17th INTERNATIONAL SCIENTIFIC CONFERENCE

# iNDiS 2026

integration
Novelty
Design
interdisciplinarity
Sustainability

## PROCEEDINGS

**November 4–6, 2026**

Hotel Fruške Terme, Vrdnik

University of Novi Sad · Faculty of Technical Sciences
Department of Civil Engineering and Geodesy

17th INTERNATIONAL SCIENTIFIC CONFERENCE

# iNDiS 2026

*Integration, Novelty, Design, Interdisciplinarity, Sustainability*

# PROCEEDINGS

Hotel Fruške Terme, Vrdnik, Serbia

4–6 November 2026

University of Novi Sad
Faculty of Technical Sciences
Department of Civil Engineering and Geodesy

| | |
|---|---|
| **Editors:** | Andrija Rašeta<br>Igor Džolev<br>Milan Jovin<br>University of Novi Sad, Faculty of Technical Sciences, Department of Civil Engineering and Geodesy, Novi Sad, Serbia |
| **Technical organization of the meeting:** | Department of Civil Engineering and Geodesy, Faculty of Technical Sciences, University of Novi Sad |
| **Technical editor of the proceedings:** | Milan Jovin |
| **Graphic design:** | Jelena Mirjanić |
| **Publisher:** | University of Novi Sad, Faculty of Technical Sciences, Department of Civil Engineering and Geodesy, Trg Dositeja Obradovića 6, Novi Sad, Serbia |
| **Edition:** | Electronic edition (PDF) |
| **Available at:** | https://indis.gradjevinans.net/conference-proceedings-2026/ |
| **ISBN:** | 978-86-6022-828-6 |

Novi Sad, 2026

**The publication was co-financed by the Ministry of Science, Technological Development and Innovation of the Republic of Serbia.**

**Publisher's note:** The publisher makes no representation, express or implied, with regard to the accuracy of the information contained in this book and cannot accept any legal responsibility or liability for any errors or omissions that had been made.

CIP - Каталогизација у публикацији
Библиотека Матице српске, Нови Сад

69.05(082)
624(082)
72:502.1(082)

**INTERNATIONAL Scientific Conference "Integration, Novelty, Design, Interdisciplinarity, Sustainability" (17 ; 2026 ; Vrdnik)**
Proceedings [Elektronski izvor] / 17th International Scientific Conference iNDiS 2026 "Integration, Novelty, Design, Interdisciplinarity, Sustainability", Vrdnik, 4-6 November 2026 ; [editors Andrija Rašeta, Igor Džolev, Milan Jovin]. - Novi Sad : Faculty of Technical Sciences, 2026

Način pristupa(URL): https://indis.gradjevinans.net/conference-proceedings-2026/. - Opis zasnovan na stanju na dan 25.11.2026. - Nasl. sa naslovnog ekrana. - Bibliografija uz svaki rad. - Rezime na srp. jeziku uz svaki rad. - Registar.

ISBN 978-86-6022-828-6

а) Индустријска градња - Зборници б) Грађевинске конструкције - Зборници в) Архитектура - Еколошка градња - Зборници

COBISS.SR-ID 206316809

## PROGRAM COMMITTEE

Andrija Rašeta, Chair
Milan Trivunić
Igor Peško
Igor Džolev
Mehmed Batilović
Vladimir Mučenski
Đorđe Jovanović
Ljubomir Budinski
Milan Marinković
Vladimir Bulatović
Vladimir Vukobratović
Mirjana Laban
Miloš Šešlija
Miro Govedarica
Dragana Konstantinović
Miljana Zeković
Milena Krklješ

## ORGANIZING COMMITTEE

Igor Džolev, Chair
Jovana Topalić, Technical Secretary
Tiana Milović
Marko Marković
Đuro Krnić
Vladimir Živaljević
Danilo Stipić
Jelena Mirjanić
Suzana Draganić
Slobodan Kolaković
Mirjana Terzić
Milan Jovin
Vladan Pantić
Panta Krstić
Olivera Bedov
Dragana Stanojević
Goran Jeftenić
Višnja Žugić
Željko Bugarinović
Ljiljana Popović
Nenad Medić
Tanja Perčić
Marina Davidović Manojlović
Nikolina Ćirić
Dragan Manojlović
Petar Lazičić
Sara Havzi
Marijana Milić
Tamara Pantić
Sara Krsmanović
Cveta Lazić
Anastasija Božić
Nikolina Gajić

*All members of the Program Committee and the Organizing Committee are affiliated with: University of Novi Sad, Faculty of Technical Sciences, Novi Sad, Serbia.*

## SCIENTIFIC COMMITTEE

| | |
|---|---|
| Aleksandar Pavić | University of Sheffield, UK |
| Ana Baričević | University of Zagreb, Croatia |
| Ana Trombeva-Gavriloska | University of Skopje, North Macedonia |
| Anka Starčev-Ćurčin | University of Novi Sad, Serbia |
| Asterios Liolios | University of Thrace, Greece |
| Baofeng Huang | Shanghai Normal University, China |
| Biljana Šćepanović | University of Podgorica, Montenegro |
| Bojana Grujić | University of Banja Luka, Bosnia and Herzegovina |
| Chiara Bedon | University of Trieste, Italy |
| Damir Markulak | University of Osijek, Croatia |
| Danijel Kukaras | University of Novi Sad, Serbia |
| Darko Nakov | University of Skopje, North Macedonia |
| Dragan Bojović | Institute for Materials Testing, Serbia |
| Dragan Milašinović | University of Novi Sad, Serbia |
| Dušan Kovačević | University of Novi Sad, Serbia |
| Duško Lučić | University of Podgorica, Montenegro |
| Goran Ćirović | University of Novi Sad, Serbia |
| Gordana Jakovljević | University of Banja Luka, Bosnia and Herzegovina |
| György Balázs | University of Budapest, Hungary |
| Igor Džolev | University of Novi Sad, Serbia |
| Judith Fauth | Technical University of Munich, Germany |
| Koce Todorov | University of Skopje, North Macedonia |
| Ksenija Janković | Institute for Materials Testing, Serbia |
| Marijana Lazarevska | University of Skopje, North Macedonia |
| Marina Carević Tomić | University of Novi Sad, Serbia |
| Marko Mihić | University of Belgrade, Serbia |
| Meri Cvetkovska | University of Skopje, North Macedonia |
| Miha Tomaževič | University of Ljubljana, Slovenia |
| Milan Trivunić | University of Novi Sad, Serbia |
| Miloš Knežević | University of Podgorica, Montenegro |
| Miloš Šešlija | University of Novi Sad, Serbia |
| Milutin Pejović | University of Belgrade, Serbia |
| Mirjana Laban | University of Novi Sad, Serbia |
| Miro Govedarica | University of Novi Sad, Serbia |
| Mitesh Surana | Indian Institute of Technology Ropar, India |
| Mladena Luković | Delft University of Technology, Netherlands |

| | |
|---|---|
| Ognjen Mijatović | University of Banja Luka, Bosnia and Herzegovina |
| Radovan Đurović | University of Podgorica, Montenegro |
| Sergio Ruggieri | Polytechnic University of Bari, Italy |
| Slaviša Trajković | University of Niš, Serbia |
| Sofija Kekez-Baran | Silesian University of Technology, Gliwice, Poland |
| Tomaž Hozjan | University of Ljubljana, Slovenia |
| Tomo Cerovšek | University of Ljubljana, Slovenia |
| Vesna Bulatović | University of Novi Sad, Serbia |
| Vladimir Mandić | University of Kragujevac, Serbia |
| Vladimir Vukobratović | University of Novi Sad, Serbia |
| Vlatko Šešov | Institute of Earthquake Engineering & Engineering Seismology, North Macedonia |
| Wang Guoxin | West Yunnan University of Applied Sciences, China |
| Zoran Sušić | University of Novi Sad, Serbia |

## REVIEWERS

All papers in these proceedings were reviewed by members of the Scientific Committee. Their institutions and countries are listed above.

# PREFACE

The 17th International Scientific Conference iNDiS was held from 4 to 6 November 2026 at Hotel Fruške Terme in Vrdnik. This year the conference marked half a century of work: the first meeting, held in 1976, was devoted to the industrialised construction of housing, and its scope has since grown to cover the whole life cycle of the built environment, from planning and design to construction, maintenance and risk management.

The papers in these proceedings show how wide that scope remains. Several contributions deal with existing structures and their second life: the assessment and repair of Hall 7 of the Novi Sad Fair after the supercell storms of July 2023, the assessment of a road bridge over the Sava River in Obrenovac and the evaluation of contemporary timber bridges. Experience from the Iriški Venac tunnel shows how large convergences in squeezing ground are controlled in practice, while the analysis of the nightclub fires in Kočani and Crans-Montana is a reminder that the safety of public buildings depends on materials, design and management working together.

The digital transformation of the profession is strongly represented: artificial intelligence in construction cost estimation and in satellite radar interferometry, BIM in crane inspection and in the documentation of cultural heritage, laser scanning and unmanned aerial vehicles in geodesy. The circular economy runs through papers on the use of dredged river sediment in road construction, recycled concrete aggregates and low-clinker cement. Contributions in architecture and urban planning address industrial heritage, public space and the transformation of cities, while papers on disaster risk management cover evacuation, education and the role of volunteers.

The iNDiS 2026 proceedings are published in two books. This book, in English, contains 81 papers, including four plenary lectures, and the companion book in Serbian (Zbornik radova) contains 10 papers, which makes 91 papers in total. The papers were written by authors from more than ten countries.

The editors thank the authors, the reviewers, the members of the committees and everyone who supported the conference.

*Editors of the Proceedings*

## SUPPORT AND SPONSORS

**The publication was co-financed by the Ministry of Science, Technological Development and Innovation of the Republic of Serbia.**

The organization of the 17th International Scientific Conference iNDiS was supported by:

**Ministry of Science, Technological Development and Innovation of the Republic of Serbia**

**Engineering Chamber of Serbia**

**Society for Structural Integrity and Life (DIVK)**

### Gold sponsors

Integrated Project Consulting

TeamCAD

### Silver sponsors

IMS Institute

PRO-ING

Sika Serbia

### Bronze sponsors

Baldinistudio International

Hidrozavod DTD

Piramida

Република Србија
МИНИСТАРСТВО НАУКЕ,
ТЕХНОЛОШКОГ РАЗВОЈА И ИНОВАЦИЈА

## Ministry of Science, Technological Development and Innovation

Shaping and implementing policy in science, research, technology and innovation towards a knowledge-based society.

**www.nitra.gov.rs**

ИНЖЕЊЕРСКА
КОМОРА
СРБИЈЕ

## Engineering Chamber of Serbia

Bringing engineers together to advance engineering standards, professional practice and continuing professional development.

**www.ingkomora.org.rs**

DIVK

## Society for Structural Integrity and Life (DIVK)

Integrity, reliability and remaining life of structures and materials – connecting science with practice. Publisher of the journal Structural Integrity and Life.

**divk.inovacionicentar.rs**

# TeamCAD
## Vaš pouzdani partner za digitalnu transformaciju

Tražite pouzdanog partnera koji razume vašu industriju, poznaje put ka digitalnoj transformaciji i govori jezik vaših inženjera?

Mi smo **Autodesk Gold Solution Provider**, **Autodesk Platform Services Certified Partner** i vodeći **Autodesk partner na Zapadnom Balkanu**.

Naša ekspertiza obuhvata prodaju softvera, razvoj softvera, BIM i Vault implementaciju, prilagođavanje i obuku - sve pod jednim krovom.

TeamCAD je tu da vam pomogne.

Naši klijenti nas biraju zbog naše stručnosti i ostaju sa nama zbog naše osnovne i strukovne tehničke podrške.

Budućnost je digitalna, hajde da je izgradimo zajedno.

**Započnite svoju transformaciju sa nama!**

**www.TeamCAD.rs**

TeamCAD

AUTODESK
Gold Partner
Authorized Training Center
Autodesk Platform Services
(APS) Certified Partner

## Consulting & engineering for every phase of your investment project

From design to construction supervision – reliable consulting and engineering services for public and private investors.

Integrated Project Consulting

PRO ING

# Design, Consulting, & Construction



office@pro-ing.rs
+381 (21) 489 4200
www.pro-ing.site
Bulevar Mihajla Pupina 3/II, 21000 Novi Sad, Serbia

IMC IMS

# SIGURNI U GRADNJI

## SA INSTITUTOM ZA ISPITIVANJE MATERIJALA

institutims.rs

+381 (0)11 26 50 322
office@institutims.rs
Bulevar vojvode Mišića 43
11040 Beograd, Srbija

SKENIRAJ

Vaš BIM partner u digitalizaciji

www.baldinistudio.rs

Baldinistudio International

Sika®

BUILDING TRUST

PIRAMIDA

Building construction since 1996

Sremska Mitrovica, Serbia

piramidasm.rs

HIDROZAVOD DTD

AD za studije, istraživanja,
projektovanje, i inženjering

+381 21 300 1 300
Petra Drapšina 56
Novi Sad, Srbija
**hidrozavoddtd.rs**

# CONTENTS

## PLENARY LECTURES

*Meri Cvetkovska*
**FIRE SAFETY AND USE OF COMBUSTIBLE MATERIALS IN PUBLIC BUILDINGS: LESSONS FROM KOČANI AND CRANS-MONTANA NIGHTCLUB FIRES** 21

*Tomo Cerovšek*
**THE TWIN TRANSITION: DIGITALISATION AND AI FOR REAL-TIME ENVIRONMENTAL DECISION INTELLIGENCE IN CIRCULAR CONSTRUCTION** 36

*Teo Beker*
**FROM DETECTION ACCURACY TO USEFUL SCREENING: LESSONS FROM INSAR VOLCANIC DEFORMATION CLASSIFICATION** 49

*Milan Uljarević, Andrija Rašeta and Dragan Bojović*
**CONTROLLING LARGE CONVERGENCES IN SQUEEZING GROUND – A CASE STUDY OF THE IRIŠKI VENAC TUNNEL** 59

## CIVIL ENGINEERING

*Aleksandar Sedmak, Simon Sedmak, Dorin Radu, Dragan Bojović and Boris Folic*
**STRUCTURAL INTEGRITY ASSESSMENT OF CIVIL ENGINEERING CONSTRUCTIONS – TWO CASE STUDIES** 70

*Tanja Perčić, Đorđe Jovanović, Drago Žarković and Dragan Manojlović*
**IMPLEMENTATION OF THE NONLINEAR ANALYSIS WITH THE SEVENTH DEGREE OF FREEDOM IN THE ACADEMIC SOFTWARE MATRIX 3D** 78

*Gojko Drljača and Milivoje Rogač*
**END PATCH LOADING – INFLUENCE OF GIRDER GEOMETRY ON BUCKLING COEFFICIENT** 91

*Nikola Postolov, Koce Todorov and Ljupcho Lazarov*
**DISCRETIZATION-INDEPENDENT STRAIN-BASED LIMIT STATE CRITERIA FOR MVLEM MODELS OF RC WALLS** 102

*Dragan Manojlović, Tanja Perčić, Miloš Milić and Radovan Perić*
**PREDICTION OF THE LOAD-SLIP RELATIONSHIP FOR TIMBER-STEEL CONNECTIONS WITH OUTER STEEL PLATES** 114

*Riste Volchev, Koce Todorov and Ljupcho Lazarov*
**COMPARISON OF PROCEDURES FOR DETERMINING PLAN REGULARITY PARAMETERS ACCORDING TO EUROCODE 8** 128

*Željana Kužet, Vladimir Mučenski, Jovana Topalić, Goran Bošković and Dragan Živanić*
**SMART CRANE INSPECTION: THE POTENTIAL OF BIM-BASED FRAMEWORK FOR CRANE INSPECTION IN CONSTRUCTION** 141

*Jovana Topalić, Danijela Gračanin, Danijela Ćirić Lalić, Luka Vidaković, Marijana Dukić Mijatović and Andrea Ivanišević*
**VALIDATION OF A PRELIMINARY RISK ASSESSMENT MODEL FOR WWTP CONSTRUCTION AND PROSPECTS FOR DIGITAL OPERATIONALIZATION** **151**

*Milan Jovin, Tatjana Grbić, Igor Peško and Andrija Rašeta*
**POSSIBILISTIC LINEAR REGRESSION FOR INTERVAL-BASED PRELIMINARY ESTIMATION OF URBAN ROAD COST AND DURATION** **161**

*Dragana Tomašević Pilipović, Miloš Šešlija, Panta Krstić, Nataša Slijepčević and Dunja Rađenović Veselić*
**TECHNO-ECONOMIC ASSESSMENT OF DREDGED SEDIMENT IN ROAD INFRASTRUCTURE** **183**

*Nermin Palić, Meri Cvetkovska, Milica Jovanoska-Mitrevska and Mirzo Selimić*
**CIRCULAR ECONOMY ASSESSMENT OF TRAFFIC NOISE BARRIERS IN ROAD INFRASTRUCTURE** **190**

*Nataša Kopitović Vuković, Strahinja Ilić, Radomir Zejak and Goran Gorašević*
**INFLUENCE OF OPTICAL GLASS FIBERS ON THE POST-FIRE BEHAVIOUR OF CONCRETE PRODUCED WITH LOCAL SILICEOUS AGGREGATE** **198**

*Anja Terzić, Ksenija Janković and Aleksandar Savić*
**CONCRETE FOR COOLER CITIES: NEW INSIGHTS** **207**

*Ivana Šalić, Šime Serdarević, Nina Šantek and Dalibor Gelo*
**STATIC AND DYNAMIC CALCULATION OF THE LOAD-BEARING STRUCTURE OF A RESIDENTIAL BUILDING** **217**

*Vladimir Živaljević, Andrija Rašeta and Igor Džolev*
**HALL 7 OF THE NOVI SAD FAIR – PART I: THE ASSESSMENT OF THE LOAD-BEARING STRUCTURE** **229**

*Vladimir Živaljević, Andrija Rašeta and Igor Džolev*
**HALL 7 OF THE NOVI SAD FAIR – PART II: STRENGTHENING AND REPAIR OF THE LOAD-BEARING STRUCTURE** **238**

*Slobodan Šupić, Vladan Pantić, Danijel Kukaras and Dragana Stanojević*
**THE ASSESSMENT OF A ROAD BRIDGE STRUCTURE OVER THE SAVA RIVER IN OBRENOVAC** **246**

*Milan Marinković and Marija Milanović*
**ASSESSMENT OF THE CONDITION OF THE PAVEMENT IN MIŠE DIMITRIJEVIĆA STREET ACCRODING TO THE PCI METHODOLOGY** **257**

*Tomaž Pazlar, Martin Capuder, Jaka Gašper Pečnik and Boris Azinović*
**ASSESSMENT OF CONTEMPORARY TIMBER BRIDGES** **264**

*Snežana Ilić, Igor Džolev, Biljana Ilić, Mirjana Laban and Milica Mirković Marjanović*
**THERMAL AND ENERGY PERFORMANCE OF AN EXTENSIVE GREEN ROOF IN NOVEMBER 2025** **276**

*Slobodan Kolaković, Marijana Milić, Ljubomir Budinski, Goran Jeftenić, Danilo Stipić and Tamara Pantić*
**SEEPAGE STABILITY ASSESSMENT OF A FLOOD PROTECTION EMBANKMENT IN THE BRIDGE PIER INFLUENCE ZONE: A CASE STUDY OF THE TISZA RIVER** **291**

*Sofija Kekez-Baran*
**CERTIFICATION OF RECYCLED CONCRETE AGGREGATES FOR APPLICATION IN STRUCTURAL CONCRETE** **310**

*Tiana Milović*
**INDIVIDUAL AND COMBINED EFFECTS OF ZEOLITIC TUFF, FLY ASH AND LIMESTONE ON COMPRESSIVE STRENGTH OF REPAIR CEMENT-BASED MORTARS** **317**

*Tiana Milović, Olja Šovljanski, Miroslav Dramićanin, Marko Radenković and Ana Tomić*
**AUTOGENOUS HEALING PROPERTY OF LOW-CLINKER CEMENT: THE MICROCRACKS REPAIR EFFICIENCY** **324**

*Olivera Bedov, Suzana Draganić and Marijana Serdar*
**MIX DESIGN OF SLAG MORTARS ACTIVATED BY SUNFLOWER HUSK ASH AND SODIUM SILICATE FOR TARGET COMPRESSIVE STRENGTH** **332**

*Aleksandar Pujović, Tiana Milović and Anka Starčev-Ćurčin*
**CONTEMPORARY REPAIR MORTARS: A REVIEW OF REQUIREMENTS, PROPERTIES AND DEVELOPMENT TRENDS** **343**

*Tamara Pantić, Marijana Milić, Ljubomir Budinski, Goran Jeftenić and Danilo Stipić*
**EPA SWMM-BASED MODELING OF FLOODING PROCESSES IN RECLAIMED DRAINAGE AREAS: A CASE STUDY OF THE KNIĆANIN-ČENTA BASIN** **356**

*Ivan Mesarović, Goran Jeftenić, Vladimir Mandić and Slobodan Kolaković*
**APPLICATION OF SPATIAL INTERPOLATION METHODS IN THE GREAT MORAVA RIVER BASIN** **372**

*Slobodan Kolaković, Vladimir Mandić, Marijana Milić, Ljubomir Budinski, Goran Jeftenić, Danilo Stipić and Tamara Pantić*
**ASSESSMENT OF CLIMATE CHANGE IMPACTS ON HYDROLOGICAL AND CLIMATOLOGICAL VARIABLES: A CASE STUDY FROM THE SJENICA REGION, SERBIA** **383**

*Anica Milanović and Petar Praštalo*
**FLOW ANALYSIS IN A LABORATORY CHANNEL USING VIDEO PROCESSING AND HEC-RAS MODELLING** **401**

*Ivan Dolibašić, Željko Lebo, Jure Galić and Ivan Volarić*
**STRUCTURAL FAILURE OF A REINFORCED CONCRETE RETAINING WALL** **415**

*Igor Džolev, Vladimir Živaljević, Jelena Mirjanić, Petar Lazičić and Andrija Rašeta*
**NUMERICAL ANALYSIS OF FIRE-INDUCED BUCKLING OF A COLD-FORMED STEEL COLUMN** **428**

*Sara Krsmanović, Miloš Šešlija and Panta Krstić*
**ANALYSIS OF THE INFLUENCE OF PAVEMENT SURFACE MACROTEXTURE ON FRICTION USING THE MPD INDICATOR** **441**

*Nikola Marjanović, Jelena Mirjanić and Aleksandra Radujković*
**COMPARATIVE ANALYSIS OF MAIN TRUSS GIRDER CONFIGURATIONS FOR THE ROOF OF A LONG-SPAN SPORTS HALL** **453**

*Dragana Stanojević, Vladimir Mučenski, Mirjana Terzić, Milena Senjak Pejić and Jovana Topalić*
**RESEARCH TRENDS IN THE APPLICATION OF ARTIFICIAL INTELLIGENCE FOR CONSTRUCTION COST ESTIMATION** **462**

*Jelena M. Andrić*
**BLOCKCHAIN - BASED FRAMEWORK FOR DAILY PROJECT INFORMATION SYNCHRONIZATION IN AEC PROJECTS** **471**

*Jelena M. Andrić and Hejing Feng*
**FROM GREEN TO SUSTAINABILITY: AN INTEGRATED AHP AND AI FRAMEWORK FOR PRIORITISING SUSTAINABILITY INDICATORS** **482**

*Panta Krstić, Miloš Šešlija, Dragana Tomašević Pilipović, Nikolina Ćirić and Sara Krsmanović*
**INFLUENCE OF LIME BINDER PROPORTION ON STRENGTH DEVELOPMENT OF STABILIZED RIVER SEDIMENT** **495**

*Aleksandar Andonov Sarev, Jovan Br. Papić, Kemal Edip, Viktorija Velinska, Miloš Šešlija and Marjan Matić*
**WELCOMING THE SECOND GENERATION OF EUROCODE 7 – RETAINING WALLS' ADDRESSING** **504**

*Branko Ranković, Miloš Šešlija, Milan Draganović and Nikola Grubić*
**THE INFLUENCE OF SEDIMENT-DERIVED MINERAL ADMIXTURES ON BITUMEN-FILLER INTERACTION AND THE PERFORMANCE OF ASPHALT MIXTURES: A SYSTEMATIC REVIEW OF THE LITERATURE** **512**

*Nikolina Ćirić Avramović, Panta Krstić and Sara Krsmanović*
**INTEGRATION OF TECTONIC AND SEISMOLOGICAL DATA OF THE WIDER KOSMAJ MOUNTAIN AREA: A REGIONAL APPROACH TO GEOHAZARD ASSESSMENT** **519**

## ARCHITECTURE AND URBAN PLANNING

*Željko Jakšić, Milan Trivunić and Dušanka Plazina-Pevač*
**TENDENCIES AND URBAN DEVELOPMENT UNDER MODERN TRAFFIC CONDITIONS: THE CASE OF NOVI SAD** **527**

*Marijana Divljak, Milena Krklješ and Dejana Nedučin*
**EDUCATIONAL MODELS AND THE TRANSFORMATION OF PRIMARY SCHOOL ARCHITECTURAL PROGRAMS: THE INFLUENCE OF THE MONTESSORI METHOD** **538**

*Dragana Konstantinović, Slobodan Jović and Boško Ristić*
**FROM REGIONAL RESOURCE TO SPATIAL STRATEGY: A NEW CONTEXTUAL READING OF DTD CANAL** **548**

*Petar Mitrović and Višnja Žugić*
**HOW DOES ARCHITECTURE REMEMBER? NARRATIVE ARTICULATION IN MEMORIAL SITES WITHIN TRANSFORMING URBAN LANDSCAPES** **557**

*Mia Stantić*
**BETWEEN BUILDING DENSITY AND HOUSING QUALITY: A COMPARATIVE ANALYSIS OF RESIDENTIAL BLOCKS OF BISTRICA AND PODBARA** **567**

*Jovana Đurovski and Miljana Zeković*
**BUILT STRUCTURE AND FUNCTIONAL TRANSFORMATION IN THE ADAPTIVE REUSE OF THERMAL POWER STATION "SNAGA I SVETLOST" IN BELGRADE** **576**

*Una Radivojević and Mirjana Sladić Todorov*
**TYPOLOGY OF DAMAGE TO ORTHODOX SACRED BUILDINGS DURING THE SECOND WORLD WAR: A CASE STUDY OF THE MUNICIPALITY OF PEĆINCI** **587**

*Miralem Bećić*
**THE ROOF AS ACTIVE URBAN INFRASTRUCTURE: TOWARDS THE REINTEGRATION OF TECTONICS, PROGRAM, AND SUSTAINABILITY** **603**

*Vladimir Savić*
**REINTERPRETING MARGINAL URBAN SPACES: FROM THE HISTORICAL TO THE SUBCULTURAL GHETTO** **614**

*Darko Sekulić*
**TENNIS COURT AS A TYPOLOGY IN SCENE ARCHITECTURE – SPATIAL TRANSFORMATIONS IN THE CULTURAL AND SOCIAL CONTEXT OF THE 18TH CENTURY** **627**

*Ranka Medenica Todorović, Milica Vračarić and Marina Carević Tomić*
**CENTRALITY OF SUBURBAN SETTLEMENTS UNDER URBAN EXPANSION: THE CASE STUDY OF VETERNIK** **640**

*Ilija Lalošević*
**SUSTAINABILITY OF CULTURAL HERITAGE OF KOTOR REGION ON THE WORLD HERITAGE LIST** **649**

*Sandra Šlegl and Đuro Krnić*
**VERTICAL ARCHITECTURE AS AN EXPRESSION OF INVESTMENT SYSTEMS: THE TRANSFORMATION OF BELGRADE SKYLINE** **659**

## GEODESY AND GEOINFORMATICS

*Vesko Đorđević, Vladan Komatović and Dejan Pavlović*
**SCAN-TO-BIM FOR CULTURAL HERITAGE PRESERVATION: DIGITAL RECONSTRUCTION AND BIM MODELING OF A HISTORICAL CHURCH IN RAMSEL, BELGIUM** **674**

*Gordana Nataroš, Mirjana Bajić and Marina Davidović Manojlović*
**EXPROPRIATION FOR THE PURPOSE OF INFRASTRUCTURE DEVELOPMENT** **684**

*Jelena Tatalović, Bogdan Bojović and Milica Malešić Petković*
**"SMART PARCEL" SYSTEM – A FOUNDATION FOR DIGITAL LAND MANAGEMENT IN SERBIA** **695**

*Radovan Đurović, Marija Delić, Gojko Nikolić, Andrea Buntić and Zoran Sušić*
**INTEGRATION OF BIM AND GIS IN GEODESY: TECHNOLOGICAL PERSPECTIVES AND THE NEED FOR EDUCATIONAL CURRICULUM REFORM** **708**

*Erta Kushta, Arli Llabani, Marin Allaraj and Fation Kurti*
**DIGITAL DOCUMENTATION AND CRACK MAPPING OF A HISTORIC FORTIFICATION USING PHOTOGRAMMETRY: A CASE STUDY OF THE KRONACH WALL** **725**

*Nikola Santrač, Mehmed Batilović, Pavel Benka, Marko Marković and Željko Bugarinović*
**BUILDINGS FOOTPRINT EXTRACTIONS USING SEGMENT ANYTHING MODEL** **737**

*Arli Llabani, Bledar Sina, Eduart Blloshmi, Radovan Đurović and Marko Z. Marković*
**UAV-BASED DOCUMENTATION OF CULTURAL HERITAGE SITES: A CASE STUDY OF KRUJA CASTLE** **753**

*Mladen Amović, Gordana Jakovljević, Miro Govedarica and Miloš Tutnjević*
**EVOLUTION OF THE UTILITY CADASTRE IN THE REPUBLIC OF SRPSKA: FROM LEGISLATION TO INTEROPERABILITY** **772**

*Vasilije Ilić and Milutin Pejović*
**SPATIALLY-ENRICHED HOUSING PRICE MODELING: ASSESSING THE ROLE OF LANDSCAPE METRICS AND LAND COVER ATTRIBUTES** **783**

*Oleg Odalović, Dejan Vasić, Dušan Petković, Slavko Vasiljević and Miljana Todorović-Drakul*
**THE ACCURACY FLOOR IN LEGACY-TO-ETRS89 DATUM TRANSFORMATION: RESIDUAL DISTORTION MODELLING FOR THE REPUBLIC OF SRPSKA** **800**

*Oleg Odalović, Marko Stanković, Dejan Vasić, Sanja Grekulović and Stefan Krstić*
**A PRELIMINARY COMPLETE BOUGUER ANOMALY MAP OF THE REPUBLIC OF SRPSKA** **819**

*Eduart Blloshmi, Bledar Sina and Arli Llabani*
**MULTI-SOURCE ASSESSMENT OF CADASTRAL PARCEL POSITIONAL ACCURACY USING GNSS SURVEYS AND ORTHOPHOTO DATA: A CASE STUDY FROM HIMARA, ALBANIA** **830**

*Bledar Sina, Eduart Blloshmi and Arli Llabani*
**DEVELOPMENT OF THE LOCAL GEODETIC REFERENCE NETWORK FOR THE CITY OF GRAMSH BASED ON GNSS MEASUREMENTS** **842**

*Željko Bugarinović, Aleksandar Ristić, Milan Vrtunski, Milan Gavrilović and Miro Govedarica*
**GENERATION OF SYNTHETIC B-SCANS USING GPRMAX AND THEIR APPLICATION IN DIFFERENT SCENARIOS** **859**

*Milan Gavrilović, Igor Ruskovski, Milka Šarkanović Bugarinović, Dušan Jovanović and Miro Govedarica*
**MONITORING THE SPATIO-TEMPORAL DYNAMICS OF FOREST AREAS USING LANDTRENDR SEGMENTATION OF SATELLITE IMAGE TIME SERIES** **867**

*Vesko Đorđević and Dejan Pavlović*
**INVESTIGATION OF TRANSMISSION LINE POLE VERTICALITY USING UAV LIDAR POINT CLOUDS** **882**

*Anastasija Božić, Mehmed Batilović, Marko Marković, Zoran Sušić and Vladimir Bulatović*
**DEFORMATION ANALYSIS OF THE ŠELEVRENAC DAM USING THE IWST METHOD** **895**

*Nikolina Gajić, Đuro Krnić, Marina Davidović Manojlović, Vladimir Bulatović and Zoran Sušić*
**INFLUENCE OF TEMPERATURE AND LEVELLING STAFF MATERIAL ON THE COLLIMATION ERROR OF THE LEICA DNA03 DIGITAL LEVEL** **910**

*Đuro Krnić, Miro Govedarica, Mehmed Batilović, Andrija Kljajić and Marko Marković*
**COMPARATIVE ACCURACY ANALYSIS OF A MOBILE SLAM SYSTEM AND TERRESTRIAL LASER SCANNING TECHNOLOGY: A MUSEUM CASE STUDY** **923**

**DISASTER RISK MANAGEMENT AND FIRE SAFETY**

*Cveta Lazić and Tanja Vranić*
**PYTHON-BASED AGENT MODELLING IN DISASTER RISK MANAGEMENT EDUCATION: A COURSE-BASED CASE STUDY** **939**

*Teodora Vojnović, Mirjana Laban, Suzana Draganić and Olivera Bedov*
**EVACUATION AS A SYSTEM OF MOVEMENT AND BEHAVIOUR: A CASE STUDY OF THE SERBIAN NATIONAL THEATRE IN NOVI SAD** **946**

*Jelena Mirjanić, Igor Džolev, Jovana Topalić, Tiana Milović and Mirjana Laban*
**VOLUNTEERS IN DISASTER RISK MANAGEMENT IN SERBIA: COOPERATION, PUBLIC PERCEPTION AND YOUTH ENGAGEMENT** **956**

*Dragan Hristovski and Vesna Nikolić*
**INTEGRATION OF KNOWLEDGE MANAGEMENT AND LEAN SIX SIGMA METHODOLOGY IN THE FUNCTION OF CONTINUOUS IMPROVEMENT OF FIRE SAFETY** **964**

**REGISTER OF AUTHORS** **975**

# PLENARY LECTURES

iNDiS 2026

https://doi.org/10.24867/INDIS-2026-EN-019



# FIRE SAFETY AND USE OF COMBUSTIBLE MATERIALS IN PUBLIC BUILDINGS: LESSONS FROM KOČANI AND CRANS-MONTANA NIGHTCLUB FIRES

*Meri Cvetkovska*[1]

***Summary:***

Fire safety in public assembly and entertainment buildings depends not on a single protective measure, but on the interaction of construction materials, interior finishes, fire detection, smoke control, fire suppression, emergency lighting and evacuation provisions. When several of these layers are simultaneously deficient, a relatively localized ignition can develop into a mass-casualty event.

This paper examines two recent nightclub fires: the fire at the Pulse nightclub in Kočani, North Macedonia, on 16 March 2025, and the fire at the Le Constellation bar in Crans-Montana, Switzerland, on 1 January 2026. The analysis focuses particularly on the role of combustible interior materials, acoustic finishes, smoke development, fire-protection systems and evacuation conditions. The paper concludes that effective fire safety requires demonstrable compliance throughout the entire chain: material selection, design, installation, inspection, maintenance, detection, suppression and evacuation.

*Keywords: fire safety, combustible materials, reaction to fire, public buildings*

# ZAŠTITA OD POŽARA I UPOTREBA ZAPALJIVIH MATERIJALA U JAVNIM OBJEKTIMA: POUKE IZ POŽARA U NOĆNIM KLUBOVIMA U KOČANIMA I KRANS-MONTANI

***Rezime:***

Zaštita od požara u javnim objektima namenjenim okupljanju i zabavi ne zavisi od jedne zaštitne mere, već od međusobnog delovanja građevinskih materijala, unutrašnjih obloga, sistema za dojavu požara, odvođenja dima, sistema za gašenje požara, nužne rasvete i uslova za evakuaciju. Kada je više ovih zaštitnih slojeva istovremeno neadekvatno ili nedovoljno primenjeno, relativno ograničen izvor paljenja može prerasti u događaj sa velikim brojem ljudskih žrtava.

Ovaj rad analizira dva nedavna požara u noćnim klubovima: požar u noćnom klubu Pulse u Kočanima, u Severnoj Makedoniji, 16. marta 2025. godine, i požar u baru Le Constellation u Krans-Montani, u Švajcarskoj, 1. januara 2026. godine. Posebna pažnja posvećena je ulozi zapaljivih materijala u enterijeru, akustičnih obloga, razvoju dima, sistema zaštite od požara i uslovima za evakuaciju. Rad zaključuje da efikasna zaštita od požara zahteva dokazivu usklađenost svih elemenata sistema – od izbora materijala, projektovanja i ugradnje, do inspekcijskog nadzora, održavanja, ranog otkrivanja požara, gašenja i bezbedne evakuacije.

*Ključne reči: zaštita od požara, zapaljivi materijali, reakcija na požar, javni objekti*

[1] Prof., Ss. Cyril and Methodius University in Skopje, Faculty of Civil Engineering, Skopje, North Macedonia, e-mail: cvetkovska@gf.ukim.edu.mk, ORCID number: 0000-0002-9155-6420

## 1. INTRODUCTION

Public entertainment buildings present a particularly demanding fire-safety environment. They may accommodate large numbers of people within relatively limited areas, often under conditions of reduced visibility, loud music, artificial lighting, temporary installations, and extensive decorative treatment. The consequences of fire in such buildings are therefore strongly influenced not only by the ignition source, but also by the materials present, the geometry of the space, the development of smoke and heat, the effectiveness of fire detection and suppression systems, and the ability of occupants to evacuate rapidly.

The fire at the Puls nightclub in Kočani, North Macedonia, on 16 March 2025, demonstrated the consequences of multiple simultaneous deficiencies in a public entertainment facility. The available expert documentation identifies combustible synthetic materials, acoustic sponge, blocked windows, inadequate smoke-control measures, absence of automatic fire detection and alarm systems, deficiencies in hydrant protection, insufficient portable extinguishers, and inadequate evacuation arrangements. The report concludes that the establishment did not meet prescribed fire-protection requirements and that the presence of combustible materials increased the fire load and contributed to more rapid fire development.

The scale of the tragedy makes the case particularly relevant for fire-safety engineering. The final number of fatalities was 63, while the World Health Organization subsequently reported 193 injuries in relation to the disaster.

Less than one year later, on 1 January 2026, a major fire occurred at the Le Constellation bar in Crans-Montana, Switzerland. Swiss federal authorities reported 41 fatalities and 115 injured persons. The investigation has focused on the ignition of combustible acoustic material by pyrotechnic devices. At the same time, authorities acknowledged that periodic safety inspections had not been conducted at the venue between 2020 and 2025, despite the existence of inspection requirements.

These two cases therefore provide an opportunity to examine a fundamental fire-safety question: **To what extent can the consequences of a fire in a public building be determined not by the initial ignition itself, but by the materials, building conditions, evacuation arrangements and regulatory failures that allow the fire to develop into a disaster?**

Although the two incidents occurred in different countries and under different regulatory systems, both demonstrate the fundamental principle that **fire safety is a system, not a single technical measure**. From this perspective, a particular methodological distinction must be made between the presence of a combustible material and proof of regulatory non-compliance. Therefore, the purpose of this paper is not simply to identify “flammable materials” as the cause of a fire. Instead, it examines how material selection interacts with the other layers of fire protection and how failures in several layers can transform an initial ignition into a mass-casualty event.

## 2. FIRE SAFETY AS A SYSTEM

Fire safety should not be regarded as a single technical measure. It is a system consisting of several mutually dependent layers. These layers include:

- prevention of ignition,
- limitation of combustible materials and fire load,
- limitation of fire development and spread,
- early fire detection,

- warning of occupants,
- smoke and heat control,
- active fire suppression,
- safe and sufficiently wide evacuation routes,
- emergency lighting and signage,
- organisational preparedness and maintenance.

The failure of one layer does not necessarily produce a disaster. However, simultaneous failure of several layers substantially increases the probability of catastrophic consequences. This can be represented by the following chain (Figure 1):

**Ignition → combustible material → rapid fire development → smoke and heat → delayed detection/inadequate warning → inadequate suppression → impaired evacuation → mass casualties**

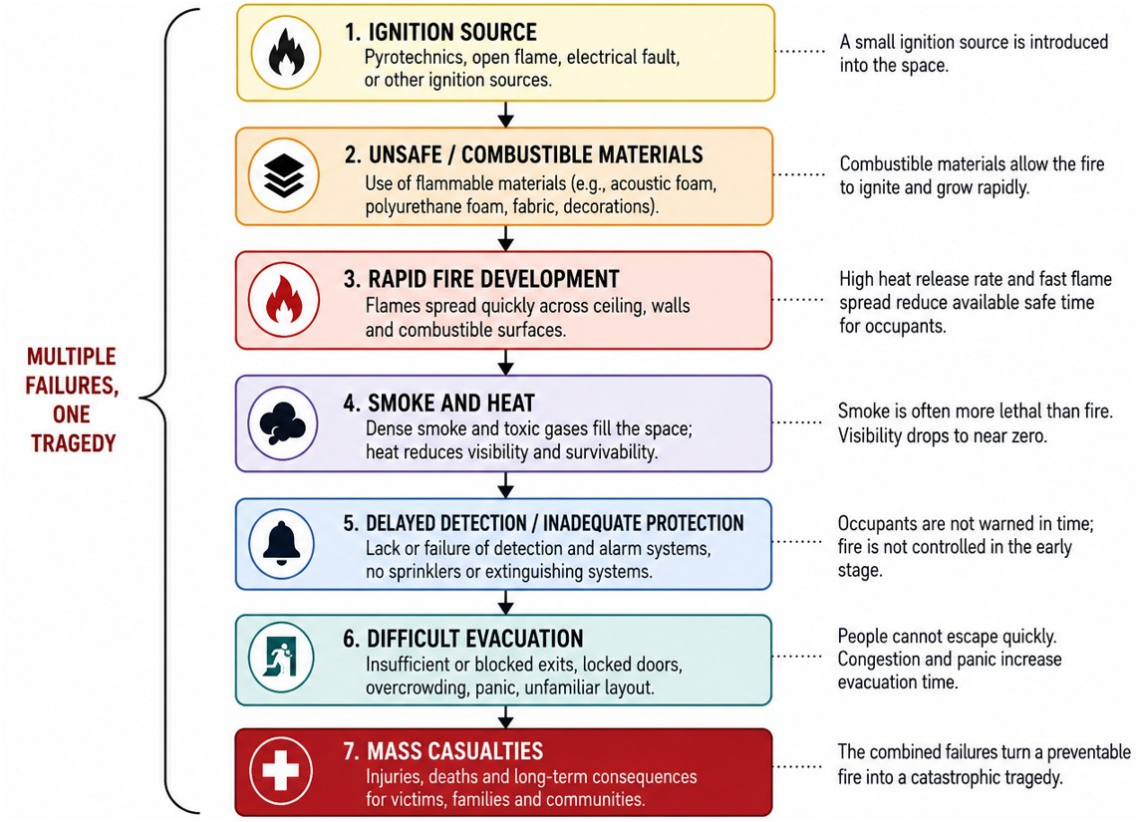


*Fig. 1 Chain of failures leading to mass casualties in nightclub fires*

The importance of this approach is that it separates the cause of ignition from the causes of catastrophic consequences. For example, pyrotechnics may initiate a fire, but pyrotechnics alone do not explain why hundreds of people may become trapped or why a fire may spread throughout an entire venue within a very short period.

The Kočani case is particularly important because the expert report does not identify a single isolated deficiency. Instead, it documents a combination of material, technical and evacuation-related deficiencies. The report specifically states that the building lacked smoke and heat extraction while containing a high presence of combustible synthetic materials, which increased the fire load and contributed to more rapid temperature rise and fire development.

The Crans-Montana case is similarly important because the tragedy cannot be understood solely in terms of the initial ignition source. Instead, it highlights the interaction between combustible interior materials, fire development, the conditions within a crowded entertainment venue, and the effectiveness of preventive and

protective measures. The rapid development of the fire significantly reduced the available time for occupants to recognize the danger and evacuate, demonstrating how failures or limitations at several levels of the fire-safety chain can transform a localized ignition into a mass-casualty event.

## 3. THE ROLE OF MATERIALS IN FIRE DEVELOPMENT

The selection of construction and interior materials is one of the fundamental elements of fire safety in buildings. The behaviour of a material when exposed to fire directly influences the rate of fire development, heat release, smoke production and the time available for occupants to evacuate.

The distinction between ignition and fire development is particularly important. The fact that a combustible material can ignite does not necessarily mean that it will produce a catastrophic fire. However, when combustible materials are used extensively on ceilings, walls or other large surfaces, they can contribute to rapid flame spread, increased heat release and the production of smoke and toxic combustion products.

This is especially important in public buildings. Interior finishes and acoustic treatments may be selected primarily for aesthetic, acoustic or economic reasons, while their reaction-to-fire characteristics may receive insufficient attention. Materials that are acceptable in one application may present an unacceptable risk when installed in large quantities, exposed to ignition sources or used without appropriate protective layers.

### 3.1. REACTION TO FIRE OF CONSTRUCTION AND INTERIOR MATERIALS

Two concepts must be distinguished in fire engineering: **reaction to fire** and **fire resistance.**

*Reaction to fire* describes how a material or product contributes to the development of a fire. Relevant characteristics include ignition, flame spread, heat release, smoke production and flaming droplets.

*Fire resistance*, in contrast, describes the ability of a building element or construction assembly to maintain specified functions for a defined period when exposed to fire, such as load-bearing capacity, integrity and insulation.

These concepts should not be confused. A material may have a particular reaction-to-fire classification while a complete building element has a separate fire-resistance classification. A concrete structural element may have excellent fire resistance, while an interior finish installed beneath it may still contribute significantly to fire development.

The fire classification of a construction product cannot be established solely from a generic material description such as “sponge”, it must be determined from the product’s certified performance and its specific end-use application.

This approach is consistent with MKC EN 13501-1:2019 [1], which classifies construction products according to reaction-to-fire test data and considers their intended end-use application. The principal Euroclasses are given in Figure 2.

The classification may be supplemented by two additional parameters:

- s1–s3 — smoke production,
- d0–d2 — flaming droplets/particles.

The **s-class** describes smoke production, where s1 represents the lowest level of smoke production and s3 the highest. The **d-class** describes flaming droplets or particles, where d0 represents no flaming droplets or particles, while d1 and d2 indicate progressively less favourable behaviour.

Consequently, a classification such as **A2-s1,d0** represents a product with very limited contribution to fire, low smoke production and no flaming droplets or particles.

| Class | Fire behaviour (reaction to fire) | Smoke production | Flaming droplets | Typical materials / examples |
|---|---|---|---|---|
| A1 | Non-combustible (no contribution to fire) | – | – | Concrete, natural stone, ceramics, glass, steel |
| A2 | Very limited contribution to fire | s1–s2 | d0–d1 | Gypsum board, cement boards, some mineral wool products |
| B | Very limited contribution to fire | s1–s2 | d0–d1 | Fire-retardant treated timber, some high-performance panels |
| C | Limited contribution to fire | s1–s3 | d0–d2 | Treated wood, certain plastics, laminates (with fire retardants) |
| D | Significant contribution to fire | s2–s3 | d0–d2 | Wood, many plastic products, insulation materials |
| E | High contribution to fire (easily ignitable) | s2–s3 | d2 | Foams, many synthetic materials, textiles, decorative elements |
| F | No determined performance or fails test | – | – | Materials without tested classification or of unknown performance |

**Additional classification parameters**

**Smoke production (s)**
**s1** – low smoke production
**s2** – medium smoke production
**s3** – high smoke production

**Flaming droplets/particles (d)**
**d0** – no flaming droplets
**d1** – limited flaming droplets
**d2** – high amount of flaming droplets

*Fig. 2 EUROCLASS System (EN 13501-1)-Reaction to fire classification of construction products*

The statement that a particular material is “fire resistant” or “flammable” is insufficient. It is important to emphasise that the Euroclass of a product cannot be determined solely from its generic material name. The classification belongs to a specific tested product or product system and depends on its composition, thickness, mounting conditions and intended end use. Therefore, statements such as "polyurethane foam is always class E" or "gypsum board is always class A2" are technically insufficient without reference to the specific certified product. For example, the term “acoustic sponge” may refer to products with different compositions, densities, thicknesses, surface treatments and mounting configurations. Its reaction-to-fire classification must therefore be established from the relevant product documentation, test report or certification.

## 4. CASE STUDY- FIRE AT THE PULS NIGHTCLUB IN KOČANI

### 4.1. REGULATORY REQUIREMENTS FOR PUBLIC BUILDINGS IN NORTH MACEDONIA

The *Rulebook on Fire, Explosion and Hazardous Materials Protection Measures*, published in the Official Gazette of the Republic of North Macedonia No. 231/2020 [2], establishes fire-protection measures to be considered in design documentation for construction, reconstruction and change of use of buildings. The regulatory framework specifically does not address construction materials used for wall, ceiling and floor finishes and does not require appropriate fire-safety measures.
This regulation only requires that, where a suspended ceiling is envisaged in the premises, it must be designed and constructed using a material with a “fire resistance” rating of at least 30 minutes, which is not appropriate. This regulation does not specify any requirements regarding the reaction-to-fire performance of materials, which is

particularly important in public buildings such as nightclubs, where large numbers of occupants may be present and where ceilings, acoustic treatments, decorative elements, and wall coverings can constitute significant exposed combustible surfaces.

## 4.2. CONSTRUCTION AND INTERIOR MATERIALS AT PULS NIGHTCLUB

The fire at the Pulse nightclub in Kočani (Figure 3) provides an important case study for examining the relationship between material selection and regulatory compliance. Based on the available expert documentation [3,4] and additional building information, the following construction and interior materials were identified.

*Tab. 1 Principal materials at the Puls nightclub and their fire-safety relevance*

| Building element | Material identified/reported | Fire-safety relevance | Assessment |
|---|---|---|---|
| Ceiling | Acoustic sponge | Potential combustible contribution; may influence flame spread, heat release and smoke development | Exact reaction-to-fire class must be established from product documentation |
| Roof | Steel and wooden beams with “Salonit” roofing sheets | Steel has limited combustible contribution; timber contributes to fire load; complete assembly determines performance | Requires assessment of the complete roof assembly |
| Structural system | Reinforced concrete | Generally provides substantial fire resistance when properly designed and detailed | Structural fire performance requires verification |
| External walls | Brick masonry | Generally limited contribution to fire development | Complete wall build-up and interior finishes must also be considered |
| Window openings | Styrofoam, gypsum board, glass wool and decorative sheet metal | Changed the original opening conditions and introduced additional materials; blocked natural ventilation | Significant fire-safety concern |
| Interior finishes | Synthetic/combustible materials | Increased fire load and potential contribution to rapid fire development | Specifically identified as a concern in the expert report |
| Ceiling acoustic treatment | Sponge/acoustic lining | Directly located within the occupied space and potentially exposed to heat/flame | Requires product-specific fire classification |

The expert report documents that the ceiling had been covered with acoustic sponge and includes photographic evidence of the ceiling treatment (Figure 4). The report also documents that windows in the occupied area were internally blocked using styrofoam, glass wool, gypsum board and decorative sheet metal (Figure 5). This is significant for two reasons. First, the materials themselves increased the amount of combustible or

potentially combustible material within the occupied space. Second, the modification of the openings influenced ventilation and smoke behaviour. The expert report specifically notes that the blocked windows required effective mechanical ventilation and smoke extraction, but that appropriate measures for smoke extraction and ventilation of the large occupant area had not been implemented.



*Fig. 3 Puls nightclub in Kočani after the fire, showing the extent of damage to the roof and building structure*



*Fig. 4 Acoustic sponge on the ceiling of the Puls nightclub in Kočani before the fire*



*Fig. 5 Internally blocked windows at the Puls nightclub in Kočani using styrofoam, glass wool, gypsum board, and decorative sheet metal*

### 4.2.1. The acoustic sponge on the ceiling: why location matters

The fire at the Pulse nightclub in Kočani provides an important case study for examining the relationship between material selection and regulatory compliance.
Immediately after the disaster, authorities reported that the fire spread after pyrotechnic devices ignited combustible material on the ceiling (acoustic sponge).
More recent expert evidence presented during the judicial proceedings in August 2026 is particularly relevant to the material analysis. According to the reported expert findings, polyurethane foam was present in the suspended ceiling of the Pulse nightclub. The expert stated that the conclusion was based on photographic documentation (Figure 6), video recordings, results of other expert examinations and traces identified during the investigation, since the building was completely destroyed by the fire.



*Fig. 6 Pyrotechnic devices producing sparks that reached the ceiling during the concert at the Pulse nightclub. The footage shows the beginning of the fire and subsequent rapid fire development*

Polyurethane foam is a polymeric material whose fire behaviour depends strongly on its formulation, density, additives, protective layers and installation system. Therefore, the mere identification of polyurethane foam does not, by itself, prove a violation of the regulations. The decisive question is whether the specific product installed in the ceiling possessed an appropriate reaction-to-fire classification and whether it was permitted for that particular application under the approved fire-safety design.
From a fire-engineering perspective, the location of a combustible material can be as important as its total quantity. A combustible material installed close to the ceiling may be exposed to the hot upper smoke layer and rising thermal plume. Once ignition occurs, a material positioned continuously over a large ceiling area can provide a pathway for rapid fire development.
A technically correct conclusion requires four steps:

1. Identify the actual product.
2. Establish its certified reaction-to-fire classification.
3. Establish the required performance for its intended application.
4. Compare the certified performance with the actual installation.

Therefore, the appropriate scientific formulation is not: “The sponge was illegal because it was combustible.” The appropriate formulation is: “The presence and extensive use of acoustic sponge gives a significant fire-safety concern because of its potential contribution to fire development; final assessment of regulatory compliance requires

identification of the specific product, its certified reaction-to-fire performance, its installation configuration and the performance requirement applicable to that location."
However, the case demonstrates a more fundamental problem:
„F**ire safety cannot be assessed only by examining whether a building has a fire-safety certificate. The actual materials installed in the building must correspond to the materials specified in the approved design and must possess the required certified fire performance".**

### 4.2.2. From material classification to fire consequences

The significance of the material used in the Puls nightclub becomes clearer when considered together with the other conditions present during the fire. The initial ignition source was associated with pyrotechnics. When a rapidly ignitable combustible material is located directly above an ignition source, the time between ignition and extensive flame spread can become extremely short. The resulting heat and smoke can then reduce visibility and survivability while simultaneously reducing the available time for evacuation (Figure 7).

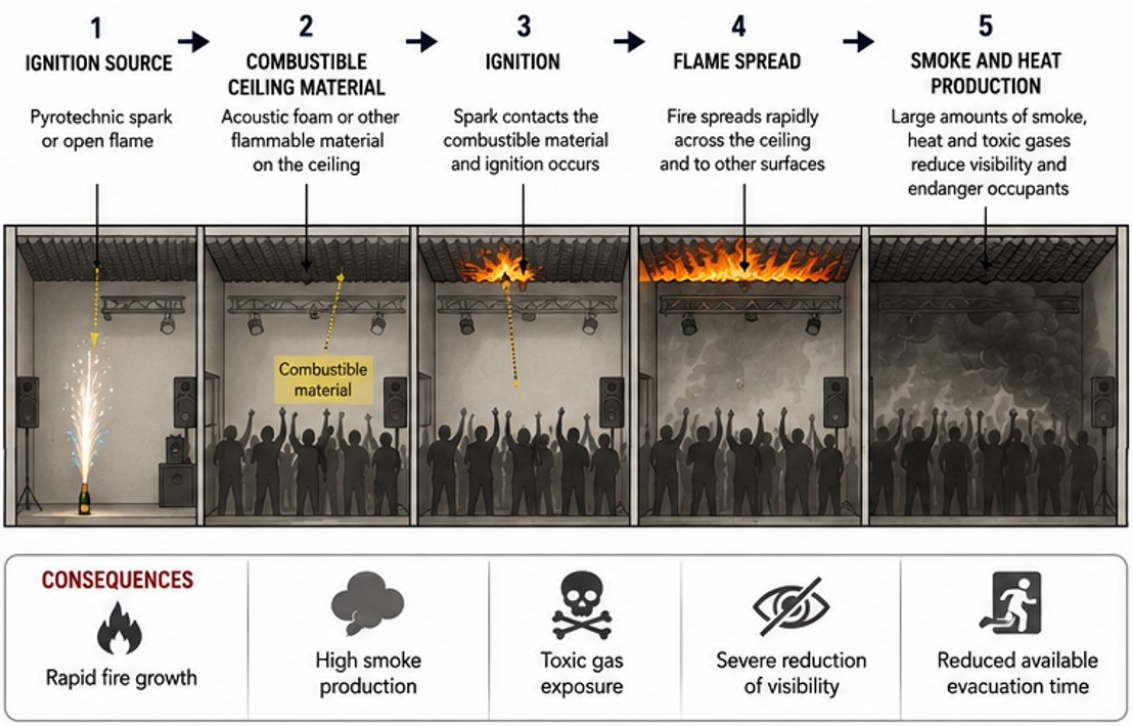


*Fig. 7 The role of combustible ceiling materials in rapid fire development*

Thus, the technical chain can be expressed as: **Ignition source → combustible material → rapid flame spread → heat and smoke → reduced available evacuation time → increased probability of casualties.**
This chain demonstrates why the selection of interior materials should be considered an essential component of life-safety design rather than merely an architectural or acoustic decision.
The Kočani case therefore illustrates that the question of compliance should not be limited to: **"Was a particular material combustible?"** The more appropriate engineering question is: **"Was the material, in its specific form and location of use, capable of satisfying the required reaction-to-fire performance for the building and its intended occupancy?"**

## 4.3. OTHER FIRE-SAFETY DEFICIENCIES IDENTIFIED AT PULS

### 4.3.1. Ventilation and smoke extraction

The expert report identifies four fans at the upper level and additional ordinary fans in the stage area, but states that their capacity was unknown. It further notes that some fans were partially enclosed with gypsum board and sponge, reducing ventilation capacity.
Most importantly, the report states that the building did not have appropriate measures for smoke extraction and ventilation of an area intended for a large number of occupants. This is a critical issue because smoke is frequently a more immediate threat to occupants than direct flame contact.
A fire in a crowded entertainment facility can rapidly produce:

- reduced visibility;
- toxic combustion products;
- elevated temperature;
- disorientation;
- panic;
- reduced walking speed;
- congestion at exits.

Thus, smoke control must be considered an essential component of evacuation safety.

### 4.3.2. Emergency lighting

The expert inspection did not identify emergency/escape lighting at the required locations. The report also specifically notes the absence of the required emergency lighting at the main Exit.
Loss of normal lighting during a fire can make evacuation significantly more difficult, particularly in an unfamiliar, crowded environment.

### 4.3.3. Automatic fire detection and alarm

The expert report states that the building had:

- no automatic fire detection system;
- no audible fire-warning system;
- no fire-protection control panel;
- no integrated control logic for the relevant fire-safety systems.

The absence of automatic detection is particularly significant in an entertainment venue because music, crowd noise and visual effects can delay recognition of a developing fire. Early detection is therefore not merely a technical convenience. It is directly connected to the time available for evacuation.

### 4.3.4. Electrical backup

The report states that no reserve power generator was installed and identifies this as a deficiency under the applicable regulatory provisions. It further describes the role of a reserve power source for critical fire-safety consumers such as smoke-extraction fans, emergency lighting and other systems.
This illustrates an important principle of fire protection: **A safety system that depends on electricity must itself remain available when the normal electrical supply is compromised.**

### 4.3.5. Hydrant system and fire suppression

The inspection found no external hydrant network. The internal hydrant lacked the necessary initial firefighting equipment, and the report states that its location did not

provide sufficient coverage for the entire building. The internal hydrant system was also considered non-functional.
The stage was not treated as a separate fire sector, and there was no automatic fixed extinguishing arrangement separating the stage from the audience area, such as a water curtain, water-cooling system or other fixed system. This is particularly important because the stage was the location associated with the initial fire development.

### 4.3.6. Portable fire extinguishers

The expert inspection identified only two portable fire extinguishers: one S-9 and one $CO_2$ extinguisher. The report considered this insufficient and refers to the applicable table indicating four extinguishers for an area of 301–500 m², subject to fire load and compartmentation.
Portable extinguishers are intended primarily for early-stage intervention. Their effectiveness is therefore strongly dependent on the time between ignition and discovery of the fire. Where automatic detection and alarm are absent, the importance of rapid human detection and immediate intervention becomes even greater.

### 4.3.7. Evacuation as the final layer of protection

A building may contain adequate construction materials and fire-protection systems, but if occupants cannot leave quickly and safely, the overall fire-safety strategy can still fail.
The expert report states that the building had three exits, but that none could be treated as a safe evacuation exit because the exits did not satisfy the prescribed conditions regarding width and safe evacuation to a predetermined safe location.
The report further states that:

- main Exit lacked required emergency lighting;
- evacuation doors were not installed to open in the direction of evacuation;
- additional partition walls had been constructed;
- a double-leaf, two-directional door created an obstruction along the evacuation route toward exits.

The main entrance itself consisted of a double-leaf aluminium/glass door with an approximate total width of 230 cm and height of 250 cm, leading through a vestibule to another double-leaf swinging door. A secondary metal door at the rear had an approximate width of 100 cm and height of 205 cm and led directly outside.
These observations illustrate why the nominal number of exits is not sufficient to establish evacuation safety.
The relevant question is: **Can the required number of occupants reach a safe place within the available safe evacuation time?**
This depends on exit width, door opening direction, travel distance, route geometry, obstructions, smoke conditions, emergency lighting, occupant behaviour and the time at which evacuation begins.

## 5. CASE STUDY - FIRE AT THE CONSTELLATION BAR IN CRANS-MONTANA

On 1 January 2026, a major fire occurred at the Le Constellation bar in Crans-Montana, Switzerland. According to the Swiss Federal Office of Public Health, 41 people lost their lives and 115 were injured in the fire [5,6].
The incident is relevant to this study because it again demonstrates the vulnerability of crowded entertainment spaces to rapid fire development.

According to the current investigative hypothesis, pyrotechnic devices attached to champagne bottles came into contact with combustible acoustic foam on the ceiling, causing rapid fire development.

What makes the case particularly important from a fire-safety perspective is the subsequent revelation concerning inspections. Municipal authorities acknowledged that periodic inspections had not been carried out between 2020 and 2025. This raises an important distinction between **having regulations** and **enforcing regulations**.

A regulation requiring periodic inspection has little practical value if inspections do not actually occur. Similarly, a requirement for appropriate materials cannot protect occupants if changes to the building are not identified and assessed during subsequent inspections.

The purpose of including Crans-Montana is not to suggest that the two incidents had identical technical causes. They did not. The buildings, regulatory frameworks, construction conditions and ignition circumstances were different. Rather, the cases are comparable at the system level. Both demonstrate the consequences that can arise when:

- combustible or otherwise fire-relevant interior materials are present;
- ignition occurs in a crowded entertainment environment;
- fire development is rapid;
- occupants have limited time to react;
- detection, warning, smoke control, suppression or evacuation measures are insufficient.

The Crans-Montana tragedy therefore provides an important international comparison: even in a different regulatory environment, the effectiveness of fire safety ultimately depends on whether requirements are implemented, maintained and verified in practice.

The Crans-Montana case therefore demonstrates that even a highly regulated environment remains vulnerable when a critical component of the safety system — inspection and verification — fails.

## 6. COMPARATIVE ANALYSIS: KOČANI AND CRANS-MONTANA

The comparison of both fire cases (Figure 8) demonstrates that fire safety cannot be reduced to material selection alone. The material question is important because combustible materials can accelerate fire development. However, the consequences depend on whether the building contains effective compensating systems.

For example, a combustible material in a building with:

- automatic detection;
- rapid alarm;
- effective smoke control;
- compartmentation;
- fixed suppression;
- adequate emergency lighting;
- sufficient and unobstructed exits;

may produce a very different outcome from the same material installed in a building where these systems are absent or ineffective. This is the essential engineering lesson.

One of the most important conclusions from the Kočani case is that regulatory compliance cannot exist only on paper. A robust fire-safety assessment should be based on a chain of demonstrable evidence:

**Design requirement → specified product → certified performance → correct installation → inspection → maintenance → operational readiness**

| FACTOR | KOČANI – PULSE NIGHTCLUB (16 MARCH 2025) | CRANS-MONTANA – LE CONSTELLATION BAR (1 JANUARY 2026) |
|---|---|---|
| Ignition source | Pyrotechnic devices used during a concert. | Pyrotechnic sparklers on champagne bottles. |
| Combustible materials | Combustible ceiling and interior materials. Polyurethane foam identified in the suspended ceiling. | Combustible acoustic foam on the ceiling (leading investigative hypothesis). |
| Fire spread | Very rapid – flames spread across the ceiling and the entire venue within seconds. | Very rapid – flames spread across the ceiling and throughout the bar. |
| Evacuation | Severely compromised: limited exits, locked/unusable doors, overcrowding. | Severely compromised: narrow exits, panic, smoke and rapid fire development. |
| Safety inspection / compliance | Major compliance concerns; questions about licensing, capacity and fire safety measures. | No mandatory safety inspections conducted between 2020 and 2025. |
| Regulatory enforcement | Serious questions about oversight, licensing and enforcement by authorities. | Inspection requirements existed, but enforcement failed over several years. |
| Result | Mass casualities: 62 deaths and more than 190 injuries. | Mass casualities: 41 deaths and more than 100 injuries. |
| Key lesson | Unsafe materials + regulatory failures + poor evacuation turn a small fire into a disaster. | Strong regulations are ineffective without regular inspections and enforcement. |

*Fig.8 Kočani (North Macedonia) vs. Crans-Montana (Switzerland): Comparative overview*

Failure at any point can compromise the final safety outcome. This is particularly important for interior materials. It is not sufficient to state: “The material is fire resistant.” The technical documentation should identify:

- the exact product;
- manufacturer;
- product composition;
- reaction-to-fire classification;
- test standard;
- test configuration;
- thickness/density;
- method of installation;
- substrate;
- intended end-use;
- required performance under the applicable regulations.

Only then can a meaningful compliance assessment be made.

MKS EN 13501-1:2019 is particularly relevant because its classification procedure is explicitly related to the end-use application of construction products.

**The central lesson of the Kočani case** is not that one combustible material “caused” the disaster. A more technical interpretation is that the material environment formed one component of a larger system of vulnerabilities.

The sequence can be understood as follows:

- **Stage 1 – Ignition**

An ignition source initiates fire development.

- **Stage 2 – Material involvement**

Combustible synthetic materials and ceiling/interior finishes become involved in the fire.

- **Stage 3 – Rapid fire development**

The available combustible surface area and material configuration contribute to rapid heat release and fire spread.

- **Stage 4 – Smoke and heat accumulation**

Inadequate smoke extraction prevents effective removal of combustion products and heat.

- **Stage 5 – Delayed warning**

Without automatic fire detection and an integrated alarm system, occupants may not receive sufficiently early warning.

- **Stage 6 – Limited firefighting capability**

Deficiencies in hydrant protection, fixed suppression and portable extinguishers reduce the ability to control the fire at an early stage.

- **Stage 7 – Evacuation impairment**

Smoke, heat, inadequate emergency lighting, insufficient exit conditions and obstructions reduce the effective evacuation capacity.

- **Stage 8 – Mass casualties**

The available safe evacuation time becomes shorter than the time required for occupants to reach safety.

This is the fundamental fire-safety problem in mass-casualty building fires: **The fire develops faster than the occupants can recognize the danger and reach safety.**

## 7. CONCLUSIONS

The analysis of the Kočani and Crans-Montana nightclub fires demonstrates that catastrophic fire events in public entertainment buildings are rarely the result of a single technical deficiency.

The Kočani expert report documents a combination of deficiencies involving combustible synthetic materials, acoustic sponge, blocked windows, smoke extraction, emergency lighting, automatic fire detection and alarm, hydrant protection, portable extinguishers, fire-sector separation and evacuation routes.

The acoustic sponge installed on the ceiling is particularly relevant because its location within the occupied space could contribute to rapid fire development. However, the scientific assessment must not assign a Euroclass solely from the generic description “sponge”. The actual product, certified classification, installation configuration and required performance must be established. This distinction is fundamental to responsible fire-safety engineering.

The second major conclusion is that **material safety cannot be separated from system safety.**

Even a material with acceptable reaction-to-fire characteristics cannot compensate for the absence of automatic detection, smoke control, suppression, emergency lighting or adequate evacuation routes. Conversely, effective fire-safety systems can reduce the consequences of an otherwise unavoidable ignition.

The third conclusion is that **regulatory compliance must be demonstrable**. A building should not be considered fire safe simply because a project or permit indicates compliance. Compliance must be verified through the actual building condition, approved materials, certified performance, installation, inspection and maintenance.

The comparison with Crans-Montana reinforces this principle. The two tragedies occurred in different countries and cannot be considered technically identical. Nevertheless, both demonstrate the vulnerability of crowded entertainment spaces when fire develops faster than occupants can respond.

The fundamental lesson is therefore simple:

**A fire-safety regulation has value only when it is translated into practice.**

For public entertainment buildings, this means that every stage of the safety chain must be treated as essential:

**appropriate materials → compliant design → certified products → correct installation → functional detection → effective warning → smoke control → fire suppression → emergency lighting → unobstructed evacuation → regular inspection and maintenance.**

If several links in this chain fail simultaneously, the result can be catastrophic.

## REFERENCES

[1] Institute for Standardization of the Republic of North Macedonia (ISRSM). MKS EN 13501-1:2019 – Fire classification of construction products and building elements – Part 1: Classification using data from reaction to fire tests. Published 30 March 2019.

[2] Republic of North Macedonia. Rulebook on measures for protection against fires, explosions and hazardous substances. Official Gazette of the Republic of North Macedonia No. 231/2020.

[3] **Expert report – Pulse nightclub, Kočani.** Technical documentation and site findings concerning fire protection, ventilation, emergency lighting, fire detection, hydrant systems, extinguishers, fire sectors and evacuation.

[4] World Health Organization (WHO). North Macedonia: strengthening mass-casualty preparedness following the Kočani nightclub fire. 2026.

[5] Swiss Federal Office of Public Health (FOPH). **Crans-Montana fire.** Updated 2 February 2026.

[6] Swiss Confederation. **Crans-Montana: useful information.** Federal information regarding the 1 January 2026 fire and its consequences.

https://doi.org/10.24867/INDIS-2026-EN-034

**INTERNATIONAL SCIENTIFIC CONFERENCE**

INTEGRATION, NOVELTY, DESIGN,
INTERDISCIPLINARITY, SUSTAINABILITY

iNDiS 2026

# THE TWIN TRANSITION: DIGITALISATION AND AI FOR REAL-TIME ENVIRONMENTAL DECISION INTELLIGENCE IN CIRCULAR CONSTRUCTION

*Tomo Cerovšek*[1]

***Summary:***

The twin transition combines the digital and green transformation of the construction sector with the aim of moving from retrospective reporting toward data-driven environmental decision-making in real or near-real time. This paper proposes an integrated framework that connects BIM/openBIM, GIS, 3D cadastre, building and demolition permits, waste-flow records, weighing data, and other digital sources into a spatiotemporal model of material stocks and flows. Spatial statistics, probabilistic models, and artificial intelligence can be used to estimate the quantity, location, and future availability of secondary materials, while continuously updating predictions with newly available data. Particular emphasis is placed on analysing spatial dependence, predicting locked and hidden material stocks, modelling building lifetimes, and simulating future material flows with an increasing accuracy. The proposed approach enables predictive urban mining and supports the reduction of environmental impacts.

*Keywords: twin transition; circular construction; environmental decision intelligence; building lifecycle; predictive urban mining*

# DVOSTRUKA TRANZICIJA: DIGITALIZACIJA I AI ZA DONOŠENJE EKOLOŠKIH ODLUKA U REALNOM VREMENU U CIRKULARNOJ GRADNJI

***Rezime:***

Dvostruka tranzicija povezuje digitalizaciju i zelenu transformaciju građevinskog sektora sa ciljem prelaska sa naknadnog izveštavanja na donošenje ekoloških odluka u realnom ili približno realnom vremenu, zasnovano na podacima. Rad predlaže integrisani okvir koji povezuje BIM/openBIM, GIS, 3D katastar, podatke o građevinskim dozvolama i dozvolama za rušenje, tokovima otpada, vaganju, kao i drugim digitalnim izvorima u prostorno-vremenski model zaliha i tokova materijala. Prostorna statistika, probabilistički modeli i veštačka inteligencija koriste se za procenu količina, lokacije i vremena buduće dostupnosti sekundarnih materijala, kao i za kontinuirano ažuriranje procena novim podacima. Poseban naglasak stavljen je na analizu prostorne zavisnosti, predikciju skrivenih zaliha materijala, modeliranje životnog veka građevina i simulaciju budućih tokova materijala. Predloženi pristup omogućava prediktivno urbano rudarstvo i pruža podršku odlukama o upotrebi, reciklaži, logistici i smanjenju uticaja na životnu sredinu.

[1] Assoc. Prof. dr., University of Ljubljana, Slovenia,
tomo.cerovsek@fgg.uni-lj.si, ORCID 0000-0003-0523-0473

*Ključne reči: dvostruka tranzicija; cirkularna gradnja; donošenje ekoloških odluka; životni vek zgrada; prediktivno urbano rudarstvo*

## 1. INTRODUCTION

The construction sector is entering a phase in which environmental sustainability cannot be addressed independently from digital transformation. Buildings and infrastructure consume large quantities of raw materials, generate substantial waste streams, and create environmental impacts throughout their entire life cycle. In the European Union, the built environment accounts for approximately half of all extracted materials and more than one third of total waste generation, making construction a central domain for climate mitigation, resource efficiency, and circular-economy policies.

At the same time, sustainability requirements are becoming increasingly life-cycle-oriented. Circular construction extends the conventional focus on operational energy toward material extraction, product manufacturing, construction, maintenance, renovation, reuse, recycling, and end-of-life processes. European initiatives such as Level(s) [1] explicitly promote life-cycle thinking and provide a common framework for assessing carbon, materials, water, climate resilience, and other sustainability dimensions throughout the life cycle of buildings. This evolution implies a fundamental change in environmental decision-making: it is no longer sufficient to determine environmental performance retrospectively, after a building has been designed, constructed, renovated, or demolished. Circularity requires the ability to anticipate future material stocks, flows, recovery opportunities, and environmental consequences before decisions are made.

This transformation requires a systems perspective that recognises buildings and infrastructure not only as functional assets but also as long-term repositories of material resources. The circular economy framework proposed by Pomponi and Moncaster [2] identifies the technological, environmental, economic and societal interdependencies that characterise circularity in the built environment. Kirchherr et al. [3] demonstrate that circular economy definitions extend beyond recycling and resource recovery towards broader systemic changes in production and consumption.

These perspectives suggest that circular construction should be approached as a dynamic socio-technical system in which physical resources, digital information, lifecycle processes, stakeholder decisions and environmental consequences are interconnected.

### 1.1. THE IMPORTANCE OF TWIN TRANSITION

These challenges create a direct connection between the green transition and the digital transition. The green transition defines objectives such as decarbonisation, resource efficiency, waste prevention, reuse, recycling, and preservation of material value. Digitalisation provides the information infrastructure required to operationalise these objectives. Building Information Modelling (BIM), geographic information systems (GIS), digital twins, common data environments, Digital Building Logbooks (DBLs), sensors, material databases, and Digital Product Passports (DPPs) increasingly make it possible to represent the built environment as a continuously evolving information system rather than as a collection of static physical assets. This convergence is increasingly reflected in EU regulation. The revised Construction Products Regulation was explicitly designed to support both the green and digital transition and introduces machine-readable DPPs containing product-performance, conformity, and environmental information across the product life cycle.

However, digitalisation alone does not create sustainability. Much of the currently available digital information remains fragmented across models, registers, permits, waste

records, product databases, logistics systems, and individual organisations. BIM may describe what is designed, GIS where assets are located, product passports what products contain, waste records what has already left the system, and sensors what is occurring at a particular moment. The greater opportunity lies in connecting these heterogeneous sources and transforming them into actionable environmental knowledge. Advanced digitalisation can therefore be understood not merely as the digitisation of documents and processes, but as the creation of an interoperable, machine-readable and continuously updated information environment capable of supporting environmental reasoning.

Circular resource management requires information to remain consistent across spatial scales, levels of detail and lifecycle stages. Individual building components, urban material stocks and regional resource flows represent different but interconnected levels of the same system. Their integration is complicated by differences in geometry, semantics, spatial resolution, temporal validity and data ownership. Research on BIM–GIS integration demonstrates that these challenges extend beyond geometric conversion to the management of information relationships and flows [4, 5]. Addressing them is essential for linking building-level observations with spatially distributed resource inventories and for maintaining reliable material information as the built environment changes. DBLs and DPPs complement this integration by supporting the continuity and traceability of information at building and product levels. The European Commission [6] identifies the DBL as a common repository of relevant building information, while the European ecodesign framework [7] establishes principles for interoperable product-level information. Within the construction sector, Regulation (EU) 2024/3110 [8] establishes the framework for a construction digital product passport system. Collectively, these developments provide a foundation for linking physical assets, digital representations and verified product information throughout their lifecycle.

## 1.2. ADVANCING CIRCULAR CONSTRUCTION

A fundamental characteristic of circular construction is the distinction between materials physically present in buildings and resources that may become available for future use. Materials remain embedded in assets for different periods, while their release depends on renovation, replacement, demolition and changing functional requirements. Even after release, their practical availability is constrained by condition, accessibility, ownership, recovery technologies and market demand. Consequently, material stock quantities cannot be interpreted directly as secondary resource supply. Circular resource management must consider both the preservation of materials in existing functions and their potential future recovery, recognising that premature release may reduce rather than increase environmental value. This distinction establishes the basis for predictive urban mining, in which spatial and temporal models connect the estimation of future material availability with the evaluation of alternative circular interventions. Spatial statistics can reveal spatial dependencies and estimate unobserved material stocks; probabilistic lifetime and material-release models can describe when currently embedded materials may enter future secondary-material streams. Koutamanis et al. [9] demonstrate that urban mining requires more reliable information about existing buildings and their material composition than conventional aggregated inventories can provide.

Artificial intelligence (AI) can complement these approaches by identifying patterns in heterogeneous data, classifying building and material archetypes, detecting anomalies, predicting changes and continuously updating estimates when new evidence becomes

available. In this role, AI should not be regarded simply as an additional prediction technique, but as a component of a broader digital decision architecture connecting observations, models, uncertainty and environmental objectives.

The integration of building-level information with spatially explicit stock models can support the identification and quantification of potentially recoverable materials. Pei et al. [10] further highlight the relevance of integrating urban building material stock analysis with Life Cycle Assessment (LCA) to connect material availability with environmental consequences. Together, these approaches provide a foundation for extending urban mining from end-of-life material recovery towards predictive and lifecycle-oriented resource management.

## 1.3. CONTRIBUTION

Against this background, the paper proposes an integrated conceptual and methodological framework for environmental decision intelligence in circular construction. The framework consequently shifts the emphasis from the availability of digital information towards its capacity to support informed decisions across different spatial scales and lifecycle stages.

The proposed approach distinguishes material stocks currently embedded in buildings from future material releases and technically recoverable secondary resources. This distinction recognises that physical material quantities cannot be equated with available resources without considering intervention timing, accessibility, technical condition and recovery constraints. It is operationalised through a six-stage spatio-temporal predictive urban mining framework combining heterogeneous data integration, spatial dependence analysis, geostatistical estimation, probabilistic building lifetime modelling and Monte Carlo uncertainty propagation. Rather than generating deterministic inventories, the approach produces spatially and temporally explicit estimates accompanied by measures of uncertainty. These predictions provide a quantitative basis for evaluating interventions according to the 5R hierarchy—Rethink, Reduce, Reuse, Repurpose and Recycle—while distinguishing resource recovery opportunities from strategies that preserve the functionality and embodied value of existing assets.

A further contribution is the interpretation of real-time environmental intelligence as an event-driven capability rather than the continuous measurement of every physical process. Relevant events, including demolition permits, building modifications, revised BIM information, newly available DPPs and recorded material outflows, can trigger updates to material stock estimates, release forecasts and associated environmental evaluations. Such updates may alter not only expected material quantities and their timing but also the relative attractiveness of alternative circular interventions. The framework therefore distinguishes observation, prediction and decision-making while connecting them through feedback, allowing newly acquired evidence to challenge earlier assumptions and improve subsequent assessments. This enables environmental assessments to remain aligned with changing resource conditions and intervention opportunities.

The methodological proposal is conceptual and requires empirical validation, particularly regarding incomplete building information, spatial estimation uncertainty, lifetime distributions and recovery assumptions. Its practical performance will depend on data availability, model calibration, interoperability and the sensitivity of environmental decisions to prediction uncertainty. Nevertheless, the framework provides a structured

basis for investigating how continuously updated information and predictive methods can improve resource planning and the evaluation of circular strategies. It thereby establishes a pathway from retrospective environmental reporting towards prospective, adaptive and uncertainty-aware circular resource management.

## 2. SYSTEMS THINKING FOR CIRCULAR CONSTRUCTION WITH 5R

Circular construction requires a systems perspective in which buildings and infrastructure are understood as both functional assets and long-term material repositories. Construction, operation, renovation, and deconstruction continuously transform material stocks and flows. Circularity therefore extends beyond waste management towards preserving asset functionality and material value while minimising resource consumption, energy use, and lifecycle environmental impacts.

The proposed 5R framework (Rethink, Reduce, Reuse, Repurpose, and Recycle) provides a hierarchy for circular interventions. Rethink challenges the need for new construction or replacement, while Reduce minimises material consumption and extends asset lifetimes. Reuse preserves components in their original functions, Repurpose enables alternative applications, and Recycle recovers materials through processing. The hierarchy prioritises functional and embodied value retention, although environmental benefits must be verified through LCA. Rethink and Reduce primarily influence future resource demand, whereas Reuse, Repurpose, and Recycle determine how existing resources remain in circulation. Implementing these strategies requires information on material quantities, composition, condition, location, and future availability, directly linking circular construction with predictive urban mining [9, 10].

As illustrated in Figure 1, the proposed systems approach connects physical assets, BIM, GIS, DBLs, DPPs, AI-supported analytics, and circular decisions. Feedback between physical interventions and digital information enables continuous updates of material stocks, environmental assessments, and resource management decisions, supporting environmental, economic, and societal outcomes.

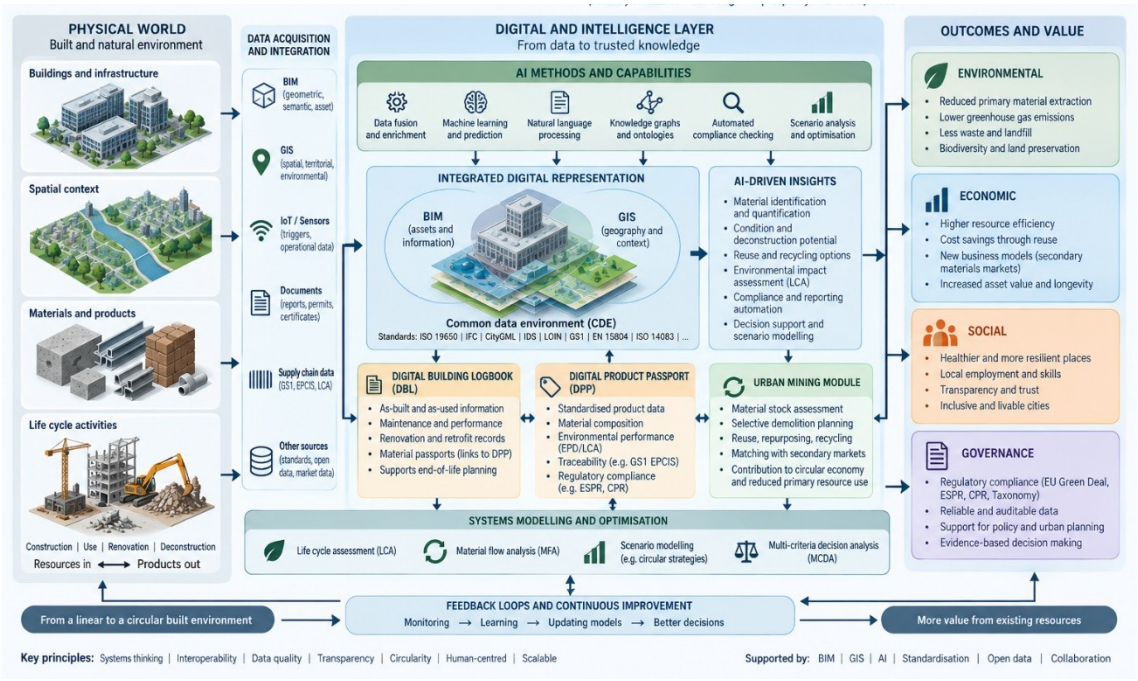


*Fig 1. AI-enabled circular built environment: A systems-based conceptual framework integrating the physical built environment, BIM, GIS, artificial intelligence, Digital Building Logbooks, Digital Product Passports, urban mining, lifecycle assessment, and feedback mechanisms to support circular resource management, triple bottom line and governance.*

## 3. DIGITALISATION AND AI AS ENABLERS OF CIRCULAR CONSTRUCTION

### 3.1. INTEGRATED DIGITAL INFORMATION: BIM, GIS, DBLs, AND DPPs

The principal challenge for digital circular construction is to establish a coherent information environment from heterogeneous sources that were originally developed for different purposes. BIM describes asset geometry, components and technical properties, while GIS provides spatial referencing and supports the representation of building stocks, infrastructure networks and urban processes. Their integration must reconcile differences in data structures, semantic classifications and granularity while preserving relationships between individual components, buildings and spatial units [4, 5].

DBLs and DPPs provide complementary information about building histories, product characteristics, environmental performance and traceability [6–8]. However, their value for predictive urban mining depends on whether information can be reliably associated with identifiable assets, products, locations and lifecycle events. Persistent identifiers, interoperable classifications, temporal records, provenance metadata and explicit uncertainty descriptions are therefore as important as geometric or semantic interoperability. A sufficiently integrated information environment should support both the reconstruction of past changes and the incorporation of newly observed events, enabling material stock estimates and forecasts to evolve as additional evidence becomes available.

However, existing building stocks rarely possess complete digital documentation. Consequently, digital integration must combine detailed information where available with

statistical and computational methods capable of estimating missing material characteristics and quantities. This distinction is fundamental for the development of predictive urban mining models.

### 3.2. AI AND ENVIRONMENTAL KNOWLEDGE INTEGRATION

AI contributes to environmental decision intelligence by transforming incomplete and heterogeneous information into usable observations and model inputs. Machine learning, computer vision, natural language processing and knowledge-based approaches can support the extraction of material attributes from documents, classification of buildings and components, identification of inconsistent records, and estimation of missing information. Research on construction and demolition waste demonstrates the potential of data-driven methods for material classification and resource-related predictions [11].

However, predictive accuracy alone does not ensure physical consistency or decision relevance. Material Flow Analysis (MFA) provides mass-balance constraints, while System Dynamics (SD) represents interactions, delays and feedback between stocks, flows and interventions. Their integration supports the analysis of complex circular resource systems in which changes in recovery, demand and material availability influence one another [12]. AI can complement these models through estimation and continuous data assimilation.

A critical methodological requirement is therefore to connect observed building characteristics, inferred material quantities and probabilistic intervention scenarios within a consistent spatial and temporal representation. This requires explicit treatment of missing information, spatial dependence and uncertainty, providing the analytical foundation for the predictive framework developed in the following chapter.

## 4. SPATIO-TEMPORAL PREDICTIVE URBAN MINING FRAMEWORK

The proposed predictive urban mining methodology is organised into six interdependent stages (Fig. 2), progressing from observed spatial and lifecycle information to probabilistic estimates of future material availability. Particular emphasis is placed on the relationship between spatially uncertain material quantities, the timing of building interventions and the technical recoverability of released resources.

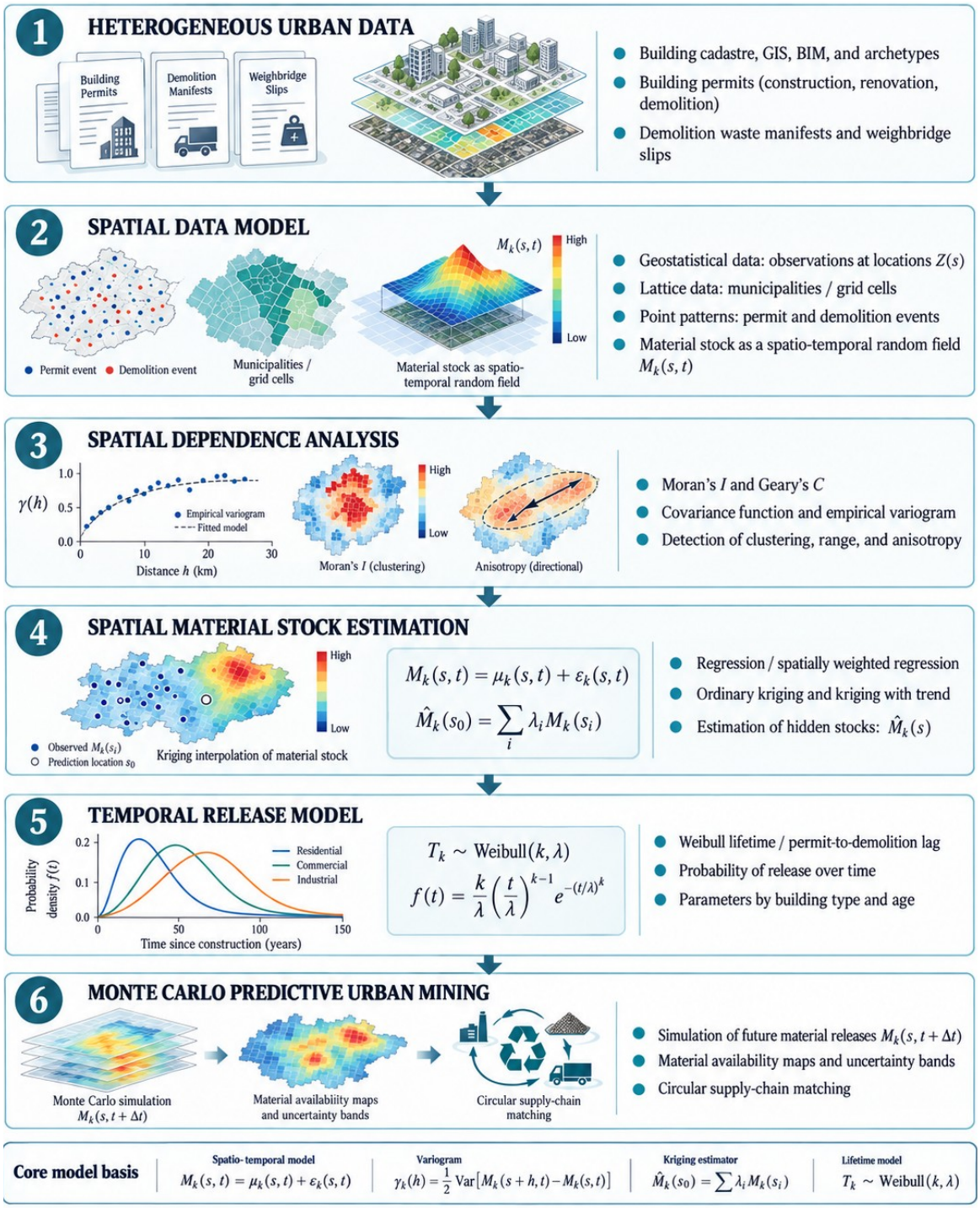


*Fig. 2. Proposed six-stage spatio-temporal framework for predictive urban mining: (1) heterogeneous urban data integration, (2) spatial data modelling, (3) spatial dependence analysis, (4) geostatistical material stock estimation, (5) probabilistic temporal release modelling, and (6) Monte Carlo simulation of future material availability, and uncertainty.*

The six stages form a connected analytical sequence in which observed building characteristics inform estimates of spatial material stocks, while probabilistic intervention models transform these stocks into potential future material releases. Recovery assumptions subsequently distinguish expected outflows from technically recoverable

quantities. This separation enables uncertainty to be traced from incomplete source information through spatial estimation and temporal forecasting to the resulting predictions of secondary resource availability. The framework thus supports spatially differentiated scenarios for material recovery, logistics planning and circular resource management:

- Stage 1 (Heterogeneous data integration): Integrates diverse data sources, including building cadastres, GIS, BIM, building archetypes, construction and demolition permits, waste manifests, and weighbridge records. These sources provide observations concerning building characteristics, material composition, intervention events, and material outflows. Their harmonisation establishes an information layer linking building-level spatial and temporal observations.
- Stage 2 (Spatial data modelling): Establishes a spatial data model incorporating geostatistical observations, areal units such as municipalities or grid cells, and point patterns representing construction or demolition events. For material category k, the spatially distributed material stock is conceptualised as a spatio-temporal random field $M_k(s,t)$, where s denotes spatial location and t time.
- Stage 3 (Spatial dependence analysis): Investigates spatial dependence through indicators such as Moran's I and Geary's C, together with covariance functions and empirical variograms. These methods support the identification of spatial clustering, dependence ranges, and anisotropy, providing the statistical foundation for estimating material quantities at unobserved locations.
- Stage 4 (Spatial material stock estimation): Applies regression and geostatistical methods, including ordinary kriging and kriging with a trend, to estimate spatial material stocks. The model captures spatially structured residual variation, providing predictions at unobserved locations together with uncertainty estimates to extend incomplete building-level information into spatially continuous or aggregated representations.
- Stage 5 (Temporal release modelling): Formulates probabilistic lifetime and material-release models to capture future renovation, replacement, or demolition events. Probabilistic lifetime models, such as Weibull distributions, describe the timing of future interventions according to building type, age, and relevant characteristics, while explicitly conditioning release probabilities on survival to the current age.
- Stage 6 (Monte Carlo predictive urban mining): Employs Monte Carlo simulation to propagate uncertainties associated with material quantities, spatial estimation, lifetime distributions, and intervention scenarios. Repeated simulations generate predictive distributions of material releases, enabling the generation of future material availability maps, expected quantities, and uncertainty intervals, with recovery factors distinguishing gross material outflows from technically recoverable resources.

The resulting framework extends conventional material inventories towards predictive urban mining by addressing four fundamental questions: what materials exist, where they are located, when they may become available, and with what degree of uncertainty. Its event-driven implementation would allow new building records, permits, digital model updates, and observed material flows to revise estimates and forecasts.

## 5. ENVIRONMENTAL DECISION INTELLIGENCE AND CONCLUSIONS

The value of predictive urban mining depends on how forecasts inform decisions, not simply on their numerical accuracy. Estimated material releases must be assessed against the 5R hierarchy, technical feasibility, environmental impacts and economic consequences. Crucially, retaining an asset in use may outperform recovering its materials, even where recovery is technically possible. MFA provides mass-balance consistency between stocks and flows, while LCA and Life Cycle Costing (LCC) evaluate alternative interventions across environmental and economic dimensions. Decision intelligence therefore requires links between forecast uncertainty, recovery constraints, transport requirements and demand for secondary materials. Event-driven observations, such as demolition permits, BIM revisions, DPP updates and measured recovery quantities, can revise both predicted availability and the ranking of circular options. This creates a feedback process in which decisions are reconsidered when evidence or operating conditions change.

Making such decisions credible requires information that remains identifiable, traceable and interpretable across organisational and lifecycle boundaries. DBLs, DPPs, BIM and GIS need persistent identifiers, common semantics, machine-readable structures and records of when information was created or revised. Regulation (EU) 2024/3110 [8] provides provisions for construction DPPs and their interoperability with BIM, while European DBL initiatives [6] seek greater continuity of building information. CEN/TC 442 addresses semantic interoperability, lifecycle information and information exchange [13]; the European Commission's 2026 Rolling Plan for ICT Standardisation also recognises these priorities [14]. Beyond technical standards, responsibility for information quality, access, verification and updating must be allocated among asset owners, designers, contractors and public authorities. The European Commission's proposed EU Public Procurement Act, COM(2026) 590, published on 9 September 2026 [15], could create opportunities for greater emphasis on verifiable lifecycle information in public procurement. However, procurement requirements should specify the decisions information must support, rather than prescribe digital deliverables without a demonstrated purpose.

In conclusion, the twin transition should be judged by its capacity to improve resource decisions, rather than by the volume of digital data collected. The proposed six-stage framework establishes a methodological bridge between fragmented observations of buildings and spatially explicit, probabilistic forecasts of material releases. Its distinction between embedded stocks, expected outflows and recoverable resources is essential: material presence alone neither establishes future availability nor justifies demolition or recovery. The 5R hierarchy gives these forecasts a decision context that favours preserving functional and embodied value, subject to comparative lifecycle evidence. Practical implementation will require empirical calibration of building lifetimes and material intensities, validation against observed interventions, and transparent treatment of spatial, temporal and recovery uncertainties. Future studies should test whether event-driven updates measurably improve forecast reliability, supply-demand matching and the environmental performance of selected interventions. They should also examine sensitivity to uncertain demolition schedules, changing market conditions and incomplete product information. Interoperable records and clear institutional responsibilities will be necessary, but their effectiveness must ultimately be demonstrated through measurable

outcomes. The aim is a resource management system capable of learning from interventions and guiding timely, evidence-based circular decisions.

## LITERATURE

[1] European Commission. (n.d.). Level(s): What's in it for you? The European framework for sustainable buildings. Directorate-General for Environment. Retrieved from https://environment.ec.europa.eu/topics/circular-economy/levels_en

[2] Pomponi, F., & Moncaster, A. (2017). Circular economy for the built environment. Journal of Cleaner Production, 143, 710–718. https://doi.org/10.1016/j.jclepro.2016.12.055

[3] Kirchherr, J., Reike, D., & Hekkert, M. (2017). Conceptualizing the circular economy: An analysis of 114 definitions. Resources, Conservation and Recycling, 127, 221–232. https://doi.org/10.1016/j.resconrec.2017.09.005

[4] Zhu, J., Wright, G., Wang, J., & Wang, X. (2018). A critical review of the integration of Geographic Information System and Building Information Modelling at the data level. ISPRS Intl. Journal of Geo-Information, 7(2), 66. https://doi.org/10.3390/ijgi7020066

[5] Zhu, J., & Wu, P. (2022). BIM/GIS data integration from the perspective of information flow. Auto. in Construction, 136, 104166. https://doi.org/10.1016/j.autcon.2022.104166

[6] European Commission. (2020). Study on the development of a European Union framework for digital building logbooks: Final report. Publications Office of the European Union. https://data.europa.eu/doi/10.2826/659006

[7] European Parliament, & Council of the European Union. (2024). Regulation (EU) 2024/1781 of 13 June 2024 establishing a framework for the setting of ecodesign requirements for sustainable products and amending Directive (EU) 2020/1828 and Regulation (EU) 2023/1542 and repealing Directive 2009/125/EC. Official Journal of the European Union, L series. https://eur-lex.europa.eu/eli/reg/2024/1781/oj

[8] European Parliament, & Council of the European Union. (2024). Regulation (EU) 2024/3110 of 27 November 2024 laying down harmonised rules for the marketing of construction products and repealing Regulation (EU) No 305/2011. Official Journal of the European Union, L series. https://eur-lex.europa.eu/eli/reg/2024/3110/oj

[9] Koutamanis, A., van Reijn, B., & van Bueren, E. (2018). Urban mining and buildings: A review of possibilities and limitations. Resources, Conservation and Recycling, 138, 32–39. https://doi.org/10.1016/j.resconrec.2018.06.024

[10] Pei, W., Biljecki, F., & Stouffs, R. (2024). Techniques and tools for integrating building material stock analysis and life cycle assessment at the urban scale: A systematic literature review. Building and Env., 262, 111741. https://doi.org/10.1016/j.buildenv.2024.111741

[11] Gao, Y., Wang, J., & Xu, X. (2024). Machine learning in construction and demolition waste management: Progress, challenges, and future directions. Automation in Construction, 162, 105380. https://doi.org/10.1016/j.autcon.2024.105380

[12] Alfarisi, S., Koide, R., Hawkin, J. L., Meng, F., & Watari, T. (2026). An integrated modelling framework for feedback-driven and mass-balanced circular economy analysis. Journal of Cleaner Production, 574, 149117. https://doi.org/10.1016/j.jclepro.2026.149117

[13] CEN-CENELEC (2026). Construction products: Digital construction and CEN/TC 442 Building Information Modelling (BIM). European Committee for Standardization and European Committee for El. Standardization. https://www.cencenelec.eu/areas-of-work/cen-sectors/construction/construction-products/

[14] European Commission. (2026). Rolling Plan for ICT Standardisation 2026: Construction – Building Information Modelling. Interoperable Europe Portal. https://interoperable-

europe.ec.europa.eu/collection/rolling-plan-ict-standardisation/construction-building-information-modelling-rp-2026

[15] European Commission. (2026). Proposal for a Regulation of the European Parliament and of the Council on public contracts and concessions (Public Procurement Act). COM(2026) 590 final, 9 September 2026. https://single-market-economy.ec.europa.eu/publications/proposal-regulation-public-contracts-and-concessions_en

https://doi.org/10.24867/INDIS-2026-EN-047



# FROM DETECTION ACCURACY TO USEFUL SCREENING: LESSONS FROM INSAR VOLCANIC DEFORMATION CLASSIFICATION

*Teo Beker*[1]

***Summary:***

Satellite radar interferometry (InSAR) measures ground movement around volcanoes, and artificial intelligence can automatically identify possible deformation for expert review. We examine how to reduce review candidates while retaining deformation detections. We evaluate our model predictions for 775 overlapping image patches using three processing versions of the same data and four combination rules. A rule requiring agreement across versions reduces patches selected for review from 297 to 251 relative to an unfiltered input, while detecting 95.07% of positive patches. The filtered input selects fewer patches when all positive patches must be detected and fewer whole frames at fixed patch thresholds. When thresholds are transferred between spatial groups, the agreement rule detects 92.96% of positive patches. These results show that useful screening depends on the detection target, the unit reviewed and geographic transfer.

*Keywords: InSAR, volcanic deformation, screening, recall, geographic transfer*

# OD TAČNOSTI DETEKCIJE DO IZDVAJANJA PODATAKA ZA STRUČNI PREGLED: POUKE IZ KLASIFIKACIJE VULKANSKIH DEFORMACIJA POMOĆU INSAR-A

***Rezime:***

Satellitska radarska interferometrija (InSAR) meri pomeranja tla oko vulkana, a veštačka inteligencija može automatski da izdvoji moguće deformacije za stručni pregled. Ispitujemo kako smanjiti broj podataka za pregled uz što manje propuštenih deformacija. Analiziramo rezultate našeg modela za 775 preklapajućih isečaka, koristeći tri različito obrađena prikaza istih podataka i četiri pravila kombinovanja. Pravilo koje zahteva saglasnost svih prikaza smanjuje broj izdvojenih isečaka sa 297 na 251 u odnosu na nefiltrirani prikaz, uz detekciju 95,07% pozitivnih isečaka. Filtrirani prikaz izdvaja manje isečaka kada se zahteva detekcija svih pozitivnih isečaka i manje celih frejmova pri fiksnim pragovima za isečke. Pri prenosu pragova između prostornih grupa, pravilo saglasnosti otkriva 92,96% pozitivnih isečaka. Ovi rezultati pokazuju da korisnost selekcije zavisi od zahtevanog odziva, jedinice pregleda i prenosivosti na druga područja.

*Ključne reči: InSAR, vulkanske deformacije, selekcija podataka, odziv, geografska prenosivost*

[1] Teo Beker, PhD candidate, Chair of Data Science in Earth Observation, Technical University of Munich (TUM), Arcisstraße 21, 80333 Munich, Germany; e-mail: teobeker@hotmail.com; ORCID: 0000-0003-1907-4045.

# 1. INTRODUCTION

Ground movement around volcanoes is one of the observations used to assess volcanic activity. Satellite interferometric synthetic aperture radar (InSAR) compares radar observations acquired at different times to measure movement along the radar viewing direction, called the line of sight (LOS). It can reveal deformation across broad areas, including volcanoes with limited ground instrumentation. Atmospheric effects and other unwanted signals can complicate interpretation, so a pattern in an InSAR image still requires expert assessment [1].

Artificial intelligence can help select which images deserve that assessment. A convolutional neural network (CNN) assigns each image a score indicating how strongly it resembles deformation examples learned during training [2]. Comparing this score with a threshold determines whether an image is selected. Lower thresholds select more images and miss fewer positives, but send more negatives for review. Balancing detection and inspection is relevant to geodetic and civil engineering monitoring; here, we evaluate volcanic patterns.

Beker et al. [3] developed training and input-preparation approaches to identify subtle volcanic deformation in the Andean Central Volcanic Zone. Here, we use our model predictions and the same working dataset to study how detections become review selections. We ask which input version or combination retains a chosen number of positive examples with fewer images to inspect, and how that answer changes with the detection target, review unit and geographic setting.

## 1.1. RELATED WORK AND SCREENING EVALUATION

CNN classification of volcanic InSAR imagery [4] and training with synthetic deformation and atmospheric noise [5] established the underlying approach. Changing the number of phase cycles in an input image, known as over-wrapping, has helped detect slow deformation when predictions from different versions are averaged [6]. These studies motivate examining how input preparation affects the number and identity of images selected for review.

Joint classification and localization [7], anomaly detection [8] and the Hephaestus dataset [9] broaden the available approaches. They address different image populations and output tasks, so their reported performance cannot be compared directly with the patch-level results here. They provide context for the screening problem rather than a common numerical benchmark.

## 1.2. STUDY OBJECTIVE

We use our model predictions to examine four practical questions. First, how many images must be reviewed to retain at least 95% of positive patches, and how much larger is the review set when every positive patch must be detected? Comparing the three input versions and four combination rules at these targets shows the consequences of the detection requirement.

Second, does selecting fewer patches also mean reviewing fewer whole frames? Third, do methods detecting the same number of positive patches select the same examples? Fourth, do thresholds fitted in other parts of the study region retain their detection target in an excluded area? Together, these experiments connect classification results to the choices made in a review workflow.

## 2. DATA AND EVALUATION

### 2.1. DATASET AND INPUT REPRESENTATIONS

We use predictions from our fine-tuned InceptionResNetV2 CNN (FT1), developed in Beker et al. [3]. Initial training used synthetic deformation and noise; fine-tuning adapted the model using real backgrounds with and without added synthetic deformation. FT denotes fine-tuning, and the same FT1 model supplies predictions for all three input versions. This paper evaluates its existing predictions.

The underlying Sentinel-1 observations span October 2014 to June 2020, with individual stacks covering 4.5–5.7 years. After corrections for atmospheric and other errors, multiple observations were combined to estimate average LOS ground-motion rates, expressed in mm/year [3]. A rate map is multiplied by a chosen duration to represent accumulated displacement, then converted into wrapped radar phase between $-\pi$ and $\pi$. Phase wrapping represents displacement through repeating cycles; the colors in the model-input images repeat with those cycles. The LOS-rate maps retain the movement-rate values.

The evaluation dataset contains 775 image patches from 31 cropped frames, with 142 positive and 633 negative labels. A frame is a larger map area from which overlapping patches are extracted. Each 256 × 256-pixel patch covers a square with 51.2 km sides at 200 m spacing. A 64-pixel extraction stride produces 25 patches per frame. Several patches can show parts of the same deformation pattern, so the 142 positive patches are not 142 independent deformation events.

We labeled the frames and reviewed the derived patches, consulting geoscience experts at GFZ when judgments were uncertain. Patches were labeled negative when the visible volcanic deformation was judged insufficiently complete. Negative labels can therefore include partial volcanic signals and non-volcanic motion. Reported detections and false positives are assessed against these reference labels.

The three input versions are FT 5y, FT 4y and filtered FT 5y, the last using the published 50-pixel median-filter condition. The 4y and 5y labels describe rescaling of the same observations. Before wrapping, FT 4y represents 80% of the displacement in FT 5y; this changes the phase pattern presented to the model. Median filtering smooths spatial detail. It can reduce unwanted texture but can also alter weak deformation patterns. Comparing these versions tests whether such processing choices improve screening for the same patches.

The processing sequence rescales each cropped input, applies optional filtering before phase wrapping, and normalizes the result to $[-1, 1]$. These dimensionless input values are distinct from the mm/year values in the LOS-rate maps. All calculations use the existing scores for the same 775 labeled patches; training and prediction are not repeated. Fig. 1 summarizes the workflow from input versions and model scores to review selections and geographic evaluation.

## 2.2. SCREENING THRESHOLDS AND COMBINATION RULES

A flag is a patch selected for expert review because its score meets or exceeds a threshold. It is a request for inspection, not confirmation of volcanic deformation. A flagged patch with a positive reference label is a true positive (TP); a flagged patch with a negative label is a false positive (FP). A positive patch below the threshold is a false negative (FN). The total number of flags is therefore TP + FP.

Recall, TP/(TP + FN), is the fraction of positive patches detected and complements measures of overall discrimination [10]. We use 95% as a common comparison target for methods: on this dataset, it requires 135 of the 142 positive patches, giving 95.07% recall and seven missed positives. Complete recall requires all 142. Comparing these targets reveals how many additional review candidates are needed to recover the final positives.

Each method receives its own threshold. We choose the highest threshold that still meets the recall target, keeping tied scores together. For example, FT 4y at a score threshold of 0.41602227 selects 297 patches: 135 true positives and 162 false positives. Minimum rank at its threshold of 0.500000 selects 251: the same count of 135 true positives and 116 false positives. These cutoffs define the matched-detection comparison; complete recall requires a lower cutoff for each method.

To combine input versions, we first put their scores on a common relative scale, following classifier-combination concepts [11]. A normalized rank expresses where a score lies among a reference collection of scores: values near one are high relative to that collection, and values near zero are low. Equal scores receive the midpoint of their tied positions. A rank describes relative position rather than a calibrated probability of deformation. For score s and reference scores R, we use

$$r(s;R)=\frac{\#\{x\in R: x<s\}+0.5\#\{x\in R: x=s\}}{|R|} \quad (1)$$

Mean rank (3) is the average of the normalized ranks from all three versions: FT 5y, FT 4y and filtered FT 5y. Mean rank (2) averages only FT 4y and filtered FT 5y. The numbers in parentheses therefore state how many versions are combined. Averaging allows a high rank in one version to compensate for a lower rank in another.

Minimum rank takes the lowest of the three ranks. A patch passes only when every version reaches the threshold, requiring agreement across inputs. This may remove selections supported by only one version, but can also reject a positive patch when one version ranks it poorly. Maximum rank takes the highest rank and selects a patch when any version reaches the threshold. These four rules and the three individual input versions give seven methods.

For the screening curves and matched-detection counts, ranks are calculated using all 775 scores for each version, and thresholds are chosen using the corresponding reference labels. This describes the tradeoff attainable on the evaluation dataset. Table 1 gives the cutoffs for the 135-detection comparison; input rows use model scores and combination rows use normalized ranks. The geographic test below estimates ranks and thresholds using other spatial groups instead.

Paired comparisons record which patches change selection. The illustrated cases are the first of each transition in a previously inspected 17-case roster; they explain decisions rather than error frequencies.

## 2.3. FROM PATCHES TO FRAMES

The frame experiment asks whether reducing patch selections also reduces the number of larger maps sent for review. A frame is selected if any patch meets the method's threshold. Its reference label is positive if it contains at least one positively labeled patch. The 31 frames comprise ten positive and 21 negative frames. Overlapping patch selections can collapse into a single frame selection.

We retain each method's threshold for 135/142 positive-patch detections when counting frames, so the comparison changes the review unit without changing patch decisions. We also check whether a positively labeled patch is detected within each positive frame: selecting a frame through a negative patch alone would not establish that its labeled deformation was detected. This any-patch selection rule differs from the weighted spatial fusion used in the original study [3].

## 2.4. TESTING THRESHOLDS ACROSS SPATIAL GROUPS

The geographic experiment asks whether screening settings chosen in other areas retain their detection target. Frames with overlapping footprints are grouped together, including chains of overlap through intermediate frames. Keeping this shared coverage together prevents neighboring views of the same area from entering both the fitting and evaluation sets [12].

We leave out each of the seven groups in turn. Using only the remaining groups, we calculate the rank reference distributions and choose a threshold targeting at least 95% recall. We then apply those settings to the excluded group, whose labels and scores did not enter that fitting step. Repeating this procedure gives one held-out decision for every patch.

Only rank references and thresholds are fitted in these splits; the classifier is unchanged. Independent evaluation must also account for model and rule choices developed using the dataset [13]. We combine decisions from all excluded groups to report recall and selected-patch counts. Groups without positives contribute to review counts but have no defined recall. Overlapping patches are not treated as independent observations in significance tests.

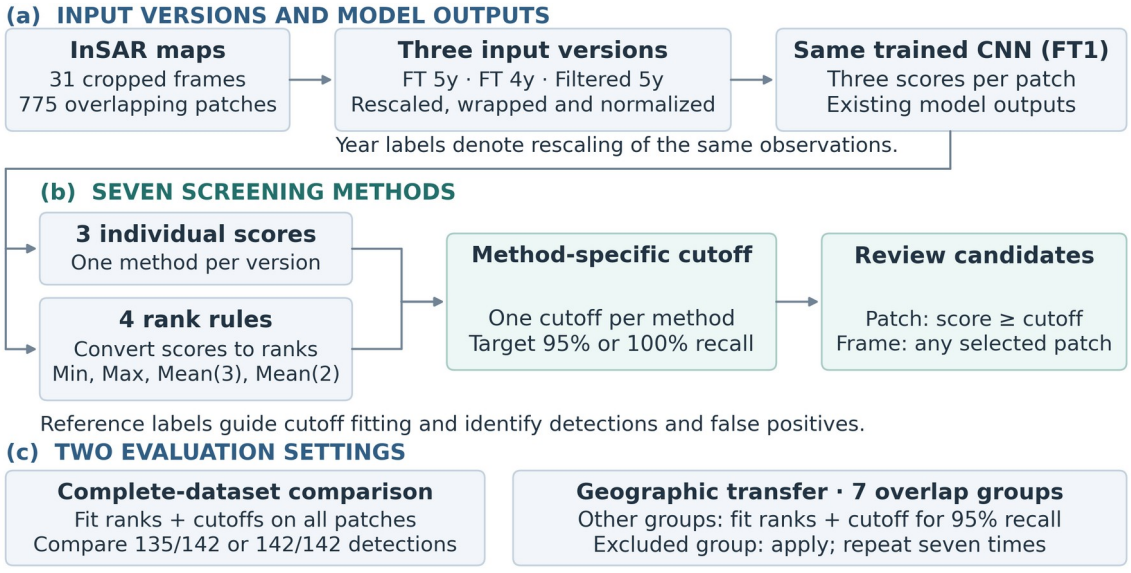


*Fig. 1 Methodology overview: existing model scores, screening choices and evaluation settings. Frame counts use the 95% patch cutoffs. Geographic fitting uses other overlap groups to set rank references and cutoffs; the classifier is unchanged.*

## 3. SCREENING TRADEOFFS

The first experiment compares review counts at the same detection target. At 135/142 detections (95.07%), minimum rank selects 251 patches versus 297 for FT 4y (Fig. 2; Tab. 1). False positives fall from 162 to 116: 46 fewer review candidates (15.5%) and 28.4% fewer false positives. Both methods retain 135 positive patches.

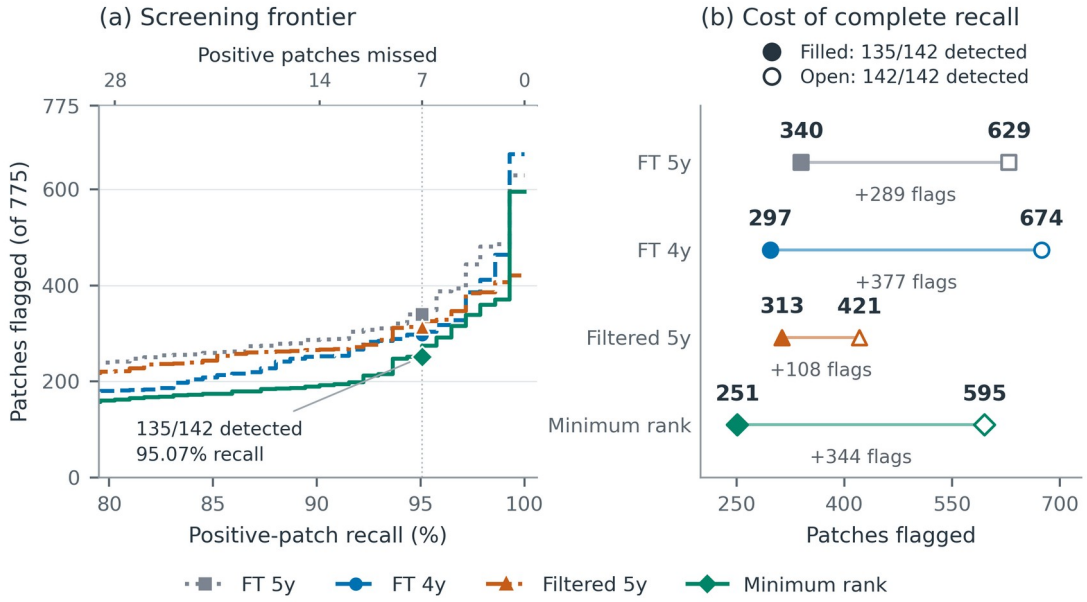


*Fig. 2 Screening tradeoffs on the evaluation dataset. Flags are patches selected for review. (a) Fewest flags at each attainable recall; markers show 135/142 detections; upper axis counts missed positives. (b) Filled/open symbols show 135/142 and 142/142 detections. Thresholds use evaluated labels; year labels denote rescaling.*

*Tab. 1 Thresholds and patch counts on the 775-patch dataset. Cutoffs at 135/142 detections are rounded to six decimals; the 142-detection column uses lower cutoffs. Held recall uses separately fitted geographic thresholds. Exact cutoffs are in the supplement.*

| Method | Cutoff at 135 TP | FP at 135 TP | Selected at 135 TP | Selected at 142 TP | Held recall (%) |
|---|---|---|---|---|---|
| FT 5y | 0.495007 | 205 | 340 | 629 | 92.96 |
| FT 4y | 0.416022 | 162 | 297 | 674 | 97.18 |
| Filtered 5y | 0.029305 | 178 | 313 | 421 | 95.07 |
| Minimum rank | 0.500000 | 116 | 251 | 595 | 92.96 |
| Mean rank (3) | 0.629462 | 128 | 263 | 583 | 92.25 |
| Mean rank (2) | 0.620000 | 135 | 270 | 545 | 93.66 |
| Maximum rank | 0.737419 | 190 | 325 | 516 | 92.25 |

Requiring every positive patch to be detected changes the preferred input. At lower cutoffs, filtered 5y selects 421 patches, minimum rank 595 and FT 4y 674. Recovering the last seven positives adds 108 filtered-input flags and 344 minimum-rank flags. Retaining those positives therefore requires many additional review candidates; analyst time was not measured.

## 4. GEOGRAPHIC THRESHOLD TRANSFER

The geographic experiment transfers settings between seven overlap groups formed by the 31 frame footprints (Fig. 3). G01, G03 and G04 contain 77, 62 and 3 positive patches; the other four contain none. Thus, 139 of 142 positives lie in two groups. Keeping overlapping coverage together avoids fitting and evaluating on neighboring views of the same area.

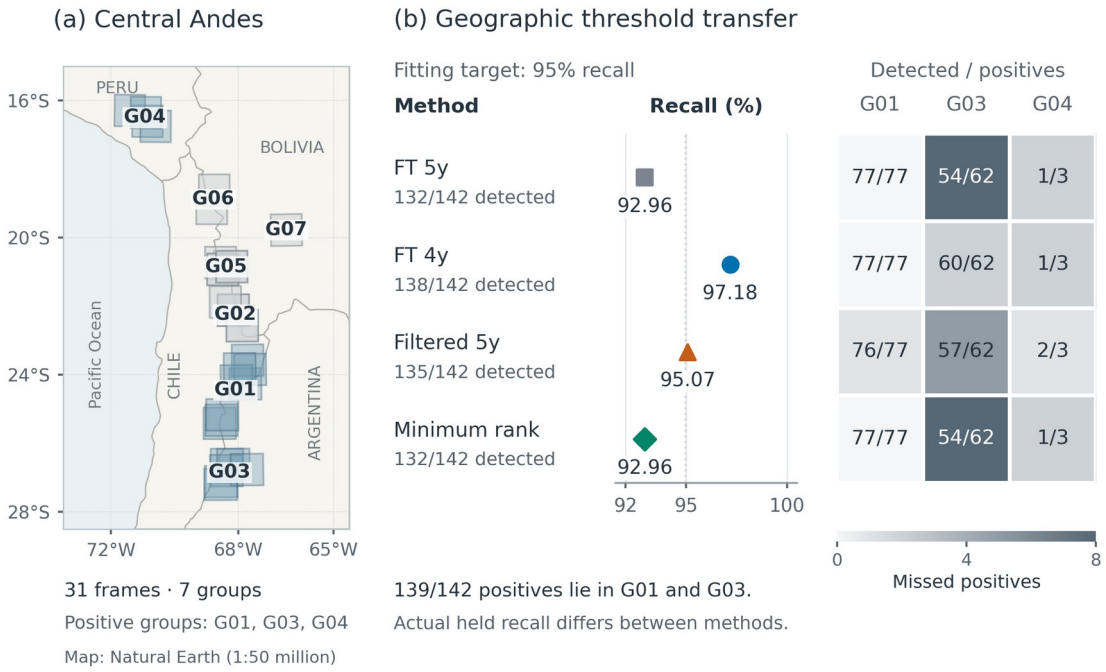


*Fig. 3 Geographic support and threshold transfer. (a) Frame footprints and groups over Natural Earth 1:50m boundaries, version 5.1.1 [14]. SIRGAS-Chile 2016 / UTM 19S footprints are inverse-projected for display. (b) Recall on excluded groups after fitting on other groups to a 95% target. Cells give detected/available positives; shading counts misses. Four groups have no positives. Only rank references and thresholds are fitted.*

When settings are transferred between geographic groups, minimum rank detects 132/142 positive patches (92.96%), compared with 138/142 (97.18%) for FT 4y and 135/142 (95.07%) for filtered 5y. Minimum rank selects fewer patches (260 versus 321 for FT 4y), but it also detects fewer positives. These counts therefore do not establish a reduction in review candidates at equal recall. None of the four combination rules reaches 95% overall held-out recall; their values range from 92.25% to 93.66% (Tab. 1). For minimum rank, detections in G01/G03/G04 are 77/77, 54/62 and 1/3; FT 4y gives 77/77, 60/62 and 1/3. The six-detection difference is concentrated in G03. Both methods detect only one of the three G04 positives. For such a small positive group, the counts communicate the available evidence more clearly than a percentage alone.

A threshold fitted to a 95% target elsewhere does not guarantee 95% detection in the excluded area. The test separates overlapping footprints when fitting rank references and cutoffs, while regional dependence and earlier model choices remain. It assesses transfer of screening settings for the existing outputs. Independently collected data are needed to assess performance beyond this study region.

## 5. DETECTION CHANGES AND ILLUSTRATIVE CASES

The paired experiment checks whether equal detection counts select the same patches. At 135/142 detections, minimum rank removes 71 FT 4y false positives, introduces 25 and retains 91. It loses two positive detections and gains two others (Tab. 2). Fig. 4 illustrates these decision changes.




*Fig. 4 Decisions at 135/142 positive detections: C04, resolved false positive; C13, lost positive; C07, retained false positive. Columns show FT 4y input, filtered FT 5y input and LOS rate. Boxes mark the lowest of all three ranks (FT 5y unshown). Squares are 51.2 km wide, north up; LOS colors saturate beyond ±10 mm/year. Cases illustrate rules, not physical causes or frequencies.*

C04's filtered rank (0.015) removes its false-positive flag. For positive C13, the minimum rank is 0.457, below the 0.500 cutoff, so agreement rejects it. All C07 ranks exceed 0.500, retaining its false-positive flag. C14 is limited by unfiltered FT 5y (0.428); both missed positives share one PEINADO frame.

*Tab. 2 Paired patch selections at the FT 4y and minimum-rank thresholds for 135/142 detections. Yes/No denotes each method's decision; rows count separate groups. The columns total 633 negative and 142 positive patches.*

| FT 4y selected | Minimum-rank selected | Negative patches | Positive patches |
|---|---|---|---|
| No | No | 446 | 5 |
| No | Yes | 25 | 2 |
| Yes | No | 71 | 2 |
| Yes | Yes | 91 | 133 |

## 6. DISCUSSION

For example, the Yes/No row contains 71 negative and two positive patches selected by FT 4y but rejected by minimum rank. Removing 71 false positives and adding 25 gives the net reduction of 46. Each method has its own cutoff. Exchanging two positive detections preserves their count while changing their identity.

Counting whole frames changes the preferred method. At unchanged patch thresholds (Sect. 2.3), FT 4y selects 28/31 frames, minimum rank 24/31 and filtered 5y 22/31, including 18/21, 14/21 and 12/21 negative frames. All seven methods detect a positive patch in every positive frame (10/10). Minimum rank selects the fewest patches; filtered 5y selects the fewest frames. Both missed positives share a frame with other detections. Repeated patch coverage helps explain the change in preferred method.

Input versions, cutoffs and review units should be chosen together, with expert interpretation [1, 2] and lessons from earlier input-combination work [6]. Other applications require their own labels and evaluation; counts alone do not measure review time.

## 7. CONCLUSION

Automated screening helps direct expert attention to candidate images in large InSAR datasets. For 775 patches, agreement across three input versions reduces selections from 297 to 251 relative to FT 4y at 135/142 positive detections, with 46 fewer false positives.

Filtered 5y selects the fewest patches at complete recall and reduces selected frames from 28 to 22 relative to FT 4y at the fixed patch cutoffs. All seven methods detect a positive patch in all ten positive frames. The preferred method depends on the detection target and review unit; equal counts can conceal different detections.

Geographic recall is 92.96% for minimum rank and 97.18% for FT 4y. These findings support choosing inputs and thresholds around the review task, assessing their transfer across areas, and evaluating detection coverage alongside candidate counts and selected examples. Expert interpretation completes the assessment.

### DATA AND CODE AVAILABILITY

A portable local supplement contains the prediction scores used here, reference labels, patch/frame identifiers, overlap groups, source hashes and standalone code reproducing the tables and case annotations. It runs without the original drive or project. Public release remains pending.

## REFERENCES

[1] Biggs J., Anantrasirichai N., Anderson K. R. et al. (2026). Advances in volcano monitoring driven by the first decade of Sentinel-1 observations. Remote Sensing of Environment, 339, 115377. https://doi.org/10.1016/j.rse.2026.115377

[2] Biggs J., Anantrasirichai N., Albino F. et al. (2022). Large-scale demonstration of machine learning for the detection of volcanic deformation in Sentinel-1 satellite imagery. Bulletin of Volcanology, 84, 100. https://doi.org/10.1007/s00445-022-01608-x

[3] Beker T., Ansari H., Montazeri S. et al. (2023). Deep Learning for Subtle Volcanic Deformation Detection With InSAR Data in Central Volcanic Zone. IEEE Transactions on Geoscience and Remote Sensing, 61, 1-20. https://doi.org/10.1109/tgrs.2023.3318469

[4] Anantrasirichai N., Biggs J., Albino F. et al. (2018). Application of Machine Learning to Classification of Volcanic Deformation in Routinely Generated InSAR Data. Journal of Geophysical Research: Solid Earth, 123, 6592-6606. https://doi.org/10.1029/2018jb015911

[5] Anantrasirichai N., Biggs J., Albino F. et al. (2019). A deep learning approach to detecting volcano deformation from satellite imagery using synthetic datasets. Remote Sensing of Environment, 230, 111179. https://doi.org/10.1016/j.rse.2019.04.032

[6] Anantrasirichai N., Biggs J., Albino F. et al. (2019). The Application of Convolutional Neural Networks to Detect Slow, Sustained Deformation in InSAR Time Series. Geophysical Research Letters, 46, 11850-11858. https://doi.org/10.1029/2019gl084993

[7] Gaddes M., Hooper A., Albino F. (2024). Simultaneous Classification and Location of Volcanic Deformation in SAR Interferograms Using a Convolutional Neural Network. Earth and Space Science, 11, e2024EA003679. https://doi.org/10.1029/2024ea003679

[8] Popescu R., Anantrasirichai N., Biggs J. (2025). Unsupervised Anomaly Detection for Volcanic Deformation in InSAR Imagery. Earth and Space Science, 12, e2024EA003892. https://doi.org/10.1029/2024ea003892

[9] Bountos N. I., Papoutsis I., Michail D. et al. (2022). Hephaestus: A large scale multitask dataset towards InSAR understanding. 2022 IEEE/CVF Conference on Computer Vision and Pattern Recognition Workshops (CVPRW), 1452-1461. https://doi.org/10.1109/cvprw56347.2022.00151

[10] Fawcett T. (2006). An introduction to ROC analysis. Pattern Recognition Letters, 27, 861-874. https://doi.org/10.1016/j.patrec.2005.10.010

[11] Kittler J., Hatef M., Duin R. et al. (1998). On combining classifiers. IEEE Transactions on Pattern Analysis and Machine Intelligence, 20, 226-239. https://doi.org/10.1109/34.667881

[12] Roberts D. R., Bahn V., Ciuti S. et al. (2017). Cross-validation strategies for data with temporal, spatial, hierarchical, or phylogenetic structure. Ecography, 40, 913-929. https://doi.org/10.1111/ecog.02881

[13] Cawley G. C., Talbot N. L. C. (2010). On Over-fitting in Model Selection and Subsequent Selection Bias in Performance Evaluation. Journal of Machine Learning Research, 11, 2079–2107. https://www.jmlr.org/papers/v11/cawley10a.html

[14] Natural Earth. Admin 0 – Countries, 1:50m, version 5.1.1. https://www.naturalearthdata.com/downloads/50m-cultural-vectors/50m-admin-0-countries-2/ (accessed 3 October 2026).

https://doi.org/10.24867/INDIS-2026-EN-057



# CONTROLLING LARGE CONVERGENCES IN SQUEEZING GROUND – A CASE STUDY OF THE IRIŠKI VENAC TUNNEL

*Milan Uljarević[1], Andrija Rašeta[2], Dragan Bojović[3]*

***Summary:***

The paper presents the experience gained in controlling large convergences during the NATM excavation of the twin-tube Iriški Venac road tunnel in Serbia. In intensely fractured Cretaceous claystones and siltstones (RMR 17–18, GSI 10–20) under about 215 m of overburden, convergences reached approximately 450 mm despite the heaviest design support classes. Two successive series of 6 m and 8 m long radial anchors did not reduce the deformation rate, and extensometers showed that the yielded zone extended beyond the anchors. The convergence rate dropped from about 10 mm/day to below 0.5 mm/day only after invert closure. The support concept was therefore shifted from ground reinforcement to structural resistance, using closed HEA200 steel rib rings and early ring closure. The governing mechanisms and the lessons learned are discussed.

*Keywords: Tunnel, squeezing ground, large convergence, NATM, ring closure, steel ribs*

# KONTROLA VELIKIH KONVERGENCIJA PRI ISTISKIVANJU STENSKE MASE – STUDIJA SLUČAJA TUNELA IRIŠKI VENAC

***Rezime:***

U radu je prikazano iskustvo u kontroli velikih konvergencija tokom iskopa dvocevnog drumskog tunela Iriški Venac primenom NATM-a. U intenzivno ispucalim krednim glincima i alevrolitima (RMR 17–18, GSI 10–20), pri nadsloju od oko 215 m, konvergencije su dostigle oko 450 mm uprkos primeni najjačih projektovanih kategorija podgrade. Dve uzastopne serije radijalnih ankera dužine 6 m i 8 m nisu smanjile brzinu deformacija, a ekstenzometri su pokazali da se plastifikovana zona prostire izvan ankera. Brzina konvergencije opala je sa oko 10 mm/dan na manje od 0,5 mm/dan tek nakon zatvaranja podnožnog svoda. Koncept podgrade je zato promenjen od ojačanja stenske mase ka konstruktivnoj nosivosti, primenom zatvorenih prstenova od čeličnih lukova HEA200 i ranog zatvaranja prstena. Razmatrani su merodavni mehanizmi i stečena iskustva.

*Ključne reči: Tunel, istiskivanje stenske mase, velike konvergencije, NATM, zatvaranje prstena, čelični lukovi*

[1] MSc CE, PhD candidate, Power China – Stecol, Novi Sad, Serbia, umilan89@gmail.com, ORCID 0009-0002-7627-1790
[2] Assoc. Prof., Faculty of Technical Sciences, University of Novi Sad, Novi Sad, Serbia, araseta@gmail.com
[3] Principal Research Fellow, Institute for Testing of Materials IMS, Belgrade, Serbia, dragan.bojovic@institutims.rs

## 1. INTRODUCTION

The New Austrian Tunnelling Method (NATM) is based on the principle that the ground surrounding an opening is not only a source of load but also the main load-bearing element. A relatively flexible primary support, composed mainly of shotcrete and rock bolts, is installed in good time to mobilise the self-supporting capacity of the rock mass, while the deformation response is continuously monitored and the support is adjusted to the encountered conditions [1–3]. Within this framework, lattice girders and steel ribs are regarded as auxiliary elements that provide early support before the shotcrete hardens and ensure the correct profile geometry [2, 4].

This concept performs well as long as the rock mass retains sufficient strength in relation to the in situ stress. When the ratio of rock mass strength to in situ stress becomes low, the ground around the opening yields over a large zone and squeezing develops: large, time-dependent convergences, overstressing of the support, loss of the excavation profile and, in extreme cases, collapse [5, 6]. Two basic strategies are available in such conditions – to allow controlled deformation by means of yielding support, or to resist the ground pressure by a stiff support system combined with pre-confinement of the face and early closure of the support ring [5, 7]. The appropriate choice depends, among other things, on whether ground reinforcement by rock bolts can actually be mobilised.

This paper presents a case study of the Iriški Venac tunnel in Serbia, where large convergences were recorded in a zone of intensely fractured claystones and siltstones. The geological setting, the observed behaviour of the ground and of the original support, the interpretation of the monitoring data and the resulting change of the support concept are described. The emphasis is on practical engineering reasoning based on field observations, with the aim of summarising lessons that may be useful for similar projects.

## 2. THE IRIŠKI VENAC TUNNEL

### 2.1. PROJECT OVERVIEW

The Iriški Venac tunnel is the central structure of the Fruška Gora Corridor, a new state road approximately 47.7 km long which crosses the Fruška Gora mountain and the Danube between Novi Sad and Ruma. The tunnel consists of two tubes, each approximately 3,550 m long, which makes it the longest road tunnel in Serbia. The excavated cross-section is approximately 110 m², and the tubes are connected by 12 cross-passages (9 pedestrian and 3 vehicular). The alignment runs entirely within the Fruška Gora National Park, a protected area since 1960, so that the works had to be planned and executed with strict environmental requirements and minimal surface disturbance.

The tunnel was excavated by NATM. Depending on the support class, the primary support consisted of shotcrete C25/30 with a thickness of 100–350 mm reinforced with wire mesh, self-drilling radial anchors 4–8 m long, and lattice girders or steel ribs, supplemented by forepoling or a pipe umbrella in the weakest ground. The secondary lining is a 350 mm thick concrete C25/30 shell, reinforced in zones with higher expected loads.

## 2.2. GEOLOGICAL AND GEOTECHNICAL CONDITIONS

The geotechnical investigations comprised 12 boreholes with a total length of 1,105 m. They revealed pronounced geological heterogeneity, with frequent lithological changes over short distances: competent Miocene limestones and dolomites, weak and sheared serpentinites, highly deformable marls and claystones, and numerous tectonised contact zones. Sixteen fault zones were predicted along the alignment, and several karstified limestone sections were identified as water-bearing. During excavation, local groundwater inflows of 1,500–2,500 L/min were indeed encountered in fractured limestone.

The section discussed in this paper was excavated through Cretaceous claystones with interlayers of siltstone (alevrolite) and sandstone. The rock mass was intensely fractured and locally crushed, with slickensided discontinuities and soft, completely decomposed infilling. Geological face mapping in this zone gave RQD ≈ 10 %, uniaxial compressive strength of the intact rock estimated at less than 5 MPa, RMR = 17–18, i.e. rock mass class V – very poor rock [8], and GSI = 10–20 [6]. The overburden was approximately 215–218 m and the face was generally dry, while small block falls from the face and the crown were common.

# 3. OBSERVED BEHAVIOUR OF THE GROUND AND THE ORIGINAL SUPPORT

## 3.1. SUPPORT AND EXCAVATION SEQUENCE

The critical section was excavated with support types 5b and 6, the heaviest support categories envisaged by the design. Both types consisted of a reinforced shotcrete shell with lattice girders and systematic self-drilling radial anchors, 6 m long in type 5b and 8 m long in type 6, while a pipe umbrella was used in the most demanding sections. The cross-section was excavated in top heading, bench and invert, so that the support ring was closed at a certain distance behind the face.

## 3.2. MONITORING RESULTS

Displacements of the primary lining were measured by systematic 3D optical monitoring of convergence sections. Along most of the alignment the measured convergences did not exceed approximately 150 mm. In the zone of fractured claystones and siltstones, however, convergences reached approximately 450 mm and showed a continuous increasing trend over an extended period, despite the application of support types 5b and 6. Cracking, spalling and local buckling of the shotcrete shell were observed, particularly in the sidewalls and at the junction between the top heading and the bench (Fig. 1). Such deformations reduce the clearance for the secondary lining, require reprofiling and threaten both construction safety and the schedule.



(a) (b)

*Fig. 1 Deformation of the primary lining in the squeezing zone: (a) sidewall at the top heading – bench junction; (b) buckled and spalled shotcrete shell*

### 3.3. SEVERITY OF SQUEEZING

The severity of squeezing can be assessed by the tunnel strain $\varepsilon$, defined as the percentage ratio of tunnel closure to tunnel diameter [5, 6]:

$$\varepsilon = 100 \cdot \frac{C}{D_{eq}} \ [\%] \tag{1}$$

where $C$ is the measured convergence (shortening of the measuring chord) and $D_{eq}$ is the diameter of a circle with the same area $A$ as the excavated cross-section:

$$D_{eq} = \sqrt{\frac{4\,A}{\pi}} \tag{2}$$

For $A \approx 110$ m², Eq. (2) gives $D_{eq} \approx 11.8$ m. Since the zero reading of a convergence section is taken after the face has passed, the part of the displacement that develops ahead of and at the face – typically one quarter to one third of the final value [9] – is not recorded. The strains in Tab. 1 are therefore lower-bound values. Even so, the critical zone falls into class C – severe squeezing problems [6], and the strains are well above the level of approximately 1 % that Sakurai [10] associated with the onset of support difficulties.

*Tab. 1 Squeezing classification of the measured convergences according to Hoek and Marinos [6]*

| Section | Convergence $C$ [mm] | Strain $\varepsilon$ [%] | Class [6] |
|---|---|---|---|
| Typical sections | ≤ 150 | ≤ 1.3 | A–B: few support problems to minor squeezing |
| Monitoring section (Fig. 3) | 313 | 2.6 | C: severe squeezing |
| Most critical sections | ≈ 450 | ≈ 3.8 | C: severe squeezing |

## 4. INTERPRETATION OF THE MONITORING DATA

### 4.1. ANCHORS AND THE EXTENT OF THE PLASTIC ZONE

Extensometers installed in the critical sections showed that displacements of the rock mass extended beyond the anchorage length, i.e. beyond both the 6 m and the 8 m long anchors of support types 5b and 6. This finding is essential for understanding the support mechanism. The effectiveness of radial bolting depends on the length of the bolts relative to the thickness of the plastic zone around the opening [7]. If the bolts extend beyond the plastic zone, their ends are anchored in undisturbed, elastically behaving ground and they provide direct confinement of the cavity (Fig. 2a). If the bolts are shorter than the plastic zone, they are fully embedded in yielded material and can act only indirectly, by stiffening the reinforced plastic ring (Fig. 2b). In an intensely fractured rock mass with a low residual strength this indirect effect is small, and the support then depends mainly on the shotcrete shell with embedded lattice girders – a relatively flexible structure whose stiffness is low at early age. This agrees with the observation of Hoek [5] that squeezing is associated with very poor quality rock masses in which rock bolts are ineffective.

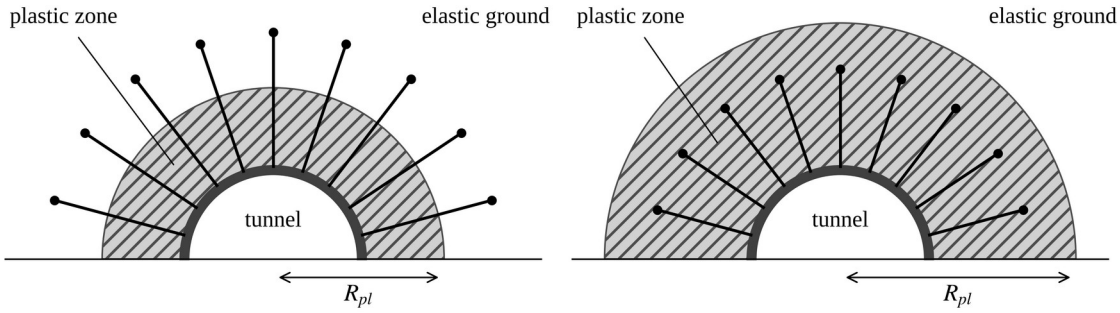


(a) $L > R_{pl} - R$: anchor ends in stable ground (b) $L < R_{pl} - R$: anchors fully within yielded ground

*Fig. 2 Effect of anchor length L relative to the plastic radius $R_{pl}$ (R – tunnel radius), after the concept described by Lunardi [7]*

### 4.2. EFFECT OF ANCHORS AND OF INVERT CLOSURE

Fig. 3 shows the convergence of a representative monitoring section in the critical zone. The section was initially supported with 6 m long anchors (type 5b), installed at the time of the zero reading. Since the deformations continued, a second series of 8 m long anchors was added after 14 days. Neither intervention reduced the deformation rate: the convergence developed at approximately 9 mm/day during the first 14 days and at approximately 17 mm/day during the following week, concurrently with the excavation of the lower parts of the cross-section. The rate began to decrease in the week preceding ring closure (approximately 4 mm/day). After the invert was concreted and the support ring was closed (day 28), it fell to approximately 2 mm/day in the first week and averaged less than 0.5 mm/day over the remaining 84 days, i.e. about twenty times less than the average of approximately 10 mm/day between the second anchor series and ring closure. Of the total 313 mm recorded after 112 days, about 88 % occurred before ring closure.

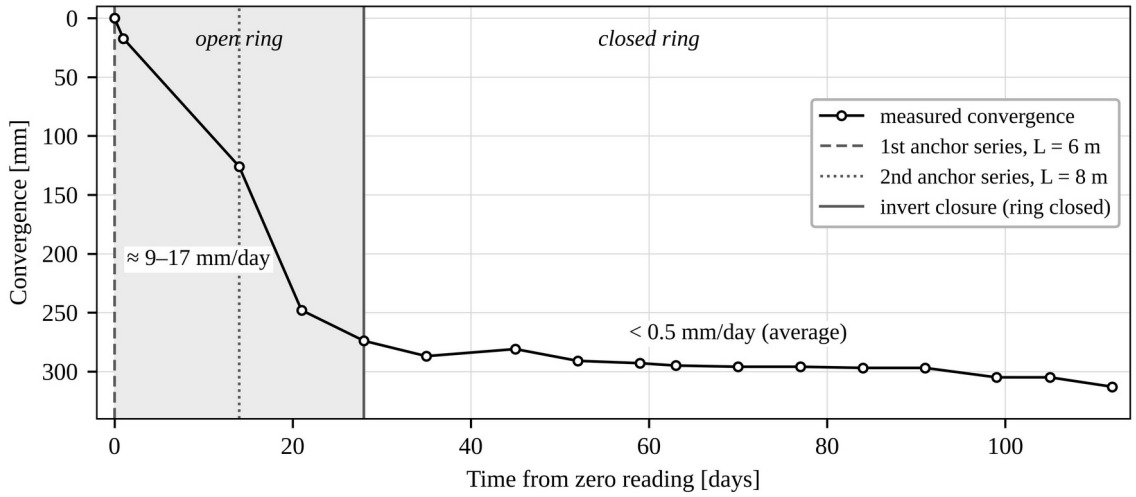


*Fig. 3 Convergence – time diagram of a monitoring section in the squeezing zone of the Iriški Venac tunnel*

The decisive change in the deformation rate thus coincided with the closure of the ring and not with the installation of the anchors. This field evidence is consistent with the extensometer results: in the critical zone the excavation was stabilised by the ring action of the support, while the contribution of the anchors was marginal. It also confirms the value of evaluating displacement rates and trends, and not only absolute values, when decisions about support adjustments are made during construction [11].

## 5. ENGINEERING RESPONSE: A STIFF CLOSED-RING SUPPORT

### 5.1. CHANGE OF THE SUPPORT CONCEPT

The monitoring results indicated that the basic assumption of the original support concept – the transfer of load from the yielded ground to the stable rock mass through anchors – was not fulfilled in the critical zone. Adding more or longer anchors would therefore not have solved the problem. Instead, the support philosophy was changed from one based on the participation of the reinforced rock mass towards one based on the structural resistance of the support itself. Steel ribs acting as primary load-bearing members are, in fact, the oldest form of tunnel support [12], and modern case histories from squeezing ground confirm that stiff closed support rings combined with appropriate excavation measures can substantially reduce convergences [13].

### 5.2. COMPOSITION OF THE NEW SUPPORT TYPE

On this basis, a new support type designated 5b.1 was introduced for the critical sections (Tab. 2, Fig. 4). Its main load-bearing element is a closed ring of HEA200 steel ribs at a spacing of not more than 0.80 m, embedded in 300 mm of shotcrete reinforced with two layers of R424 mesh. The radial self-drilling anchors were reduced to R32N, 3.0 m long; their purpose is no longer deep ground reinforcement but local confinement of the rock immediately behind the lining and good contact between the ground and the support. A combination of 3 m and 6 m long anchors was kept as an option. Type 5b.1 is the stiffest support type applied in the tunnel.

*Tab. 2 Comparison of the original and the modified support concept*

| Feature | Types 5b and 6 (original) | Type 5b.1 (modified) |
|---|---|---|
| Governing mechanism | Ground reinforcement, flexible shell | Structural resistance of a stiff ring |
| Radial anchors | Systematic SDA, $L$ = 6 m (5b) and 8 m (6) | SDA R32N, $L$ = 3.0 m (optionally 3 + 6 m) |
| Steel elements | Lattice girders | HEA200 ribs, closed ring, $e$ ≤ 0.80 m |
| Shotcrete | Reinforced shotcrete shell | 300 mm, two layers of mesh R424 |
| Face and pre-support | Pipe umbrella in the weakest sections | Full-face with face reinforcement, or staged with temporary footings |
| Ring closure | At a distance behind the face | Early, as close to the face as possible |

Type 5b.1 can be executed either full-face, with core-face reinforcement, or in stages with temporary support measures. Full-face excavation is preferred because it allows the complete support ring to be installed immediately behind the face and minimises the unsupported length, while the reinforced core-face limits the extrusion and the pre-convergence that develop ahead of the face [7, 14].

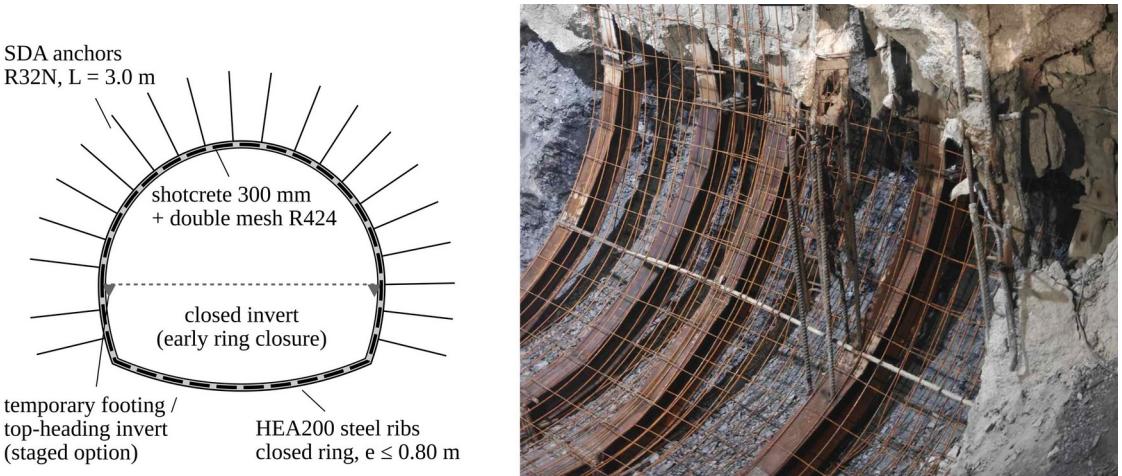


*Fig. 4 Support type 5b.1: (a) principal scheme of the cross-section; (b) HEA200 steel ribs in the invert before shotcreting*

## 5.3. EARLY RING CLOSURE AND TEMPORARY FOOTINGS

The performance of a heavy steel rib support depends fundamentally on the formation of a closed ring. Without the invert, the ribs act as open frames subjected to large bending moments, with a tendency towards settlement and inward movement of their feet. Once the ring is closed, the support works predominantly in compression and its stiffness and load-carrying capacity increase considerably. Ring closure as early as possible was therefore defined as a mandatory requirement for type 5b.1. When staged excavation is unavoidable, the rib footings must be temporarily supported – by enlarged

footings, a temporary top-heading invert or feet-lock pipes – in order to limit the settlement and rotation of the ribs until the invert is completed. Analytical and field studies show that feet-lock pipes effectively reduce the load concentration and settlement at the foot of steel ribs in weak ground [15].

### 5.4. ROLE OF LIGHT STEEL ELEMENTS IN THE INVERT

It should be emphasised that the ring is closed by the concrete invert itself, and not by light steel elements embedded in it. The contribution of a lattice girder to the stiffness of a shotcrete lining can be estimated by the rule of mixtures:

$$E_{eq} = (1 - \rho) E_c + \rho E_s \tag{3}$$

where $E_c$ and $E_s$ are the moduli of elasticity of shotcrete and steel and $\rho$ is the ratio of the steel area to the cross-sectional area of the lining, averaged per metre of tunnel length. For young shotcrete with $E_c$ = 15 GPa, $E_s$ = 200 GPa and a typical ratio $\rho$ = 0.3 % (one girder per 1 m round), Eq. (3) gives $E_{eq} \approx 15.6$ GPa, i.e. an increase of only about 4 %. The girder thus adds little stiffness that could not be provided equally well by conventional reinforcement. This was confirmed in the tunnel by a 10 m long trial section in soft ground (RMR ≈ 20), in which the lattice girders in the invert were replaced by conventional reinforcement. The convergence stopped shortly after the invert was concreted, in the same way as in the adjacent sections with lattice girders. Similar detailing, with steel arches in the top heading and bench and a shotcrete invert reinforced with two layers of mesh, was used in the design of the Ljubno tunnel in Slovenia [16]. Light lattice girders in the invert can therefore be replaced by conventional reinforcement, while heavy steel ribs are justified where high stiffness is required immediately, before the shotcrete gains strength.

## 6. DISCUSSION AND LESSONS LEARNED

The case of the Iriški Venac tunnel shows that the response of the ground to the applied support measures, rather than the nominal strength of the support class, should govern decisions in squeezing ground. The main observations and their practical implications are summarised in Tab. 3.

*Tab. 3 Observations from the Iriški Venac tunnel and their practical implications*

| Observation | Implication for design and construction |
|---|---|
| Deformation rate unchanged after installation of additional or longer anchors | Verify the extent of the plastic zone by extensometers before relying on further bolting |
| Sharp drop in deformation rate after invert closure | Ring closure governs stability; minimise the time and distance to closure |
| Lower-bound tunnel strain above 2.5 % | Severe squeezing; flexible support classes are insufficient and a stiffer or yielding concept is required |
| Settlement and inward movement of rib feet in staged excavation | Provide temporary footings or feet-lock pipes until the invert is completed |
| Similar response with and without lattice girders in the invert | Light girders add little stiffness and can be replaced by conventional reinforcement |

An alternative to the adopted resistance-based solution would have been a yielding support with deformable elements, which allows larger controlled convergences and reduces the ground pressure acting on the lining [5]. Such a solution, however, requires a corresponding overexcavation and a reliable prediction of the final deformation. In the Iriški Venac tunnel, where the convergences had already reduced the clearance and the aim was to preserve the excavation profile, a stiff closed ring with early closure was considered the more robust choice.

It should also be noted that heavy steel ribs are not a universal solution. In competent ground, where anchors can develop their capacity beyond the plastic zone, the classical flexible NATM support remains more economical and more efficient, and steel elements should retain their auxiliary role [2, 4]. The decision to change the support concept must therefore be based on monitoring evidence, as in the case presented here.

## 7. CONCLUSIONS

Based on the experience from the Iriški Venac tunnel, the following conclusions can be drawn:

- in intensely fractured claystones and siltstones under approximately 215 m of overburden, convergences reached approximately 450 mm and the lower-bound tunnel strain (≈ 3.8 %) corresponded to severe squeezing, although the heaviest design support classes were applied,
- extensometers showed that the yielded zone extended beyond the 6 m and 8 m long anchors, which explains why the additional anchor series did not reduce the convergence rate,
- the convergence rate decreased from approximately 10 mm/day to less than 0.5 mm/day only after the invert was closed, which indicates that stability was governed by ring action,
- the support concept in the critical zones was therefore changed from ground reinforcement to structural resistance by introducing support type 5b.1 with closed HEA200 steel rib rings, 300 mm of reinforced shotcrete and short radial anchors,
- early ring closure and temporary support of the rib footings are essential conditions for the effectiveness of a stiff steel rib support, whereas light lattice girders in the invert contribute little and can be replaced by conventional reinforcement.

The presented approach – continuous evaluation of displacement trends, verification of the anchorage conditions and a timely change of the support concept – can be recommended for other tunnels in weak, squeezing rock masses.

## REFERENCES

[1] Rabcewicz L. (1964–1965). The New Austrian Tunnelling Method, Parts 1–3. *Water Power*, Volume 16, pp. 453–457 and 511–515; Volume 17, pp. 19–24.

[2] Austrian Society for Geomechanics (2010). *NATM – The Austrian Practice of Conventional Tunnelling*, Austrian Society for Geomechanics, Salzburg, Austria.

[3] Kovačević J. (2014). *Savremeno građenje u podzemlju* (in Serbian), AGM knjiga, Belgrade, Serbia.

[4] Federal Highway Administration (2009). *Technical Manual for Design and Construction of Road Tunnels – Civil Elements*, Publication No. FHWA-NHI-10-034, U.S. Department of Transportation, Washington, D.C., USA.

[5] Hoek E. (2001). Big tunnels in bad rock. *Journal of Geotechnical and Geoenvironmental Engineering*, Volume 127, No. 9, pp. 726–740. https://doi.org/10.1061/(ASCE)1090-0241(2001)127:9(726)

[6] Hoek E., Marinos P. (2000). Predicting tunnel squeezing problems in weak heterogeneous rock masses. *Tunnels and Tunnelling International*, Volume 32, No. 11, pp. 45–51 (Part 1) and No. 12, pp. 33–36 (Part 2).

[7] Lunardi P. (2008). *Design and Construction of Tunnels – Analysis of Controlled Deformations in Rock and Soils (ADECO-RS)*, Springer, Berlin, Germany. https://doi.org/10.1007/978-3-540-73875-6

[8] Bieniawski Z. T. (1989). *Engineering Rock Mass Classifications*, John Wiley & Sons, New York, USA.

[9] Vlachopoulos N., Diederichs M. S. (2009). Improved longitudinal displacement profiles for convergence confinement analysis of deep tunnels. *Rock Mechanics and Rock Engineering*, Volume 42, No. 2, pp. 131–146. https://doi.org/10.1007/s00603-009-0176-4

[10] Sakurai S. (1983). Displacement measurements associated with the design of underground openings. *Proceedings of the International Symposium on Field Measurements in Geomechanics*, Zurich, Switzerland, 5–8 September, Volume 2, pp. 1163–1178.

[11] ITA Working Group 2 (2011). *Monitoring and Control in Tunnel Construction*, ITA Report No. 9, ITA-AITES, Lausanne, Switzerland.

[12] Proctor R. V., White T. L. (1946). *Rock Tunneling with Steel Supports, with an Introduction to Tunnel Geology by Karl Terzaghi*, The Commercial Shearing and Stamping Co., Youngstown, Ohio, USA.

[13] Li S., Tan Z., Wang Y., Yang Y. (2024). Large deformation failure characteristics and control measures for squeezing tunnels with steeply inclined and layered rock in strong and active fault zones: a case study. *International Journal of Civil Engineering*, Volume 22, pp. 1771–1790. https://doi.org/10.1007/s40999-024-00953-6

[14] Panet M. (2023). *The Tunnel Behavior at the Face of Excavation*, Muir Wood Lecture 2023, ITA-AITES, Lausanne, Switzerland.

[15] Chen L., Chen J., Luo Y., Li Y., Hu T. (2019). Vertical load and settlement at the foot of steel rib with the support of feet-lock pipe in soft ground tunnel. *Advances in Civil Engineering*, Volume 2019, Article ID 6186748. https://doi.org/10.1155/2019/6186748

[16] Likar J., Likar A., Žarn J., Marolt Čebašek T. (2015). Analysis of shallow tunnels construction in swelling grounds. *RMZ – Materials and Geoenvironment*, Volume 62, pp. 175–191.

# CIVIL ENGINEERING

iNDiS 2026

https://doi.org/10.24867/INDIS-2026-EN-068



# STRUCTURAL INTEGRITY ASSESSMENT OF CIVIL ENGINEERING CONSTRUCTIONS – TWO CASE STUDIES

*Aleksandar Sedmak[1], Simon Sedmak[2], Dorin Radu[3], Dragan Bojović[4], Boris Folic[2]*

***Summary:***

Structural integrity of civil engineering constructions evolved in last 4,500 years from antient wonders, best represented by pyramids in Egypt to the modern wonders, such as Burj Kalifa in Dubai. In the meantime, bridges, dams, temples, buildings and other spectacular and beautiful construction have proved human ingeniosity and ever-lasting desire to reach stars, at least symbolically. In this paper two civil constructions are briefly analysed (historical steel bridge in Transylvania and prestressed concrete dome of the Hall 1 of the Belgrade fair), mostly from the point of view of structural integrity.

*Keywords: Structural integrity, Civil engineering constructions, Historical steel bridge, Prestressed concrete dome, Hall 1 of the Belgrade fair, cracks*

# PROCENA INTEGRITETA GRAĐEVINSKIH KONSTRUKCIJA – DVE STUDIJE SLUČAJA

***Rezime:***

Integritet građevinskih konstrukcija evoluirao je u poslednjih 4.500 godina od antičkih čuda, najbolje predstavljenih piramidama u Egiptu, do modernih čuda, poput Burž Kalife u Dubaiju. U međuvremenu, mostovi, brane, hramovi, zgrade i druge spektakularne i lepe građevine dokazale su ljudsku domišljatost i večnu želju da se dosegnu zvezde, barem simbolično. U ovom radu su ukratko analizirane dve građevinske konstrukcije (istorijski čelični most u Transilvaniji i prenapregnuta betonska kupola hale 1 na Beogradskom sajmu), uglavnom sa stanovišta integriteta.

*Ključne reči: Integritet konstrukcija, Građevinske konstrukcije, Istorijski čelični most, Prenapregnuta betonska kupola, Hale 1 Beogradskog sajma, prsline*

[1] Prof. emeritus, Faculty of Mechanical Engineering, University of Belgrade, Serbia, asedmak@mas.bg.ac.rs 0000-0002-5438-1895
[2] Senior scientific researcher, Innovation center of the Mechanical Engineering, Belgrade, Serbia, simon.sedmak@yahoo.com, 0000-0002-2674-541X, boris.folic@gmail.com, 0000-0003-2127-0264
[3] Assoc. Prof., Faculty of Civil Engineering, University of Transilvania, Brasov, Romania, dorin.radu@unitbv.ro, 0000-0001-5043-2723
[34] Senior scientific researcher, Institute IMS, Belgrade, Serbia, dragan.bojovic@institutims.rs 0000-0002-4900-6177

## 1. INTRODUCTION

The term “structural integrity” has been introduced to prevent important problems in the case of failure, often without warning. As a scientific discipline, structural integrity was established in the early Eighties of XX Century, to solve the problem of unacceptable defects in Alaska pipeline, [1, 2]. It has been based on application of fracture mechanics parameters, such as stress intensity factor, K, crack tip opening displacement, CTOD, and J integral, comparing their values as crack driving forces vs. material resistance to crack growth, providing useful tool to assess integrity of a structure with a crack, [2]. One of the most commonly used tools is so-called Failure Assessment Diagram (FAD), based on elastic-plastic behaviour of material, combining thereby the stress intensity factor and CTOD into a single criterion, leading also to risk-based assessment of structural integrity, [3-8]. One should keep in mind that structural integrity analysis is not limited to cracked components only, but rather to any construction if crack existence is just assumed, [9]. This is reasonable assumption keeping in mind the fact that not all defects are always detected and especially important one if crack can initiate during service due to corrosion, fatigue or any other mechanism, including their combined action.
This approach is explained and illustrated here using two case studies, prestressed concrete dome of the Hall 1 at the Belgrade Fair, the masterpiece of Serbian legendary civil engineer, professor and academician Branko Žeželj, [10], and the old steel bridge in Transylvania, [11, 12].

## 2. FAILURE ASSESSMENT DIAGRAM AND RISK MATRIX

The FAD maps a cracked component state into a 2D coordinate system where the horizontal axis is a normalized net stress and the vertical axis is a normalized crack driving force. The relative position of the service point with respect to the FAD limit curve indicates likelihood of failure, [13, 14]. Normalized net stress ratio (X coordinate) is defined as:

$$S_r = \frac{\sigma_n}{\sigma_c} \tag{5}$$

where $\sigma_n$ is the net-section (nominal) stress and $\sigma_c$ is the critical stress. Normalized stress intensity factor ratio (Y coordinate) is defined as:

$$K_r = \frac{K_I}{K_{Ic}} \tag{6}$$

where $K_I$ is the stress intensity factor for the crack and $K_{Ic}$ is the fracture toughness. The FAD limit curve defines safe and non-safe regions: assessment points lying below the curve are considered SAFE, Fig. 1. It is defined by the following expression, [2]:

$$K_r = S_r \left[ \frac{8}{\pi^2} \ln \sec\left( \frac{\pi}{2} S_r \right) \right]^{\frac{-1}{2}} \tag{7}$$

The FAD can also be used as a probability/likelihood measure: using a simple ratio OA/OB, Fig. 1, one can see how close a service point is to failure, [13, 14], and by reasoning that likelihood is 0 at (0,0) point and 1 at point B, conclude that in between there is the linear correlation between them.

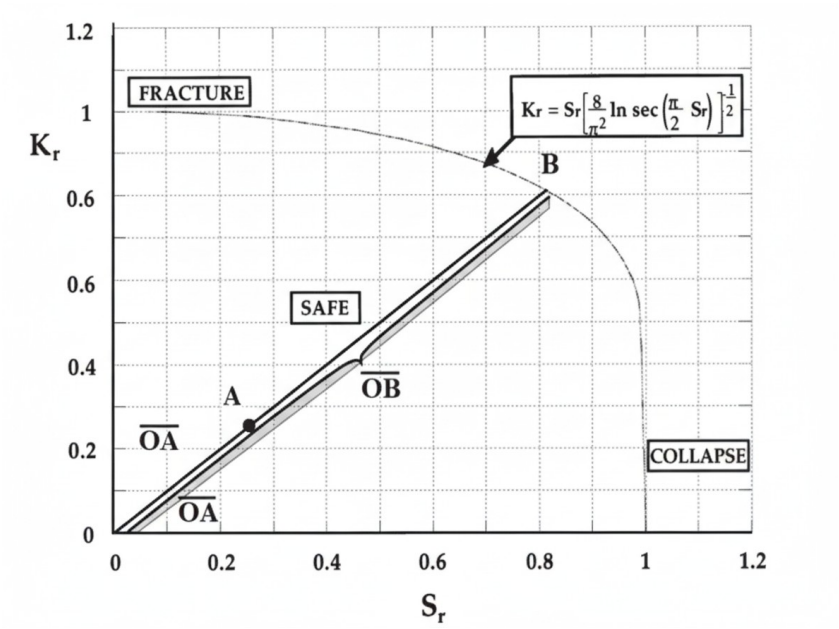


*Figure 1. FAD with service point A and corresponding point on limit curve, [14]*

## 3. PRESTRESSED CONCRETE DOME

Prestressed dome of the Hall 1 of the Belgrade Fair was designed by a Serbian scientist, engineer, inventor and academic Branko Žeželj, one of the founders of the Institute for testing of materials IMS in Belgrade.
Basic dimensions of the Dome are: height of 27.8 m and diameter of 106 m. The upper galleries around the perimeter, which are 4.7 m and 8.7 m above the ground, form the outer contour of the Hall 1 enclosed by glass walls, 117 m in diameter.
For Hall 1 of the Belgrade Fair and Žeželj's (Arch) Bridge in Novi Sad Prof. Branko Žeželj was awarded The Gold medal FIP (Fédération Internationale de la Précontrainte - International Federation for Prestressing) in the 60s of XX century. In 2009, an official decree by the Government of the Republic of Serbia declared the Hall 1 a monument of culture. Every year Institute IMS gets the Guinness World Records certificate for the largest prestressed concrete dome in the world, Fig. 2.




*Figure 2. Guinness certificate*

Prestressed concrete dome of the Belgrade Fair Hall is shown as a cross section of the foundation in Fig. 3a, cross section of the roof, Fig. 3b and cross section of (semi) arch at the bottom right.

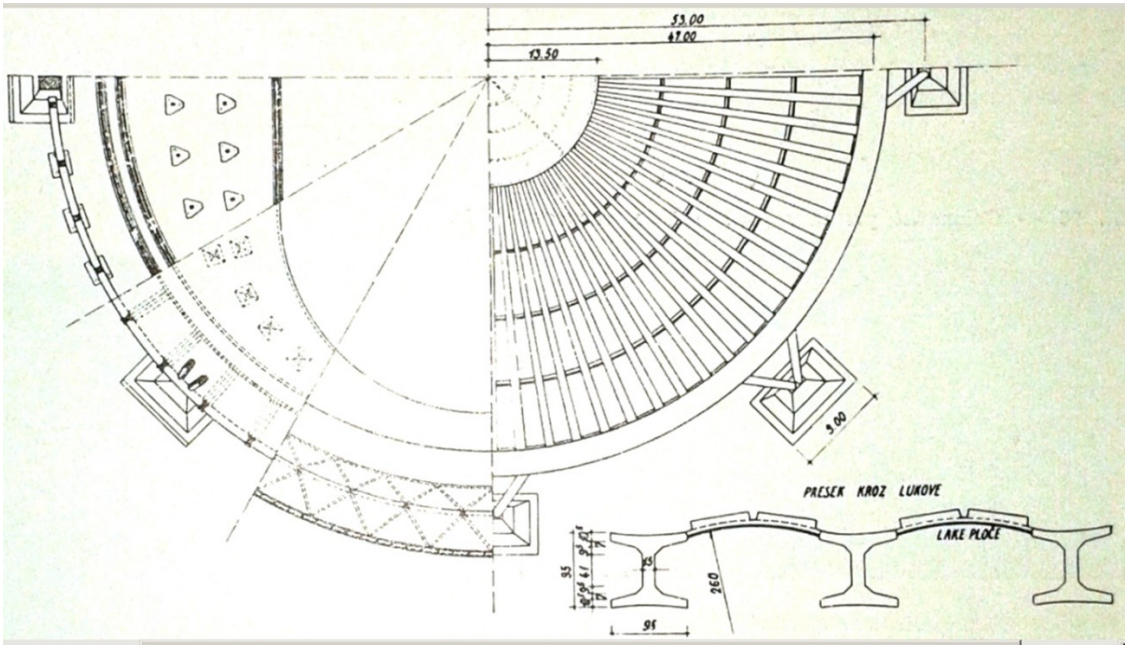


*Figure 3. Cross sections of the Hall 1 of the Belgrade Fair, [18]*

Recently, numerical simulation of the stress state was performed using FEM, and compared with the original calculations done by hand by Branko Zezelj. Agreement was almost perfect, as shown in details in [15-17]. Here we focus attention to the structural integrity, also assessed by numerical simulation of imaginary crack positioned in so-called “V” column. It was performed by using 2D extended Finite Element Method (xFEM), based on calculations of forces, moments and support displacements.
An edge crack of 2.5 mm length was assumed to be located in one of the reinforcement bars (5 mm in diameter). The main goal was to determine how the column behaves with a loading defined by predefined support displacement of 2 cm, corresponding to remote stress of 150 MPa. The crack was located to pass first through the concrete part, and then through the steel bar. Steel bar was modelled with different number of elements, from 3 to 8, to minimize the effect of mesh. One can see that the crack reached and entered the steel bar, with maximum stress value just above 600 MPa at the crack tip in the Fig. 4. More detailed analysis is given in [17].

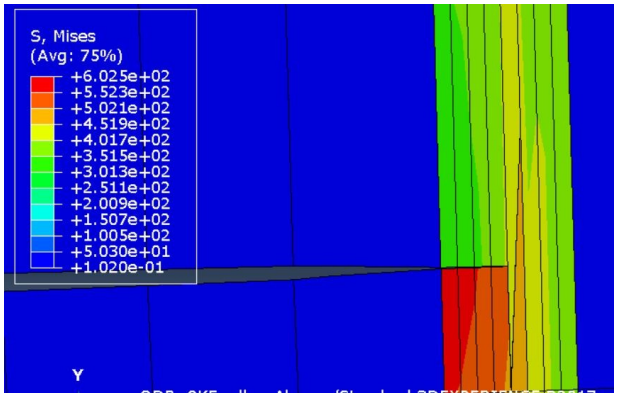


*Figure 4. Results of xFEM analysis, distribution of von Mises stress, [17].*

As for the structural integrity, a simple conservative linear elastic fracture mechanics analysis can provide the minimum fracture toughness value of a bar steel to sustain an edge crack with a length up to the half bar thickness (a=2.5 mm):

$K_I = Y\sigma\sqrt{\pi a} = 1139$ MPa√mm,

where $K_I$ is the stress intensity factor, Y is the geometry factor, Y=2.71 for a/W=0.5, σ=150 MPa is the remote stress, crack length a=2.5 mm. Therefore, the minimum value of a bar steel fracture toughness is 1139 MPa√mm, being 88% of the value reported in [17], $K_{Ic}$=1296 MPa√mm.
Additional analysis can be performed by applying the Failure Assessment Diagram. Calculating the net stress (602 MPa) and dividing it by the critical stress (1375 MPa) ($\sigma_n/\sigma_c$=0.43), one gets the coordintes of the service point (0.43, 0.88) which is still in the safe zone, Fig. 5. More detailed analysis is given in [17].

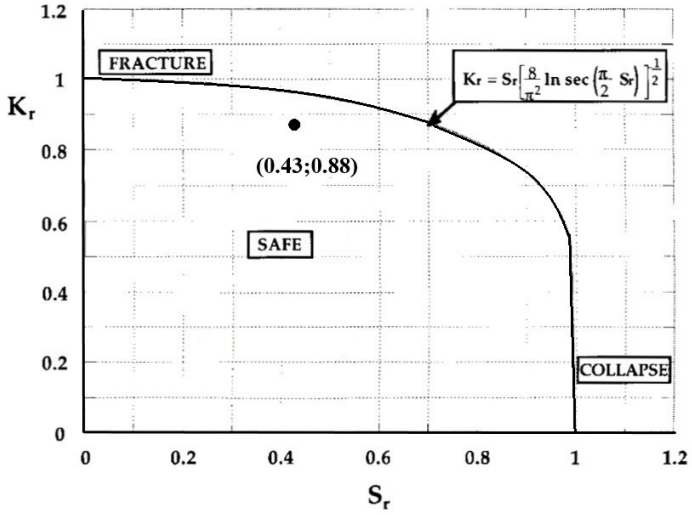


*Figure 5. The FAD for a cracked "V" column, [17]*

## 4. HISTORICAL STEEL BRIDGE IN TRANSYLVANIA

Historical steel bridge in Transylvania, build in 1925, is presented here, including stress analysis and structural integrity assessment, as described in more details in [11, 12]. In this paper following topics will be briefly presented:

- Structural analysis of the existing bridge, Fig. 6.
- Structural analysis of the proposed solution - retrofitted bridge.
- Engineering Critical Assessment considering common possible crack-like defects.



*Figure 6. View of the existing structure, [11]*

The bridge is a riveted type and has a parabolic truss main beam structure, with descending diagonals with an opening of L = 27.86 m. Stress analysis indicated the most critical part, the lower chord, as shown in Fig. 7, where stress reached 183.2 MPa.

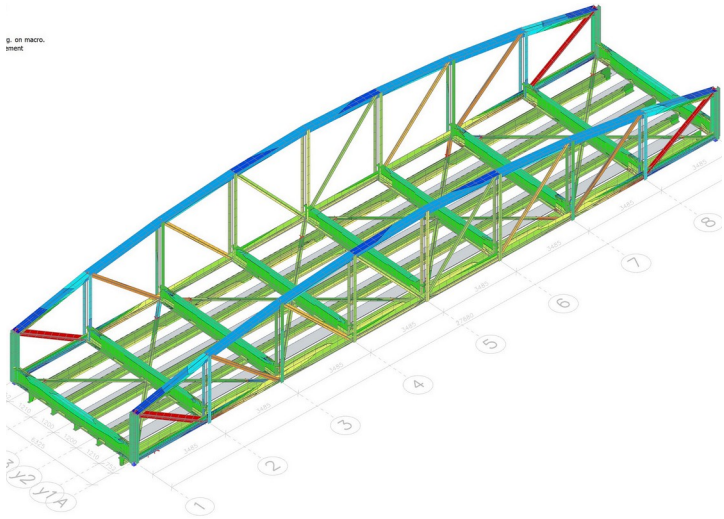

*Figure 7. FEM results with critical cross-sections (red), [11].*

Therefore, it was decided to install additional supporting central beam, made of stronger steel, as shown in Fig. 8, which would carry 291.8 MPa, reducing at the same time the maximum stress in the lower chord to 162.2 MPa. More details are given in [11, 12].

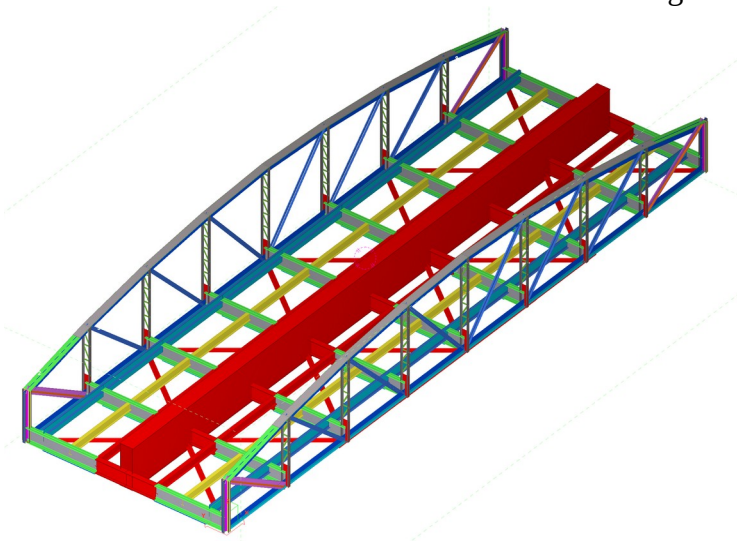

*Figure 8. Proposed retrofit solution, [11]*

Based on this calculation, further analysis was performed taking into account several potentially dangerous cracks, as shown in more details in [11, 12]. Here the FAD level 2 is presented, being slightly modified from the FAD presented in previous chapters. Modification takes into account plasticity effects which is reasonable concept for structural steels. Through-thickness cracks in the area nearby the rivet were considered, with locations and lengths defined in Table 1. As one can see form the results presented in FAD, Fig. 9, crack TTF-5 is the most critical one, and the only one which can lead to the failure.

*Table 1 Data of the assumed crack-like defects*

| Case no. | Name | location of crack | Crack length 2a |
|---|---|---|---|
| **Case 1** | (TTF-1) | Main truss beam - lower chord | **30** |
| **Case 2** | (TTF-2) | Main truss beam - upper chord | 30 |
| **Case 3** | (TTF-3) | Main truss beam – Diagonal 1 | 10 |
| **Case 4** | (TTF-4) | Deck transversal beam | 30 |
| **Case 5** | (TTF-5) | Deck longitudinal beam | 30 |

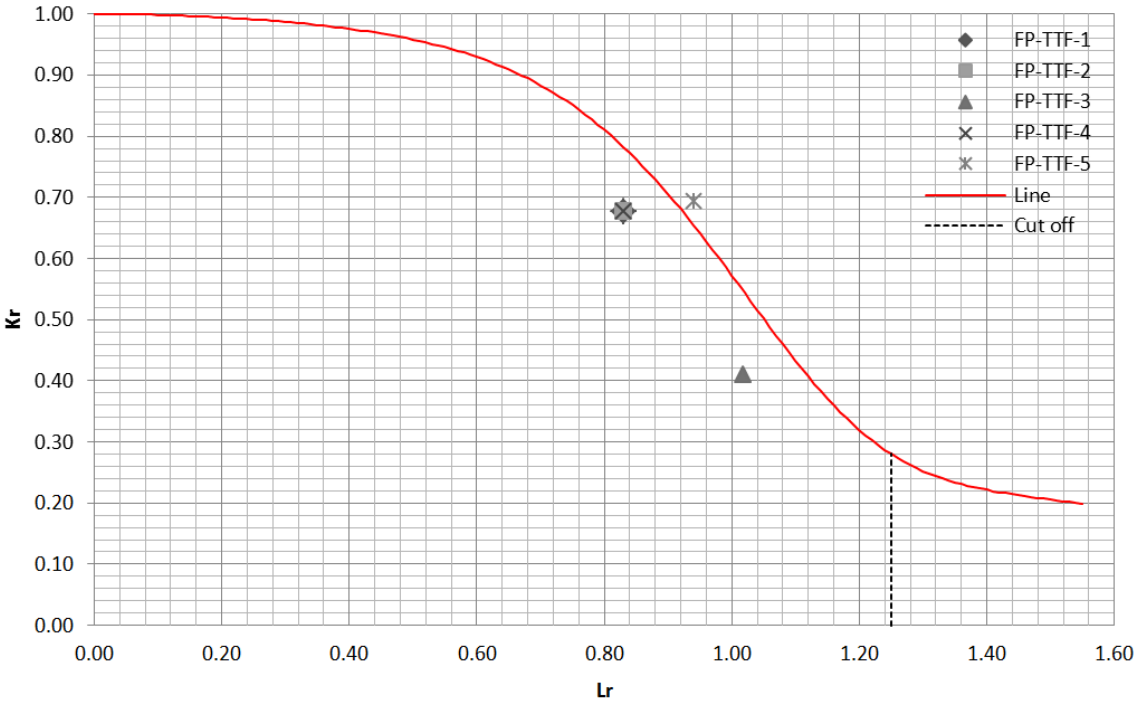


*Figure 9. The FAD level 2 indicating positions of assumed crack-like defects*

## 5. CONCLUSIONS

Based on the presented case studies and results, one can conclude the following:

- Structural integrity is well advanced scientific and engineering discipline which can provide reliable assessment of the effect of cracks on behaviour and serviceability of civil engineering constructions
- Old and historically important constructions can used well beyond their original design life if properly monitored and retrofitted when necessary.

## ACKNOWLEDGEMENT

This paper is dedicated to Academician Branko Žeželj, the mastermind of prestressed concrete constructions and the world champion in free-supported dome spans.

## REFERENCES (STYLE: LITERATURA)

[1] Reed R.P. et al, (1983), Fitness-for-Service Criteria for Pipeline Girth-Weld Quality, Final Report to the U.S.DOT, NBS, Boulder, USA, 1983

[2] Sedmak A., (2003), Primena mehanike loma na integritet konstrukcija, Mašinski fakultet Univerziteta u Beogradu, 2003

[3] Reynoza V., Acero J., (2025), Evaluation and seismic risk of confined masonry buildings in the city of Eten - Chiclayo - Peru, 2023, Structural Integrity and Life, Vol. 25(2), pp. 297–300, https://doi.org/10.69644/ivk-2025-02-0297

[4] Kraedegh A.M. et al, (2024), Integrity and risk assessment of offshore jacket structures, Structural Integrity and Life, Vol. 24(3), pp. 380–385, https://doi.org/ 10.69644/ivk-2024-03-0380

[5] Jovanović A. et al, (2023), Inspection of damage and risk analysis of containers in a coal drying facility in exploitation, Structural Integrity and Life, Vol. 23(2), pp. 111–115

[6] Pavišić M., (2007) Risk based integrity assessment of concrete structures, Structural Integrity and Life, Vol. 7(1), pp. 29–36

[7] Đorđević P. et al, Risk analysis in structural integrity, Structural Integrity and Life, Vol. 11(2), pp. 134–138

[8] Radu., D., Sedmak, A., Băncilă, R., (2018), Determining the crack acceptability in the welded joints of a wind loaded cylindrical steel shell structure, Engineering Failure Analysis, 10.1016/j.engfailanal.2018.04.032

[9] Mijatović T. et al, (2019), Structural Integrity Assessment from the Aspect of Fracture Mechanics. Structural integrity and life Vol. 19(2), pp. 121–124.

[10] Jelić M., Common characteristics of main contributions of Roger Boscovich, Milutin Milanković and Branko Žeželj to the development of civil engineering, Structural Integrity and Life, Vol. 17(2), pp. 157–169

[11] Dorin Radu et al. (2022), Solution for consolidation and retrofitting a historical steel bridge Procedia Structural Integrity, Vol. 37, pp. 771–778

[12] Sedmak A. et al, (2023), Residual life assessment of the historical road riveted bridges Engineering Fracture Mechanics, Vol. 299, 109960, https://doi.org/10.1016/j.engfracmech.2024.109960

[13] Golubović, T., Sedmak, A., Spasojević Brkić, V., Kirin, S., Rakonjac, I. (2018), Novel risk based assessment of pressure vessels integrity, Technical Gazette, Vol. 25(3), pp. 803-807.

[14] Kirin S., Sedmak A., Zaidi R., Grbović A., Šarkočević Ž., (2020), Comparison of experimental, numerical and analytical risk assessment of oil drilling rig welded pipe based on fracture mechanics parameters, Engineering Failure Analysis, Vol. 112, Article number 104508, https://doi.org/10.1016/j.engfailanal.2020.104600

[15] Jelic M., Sedmak A., (2020), The largest pre-stressed concrete Dome in the world – the case study of “Hall 1 of the Belgrade Fair“, Procedia Structural Integrity, Vol. 28, pp. 1833-1838, https://doi.org/10.1016/j.prostr.2020.11.006

[16] Jelic M. et al, (2021) Numerical simulation of “Hall 1 of the Belgrade Fair“, Engineering Failure Analysis, Vol. 127, 105570, https://doi.org/10.1016/j.engfailanal.2021.105570

[17] Jelic M. et al, (2024) Structural integrity analysis of the pre-stressed concrete dome of the Belgrade fair hall 1, Frattura ed Integrità Strutturale, 67 (2024) 337-351; DOI: 10.3221/IGF-ESIS.67.24

[18] Žeželj, B., 1960. A Large Dome at Belgrade. Concrete and Constructional Engineering 7, 263–270.

https://doi.org/10.24867/INDIS-2026-EN-076



# IMPLEMENTATION OF THE NONLINEAR ANALYSIS WITH THE SEVENTH DEGREE OF FREEDOM IN THE ACADEMIC SOFTWARE MATRIX 3D

*Tanja Perčić[1], Đorđe Jovanović[2], Drago Žarković[3], Dragan Manojlović[4]*

***Summary:***

Steel structures are commonly composed of thin-walled members with open cross-sections, which have low torsional stiffness and are therefore susceptible to non-uniform torsion, requiring the introduction of an additional degree of freedom warping, known as the seventh degree of freedom. This paper presents the implementation of a geometrically nonlinear analysis that accounts for the seventh degree of freedom in the academic software Matrix 3D, based on the elastic and geometric stiffness matrices that incorporate non-uniform torsion and on the link elements that model the warping transmission at the joints. The analysis is carried out for three beam-to-column joint configurations: with diagonal, box and diagonal/box stiffening and validated by comparison with geometrically nonlinear shell finite-element analyses in the software Abaqus.

*Keywords: nonlinear analysis, seventh degree of freedom, Matrix 3D*

# IMPLEMENTACIJA NELINEARNE ANALIZE SA SEDAM STEPENI SLOBODE U AKADEMSKOM SOFTVERU MATRIX 3D

***Rezime:***

Čelične konstrukcije se najčešće izrađuju od tankozidnih elemenata otvorenog poprečnog preseka, koji imaju malu torzionu krutost i stoga su podložni neuniformnoj torziji, što zahteva uvođenje dodatnog stepena slobode, vitoperenja, poznatog kao sedmi stepen slobode. U ovom radu prikazana je implementacija geometrijski nelinearne analize za linijske elemente koja obuhvata sedmi stepen slobode u akademskom softveru Matrix 3D, zasnovana na matricama elastične i geometrijske krutosti koje obuhvataju neuniformnu torziju i na veznim (link) elementima koji modeliraju prenos vitoperenja u čvorovima. Analiza je sprovedena za tri konfiguracije veze grede i stuba-sa dijagonalnim, kutijastim i dijagonalnim-kutijastim ukrućenjem i validirana poređenjem sa geometrijski nelinearnim analizama sa površinskim konačnim elementima u softveru Abaqus.

*Ključne reči: nelinearna analiza, sedmi stepen slobode, Matrix 3D*

[1] Teaching Assistant, Faculty of Technical Sciences, University of Novi Sad, Novi Sad, Serbia, nozica.tanja@uns.ac.rs, ORCID 0000-0001-5517-9659
[2] Asst. prof., Faculty of Technical Sciences, University of Novi Sad, Serbia, Novi Sad, djordje.jovanovic@uns.ac.rs, ORCID 0000-0002-6741-0042
[3] Asst. prof., Faculty of Technical Sciences, University of Novi Sad, Novi Sad Serbia, dragozarkovic@uns.ac.rs, ORCID 0000-0002-0560-5231
[4] Teaching Assistant with PhD, Faculty of Technical Sciences, University of Novi Sad, Novi Sad, Serbia, manojlovic.dragan@uns.ac.rs, ORCID 0000-0003-1269-7477

## 1. INTRODUCTION

Steel structures are most often assembled from thin-walled members with open cross-sections (I, channel and similar profiles), which combine high bending efficiency with very low torsional stiffness. In such members, the torsion is resisted not only by uniform (Saint-Venant) torsion but also, to a large extent, by non-uniform (warping) torsion. When warping is restrained, longitudinal warping normal stresses and an additional internal force, the bimoment, develop. Describing this behaviour requires an additional kinematic quantity at each node the warping degree of freedom, frequently referred to simply as the seventh degree of freedom. It extends the classical six degree of freedom beam element and is based on Vlasov's thin-walled beam theory [1].

Most conventional beam-column finite elements available in commercial software account for only six degrees of freedom per node and for uniform torsion, which may lead to a considerable overestimation of the stiffness and the buckling resistance of open thin-walled members. A rigorous alternative is to model the structure with shell finite elements; however, the associated modelling effort and computational cost are prohibitive for routine design and, in particular, for parametric or nonlinear studies. Beam elements enriched with the warping degree of freedom therefore offer a favourable compromise between accuracy and efficiency.

The theoretical and numerical treatment of non-uniform torsion in thin-walled members has been developed over several decades. Baigent and Hancock [2] formulated a matrix displacement method incorporating warping torsion and introduced warping as the seventh degree of freedom at the member ends. McGuire et al. [3] presented the stiffness formulation for non-uniform torsion and implemented it, together with second-order effects, in the program MASTAN2 v5.2, where constraint conditions must be established between the warping degrees of freedom of the connected end sections. Basaglia et al. [4] proposed simple kinematic models that describe the warping transmission or restraint at such joints for the most common configurations, and validated them using shell finite-element analyses.

In a previous study [5], the authors implemented the warping (seventh) degree of freedom in the academic software Matrix 3D for the purpose of linear buckling analysis. To this end, the 14×14 elastic and geometric stiffness matrices accounting for non-uniform torsion were introduced at the beam level, and the warping transmission at the frame joints was enforced by means of link elements whose stiffness depends on the joint configuration (diagonal, box and diagonal/box-stiffened). The resulting linear buckling analysis was then validated by comparison with shell finite-element models in Abaqus for several plane and space frames, showing good agreement in both the critical loads and the buckling modes.

The present paper extends this implementation from linear buckling analysis to a fully geometrically nonlinear analysis that accounts for the seventh degree of freedom and the warping transmission at the joints. The element formulation, comprising the geometric stiffness matrix including warping and the joint link elements, together with the incremental–iterative solution procedure implemented in Matrix 3D, is described, and the obtained results are validated by comparison with geometrically nonlinear shell finite-element analyses carried out in Abaqus. Three beam-to-column joint configurations are considered: diagonal, box and diagonal/box stiffened, since the joint detailing governs the warping transmission and, consequently, the nonlinear response of the frame.

## 2. THEORETICAL FORMULATION OF THE NONLINEAR ANALYSIS IN MATRIX 3D

This section summarises the element formulation and the solution procedure used in Matrix 3D for the geometrically nonlinear analysis of thin-walled frames with the seventh degree of freedom.

### 2.1. BEAM ELEMENT WITH THE SEVENTH DEGREE OF FREEDOM

Each two-node beam element is described by the six classical degrees of freedom per node (three translations and three rotations), augmented by one warping degree of freedom θ′ (the derivative of the torsional rotation) at each end, giving fourteen degrees of freedom per element. The elastic stiffness matrix is obtained by augmenting the conventional 12×12 stiffness matrix with the contribution of non-uniform torsion, which is expressed through the torsion constant It and the warping constant Iw [2].
At the global level, the warping degree of freedom is introduced through two additional global degrees of freedom per member, so that the total number of system degrees of freedom increases by twice the number of such members.

### 2.2. WARPING TRANSMISSION AT THE JOINTS

At a joint connecting non-aligned members, the warping displacements of the connected end sections are coupled by means of link elements whose 2×2 stiffness matrix depends only on the joint configuration [4], [6].

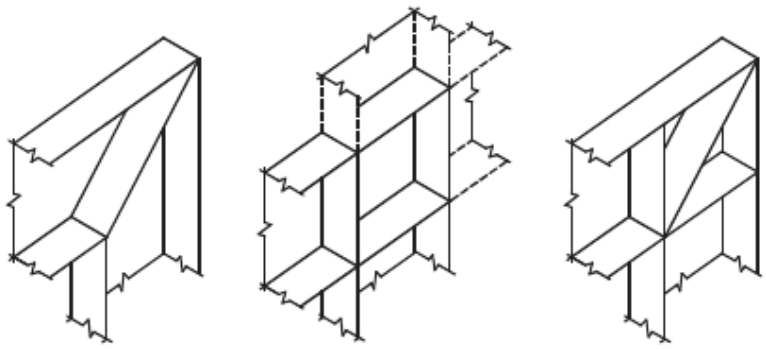

*Fig. 1 Diagonal-stiffened, box and diagonal/box stiffened joints*

These link elements couple, or decouple, the warping degrees of freedom of the member ends meeting at the joint and thus represent the complete-direct, complete-inverse and suppressed warping transmission characteristic of the diagonal, box and diagonal/box stiffened joints, respectively. The link element matrices for the three joint configurations (Fig. 1) are shown below:

$$k_{link\,1}=\begin{bmatrix} 1E+10 & -1E+10 \\ -1E+10 & 1E+10 \end{bmatrix} \tag{1}$$

$$k_{link\,2}=\begin{bmatrix} 1E+10 & 1E+10 \\ 1E+10 & 1E+10 \end{bmatrix} \tag{2}$$

$$k_{link\,3}=\begin{bmatrix} 1E+10 & 0 \\ 0 & 1E+10 \end{bmatrix} \tag{3}$$

where the first matrix $k_{link1}$ is used for the diagonal stiffened joints, the second $k_{link2}$ for the box-stiffened joints and the third $k_{link3}$ for the diagonal/box stiffened joints. The coefficient $k = 10^{10}$ in Eqs. (1)–(3) is a penalty warping stiffness ($kNm^3$) through which the kinematic warping constraints between the connected member ends are imposed. The penalty method is a standard alternative to the Lagrange multiplier technique for enforcing multi-freedom constraints: the constraint is satisfied approximately by assigning the coupling a stiffness much larger than that of the surrounding structure. Following the common recommendation that the penalty be several orders of magnitude (typically $10^4$–$10^8$ times) larger than the largest stiffness coefficient it couples, k is chosen well above the warping stiffness $EI_w/L$ of the connected members. For the I200×5 members considered here ($E = 205$ GPa, $I_w = 7.94 \cdot 10^{-9}$ $m^6$, element length 0.5 m), $EI_w/L \approx 3.3$ $kNm^3$, so that the adopted value of k lies about nine orders of magnitude above the member warping stiffness.

## 2.3. GEOMETRIC STIFFNESS AND THE NONLINEAR SOLUTION PROCEDURE

The geometrically nonlinear analysis in Matrix 3D is formulated as an incremental–iterative procedure [7]. The total load is applied in a sequence of increments, and within each increment equilibrium is restored by Newton–Raphson iterations performed on the updated tangent stiffness matrix, while the equilibrium path is traced by an arc-length scheme [8] (Fig. 2). In the present study the analysis is geometrically nonlinear only: the material is assumed to remain linearly elastic, and the nonlinearity is introduced through a geometric (initial-stress) stiffness matrix that depends on the current element internal forces, the element matrices being formed on the reference (undeformed) configuration under a small-strain, moderate-rotation (second-order) assumption. This geometric stiffness matrix couples the axial force N and the end bending moments $M_{y1}$, $M_{y2}$, $M_{z1}$ and $M_{z2}$ with the torsion–warping degrees of freedom, so that the second-order interaction of axial load and bending with warping torsion is accounted for.

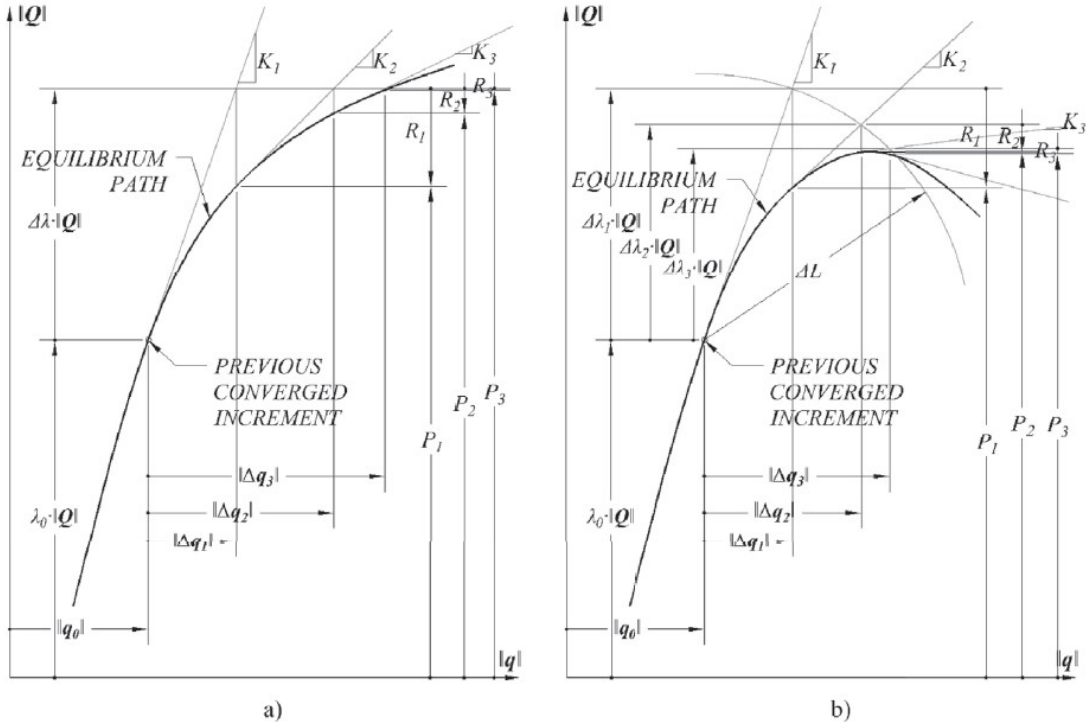


*Fig. 2 a) Newton-Raphson iterations; b) Arc-length iterations [8]*

For members with activated warping, both the elastic ($K_e$) and geometric ($K_G$) element stiffness matrices are of order 14×14. The geometric matrix is an initial-stress matrix: it is recomputed in every iteration from the current internal forces of the element, primarily the axial force N and the end bending moments $M_{y1}$, $M_{y2}$, $M_{z1}$ and $M_{z2}$, together with the cross-section properties.
The solution algorithm proceeds as follows:

- **Assembly of the linear model**. The elastic system stiffness matrix is assembled from the element matrices, including the additional warping degrees of freedom and the joint link elements. The load history is discretised into increments, and an initial geometric imperfection may be imposed so that a geometrically nonlinear analysis with imperfections (GNIA) is carried out.
- **Load increment (predictor)**. A new increment is started with a trial load-factor increment $\Delta\lambda$ and the corresponding trial displacement increment, obtained by solving the system with the current tangent stiffness.
- **Predictor correction.** From this trial displacement the element end forces are evaluated, the 14×14 geometric stiffness matrix is formed from the axial force and end moments and transformed to global coordinates, the tangent stiffness $K_T = K_e + K_G$ is updated, and the system is re-solved with the corrected tangent matrix. This step is performed once at the beginning of each increment.
- **Element state determination**. In every iteration, the element internal forces are evaluated for the current displacement state, the geometric stiffness matrix is recomputed from these forces and the tangent stiffness $K_T = K_e + K_G$ is updated accordingly, the global internal-force vector and the tangent stiffness are assembled, and the residual (out-of-balance) force vector $g = \lambda \cdot F_{ext} - F_{int}$ is computed, together with the reactions.
- **Convergence check**. The increment is considered converged when the norm of the residual force, normalised by the norm of the applied load, falls below a prescribed tolerance. If it is, the iteration is terminated, otherwise, a displacement correction is computed and the procedure returns to element state determination, in which the geometric stiffness is again updated.
- **Arc-length control and line search**. Because the load factor $\lambda$ is treated as an additional unknown, a spherical arc-length constraint is imposed to allow the analysis to pass limit points (snap-through and snap-back). In each iteration the constraint yields a quadratic equation for the load-factor correction, and the physically correct root is selected from the direction of the displacement increment so that the solution does not reverse along the path. A line search additionally scales the correction to minimise the residual force and improve robustness near limit points.
- **Adaptive step control**. If the Newton–Raphson iterations of an increment do not converge, the increment is automatically subdivided into smaller steps and recomputed. If the step size reaches a prescribed minimum without convergence, the analysis is terminated.
- **Storage of the converged state**. For every converged increment the displacements, member internal forces, reactions and the corresponding point of the equilibrium path (load factor versus displacement) are stored. The smallest eigenvalue of the tangent stiffness is also monitored along the path, which makes it possible to detect the approach of limit and bifurcation points.

The output of the analysis is the complete nonlinear equilibrium path, that is, the force–displacement (or load-factor–displacement) response, together with the internal forces, reactions and warping (bimoment) results at each converged step. The procedure is summarised in the flowchart in Fig. 3.

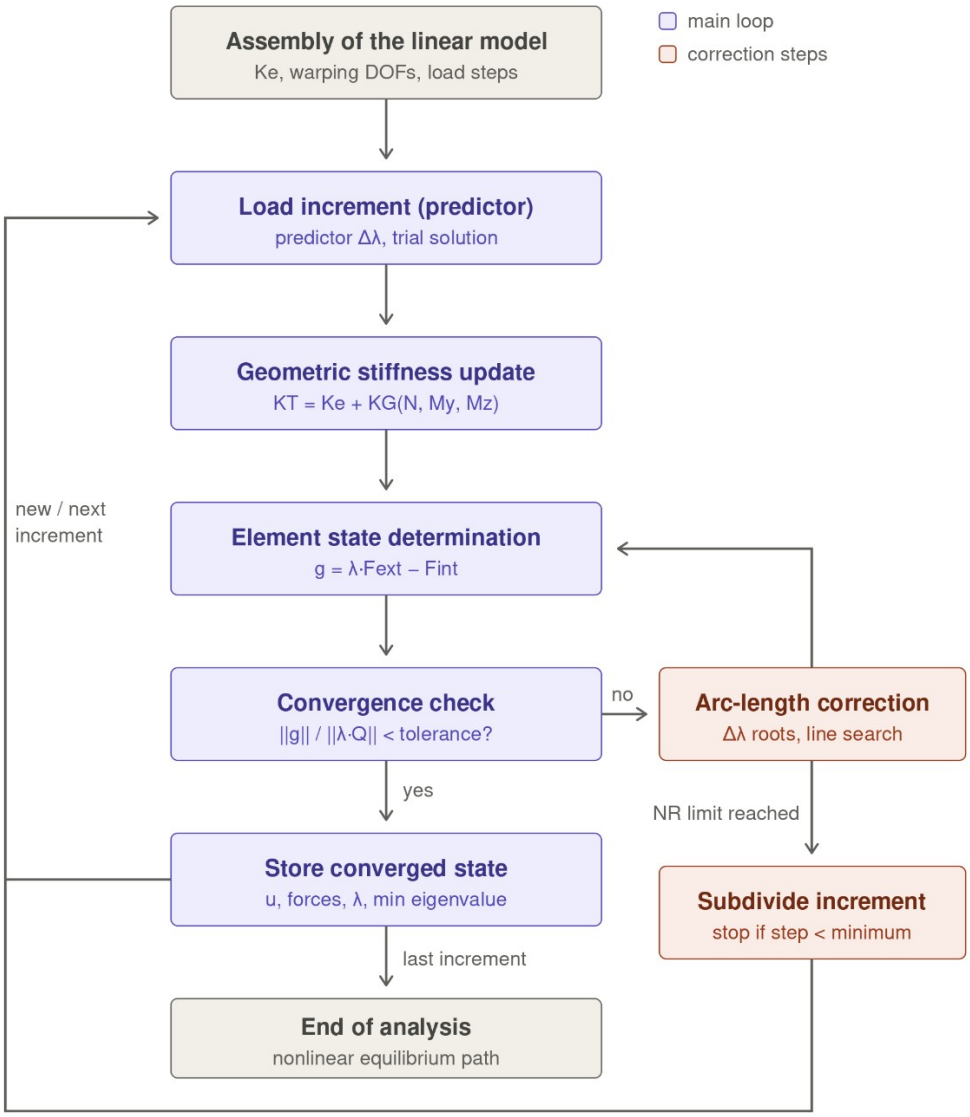


*Fig. 3 Flowchart of the incremental–iterative nonlinear solution with the seventh degree of freedom in Matrix 3D*

## 3. VALIDATION OF THE NONLINEAR ANALYSIS WITH THE SEVENTH DEGREE OF FREEDOM

To validate the geometrically nonlinear analysis with the seventh degree of freedom implemented in Matrix 3D, two examples are presented in this section. In the first example, a simply supported beam loaded at both ends by biaxial bending moments is analysed, and the resulting moment–displacement response is compared with reference values from the literature [3] and with a shell finite-element model in Abaqus. In the second example, an L-shaped frame [4] is analysed by a geometrically nonlinear analysis with imperfections (GNIA) for three beam-to-column joint configurations: diagonal, box and diagonal/box stiffened, and the force–displacement response obtained with the beam element model in Matrix 3D is compared with the beam element results from MASTAN2 v5.2 and with the shell finite-element results from Abaqus.

### 3.1. SIMPLY SUPPORTED BEAM

The first example considers a simply supported beam, with free warping at the ends, loaded at both ends by strong-axis bending moments of 1500 kNm and weak-axis bending moments of 1.5 kNm (0.001 of the strong-axis value). The beam has a length of 6.096 m and a W27×102 cross-section, with a modulus of elasticity of 200 GPa [3]. In Matrix 3D, beam finite elements with a mesh size of 0.5 m were employed, whereas in Abaqus, S4R shell finite elements with a mesh size of 0.05 m were used.

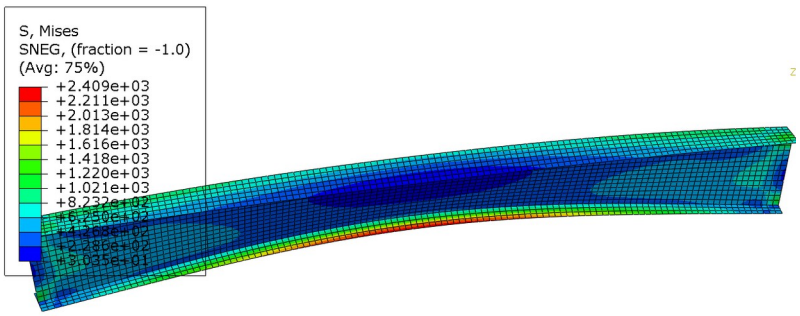


*Fig. 4 Deformed configuration of the simply supported beam from the nonlinear analysis in Abaqus*

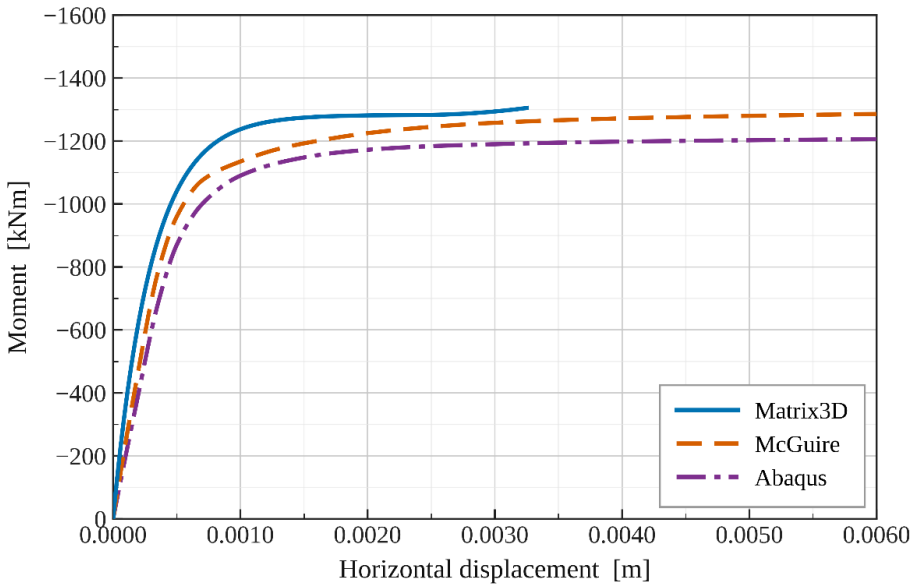


*Fig. 5 Moment-displacement diagram*

Fig. 5 presents the moment–midspan displacement diagram. Taking the Matrix 3D result as the reference, the moment at a lateral displacement of 3 mm obtained with the beam element model from the literature [3] differs by only about 2.6%, whereas the shell model in Abaqus gives a moment about 7.1% lower. The close agreement with the reference beam solution provides a verification of the implemented beam formulation. The larger difference with respect to the shell model can primarily be attributed to the additional cross-sectional deformation modes captured by the shell discretisation. The shell model is not subject to this assumption: the walls of the cross-section can also bend and distort locally (cross-sectional distortion, bending of the web and flanges) (Fig. 4). These additional deformations make the shell model more flexible, so that for the same displacement it yields a lower moment.

## 3.2. L-FRAME

The frame consists of a column with a length of 6 m and a beam with a length of 6 m. Both the column and the beam are fixed at their ends. At the fixed ends, all translations and rotations are fully restrained, including the torsional rotation. Warping is also restrained ($\theta' = 0$) at these supports. The cross-section is I200×5 [4]. It is a doubly symmetric I-section with a web height of 200 mm and two flanges of 100 mm width, with both the web and the flanges having a uniform thickness of 5 mm. The modulus of elasticity is 205 GPa. The frame is subjected to a vertical load of 40 kN (Fig. 6). Lateral displacement is restrained at the joints. A geometrically nonlinear analysis with imperfection (GNIA) was performed, the imperfection being introduced by imposing a lateral displacement of 6 mm at the mid-length of the beam (Fig. 6). The results obtained from Abaqus, MASTAN2 v5.2 and the academic software Matrix 3D are compared.

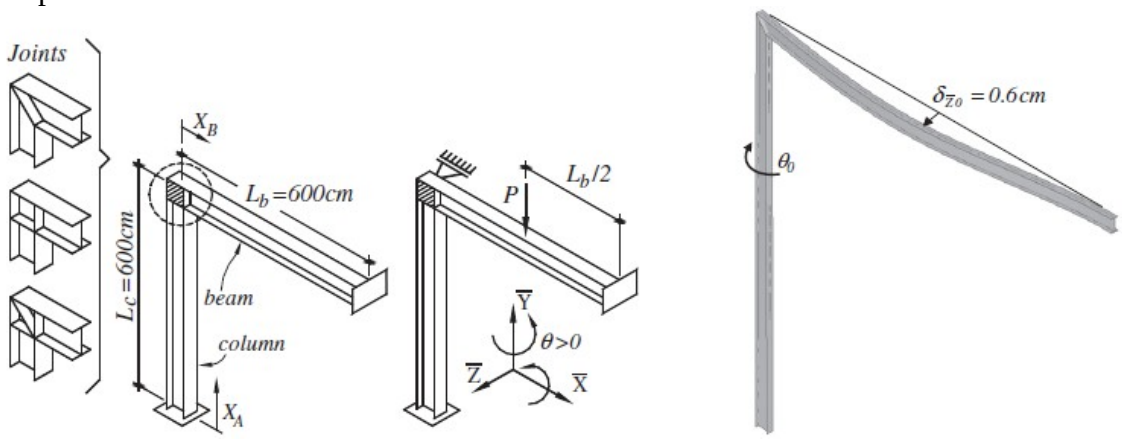


*Fig. 6 L-frame characteristics*

In Matrix 3D and MASTAN2 v5.2, a geometrically nonlinear analysis with imperfections (GNIA) was performed using a beam element model with seven degrees of freedom and a finite element size of 0.5 m. In Abaqus, a static nonlinear analysis was carried out using a shell element model of the frame with a S4R finite element mesh.
Figs. 7-9 show the results of the nonlinear analyses in all three software programs for three types of beam-to-column connections (diagonal stiffener, box stiffener, and diagona/box stiffener). In MASTAN2 v5.2, the warping condition at a joint is specified through the Torsion option within the Define Connections menu, which offers free, fixed or continuous warping restraint at the member ends. These correspond, respectively, to the diagonal-stiffened joint, modelled as continuous warping restraint that provides direct warping transmission, and the diagonal/box-stiffened joint, modelled as fixed warping restraint that fully restrains warping. MASTAN2 v5.2 does not provide an option reproducing the inverse warping transmission that characterises the box-stiffened joint; therefore, only the diagonal and diagonal/box configurations were modelled in MASTAN2 v5.2. The lateral displacement plotted in Figs. 7-9 is measured from the initial imperfect configuration, it is the additional displacement developed under load and does not include the 6 mm initial imperfection.

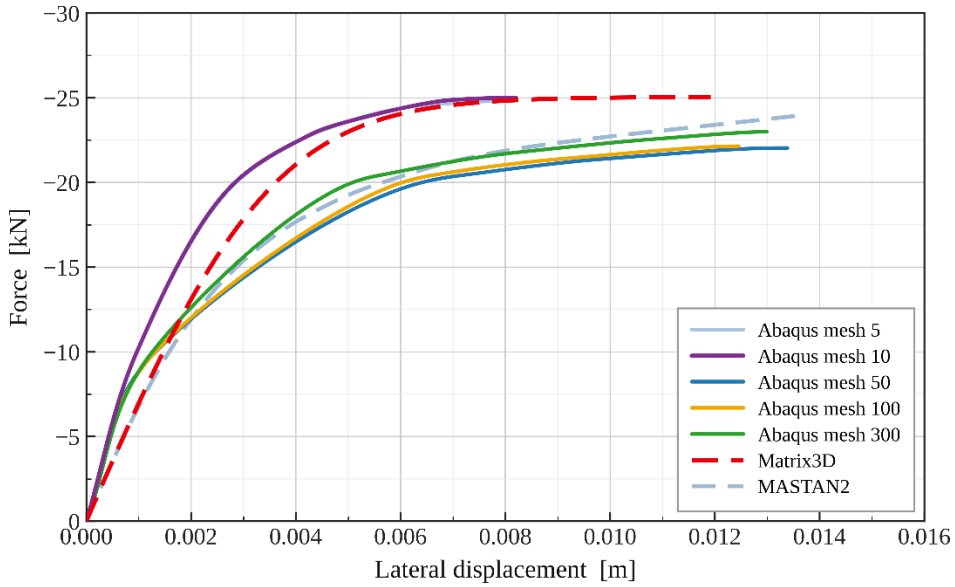


*Fig. 7 Force–midspan displacement diagram for the L-frame with a diagonal stiffener*

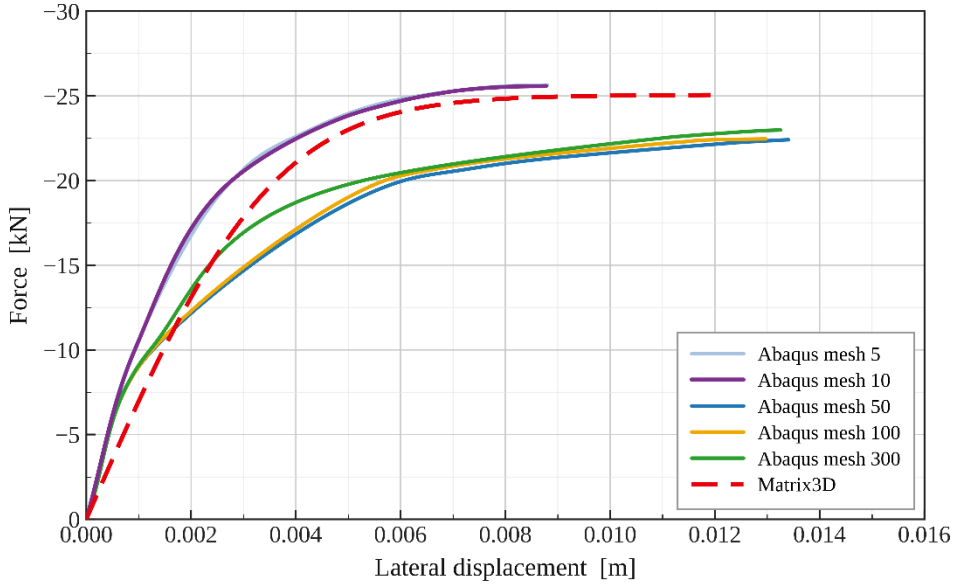


*Fig. 8 Force–midspan displacement diagram for the L-frame with a box stiffener*

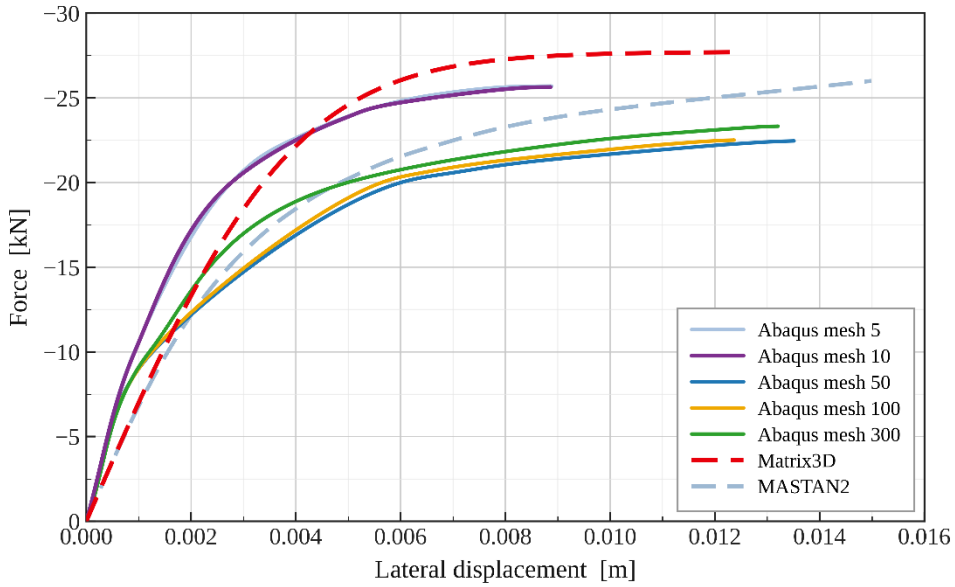


*Fig. 9 Force–midspan displacement diagram for the L-frame with a diagonal/box stiffener*

For this frame, the forces obtained in Matrix 3D, MASTAN2 v5.2 and Abaqus were compared, taking the Matrix 3D beam model as the reference. The Matrix 3D results are in very good agreement with the finer Abaqus shell meshes (mesh 5mm and 10mm): the force at a lateral displacement of 8 mm differs by only about 1% for the diagonal stiffened joint, about 3% for the box-stiffened joint, and about 6–7% for the diagonal/box stiffened joint. These two meshes are considered to represent the converged shell solution, since their element size is small enough to describe the deformation of the individual walls of the I200×5 section, and further refinement from 10 mm to 5 mm changes the response only marginally. The difference between the 5 mm and 10 mm meshes remains below about 2% over the relevant part of the equilibrium path (and below 1% at a lateral displacement of 8 mm), which confirms that the shell solution is essentially mesh-converged. In contrast, the coarser shell meshes (mesh 50mm, 100mm and 300mm) yield a markedly lower force at a lateral displacement of 8 mm, between about 13% and 23% below the Matrix 3D value, the largest deviation occurring for the diagonal/box stiffened joint. The MASTAN2 v5.2 results lie close to these coarser meshes, about 12% (diagonal) to 15% (diagonal/box) below Matrix 3D. All models nevertheless reproduce the same influence of the joint configuration, the diagonal/box stiffened joint, which fully restrains the warping transmission, being the stiffest and developing the highest force.

The full restraint of warping transmission is what makes the diagonal/box-stiffened joint the stiffest and strongest, but it is also what concentrates local and distortional deformation in the joint region. It is therefore expected that this joint shows both the highest capacity and the largest difference between the beam and shell models. The larger differences obtained with the coarser meshes should be attributed to the shell model rather than to the beam formulation, as the 7-DOF beam model can only be assessed fairly against a mesh-converged shell solution. When such a solution is used as the reference, the beam model describes the behaviour of all three joints well, and larger differences appear only where cross-sectional distortion becomes significant, which a beam element cannot describe.

Figs. 10 and 11 show the deformed shapes of the L-frame in the academic software Matrix 3D for different joint configurations. The figures show that the beam element model in the academic software Matrix 3D also displays the torsional rotation of the cross-section, where it can be clearly seen that the largest torsion occurs at the mid-span of the beam.

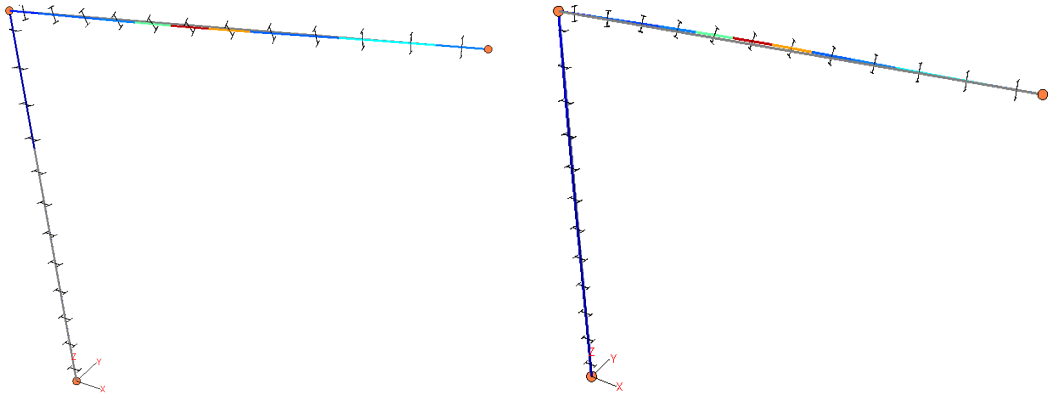

*Fig. 10 Deformed shape of the L-frame with a diagonal stiffener (left) and a box stiffener (right) in Matrix 3D*

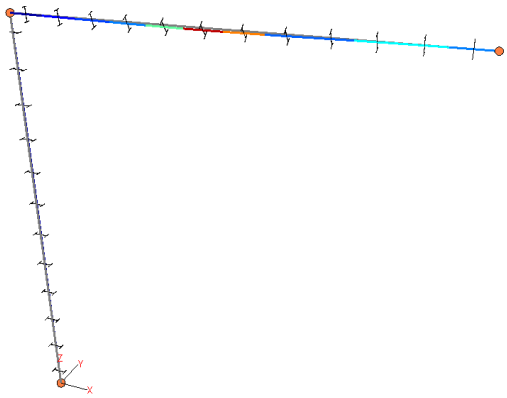

*Fig. 11 Deformed shape of the L-frame with a diagonal/box stiffener in Matrix 3D*

Fig. 12 shows the deformed shapes obtained with meshes ranging from 300 mm to 5 mm. With the coarser meshes the cross-section remains essentially undistorted and the member deforms in a global manner, whereas as the mesh is refined the local deformation and distortion of the cross-section (twisting of the flanges and out-of-plane deformation of the walls, most pronounced along the beam and near the joint) become progressively visible. This confirms that only the finer meshes capture the local behaviour, which explains the systematically lower force predicted by the coarser meshes

Overall, the beam finite-element model with the seventh degree of freedom implemented in Matrix 3D accurately describes the converged (finer-mesh) shell response with a maximum difference of about 7%, at a small fraction of the modelling and computational cost of a shell model.

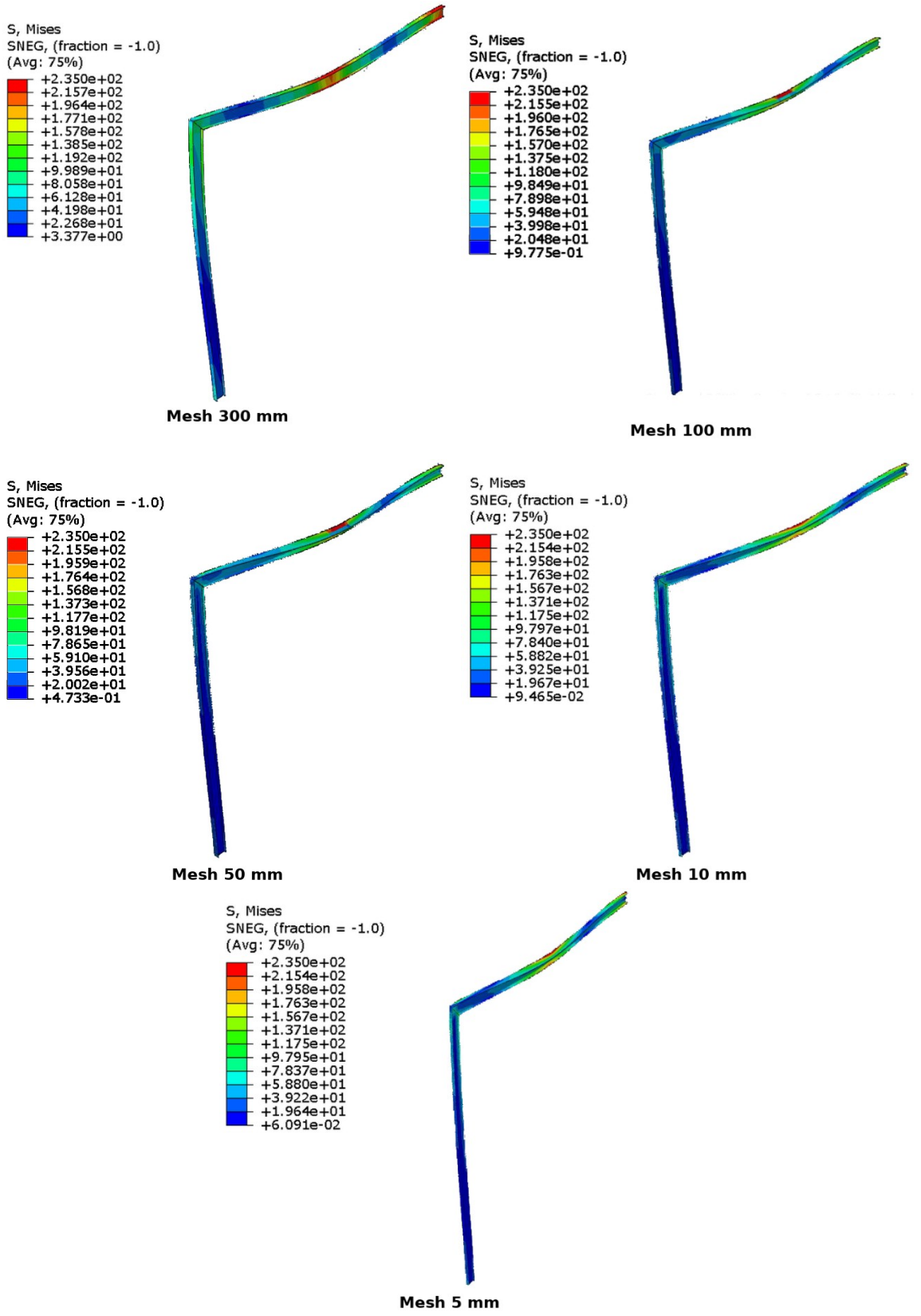


*Fig. 12 Deformed shapes for the L-frame with a diagonal stiffener obtained with meshes ranging from 300 mm to 5 mm*

## 4. CONCLUSION

The presented implementation extends Matrix 3D from linear buckling analysis to geometrically nonlinear analysis of thin-walled frames while explicitly accounting for warping and its transmission through joints. The comparisons demonstrate that the proposed 14-DOF beam formulation can reproduce the global nonlinear response obtained from converged shell models with differences below approximately 7%, while retaining the substantially lower modelling and computational cost characteristic of beam models.

### ACKNOWLEDGEMENT

This research has been supported by the Ministry of Science, Technological Development and Innovation (Contract No. 451-03-34/2026-03/200156) and the Faculty of Technical Sciences, University of Novi Sad through project “Scientific and Artistic Research Work of Researchers in Teaching and Associate Positions at the Faculty of Technical Sciences, University of Novi Sad 2026” (No. 01-3609/1).

## REFERENCES

[1] Vlasov V.Z. (1961). Thin-walled elastic beams (2nd edition), Israel Program for Scientific Translations, Jerusalem, Israel.

[2] Baigent A.H., Hancock G.J. (1982). Structural analysis of assemblages of thin-walled members. Engineering Structures, Volume 4, pp. 207–216. https://doi.org/10.1016/0141-0296(82)90010-4

[3] McGuire W., Gallagher R.H., Ziemian R.D. (2000). Matrix structural analysis (2nd edition), John Wiley & Sons, New York, USA.

[4] Basaglia C., Camotim D., Silvestre N. (2012). Torsion warping transmission at thin-walled frame joints: Kinematics, modelling and structural response. Journal of Constructional Steel Research, Volume 69, pp. 39–53. https://doi.org/10.1016/j.jcsr.2011.07.016

[5] Nožica T., Jovanović Đ., Žarković D., Rašeta A. (2023). Verification of buckling analysis of beam finite element model including warping in Matrix 3D. International Scientific Conference iNDiS 2023 – Planning, Design, Construction and Building Renewal, Faculty of Technical Sciences, Novi Sad, Serbia, 16–17 November, pp. 630–639.

[6] Shayan S., Rasmussen K.J.R. (2014). A model for warping transmission through joints of steel frames. Thin-Walled Structures, Volume 82, pp. 1–12. https://doi.org/10.1016/j.tws.2014.03.017

[7] Žarković D. (2022). P-Delta analysis using Matrix 3D non-linear structural analysis software. https://www.researchgate.net/publication/364225116, accessed on 15 July 2026.

[8] Žarković D., Jovanović Đ., Vukobratović V., Brujić Z. (2019). Convergence improvement in computation of strain-softening solids by the arc-length method. Finite Elements in Analysis and Design, Volume 164, pp. 55–68. https://doi.org/10.1016/j.finel.2019.06.005

https://doi.org/10.24867/INDIS-2026-EN-089



# END PATCH LOADING – INFLUENCE OF GIRDER GEOMETRY ON BUCKLING COEFFICIENT

*Gojko Drljača[1], Milivoje Rogač[2]*

***Summary:***

The present study investigates a specific case of locally loaded I-girders, namely end patch loading. A linear elastic stability analysis was performed to determine the critical load, i.e. the buckling coefficient $k_f$. The analysis was carried out numerically using the finite element software Abaqus. In the previous study by Lagerqvist, on which the expression for calculating $k_f$ given in the current Eurocode is based, it was shown that the coefficient β, representing the ratio between the torsional stiffness of the flange and the flexural stiffness of the web, adequately quantifies the influence of the girder geometry on $k_f$. Certain limitations of Lagerqvist's study were identified, particularly regarding the influence of the flange stiffness/width and the range of parameters considered. In the present study, these limitations were investigated through an individual and systematic analysis of the three geometric parameters defining β (flange thickness ($t_f$), web thickness ($t_w$), and flange width ($b_f$)) and it was concluded that their effects on $k_f$ are adequately quantified by the parameter β.

*Keywords: End patch load, Buckling coeficient, Welded I-girder, Parametric numerical anlysis*

# END PATCH LOADING – UTICAJ GEOMETRIJE NOSAČA NA KOEFICIJENT IZBOČAVANJA

***Rezime:***

U ovom radu analiziran je poseban slučaj lokalno opterećenih I-nosača, odnosno end patch loading. Sprovedena je linearno-elastična analiza stabilnosti radi određivanja kritičnog opterećenja, odnosno koeficijenta izbočavanja $k_f$. Analiza je sprovedena numerički primjenom metode konačnih elemena*ta* u programskom paketu Abaqus. U prethodnom istraživanju Lagerqvista, na kojem se zasniva izraz za proračun $k_f$ dat u važećem Evrokodu, pokazano je da koeficijent β, koji predstavlja odnos torzione krutosti nožice i savojne krutosti rebra, na adekvatan način kvantifikuje uticaj geometrije nosača na $k_f$. Uočena su određena ograničenja Lagerqvistovog istraživanja, naročito u pogledu uticaja krutosti/širine nožice i opsega analiziranih parametara. U ovom radu navedena ograničenja istražena su kroz pojedinačnu i sistematičnu analizu tri geometrijska parametra koji definišu β (debljine nožice ($t_f$), debljine rebra ($t_w$) i širine nožice ($b_f$)) pri čemu je zaključeno da su njihovi uticaji na $k_f$ adekvatno kvantifikovani parametrom β.

*Ključne riječi: End patch loading, Koeficijent izbočavanja, Zavareni I-nosač, Parametarska numerička analiza*

[1] Student, Faculty of Civil Engineering, University of Montenegro, Podgorica, Montenegro, gojko.drljaca27@gmail.com, ORCID 0009-0006-5555-3456
[2] Assoc. Prof., Faculty of Civil Engineering, University of Montenegro, Podgorica, Montenegro, milivojer@ucg.ac.me, ORCID 0000-0002-6853-6712

## 1. INTRODUCTION

The paper analyzes the problem of locally loaded thin-walled steel I-girders, commonly referred to as patch loading. This problem has been investigated for more than 100 years. Failure occurs after local buckling of the web in the load introduction zone (Figure 1). The problem is highly nonlinear with respect to both geometry and material behavior. A large number of material and geometric parameters influence the ultimate load.

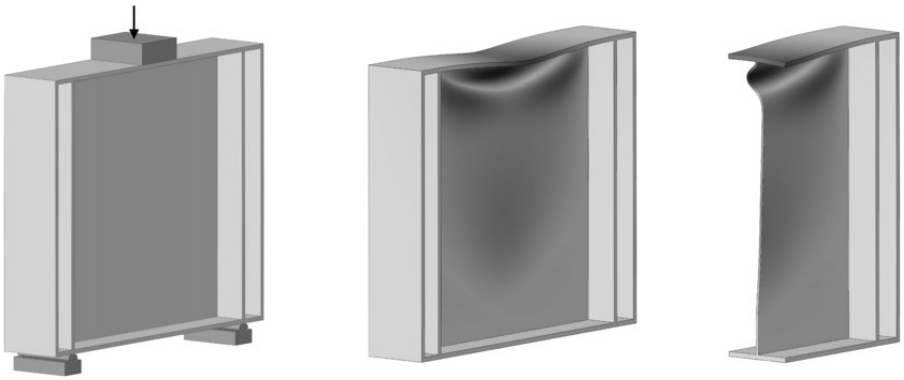

*Fig. 1 Web buckling due to patch loading*

Eurocode 3, Part 1-5 [1], addresses this issue. The design procedure proposed in [1] is harmonized with the other design procedures in Eurocode 3 dealing with stability problems. The plastic resistance and the elastic critical load are related through the reduction factor $\chi$, which was obtained by calibration against an extensive experimental database [2,3,4]. The semi-empirical nature of the reduction factor, as well as the fact that no closed-form solution of the problem exists, clearly confirms that the problem remains relevant.

Thus, the design model given in Eurocode [1] requires the elastic critical load of a patch-loaded girder to be calculated in order to determine its ultimate resistance. The main parameter in the calculation of the critical load is the buckling coefficient ($k_f$), which depends on the girder geometry, loading type and boundary conditions [5].

Eurocode distinguishes three different types of patch loading (Figure 2). The subject of this paper is the calculation of the buckling coefficient for end patch loading, i.e. loading type (c) shown in Figure 2.

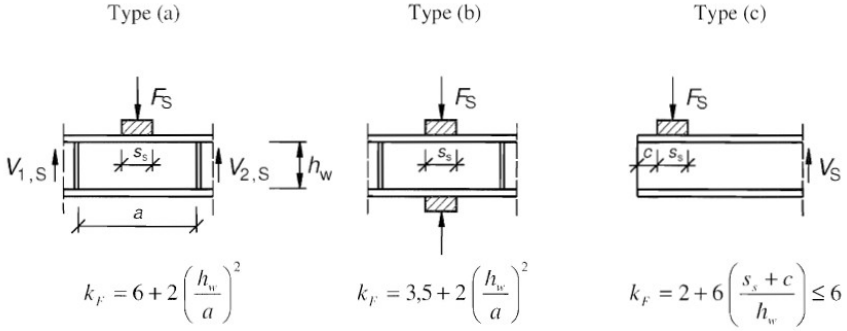


*Fig. 2 Buckling coefficients for different types of load application [1]*

The expression for $k_f$ given in [1] is based on the research conducted by Lagerqvist [6]. The influence of the girder geometry ($t_f$ – flange thickness, $t_w$ – web thickness, $b_f$ – flange width) on the buckling coefficient $k_f$ was analyzed through the derived parameter β, which represents the ratio between the torsional stiffness of the flange and the flexural stiffness of the girder web (see the following section). It was concluded that the parameter β provides a sufficiently reliable measure for estimating the influence of flange stiffness/width on $k_f$. However, certain deviations were observed for cross-sections with significantly wider flanges, indicating that the influence of flange stiffness/width is not fully captured by β alone. In addition, certain limitations of the parametric analysis conducted in [6] can be identified, particularly with regard to the selection and range of the analyzed parameters.

The main objective of this study is to perform a detailed analysis of the three geometric parameters $t_f$, $t_w$, and $b_f$, which are systematically varied in order to investigate their individual influence on $k_f$. The main research hypothesis is that the influence of the analyzed geometric parameters can be adequately quantified by the parameter β. The study was carried out using the finite element method in the Abaqus software package [7].

## 2. REVIEW OF LAGERQVIST'S RESEARCH [6]

After analyzing the experimental results for end patch loading, Lagerqvist adopted the 3D numerical model shown in Figure 3. The adopted model simulates simply supporter beam at one end. The following mechanical properties were assigned to all models: Young's modulus E = 210 GPa and Poisson's ratio ν = 0.3 [6].

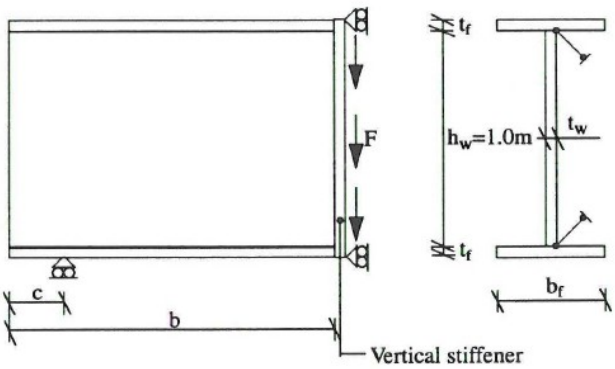


*Fig. 3 Adopted model used by Lagerqvist in [6]*

In all analyses, the distance between the flange centrelines (h) was 1m, and therefore the web depth ($h_w$) was equal to 1m minus the flange thickness. Different girder lengths were considered (dimension b in Fig. 3). It was concluded that, for $b/h_w \geq 4$, the transverse stiffener at the right end of the girder (Fig. 3) has no influence on the buckling coefficient. The values of $k_f$ were obtained using Eq. (1).

$$F_{cr} = k_f * \frac{\pi^2 E}{12\left(1-\nu^2\right)} * \frac{t_w^3}{h_w} \tag{1}$$

In addition to the 3D girder model, Lagerqvist developed reference 2D models of the I-girder web without flanges, with the same boundary conditions as those used for the model shown in Fig. 3 ($b/h_w = 4$ and $c/h_w = 0.2$), while varying only the plate thickness (1, 2, 4 and 6mm). By comparing the results obtained from the 2D and 3D models, Lagerqvist observed that the buckling coefficient $k_f$ was approximately three times higher for the 3D model than for the corresponding 2D model. This increase in $k_f$ is attributed to the beneficial influence of the flanges, which reduce the rotation of the longitudinal edges of the web and enable a more effective distribution of stresses along the web. Lagerqvist assumed that the beneficial influence of the flanges could be quantified as a function of the ratio between the torsional stiffness of the flange and the flexural stiffness of the web, as given in Eq. (2).

$$\frac{GK}{D h_w} = \frac{12 * \left(1-\nu^2\right) * E * b_f * t_f^3}{E * h_w * t_w^3 * 6 * \left(1+\nu\right)} \tag{2}$$

By evaluating Eq. (2) a new parameter β is obtained together with the numerical constant 1.4. Equation (3) shows the geometric parameters on which the parameter β depends.

$$\beta = \frac{b_f * t_f^3}{h_w * t_w^3} \tag{3}$$

To verify the validity of the parameter β, Lagerqvist analyzed a set of I-girders for which $\beta = 16$ and $h_w = 1$m were kept constant, while $t_w$, $b_f$ and $t_f$ were varied. The resulting values of the buckling coefficient $k_f$ ranged from 3.87 to 3.93, corresponding to a difference of approximately 2%. This variation in the results was considered acceptable, and the parameter β was subsequently adopted for further analyses.
Lagerqvist then investigated the variation of the buckling coefficient with the parameter β. The values of β considered in the analysis ranged from 1 to 54. Lagerqvist selected different values of $b_f$, $t_f$ and $t_w$ randomly, so as to satisfy Eq. (3) This may be regarded as one of the limitations of his analysis. Table 1, reproduced from Lagerqvist's work, presents the values of the geometric parameters relevant to the determination of β within his analysis.

*Tab. 1 Values of the geometric parameters used to determine the parameter β in [6]*

| $t_w$ m | $t_f$ m | $b_f$ m | β |
|---|---|---|---|
| 0.02 | 0.04 | 0.125 | 1 |
| 0.02 | 0.04 | 0.250 | 2 |
| 0.01 | 0.04 | 0.125 | 8 |
| 0.01667 | 0.05 | 0.500 | 13.5 |
| 0.01 | 0.05 | 0.125 | 15.625 |
| 0.01 | 0.04 | 0.250 | 16 |
| 0.01 | 0.06 | 0.125 | 27 |
| 0.01 | 0.05 | 0.250 | 31.25 |
| 0.01 | 0.06 | 0.250 | 54 |

The analysis indicated that the parameter β does not completely account for the effect of flange stiffness/width on the value of $k_f$. However, for end patch loading, β was found to provide a sufficiently reliable representation of the influence of the flanges on the elastic critical load.
In Lagerqvist's study, the parameter β was not investigated by systematically varying one geometric parameter while keeping the remaining parameters constant. Instead, different combinations of the geometric parameters defining β were considered. This may be regarded as a limitation of the analysis, since such an approach does not enable the individual influence of each parameter on β, and consequently on $k_f$, to be clearly isolated.

## 3. NUMERICAL ANALYSIS

The numerical analysis was performed using the finite element software Abaqus [7]. The software allows both material and geometric nonlinearities to be included in the analysis. However, since the present study focuses on the elastic critical load, material nonlinearity was not considered, and all models were analyzed within the elastic range.

### 3.1. DEVELOPMENT AND VALIDATION OF THE NUMERICAL MODEL

A 3D numerical model adopted from [6] (Fig. 3) was used in the analysis. The girder was modeled using shell elements, with the web and flanges represented by their mid-surfaces. The material properties were defined in accordance with [6], with Young's modulus E = 210 GPa and Poisson's ratio ν = 0.3. The I-girder height was set to 1m, while the remaining geometric parameters were $b_f$ = 0.25m, $t_w$ = 0.01m and $t_f$ = 0.04m. The parameter c was fixed at 0.2m.
The boundary conditions were defined in accordance with [6]. At a distance c from the free end, a line support extending in the transverse direction was introduced to restrain vertical displacement. At the opposite end of the girder, a transverse stiffener with a thickness equal to the web thickness $t_w$ was included. In the longitudinal direction, the displacement was restrained at two points located at the centroids of the flanges, at the position of the transverse stiffener. The external load was applied as vertical forces acting along the web centreline, also at the position of the transverse stiffener.
Buckling analysis was performed using an Eigenvalue Buckling analysis [7], which determines the elastic critical load and the corresponding buckling modes of the structure. The procedure is based on a linear bifurcation analysis, in which the critical load is obtained from the eigenvalues, i.e. the load multipliers applied to the prescribed reference load.
Two load discretization schemes were analyzed: one with a smaller number of larger forces and another with a larger number of smaller forces, while maintaining the same total applied load. The obtained results showed that the density of the force distribution has no influence on the value of the buckling coefficient $k_f$. Finally, as in [6], the web was laterally restrained along three sides in order to eliminate the influence of lateral-torsional buckling of the girder. Figure 4 shows the I-girder model developed in Abaqus, together with the defined boundary conditions and first buckling mode.

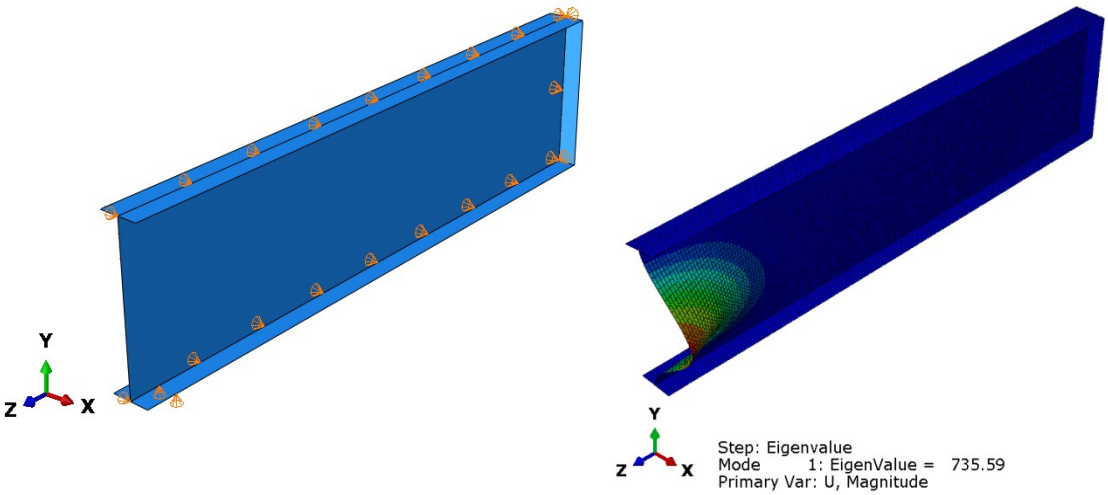


*Fig. 4 Numerical model of the I-girder in Abaqus: model boundary conditions (left); elastic buckling mode for end patch loading (right)*

For validation of the numerical model, girder lengths of b = 4m and b = 5m were considered, using different finite element sizes of 10 mm, 25 mm and 50 mm. Table 2 presents the values of the elastic critical load $F_{cr}$, together with the corresponding values of the buckling coefficient $k_f$ calculated according to Eq. (1). For comparison, the values of $k_f$ reported in [6] for girders with the same geometry are also included in the table.
When applying Eq. (1), the web depth $h_w$ = 960mm was used. This value was obtained from the girder height h = 1000mm by subtracting half of the flange thickness at the top and half at the bottom, corresponding to a total flange thickness of $t_f$ = 40mm.

*Tab. 2 Comparison of $k_f$ values obtained from the present numerical analysis and those reported in [6]*

| b (mm) | FE size (mm) | $F_{cr}$ (N) | $k_f$ | $k_f$ [6] |
|---|---|---|---|---|
| 4000 | 10 | 732500 | 3.705 | 3.74 |
| | 25 | 735590 | 3.72 | |
| | 50 | 745880 | 3.77 | |
| 5000 | 10 | 731520 | 3.7 | 3.74 |
| | 25 | 734590 | 3.715 | |
| | 50 | 744820 | 3.767 | |

Table 2 presents the values of the buckling coefficient obtained from the numerical models developed in this study together with those reported in [6]. The difference is less than 1%, indicating excellent agreement between the results. Differences in the absolute values are expected due to the different finite element mesh densities. In the present study, a uniform mesh size of 10 × 10mm was used, resulting in a total of 78,600 elements, whereas Lagerqvist reported a total number of elements ranging from 720 to 820, without providing a detailed description of the mesh distribution.
Lagerqvist performed his analyses using ANSYS software with the SHELL63 element, a four-node shell element with full 2 × 2 integration, whereas the present study was carried out in Abaqus software [7] using the S4R element, a four-node shell element with reduced integration and a single integration point. Despite the differences in the integration schemes, the deviation of less than 1% demonstrates very good agreement

between the two numerical approaches and confirms the suitability of present element formulations for the analysis of end patch loading.

## 3.2. PARAMETRIC ANALYSIS

The dimensionless parameter β was analyzed by Lagerqvist in [6], who concluded that it does not fully account for the influence of flange stiffness on the value of the buckling coefficient, but provides sufficiently accurate results for determining $k_f$ in the case of end patch loading.

In the present study, the parameter β was investigated in detail by varying the flange thickness $t_f$, web thickness $t_w$ and flange width $b_f$. The parameter $h_w$ was not directly included in the parametric analysis because, in the final expression proposed in [6] for $k_f$ under end patch loading, Eq. (4), $h_w$ appears in both factors of the expression. Consequently, varying $h_w$ would lead to a scatter in the β–$k_f$ diagram, unlike the expected agreement obtained when varying $t_w$, $t_f$ and $b_f$. Web depth ($h_w$) was varyed indirectly when parameter $t_f$ was investigated (see subsection 3.2.1). Since the range of variation was small ($h_w$ = 970–993mm), it was assumed that its influence would not be significant. Further study is needed for the influentional parameter $h_w$.

$$k_f = \left(1 + 3 * \frac{c + s_s}{h_w}\right) * \left(1.6 + 0.3 * \sqrt[4]{\beta}\right) \tag{4}$$

Equation (4) was adopted in [1] as the final expression, with a minor modification consisting of the adoption of a fixed value β = 3.16. In [6], it was shown that for $b/h_w > 4$, the value of the buckling coefficient $k_f$ remains constant. For the analyses carried out in the present study, the values b = 5m, h = 1m and c = 0.2m were adopted.

As can be seen from Table 1, the parameters included in the expression for β were not varied systematically by keeping two parameters constant while varying the third. Instead, several parameters were varied simultaneously, which may be regarded as a limitation of the analysis conducted in [6]. In the present study, for all analyses of the parameter β, the values of b, h and two of the remaining three parameters were kept constant, while the third parameter was varied.

### 3.2.1. Flange thickness ($t_f$)

The influence of the flange thickness on the buckling coefficient $k_f$ was analyzed first. The obtained values of the buckling coefficient are presented in Table 3, while their graphical representation is shown in Fig. 5.

*Tab. 3 Variation of flange thickness*

| $b_f$ = 300mm | $t_w$ = 5mm | b = 5000mm | $h_w$ = 970–993mm |
|---|---|---|---|
| $t_f$ (mm) | β | $k_f$ | $k_f$ EC3 |
| 7 | 0.83 | 2.83 | 3.21 |
| 9 | 1.76 | 3.19 | 3.21 |
| 12 | 4.20 | 3.52 | 3.21 |
| 15 | 8.22 | 3.71 | 3.22 |
| 19 | 16.78 | 3.85 | 3.22 |
| 24 | 33.99 | 3.94 | 3.23 |
| 27 | 48.55 | 3.98 | 3.23 |
| 30 | 66.80 | 4.01 | 3.24 |

| | | | |
|---|---|---|---|
| | | | |

Based on the results presented in Table 3 and Fig. 5, it can be concluded that the adoption of a constant value β = 3.16 in [1] is not an ideal solution, but provides sufficiently accurate results for engineering practice. For β = 0.82, lower values of the buckling coefficient $k_f$ are obtained compared with those given by [1], resulting in a non-conservative prediction. It should be emphasized that a flange thickness of $t_f$ = 7 mm is not common for a girder with web thickness of $t_w$ = 5 mm ($t_f$ / $t_w$ = 1.4); therefore, this case was analyzed solely for theoretical purposes. The unrealistic nature of such geometric proportions may justify the adoption of a constant value of β in [1]. Similar unrealistic combinations of dimensions also occur in Tables 4 and 5, which present the variation of the web thickness and flange width, respectively.

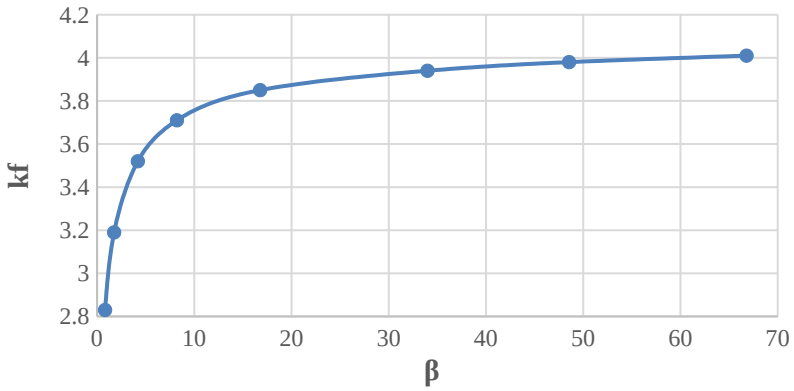


*Fig. 5 Influence of flange thickness $t_f$ (through the parameter β) on the buckling coefficient*

### 3.2.2. Web thickness ($t_w$)

In the subsequent analysis, the influence of the web thickness on the buckling coefficient $k_f$ was investigated. The obtained results are presented in Table 4, while their graphical representation is shown in Fig. 6.

*Tab. 4 Variation of web thickness*

| $b_f$ = 300mm | $t_f$ = 20mm | b = 5000mm | $h_w$ = 980mm |
|---|---|---|---|
| $t_w$ (mm) | β | $k_f$ | $k_f$ EC3 |
| 3.5 | 57.12 | 3.98 | 3.22 |
| 4 | 38.26 | 3.95 | |
| 5 | 19.59 | 3.87 | |
| 6 | 11.34 | 3.78 | |
| 7 | 7.14 | 3.67 | |
| 8 | 4.78 | 3.56 | |
| 11 | 1.84 | 3.18 | |
| 14 | 0.89 | 2.82 | |

As the web thickness decreases, the value of the buckling coefficient $k_f$ increases, which can be attributed to a more pronounced restraint of the web at the junction with the flanges. On the other hand, increasing the web thickness increases the overall load-carrying capacity of the girder, while the value of the buckling coefficient $k_f$ decreases.

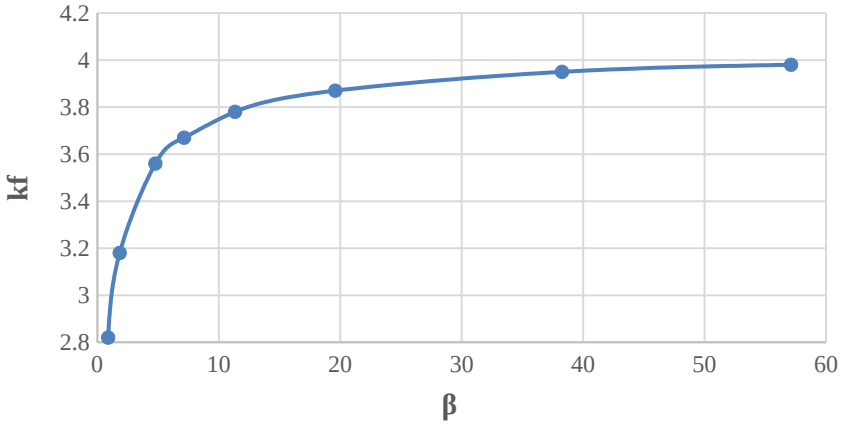


*Fig. 6 Influence of web thickness $t_w$ (through the parameter β) on the buckling coefficient*

### 3.2.3. Flange width ($b_f$)

In the final analysis, the influence of the flange width on the buckling coefficient $k_f$ was investigated. The obtained results are presented in Table 5, while their graphical representation is shown in Fig. 7.

*Tab. 5 Variation of flange width*

| $t_w$ = 5mm | $t_f$ = 20mm | b = 5000mm | $h_w$ = 980mm |
|---|---|---|---|
| $b_f$ (mm) | β | $k_f$ | $k_f$ EC3 |
| 15 | 0.98 | 2.65 | 3.22 |
| 25 | 1.63 | 3.04 | |
| 65 | 4.24 | 3.52 | |
| 125 | 8.16 | 3.71 | |
| 250 | 16.33 | 3.84 | |
| 500 | 32.65 | 3.93 | |
| 1000 | 65.31 | 3.98 | |

Increasing the flange width provides greater restraint to the web and leads to an increase in the buckling coefficient $k_f$, which is consistent with the expected structural behavior.

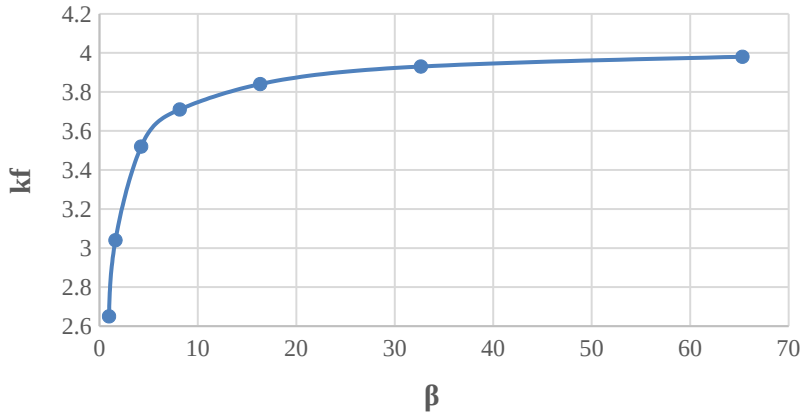


*Fig. 7 Influence of flange width $b_f$ (through the parameter β) on the buckling coefficient*

### 3.2.4. Discussion of Results

Lagerqvist concluded in [6] that the parameter β is not ideal for quantifying $k_f$ in the case of end patch loading, although it provides satisfactory results. The results presented in this study confirm Lagerqvist's conclusion. Finally, the results of the numerical analyses conducted for all three parameters are summarized in Fig. 8.

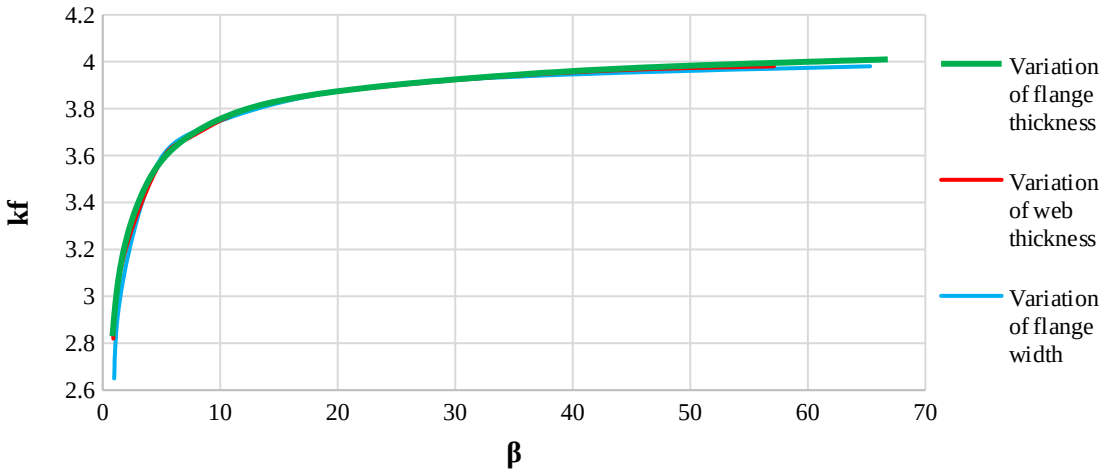


*Fig. 8 β–$k_f$ diagrams for c = 0.2m corresponding to different variations of the geometric parameters*

The previous three diagrams show an almost complete agreement between the results, indicating that the influence of the geometric parameters $t_f$, $t_w$ and $b_f$ on the buckling coefficient $k_f$ is adequately captured by the parameter β.
In [1], a value of β = 3.16 was adopted. Based on the results presented in Fig. 8, it can be concluded that, despite the simplification of the expression for the buckling coefficient $k_f$, the adopted solution provides satisfactory and conservative results for values of $\beta \geq 2$.

## 4. CONCLUSIONS

Based on the conducted numerical analyses, it can be concluded that the parameter β adequately captures the influence of the geometric characteristics of the flange and web on the value of the buckling coefficient $k_f$. Thus, the initial hypothesis was confirmed and the main objective of the study was achieved. The obtained results show that the effects of $t_w$, $t_f$ and $b_f$ on $k_f$ are reliably described by the parameter β for the investigated range of these parameters.
Future research should focus on a more detailed investigation of the influence of the remaining geometric and loading parameters, particularly the web depth $h_w$, the loaded length $s_s$, and the distance of the load application point from the free end c. Their inclusion may further improve the description of the girder behavior and enable a more precise definition of the relationship between the buckling coefficient $k_f$ and the relevant parameters.

## REFERENCES

[1] CEN. EN 1993-1-5:2006, Eurocode 3: Design of steel structures – Part 1-5: Plated structural elements. Brussels: European Committee for Standardization; 2006.

[2] O. Lagerqvist, B. Johansson, (1996). Resistance of I-girders to concentrated loads, Journal of Constructional Steel Research

[3] Gozzi, J. (2007). Patch Loading Resistance of Plated Girders – Ultimate and Serviceability Limit State, Doctoral Thesis, LTU.

[4] Rogač, M., Aleksić, S., Lučić, D. (2020). “Influence of patch load length on resistance of I-girders. Part I: Experimental research.” Journal of Constructional Steel Research

[5] Timoshenko, S. P., Gere, J. M. (1961). Theory of Elastic Stability. 2nd ed., McGraw-Hill Book Company, New York.

[6] Lagerqvist, O. (1994). Patch Loading – Resistance of Steel Girders Subjected to Concentrated Forces. Doctoral Thesis 1994:159D, Division of Steel Structures, Luleå University of Technology, Luleå, Sweden.

[7] Dassault Systèmes SIMULIA Corp. ABAQUS/CAE 2020, Dassault Systèmes, Providence, RI, USA.baqus

https://doi.org/10.24867/INDIS-2026-EN-100



# DISCRETIZATION-INDEPENDENT STRAIN-BASED LIMIT STATE CRITERIA FOR MVLEM MODELS OF RC WALLS

*Nikola Postolov[1], Koce Todorov[2], Ljupcho Lazarov[3]*

***Summary:***

The Multiple-Vertical-Line-Element Model (MVLEM) provides direct access to boundary element strains of reinforced concrete walls. However, the strain in a single base element is mesh dependent. This paper examines an approach that leaves the numerical model and material laws unchanged and instead prescribes the gauge length and position at which each strain criterion is evaluated. The approach is evaluated on three cyclic wall tests of Dazio et al. The global response is reproduced accurately and is practically independent of discretization. Base element strains differ between meshes by factors exceeding 20, whereas strains averaged over half the wall length and extrapolated to the reading position differ by less than a factor of 1.4 over most of the drift range. Limit states for reinforcement yielding, cover spalling, bar fracture and core crushing are defined using limit values from the material laws and EN 1998-1-1:2024. The criteria reproduce the drifts at yielding and spalling, predict the drift at failure within 8 % and identify the governing failure mechanism.

*Keywords: MVLEM, RC walls, discretization sensitivity, strain-based limit states, mesh independence, Eurocode 8*

# KRITERIJUMI GRANIČNIH STANJA NA OSNOVU DILATACIJA NEZAVISNI OD DISKRETIZACIJE ZA MVLEM MODELE AB ZIDOVA

***Rezime:***

Model sa više vertikalnih linijskih elemenata (MVLEM) omogućava direktan pristup dilatacijama u graničnim elementima armiranobetonskih zidova. Međutim, dilatacija u jednom elementu u osnovi zavisi od mreže. U radu se razmatra pristup koji numerički model i konstitutivne zakone materijala ostavlja nepromenjenim, a umesto toga propisuje mernu dužinu i položaj na kojem se svaki kriterijum ocenjuje. Pristup je evaluiran na tri ciklična ispitivanja zidova Dazia i dr. Globalni odgovor je reprodukovan sa dobrom tačnošću i praktično nezavisan od diskretizacije. Dilatacije u elementu u osnovi razlikuju se između mreža više od 20 puta, dok se dilatacije osrednjene na polovini dužine zida i ekstrapolirane do položaja očitavanja razlikuju manje od faktora 1,4 u najvećem delu opsega pomeranja. Granična stanja tečenja armature, otpadanja zaštitnog sloja, kidanja armature i drobljenja jezgra definišu se primenom graničnih vrednosti iz konstitutivnih zakona i EN 1998-1-1:2024. Kriterijumi reprodukuju pomeranja pri tečenju i otpadanju, predviđaju pomeranje pri lomu sa odstupanjem manjim od 8% i identifikuju merodavni mehanizam loma.

*Ključne reči: MVLEM, AB zidovi, osetljivost na diskretizaciju, granična stanja na osnovu dilatacija, nezavisnost od mreže, Evrokod 8*

[1]MSc, Faculty of Civil Engineering, Ss. Cyril and Methodius University in Skopje, Skopje, Macedonia, e-mail, postolov@gf.ukim.edu.mk ORCID 0000-0002-4681-5980,
[2]PhD, Faculty of Civil Engineering, Ss. Cyril and Methodius University in Skopje, Skopje, Macedonia, e-mail, todorov@gf.ukim.edu.mk ORCID 0000-0003-1736-4989,
[3]PhD, Faculty of Civil Engineering, Ss. Cyril and Methodius University in Skopje, Skopje, Macedonia, e-mail, lazarov@gf.ukim.edu.mk ORCID 0009-0003-7621-8161

## 1. INTRODUCTION

Nonlinear analysis of reinforced concrete (RC) wall and dual wall-frame systems increasingly relies on macro-models, among which the Multiple-Vertical-Line-Element Model (MVLEM) is widely used [1]. It reproduces the flexural response of slender walls with several degrees of freedom comparable to that of a frame element, while providing direct access to strains in the boundary elements. This feature makes the model particularly attractive for performance-based assessment, in which limit states such as reinforcement yielding, cover spalling, bar fracture, and core crushing are defined through strain-based criteria, as in the new generation of Eurocode 8 [2].

The reliability of such criteria, however, depends on a quantity that the model does not define uniquely. The strain computed in a single element at the wall base is mesh dependent. In the presence of concrete softening, deformation localizes in the shortest element, so that the same limit strain corresponds to different top displacements for different meshes. A common remedy is regularization of the material laws, in which the softening branch is adjusted to the element length so that the dissipated energy per unit crack area is preserved [3]. However, regularized parameters lose their direct link to the material test data and must be recalculated whenever the mesh is changed, which is inconvenient in parametric studies of complete structural systems where wall discretization is not the primary variable.

This paper examines an alternative approach that leaves the numerical model and material laws unchanged and instead fixes the way in which the response is evaluated. Each strain criterion is assessed over a prescribed gauge length and at a prescribed position in the cross section, consistent with the basis used to define its limit value. None of the individual components of the rule is new. Averaging over half the wall length, reading strains at the hoop axis, and adopting a base gauge length of a few wall thicknesses are all supported by previous studies. The objective here is to evaluate whether their combined use in an unregularized macro-model can provide practically mesh-independent strain measures and reliable limit-state predictions when compared with experimental results.

The approach is evaluated against three quasi-static cyclic wall tests by Dazio et al. [4], comprising a confined ductile wall (WSH3), an unconfined wall (WSH4), and a wall with higher axial load and extended confinement (WSH6). For each wall, the sensitivity of global and local response quantities to discretization along the height and across the section is quantified, a reading rule is established for obtaining practically mesh-independent strains, and a set of strain-based limit states using limit values from the material laws and Eurocode 8 is verified against the observed damage and drift at failure.

## 2. NUMERICAL MODEL AND TEST SPECIMENS

### 2.1. WALL ELEMENT AND MATERIAL LAWS

In the MVLEM, the flexural response of a wall segment is represented by vertical uniaxial macro-fibres under the plane-sections hypothesis, allowing direct evaluation of boundary-element strains. The relative rotation between the element ends is assumed to occur at a height $c \cdot h$ above the bottom edge. The value $c = 0.4$ [1] is calibrated to reproduce the non-uniform curvature distribution of flexure-dominated walls; standard fibre-based beam elements do not include an equivalent parameter. Shear is represented by a linear elastic spring, while shear-flexure interaction and bond slip in the anchorage zone are not included [1].

Concrete is modelled using the uniaxial Concrete02 material [5], which follows the Kent-Scott-Park backbone [6], consisting of a parabolic ascending branch up to the peak stress, a linear descending branch to a residual strength, linear tension softening, and

unloading/reloading rules with stiffness degradation. Confinement is represented through increased strength and ultimate strain of the concrete core. The cover is not modelled as a separate fibre. Instead, the entire boundary zone is assigned to the confined concrete law. Reinforcement is modelled using Steel02, based on the Menegotto-Pinto model [7] with the extension of Filippou et al. [8], including a bilinear envelope, strain hardening, and the Bauschinger effect.

Two consequences of these material models are important for the subsequent analysis. First, the hysteretic response degrades in stiffness but not in strength under cyclic loading. Hoop fracture is not represented, and the confined core does not lose its confinement. Second, Steel02 is symmetric in tension and compression and does not account for bar buckling, fracture, or fatigue. Consequently, the physical mechanisms that cause strength loss in real walls, such as hoop fracture and fracture or buckling of longitudinal reinforcement, are not represented explicitly in the model. Local concrete degradation is confined to a relatively small part of the section ($c/l_w \approx 0.15–0.21$), while the tensile reinforcement continues to harden and sustain the flexural resistance. The computed response therefore does not exhibit a pronounced strength drop and continues beyond the stage at which the experimental response begins to degrade. For this reason, the relevant limit states are tracked through strain-based criteria during the analysis rather than inferred from the shape of the hysteresis loops. Once a near-collapse criterion is exceeded, the subsequent computed response is outside the physically meaningful range of the model and is not used.

## 2.2. TEST SPECIMENS AND DISCRETIZATIONS

The three specimens are taken from the experimental series of Dazio, Beyer, and Bachmann [4, 9]. All specimens have the same cross-sectional dimensions, with wall length $l_w = 2.0$ m and thickness $t_w = 150$ mm, while the shear span is $L_V = 4.56$ m for WSH3 and WSH4 and 4.52 m for WSH6. The specimens differ in the longitudinal and transverse reinforcement of the boundary elements and in the applied axial load. WSH3 represents a confined ductile reference wall; WSH4 has no confinement and lies outside typical seismic design practice but is included to examine the criteria for an unconfined section; WSH6 is subjected to a higher axial load ratio ($\nu = 0.108$) and has extended confinement. Each numerical model is subjected to the same displacement protocol as used in the tests, consisting of two complete cycles per ductility level with amplitude increments of $\Delta y = 15.4$ mm for WSH3 and WSH4 and 12.75 mm for WSH6 [4].

The measured mean material properties reported in [4] are used: $f'_c$=39.2/40.9 /45.6 MPa, $R_{p0.2}$=601/576/576 MPa and $A_{gt}$=7.69/7.29/7.29 % for the Ø12 boundary bars of WSH3/WSH4/WSH6, respectively. Transverse reinforcement consists of Ø6 hoops at 75 mm spacing in WSH3 and 50 mm in WSH6, while WSH4 has no confinement, resulting in confinement factors K=1.13/1.00/1.18.

The reference model uses elements 50 cm in height and nine vertical macro-fibres across the section, with two fibres assigned to each boundary element (h050/m09). The notation h050 denotes an element height of 50 cm, while m09 denotes a total of 9 vertical macro-fibres across the wall section. Sensitivity to the discretization along the wall height is investigated using six meshes with element heights ranging from 10 to 100 cm (h010–h100), all with the m09 section discretization, up to a top drift of 2.0%. Sensitivity to the section discretization is examined at the h050 height mesh by progressively subdividing the confined boundary regions, using configurations m07–m31 for WSH3 and WSH4 and m07–m41 for WSH6. Together, these two refinement studies quantify the sensitivity of both global and local response quantities, including strength, stiffness, and boundary element strains.

## 3. DISCRETIZATION SENSITIVITY

### 3.1. GLOBAL RESPONSE

The global response is reproduced accurately and is largely independent of discretization. Table 1 presents the deviation of the computed peak lateral force from the experimental value for the reference model, together with the range obtained for the height and section discretizations. For the reference model, the peak force is underestimated by 1–4 %. Across the six height meshes, the maximum deviation remains within 1.9 % for WSH3, 7.3 % for WSH4, and 3.9 % for WSH6.

The section discretization has a smaller influence than the element height. The spread in peak force across all section discretizations is 0.8% for WSH3 and 1.6% for WSH6. For WSH4, the spread reaches 7.9%, but this is caused entirely by the coarsest discretization, m07; when this case is excluded, the spread reduces to 0.2%. In model m07, each boundary element is represented by a single fibre, so the strain is evaluated at the fibre centroid and therefore underestimates the edge strain. Because the unconfined concrete has a steep descending branch, degradation begins later and the strength is consequently overestimated. The adopted m09 discretization, with two fibres in each boundary element, is not affected by this issue.

*Tab. 1 Deviation of the computed peak lateral force from the experimental value*

| Wall | Reference model h050/m09 | Range over height meshes h010–h100 (m09) | Spread over section discretizations (h050) |
|---|---|---|---|
| WSH3 | –1 % | up to –1.9 % | 0.8 % |
| WSH4 | –4 % | up to –7.3 % | 7.9 % (0.2 % without m07) |
| WSH6 | –3 % | up to –3.9 % | 1.6 % |

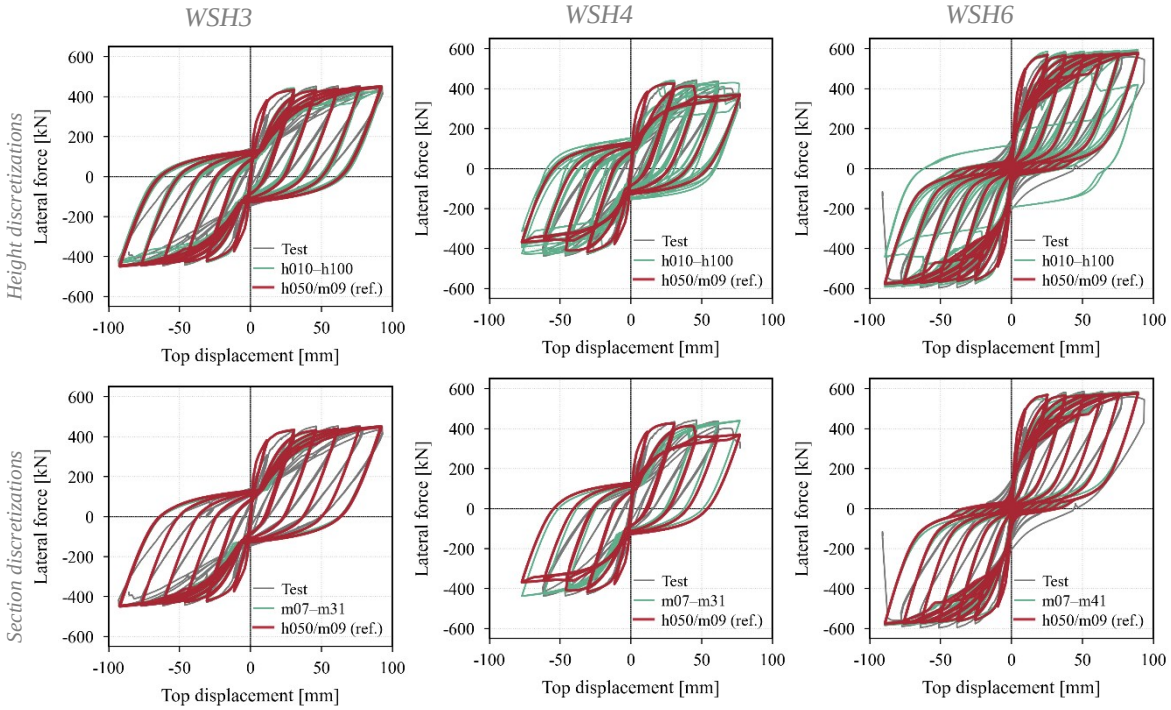


*Fig. 1 Lateral force - top displacement response of WSH3, WSH4 and WSH6: experimental response and height discretizations (top row) and section discretizations (bottom row)*

## 3.2. LOCAL STRAINS AND THE READING RULE

Local strains can be used consistently only if a fixed reading rule is adopted, defining both the gauge length along the wall height and the position in the cross section at which the strain is evaluated. Along the wall height, the strain taken directly from a single base element is strongly mesh-dependent. For example, at 2.0% drift the compressive strain in WSH6 differs by more than a factor of 20 among the six height meshes, because the same inelastic deformation is distributed over element heights ranging from 10 to 100 cm. To reduce this dependence, the strain is averaged over the lower length Lav of the wall, measured from the base, using a height-weighted average of the strains in the elements contained within this length, with partial contribution from the last element where necessary. For Lav=lw/2 [11], the mesh dependence is greatly reduced. The averaged curvature differs by only about 2–7% among the meshes, while the corresponding averaged strains differ by less than a factor of 1.4 over most of the drift range. Larger differences, reaching up to a factor of 2.7, occur only on the compression side at the largest drift levels. The notation Lav is used to distinguish the averaging length from the plastic hinge length Lpl defined by EN 1998-1-1:2024 expression (7.13). For the three walls, the two lengths are numerically very similar (Lav = 1000 mm and Lpl ≈ 984–1016 mm), although they are conceptually different. Figures 2 and 3 compare the direct base-element strain with the strain averaged over Lav. As the element height decreases, the direct base-element strain becomes increasingly mesh-dependent, whereas the averaged values remain closely grouped for all six meshes. In WSH4, the finest mesh reaches the residual branch of the concrete law at about 1.4% drift, after which the localization shifts to the element above.

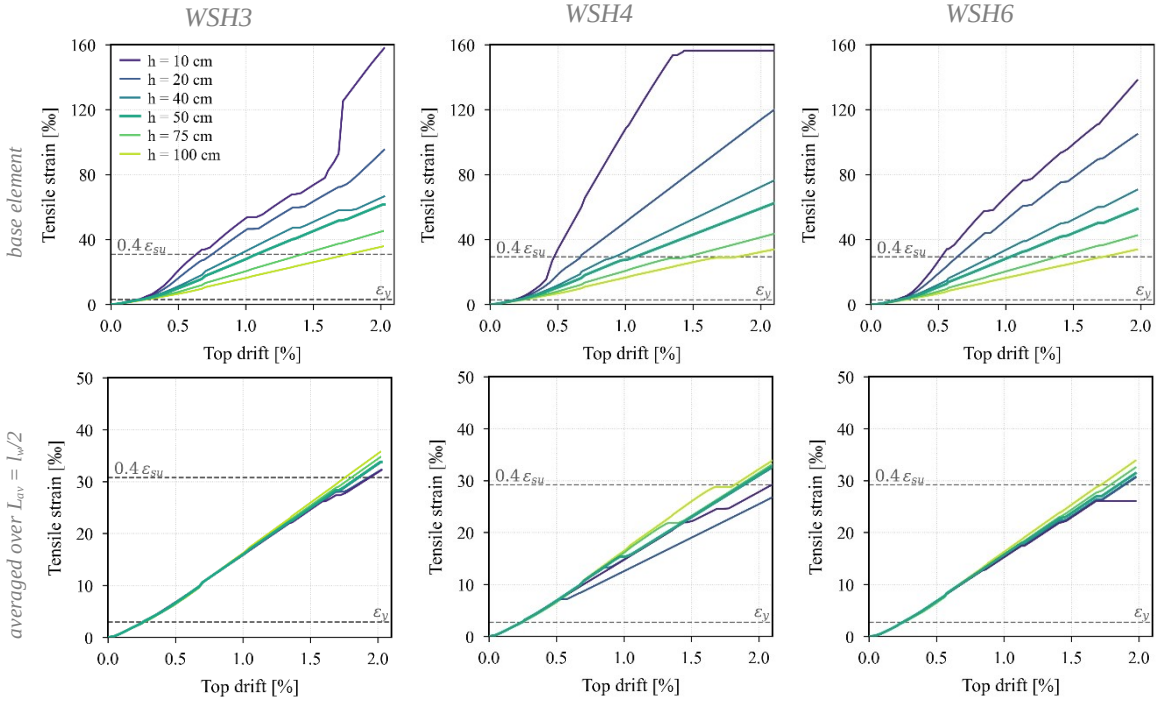


*Fig. 2 Tensile strain at the centroid of the first bar for the six height meshes h010–h100: read in the base element and averaged over $L_{av} = l_w/2$; dashed lines εy and $0.4{\cdot}\varepsilon_{su}$*

The second component of the reading rule concerns the position across the wall section. Because the strain distribution is linear, the strain at the centroid of the outermost fibre differs systematically from the strain at the physical reading position. For the m09 discretization, the fibre strain underestimates the strain at the prescribed reading position by approximately 20% on the compression side and by 2–4% on the tension side. For the unconfined WSH4 wall, the compression-side difference is about 12%. The larger discrepancy on the compression side results from the relatively shallow compression zone

($c/l_w \approx 0.15–0.21$), so that the distance between the fibre centroid and the section edge represents a larger fraction of the compression-zone depth. With only one fibre in each boundary element, as in m07, the discrepancy reaches about 70% on the compression side. Because the strain profile is linear, extrapolation to the prescribed reading position removes most of this discretization effect. For m09 and finer discretizations, the remaining variation is below 0.2% on the tension side and within 5% on the compression side. The larger differences observed for m07 reflect the coarse section representation itself rather than the strain-reading procedure (Figure 4).

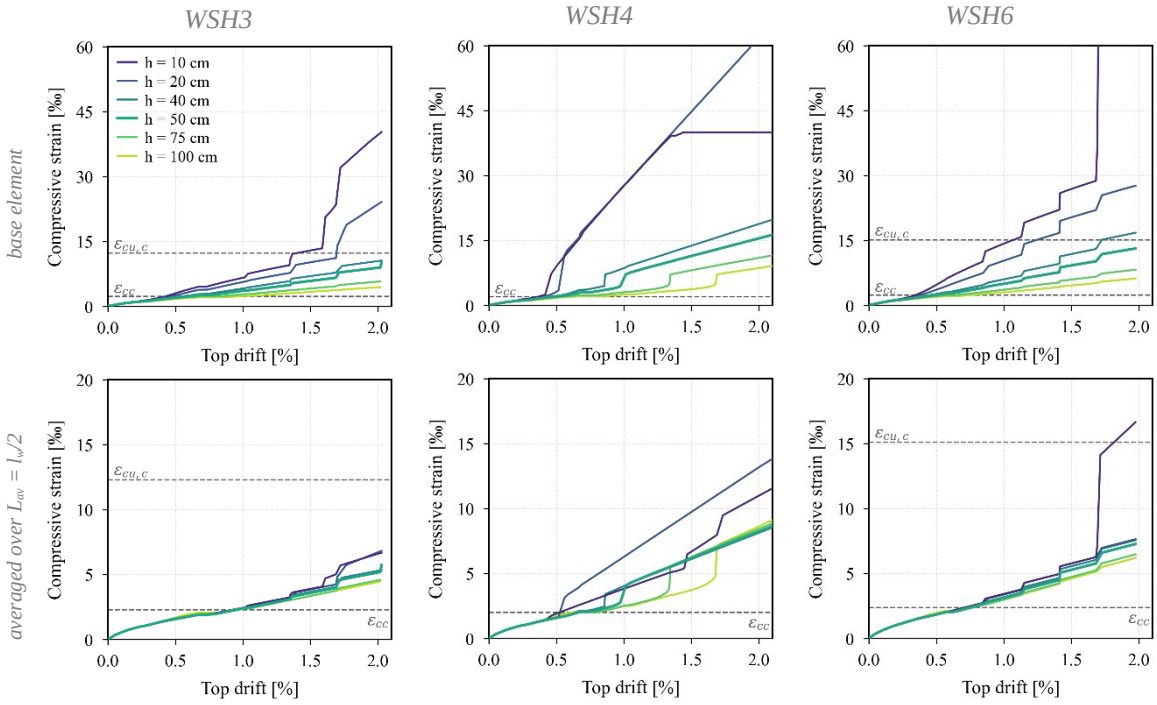


*Fig. 3 Compressive strain at the hoop axis for the six height meshes h010–h100, read in the base element and averaged over $L_{av} = l_w/2$; dashed lines $\varepsilon_{cc}$ and $\varepsilon_{cu,c}$*

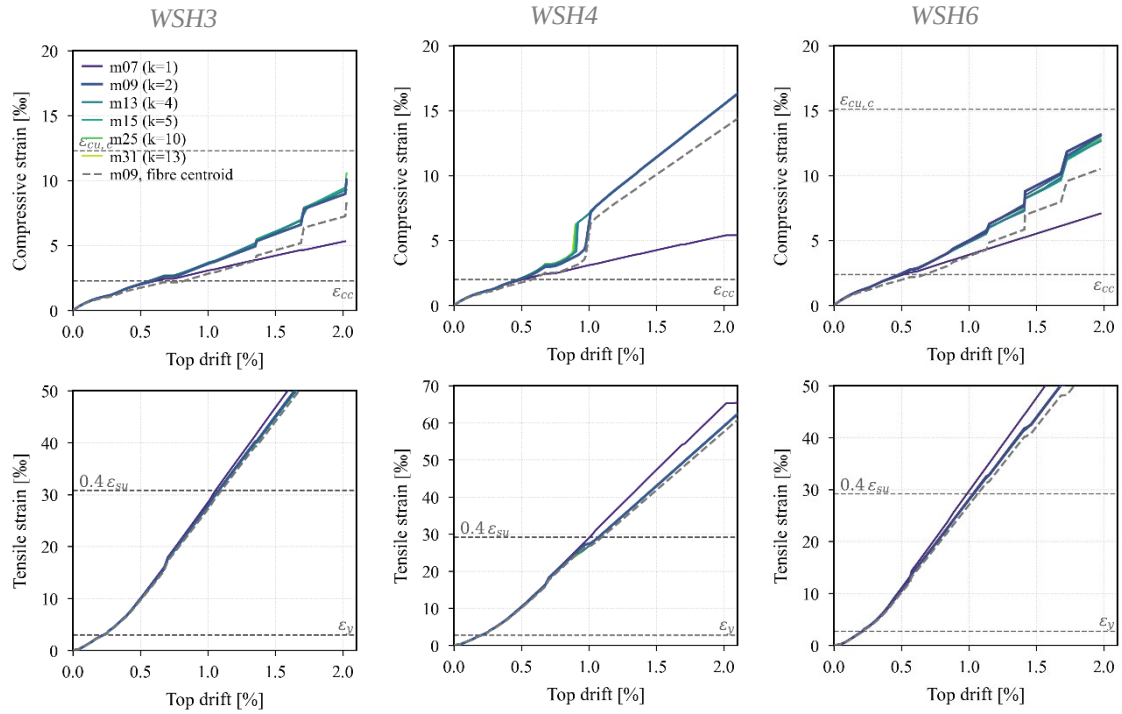


*Fig. 4 Base-element strain extrapolated to the reading position for the section discretizations m07–m31 (WSH6: m07–m41); dashed line: strain at the outer fibre centroid of m09*

On the compression side, the averaged strain reflects two competing effects. The model does not include bond slip in the anchorage zone or the spread of nonlinearity associated with diagonal cracking. Consequently, part of the imposed top displacement that is accommodated by these mechanisms in the experiment must, in the numerical model, be reproduced through increased curvature in the base region. The base curvature is therefore overestimated independently of the mesh. Approximately 91–92% of the rotation over the instrumented height is concentrated within the bottom 1.0 m of the wall in the model, compared with about 81% in the test.

Averaging over the element height acts in the opposite direction by reducing the influence of the local concentration of compressive deformation. The net effect cannot be established from the model formulation alone and must therefore be assessed through comparison with the experimental response. In the specimen for which crushing governed, the crushing criterion is reached before the observed failure drift, indicating a conservative prediction. For this reason, the limit states are not associated with raw local strains. Instead, each criterion is defined together with a prescribed gauge length and reading position and is verified as a complete criterion against the experimentally observed top drift. Mesh dependence is therefore reduced through post-processing, while the numerical model and material laws remain unchanged. Regularization [3] provides an alternative by addressing the dependence within the constitutive formulation itself. However, the regularized softening parameters depend on the element length for which they are derived and would therefore introduce mesh-specific material parameters into system-level models. In addition, regularization modifies the compressive softening branch, which is particularly relevant for analyses extending well into the strength-degradation range, whereas the limit states considered here are reached before pronounced degradation occurs.

The strain underestimation reported by Orakcal and Wallace [12] refers to direct comparison with instrumental measurements, which include contributions from base-crack opening, local wall-foundation effects, and the localization of compressive deformation over a short length. The criteria adopted here, by contrast, are based on strains derived from section analysis, which are also systematically lower than the directly measured strains in the Dazio tests [4]. The two comparisons therefore refer to different strain measures and are not contradictory.

## 4. STRAIN-BASED LIMIT STATE CRITERIA

On this basis the limit states are defined as criteria on computed strains, with limit values calculated for each wall from its own material properties and confinement, and with a fixed reading rule that follows one principle: each criterion is evaluated over a gauge length consistent with the basis used to define its limit value, and at the position where the material it refers to actually exists (Table 2). Reinforcement yielding and cover spalling take their limit values directly from the reinforcement stress–strain law and from the strain at peak stress of the unconfined boundary concrete, respectively. The two near-collapse states, bar fracture and core crushing, take theirs from the normative expressions of EN 1998-1-1:2024 [2]. All four criteria are compared with the drifts at which the corresponding event was recorded in the tests [4, 9].

*Tab. 2 Limit states of the wall: limit values and reading rule*

| Limit state | Limit value | Reading rule |
|---|---|---|
| Yielding of reinforcement | $\varepsilon_y$ – yield strain from the reinforcement stress–strain law | averaged along height over $L_{av}$, at the centroid of the first longitudinal bar |
| Cover spalling | $\varepsilon_{cc}$ – strain at peak stress of unconfined concrete | averaged along height over $L_{av}$, at the axis of the hoop |
| Bar fracture | $\varepsilon_{su}$ – EN 1998-1-1 (7.8), i.e. strain amplitude $0.5–0.6 \cdot A_{gt}$ | averaged along height over $L_{av}$, at the centroid of the first longitudinal bar |
| Core crushing | $\varepsilon_{cu,c}$ – EN 1998-1-1 (7.12) from the confinement of the wall | base element $h$ = 500 mm, at the axis of the hoop |

## 4.1. READING POSITIONS

The compressive strain is evaluated at the axis of the outermost hoop, located at a distance from the section edge equal to the concrete cover plus half the hoop diameter (17.1 mm). The tensile strain is evaluated at the centroid of the outermost row of longitudinal reinforcement, located at a distance equal to the cover plus the hoop diameter plus half the longitudinal bar diameter (25.2 mm). The same reading positions are used for all three walls. Both positions follow the same physical principle. The confined concrete strain εcu,c according to expression (7.12) refers to the confined core, whose geometric boundary is defined by the hoop axis, while εy and εsu are properties of the reinforcing bar and should therefore be evaluated at the bar centroid. Evaluating the strain at the extreme concrete fibre would imply checking a criterion at a position where, depending on the limit state, the relevant material either no longer exists because of cover spalling or is not present in the first place.

## 4.2. GAUGE LENGTH FOR THE STRAIN-AVERAGED CRITERIA

The averaging length Lav = lw/2 is supported by three arguments. First, it corresponds to the empirical recommendation of Abdullah [11], derived from a large database of rectangular flexure-dominated walls, which is the class of elements considered here. Second, for the three walls analysed, Lav is close to the plastic hinge length Lpl given by EN 1998-1-1:2024 expression (7.13): Lpl=1015/1016/992 mm for WSH3/WSH4/WSH6, compared with Lav=1000 mm. This agreement is numerical rather than definitional, but it is important because it allows the computed strains to be evaluated over a gauge length comparable to that associated with the derivation of the code limit strains. The code limit strains are not direct local material measurements. Grammatikou et al. [10] determined ultimate curvature over a finite base length of the order of the plastic hinge length and converted it to strain through moment-curvature analysis. The resulting strain limits therefore represent deformation over a finite gauge length rather than the response of an infinitesimal section, although the authors also note that the values may be applied to the end section. Once anchorage-slip rotation is removed, the measured ultimate curvature shows no systematic dependence on the adopted base length, provided that this length remains of the order of the plastic hinge length. Third, the numerical results confirm the need for averaging. Without averaging, the base-element strain varies by more than a factor of 20 between meshes, whereas averaging over Lav reduces the differences to less than a factor of 1.4 over most of the drift range (Figures 2 and 3). The averaged strain therefore provides a sufficiently stable quantity for use with a prescribed limit value.

## 4.3. GAUGE LENGTH FOR THE CRUSHING CRITERION

The crushing criterion is associated with a different characteristic length from that used for the tension-based criteria. In thin walls, approximately those with thicknesses below 300 mm and length-to-thickness ratios of about 10–15, for which the compression-zone depth c is comparable to the wall thickness tw, compression-side damage such as cover spalling, concrete crushing, and bar buckling tends to localize over a height of the order of a few wall thicknesses. In the tests reported by Segura and Wallace [13], compressive strains were concentrated within the bottom 356 mm of walls 152–229 mm thick, corresponding to approximately 1.6–2.3·tw, while the average strain above that region remained below about 2 ‰. This behaviour forms the basis of plastic hinge formulations of the type lc = α·tw proposed for thin walls [13, 14]. The specimens considered here fall within the same general range. With lw/tw=13.3 and c/lw=0.15–0.21, the ratio c/tw is approximately 2.0–2.8. This is close to the threshold of about 2.5 identified in [13], above which compression-side damage may become critical for drift capacity. This observation is consistent with the experimentally observed failure mechanisms. Fracture of the tension reinforcement governed in WSH3, whereas compression failure governed in WSH6. As with Lpl, the length lc should be interpreted as a characteristic length associated with the adopted limit strain rather than as a directly measured damage height. In [14], the value α = 2.5 was calibrated together with a concrete ultimate strain of 7‰ for walls with limited confinement. For better confined walls, measured edge strains may exceed 20‰ [13], indicating that the same characteristic length may provide a conservative estimate of deformation capacity.

The observed damage patterns of the Dazio specimens provide an additional check. In WSH6, where crushing governed, the compression damage zone extended over approximately 450–550 mm, corresponding to 3.0–3.7·tw. In WSH4, the observed zone was about 330–350 mm (2.2–2.3·tw), while in WSH3 the reported 250 mm does not represent a fully developed crushing zone because failure was governed by fracture of the tension reinforcement. The characteristic length lc = 2.5·tw = 375 mm therefore lies below the measured height of the fully developed crushing zone in WSH6, consistent with its conservative basis.

On this basis, the crushing strain is evaluated over a fixed 500 mm base element. This length lies within the experimentally observed height of the crushing zone in WSH6 and is therefore of the same order as the physical localization region. It avoids both excessive dilution of compressive strain over a long element and excessive localization in a very short element. The 500 mm length is treated as a gauge length for the criterion rather than as a numerical discretization parameter. The tension-based and crushing criteria therefore use different gauge lengths because they represent different physical mechanisms. Tension-related inelasticity spreads over a larger height governed by the moment gradient and distributed cracking, whereas crushing is a local instability of the compression zone whose characteristic dimension is of the order of the wall thickness.

## 4.4. LIMIT VALUES FROM EN 1998-1-1

EN 1998-1-1:2024 provides two expressions for the ultimate strain of tensile reinforcement: expression (7.8), applicable before cover spalling, and expression (7.10), applicable after spalling. In the walls considered here, reinforcement fracture occurs after cover spalling. However, direct application of expression (7.10) gives approximately 0.262·εsu,nom, which is substantially lower than the strain range associated with fracture in the experimental observations. The calibration basis of expression (7.10) should also be considered. According to Grammatikou et al. [10], the underlying database is dominated by columns and relatively small sections, with a mean section depth of approximately 0.5

m in the cyclic tests. Its direct application to walls with lw = 2.0 m therefore represents an extrapolation beyond the main calibration range.

Under cyclic loading, each tensile excursion starts from a previously compressed state, and repeated reversals progressively consume the ductility capacity of the reinforcement. In the Dazio tests [4], fracture was associated with a tensile strain excursion of approximately 0.5–0.6·Agt, rather than with the total uniform elongation Agt. Expression (7.10) gives a value less than half of this experimentally observed range. For the present limit-state criterion, a value of 0.4·εsu,nom, corresponding to expression (7.8), is therefore adopted, with εsu,nom taken as the measured Agt. The criterion is evaluated in terms of total tensile strain. At the point at which it is reached, the strain excursion εs − εc is larger by the magnitude of the compressive strain from the preceding half-cycle, approximately 6‰, giving an excursion of about 0.48·Agt. This remains slightly below the experimentally observed range of 0.5–0.6·Agt, and is therefore conservative. Expression (7.10) is retained for its intended role in the normative calculation of ultimate rotation but is not used here as a directly tracked fracture criterion. For concrete, the input value εcu in expression (7.9) is taken as 3.5‰ for all three walls, corresponding to the lower-bound value obtained for sections of ordinary dimensions [10]. The confined concrete strain εcu,c is calculated from expression (7.12) using the confinement effectiveness factor and volumetric ratio of transverse reinforcement, both referred to the axis of the outer hoop. This is the same reference position at which the compressive strain is evaluated in the numerical model. The resulting values are εcu,c=12.3 ‰ for WSH3 and 15.1 ‰ for WSH6.

## 5. VERIFICATION AGAINST THE OBSERVED FAILURE

The proposed limit-state framework is verified against the experimental observations. For WSH3, the bar fracture criterion predicts a top drift of 1.85%, compared with the observed value of 2.02%. For WSH6, the crushing criterion predicts 1.91%, compared with the observed 2.08%. Both predictions are approximately 8% conservative, using the averaging and reading rules defined in advance and without calibration to the observed failure drifts. In WSH3, only the criterion corresponding to the experimentally observed failure mechanism is activated. The specimen failed by fracture of the tensile reinforcement, while the crushing criterion remains below its limit value. This indicates that the framework is able not only to predict the failure drift, but also to distinguish between competing failure mechanisms. The result also provides an internal consistency check of the adopted limit values. If the compressive-strain limit were set too low, the crushing criterion would be triggered prematurely, and the predicted failure mechanism would be incorrect.

The earlier limit states are assessed against the experimentally recorded events [4]. The reinforcement-yielding criterion is reached at drifts of 0.25%, 0.24%, and 0.25% for WSH3, WSH4, and WSH6, respectively, compared with recorded first-yield drifts of 0.25%, 0.25%, and 0.22%. The cover-spalling criterion is reached at 1.00% for WSH3, compared with an observed onset at 1.02%, and at 0.83% for WSH6, compared with a mean observed drift of 0.86% over the spalling cycles. For the unconfined WSH4 wall, the spalling criterion is reached earlier, at 0.60% drift compared with the observed 1.02%. This conservative discrepancy reflects the use of the strain at peak stress of the unconfined concrete law, approximately 2.0‰, which is lower than the strain of about 3‰ inferred by Dazio et al. [4] from section analysis at the onset of spalling.

Two additional checks are independent of the numerical model and of the adopted averaging length. First, the confined concrete ultimate strains calculated from expression (7.12) differ by only 3-5% from the values obtained independently from the section

analysis reported by Dazio et al. [4]. Second, the choice of expression (7.8) instead of (7.10) for the bar fracture criterion is supported by the corresponding predicted drift. With expression (7.8), fracture is reached at 1.85% drift compared with the observed 2.02%, whereas expression (7.10) would trigger the criterion at approximately 1.25%.

The scope of these results is subject to several limitations. The numerical model does not reproduce the strength drop observed experimentally at member level, so the conventional definition of near collapse based on a 20% reduction in strength cannot be applied directly. In the present framework, this role is instead taken by the strain-based limit-state criteria, and the computed response beyond the first exceedance of a near-collapse criterion is not considered.

Anchorage slip and shear-flexure interaction are not included in the model. The omission of anchorage slip is reflected in the overestimation of base curvature discussed in Section 3.2. Nevertheless, the global response is reproduced with good accuracy, and the predicted failure drifts remain close to the experimental values for the walls considered here. Since these specimens do not enter the nonlinear shear range, the influence of the neglected shear-flexure interaction is expected to be limited within the scope of the present study.

Finally, each of the two near-collapse criteria is verified against only one specimen: bar fracture in WSH3 and core crushing in WSH6. The present results therefore demonstrate that the framework can distinguish between the two observed failure mechanisms, but broader validation is required before the criteria can be generalized to a wider range of wall geometries, reinforcement layouts, axial load levels, and confinement conditions.

## 6. CONCLUSIONS

The verification of the MVLEM against three quasi-static cyclic wall tests leads to the following conclusions. The global response is reproduced with good accuracy and shows limited sensitivity to discretization. For the reference models, the computed peak lateral force differs from the experimental value by 1–4%, while the spread across six height meshes and up to eleven section discretizations remains below 8%. The base curvature is systematically overestimated due to model formulation. However, this effect is largely mesh-independent, has a known physical origin, and leads to conservative strain estimates.

Local strains can be used consistently only when a fixed reading rule is adopted. For the strain-averaged criteria, averaging over Lav = lw/2 and extrapolating the strain to the prescribed reading position substantially reduces the dependence on both height and section discretization. For the crushing criterion, the strain is evaluated over a 500 mm base element, corresponding to a gauge length of the same order as the observed compression-damage zone. In this way, practically mesh-independent strain measures are obtained without regularization of the material laws.

The limit states are defined through strain-based criteria, with limit values taken from the material laws and EN 1998-1-1:2024 and evaluated using the prescribed gauge lengths and reading positions. The criteria reproduce the experimentally observed drifts at reinforcement yielding and cover spalling with good accuracy, predict the failure drift within about 8% of the measured value, and correctly identify the governing failure mechanism in the specimens brought to failure.

The proposed reading rule does not introduce calibration parameters fitted to the observed failure drifts. The averaging length Lav is derived from the wall geometry, while the limit values are determined from the material properties and confinement of each specimen. For the wall class investigated here, a practical discretization consists of a 500 mm base element, with elements of comparable height over the plastic region, and at least two

vertical macro-fibres in each boundary element. A single-fibre boundary representation may underestimate the edge strain and, for an unconfined section, may overestimate the lateral strength, whereas finer subdivision has little influence once the strain is extrapolated to the prescribed reading position.

The results indicate that the proposed framework provides a practical basis for strain-based limit-state assessment of MVLEM wall models while reducing sensitivity to discretization. Its application to walls with substantially different geometries, confinement conditions, axial load levels, and failure mechanisms requires broader validation, particularly for the fixed gauge length adopted for the crushing criterion. The approach is therefore considered suitable for further application and validation in parametric analyses of dual wall-frame systems, where wall discretization is not the primary variable.

## REFERENCES

[1] Orakcal K., Wallace J. W., Conte J. P. (2004). Flexural Modeling of Reinforced Concrete Walls - Model Attributes. ACI Structural Journal, 101(5), pp. 688-698.

[2] EN 1998-1-1:2024. Eurocode 8: Design of structures for earthquake resistance - Part 1-1: General rules and seismic action. CEN, Brussels.

[3] Pugh J. S., Lowes L. N., Lehman D. E. (2015). Nonlinear line-element modeling of flexural reinforced concrete walls. Engineering Structures, Volume 104, pp. 174-192. https://doi.org/10.1016/j.engstruct.2015.08.037

[4] Dazio A., Beyer K., Bachmann H. (2009). Quasi-static cyclic tests and plastic hinge analysis of RC structural walls. Engineering Structures, 31(7), pp. 1556-1571. https://doi.org/10.1016/j.engstruct.2009.02.018

[5] Yassin M. H. M. (1994). Nonlinear Analysis of Prestressed Concrete Structures under Monotonic and Cyclic Loads. Doctoral thesis, University of California, Berkeley, USA.

[6] Scott B. D., Park R., Priestley M. J. N. (1982). Stress-Strain Behavior of Concrete Confined by Overlapping Hoops at Low and High Strain Rates. ACI Journal, 79(1), pp. 13-27.

[7] Menegotto M., Pinto P. E. (1973). Method of Analysis for Cyclically Loaded R.C. Plane Frames Including Changes in Geometry and Non-Elastic Behavior of Elements under Combined Normal Force and Bending. IABSE Symposium on Resistance and Ultimate Deformability of Structures, Lisbon, pp. 15-22.

[8] Filippou F. C., Popov E. P., Bertero V. V. (1983). Effects of Bond Deterioration on Hysteretic Behavior of Reinforced Concrete Joints. Report UCB/EERC-83/19, University of California, Berkeley, USA.

[9] Dazio A., Wenk T., Bachmann H. (1999). Versuche an Stahlbetontragwänden unter zyklisch-statischer Einwirkung. IBK Bericht Nr. 239, ETH Zürich, Switzerland.

[10] Grammatikou S., Biskinis D., Fardis M. N. (2016). Ultimate Strain Criteria for RC Members in Monotonic or Cyclic Flexure. Journal of Structural Engineering, 142(9), 04016046. https://doi.org/10.1061/(ASCE)ST.1943-541X.0001507

[11] Abdullah S. A. (2019). Reinforced Concrete Structural Walls: Test Database and Modeling Parameters. Doctoral thesis, University of California, Los Angeles, USA.

[12] Orakcal K., Wallace J. W. (2006). Flexural Modeling of Reinforced Concrete Walls - Experimental Verification. ACI Structural Journal, 103(2), pp. 196-206.

[13] Segura C. L., Wallace J. W. (2018). Impact of Geometry and Detailing on Drift Capacity of Slender Walls. ACI Structural Journal, 115(3), pp. 885-895.

[14] Takahashi S., Yoshida K., Ichinose T., Sanada Y., Matsumoto K., Fukuyama H., Suwada H. (2013). Flexural Drift Capacity of Reinforced Concrete Wall with Limited Confinement. ACI Structural Journal, 110(1), pp. 95-104.

https://doi.org/10.24867/INDIS-2026-EN-112



# PREDICTION OF THE LOAD-SLIP RELATIONSHIP FOR TIMBER-STEEL CONNECTIONS WITH OUTER STEEL PLATES

*Dragan Manojlović[1], Tanja Perčić[2], Miloš Milić[3], Radovan Perić[4]*

***Summary:***

The load-slip behaviour of connections represents an indispensable input for analytical models and numerical simulations in the design of timber structures. As these connections demonstrate strongly nonlinear behaviour even under relatively small loads, and given that the bilinear model proposed by Eurocode 5 is unable to adequately capture such response, the characterisation and prediction of the complete load-slip curve for timber connections is of great importance. For this reason, researchers in this field have employed suitable exponential functions to describe this behaviour and have developed numerical models based on the beam-on-elastic-foundation theory, with input parameters derived from experimental data and/or empirical relations. This paper presents a numerical model for predicting the complete load-slip response of timber-to-steel connections with outer steel plates, developed on the basis of the European Yield Model and accounting for the nonlinear behaviour of all materials involved.

*Keywords: timber-steel connections, outer steel plates, load-slip relationship, model*

# PREDVIĐANJE ZAVISNOSTI SILA-POMERANJE KOD VEZA DRVO-ČELIK SA SPOLJAŠNJIM ČELIČNIM PLOČAMA

***Rezime:***

Pri projektovanju drvenih konstrukcija, ponašanje veza opisano preko zavisnosti sila-pomeranje predstavlja jedan od neizostavnih ulaznih podataka za analitičke modele i numeričke simulacije. Budući da ove veze pokazuju veoma izraženo nelinearno ponašanje čak i pri malim silama, a bilinearni model predložen od strane Evrokoda 5 nije u mogućnosti da opiše ovakvo ponašanje, opisivanje i predviđanje kompletne zavisnosti sila-pomeranje za drvene veze je od izuzetnog značaja. Stoga istraživači u oblasti su primenjivali adekvatne eksponencijalne funkcije za njihovo opisivanje i razvijali numeričke modele zasnovane na teoriji grede na elastičnoj podlozi, sa ulaznim podacima baziranim na eksperimentalnim rezultatima i/ili empirijskim izrazima. U ovom radu razvijen je numerički model za predviđanje kompletne krive sila-pomeranje kod veza drvo-čelik sa spoljašnjim čeličnim pločama, zasnovan na Evropskom modelu tečenja, uzimajući u obzir nelinearno ponašanje svih primenjenih materijala.

*Ključne reči: veze drvo-čelik, spoljašnje čelične ploče, zavisnost sila-pomeranje, model*

[1] Teach. Assist. with PhD, Faculty of Technical Sciences, University of Novi Sad, Novi Sad, Serbia, manojlovic.dragan@uns.ac.rs, ORCID 0000-0003-1269-7477
[2] Teach. Assist., Faculty of Technical Sciences, University of Novi Sad, Novi Sad, Serbia, nozica.tanja@uns.ac.rs, ORCID 0000-0001-5517-9659
[3] Asst. Prof., University of Niš, Faculty of Civil Engineering and Architecture, Niš, Serbia, milos.milic@gaf.ni.ac.rs, ORCID 0000-0003-3028-0915
[4] Teach. Assoc., University of Niš, Faculty of Civil Engineering and Architecture, Niš, Serbia, radovan.peric@gaf.ni.ac.rs, ORCID 0009-0003-3022-7898

## 1. INTRODUCTION

As one of the oldest and most widely used construction materials, timber has experienced a significant revival in modern structural engineering over recent decades, driven by growing sustainability demands and advances in engineered wood products [1]. In contemporary timber structures, connections between structural members play a crucial role, as they largely govern the overall stiffness, strength, and ductility of the structure. Among the various connection types, dowel-type fasteners such as bolts, nails, screws, and dowels are the most commonly used in practice due to their simplicity, reliability, and ease of installation. In the case of timber-to-steel connections with outer steel plates, which are frequently employed in modern mass timber structures, this characterisation is of particular importance due to the complex interaction between the timber and steel components [2]. The load-slip behaviour of connections is a key parameter governing the structural response of timber structures, and its accurate characterisation is therefore essential for reliable structural analysis and design.

Experimental studies have shown that timber connections exhibit strongly nonlinear load-slip behaviour even under relatively small loads. This nonlinearity arises from various physical mechanisms, including the embedment behavior of the fastener into the timber (characterised by the localised crushing of wood fibres), the plastic bending and yielding of the fastener through plastic hinge formation, and the nonlinear response of the steel plates [3]. The bilinear model proposed by Eurocode 5 [4] is unable to adequately capture this response, as it oversimplifies the actual behavior of the connection and can lead to non-conservative results. To overcome this limitation, researchers have proposed the use of adequate exponential functions [5], which are widely used in timber engineering to accurately model the nonlinear load-slip behaviour of dowel-type timber connections, as they provide a smooth and continuous transition from the initial elastic stage to the plastic yield plateau, capturing the mechanical behaviour that simplified bilinear models fail to represent. These functions have proven to be well suited for fitting experimental data and are widely adopted in the literature due to their mathematical simplicity and good agreement with experimental results. However, their reliable application requires accurate and adequate input parameters, which are typically obtained from experimental testing or empirical relations. Since general analytical expressions for these parameters are scarce and often lack broad applicability, their use is largely limited to cases where experimental data are available or if empirical dependencies exist, which restricts their wider adoption in engineering practice [6].

In parallel, sophisticated numerical models based on the beam-on-elastic-foundation (BOEF) theory have been developed to predict the load-slip response of dowel-type connections. In these models ([3],[7],[8],[9]), the fastener is treated as a beam element supported by a nonlinear elastic foundation representing the embedment behaviour of the timber, while the steel plates are modelled using a linear elastic foundation representing their bearing behaviour, with the stiffness of the foundation depending on the plate thickness and the assumed boundary conditions. These models typically require input parameters derived from experimental data and/or empirical relations, including the embedment strength and stiffness of timber, as well as the bending resistance of the fastener. In order to more accurately capture the behaviour and interaction of the fastener and the steel plates, more advanced finite element models have been proposed [10], employing solid elements for both components and a nonlinear elastic foundation to represent the embedment behaviour of the timber. While BOEF-based models offer a high level of accuracy, their implementation requires the use of specialised finite element software that demands considerable expertise, which limits their accessibility in everyday

engineering practice and motivates the development of simpler alternative approaches capable of achieving a comparable level of reliability and accuracy.

The European Yield Model (EYM), originally established through Johansen's yield theory [11] and later incorporated into Eurocode 5, provides a theoretical framework for predicting the load-carrying capacity of dowel-type connections based on the governing yield mechanisms, namely the formation of plastic hinges in the fastener and the embedment of the fastener into the timber. Although the EYM was originally formulated for the prediction of ultimate load capacity only, based on rigid-plastic assumptions for both the fastener and the timber, several researchers ([12],[13],[14],[15],[16]) have extended it to describe the full load-slip response by incorporating realistic constitutive behaviour of all components involved, thereby enabling the quantification of displacements throughout the entire loading process and providing a more complete characterisation of connection behaviour. These extended formulations ([13],[14],[16]) have shown considerable promise, especially when paired with appropriate constitutive models capturing the nonlinear behaviour of both the timber and the fastener. It should be noted, however, that despite incorporating these material nonlinearities, while certain models retain the fundamental assumptions of Johansen's yield theory, in which the timber embedment stress acting on the fastener is assumed to be uniformly distributed, rather than reflecting the actual stress distribution. Despite these advances, the accurate prediction of the full load-slip curve of timber-to-steel connections with outer steel plates, while accounting for the nonlinear behaviour of all materials involved, remains a challenging task, particularly given that the actual behaviour of the steel plates is not explicitly considered in these models.

The present paper addresses these shortcomings by proposing a numerical model based on the EYM, extended to incorporate the actual distribution of the nonlinear embedment stress along the fastener in timber, the nonlinear behaviour of the fastener in bending due to its rotation, and the actual distribution of the bearing stress along the fastener through the thickness of the steel plates, with the aim of predicting the complete load-slip response of timber-to-steel connections with outer steel plates. The model proposed in this paper is intentionally kept simple, allowing it to be applied manually or implemented in commonly used tools such as Matlab, Python, or Microsoft Excel, while relying only on a set of well-defined input parameters, namely the embedment behaviour of the timber ([3], [5],[6],[9]) and the steel plates [17] and the bending behaviour of the fastener ([6],[18]), which can be obtained either from experimental testing or from theoretical expressions that have been shown to be in good agreement with experimental data. In the absence of experimental data for direct comparison, the proposed model was validated using numerical simulations of timber-steel connections ([21],[22]).

## 2. THEORETICAL FORMULATION OF THE PROPOSED NUMERICAL MODEL FOR TIMBER-TO-STEEL CONNECTIONS

This section presents the theoretical formulation of the proposed model, with focus on timber-to-steel connections with outer steel plates in single shear. The rope effect is deliberately omitted, such that only the Johansen component of the load-carrying capacity is considered, as the rope effect represents an additional contribution that can significantly increase the load-carrying capacity and alter the governing failure mode, and its inclusion would obscure the primary mechanical behaviour of the connection.

The proposed model builds upon previously developed formulations ([13],[14],[16]), adopting an approach based on the EYM, which represents the equilibrium condition on an isolated segment of the fastener for the adopted failure mode of the connection. By incorporating the actual nonlinear material behaviour of the timber, the steel plate and the

fastener into the EYM framework, the model can be extended beyond its original formulation to predict the complete load-slip relationship of the connection over the entire displacement domain.

## 2.1. NONLINEAR BEHAVIOR OF MATERIALS

To describe the nonlinear material behaviour, theoretical expressions were adopted where available, while numerical or experimental relations were employed in their absence. The embedment behaviour of the fastener in timber, characterised by the localised crushing of wood fibres, is described by the Richard-Abbott exponential function [5], in which the nonlinear behaviour is defined as a function of the curve shape parameter *a* and the embedment parameters [3] obtained from analytical expressions (Tab. 1) developed as a function of timber density $\rho$ [kg/m$^3$]. For loading at an angle α to the grain, the Hankinson equation (see Tab. 1) can be applied to account for the directional dependence of the embedment parameters. The embedment stress $f_h$ [MPa] at a given displacement $u$ [mm] is determined using the Richard-Abbott function (Eq. 1), with the corresponding embedment parameters as defined in Fig. 1.

$$f_h(u) = \frac{(k_{f,el} - k_{f,pl}) \cdot u}{\left[1 + \left(\frac{(k_{f,el} - k_{f,pl}) \cdot u}{f_{h,inter}}\right)^a\right]^{\frac{1}{a}}} + k_{f,pl} \cdot u \tag{1}$$

where:

$f_h$ is the embedment strength as a function of displacement u;
$u$ is the embedment displacement;
$k_{f,el}$ is the elastic stiffness of the embedment curve;
$k_{f,pl}$ is the plastic (post-yield) stiffness of the embedment curve;
$f_{h,inter}$ is the intercept (reference) embedment strength;
$a$ is the shape (curvature) parameter of the Richard-Abbott function.

*Tab. 1 Embedment parameter expressions for loading parallel, perpendicular, and at an angle α to the grain (Hankinson equation)*

| Parameters | Parallel (α=0°) | Perpendicular (α=90°) | Hankinson equation |
|---|---|---|---|
| $k_{f,el}$ [N/mm$^3$] | 0.1374·$\rho$-12.29 | 0.0922·$\rho$-18.20 | $F(\alpha) = \frac{F_0 \cdot F_{90}}{F_0 \cdot \sin^2(\alpha) + F_{90} \cdot \cos^2(\alpha)}$ with $F$ as the generic parameter representing $k_{f,el}$, $k_{f,pl}$ and $f_{h,inter}$ |
| $k_{f,pl}$ [N/mm$^3$] | 0.0047·$\rho$-2.00 | 0.0084·$\rho$-2.21 | |
| $f_{h,5mm}$ [N/mm$^2$] | 0.1253·$\rho$-20.32 | 0.1108·$\rho$-28.47 | |
| $f_{h,inter}$ [N/mm$^2$] | $f_{h,5mm,0}$ - 5· $k_{f,pl,0}$ | $f_{h,5mm,90}$ - 5· $k_{f,pl,90}$ | |

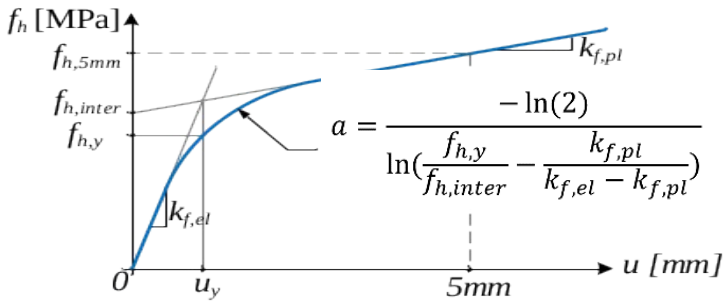


*Fig. 1 Definition of the principal embedment parameters for the nonlinear behaviour of timber*

The bearing behaviour of the fastener within the steel plate can be described using the exponential function proposed by Može and Piculin [17], in which the nonlinear bearing stress $\sigma_b = \overline{\sigma}_b \cdot f_u$ is defined as a function of the hole elongation $u$ (Eq. 2). The corresponding bearing parameters, namely the relative hole elongation at maximum resistance $\alpha_b$ (at $u_u$) and the material factor $k_m$, defined in accordance with prEN 1993-1-8:2023 [19], are used to characterise the nonlinear relationship $\overline{\sigma}_b(u)$ given in Eq. 2 and are presented in Fig. 2.

$$\sigma_b(u) = \overline{\sigma}_b(\overline{u}) \cdot f_u = \frac{126 \cdot \overline{u}}{\left(1 + \sqrt{30 \cdot \overline{u}}\right)^2} \cdot f_u \tag{2}$$

where:

$\overline{\sigma}_b$ is the relative average bearing stress as a function of $\overline{u} = u/d$ (where u is hole elongation or embedment displacement in steel plate);
$\overline{u}$ is relative hole elongation;
$d$ is fastener diameter;
$d_0$ is hole diameter;
$f_u$ is tensile strength of plate material;
$f_b$ is tensile strength of fastener.

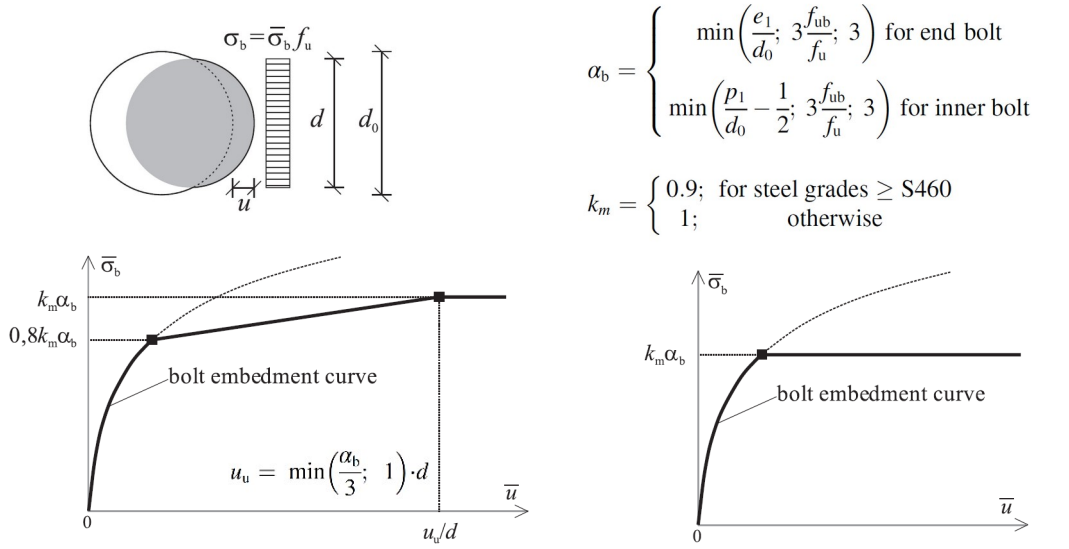


a) steels up to S460 ($k_m = 1$) b) steels S460 and greater ($k_m = 0.9$)

*Fig. 2 Presentation of the analytical bearing stress model for the steel plate [17]*

The nonlinear behaviour of the fastener in bending, typically described as a relationship between the bending moment and the rotation angle of the fastener ($M_y$-$\alpha$), can be predicted using the analytical exponential expressions proposed by Blass et al. [18] for dowels and bolts, or by Bjetka [20] and Manojlović [6] for screws (see Fig. 3). It should be noted that these relationships have inherent limitations, as they were derived from regression analyses and for specific fasteners and limited ranges of diameters and materials from which they are manufactured, and therefore their application to the wider variety of fasteners used in timber connections remains limited. Since the initial slope of the $M_y$-$\alpha$ curve in the aforementioned functions lacks a theoretical background ([18], [20]), an exponential expression proposed by Manojlović [6] was formulated to more accurately describe the experimentally obtained $M_y$-$\alpha$ curves. By examining the linear portion of the $M_y$-$\theta$ curve up to the elastic moment $M_{el} = f_y \cdot (\pi \cdot d^3/32)$, and treating the rotation of the fastener cross-section above the support $\theta_1$ as a result of the concentrated

force applied at midspan, the initial slope $K_b=M_{el}/\theta_{el}$ (where $\theta_{el}=2\cdot\theta_1$) can be derived directly from elastic theory (Fig. 3c). Knowing the elastic moment $M_{el}$ and the plastic bending moment capacity $M_{pl}=M_{y,eff}=f_{y,eff}\cdot(d^3/6)$, together with the initial slope $K_b$ derived from elastic theory, the complete theoretical $M_y$-$\alpha$ relationship can be obtained using an appropriate exponential function. In this way, the theoretical $M_y$-$\alpha$ relationship can be extended to a wider range of fasteners, overcoming the limitations inherent in the previously proposed analytical models ([18], [20]).

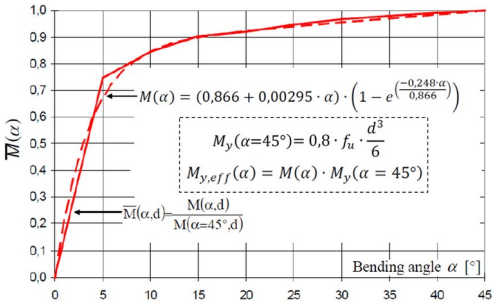


*a) Blass et al. [18]*

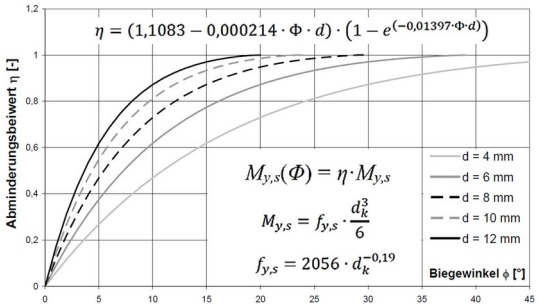


*b) Bjetka [20]*

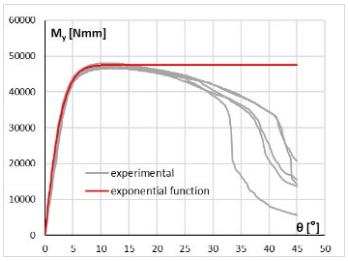


$$M_y(\theta) = M_{y,eff} \cdot \left(1 - e^{\left(-\left(\frac{K_B}{M_{y,eff}} + a_1 \cdot \theta\right) \cdot \theta\right)}\right)$$

$$a_1 = \frac{d}{d_{ref} \cdot (\alpha_{max})} \cdot \frac{K_b}{M_{y,eff}}$$

$$M_{y,eff} = M_{pl} = (f_{y,eff} \cdot {d_{eff}}^3)/6$$

$$f_{y,eff} = \begin{cases} \frac{0{,}9 \cdot (f_y + f_u)}{2} & \text{за } f_u < 450\ MPa \\ 0{,}9 \cdot f_u & \text{за } f_u > 450\ MPa \end{cases}$$

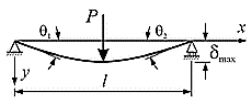


$$\Theta_1 = \Theta_2 = \frac{Pl^2}{16EI}$$

$$\theta_{el} = 2 \cdot \theta_1 = 2 \cdot \frac{P_{el} \cdot L_0^2}{16 \cdot E \cdot I} = \frac{M_{el} \cdot L_0}{2 \cdot E \cdot I} = \frac{4 \cdot f_u \cdot L_0}{5 \cdot d_{eff} \cdot E} \quad [rad]$$

$$K_b = \frac{M_{el}}{\theta_{el}} = \left(\frac{\pi^2 \cdot {d_{eff}}^4}{5760}\right) \cdot \frac{E}{L_0} = \frac{E \cdot I \cdot \pi}{90 \cdot L_0} \quad [Nmm/deg]$$

*c) Manojlović [6]*

*Fig. 3 Analytical relationships $M_y$-$\alpha$ for bending behaviour of the fastener*

In the absence of the theoretical $M_y$-$\theta$ relationship, it may alternatively be determined through experimental testing or numerical simulations (*[6],[21]*). The determination of the $M_y$-$\theta$ relationship through experimental testing or numerical simulations is typically carried out by bending the fastener in accordance with the procedure specified in EN 409 *[23]*, or other relevant standards used for determining the yield moment $M_y$ required for application in the Johansen expressions. This is typically achieved through a three-point bending test, illustrated in Fig. 4, in which the applied force $P$ and the corresponding midspan displacement $u$ are recorded, allowing the $M_y$-$\theta$ relationship to be derived using the expressions provided therein.



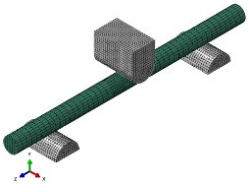

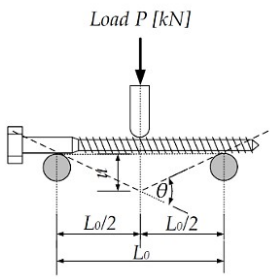


Transformation of the measured $P$-$u$ response into the $M_y$-$\theta$ relationship:

$$M_y = (P \cdot L_0)/4$$

$$\theta = 2 \cdot \tan^{-1}(2 \cdot u/L_0)$$

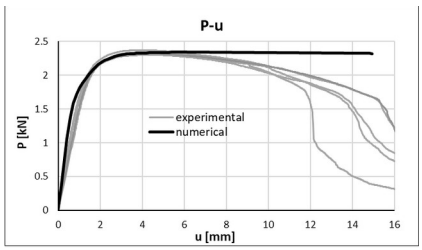


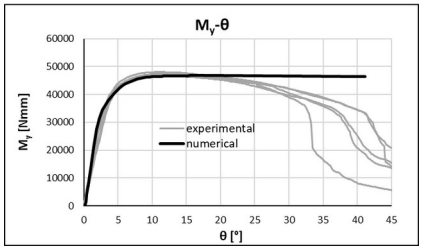


*Fig. 4 Experimental and numerical determination of the $M_y$-$\theta$ relationship [6]*

## 2.2. PROCEDURE FOR DETERMINING THE LOAD-SLIP RESPONSE

In contrast to the original EYM, which assumes rigid-plastic behaviour of the timber and the fastener while approximating the steel plate response through simplified rotational boundary conditions, the proposed numerical model introduces certain modifications to the EYM and incorporates nonlinear constitutive relationships for all materials involved, as defined in Section 2.1.

The model retains the fundamental kinematic assumptions of the EYM, in which the fastener is treated as a rigid body, with all bending deformation represented as a concentrated nonlinear rotations at discrete points corresponding to the locations of plastic hinge formation, while elastic bending deformations of the fastener between these points are neglected. In order to account for the complete stress distribution along the fastener, and for the influence of the balancing load located beyond the plastic hinges, the fastener's rotation point, which is often neglected, is incorporated into the model, whereby the bending deformation of the fastener at this point is considered as a concentrated nonlinear rotation, representing the modification introduced to the EYM model. These modifications enables the model to cover several different failure modes, as well as their transition modes. At this stage, however, the proposed model has been developed only for the failure modes characterised by the formation of plastic hinge in the thick outer steel plates, while cases involving thin and intermediate-thickness plates require further refinement.

Following the principles of EYM theory, this enables the determination of the load-carrying capacity corresponding to a given displacement, through equilibrium conditions along the fastener, and consequently the derivation of the complete load-slip curve. To obtain the load-slip curve $w_{sp}$–$R$, an iterative process must be employed, because determining the load-carrying capacity for a given displacement requires satisfying the equilibrium conditions on the isolated fastener segments at each step. Owing to the complexity of this procedure, its implementation generally requires a solver based on an algorithm such as Generalized Reduced Gradient (GRG) Nonlinear, available in certain software packages (e.g., Microsoft Excel Solver), or custom-written code. The corresponding steps for determining the forces in each segment, related to one displacement increment, are presented below according to Figure 5. For the timber member, the known value is $L_t$ (timber member thickness), and the assumed values are $w_3$, $t_1$, and $b_1$; for the steel plate, the known value is $t_{sp}$ (steel plate thickness), and the assumed value is $b_{1,sp}$. Based on these values, the following quantities are calculated from the geometry of the timber member and the steel plate:

1) From $w_3$ and $t_1$ → rotation of the fastener in *SEGMENT-A* is $\theta_3 = \arctan(w_3/t_1)$.
2) From the equilibrium condition of *SEGMENT-A*, the moment $M_{yAB}=F_A \cdot e_A$ is calculated, and from the $M_y$-$\theta$ relationship, the rotation angle $\theta_2$ is determined, thereby also the angle $\theta_{2+3}=\theta_2+\theta_3$, based on which the displacement $w_2= t_2 \cdot \tan(\theta_{2+3})$ and resultant force $F_B$ of the *SEGMENT-B* are determined (where $t_2 = L_t - t_1 - b_1$). In this process, the condition $F_A=F_B$ must be satisfied, which is achieved by varying the assumed values of $t_1$ and $b_1$ (which directly affect $t_2$ and $w_2$). Once the condition $F_A=F_B$ is satisfied, the procedure proceeds to the next step.
3) From the equilibrium condition of *SEGMENT-B*, the moment $M_{yt}=M_{yAB}+F_B \cdot e_A$ is calculated, and from the $M_y$-$\theta$ relationship, the rotation angle $\theta_4$ is determined, thereby also the angle $\theta_1=\theta_4+\theta_{2+3}$, based on which the embedment displacement in the timber $w_1=w_2+ b_1 \cdot \tan(\theta_1)$ is determined. Additionally, for the known angle $\theta_1$, the bending moment $M_{ysp}$ in the steel plate is determined from the $M_y$-$\theta$ relationship, along with the embedment displacement $w_{1,sp}$ and resultant force $F_D$.

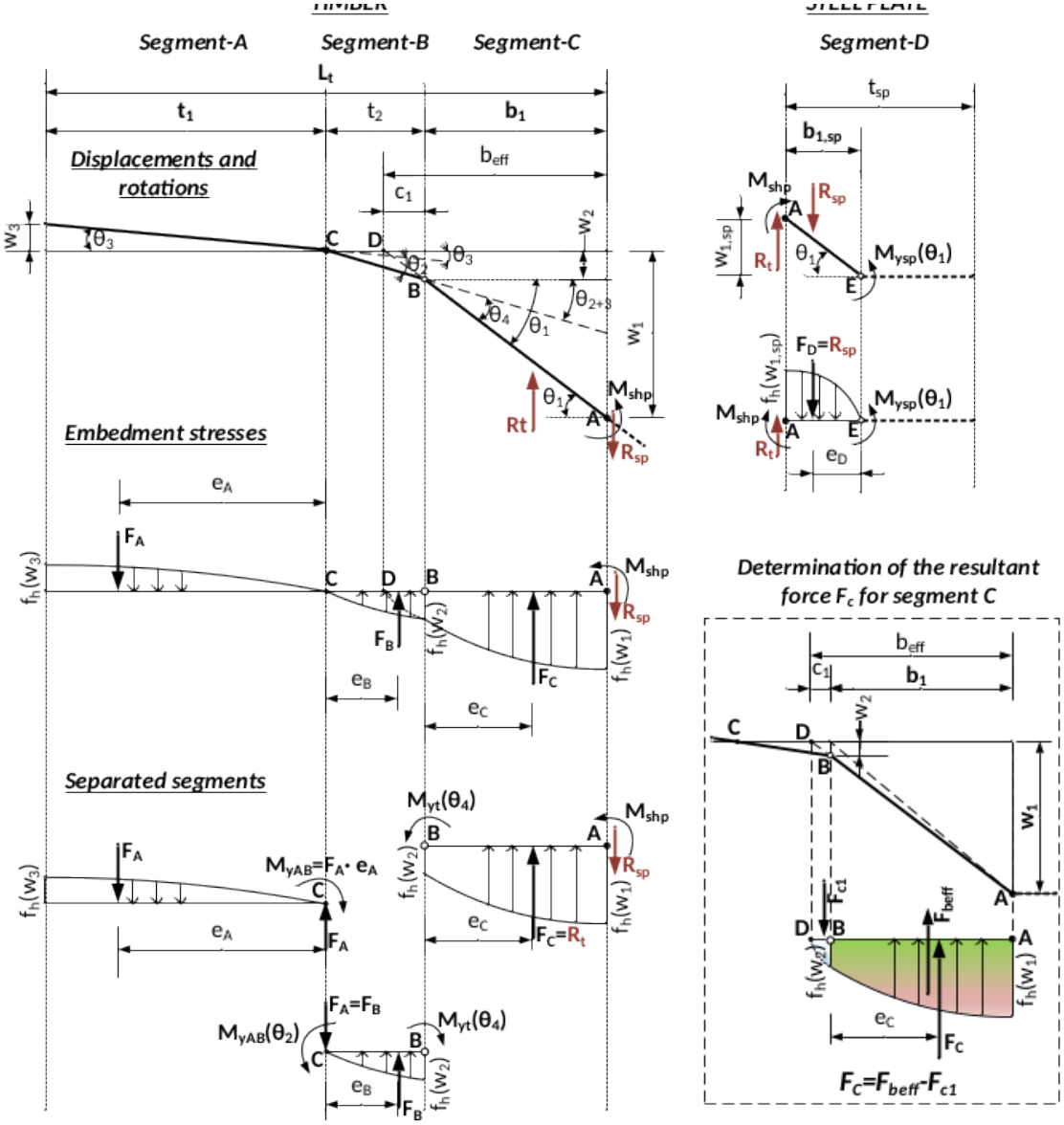


*Fig. 5 Scheme illustrating the assumed deformed shape of the fastener and the corresponding displacements, rotations and stress distribution*

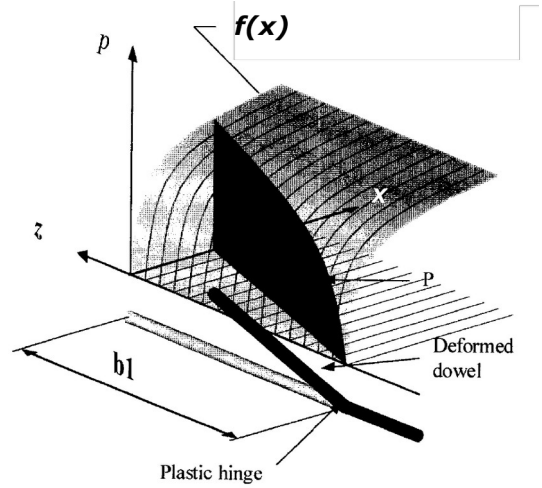


*Embedment displacement along the segment*

$$x(z)=\frac{w}{b_1}\cdot z$$

*Embedment force*

$$F_{emb}=\int_0^{b_1} f(x)\,dz$$

*f(x) – embedment function for the timber Eq.(1) or for the steel plate Eq.(2), as defined in Section 2.1.*

*Fig. 6 Illustration of the determination of resultant forces for each segment using the nonlinear behavior of the timber and steel plate [12]*

4) For the known geometry, $c_1=w_2/\tan(\theta_1)$ and $b_{eff}=b_1+c_1$ are determined in order to calculate the resultant force $F_C$. The force $F_C$ is obtained by determining the forces $F_{beff}$ and $F_{c1}$ (see Fig. 5 and Fig. 6), i.e., $F_C=F_{beff}-F_{c1}$.
5) All forces acting on the *SEGMENT-C* and *SEGMENT-D* are now known, and the equilibrium conditions are checked at point A, i.e., $\Sigma M_A=0$ and $\Sigma V=0$ for both sides (the timber member and the steel plate).
6) If all equilibrium conditions are satisfied for both side, the load-carrying capacity $R$ is $R=R_t=R_{sp}=F_C=F_D$, and displacement in the shear plane is $w_{sp}=w_1+w_{1,sp}$. The point ($w_{sp}$, $R$) is obtained on the load-slip curve, which corresponds to one displacement increment.

Following the procedure described above, it should be emphasized that the forces $F_A$, $F_B$, $F_C$ and $F_D$ (see Fig. 6), as well as the corresponding positions of the centroids $e_A$, $e_B$, $e_C$ and $e_D$ of the resultant forces, are determined based on the known $f_h$-$w$ relationship, i.e., using the stress $f_h(w_i)$ as a function of displacement. Furthermore, for *SEGMENT-C*, the force $F_C$ is obtained by integrating the embedment stress over the full area swept by the rotation of the fastener about point D, located beyond the point of maximum moment $M_{yt}$ (point B) in the timber member. This represents the modification introduced to the EYM model by incorporating the contribution due to the adopted rotation about point C. The overlapping embedded region between point D and point B is subsequently subtracted to avoid double-counting, resulting in the correct resultant force for this segment [14]. Using the $M_y$-$\theta$ relationship, the steps involve determining the rotation angle based on a known moment, or vice versa, with the modification that a different $M_y$-$\theta$ relationship is used for the bending behaviour of the fastener in the timber (points C and B) compared to that in the steel plate (point E). This is done in order to account for the different bending behaviour of the fastener in the timber and in the steel plate, i.e. the different bending radii of its deformed shape. A similar effect was observed by Kuck and Sandhaas [1] for fasteners in softwood and hardwood, and by Riepe et al. [16], who found, using a BOEF model, that the plastic hinges next to the steel plate and in the timber form at significantly different rotations.

## 3. NUMERICAL SIMULATION OF TIMBER-TO-STEEL CONNECTIONS

The presented algorithm for determining the complete load-slip curve was implemented in Excel through a custom-written code based on the built-in GRG nonlinear solver, and numerical simulations were subsequently performed using the proposed model. The proposed model was validated against reference numerical simulations of timber-to-steel connections presented in [22], performed using the finite element method (FEM) in the FEMAP with NX NASTRAN software package. These simulations represent modifications of the numerical models originally developed in the doctoral dissertation by Milić ([10],[21]). For further details on the FE models, the reader is referred to [22]. As in the analytical model, the rope effect was also omitted in the FEM models used for comparison, in order to isolate and focus solely on the Johansen component of the load-carrying capacity. Furthermore, friction was not considered at any of the contact interfaces, i.e., between the timber and the fastener, between the steel plate and the fastener, and between the steel plate and the timber.
In order to demonstrate the model's capability to predict the complete curve, as well as the failure mode and stress distribution, two connections were selected, designated 4.6/S235-12mm/C18 and 12.9/S235-12mm/C18. These connections consisted of softwood of strength class C18 ($\rho_m$=380kg/m$^3$) with a thickness of 100 mm, a fastener with a diameter of 10 mm in two bolt grades (4.6 and 12.9), and a steel plate with a thickness of 12 mm and

strength grade S235. In order to ensure a consistent and reliable comparison, all input data required for the proposed model, including material properties and connection geometry, were taken directly from the aforementioned study (see [22]). Some of the most relevant input data are shown in Fig. 7: (a) the relationship between the bolt yield moment $M_y$ and the rotation angle $\theta$ for bolt grades 4.6 and 12.9, with different behaviour in the timber and the steel plate, (b) the adopted embedment stress-displacement curves for timber strength class C18 and the bearing stress-displacement curve of the steel plate.

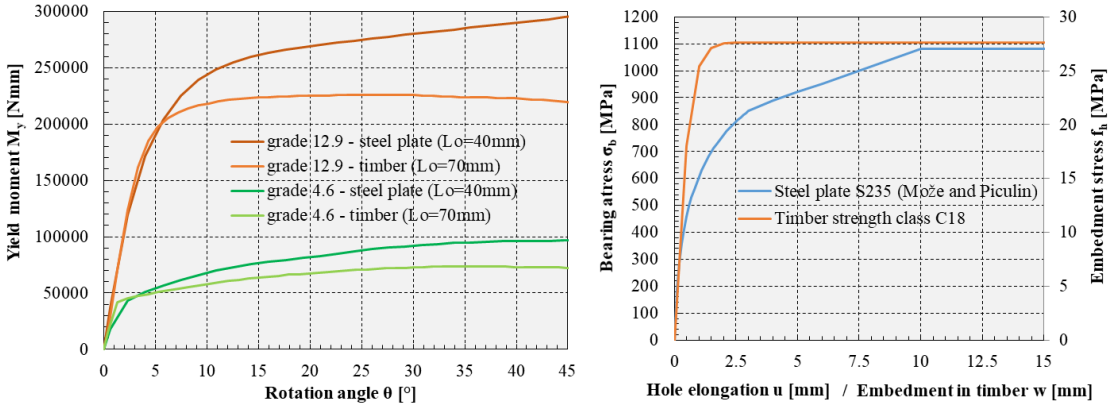


*Fig. 7 (a) $M_y$-$\theta$ relationship for bolt grades 4.6 and 12.9, (b) embedment stress-displacement curves for timber class C18 and the bearing stress-displacement curve of the steel plate*

## 4. COMPARATIVE RESULTS AND DISCUSSION

The following figures present the load-slip diagrams (Fig. 8) and, at a slip of $w_{sp}$≈16 mm, the deformed shapes of the fastener (Fig. 9), the embedment stress in the timber (Fig. 10) the bearing stress in the steel plate (Fig. 11), as well as the distribution of the bending moment along the fastener (Fig. 12), in which the results obtained using the proposed model are superimposed on those of the FE simulations of the connections from [23].
Considering the load-slip diagram shown in Fig. 8, it can be observed that the proposed model provides a very good prediction, i.e., it follows the trend of the numerical simulations. In the initial phase, the agreement is very good, whereas for the connection with bolt grade 12.9, a slight drop in force can be observed after 4 mm (at $w_{sp}$≈16 mm, the difference reaches -9.1%).

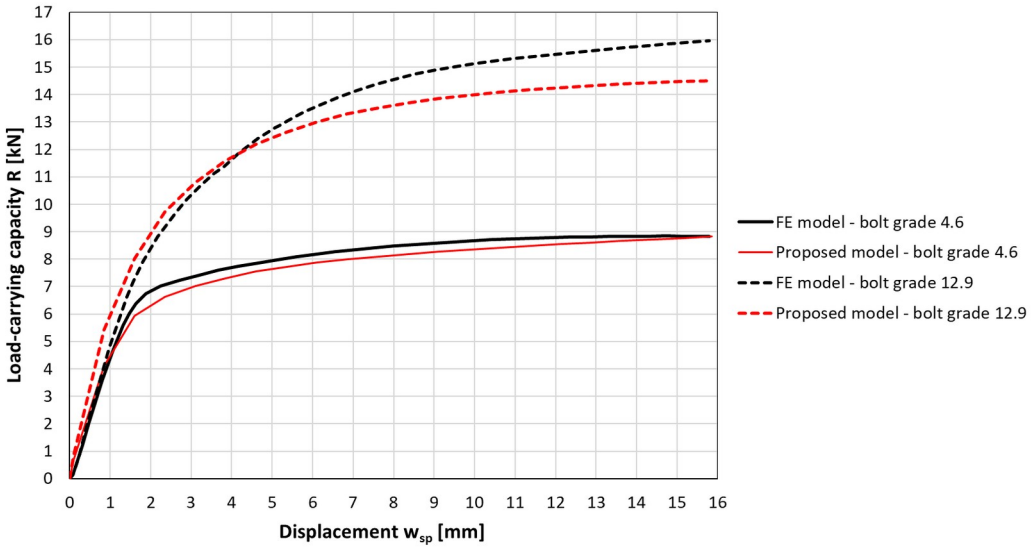


*Fig. 8 Load-slip curves ($w_{sp}$-R) for bolt grades 4.6 and 12.9*

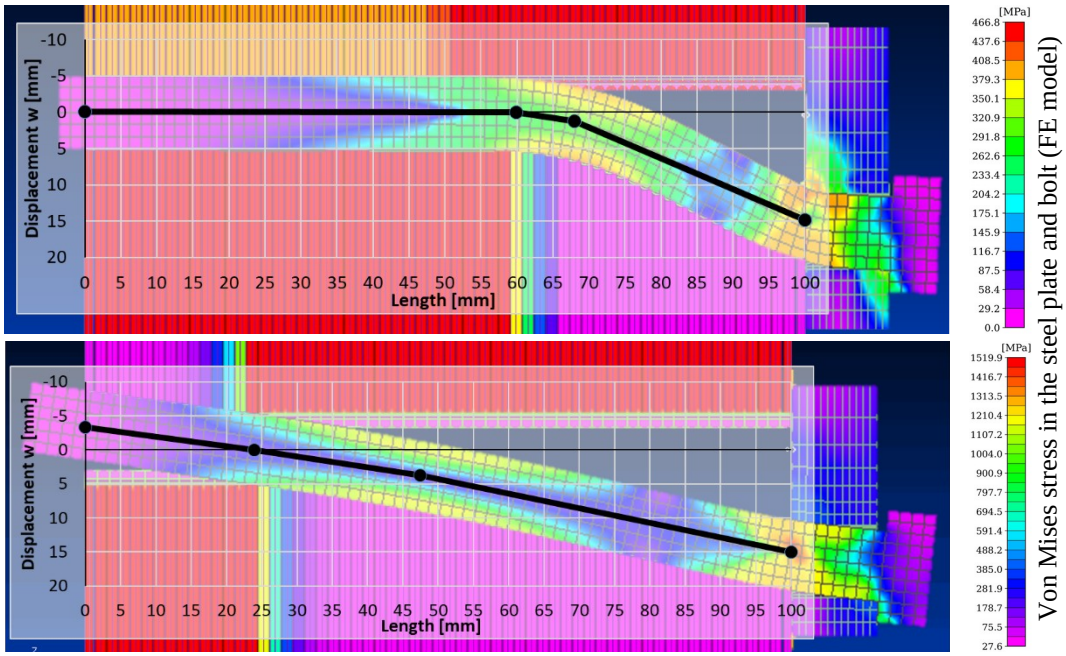


*Fig. 9 Deformed shapes of the fastener for bolt grades 4.6 and 12.9*

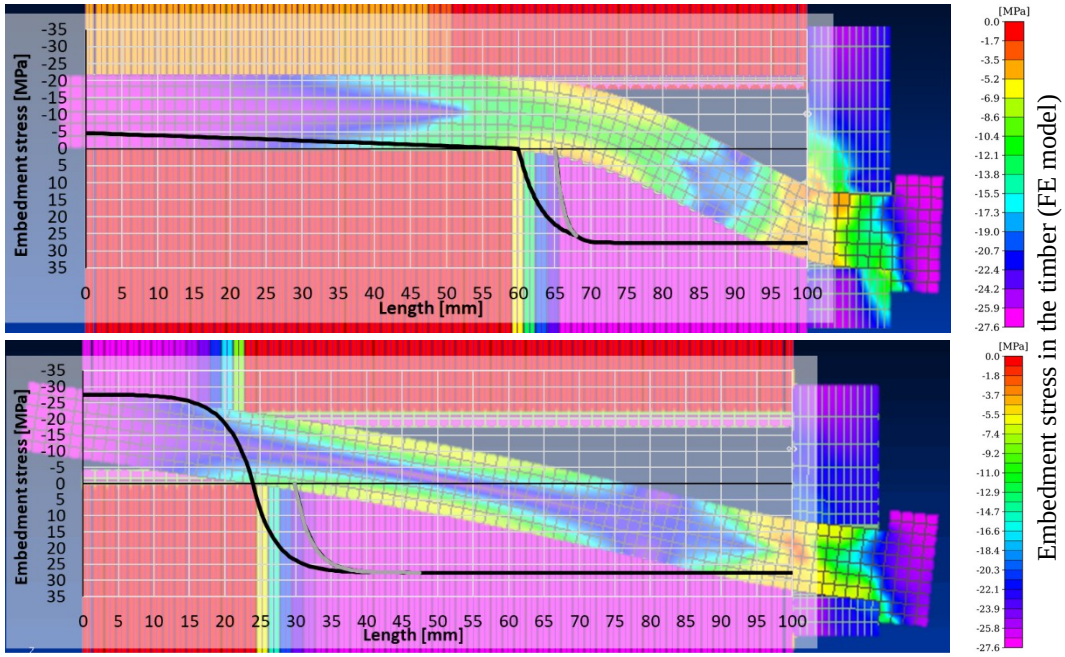


*Fig. 10 Embedment stress in the timber for bolt grades 4.6 and 12.9*

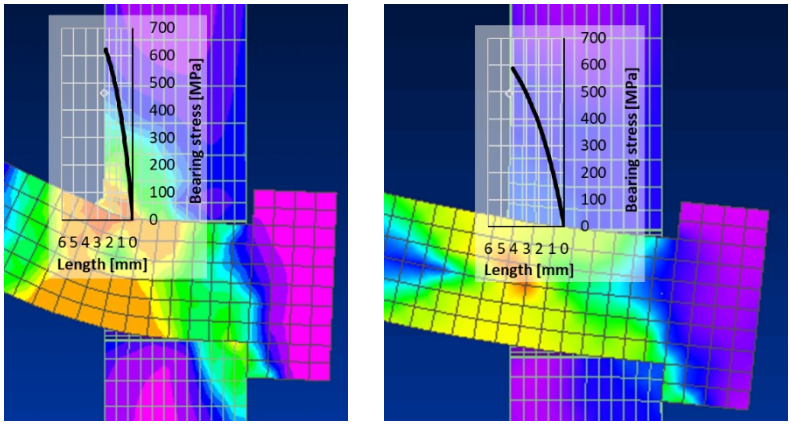


*Fig. 11 Bearing stress in the steel plate for bolt grades 4.6 and 12.9*

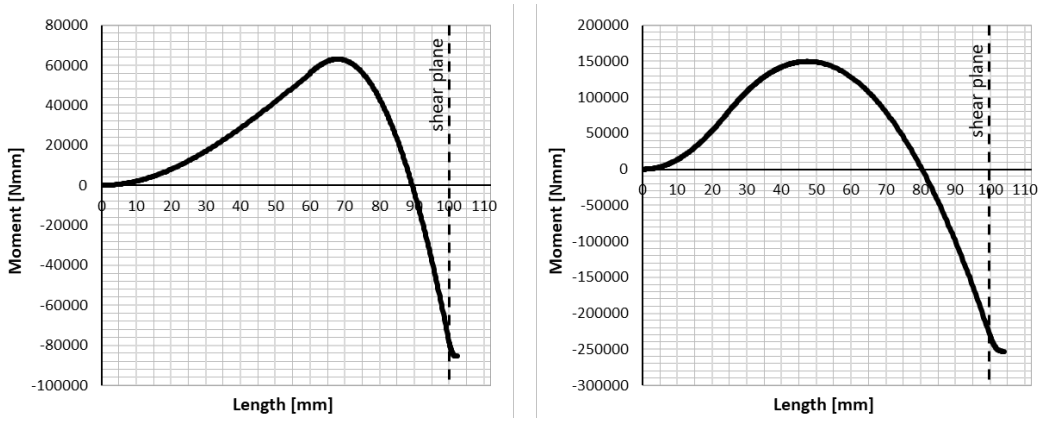


*Fig. 12 Bending moment distribution along the fastener for bolt grades 4.6 and 12.9*

Comparing the fastener displacements, it can be observed that the proposed model is able to describe the actual displacement and the deformed shape of the fastener in both cases (different bolt grades), taking into account the exact location of the fastener rotation point and the position of the plastic hinges. As previously mentioned, the introduced modification (adopting the fastener rotation point beyond the plastic hinge) helped capture this rotation in certain situations and demonstrated that this effect must not be neglected (as is the case for bolt grade 12.9). This makes it possible not only to account for the change in bolt grade, but also for the change in the thickness of the timber member, and its influence on the change in the governing failure mode, as well as on the transition modes. Furthermore, owing to the introduced modification, it is possible to determine a more realistic stress distribution along the fastener, as well as the influence of the fastener on the surrounding timber. From Fig. 10, it can be observed that embedment for bolt grade 4.6 occurs predominantly below the fastener, while the very small rotation induced stresses (~5 MPa) on the opposite side, that remain within the linear elastic range. On the other hand, considering bolt grade 12.9, it can be observed that, in addition to the embedment on the lower side occurring over a length greater than the location of the plastic hinge embedment also occurs on the opposite side; however, it can now be seen that plastification of the timber has occurred over a certain length. In Fig. 11, the stress distribution in the steel plate can be seen only up to the plastic hinge, since the remainder of the plate was neglected in the model. Despite this approximation, the position of the plastic hinge within the steel plate is accurately predicted, and it can be observed that the hinge forms within the zone of the largest embedment of the fastener into the plate. Considering the magnitude of the stresses, it can be noted that the values in both cases are around ~600 MPa. It is also worth noting, at this point, that the bending behaviour of the fastener in the steel plate and in the shear plane differs from that in the timber, i.e., a smaller radius of curvature can be observed. For this reason, the additional modification introduced in the proposed model, whereby a different $M_y$-$\theta$ relationship is used to describe the bending behaviour of the fastener in the timber (points C and B) compared to that in the steel plate (point E), has proven justified based on the observed results. Furthermore, the performed calculations demonstrate that one of the capabilities of the proposed model is the determination of the bending moment distribution along the fastener, as shown in Fig. 12. Unlike conventional models, which typically provide only the final load-carrying capacity, the proposed model enables insight into the complete moment distribution along the fastener at each load level, thereby providing a deeper understanding of the underlying failure mechanism and allowing for verification of the exact location and magnitude of the plastic hinges, which is not directly attainable using the classical EYM approach.

## 5. CONCLUSION

This paper presented a numerical model, based on the EYM, for predicting the complete load-slip response of timber-to-steel connections with outer steel plates. The proposed model extends the original EYM by incorporating the nonlinear embedment behaviour of the timber, the nonlinear bearing behaviour of the steel plate, and the nonlinear bending behaviour of the fastener, thereby enabling the prediction of the full load-slip curve rather than only the ultimate load-carrying capacity. A key contribution of the model is the introduction of the fastener's rotation point beyond the plastic hinge, an aspect commonly neglected in existing formulations. This modification allows for a more realistic representation of the deformed shape of the fastener and enables the model to capture several failure modes, as well as their transition modes. In addition, the model distinguishes between the bending behaviour of the fastener in the timber and in the steel plate through the use of separate $M_y$-$\theta$ relationships, accounting for the different bending radii observed in each material. The proposed model was validated against reference finite element (FE) simulations of timber-to-steel connections with two bolt grades (4.6 and 12.9). The results showed very good agreement between the proposed model and the FE simulations, both in terms of the load-slip curves, the deformed shape of the fastener, and the stresses in the timber and in the steel plate. For bolt grade 4.6, the agreement remained excellent throughout the entire displacement range, while for bolt grade 12.9 a difference of approximately 9% was observed at larger displacements, indicating that the influence of the fastener's rotation beyond the hinge becomes more pronounced for stiffer, higher-grade fasteners and should therefore not be neglected. Furthermore, unlike the classical EYM approach, the proposed model provides the complete distribution of bending moments along the fastener, offering additional insight into the underlying failure mechanism and allowing verification of the location and magnitude of the plastic hinges. At the present stage, the proposed model is applicable to failure modes governed by the formation of a plastic hinge in thick outer steel plates, while its extension to thin and intermediate-thickness plates, as well as to configurations including the rope effect, requires further development. Future work will focus on extending the model to a wider range of failure modes, plate thicknesses, and timber thicknesses, as well as on its validation against experimental data.

### ACKNOWLEDGEMENT

The research has been conducted within the project "Enhancement of teaching and scientific research capacities through the application of modern technologies in the fields of civil engineering, geodesy, and disaster risk management and fire safety", developed at the Department of Civil Engineering and Geodesy, Faculty of Technical Sciences, University of Novi Sad, Serbia.

This research was supported by the Ministry of Science, Technological Development and Innovation of the Republic of Serbia, under the Agreement on Financing the Scientific Research Work of Teaching Staff at the Faculty of Civil Engineering and Architecture, University of Niš - Registration number: 451-03-34/2026-03/200095 dated 05/02/2026.

## REFERENCES

[1] Kuck E., Sandhaas C. (2022). Load-bearing behaviour of partially threaded screws in hardwood. Wood Material Science & Engineering, Volume 17, Issue 4, pp. 283–298.
[2] Ho A.-P., Ziegler J.W., Seim W. (2026). Extended analytical model for shear-loaded steel-to-timber connections with screws and profiled nails. Eng. Struct., Volume 364, 123160.
[3] Gikonyo J.W., Schweigler M., Bader T.K. (2024). Beam-on-foundation modelling of dowel-type single fastener connections in cross laminated timber. Eng. Struct., Volume 303, 117519.

[4] EN 1995-1-1 (2004). Eurocode 5: Design of timber structures – Part 1-1: General – Common rules and rules for buildings. European Committee for Standardization (CEN), Brussels, Belgium.
[5] Schweigler M., Bader T.K., Hochreiner G., Lemaître R. (2018). Parameterization equations for the nonlinear connection slip applied to the anisotropic behaviour of wood. Composites Part B: Engineering, Volume 142, pp. 142–158.
[6] Manojlović D. (2024). Novi model za simulaciju ponašanja spregnutih veza drvo-beton ostvarenih štapastim spojnim sredstvima pri statičkom dejstvu. Doctoral thesis (in Serbian), Faculty of Technical Sciences, University of Novi Sad, Serbia.
[7] Lemaître R., Bocquet J.F., Schweigler M., Bader T.K. (2018). Beam-on-foundation modelling as an alternative design method for timber joints with dowel-type fasteners – Part 1: Strength and stiffness per shear plane of single-fastener joints. INTER – International Network on Timber Engineering Research, Meeting 51, Paper 51-7-13, Tallinn, Estonia.
[8] Basterrechea-Arévalo M., Schweigler M., Lemaître R., Bader T.K. (2023). Numerical modelling of moment transmitting timber connections. Eng. Struct., Volume 297, 116923.
[9] Aquino C.D., Schweigler M., Rodrigues L.G., da Silva L.C.M., Branco J.M., Bader T.K. (2025). Numerical and fracture mechanics-based simulations of brittle failure in dowelled timber connections under in-plane multiaxial forces and bending moment. Engineering Structures, Volume 343, Part B, 120987.
[10] Milić M., Vacev T., Petronijević P., Nešović I., Zorić A., Paunović S., Matejević Nikolić B. (2024). Experimental research and FE model of a bolted steel-CLT composite connection. Periodica Polytechnica Civil Engineering, Volume 68, Issue 1, pp. 8–22.
[11] Johansen K.W. (1949). Theory of timber connections. International Association for Bridge and Structural Engineering (IABSE) Publications, Volume 9, pp. 249–262.
[12] Heine C.P., Dolan J.D. (2001). A new model to predict the load-slip relationship of bolted connections in timber. Wood and Fiber Science, Volume 33, Issue 4, pp. 534–549.
[13] Kobel P. (2019). Dowel-type connections in beech LVL. Doctoral thesis, ETH Zurich, Switzerland.
[14] Vella N., Gardner L., Buhagiar S. (2021). Analytical modelling of cold-formed steel-to-timber connections with inclined screws. Engineering Structures, Volume 249, 113187.
[15] Manojlović D., Rašeta A., Vukobratović V., Čeh A., Kozarić L., Jovanović Đ., Starčev-Ćurčin A. (2023). Simulation of load-slip capacity of timber-concrete connections with dowel-type fasteners. Buildings, Volume 13, Issue 5, 1171.
[16] Riepe J., Díaz J., Schänzlin J. (2025). An elasto-plastic model for the deformation of dowel-type fasteners based on Johansen's theory. Engineering Structures, Volume 344, 121315.
[17] Može P., Piculin S. (2024). Analytical prediction of load-deformation behaviour for bearing at bolt holes. Journal of Constructional Steel Research, Volume 60, 105968.
[18] Blass H.J., Bienhaus A., Krämer V. (2001). Effective bending capacity of dowel-type fasteners. PRO 22: International RILEM Symposium on Joints in Timber Structures, RILEM Publications, Stuttgart, Germany, pp. 71–80.
[19] prEN 1993-1-8 (2023). Eurocode 3: Design of steel structures – Part 1-8: Design of joints. European Committee for Standardization (CEN), Brussels, Belgium.
[20] Bejtka I. (2005). Verstärkung von Bauteilen aus Holz mit Vollgewindeschrauben. Doctoral thesis (in German), University of Karlsruhe, Germany.
[21] Milić M. (2023). Predlog novog rešenja za sprezanje čelika i unakrsno lameliranog drveta primenom ojačanih moždanika. Doctoral thesis (in Serbian), Faculty of Civil Engineering and Architecture, University of Niš, Serbia.
[22] Perić R., Perčić T., Milić M., Manojlović D. (2026). Improvement of an analytical model for determining the load-carrying capacity of timber-steel connections with dowel-type fasteners. 17th Congress of the Association of Structural Engineers of Serbia (ASES), Zlatibor, Serbia, 23–25 September, pp. 436–447.
[23] EN 409 (2009). Timber structures – Test methods – Determination of the yield moment of dowel type fasteners. European Committee for Standardization (CEN), Brussels, Belgium.

https://doi.org/10.24867/INDIS-2026-EN-126



# COMPARISON OF PROCEDURES FOR DETERMINING PLAN REGULARITY PARAMETERS ACCORDING TO EUROCODE 8

*Riste Volchev[1], Koce Todorov[2], Ljupcho Lazarov[3]*

***Summary:***

Six procedures for determining the centre of stiffness, structural eccentricity and torsional radius of multi-storey buildings are compared with respect to their influence on plan regularity assessment according to Eurocode 8. Nine idealised six-storey RC dual systems with different stiffness distributions in plan were analysed. The results show that the adopted procedure can significantly affect the classification, with discrepancies generally increasing with the degree of irregularity. The simplified procedure based on cross-sectional moments of inertia gives the most conservative results, while the use of a procedure based on a reference level at 0.8H may fail to capture the governing first-storey values. The second-generation procedure additionally captures sign reversals of interstorey rotation increments. Since torsional flexibility affects the behaviour factor, and consequently the design seismic forces, a clearly defined procedure for determining the relevant torsional parameters is essential for consistent seismic design.

*Keywords: plan irregularity; structural eccentricity; centre of stiffness; torsional radius; torsional flexibility; Eurocode 8*

# POREĐENJE POSTUPAKA ZA ODREĐIVANJE PARAMETARA REGULARNOSTI U OSNOVI PREMA EVROKODU 8

***Rezime:***

U radu je upoređeno šest postupaka za određivanje centra krutosti, konstrukcijskog ekscentriciteta i torzionog radijusa višespratnih zgrada, sa aspekta njihovog uticaja na kontrolu regularnosti u osnovi prema Evrokodu 8. Analizirano je devet idealizovanih šestospratnih AB dvojnih sistema sa različitom raspodelom krutosti u osnovi. Rezultati pokazuju da izbor postupka može značajno uticati na klasifikaciju, pri čemu razlike generalno rastu sa stepenom neregularnosti. Pojednostavljeni postupak zasnovan na momentima inercije preseka daje najkonzervativnije rezultate, dok primena postupka zasnovanog na referentnom nivou od 0,8H može dovesti do izostavljanja merodavnih vrednosti na prvoj etaži. Postupak druge generacije dodatno registruje promenu znaka međuspratnog priraštaja rotacije. Budući da torziona fleksibilnost utiče na faktor ponašanja, a time i na vrednosti projektnih seizmičkih sila, jasno definisan postupak za određivanje relevantnih torzionih parametara od značaja je za dosledno seizmičko projektovanje.

*Ključne reči: neregularnost u osnovi; konstrukcijski ekscentricitet; centar krutosti; torzioni radijus; torziona fleksibilnost; Evrokod 8*

[1] PhD student, Ss. Cyril and Methodius University in Skopje, Faculty of Civil Engineering, Skopje, Macedonia, volcev@gf.ukim.edu.mk ORCID 0000-0001-9815-9914
[2] Full Prof., Ss. Cyril and Methodius University in Skopje, Faculty of Civil Engineering, Skopje, Macedonia, todorov@gf.ukim.edu.mk ORCID 0000-0003-1736-4989
[3] Full Prof., Ss. Cyril and Methodius University in Skopje, Faculty of Civil Engineering, Skopje, Macedonia, lazarov@gf.ukim.edu.mk ORCID 0009-0003-7621-8161

## 1. INTRODUCTION

Structural irregularity can contribute to severe earthquake damage and, in some cases, structural collapse. Plan irregularity is characterised by a non-uniform distribution of stiffness, mass and strength within the structural system. The associated structural eccentricity, defined as the distance between the centre of mass and the centre of stiffness, gives rise to torsional moments about the vertical axis under seismic loading. Although the distributions of stiffness, mass and strength can be determined and explicitly incorporated into the model for structural analysis, several other influential factors are difficult to quantify. These include differences in ground motion between supports; non-structural elements that are omitted from the design model but affect the stiffness and strength of the system; unforeseen distributions of imposed loads; and differences between the actual and assumed distributions of mass, stiffness and strength [1,2].

Post-earthquake observations over the past decade have reaffirmed the practical significance of plan irregularity. Following the Puebla earthquake in Mexico (September 2017, Mw 7.1), 43% of the 44 collapsed buildings in Mexico City were corner buildings with an asymmetric arrangement of masonry infills [3]. After the Durres earthquake in Albania (November 2019, Mw 6.4), torsional irregularity was identified as a factor contributing to severe damage in multi-storey RC frame buildings [4]. Following the Kahramanmaras earthquakes in Turkey (February 2023, Mw 7.8 and 7.5), a systematic analysis of collapsed buildings found that more than half exhibited pronounced torsional irregularity. These included a 13-storey building in Iskenderun, whose twisting during collapse was directly attributed to this phenomenon [5]. In most of these cases, plan irregularity occurred in combination with other structural deficiencies. Nevertheless, its frequent identification in post-earthquake investigations highlights the need for appropriate analysis and treatment in modern seismic codes [3–5].

Seismic design codes are continuously revised and developed in response to scientific advances and findings from post-earthquake field investigations. The first relevant studies on plan irregularity date back to the 1950s, while code provisions addressing the issue were introduced approximately three decades later [6]. Although modern codes differ in their approaches to plan regularity and in the criteria, they prescribe, their provisions are precautionary in nature. These provisions include analysis procedures involving increased design forces and displacement amplification methods, among other measures [7–9].

This study compares six procedures for determining the centre of stiffness, structural eccentricity and torsional radius of multi-storey buildings, with particular emphasis on their influence on the assessment of regularity in plan according to Eurocode 8. The comparison includes five procedures associated with the first generation and the procedure specified in Annex B of the second generation. Nine idealised six-storey RC dual systems with different wall arrangements are analysed to examine how the choice of procedure affects the calculated parameters and the resulting classification of plan regularity and torsional flexibility.

## 2. CRITERIA FOR REGULARITY IN PLAN ACCORDING TO EUROCODE 8

The structural engineer plays a central role in the design of earthquake-resistant structures, but effective coordination with the other design participants is also essential because the design phases are interconnected. Parameters that significantly influence the structural response should therefore be clearly defined at an early stage of the design process. As the second generation of Eurocode 8 approaches full implementation, differences in the formulation and status of the criteria for regularity in plan warrant consideration. The principal qualitative and quantitative criteria are outlined below.

- With respect to the distribution of lateral stiffness and mass, the structure should be approximately symmetrical in plan about two orthogonal axes. Accordingly, the centre of stiffness and the centre of mass should coincide or lie close to each other.
- The plan configuration should be compact. In the second generation, the area between the floor outline and the enveloping convex polygonal line at each setback is limited to 15% of the floor area. This represents a relaxation of the corresponding first-generation limit of 5%.
- The in-plane stiffness of the floors must be sufficiently high relative to the lateral stiffness of the vertical structural elements to ensure that floor deformation does not significantly affect the distribution of forces among those elements. The second generation defines this requirement more precisely: the effect may be considered small if the forces in the vertical structural elements differ by no more than 20% from those calculated assuming an infinitely stiff diaphragm. Floors with L, C, H, I, X or other irregular plan shapes require particular attention. The stiffness of their lateral branches must be comparable to that of the central part to satisfy the rigid diaphragm condition.
- The slenderness of the building in plan, $\lambda = L_{max} / L_{min}$, must not exceed 4, where $L_{max}$ and $L_{min}$ are the larger and smaller plan dimensions, respectively. In the second generation, this condition need not be satisfied if the number of alignments of primary seismic structures perpendicular to the longer side exceeds $0.5\,\lambda$. Long industrial halls with numerous parallel frames are an example of such structures.
- At each storey level and in both directions, *x* and *y*, the distance between the centre of stiffness and the centre of mass should not exceed 30% of the corresponding torsional radius. The torsional radius should also be at least equal to the radius of gyration of the floor mass in plan:

$$e_{0x,i} \le 0.30\, r_{x,i} \qquad e_{0y,i} \le 0.30\, r_{y,i} \tag{1}$$

$$r_{x,i} \ge l_{s,i} \qquad r_{y,i} \ge l_{s,i} \tag{2}$$

  where $e_{0x,i}$ and $e_{0y,i}$ are the structural eccentricities at storey $i$, $r_{x,i}$ and $r_{y,i}$ are the corresponding torsional radii, and $l_{s,i}$ is the radius of gyration of the floor mass in plan [10–13].

The first generation does not prescribe a specific procedure for determining the centre of stiffness and the torsional radius but allows the National Annexes to refer to documents providing suitable methods. The second generation specifies a procedure in Annex B. A further important distinction concerns the status of the criteria within the code. In the first generation, non-compliance with the criteria for regularity in plan directly affects the choice of structural model and analysis method and indirectly affects the behaviour factor (q). In the second generation, the general criteria for regularity in plan (symmetry, compactness, diaphragm stiffness, slenderness and eccentricity) are presented in an informative annex as non-mandatory rules of good engineering practice. By contrast, the torsional flexibility criterion in Eq. (2), previously included among the criteria for regularity in plan, is addressed separately in Clause 4.4.3 as an explicit requirement [10, 13]. This clause primarily defines torsional flexibility through the modal properties of the structure, namely the predominant modes and their periods, while Eq. (3) provides a simplified sufficient condition:

$$\frac{r_i}{l_{s,i}} \ge 1 \tag{3}$$

The torsional flexibility criterion directly affects the determination of the behaviour factor (q) through the component $q_R$, which accounts for the overstrength associated with the redistribution of seismic action effects [13]. Since the torsional flexibility check is mandatory, whereas the general assessment of regularity in plan is recommended, accurate determination of the torsional radius remains an important research question.

## 3. METHODS FOR DETERMINING THE CENTRE OF STIFFNESS AND THE TORSIONAL RADIUS

In multi-storey buildings, the position of the centre of stiffness and the torsional radii are not uniquely defined, since they depend on the distribution of lateral loads along the height. Two conditions should be satisfied when defining the centre of stiffness. First, any distribution of lateral loads acting through this centre should produce purely translational floor displacements in the direction of loading. Second, any distribution of torsional moments about the vertical axis (z) should produce floor rotations about a vertical axis passing through the centre of stiffness. The torsional radius characterises the susceptibility of the structure to torsional vibrations under earthquake action. It is determined as the square root of the ratio of torsional stiffness to lateral stiffness in the direction considered [10–13]:

$$r_x = \sqrt{K_\theta / K_y} \qquad r_y = \sqrt{K_\theta / K_x} \tag{4}$$

As noted above, the first generation of Eurocode 8 does not prescribe a specific procedure for determining these parameters in multi-storey buildings. Five procedures available in the literature are presented below, followed by the procedure specified in the second generation. A simplified definition for assessing regularity in plan and approximately evaluating torsional effects is possible if two conditions are satisfied: (1) all lateral-load-resisting systems, such as cores, walls and frames, extend continuously from the foundations to the top of the building; and (2) their deflected shapes under horizontal loading do not differ significantly [10, 13]. The loading patterns adopted in the relevant procedures are illustrated in Fig. 1.

- **Procedure G1.1**

For single-storey buildings, the first generation of Eurocode 8 permits the centre of stiffness and the torsional radius to be determined with respect to a reference point in plan. Lateral stiffness is represented by the cross-sectional moments of inertia of the vertical load-bearing elements, while the contribution of the beams is neglected [14]. In frames and systems of slender walls dominated by flexural deformation, the centre of stiffness and the torsional radius at each storey may be calculated from the cross-sectional moments of inertia of the vertical elements. Where shear deformation is also significant, its contribution may be included by using an equivalent cross-sectional moment of inertia [10].

$$x_{CS} = \frac{\sum x E I_y}{\sum E I_y} \qquad y_{CS} = \frac{\sum y E I_x}{\sum E I_x} \tag{5}$$

$$r_x = \sqrt{\frac{\sum \left( \left(x - x_{cs}\right)^2 E I_y + \left(y - y_{cs}\right)^2 E I_x \right)}{\sum E I_y}}$$
$$r_y = \sqrt{\frac{\sum \left( \left(x - x_{cs}\right)^2 E I_y + \left(y - y_{cs}\right)^2 E I_x \right)}{\sum E I_x}} \tag{6}$$

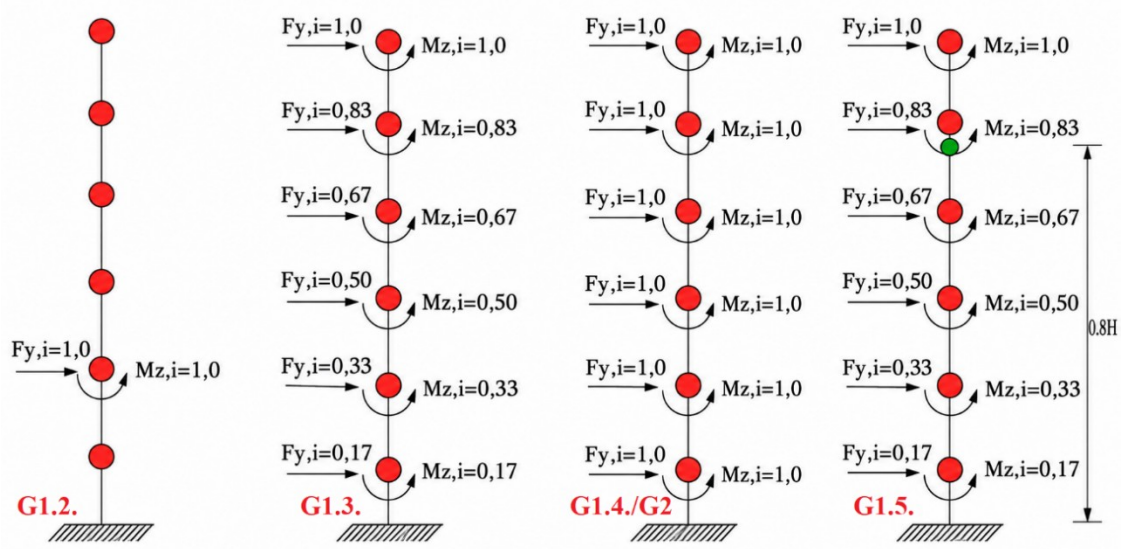


*Fig. 1 Schematic representation of the loading patterns adopted in the considered procedures*

- **Procedure G1.2**

In the second procedure, described by Fajfar et al. [15] and adopted in this study, the centre of stiffness and the torsional radius are determined separately for each storey. To determine the structural eccentricity, three separate static load cases are defined at the storey under consideration: a unit lateral force in each of the x and y directions and a unit torsional moment about the vertical axis, all applied at the centre of mass. Once the centre of stiffness and the corresponding structural eccentricity have been determined, the analysis is repeated with the loads applied at the centre of stiffness to obtain the torsional radius.

- **Procedure G1.3**

The third procedure follows the same approach as G1.2, except that the lateral forces and torsional moments are applied simultaneously to all storeys rather than to each storey separately. A triangular load distribution is adopted along the height [16].

- **Procedure G1.4**

The fourth procedure is closely related to G1.3. If the triangular load distribution produces substantial storey-to-storey variations in the position of the centre of stiffness or in the torsional radius, the analysis should be repeated using a uniform load distribution along the height. The results for dual systems may be particularly sensitive to this change [16].

- **Procedure G1.5**

In the fifth procedure, the centre of stiffness and the torsional radius are determined for the structure as a whole, rather than separately for each storey. In the first step, the lateral forces ($F_{x,i}$ and $F_{y,i}$) are calculated using the lateral force method of analysis. Torsional moments proportional to these forces, ($T_i = F_i \cdot c$), are then applied at each storey. The resulting centre of rotation is determined geometrically for each storey. The horizontal projection of the centre of rotation at (z=0.8H), corresponding to 80% of the total structural height, is adopted as the centre of stiffness of the entire structure. In the second step, lateral forces in both directions, proportional to the torsional moments used in the first step, are applied at the centre of stiffness. The resulting displacements and rotations are used to determine the torsional radius [11, 17]:

$$r_x = \sqrt{\delta_{y,0.8H}/\theta_{0.8H}} \qquad r_y = \sqrt{\delta_{x,0.8H}/\theta_{0.8H}} \tag{7}$$

- **Procedure G2**

Annex B of the second generation of Eurocode 8 provides a simplified procedure based on the lateral stiffnesses of the individual vertical members at each storey. This procedure applies to structures composed of the same type of primary bracings extending continuously from the base to the level under consideration. Annex B also provides a procedure for determining the structural eccentricity and the torsional radius using a 3D model, provided that the floors can be considered rigid in their planes. Three load cases are defined, with the loads applied simultaneously to all storeys. The first two consist of lateral forces acting in the (X) and (Y) directions at the centres of mass. At each storey, the force is calculated as the product of the storey mass and a unit acceleration. These load cases yield the interstorey rotation increments $\Delta\theta_{x,i}$ and $\Delta\theta_{y,i}$, respectively. The third load case consists of moments about the vertical axis, numerically equal to the previously calculated forces, and yields $\Delta\theta_{z,i}$. The structural eccentricities are then calculated as:

$$e_{0x,i}=\frac{\Delta\theta_{y,i}}{\Delta\theta_{z,i}} \qquad e_{0y,i}=\frac{\Delta\theta_{x,i}}{\Delta\theta_{z,i}} \tag{8}$$

The torsional radius $r_{x,i}$ can be determined from the following formula:

$$r_{x,i}=\sqrt{\frac{\Delta d_{y,C,i}}{\Delta\theta_{z,i}}}, \tag{9}$$

where $\Delta d_{y,C,i}=\left(\Delta d_{y,G,i}-\Delta\theta_{y,i}\cdot e_{0x,i}\right)$ is the interstorey displacement difference at the centre of stiffness (C), obtained from the second load case (Y direction), and $\Delta d_{y,G,i}$ is the corresponding difference at the centre of mass (G). The same procedure can be applied to determine $r_{y,i}$ [13]. Unlike the preceding procedures, which use response quantities at each level measured relative to the base, the second-generation procedure uses relative interstorey quantities to determine the centre of stiffness and the torsional radius. This is an essential methodological distinction between the procedures.

## 4. NUMERICAL EXAMPLE

### 4.1. DESCRIPTION OF THE ANALYSED STRUCTURES

Six-storey structures with different degrees of plan irregularity were defined to compare the procedures presented in Section 3. All structures have a rectangular plan comprising three frames in the X direction and six frames in the Y direction. The frames are spaced at 5 m in both directions, giving overall plan dimensions of 25 × 10 m. All structures are symmetrical about the X axis. A constant storey height of 3 m gives a total structural height of 18 m. The columns have a square cross-section of 60 × 60 cm throughout the height, while the beams have a rectangular cross-section of 40 × 50 cm. The slab thickness is 15 cm. Different degrees of plan irregularity were obtained by replacing the middle column in two of the six frames in the Y direction with an RC wall. Each wall has a rectangular cross-section of 300 × 25 cm, with its longer side oriented in the Y direction. This arrangement yields 15 possible wall-layout combinations. Three are also symmetrical about the Y axis: walls in axes Ry1 and Ry6 (Str.W1/6), Ry2 and Ry5 (Str.W2/5), and Ry3 and Ry4 (Str.W3/4). The remaining 12 combinations form six mirror pairs: Str.W1/2–Str.W5/6, Str.W1/3–Str.W4/6, Str.W1/4–Str.W3/6, Str.W1/5–Str.W2/6, Str.W2/3–Str.W4/5 and Str.W2/4–Str.W3/5. The first structure in each pair was analysed together with the three symmetrical structures, giving a total of nine analysed structures (Fig. 2).

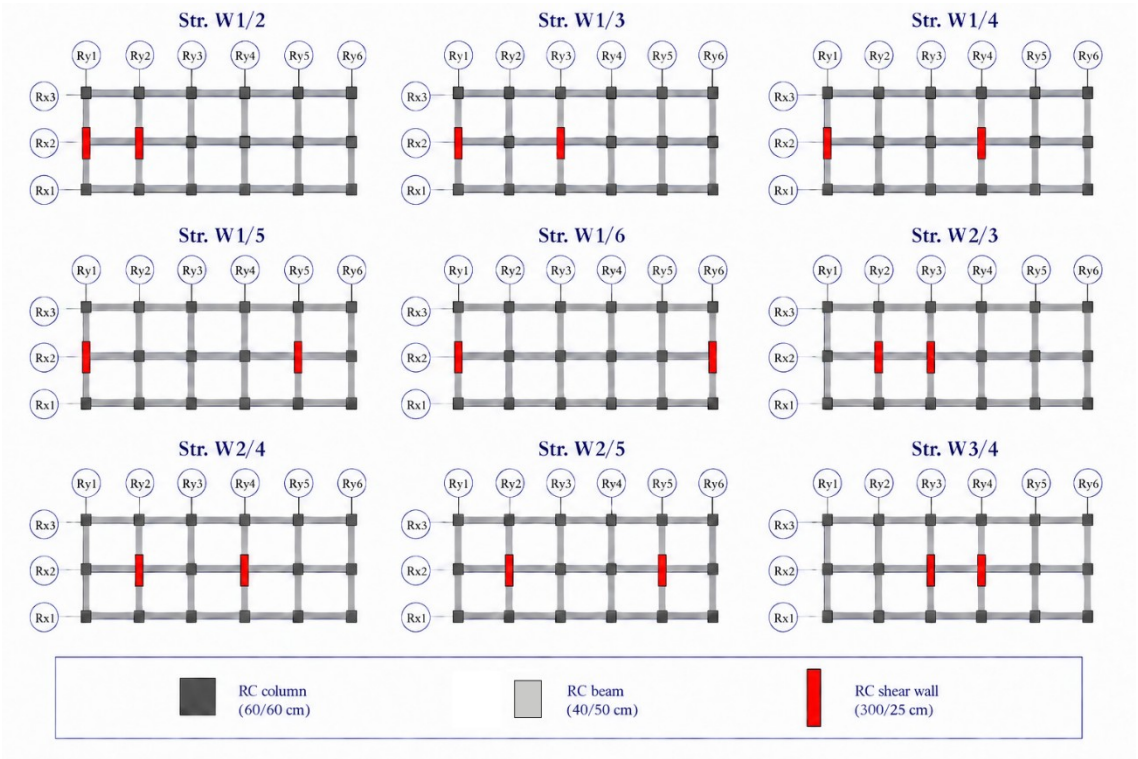


*Fig. 2 Plan layouts of the vertical structural elements in the analysed structures*

The models were analysed using SeismoStruct. Linear-elastic static analysis was used to determine the structural response, while modal analysis provided the natural periods and mode shapes. A rigid diaphragm was assigned at each floor level, and concrete class C25/30 was adopted for all structural elements. At each storey, all frames in the Y direction were subjected to a line load of 25 kN/m and concentrated loads of 125 kN at each node. The self-weight of the structural elements was neglected. The structural mass was determined from the applied gravity loads. Consequently, the centre of mass occupies the same position in all analysed structures, allowing the influence of the stiffness distribution in plan to be examined independently. The stiffness of all elements was taken as 50% of the corresponding uncracked stiffness [10]. Since this reduction was applied uniformly, it does not alter the relative stiffness distribution and therefore does not affect the centre of stiffness or the torsional radius. It does, however, affect the natural periods. The models are intended as idealised parametric systems for comparing the procedures rather than as fully designed buildings.

## 4.2. COMPARISON OF RESULTS

All structures are regular with respect to the X axis because their distributions of mass, loads, stiffness and strength are symmetrical about this axis. The regularity criteria were therefore checked with respect to the Y axis. For the rectangular plan, with dimensions $L \times B = 25 \times 10\,m$ and uniformly distributed floor masses, the radius of gyration of the floor mass is:

$$l_s = \sqrt{\frac{L^2 + B^2}{12}} = \sqrt{\frac{25^2 + 10^2}{12}} = 7.77\,m \tag{10}$$

The structural eccentricity and the torsional radius were calculated using the six procedures described in Section 3. For the analysed structures, G1.5 and G1.3 have the same triangular load distribution, while G2 and G1.4 have the same uniform distribution. Since the gravity loading is identical at all storeys, the storey masses are equal. The

height-dependent force distribution used in G1.5 therefore gives a triangular profile, whereas the mass-proportional forces obtained using a unit acceleration in G2 give a uniform profile. This equivalence concerns only the loading patterns. The procedures use the resulting response quantities differently, so the calculated structural parameters need not coincide.

The structural eccentricities $e_{0x,i}$ shown in Fig. 3 range from −1.30 m to 8.50 m. Procedure G1.1 gives constant values along the height because the cross-sectional dimensions of the vertical structural elements are unchanged. In the other procedures, the eccentricity decreases with height, making the first storey critical for the assessment of regularity in plan. The differences between the procedures increase with the degree of irregularity. At the first storey, the maximum difference is less than 1 m for Str.W1/5 but almost 3 m for Str.W1/2. Procedures G1.3 and G1.4 give nearly identical values. In G1.5, the reference level at (0.8H) lies between the fourth and fifth storeys and therefore does not capture the governing first-storey eccentricity. Procedure G2 alone produces negative eccentricities at the top storey. These arise from wall–frame interaction, which causes a reversal in the sign of the interstorey rotation increment. This raises an issue concerning the application of the criterion that is not addressed in Annex B: for a negative eccentricity, the interpretation of the check $e_{0x} \leq 0.3 r_x$ becomes ambiguous. The absolute value $|e_{0x,i}|$ is therefore used in this study.

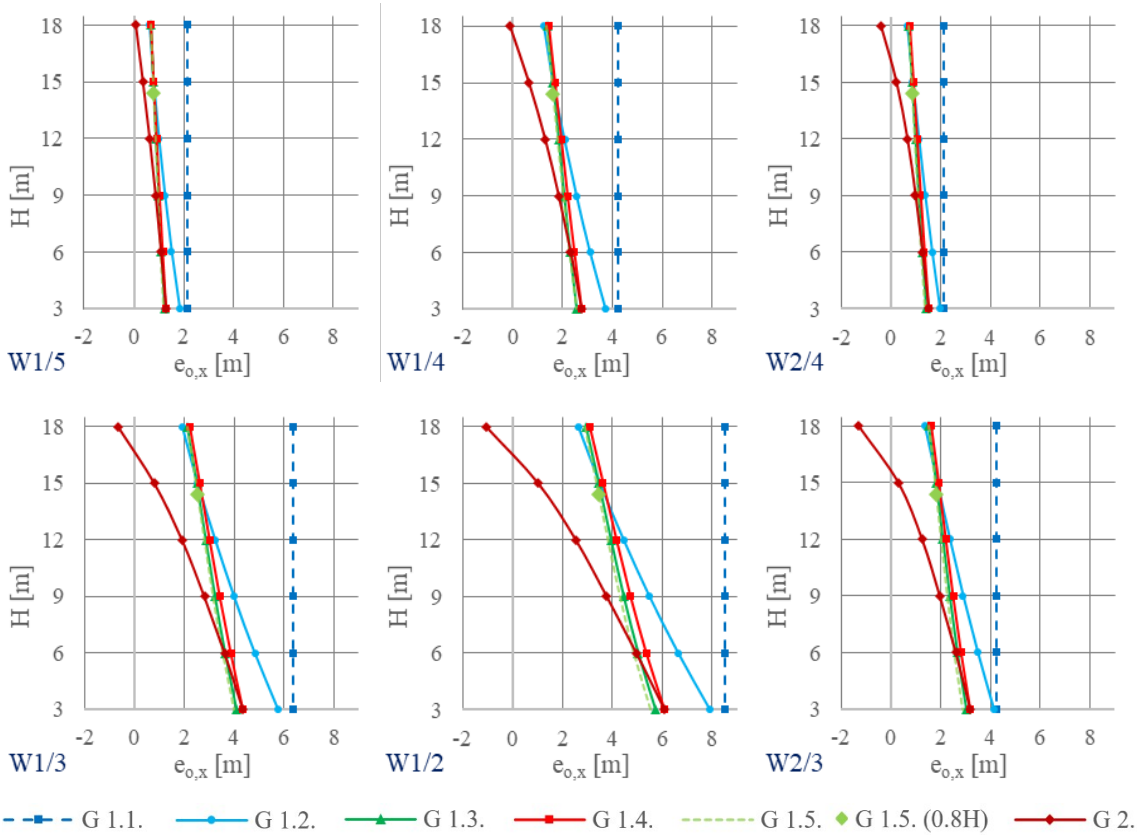


*Fig. 3 Structural eccentricity $e_{0x,i}$ obtained by different procedures*

The torsional radii $r_{x,i}$ shown in Fig. 4 range from 4.3 m to 12.1 m. The torsional radius increases with height in all structures except the symmetrical structure Str.W1/6, where it decreases. In this structure, the RC walls are in the end frames, resulting in substantially higher torsional stiffness at the lower storeys than at the upper ones. Procedure G1.1 gives constant values along the height and generally lower torsional radii than the other procedures. The exception is Str.W1/6, for which it gives larger values. This difference

results from neglecting the contribution of the beams to the stiffness of the dual systems, for which the procedure is not formally intended. As with the structural eccentricity, the differences between the procedures increase with the degree of irregularity. For Str.W1/5, all procedures give torsional radii of approximately 10 m at all storeys, whereas for Str.W1/2 the difference exceeds 4 m. Procedures G1.3, G1.4 and G1.5 give closely comparable values. Procedure G2 produces the highest values at the upper storeys and the most pronounced increase with height. At the first storey, however, its values approach those obtained using the other procedures.

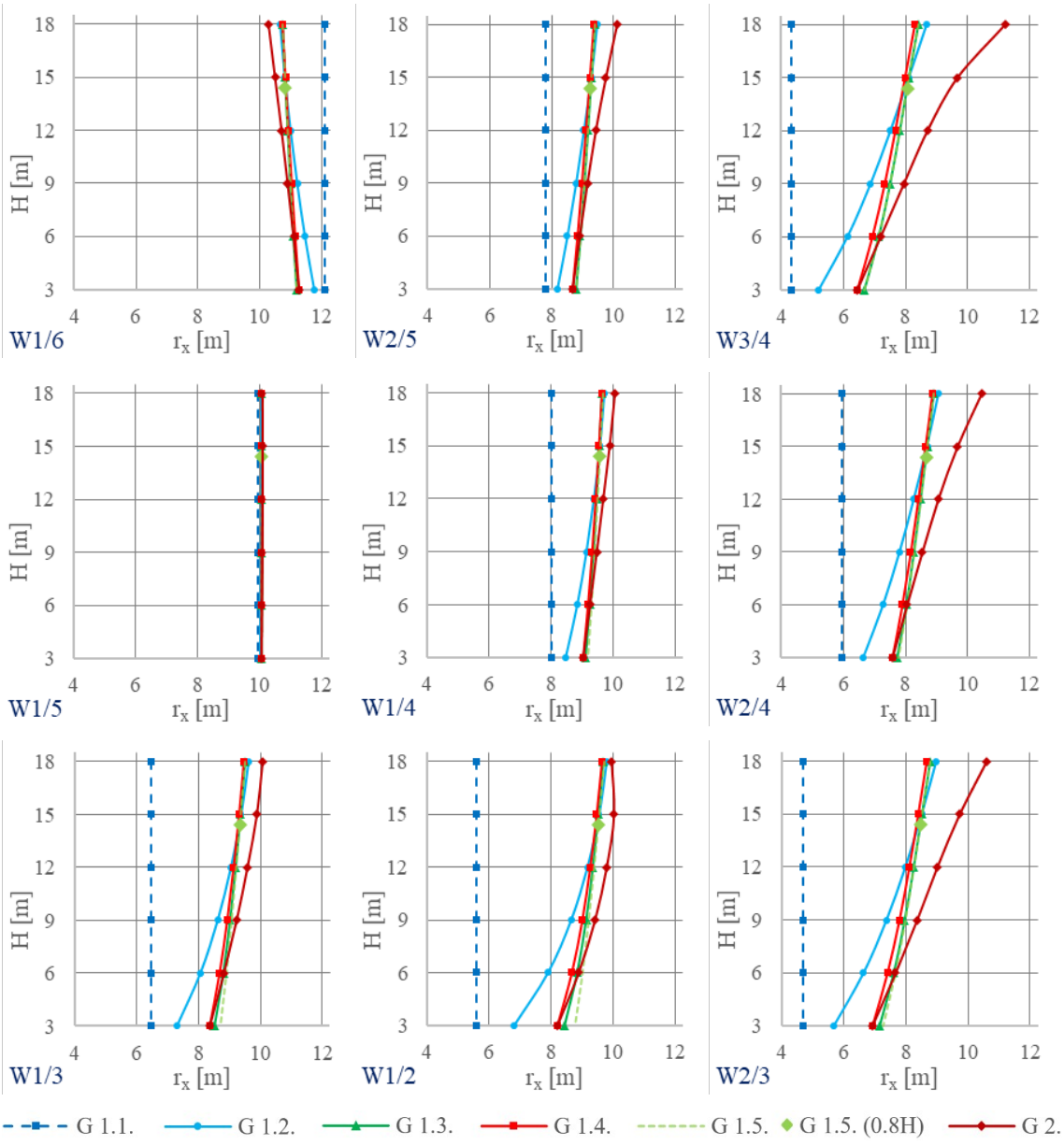


*Fig. 4 Torsional radius $r_{x,i}$ obtained by different procedures*

The results in Table 1 demonstrate that the choice of procedure significantly affects the classification of regularity in plan. The values are normalised, with values above 1.00 indicating that the corresponding criterion is not satisfied and values below 1.00 indicating that it is satisfied. Procedure G1.1 generally gives the highest ratios. For the eccentricity criterion, these exceed twice the values obtained using procedures that load all storeys simultaneously. It is therefore the most conservative procedure and classifies six of the nine structures as irregular. Procedure G1.2, in which each storey is loaded

separately, gives lower ratios than G1.1 but the same classification for torsional flexibility. Procedures G1.3, G1.4 and G2 give similar values and almost identical classifications. The only difference concerns the eccentricity criterion for Str.W1/4: the ratio is 0.94 for G1.3 and 1.02 for G1.4 and G2, indicating slightly higher values under uniform loading than under triangular loading. The results of G1.4 and G2 coincide because the first storey governs and, at this level, the relative interstorey and absolute response quantities are equal. Procedure G1.5 shows the largest departure from the other procedures when the assessment is performed at (0.8H), where only one structure is classified as irregular. When the first-storey values are used instead, as shown in parentheses in Table 1, its classification coincides with that of G1.3. Overall, the differences between the procedures are greater for the eccentricity criterion than for the torsional flexibility criterion. Structures Str.W1/6, Str.W1/5 and Str.W2/5 are regular according to all six procedures.

*Tab. 1 Check of plan regularity criteria (normalised values)*

| | $\frac{\lvert e_{0,x}\rvert}{0{,}3r_x}$ | $\frac{l_s}{r_x}$ | $\frac{\lvert e_{0,x}\rvert}{0{,}3r_x}$ | $\frac{l_s}{r_x}$ | $\frac{\lvert e_{0,x}\rvert}{0{,}3r_x}$ | $\frac{l_s}{r_x}$ | $\frac{\lvert e_{0,x}\rvert}{0{,}3r_x}$ | $\frac{l_s}{r_x}$ | $\frac{\lvert e_{0,x}\rvert}{0{,}3r_x}$ | $\frac{l_s}{r_x}$ | $\frac{\lvert e_{0,x}\rvert}{0{,}3r_x}$ | $\frac{l_s}{r_x}$ |
|---|---|---|---|---|---|---|---|---|---|---|---|---|
| **Str. W1/6** | ☑ 0.00 | ☑ 0.64 | ☑ 0.00 | ☑ 0.73 | ☑ 0.00 | ☑ 0.73 | ☑ 0.00 | ☑ 0.72 | ☑ 0.00 (0.00) | ☑ 0.72 (0.69) | ☑ 0.00 | ☑ 0.76 |
| **Str. W2/5** | ☑ 0.00 | ☑ 0.99 | ☑ 0.00 | ☑ 0.95 | ☑ 0.00 | ☑ 0.89 | ☑ 0.00 | ☑ 0.90 | ☑ 0.00 (0.00) | ☑ 0.84 (0.89) | ☑ 0.00 | ☑ 0.90 |
| **Str. W3/4** | ☑ 0.00 | ✗ 1.80 | ☑ 0.00 | ✗ 1.49 | ☑ 0.00 | ✗ 1.17 | ☑ 0.00 | ✗ 1.21 | ☑ 0.00 (0.00) | ☑ 0.96 (1.17) | ☑ 0.00 | ✗ 1.21 |
| **Str. W1/5** | ☑ 0.71 | ☑ 0.78 | ☑ 0.61 | ☑ 0.78 | ☑ 0.40 | ☑ 0.77 | ☑ 0.43 | ☑ 0.77 | ☑ 0.26 (0.40) | ☑ 0.77 (0.77) | ☑ 0.43 | ☑ 0.77 |
| **Str. W1/4** | ✗ 1.77 | ☑ 0.97 | ✗ 1.47 | ☑ 0.92 | ☑ 0.94 | ☑ 0.85 | ✗ 1.02 | ☑ 0.86 | ☑ 0.57 (0.92) | ☑ 0.81 (0.85) | ✗ 1.02 | ☑ 0.86 |
| **Str. W2/4** | ✗ 1.19 | ✗ 1.31 | ☑ 0.99 | ✗ 1.17 | ☑ 0.60 | ✗ 1.005 | ☑ 0.66 | ✗ 1.03 | ☑ 0.33 (0.58) | ☑ 0.90 (1.01) | ☑ 0.66 | ✗ 1.03 |
| **Str. W1/3** | ✗ 3.29 | ✗ 1.20 | ✗ 2.63 | ✗ 1.06 | ✗ 1.60 | ☑ 0.91 | ✗ 1.74 | ☑ 0.93 | ☑ 0.90 (1.54) | ☑ 0.83 (0.89) | ✗ 1.74 | ☑ 0.93 |
| **Str. W1/2** | ✗ 5.05 | ✗ 1.39 | ✗ 3.87 | ✗ 1.14 | ✗ 2.26 | ☑ 0.92 | ✗ 2.47 | ☑ 0.95 | ✗ 1.20 (2.10) | ☑ 0.82 (0.88) | ✗ 2.47 | ☑ 0.95 |
| **Str. W2/3** | ✗ 3.03 | ✗ 1.66 | ✗ 2.43 | ✗ 1.37 | ✗ 1.41 | ✗ 1.09 | ✗ 1.55 | ✗ 1.12 | ☑ 0.71 (1.31) | ☑ 0.92 (1.07) | ✗ 1.55 | ✗ 1.12 |
| | **Procedure G 1.1.** | | **Procedure G 1.2.** | | **Procedure G 1.3.** | | **Procedure G 1.4.** | | **Procedure G 1.5.** | | **Procedure G 2.** | |

Figure 5 presents the periods of the first three vibration modes and the corresponding effective modal mass participation ratios in the three directions for all nine structures. In the asymmetric structures, translation in the Y direction is coupled with torsion, and this coupling becomes more pronounced as the eccentricity increases. For structures with RC walls located closer to the centre of the plan (Str.W2/5, Str.W2/4, Str.W2/3 and Str.W3/4) the torsional period exceeds the translational period in the Y direction, with $\left(T_\theta/T_y\right)$ ranging from 1.01 to 1.25. These structures are therefore torsionally flexible according to criterion b) of Clause 4.4.3(1). Criterion a) gives the same classification because their largest effective modal mass in the Y direction corresponds to the third mode. The modal classification generally agrees with the results of G1.3, G1.4 and G2. The exception is Str.W2/5, which is classified as regular by the static procedures, although its $l_s/r_x$ ratios range from 0.84 to 0.99 and are therefore close to the limiting value.

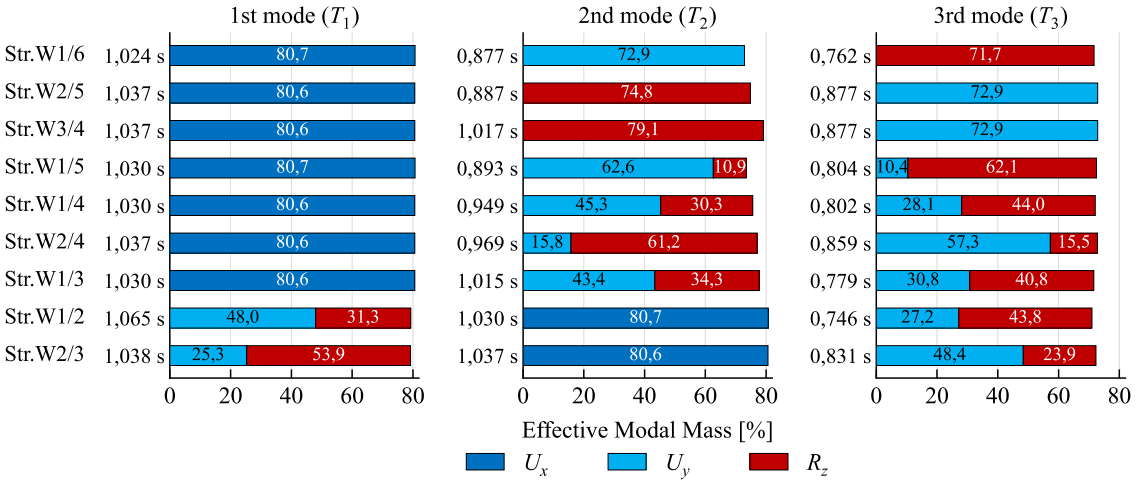


*Fig. 5 Periods and effective modal mass participation ratios of the first three modes*

## 5. CONCLUSION

In multi-storey structures, the centre of stiffness and the torsional radius are not uniquely defined. The results of this study demonstrate that the procedure adopted for their determination can significantly affect the classification of regularity in plan. The same structure may be classified as regular by one procedure and irregular by another. The discrepancies increase with the degree of irregularity, making the choice of procedure particularly important for structures in which the regularity assessment is most relevant.

Procedure G1.1 generally gives larger structural eccentricities and smaller torsional radii than the other procedures because it neglects the contribution of the beams. Its applicability to the analysed dual systems is therefore limited. Procedures G1.3, G1.4 and G2 produce almost identical classifications, indicating that the shape of the lateral load distribution has a minor influence for the structures considered. Procedure G1.5 gives a less restrictive classification when the assessment is performed at (0.8H), because this reference level does not capture the governing first-storey values. When the first-storey values are used, its classification coincides with that of G1.3. Procedure G2 alone captures the reversal in the sign of the interstorey rotation increment caused by wall–frame interaction. The resulting negative eccentricities make the interpretation of the check $e_{0x} \leq 0.3\, r_x$ ambiguous, an issue not addressed in Annex B. The modal criteria of Clause 4.4.3 generally agree with the static procedures, except for Str.W2/5, which lies close to the limiting value. This exception shows that the static and modal criteria within the same clause may yield different classifications near the limit.

Although the differences between the procedures are greater for the eccentricity criterion, which the second generation retains as a rule of good engineering practice, the classification of torsional flexibility also depends on the procedure adopted. The torsional flexibility criterion is mandatory and directly affects the behaviour factor through the component $q_R$. The choice of procedure therefore has implications for the design seismic forces, highlighting the need for a clearly defined and unambiguous procedure for determining the relevant torsional parameters. Further research should use nonlinear analyses to establish which procedure best reflects the actual torsional response of dual systems. The study should also be extended to buildings of different heights and structural systems.

## REFERENCES

[1] Anagnostopoulos S.A., Kyrkos M.T., Papalymperi A., Plevri E. (2015). Should accidental eccentricity be eliminated from Eurocode 8? Earthquakes and Structures, Volume 8, No. 2, pp. 463–484. https://doi.org/10.12989/eas.2015.8.2.463

[2] Volchev R., Postolov N., Todorov K., Lazarov Lj. (2025). The influence of structural eccentricity on the seismic behavior of torsionally sensitive structures. 3rd Croatian Conference on Earthquake Engineering, University of Zagreb Faculty of Civil Engineering, Split, Croatia, 19–22 March, pp. 578–588. https://doi.org/10.5592/CO/3CroCEE.2025.87

[3] Galvis, F.A., Miranda, E., Heresi, P., Dávalos, H., Ruiz-García, J. (2020). Overview of collapsed buildings in Mexico City after the 19 September 2017 (Mw7.1) earthquake. Earthquake Spectra, 36(2_suppl), pp. 83–109. https://doi.org/10.1177/8755293020936694

[4] Marinković M., Baballëku M., Isufi B., Blagojević N., Milićević I., Brzev S. (2022). Performance of RC cast-in-place buildings during the November 26, 2019, Albania earthquake. Bulletin of Earthquake Engineering, Volume 20, pp. 5427–5480. https://doi.org/10.1007/s10518-022-01414-y

[5] Atmaca B., Altunişik A.C., Ertürk Atmaca E., Başağa H.B., Günaydin M., et al. (2025). What is the reason for collapses on February 6, 2023, Kahramanmaraş earthquakes: Insights from a dataset of 400 collapsed RC buildings post-earthquake analysis. Journal of Building Engineering, Volume 107, 112660. https://doi.org/10.1016/j.jobe.2025.112660

[6] Anagnostopoulos S.A., Kyrkos M.T., Stathopoulos K.G. (2015). Earthquake induced torsion in buildings: critical review and state of the art. Earthquakes and Structures, Volume 8(2), pp. 305–377. https://doi.org/10.12989/eas.2015.8.2.305

[7] Alecci V., De Stefano M. (2019). Building irregularity issues and architectural design in seismic areas. Frattura ed Integrità Strutturale, Volume 47, pp. 161–168. https://doi.org/10.3221/IGF-ESIS.47.13

[8] Das P.K., Dutta S.C., Datta T.K. (2021). Seismic behavior of plan and vertically irregular structures: State of art and future challenges. Natural Hazards Review, Volume 22(2), 04020062. https://doi.org/10.1061/(ASCE)NH.1527-6996.0000440

[9] Mrdak I., Rakočević M., Lađinović Đ. (2024). Assessment of torsional irregularity provisions for buildings in accordance with Eurocode 8. Journal of Applied Engineering Science, Volume 22(2), pp. 310–315. https://doi.org/10.5937/jaes0-50820

[10] CEN (2004). EN 1998-1:2004 Eurocode 8: Design of structures for earthquake resistance – Part 1: General rules, seismic actions and rules for buildings. Comité Européen de Normalisation, Brussels, Belgium.

[11] Fardis M.N., Carvalho E.C., Fajfar P., Pecker A. (2015). *Seismic Design of Concrete Buildings to Eurocode 8*, CRC Press, Boca Raton, USA.

[12] Penelis G.G., Penelis G.G. (2019). *Concrete Buildings in Seismic Regions* (2nd edition), CRC Press, Boca Raton, USA.

[13] CEN (2025). FprEN 1998-1-2:2025 Eurocode 8: Design of structures for earthquake resistance – Part 1-2: Buildings. CEN/TC 250/SC 8 N1396, Comité Européen de Normalisation, Brussels, Belgium.

[14] Postolov N., Volcev R., Todorov K., Lazarov Lj. (2020). Effects of modelling assumptions on the plan irregularity criteria for single storey buildings. In: Köber D., De Stefano M., Zembaty Z. (eds.), Seismic Behaviour and Design of Irregular and Complex Civil Structures III, Geotechnical, Geological and Earthquake Engineering, Volume 48, Springer, Cham, Switzerland, pp. 233–248. https://doi.org/10.1007/978-3-030-33532-8_19

[15] Bisch P., Carvalho E., Degee H., Fajfar P., Fardis M., Franchin P., Kreslin M., Pecker A., Pinto P., Plumier A., Somja H., Tsionis G. (2012). Eurocode 8: Seismic Design of Buildings – Worked examples, Carvalho E., Fardis M., Acun B., Athanasopoulou A., Pinto Vieira A. (eds.), EUR 25204 EN, Publications Office of the European Union, Luxembourg. https://doi.org/10.2788/91658

[16] IStructE, AFPS (2010). Manual for the seismic design of steel and concrete buildings to Eurocode 8, The Institution of Structural Engineers, London, Great Britain.

[17] OASP (2003). Greek Code for Seismic Resistant Structures – EAK 2000, Earthquake Planning and Protection Organization, Ministry of Environment, Planning and Public Works, Athens, Greece.

https://doi.org/10.24867/INDIS-2026-EN-139



# SMART CRANE INSPECTION: THE POTENTIAL OF BIM-BASED FRAMEWORK FOR CRANE INSPECTION IN CONSTRUCTION

*Željana Kužet[1], Vladimir Mučenski[2], Jovana Topalić[3], Goran Bošković[4], Dragan Živanić[5]*

***Summary:***

Given the ongoing technological transformation in the construction industry and the high incidence of crane-related accidents due to inadequate inspection, the study presents an integrated monitoring system that combines Building Information Modeling (BIM) with Industry 4.0 technologies to track, manage, and assess the technical condition of cranes throughout their operational lifecycle on construction sites. The proposed framework is based on a BIM digital model of a crane, enriched with component-level technical, operational, and safety-related data. The three-layer system: (1) data acquisition layer, (2) BIM layer, and (3) output layer, enables inspectors to access relevant information efficiently, thus ensuring the transition from traditional crane inspections to the principles of Industry 4.0 and Industry 5.0.

*Keywords: Building Information Modeling, Crane inspection, Construction safety, Industry 4.0, Industry 5.0*

# PAMETNA INSPEKCIJA DIZALICA: POTENCIJAL BIM OKVIRA ZA INSPEKCIJU DIZALICA U GRAĐEVINARSTVU

***Rezime:***

S obzirom na tekuću tehnološku transformaciju građevinske industrije i visoku učestalost nesreća povezanih sa dizalicama usled neadekvatnih inspekcijskih postupaka, u radu je predstavljen integrisani sistem za monitoring koji kombinuje modelovanje informacija o građevinama (BIM) sa tehnologijama Industrije 4.0 u cilju praćenja, upravljanja i procene tehničkog stanja kranova tokom celokupnog njihovog operativnog životnog ciklusa na gradilištima. Predloženi okvir zasniva se na digitalnom modelu dizalice razvijene u BIM okruženju, obogaćenom tehničkim, operativnim i bezbednosnim podacima na nivou pojedinačnih komponenti. Troslojnom strukturom sistema: (1) sloj za prikupljanje podataka, (2) BIM sloj i (3) izlazni sloj, inspektorima se omogućava efikasan pristup relevantnim informacijama, tako obezbeđujući prelazak sa tradicionalnih pregleda dizalica ka principima Industrije 4.0 i Industrije 5.0.

*Ključne reči: Building Information Modeling (BIM), Inspekcija dizalica, Bezbednost u građevinarstvu, Industrija 4.0, Industrija 5.0*

[1] PhD Student, Scholarship holder of the Ministry of Science, Technological Development and Innovation, Faculty of Technical Sciences, University of Novi Sad, Republic of Serbia, zeljana.kuzet.12@outlook.com, ORCID: 0009-0004-0958-517X
[2] PhD, Full professor, Faculty of Technical Sciences, University of Novi Sad, Republic of Serbia, mucenskiv@uns.ac.rs, ORCID: 0000-0001-9830-4747
[3] PhD, Research Associate, Faculty of Technical Sciences, University of Novi Sad, Republic of Serbia, jovanatopalic90@uns.ac.rs, ORCID: 0000-0001-7854-3257
[4] PhD, Assistant Professor, Faculty of Mechanical and Civil Engineering in Kraljevo, University of Kragujevac, Republic of Serbia, boskovic.g@mfkv.rs, ORCID: 0000-0002-4597-922X
[5] PhD, Full professor, Faculty of Technical Sciences, University of Novi Sad, Republic of Serbia, zivanic@uns.ac.rs, ORCID: 0000-0003-2570-0727

## 1. INTRODUCTION

For more than 200 years, the industrial process has undergone several revolutions at a rapid pace. Since industry developed rapidly from the “Steam Age” (Industry 1.0) and “Electric Age” (Industry 2.0) to the information technology (IT) era (Industry 3.0), the IT era serves as a baseline for Industry 4.0 and Industry 5.0 [1,2]. Industry 4.0 is the convergence of IT and Operational Technology (OT). It has undergone enormous evolution through numerous innovations (e.g., Artificial Intelligence (AI), robotics, blockchain, Internet of Things (IoT)), which have brought innovation, quality, complete autonomy, and a safe environment [3-5].

Unlike Industry 4.0, which focuses on automation, Industry 5.0 reintroduces humans into production processes, combining their creativity and intelligence with the efficiency and autonomy of machines. By enabling cooperation between human and autonomous systems, it is possible to enhance efficiency, reduce costs and waste, and develop reliable autonomy [6]. As a dynamic, continuously evolving concept, Industry 5.0 drives the World Industrial System toward a future built on collaboration and co-creation. Human–centricity, sustainability, and resiliency are the main characteristics of Industry 5.0 [7]. Since the essence of Industry 5.0 lies in collaborative intelligence, multi-objective interweaving, multi-technology restructuring, multi-discipline integration, multi-sector symbiosis, and multi-systems heterogeneity [7], its principles naturally extend across various industries and professional fields [8].

The construction industry is currently undergoing a significant transformation, driven by the adoption of advanced Industry 4.0 technologies and further shaped by emerging Industry 5.0 principles [9]. Regardless of rapid technological improvements, the construction industry remains one of the most hazardous industries due to a high rate of fatal incidents and serious injuries caused by various hazards. One of the hazards contributing to the growth in the incident rate are cranes, which are associated with increased accidents due to overturning, overloading, inadequately trained crane operators, and inadequate inspections and checks of the crane [10]. It can be concluded that a more advanced, data-driven safety management approach is needed. This makes Industry 4.0 and 5.0 particularly relevant in the construction and engineering sector, where the integration of advanced digital tools, such as Building Information Modeling (BIM), can be applied across specialized domains, including health and safety engineering and crane inspection and verification.

BIM serves as a comprehensive information system encompassing the entire asset lifecycle, from design and modeling to project delivery and virtual construction [11]. Beyond its core 3D modeling capabilities, BIM technology enables integration with additional project data (e.g., scheduling-4D, cost estimation-5D) [12-14]. Within the Construction 4.0 framework, BIM stands out as a key digital technology, integrated alongside tools such as IoT, AI, and data analytics to drive the digital transformation of the construction industry [15].

Unlike traditional 3D CAD software, 3D-BIM models go beyond simple geometric representation by attaching attributes to each component, where any change in one element is automatically reflected across all related information throughout the project. Building on this, 4D-BIM connects the 3D model with the construction schedule, simulating the construction process over time and enabling early detection of errors, risks, and scheduling inconsistencies, ultimately contributing to a safer, more efficient construction process [16]. In addition, other technologies are currently being implemented combined with BIM methodology, such as IoT, Big Data (BD), Cloud Computing (CC), and Facility Management (FM) techniques. The combined use of these

technologies, together with BIM, offers significant advancements in construction and civil engineering [17] and in occupational safety and health engineering [16].
As a significant workplace hazard in the infrastructure construction industry, cranes directly affect project progress and personnel safety [18, 19]. Due to various structural and mechanical failures, design errors, failures of periodic controls, and maintenance deficiencies [20-22], the rate of crane accidents is increasing, causing major adverse effects on construction projects and the workforce [23]. Therefore, cranes should be regularly inspected and maintained [24, 25] to verify that all components meet required safety and quality standards. After inspection, an examination report is issued to confirm that the crane has been tested [26]. Therefore, to improve construction safety through construction safety management, Building Information Modeling (BIM) enables early identification and visual assessment of potential hazards, supporting proactive risk control throughout the construction process [27]. To reduce on-site crane accidents and ensure a safe environment, this research examines the potential of BIM, in combination with Industry 4.0 technologies, as a basis for a more integrated and data-driven approach to crane inspection in the construction industry.

## 2. INTEGRATION OF BIM INTO SAFETY MANAGEMENT

Safety management in construction needs to be revised and upgraded from manual processes to digitalization across all construction project phases [28]. To enhance safety management throughout the project life cycle, diverse technologies from Industry 4.0 have been developed [29], bringing automation and new opportunities to reduce costs, enhance safety, and improve productivity [30,31]. Some of the most widely used technologies in safety management include wearable technology, plant-based sensors (e.g., on safety-critical equipment to determine maintenance and servicing schedules), and aerial drones that perform visual inspections of safety–critical assets [32-34]. Apart from physical systems, Industry 4.0 is also characterized by digital transformation. Digital transformation is a tool that greatly improves safety in the industry by applying technologies (data analytics, IoT, AI) to connect data from different sources, creating integrated, flexible, and intelligent systems that enhance collaboration and decision-making [35]. In this context, BIM can be seen as a digital platform that enables the integration and visualization of data on equipment, processes, and risks in construction projects with the aim of effective safety management on the construction site.
Considering BIM as the most promising technology and its supporting software as a tool to simplify construction project planning [29, 36], it is recommended as a starting point for safety management planning. By desegregating existing safety rules and guidelines and applying them to 3D models and 4D planning, more illustrative site layouts and safety plans are provided, enabling the development of checklists to identify and eliminate potential hazards in the planning phase [28,36]. During the realization phase, thanks to BIM implementation, it is possible to conduct continuous monitoring, visualize risk zones, streamline decision–making, and implement appropriate preventive measures [28]. Indirectly, BIM can affect other project participants (e.g., designers, subcontractors, and safety specialists) in both safety and construction management [37].
In construction safety management, 3D and 4D BIM are primarily linked to safety management, hazard identification, on-site monitoring, communication, and collaboration. Therefore, in the field of implementing BIM into crane inspection procedures, 3D BIM can be used for the visualization of equipment (crane), supplemented with information on equipment (cranes), allowing real-time observation and analysis of potential conflicts within the model. Furthermore, 4D BIM allows safety analysis of construction dynamics and the planning of protective measures [16].

To improve work safety, it is necessary to implement contemporary digital technologies that enable the collection and analysis of data on crane operations and construction site conditions in real time. Technologies such as AI, IoT, machine learning, and digital twin systems can significantly advance safety and operational performance. For example, findings from Karsley and Oktem [38] underscore the transition toward continuous monitoring of crane operations, which serves as the basis for data-driven inspection approaches.

In that context, BIM is used as an integrated platform that unifies crane data. By combining data from sensors, cameras, and an object identification system, BIM enables continuous updates to the digital construction site view and the identification of potential safety risks. A framework for comprehensive crane safety management includes collecting physical data on a real construction site from people, machines, hoisted objects, and the environment using sensors, cameras, AutoID, UWB, laser scanning, and other advanced technologies. Then, the acquired data is transmitted across wired and wireless networks for processing. After processing, the data is integrated and visualized by a BIM-based environment, forming a virtual simulation of the construction site. In this way, the real construction site relates to its digital counterpart, enabling continuous interaction and feedback while supporting application services (risk dynamic analysis, risk prediction and warning, risk control, etc.). Based on this approach, it is possible to develop systems for risk analysis and early warning that improve safety and control of the crane operation process [39]. While the framework by Zhang and Chen [39] integrates real-time data within a BIM-based environment for safety monitoring and risk analysis, the proposal by Wu et al. [40] shifts the focus to the management and automation of inspection data, without a connection to a structured digital crane model.

Wu et al. [40] stated that no existing solution ensures inspections are conducted or that inspection data is adequately maintained. Although this research and formation of the proposed framework aimed to ensure that crane inspections are performed automatically on schedule, ensuring that inspection records are kept in an immutable, transparent, and traceable manner, its three-layered structure consists of:

1. Data collection layer, which represents input for semi-automated inspection data gathered by IoT technology and UAVs equipped with cameras,
2. Blockchain layer, also known as the core of the proposed framework, that uses: hashing algorithms, peer-to-peer networks, public-private key encryption, consensus mechanisms, and smart contracts,
3. Application layer, which represents the user-facing layer, used by five participants who interact with the system (the owner, contractor, sub-contractor, supervisor, and supplier). The system provides them with three services: triggering safety inspections, recording inspection information, and querying inspection history.

Analyzing the proposed three-layer framework, it is observed that the inspection results are recorded as isolated records without a physical model of the crane. In addition, the proposed framework prevents integration with data on crane components throughout their entire life cycle, as it includes only the exploitation phase.

A review of the literature shows that no existing framework positions crane inspection activities within a structured, model-based digital representation of the crane. For this reason, BIM provides a logical basis for a formation-integrated monitoring system that leverages BIM alongside IoT and sensors to track, manage, and assess the technical condition of cranes throughout their operational lifecycles on construction sites.

## 3. PROPOSED FRAMEWORK FOR BIM-INTEGRATED CRANE INSPECTION

Based on gaps identified in the existing literature, this study proposes a framework for an integrated monitoring system that leverages BIM alongside Industry 4.0 technologies to track, manage, and assess the technical condition of cranes throughout their operational lifecycles on construction sites, rather than treating crane inspection as a periodic, independent activity, as shown in Figure 1. The proposed framework is based on a digital model of the crane built in the BIM environment, enhanced with technical, operational, and safety-related data for each crane component, and can be considered a three-layered system. For establishing 3D-BIM models, Toan et al. [16] suggest using various software, including Navisworks (Autodesk), ArchiCAD (Graphisoft), Solibri Model Checker (Solibri Inc.), and Google SketchUp.

The data acquisition layer contains both preventive and periodic crane inspection inputs and real-time monitoring data, which serve as the system's primary base. These data are then processed and combined within the BIM, which serves as a central hub, linking all information to a structured digital representation of crane components. Based on this synthesis, the system produces outputs (e.g., safety indicators, anomaly detection, and maintenance recommendations) that support informed decision-making in crane safety management.

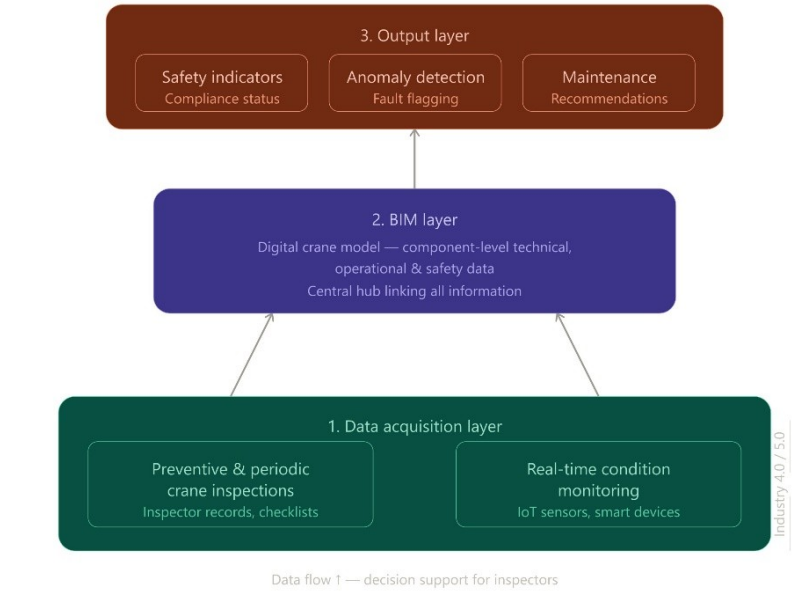


*Fig. 1 Proposed framework for BIM-integrated crane inspection*

The proposed system works through two separate but connected streams of data:

- Preventive and periodic crane inspection inputs – in which results from preventive and periodic inspections are recorded directly into the BIM model, enabling a structured, accessible data source that all relevant stakeholders can reference, and also serves as a starting point for the crane status in the scope of safety;
- Real-time condition monitoring – collecting and continuously uploading data of crane status to BIM model through IoT sensors, smart devices, and other monitoring technologies in real time, enabling continuous following of crane performance, earlier disclosure of developing faults, and a timelier response before minor issues expand into safety risks.

The conceptual framework also proposes the use of modern digital tools during the inspection process to improve efficiency and the certainty of each examination. The combination of data from preventive and periodic crane inspections with continuous, real-time data results in a dynamic, transparent, crane condition check that can always be followed and kept up to date. Therefore, safety management is supported by a more proactive approach, reducing the likelihood of accidents caused by undetected deterioration and improving overall compliance with applicable regulatory requirements. It can be concluded that the proposed framework shifts the crane inspection process towards the broader principles of Industry 4.0 and Industry 5.0, not by fully automating crane inspection, but by providing inspectors with the tools and information they need to work with.

## 4. DISCUSSION

The reviewed literature consistently points to the same underlying problem: crane inspection systems are built around scheduled visits and isolated records, with no structured digital representation of the crane itself as a reference point. Frameworks like the one proposed by Wu et al. [40] have made genuine progress in addressing the enforcement and record-keeping side of the problem, and the real-time monitoring approach demonstrated by Zhang and Chen [39] shows what becomes possible when sensor data is brought into a BIM environment. Neither of these, nor any other framework identified in the literature, offers a complete solution—one that anchors inspection data to the crane's physical structure, tracks its condition over time, and integrates seamlessly with the day-to-day work of inspectors on site. Therefore, the framework proposed in this study treats the crane's BIM model not as a visualization tool but as a living record of its technical condition, continuously updated through periodic inspections and real-time IoT data streams.

The dual-mode data structure — combining preventive and periodic inspection records with continuous real-time monitoring — is one of the framework’s most practically significant features. Since crane damage and cracks are often hidden and hard to detect, the current system updates only when an inspector checks the crane on-site under certain conditions. Therefore, by enabling real-time monitoring with IoT sensors and other Industry 4.0 technologies, the proposed framework ensures the crane's digital representation remains up to date rather than being updated only periodically. For safety managers and contractors, this translates into a fundamentally different decision-making environment — one where maintenance scheduling, operational restrictions, and early interventions can be grounded in live data rather than reports that may already be weeks old.

Furthermore, not just relying on advanced technologies of Industry 4.0, the Industry 5.0 dimension of the framework deserves particular attention – it is overlooked in the fact that an automated, sensor-driven monitoring system does not mean replacing the inspector, but supplying the inspector with a digital model of the crane that shows them the current condition and any anomalies or flags detected since the last inspection. When an inspector arrives on site, the BIM model can already show the crane’s condition trajectory since the last visit, flag any sensor anomalies detected in the interim, and highlight components approaching the end of their service intervals. This is precisely the kind of human-machine collaboration that Industry 5.0 describes [6], and crane inspection is a domain where it applies very naturally.

At the same time, the study acknowledges that the proposed framework has not yet been tested on a real construction crane and remains at the conceptual level. Moving from concept to implementation involves challenges, with the cost dimension perhaps the

biggest. Larger construction firms may be well-positioned to invest in this kind of infrastructure, but smaller companies often are not, and they make up a significant portion of the industry [41]. Without broader incentives — whether from regulators, insurers, or clients — the adoption of such a system is likely to remain uneven. Apart from cost-related challenges, there are technical limitations, as both the network and sensors can fail, drift out of calibration, or be affected by environmental conditions on site.
None of this is a reason to abandon the approach — but it does mean that empirical validation in real construction settings, alongside regulatory alignment that formally recognizes BIM-based outputs as valid inspection documentation, are necessary conditions before the framework can move beyond a proof of concept.

## 5. CONCLUSION

This study identified a structural gap in existing crane inspection frameworks and proposed a BIM-integrated, three-layer conceptual solution that combines periodic inspection data with continuous real-time monitoring, anchored to a component-level digital model of the crane. By aligning with both Industry 4.0 and Industry 5.0 principles, the framework positions BIM not as a visualization tool but as an active, updatable record of crane condition — one that supports rather than replaces the inspector's professional judgment. The immediate next step toward practical realization of this concept is the development of an actual digital crane model in Autodesk software, serving as the operational foundation for the BIM layer, complemented by review and verification tools such as Autodesk Navisworks or Solibri Model Checker as integral components of the framework. Empirical validation in real construction settings, assessment of implementation costs at enterprise scale, and alignment with applicable inspection regulations remain critical for demonstrating whether BIM-integrated crane inspection can deliver measurable improvements in construction safety.

**ACKNOWLEDGEMENT**

This research was supported by the Ministry of Science, Technological Development, and Innovation under Contract Nos. 451-03-34/2026-03/200156 and 451-03-34/2026-03/200108, as well as by the Faculty of Technical Sciences, University of Novi Sad, through the project "Scientific and Artistic Research Work of Researchers in Teaching and Associate Positions at the Faculty of Technical Sciences, University of Novi Sad 2026" (No. 01-3609/1). The research contributes to achieving the ninth Sustainable Development Goal of the UN 2030 Agenda — building resilient infrastructure, promoting inclusive and sustainable industrialization, and fostering innovation.

## REFERENCES

[1] Breque, M., L. De Nul, A. Petridis (2021). Industry 5.0: Towards a sustainable, humancentric and resilient European industry (https://msu.euramet.org/current_calls/documents/EC_Industry5.0.pdf)

[2] Müller, J. (2020). Enabling Technologies for Industry 5.0 (https://www.4bt.us/wp-content/uploads/2021/04/INDUSTRY-5.0.pdf)

[3] Choi, T. M., Kumar, S., Yue, X., & Chan, H. L. (2022). Disruptive technologies and operations management in the Industry 4.0 era and beyond. *Production and operations management*, 31(1), 9-31.

[4] Duggal, A. S., Malik, P. K., Gehlot, A., Singh, R., Gaba, G. S., Masud, M., & Al-Amri, J. F. (2022). A sequential roadmap to Industry 6.0: Exploring future manufacturing trends. *Iet Communications*, 16(5), 521-531.

[5] De Felice F., Travaglioni M, Petrillo A. (2021). Innovation trajectories for a Society 5.0. Data; 6(11):115.

[6] Mourtzis D, Angelopoulos J, Panopoulos N. (2022). Operator 5.0: a survey on enabling technologies and a framework for digital manufacturing based on extended reality. *J Mach Eng*; 22(1):43–69.

[7] Leng, J., Sha, W., Wang, B., Zheng, P., Zhuang, C., Liu, Q., ... & Wang, L. (2022). Industry 5.0: Prospect and retrospect. *Journal of Manufacturing Systems*, 65, 279-295.

[8] Papetti, A., Gregori, F., Pandolfi, M., Peruzzini, M., & Germani, M. (2020). A method to improve workers' well-being toward human-centered connected factories. *Journal of Computational Design and Engineering*, *7*(5), 630-643.

[9] Chandran, J. C., & Selvaraj, K. (2025). A study on the role of industry 4.0 and 5.0 in enhancing health and safety of construction workers. *Cutting-edge research in commerce and management: a technology perspective*, 76.

[10] Mučenski, Lj. V. (2018). Theoretical foundations of occupational health and safety in construction. Faculty of Technical Sciences, Novi Sad.

[11] Nizam R.S., Zhang C., Tian L. (2018). A BIM-based tool for assessing embodied energy for buildings, *Build. Energy Efficiency* 170 1–14, https://doi.org/10.1016/J.ENBUILD.2018.03.067.

[12] Ibrahim M., Abdulkareem A. (2013). A knowledge-based BIM system for building maintenance, Automation in construction, 29, 173-182

[13] Zhang, Z., Hu Z. (2011). BIM-and 4 D-based integrated solutions of analysis and management for conflicts and structural safety problems during construction: 1. Principles and methodologies, *Automation in construction*, 20 (2): 155-166

[14] Bilal S. (2009). Building information modeling framework: A research and delivery foundation for industry stakeholders, Automation in construction, 18(3): 357-375

[15] Sawhney, A., Riley, M., & Irizarry, J. (2020). Construction 4.0: an innovation platform for the built environment. *Routledge*.

[16] Toan, N. Q., Dung, N. T. T., & Hanh, N. T. M. (2021). 3D-BIM and 4D-BIM models in construction safety management. In *E3S Web of Conferences* (Vol. 263, p. 02005). EDP Sciences.

[17] Cepa, J. J., Pavon, R. M., Alberti, M. G., Ciccone, A., & Asprone, D. (2023). A review on the implementation of the BIM methodology in the operation maintenance and transport infrastructure. *Applied Sciences*, 13(5), 3176.

[18] He, W., Lin, Z., Li, W., Wong, C. J., Kong, D., & Loh, W. E. (2025). The comprehensive safety assessment method for complex construction crane accidents based on scenario analysis–A case study of crane accidents. Computers & Industrial Engineering, 199, 110716.

[19] Im, S. & Park, D. (2020). Crane Safety Standards: Problem Analysis and Safety Assurance Planning. *Safety Science*, 127(July), Article 104686. https://doi.org/10.1016/j.ssci.2020.104686

[20] Alveriuse C, A. Kadir Z, A. Malambut N. (2023). Hazard Identification, Risk Assessment and Risk Control (Hirarc) for Lifting Operation at Condominium Construction in Sabah. *Progress in Engineering Application and Technology*; 4: 107–120.

[21] Wang J, Guo F, Song Y, et al. (2022). Safety Risk Assessment of Prefabricated Buildings Hoisting Construction: Based on IHFACS-ISAM-BN. *Buildings*; 12: 811.

[22] Yılmaz F, Ozcan M. (2019). A Risk Analysis and Ranking Application for Lifting Vehicles Used in Construction Sites with Integrated AHP and Fine-Kinney Approach. *Adv Sci Technol Res J* 2019; 13: 152–161.

[23] IIF Home: U.S. Bureau of Labor Statistics. n.d. Accessed April 3, 2026. https://www.bls.gov/iif/home.htm.

[24] Amilia N. (2023). Application of Construction Safety Analysis (CSA) Method to assess occupational risk in lifting and transporting activities using freestanding tower crane.

Doctoral Dissertation, Universitas Islam Indonesia, https://dspace.uii.ac.id/handle/123456789/47330

[25] Herrera-P´erez, Virginia, Francisco Salguero-Caparros, ´ María del Carmen Pardo-Ferreira, and Juan Carlos Rubio-Romero. (2023). "Key Factors in Crane-Related Occupational Accidents in the Spanish Construction Industry (2012–2021)." *International Journal of Environmental Research and Public Health* 20 (22): 7080. https://doi.org/10.3390/ijerph20227080 .

[26] Health and Safety Executive (1998). Lifting Operations and Lifting Equipment Regulations 1998 (LOLER), https://www.legislation.gov.uk/uksi/1998/2307/contents/made

[27] Mučenski, V., Peško, I., & Kolaković, S. (2020). Application of BIM methodology for improving occupational safety education in construction. In *Proceedings of the XXVI Conference "Trends in the Development"*, University of Novi Sad.

[28] Teizer, J., & Melzner, J. (2018). BIM for construction safety and health. In *Building Information Modeling: Technology Foundations and Industry Practice* (pp. 349-365). Cham: Springer International Publishing.

[29] Martínez-Aires, M. D., López-Alonso, M., & Martínez-Rojas, M. (2018). Building information modeling and safety management: A systematic review. *Safety science*, 101, 11-18.

[30] Forcina A., Silvestri L., De Felice F., Falcone D. (2024). Exploring industry 4.0 technologies to improve manufacturing enterprise safety management: A TOPSIS-based decision support system and real case study, *Saf. Sci*. 169 106351.

[31] Wang B. (2021). Safety intelligence as an essential perspective for safety management in the era of safety 4.0: From a theoretical to a practical framework, *Process Safety Environ. Protect*. 148 189–199.

[32] Qian Y., Vaddiraju S., Khan F. (2023). Safety education 4.0–a critical review and a response to the process industry 4.0 need in chemical engineering curriculum: safety, *Science* 161 106069.

[33] Musarat M.A., Alaloul W.S., Irfan M., Sreenivasan P., Rabbani M.B.A. (2022). Health and safety improvement through industrial revolution 4.0: Malaysian construction industry case, Sustainability 15 (1) 201.

[34] Romero D., Mattsson S., Fast-Berglund Å., Wuest T., Gorecky D., Stahre J. (2018). Digitalizing occupational health, safety and productivity for the operator 4.0, in: *Advances in Production Management Systems. Smart Manufacturing for Industry 4.0: IFIP WG 5.7 International Conference*, *APMS* 2018, Seoul, Korea, August 26-30, Proceedings, Part II, Springer International Publishing, pp. 473–481.

[35] Haleem, A., Javaid, M., & Singh, R. P. (2025). Encouraging Safety 4.0 to enhance industrial culture: An extensive study of its technologies, roles, and challenges. *Green Technologies and Sustainability*, 3(3), 100158.

[36] Azhar, S., Behringer, A., Sattineni, A., & Mqsood, T. (2012). BIM for facilitating construction safety planning and management at jobsites. In *Proceedings of the CIB-W099 international conference: modelling and building safety*, Singapore (pp. 10-11).

[37] Sulankivi, K., Mäkelä, T. and Kiviniemi, M. (2009). BIM-based site layout and safety planning. *Proceedings of the First International Conference on Improving Construction and Use through Integrated Design Solutions, CIB IDS 2009*, 10-12 June. Espoo,Finland.

[38] Karslı, E., & Oktem H. (2024). Advanced Crane Systems: The Impact of Modern Technologies on Performance and Safety. In *F. Zerrin Saltan, H. Arıkan & Y. Uzun (Eds.), Current Studies in Basic Sciences, Engineering and Technology 2024* (pp. 113-129). ISRES Publishing.

[39] Zhang, Y., & Chen, K. (2023). Digital technologies for enhancing crane safety in construction: a combined quantitative and qualitative analysis. *Journal of Civil Engineering and Management*, 29(7), 604-620.

[40] Wu, H., Zhong, B., Li, H., Chi, H. L., & Wang, Y. (2022). On-site safety inspection of tower cranes: A blockchain-enabled conceptual framework. *Safety Science*, 153, 105815.

[41] Perera, C., Udagedara, S., & Attanayake, U. (2020). Challenges in adopting Industry 4.0 technologies in construction SMEs. *Engineering, Construction and Architectural Management*, 28(4), 1209–1229.

https://doi.org/10.24867/INDIS-2026-EN-149



# VALIDATION OF A PRELIMINARY RISK ASSESSMENT MODEL FOR WWTP CONSTRUCTION AND PROSPECTS FOR DIGITAL OPERATIONALIZATION

*Jovana Topalić[1], Danijela Gračanin[2], Danijela Ćirić Lalić[3], Luka Vidaković[4], Marijana Dukić Mijatović[5], Andrea Ivanišević[6]*

***Summary:***

Wastewater treatment plants (WWTPs) are complex infrastructure projects whose construction processes are exposed to interrelated risks that are rarely captured by conventional frameworks. This paper presents the structure and validation of a preliminary risk assessment model developed for the WWTP construction process. The model encompasses 37 risks in six groups: legal, financial and economic, logistical, ecological, managerial, and design, developed through a two-round Delphi method involving 33 domain experts. Validation of the model on six real WWTP projects in Serbia and Bosnia and Herzegovina, involving 10 practitioners across designer, contractor, and investor roles, confirmed its practicality and applicability. The paper discusses the model's potential for digital operationalization as a cloud-based decision-support platform.

***Keywords:*** *validation, risk assessment, wastewater treatment plant, construction, digital platform*

# VALIDACIJA MODELA PRELIMINARNE PROCJENE RIZIKA ZA PROCES GRAĐENJA POSTROJENJA ZA PREČIŠĆAVANJE OTPADNIH VODA I POTENCIJAL ZA DIGITALIZACIJU

***Rezime:***

Postrojenja za prečišćavanje otpadnih voda (PPOV) predstavljaju složene infrastrukturne projekte čiji su procesi građenja izloženi međusobno povezanim rizicima koji se rijetko obuhvataju konvencionalnim okvirima. U radu je predstavljena struktura i validacija modela preliminarne procjene rizika razvijenog za proces građenja PPOV-a. Model obuhvata 37 rizika u šest grupa: pravnih, finansijskih i ekonomskih, logističkih, ekoloških, menadžerskih i projektantskih, razvijenih primjenom dvostrukog kruga Delfi metode uz 33 eksperta. Validacija na šest stvarnih projekata u Srbiji i Bosni i Hercegovini, uz učešće deset ispitanika, potvrdila je praktičnost i primjenjivost modela. Rad razmatra potencijal digitalizacije modela u cloud platformu za podršku procesima odlučivanja.

***Ključne reči:*** *validacija, procjena rizika, postrojenje za prečišćavanje otpadnih voda, građenje, digitalna platforma*

[1] Research Associate, Faculty of Technical Sciences, University of Novi Sad, Serbia, jovanatopalic90@uns.ac.rs, ORCID 0000-0001-7854-3257
[2] Full Prof., Faculty of Technical Sciences, University of Novi Sad, Serbia, gracanin@uns.ac.rs, ORCID 0000-0002-2150-4852
[3] Assistant Prof., Faculty of Technical Sciences, University of Novi Sad, Serbia, danijela.ciric@uns.ac.rs, ORCID 0000-0002-4834-6487
[4]Labsoft Novi Sad Serbia, luka.vidakovic@labsoft.ai, ORCID 0009-0003-6591-2254
[5] Full Prof., Faculty of Technical Sciences, University of Novi Sad, Serbia, marijana.mijatovic@uns.ac.rs, ORCID 0000-0003-1327-0889
[6] Full Prof., Faculty of Technical Sciences, University of Novi Sad, Serbia, andreai@uns.ac.rs, ORCID 0000-0003-3342-7257

## 1. INTRODUCTION

Every community produces both liquid and solid waste as well as air emissions. The issue of protecting water from pollution is directly dependent on industrial and technological development, which results in the creation of legislative regulations in this area. The creation and implementation of laws to protect water from pollution have a significant impact on the proper and efficient functioning of water protection [1]. Nowadays, many engineers are involved in planning, designing, and constructing wastewater treatment plants. The construction of a wastewater treatment plant is a complex and extensive project, which sometimes takes several years. Plants represent multi-million-dollar investments due to their complexity, equipment, and the large number of people involved across all parts of the project [2]. The construction of wastewater treatment plants (WWTPs) connects environmental engineering, public infrastructure investment, and multi-stakeholder governance. Delivering a functional WWTP requires integrating structural, mechanical, electrical, technological, and environmental engineering within a regulatory framework that emphasizes local spatial planning, national water law, environmental impact assessment, and European environmental standards. Despite this complexity, the risk management literature specific to WWTP construction remains focused mainly on operational and technological risks [3-7] such as effluent quality, treatment process efficiency, and energy consumption, while the construction-phase risks that govern whether a project is delivered on time, within budget, and fully functional are rarely identified, structured, or quantified.

European Union has legal regulations to ensure the effective treatment of urban wastewater before discharge into the environment. All urban wastewater from agglomerations of 1 000 PE and above should be collected in collecting systems [8]. Significant investments will be necessary to implement the new requirements introduced by [8]. Recognizing the burden this places on Member States with many small agglomerations (1,000–2,000 PE), the Directive allows extended compliance deadlines for such cases within the first national implementation program.

The regulatory framework governing WWTP construction in Serbia operates at three levels: EU-level directives transposed through the accession process; national legislation, primarily the Water Law [9] and the Environmental Protection Law [10]; and local spatial planning instruments.

For countries such as Serbia, which must align national legislation with [8] as part of the accession process, the practical implication is a substantially enlarged construction pipeline, with more stringent technical requirements and shorter planning horizons than the earlier directive. This investment pressure makes the early-stage identification and assessment of construction risks not merely good practice, but a prerequisite for viable project planning. According to [11], risk exposure is highest and the cost of effective mitigation lowest during the early planning and design phases of infrastructure projects. A structured preliminary risk assessment model applied at project initiation can prevent the delays, cost overruns, and post-completion non-functionality that have characterized a significant share of WWTP projects in the region [12].

While the model structure was established in [12], this paper presents its first multi-role empirical validation and develops the rationale for its digital operationalization.

## 2. THE STRUCTURE OF THE RISK ASSESSMENT MODEL

The preliminary risk assessment model was developed in [12], combining a systematic literature review, legal and regulatory analysis, and expert consensus via a two-round Delphi process involving 33 domain experts from Serbia and Bosnia and Herzegovina.

The model encompasses 37 construction-relevant risks, structured into six thematic groups. Each risk is assigned a weight coefficient derived from the Delphi consensus, and the coefficients are normalized so that the sum of all individual risk weights equals 100 credits. A total project score below 50 credits indicates that construction-phase risks have been adequately identified and managed.
Tab 1 presents the complete risk inventory with weight coefficients, as established in [12].

*Tab 1: Preliminary risk assessment model: complete risk inventory with weight coefficients*

| Code | Risk Description | Weight |
|---|---|---|
| | *LEGAL RISKS — Max. credits: 16.1* | |
| 1.1 | Frequent changes and modifications of laws and sub-legal acts | 1.1 |
| 1.2 | Misalignment between foreign financier regulations and host country regulations | 1.2 |
| 1.3 | Lack of knowledge of current legal and sub-legal acts | 1.3 |
| 1.4 | Delays in resolving contractual disputes between the investor and the designer during the design phase | 1.1 |
| 1.5 | The untimely issuance of conditions and permits by public enterprises for design purposes | 1.2 |
| 1.6 | Inadequate connection conditions for linking the facility to the infrastructure system | 1.2 |
| 1.7 | Inadequate assessment of the impact of public procurement on the project schedule | 1.1 |
| 1.8 | Inadequate criteria for the selection of the works supplier | 1.3 |
| 1.9 | Inadequate criteria for the selection of the plant designer | 1.4 |
| 1.10 | Inadequate criteria for the selection of the contractor | 1.4 |
| 1.11 | Inadequate consideration of the optimal contracting method for project realization | 1.2 |
| 1.12 | Inadequate municipal spatial plan (regarding location, size, and dimensions) | 1.4 |
| 1.13 | Problems in obtaining the building permit | 1.1 |
| | *FINANCIAL AND ECONOMIC RISKS — Max. credits: 16.0* | |
| 2.1 | Inadequate budget (insufficient funds) for the construction of modern facilities | 3.7 |
| 2.2 | Uncontrolled cash flow for individual project phases | 3.3 |
| 2.3 | Inflation and unexpected changes in prices | 3.0 |

| Code | Risk Description | Weight |
|---|---|---|
| 2.4 | Incomplete or incorrect estimates of financial benefits | 3.1 |
| 2.5 | Incomplete or incorrect estimates of economic benefits | 3.0 |
| | *LOGISTICAL RISKS — Max. credits: 17.1* | |
| 3.1 | Lack of communication with public utility companies regarding changes to initial design parameters | 8.2 |
| 3.2 | Shortage of qualified designers for WWTP projects | 8.9 |
| | *ECOLOGICAL RISKS — Max. credits: 18.3* | |
| 4.1 | WWTP location is inadequate from the perspective of environmental protection (ecosystem disruption) | 9.2 |
| 4.2 | WWTP location is inadequate regarding proximity and position relative to populated areas | 9.1 |
| | *MANAGERIAL RISKS — Max. credits: 16.3* | |
| 5.1 | Shortage of qualified staff employed in public utility companies | 2.4 |
| 5.2 | Poor communication among project participants (designers) | 2.4 |
| 5.3 | Insufficient competence of the investor in the design phase in providing information to the designer | 2.1 |
| 5.4 | Slow investor decisions are causing delays in the design process | 2.1 |
| 5.5 | Inadequate investment team structure | 2.4 |
| 5.6 | Absence of a project manager on behalf of the investor | 2.4 |
| 5.7 | Unrealistic project scheduling by the investor | 2.5 |
| | *DESIGN RISKS — Max. credits: 16.3* | |
| 6.1 | Insufficient data on wastewater quantities | 2.2 |
| 6.2 | Lack of data on the receiving water body (flow, water level, water quality) | 2.0 |
| 6.3 | Incorrect demographic projection | 2.2 |
| 6.4 | Insufficient data on the existing sewerage system | 2.0 |
| 6.5 | Uncoordinated work among different types of designers | 2.0 |
| 6.6 | Designers' unfamiliarity with the planned/desired equipment | 2.1 |
| 6.7 | Excessive distance of settlements connected to the treatment plant | 1.8 |
| 6.8 | Change in wastewater treatment technology | 2.1 |

| Code | Risk Description | Weight |
|---|---|---|
| | | |

*Note: Individual weight coefficients are rounded to one decimal place; the sum of individual weights within a group may therefore differ from the stated group maximum by ±0.1 credits.*

The ecological risk group carries the highest maximum credit score (18.3), reflecting expert consensus that site-specific environmental conditions, particularly the adequacy of WWTP location with respect to ecosystem protection and proximity to populated areas, represent the most consequential and least routinely managed category of construction-phase risk. Logistical risks rank second (17.1), underscoring the critical importance of communication with public utility companies and the availability of qualified WWTP designers. Design and managerial risks carry equal maximum credits (16.3 each), reflecting their functional interdependence. Legal and financial risks, while individually significant, ranked lowest in the expert consensus, consistent with the observation that these dimensions are typically regularized through contractual mechanisms and regulatory compliance at the outset of the investment process, reducing residual uncertainty relative to technical and site-specific risk categories.

## 3. MODEL VALIDATION

### 3.1. WHY VALIDATION IS NECESSARY: ARGUMENTS FROM THE LITERATURE

The scientific literature on construction risk management consistently identifies the gap between risk model development and empirical validation as a critical methodological weakness. In [13], guidelines for Delphi-based research in construction engineering and management emphasize that the rigor of the elicitation procedure alone does not guarantee external validity. Models derived from expert judgment, therefore, require independent empirical testing before their outputs can be interpreted as reliable indicators of project performance. Also, [14] notes that generic construction risk frameworks, however methodologically sound, tend to lose discriminatory power when applied to infrastructure types with specific risk profiles: validation on domain-specific project samples is the mechanism by which this specificity is confirmed or challenged. In [15], the context of BIM-based digital risk platforms for tunnel construction argues that the credibility of any risk management tool with regulatory or investment stakeholders depends fundamentally on empirical performance data; theoretical derivation alone is insufficient for institutional adoption.

In the specific context of WWTP construction, validation serves an additional function: it tests whether a model built on expert knowledge captures the risk realities of actual projects in a region with limited documentation of completed works and institutional fragmentation among investor, designer, and contractor roles. In [16], it is emphasized that construction risk perceptions differ substantially across stakeholder roles: investors, designers, and contractors operate under different contractual exposures and information environments, and that a practically useful risk model must be interpretable and consistent for all three groups. Validation on multi-role project samples directly tests this cross-role consistency.

### 3.2. VALIDATION METHODOLOGY

A dedicated validation questionnaire was developed for each of the 37 model risks, providing for each: a concise risk description; the applicable weight coefficient; one or

more operationalized questions through which the presence or degree of the risk on the evaluated project could be assessed; and a binary scoring rule (0 = risk condition absent or adequately managed; 1 = risk condition present and insufficiently managed). The weighted credit score for each risk equals the product of the binary response and the weight coefficient; the total project score is the sum across all 37 risks, with a maximum of 100 credits. The threshold of 50 credits represents the midpoint of the scoring range and was adopted as the classification boundary: projects scoring below 50 credits are classified as having adequately managed their construction-phase risk exposure. A parallel structured interview instrument collected qualitative assessments of the model's clarity, comprehensiveness, ease of use, and practical relevance.

Six WWTP projects were purposively selected as examples of good practice and were included in the validation process. All of them are operational or under active construction in Serbia or Bosnia and Herzegovina. They were built or were under construction during 2015-2022, with capacities up to 150,000 PE and estimated construction costs up to €7,000,000. This selection strategy is designed to test specificity rather than sensitivity; the capacity to identify high-risk projects will require a complementary sample of failed or delayed projects in future work. Ten practitioners participated: designers, contractors, and investor or local government representatives, all with direct project involvement. For three projects (WWTP 1, 3, and 5), assessments were obtained from multiple practitioners, enabling an inter-rater reliability analysis. The purposive selection strategy was designed to validate the model's specificity, its ability to classify well-managed projects as low risk correctly. Testing the complementary dimension (sensitivity: the capacity to identify high-risk projects) requires a sample of failed or significantly delayed projects. It is acknowledged as a direction for future research.

## 3.3. VALIDATION RESULTS AND DISCUSSION

Tab 2 presents the validation results by project and participant.

*Tab 2: Validation results: total weighted risk scores per project and practitioner*

| WWTP | Capacity | Est. Value | Practitioner 1 | Practitioner 2 | Practitioner 3 |
|---|---|---|---|---|---|
| WWTP 1 | ≤150,000 PE | ≤€7M | 34.65 (designer) | 51.95 (investor) | 17.55 (contractor) |
| WWTP 2 | ≤150,000 PE | ≤€7M | 40.60 | — | — |
| WWTP 3 | ≤150,000 PE | ≤€7M | 31.20 | 31.45 | — |
| WWTP 4 | ≤150,000 PE | ≤€7M | 16.75 | — | — |
| WWTP 5 | ≤150,000 PE | ≤€7M | 26.20 | 27.45 | — |
| WWTP 6 | ≤150,000 PE | ≤€7M | 25.70 | — | — |

*Note: Estimated construction values are project cost estimates at the time of construction (for projects completed in the period 2015–2022) and do not reflect current market prices.*

Nine out of ten assessments (90%) produced total scores below the 50-credit threshold, confirming that the selected good-practice projects had adequately managed

construction-phase risk exposure, consistent with their operational or on-schedule status. If a project has fewer than 50 credits, it is considered that the risks have been identified and analyzed on time [12]. High inter-rater consistency was observed for multi-participant projects: WWTP 3 yielded 31.20 and 31.45; WWTP 5 yielded 26.20 and 27.45. This near-identical scoring by different practitioners on the same project constitutes preliminary evidence of reproducibility and internal consistency.

The results for WWTP 1 suggest a role-specific exposure pattern consistent with the theoretical literature [16]: the investor representative had direct responsibility for regulatory compliance, financial management, and logistical coordination, all of which activated a broader set of risks than were visible to the contractor (17.55) or designer (34.65). This divergence illustrates the model's sensitivity to the full scope of investment-phase risk and suggests its potential as a coordination instrument: systematically comparing scores across stakeholder roles could surface risk perception gaps before they materialize as project disputes. This interpretation remains a hypothesis requiring confirmation through larger multi-role samples.

The qualitative interview component confirmed a near-unanimous positive assessment: all ten participants rated the questionnaire as clear, comprehensive, and relevant; all stated they would have found it useful at project initiation. The ecological and logistical groups, which were weighted most heavily in the model, were independently identified by practitioners as the categories most likely to cause delays and cost escalation in WWTP construction, providing convergent validity for the expert-derived weight coefficients.

The principal limitations are: (i) the purposive sample validates specificity but not sensitivity; (ii) the sample is geographically bounded to two countries and all projects are below 150,000 PE; (iii) binary scoring does not capture gradations of risk severity within individual items. These constraints point directly toward the research directions described in the following section.

## 4. TOWARDS DIGITAL OPERATIONALIZATION: WHY IT MATTERS

The validated model demonstrates that structured, expert-derived risk assessment yields reliable, reproducible outputs for WWTP construction projects. This empirical confirmation is the necessary precondition for a further step: the transition from a paper-based scoring instrument to a digitally operationalized decision-support platform. The argument for this transition is grounded in three converging rationales, one methodological, one institutional, and one regulatory.

Methodologically, the current model's boundary condition is the absence of a project case database. The validated 37-risk framework and normalized scoring algorithm constitute a deterministic, transparent, and auditable core. Still, they cannot contextualize a project's score against comparable historical projects, propose risk-response measures calibrated to specific site or regulatory conditions, or evolve in response to new patterns in construction risk. In [15], it is demonstrated that integrating structured risk models with digital data platforms enables progressive enrichment through machine learning and pattern recognition across accumulated project data, without compromising the reliability of the base scoring algorithm. A cloud-based WWTP risk platform would, over time, build precisely this case database, enabling risk benchmarking across projects of varying scales, locations, and regulatory contexts.

Institutionally, the validation results directly motivate the development of digital coordination functionality. The WWTP 1 case, with investor, designer, and contractor scores ranging from 17.55 to 51.95 credits for the same project, illustrates that different project stakeholders operate with substantially different risk-awareness profiles. A shared digital platform through which all parties enter and compare their assessments

transforms the model from an individual scoring exercise into a structured, pre-contractual dialogue mechanism.

The proposed platform implements a layered, serverless architecture on Amazon Web Services infrastructure, organized into five functional units shown in Figure 1. The client application layer communicates with the system through API Gateway, while authentication and authorization are implemented through Amazon Cognito, with users separated by tenant and role (investor, designer, contractor). The central domain services, implemented as stateless functions (AWS Lambda), communicate exclusively via an event bus (Amazon EventBridge), achieving loose coupling between components and enabling independent development of modules for risk assessment, multi-role coordination, and document generation. The risk assessment module implements the scoring algorithm described in the previous chapter as a separate, versioned software component, ensuring traceability between assessment results and the exact version of the applied model. The artificial intelligence layer is implemented through an abstract interface (AI Gateway) that enables independence from any specific language model provider, with Amazon Bedrock as the primary implementation and a Retrieval-Augmented Generation mechanism operating over a corpus of applicable regulations. Traceability and compliance with the requirements of the ISO/IEC 27001 and ISO 31000 standards are ensured through immutable logging of every transaction (Amazon Aurora PostgreSQL) and continuous monitoring of data access and modifications (AWS CloudTrail, AWS Config).

In [17], it is demonstrated that integrating risk information with digital project data environments improves stakeholder accountability and coordination, reducing the information asymmetries that generate disputes. For regulatory bodies overseeing multiple concurrent WWTP investments, aggregated platform data would further support portfolio-level prioritization, a capability entirely beyond the reach of a paper questionnaire.

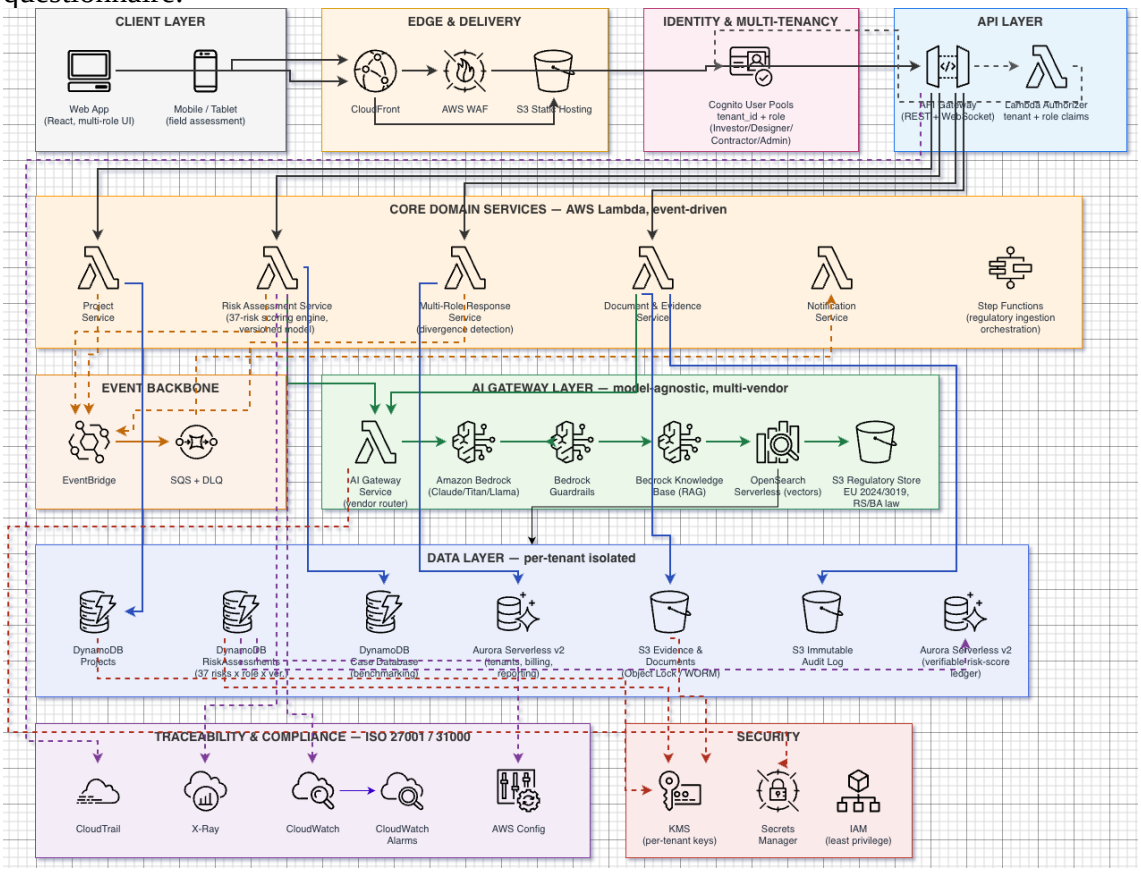


*Fig. 1 The architecture of a digital platform*

Regulatorily [8] introduces enhanced monitoring obligations, mandatory data transparency requirements, and risk-based approaches to wastewater collection and treatment planning. These provisions imply a digital data infrastructure for WWTP investment management that currently does not exist in most municipalities in the Western Balkans. A cloud-based risk platform aligned with the model validated in this study would directly support compliance with these emerging requirements, providing structured, auditable risk records for planning permits, environmental impact assessments, and financing applications. The investment pipeline implied by [8]-more plants, higher standards, and tighter deadlines-makes the case for digitized, scalable risk assessment tools compelling at the system level, not only at the level of individual projects.

## 5. CONCLUSIONS

The following conclusions are drawn from this study:

- The presented model provides a complete, validated inventory of 37 WWTP-specific construction risks across six thematic groups, with quantitative weight coefficients derived from a 33-expert Delphi consensus. Ecological and logistical risks carry the highest weights, reflecting expert consensus that site conditions and utility infrastructure prerequisites are the most consequential and most frequently underestimated categories.
- Empirical validation on six real WWTP projects confirmed the model's specificity: 90% of assessments produced scores below the 50-credit threshold, with high inter-rater consistency across comparable practitioner roles. All ten validation participants assessed the model as clear, comprehensive, and practically useful for early-stage project planning.
- Role-specific score divergence (WWTP 1: 17.55–51.95 credits) suggests the model's responsiveness to stakeholder-specific risk exposure profiles and its potential as a pre-contractual coordination instrument, pending confirmation through larger multi-role samples.
- The validated scoring algorithm provides the deterministic foundation for digital operationalization as a cloud-based platform. Digitalization would enable progressive case-database enrichment, machine-learning-based risk benchmarking, multi-stakeholder coordination, and alignment with the monitoring and data-transparency obligations introduced by Directive 2024/3019, thereby advancing the model from a validated research instrument to an operational infrastructure-planning tool.

**ACKNOWLEDGEMENT**

This research has been supported by the Provincial Secretariat for Higher Education and Scientific Research Activity of the Autonomous Province of Vojvodina, during the project, "Application of Machine Learning and Data Analytics in Risk Assessment for the Optimization of Planning and Design of Wastewater Treatment Plants" number 003829785 2025 09418 003 000 000 001.

## 6. REFERENCES

[1] Ministry of Environmental Protection of Serbia "Treatment of communal wastewater, technological view and critical view of actual objects, giving the optimal proposal for wastewater treatment plants, with aspects for protection of water, air and land of settlements in Serbia", Ministry of Environmental Protection of Serbia, Belgrade, Serbia, 1999. (in Serbian)

[2] Topalić Marković J., Mučenski V., Savić D., Velkovski T., Peško I., Tomaš L. (2021). Risk Assessment Model for Planning and Design Processes of Wastewater Treatment Plants. Periodica Polytechnica Civil Engineering, 65(1), 181–190. https://doi.org/10.3311/PPci.16740

[3] Belia, E., Neumann, M. B., Benedetti, L., Johnson, B., Murthy, S., Weijers, S., Vanrolleghem, P. A. "Uncertainty in Wastewater Treatment Design and Operation", [e-book] IWA Publishing, London, UK, Rep. 21, 2020.

[4] Van der Merwe-Botha, M., Manus, L. "Wastewater Risk Abatement Plan, W2RAP Template", [pdf] Water Research Commission, Pretoria, South Africa, 2011. Available at: http://www.wrc.org.za/wp-content/ uploads/mdocs/TT%20624.pdf

[5] Van der Merwe-Botha, M., Manus, L. "Wastewater Risk Abatement Plan A W2RAP GUIDELINE To plan and manage towards safe and complying municipal wastewater collection and treatment in South Africa", [pdf] Water Group Holdings (Pty) Ltd, Department of Water Affairs, Pretoria, South Africa, Rep. TT 489/11, 2011. Available at: http://www.wrc.org.za/wp-content/uploads/mdocs/TT%20489-11.pdf

[6] Belia. E., Johnson. B. "Uncertainty Evaluations in Model-Based WRRF Design for High Level Nutrient Removal", [pdf] Water Environment Research Foundation, Alexandria, VA, USA, Rep. NUTR1R06q, 2013. Available at: https://modeleau.fsg.ulaval.ca/ fileadmin/modeleau/documents/Publications/pvr1116.pdf

[7] Grady, Jr., C. P. L., Daigger, G. T., Love, N. G., Filipe, C. D. M. "Biological Wastewater Treatment", 3rd ed., IWA Publishing, London, UK, 2011.

[8] European Parliament and Council. (2024). Directive (EU) 2024/3019 of the European Parliament and of the Council of 27 November 2024 concerning urban wastewater treatment (recast). Official Journal of the European Union, OJ L 2024/3019, 12.12.2024.

[9] Republic of Serbia. (2010, amended 2016). Zakon o vodama (Water Law). Official Gazette of the Republic of Serbia, No. 30/2010, 93/2012, 101/2016.

[10] Republic of Serbia. (2004, amended 2018). Zakon o zaštiti životne sredine (Law on Environmental Protection). Official Gazette of the Republic of Serbia, No. 135/2004, 36/2009, 72/2009, 43/2011, 14/2016, 76/2018, 95/2018.

[11] PMI – Project Management Institute. (2021). A Guide to the Project Management Body of Knowledge (PMBOK® Guide), 7th ed. PMI, Newtown Square, PA.

[12] Topalić Marković J. (2022). Preliminary Risk Assessment Model for the Wastewater Treatment Plant Construction Process. Doctoral dissertation, Faculty of Technical Sciences, University of Novi Sad, Serbia.

[13] Hallowell M.R., Gambatese J.A. (2010). Qualitative research: application of the Delphi method to CEM research. Journal of Construction Engineering and Management, 136(1), 99–107. https://doi.org/10.1061/(ASCE)CO.1943-7862.0000137

[14] Renault B.Y., Agumba J.N. (2016). Risk management in the construction industry: a new literature review. MATEC Web of Conferences, 66, 00008. https://doi.org/10.1051/matecconf/20166600008

[15] Liu N., Guo D., Song Z., Zhong S., Hu R. (2023). BIM-based digital platform and risk management system for mountain tunnel construction. Scientific Reports, 13, 7504. https://doi.org/10.1038/s41598-023-34525-w

[16] Cerić A., Marić T. (2011). Determining priorities for managing risk on construction projects. Građevinar, 63(3), 265–271. (in Croatian)

[17] Yasser M., Rashid I.A., Nagy A.M., Elbehairy H.S. (2022). Integrated model for BIM and risk data in construction projects. *Engineering Research Express*, 4(4), 045044. https://doi.org/10.1088/2631-8695/acae1e

https://doi.org/10.24867/INDIS-2026-EN-159



# POSSIBILISTIC LINEAR REGRESSION FOR INTERVAL-BASED PRELIMINARY ESTIMATION OF URBAN ROAD COST AND DURATION

*Milan Jovin[1], Tatjana Grbić[2], Igor Peško[3], Andrija Rašeta[4]*

***Summary:***

Early-stage cost and duration estimation of urban-road projects is performed under sparse information. For Novi Sad, Peško et al. developed ANN and SVM point predictors based on bill-of-quantities inputs. This paper applies Tanaka-type possibilistic linear regression to 35 Novi Sad projects using functional parameters available before a bill of quantities exists. The cost model is fitted on log-cost and back-transformed to Serbian dinars; OLS serves as the centre baseline. Leave-one-out validation shows OLS as the stronger centre predictor, while Tanaka contributes an h-level possibility band at h = 0.5 that covers 85.7% of held-out observations but remains wide. Offered duration is reported as an exploratory secondary result. The contribution is interval information for an earlier estimation phase, not improved point accuracy.

*Keywords: preliminary cost estimation, urban road construction, possibilistic linear regression, fuzzy regression, functional parameters, uncertainty*

# POSIBILISTIČKA LINEARNA REGRESIJA ZA INTERVALNU PROCENU TROŠKOVA I TRAJANJA IZGRADNJE GRADSKIH SAOBRAĆAJNICA

***Rezime:***

Preliminarna procena troškova i trajanja izgradnje gradskih saobraćajnica sprovodi se u uslovima ograničenih informacija. Za Novi Sad, Peško i saradnici razvili su ANN i SVM modele tačkaste procene na osnovu predmera i predračuna. Ovaj rad primenjuje mogućnosnu linearnu regresiju Tanaka tipa na 35 novosadskih projekata, koristeći funkcionalne parametre dostupne pre izrade predmera. Model troškova dobijen je na logaritmu troška i transformisan u dinare; OLS služi kao centralna referenca. OLS daje bolju centralnu procenu, dok Tanaka doprinosi mogućnosnim pojasom na h = 0,5 koji pokriva 85,7% opservacija, ali je širok. Doprinos rada je intervalna informacija u ranijoj fazi procene, ne veća tačnost tačkaste procene.

*Ključne reči: preliminarna procena troškova, izgradnja gradskih saobraćajnica, mogućnosna linearna regresija, fazi regresija, funkcionalni parametri, neizvesnost*

[1] Teaching Assistant, University of Novi Sad, Faculty of Technical Sciences, Department of Civil Engineering and Geodesy, Novi Sad, Serbia, mjovin@uns.ac.rs, ORCID 0009-0004-4422-4230.
[2] Full Professor, University of Novi Sad, Faculty of Technical Sciences, Department of Fundamentals Sciences, Novi Sad, Serbia, tatjana@uns.ac.rs, ORCID 0000-0002-4236-7164.
[3] Full Professor, University of Novi Sad, Faculty of Technical Sciences, Department of Civil Engineering and Geodesy, Novi Sad, Serbia, igorbp@uns.ac.rs, ORCID 0000-0001-9098-3642.
[4] Full Professor, University of Novi Sad, Faculty of Technical Sciences, Department of Civil Engineering and Geodesy, Novi Sad, Serbia, araseta@uns.ac.rs, ORCID 0000-0002-4535-1379.

## 1. INTRODUCTION

Preliminary estimation of cost and duration in urban-road construction is the engineering decision that opens, scopes and constrains every project that follows it. In the conceptual phase, an investor must decide whether to launch a tender and a contractor must decide whether to bid, and both decisions are taken on the basis of information that is, by construction, sparse: typically functional and dimensional descriptions of the future object rather than a finished bill of quantities. The accuracy that is achievable at this phase is correspondingly modest, and standard practice in the construction-cost literature accepts a relatively wide error band at the conceptual stage [3, 4]. What matters most for the decisions taken at this point is therefore not only the quality of the centre estimate but also a transparent representation of the uncertainty that surrounds it.

For urban-road projects in Novi Sad, the empirical and methodological foundation has been established by the Peško research line. Peško et al. [1] trained artificial-neural-network models on 130 completed urban-road projects, using bill-of-quantities material amounts and qualitative work-level descriptors as inputs and producing point estimates of total realisation cost and total construction time. Peško et al. [2] extended this work to 166 projects realised for the same municipal investor over the period January 2005 – December 2012, and compared artificial neural networks with support-vector machines on a richer twelve-input feature set drawn from the bill of quantities. Both papers are valuable for the detailed pre-contract phase in which a complete design and a finished bill of quantities are already available. They are, however, not designed for use at the earliest, functional-parameter stage of estimation, in which the bill of quantities does not yet exist, and they produce a single deterministic number rather than an explicit representation of the uncertainty that is, by hypothesis, largest at the same conceptual stage.

Two complementary observations follow. First, estimation by the functional parameters of a future object (features such as road length, predicted parking-space count, parking type, or parking position) has been identified by Peško et al. [2] themselves as a natural extension of the research line, but it remains comparatively underdeveloped in the urban-road context. Second, even where centre-of-line estimators perform well, point estimates do not communicate the uncertainty that the conceptual phase is known to carry, and an estimator whose output is an interval rather than a single number may therefore add useful information for early-phase decision-making. These two observations together define the gap addressed by the present paper. They do not, individually or jointly, imply that an interval-based fuzzy-regression formulation will be more accurate than the existing ANN and SVM point predictors; the question that is open is whether such a formulation can provide complementary interval information at the earlier phase, on the same domain, in a defensible form.

The aim of this paper is to examine the applicability of Tanaka-type possibilistic linear regression [5, 6] for interval-based early-stage estimation of cost and duration in urban-road construction. The paper is positioned as a complementary extension of the Peško research line. It applies Tanaka-type possibilistic regression to a dataset of 35 Novi Sad urban-road projects, made available through the Peško research line, using early functional parameters that are available before a bill of quantities is produced. The headline cost model is fitted on log-cost and back-transformed to RSD for reporting; the methodological justification for this choice is developed in §3. An Ordinary Least Squares (OLS) model is fitted on the same data as a centre-line baseline, and the Tanaka model is evaluated alongside it for the h-level possibility band that OLS does not

provide. Offered duration is reported as a secondary, exploratory target. Rather than displacing the ANN and SVM point predictors of the Peško research line, this paper asks whether a possibilistic model can complement them with explicit interval information at an earlier estimation phase.

The remainder of the paper is structured as follows. Section 2 reviews the background and the related work. Section 3 presents the data and the methodology, including the OLS baseline, the Tanaka possibilistic linear regression formulation, the choice of the possibility level h, and the evaluation protocol. Section 4 reports the results: OLS and Tanaka log-cost estimates at h = 0.5, an h-level sensitivity diagnostic, a trimmed-sample robustness check, an original-scale sensitivity result, and an exploratory duration model. Section 5 discusses the interpretation and the limitations. Section 6 concludes and identifies directions for further work.

## 2. BACKGROUND AND RELATED WORK

### 2.1. PRELIMINARY COST AND DURATION ESTIMATION IN URBAN-ROAD CONSTRUCTION

Preliminary estimation of cost and duration in construction is the engineering decision that opens, scopes, and constrains every project that follows it. Two practical considerations make it especially load-bearing for road infrastructure. First, the conceptual phase is the phase in which an investor decides whether to tender and a contractor decides whether to bid, and these decisions are taken on the basis of information that is, by construction, sparse: typically functional and dimensional descriptions of the future object rather than a finished bill of quantities. Second, the same conceptual phase is the phase in which uncertainty is at its largest, and standard practice in the construction-cost literature accepts a relatively wide error band at this stage: the often-cited Ashworth benchmark of ±15 % for conceptual cost estimation has been adopted as a reference value in domain studies of urban-road tendering [2]. The present paper refers to this benchmark as background context for the conceptual-estimating phase and does not adopt it as an evaluation target for the models reported here. Recent systematic reviews of transport-infrastructure cost estimation reinforce the same picture: methods for the conceptual phase are dominated by parametric and machine-learning models, and the central methodological tension is between richer feature sets that arrive later in the design cycle and leaner feature sets that are available earlier [3, 4].

Urban-road construction is a particularly suitable empirical domain for this question. Projects are well delimited in scope, recur within the portfolio of a single municipal investor, share a common contractual structure, and offer a stable mix of cost-significant items: earthworks, pavement structure, surfacing, drainage, landscaping. These features are precisely what made the Peško research line at the University of Novi Sad possible. Peško, Trivunić, Ćirović and Mučenski [1] built an artificial-neural-network model on a database of 130 completed urban-road projects in Novi Sad, using bill-of-quantities material amounts and qualitative work-level descriptors as inputs and reporting cost and construction time as separate outputs. Peško, Mučenski, Šešlija, Radović, Vujkov, Bibić and Krklješ [2] extended that work to 166 projects realised for the same municipal investor over the period January 2005 – December 2012, compared Multi-Layer Perceptron (MLP)-style artificial neural networks against support-vector machines under both min-max and zero-mean normalisations, and used twelve inputs drawn from the bill of quantities: five material amounts (crushed stone, curbs, asphalt base layer, asphalt surface layer, prefabricated concrete elements), five percentage shares of work

groups (preparation, earthworks, drainage, traffic-signal installation, other), the works-realisation zone, and a binary project-category indicator. Both papers produce point estimates of total offered revalorised price and offered duration.

The Peško research line therefore sets the empirical baseline for the present paper in two senses. It defines the domain, the modelling conventions and the empirical reference point that any extension paper on Novi Sad urban-road cost and duration estimation has to respect, and it explicitly identifies the direction in which the line should be extended. In the closing section of Peško et al. [2], the authors flag the introduction of further input parameters that describe the functional features of the future object (section length, roadway width, urban-road category, cycling-lane length, pedestrian-lane and parking areas, plateaus) as the natural next step, and note that such functional features would enable estimation at a still earlier phase, when the bill of quantities is not yet defined. The present paper takes that future-work direction as its starting point.

## 2.2. FROM BILL-OF-QUANTITIES INPUTS TO FUNCTIONAL PARAMETERS

The bill of quantities is the project document that fixes the quantities of every work item priced in the tender. Its existence presupposes a substantially complete design, and its preparation is a non-trivial engineering effort in its own right. Models trained on bill-of-quantities inputs (including the ANN and SVM models of Peško et al. 2013, 2017) therefore operate at a relatively late point in the pre-contract cycle. They are well suited to detailed preliminary estimation, where the design is fixed and the question is to price it; they are not available for use at the earlier conceptual phase, where the bill of quantities does not yet exist.

Functional parameters of a future object (features such as the length of the planned road, the predicted number of parking spaces, the type of parking, and the position of parking relative to the carriageway) describe the object at the level of feasibility studies, urban-planning briefs, and indicative client requirements. They carry meaningfully less information per project than a bill of quantities, and any model trained on them must accept correspondingly wider prediction uncertainty. They are, however, available earlier, sometimes by years, than the bill-of-quantities inputs used in the Peško research line. A model that uses only functional parameters is therefore not a substitute for a model that uses the bill of quantities; it is a tool for a different phase of the same estimation problem, with a correspondingly different acceptable error band. The empirical case of the present paper is constructed in exactly this spirit: it retains the targets and the domain of Peško et al. [2], namely total offered revalorised price and offered duration of urban-road projects in Novi Sad, but moves the predictor set to functional parameters that survive a variation rule on a 35-record sample (road length and predicted parking-space count after the rule of §3.2).

## 2.3. FUZZY AND POSSIBILISTIC REGRESSION

Fuzzy regression is a family of regression models in which one or more of the regression coefficients, the inputs or the output are represented as fuzzy quantities rather than as real numbers. The family was introduced as a way to model relationships in which the deviations between observed and estimated values are interpreted not as random measurement error but as a fuzziness of the underlying system itself. The seminal reference is Tanaka, Uejima and Asai [7]; the formulation used in the present paper follows the possibilistic linear-regression line developed in Tanaka [5], Tanaka and Watada [6], and Tanaka, Hayashi and Watada [8]. In its basic form, each regression coefficient is modelled as a symmetric triangular fuzzy number with a centre and a non-

negative spread, the regression coefficients are estimated by solving a linear programme that minimises the total fuzziness of the model subject to the requirement that every observation lies inside an inclusive interval at a chosen possibility level h, and the model output at a new point is an h-level interval rather than a single number. The full formulation, including the equations, is given in §3.4.

Two properties of the Tanaka family are load-bearing for the way the present paper interprets its results. First, the output of the model is a possibility band in the sense of Tanaka [5]; it is not a statistical confidence interval and should not be reported or read as one. Comparative reviews of fuzzy-regression formulations [11] draw exactly this distinction and treat the possibility interpretation as the defining feature of the family. Second, the Tanaka linear programme has well-documented sensitivities: Redden and Woodall [9] show that the fitted band depends on the chosen possibility level h, and Hung and Yang [10] document that a single influential observation can substantially inflate the fitted spreads and therefore the width of the band. These two properties are taken seriously in §3.5 (h-level sensitivity reported empirically) and §3.6 (outlier diagnostics reported transparently).

## 2.4. FUZZY METHODS IN CONSTRUCTION COST AND INFRASTRUCTURE ESTIMATION

Fuzzy and hybrid fuzzy approaches have been applied to construction cost estimation across a range of project types. In the capital-cost estimation of treatment facilities, Chang, Chen and Yang [12] and Chang, Chen and Chen [13] used fuzzy and fuzzy goal regression formulations for municipal waste incinerators and wastewater treatment plants. In conceptual building-cost estimation, hybrid neuro-fuzzy and evolutionary fuzzy neural inference models have been developed on historical project portfolios [15, 16, 17]. Closer to the present paper's domain, fuzzy regression has been applied to road freight modelling [18] and to bridge-condition prediction [19, 20], and Hassim et al. [14] report a fuzzy neural-network application to national-scale tender-price standardisation. Two recent systematic reviews place these approaches in the broader landscape of AI and parametric construction-cost modelling [4, 21].

What this body of work shows is that fuzzy approaches are an established methodological family in construction-cost estimation, with applications spanning building, infrastructure, and tender pricing. What it does not show is a direct application of Tanaka-type possibilistic linear regression to the cost or duration estimation of urban-road projects, and in particular no application of the formulation as an interval-output companion to the ANN- and SVM-based Peško research line on this exact domain. The construction-fuzzy literature therefore validates the broad methodological choice (interval-based, possibility-grounded regression has a long track record in this field) without pre-empting the specific contribution that the present paper makes.

## 2.5. POSITIONING OF THE PRESENT PAPER

Three strands of literature converge on the position of the present paper. The Peško research line provides a well-characterised empirical foundation in the same Novi Sad urban-road domain [1, 2], with ANN and SVM point-prediction models trained on bill-of-quantities inputs and an explicitly flagged future-work direction toward functional-parameter inputs. The wider construction-cost-estimation literature treats early-phase functional-parameter estimation as comparatively underdeveloped and acknowledges the corresponding need for honest uncertainty reporting [3, 4]. The fuzzy-regression literature, in turn, offers an interval-output formulation that operationalises that uncertainty in a way that classical OLS cannot, with the Tanaka family in particular

providing the most directly applicable methodology [5, 6, 8, 11], together with documented caveats on h-level dependence [9] and outlier sensitivity [10] that any application has to confront.

Against that triangulation, the gap addressed by the present paper is specific. The Peško-line models provide point predictions of cost and duration using richer bill-of-quantities inputs. Early functional-parameter estimation on the same domain remains less developed. The fuzzy-regression literature supports interval-based modelling under early-phase uncertainty but, to the authors' knowledge, has not been applied to urban-road cost and duration estimation in the Tanaka-type possibilistic form. The present paper fills exactly this position: it is a complementary extension of the Peško research line in which Tanaka-type possibilistic linear regression is fitted to the early functional parameters that the bill of quantities does not yet contain, and the output is an h-level possibility band rather than a point estimate. The paper does not claim superior centre-prediction accuracy against OLS, ANN or SVM; the contribution is the addition of an explicit possibility band, evaluated alongside an OLS centre-line baseline on the same data. The data, the model formulation, the evaluation protocol and the outlier diagnostics needed to support that contribution are developed in §3.

## 3. DATA AND METHODOLOGY

### 3.1. DATASET AND RESEARCH CONTEXT

The empirical basis for this paper is a dataset of 35 urban-road construction projects from the same research domain as Peško et al. [1] and Peško et al. [2], namely the construction and reconstruction of urban roads in the city of Novi Sad, Republic of Serbia. The dataset was made available by the co-authoring research team within the Peško et al. research line. The records were compiled from contractor offers published on the Serbian Public Procurement Portal during earlier studies in this research line on preliminary cost and duration estimation of urban road construction projects.

The two target variables follow the convention used throughout the Peško research line. The first target is the **total offered revalorised price**, that is, the realisation value offered by the contractor in the accepted bid, expressed in Serbian dinars (RSD) and revalorised to a common reference date; Peško et al. [2] justify the use of contractor-offered prices rather than actually paid realisation values on the grounds that paid values are not consistently available, are often not properly recorded, and can drift relative to the contracted price during realisation. The second target is the **offered duration** of the works, expressed in calendar days. As Peško et al. [2] explicitly note, the offered duration is not, in general, the result of an independent estimation by the contractor: the investor typically sets a maximum duration in the tender conditions, and contractors tend to adopt that maximum value. Any model trained on offered duration therefore predicts the offered figure, not the realised one. This caveat is carried forward into the present analysis: the cost model carries the headline of this paper, while the duration model is presented as a secondary, exploratory result.

**Cost target and the log transformation.** Cost is recorded on the original RSD scale, but the main cost model in this paper is fitted on the natural logarithm of cost, log(cost_rsd), with predictions and possibility bands back-transformed to RSD by the exponential function for reporting. Three reasons motivate this choice: (i) construction cost is strictly positive and right-skewed in this domain, so a multiplicative error structure is more natural than an additive one; (ii) the unconstrained Tanaka linear programme has no positivity constraint on the lower bound of the possibility band, and fitting on log-cost guarantees a strictly positive back-transformed band; and (iii) the log

transformation stabilises percentage errors by reducing the leverage of very small projects on MAPE. The original-scale cost model is retained as a sensitivity result (§4); the log-cost model is the headline.

The 35-record dataset is a project subset compiled within the same Peško research line on Novi Sad urban-road construction. Peško et al. [2] report a procurement window of January 2005 – December 2012 for their 166-project dataset; the present paper makes no further claim about the procurement window of its own 35-record subset. The revalorisation procedure follows the method used in the Peško research line: contractor-offered prices are adjusted to a common reference date using the general retail price index for the Republic of Serbia, as described in Peško et al. [2]. The base date used for the present 35-record dataset follows the Peško research-line convention and is available from the authors upon request.

The present dataset differs from the earlier Peško datasets in two respects relevant to the methodology. First, the predictor set consists exclusively of **functional project parameters** (road length, predicted number of parking spaces, parking type, and parking position) known before a bill of quantities is produced, rather than the bill-of-quantities material quantities and work-group shares used in Peško et al. [1, 2]. This responds to the future-work direction stated in the closing section of Peško et al. [2], where estimation "by functional parameters of a future object" is identified as the next step. Second, the two targets are modelled separately, following the Peško et al. [2] finding that separate models for cost and duration are more accurate than a single joint model.

## 3.2. VARIABLES AND ENCODING

Table 1 summarises the six variables used in this study, together with their type and encoding. The two numerical predictors (preliminary road length and predicted number of parking spaces) are standardised (zero mean, unit variance) before being used in any model, to prevent the difference in scale from dominating the optimisation in the Tanaka linear-programming formulation introduced in §3.4. The two categorical predictors are recoded as binary dummy variables.

*Tab. 1 Variables, roles, types, units and encoding.*

| Variable | Role | Type | Unit | Encoding / notes |
|---|---|---|---|---|
| Total offered revalorised price | Cost on original scale; sensitivity only (§4). | Continuous | RSD | Revalorised offered price, per Peško et al. (2017). |
| log(cost_rsd) | Target $Y_1$ — main cost-model target (headline). | Continuous | log RSD | Natural logarithm of cost; back-transformed by exp(·). |
| Offered duration | Target $Y_2$ — secondary / exploratory target. | Continuous | days | Offered (tender) duration; caveat from Peško et al. (2017). |
| Preliminary road length | Predictor $X_1$ | Continuous | m | Standardised (z-score) before model fitting. |
| Predicted parking spaces | Predictor $X_2$ | Continuous | count | Standardised (z-score) before model fitting. |
| Parking type | Predictor $X_3$ | Binary | — | Dummy: oblique = 1, longitudinal = 0. Inclusion |

| Variable | Role | Type | Unit | Encoding / notes |
|---|---|---|---|---|
| | | | | subject to §3.2 rule. |
| Parking position | Predictor $X_4$ | Binary | — | Dummy: two-sided = 1, one-sided = 0. Inclusion subject to §3.2 rule. |

The inclusion of the two binary predictors in the final model is conditional on their showing sufficient variation in the 35-record sample. If either category is nearly constant, the main model will be estimated using only the numerical functional parameters (road length and parking spaces), and the categorical variables will be reported as a data limitation and used only as exploratory sensitivity variables. No interaction terms are included in the baseline specification, and the model is kept linear in the predictors; with n = 35, every additional degree of freedom is expensive.

### 3.3. CLASSICAL OLS BASELINE

An ordinary least squares (OLS) multiple linear regression model is fitted separately to each target on the same standardised predictors. OLS is fitted primarily to log-cost (the main cost target) and secondarily to offered duration (the exploratory target). OLS plays two complementary roles in this paper:

- It is the fair centre-line baseline against which the centre of the Tanaka possibilistic linear regression model (§3.4) is compared on the same sample under the same evaluation protocol (§3.7).
- It is the estimator used for direction-of-effect interpretation. OLS coefficients (sign and significance) carry the substantive reading of how road length and parking-space count are associated with cost (on the log scale) and with duration. Direction-of-effect claims in §5 are sourced from OLS, not from the Tanaka centre line (see the methodological caveat at the end of §3.4).

For each OLS model the estimated coefficients, their standard errors, the coefficient of determination $R^2$, and the leave-one-out cross-validation values of Mean Absolute Error (MAE), Mean Absolute Percentage Error (MAPE) and Root Mean Squared Error (RMSE) are reported in §4. The Peško et al. [2] ANN and SVM results are referred to in §5 only in a contextual sense, because the input regimes (functional parameters versus bill-of-quantities inputs) and the sample sizes (n = 35 versus n = 166) differ; the within-paper, like-for-like numerical comparison is OLS versus Tanaka on the same data.

### 3.4. TANAKA-TYPE POSSIBILISTIC LINEAR REGRESSION

The fuzzy regression model used in this paper follows the possibilistic linear formulation introduced by Tanaka, Uejima and Asai [7] and developed in Tanaka [5] and Tanaka and Watada [6]. For a vector of predictors $x = (x_0, x_1, \ldots, x_k)^T$, with $x_0 = 1$ for the intercept, the fuzzy output $\tilde{Y}$ is written as a linear combination of fuzzy coefficients:

$$\tilde{Y}(x) = \tilde{A}_0 x_0 + \tilde{A}_1 x_1 + \cdots + \tilde{A}_k x_k \qquad (1)$$

where each coefficient $\tilde{A}_j$ is a symmetric triangular fuzzy number characterised by a centre $a_j$ and a non-negative spread $c_j \geq 0$. For $c_j > 0$, the membership function of $\tilde{A}_j$ is

$$\mu_{\tilde{A}_j}(a) = \max\{0, 1 - |a - a_j| / c_j\} \qquad (2)$$

If c_j = 0, the coefficient is treated as crisp at a_j, with no spread; in that case x_j contributes only to the centre prediction and not to the width of the possibility band. For a fixed possibility level h ∈ [0, 1], the h-level interval of the fuzzy output at point x is

$$\left[\sum_j a_j x_j - (1-h)\sum_j c_j|x_j|, \sum_j a_j x_j + (1-h)\sum_j c_j|x_j|\right] \qquad (3)$$

The centre line of the fuzzy model at x is Σ_j a_j x_j; the half-width of the h-level interval at x is (1 − h) Σ_j c_j |x_j|. The width therefore depends both on the fitted spreads c_j and on the chosen possibility level h.

Following Tanaka [5], the coefficients (a_j, c_j) are obtained by solving a linear programming (LP) problem that minimises the total fuzziness of the model subject to the requirement that every observed (x_i, y_i) lies inside the h-level interval at x_i. Formally, for a sample of n observations,

$$\begin{aligned} &\text{minimise} \sum_{i=1}^{n}\sum_{j=0}^{k} c_j|x_{ij}| \\ &\text{subject to} \sum_j a_j x_{ij} + (1-h)\sum_j c_j|x_{ij}| \geq y_i, i=1,\ldots,n, \\ &\quad \sum_j a_j x_{ij} - (1-h)\sum_j c_j|x_{ij}| \leq y_i, i=1,\ldots,n, \\ &\quad c_j \geq 0, j=0,1,\ldots,k. \end{aligned} \qquad (4)$$

Two separate Tanaka models are fitted: one for the cost target $Y_1$ = log(cost_rsd) (main result) and one for the duration target $Y_2$ (secondary result), each on the same standardised predictors. The LP problems are solved in Python. For the main cost model, the LP is fitted on log-cost and the centre and h-level bounds produced by equation (3) are subsequently back-transformed to RSD by the exponential function before being reported and plotted. For duration, no transformation is applied. At any new x the model returns a centre prediction Σ_j a_j x_j and an h-level **possibility band** given by equation (3); this interval is interpreted as a possibility band at level h in the sense of Tanaka [5] and is **not a statistical confidence interval**.

**Methodological caveat — centre line.** The Tanaka LP minimises total fuzziness, not squared error. The fitted centre vector a is therefore not a least-squares estimate and can differ from the OLS coefficients in sign as well as magnitude. In this paper, OLS provides the centre prediction used for point-prediction interpretation (§3.3); the Tanaka model is used primarily to obtain the possibility band that the OLS centre alone cannot provide. Substantive direction-of-effect claims in §5 are sourced from OLS, not from the Tanaka centre line.

### 3.5. H-LEVEL SELECTION

The possibility level h is a modelling choice rather than a quantity estimated from the data. For a fixed set of coefficients (a_j, c_j), equation (3) implies that the h-level interval is non-increasing in h. However, in the basic Tanaka possibilistic LP formulation used in this paper, the LP problem (4) is re-solved at each value of h, and a change in h rescales the fitted coefficient spreads c_j; because the (1 − h) factor in the half-width of the h-level interval is cancelled by this rescaling of the spreads, the band half-width may remain invariant in h. This is a structural property of the basic Tanaka LP formulation adopted here, not a property that should be assumed a priori. The sensitivity analysis in §4 reports the fitted spreads, the back-transformed bands and the leave-one-out cross-validation (LOO-CV) diagnostics across h ∈ {0, 0.25, 0.5, 0.75}, and serves to demonstrate this structural property transparently on the fitted model. The headline results are reported for h = 0.5 as a conventional mid-band choice for

comparability and interpretability, not because it would, within this formulation, yield a qualitatively different band, consistent with the broader literature on the h-dependence of this family of models [9].

### 3.6. OUTLIER DIAGNOSTICS

It is well established that Tanaka-type possibilistic regression is sensitive to outliers: a single extreme observation can substantially inflate the fitted spreads c_j and therefore the width of the possibility band [10]. To surface this effect transparently, a two-pass procedure is used. In the first pass, OLS residual diagnostics are computed: Cook's distance D_i and externally studentised residuals t_i for every observation i. Observations with D_i > 4/n (here, 4/35 ≈ 0.114) or |t_i| > 3 are flagged. In the second pass, both the OLS and the Tanaka models are refitted with the flagged observations removed. The full-sample fit remains the headline result in §4; the trimmed-sample fit is reported alongside it as a robustness check, not as the headline. No observation is removed silently; the diagnostic and the effect of removal are both shown so that the reader can assess the sensitivity of the bands and the centre-line errors to the flagged rows.

### 3.7. LEAVE-ONE-OUT CROSS-VALIDATION

With n = 35, a fixed train/test split would leave too few test observations to yield stable estimates. Leave-one-out cross-validation (LOO-CV) is therefore used: for each $i \in \{1, \ldots, 35\}$, each model is fitted on the remaining 34 observations and used to predict the held-out observation i, and the held-out predictions are aggregated to compute the metrics of §3.8. For the Tanaka model, the centre prediction and the lower and upper bounds of the h-level interval at h = 0.5 are recorded at each fold, so that band coverage and band width are evaluated out of sample. For the main cost model, both OLS and Tanaka are trained on log(cost_rsd), and the held-out predictions (centre, lower, upper) are back-transformed by exp(·) before any error metric is computed; the reported MAE, MAPE, RMSE, coverage and band-width statistics for cost are therefore on the original RSD scale. For duration, no transformation is applied. The two passes of §3.6 (full sample and trimmed sample) are both evaluated under LOO-CV. The reported errors should be read as indicative out-of-sample estimates given the small sample, not as unbiased generalisation errors.

### 3.8. EVALUATION METRICS

Two families of metrics are used. The first family characterises the accuracy of the **centre prediction** and is applicable to both OLS and Tanaka: mean absolute error (MAE), mean absolute percentage error (MAPE), and root mean squared error (RMSE). For the cost model, all three centre metrics are reported on the original RSD scale, after back-transformation of the log-cost predictions by exp(·); this preserves comparability with the Peško research line, in which MAPE is the standard reporting metric [1, 2]. For duration, the same three metrics are reported in days. MAE is the primary error metric in this paper; MAPE is reported for comparability and is interpreted with caution on the cost model because small projects can inflate it; RMSE is reported for completeness. The second family characterises the **possibility band** and is applicable only to the Tanaka model. For the cost model, all three band metrics are reported on the original RSD scale, after back-transformation of the lower and upper bounds by exp(·):

- Coverage — the proportion of LOO held-out observations whose true value lies inside the predicted h-level interval at h = 0.5 (computed on the RSD scale for cost; on the day scale for duration).

- Average band width — the mean of (upper − lower) over the LOO held-out predictions at h = 0.5 (back-transformed to RSD for cost; in days for duration).
- Relative band width — the average band width divided by the sample mean of the target on the reporting scale, allowing direct comparison between the cost and duration models on a common scale.

All evaluation metrics are computed for the cost and the duration models, in both the full-sample and the trimmed-sample passes, and at $h \in \{0, 0.25, 0.5, 0.75\}$ for the sensitivity check of §3.5. The cost model is the headline; the duration model is reported alongside it but framed as a secondary, exploratory result in light of the offered-duration caveat from Peško et al. [2].

## 4. RESULTS

### 4.1. DATA AUDIT AND PREDICTOR SELECTION

The dataset comprises n = 35 records with no missing values across the six variables defined in §3.2. The two binary predictors are strongly imbalanced: parking type splits into 33 longitudinal and 2 oblique projects (minority share 5.7%), and parking position into 34 one-sided and 1 two-sided project (minority share 2.9%). Both binaries fall below the 10% minority-share inclusion threshold defined in §3.2 and are therefore excluded from the main model. The headline OLS and Tanaka models are estimated on the two numerical functional predictors only (preliminary road length and predicted number of parking spaces, both standardised), with parking type and parking position carried forward to §5 as a data limitation.

### 4.2. DESCRIPTIVE STATISTICS

Table 2 summarises the four variables that enter the main models. Cost spans an order of magnitude (RSD 2.36 M to 49.64 M), duration ranges from 8 to 75 calendar days, road length from 62 m to 1 050 m, and the predicted parking-space count from 3 to 125 spaces. All four variables are strictly positive. Cost and parking-space counts are right-skewed, with the mean noticeably above the median; road length and duration are closer to symmetric within the observed range, although the maxima exceed the means in both cases. The overall pattern is consistent with the project-size mix expected in the Novi Sad urban-road portfolio [2].

*Tab. 2 Descriptive statistics for the four variables that enter the main models (n = 35).*

| Variable | Unit | Min | Median | Mean | Max | SD |
|---|---|---|---|---|---|---|
| Total offered revalorised price | RSD | 2,362,887 | 11,238,812 | 14,672,884 | 49,638,700 | 10,697,485 |
| Offered duration | days | 8 | 25 | 27.11 | 75 | 13.84 |
| Preliminary road length | m | 62 | 481 | 509.71 | 1,050 | 301.92 |
| Predicted parking spaces | count | 3 | 21 | 29.94 | 125 | 25.51 |

### 4.3. OLS BASELINE FOR LOG-COST

Table 3 reports the OLS coefficients of the log-cost model on the two standardised predictors. The intercept of 16.2190 (in log RSD) corresponds to a back-transformed value of exp(16.2190) ≈ RSD 11.0 M for the mean project. The coefficient on

standardised road length is 0.5186 (p = 0.0001); the coefficient on standardised parking spaces is small (0.0405) and not significant (p = 0.7372). Within this two-predictor specification, road length is the only statistically supported predictor of log-cost. The model explains $R^2 = 0.4581$ of the variation in log-cost, with adjusted $R^2 = 0.4242$.

*Tab. 3 OLS log-cost coefficients (log RSD per +1 SD of predictor; intercept in log RSD).*

| Predictor | Coefficient (log RSD) | Std. error | p-value |
|---|---|---|---|
| Intercept | 16.2190 | 0.1038 | < 0.0001 |
| road_length_z | 0.5186 | 0.1195 | 0.0001 |
| parking_spaces_z | 0.0405 | 0.1195 | 0.7372 |

Under leave-one-out cross-validation, the back-transformed centre prediction yields MAE = RSD 6 020 714, RMSE = RSD 9 941 689, and MAPE = 48.20%. A more substantive reading is deferred to §5.

## 4.4. TANAKA POSSIBILISTIC REGRESSION FOR LOG-COST

The Tanaka possibilistic linear regression model (§3.4) was fitted on log(cost_rsd) and the resulting centre and h-level bounds were back-transformed to RSD. At the headline level h = 0.5, the leave-one-out diagnostics summarised in Table 4 are: MAE = RSD 8 617 330, RMSE = RSD 12 025 870, MAPE = 97.12%, coverage 85.7% (30 of 35 held-out observations contained in the possibility band), average band width RSD 52 492 715, and relative band width 3.578 of the mean cost. The minimum lower bound over the 35 LOO folds is RSD 2 022 603, and no fold produces a negative lower bound; the back-transformation by exp(·) eliminates the artefact present in the original-scale model (see §4.7).

*Tab. 4 Headline LOO-CV diagnostics for the cost models (h = 0.5).*

| Metric | OLS log-cost | Tanaka log-cost |
|---|---|---|
| MAE (RSD) | 6,020,714 | 8,617,330 |
| RMSE (RSD) | 9,941,689 | 12,025,870 |
| MAPE | 48.20% | 97.12% |
| Coverage | — | 85.7% |
| Average band width (RSD) | — | 52,492,715 |
| Relative band width | — | 3.578 |
| Minimum lower bound (RSD) | — | 2,022,603 |

For transparency, the fitted Tanaka log-cost coefficients at h = 0.5 are reported in Table 5. The centre vector a is the LP-fitted minimum-fuzziness centre; it is not a least-squares estimate and should not be read as a direction-of-effect estimate (see the methodological caveat in §3.4). The spread vector c determines the half-width of the possibility band: predictors with c = 0 are treated as crisp and contribute only to the centre prediction.

*Tab. 5 Fitted Tanaka log-cost coefficients at h = 0.5 (intercept and the two standardised predictors).*

| Predictor | Centre a (log RSD) | Spread c (log RSD) |
|---|---|---|

| | | |
|---|---|---|
| Intercept | 16.3942 | 2.0031 |
| road_length_z | −0.0905 | 0.8586 |
| parking_spaces_z | 0.3530 | 0.0000 |

On centre-prediction accuracy OLS performs better than the Tanaka model on every metric in Table 4: lower MAE, lower RMSE, and lower MAPE. The Tanaka model contributes a different quantity, the possibility band at h = 0.5, which OLS does not provide. Figure 1 shows the back-transformed band against the observed cost values, sorted by observed cost; the five non-covered observations sit at both tails of the cost distribution. The interpretation of this complementarity is taken up in §5.

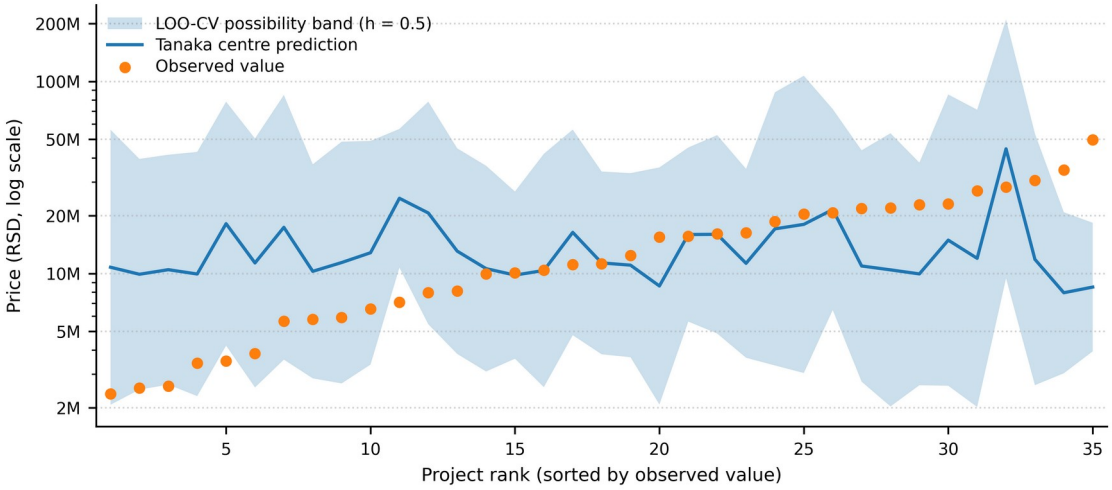


*Fig. 1 Observed cost vs. LOO-CV Tanaka possibility band at h = 0.5, log-cost model back-transformed to RSD (log y-axis).*

## 4.5. H-LEVEL SENSITIVITY

The sensitivity analysis at h ∈ {0, 0.25, 0.5, 0.75} for the log-cost model returned identical back-transformed bands and identical LOO-CV diagnostics at every h-level. Inspection of the fitted coefficients confirmed the mechanism: when the LP problem (4) is re-solved at successive h-values the fitted centres a remain unchanged and the spreads c rescale by exactly the factor 1/(1 − h), so the half-width (1 − h) · |x| · c is invariant. This is not a property specific to the present 35-record dataset; it is a structural consequence of the basic Tanaka LP formulation: because the spreads c rescale by the factor 1/(1 − h), the (1 − h) factor in the band half-width is cancelled. The flat sensitivity profile across h should therefore be read as a structural property of the adopted formulation, not as evidence of empirical robustness across substantively different bands; the check across h-levels is retained as a transparency demonstration of that property on the fitted model.

## 4.6. TRIMMED-SAMPLE ROBUSTNESS CHECK

The OLS residual diagnostics of §3.6 flagged three observations as potentially influential: ids 2, 17 and 35 (Cook's D > 4/n and / or externally studentised residual outside ±3 in at least one of the OLS models). Refitting both OLS and Tanaka log-cost on the trimmed sample (n = 32) gives the values in Table 6.

*Tab. 6 Full-sample (n = 35) vs. trimmed-sample (n = 32, ids 2/17/35 removed); log-cost model, h = 0.5 for Tanaka.*

| Metric | OLS full | OLS trimmed | Tanaka full | Tanaka trimmed |
|---|---|---|---|---|
| MAE (RSD) | 6,020,714 | 5,112,683 | 8,617,330 | 7,230,820 |
| RMSE (RSD) | 9,941,689 | 7,102,445 | 12,025,870 | 10,251,636 |
| MAPE | 48.20% | 45.93% | 97.12% | 71.34% |
| $R^2$ (in-sample) | 0.4581 | 0.5818 | — | — |
| Adjusted $R^2$ | 0.4242 | 0.5530 | — | — |
| Coverage | — | — | 85.7% | 81.3% |
| Average band width (RSD) | — | — | 52,492,715 | 38,382,313 |
| Relative band width | — | — | 3.578 | 2.957 |

Trimming the three flagged observations narrows both centre-prediction errors and band widths: the OLS in-sample $R^2$ rises from 0.4581 to 0.5818, the Tanaka LOO MAPE falls from 97.12% to 71.34%, the average band width contracts from RSD 52.5 M to RSD 38.4 M, and the relative band width from 3.578 to 2.957. Band coverage falls only slightly (85.7% → 81.3%). Figure 2 shows the trimmed-sample band on the same log y-axis as Figure 1. The trimmed model is reported as a robustness check and not as the headline result; the full-sample fit remains the reference for the rest of the paper.

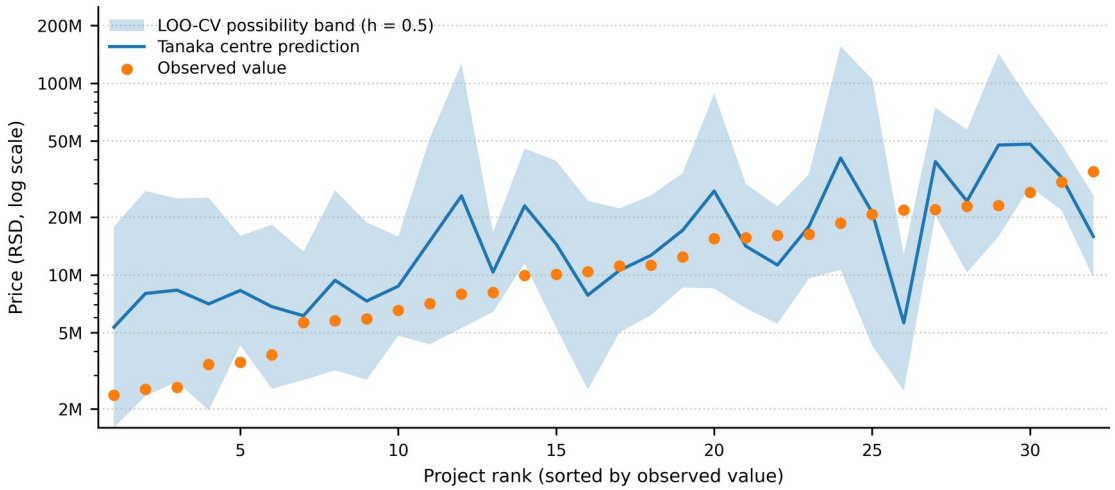


*Fig. 2 Observed cost vs. LOO-CV Tanaka possibility band at h = 0.5, trimmed (n = 32) log-cost model back-transformed to RSD (log y-axis).*

## 4.7. ORIGINAL-SCALE COST: SENSITIVITY RESULT

For completeness, the Tanaka model was also fitted on the original RSD scale, as specified in §3.1 as a sensitivity result. At h = 0.5, the LOO-CV diagnostics give MAPE = 239.49%, average band width 44.854 M RSD and relative band width 3.057 of the mean cost. The dominant artefact is that the unconstrained LP produces a possibility band whose lower bound falls below zero for several small projects, which is not meaningful for construction cost. The log-cost formulation of §4.4 was adopted

precisely to remove this artefact and to stabilise MAPE on small projects; the original-scale model is therefore retained only for traceability and is not the basis of any substantive claim.

## 4.8. EXPLORATORY DURATION MODEL

The duration model is reported as a secondary, exploratory result. OLS on the same two standardised predictors gives $R^2 = 0.2155$ and adjusted $R^2 = 0.1665$; neither predictor is significant at the 5% level (road_length_z: coefficient 2.9322, p = 0.2420; parking_spaces_z: coefficient 4.3459, p = 0.0868). LOO-CV centre-prediction errors are MAE = 10.920 days, RMSE = 14.752 days and MAPE = 49.28%. The Tanaka duration model at h = 0.5 returns LOO-CV MAE = 12.495 days, RMSE = 15.445 days, MAPE = 63.35%, coverage = 85.7%, average band width 40.796 days and relative band width 1.505. The OLS and Tanaka diagnostics for the exploratory duration model are summarised in Table 7. Figure 3 shows the observed duration values against the LOO-CV band.

*Tab. 7 Exploratory duration model — OLS and Tanaka (h = 0.5) LOO-CV diagnostics.*

| Metric | OLS duration | Tanaka duration |
|---|---:|---:|
| MAE (days) | 10.920 | 12.495 |
| RMSE (days) | 14.752 | 15.445 |
| MAPE | 49.28% | 63.35% |
| $R^2$ (in-sample) | 0.2155 | — |
| Adjusted $R^2$ | 0.1665 | — |
| Coverage | — | 85.7% |
| Average band width (days) | — | 40.796 |
| Relative band width | — | 1.505 |

The signal is weak: neither predictor is individually significant in OLS, and adjusted $R^2$ is low. In addition, the duration target carries the substantive caveat noted in §3.1; Peško et al. [2] report that the offered duration in this domain tends to follow the maximum duration set by the investor in the tender conditions rather than an independent contractor estimate. For both reasons, interpretation of the duration model is deferred to §5 and the cost model carries the headline.

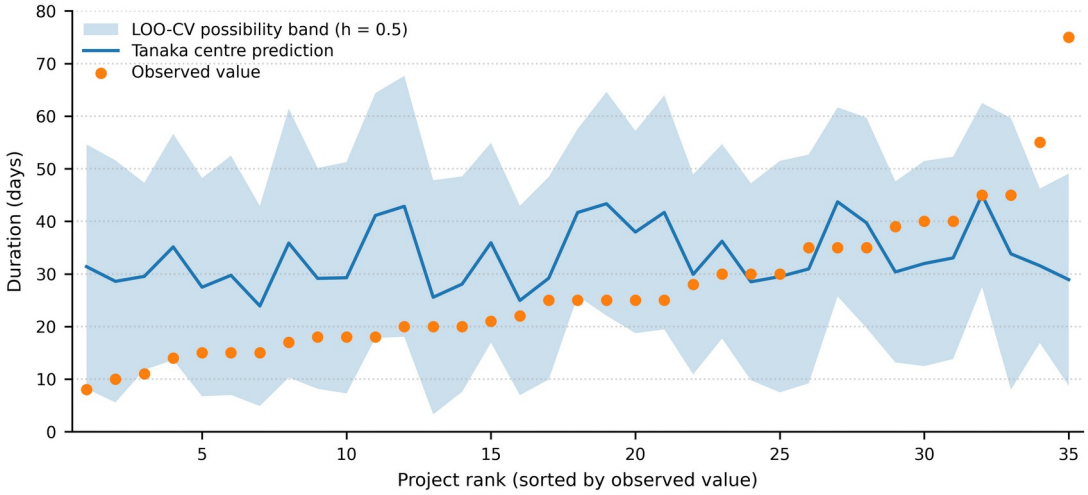


*Fig. 3 Observed duration vs. LOO-CV Tanaka possibility band at h = 0.5 (days).*

### 4.9. EMPIRICAL SUMMARY

The empirical results above can be summarised in five observations, each of which is taken up in the Discussion (§5):

- On centre-prediction accuracy the OLS log-cost model outperforms the Tanaka log-cost model on every reported metric (MAE, RMSE, MAPE) under leave-one-out cross-validation.
- The Tanaka log-cost model provides a possibility band that OLS does not. At h = 0.5 the band covers 85.7% of held-out observations on the full sample (81.3% on the trimmed sample), at the cost of substantial average width (RSD 52.5 M full; RSD 38.4 M trimmed), roughly 3.0 to 3.6 times the sample mean cost.
- Re-fitting Tanaka on log-cost and back-transforming by exp(·) eliminates the negative-lower-bound artefact of the original-scale model and reduces MAPE from 239.49% to 97.12%.
- The bands remain wide because the model uses only two early functional parameters (road length and parking spaces). Within this specification, road length is the only statistically supported predictor of log-cost; the contribution of parking spaces is small and not significant in OLS.
- The duration model is reported as a secondary, exploratory result. The signal is weak (adjusted $R^2 = 0.1665$; neither predictor significant at the 5% level), and the offered-duration caveat from Peško et al. [2] limits substantive interpretation.

## 5. DISCUSSION

### 5.1. WHAT THE COST RESULTS SHOW

The headline cost result of this paper is the Tanaka possibilistic linear regression fitted on log(cost_rsd), back-transformed to RSD (§4.4). Under leave-one-out cross-validation, the OLS centre prediction is more accurate than the Tanaka centre prediction on every reported metric (MAE, RMSE and MAPE) at h = 0.5. The Tanaka model does not, on this dataset, deliver better point accuracy than OLS, and the paper does not claim that it does. What the Tanaka model contributes is a different type of output: a possibility band at h = 0.5 that OLS does not provide. The complementarity is the substantive contribution, not a head-to-head accuracy gain.

Within the two-predictor specification adopted in §3.2, road length is the only statistically supported predictor of log-cost: the OLS coefficient on standardised road length is positive and significant ($p = 0.0001$), while the coefficient on standardised parking spaces is small and not significant ($p = 0.7372$). Parking spaces therefore do not carry an independent signal once road length is accounted for. This does not mean that parking provision is irrelevant to construction cost in general; only that, in this 35-record sample and conditional on road length, it provides no additional explanatory power that the linear-in-z model can identify.

## 5.2. PRACTICAL MEANING OF THE POSSIBILITY BAND

The Tanaka band at $h = 0.5$ is a possibility band in the sense of Tanaka [5]: it characterises the range of cost values that the fitted possibilistic linear system regards as compatible with the observed data at possibility level 0.5. It is **not** a statistical confidence interval, and it should not be reported or read as one. In early-stage tendering, where bill-of-quantities data are not yet available, the practical value of such a band is that it returns an explicit possibility range (a lower bound, an upper bound and a centre) instead of a single point prediction that hides its own uncertainty. A range supports phase-appropriate decisions: a contractor can compare the upper bound against a plausible budget envelope, an investor can compare the lower bound against minimum-cost expectations, and both parties can read the width of the band as a quantitative signal of how informative the available functional parameters actually are. Such a band has value primarily as a proof of concept: it provides explicit interval information in an early estimation phase, in which the alternative would be a point prediction whose uncertainty remains implicit. However, given that the average band width is large (§4), the band in its present form should not be presented as ready for direct use in decision-making without further model refinement. It is more appropriately read as a transparent representation of uncertainty than as a precise prediction tool: methodologically useful, but not yet operationally mature.

The bands reported in §4 are wide. On the full sample ($n = 35$) the average LOO-CV band width at $h = 0.5$ is RSD 52.5 M, roughly 3.58 times the sample mean cost; on the trimmed sample ($n = 32$) it falls to RSD 38.4 M ($\approx 2.96$ times mean cost). These widths reflect the lean predictor set (only road length and predicted parking-space count survive the variation rule of §3.2) and the small sample. The width should be read as a faithful quantification of preliminary-phase uncertainty given the information actually available, not as a result to be hidden. A narrow band on the same lean inputs would be misleading; a wide band is the honest representation.

## 5.3. WHY LOG-COST IS THE DEFENSIBLE HEADLINE MODEL

The original-scale cost model was retained only as a sensitivity result (§4.7) for two reasons documented there. First, the back-transformed centre-prediction performance was poor in percentage terms (MAPE = 239.49% under LOO-CV), driven by very small projects in the denominator. Second, the unconstrained Tanaka LP has no positivity constraint on the lower bound of the band; for several small projects the lower bound of the fitted possibility band fell below zero, which is not meaningful for construction cost. Re-fitting both OLS and Tanaka on log(cost_rsd) and back-transforming centre and bounds by the exponential function addresses both problems. The choice is methodologically justified on four grounds: (i) construction cost in this domain is strictly positive; (ii) the cost distribution in the sample is right-skewed (§4.2), so a multiplicative error structure is more natural than an additive one; (iii) the exponential back-transformation guarantees a strictly positive band (the minimum lower bound

across the 35 LOO folds in §4.4 is RSD 2 022 603, with no fold producing a negative bound); and (iv) the log transformation stabilises MAPE by reducing the leverage of small projects in the denominator (MAPE falls from 239.49% to 97.12% on the full sample). The log-cost model is therefore the headline of the paper; the original-scale model is reported for traceability only and carries no substantive claim.

## 5.4. RELATION TO PEŠKO ET AL. [1, 2]

This paper is positioned as a complementary extension of the Peško research line on preliminary cost and duration estimation of urban-road projects in Novi Sad [1, 2], not as a replacement for its ANN and SVM models. Peško et al. [2] train ANN and SVM models on a richer 12-input feature set drawn from the bill of quantities (material quantities and percentage shares of work groups), with n = 166 projects, and produce point estimates of cost and duration. The present paper uses only four candidate functional parameters known before a bill of quantities exists (and, after the variation check of §3.2, only two of those predictors enter the main model), with n = 35 projects, and produces a possibility band in addition to a point estimate. The two studies therefore address two different phases of the same estimation problem: Peško et al. [2] address detailed pre-contract estimation when bill-of-quantities data are available, while this paper addresses an earlier, functional-parameter-only phase in which the bill of quantities does not yet exist.

For exactly that reason any quantitative comparison between this paper's centre-line MAPE and the ANN/SVM MAPEs reported in Peško et al. [2] is contextual rather than head-to-head: the input regimes differ, the sample sizes differ, and the type of output differs (point estimate versus possibility band). The framing throughout has been that of a complementary extension to a research line that Peško et al. [2] themselves flagged as a future-work direction, estimation "by functional parameters of a future object", and the results of §4 should be read against that framing.

## 5.5. DURATION MODEL AS EXPLORATORY EVIDENCE

The duration model (§4.8) is presented as a secondary, exploratory result rather than as a parallel main result. Three reasons support this framing. First, the statistical signal is weak: OLS adjusted $R^2$ is 0.1665 and neither predictor is significant at the 5% level (road length $p = 0.2420$; parking spaces $p = 0.0868$). Second, the LOO-CV centre errors and the Tanaka band width are large relative to the mean duration (Tanaka MAPE = 63.35%; relative band width 1.505). Third, and substantively most important, Peško et al. [2] explicitly observe that in this domain the offered duration is typically not the result of an independent estimation by the contractor: investors set a maximum duration in the tender conditions, and contractors tend to adopt that maximum value. A model trained on offered duration therefore predicts the offered figure, not an independently estimated realised duration.

The cost model therefore carries the main contribution of the paper, while the duration model shows that the same possibilistic framework can be applied to the duration target but would require either better target data (for example, realised durations alongside offered ones) or a richer set of predictors before it can carry an independent substantive claim.

## 5.6. LIMITATIONS AND METHODOLOGICAL IMPLICATIONS

Seven limitations and methodological caveats inform how the results above should be read:

- Small sample size. With n = 35 the LOO-CV diagnostics are indicative out-of-sample estimates rather than unbiased generalisation errors. The cost model's headline metrics carry the corresponding uncertainty, and the trimmed-sample refit in §4.6 should be read as a robustness check, not as a stronger basis for inference.
- Only two usable numerical predictors. Road length and predicted parking-space count are the only predictors that enter the main model; even within this pair, parking spaces do not provide independent signal in OLS. The wide possibility bands are a faithful consequence of this lean predictor set, not of an arbitrary choice.
- Excluded categorical predictors. Parking type (33 longitudinal / 2 oblique) and parking position (34 one-sided / 1 two-sided) are essentially constant in the sample and were excluded from the main model. They cannot be ruled out as substantively relevant predictors in a larger, more balanced sample, but in this sample they cannot be tested.
- Sensitivity to influential observations. Three records (ids 2, 17, 35) were flagged in the OLS diagnostics of §3.6. Trimming them tightens both OLS and the Tanaka band (for example, the Tanaka relative band width falls from 3.578 to 2.957) without changing the qualitative picture. The full-sample fit remains the headline; the trimmed fit documents the sensitivity transparently rather than removing it silently [10].
- The Tanaka centre line is not a least-squares trend. The LP minimises total fuzziness, not squared error, and the fitted centre vector can differ in sign from the OLS coefficients (the centre-line caveat of §3.4). In this paper, OLS is used for direction-of-effect interpretation and the Tanaka model is used to obtain the band; the Tanaka centre coefficients in Table 5 should not be read as effect estimates.
- h-level invariance is a structural property of the basic Tanaka LP formulation. The invariance of the back-transformed bands across $h \in \{0, 0.25, 0.5, 0.75\}$ reported in §4.5 is not specific to the present sample; it is a consequence of the structure of the basic Tanaka LP formulation: the coefficient spreads rescale by the factor $1/(1 - h)$, which cancels the $(1 - h)$ factor in the band half-width. The flat sensitivity profile across h should therefore be read as a structural property of the adopted formulation, not as evidence of empirical robustness across substantively different bands; the check across h-levels is retained as a transparency demonstration. More generally, the h-dependence of fitted Tanaka models is a known and well-discussed property of the family [9].
- Geographical and contractual scope. The dataset is drawn from urban-road projects in a single municipality (Novi Sad) and uses contractor-offered, revalorised prices in RSD. Transferability of the centre coefficients or the band widths to other cities, to highway-scale projects, or to projects under different contracting regimes is not demonstrated here and should not be assumed.

## 5.7. IMPLICATIONS FOR FURTHER WORK

Four directions are well aligned with both the empirical limitations of §5.6 and the structure of the Peško research line:

- Enlarging the dataset. A larger sample drawn from the same Novi Sad portfolio (or, if available, from comparable Serbian municipalities) could tighten the bands, could allow stricter cross-validation, and could re-open the question of which categorical predictors can be tested at meaningful balance.
- Adding further functional parameters. Peško et al. [2] explicitly flagged the introduction of additional functional parameters of the future object (roadway width, urban-road category (boulevard, side alley, …), cycling-lane length,

pedestrian-lane areas, and plateau areas) as a natural next step. Each of these is, in principle, available at the same early stage as the predictors used here, and each could narrow the bands meaningfully.

- Robust and alternative fuzzy-regression formulations. The outlier sensitivity of the basic Tanaka LP can be addressed using the outlier-omission approach of Hung and Yang [10] or one of the weighted / least-absolute-deviation reformulations in the wider fuzzy-regression literature. Such variants could, on this kind of dataset, target the band-width inflation observed in §4 directly.
- Integration with existing point-prediction models. The most natural integration with the Peško research line is to keep ANN or SVM as the point-prediction engine where bill-of-quantities data are available [2] and to add a Tanaka possibility band over the same projects to communicate phase-appropriate uncertainty. Any such integration would require either a matched-input experimental setting (in which all models are trained on the same predictor regime and the same project sample) or a deliberately designed hybrid workflow in which each model is used at the estimation phase appropriate to its inputs. Without one of those two designs, the comparison would not be head-to-head and should not be presented as such; this also clarifies that no head-to-head comparison with the ANN/SVM results of Peško et al. [2] is performed in this paper or implied by this future-work direction. Such a hybrid is outside the scope of the present paper but is a defensible next step that uses both methodological lines for what each does best.

## 6. CONCLUSIONS AND FURTHER WORK

This paper examined the applicability of Tanaka-type possibilistic linear regression to the early-stage estimation of cost and duration of urban-road construction projects. It is positioned as a complementary extension of the Peško et al. research line on the same domain [1, 2]: where the earlier studies fit ANN and SVM models to detailed bill-of-quantities inputs and produced point estimates, the present paper fits OLS and Tanaka models to a small set of functional project parameters that are known before a bill of quantities exists, and produces an interval-based possibility output in addition to a point estimate. The empirical case used 35 urban-road projects from the Novi Sad domain, made available through the Peško research line, with road length and predicted parking-space count as the two surviving numerical predictors after the variation rule of §3.2.

The headline result of the paper is the Tanaka possibilistic linear regression fitted on log(cost_rsd) and back-transformed to RSD. On centre-prediction accuracy OLS performed better than the Tanaka model on every reported metric under leave-one-out cross-validation; the paper does not claim that Tanaka delivers superior point accuracy. The substantive contribution of the Tanaka model is the h-level possibility band that OLS does not provide, presented here at h = 0.5 as the headline level and supported by an h-level sensitivity diagnostic. The log-cost formulation eliminated the negative-lower-bound artefact of the unconstrained original-scale Tanaka model and stabilised the percentage-error metric on small projects; the original-scale model is retained only as a sensitivity result. The fitted bands remain wide, a faithful reflection of the limited information that is available in the early estimation phase, not a result to be hidden.

The duration model is reported as a secondary, exploratory result. Offered duration is a weaker target than offered price in this domain because, as Peško et al. [2] note, contractors tend to adopt the maximum duration set by the investor in the tender conditions rather than producing an independent estimate; the duration model therefore predicts the offered figure rather than an independently estimated realised duration. The main limitations of the empirical work are the small sample size (n = 35), the lean

predictor set (only two numerical predictors enter the main model), the heavily imbalanced categorical predictors that had to be excluded, the sensitivity of both OLS and the Tanaka band to a small number of influential observations, and the single-municipality (Novi Sad) scope of the dataset, which limits transferability to other cities or to highway-scale projects.

Four directions for further work follow naturally from these limitations. First, the dataset could be enlarged, ideally from the same Novi Sad portfolio or from comparable Serbian municipalities, to permit stricter cross-validation and to re-test the categorical predictors at a more balanced distribution. Second, the predictor set could be enriched with additional functional parameters explicitly flagged in Peško et al. [2] (road width, urban-road category, cycling-lane length, pedestrian-lane areas, and plateau areas), each of which is, in principle, available at the same early stage as the predictors used here. Third, robust or alternative fuzzy-regression formulations could be tested, including the outlier-omission approach of Hung and Yang [10] and the weighted or least-absolute-deviation reformulations in the wider fuzzy-regression literature. Fourth, future integration with ANN or SVM point-prediction models should be undertaken only in a matched-input experimental setting, in which all models are trained on the same predictors and the same project sample, or in a deliberately designed hybrid workflow in which each method is used at the estimation phase appropriate to its inputs; without one of these two designs, the comparison would not be head-to-head and should not be presented as such.

Within the scope demonstrated here, possibility bands of the Tanaka type are best understood not as a substitute for established point-prediction models, but as an interval-based companion to them, a transparent way to attach phase-appropriate uncertainty to early-stage cost estimation in urban-road construction.

## 7. REFERENCES

[1] Peško I., Trivunić M., Ćirović G., Mučenski V. (2013). A preliminary estimate of time and cost in urban road construction using neural networks. Tehnički Vjesnik 20(3): 563–570.

[2] Peško I., Mučenski V., Šešlija M., Radović N., Vujkov A., Bibić D., Krklješ M. (2017). Estimation of costs and durations of construction of urban roads using ANN and SVM. Complexity 2017, Article 2450370, 13 pp. DOI: 10.1155/2017/2450370.

[3] Barakchi M., Torp O., Belay A.M. (2017). Cost estimation methods for transport infrastructure: a systematic literature review. Procedia Engineering 196: 270–277. DOI: 10.1016/j.proeng.2017.07.199.

[4] Elmousalami H.H. (2020). Artificial intelligence and parametric construction cost estimate modeling: state-of-the-art review. Journal of Construction Engineering and Management 146(1): 03119008. DOI: 10.1061/(ASCE)CO.1943-7862.0001678.

[5] Tanaka H. (1987). Fuzzy data analysis by possibilistic linear models. Fuzzy Sets and Systems 24: 363–375.

[6] Tanaka H., Watada J. (1988). Possibilistic linear systems and their application to the linear regression model. Fuzzy Sets and Systems 27: 275–289.

[7] Tanaka H., Uejima S., Asai K. (1982). Linear regression analysis with fuzzy model. IEEE Transactions on Systems, Man, and Cybernetics SMC-12(6): 903–907.

[8] Tanaka H., Hayashi I., Watada J. (1989). Possibilistic linear regression analysis for fuzzy data. European Journal of Operational Research 40: 389–396.

[9] Redden D.T., Woodall W.H. (1994). Properties of certain fuzzy linear regression methods. Fuzzy Sets and Systems 64: 361–375.

[10] Hung W.-L., Yang M.-S. (2006). An omission approach for detecting outliers in fuzzy regression models. Fuzzy Sets and Systems 157: 3109–3122.

[11] Chang Y.-H.O., Ayyub B.M. (2001). Fuzzy regression methods — a comparative assessment. Fuzzy Sets and Systems 119: 187–203.

[12] Chang N.-B., Chen Y.L., Yang H.H. (1996). A fuzzy goal regression model for the construction cost estimation of municipal waste incinerators. International Journal of Systems Science 27(5): 433–445. DOI: 10.1080/00207729608929235.

[13] Chang N.-B., Chen Y.L., Chen H.W. (1997). A fuzzy regression analysis for the construction cost estimation of wastewater treatment plants (I) theoretical development. Journal of Environmental Science and Health Part A 32(4): 885–899. DOI: 10.1080/10934529709376584.

[14] Hassim S., Muniandy R., Alias A.H., Abdullah P. (2018). Construction tender price estimation standardization (TPES) in Malaysia: modeling using fuzzy neural network. Engineering, Construction and Architectural Management. DOI: 10.1108/ECAM-09-2016-0215.

[15] Cheng M.-Y., Tsai H.-C., Hsieh W.-S. (2009). Web-based conceptual cost estimates for construction projects using evolutionary fuzzy neural inference model. Automation in Construction 18(2): 164–172.

[16] Yu W.-D., Skibniewski M.J. (2010). Integrating neurofuzzy system with conceptual cost estimation to discover cost-related knowledge from residential construction projects. Journal of Computing in Civil Engineering, ASCE, 24(1): 35–44. DOI: 10.1061/(ASCE)0887-3801(2010)24:1(35).

[17] Wang W.-C., Bilozerov T., Dzeng R.-J., Hsiao F.-Y., Wang K.-C. (2017). Conceptual cost estimations using neuro-fuzzy and multi-factor evaluation methods for building projects. Journal of Civil Engineering and Management 23(1): 1–14.

[18] Najaf P., Famili S. (2013). Application of an intelligent fuzzy regression algorithm in road freight transportation modelling. Promet — Traffic & Transportation 25(4): 311–322.

[19] Pan N.-F., Wang H., Yang M.-D., Hsu K.-C. (2008). Estimates of bridge girder conditions based on fuzzy inspection data. In: Proceedings of the Fifth International Conference on Fuzzy Systems and Knowledge Discovery (FSKD 2008), Jinan, China, 18–20 October 2008, IEEE.

[20] Wang H., Pan N.-F. (2008). A fuzzy regression model for predicting non-crisp variable. In: Proceedings of the Fifth International Conference on Fuzzy Systems and Knowledge Discovery (FSKD 2008), Jinan, China, 18–20 October 2008, IEEE.

[21] Hashemi S.T., Ebadati O.M., Kaur H. (2020). Cost estimation and prediction in construction projects: a systematic review on machine learning techniques. SN Applied Sciences 2: 1703. DOI: 10.1007/s42452-020-03497-1.

https://doi.org/10.24867/INDIS-2026-EN-181



# TECHNO-ECONOMIC ASSESSMENT OF DREDGED SEDIMENT IN ROAD INFRASTRUCTURE

*Dragana Tomašević Pilipović[1], Miloš Šešlija[2], Panta Krstić[3], Nataša Slijepčević[4], Dunja Rađenović Veselić[5]*

***Summary:***

Maintenance dredging of inland waterways is critical for sustaining channel flow and navigational depth. While global circular practices reuse up to 90% of dredged sediments, standard practice in Serbia relies exclusively on landfilling. This study presents a comparative techno-economic assessment of utilizing dredged river sediment as an alternative subbase material for cycling path infrastructure versus conventional sand replacement and direct landfill disposal. A two-tier cost model was established using standardized unit rates. On a macro-management level, valorising 1,000 m³ of sediment into cycling paths requires €30,813.58 compared to €39,808.07 for landfill disposal, achieving an immediate saving of 22.6%. On a linear construction level, stabilized sediment for a 2.50 m wide track reduces total costs a 30.4% net saving, driven by a 69.9% reduction in earthwork expenses. Reusing dredged sediment resolves critical siltation bottlenecks and conserves virgin aggregates.

*Keywords: Sediment, Circular economy, Techno-economic analysis, Road infrastructure, Cost estimation*

# TEHNO-EKONOMSKA PROCENA PRIMENE SEDIMENTA U PUTNOJ INFRASTRUKTURI

***Rezime:***

Redovno izmuljivanje plovnih puteva ključno je za održavanje proticajnog profila i dubine kanala. Dok se u svetu ponovo iskoristi do 90% izmuljenog sedimenta, u Srbiji se praksa isključivo oslanja na deponovanje. Ovaj rad daje uporednu tehno-ekonomsku procenu primene izmuljenog sedimenta za donji sloj biciklističkih staza u odnosu na zamenu tla peskom i odlaganje na deponiju. Razvijen je dvostepeni model troškova prema standardnim jediničnim cenama. Na makro nivou, valorizacija 1.000 m³ sedimenta u telu staze košta 30.813,58 € u poređenju sa 39.808,07 € za deponovanje, uz uštedu od 22,6%. Na nivou staze širine 2,50 m, stabilizovani sediment smanjuje ukupnu cenu izgradnje uz neto uštedu od 30,4%, zahvaljujući smanjenju troškova zemljanih radova za 69,9%. Ponovna upotreba sedimenta rešava problem taloženja i štedi primarne agregate.

*Ključne reči: Sediment, Cirkularna ekonomija, Tehno-ekonomska analiza, Putna infrastruktura, Analiza troškova*

[1] Full Professor, Faculty of Sciences, University of Novi Sad, dragana.tomasevic@dh.uns.ac.rs, ORCID 0000-0002-8275-3297
[2] Associate Professor, Faculty of Technical Sciences, University of Novi Sad, Novi Sad, Serbia, sele@uns.ac.rs, ORCID 0000-0002-8857-8952
[3] Teaching Assistant, Department of Civil Engineering and Geodesy – Faculty of Technical Sciences, University of Novi Sad, Serbia, panta.krstic@uns.ac.rs , ORCID 0000-0001-5519-391X
[4] Research Associate, Faculty of Sciences, University of Novi Sad, natasa.slijepcevic@dh.uns.ac.rs, ORCID 0000-0002-3866-1205
[5] Research Associate, Faculty of Sciences, University of Novi Sad, dunja.radjenovic@dh.uns.ac.rs, ORCID 0000-0002-6862-4691

## 1. INTRODUCTION

Sediment dredging is an indispensable hydrological and civil engineering intervention required for the maintenance and development of inland waterways, navigation canals, ports, and flood mitigation corridors [1, 2]. Globally, dredging operations extract hundreds of millions of cubic meters of mineral sediment each year. In certain European Union countries alone, dredging yields approximately 200 million tons of sediment annually [3, 4]. Traditionally, dredged materials have been classified and treated as problematic waste streams. Due to fine grain sizing, organic matter presence, and elevated moisture content, common historical management has relied almost exclusively on landfill disposal or confined disposal facilities (CDFs). However, the continuous disposal of large sediment volumes is increasingly constrained by escalating tipping fees, stringent land-use planning regulations, and high environmental protection standards [5].

Under modern circular economy principles, the new EU Circular Economy Action Plan [6], the European Green Deal, and Green Public Procurement guidelines [7, 8], dredged sediment is increasingly recognized as a valuable secondary mineral resource rather than a waste requiring permanent containment [3, 9]. At a global level, beneficial sediment reuse has reached high maturity across numerous economies: the Netherlands beneficially reuses 80–90% of its dredged sediment, China valorizes 60–70%, Japan 50–60%, France and South Korea 40–50%, and the United Kingdom and Australia 30–40% [4, 5]. In contrast, beneficial sediment valorization remains largely undeveloped in the Republic of Serbia, where public utility enterprises and water management authorities continue to rely exclusively on landfilling.

In the Autonomous Province of Vojvodina (Serbia), the regional canal network (the Danube-Tisa-Danube - DTD system) spans over 960 km of artificial waterways. Maintaining standard hydraulic design profiles across this network requires dredging an estimated 1,765,000 $m^3$/year (or ~1.0 million tons of dry matter/year). However, due to significant budgetary constraints, disposal limitations, and logistical challenges, actual dredging output is limited to approximately 300,000 $m^3$/year (~410,000 t dry matter/year). Regional sediments typically comprise 20–50% clay, 2–30% sand, and up to 3% gravel. Repurposing these accumulated sediments as alternative embankment and subgrade materials in transport infrastructure—specifically recreational cycling paths along canal banks—presents an exceptional circular engineering opportunity. Such initiatives directly support the United Nations Sustainable Development Goals (SDGs), notably SDG 9 (Resilient Infrastructure), SDG 11 (Sustainable Cities), and SDG 12 (Responsible Consumption and Production) [10], while significantly reducing construction material carbon footprints and conserving virgin mineral resources [11, 12].

This paper presents a techno-economic feasibility study evaluating the beneficial use of dredged sediment in cycling path construction compared to conventional natural sand replacement and direct landfill disposal. The study establishes a two-tier cost estimation model (in Euros) based on detailed bills of quantities and real-world construction market data.

## 2. METHODOLOGY AND COST ESTIMATION FRAMEWORK

### 2.1 Infrastructure Profile and Cross-Section Design

To establish an engineering and economic comparison, a standardized cycling path cross-section was designed along an active waterway embankment crown. A comparative overview of the embankment and pavement cross-sections is presented in Fig. 1, showing the beneficial use of stabilized dredged sediment (Fig. 1a) alongside the conventional

sand replacement approach (Fig. 1b).The cross-section geometry comprises an overall embankment crown width of 3.00 m, an effective paved cycling track width of 2.50 m, lateral berms of 0.80 m, and embankment side slopes of 1:2. The comparative engineering model evaluated two structural foundation options for the 40 cm subgrade layer:

- Option A (Beneficial Sediment Use): In-situ stabilization of dredged river sediment using hydraulic road binders at an engineered layer thickness of d = 40 cm.
- Option B (Conventional Construction): Complete excavation of the weak subgrade and replacement with imported commercial natural sand compacted at an equivalent layer thickness of d = 40 cm.

The upper pavement structure for both options was designed according to European and Serbian road engineering standards for asphalt and unbound road courses [13, 14], consisting of:

- Wearing course: 4 cm Asphalt Concrete AC 11 with bitumen BIT 50/70;
- Bituminized base layer: 6 cm Bituminized Base Layer BBL 22sA (BBL 22A) with BIT 50/70;
- Unbound crushed stone base: 20 cm crushed stone aggregate fraction 0/31.5 mm (DKA 0/31.5 mm), compacted to achieve a minimum modulus $E_{v2} \geq 70$ MPa;
- Slope protection: 20 cm topsoil spreading (humification) and hydroseeding on embankment flanks.

a)

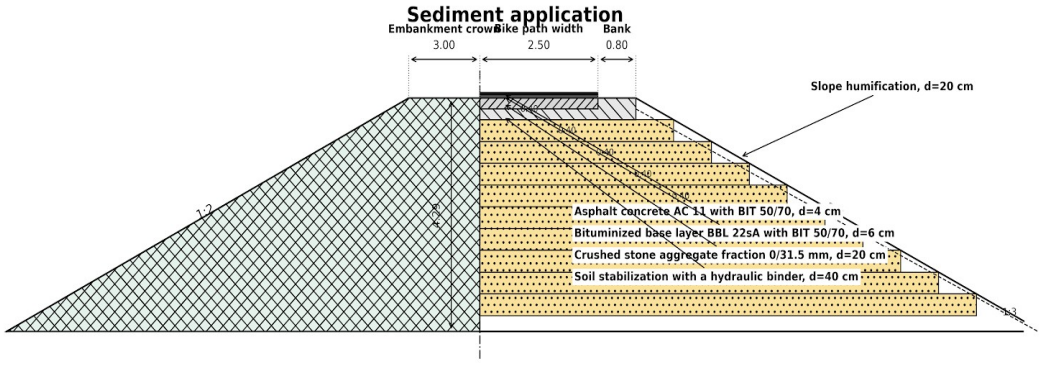


b)

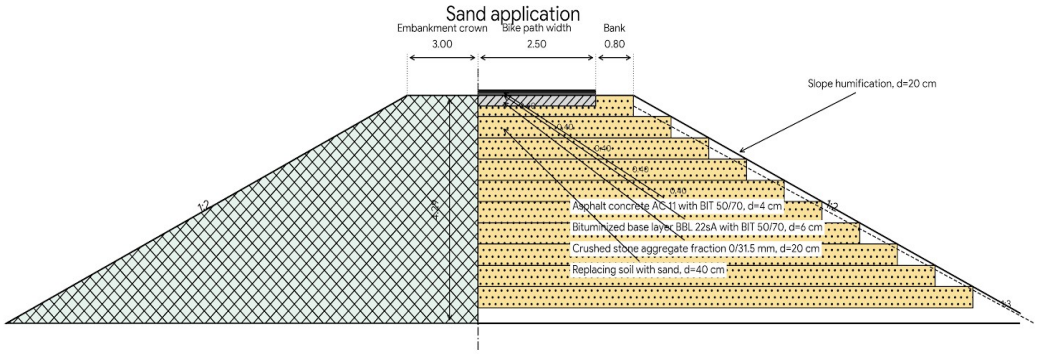


*Fig. 1 Comparative cross-sectional layout of the cycling path embankment: (a) beneficial use of stabilized dredged sediment; (b) conventional sand replacement*

### 2.2 Two-Tier Techno-Economic Evaluation Framework

The financial feasibility is evaluated using a cost estimation framework structured into two analytical tiers:

- Macro-Management Tier: Evaluation of the total differential costs for managing a standardized batch of 1,000 m³ of dredged sediment via direct Landfill Disposal versus Beneficial Reuse in cycling path construction.
- Linear Construction Tier: Direct unit cost comparison per linear meter (€/m) for a 2.50 m wide cycling path, comparing stabilized sediment against conventional sand across three standard construction phases: I. Preparatory Works, II. Earthworks, and III. Pavement Superstructure.

## 3. RESULTS AND ECONOMIC EVALUATION

### 3.1 Macro-Level Cost Comparison (1,000 m³ Sediment Management)

The macro-level analysis compares the total expenditure of disposing 1,000 m³ of dredged sediment in a regulated landfill against utilizing the same volume for local infrastructure development. Landfill disposal involves hauling to a landfill site, tipping fees, and site containment earthworks. In contrast, beneficial use integrates the material directly into the embankment subgrade.

As summarized in Table 1, landfill disposal of 1,000 m³ of dredged sediment incurs an estimated total cost of €39,808.07. Conversely, beneficial utilization of the same volume for cycling path construction requires €30,813.58. This results in an immediate direct financial saving of €8,994.49 per 1,000 m³ (a 22.6% reduction). Beyond capital cost savings, the beneficial reuse option creates a tangible community asset (recreational cycling infrastructure) while avoiding the consumption of municipal landfill space [4].

*Tab. 1 Macro-economic cost comparison for 1,000 m³ of dredged sediment management*

| Sediment Management Option | Volume [m³] | Total Cost [EUR] | Financial Balance [EUR] |
|---|---|---|---|
| Landfill Disposal (Landfilling) | 1,000 | €39,808.07 | Baseline Option |
| Beneficial Reuse (Cycling Path) | 1,000 | €30,813.58 | - €8,994.49 (-22.6%) |

### 3.2 Detailed Analysis per Linear Meter

To determine the exact cost drivers at the construction stage, Table 2 details the unit costs per linear meter of cycling path (width 2.50 m) comparing the sediment option against conventional sand replacement.

*Tab. 2 Comparative unit cost analysis per linear meter of cycling path*

| No. | Construction Work Phase | Sediment [EUR/m] | Natural Sand [EUR/m] | |
|---|---|---|---|---|
| I | Preparatory Works (geodetic marking, bush clearing) | €24.53 | €24.53 | |
| II | Earthworks & Subgrade (excavation, fill, grading) | €68.88 | €228.91 | |
| III | Pavement Superstructure (stabilization/sand, DKA, asphalt) | €127.52 | €64.17 | |
| | **Total construction cost per meter** | **€220.93** | **€317.61** | |
| | **Net Financial Saving per Linear Meter** | **-** | **-** | **€96.68 / m (30.4%)** |

A granular examination of the three construction phases reveals distinct financial trade-offs:

- Phase I - Preparatory Works (€24.53/m): Geodetic site alignment, stakeout, and mechanical bush/vegetation clearing are identical for both construction variants.
- Phase II - Earthworks and Subgrade (€68.88/m vs. €228.91/m): Utilizing dredged sediment produces a 69.9% cost reduction (€160.03/m saving). In conventional construction, procuring, hauling, and compacting 8.86 $m^3$/m of natural sand accounts for €173.87/m alone. Utilizing locally available dredged sediment completely eliminates commercial aggregate purchasing costs.
- Phase III - Pavement Superstructure (€127.52/m vs. €64.17/m): The sediment option exhibits higher superstructure costs due to the need for specialized in-situ stabilization machinery (soil recycler/stabilizer train with pressurized water injection) and hydraulic binder acquisition (€63.35/m). However, this increase is outweighed by the earthwork savings.
- Net Economic Balance (€220.93/m vs. €317.61/m): Overall, incorporating dredged sediment achieves a net financial saving of €96.68 per linear meter (a 30.4% total project cost reduction).

## 4. ENVIRONMENTAL AND SOCIO-ECONOMIC CO-BENEFITS

Beyond direct construction savings, valorizing dredged sediment establishes a closed-loop circular model that yields multidisciplinary benefits. To evaluate the broader sustainability impact, a comparative matrix benchmarked conventional landfill disposal against beneficial reuse in cycling path infrastructure (Tab. 3). The analysis demonstrates that repurposing local sediment simultaneously eliminates quarry extraction pressures, reduces heavy transport GHG emissions, and mitigates waterway flood risks while delivering valuable recreational assets for the local community [6, 7, 10, 11, 12].

*Tab. 3 Multidisciplinary sustainability impact matrix: landfill disposal vs. beneficial sediment reuse*

| Sustainability Dimension | Conventional Practice (Landfill Disposal) | Circular Valorization (Cycling Path Subbase) | Environmental and Socio-Economic Impact |
|---|---|---|---|
| Hydrological and Flood Control | Dredged sediment is relocated to land; risk of back-siltation remains high. | Regular desiltation deepens the bed, raises flow velocity, and lowers flood risk. | **Positive:** Mitigates waterway flooding and enhances discharge capacity. |
| Virgin Material Depletion | High demand for primary sand extraction from natural riverbeds/quarries. | 100% of subgrade sand replacement is substituted with stabilized local sediment. | **Positive:** Conserves scarce natural mineral resources. |
| Transport and GHG Emissions | Long haulage distances to designated landfills (>15 km). | Material is utilized in-situ directly along the canal embankment crown. | **Positive:** Substantial decrease in transport fuel and heavy vehicle $CO_2$ emissions. |
| Land and Waste Management | Consumes municipal landfill capacity; potential long-term liability. | Zero landfilling; sediment is safely bound into a stable structural asset. | **Positive:** Preserves landfill space and supports EU Green Deal targets. |
| Community and Eco-Tourism | No public utility or economic return generated for local community. | Delivers multi-functional recreational infrastructure along waterways. | **Positive:** Promotes active mobility, public health, and local tourism. |

## 5. CONCLUSIONS

This study validates the techno-economic viability of replacing linear sediment disposal with circular valorization in transport infrastructure. The main findings are:

- On a macro-management tier, valorizing 1,000 m³ of dredged sediment for cycling path construction costs €30,813.58 compared to €39,808.07 for landfill disposal, yielding an immediate direct saving of 22.6% (€8,994.49) while avoiding the consumption of municipal landfill volume.
- On a linear construction tier, stabilized sediment construction costs €220.93/m compared to €317.61/m for conventional natural sand construction—a net saving of €96.68/m (30.4%), driven by a ~70% reduction in earthwork and aggregate haulage expenses.
- The higher unit cost of in-situ hydraulic stabilization (€127.52/m vs. €64.17/m) is heavily compensated by the complete elimination of commercial sand purchase and long-haul transport (€68.88/m vs. €228.91/m).
- Beneficial sediment reuse resolves waterway siltation bottlenecks, lowers primary aggregate extraction pressure, and provides a sustainable construction model for transport infrastructure in Serbia and the broader region.

## ACKNOWLEDGEMENT

The authors gratefully acknowledge the financial support of the Ministry of Science, Technological Development and Innovation of the Republic of Serbia (Grants No. 451-03-137/2025-03/200125 and 451-03-136/2025-03/200125).

## REFERENCES

[1] CEDA (2019a). Assessing the Benefits of Using of Contaminated Sediments. Central Dredging Association Position Paper. https://www.ecoshape.org/app/uploads/sites/2/2019/07/2019-05-BUSC-pp.pdf

[2] Suedel B.C., McQueen A.D., Wilkens J.L., Saltus C.L., Bourne S.G., Gailani J.Z., King J.K., Corbino J.M. (2022). Beneficial use of dredged sediment as a sustainable practice for restoring coastal marsh habitat. Integrated Environmental Assessment and Management, Volume 18, pp. 1162–1173. https://doi.org/10.1002/ieam.4501

[3] CEDA (2019b). Sustainable Management of the Beneficial Use of Sediments. Central Dredging Association Information Paper. https://dredging.org/media/ceda/org/documents/ceda/2019-05-bus-ip.pdf

[4] Wijdeveld A., Lemière B., Coftier A. et al. (2024). Beneficial use of sediments, tools, pilot sites and measuring techniques developed and used within seven European Union INTERREG projects. Journal of Soils and Sediments, Volume 24, pp. 1500–1516. https://doi.org/10.1007/s11368-024-03811-z

[5] Yang H., Feng Q., Zhu J., Liu G., Dai Y., Zhou Q., Xia S., Wu Z., Zhang Y. (2024). Towards sustainable futures: A review of sediment remediation and resource valorization techniques. Journal of Cleaner Production, Volume 435, 140529. https://doi.org/10.1016/j.jclepro.2023.140529

[6] European Commission (2020). A new Circular Economy Action Plan: For a cleaner and more competitive Europe. Communication from the Commission to the European Parliament, the Council, the European Economic and Social Committee and the Committee of the Regions, COM(2020) 98 final. https://eur-lex.europa.eu/legal-content/EN/TXT/HTML/?uri=CELEX:52020DC0098

[7] European Commission (2016). Criteria for Green Public Procurement for the Design, Construction and Maintenance of Roads. Procurement practice guidance document, EUR 28028 EN. https://doi.org/10.2791/201271

[8] Garbarino E., Rodriguez Quintero R., Donatello S., Wolf O. (2016). Revision of Green Public Criteria for Road Design, Construction and Maintenance. JRC Technical Reports, EUR 28028 EN.

[9] Almokdad M., Zentar R. (2023). Characterization of recycled dredged sediments: Toward circular economy in road construction. Construction and Building Materials, Volume 402, 132974. https://doi.org/10.1016/j.conbuildmat.2023.132974

[10] United Nations (2019). The Sustainable Development Goals Report 2019. United Nations Department of Economic and Social Affairs, New York, USA. https://unstats.un.org/sdgs/report/2019/The-Sustainable-Development-Goals-Report-2019.pdf

[11] United Nations Environment Programme (UNEP) & Yale Center for Ecosystems + Architecture (2023). Building Materials and the Climate: Constructing a New Future. UNEP, Nairobi, Kenya. https://wedocs.unep.org/items/effe9d8d-a949-4397-bed6-7afda856e261

[12] Rađenović Veselić D., Slijepčević N., Tenodi S., Pejin Đ., Jevrosimov I., Marjanović Srebro T., Tomašević Pilipović D. (2025). From sink to strategy: Sediments at the nexus of carbon sequestration and climate action. Earth-Science Reviews, Volume 271, 105310. https://doi.org/10.1016/j.earscirev.2025.105310

[13] CEN (2016). EN 13108-1: Bituminous mixtures - Material specifications - Part 1: Asphalt Concrete. European Committee for Standardization, Brussels, Belgium.

[14] CEN (2013). EN 13242: Aggregates for unbound and hydraulically bound materials for use in civil engineering work and road construction. European Committee for Standardization, Brussels, Belgium.

https://doi.org/10.24867/INDIS-2026-EN-188



# CIRCULAR ECONOMY ASSESSMENT OF TRAFFIC NOISE BARRIERS IN ROAD INFRASTRUCTURE

*Nermin Palić[1], Meri Cvetkovska[2], Milica Jovanoska-Mitrevska[3], Mirzo Selimić[4]*

***Abstract***

Traffic noise barriers are conventionally designed and procured as single-purpose acoustic infrastructure, with material selection driven primarily by sound-reduction performance, cost and structural durability, while end-of-life management receives comparatively little attention at the design stage. This paper examines traffic noise barriers through the lens of the circular economy, treating them not only as noise-mitigation devices but as material stocks circulating, or failing to circulate, within the built environment. Drawing on published life-cycle assessment (LCA) studies, embodied-energy data and recent applied research, including the use of decommissioned wind-turbine blade composites in noise barrier construction, the paper reviews the principal barrier typologies in use today, concrete, steel and aluminium panels, transparent acrylic and glass, timber, composite and green/vegetated terraced systems, and evaluates each against four circularity-relevant criteria: recyclability of constituent materials, embodied energy and carbon, feasibility of reuse or material recovery, and realistic end-of-life pathways. The analysis shows that current practice remains predominantly linear: concrete and acrylic systems, although acoustically effective, present the most limited circular pathways, typically ending in downcycling or landfill, whereas aluminium, modular steel and selected composite-reuse systems offer substantially higher recovery potential due to established scrap markets and the comparatively low energy cost of secondary processing. The paper further argues that design for disassembly, principles already established in building construction, ranging from reversible mechanical connections to modular panel systems, can be transferred to noise barrier design with limited additional cost, and proposes a four-stage circular economy assessment framework for transport noise barriers covering material selection, design for disassembly, end-of-life routing and procurement criteria. The paper concludes with recommendations for embedding circularity indicators into public procurement specifications for road and rail noise mitigation infrastructure, positioning circular barrier design as a measurable contribution to broader sustainable transport infrastructure targets.

*Keywords: Traffic noise barriers; circular economy; life cycle assessment; design for disassembly; recycling; road infrastructure.*

[1] *Assistant Professor, University College „CEPS-Center for Business Studies“, Kiseljak, Bosnia and Herzegovina, nermin.palic@ceps.edu.ba, https://orcid.org/0000-0001-8839-4910*
[2] *Professor Doctor, Ss. Cyril and Methodius University in Skopje, Faculty of Civil Engineering, Skpoje, N. Macedonia, cvetkovska@gf.ukim.edu.mk, https://orcid.org/0000-0002-9155-6420*
[3] *Professor Doctor, Ss. Cyril and Methodius University in Skopje, Faculty of Civil Engineering, Skpoje, N. Macedonia, m.jovanoska@gf.ukim.edu.mk, https://orcid.org/0009-0001-2273-5062*
[4] *Assistant Professor, University College „CEPS-Center for Business Studies“, Kiseljak, Bosnia and Herzegovina, mirzo.selimic@ceps.edu.ba, https://orcid.org/0000-0003-0267-9670*

## 1. INTRODUCTION

Road and rail traffic noise barriers are widely deployed obstacles placed between noise sources and receivers, such as residential areas or sensitive facilities, and are generally regarded as the most effective engineering solution for noise propagation where space for vegetation belts or earth embankments is unavailable [1]. Acoustic effectiveness depends on barrier material, height, length, placement and shape, while non-acoustic considerations, including visual impact, safety, maintenance access and air quality in fully enclosed sections, must be balanced against the acoustic design [1]. Figure 1 illustrates the basic acoustic mechanism through which a barrier interrupts the direct sound path, creating a shadow zone at the receiver while generating reflection, diffraction and partial transmission components.

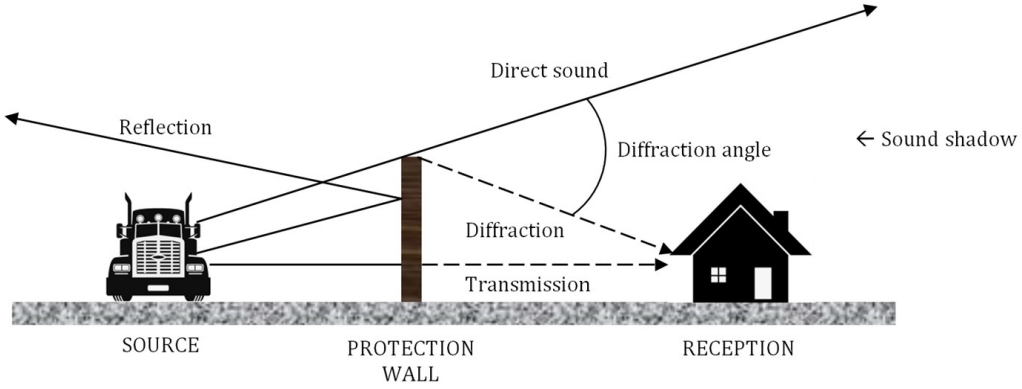


*Figure 1. Acoustic mechanism of a noise barrier: direct sound, reflection, diffraction and transmission [2]*

While the acoustic design of noise barriers is well established in engineering practice and standards, the materials used to build them are rarely evaluated against circularity criteria at the procurement stage. Global infrastructure expansion and the renewal of ageing barrier stock installed decades ago mean that growing volumes of barrier material will reach end-of-life in the coming years, making the choice between landfill, downcycling, material recovery and reuse an increasingly material question for transport agencies. This paper applies a circular economy perspective to traffic noise barriers, asking how circular current systems are, which materials offer the greatest potential for reuse and recycling, and how design for disassembly can be integrated into barrier construction without compromising acoustic performance.

## 2. NOISE BARRIER TYPOLOGIES AND MATERIALS

Noise barrier construction materials include reinforced concrete, plain concrete, brick, stone, wood, aluminum, glass, transparent plastic and various composite constructions. Figure 2 illustrates the comparative acoustic performance commonly cited for different wall materials and thicknesses, ranging from approximately 60 dB for a 1.0 m gabion wall to 17 dB for thin corrugated iron, demonstrating that material choice has a direct and substantial effect on acoustic outcomes, independent of any circularity considerations [3].




*Figure 2. Indicative noise reduction by barrier material and thickness [3]*

Beyond solid panel systems, terraced and vegetated barriers, typically constructed from reinforced concrete, metal or recycled prefabricated structural modules filled with soil and planted with shrubs or creepers, combine acoustic and visual screening with ecological co-benefits such as biodiversity support, stormwater attenuation and a degree of carbon sequestration in the substrate [1]. Figure 3 shows a terraced green barrier in which a modular shell supports vegetated growing chambers; the structural shell can in principle be disassembled and the modules reused or relocated, while the substrate and vegetation re-enter the local landscape cycle independently of the panel material.

A further multifunctional variant integrates photovoltaic panels into the barrier structure itself, converting a single-purpose acoustic asset into a combined noise-mitigation and renewable-energy installation, as shown in Figure 4 for a barrier section along an Alpine motorway. Such systems do not by themselves resolve end-of-life material questions, since the supporting structure is typically aluminum or steel and the panels contain their own embedded materials, but they illustrate that the functional life of barrier infrastructure can be extended in value terms even where the physical material stock remains unchanged.



*Figure 3. Terraced/vegetated noise barrier with modular planted chambers [4] and Figure 4. Photovoltaic-integrated noise barrier on a motorway embankment [5]*

## 3. LIFE-CYCLE AND CIRCULARITY EVIDENCE FROM THE LITERATURE

### 3.1. LIFE-CYCLE ASSESSMENT OF BARRIER MATERIALS

Life-cycle assessment (LCA) studies of noise barriers remain comparatively scarce relative to the broader pavement and structural-materials literature, but available evidence indicates substantial differences between conventional and alternative mix designs. A life-cycle assessment of a low-height noise barrier for railway traffic compared a baseline precast Portland cement concrete design against precast and additively manufactured geopolymer composite alternatives across global warming potential, fossil depletion, photochemical ozone formation and acidification impact categories [6]. Over a fixed 40-year service life, the most advanced additive-manufactured geopolymer alternative

achieved a 73% reduction in global warming potential relative to the conventional concrete baseline, with the advantage persisting across a sensitivity analysis varying assumed service life between 10 and 40 years [6]. This finding indicates that within a single barrier typology, conventional concrete, the choice of binder chemistry and manufacturing process alone can produce an order-of-magnitude difference in embodied climate impact, independent of any change in acoustic performance.

At the level of broader transport infrastructure, life-cycle assessment of highway projects consistently identifies material extraction and processing, particularly cement, aggregate, steel and bitumen, as the dominant contributors to total carbon footprint, with concrete production alone accounting for a large share of pavement-related emissions and steel reinforcement and barrier elements contributing a further significant fraction [7]. This pattern suggests that the embodied-carbon profile of noise barrier elements should not be assessed in isolation but understood as part of the same high-impact materials category that dominates road infrastructure emissions more generally.

### 3.2. CIRCULAR ECONOMY APPLICATIONS: THE WIND-TURBINE BLADE CASE

A directly relevant applied case is provided by recent research developing road noise barriers from composite material recovered from decommissioned wind-turbine blades [11]. The study assessed whether the structural strength of blade-derived composite panels was sufficient to withstand wind and traffic loading in compliance with current standards, finding that the recovered composite could meet the relevant load requirements with sufficient resistance margin [11]. The same study quantified embodied energy and embodied carbon for several noise barrier types using life-cycle assessment, framing the blade-to-barrier pathway explicitly as a circular economy model in which a end-of-life structural asset, the blade, is given a second functional life as transport infrastructure rather than being landfilled or incinerated, the two dominant disposal routes for glass-fibre reinforced composite blades at present [11]. This example demonstrates that material recovery for noise barriers need not be limited to recycling barrier materials themselves, but can extend to absorbing waste streams from other infrastructure sectors, in this case the wind energy sector, into noise barrier construction.

### 3.3. RECYCLABILITY AND EMBODIED ENERGY BY MATERIAL CLASS

Among conventional barrier materials, aluminium offers the most favourable circularity profile on energy grounds. Producing recycled aluminium requires only approximately 5% of the energy needed to produce primary aluminium from bauxite, a saving on the order of 95% [8], [9]. Aluminium also retains its physical and chemical properties through repeated recycling cycles without quality degradation, and an estimated three-quarters of all aluminium ever produced remains in use today following one or more recycling cycles [10]. These properties make aluminium-framed barrier panels, including the reflective and glazed panel types shown in typical noise barrier installations, comparatively well suited to closed-loop recovery at end-of-life, provided collection and sorting infrastructure is available.

Concrete, by contrast, is technically recyclable in the sense that demolished material can be crushed into aggregate for use in road sub-base or new concrete production, but this constitutes downcycling rather than closed-loop recycling, since the recovered aggregate rarely re-enters a structurally equivalent application. Mixed-material precast panels incorporating steel reinforcement, sealants or composite facings further complicate separation at end-of-life. Transparent acrylic and laminated glass panels, valued acoustically and visually for permitting visibility through the barrier, present the least favourable circularity profile among common materials: acrylic is petroleum-derived and is rarely recycled in practice at the volumes generated by barrier replacement, while laminated or coated glass panels require specialised separation processes that are not widely available in current waste-management infrastructure.

## 4. DESIGN FOR DISASSEMBLY IN NOISE BARRIER CONSTRUCTION

Design for disassembly (DfD) is an established principle in building construction that prioritises reversible mechanical connections, such as bolts, clips and screws, over permanent or chemically bonded joints, modular and standardised component geometries, and material choices with known, accessible recovery routes, in order to facilitate future dismantling for reuse, remanufacture or recycling rather than demolition [12]. Reviews of design for disassembly in concrete construction note that a large proportion of structures are removed while their constituent elements retain substantial residual service life, and argue that reconsidering structural design to support future disassembly is necessary to shift the sector from a linear to a cyclical materials model [13].

These principles transfer naturally to noise barrier construction, which already relies on modular, panelised assembly in most contemporary systems, including the post-and-panel aluminium and acrylic systems and the prefabricated terraced/vegetated wall systems described in Section 2. Cantilever-top barrier configurations, which incorporate a specially shaped upper element to increase the effective diffraction angle and have been shown to increase acoustic protection by 1.4 to 3.6 dB(A) relative to an equivalent flat barrier of the same height, illustrate that acoustic performance gains and modular, demountable construction are not mutually exclusive design objectives; the cantilever element itself can in principle be designed as a separable, reusable component. Embedding design-for-disassembly criteria into noise barrier specifications would primarily require specifying reversible fixings at panel-to-post and post-to-foundation connections, standardising panel dimensions across projects to support a secondary market for reclaimed panels, and avoiding composite material combinations that cannot be separated without specialised processing.

## 5. A CIRCULAR ECONOMY ASSESSMENT FRAMEWORK FOR NOISE BARRIERS

Building on the evidence reviewed above, this paper proposes a four-stage circular economy assessment framework intended to support both the comparative evaluation of existing barrier systems and the specification of new procurement. The first stage, material selection, requires explicit comparison of candidate materials against recyclability, embodied energy and recovered-material availability, rather than acoustic performance and unit cost alone, drawing on data of the type summarised in Table 1. The second stage, design for disassembly, requires that connection details, panel modularity and material combinations be assessed for ease of future separation at the design stage, following the principles outlined in Section 4. The third stage, end-of-life routing, requires that a designated pathway, reuse, closed-loop recycling, downcycling or, as a last resort, landfill, be identified and documented for each major material component before installation, rather than left to be determined reactively at removal. The fourth stage, procurement criteria, requires that public tenders for noise barrier supply and installation include explicit circularity indicators, such as minimum recycled content, documented end-of-life recovery routes and design-for-disassembly compliance, alongside conventional acoustic and structural specifications.

Table 1 summarises the circularity profile of the principal barrier material classes discussed in Sections 2 and 3, synthesising the acoustic, recyclability, embodied energy and end-of-life evidence reviewed above into a single comparative reference.

*Tab. 1. Comparative circular economy profile of common traffic noise barrier materials*

| Material | Acoustic performance | Recyclability | Embodied energy / carbon | End-of-life pathway |
|---|---|---|---|---|
| Reinforced concrete | High (≈60 dB for 1 m gabion-equivalent mass; widely | Moderate – crushable to aggregate, but mixed-material panels complicate | High; cement clinker production is carbon-intensive | Downcycling to road sub-base aggregate; landfill if |

| | | | | |
|---|---|---|---|---|
| | used baseline) | separation | | contaminated |
| Steel / aluminium panel | Moderate to high, depends on cladding and absorptive lining | High – aluminium and steel are infinitely recyclable without quality loss | High primary production energy, but recycling uses only 5–20% of primary energy | Established scrap markets; high recovery value supports collection |
| Transparent acrylic / glass | Moderate; often used where visual permeability is required | Low to moderate – acrylic is petroleum-based and rarely recycled in practice; glass is recyclable but panels are laminated/coated | Moderate; lighter than concrete, lower transport emissions | Mostly landfill or incineration; mechanical recycling technically possible but underused |
| Timber / timber composite | Moderate, good absorption when porous | High if untreated; treated/composite timber recycling is limited | Low embodied carbon; can sequester carbon if sourced sustainably | Reuse, chipping for particleboard, or bioenergy recovery |
| Composite (e.g. recycled wind-turbine blade material) | High; comparable structural performance to conventional composites under wind and traffic loads [11] | Currently low – thermoset composites are difficult to recycle, but reuse as a barrier panel itself constitutes a circular pathway | Substantially reduced relative to virgin composite production, since the embodied energy of the blade is reused rather than discarded [11] | Second-life application; eventual disposal challenge remains unresolved |
| Green / vegetated terraced wall | Variable; primarily relies on mass and surface absorption of substrate and vegetation | High for structural shell (concrete, metal or recycled plastic modules); biological component is renewable | Moderate; offset partly by carbon sequestration and stormwater/biodiversity co-benefits | Modular disassembly of shell; soil and vegetation returned to landscape use |

## 6. DISCUSSION

The evidence reviewed indicates that current noise barrier practice remains predominantly linear in its treatment of materials, with circularity emerging more often as an incidental property of material choice, aluminium's favourable recycling economics, for example, than as a deliberate design objective. The geopolymer composite and wind-turbine-blade composite cases reviewed in Section 3 show that substantial reductions in embodied climate impact, in the order of 70% or more relative to conventional baselines, are achievable using materials and processes that already exist, suggesting that the barrier to wider adoption is more a matter of procurement specification and market awareness than of fundamental technical feasibility.

A reasonable objection is that acoustic performance, safety and cost will continue to dominate barrier specification, and that circularity criteria risk being treated as a secondary, easily deprioritised consideration. The framework proposed in Section 5 addresses this by integrating circularity into the same procurement stage at which acoustic and structural criteria are already specified, rather than treating it as a separate, voluntary add-on; minimum recycled content and documented end-of-life routing can be expressed

as binding tender requirements in the same manner as minimum sound transmission class or wind load resistance. This positions circular economy assessment as a complement to, rather than a competitor with, established acoustic engineering practice.

## 7. CONCLUSION

Traffic noise barriers are an established and effective acoustic mitigation technology, but they are rarely assessed as material stocks within a circular economy. This paper has reviewed the principal barrier typologies, concrete, aluminium and steel, transparent acrylic and glass, timber, composite and vegetated terraced systems, against recyclability, embodied energy and end-of-life criteria, drawing on life-cycle assessment evidence and the applied case of wind-turbine-blade composite reuse in barrier construction. The analysis shows clear differentiation between material classes: aluminium and modular steel systems offer the strongest circular pathways through established recycling markets, while transparent acrylic and conventional precast concrete present the most limited options absent specific intervention. The four-stage assessment framework proposed, covering material selection, design for disassembly, end-of-life routing and procurement criteria, offers a practical structure for transport agencies to embed circularity into noise barrier specification without displacing acoustic and structural requirements. Future work should extend the comparative life-cycle evidence base for barrier-specific applications, which remains thinner than for pavements and structural concrete, and should pilot circularity-weighted procurement criteria in real infrastructure tenders to test their practical effect on material selection.

## LITERATURE

[1] Palić, N.: "*Protective and safety measures against negative effects of traffic noise – A review*", SECURITY HORIZONS, University "St. Kliment Ohridski", Bitola Faculty of Security, pp. 47-63, Skopje, 2022.

[2] Lärmschutz an Straßen, Retrieved from http://leisea81.de/legacy_I/pdf/Zueblin-LS-Decke_Info.pdf

[3] Başdoğan, G., Çiğ, A.: "*Noise Barrier in Intra-City Transportation*", Yüzüncü Yıl Üniversitesi Tarım Bilimleri Dergisi. 25. 98-104., 2015. DOI: 10.29133/yyutbd.236261

[4] Durisol: "*Future-ready noise walls*", Retrieved from https://www.durisol.com/

[5] Hatko: "*How to Make Electricity Generation from Noise with Noise Barriers?*", Retrieved from https://www.hatkosoundbarrier.com/electricty-generation-from-noise/

[6] Abdulkareem, M., Havukainen, J., Nuortila-Jokinen, J., Horttanainen, M.: "*Life Cycle Assessment of a Low-Height Noise Barrier for Railway Traffic Noise*", Journal of Cleaner Production, Volume 323, 2021, DOI: https://doi.org/10.1016/j.jclepro.2021.129169.

[7] Cerclos: "*Highway (Infrastructure) Example Life Cycle Assessment*", 2025.

[8] Recycling Today: "*Aluminium's Life Cycle Advantages*", industry report, Retrieved from: https://www.recyclingtoday.com/news/aluminium-construction-life-cycle-recycling/

[9] Al-Alimi, S., et.al.: "*Recycling aluminium for sustainable development: A review of different processing technologies in green manufacturing*", Results in Engineering, Volume 23, 2024, DOI: https://doi.org/10.1016/j.rineng.2024.102566

[10] Stacbond: "The Contribution of Recycled Aluminium to the Circular Economy in the Construction Sector", 2024., Retrieved from: https://stacbond.com/en/blog/the-contribution-of-recycled-aluminium-to-the-circular-economy-in-the-construction-sector/

[11] Broniewicz, M., Halicka, A., Buda-Ożóg, L., Broniewicz, F., Nykiel, D., Jabłoński, Ł,.: "*The Use of Wind Turbine Blades to Build Road Noise Barriers as an Example of a Circular Economy Model*", PMC, National Library of Medicine, 2024., DOI: 10.3390/ma17092048

[12] Dassault Systèmes: "Design for Disassembly in the Age of Circularity", 2025., Retrieved from: https://www.3ds.com/sustainability/circular-economy/design-for-disassembly

[13] Salama, W.: "*Design of Concrete Buildings for Disassembly: An Explorative Review*", International Journal of Sustainable Built Environment, Volume 6, Issue 2, 2017, Pages 617-635, DOI: https://doi.org/10.1016/j.ijsbe.2017.03.005

https://doi.org/10.24867/INDIS-2026-EN-196



# INFLUENCE OF OPTICAL GLASS FIBERS ON THE POST-FIRE BEHAVIOUR OF CONCRETE PRODUCED WITH LOCAL SILICEOUS AGGREGATE

*Nataša Kopitović Vuković[1], Strahinja Ilić[2], Radomir Zejak[3], Goran Gorašević[4]*

***Summary:***

This study investigates the post-fire behaviour of concrete produced with locally available quartz–keratophyre aggregate and reinforced with optical glass fibers. Specimens were exposed to temperatures ranging from 100°C to 1100°C and tested after cooling. The experimental program included visual assessment, ultrasonic pulse velocity measurements and determination of residual compressive strength and modulus of elasticity. The results showed progressive deterioration as the temperature increased. At 700°C, the optical fiber-reinforced concrete exhibited higher compressive strength and modulus of elasticity than the polypropylene fiber-reinforced mixture. However, its compressive strength remained lower than that of the reference concrete throughout the investigated temperature range. The findings indicate that the effect of optical glass fibers depends on the level of thermal exposure and provide further insight into the residual behaviour of concrete containing locally available siliceous aggregate.

*Keywords: concrete; siliceous aggregate; optical glass fibers; post-fire behaviour; elevated temperatures; residual mechanical properties*

# UTICAJ OPTIČKIH STAKLENIH VLAKANA NA PONAŠANJE BETONA SA LOKALNIM SILIKATNIM AGREGATOM NAKON DEJSTVA POŽARA

***Rezime:***

U ovom radu ispituje se ponašanje betona nakon požara, proizvedenog sa lokalno dostupnim kvarc–keratofirskim agregatom i ojačanog optičkim staklenim vlaknima. Uzorci su izlagani temperaturama od 100°C do 1100°C, a zatim ispitivani nakon hlađenja. Eksperimentalni program obuhvatio je vizuelnu procjenu, mjerenje brzine ultrazvučnog impulsa i određivanje rezidualne čvrstoće pri pritisku i modula elastičnosti. Rezultati su pokazali progresivnu degradaciju sa porastom temperature. Na 700°C beton sa optičkim vlaknima pokazao je veću čvrstoću pri pritisku i modul elastičnosti od mješavine sa polipropilenskim vlaknima. Međutim, njegova čvrstoća pri pritisku bila je niža od referentnog betona u cijelom ispitivanom temperaturnom opsegu. Rezultati ukazuju da efekat optičkih staklenih vlakana zavisi od nivoa termičkog izlaganja i doprinose boljem razumijevanju rezidualnog ponašanja betona sa lokalnim silikatnim agregatom.

*Ključne riječi: beton; optička staklena vlakna; ponašanje nakon požara; silikatni agregat; povišene temperature; rezidualna mehanička svojstva*

[1] Assis. Prof., Faculty of Civil Engineering, University of Montenegro, Montenegro, nataly@ucg.ac.me, ORCID 0000-0002-6152-4073
[2] MSc in Civil Engineering, Skill Inženjering Podgorica, straleilic6@gmail.com
[23] Full Prof., Faculty of Civil Engineering, University of Montenegro, Montenegro, rzejak@t-com.me
[34] PhD student, Faculty of Civil Engineering, University of Montenegro, ggorasevic@gmail.com
[4]

## 1. INTRODUCTION

Concrete is generally considered a material with relatively favourable behaviour under fire exposure. Nevertheless, elevated temperatures cause progressive physical, chemical and mechanical changes that may significantly affect its residual properties after cooling. The extent of deterioration depends on several parameters, including the maximum temperature, duration and rate of heating, cooling conditions, moisture content, composition of the cementitious matrix, aggregate characteristics and the presence of fibers [1].

The type of aggregate is particularly important because aggregate mineralogy and its thermal behaviour influence the response of concrete exposed to elevated temperatures [2,3]. For this reason, the investigation of concrete produced with locally available quartz–keratophyre aggregate is relevant for assessing the residual behaviour of this material following thermal exposure.

The incorporation of fibers represents one of the approaches used to modify the behaviour of concrete exposed to high temperatures. Polypropylene fibers have been extensively investigated, particularly because their melting at relatively low temperatures may increase the permeability of concrete and facilitate the release of water vapour, thereby reducing the build-up of internal pore pressure and the risk of explosive spalling [4,5]. This mechanism and the influence of polypropylene fibers on the behaviour of concrete exposed to elevated temperatures have also been widely discussed in previous experimental investigations [6,7].

In the authors' previous investigation, concrete produced with the same aggregate and containing polypropylene fibers was exposed to elevated temperatures [8,9].

The present study builds upon that experimental program by examining concrete containing optical glass fibers in order to investigate their influence on the residual properties of concrete after exposure to elevated temperatures. Unlike polypropylene fibers, optical glass fibers do not provide the same low-temperature melting mechanism that creates pathways for vapour release within the cementitious matrix. Their role in construction is primarily associated with aesthetic applications and the development of technologies that enable deformation measurement and structural condition monitoring using optical fibers [10].

The experimental program includes visual assessment of thermally induced deterioration, ultrasonic pulse velocity measurements as an indicator of internal deterioration, and the determination of residual compressive strength and modulus of elasticity. The results obtained for concrete containing optical glass fibers are considered together with the corresponding results for reference concrete and polypropylene fiber-reinforced concrete produced with the same aggregate.

Particular attention is given to the temperature-dependent response of the investigated mixtures and to the comparison of the experimentally determined residual compressive strength with the reduction factors given in MEST EN 1992-1-2 [11]. Since the present investigation was performed on specimens tested after cooling, this comparison is considered indicative and should not be interpreted as a direct validation of the Eurocode provisions.

## 2. MATERIALS AND EXPERIMENTAL PROGRAM

### 2.1. MATERIALS

Concrete mixtures were prepared using locally available siliceous aggregate, cement, chemical admixtures and optical glass fibers. The behaviour of concrete exposed to

elevated temperatures is strongly influenced by the mineralogical composition and thermal stability of the aggregate, making the investigation of locally available aggregate particularly relevant [12].

The aggregate used in this investigation belongs to the quartz–keratophyre group characterized by a high content of siliceous minerals and a low percentage of carbonate impurities. It originated from the "Okrugličkи krš", quarry near Štitarica (Mojkovac, Montenegro).

All concrete mixtures were produced using CEM III/B 32.5N SRLH cement manufactured by Dalmacija Cement (Split, Croatia). This cement was selected for the experimental program because of its composition and suitability for the investigated concrete mixtures exposed to elevated temperatures.

Two commercially available admixtures were incorporated into all concrete mixtures. Sika ViscoCrete 4077 was used as a high-range water-reducing admixture to improve workability while maintaining a low water-to-cement ratio. Sika Air was added to provide controlled air entrainment and improve the behaviour of fresh concrete.

In this study, glass optical fibers from the CNBM manufacturer were used in the form of thin needles (Figure 1). Unlike polypropylene fibers, they do not provide a low-temperature melting mechanism for the formation of vapour-release pathways within the cementitious matrix. Their application in the experiment enabled an assessment of their influence on the behaviour of concrete exposed to elevated temperatures.




*Figure 1. Optical glass fibers used in the experimental investigation*

## 2.2. SPECIMEN PREPARATION

Three concrete mixtures with siliceous aggregate were considered: a reference mixture without fibers (S-E), a mixture containing polypropylene fibers (S-PP) and a mixture containing optical glass fibers (S-O). All mixtures had identical aggregate grading, cement content, water-to-cement ratio and admixture dosage, while the type of fiber represented the variable parameter. The optical glass fiber dosage was 30 g per batch, corresponding to approximately 1.0 kg/m³. Particular attention was paid to achieving a uniform fiber distribution and avoiding fiber agglomeration.

After casting, all specimens were cured under laboratory conditions for 28 days. Cylindrical cores with dimensions Ø54×100 mm were subsequently extracted from larger concrete elements in order to simulate the concrete cover zone of reinforced concrete structural members.

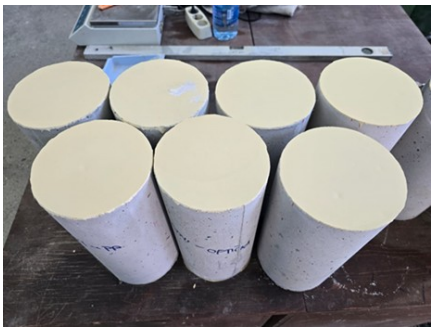

*Figure 2. Preparation of cylindrical core specimens*

The specimens were exposed to temperatures of 100°C, 200°C, 500°C, 700°C and 1100°C. Each temperature level was maintained for 90 minutes, followed by gradual cooling to room temperature. High-temperature exposure was performed in the laboratory of ABG TEST Ltd., Podgorica.
Heating procedures and the furnaces used for high-temperature exposure are presented in Figures 3 and 4.



*Figure 3. Laboratory furnace at the Faculty of Civil Engineering in Podgorica, used for exposing samples to temperatures up to 200℃*



*Figure 4. Furnace in the ABG test laboratory, used for testing at temperatures up to 1100℃*

## 2.3. SPECIMEN TESTING

Following thermal exposure and cooling to room temperature, the specimens were subjected to ultrasonic pulse velocity measurements and compressive strength testing. Ultrasonic pulse velocity was used as a non-destructive indicator of changes in the internal condition of concrete after exposure to elevated temperatures. Selected specimens exposed to 200°C and 700°C were additionally tested to determine the modulus of elasticity (Figure 5).



*Figure 5. Testing machine*

The experimental results were compared with the reduction factors specified in Eurocode 2 (MEST EN 1992-1-2) [11] and discussed in relation to the authors' previously published results for concrete reinforced with polypropylene fibers.

## 3. RESULTS AND DISCUSSION

### 3.1. VISUAL ASSESSMENT OF CONCRETE DEGRADATION

The visual appearance of the specimens revealed progressive changes in the concrete surface with increasing temperature. Up to 200°C, no significant visible deterioration was observed. More pronounced changes in colour and surface appearance occurred after exposure to 500°C and 700°C. At 1100°C, severe thermal degradation of the concrete surface was evident. Nevertheless, the core specimens largely retained their shape and could subsequently be subjected to mechanical testing.

*Table 1. Visual observations of specimens after exposure to different temperatures*

| Temperature (℃) | Specimens |
|---|---|
| 25 | No changes |
| 100 | No visible changes |
| 200 | Surface slightly rough; microcracks possible, but hardly noticeable |
| 500 | Cracks hard to see; discoloration |
| 700 | Appearance of visible cracks, disintegration of two standard samples |
| 1100 | The core shape preserved, one standard sample has disintegrated |



*Figure 6. Visual appearance and progressive thermal degradation of concrete specimens after exposure to different temperatures: 500℃, 700℃ and 1100℃, respectively.*

## 3.2. ULTRASONIC PULSE VELOCITY

The ultrasonic pulse velocity (UPV) decreased progressively with increasing temperature for all investigated mixtures, indicating progressive deterioration of the internal concrete structure [8]. The reduction was relatively moderate up to 200°C, whereas a more pronounced decrease occurred after exposure to 500°C.

A more pronounced reduction in ultrasonic pulse velocity was observed at higher temperatures, indicating progressive internal deterioration of the concrete matrix. At 700°C, the S-O mixture exhibited a higher ultrasonic pulse velocity than both the reference mixture (S-E) and the polypropylene fiber-reinforced mixture (S-PP), suggesting a comparatively better preserved internal structure under these test conditions.

## 3.3. RESIDUAL COMPRESSIVE STRENGTH

The progressive reduction in compressive strength with increasing temperature is consistent with the general behaviour of concrete subjected to elevated temperatures, which has been extensively reported in previous experimental studies [1,5,13].

*Table 2. Compressive strength of concrete mixtures with siliceous aggregate after exposure to elevated temperatures*

| Specimen label | Temperature (°C) / Compressive strength (MPa) | | | | | |
|---|---|---|---|---|---|---|
| | 25°C | 100°C | 200°C | 500°C | 700°C | 1100°C |
| S-E | 55.45 | 55.38 | 52.91 | 49.56 | 32.86 | 10.59 |
| S-PP | 57.2 | 53.27 | 50.14 | 39.95 | 21.54 | 9.46 |
| S-O | 53.71 | 52.54 | 52.18 | 42.94 | 25.54 | 7.35 |

For the S-O mixture, the compressive strength remained almost unchanged up to 200°C and decreased more significantly at higher temperatures. The residual strength ratios, calculated relative to the strength at 25°C, were 0.97 at 200°C, 0.80 at 500°C, 0.48 at 700°C and 0.14 at 1100°C.

For an indicative comparison, these residual values were considered alongside the reduction factors for concrete with siliceous aggregate provided in MEST EN 1992-1-2 [11], which are 0.95 at 200°C, 0.60 at 500°C and 0.30 at 700°C. However, this comparison should be interpreted with caution because the present results represent residual properties determined after cooling, whereas the Eurocode provisions describe the temperature-dependent behaviour of concrete at elevated temperatures.

The influence of optical glass fibers was temperature-dependent. The S-O mixture did not exhibit higher compressive strength than the reference concrete at any of the investigated temperature levels. Nevertheless, at 700°C, it retained a higher compressive strength than the polypropylene fiber-reinforced mixture. This comparison is also relevant in the context of the authors' previous investigation of polypropylene fiber-reinforced concrete produced with the same local aggregate [9].

## 3.4. MODULUS OF ELASTICITY

The effect of elevated temperature on the deformation behaviour of the investigated concrete was evaluated through the modulus of elasticity determined on cylindrical specimens with dimensions Ø54×100 mm. Additional tests were performed at 200°C and 700°C after 90 minutes of thermal exposure, with three specimens tested for each of the three concrete mixtures. The results are presented in Table 3.

*Table 3. Modulus of elasticity of concrete mixtures with siliceous aggregate*

| Specimen label | Temperature (°C) / Modulus of elasticity (GPa) | |
|---|---|---|
| | 200°C | 700°C |
| S-E | 36.67 | 10.64 |
| S-PP | 31.63 | 8.99 |
| S-O | 33.93 | 10.70 |

The results demonstrate a clear temperature-dependent influence of fiber type on concrete stiffness. At 700°C, the S-O mixture exhibited the highest modulus of elasticity among the three siliceous aggregate mixtures, although the difference compared with the reference mixture was small. This result should therefore be interpreted as a comparatively favourable response rather than as a significant improvement in stiffness. The pronounced reduction in the modulus of elasticity after thermal exposure is consistent with previous studies showing that concrete modulus of elasticity is particularly sensitive to thermally induced microstructural damage [1,5,14].

## 4. CONCLUSIONS

This study investigated the post-fire behaviour of concrete produced with locally available siliceous aggregate and containing optical glass fibers. Based on the experimental results, the following conclusions can be drawn:

- Increasing temperature resulted in progressive deterioration of the investigated concrete, with substantial reductions in compressive strength and modulus of elasticity at higher temperature levels.
- The incorporation of optical glass fibers did not increase the residual compressive strength compared with the reference concrete throughout the investigated temperature range. However, at 700°C, the S-O mixture exhibited higher compressive strength and modulus of elasticity than the polypropylene fiber-reinforced mixture.
- The results indicate that the influence of optical glass fibers on the residual mechanical behaviour of concrete is temperature-dependent. At 700°C, the S-O mixture showed a comparatively favourable response among the investigated fiber-reinforced concretes, whereas severe degradation was observed at 1100°C.

- The results contribute to the understanding of the post-fire behaviour of concrete produced with locally available quartz–keratophyre aggregate and provide a basis for further investigation of optical glass fibers in concrete exposed to elevated temperatures, which may contribute to more sustainable and safer construction practices in Montenegro.

## LIMITATIONS AND RECOMMENDATIONS FOR FUTURE RESEARCH

Further testing of combined mixtures containing polypropylene and optical glass fibers is justified in order to investigate their potential combined effect on high-temperature behaviour and residual mechanical properties. In addition, research should be extended to different cement types to compare the influence of cement composition and mineral additions on the behaviour of concrete exposed to elevated temperatures.
It should also be noted that the tests were conducted on cooled specimens; therefore, the measured values represent residual mechanical properties, whereas Eurocode 2 provides temperature-dependent material properties for concrete at elevated temperatures [11].
It is recommended to increase the number of specimens per temperature level in order to obtain more reliable statistics and to investigate different cooling regimes—natural cooling, forced-air cooling and water quenching—to assess their influence on the final mechanical properties.

## REFERENCES

[1] Wang W., Yang L., Zhao Y. (2020). Performance of Concrete with Fibers Under Elevated Temperatures: A Review of Recent Advances. *Journal of Structural Fire Engineering,* Volume 11(2), pp.123-136.

[2] Shao Y., Liu J., Liu Y. (2017). Effect of Mineral Aggregate Types on the Fire Resistance of Concrete. *Journal of Fire Sciences,* Volume 35(4), pp.402-418.

[3] Wu X., Chen B., Wang, Z. (2021). Effects of Aggregate Types on the Fire Resistance of Concrete: A Comparative Study. *Journal of Materials in Civil Engineering,* Volume 33(5).

[4] Rashid M., Li X. (2017). Fire Resistance of Concrete with Polypropylene and Glass Fibers: A Review. *Fire Safety Science,* Volume 9, pp.53-61.

[5] Liu Y., Li S. (2018). The Influence of Polypropylene and Glass Fibers of Concrete Behavior Under High-Temperature Exposure. *Construction and Building Materials,* Volume 174, pp.472-479.

[6] Phan L.T., Carino N.J. (2002). Effects of Test Conditions and Mixture Proportions on High-Strength Concrete Exposed to High Temperatures. *ACI Materials Journal,* Volume 99(1). pp.54-66.

[7] Arisoy B., Wu H. C. (2008). High temperature resistance of normal strength concrete with silica fume and steel fibers. *Construction and Building Materials,* Volume 22(3), pp.504-512.

[8] Ilić S. (2025). Uticaj tipa agregata i vlakana na protivpožarnu otpornost betona. Master thesis, University of Montenegro, Montenegro.

[9] Ilić S., Zejak R., Kopitović Vuković N., Zejak M. (2026). Experimental Study on the Fire Resistance of Concrete with Local Siliceous Aggregate and Polypropylene Fibers. *$10^{th}$ International Conference –GNP*, Budva, Montenegro.

[10] Mallick A. et al. (2019). Fiber Optic Sensors for Structural Health Monitoring of Concrete. *Journal of Civil Structural Health Monitoring,* Volume 9(3), pp.315-329.

[11] MEST EN 1992-1-2: Eurokod 2 – Projektovanje betonskih konstrukcija – Dio 1-2: Opšta pravila – Projektovanje konstrukcija na dejstvo požara.

[12] Alhamad A., Yehia S., Lublóy É., Elchalakani M. (2022). Performance of Different Concrete Types Exposed to Elevated Temperatures: A Review. *Materials,* Volume 15(14), Article 5032.

[13] Khoury G.A (1992). Compressive strength of concrete at high temperatures: a reassessment. *Magazine of Concrete Research,* Volume 44(161), pp.291-309.

[14] Babalola O.E., Awoyera P.O., Le D.-H., Bendezú Romero L.M. (2021). A review of residual strength properties of normal and high strength concrete exposed to elevated temperatures: Impact of materials modification on behaviour of concrete composite. *Construction and Building Materials,* Volume 296, Article 123448.

https://doi.org/10.24867/INDIS-2026-EN-205

**INTERNATIONAL SCIENTIFIC CONFERENCE**
INTEGRATION, NOVELTY, DESIGN,
INTERDISCIPLINARITY, SUSTAINABILITY

iNDiS 2026

# CONCRETE FOR COOLER CITIES: NEW INSIGHTS

*Anja Terzić[1], Ksenija Janković[2], Aleksandar Savić[3]*

***Summary:***

Rapid global urbanization, with over half the world's population now living in cities, poses significant environmental challenges such as air pollution and urban heat islands (UHI). UHI predominantly result from reduced greenery in the cities, $CO_2$ emissions from construction sector, and greenhouse gases procused within the city. This paper reviews the use of construction and demolition waste (C&DW) based concrete to mitigate UHI by enhancing thermal and environmental performance through innovative recycling techniques. Focusing on reflective concrete pavers made from C&DW, the study explores their role in increasing albedo and lowering urban temperatures, addressing waste management and reducing greenhouse gas emissions in line with net-zero targets. It also examines situation with UHI in Republic of Serbia and globally, thermal benefits, urban microclimate effects, challenges, and future research directions, offering insights for sustainable urban infrastructure and climate adaptation.

*Keywords: Concrete pavements; Urbanisation; Thermal performance; Modelling.*

# BETON ZA HLADNIJE GRADOVE: NOVI UVIDI

***Rezime:***

Brza globalna urbanizacija i preko polovine svetske populacije koja sada živi u gradovima predstavljaju značajne ekološke izazove kao što su zagađenje vazduha i urbana toplotna ostrva (UTO). UTO su pretežno rezultat smanjenog zelenila u gradovima, emisije $CO_2$ iz građevinskog sektora i gasova staklene bašte koji nastaju u gradu. Ovaj rad razmatra upotrebu betona na bazi građevinskog i ruševinskog otpada (GIO) za ublažavanje UTO poboljšanjem termičkih i ekoloških performansi kroz inovativne tehnike reciklaže. Fokusirajući se na reflektujuće betonske ploče napravljene od GIO, studija istražuje njihovu ulogu u povećanju albeda i snižavanju urbanih temperatura, rešavajući problem upravljanja otpadom i smanjenju emisije gasova staklene bašte u skladu sa ciljevima neto nulte emisije. Takođe, ispituje situaciju sa UTO u Republici Srbiji i globalno, termalne koristi, efekte urbane mikroklime, izazove i buduće pravce istraživanja, nudeći uvide za održivu urbanu infrastrukturu i klimatsku adaptaciju.

*Ključne reči: Betonski pločnici; Urbanizacija; Termičke performanse; Modeliranje.*

[1] Principal Research Fellow, IMS Institute, Belgrade, Serbia, anja.terzic@institutims.rs, ORCID 0000-0002-4762-7404
[2] Principal Research Fellow, IMS Institute, Belgrade, Serbia, ksenija.jankovic@institutims.rs, ORCID 0000-0003-3744-3799
[3]Assoc. Prof., University of Belgrade, Faculty of Civil Engineering, Belgrade, Serbia, sasha@grf.bg.ac.rs, ORCID 0000-0002-1777-6775

## 1. INTRODUCTION: THE URBAN HEAT ISLAND SURGE - TRACING THE EFFECTS OF EXPANDING CITIES

Rapid global urbanization is a key factor shaping the future of sustainable civil engineering and urban planning. Currently, over half of the world's population lives in cities, a figure expected to reach 70% by 2050 [1, 2]. Urbanization poses major challenges to sustainability and urban liveability, primarily through environmental issues like surface warming and air pollution caused by urban heat islands (UHI) [3]. Since 1850, Earth's temperature has risen by 0.06°C per decade, accelerating to over three times that rate since 1982. The warmest ten years on record occurred in the past decade (2015–2025) [4]. Fossil $CO_2$ emissions surged 1.1% from 2022 to 36.8 billion tons in 2023, with global efforts to reduce fossil fuel use lagging behind what is needed to prevent severe climate change, despite declines in some regions (EU, USA). While afforestation and reforestation help curb greenhouse gas emissions from deforestation, current efforts remain insufficient [5]. At the current emission rate, there is a 50% chance global warming will exceed 1.5°C within seven years, nearing critical thresholds. Rising atmospheric $CO_2$ continues to drive worsening climate impacts, including extreme weather, floods, and sea level rise [6]. To avoid catastrophic outcomes, rapid global decarbonization is imperative. It is necessary to use innovative materials and solutions that support the Green Agenda [7, 8].

The Urban Heat Island (UHI) (Figure 1, [9]) phenomenon occurs when urban areas experience higher temperatures than surrounding rural zones due to factors like increased human-generated heat, greater solar absorption, reduced reflectance, lower heat capacity, and limited heat dispersion. UHI intensity ranges from 0.4 to 11°C and poses growing health risks, exacerbated by climate change. Key objectives include creating detailed UHI maps for specific cities and developing innovative construction materials aligned with Zero Waste principles to mitigate temperature rises in critical areas.

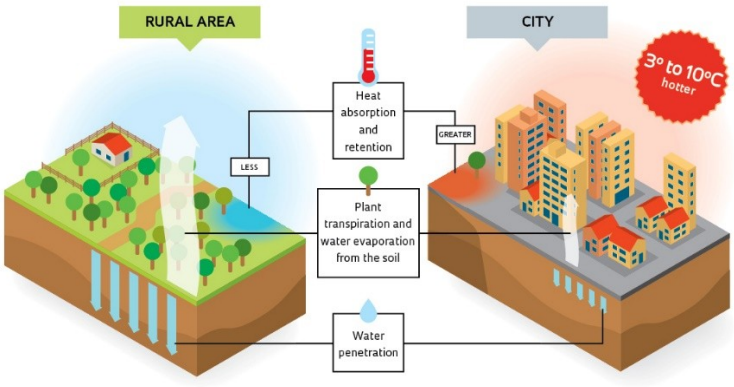


*Figure 1. Why the urban heat island effect occurs? [9].*

## 2. RECENT INSIGHTS INTO URBAN HEAT ISLAND DYNAMICS AND MITINGATION

Researchers have approached UHI mitigation from various angles. Wu et al. [1] explored using green infrastructure, such as urban greenery and green roofs, to reduce UHI by integrating it with building and urban geography features; however, greenery installation is sometimes impractical. Cheng et al. [10] highlighted digital technologies (e.g., Digital Twin, ENVI-met software) as crucial for linking urban economic

resilience and UHI mitigation, though resource constraints limit adoption in low- and middle-income countries. Aghazadeh et al. [11] analysed land-use changes via Landsat data (2000–2021), showing urbanization intensifies UHI by replacing cooling green spaces. Jayasooriya et al. [12] studied urban fabric effects, noting that certain rooftop colours (e.g., red) raise surface temperatures by over 5°C compared to lighter colours, while high-rise buildings can create cooler urban pockets.

Perez et al. [13] examined London's UHI trends over 33 years, finding city centre temperatures up to 6.8°C higher than surrounding areas, influenced by weather patterns. Effective UHI mitigation materials must consider diurnal temperature variations, seasons, sunlight, and wind. Li et al. [14] proposed a multi-level urban ecological cooling network using circuit theory and spatial analysis to guide sustainable urban planning, demonstrated in Hefei City. Additional global case studies [15-18] have employed weather data, simulations, and urban design strategies to address UHI effects.

These approaches highlight the importance of integrating ecological principles into urban development. By leveraging innovative design and technology, cities can effectively reduce heat retention and enhance liveability for their residents.

## 3. ENHANCING URBAN COOLING THROUGH SMART MATERIAL CHOICES: RESEARCH GAP AND INITIATIVES.

To date, global urban case studies have predominantly acknowledged the role of surface colour in influencing temperature increases. However, there remains a significant knowledge gap regarding the comprehensive investigation of construction materials specifically designed to optimize the albedo effect and their scalable implementation. On a national level, efforts to address the Urban Heat Island phenomenon through material innovation have been limited and sporadic, with only a few isolated case studies conducted that have had minimal impact and recognition on an international scale.

Notably, there has been no coordinated national initiative aimed at mitigating UHI through the deployment of building materials engineered to enhance albedo. Furthermore, based on the current state of the art, international endeavours in this domain remain scarce and underdeveloped. Researchers should seek to fill these gaps by advancing the scientific understanding and practical application of high-albedo construction materials to achieve meaningful reductions in urban temperatures. Primary objective should be to explore the development and application of waste-based paving materials in carefully selected light hues to effectively mitigate elevated temperatures within urban environments. The mentioned goal extends beyond conducting case studies to developing practical and innovative solutions, specifically novel concrete paving units, that effectively reduce ambient temperatures in surrounding environments, thereby enhancing environmental sustainability on a broader scale. These efforts not only enhance urban aesthetics but also improve public health by mitigating heat-related issues. Ultimately, this approach fosters a more resilient and adaptive infrastructure for future generations.

This goal should be achieved through the strategic utilization of both primary and secondary raw materials characterized by pale coloration, which are instrumental in enhancing the albedo effect. Urban albedo refers to the proportion of incoming solar radiation that is reflected by various surfaces within the urban landscape, quantitatively expressed as the ratio of reflected to incident radiation. Surfaces with an albedo value of 0 absorb the entirety of incoming solar radiation, exhibiting no reflectivity and typically corresponding to darker colours, whereas surfaces with an albedo value of 1 reflect all incoming solar radiation, corresponding to lighter colours (Figure 2. [19])

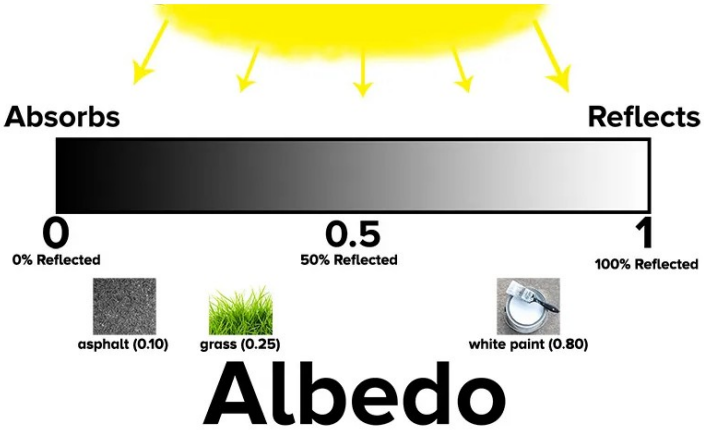


*Figure 2. Albedo effect [19]*

As cities continue to grapple with rising temperatures, the need for a cohesive strategy that incorporates high-albedo materials in urban planning becomes increasingly critical. A comprehensive national initiative could pave the way for more effective implementation, potentially transforming urban environments and significantly mitigating the heat island effect.

## 4. CASE STUDY OF SERBIA

Materials applied for UHIs in Serbia, particularly in the cities of Belgrade and Novi Sad, manifest as significantly elevated temperatures compared to surrounding rural areas. This phenomenon primarily results from the high concentration of heat-absorbing materials such as concrete, asphalt, and glass, combined with a notable deficiency in urban green spaces. In Belgrade, central districts can experience temperature increases of up to *7°C* above those in adjacent rural zones. Projections indicate that by the middle of this century, these urban centers may be increasingly vulnerable to extreme and potentially lethal heatwaves.

The most severely affected areas within Belgrade include New Belgrade, Terazije, Slavija, and sections of Palilula. These districts are characterized by dense urban development and extensive use of materials with high thermal mass, which absorb and subsequently re-radiate heat, exacerbating local temperature elevations. Empirical studies reveal that central Belgrade consistently exhibits higher temperatures than its peripheral surroundings. The intensity of the heat island effect peaks during winter months, with average temperature differentials reaching up to 1.4°C, and remains pronounced during evening hours when heat retention is most evident.

Central Belgrade suffers from a significant scarcity of green areas, with only approximately 2.83% of its surface dedicated to vegetation, in stark contrast to the broader metropolitan region where green spaces constitute about 12%. This imbalance contributes substantially to heat retention and reduced urban cooling capacity.

Similar patterns are observed in Novi Sad, where urban heat island intensity correlates strongly with densely built central and industrial zones. Research confirms that areas with higher building density experience markedly elevated temperatures, underscoring the role of urban morphology in UHI formation.

The primary drivers of the urban heat island effect in Serbian cities include suboptimal urban planning, insufficient incorporation of green infrastructure, and the prevalence of impermeable surfaces that hinder natural cooling processes. To address these challenges, experts advocate for a multifaceted approach encompassing the strategic

planting of native tree species, implementation of mandatory green roofs and green walls on buildings, and the creation of interconnected green corridors. These measures aim to enhance urban biodiversity, increase evapotranspiration, and reduce surface and air temperatures. Without the adoption of effective mitigation strategies, Serbian urban centers risk experiencing increasingly severe heat events. Forecasts suggest that temperatures could reach as high as 50°C under conditions of low humidity, posing serious public health risks and necessitating urgent urban resilience planning [20, 21].

## 5. MATERIALS AND MODELLING

Paver units, including blocks, bricks, and pavers, classified based on their dimensions and manufacturing processes, are frequently examined in material science research. Numerous studies have explored their properties; however, the interpretations of these findings vary widely, reaching diverse end-user groups.

Estolano et al. [22] conducted a comprehensive analysis of concrete paving blocks incorporating metakaolin (MK). Their investigation covered structural, fluorescence, optical, and mechanical characteristics. The MK-modified blocks demonstrated superior compressive strength, measuring 36.5 MPa, compared to conventional counterparts. Notably, blocks with a 20-30% MK replacement exhibited significant blue fluorescence, indicative of incomplete hydration reactions. Additionally, the inclusion of MK increased the cavity width within the blocks by approximately 10% relative to the reference samples. However, albedo reflectance was not assessed in this study.

Marinelli et al. [23] focused on the environmental implications of applying porous materials in urban areas dominated by impermeable concrete surfaces, which hinder precipitation infiltration, restrict vegetation growth, and exacerbate the urban heat island (UHI) effect. Their research, tailored to Scotland's challenging climatic conditions, produced paver units with limited compressive strength (below 20 MPa). Despite this limitation, the study proposed innovative applications for these pavements, including pedestrian walkways, bicycle paths, parking areas, flood control infrastructure, vegetation supports, and aesthetic landscaping features. The materials demonstrated excellent workability, enhanced permeability, and preliminary indications of improved durability, particularly resistance to freeze-thaw cycles. Nonetheless, the study did not conclusively determine the materials’ impact on mitigating UHI.

Asphalt concrete (AC) has been extensively studied concerning its thermal properties and contribution to the UHI phenomenon. In a review by Mohajerani et al. [24], densely graded AC was identified as a significant contributor to elevated surface temperatures, reaching up to 60°C during hot summer days due to its high volumetric heat capacity and low albedo. The authors highlighted that employing “cool” AC pavements, either porous or reflective, can effectively reduce surface temperatures. However, the selection of these mitigation strategies must consider local climatic conditions and urban morphology.

Tan et al. [25] enhanced the cooling capabilities of pervious concrete (PC) by incorporating biochar (BC) derived from waste biomass as a hygroscopic filler. Their study examined the effects of substituting 5% BC by weight of cement on albedo, emissivity, porosity, microstructural morphology, water absorption, and evaporation rates. Theoretically, such modified PC could contribute to UHI reduction, water pollution remediation, and decreased surface runoff. However, while BC addition significantly diminished the albedo of PC, it did not alter its porosity. The study also raised concerns regarding the cost-effectiveness and sustainability of BC production for widespread application.

Yaghmour et al. [26] investigated the pressure drop and heat transfer characteristics of both normal and lightweight pervious concretes under forced air flow conditions, aiming to understand their heating and cooling performance. The pressure drops values ranged from 500 to 8000 Pa/m at an airflow velocity of 0.35 m/s. Variations in paste-to-aggregate ratio and water-to-cement ratio influenced the porosity and void structure, thereby affecting the pressure drop. Notably, the study did not address the implications for the UHI effect.

Adresi et al. [27] evaluated the efficacy of an improved pervious concrete pavement (IPCP) system in mitigating UHI, addressing freeze-thaw susceptibility, and facilitating de-clogging. Utilizing a physical model apparatus simulating temperature fluctuations, de-icing processes, and clogging scenarios, the study demonstrated that selecting appropriate subbase materials enhanced evaporative cooling, reducing temperature rise by up to 37% under varying environmental conditions. The IPCP system incorporated a dual-function drainage mechanism that managed water levels, applied air pressure to restore permeability (achieving up to 97% permeability recovery), and used hot water injection for de-icing, thereby effectively addressing common pavement challenges.

Y. Chen et al. [28] developed a sun thermal reflective coating (STRC) designed to lower asphalt surface temperatures. Thermal performance was evaluated using a custom-built testing apparatus, while optical properties were analysed via UV-Vis-NIR spectroscopy. Durability assessments, including radiation cycling and thermal shock endurance tests, confirmed the coating's long-term stability. The pigment $CrO_3$, a key component of STRC, exhibited low visual reflectance (10.22%) but high near-infrared reflectance (54.76%). Application of STRC5 on asphalt concrete samples resulted in a significant temperature reduction, maintaining an average surface temperature of 49.51°C compared to 60.07°C for untreated samples. The coating demonstrated resilience to extreme temperature variations ranging from -20°C to 60°C.

J. Chen et al. [29] explored the use of high-conductivity permeable concrete pavement reinforced with steel fibres to mitigate UHI effects. Laboratory thermal transfer models and temperature measurements under controlled dry and wet conditions assessed the thermal conductivity and surface temperature behaviour of permeable concrete slabs subjected to heat radiation and water spray.

Kopel et al. [30] examined the transmission and reflection characteristics of various building materials at 2.4 GHz frequency using a setup with three antennas. Concrete samples exhibited the lowest transmittance, with only 34% of electromagnetic waves passing through and 35% being reflected. Composite boards demonstrated higher reflectance values.

Calis et al. [31] investigated the incorporation of colour pigments into roller-compacted high-performance concrete (RCHPC) to improve albedo and thereby mitigate UHI. Traditional asphalt pavements, characterized by low albedo, contribute significantly to urban heat accumulation. The RCHPC sample with the highest albedo (0.69) contained 0.75% pigment by weight of cement. Using ENVI-met software, two urban scenarios were modelled, simulating air temperature, relative humidity, surface temperature, and reflected radiation. Results indicated that the use of colour-pigmented RCHPC led to reductions of 1.63°C in air temperature and 9.69°C in surface temperature within the modelled area.

Shamsaei et al. [32] addressed the reduction of asphalt pavement's adverse impact on UHI through the utilization of waste materials from construction and demolition waste (C&DW). Laboratory analyses included thermal property measurements, solar simulation cooling tests, and UV-visible-NIR spectrometer reflectance assessments. Field experiments employed pyranometers and thermocouples to evaluate albedo and cooling effects. Indoor reflectance tests revealed that concrete chip sealing exhibited

80% higher solar reflectance than aged asphalt pavement, while yellow and red bricks reflected approximately 136% more. Surface temperature measurements showed that concrete chip sealing, red brick, and yellow brick surfaces were 23%, 18%, and 15% cooler, respectively, compared to hot mix asphalt (HMA) specimens. Notably, concrete chip seals emitted the most heat during nighttime, whereas clay brick chip seals emitted the least. Field data further indicated that yellow brick surfaces had albedo values two to six times greater than new and aged HMA, resulting in surface temperature reductions of 17% and 27%, respectively.

Regarding models for UHI, traditional models struggle to capture the complex, multidimensional nature of UHI effects, driving a shift towards more advanced machine learning (ML) and deep learning (DL) approaches. ML models, such as Random Forest and Support Vector Machines, excel at identifying hidden patterns from diverse datasets, while DL models, including CNNs and LSTMs, handle larger, more complex data with improved accuracy. These models support two key UHI tasks: classifying high-risk areas for targeted mitigation and forecasting future heat patterns for proactive urban planning [33]. Despite their advantages, DL models face challenges like high computational costs and limited interpretability.

Traditional models face limitations in addressing the complex, multidimensional nature of the Urban Heat Island (UHI) effect. Consequently, the increasing threats posed by UHI have driven the development of more sophisticated modelling approaches. Recently, there has been a shift from physical models to machine learning (ML) models, which are favoured for their accuracy and ability to uncover hidden patterns in large, diverse datasets. ML models handle various data types, including numerical, categorical, satellite imagery, and locally sensed environmental variables, aiding in effective mitigation strategies [33, 34].

As UHI dynamics grow more complex and datasets expand, there is a rising demand for even more precise modelling. Deep learning (DL), a subset of ML, can process larger, more complex data and has seen increased application. These advanced models reveal intricate patterns and multi-scale relationships but introduce challenges such as high computational costs, limited interpretability, and inconsistent performance reporting. Addressing these issues is essential to ensure DL models remain reliable and practical for urban climate analysis. Recent UHI studies [34-38] apply ML and DL to two key tasks: classifying high-risk heat areas and forecasting future UHI patterns. Classification identifies vulnerable urban zones for targeted interventions, while prediction estimates future heat intensity, supporting early warning systems and long-term planning. These complementary tasks require distinct model architectures and data inputs. As ML and DL use in UHI modelling expands, evaluating their effectiveness in capturing spatial and temporal dynamics becomes critical.

Thereby, hybrid modelling approaches are necessary for enhancing urban heat mitigation strategies and decision-making.

## 6. FORESEEN RESEARCH AND CONCLUSIONS

A broader investigation is underway, focusing on critical locations and the development of an interactive map of the Urban Heat Island (UHI) effect for the city of Belgrade. Concrete paving elements (based on inorganic construction waste – IWC) were prepared and tested, followed by the optimization of their composition. While construction waste is frequently used in the production of paving elements, very few publications address the impact of color and albedo on such materials. Existing literature largely focuses on asphalt concrete, whereas the aim of this study is to produce elements using normal-weight concrete. The optimal IWC mixture composition

was determined by varying the water/cement ratio (0.4–0.55), filler content (10–30%) and type (ground tiles, stone, or sanitary ware), recycled concrete aggregate content (0–50%), and admixtures (superplasticizers). Laboratory testing of the samples covered hydration mechanisms and mineralogical changes, microstructural characteristics, workability, slump testing, density, water penetration depth under pressure, rebound number, ultrasonic pulse velocity, and mechanical strength. Sample durability was assessed through freeze-thaw cycle testing, both with and without the use of de-icing salts. Reflectometric characterization of the samples was conducted in accordance with the ASTM C1549 standard. The performance of the paving elements complies with EN and SRPS standards. Future activities include installing the acquired elements at selected pilot sites affected by the urban heat island effect, as well as monitoring and evaluating their impact on reducing ambient temperature.

## ACKNOWLEDGEMENT

This investigation is financially supported by the Ministry of Science, Technological Development and Innovation of the Republic of Serbia under Contract No.: 451-03-33/2026-03/200012.

## REFERENCES

[1] Q. Wu, Y. Huang, P. Irga, P. Kumar, W. Li, W. Wei, H. K. Shon, C. Lei, J. L. Zhou, (2024). Synergistic control of urban heat island and urban pollution island effects using green infrastructure, *Journal of Environmental Management*, Volume 370, 122985, https://doi.org/10.1016/j.jenvman.2024.122985.2018

[2] Revision of World Urbanization Prospects, website: https://www.un.org/en/desa/2018-revision-world-urbanization-prospects, accessed on 29.04.2026.

[3] Heat island effect, website: https://www.epa.gov/heatislands, accessed on 29.04.2026.

[4] Climate change, website: https://www.climate.gov/news-features/understanding-climate/climate-change-global-temperature, accessed on 29.04.2026.

[5] Global Carbon Project, website: https://globalcarbonbudget.org/fossil-co2-emissions-at-record-high-in-2023/, accessed on 29.04.2026.

[6] United Nations climate change, website: https://unfccc.int/, accessed on 29.04.2026.

[7] UN Sustainable development goals, website: https://www.undp.org/?gad_source=1, accessed on 29.04.2026.

[8] UN – 2050 long-term strategy, website: https://climate.ec.europa.eu/eu-action/climate-strategies-targets/2050-long-term-strategy_en, accessed on 29.04.2026.

[9] Urban Heat Islands; website: https://land8.com/how-landscape-architecture-mitigates-the-urban-heat-island-effect/, accessed on 29.04.2026)

[10] Cheng, X.; Ge, F.; Xu, M.; Li, Y. (2024). The heat island effect, digital technology, and urban economic resilience: Evidence from China. *Technological Forecasting and Social Change*, Volume 209, 123802. https://doi.org/10.1016/j.techfore.2024.123802.

[11] Aghazadeh, F.; Mashayekh, H.; Akbari, M. A.; Boroukanlou, S.; Habibzadeh, N.; Ghasemi, M.; Goswami, A. A(2024). GIRS-based analysis of urban green space losses with land-use changes and its relationship with surface urban heat island in the city of Tabriz. *Advances in Space Research*, Volume 75 (2), pp. 1804–1824. https://doi.org/10.1016/j.asr.2024.10.018.

[12] Jayasooriya, V. M.; Adams, M. D. (2024). From urban heat islands to intra-urban heat islands: Role of urban fabric in redefining microclimates of tomorrow's compact cities. *Energy and Buildings*, Volume 324, 114900. https://doi.org/10.1016/j.enbuild.2024.114900.

[13] Pérez, I. A.; García, M. Á.; Rasekhi, S.; Pazoki, F.; Fernández-Duque, B. (2024). Extension and trend of the London urban heat island under Lamb weather types.

*Sustainable Cities and Society*, Volume 114, 105743. https://doi.org/10.1016/j.scs.2024.105743.

[14] Li, Y.; Wang, S.; Zhang, S.; Wei, M.; Chen, Y.; Huang, X.; Zhou, R. (2024). The creation of multi-level urban ecological cooling network to alleviate the urban heat island effect. *Sustainable Cities and Society*, Volume 114, 105786. https://doi.org/10.1016/j.scs.2024.105786.

[15] Zhao, S.; Zhou, D.; Liu, S. (2015). Data concurrency is required for estimating urban heat island intensity. *Environmental Pollution*, Volume 208 (Pt A), 118–124. https://doi.org/10.1016/j.envpol.2015.07.037.

[16] Zhou, W.; Cao, W.; Wu, T.; Zhang, T. (2022). The win-win interaction between integrated blue and green space on urban cooling. *The Science of the Total Environment 2022*, Volume 863, 160712. https://doi.org/10.1016/j.scitotenv.2022.160712.

[17] Kumar, P.; Druckman, A.; Gallagher, J.; Gatersleben, B.; Allison, S.; Eisenman, T. S.; Hoang, U.; Hama, S.; Tiwari, A.; Sharma, A.; Abhijith, K. V.; Adlakha, D.; McNabola, A.; Astell-Burt, T.; Feng, X.; Skeldon, A. C.; De Lusignan, S.; Morawska, L. (2019). The nexus between air pollution, green infrastructure and human health. *Environment International*, Volume 133 (Pt A), 105181. https://doi.org/10.1016/j.envint.2019.105181.

[18] Deilami, K.; Kamruzzaman, Md.; Liu, Y. (2018). Urban heat island effect: A systematic review of spatio-temporal factors, data, methods, and mitigation measures. *International Journal of Applied Earth Observation and Geoinformation*, Volume 67, 30–42. https://doi.org/10.1016/j.jag.2017.12.009.

[19] Albedo effect; website: https://www.sciencefriday.com/educational-resources/the-albedo-effect-urban-heat-islands-and-cooling-down-your-playground/, accessed on 29.04.2026

[20] Milovanovic, B.; Radovanovic, M.; Schneider, C. (2020). Seasonal distribution of urban heat island intensity in Belgrade (Serbia). *Journal of the Geographical Institute Jovan Cvijic SASA*, Volume 70 (2), 163–170. https://doi.org/10.2298/ijgi2002163m.

[21] Savić, S.; Unger J.; Gál T.; Milošević D.; Popov Z. (2013). Urban heat island research of Novi Sad (Serbia): A review, *Geographica Pannonica*, Volume 17, Issue 1, 32-36

[22] Estolano, A. M. L.; Lima, N. B.; Lima, N. B.; VA, R., Junior; Belarmino, M. K. D. L.; Silva, A. I. S.; Nascimento, C. F. G.; Oliveira, N. T. C.; Lima, V. M. E.; Ioras, R. U. F.; Oliveira, R. A.; Lima, N. B. D.; Lima, N. B. D. (2019). Concrete paving blocks: Structural, thermodynamic, fluorescence, optical and mechanical properties. *Journal of Molecular Structure*, 1184, pp.443–451. https://doi.org/10.1016/j.molstruc.2019.02.048.

[23] Marinelli, A.; Rasheed, L. P. H. (2024). Considering Environmental Effects on porous concrete Applications: An Experimental investigation. *Procedia Structural Integrity*, Volume 54, pp.332–339. https://doi.org/10.1016/j.prostr.2024.01.091.A

[24] Mohajerani, A.; Bakaric, J.; Jeffrey-Bailey, T. (2017). The urban heat island effect, its causes, and mitigation, with reference to the thermal properties of asphalt concrete. *Journal of Environmental Management*, Volume 197, pp.522–538. https://doi.org/10.1016/j.jenvman.2017.03.095.

[25] Tan, K.; Qin, Y.; Du, T.; Li, L.; Zhang, L.; Wang, J. (2021). Biochar from waste biomass as hygroscopic filler for pervious concrete to improve evaporative cooling performance. *Construction and Building Materials*, Volume 287, 123078. https://doi.org/10.1016/j.conbuildmat.2021.123078.

[26] Yaghmour, E.; Qamar, M. A.; Naito, C.; Suleiman, M.; Fox, J.; Romero, C.; Neti, S. (2024). Pressure drop and heat transfer properties for normal weight and lightweight pervious concrete. *Construction and Building Materials*, Volume 425, 135947. https://doi.org/10.1016/j.conbuildmat.2024.135947.

[27] Adresi, M.; Yamani, A. R.; Tabarestani, M. K. (2024). Evaluating the effectiveness of innovative pervious concrete pavement system for mitigating urban heat island effects, de-icing, and de-clogging. Construction and Building Materials 2024, 449, 138361. https://doi.org/10.1016/j.conbuildmat.2024.138361.

[28] Chen, Y.; Sha, A.; Jiang, W.; Du, P.; Lu, Q.; Hu, K. (2024). Development and evaluation of STRC coating for cooling asphalt pavement and mitigating urban heat island effects. *Construction and Building Materials*, Volume 449, 138494. https://doi.org/10.1016/j.conbuildmat.2024.138494.

[29] Chen, J.; Chu, R.; Wang, H.; Zhang, L.; Chen, X.; Du, Y. (2019). Alleviating urban heat island effect using high-conductivity permeable concrete pavement. *Journal of Cleaner Production*, Volume 237, 117722. https://doi.org/10.1016/j.jclepro.2019.117722.

[30] Koppel, T.; Shishkin, A.; Haldre, H.; Toropovs, N.; Vilcane, I.; Tint, P. (2017). Reflection and transmission properties of common construction materials at 2.4 GHz frequency. *Energy Procedia*, Volume 113, pp.158–165. https://doi.org/10.1016/j.egypro.2017.04.045.

[31] Calis, G.; Yildizel, S. A.; Keskin, U. S. (2022). Investigation of color pigment incorporated roller compacted high performance concrete as a mitigation tool against urban heat island. *Case Studies in Construction Materials*, Volume 17, e01479. https://doi.org/10.1016/j.cscm.2022.e01479.

[32] Shamsaei, M.; Carter, A.; Vaillancourt, M. (2024). Using construction and demolition waste materials to alleviate the negative effect of pavements on the urban heat island: A laboratory, field, and numerical study. *Case Studies in Construction Materials*, Volume 20, e03346. https://doi.org/10.1016/j.cscm.2024.e03346.

[33] Samad, N.; Farnaghi, M.; Ostermann, F. O.; Zurita-Milla, R. (2026). A systematic literature review of machine learning and deep learning for urban heat island modelling. *Discover Cities*, Volume 3 (1). https://doi.org/10.1007/s44327-026-00223-1.

[34] Alzubaidi, L.; Zhang, J.; Humaidi, A. J.; Al-Dujaili, A.; Duan, Y.; Al-Shamma, O.; Santamaría, J.; Fadhel, M. A.; Al-Amidie, M.; Farhan, L. (2021). Review of deep learning: concepts, CNN architectures, challenges, applications, future directions. *Journal of Big Data*, Volume 8 (1), 53. https://doi.org/10.1186/s40537-021-00444-8.

[35] Sahana, V.; Mondal, A.; Sreekumar, P. (2021). Drought vulnerability and risk assessment in India: Sensitivity analysis and comparison of aggregation techniques. *Journal of Environmental Management*, Volume 299, 113689. https://doi.org/10.1016/j.jenvman.2021.113689.

[36] Zhuang, F.; Qi, Z.; Duan, K.; Xi, D.; Zhu, Y.; Zhu, H.; Xiong, H.; He, Q. (2020). A comprehensive survey on transfer learning. *Proceedings of the IEEE 2020*, Volume 109 (1), pp.43–76. https://doi.org/10.1109/jproc.2020.3004555.

[37] Jia, H.; Yang, D.; Deng, W.; Wei, Q.; Jiang, W. (2020). Predicting land surface temperature with geographically weighed regression and deep learning. Wiley,*Interdisciplinary Reviews Data Mining and Knowledge Discovery*, Volume 11 (1). https://doi.org/10.1002/widm.1396.

[38] Fu, S.; Wang, L.; Khalil, U.; Cheema, A. H.; Ullah, I.; Aslam, B.; Tariq, A.; Aslam, M.; Alarifi, S. S. (2024). Prediction of surface urban heat island based on predicted consequences of urban sprawl using deep learning: A way forward for a sustainable environment. *Physics and Chemistry of the Earth Parts a/B/C*, Volume 135, 103682. https://doi.org/10.1016/j.pce.2024.103682.

https://doi.org/10.24867/INDIS-2026-EN-215



# STATIC AND DYNAMIC CALCULATION OF THE LOAD-BEARING STRUCTURE OF A RESIDENTIAL BUILDING

*Ivana Šalić[1], Šime Serdarević[2], Nina Šantek[3], Dalibor Gelo[4]*

***Summary:***

This paper presents static and dynamic analysis of a residential building. The building has a floor plan area of 11.17 × 8.72 m and consists of two above-ground floors: the ground floor and the first floor. Based on the prepared architectural documentation, the geometry of the house was modeled using global and local calculation models. The structural system of the residential building is based on reinforced concrete elements with brick masonry infill and a timber roof. Structural elements, both horizontal and vertical, as well as the roof structure, were dimensioned in accordance with applicable standards and regulations. The entire modelling, structural analysis and design of the reinforced concrete and timber structural elements were carried out using SCIA Engineer 26.0 (SCIA nv, Hasselt, Belgium). The calculation of wind actions was performed using the "Opterećenja" software developed by Željko Finžgar, which provides calculation of permanent, snow and wind actions in accordance with HRN and HRN EN 1991.

*Keywords: static analysis, dynamic analysis, earthquake, SCIA Engineer, Eurocode*

# STATIČKI I DINAMIČKI PRORAČUN NOSIVE KONSTRUKCIJE OBITELJSKE KUĆE

***Rezime:***

U radu je prikazan statički i dinamički proračun stambene građevine. Građevna je tlocrtne površine 11,17x8,72 m, sastoji se od dvije nadzemne etaže: prizemlje i I. kat. Temeljem izrađenih arhitektonskih podloga geometrija kuće modelirana je primjenom globalnih i lokalnih proračunskih modela. Konstrukcijski sustav stambene građevine temelji se na armiranobetonskim elementima, uz zidanu ispunu od opeke te drveni krov. Nosivi elementi konstrukcije, kako horizontalni, tako i vertikalni, kao i krovna konstrukcija dimenzionirat će se u skladu sa važećim normama i propisima. Cjelokupno modeliranje, proračun konstrukcije i dimenzioniranje elemenata od armiranog betona i drva provedeni su pomoću računalnog programa SCIA Engineer 26.0 (SCIA nv, Hasselt, Belgija). Proračun djelovanja vjetra proveden je pomoću softvera „Opterećenja" autora Željka Finžgara, koji omogućuje proračun stalnih opterećenja, opterećenja snijegom i vjetrom u skladu s normama HRN i HRN EN 1991.

*Ključne reči: statički proračun, dinamički proračun, potres, SCIA Engineer, Eurokod*

[1] Civil Engineer, Vodoopskrba i odvodnja d.o.o., Zagreb, Croatia, ivana.salic@zgh.hr
[2] Senior Lecturer, Zagreb University of Applied Sciences, Zagreb, Croatia, sime.serdarevic@tvz.hr, ORCID 0009-0004-9873-4658
[3] Lecturer, Zagreb University of Applied Sciences, Zagreb, Croatia, nina.santek@tvz.hr, ORCID 0009-0007-6661-6616
[4] Senior Lecturer, Zagreb University of Applied Sciences, Zagreb, Croatia, dalibor.gelo@tvz.hr, ORCID 0009-0008-5261-107X

## 1. INTRODUCTION

Building's structure is a less complex residential building containing two residential units. The building is located on cadastral plot no. 2121/17, cadastral municipality Klara Nova, with a total area of 340 m² (Fig. 1). The terrain is predominantly flat with no significant slopes. According to the General Urban Development Plan of the City of Zagreb (SGGZ 28/2025), the plot is located within the M1 mixed-use predominantly residential zone. The building is designed as a detached structure with a gable roof, two above-ground floors (ground floor and first floor) and a basement under part of the building. The foundations and basement of this building are not included in the analysis, therefore, for the purposes of the calculation model, supports under the columns and walls of the structure will be used in order to properly distribute the loads on the ground.




*Fig. 1. Building location*

## 2. RESIDENTIAL BUILDING (LOCATION: KUČAR III. 19, ZAGREB)

### 2.1. LOCATION AND BASIC TECHNICAL DATA

The building is rectangular in shape with floor plan dimensions of 11.17 × 8.72 m (Fig. 2). It consists of a basement, ground floor, and first floor. The structural system is based on reinforced concrete elements with 25 cm thick brick masonry infill. The reinforced concrete elements were designed using concrete C25/30. Columns have cross-sectional dimensions of 25/25 cm, while beams dimensions are 25/30 cm. Concrete slab is 20 cm thick. Reinforcement meshes and reinforcing bars of class B500B were used. The roof structure is gable-shaped and made of timber classes C24 and GL28h.

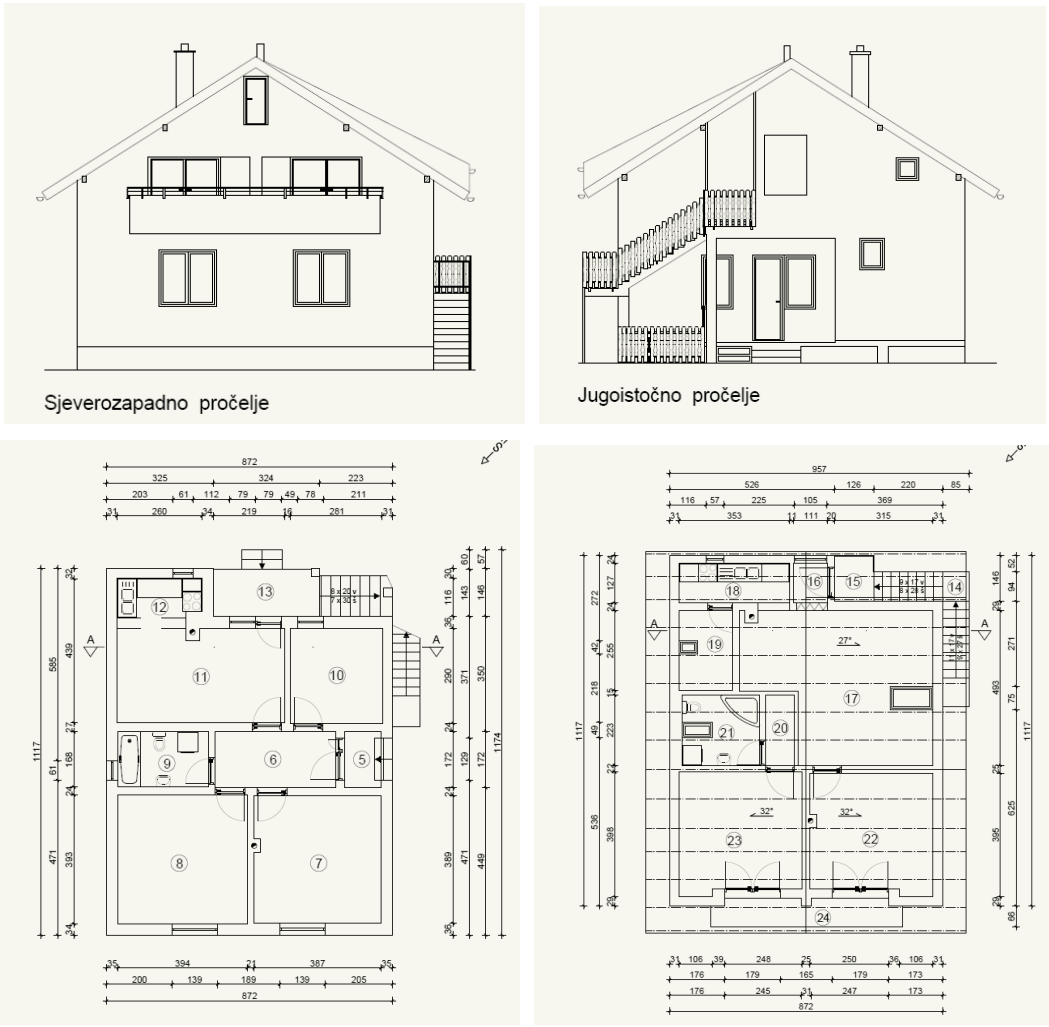


*Fig 2 . Architectural drawings*

## 2.2. VERIFICATION OF MECHANICAL RESISTANCE AND STABILITY

A verification and analysis of the fulfilment of the basic requirements regarding mechanical resistance and stability, as well as seismic resistance, were carried out using modal analysis within the SCIA Engineer 26.0 software package.

### 2.2.1. Loads

Loads on the structure such as wind, snow, fire, operational loads, and other loads were considered according to the Croatian standards based on HRN EN 1991.
**Permanent load:** the most significant permanent load is the self-weight of the structure, calculated according to the dimensions and material densities. The self-weight of structural elements was automatically generated in SCIA Engineer 26.0.
**Additional permanent load:** additional permanent loads include the weight of construction layers, roof coverings, installations, and floor layers according to HRN EN 1991-1-1:2012: Eurocode 1: Actions on structures – Part 1-1: General actions – Densities, self-weight, imposed loads for buildings. The calculated additional permanent load for the roof structure was $\Delta g = 1.798$ kN/m², while the additional permanent load for the slab structure was $\Delta g = 2.340$ kN/m² (Tab. 1).

*Tab. 1. Additional permanent load – slab structure*

| | FLOOR STRUCTURE | d [m] | γ [kN/m$^3$] | dx γ [kN/m$^2$] |
|---|---|---|---|---|
| 1. | Floor finish | 0,025 | 9,60 | 0,240 |
| 2. | Cement screed | 0,065 | 22,00 | 1,430 |
| 3. | PE foil | / | / | / |
| 4. | Thermal insulation | 0,02 | 2,0 | 0,040 |
| 5. | Plaster | 0,02 | 19,00 | 0,380 |
| 6. | Service installations | / | / | 0,250 |
| Σ | | | Δg = | 2,340 kN/m$^2$ |

**Imposed load:** the imposed load was calculated according to HRN EN 1991-1-1:2012: Eurocode 1: Actions on structures – Part 1-1: General actions – Densities, self-weight, imposed loads for buildings; for residential buildings (Category A), with a floor load of 2.0 kN/m² and a balcony load of 4.0 kN/m².
**Snow load:** the characteristic snow load for the relevant snow zone (III. snow zone and ) was adopted as $s_k$ = 1.00 kN/m² , according to HRN EN 1991-1-3:2012: Eurocode 1: Actions on structures – Part 1-3: General actions – Snow loads.
**Wind load:** wind load was calculated using the software package named 'Opterećenja' (eng. 'Loads') (Fig. 3 and 4).

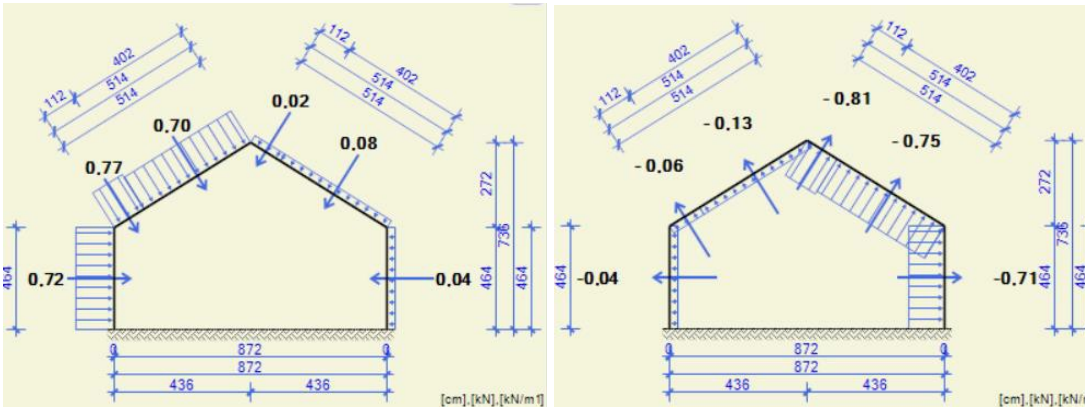


*Fig. 3. Wind load calculation in the software "Opterećenja"*

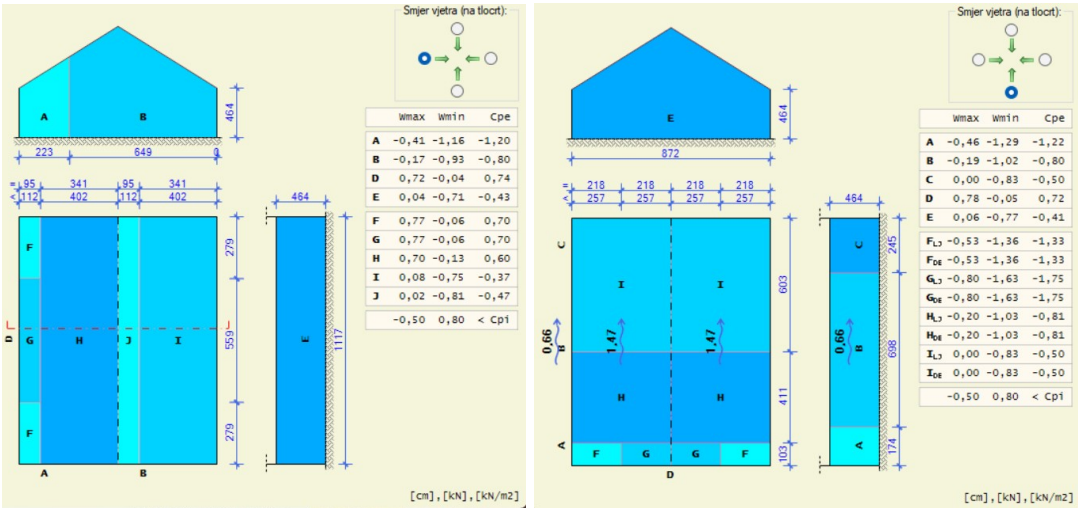


*Fig. 4. Wind load values in the software "Opterećenja" [8]*

**Seismic load:** seismic load was calculated in accordance with the standard HRN EN 1998-1-1:1994: Eurocode 8: Design of structures for earthquake resistance – Part 1: General rules, seismic actions and rules for buildings. The structure is designed for horizontal seismic action described by two perpendicular components, $F_x$ and $F_y$, acting in two orthogonal planes. The values of the seismic forces are determined by applying the design response spectrum, which depends on the seismic characteristics of the location, the soil category, the importance class of the structure, and the total weight of the structure, all in accordance with Eurocode 8. In the city of Zagreb, the characteristic soil type is classified as C – layers of dense or medium – dense sand, gravel, or stiff clay with thicknesses ranging from several tens to several hundreds of meters. The importance class is II – ordinary buildings, i.e. buildings that do not belong to other categories, while the reference peak ground acceleration for the given location, corresponding to a return period of 475 years, is $a_{gR}$ = 0.234g.

### 2.2.2. Structural Modeling in SCIA Engineer 26

Modeling was performed with two separate models (timber roof structure+main load-bearing RC structure). Timber roof structure modeling consists of two separate models, one for timber roof rafter element and other for timber roof purlin element (Fig. 5). The objective of the timber roof structure analysis was to verify the selected elements (cross sections, elements and material) for ultimate and serviceability limit state requirements and to determine support reactions for transfer to the main load-bearing RC structure.

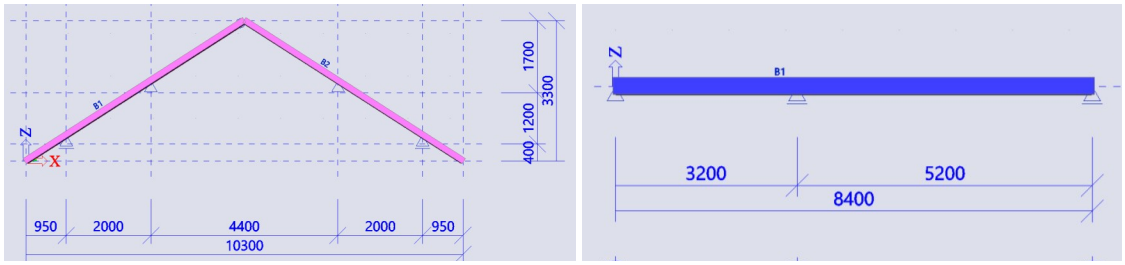


*Fig. 5. Timber rafter and purlin*

The assumed loads were defined, the verification of internal forces and bending moments was carried out, and finally, the utilization check of the elements was performed. It was

concluded that the selected elements satisfy the assumed ultimate and serviceability limit state requirements. (Fig. 6, 7 and 8)

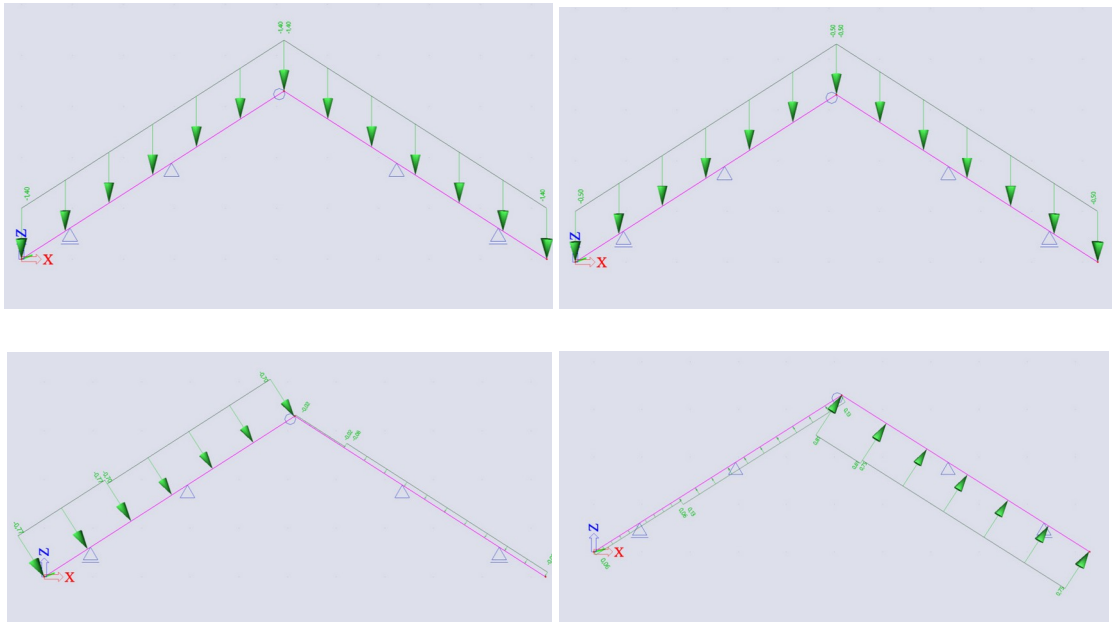

*Fig. 6. Loads – timber rafter*

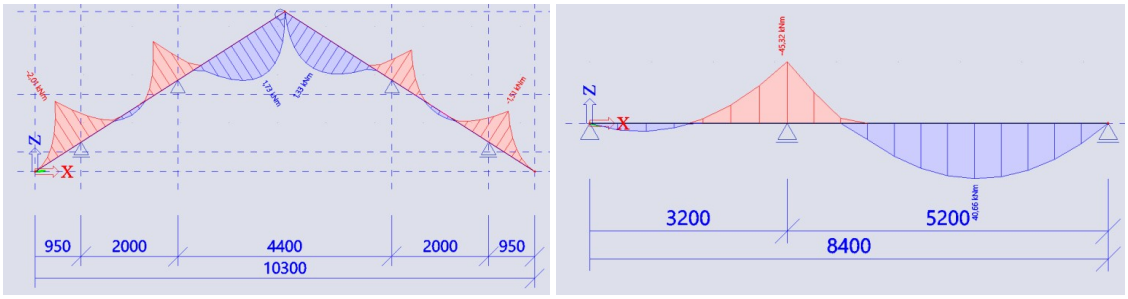


*Fig. 7. Bending moment – rafter and purlin*

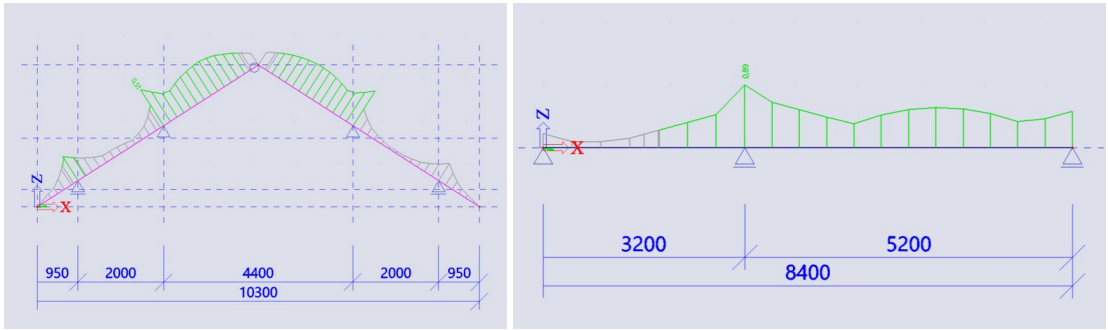


*Fig. 8. ULS utilization – rafter and purlin*

Main-load bearing RC structure consists of vertical, inclined, and horizontal reinforced concrete elements as shown in Fig. 9. For the modelling of vertical elements, reinforced concrete class C25/30 and square cross-sections with dimensions b/h = 25/25 cm were selected, while the horizontal and inclined elements were also designed in reinforced concrete class C25/30, but with dimensions b/h = 25/30 cm.

Loads from the analysis and calculation of the timber roof structure (Fig. 10) were applied to the model. For the seismic load spectrum, type 2 was selected because, for the considered natural vibration periods, it provides more unfavorable (higher) values of spectral acceleration and consequently higher seismic forces within the structure. By adopting this spectrum type, a more conservative and therefore safer approach to determining seismic load is ensured (Fig. 11).

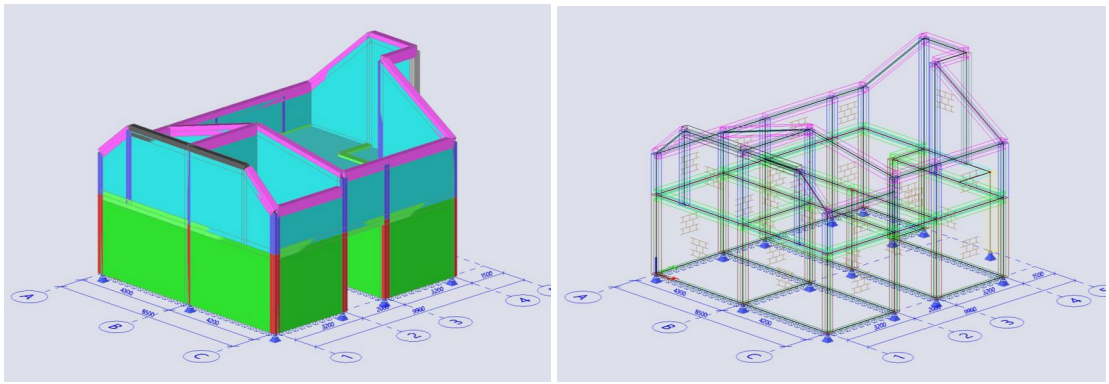

*Fig. 9. Main load – bearing RC structure model*

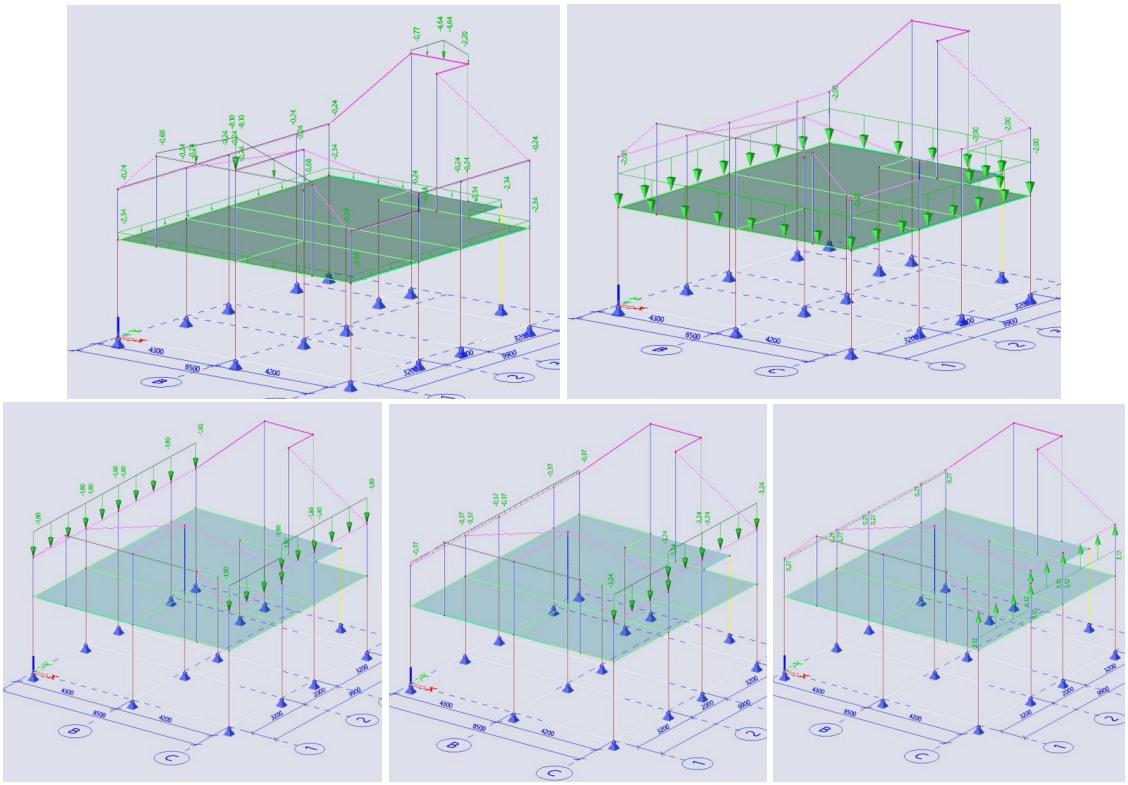

*Fig. 10. Loads – main load-bearing RC structure*

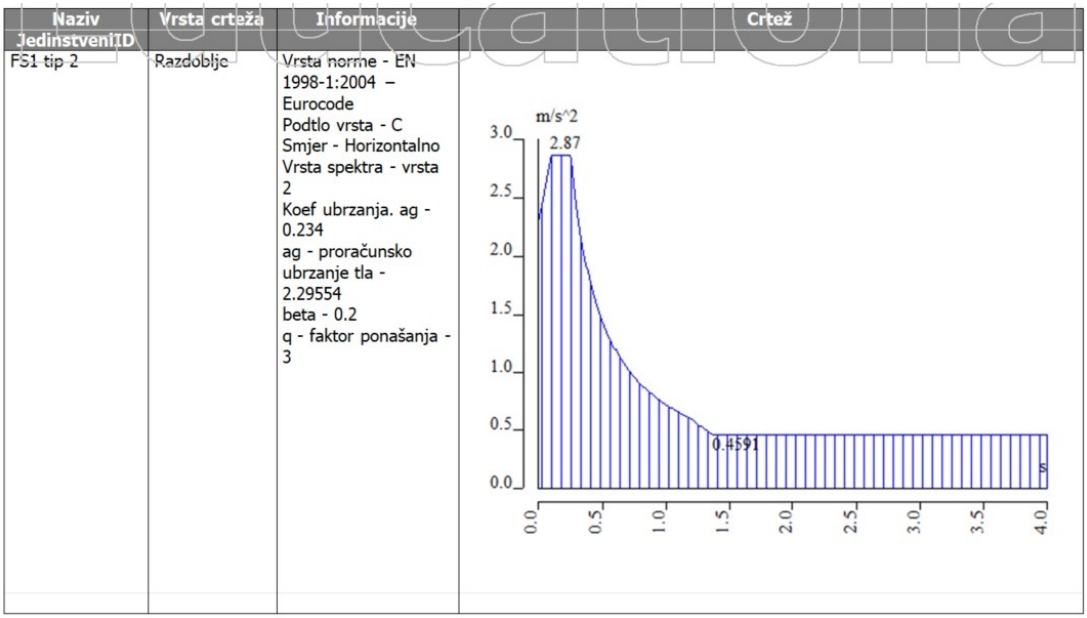


*Fig. 11. Seismic spectrum*

The modal analysis was performed to determine the natural vibration characteristics of the main load-bearing structure and to obtain the modal response of the building under seismic excitation. The calculated natural vibration modes were subsequently used in the seismic response spectrum analysis. The first relevant translational modes describe the predominant response of the structure in the horizontal X and Y directions, while the torsional mode provides information on the torsional response of the building.

The second vibration mode predominantly activates the Y direction, the third mode activates the X direction, while the fourth mode is predominantly torsional. The modal participating mass ratios were considered in the seismic response analysis in order to account for the dynamic response of the structure in both principal horizontal directions.

The seismic effects obtained from the response spectrum analysis were not considered as a separate verification only, but were included in the governing load combinations used for the structural design. The resulting seismic combinations generated internal forces in the structural members, including axial forces, bending moments and shear forces. These internal forces were then used for the ultimate and serviceability limit state checks of the reinforced concrete elements.

For the member design, the critical vertical and horizontal reinforced concrete elements were selected based on the governing combinations and the highest resulting internal forces. The reinforcement was subsequently determined from these design actions. In this way, the modal analysis directly contributes to the seismic design of the structural members by defining the dynamic seismic actions that are transferred into the member forces used for the final reinforcement and utilization checks.

For the floor structure Q335 reinforcement mesh was selected for both the upper and lower reinforcement zones, with the note that local extreme values were neglected and that additional reinforcement bars should be provided at locations where the defined reinforcement mesh is insufficient. The verification of the required slab reinforcement in the x and y directions is shown in Fig. 12 and 13.

The critical vertical and horizontal elements were selected based on the governing internal forces obtained from the complete set of load combinations, including the seismic combinations resulting from the response spectrum analysis. The design actions, primarily axial force, bending moment and shear force, were used for the ultimate limit

state verification and determination of the required reinforcement. The utilization ratios obtained from these checks were then used to verify the adequacy of the adopted cross-sections and reinforcement. For vertical element reinforcement consisting of 4Φ14 bars and Φ8/15 cm stirrups was adopted. For horizontal element reinforcement consisting of 2Φ14+2Φ14+2Φ10 bars and Φ8/15 cm stirrups was adopted. The utilization check of the ground floor vertical element as well as the ground floor horizontal element is presented in Fig. 14, while the selected cross-sections are shown in Fig. 15.

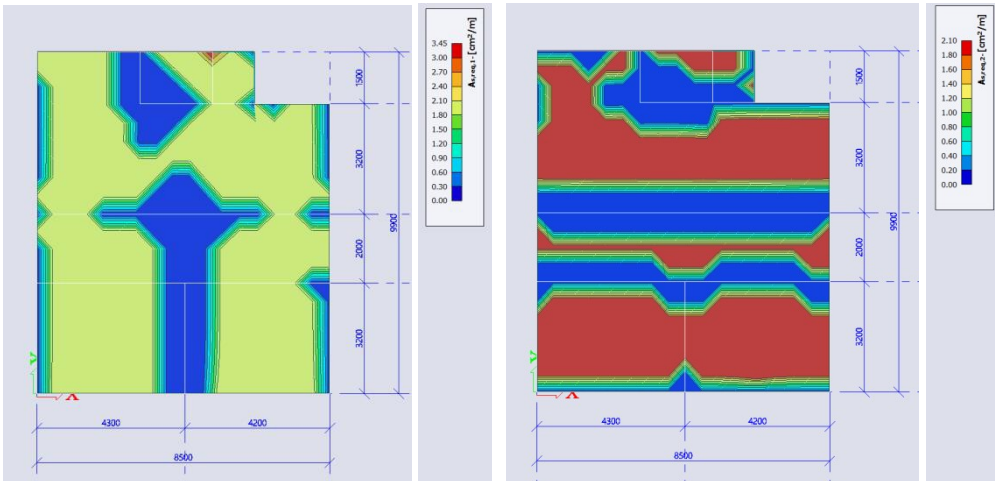


*Fig. 12. Required reinforcement – slab (bottom zone, x and y direction)*

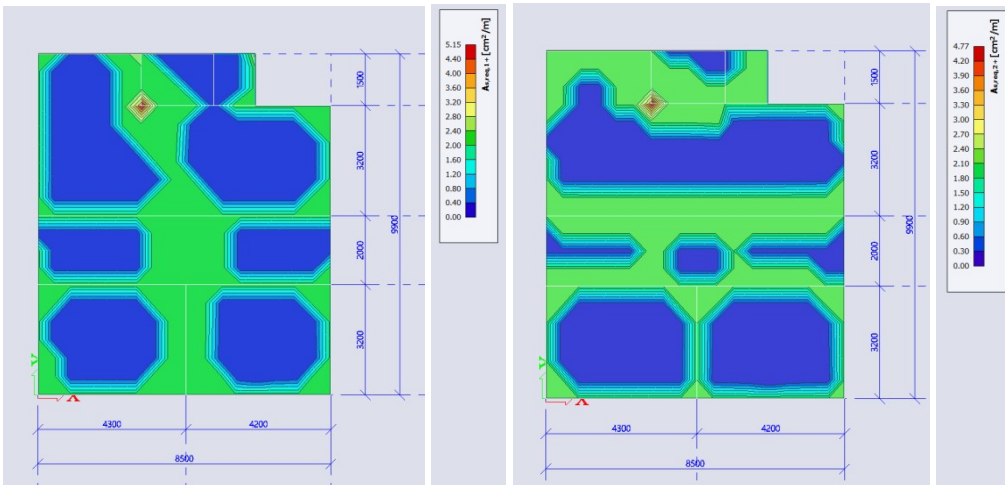


*Fig. 13. Required reinforcement – slab (top zone, x and y direction)*

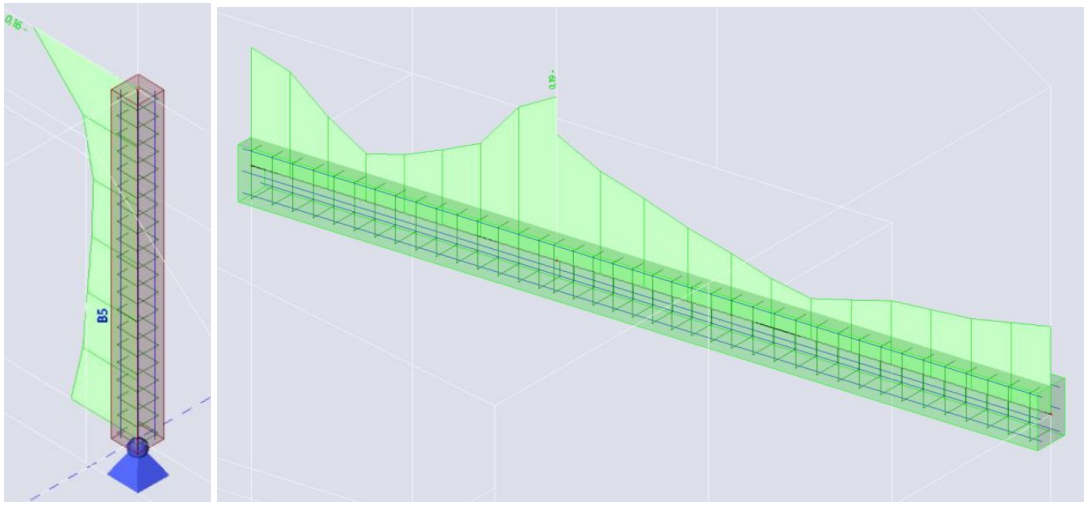


*Fig. 14. ULS utilization – horizontal and vertical RC elements*

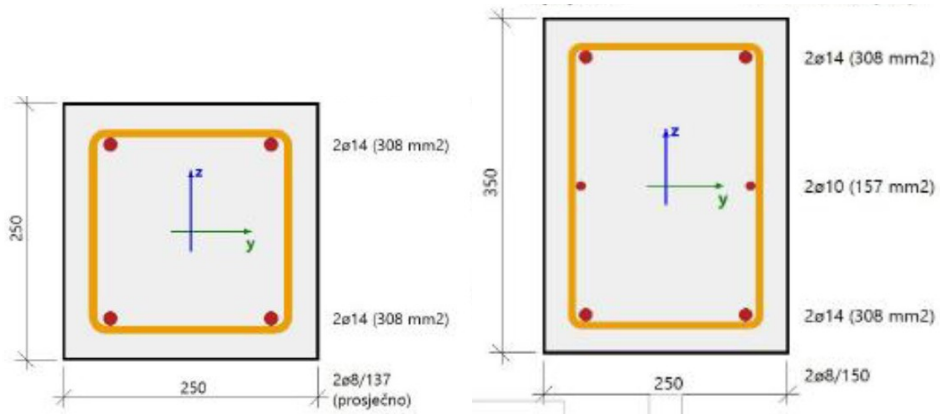


*Fig. 15. Cross-sections – horizontal and vertical RC elements*

The second vibration mode activates the Y direction, the third mode activates the X direction, while the fourth mode activates torsion. The calculation protocol with participating mass ratios is presented in Fig. 16, and the vibration modes in 3D representation are shown in Fig. 17.

**Solution of Free vibration**

| | |
|---|---|
| Number of 2D elements | 1381 |
| Number of 1D elements | 371 |
| Number of mesh nodes | 1400 |
| Number of equations | 8400 |
| Combination of mass groups | CM1 |
| Modification group | None |
| Number of frequencies | 10 |
| Method | Lanczos |
| Bending theory | Mindlin |
| Type of analysis model | Standard |
| Nodal mass matrix | Diagonal |

**Sum of masses**

| | Mass type | X [kg] | Y [kg] | Z [kg] |
|---|---|---|---|---|
| CM1 | Moving mass | 212830,51 | 212830,51 | 212830,51 |
| CM1 | Total mass | 218902,10 | 218902,10 | 218902,10 |

**Relative modal masses**

| Mode | ega [rad | Period [s] | Freq. [Hz] | Γxi | Γyi | Γzi | Wxi/Wxtot | Wyi/Wytot | Wzi/Wztot | xi_R/Wxtot | yi_R/Wytot | zi_R/Wztot |
|---|---|---|---|---|---|---|---|---|---|---|---|---|
| 1 | 38.8134 | 0,16 | 6,18 | -7,5481 | 169,3389 | 2,1974 | 0,0003 | 0,1347 | 0,0000 | 0,0404 | 0,0001 | 0,0004 |
| 2 | 62.0536 | 0,10 | 9,88 | 17,7955 | 390,0688 | -1,1726 | 0,0015 | 0,7149 | 0,0000 | 0,0013 | 0,0001 | 0,0570 |
| 3 | 74.7375 | 0,08 | 11,89 | 386,9597 | 56,3898 | -2,8800 | 0,7036 | 0,0149 | 0,0000 | 0,0002 | 0,0170 | 0,1622 |
| 4 | 80.3494 | 0,08 | 12,79 | 203,0756 | 80,8477 | -2,3010 | 0,1938 | 0,0307 | 0,0000 | 0,0003 | 0,0025 | 0,6244 |
| 5 | 95.5495 | 0,07 | 15,21 | 12,4400 | -12,5867 | -7,3658 | 0,0007 | 0,0007 | 0,0003 | 0,0004 | 0,0000 | 0,0453 |
| 6 | 108.98 | 0,06 | 17,34 | 1,0363 | 19,5650 | -0,1306 | 0,0000 | 0,0018 | 0,0000 | 0,0005 | 0,0000 | 0,0102 |
| 7 | 116.053 | 0,05 | 18,47 | -2,6948 | -88,3296 | -5,0186 | 0,0000 | 0,0367 | 0,0001 | 0,0343 | 0,0000 | 0,0012 |
| 8 | 137.402 | 0,05 | 21,87 | 36,7856 | -0,4350 | -5,1693 | 0,0064 | 0,0000 | 0,0001 | 0,0000 | 0,0023 | 0,0002 |
| 9 | 147.247 | 0,04 | 23,44 | -1,3170 | -15,6229 | 23,8735 | 0,0000 | 0,0011 | 0,0027 | 0,0006 | 0,0012 | 0,0023 |
| 10 | 149.164 | 0,04 | 23,74 | -18,6620 | 9,1797 | -35,8049 | 0,0016 | 0,0004 | 0,0060 | 0,0038 | 0,0017 | 0,0003 |
| | | | | | | | 0,9078 | 0,9360 | 0,0093 | 0,0819 | 0,0249 | 0,9034 |

*Fig. 16. Modal analysis – calculation protocol*

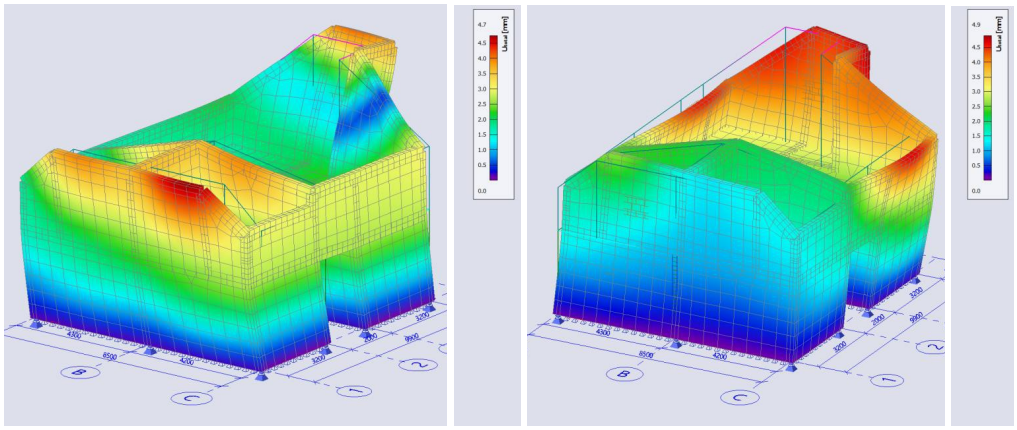

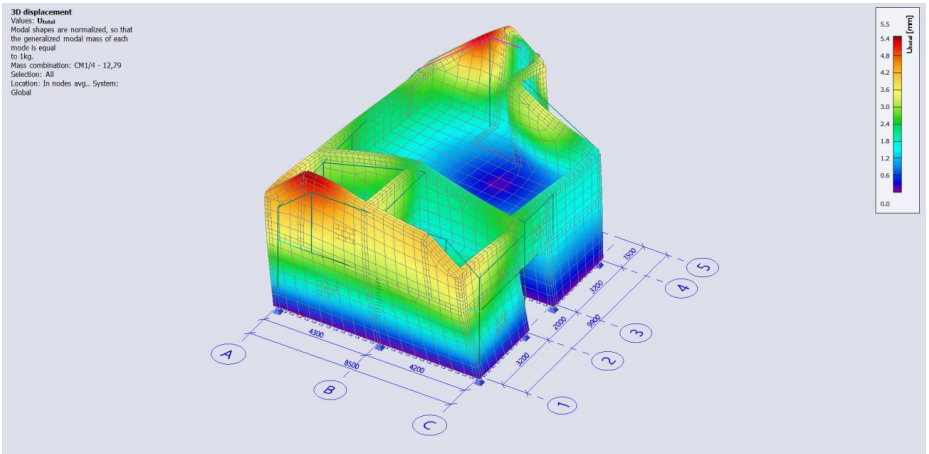


*Fig. 17. Vibration modes*

## 3. CONCLUSION

Based on the presented calculations and detailed structural analysis, it can be concluded that all load-bearing elements satisfy the assumed requirements of ultimate and serviceability limit states by the Eurocode standards. The obtained results of the static and dynamic analysis confirm the expected structural behavior under seismic loading while ensuring the necessary conditions of stability, stiffness, and durability. The modal analysis provided the dynamic characteristics of the structure and the corresponding seismic response used in the response spectrum analysis. The resulting seismic effects were incorporated into the governing design load combinations and subsequently used for the verification and dimensioning of the reinforced concrete structural members. Therefore, the modal analysis represents an integral part of the design procedure rather than an independent assessment of the structural dynamic characteristics.
During the dimensioning of structural elements and the selection of reinforcement and construction materials, an approach combining technical reliability and economic efficiency was applied. Based on the presented analysis, it can be concluded that the designed structure fully complies with the applicable technical regulations and is suitable for safe and long-term use in accordance with its intended purpose.

## REFERENCES

[1] HRN EN 1990:2011 Eurocode: Basis of structural design (EN 1990:2002+A1:2005+A1 :2005/AC:2010); Croatian Standards Institute (HZN); Zagreb, 2011.

[2] HRN EN 1991-1-1 Eurocode 1: Actions on structures -- Part 1-1: General actions -- Densities, self-weight and imposed loads for buildings (EN 1991-1-1:2002+AC:2009); Croatian Standards Institute (HZN); Zagreb, 2012.

[3] HRN EN 1991-1-3 Eurocode 1: Actions on structures -- Part 1-3: General actions -- Snow loads (EN 1991-1-3:2003+AC:2009); Croatian Standards Institute (HZN); Zagreb, 2012.

[4] HRN EN 1991-1-4 Eurocode 1: Actions on structures -- Part 1-4: General actions -- Wind actions (EN 1991-1-4:2005+AC:2010+A1:2010); Croatian Standards Institute (HZN); Zagreb, 2012.

[5] HRN EN 1995-1-1 Eurocode 5: Design of timber structures -- Part 1-1: General -- Common rules and rules for buildings (EN 1995-1-1:2004+AC:2006+A1:2008); Croatian Standards Institute (HZN); Zagreb, 2013.

[6] HRN EN 1992-1-1 Eurocode 2: Design of concrete structures -- Part 1-1: General rules and rules for buildings (EN 1992-1-1:2004+AC:2010); Croatian Standards Institute (HZN); Zagreb, 2013.

[7] HRN EN 1998-1 Eurocode 8: Design of structures for earthquake resistance -- Part 1: General rules, seismic actions and rules for buildings (EN 1998-1:2004+AC:2009); Croatian Standards Institute (HZN); Zagreb, 2011.

[8] SCIA Engineer 26.0, SCIA nv, Hasselt, Belgium, 2025.

[9] Opterećenja, Željko Finžgar, version 3.4.2.1, available at: er-ef.net/opterecenja.html

https://doi.org/10.24867/INDIS-2026-EN-227



# HALL 7 OF THE NOVI SAD FAIR – PART I: THE ASSESSMENT OF THE LOAD-BEARING STRUCTURE

*Vladimir Živaljević[1], Andrija Rašeta[2], Igor Džolev[3]*

***Summary:***

Hall 7 of the Novi Sad Fair had suffered severe structural damage during the supercell storms in July 2023. The extreme wind loading caused partial failure of the roof structure and destruction of roof coverings. In order to evaluate the structural condition and define appropriate rehabilitation measures, a detailed visual inspection and numerical assessment of the load-bearing steel structure were carried out. The inspection included the examination of all primary and secondary steel structural members. A three-dimensional finite element model of the existing structure was developed and analysed in accordance with the relevant Eurocode standards. The acquired results revealed weaknesses in the load-bearing capacity of many structural elements, confirming the need for strengthening measures.

*Keywords: structural assessment, steel structures, rehabilitation, finite element analysis*

# HALA 7 NOVOSADSKOG SAJMA – DEO I: PROCENA STANJA NOSEĆE KONSTRUKCIJE

***Rezime:***

Hala 7 Novosadskog sajma pretrpela je značajna oštećenja tokom superćelijskih oluja u julu 2023. godine. Ekstremno dejstvo vetra izazvalo je delimično urušavanje krovne konstrukcije, kao i uništenje krovnog pokrivača. U cilju procene stanja konstrukcije i definisanja mera sanacije sprovedeni su detaljan vizuelni pregled i numerička analiza noseće čelične konstrukcije. Pregledom su obuhvaćeni svi primarni i sekundarni čelični elementi konstrukcije. Formiran je trodimenzionalni model postojeće konstrukcije pomoću softvera baziranog na metodi konačnih elemenata i izvršene su analize u skladu sa relevantnim Evrokod standardima. Dobijeni rezultati pokazali su nedovoljnu nosivost mnogih elemenata konstrukcije, čime je potvrđena potreba za sprovođenjem mera ojačanja.

*Ključne reči: procena stanja, čelične konstrukcije, sanacija, metod konačnih elemenata*

[1] Assistant Prof., Faculty of Technical Sciences, University of Novi Sad, Serbia, zivaljevic.vladimir@uns.ac.rs, ORCID 0000-0002-2808-2664
[2] Full Prof., Faculty of Technical Sciences, University of Novi Sad, Serbia, araseta@uns.ac.rs, ORCID 0000-0002-4535-1379
[3] Associate Prof., Faculty of Technical Sciences, University of Novi Sad, Serbia, idzolev@uns.ac.rs,, ORCID 0000-0002-7622-7936

## 1. INTRODUCTION

In July 2023, Serbia and the wider Balkan region were struck by several severe supercell storms, which were among the strongest ever recorded in the area. The storms brought hurricane-force winds, intense rainfall and large hail. Wind gusts in some locations exceeded 27 m/s, causing widespread destruction across Serbia, Croatia, Bosnia and Herzegovina, and Slovenia. The storms caused significant damage to residential, commercial, and industrial buildings, including roof failures, and collapsed structures. Large areas of forests and agricultural land were devastated, while thousands of trees and utility poles were dislodged. Transportation and power infrastructure suffered major disruptions, leading to road blockages, railway interruptions, and prolonged electricity outages in many regions. Several people lost their lives and many were injured due to falling trees, debris, and structural failures.
During these severe storms, Hall 7 of the Novi Sad Fair suffered significant structural damage. Extremely strong wind gusts caused partial failure of the roof structure and damage to roof cladding and facade elements. Parts of the steel roof system were deformed, while certain secondary structural elements and roof coverings were detached or displaced by the wind (Fig. 1). The storm also caused damage to the surrounding infrastructure and installations within the fair complex. Following the event, the detailed inspection and structural assessment were carried out in order to evaluate the extent of the damage of the structure, determine the structural safety of the building, and define the necessary rehabilitation and reconstruction measures.



*Fig. 1 Collapsed roof structure overthrown in front of the building (source: https://nova.rs)*

In this paper the assessment of the load-bearing steel structure of Hall 7 of the Novi Sad Fair after the supercell storm event of July 2023 is presented [1]. Detailed visual inspection of the structural system, identification of the observed damage and defects, development of a three-dimensional numerical model, and structural verification in accordance with the relevant Eurocode provisions were included in the study. Based on the results of the assessment, the structural safety and load-bearing capacity of the existing structure were evaluated and the necessity of rehabilitation and strengthening measures was determined.

## 2. DESCRIPTION OF THE STRUCTURAL SYSTEM

The ground plan of the hall is measuring 50.0 × 50.0 m. The load-bearing steel structure consists of four main steel four-legged lattice columns positioned at an axial distance of 7.5 m from the edge of the building. This means that the axial spacing between these columns in both directions is 35.0 m. Roof structure is formed from four pairs of steel

trusses resting on the corresponding lattice columns. In this way, four main lattice frames are formed, each consisting of a pair of lattice frames spaced 50 cm apart, connected at node locations by welded transverse bracings (L-profiles or steel plates).
The secondary roof steel structure is grillage consisting of four steel trusses in each direction. These trusses are spaced 7.0 m apart. Additionally, roof girders are placed between the trusses. Along the main diagonal directions of the building, "R" girders are installed, while along the perimeter of the entire structure, "R" columns are placed beneath the primary and secondary lattice roof girders. All structural steel elements are connected by welding, either through connection plates or by direct welded joints.
The foundations of the four main lattice columns are made of reinforced concrete isolated footings with a cruciform plan shape. Along the perimeter of the building, a strip footing was designed for the parapet and gable walls. Above the foundations, a 10 cm thick ground concrete slab was constructed over a 10 cm gravel layer. The load-bearing steel structure is shown in Fig. 2.

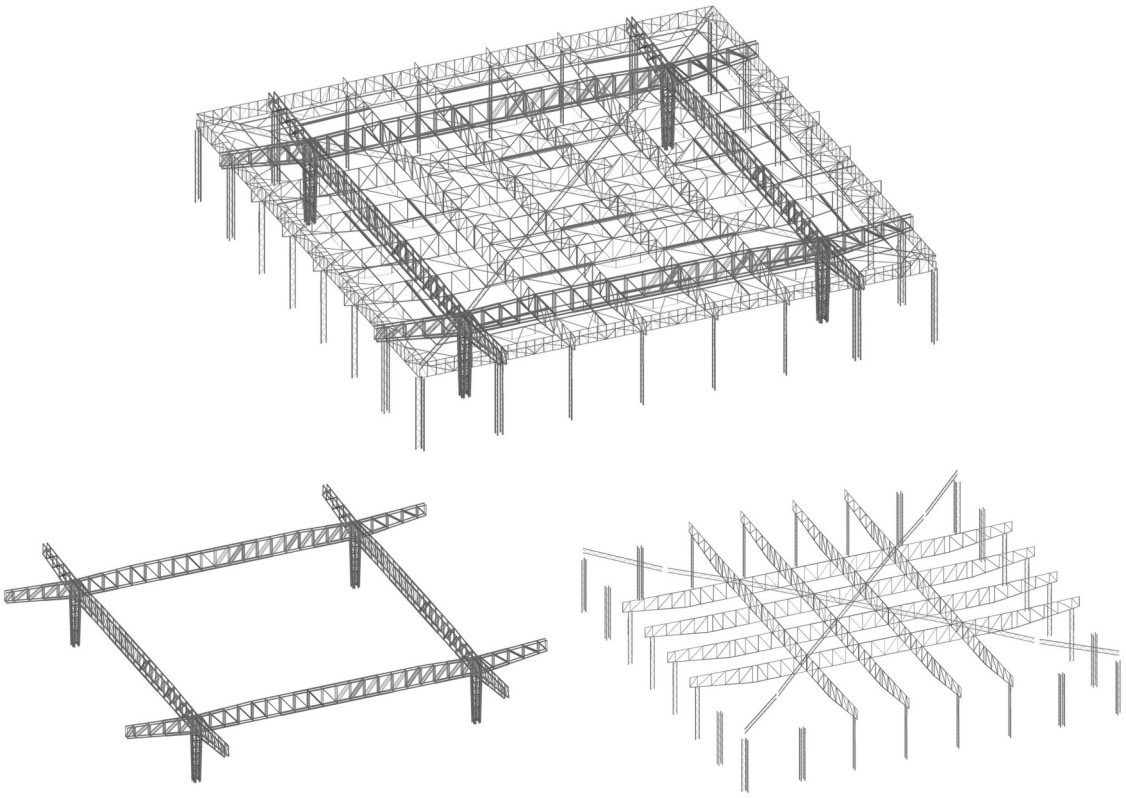

*Fig. 2 Bearing structure of the hall: all structural elements (top), main lattice columns and roof girders (bottom left), secondary roof grillage, “R” girders and “R” columns (bottom right)*

## 3. VISUAL INSPECTION

The visual examination included all accessible above-ground structural elements of the facility, such as the main steel lattice columns and truss girders, steel truss grillage, perimeter "R" columns, diagonal "R" roof girders, as well as the secondary steel roof components and roof surface.
The visual inspection of four main steel four-legged lattice columns and four pairs of steel trusses revealed no significant defects or damage. The corrosion protection coating was found to be in good condition. The general views of a main column and truss girder pairs are depicted in Fig. 3 and Fig. 4, respectively.



*Fig. 3 General view of the main four-legged column (left) and the connection zone of the truss girder pairs and main column (right)*



*Fig. 4 General view of the main truss girder pairs*

The main defect identified considering the roof grillage trusses is the deviation of their overall geometry from the geometric straightness. Aside this defect, the visual examination indicated no major defects, except the deformation of two diagonal members, which is shown in Fig. 5.

Inspection of the "R" columns along the perimeter revealed deterioration and peeling of the protective coating on all inspected "R" columns, as well as significant areas of several columns on which the corrosion protection had completely failed (Fig. 6). These phenomena were to be expected, since "R" columns are exposed to the external environment. In addition, several columns were found to have been partially recoated with a new anticorrosion protective layer (Fig. 7).



*Fig. 5 Deformation of two diagonal members of the roof grillage truss*




*Fig. 6 Corosion of the "R" column*




*Fig. 7 New protective coating on the "R" column*

An exterior inspection of the roof structure revealed that a previous rehabilitation intervention had been carried out in which a new timber substructure and roofing panels were installed above the original steel structure and roof panels. During the supercell storm, this timber substructure and the newly installed roof panels were completely destroyed and detached from the main roof structure. The detachment process also caused a severe damage to the original roof covering located beneath the timber substructure. As a consequence of these failures, water penetration into the building occurred, resulting in substantial damage to the facility and disruption of its intended use. Furthermore, an additional layer of lightweight concrete was observed on the roof surface, having been subsequently added within the roof valleys, which had been originally designed for the drainage of stormwater. This intervention had been undertaken to level the originally designed roof surface, thereby altering the intended drainage configuration of the roof. Damaged roof surface and the layer of the lightweight concrete are shown in Fig. 8.



*Fig. 8 Damaged roof surface (left) and the layer of the lightweight concrete in the roof valleys (right)*

## 4. NUMERICAL ANALYSIS OF THE EXISTING STRUCTURE

Structural analysis was carried out with the aim to evaluate the load-bearing capacity of the existing steel structure and to propose the possible rehabilitation measures.

### 4.1. NUMERICAL MODEL

The three-dimensional numerical model was developed using the software Radimpex Tower [2]. In order to describe the behaviour of steel structural elements, numerical model was developed using beam finite elements (FE). All beam FEs were positioned along the centroidal axes of the corresponding structural members and were assigned geometric properties based on the available archival design documentation and on-site verification measurements. The mechanical properties of steel were conservatively assumed. Structural steel grade S235 was adopted, with a modulus of elasticity of $E = 210.0$ GPa and a Poisson's ratio of $\nu = 0.30$. The structure was modelled with fixed supports at the bases of the main columns, while the lower ends of the tie rods were represented by pinned connections.

The load analysis was performed in accordance with SRPS EN 1991-1-1 [3], SRPS EN 1991-1-3 [4], SRPS EN 1991-1-4 [5], and SRPS EN 1998-1 [6]. Load combinations were generated by applying the relevant partial safety factors for actions prescribed in SRPS EN 1990 [7]. In Fig. 9 the numerical model of the existing steel structure is shown.

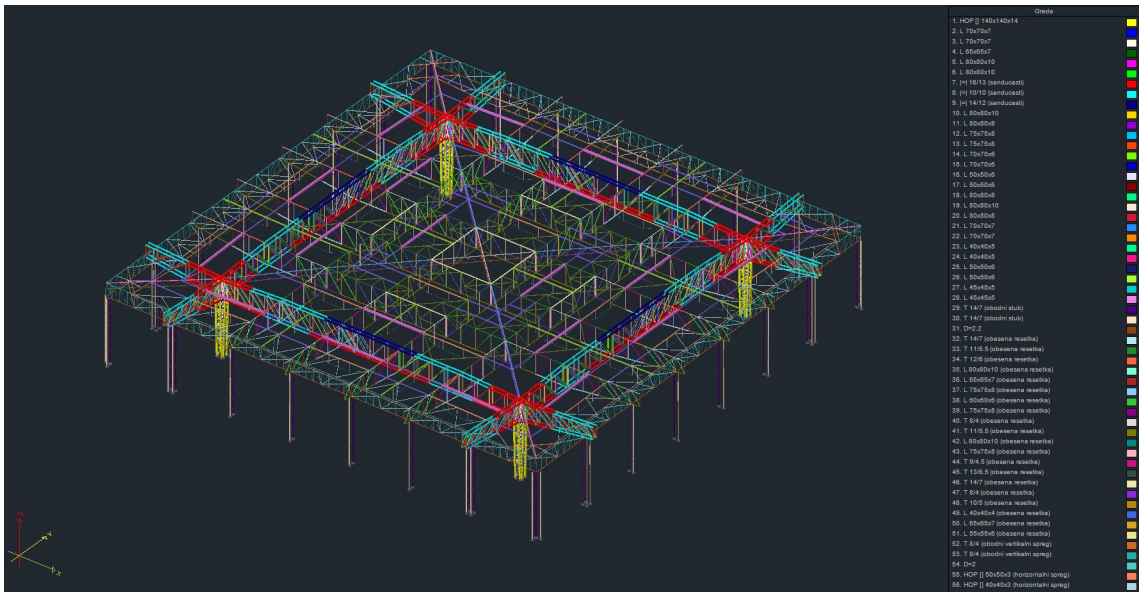

*Fig. 9 Numerical model of the existing steel structure*

The structural verification analysis was conducted by means of linear static analysis.

## 4.2. RESULTS

The load-bearing capacity of individual structural members was assessed in accordance with the provisions of SRPS EN 1993-1-1 [8], using the corresponding partial safety factors for materials. In Figs. 10 to 13, some of the selected results of the structural analysis and the design verification of the structure are presented.

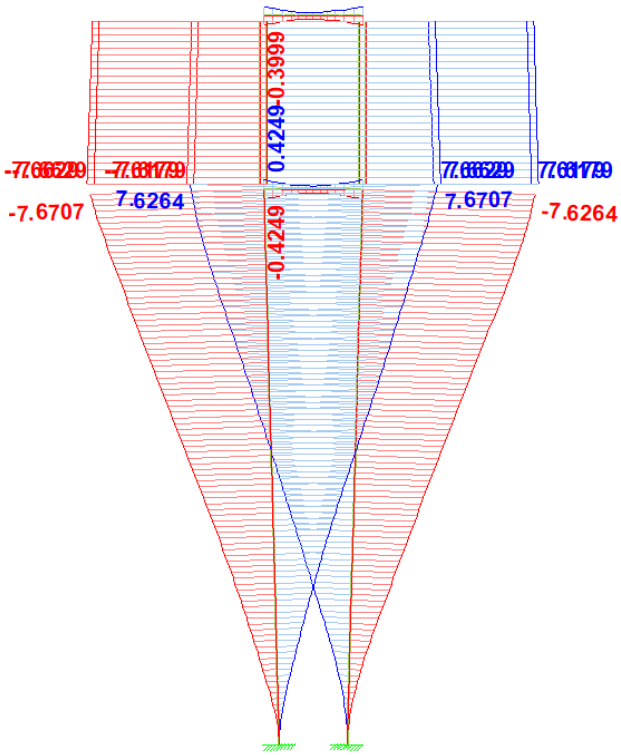


*Fig. 10 Envelope of the horizontal displacements [mm] of main four-legged lattice column for seismic load combinations*

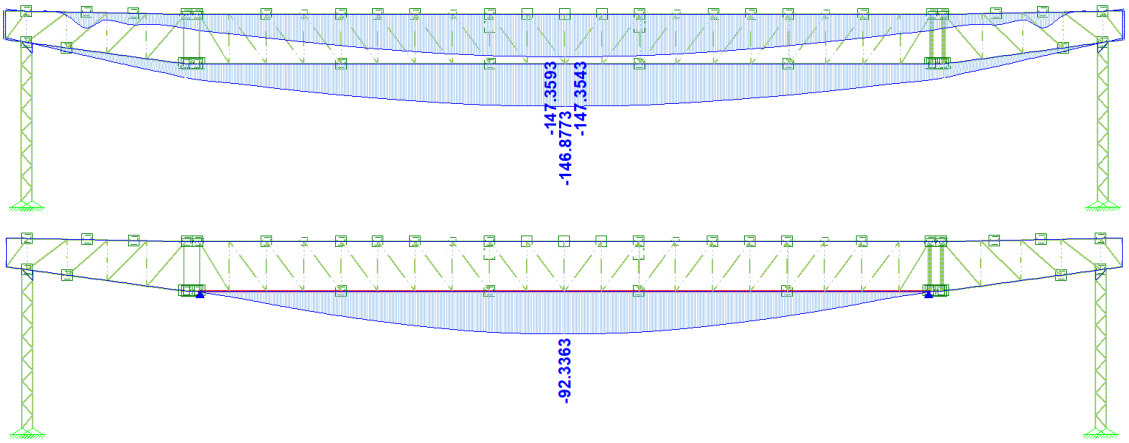


*Fig. 11 Vertical deflection [mm] of the secondary roof truss for serviceability limit state combinations: absolute (above) and relative to the support, i.e. main columns (below)*

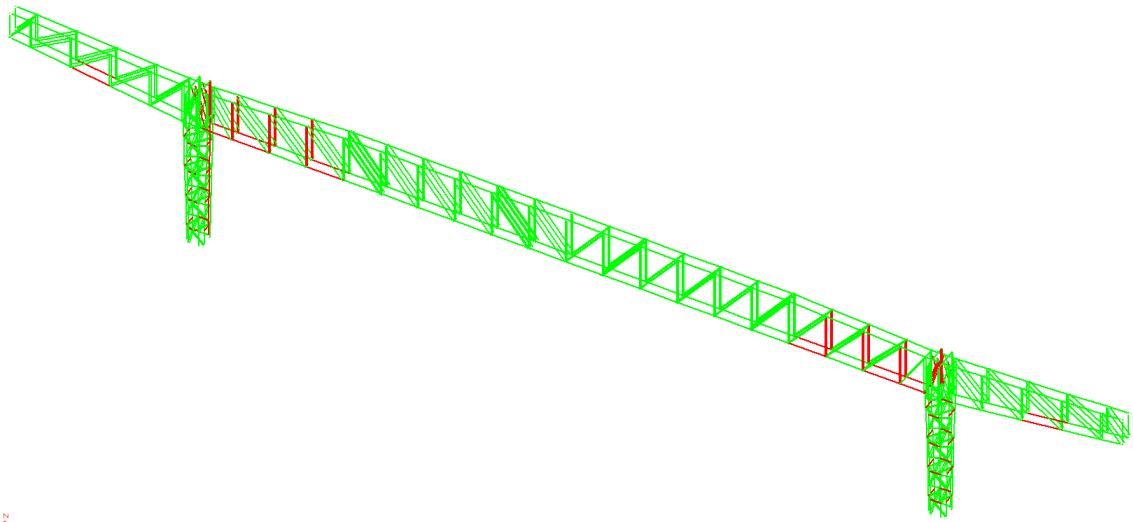

*Fig. 12 Critical utilisation of members of the main columns and main pairs of truss girders (green – utilisation below 100%; red – utilisation above 100%)*

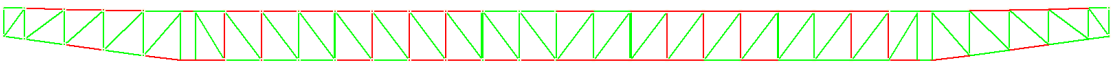

*Fig. 13 Critical utilisation of members of the secondary roof grillage truss girder (green – utilisation below 100%; red – utilisation above 100%)*

The results of the numerical analysis indicate that the global structural behaviour of the hall is not satisfactory with respect to overall ultimate and serviceability limit states. The member verification performed according to SRPS EN 1993-1-1 [8] showed that a number of structural elements, particularly within the secondary roof grillage and certain members of the primary load-bearing system, exceed the allowable utilisation ratio. These results are consistent with the observations obtained during the visual inspection and confirm that the load-bearing capacity of the existing structure under the prescribed design loading is insufficient. Consequently, the implementation of strengthening measures was necessary in order to restore the required level of structural safety and ensure reliable future operation of the facility.

## 5. CONCLUSIONS

The assessment of Hall 7 of the Novi Sad Fair demonstrated the importance of a comprehensive structural evaluation following extreme weather events. The visual inspection revealed that the main load-bearing system remained largely preserved despite the severe storm action, while significant damage was identified on the secondary structural elements and roof covering. In addition, deterioration of corrosion protection was observed on several perimeter steel members, indicating the need for maintenance interventions regardless of the storm-induced damage.

Although the verification of the foundation structure is beyond the scope of this study, it is important to note that the removal of the damaged roof structure together with the lightweight concrete infill resulted in a reduction of the permanent load acting on the foundation system, thereby providing additional relief to the existing foundation system.

The numerical analyses provided a detailed insight into the structural performance of the existing steel structure. Although the global stability of the structure was not compromised, the verification of individual members revealed insufficient resistance of many structural elements. The obtained utilisation ratios clearly indicated that the existing structural configuration does not fully satisfy the requirements for load-bearing capacity prescribed by the applicable standards.

The presented case study also highlights the vulnerability of existing structures to extreme climatic events and emphasizes the necessity of systematic inspections, structural assessments and rehabilitation measures in order to preserve the safety and serviceability of public facilities.

### ACKNOWLEDGEMENT

The research has been conducted within the project "Enhancement of teaching and scientific research capacities through the application of modern technologies in the fields of civil engineering, geodesy, and disaster risk management and fire safety", developed at the Department of Civil Engineering and Geodesy, Faculty of Technical Sciences, University of Novi Sad, Serbia.

## REFERENCES

[1] Elaborat postojećeg stanja sa preporukama za sanaciju konstrukcije Hale 7 Novosadskog sajma (2023), Faculty of Technical Sciences, Novi Sad, Serbia

[2] Radimpex Tower User’s Manual, Ver. 8597 (2026)

[3] European Committee for Standardization (2012). Eurocode 1: Actions on structures – Part 1-1: General actions – Densities, self-weight, imposed loads for buildings, Brussels, Belgium.

[4] European Committee for Standardization (2017): Eurocode 1: Actions on structures – Part 1-3: General actions – Snow loads – National Annex, Brussels, Belgium.

[5] European Committee for Standardization (2012): Eurocode 1: Actions on structures – Part 1-4: General actions – Wind actions, Brussels, Belgium.

[6] European Committee for Standardization (2018): Eurocode 8: Design of structures for earthquake resistance – Part 1: General rules, seismic actions and rules for buildings – National Annex, Brussels, Belgium.

[7] European Committee for Standardization (2012): Eurocode – Basis of structural design – National Annex, Brussels, Belgium.

[8] European Committee for Standardization (2021): Eurocode 3: Design of steel structures – Part1-1: General rules and rules for buildings - National Annex, Brussels, Belgium.

https://doi.org/10.24867/INDIS-2026-EN-236



# HALL 7 OF THE NOVI SAD FAIR – PART II: STRENGTHENING AND REPAIR OF THE LOAD-BEARING STRUCTURE

*Vladimir Živaljević*[1], *Andrija Rašeta*[2], *Igor Džolev*[3]

***Summary:***

Based on the structural condition assessment and numerical analysis, which identified a great deal of deficiencies of the load-bearing structure of Hall 7 of the Novi Sad Fair following the 2023 supercell storms, rehabilitation and strengthening measures are presented. The strict sequence of construction works was defined within the strengthening solution. Strengthening measures were implemented on the main truss girders, secondary roof grillage trusses, diagonal "R" girders, perimeter "R" columns, and through the installation of additional bracing systems in both the upper and lower planes of the trusses. Furthermore, repair measures for secondary structural elements were applied. This rehabilitation concept was verified through additional structural analyses, demonstrating the adequacy of the strengthened structural system.

*Keywords: structural rehabilitation, strengthening measures, steel structures*

# HALA 7 NOVOSADSKOG SAJMA – DEO II: SANACIJA NOSEĆE KONSTRUKCIJE

***Rezime:***

Nakon procene stanja i numeričke analize konstrukcije, kojima je utvrđena nedovoljna nosivost pojedinih elemenata Hale 7 Novosadskog sajma, nakon superćelijskih oluja tokom 2023. godine, u ovom radu prikazane su projektovane mere sanacije i ojačanja konstrukcije. Definisan je i detaljan redosled izvođenja radova. Ojačanja su sprovedena na glavnim rešetkastim nosačima, sekundarnoj krovnoj roštiljnoj konstrukciji, dijagonalnim „R” nosačima, obodnim „R” stubovima, kao i kroz uvođenje dodatnih elemenata spregova u gornjoj i donjoj ravni krovnih nosača. Takođe, primenjene su mere sanacije i na drugim sekundarnim elementima konstrukcije. Koncept sanacije je verifikovan dodatnim statičkim proračunima, čime je potvrđena valjanost ojačanog konstrukcijskog sistema.

*Ključne reči: sanacija konstrukcija, ojačanje konstrukcija, čelične konstrukcije*

[1] Assistant Prof., Faculty of Technical Sciences, University of Novi Sad, Serbia, zivaljevic.vladimir@uns.ac.rs, ORCID 0000-0002-2808-2664
[2] Full Prof., Faculty of Technical Sciences, University of Novi Sad, Serbia, araseta@uns.ac.rs, ORCID 0000-0002-4535-1379
[3] Associate Prof., Faculty of Technical Sciences, University of Novi Sad, Serbia, idzolev@uns.ac.rs,, ORCID 0000-0002-7622-7936

## 1. INTRODUCTION

In the first part of this comprehensive research, a detailed visual inspection and numerical evaluation of the existing load-bearing steel structure of Hall 7 were presented [1, 2]. The three-dimensional finite element analysis, conducted in accordance with Eurocode standards, confirmed that while the global stability of the hall was not compromised, numerous structural elements failed to meet the required safety demands. Overload and geometric deviations were identified within certain members of the primary lattice frame system and secondary roof grillage trusses, highlighting the high vulnerability of the structure under extreme wind actions.

To restore the facility to its full operational capacity and comply with the current standards in terms of structural load-bearing capacity, a robust engineering solution was mandatory. Therefore, a complete rehabilitation strategy was developed, aiming not only to repair the storm-induced damage but also to systematically strengthen the necessary structural elements and enhance the overall bearing capacity of the structure.

In this paper, the specific rehabilitation measures designed for the strengthening and repair of the load-bearing structure of the Hall 7 are presented in detail. The structural interventions implemented on the main truss girders, secondary grillage trusses, diagonal "R" girders, perimeter "R" columns, and the newly introduced horizontal bracing systems are described in the study. Furthermore, the precise sequence of works required to relax the existing stresses during the intervention is outlined.

## 2. REHABILITATION MEASURES

Based on the findings and conclusion of the visual inspection and numerical analysis of the existing structure, several rehabilitation alternatives were analysed using numerical simulations based on finite element method. As in Part I, the load analysis was performed in accordance with relevant Eurocode standards [3-8]. General rehabilitation measures aimed to improve the bearing capacity and the durability of the structure are proposed in terms of strengthening and repair of the following structural members:

- main truss girders,
- secondary roof grillage girders,
- diagonal "R" girders,
- "R" columns at a perimeter of the structure,
- horizontal bracing members,
- secondary roof beams.

In order to ensure that the as-built state corresponds as closely as possible to the designed rehabilitated state, the strengthening of the roof steel structure shall be carried out in the following sequence:

1. erection of the temporary scaffolding beneath the existing roof structure,
2. temporary shoring of the structure,
3. lifting of the structure to its design ("zero") geometry using hydraulic jacks,
4. execution of the rehabilitation and strengthening works,
5. gradual release of the hydraulic jacks and reactivation of the structural system.

This procedure is intended to restore the geometry of the structure prior to strengthening and relax existing members from the current stresses, thereby ensuring that the newly installed strengthening elements are engaged in load transfer in accordance with the design assumptions.

## 2.1. MAIN LATTICE COLUMNS AND "R" COLUMNS AT A PERIMETER OF A STRUCTURE

At locations along the main lattice columns, where the finishing coating has been locally damaged, steel members were cleaned of corrosion and contaminants and recoated with an appropriate anticorrosion protection system.
All diagonal "R" columns at a perimeter were cleaned to remove deteriorated paint layers, dirt, and corrosion products. Following the surface preparation, a new corrosion protection system was applied.

## 2.2. MAIN TRUSS GIRDERS

The top chord (RHS composed of 2 U160 channels) and the bottom chord (RHS whose configuration varies depending on the truss panel, 2 U140 to 2 U180 channels) were strengthened by attaching 100 × 10 mm steel plates to both sides of the hollow section. The plates were continuously welded to the existing members along their perimeter using fillet welds. The strengthening was applied within the regions adjacent to the main four-legged lattice columns.
Additionally, the four vertical members closest to the main column, within the central span, were strengthened by welding steel angle sections L80×80×8. The added angles, together with the existing vertical members, form square hollow section (SHS), thereby increasing the load-bearing capacity of the truss. These strengthening measures are depicted in Fig. 1.

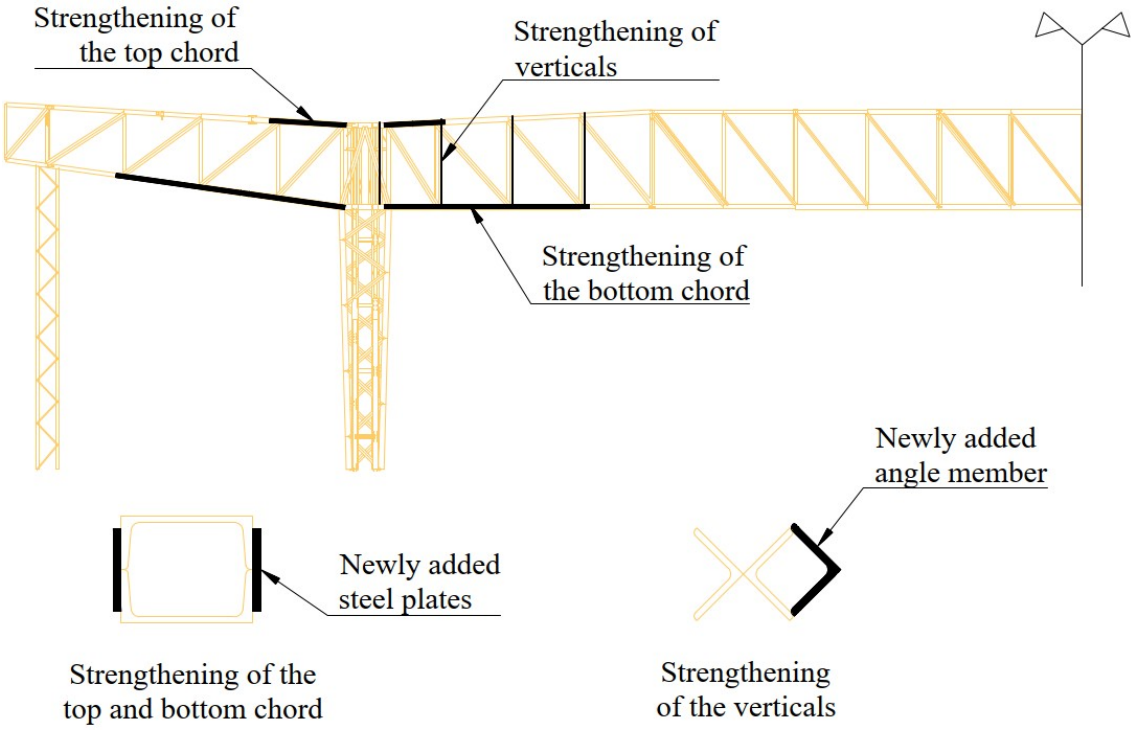


*Fig. 1 Strengthening of the top and bottom chord, and four vertical members of the main truss girders*

Finally, pairs of parallel main truss girders were interconnected at the bottom chord level at every truss node. The connection was established using L100×100×10 steel angles. The angles were welded continuously to the lower edge of the bottom chord along the perimeter of the angle section, creating a rigid connection between neighbouring trusses (Fig. 2).

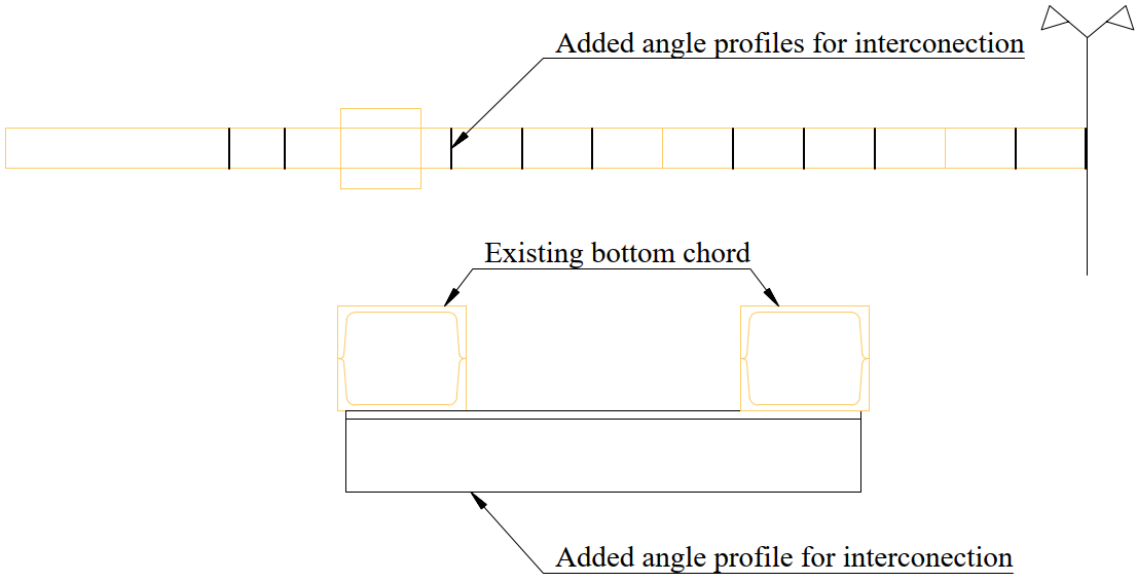


*Fig. 2 Interconnecting the pairs of the main truss girders*

## 2.3. SECONDARY GRILLAGE TRUSS GIRDERS

The rehabilitation measures for the secondary grillage truss girders include strengthening of the top and bottom chords, vertical and diagonal members, as well as the installation of additional ties (Fig. 3).

The top chord members were strengthened throughout the entire central portion of the structure by adding two steel angles of the same dimensions as the existing members. Continuous welding along the contact lines between the existing and newly added angles results in the formation of two hollow sections, thereby increasing the load-bearing capacity of the chord. The bottom chord was strengthened in all truss panels, except for the three panels closest to the main truss girders within the central portion of the structure. Strengthening was achieved by welding steel plates of varying dimensions along the length of the girder to the lower edge of the existing bottom chord.

The first seven vertical members within the central region of the truss were strengthened by adding steel angles welded continuously to the existing verticals along their lines of contact, thereby forming closed hollow sections. Additional diagonal angle profiles were installed in truss panels 2–6 of the central span and in panels 2 and 3 of the cantilever region. These diagonal members were connected to the chord members through gusset plates.

In addition to the aforementioned strengthening measures, tension ties fabricated from round steel bars were introduced at the level of the bottom chord. These ties are intended to enhance the overall stability of the structural system and to restore the girders to their designed alignment, as the noticeable deviations from straightness was revealed during visual inspection.

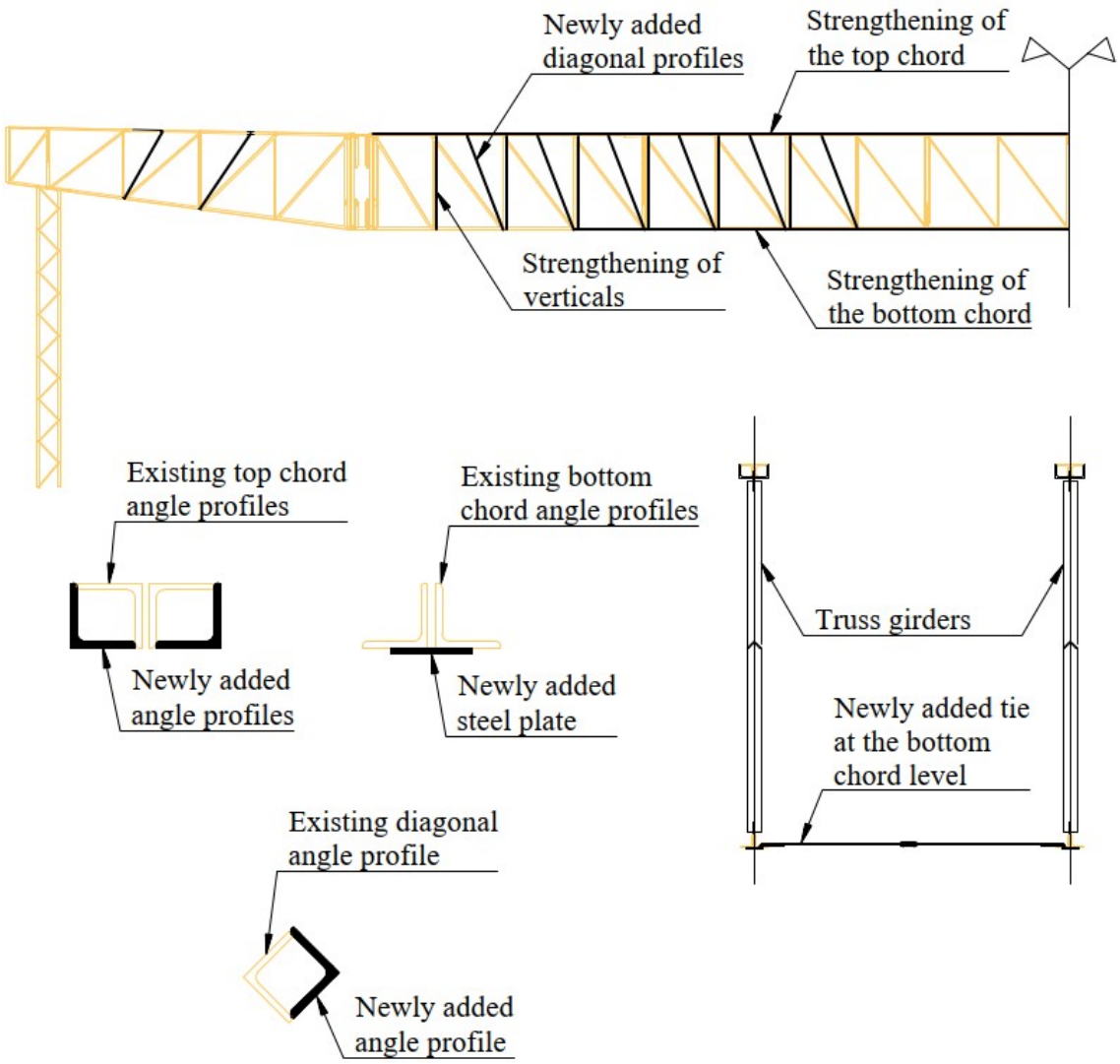


*Fig. 3 Strengthening measures for secondary truss girders*

## 2.4. DIAGONAL "R" GIRDERS

For the diagonal "R" girders, additional inclined tension ties were introduced within the central panels, while diagonal corner braces were installed at the corners of the structure. The tension ties, made from round steel bars, were at one end welded to the top chord of either a primary or secondary girder, while at the other end they were connected to the bottom chord of the diagonal "R" girder. The corner braces were fabricated from SHS profiles. In addition, the diagonal "R" girders were strengthened by introducing additional vertical members, strengthening the top chord, and reinforcing the diagonal web members. The newly added vertical members were SHS sections. The top chord, originally composed of two L55×55×6 angle sections forming a T-shaped cross-section, was strengthened by adding identical angle sections. The new profiles were welded to the existing chord, resulting in the formation of two interconnected hollow sections. The diagonal web members, originally fabricated from round steel bars, were strengthened by attaching two steel angle sections to each member, thereby forming a T-shaped cross-section. These rehabilitation measures are shown in Fig. 4.

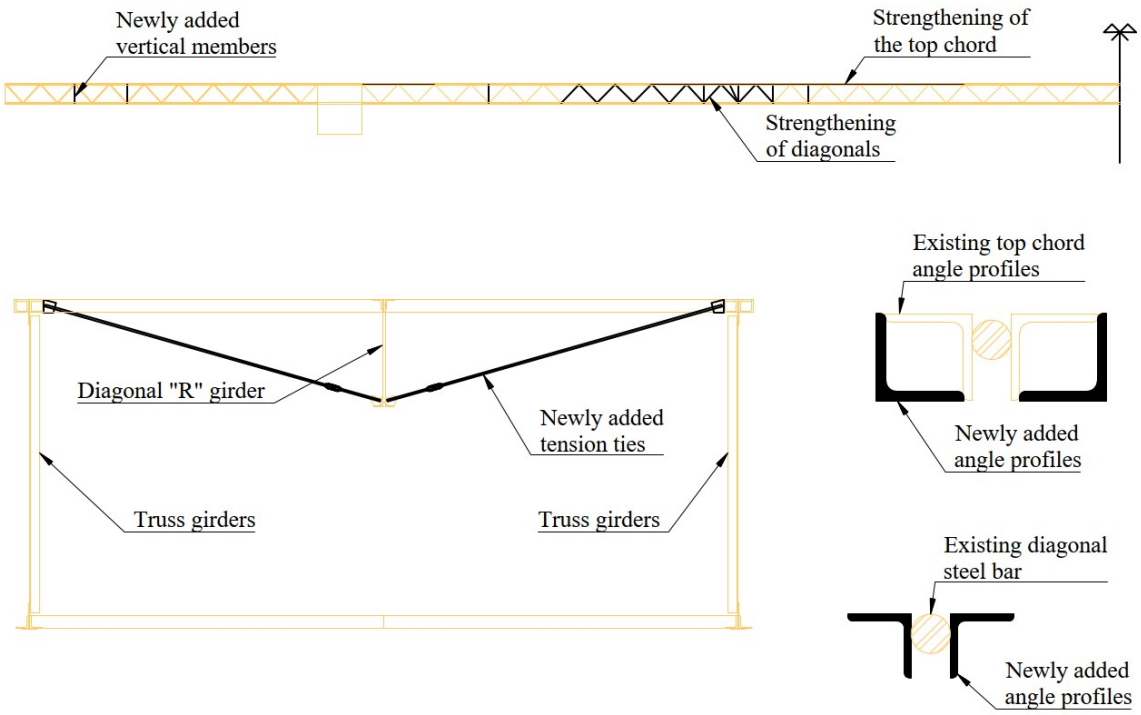


*Fig. 4 Strengthening of the diagonal "R" girders*

## 2.5. HORIZONTAL BRACING MEMBERS

In order to enhance the global stability and behaviour of the structure, additional bracing members were installed in both the upper and lower planes of the primary and secondary truss girders. The strengthening was achieved using SHS profiles of various cross-sectional dimensions. The schematic layout of the newly installed bracing members is given in Fig. 5. The existing structural members are shown in orange, whereas the newly added elements are shown in black.

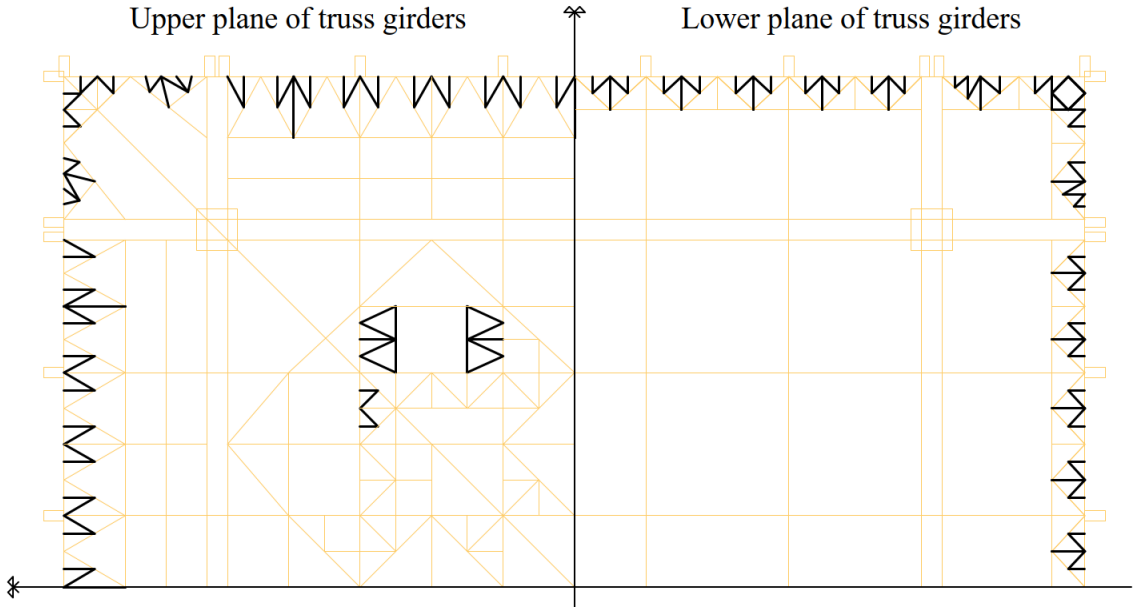


*Fig. 5 Schematic layout of the newly installed bracing members for upper (left) and lower (right) plane of truss girders*

## 2.6. ADDITIONAL STRENGTHENING AND REPAIR MEASURES

In addition to the previously described strenghtening measures, a following series of measures related to the secondary structural elements, cladding components, and other non-structural elements of the building was applied:

- In the central zone of the roof structure, the existing secondary beams formed from U100 profiles were strengthened by installing additional U100 profiles at a spacing of 100 mm from the existing members. These sections were interconnected by means of L55×55×6 steel angles welded to the lower flanges of the channel sections, thereby increasing the stiffness and load-bearing capacity of the secondary roof system.
- The layer of lightweight aggregate concrete that had previously been cast within the valleys of the original roof structure was completely removed. In addition, the remaining portions of the previously installed timber substructure and the damaged waterproofing membrane were dismantled and removed.
- Unused ventilation ducts located within the roof structure were also removed.
- The existing sheet-metal flashing along the roof perimeter was removed and replaced with new flashing elements.
- All perimeter "R" columns, as well as other steel structural members exhibiting localized damage of the protective coating, were treated with anticorrosion protection systems following appropriate surface preparation, including the removal of corrosion products and contaminants.
- All newly installed strengthening elements were protected with anticorrosion coatings in accordance with the specified corrosion protection requirements.

## 3. CONCLUSIONS

Based on the performed visual inspection and structural analysis, suitable strengthening measures were designed in order to successfully address all load-bearing capacity and stability deficiencies. The proposed engineering interventions, incorporating the installation of steel plates, additional profiles and bracing configurations, ensured that the utilization ratios of all critical members fell well within the allowable limits of ultimate and serviceability limit states.

A key factor in the success of the rehabilitation plan was the defined construction sequence, which utilizes temporary scaffolding and hydraulic jacks to restore the framework to its original "zero" geometry. This methodology effectively relieved the existing structural members of accumulated stresses and guaranteed that the newly added strengthening elements would actively participate in load transfer according to the design assumptions.

The total mass of the structural elements prior to the rehabilitation works was calculated to be 115.59 t. The structural repair of the building required an addition of new structural elements with a total mass of 15.04 t, which increased the total mass of the facility to 130.63 t, i.e., by roughly 13 %. This rational material consumption yielded a sufficient increase in structural resistance, proving that, in this case, retrofitting the existing structural system represents a technically and economically superior alternative to demolition and rebuilding. The implemented solutions have successfully restored the functionality, durability, and long-term safety of Hall 7 of the Novi Sad Fair, ensuring its reliability against future environmental actions.

**ACKNOWLEDGEMENT**

The research has been conducted within the project "Enhancement of teaching and scientific research capacities through the application of modern technologies in the fields of civil

engineering, geodesy, and disaster risk management and fire safety", developed at the Department of Civil Engineering and Geodesy, Faculty of Technical Sciences, University of Novi Sad, Serbia.

## REFERENCES

[1] Elaborat postojećeg stanja sa preporukama za sanaciju konstrukcije Hale 7 Novosadskog sajma (2023), Faculty of Technical Sciences, Novi Sad, Serbia

[2] Živaljević V., Rašeta A., Džolev I. (2026): Hall 7 of the Novi Sad Fair – Part I: The assessment of the load-bearing structure. *17th International Scientific Conference iNDiS – Integration, Novelty, Design, interdisciplinarity, Sustainability*, Faculty of Technical Sciences, Novi Sad, Serbia, 4-6 November, pp. 229–237.

[3] European Committee for Standardization (2012). Eurocode 1: Actions on structures – Part 1-1: General actions – Densities, self-weight, imposed loads for buildings, Brussels, Belgium.

[4] European Committee for Standardization (2017): Eurocode 1: Actions on structures – Part 1-3: General actions – Snow loads – National Annex, Brussels, Belgium.

[5] European Committee for Standardization (2012): Eurocode 1: Actions on structures – Part 1-4: General actions – Wind actions, Brussels, Belgium.

[6] European Committee for Standardization (2018): Eurocode 8: Design of structures for earthquake resistance – Part 1: General rules, seismic actions and rules for buildings – National Annex, Brussels, Belgium.

[7] European Committee for Standardization (2012): Eurocode – Basis of structural design – National Annex, Brussels, Belgium.

[8] European Committee for Standardization (2021): Eurocode 3: Design of steel structures – Part1-1: General rules and rules for buildings - National Annex, Brussels, Belgium.

https://doi.org/10.24867/INDIS-2026-EN-244



# THE ASSESSMENT OF A ROAD BRIDGE STRUCTURE OVER THE SAVA RIVER IN OBRENOVAC

*Slobodan Šupić[1], Vladan Pantić[2], Danijel Kukaras[3], Dragana Stanojević[4]*

***Summary:***

The paper presents the results of an assessment of a road bridge over Sava River within the premises of the "Nikola Tesla A" TPP in Obrenovac. The assessment included a detailed visual inspection of all structural components, as well as the necessary in-situ and laboratory testing to evaluate the quality of the materials. The primary objective of the inspection was to assess the condition of the structure after several decades of service, identify defects and damages affecting its structural components, and propose the necessary repair measures to restore the bridge to the required levels of structural capacity, durability, and functionality. The visual inspection revealed numerous deterioration mechanisms, including global and local deformations of the steel truss members, advanced corrosion of the bridge substructure components, as well as cracking and corrosion-related deterioration of the RC elements. The extent and severity of the damages indicate the need for both non-structural and structural repair measures.

*Keywords: assessment, road bridge, defects, damages, repair measures*

# PROCENA STANJA KONSTRUKCIJE DRUMSKOG MOSTA PREKO REKE SAVE U OBRENOVCU

***Rezime:***

U radu su prikazani rezultati procene stanja drumskog mosta preko reke Save u krugu TE „Nikola Tesla A" u Obrenovcu. Procena stanja mosta je obuhvatila detaljan vizuelni pregled svih elemenata noseće rasponske konstrukcije mosta: čelične rešetkaste konstrukcije i rečnih AB stubova, kao i potrebna terenska i laboratorijska ispitivanja kvaliteta ugrađenih materijala. Cilj glavnog pregleda konstrukcije mosta je sagledavanje stanja nakon višedecenijske eksploatacije, registrovanje manifestovanih defekata i oštećenja na vitalnim elementima, kao i predlog svih potrebnih mera sanacije koje će dovesti most u stanje projektovane nosivosti, trajnosti i funkcionalnosti. Vizuelnim pregledom su detektovani brojni defekti i oštećenja: globalne i lokalne deformacije elemenata rešetkaste čelične konstrukcije, uzapredovao proces korozije na elementima donjeg stroja mosta, kao i prsline i pukotine i korozija AB elemenata, koji uslovljavaju potrebu za nekonstrukcijskim i konstrukcijskim merama sanacije.

*Ključne reči: procena stanja, drumski most, defekti, oštećenja, mere sanacije*

[1] Associate Professor, Faculty of technical sciences, University of Novi Sad, Serbia, ssupic@uns.ac.rs ORCID 0000-0003-3029-9309
[2] Teaching Assistant, Faculty of technical sciences, University of Novi Sad, Serbia, pantic_vladan@uns.ac.rs ORCID 0000-0002-3482-9437
[3] Full Professor, Faculty of technical sciences, University of Novi Sad, Serbia, dkukaras@uns.ac.rs ORCID 0000-0003-4726-2799
[4] Teaching Assistant, Faculty of technical sciences, University of Novi Sad, Serbia, dragana.stanojevic@uns.ac.rs ORCID 0000-0003-3471-5656

## 1. INTRODUCTION

The road bridge over the Sava River in Obrenovac (Fig. 1) is located in the immediate vicinity of the "Nikola Tesla A" Thermal Power Plant, one of the most significant energy facilities in Serbia. The original design of the bridge dates from 1994, when it was initially planned as a district-heating pipeline crossing, and was subsequently redesigned as a road bridge with a 6.5m wide carriageway, whereby its previous purpose of carrying the district-heating pipeline was also retained.



*Fig. 1 View of the bridge over the Sava River in Obrenovac*

The bridge, as a whole, consists of five structural units:

1. The span structure over the river, extending from the entry structure "ST1" to pier "ST7", with spans of 2×50.0 + 140.0 + 100.0 + 2×50.0m, consists of a welded steel truss superstructure (K1–K6) supported, through steel bearings, on reinforced-concrete (RC) river piers ST2–ST7.
2. The precast RC approach structure over the left-bank inundation continues from the transitional pier "ST7" to the entry structure "ST16", with spans of 8×20.2 + 19.7m, supported on RC piers ST8–ST15.
3. The entry structures "ST1" and "ST16" are RC structures designed to carry the reactions from the main span and approach structures, while also supporting the district-heating pipeline.
4. The RC approach ramp on the left bank extends from ST16 to the adjoining embankment over a total length of 155.2m.
5. The RC approach ramp on the right bank, extending from the entry structure ST1, comprises an RC bridge carrying the roadway and district-heating utility ducts, retaining walls, and a culvert accommodating the pipeline beneath the roadway.

This paper focuses on the condition assessment of the bridge superstructure over the river. The steel superstructure over the river consists of six truss structures, designated K1–K6, with a total length of 446.50m (Fig. 2). Structures K1, K2, K5, and K6 are single-tier trusses with a simply supported structural system, each having a span of 50.0m and a structural depth of 5.5m. The main-span structures, K3 and K4, crossing the main river channel, are three-tier trusses with a total structural depth of 3 × 5.5m and form a continuous structural system with spans of 140.0m and 100.0m.

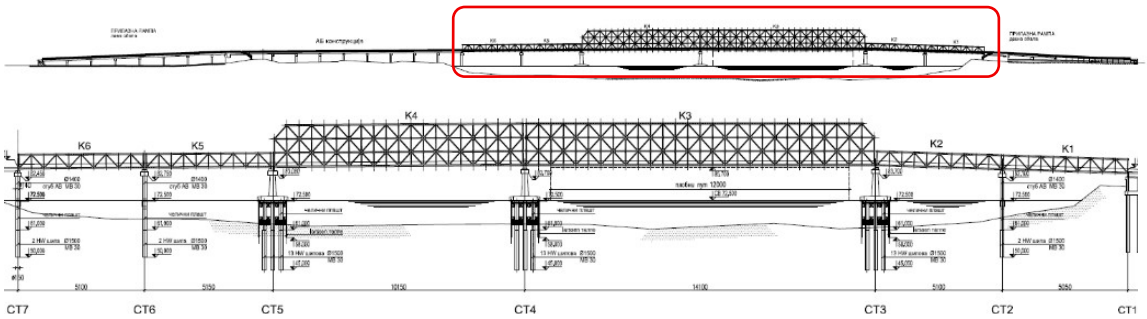


*Fig. 2 Layout of the span structure of the bridge over the Sava River in Obrenovac*

The main girders are arranged at a spacing of 8.0m and are composed of welded open sections, 500mm wide and 650–700mm deep, while the cross girders are spaced at 5.0m. Steel grades S235 and S355 were used for the load-bearing structural and deck elements. The truss structures are supported on the variable-cross-section RC river piers ST3, ST4, and ST5, as well as on two-tier RC frame piers ST2, ST6, and ST7, each consisting of two 1,400mm-diameter circular columns connected by an RC bearing girder. Longitudinal movements of the superstructure resulting from horizontal actions are accommodated by steel bearings located beneath the main chord members. Movable roller bearings are provided at pier ST1 for structures K1 and K2, at piers ST3 and ST5 for structures K3 and K4, and at pier ST7 for structures K5 and K6, while fixed tangential bearings are provided at the remaining support locations.

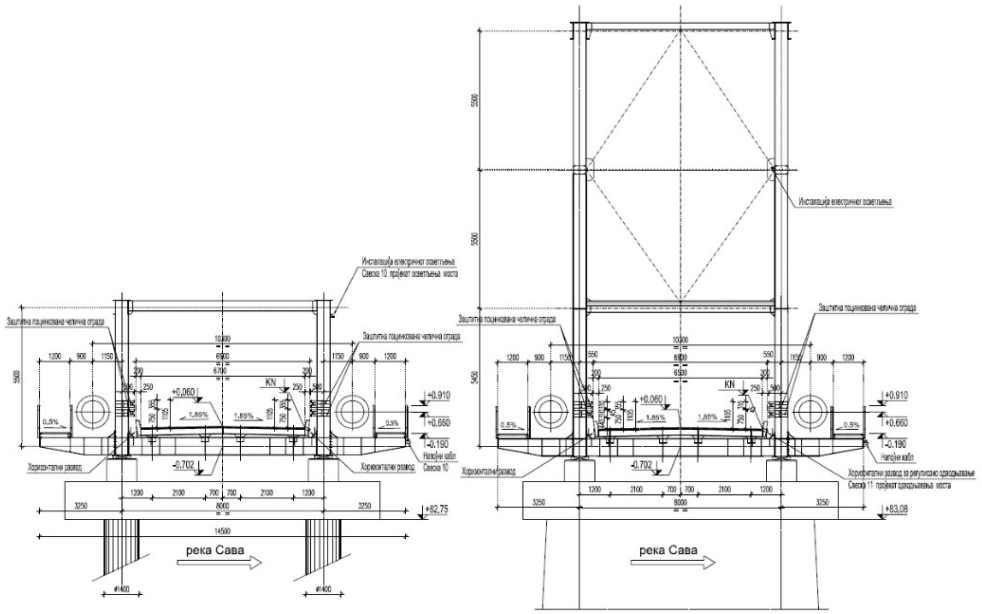


*Fig. 3 Cross-sections of the structure (left: K1, K2, K5, K6; right: K3, K4)*

The aim of the structural inspection was to assess the condition of the bridge after approximately three decades in service, with particular emphasis on the condition of the corrosion protection system, the presence and extent of significant defects and damages, and the quality of the incorporated concrete, evaluated through field and laboratory testing. To obtain the necessary data, the following activities were carried out: collection and review of the available design documentation; on-site verification of the dimensions of the load-bearing structural elements; detailed visual inspection of the steel and RC elements using an aerial work platform, mobile scaffolding, and binoculars; extraction of concrete cores from selected RC elements followed by laboratory determination of compressive strength; and measurement of the concrete carbonation depth using the colorimetric (phenolphthalein) method.

## 2. DETAILED VISUAL INSPECTION

The detailed visual inspection covered the steel truss superstructure over the river, including the chords, bracing members, bearings, deck structure, and railings, as well as the RC river piers supporting the superstructure (ST2–ST7).

### 2.1. STEEL TRUSS SUPERSTRUCTURE OF THE BRIDGE OVER THE RIVER

#### 2.1.1. Geometric Inspection

The visual inspection revealed local and global deformations of the chord members in the plane of the upper chord of structures K1, K3, K4, and K6, resulting from vehicle impacts. A total of 23 members were found to be deformed, with the affected length ranging from 10% to 100% of the total member length. The affected members and the extent of the observed deformations are summarized in Table 1 and illustrated in Figs. 4 and 5.

*Tab. 1 Deformations of steel truss members of the bridge over the river*

| Bridge | Deformed members – designation | Deformation type | Relative deformed length, % |
|---|---|---|---|
| K1 | 201, 202, 241, 102, 203, 106, 242, 243 | Global | 50 – 100 |
| K6 | 210 | Local | 30 |
| K3 | 2206, 2097, 2096, 2046, 2095, 2045, 2094, 2044, 2087, 2086, 2036,2043, 2035 | Global; Local | 30 – 100 |
| K4 | 2050 | Local | 10 |



*Fig. 4 Global deformation of a chord member, bridge K1*



*Fig. 5 Global deformations of chord members, bridge K3*

### 2.1.2. Inspection of Bolted Connections

The visual inspection of the bolted connections on structures K1, K3, and K4 revealed missing bolts at several joints of the upper-chord truss. On K1, one bolt was missing at each of three joints and two bolts at a fourth joint, while on K3 and K4, three to four bolts were missing at three joints on each structure. The missing bolts are predominantly attributed to vehicle impacts and the resulting member deformations, which compromised the integrity of the connections between the truss elements (Fig. 6).



*Fig. 6 Disturbed connection of steel elements, bridges K1, K3 and K4*

### 2.1.3. Condition of the Corrosion Protection System

The corrosion-protective coating of the steel elements has deteriorated over a significant portion of the structure and exhibits extensive spalling and detachment, while localized coating repairs are evident on some elements. Loss of the protective coating has resulted in the initiation and development of corrosion of varying severity. The observed deterioration ranges from localized shallow corrosion at locations where the protective coating has been mechanically or chemically damaged, such as at welds and splices, to non-uniform or uniform surface corrosion, most pronounced on the upper surfaces of the upper-chord elements and at locations of water retention on the lower-chord elements. Severe corrosion, accompanied by delamination and flaking of the steel and resulting in a reduction in the member cross-section, was primarily observed at plate splices of the lower-chord elements.

On the upper-chord elements of structures K1 and K2, the predominant forms of deterioration are localized shallow and uniform surface corrosion (Fig. 7), while localized shallow corrosion predominates on structures K3 and K4. Severe corrosion with steel delamination and flaking was locally observed on the lower-chord elements of all inspected structures, particularly at connections between structural elements, in areas of prolonged water retention, and on the fasteners themselves (Fig. 8).



*Fig. 7 Surface corrosion of upper-chord elements, bridge K1*



*Fig. 8 Deep corrosion accompanied by flaking of the steel at the connections of lower-chord elements, bridge K1*

### 2.1.4. Bearings

The truss structures are supported on steel bearings located beneath the main chord members. Longitudinal movements resulting from horizontal actions are accommodated by movable roller bearings at pier ST1 for structures K1 and K2, at piers ST3 and ST5 for structures K3 and K4, and at pier ST7 for structures K5 and K6, while the remaining fixed bearings are of the tangential type. The bearing elements are protected by a corrosion-protective coating, which has locally deteriorated, resulting in corrosion ranging from predominantly surface corrosion to localized severe corrosion accompanied by steel delamination and flaking. At the bearing on pier ST5, a crack was observed in the steel bearing plate, together with corrosion of the plate and bolts, resulting in a localized reduction of the effective bearing area (Fig. 9).



*Fig. 9 Corroded bearing with a cracked bearing plate, pier ST5*

### 2.1.5. Drainage system

Rainwater is collected from the bridge deck by a system of continuous steel gutters supported on the cross girders. The gutters are connected to welded circular steel pipes by stainless-steel couplings and further to ductile iron pipes, which convey the collected water to two-chamber steel filter boxes mounted on the bearing girders above the piers. From there, the water is discharged into the river through vertical downpipes installed along the piers.

The main deficiency of the drainage system is the inadequate longitudinal slope of the gutters, resulting in the accumulation of water, aggressive substances, salts, and debris rather than their proper conveyance toward the downpipes. Prolonged water retention has caused deterioration of the protective coating and initiated corrosion of the steel gutters. In some areas, the corrosion has progressed to severe section loss, accompanied by steel delamination and flaking and a significant reduction in the remaining plate thickness (Fig. 10). Corrosion has also affected the connections between the gutters, connecting pipes, and ductile iron pipes and, combined with inadequate maintenance, has resulted in the loosening and separation of several joints. Consequently, water is discharged directly onto the steel and RC elements of the structure-



*Fig. 10 Layered deep corrosion of the steel drainage gutter*

## 2.2. RC RIVER PIERS

The detailed visual inspection also covered the RC river piers ST2–ST7.

Visual inspection of the piers detected the following defects:

- insufficient thickness of the concrete cover,
- visible reinforcement,
- surface (shallow) honeycombs,
- honeycombs.

The following damages were registered:

- horizontal (transverse) and vertical cracks and fissures due to reinforcement corrosion,
- vertical cracks induced by thermal stresses and/or concrete shrinkage,
- surface corrosion of reinforcement,
- severe corrosion of reinforcement,
- delamination, cracking and spalling of the concrete cover,
- chemical corrosion of concrete: leaching of $Ca(OH)_2$,
- physical corrosion of concrete: leaching of the cement paste,
- biological corrosion of concrete.

The characteristic defect observed on all inspected piers is insufficient concrete cover, with locally exposed reinforcement, predominantly stirrups and, to a lesser extent, the main longitudinal bars. In addition, poorly compacted and porous concrete was observed along the height of the column at pier ST6. The main types of damages include transverse cracks at stirrup locations, vertical cracks attributed to thermal effects and/or restrained shrinkage (piers ST4, ST5, ST7, and ST7'), local flaking of the thin concrete cover, and spalling of the cover along corroded reinforcement bars.
Reinforcement corrosion was observed on all inspected piers, predominantly in the form of surface corrosion, with localized severe corrosion of the stirrups and, at pier ST5, of the main reinforcement in the lower part of the column. Locally, near the waterline, evidence of leaching of the cementitious matrix and calcium hydroxide [$Ca(OH)_2$], as well as minor biological growth, was also observed (Figs. 11 and 12). Similar defects and damages, of comparable extent and severity, were observed on the RC bearing girders and bearing support blocks above the piers.



*Fig. 11 View of river piers ST2 and ST2' (left) and a corroded, cracked stirrup zone with insufficient concrete cover, pier ST7 (right)*



*Fig. 12 Insufficient concrete cover thickness, locally deep corrosion of the main reinforcement bars and stirrups, cracking and spalling of the concrete cover in the lower part of pier ST5*



*Fig. 13 Insufficient concrete cover thickness, transverse cracks at stirrup locations, vertical cracks, pier ST5*

## 3. FIELD AND LABORATORY TESTING

Field and laboratory testing was carried out on the RC piers and bearing beam (piers ST7 and ST7', and the bearing girder above pier ST7) and included the determination of the in-situ concrete compressive strength by testing extracted cores, as well as the measurement of concrete carbonation depth (Fig. 14).

### 3.1. COMPRESSIVE STRENGTH

The in-situ compressive strength of the concrete in the RC piers and bearing beam was determined by testing extracted concrete cores in accordance with SRPS EN 12504-1. Data on core density, length-to-diameter ratio, core compressive strength ($f_{c,1:1,core}$), and in-situ compressive strength ($f_{c,is}$) are presented in Table 2. The characteristic in-situ compressive strength was subsequently assessed in accordance with SRPS EN 13791, following the procedure specified for a small test region.




*Fig. 14 Extraction of a concrete core from an RC element of the bridge over the river*

*Tab. 2 Density, core compressive strength and in-situ compressive strength*

| Element | Core mark | Density kg/m$^3$ | $f_{c,1:1,core}$ MPa | $f_{c,is}$ MPa | $f_{ck,cyl}$ MPa |
|---|---|---|---|---|---|
| Pier | ST7 | 2347 | 45.6 | 37.37 | 35 |
| Pier | ST7' | 2276 | 51.1 | 41.88 | |
| Bearing beam | ST7 LG | 2329 | 57.9 | 47.48 | |

Based on the analysis of the test results, the characteristic in-situ compressive strength was found to correspond to a minimum characteristic cylinder compressive strength of fck,cyl = 35 MPa. Compared with the specified design concrete grade for the piers and bearing girders (MB30, approximately equivalent to C25/30), the assessed in-situ concrete strength corresponds to strength class C35/45. Therefore, the concrete in the existing structure meets and exceeds the specified design requirement.

### 3.2. CARBONATION DEPTH

To assess whether a sufficient depth of uncarbonated concrete remains to provide adequate protection to the reinforcement throughout the remaining service life of the structure, the concrete carbonation depth was measured using the colorimetric

(phenolphthalein) method in accordance with SRPS EN 14630 (Fig. 15). The outer portions of the same cores used for the compressive strength assessment were used for carbonation testing. The measured carbonation depths are presented in Table 3.




*Fig. 15 View of sectioned specimens for carbonation depth testing*

*Tab. 3 Results of measuring the carbonation depth of concrete*

| Element | Core mark | $d_{c,i}$ mm | $d_{c,mean}$ mm | $d_{c,min}$ mm | $d_{c,max}$ mm |
|---|---|---|---|---|---|
| Pier | ST7 | 11 | 9.3 | 5 | 12 |
| Pier | ST7' | 12 | | | |
| Bearing girder | ST7 LG | 5 | | | |

The results indicate that concrete carbonation has occurred, with the depth of carbonation varying depending on the type of structural element. At the piers, the measured depths of 11 mm and 12 mm are comparable to or greater than the available concrete cover, which was found during the visual inspection to be insufficient on all inspected piers. Consequently, the carbonation front has reached or penetrated beyond the reinforcement level, resulting in the loss of the passive protection against reinforcement corrosion. In contrast, the carbonation depth measured on the bearing girder was considerably smaller (5 mm). Since insufficient concrete cover was observed only locally on this type of element, the carbonation front has generally not reached the reinforcement level, and the concrete cover therefore continues to provide passive protection against corrosion.

## 4. CONCLUSION AND GLOBAL REPAIR MEASURES

The assessment identified defects and damage affecting both the steel and RC elements of the bridge superstructure. The most significant structural damage to the steel truss consists of local and global deformations caused by vehicle impacts. A total of 23 members were found to be deformed, predominantly within the upper-chord truss and the first tier, with the affected length ranging from 10% to 100% of the member length. The resulting deformation has also affected several bolted connections. Although the overall load-bearing capacity and stability of the steel superstructure remain generally preserved, the observed deformations locally reduce structural capacity and require appropriate structural repair to restore the designed level of safety and performance.

The corrosion protection system has deteriorated over a significant portion of the steel structure, resulting in corrosion of varying severity. Surface corrosion is predominant, while localized severe corrosion accompanied by steel delamination, flaking, and section loss was observed primarily on the lower-chord members, particularly at connections and locations of prolonged water retention. Similar deterioration was identified on the steel bearings and drainage system. The inadequate longitudinal slope and poor condition of the drainage system promote water retention and direct discharge

onto structural elements, thereby accelerating deterioration. These deficiencies primarily affect the durability of the steel structure and require comprehensive rehabilitation of the corrosion protection and drainage systems.
The observed defects and damages of the RC elements, including insufficient concrete cover, cracking, spalling, honeycombs, and reinforcement corrosion, do not currently compromise their overall load-bearing capacity but adversely affect their durability. The assessed in-situ concrete strength corresponds to class C35/45 and therefore exceeds the specified design concrete grade of MB30 (approximately C25/30). However, carbonation has reached or locally penetrated beyond the reinforcement level at the inspected piers, resulting in the loss of passive protection against reinforcement corrosion.
The recommended repair measures can be classified into structural and non-structural interventions.

**Structural repair measures:**

- replacement or repair of steel truss members exhibiting significant local or global deformations;
- repair or replacement of steel members affected by severe corrosion and significant section loss;
- inspection and restoration of bolted connections affected by member deformation or missing bolts;
- structural repair of cracks in RC elements where their width, orientation, or extent indicates an adverse effect on structural performance.

**Non-structural repair measures:**

- comprehensive rehabilitation of the corrosion protection system of the steel structure and bearings;
- reconstruction and improvement of the bridge drainage system to ensure effective water discharge and prevent prolonged water retention;
- removal of deteriorated and carbonated concrete and treatment of corroded reinforcement;
- restoration or increase of insufficient concrete cover using appropriate repair materials;
- repair of non-structural cracks, spalling, and honeycombed areas in RC elements;
- application of corrosion inhibitors and protective surface systems, where appropriate, to improve the durability of the RC elements.

Implementation of the proposed structural and non-structural repair measures would restore the required structural performance of the locally damaged elements, mitigate the identified deterioration mechanisms, and significantly improve the durability of both the steel and RC components, thereby providing the conditions for the safe and reliable continued service of the bridge.

## REFERENCES

[1] Kukaras D., Šupić S., Pantić V.: Elaborat o proceni stanja noseće konstrukcije mosta preko reke Save u Obrenovcu, Centar za konstrukcije d.o.o Subotica, Obrenovac, 2026.

https://doi.org/10.24867/INDIS-2026-EN-255



# ASSESSMENT OF THE CONDITION OF THE PAVEMENT IN MIŠE DIMITRIJEVIĆA STREET ACCRODING TO THE PCI METHODOLOGY

*Milan Marinković*[1], *Marija Milanović*[2]

***Summary:***

Regular collection of data on the condition of roads is the basis for proper management of the road network. There are different ways to assess the condition of roads. These are mostly evaluations based on visual inspection, which can sometimes be subjective, and there are also indexes whose value classifies the condition of the pavement into a certain category. In this paper, the assessment of the condition of the pavement in Miše Dimitrijevića street in Novi Sad according to the PCI methodology is presented. According to that methodology, there are 19 types of distress that are registered during a visual inspection. A detailed assessment procedure is defined by the standard. The total length of the road that was inspected in 2021 is about 1000 m, and based on the PCI methodology, the rating is 66, which means that the condition of the road is fair according to the PCI scale. The same pavement was rated in 2024 and rating was 61.8.

*Keywords: rating, condition, distress, pavement management system*

# PROCJENA STANJA KOLOVOZA U ULICI MIŠE DIMITRIJEVIĆA PREMA PCI METODOLOGIJI

***Rezime:***

Redovno prikupljanje podataka o stanju saobraćajnica predstavlja temelj za pravilno upravljanje putnom mrežom. Postoje različiti načini za ocjenu stanja saobraćajnica. To su uglavnom ocjene prema vizuelnom pregledu koje ponekad mogu biti podložne subjektivnosti a postoje i indeksi čija vrijednost klasifikuje stanje kolovoza u određenu kategoriju. U ovom radu je prikazana ocjena stanja kolovoza u ulici Miše Dimitrijevića u Novom Sadu prema PCI metodologiji. Prema toj metodlogiji postoji 19 tipova oštećenja koja se registruju tokom vizuelnog pregleda. Detaljan postupak procjene stanja je definisan standardom. Ukupna dužina saobraćajnice koja je pregledana 2021 godine je oko 1000 m i na osnovu PCI metodologije ocjena je 66 što prema PCI skali znači da je stanje saobraćajnice osrednje. Ista saobraćajnica je ocijenjena i 2024 godine i dobijena ocjena je 61,8.

*Ključne reči: ocjena, stanje, oštećenja, upravljanje putevima*

[1] Assistant Professor, Department of Civil Engineering and Geodesy, Faculty of Technical Sciences Novi Sad, University of Novi Sad, Republic of Serbia, milan.marinkovic@uns.ac.rs, ORCID 0000-0002-1992-302X
[2] Serbian Railway Infrastructure, Belgrade, Republic of Serbia, marijamijailovic7@gmail.com,

## 1. INTRODUCTION

During its life cycle, the infrastructure is exposed to the effects of traffic load and atmospheric influences [1]. In addition, the quality of the built-in materials affects the rate of deterioration of the infrastructure. The basic logic is that over time the situation will deteriorate if infrastructure maintenance is not carried out (Figure 1).

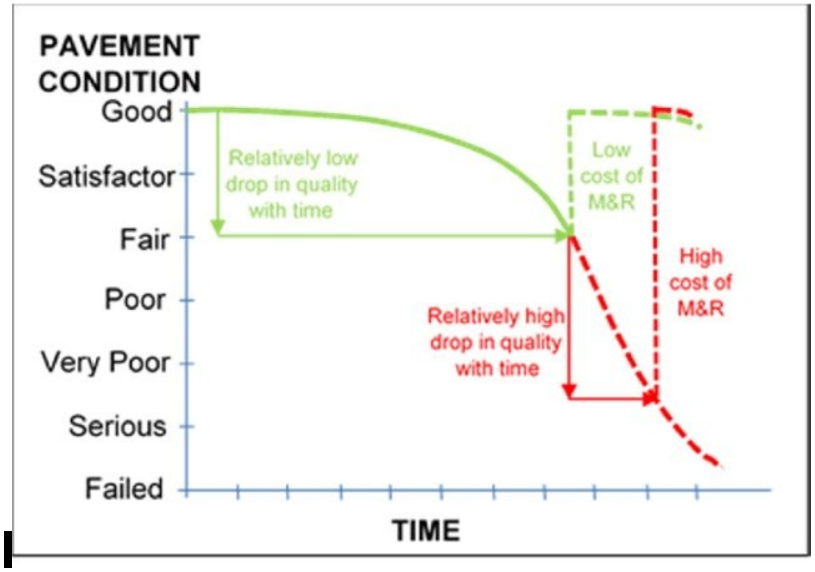


*Fig. 1 Change in pavement condition over time[2]*

The condition of the infrastructure can be expressed in different ways, in the sense that it can be expressed through some descriptions based on visual inspection, in terms of one word description, or through some quantitative parameters. Quantitative parameters are represented by a number that corresponds to a certain condition of the infrastructure. Parameters that can be used to express quality are Pavement Condition Index (PCI) [3, 4,5], Present Serviceability Index (PSI) [6, 7] or International Roughness Index (IRI) [8,9,10] .

## 2. PAVEMENT CONDITION INDEX

This paper present an assessment of the condition of Miše Dimitrijevića street in Novi Sad. The condition assessment was carried out according to the PCI methodology which is defined by the standard ASTM D6433-24 [11]. This method was developed by US Army engineers [12] and was originally intended for airports but was later adapted for roads.

According to this methodology, 19 types of distress are defined, which are registered by visual inspection on the field. The manual that describes this methodology provides example photos of all types of distress. It is important to note that all distresses have three intensities in which they can occur, namely: low, medium and high level of distress.

## 3. CASE STUDY AND RESULTS

Of the total length of the street, the condition assessment was carried out on 1000 m. Before inspecting the road and registering the distress, it is necessary to divide the road in the appropriate number of subsections, with the condition that the area of one subsection is 225±90 m$^2$[11]. Since the mentioned street has two lanes, it was adopted that it has an average width of 6m. The minimum number of subsections for inspection is:

$$n=\frac{N * s^2}{\frac{e^2}{4} * (N-1)+s^2} \quad (1)$$

where:
N- total number of subsections
e- acceptable error in estimating PCI values on a section. For the initial calculation ± 5 points
s- standard deviation of PCI values on subsections within a section. s =± 10 points for the initial calculation

For the case of this road section, it was obtained by calculation [11]:

$$n=\frac{20 * 10^2}{\frac{5^2}{4} * (20-1)+10^2}=9,14 \quad (2)$$

It was adopted that a minimum of 10 subsections should be inspected for condition assessment.

After that, it is necessary to determine which 10 subsections out of a total of 20 will be inspected. This can be determined based on the formula for the review interval:

$$i=\frac{N}{n}=2 \quad (3)$$

The resulting number indicates how much difference there will be between subsections. What can be an exception to this rule is if there is a subsection that is in significantly worse or significantly better condition than the rest of the subsections. In that case, we can skip such subsection during the review. In our case, it was decided to inspect every second subsection. This means we should review every second subsection ie. that starting with the first, we should then examine the third, fifth, seventh, etc. It is shown in more detail in Figure 2.

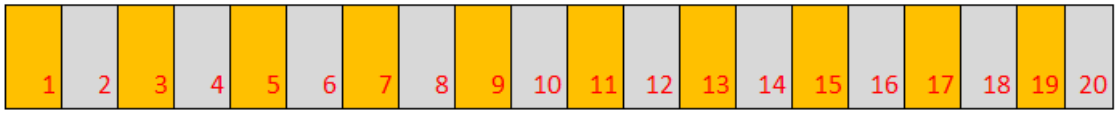


*Fig. 2 Order of subsections for visual inspection and condition rating*

After the subsections were selected for inspection on the field, a visual inspection of the pavement was carried out. The review was carried out at the end of 2021. Distress of the pavement surface were photographed. The most common distresses observed are:

alligator crackings (Figure 3), longitudinal and transverse crackings, patches and potholes.



*Fig. 3 Photos of alligator crackings in Miše Dimitrijevića Street*

After the distress was registered, the location of the distress was sketched, as well as a graphic representation of the distress on the maps as shown in Figure 4.

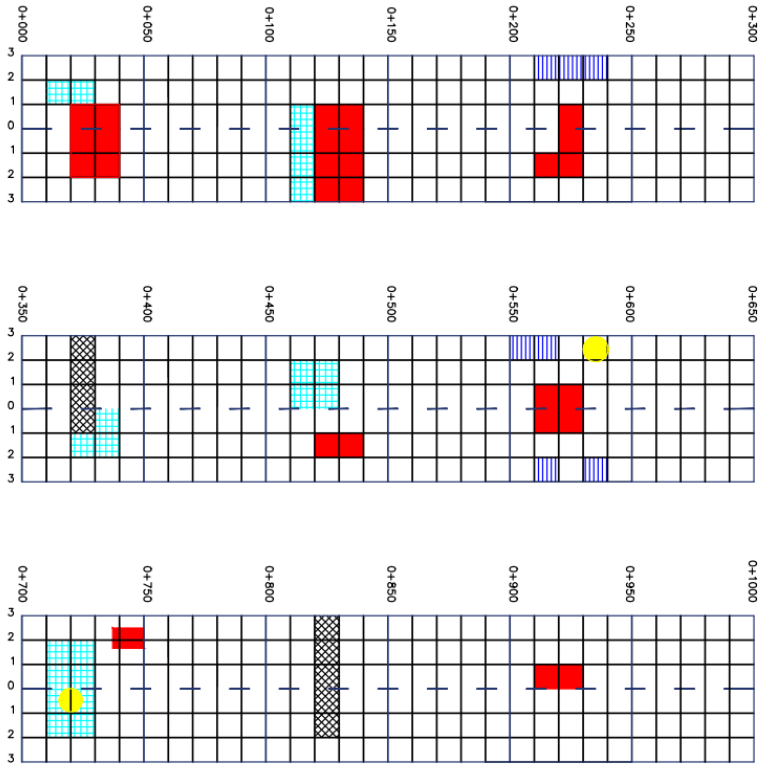


| # | DISTRESS TYPE | LEGEND |
|---|---|---|
| 1 | Alligator Cracking | AC |
| 2 | Bleeding | BL |
| 3 | Block Cracking | BC |
| 4 | Bumps and Sugs | BS |
| 5 | Corrugation | CO |
| 6 | Depression | DE |
| 7 | Edge Cracking | EC |
| 8 | Jt. Reflection Cracking | JRC |
| 9 | Lane/ Shoulder Drop Off | LSDO |
| 10 | Long & Trans Cracking | LTC |
| 11 | Patching and Util Cut Patching | PUCP |
| 12 | Polished Aggregate | PA |
| 13 | Potholes | PO |
| 14 | Railroad Crossing | RC |
| 15 | Rutting | RU |
| 16 | Shoving | SH |
| 17 | Slippage Cracking | SC |
| 18 | Swell | SW |
| 19 | Weathering / Raveling | WR |

*Fig. 4 Distress maps*

In addition to the distress drawings, a report on the inspection of each subsection was created. The data sheets are created using the form prescribed by the specified standard [11]. The table 1 shows the completed form for Subsection 17.

*Tab. 1 Data sheet for subsection 17*

| | | | | | | | |
|---|---|---|---|---|---|---|---|
| Branch | Miše Dimitrijevića Novi Sad | | | | Sketch: 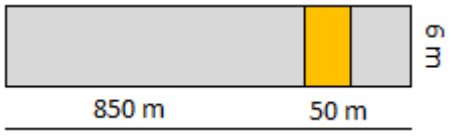  | | |
| Section | MD17 | | | | | | |
| Sample unit | SU17 | | | | | | |
| Surveyed by | M.M. | | | | | | |
| Date | 16.11.2021. | | | | | | |
| Sample area | 300 | | | | | | |
| Distress severity | Quantity | | | | Total | Density (%) | Deduct value |
| 11 M | 12 | 2 | | | 14 | 4,67 | 22 |
| 3 L | 20 | 1,2 | | | 21,2 | 7,07 | 8 |

After registering the distress, the density is determined and then based on the density of the distress, the deduct values are determined. The standard provides diagrams for each type of distress on the basis of which the deduct values are determined. Then the obtained values are ordered from maximum to minimum and it is determined how many of these values are taken into account for the PCI calculation. For this subsection it is taken into account:

$$m_i = 1 + \frac{9}{98} * (100 - max\,DV) = 8,16 \qquad (4)$$

Since we only have two values, we take them into the calculation. The next step is to calculate the corrected deduct values (Table 2). The corrected values are determined based on the sum of the deduct values and the factor q, which is the number of values greater than 2, and everything is calculated from the diagram given in the standard.

*Tab. 2 Calculation of corrected deduct values for subsection 17*

| No | Deduct value | | Total | q | CDV |
|---|---|---|---|---|---|
| 1 | 22 | 8 | 30 | 2 | 19 |
| 2 | 22 | 2 | 24 | 1 | 24 |

This procedure is determined for each of the subsections we review. Finally, the PCI value for the subsection is determined. For subsection 17 the PCI value is:

$$PCI = 100 - max\,CDV = 76 \qquad (5)$$

According to the PCI scale, this subsection is classified as a subsection with a satisfactory condition (Figure 5).

| PCI | Verbal Rating |
|---|---|
| 86–100 | Good |
| 71–85 | Satisfactory |
| 56–70 | Fair |
| 41–55 | Poor |
| 26–40 | Very Poor |
| 11–25 | Serious |
| 0–10 | Failed |

*Fig. 5 Pavement Condition Index scale [13]*

After the assessment of each of the subsections, the final assessment for the entire section was calculated:

PCI = 66

Based on the mentioned scale (Figure 5), the condition of Miše Dimitrijevića street is fair.

In the paper that has already been published [14], the same street was inspected in 2024 and the condition was assessed with a score of PCI=61.8, which means that the condition has worsened over a period of three years. There were no reconstruction or rehabilitation works on the road in question, so this conclusion is logical.

## 4. CONCLUSIONS

Monitoring the condition of roads is a very important factor when managing the road network. Monitoring the condition allows us to carry out maintenance work on the road network in a timely manner. Of course, it is understood that data collection should be constant and that data should be collected as newest as possible.

This paper presents the process of assessing the condition of Miše Dimitrijevića street according to the PCI methodology. The PCI methodology is one of several methodologies that serve to assess the condition and it is based on detailed instructions given through the standard. During the assessment of the condition, a visual inspection was carried out on the field in 2021, distress was drawn, forms were filled out, and the PCI value was calculated. The entire section is divided into 20 subsections, of which 10 subsections were inspected and evaluated. In the end, the final rate of this road is 66, which according to the PCI scale categorizes this road in fair condition. The same road was inspected three years later and was rated 61.8, which means that the condition has deteriorated.

## ACKNOWLEDGEMENT

This research was funded by the European union-NextGenerationEU, project Harmonization of Innovation and smart Traffic Infrastructure - HIPI, 581-UNIOS-73.

## REFERENCES

[1] Sarkar H., Sinha S. (2026). *State-of-the-art review of pavement deterioration models for enhancing transportation infrastructure management*. International Journal of Pavement Engineering, Volume 27. No1. https://doi.org/10.1080/10298436.2026.2633306

[2] Bazlamit S.M., Ahmad H.S., Al-Suleiman T.I. (Obaidat). (2017). *Pavement Maintenance Applications Using Geographic Information Systems*. Procedia Engineering, Volume 182, pp. 83-90. https://doi.org/10.1016/j.proeng.2017.03.123.

[3] Fareed K.M.A., Rubasi K.A.H., Saleh A.A. (2016). *The Road Pavement Condition Index (PCI) Evaluation and Maintenance: A Case Study of Yemen.* Organization, Technology and

Management in Construction. Volume 8. No 1. pp. 1446-1455. https://doi.org/10.1515/otmcj-2016-0008

[4] Pinatt J.M., Chicati M.L., Ildefonso J.S., Grégio D'arce Filetti C.R. (2020). *Evaluation of pavement condition index by different methods: Case study of Maringá, Brazil.* Transportation Research Interdisciplinary Perspectives. Volume 4. pp. https://doi.org/10.1016/j.trip.2020.100100.

[5] Temimi, F. A. R., Ali, A. H. M., Obaidi, A. H. F. (2021). *The Pavement Condition Index (PCI) Method for Evaluating Pavement Distresses of The Roads in Iraq- A Case Study in Al- Nasiriyah City*. Volume 11. No 2. pp. 17-.http://www.doi.org/10.31663/tqujes.11.2.394

[6] Isradi M., Prasetijo J., Aden T., Rifai, A. (2023). Relationship of present serviceability index for flexible andrigid pavement in urban road damage assessment using pavement condition index and international roughness index. E3s Web of Conferences, Volume 429, 03012. https://doi.org/10.1051/e3sconf/202342903012

[7] Hall K., Muñoz C. (1999). *Estimation of Present Serviceability Index from International Roughness Index*. Transportation Research Record: Journal of the Transportation Research Board, Volume 1655. No 1, pp. 93-99. https://doi.org/10.3141/1655-13

[8] Múčka, P. (2017). *International Roughness Index specifications around the world*. Road Materials and Pavement Design. Volume 18. No 4, pp. 929–965. https://doi.org/10.1080/14680629.2016.1197144

[9] Pérez-Acebo H., Isasa M., Gurrutxaga I., García H., Insausti A. (2023). International Roughness Index (IRI) prediction models for freeways. Transportation Research Procedia. Volume 71. pp. 292-299. https://doi.org/10.1016/j.trpro.2023.11.087

[10] Chen, S.-L., Lin, C.-H., Tang, C.-W., Chu, L.-P., & Cheng, C.-K. (2020). Research on the International Roughness Index Threshold of Road Rehabilitation in Metropolitan Areas: A Case Study in Taipei City. Sustainability. Volume 12. No 24. pp 10536. https://doi.org/10.3390/su122410536

[11] Advancing Standards Transforming Markets (2024). ASTM D6433-24-Standard Practice for Roads and Parking Lots Pavement Condition Index Surveys

[12] Al-Rubaee R. H. A., Shubber A. A. M., Khaleefah H. S. (2020*). Evaluation of rigid pavement using the Pavement ConditionIndex: A Case Study*. IOP Conference Series: Materials Science and Engineering, Volume 737. No 1. 012128. https://doi.org/10.1088/1757-899X/737/1/012128

[13] Zoccali, P., Loprencipe, G., Galoni, A. (2017). Sampietrini Stone Pavements: Distress Analysis Using Pavement Condition Index Method. *Applied Sciences, Volume 7,* pp. 83-90 669. https://doi.org/10.3390/app7070669

[14] Marinković M. (2026). *Methods for Assessing the Conditions of Pavement with an Example of Asssessment in Novi Sad.* Journal of Road and Traffic Engineering. Volume 72. No 5. pp. 131-138. https://doi.org/10.31075/6SKP.13

https://doi.org/10.24867/INDIS-2026-EN-262



# ASSESSMENT OF CONTEMPORARY TIMBER BRIDGES

*Tomaž Pazlar[1], Martin Capuder[2], Jaka Gašper Pečnik[3], Boris Azinović[4]*

***Summary:***

In recent years, timber has re-emerged as a viable alternative material for bridge construction, not only for the rehabilitation of existing traditional structures but also for the construction of new bridges, particularly pedestrian and bicycle bridges. Routine periodic inspections have revealed early deterioration affecting critical load-bearing elements, prompting more detailed condition assessments using advanced non-destructive testing (NDT) methods. The investigations identified inadequate design, particularly with respect to durability considerations, deficiencies in construction execution, and insufficient maintenance as the primary factors contributing to the relatively high levels of deterioration. Consequently, the service life of some these timber bridges may often be significantly shorter than originally anticipated.

*Keywords: contemporary timber bridges, assessment, durability, non-destructive methods*

# PROCENA SAVREMENIH DRVENIH MOSTOVA

***Rezime:***

Poslednjih godina drvo je ponovo prepoznato kao održiva alternativa za izgradnju mostova, ne samo u rehabilitaciji postojećih konstrukcija već i u izgradnji novih mostova, naročito pešačkih i biciklističkih. Redovni periodični pregledi ukazali su na ranu pojavu oštećenja usled degradacije na ključnim nosećim elementima, što je uslovilo sprovođenje detaljnijih procena stanja primenom savremenih metoda nedestruktivnog ispitivanja (NDT). Istraživanja su pokazala da su neadekvatno projektovanje, posebno u pogledu obezbeđenja trajnosti, nedostaci u izvođenju građevinskih radova i neadekvatno održavanje glavni uzroci relativno visokog stepena degradacije. Kao posledica toga, vek trajanja nekih drvenih mostova često je značajno kraći od projektovanog.

*Ključne reči: savremeni drveni mostovi, procjena, trajnost, nedestruktivne metode*

[1] PhD, Head of Section for Timber Structures, Slovenian National Building and Civil Engineering Institute, Dimičeva 12, 1000 Ljubljana, Slovenia, tomaz.pazlar@zag.si, ORCID 0009-0003-3857-3293
[2] MSc, Researh associate, Slovenian National Building and Civil Engineering Institute, Dimičeva 12, 1000 Ljubljana, Slovenia, martin.capuder@zag.si, ORCID 0009-0002-6984-1804
[3] PhD, Researh associate, Slovenian National Building and Civil Engineering Institute, Dimičeva 12, 1000 Ljubljana, Slovenia, jaka.pecnik@zag.si, ORCID 0000-0002-8775-8230
[4] PhD, Researh associate, Slovenian National Building and Civil Engineering Institute, Dimičeva 12, 1000 Ljubljana, Slovenia, boris.azinovic@zag.si, ORCID 0000-0002-1810-5957

## 1. INTRODUCTION

Timber bridges are among the oldest engineered structures in human history. The ability of timber to resist bending loads was recognized early, leading to the construction of some of the earliest bridge structures in order to provide permanent river crossings. In Slovenia, remains of simple timber bridges dating back to the Neolithic period have been discovered in the wetlands surrounding Ljubljana. These early bridges consisted of logs spanning single or multiple openings, a basic structural concept that has remained largely unchanged over time. The principal evolution has been in the processing of timber, with round logs gradually being replaced by hewn and, later, sawn timber members. Local available timber species were used: hardwood species, particularly oak, as well as naturally durable softwood species such as larch, were commonly used for primary load-bearing members subjected to bending and compression. Less durable species, such as spruce, were also used where a limited service life was acceptable / expected or where adequate protective design measures, such as roofed or covered bridge structures were implemented [1].

Over the course of the twentieth century, timber bridges were gradually replaced by reinforced concrete and steel bridges, primarily to improve durability and increase load-carrying capacity. Traditional timber bridges (Figure 1) generally required relatively intensive maintenance and periodic rehabilitation, which further encouraged bridge owners and infrastructure managers to adopt alternative structural materials and systems. Nevertheless, a considerable number of historic timber bridges have been preserved and are now protected as cultural heritage structures due to their historical and architectural significance.

During the past few decades, however, bridge designers in Slovenia have increasingly reconsidered timber as a primary structural material, largely driven by the growing emphasis on sustainable and environmentally responsible construction. Timber is now commonly used for pedestrian and cyclist bridges. Since 2000, Slovenia has developed an extensive network of cycling routes, while urban areas have invested in numerous pedestrian and cycling bridges as part of sustainable mobility initiatives, providing shorter and more direct connections within cities.



*Fig. 1 Traditional oak bridge vs. contemporary spruce arc bridge.*

It should be noted that pedestrian and cyclist bridges forming part of cycling infrastructure are generally required to accommodate not only pedestrians and cyclists but also maintenance and emergency service vehicles. Consequently, these structures must satisfy higher load-bearing and serviceability requirements than conventional pedestrian bridges.

The development of engineered wood products, particularly glued laminated timber (glulam), together with other advanced materials and innovative structural solutions, such as timber–concrete composite systems, has significantly expanded the potential applications of timber bridges. These technologies enable the construction of bridges with longer spans and higher load capacities, as demonstrated by numerous examples built in recent years across Europe and other parts of the world.

Bridge owners and infrastructure managers are responsible for ensuring that bridge structures remain safe and serviceable throughout their intended service life. A key component of bridge maintenance is the systematic inspection of structural condition – timber bridges might be even more prone to structural damage due to material degradation [1, 9]. Depending on the importance, function, and associated risk of the structure, different inspection regimes may be specified. In general, bridge inspections can be classified as regular inspections, main or principal inspections, detailed inspections, and special (extraordinary) inspections carried out following exceptional events or when structural defects are suspected.

## 2. GENERAL ASSESSMENT OF BRIDGES IN SLOVENIA

The Slovenian National Building and Civil Engineering Institute (ZAG) has been actively involved in bridge condition assessment since its establishment. In 1990, ZAG developed a comprehensive bridge inspection methodology that introduced a systematic approach to the assessment of all types of bridge structures [2]. This methodology forms the basis of the national bridge management system and enables standardized documentation and evaluation of bridge condition.

The inspection procedure consists of a general description of the bridge followed by a systematic documentation of all observed defects and damage. Each recorded damage is described using the following parameters:

- Structural member on which the damage was detected.
- Detailed identification of the structural member and its location.
- Type of damage.
- Location of the damaged area within the bridge (e.g., pier, girder, deck, riverbed) or a textual description of the affected area.
- Position of the damage in the longitudinal and transverse directions relative to the bridge axis, including its elevation.
- Degree (severity) of damage.
- Extent of damage.
- Recommended remedial measures.
- General inspection findings.

Each inspection parameter is assigned an alphanumeric or numerical code, thereby minimizing inspector-dependent reporting differences while enabling a consistent and objective evaluation of bridge condition. The coded information is subsequently used to calculate bridge condition ratings.

To facilitate standardized coding, each bridge is divided into a number of principal structural groups: bridge surroundings, riverbed, foundations, piers and abutments, bearings, superstructure, roadway, tunnel, expansion joints, safety equipment and traffic signage, utility installations, and drainage systems. Each principal group is further subdivided into individual structural components. For example, the superstructure includes the deck slab, main girders, secondary load-bearing members, box girders, cross beams, arches, vaults, trusses, and sidewalk structures.

Damage observed on bridge components is classified using a four-digit coding system. The first two digits identify the general damage category, including structural behaviour

deficiencies, material deterioration, and defects of structural elements. The remaining digits provide a more detailed classification of the damage. For steel structures, for example, the coding distinguishes between mechanical damage, damage to protective coatings, corrosion of structural steel, cracking, missing elements, and rotation of structural connections. In addition to the damage type, the inspector records the location, severity, and extent of the damage. Appropriate remedial measures are then proposed based on the severity of the deterioration and its potential consequences for structural safety and serviceability.

- Each recorded damage is quantitatively evaluated using four weighting factors:
- K1 – Element factor, representing the structural importance of the affected element.
- K2 – Damage intensity factor, describing the severity or stage of deterioration.
- K3 – Damage extent factor, representing the size or distribution of the damage.
- K4 – Urgency factor, indicating the required priority of remedial actions (no immediate action required, intervention within five years, immediate intervention, or urgent intervention due to potential structural failure).

These factors are combined to determine condition ratings for individual bridge components as well as for the bridge as a whole.




*Fig. 2 eBridge software.*

The methodology has been continuously updated over the years, together with the development of the accompanying software tool, eBridge (Figure 2). Today, eBridge is implemented as a web-based application in which all bridge inspection reports are

stored in a MySQL database hosted on a central server. The application provides inspectors and bridge managers with several important functionalities, including:

- access to the inspection database from any location and any internet-connected device, including directly on site during bridge inspections;
- integration of photographs linked to individual damage records;
- quantitative evaluation of damage using standardized condition indices;
- automatic calculation and graphical presentation of condition ratings for the principal bridge groups (substructure, superstructure, riverbed and surroundings, and pavement and equipment), as well as for the bridge as a whole, thereby supporting bridge ranking and maintenance prioritization according to the degree of deterioration.

The inspection summary provides condition ratings for the principal bridge groups, namely the substructure, superstructure, pavement and equipment, as well as an overall condition rating for the bridge. In addition, the overall bridge condition is expressed using a standardized five-level condition scale (1–5), enabling a rapid assessment of the bridge condition and facilitating maintenance planning and prioritization.

The Description section is intended primarily for bridge owners and infrastructure managers. Based on the detailed inspection findings, it should provide a clear, reliable, and comprehensive overview of the bridge condition. In this concise narrative, the inspector highlights the most significant defects and deterioration mechanisms, with particular emphasis on those that may adversely affect structural safety, serviceability, or durability and therefore require immediate attention or further investigation.

The Remedial Measures section summarizes all maintenance and repair actions proposed during the inspection. In addition to measures associated with specific defects, it also includes recommendations that apply to the bridge as a whole. The proposed actions are classified into general maintenance measures, standard repair works with estimated quantities and recommended implementation deadlines, urgent repairs, and non-urgent repairs, thereby providing bridge managers with a structured basis for maintenance planning.

The presented methodology is applicable to all categories of bridge inspections, including regular inspections (typically performed every two years), main / principal inspections (typically every six years), special inspections, detailed investigations, baseline (zero) inspections, and inspections carried out prior to the expiration of the warranty period. One of its greatest strengths lies in its application to periodic inspections, where the consistent use of standardized inspection procedures and condition indices enables deterioration trends to be monitored over time. This allows changes in condition to be identified at the level of individual structural elements, entire bridge structures, or across the bridge network, thereby supporting data-driven maintenance management and long-term asset planning.

## 3. ASSESSMENT OF TIMBER BRIDGES

Although the presented methodology has proven to be highly effective for the assessment of reinforced concrete and steel bridges, it was originally developed primarily for concrete bridge structures. Consequently, the numerical condition ratings do not always accurately reflect the actual condition of timber bridges, whose deterioration mechanisms differ substantially from those of conventional bridge materials. Timber structures are particularly sensitive to moisture exposure, biological degradation, and localized defects, which may not be adequately represented by the existing weighting system. Therefore, special consideration should be given to the

selection and interpretation of the weighting factors (K1–K4) when evaluating timber bridges to ensure that the resulting condition ratings accurately represent their structural performance and maintenance needs.

The presented methodology is primarily focused on the assessment and condition rating of bridge structures rather than on the inspection procedures or the specific inspection methods employed. While the assessment framework is standardized, the selection of inspection techniques and the extent of the investigation depend on the type and scope of the inspection being performed.

In practice, bridge inspectors may adopt different approaches based on their experience and professional judgment. To ensure consistency, repeatability, and comparability of inspection results over time, it is recommended that the same inspection methodology and evaluation principles be applied throughout the service life of a bridge. A consistent approach minimizes subjectivity, improves the reliability of condition ratings, and enables meaningful comparison of inspection results from successive inspection campaigns.

The inspection methods employed should be appropriate to the inspection level. Regular inspections generally rely on visual examination, whereas main / principal and detailed inspections may require more comprehensive investigations, including measurements, non-destructive testing (NDT), material sampling, or structural monitoring, depending on the observed condition of the bridge and the objectives of the assessment.

Over the past decades, a wide range of non-destructive testing (NDT) methods have been developed and documented in the literature for the assessment of timber structures. These include techniques such as stress wave timing, ultrasonic testing, Pilodyn penetration testing, resistance drilling (Resistograph), screw withdrawal testing, and several others [3, 4]. The assessment of existing timber structures has also been the focus of two major European COST Actions: COST Action E55 and COST Action FP1101 [5, 6, 7].

The literature further describes a number of specialized methodologies applied specifically to the condition assessment of timber bridges, as well as the most common deficiencies related to their design, construction, and maintenance [8, 9, 10]. Furthermore, long term monitoring of timber bridges is also subject of research [11].

## 4. CASE STUDY: ASSESSMENT OF A TIMBER CYCLING FOOTBRIDGE BRIDGE

The investigated structure is a timber pedestrian and cycling bridge crossing the Sava River near the Danica Camp in Bohinjska Bistrica, Slovenia. Constructed in 2013, the bridge has a total span of approximately 53 m and consists of two glued laminated timber arch girders (GL32c) supported by reinforced concrete abutments and intermediate piers (Figure 3) [12]. The primary load-bearing system comprises glulam arch girders, transverse glulam beams, secondary longitudinal glulam beams, and larch timber decking. The main arches are enclosed by a ventilated timber façade designed to protect the structural members from direct environmental exposure while allowing moisture dissipation. It was foreseen that transverse glulam beams and secondary longitudinal glulam beams would be made of impregnated spruce.

The bridge in question was not included in the described system of regular bridge inspections. A detailed assessment was performed in October 2025 to evaluate the structural condition of the timber elements, steel connectors, and protective cladding. The assessment was initiated following an extraordinary incident involving the structural failure of the bridge decking, transverse glulam beams and secondary longitudinal glulam beams under a maintenance vehicle.

The assessment consisted of a combination of visual inspection and non-destructive and semi-destructive testing techniques. A detailed visual survey was first performed to identify signs of deterioration such as biological decay, moisture accumulation, fungal colonization, insect attack, cracking, mechanical damage, deformation, corrosion of steel components, and deficiencies in construction detailing affecting moisture drainage and ventilation.




*Fig. 3 Cycling footbridge over the Sava River.*

To facilitate direct examination of concealed structural elements, selected sections of the timber façade were locally removed at locations exhibiting visible deterioration. This enabled inspection of the condition of the primary arch girders, façade substructure, waterproof membrane, and concealed connection details without extensive dismantling of the protective cladding.

Timber moisture content was measured using an electrical resistance moisture meter (Figure 4). Measurements were taken at representative locations on the primary arches and transverse beams to evaluate moisture conditions associated with biological deterioration. Moisture measurements provided an indication of the exposure conditions and the likelihood of fungal activity, particularly in regions susceptible to water accumulation.




*Fig. 4 Measurements of moister content (left). Resistograph measurements (right).*

Simple hand tools, including a carpenter's hammer, chisel, and knife, were used to probe timber surfaces and determine the depth and severity of localized decay. These investigations allowed confirmation of biological deterioration observed visually and provided qualitative information regarding the residual integrity of degraded members.

Internal timber condition was further evaluated using resistance drilling (Resistograph IML Resi PD500) (Figure 4). This semi-destructive technique records drilling resistance as a function of penetration depth, allowing the detection of internal decay, voids, and zones of reduced wood density while causing only minimal damage to the structural

member. Resistance drilling was employed at selected locations where visual inspection indicated possible internal deterioration or where the extent of decay could not be reliably assessed from the surface.

The inspection was complemented by a review of the available design and construction documentation, including original design drawings, as-built documentation, construction records, and previous project documentation. The observed structural configuration and deterioration patterns were compared with the original design intent to identify deviations in construction details, material selection, timber protection systems, and previous repair interventions. Where original structural calculations were unavailable, simplified engineering evaluations were used to assess the adequacy of the existing structural system and identify members requiring immediate intervention.

## 4.1. GENERAL CONDITION

The bridge is situated in a densely vegetated environment where natural growth has significantly increased since construction. Accumulation of leaves, organic debris, and dirt was observed at numerous locations, particularly between deck boards, around secondary longitudinal beams, on transverse beams, and beneath the protective façade (Figure 5). These deposits retain moisture, creating favourable conditions for fungal decay and biological deterioration of timber.




*Fig. 5 Accumulation of leaves, organic debris, and dirt.*

Evidence of inadequate maintenance was identified throughout the structure. Vegetation has begun penetrating façade elements at the bridge entrances, while erosion of the riverbank adjacent to one abutment and local deterioration of concrete protective coatings were also observed (Figure 6). The inspection concluded that regular cleaning and vegetation management have not been performed at the frequency required / expected for exposed timber bridge structures.




*Fig. 6 Erosion of the riverbank (left). Deterioration of concrete coatings (right).*

## 4.2. CONDITION OF THE MAIN ARCH GIRDERS

The primary arch girders remain structurally continuous; however, deterioration is concentrated at their exposed end regions beneath the protective cladding at bridge entrances. On the right riverbank, only limited biological degradation was observed, consisting mainly of local surface decay and complete deterioration of portions of the timber façade substructure. Moisture measurements ranged between 18 and 19 %, which is typical for protected timber exposed to outdoor conditions.

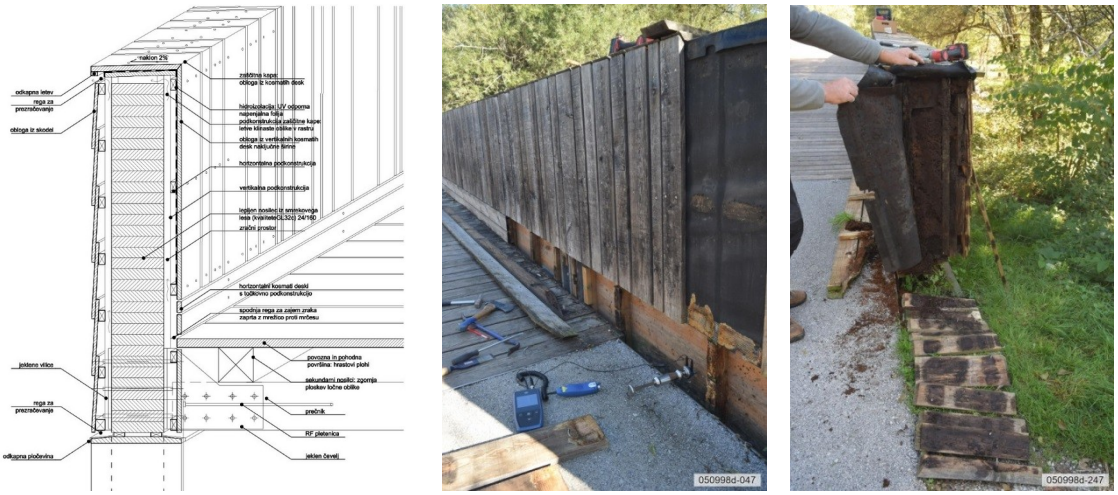


*Fig. 7 Protection of main girders with foil / façade.*

The condition of the arch girders on the left riverbank was considerably more severe (Figure 7). Removal of façade elements revealed complete decay of the supporting timber substructure, widespread fungal degradation, insect attack including larvae, and damaged waterproof membranes. Localized deterioration extended up to approximately 10 cm into the cross-section of the timber, indicating prolonged moisture exposure. The deterioration was most pronounced at the end grain, suggesting inadequate drainage and long-term water ingress most likely caused by poor execution of construction work (installation of membrane, non-impregnated or just surface-applied agent on battens used as substructure for façade). As expected, the shingles are in significantly better condition than the boards. The partial sunlight exposure of the membrane raises questions regarding its long-term durability.

The inspection further revealed deficiencies in previous repair works, including incomplete façade restoration (including metal sheeting) and unsuitable fasteners for outdoor service conditions.

## 4.3. CONDITION OF THE TRANSVERSE BEAMS

Inspection of the fourteen transverse glulam beams demonstrated widespread deterioration concentrated at the interfaces with the secondary longitudinal beams. Moisture accumulation on the upper surfaces has resulted in localized biological decay, reducing the effective structural depth of several members by up to approximately 5 cm. The most critical defect was identified in one of transverse beam (Figure 8), where pronounced deformation indicates substantial loss of structural capacity resulting from timber decay. Corresponding deformation of the bridge deck was also visible from the walking surface. This member represents the most significant immediate structural concern identified during the inspection.




*Fig. 8 Decay – assessment using Resistograph (left). Lose of structural integrity (right).*

## 4.4. CONDITION OF THE SECONDARY LONGITUDINAL BEAMS

The secondary longitudinal beams exhibited the highest overall level of deterioration among the structural timber components (Figures 9 and 10). Three principal degradation mechanisms were identified:

- biological decay at beam ends caused by moisture accumulation within debris-filled connection gaps;
- localized deterioration directly beneath the deck boards, where moisture measurements reached more than 50 %, indicating continuously saturated timber;
- longitudinal decay associated with natural timber defects and prolonged moisture exposure.




*Fig. 9 Decay in secondary longitudinal beams – at beam ends (left) and along elements (right).*




*Fig. 10 Fungi attack (left). Inappropriate repair measures (right).*

Several beams exhibited reductions in effective cross-sectional depth of up to 30 %, while fungal colonization was locally observed. In sections repaired after vehicle impact, original glued laminated members had been replaced with solid sawn timber of unknown mechanical properties, and several structural fasteners were missing (Figure 10).
Similar to the transverse beams, the longitudinal beams were not vacuum-pressure impregnated; wood preservatives were most likely surface-applied by brush or roller.

## 4.5. CONDITION OF THE DECK

The larch deck boards generally remain in satisfactory condition; however, approximately one-third of the boards exhibit defects that include excessive knots, unfavourable grain orientation, growth defects, mechanical damage, and localized biological deterioration (Figure 11). Although these defects currently have limited influence on global structural behaviour, replacement of damaged deck boards is recommended during rehabilitation process.




*Fig. 11 Decay of larch deck boards.*

## 4.6. RECOMMENDED REHABILITATION MEASURES

The inspection concluded that immediate intervention is required to maintain structural safety and prevent further deterioration. Priority measures include replacement or strengthening of the severely damaged transverse beam, restriction of any service vehicle traffic, loitering, repair of damaged façade components, restoration of waterproof detailing, replacement of deteriorated façade substructures, installation of missing structural connectors, and replacement of damaged deck boards.
A comprehensive rehabilitation programme in near future should additionally include replacement of all transverse and secondary longitudinal beams, verification of structural load capacity through updated structural analysis, stabilization of riverbank erosion near the foundations, renewal of concrete protective coatings, and reconstruction of deteriorated façade components. Future replacement members should be manufactured from pressure-treated timber or naturally durable wood species and assembled using corrosion-resistant fasteners suitable for outdoor service conditions. Several design details should be re-designed to ensure long-term durability of structure.

## 5. CONCLUSIONS

The presented assessment of contemporary timber bridge demonstrates that the observed deterioration is primarily associated with long-term moisture retention, insufficient detailing for drainage and ventilation (design and execution), biological degradation, and inadequate maintenance rather than deficiencies in the global structural

concept. Consequently, improving moisture management and implementing systematic maintenance are considered essential for extending the service life of timber pedestrian and cycling bridges operating under similar environmental conditions.
Constructing contemporary timber timber pedestrian and cycling bridges with non-durable wood species requires meticulous design, robust protective measures, high-quality construction, and rigorous long-term maintenance. Only through this comprehensive approach can timber compete effectively with alternative structural materials in bridge construction.

**ACKNOWLEDGEMENT**

This research was partly funded by the Slovenian Research and Innovation Agency (ARIS) under research programs P2-0273, and P4-0430.
The authors would also like to thank to Municipality of Bohinj.

## REFERENCES

[1] Norwegian Safety Investigation Authority: Sub-report 2 on the bridge collapse at Tretten on 15th of August 2022, Road traffic report 2024/03, https://nsia.no/Road/Published-reports/2024-03.

[2] Pazlar, T., Kramar M. (2014), Assessment of timber bridges in Slovenia. Cost timber bridge conference. Biel: Bern University of Applied Sciences, 2014.

[3] Ross, R.J., Pellerin R. F. (1994), Non-destructive Testing for Assessing Wood Members in Structures. A Review. General Technical Report FPL-GTR-70.

[4] Kasal B., Tannert T. eds. (2010), *In Situ Assessment of Structural Timber*, Springer, Netherlands, http://www.springer.com/engineering/civil+engineering/book/978-94-007-0559-3.

[5] Dietsch P., Köhler J. eds. (2009), *Assessment of Timber Structures*, COST Action E55 "Modelling of the Performance of Timber Structures".

[6] Tannert T., Dietsch P., Cestari C. B., Kasal B. (2012), COST Action FP1101 “Assessment, Reinforcement and Monitoring of Timber Structures”, World Conference on Timber Engineering, 15. - 19. 7. 2012, Auckland, New Zealand.

[7] Harte A. M., Dietsch P. (2015), *Reinforcement of Timber Structures: A state-of the-art report*, COST Action FP1101.

[8] Palma P., Steiger R. (2020), Structural health monitoring of timber structures – Review of available methods and case studies, *Construction and Building Materials*, Volume 248, https://doi.org/10.1016/j.conbuildmat.2020.118528.

[9] Ritter M. A. (1990), *Timber Bridges: Design, Construction, Inspection and Maintenance.* United states Department of Agriculture, Forest Service. Washington, DC.

[10] Abdoli F., Rashidi M., Wang J., Siddique R., Nasir. V. (2024), Structural health monitoring of timber bridges – A review. *Results in Engineering*. Volume 24 (2024) https://doi.org/10.1016/j.rineng.2024.103084.

[11] Franke B., Franke S., Műller A. (2014), Case studies: long-term monitoring of timber bridges. *J Civil Struct Health Monit* 5, 195–202. https://doi.org/10.1007/s13349-014-0093-4.

[12] Pazlar T., Capuder M., Pečnik J. G. (2026), Report ZAG 767/25-640-1 about the assessment of bicycle footbridge over Sava river at campsite Danica in Bohinjska Bistrica, Ljubljana Slovenia.

https://doi.org/10.24867/INDIS-2026-EN-274



# THERMAL AND ENERGY PERFORMANCE OF AN EXTENSIVE GREEN ROOF IN NOVEMBER 2025

*Snežana Ilić[1], Igor Džolev[2], Biljana Ilić[3], Mirjana Laban[4], Milica Mirković Marjanović[5]*

***Summary:*** Green roofs can improve the thermal performance of building envelopes by reducing temperature fluctuations and heat transfer. This study experimentally evaluates an extensive green roof compared with a conventional reference roof during November 2025. The main scientific contribution is the experimental and quantitative characterization of thermal buffering and heat-transfer attenuation through continuous in-situ monitoring under continental late-autumn conditions. The green roof exhibited lower temperature fluctuations and a more pronounced thermal phase shift than the conventional roof. Cumulative heat loss was 20,221.53 Wh/m² for the conventional roof and 14,824.24 Wh/m² for the green roof, corresponding to a reduction of 5,397.29 Wh/m² or 26.69%. The results demonstrate the value of continuous monitoring for capturing the dynamic thermal behaviour of green roofs and their potential to reduce heat transfer during late autumn.

*Keywords: Green roof; Thermal performance; Heat transfer; Energy efficiency; In-situ monitoring; Continental climate; Late-autumn conditions*

# TOPLOTNE I ENERGETSKE PERFORMANSE EKSTENZIVNOG ZELENOG KROVA U NOVEMBRU 2025.

***Rezime:*** Zeleni krovovi mogu poboljšati termičke performanse omotača zgrade smanjenjem temperaturnih oscilacija i prenosa toplote. U radu su eksperimentalno analizirane performanse ekstenzivnog zelenog krova u poređenju sa konvencionalnim referentnim krovom tokom novembra 2025. godine. Glavni naučni doprinos rada je eksperimentalna i kvantitativna karakterizacija termičkog ublažavanja i smanjenja prenosa toplote na osnovu kontinuiranog in-situ monitoringa u kontinentalnim kasnojesenjim uslovima. Zeleni krov je ostvario manje temperaturne oscilacije i izraženiji fazni pomak u odnosu na konvencionalni krov. Kumulativni toplotni gubitak iznosio je 20.221,53 Wh/m² za konvencionalni i 14.824,24 Wh/m² za zeleni krov, što predstavlja smanjenje od 5.397,29 Wh/m², odnosno 26,69%. Rezultati pokazuju značaj kontinuiranog monitoringa za praćenje dinamičkog termičkog ponašanja zelenih krovova i njihov potencijal za smanjenje prenosa toplote tokom kasne jeseni.

*Ključne reči: zeleni krov; termičke performanse; prenos toplote; energetska efikasnost; in-situ monitoring; kontinentalna klima; kasnojesenji uslovi*

[1]PhD student, Institute IMS, Belgrade, Serbia, snezana.ilic@institutims.rs, ORCID 0000-0003-1641-2301
[2]Assoc. prof., Faculty of Technical Sciences, University of Novi Sad, Serbia, idzolev@uns.ac.rs, ORCID 0000-0002-7622-7936
[3]PhD CE, Institute IMS, Belgrade, Serbia, biljana.ilic@institutims.rs, ORCID 0000-0003-0798-1748
[4]Full prof., Faculty of Technical Sciences, University of Novi Sad, Serbia, mlaban@uns.ac.rs, ORCID 0000-0001-6557-3094
[5]PhD CE, Institute IMS, Belgrade, Serbia, milica.mirkovic@institutims.rs, ORCID 0000-0001-6023-8414

## 1. INTRODUCTION

Green roofs are increasingly used as a sustainable building technology because of their potential to improve the thermal, energy, and environmental performance of buildings. In addition to ecological benefits such as stormwater retention, mitigation of urban heat island effects, and improvement of the urban microclimate, green roof systems can reduce heat transfer through the building envelope, attenuate temperature fluctuations, and increase thermal stability [1-5]. Previous experimental and numerical studies have demonstrated that green roofs can contribute to reductions in building cooling demand and roof heat flux, although the magnitude of these effects varies considerably depending on climatic conditions, roof design, substrate properties, vegetation characteristics, and moisture availability [6-8]. Therefore, green roofs should be considered dynamic building-envelope systems whose thermal performance changes in response to environmental conditions rather than as conventional static insulation layers.

The thermal behaviour of green roofs is governed by complex interactions between the roof layers, vegetation, substrate moisture, solar radiation, ambient temperature, and precipitation. In particular, substrate thickness and moisture content can substantially affect the effective thermal resistance and heat-transfer characteristics of the system [7, 9, 10]. Moisture can modify the thermal properties of the growing medium and, together with evaporation and plant transpiration, contribute to the attenuation of heat transfer. Previous research has also shown that the thermal response of green roofs is strongly dependent on seasonal and climatic conditions. Studies conducted in continental climates have reported substantial reductions in roof surface temperature and heat-flux variability, indicating an increased thermal stability of green roof systems compared with conventional roofs [11]. These findings highlight the importance of evaluating green roof performance under actual outdoor conditions and at sufficiently high temporal resolution.

From an energy-performance perspective, green roofs have been investigated as a passive strategy for reducing heating and cooling loads. Ascione et al. [6] reported reductions in annual cooling energy demand of approximately (15–30)% for different European climatic conditions, together with improvements in indoor thermal comfort. Sailor et al. [7] demonstrated that parameters such as substrate thickness and irrigation can significantly influence thermal performance, with heat-flux reductions of up to approximately 40% under favourable conditions. Regional studies have also indicated considerable energy-saving potential in buildings located in continental climates. Perović et al. [12], for example, reported annual cooling energy savings in the range of (10–20)% for a calibrated building model in Belgrade, while Guattari et al. [8] demonstrated substantial reductions in heat flux during peak summer conditions. These results confirm the potential of green roofs as a passive measure for improving building energy performance, but also emphasize that their effectiveness is highly climate- and season-dependent.

Despite the growing body of research, long-term experimental evidence describing the transient thermal behaviour of green roofs under real climatic conditions remains relatively limited. Many studies are based on numerical simulations, short-term measurement campaigns, or aggregated annual performance indicators, which may not fully capture the dynamic effects of precipitation, substrate moisture, vegetation activity, and rapidly changing outdoor temperatures [3-5, 13]. This is particularly relevant for continental climates, where pronounced seasonal variations can result in substantially different thermal responses during summer, transitional periods, and the

heating season. Detailed in-situ measurements are therefore necessary to quantify heat-transfer attenuation and thermal stability and to distinguish the actual performance of green roof assemblies from results obtained under simplified or idealized conditions.

This study investigates the thermal and energy performance of an extensive green roof installed on an existing building at the Institute IMS in Belgrade, Serbia. The green roof was implemented in December 2024 and consists of a root-resistant membrane, drainage layer, mineral wool substrate, and vegetation layer dominated by Sedum species. A conventional flat roof located on the same building was used as a reference system. This experimental arrangement enables a direct comparison of the thermal behaviour of the two roof configurations under similar outdoor conditions and minimizes the influence of differences in building use and climatic exposure.

Continuous measurements began in February 2025 and included temperatures and heat fluxes through both roof systems, together with selected environmental parameters such as substrate moisture, precipitation, and illumination. Temperature measurements were performed using Type T thermocouples, while heat flux was monitored using heat flux meters installed at representative positions on the green and reference roofs. The measurements were performed in accordance with the principles of the in-situ heat-flow-meter method specified by SRPS ISO 9869-1:2016 [14]. Data were recorded at 10-minute intervals, allowing the analysis of both short-term temperature variations and cumulative heat transfer through the investigated roof assemblies.

The present study focuses on November 2025, representing a transition from autumn toward winter conditions and the beginning of the heating season. During this period, outdoor temperatures decreased considerably, solar radiation was reduced, while precipitation and atmospheric humidity were relatively high. These conditions provide an appropriate basis for evaluating the ability of the green roof to moderate temperature fluctuations and reduce heat transfer under increasingly cold and humid outdoor conditions. At the same time, the combination of low solar gains and elevated moisture levels provides an opportunity to examine the role of the green roof layers and substrate in the transient thermal response of the assembly. In contrast to the predominantly summer-oriented assessment of green roof thermal performance reported in the literature, the present study addresses the less frequently investigated late-autumn period, when the thermal behaviour of the roof is governed primarily by heat loss and changing moisture conditions.

The main objective of this study is to evaluate the thermal response and energy performance of the extensive green roof during November 2025 and to compare its behaviour with that of the conventional flat roof. The analysis focuses on temperature profiles, heat-flux behaviour, thermal attenuation, thermal inertia, and cumulative energy transfer through the roof assemblies. The principal scientific contribution of the study is the experimental and quantitative demonstration, based on continuous in-situ monitoring, of the thermal buffering and heat-transfer attenuation provided by an extensive green roof under real continental late-autumn conditions. Rather than evaluating green roof performance solely through short-term measurements, numerical simulations, or aggregated seasonal indicators, the study uses continuous measurements at 10-minute intervals to capture the transient response of the two roof systems under naturally varying outdoor temperature, precipitation, moisture, and solar conditions. The direct comparison with a conventional roof exposed to the same climatic conditions enables the effect of the green roof assembly to be assessed while minimizing differences in external exposure. The results therefore provide experimental evidence of the dynamic thermal behaviour of an extensive green roof during a cold and humid transitional period and contribute to a more comprehensive understanding of its performance beyond the commonly investigated summer conditions.

## 2. EXPERIMENTAL SETUP AND METHODOLOGY

### 2.1. EXPERIMENTAL SITE AND ROOF SYSTEMS

The experimental investigation of the thermal performance of an extensive green roof system was conducted at the Laboratory for Thermal Engineering and Fire Protection of the Institute IMS, located at 7 Viktor Igo Street, Belgrade, Serbia (44.79372° N, 20.43521° E). The experimental site is situated within a building constructed during the 1950s and selected primarily due to the availability of a suitable flat roof area for the implementation of the green roof system and the availability of appropriate measurement equipment. The investigated building is more than 70 years old and represents a typical example of an older building for which detailed information on the thermal properties of the existing roof construction was not available.

The building was constructed at a time when regulatory requirements concerning the thermal performance of building components were not yet established. Consequently, the available technical documentation does not provide information on the thermal characteristics of the roof or the building envelope as a whole. The available documentation, preserved at the Institute IMS and the Belgrade City Archives, mainly contains load calculations for individual roof layers and technical drawings, including building plans and cross-sections. The building consists of three cascading sections with different heights. The first section, with a height of 10.825 m, includes a structural testing hall and associated office space. The second section is 5.4 m high and is predominantly used as office space, while the third section has a basic height of 9.78 m, with one segment reaching 12.22 m. Offices and testing laboratories are located within this section.

The experimental programme comprised both laboratory and in situ investigations. For the thermal assessment, an extensive green roof system was installed on a section of the existing flat roof and compared with an adjacent reference roof area representing the existing flat roof construction without the green roof layers. This configuration enabled simultaneous monitoring under essentially identical outdoor climatic conditions and provided a direct basis for evaluating the thermal effect of the green roof system.The investigated green-roof system was also subjected to a separate laboratory programme addressing its reaction to fire under controlled moisture conditions; however, the present study concerns exclusively the independent in-situ thermal-monitoring programme and the corresponding thermal and energy-performance dataset.

The investigated roof assembly represents an extensive green roof configuration consisting of four functional layers arranged above the existing roof construction: a root barrier, a drainage and water-retention layer, a mineral wool growing substrate, and a vegetated cover. The system was selected for the experimental study as a lightweight roof solution requiring relatively limited maintenance and suitable for the climatic conditions of Belgrade, Serbia. In the present study, the description of the roof assembly is provided primarily to define the boundary conditions and material configuration relevant to the thermal measurements.

The root barrier was formed by a 0.5-mm-thick low-density polyethylene (LDPE) membrane. It separated the green roof layers from the underlying waterproofing and served to prevent root penetration and associated mechanical or biological damage. Above the root barrier, a 25-mm-thick double-sided profiled drainage board made of recycled polystyrene was installed. Besides facilitating the removal of excess water, this

layer provided water-retention capacity of approximately 11.8 L/m² and enabled ventilation within the root zone.
The growing medium was composed of stone mineral wool with a nominal thickness of 40 mm and a thermal conductivity of approximately 0.040 W/(m·K). Its dry bulk density was approximately 100–110 kg/m³, corresponding to a dry mass of approximately 4–4.4 kg/m². The uppermost layer consisted of vegetation dominated by species of the Sedum genus (family Crassulaceae), with approximately 10–12 species represented. The vegetation layer was approximately 20–40 mm thick, with a mass of about 15 kg/m² under dry conditions and up to approximately 23 kg/m² when saturated. These variations in moisture and mass are relevant to the thermal behaviour of the roof and were therefore considered through the environmental monitoring programme described in the following sections.
The investigated roof configuration and the arrangement of its constituent layers are schematically presented in Figure 1.

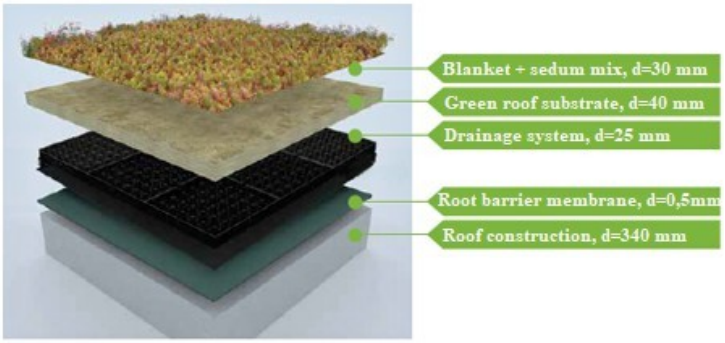


*Fig. 1 Schematic representation of the extensive green roof system and its constituent layers [15]*

## 2.2. HEAT FLUX MEASUREMENT METHOD

The thermal performance of the green and reference roofs was determined using the heat flux meter method in accordance with SRPS ISO 9869-1:2016 [14]. The method enables in situ determination of the thermal characteristics of building elements through measurements of heat flux density and temperatures at the surfaces of the investigated component. In the present study, the method was applied to quantify heat transfer through the green and reference roof assemblies under real climatic conditions.
The experimental approach was based on simultaneous measurement of heat flux density and temperatures on the external and internal sides of the monitored roof sections. This configuration enabled the thermal response of the two roof systems to be compared under the same environmental conditions. In addition to instantaneous heat flux values, temporal integration of the measured heat flux was used to evaluate accumulated energy transfer through the roof constructions. Such an approach allowed both short-term thermal fluctuations and longer-term daily and seasonal thermal behaviour to be analysed.
The green roof was installed at the end of December 2024, after which the measurement infrastructure was installed and commissioned. Between December 2024 and February 2025, the software system for automated monitoring and data recording was developed, configured, calibrated, and tested. This period was used to verify the stability and reliability of the data acquisition system and to eliminate potential measurement and communication errors. Continuous measurements commenced on 1 February 2025 following the final adjustment and verification of the system. The measurement campaign was planned for a duration of one year, with measurements performed continuously at 10-min intervals.

In addition to cumulative heat transfer, quantitative indicators were used to characterize the transient thermal response of the two roof systems. For the temperature analysis, the signals from the corresponding external/intermediate measurement positions were averaged for each roof system (T1, T2, T5 and T6 for the reference roof, and T9, T10, T13 and T14 for the green roof). The daily temperature amplitude was calculated as the difference between the maximum and minimum temperature recorded during each 24-h period, and the mean daily amplitude was subsequently determined for the entire month. Thermal attenuation was expressed as the relative reduction in the mean daily temperature amplitude of the green roof compared with the reference roof.

The characteristic thermal phase lag was evaluated from the 24-h harmonic component of the measured temperature signals. A sinusoidal harmonic with a period of 24 h, including a linear trend term, was fitted to the outdoor-temperature signal and to the averaged temperature signals of the two roof systems. The phase lag was defined as the temporal difference between the fitted daily temperature maximum of the outdoor signal and the corresponding maximum of each roof-temperature signal.

For the heat-flux analysis, the measurements from F1 and F2 were averaged to represent the reference roof, while F3 and F4 were averaged to represent the green roof. The maximum positive heat flux, mean daily heat-flux range, and mean within-day standard deviation were determined for both roof systems. The daily heat-flux range was calculated as the difference between the maximum and minimum heat flux during each 24-h period, while the within-day standard deviation was used as an indicator of short-term heat-flux variability. All calculations were performed using the 10-min measurement series recorded from 1 to 30 November 2025.

## 2.3. INSTRUMENTATION AND SENSOR ARRANGEMENT

The measurement system comprised HFS-01-05 heat flux meters, Type T thermocouples [16], and sensors for monitoring environmental conditions. The HFS-01-05 heat flux meters [17] had a measurement range of 0–50 kW/m² and a sensitivity of 0.1 μV/(W/m²). Two heat flux meters, designated F3 and F4, were installed within the green roof assembly between the root barrier membrane and the drainage layer. On the reference roof, heat flux meters F1 and F2 were installed on the concrete slab below the gravel layer.

Temperature measurements were performed using JUMO Type T (Cu-Con) thermocouples in accordance with DIN IEC 584. The thermocouples had an accuracy of ±0.5 °C over the range from −200 to 350 °C [16]. Four thermocouples were associated with each heat flux meter, with two positioned on the external, atmosphere-exposed side and two on the internal, heated side of the monitored roof section. This arrangement provided redundant temperature measurements and enabled continuous monitoring in the event of an individual sensor failure.

On the green roof, heat flux meter F3 was positioned approximately halfway across the roof at a distance of 1.0 m from the office wall, while F4 was positioned at a distance of 3.24 m from the same wall. Thermocouples 9 and 10 were installed above the root barrier membrane and below the drainage layer, approximately 100 mm from F3. Thermocouples 11 and 12 were installed on the office ceiling below the F3 measurement zone. Similarly, thermocouples 13 and 14 were positioned around F4 above the root barrier membrane, while thermocouples 15 and 16 were installed on the ceiling directly below the F4 measurement zone.

On the reference roof, heat flux meter F1 was installed on the concrete slab in the area with a roof rib, at a distance of 1.0 m from the office wall and 2.75 m from the roof parapet. Heat flux meter F2 was positioned on the concrete slab in an area without a

roof rib, 3.24 m from the office wall and 2.75 m from the parapet. Thermocouples 1 and 2 were installed approximately 100 mm from F1 on the upper surface of the concrete slab, while thermocouples 3 and 4 were positioned on the office ceiling below the F1 measurement area. Thermocouples 5 and 6 were similarly installed approximately 100 mm from F2, and thermocouples 7 and 8 were positioned on the ceiling below F2.

To account for environmental conditions influencing the thermal response of the green roof, additional sensors were installed for monitoring substrate moisture, precipitation, and light intensity. YL-69 sensors were used to measure substrate moisture over a range of (0–100)%, with an accuracy of approximately ±3% [18]. FC-37 sensors were used for precipitation detection, with a response time of less than 1 s [19]. Incident light intensity was monitored using KY-018 sensors with a measurement range of 0–1000 lx and a resolution of approximately ±5 lx [20].

To reduce the influence of edge effects and improve the comparability of the measurements, the perimeter zones of the green roof and the areas surrounding the heat flux meters on the reference roof were covered with a layer of medium-sized gravel. This arrangement provided more consistent measurement conditions and reduced the potential influence of local geometric and boundary effects.

## 2.4. DATA ACQUISITION AND MONITORING SYSTEM

A dedicated data acquisition system was developed to provide continuous and automated monitoring of the thermal and environmental parameters. The system integrated a Measurement Computing TC-32 device for temperature measurements [21], a Measurement Computing data acquisition unit for heat flux measurements, and an Arduino Uno R3 microcontroller [22] for the acquisition of signals from the environmental sensors. The thermocouples transmitted temperature signals to the TC-32 unit, while the heat flux meters were connected to the dedicated heat flux acquisition device. The light, precipitation, and substrate moisture sensors were connected to the Arduino Uno R3. The complete system was connected to a desktop computer for data acquisition, processing, monitoring, and visualisation.

Data acquisition and monitoring were implemented using LabVIEW software [23]. All measured parameters were automatically recorded at 10-min intervals. The recorded dataset included external and internal surface temperatures, heat flux density, substrate moisture, precipitation, and light intensity. The relatively short acquisition interval enabled the detection of transient thermal responses while simultaneously providing an adequate temporal resolution for the analysis of daily and seasonal trends.

The acquired data were stored in TDMS format and archived monthly on an external storage device. As an additional data protection measure, the measurements were simultaneously recorded in XLS format. An uninterruptible power supply (UPS) [24]with an autonomy of approximately one hour was incorporated into the system to maintain operation during short-term power interruptions. These measures were intended to minimise data loss and ensure continuity during the long-term experimental campaign.

The resulting monitoring system provided a comprehensive experimental basis for evaluating the thermal performance of the extensive green roof relative to the reference flat roof. The simultaneous acquisition of heat flux, surface temperatures, and environmental parameters enabled the thermal response of both roof systems to be evaluated under comparable boundary conditions. In particular, the integration of heat flux over time provided information on cumulative energy transfer, while the combined analysis of temperature and heat flux measurements allowed the influence of the green roof layers, substrate moisture, precipitation, and solar exposure on heat transmission to be assessed throughout the annual monitoring period.

## 3. RESULTS AND DISCUSSION

November 2025 marked a clear transition toward colder seasonal conditions, characterised by a substantial decrease in air temperature compared with the preceding autumn months. The minimum recorded temperature ranged from −0.9 °C on 24 November to 17.0 °C on 17 November, while the maximum temperature ranged from 1.5 °C on 22 November to 24.0 °C on 2 November. The lowest temperatures below 0 °C occurred during the final week of the month, indicating the onset of winter conditions. Solar radiation was considerably lower than during the summer and early autumn, with recorded values ranging from approximately 50 to 570 W/m². The UV index was predominantly low, generally ranging from 0 to 2–3, reflecting the reduced solar intensity characteristic of late autumn.
Relative humidity was frequently above 90%, particularly during rainy and sleet events, whereas minimum values of approximately (26–35)% occurred during drier periods. Atmospheric pressure varied between 974.8 and 1003.5 hPa. Wind speeds were generally moderate to moderately strong, ranging from approximately 4km/h to 28 km/h, with maximum gusts reaching 56 km/h. Cloud cover was highly variable, ranging from relatively clear conditions to fully overcast periods accompanied by rain or sleet. Precipitation occurred relatively frequently during the month, predominantly as rainfall, with sleet and occasional wintry precipitation recorded toward the end of November. Daily precipitation amounts ranged from 0.2mm to 9 mm, indicating relatively wet and dynamically changing late-autumn conditions.

### 3.1. THERMAL AND ENVIRONMENTAL MONITORING OF THE GREEN ROOF

Figure 2 presents the measured temperature profiles at the external and internal locations of the investigated roof assemblies during November 2025. The temperature response reflects the transition from autumn toward winter conditions. The outdoor air temperature exhibited pronounced short-term variability, generally ranging from approximately 2 °C to 15 °C during the monitored periods. Short warm intervals were still present, particularly during the first part of the month. Conversely, periods of cooling became longer and more distinct, reflecting the increasing influence of colder atmospheric conditions and reduced solar gains.

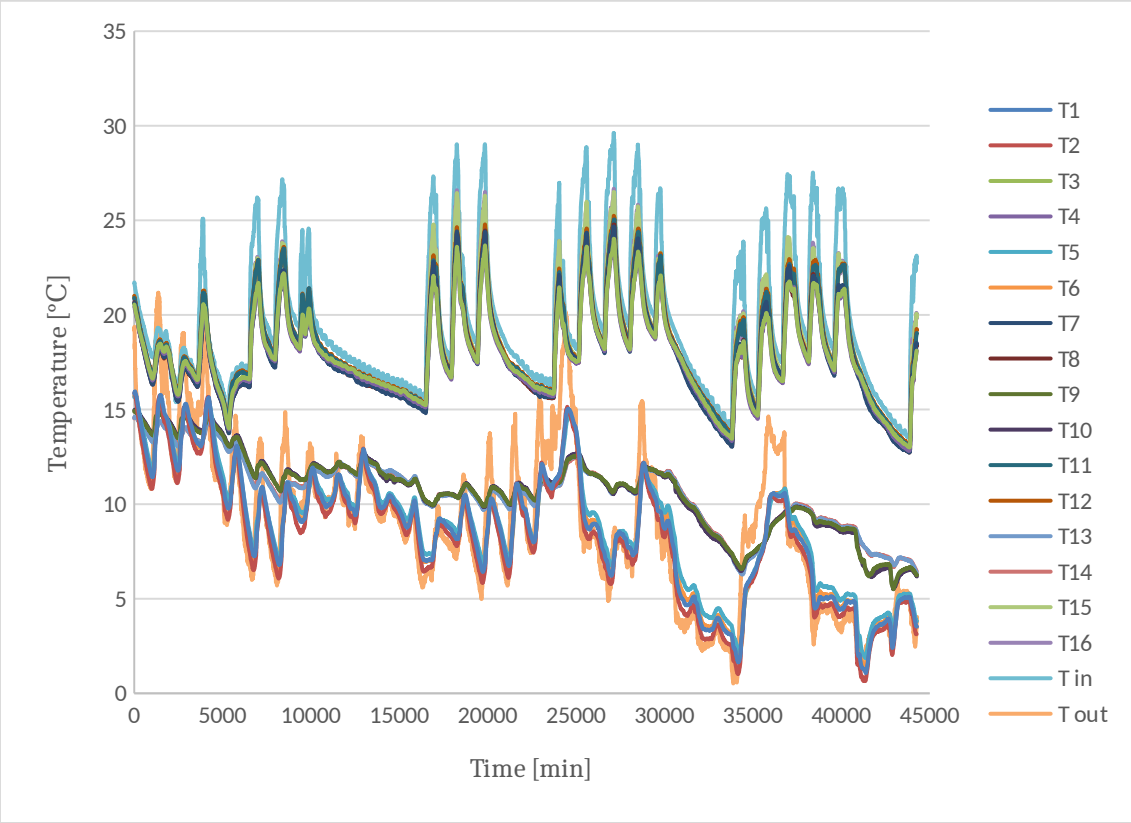


*Fig. 2 Temperature profiles of the inner and outer layers of the roof structure during November 2025*

A clear difference between the thermal responses of the green and reference roofs was maintained throughout the month. The temperatures measured at the external/intermediate positions of the green roof exhibited substantially smaller fluctuations and a more gradual response to changes in outdoor temperature than those measured at the corresponding positions of the reference roof.

Quantitative analysis of the 10-min temperature series confirmed the attenuation observed in Figure 2. The mean daily temperature amplitude, calculated as the daily difference between the maximum and minimum temperature, was 3.26 °C for the reference roof and 1.09 °C for the green roof. This corresponds to a reduction in the mean daily temperature amplitude of approximately 66.7%. Considering the complete November measurement period, the overall temperature range decreased from 14.34 °C for the reference roof to 8.49 °C for the green roof, representing a reduction of approximately 40.8%. These results quantitatively demonstrate the ability of the green roof assembly to attenuate short-term temperature variations.

The temporal response of the two roof assemblies also differed. Analysis of the 24-h harmonic component of the temperature signals indicated a characteristic phase lag of approximately 2.3 h between the outdoor temperature and the response of the reference roof, compared with approximately 3.6 h for the green roof. The green-roof assembly therefore introduced an additional thermal delay of approximately 1.3 h under the investigated late-autumn conditions. This delayed response, together with the lower temperature amplitude, indicates greater effective thermal inertia and a more pronounced thermal-buffering effect of the green-roof assembly.

In contrast, the reference flat roof showed a stronger and faster response to changes in outdoor conditions. Relatively rapid increases and decreases in temperature remained evident, particularly during short warmer periods and during pronounced day–night temperature changes. The stronger coupling between the outdoor conditions and the

reference-roof temperature confirms its lower capacity to attenuate transient thermal variations.

The indoor temperature exhibited a more pronounced decreasing trend than in October, generally declining from approximately 20 °C toward 18 °C, with occasional values below this level. Although the indoor fluctuations remained moderate, they became more noticeable as outdoor temperatures decreased and passive solar gains were reduced. Nevertheless, the reduced external/intermediate temperature amplitude and the greater thermal delay measured for the green roof indicate that the additional roof layers moderated the rate at which outdoor temperature variations were transmitted through the roof assembly.

The heat-flux measurements presented in Figure 3 provide further evidence of the different thermal behaviour of the two roof systems. As outdoor temperatures decreased, heat transfer from the heated interior toward the external environment became more pronounced. However, both the magnitude and short-term variability of the heat flux remained lower for the green roof than for the reference roof.

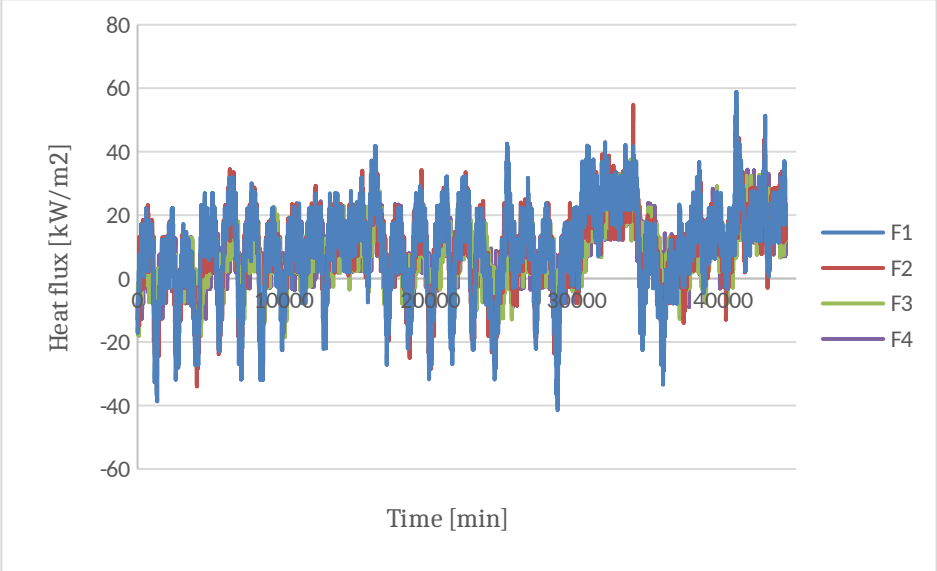


*Fig. 3 Heat flux flow through the roof structure in November2025*

Quantitative analysis of the heat-flux signals showed that the maximum positive heat flux during November was 55.14 W/m² for the reference roof and 35.16 W/m² for the green roof. The green roof therefore reduced the peak heat flux by approximately 36.2%.

The difference was also evident in the daily heat-flux variability. The mean daily heat-flux range decreased from 42.75 W/m² for the reference roof to 25.80 W/m² for the green roof, corresponding to a reduction of approximately 39.6%. In addition, the mean within-day standard deviation decreased from 9.82 W/m² to 5.35 W/m², representing a reduction of approximately 45.5%. These results indicate that the green roof not only reduced the peak magnitude of heat transfer but also damped short-term fluctuations in heat flux throughout the day.

The environmental measurements provide additional context for interpreting the thermal response of the green roof. The measured light intensity varied throughout the monitoring period, reflecting the changing atmospheric conditions during November, as shown in Figure 4. The variations in illumination affected the amount of solar energy reaching the vegetation and substrate and formed part of the environmental conditions characterizing the November monitoring period.

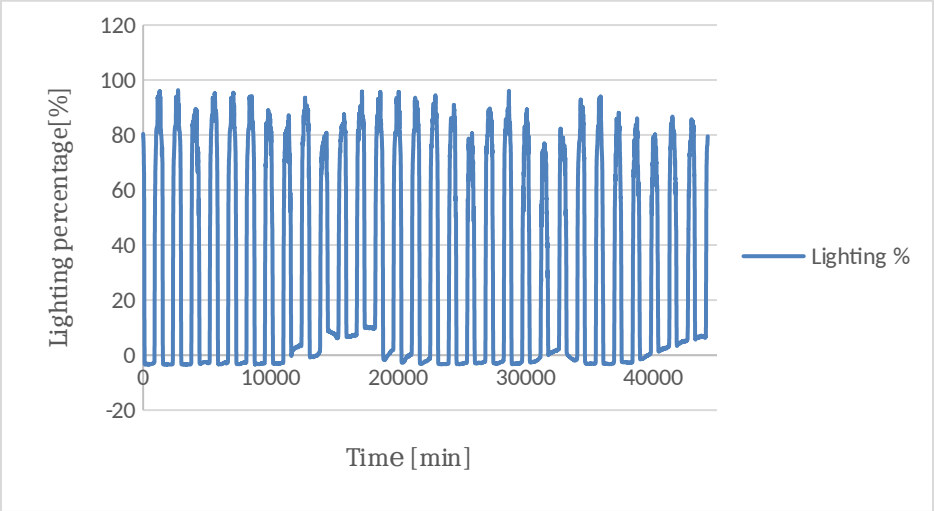


*Fig. 4 Percentage of illumination at the experimental green roof site in November 2025*

The substrate retained a measurable amount of moisture throughout the month, although the moisture content varied in response to the relatively frequent precipitation events, as shown in Figure 5. The increased moisture availability is relevant to the interpretation of the thermal behaviour because water content influences the effective thermal properties of porous materials. In particular, an increase in moisture content may increase the effective thermal conductivity of the substrate compared with dry conditions. Despite the wetter conditions prevailing during November, the green roof maintained lower heat-flux peaks and substantially lower daily heat-flux variability than the reference roof.

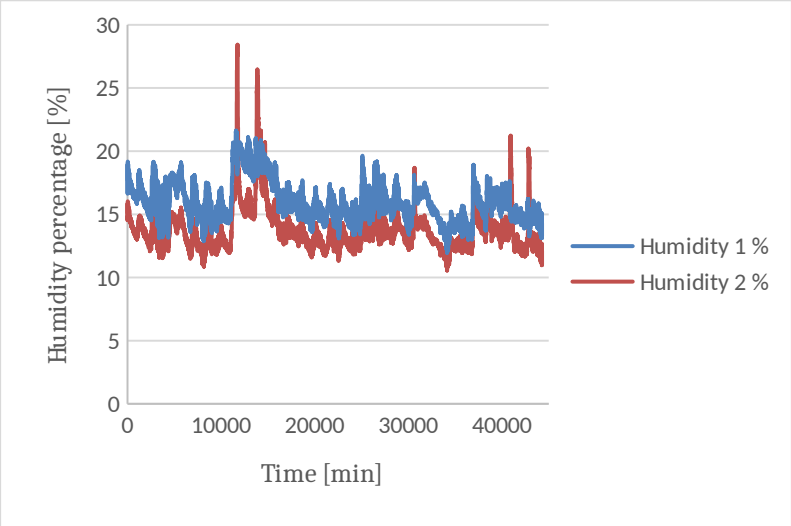


*Fig. 5 Substrate moisture percentage at two measurement points on a green roof in November 2025*

The precipitation record confirms a higher frequency of rainfall compared with the preceding months, with wintry precipitation occurring during the final part of November, as shown in Figure 6. The combined occurrence of lower temperatures and increased moisture resulted in a pronounced seasonal change in the appearance of the vegetation. A substantial proportion of the above-ground vegetation had dried out by the end of the month, leaving only limited green coverage. This behaviour is consistent with the seasonal adaptation of Sedum species to lower temperatures and reduced solar availability. Although above-ground vegetation activity was reduced, the substrate and below-ground plant structures remained integral components of the green-roof system.

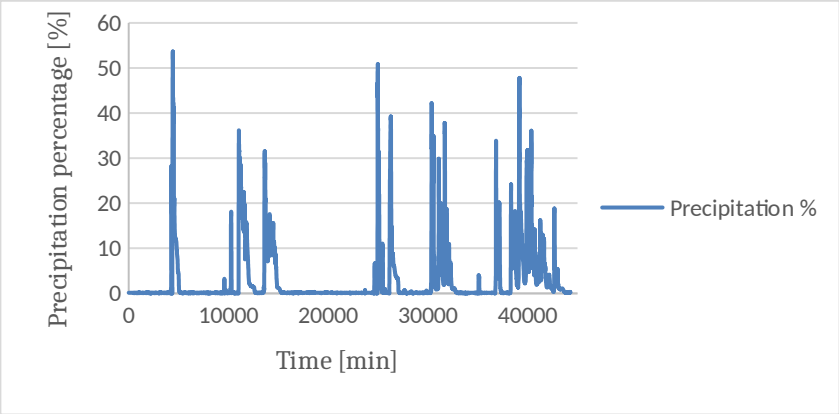


*Fig. 6 Percentage of precipitation in November 2025*

Overall, the November measurements demonstrate that the green roof maintained a pronounced thermal-buffering effect during the transition toward colder conditions. Compared with the reference roof, the green roof reduced the mean daily temperature amplitude by 66.7%, increased the characteristic thermal phase lag by approximately 1.3 h, reduced the maximum positive heat flux by 36.2%, and decreased daily heat-flux variability by approximately 40–46%, depending on the variability indicator considered. These quantitative results confirm that the green roof moderated both temperature and heat-flux fluctuations under late-autumn conditions and complement the cumulative energy-balance analysis presented in the following section.

## 3.2. ENERGY BALANCE OF THE ROOF ASSEMBLIES

The monthly energy balance was determined from the measured heat flux density using the methodology described in Section 2 and in accordance with the principles of SRPS ISO 9869-1:2016 [14]. Temporal integration of the heat flux measurements enabled the cumulative amount of heat transferred through the investigated roof areas to be quantified for November 2025.

Figure 7 compares the cumulative heat transfer through the reference flat roof and the extensive green roof. The total measured heat loss through the reference roof was 20,221.53 Wh/m², whereas the corresponding value for the green roof was 14,824.24 Wh/m². The difference between the two systems therefore amounted to 5,397.29 Wh/m², corresponding to a 26.69% reduction in cumulative heat loss for the green roof.

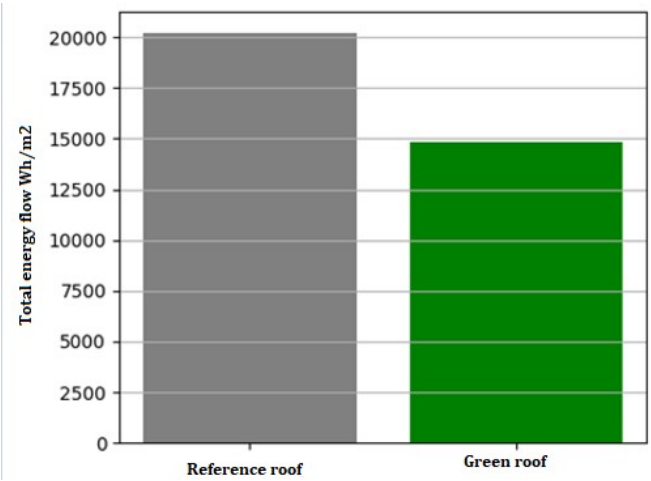


*Fig. 7 Comparison of the roof's energy balance in November 2025*

The measurements at the individual monitoring positions further support this finding. The cumulative heat fluxes measured at the green roof locations were 7,392.27 Wh/m² (F3) and 7,431.97 Wh/m² (F4), while the corresponding values for the reference roof were 10,673.90 Wh/m² (F1) and 9,547.62 Wh/m² (F2). The two green roof measurement locations produced very similar values, with a difference of only approximately 40 Wh/m². This relatively small spatial variation indicates a consistent thermal response of the investigated green roof within the monitored areas.

The lower cumulative heat transfer measured through the green roof can be attributed to the combined thermal effects of its multilayer configuration, particularly the mineral wool substrate and vegetation layer. The substrate provides additional thermal resistance and contributes to the thermal mass of the roof, while the vegetation and associated moisture dynamics modify the energy exchange at the roof surface. Under the colder November conditions, these effects resulted in a lower rate of heat transmission from the conditioned interior toward the outdoor environment.

The comparison also indicates that the thermal benefit of the green roof was maintained despite the relatively high moisture content and frequent precipitation characteristic of the month. Moisture accumulation can alter the effective thermal conductivity of porous materials and therefore represents an important factor in the seasonal thermal performance of green roofs. Nevertheless, the integrated heat flux measurements show that the overall effect of the investigated system remained favourable. The green roof reduced cumulative heat losses by more than one quarter compared with the reference roof during the analysed month.

It should be noted that the observed reduction represents the thermal performance of the complete roof systems under the specific boundary conditions prevailing in November 2025. The result therefore reflects the combined effects of outdoor temperature, solar radiation, precipitation, substrate moisture, indoor conditions, and the thermal properties of the roof assemblies rather than the contribution of an individual green roof layer alone. This is one of the principal advantages of the in-situ heat flux approach, as it captures the integrated thermal response of the roof under real climatic conditions.

The November results consequently confirm that the extensive green roof provided a measurable reduction in heat transfer during the late-autumn period. A 26.69% reduction in cumulative heat loss relative to the reference roof demonstrates that the system retained significant thermal-buffering capacity even under low solar radiation, frequent precipitation, and temperatures approaching and temporarily falling below freezing. Together with the observed attenuation and phase shift of temperature fluctuations, these results indicate that the investigated green roof can contribute to reducing heat losses and stabilising the thermal conditions of the building envelope during the transition into the heating season.

## 4. CONCLUSION

This study experimentally evaluated the thermal performance of an extensive green roof under real climatic conditions in Belgrade, Serbia, using continuous in situ measurements of heat flux, surface temperatures, and relevant environmental parameters. The green roof was compared with a reference flat roof in order to quantify its effect on heat transfer through the building envelope.

The results demonstrated that the green roof effectively attenuated temperature fluctuations and delayed the thermal response of the roof assembly to changes in outdoor conditions. Quantitatively, the mean daily temperature amplitude was reduced by approximately 66.7%, while the characteristic thermal response was delayed by an additional approximately 1.3 h compared with the reference roof. The maximum

positive heat flux was also reduced by approximately 36.2%, confirming the thermal-buffering effect observed throughout the month. The magnitude of these effects varied with seasonal conditions, solar radiation, precipitation, and substrate moisture.

The November 2025 results provide a representative example of the observed performance. The cumulative heat loss through the green roof was 14,824.24 Wh/m², compared with 20,221.53 Wh/m² for the reference roof, corresponding to a reduction of 26.69%. This confirms that the thermal benefits of the green roof were maintained even during colder and wetter late-autumn conditions.

Overall, the findings indicate that extensive green roofs can contribute to improving the thermal performance of existing flat roof constructions by reducing heat transfer and moderating temperature variations. The study also demonstrates the importance of long-term in situ monitoring for assessing the dynamic thermal behaviour of green roofs under real climatic conditions. Further research involving multi-year measurements would provide additional insight into the influence of vegetation development, moisture dynamics, and seasonal variability on long-term thermal performance.

## ACKNOWLEDGEMENT

This research has been supported by the Ministry of Science, TechnologicalDevelopment and Innovation (Contract No. 451-03-34/2026-03/200156 and Contract no. 451-03-33/2026-03/200012) and the Faculty of Technical Sciences, University of Novi Sad throughproject “Scientific and ArtisticResearch Work of Researchers in Teaching and Associate Positions at the Faculty of Technical Sciences, University of Novi Sad 2026” (No. 01-3609/1).

## REFERENCES

[1] Mentens, J., et al., Green roofs as a tool for solving the rainwater runoff problem, Landscape and Urban Planning, 77(3) (2006), pp. 217–226, doi:10.1016/j.landurbplan.2005.02.010.

[2] Mihalakakou, G., et al., Green roofs as a nature-based solution for improving urban sustainability, Renewable and Sustainable Energy Reviews, 180 (2023), 113306, doi:10.1016/j.rser.2023.113306.

[3] Shafique, M., et al., Green roof benefits, opportunities and challenges – A review, Renewable and Sustainable Energy Reviews, 90 (2018), pp. 757–773, doi:10.1016/j.rser.2018.04.006.

[4] Vijayaraghavan, K., Green roofs: A critical review on the role of components, benefits, limitations and trends, Renewable and Sustainable Energy Reviews, 57 (2016), pp. 740–752

[5] Rahman, M. A., Alim, M. A., Jahan, S., Rahman, A., Vegetated roofs as a means of sustainable urban development: A scoping review, Water, 14 (3) (2022), 420, https://doi.org/10.3390/w14030420

[6] Ascione, F., et al., Green roofs in European climates: Are effective solutions for energy savings in air-conditioning?, Applied Energy, 104 (2013), pp. 845–859, doi:10.1016/j.apenergy.2012.11.068.

[7] Sailor, D. J., et al., Exploring the building energy impacts of green roof design decisions, Journal of Building Physics, 35(4) (2012), pp. 372–391, doi:10.1177/1744259111420076.

[8] Guattari, C., et al., Experimental evaluation and numerical simulation of the thermal performance of a green roof, Applied Sciences, 10(5) (2020), 1767, doi:10.3390/app10051767.

[9] Dimitrijević, D. G., et al., Green living roof implementation and influences of the soil layer on its properties, Thermal Science, 20(5) (2016), S1511–S1520, doi:10.2298/TSCI16S5511D.

[10] Bellazzi, A., et al., Thermal resistance of growing media for green roofs: Experimental example, Journal of Building Engineering, 28 (2019), 101076, doi:10.1016/j.jobe.2019.101076.

[11] Dragićević, S., Marjanović, M., Šutić, B., Dynamic simulations of thermal behavior of conventional and green roofs, Facta Universitatis, Series: Architecture and Civil Engineering, 14 (3) (2016), pp. 310–317

[12] Perović, M., et al., Energy modeling of green roofs in continental climate: A case study of Belgrade, Applied Sciences, 13(11) (2023), 7348, doi:10.3390/app13137348.

[13] Kazemi, M., et al., Heat transfer measurement within green roof with incinerated municipal solid waste aggregates, Sustainability, 13(13) (2021), 7115, doi:10.3390/su13137115.

[14] Institute for Standardization of Serbia. (2016). SRPS ISO 9869-1:2016 – Thermal insulation – Building elements – In-situ measurement of thermal resistance and thermal transmittance – Part 1: Heat flow meter method. Belgrade: Institute for Standardization of Serbia.

[15] Knauf Insulation. (n.d.). *Urbanscape Green Roll* (Technical specifications). Retrieved 20. 3. 2025., from Knauf Insulation website: https://knauf.com/lt-LT/knauf-insulation/produktai-ir-sistemos/urbascape

[16] JUMO GmbH & Co. KG. (2023). Mineral-insulated thermocouples – Type T (Cu–Con), DIN EN 60584 / IEC 584 [Product datasheet]. Preuzeto 21. 3. 2025. sa https://www.jumo.rs/web/products/temperature/accessories/thermocouple

[17] Hukseflux Thermal Sensors B.V. (2023). HFS01 high heat flux sensor [Product specifications]. Retrieved August 22, 2025, from https://www.hukseflux.com/products/heat-flux-sensors/heat-flux-sensors/hfs01-high-heat-flux-sensor

[18] YL-69 Datasheet. (2023). *Soil moisture sensor specifications*. Random Nerd Tutorials. https://randomnerdtutorials.com/guide-for-soil-moisture-sensor-yl-69-or-hl-69-with-the-arduino/

[19] FC-37 Datasheet. (2023). *Rain sensor specifications*. Retrieved August 22, 2025, from https://randomnerdtutorials.com/guide-for-rain-sensor-fc-37-or-yl-83-with-arduino/

[20] KY-018 Datasheet. (2023). *Light sensor specifications*. Retrieved August 22, 2025, from https://fabacademy.org/2024/labs/puebla/students/andrea-hortega/assets/images/week11/KY-018-Joy-IT.pdf

[21] Measurement Computing, *TC-32 and TC-32-EXP Datasheet*. 2023. [Online]. Available: https://digilent.com/reference/_media/daq-and-datalogging/specs/ds-tc-32.pdf

[22] Arduino. (n.d.). *Arduino Uno R3 (ATmega328P)* [Microcontroller board]. Arduino. https://store.arduino.cc/products/arduino-uno-rev3

[23] National Instruments, *LabVIEW 2023 Q3 User Manual*. Austin, TX, USA: National Instruments, 2023. [Online]. Available: https://www.ni.com/docs

[24] APC by Schneider Electric. (n.d.). *Uninterruptible Power Supply (UPS)* [Electrical device]. APC. https://www.apc.com/shop/ups/

https://doi.org/10.24867/INDIS-2026-EN-289



# SEEPAGE STABILITY ASSESSMENT OF A FLOOD PROTECTION EMBANKMENT IN THE BRIDGE PIER INFLUENCE ZONE: A CASE STUDY OF THE TISZA RIVER

*Slobodan Kolaković[1], Marijana Milić[2], Ljubomir Budinski[3], Goran Jeftenić[4], Danilo Stipić[5], Tamara Pantić[6]*

***Summary:***

Bridge foundations constructed within or near flood protection embankments may modify seepage conditions and locally increase hydraulic gradients, thereby increasing the risk of internal erosion. This issue is particularly important for large river crossings founded on heterogeneous alluvial deposits. This paper presents an assessment of seepage stability for the right-bank flood protection embankment of the Tisza River, where a newly planned bridge pier is located at the protected-side toe of the embankment (a potentially critical location in terms of seepage). The assessment included determining the seepage line, filtration velocities, and critical hydraulic gradients under conditions corresponding to the 1% annual exceedance probability (100-year) flood event. Based on the results, appropriate protection measures were proposed to prevent suffusion and soil fluidization and to ensure long-term seepage stability of the embankment.

*Keywords: suffusion, embankment–pier interface, seepage stability, seepage line, SEEP/W*

# PROCENA FILTRACIONE STABILNOSTI ODBRAMBENOG NASIPA OD POPLAVA U ZONI UTICAJA MOSTOVSKOG STUBA: STUDIJA SLUČAJA NA RECI TISI

***Rezime:***

Izgradnja temelja mostova u okviru ili u neposrednoj blizini odbrambenih nasipa od poplava može izmeniti uslove filtracije i lokalno povećati hidrauličke gradijente, čime se povećava rizik od razvoja unutrašnje erozije. Ovaj problem je naročito izražen kod mostova preko velikih reka, fundiranih u heterogenim aluvijalnim naslagama. U radu je izvršena procena filtracione stabilnosti desnog odbrambenog nasipa na reci Tisi, gde je novoprojektovani mostovski stub lociran u zoni branjene nožice nasipa (potencijalno kritična lokacija sa aspekta procednih voda). Analiza je obuhvatila određivanje položaja procedne linije, brzina filtracije i kritičnih hidrauličkih gradijenata pri uslovima koji odgovaraju velikoj vodi verovatnoće pojave od 1% (stogodišnja voda). Na osnovu dobijenih rezultata predložene su odgovarajuće zaštitne mere za sprečavanje pojave sufozije i fluidizacije tla, kao i za obezbeđenje dugoročne filtracione stabilnosti nasipa.

*Ključne reči: sufozija, kontakt nasipa i mostovskog stuba, filtraciona stabilnost, procedna linija, SEEP/W*

[1] Assoc. Prof., Faculty of Technical Sciences (FTN), University of Novi Sad (UNS), Novi Sad, Serbia, kolakovic.s@uns.ac.rs, ORCID 0000-0002-9859-9669
[2] Teach. Ass., FTN, UNS, Novi Sad, Serbia, marijana.milic@uns.ac.rs, ORCID 0000-0003-1974-2461
[3] Full Prof., FTN, UNS, Novi Sad, Serbia, ljubab@uns.ac.rs, ORCID 0000-0001-7816-0889
[4] Assoc. Prof., FTN, UNS, Novi Sad, Serbia, goran.jeftenic@uns.ac.rs, ORCID 0000-0001-5639-4406
[5] Ass. Prof., FTN, UNS, Novi Sad, Serbia, danilostipic@uns.ac.rs, ORCID 0000-0001-6557-5997
[6] Teach. Ass., FTN, UNS, Novi Sad, Serbia, tamara.pantic@uns.ac.rs, ORCID 0009-0003-6341-5692

## 1. INTRODUCTION

Flood protection embankments represent one of the most important structural measures for reducing flood risk in lowland river systems. Their safety and functionality depend not only on geometric and mechanical characteristics but also on their resistance to seepage-induced instability. Internal erosion processes caused by groundwater flow through embankments and their foundations are recognized as one of the leading causes of earth structure failures worldwide [1]. Under unfavourable hydraulic conditions, seepage may lead to suffusion, piping, or soil fluidization, resulting in progressive degradation of soil structure and, ultimately, loss of stability.

Internal erosion in earth structures has been extensively studied over the past few decades. Foster et al. [1] found that seepage-related processes account for a significant share of dam and embankment failures. Richards and Reddy [2] emphasized the roles of hydraulic gradients, soil gradation, and particle migration in initiating and developing internal erosion. Bonelli [3] identified suffusion as a key concern in broadly graded soils, where fine particles are detached and transported through pores formed by coarser particles. These processes progressively increase soil porosity and permeability, potentially leading to severe geotechnical challenges.

Excessive seepage forces can also cause fluidization in cohesionless soils. When upward seepage forces approach or exceed the submerged weight of soil particles, effective stress approaches zero, resulting in a loss of shear strength and bearing capacity [4]. Soil susceptibility to suffusion or fluidization depends mainly on grain-size distribution, hydraulic conductivity, and hydraulic gradient. Studies have shown that soils with low coefficients of grain-size non-uniformity are generally more susceptible to fluidization, while highly heterogeneous soils are more prone to suffusion [5]. Contemporary engineering practice utilizes numerical seepage modelling to assess filtration stability and identify potential zones of internal erosion. Finite-element-based approaches enable the simulation of groundwater flow through complex soil profiles and engineered structures, providing detailed information on hydraulic head distribution, seepage velocities, and exit gradients [6]. These analyses are essential for designing and evaluating hydraulic structures in alluvial environments, where substantial spatial variability in soil properties can significantly affect seepage conditions.

While the seepage stability of dams and flood-protection embankments has been extensively studied, limited research has focused on the direct interaction between major transportation infrastructure and flood defence systems. The placement of bridge foundations within or near embankments can modify natural seepage paths and locally elevate hydraulic gradients, potentially increasing the risk of internal erosion. This issue is particularly significant for large river crossings constructed on heterogeneous alluvial deposits, where hydraulic and geotechnical conditions are complex.

The planned Belgrade–Zrenjanin–Novi Sad motorway features a bridge crossing over the Tisza River, with one pier located within the protected-side toe zone of the right-bank flood protection embankment. Given the potential impact of the bridge foundation system on seepage conditions, a comprehensive assessment of filtration stability was necessary. The location and engineering context of this structure are detailed in the source study [7] upon which this research was based.

The objective of this paper was to assess the filtration stability of the right-bank Tisza embankment within the bridge influence zone using numerical seepage modelling. Emphasis was placed on determining hydraulic head distribution, seepage flow characteristics, and critical exit gradients under extreme hydraulic conditions. Based on the obtained results, the susceptibility of the embankment-foundation system to suffusion and fluidization was evaluated, and appropriate mitigation measures were

proposed to ensure the long-term safety of both the flood protection embankment and the bridge structure.

## 2. QUALITATIVE ASSESSMENT OF INTERNAL STABILITY

Under specific hydraulic conditions, seepage through porous media can induce soil deformations, including changes in soil volume and porosity.
Seepage stability can be classified into two categories:

- **Local** stability refers to specific zones within a structure where seepage velocities and hydraulic gradients are elevated,
- **Global** stability refers to the overall stability of the soil mass and the potential for large-scale deformations.

Local seepage-induced deformations can be further categorized into two types:

- Non-hazardous seepage failures occur at greater depths and have little or no effect on the ground surface,
- Hazardous seepage failures develop near the ground surface and may result in significant soil deformations.

Seepage failure may manifest as fluidization or suffusion, depending primarily on the soil grain-size distribution. A fundamental criterion for the occurrence of seepage-induced deformation is the coefficient of uniformity of the soil, defined as the ratio of the particle diameters corresponding to 60 % and 10 % passing on the grain-size distribution curve ($C_u = d_{60}/d_{10}$).
The susceptibility of soil to fluidization and liquefaction, as well as suffusion, depends primarily on the exit hydraulic gradient and the soil grain-size distribution, which is commonly characterized by the coefficient of uniformity ($d_{60}/d_{10}$). Fluidization and liquefaction refer to the transition of granular soil from a stable state to a fluid-like state, whereas suffusion refers to the migration of fine soil particles induced by seepage flow [8].
These concepts form the theoretical basis for understanding seepage-induced soil deformation and its manifestations in geotechnical engineering.
The diagram used to assess fluidization and suffusion susceptibility, adapted from [8], is shown in Figure 1. The prohibited (forbidden) zone denotes the range of exit hydraulic gradients (Ie) at which the porous medium becomes unstable and seepage-induced failure occurs.

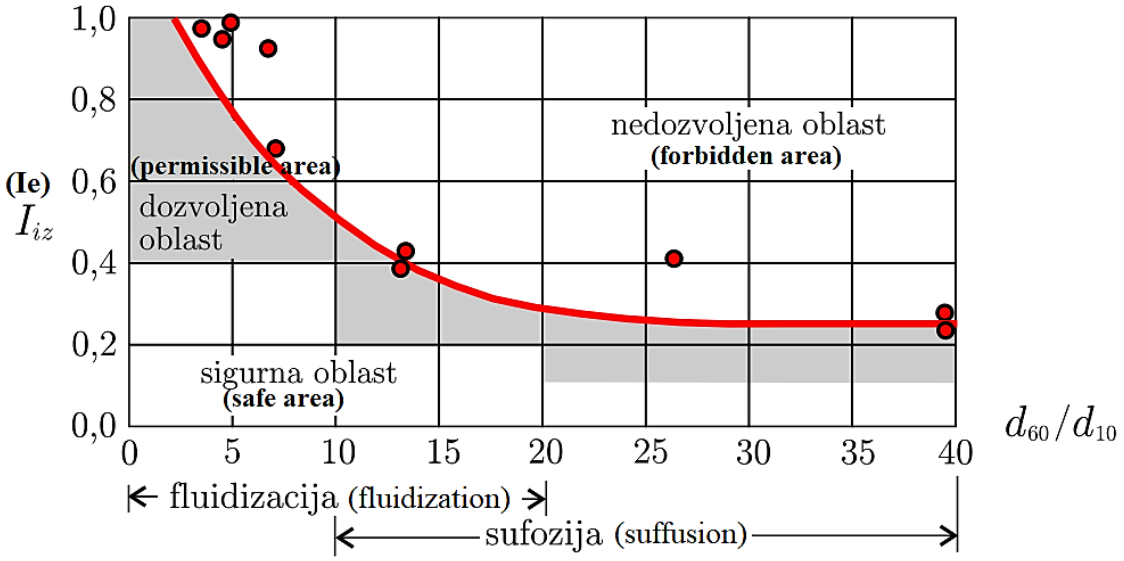


*Fig. 1 Diagram for assessing soil susceptibility to fluidization and suffusion [8]*

Among the methods for identifying internal stability based on characteristic particle sizes, the most commonly used are summarized in Table 1, adapted from [9].

*Tab. 1 Identification methods considering characteristic particle size [9]*

| Researcher | Applicable Soils | Identification Method | Stability |
|---|---|---|---|
| Istomina [10] | Sand and gravel | $C_u \leq 10$<br>$10 \leq C_u \leq 20$<br>$C_u \geq 20$ | Stable<br>Moderate stable<br>Unstable |
| Kezdi | All types of soil | $(d_{15c}/d_{85f})_{max} \leq 4$ | Stable |
| Kenney and Lau | Non-cohesive soils | $(H/F)_{min} \geq 1.0$ | Stable |
| Burenkova | Non-cohesive soils | $0.76\lg(h'')+1<h'<1.86\lg(h'')+1$ | Stable |

The Istomina identification method, used as a preliminary assessment method in this study, considers the coefficient of uniformity $C_u$ as a control variable to determine the internal stability of soils. For soils with $d_{10} > 0.5$ mm or $d_{60} > 10$ mm, most soils with $C_u < 10$ are stable, while those with $C_u > 20$ are unstable.

The diagram in Figure 1 illustrates the dependence of the exit hydraulic gradient ($I_e$) on the coefficient of uniformity ($C_u = d_{60}/d_{10}$), indicating the transition between fluidization and suffusion in soils. Fluidization occurs at lower values of $C_u$, typically below 5, where complete soil destabilization occurs due to fluid pressure. Suffusion occurs at higher values of the non-uniformity coefficient ($C_u > 20$), where fine soil particles are detached and washed out from the coarser soil matrix, potentially leading to instability.

Critical gradient values are:

- For $C_u < 10$, $I_{e,perm} = 0.4$,
- For $10 < C_u < 20$, $I_{e,perm} = 0.2$,
- For $C_u > 20$, $I_{e,perm} = 0.1$.

Based on experimental data, permissible exit hydraulic gradients were defined for unloaded materials to prevent suffusion or fluidization. When the grain-size non-uniformity coefficient ranges between 10 and 20, there is a risk of both phenomena, whereas for $C_u > 20$, the risk of suffusion becomes dominant.

These findings are essential for the design of soil stabilization systems and for mitigating geotechnical hazards. Experimental results show that suffusion in cohesive soils occurs only at higher seepage gradients, when $I_{cr,s} > 7$-10. This indicates that suffusion is relatively rare in cohesive soils due to smaller pore sizes and molecular attractive forces between particles. When the grain-size non-uniformity coefficient is low ($C_u < 10$), fluidization may occur in sandy materials. In cohesive soils, fluidization can develop at a critical seepage gradient of approximately $I_{cr,f} \approx 1$.

Cohesive soils are generally more resistant to suffusion and fluidization due to their specific particle and pore structure; however, under certain conditions, seepage failure may still occur at high hydraulic gradients.

## 3. CASE STUDY

### 3.1. STUDY AREA

The case study presented in this paper focuses on the planned bridge over the Tisza River, located along the Belgrade–Zrenjanin–Novi Sad motorway, Section 2 (Zrenjanin–Novi Sad). The bridge is situated within Sector 5 at chainage km 70+719.86

of the proposed motorway alignment. The motorway crosses the Tisza River at river kilometre 34.4, within the Special Nature Reserve "Ritovi Donjeg Potisja" (Figure 2).
The bridge alignment extends across the flood protection embankment on the left riverbank, the inundation area between the two embankments, the Tisza River itself, and the flood protection embankment on the right riverbank, which is the subject of this study.
The ground elevation in the vicinity of the bridge is approximately 75.0 m above mean sea level (a.m.s.l.).




*Fig. 2 Location of the planned bridge over the Tisza River*

From a geomorphological perspective, the entire area of Sector 5, where the motorway will be constructed, is characterized by a nearly flat terrain representing the alluvial floodplain of the Tisza River.
The most prominent geomorphological features include the existing road embankments, riverbank protection structures, and the river channel. The wider study area is intersected by a dense network of drainage and melioration canals belonging to the Tisza River catchment. The dominant topographic features are the embankments of the state and local road network. Historically, this area has been frequently affected by flooding, leading to the periodic formation of marshy, waterlogged zones [11].
The bridge alignment, pier locations, and cross-sectional layout were adopted from the bridge design documentation [7].
The main bridge structure, with a total length of 490 m (indicated by the red line in Fig. 2), spans the Tisza River and its right flood protection embankment. A composite beam bridge with extended spans was selected to satisfy the site-specific design requirements while considering the construction technology proposed by the contractor.

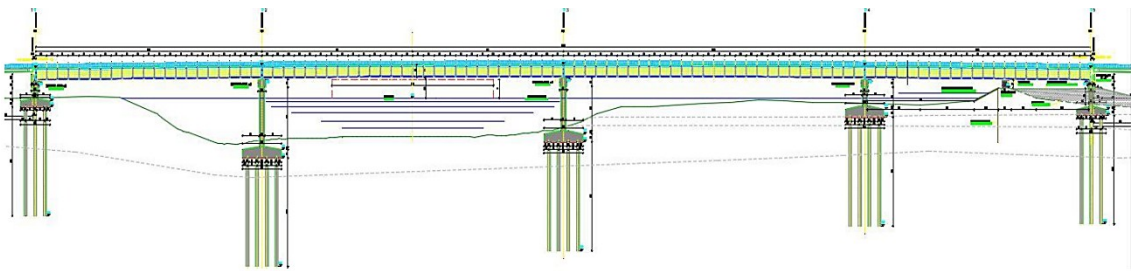

*Fig. 3 Geometry of the main bridge structure and pier locations [7]*

## 3.2. METHODOLOGY

Due to the location of the newly planned bridge pier within the protected-side toe of the right-bank Tisza River embankment, which represents a potentially critical zone with respect to seepage, a seepage analysis was performed to determine the position of the seepage line, filtration velocities, and hydraulic gradients. The objective of this case study was to evaluate the seepage stability of the right-bank flood protection embankment in the bridge crossing area.

Considering the selected structural system of the bridge, the proposed construction methodology, the site constraints associated with the motorway crossing of the existing flood protection infrastructure, and the local geomorphological conditions, bridge pier S20 was positioned at the protected-side toe of the right-bank embankment. It should be noted that, at this location, the embankment width has been increased by the addition of a sand ballast due to the presence of highly permeable alluvial fine- to medium-grained sands underlying the embankment. The total width of the embankment, including the sand ballast, is approximately 78 m.

The bridge layout was developed in accordance with the design requirements governing the motorway crossing and the flood protection system. These requirements specify minimum clearances between bridge piers and the embankment toes whenever feasible. However, owing to the embankment's considerable width and site-specific geometric constraints, compliance with the prescribed minimum distances was not technically feasible. Consequently, the adopted design required verification of the embankment's structural and seepage stability.

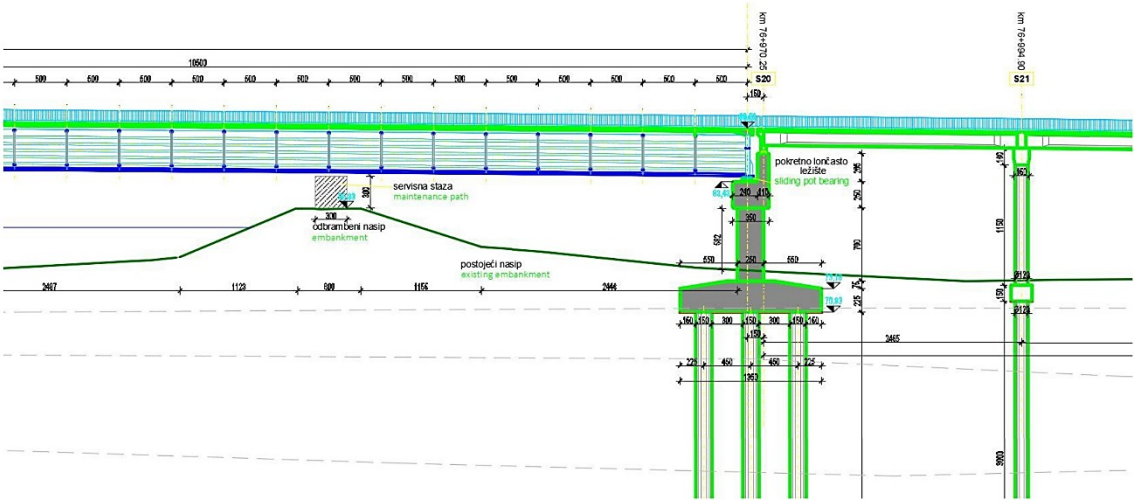


*Fig. 4 Location of bridge pier S20 at the protected-side toe of the right-bank flood protection embankment [7]*

Field observations and practical experience indicate that contact filtration tends to develop along the interface between the pier and the surrounding soil. Pier settlement, dynamic loading effects, and differential displacements can cause separation between the pier and the soil, which in turn promotes the formation of contact filtration in this region. The embankment zones adjacent to the concrete pier are generally inaccessible to large compaction equipment and construction machinery. As a result, achieving adequate compaction in these areas is challenging, which may result in subsequent settlement, the formation of voids, and an increased hydraulic (seepage) gradient [12].

The interface between the sand embankment and the concrete shaft of the pier, due to differences in material properties, serves as a preferential seepage path and compromises the embankment's filtration stability. For gradient verification, a boundary condition is applied that assumes free outflow of water at the pier location, similar to a drainage channel.

As a technical solution to ensure the embankment's filtration stability, the installation of a concrete slab revetment on the unprotected slope and the construction of a seepage control system consisting of a grout curtain (cut-off) and a sheet pile cut-off wall have been proposed. The sheet piles, 12 m in length, are driven through the embankment and the underlying foundation layer at the junction between the embankment crest and the unprotected slope.

The concrete slab revetment extends from the dam crest to the slope toe, preventing direct horizontal seepage through the embankment body. The sheet pile cut-off wall installed through the embankment and alluvial deposits reduces seepage discharge and lowers the exit hydraulic gradient at the embankment–pier interface. Considering that uplift pressures in foundations are not a governing design issue for embankment dams, the sheet pile cut-off may be positioned downstream of the unprotected embankment toe.

Furthermore, the use of multiple rows of sheet piles is not recommended, as it does not significantly increase the seepage path length [12]. Although a fully effective protective measure would involve extending the sheet pile cut-off through the entire thickness of the alluvial deposits, such a solution is not rational in this case due to the considerable depth of the alluvium. Therefore, a shorter sheet pile cut-off system is adopted to ensure adequate protection of the foundation soil downstream of the embankment.

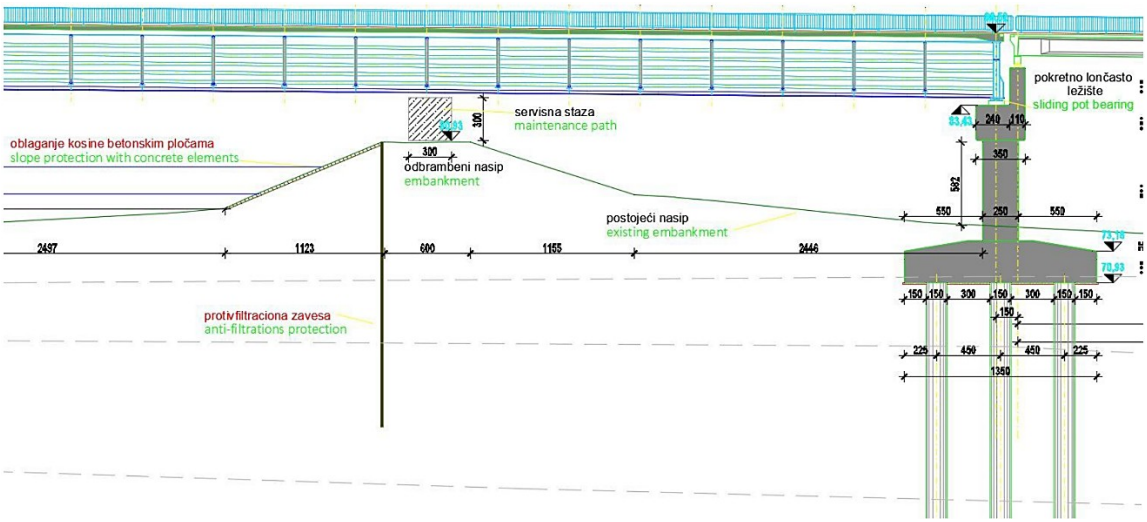


*Fig. 5 Proposed protective measures [7]*

## 4. HYDRAULIC ANALYSIS: MATHEMATICAL MODEL FORMULATION

Seepage analysis through the embankment to assess filtration stability was conducted using the two-dimensional (2D) module of the SEEP/W software package. This software enables the development of numerical models that accurately simulate water flow in porous media composed of granular materials.

### 4.1. MODEL SETUP

The first step in developing the two-dimensional model was defining the geometry of the embankment, pier, and protective measures, after which the soil lithology was defined (Figure 6).

To account for water filtration from the main channel of the Tisza River, the model geometry included the river channel, floodplain, embankment, and bridge pier, i.e., a longitudinal profile of 320 m. For modeling purposes, data obtained from sampling of

riverbed sediments at the bridge pier location were used, as reported in geological and geotechnical documentation [11].

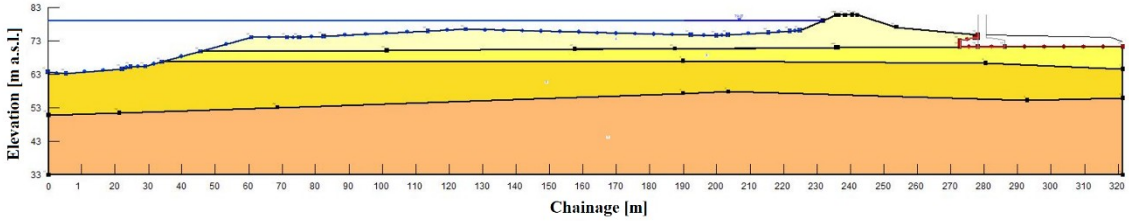


*Fig. 6 Model geometry with geological formation of alluvial sediments*

The geological structure of the wider investigation area consists of Quaternary alluvial–lacustrine sediments, alluvial deposits, loess–marsh sediments, and anthropogenic fill. Recent investigations have confirmed the site's general geological composition. The alluvial deposits (a) are represented by two main facies: floodplain facies (af) and channel facies (ac).

Alluvial deposits – floodplain facies (af)

The floodplain facies consists of silty sandy clays, sandy silts, silty sands, and silts with carbonate concretions. These deposits are characterized by irregular lateral and vertical alternation and are formed during overbank flooding events. Compared to channel deposits, they exhibit finer grain size, thin lenticular lamination, horizontal stratification, the presence of marsh–terrestrial fauna, and elevated $CaCO_3$ content. Grain-size distribution depends on distance from the main channel, with coarser fractions deposited closer to the channel and finer fractions in distal areas.

From a hydrogeological perspective, these deposits (typically 5–9 m thick) are characterized by subcapillary porosity and low to medium permeability, with filtration coefficients ranging from $10^{-7}$ to $10^{-4}$ cm/s, classifying them as semi-permeable media. Groundwater within these deposits occurs as a temporary, perched aquifer with a free water table, which may hydraulically connect with the main aquifer under high groundwater conditions, while such connectivity is lost during low water levels. Recharge is mainly governed by precipitation infiltration, while discharge occurs via evapotranspiration and drainage toward the main aquifer. In low-lying areas, high groundwater levels can lead to waterlogging and marsh formation.

Alluvial deposits – channel facies (ac)

The channel facies consists of silty sands, sands, and sand–silt mixtures with occasional interlayers of fine-grained gravel. These deposits (with thicknesses exceeding 10 m) exhibit irregular vertical and horizontal alternations and are formed by deposition of coarser fluvial material within active or abandoned river channels.

They are characterized by capillary to supercapillary porosity and good permeability, with hydraulic conductivity values ranging from $10^{-2}$ to $10^{-5}$ cm/s. Locally, less permeable clay lenses or interlayers may occur.

At the site of interest, the ground is composed of floodplain facies deposits (af) represented by silty sands ($af^{s,s}$) to an average depth of approximately 3.5 m, underlain by silty–sandy–muddy deposits ($af^{s,s,m}$) to an average depth of about 8.0 m, while the underlying stratum consists of channel facies deposits (ac), predominantly silty sands ($ac^{s}$).

Laboratory geomechanical testing of samples from this medium produced permeability coefficient values determined by the USBR and Hazen methods [11]. Numerical analyses were conducted using both approaches. The permeability coefficients for each layer are provided in Table 2. The colors used in the formatted table correspond to the layer colors shown in Figure 6, where each layer is consistently color-coded with its respective table entry.

*Tab. 2 Permeability coefficients by layers [11]*

| Layer | USBR [m/s] | Hazen [m/s] |
|---|---|---|
| $af^{s,s}$ | $2.16e^{-05}$ | $2.42e^{-05}$ |
| $af^{s,s,m}$ | $2.83e^{-06}$ | $1.89e^{-06}$ |
| $ac^{s}$ (1) | $2.9e^{-06}$ | $1.31e^{-06}$ |
| $ac^{s}$ (2) | $1.29e^{-06}$ | $5.47e^{-07}$ |

In the second step, the computational grid was generated. The SEEP/W 2D module uses the finite element method as its numerical approach, with the computational grid formed from square and triangular elements of varying sizes and orientations. The finite element method offers significant advantages over other methods when dealing with irregular flow domains and abrupt changes in the primary field variable near specific locations. The example in Figure 7 shows the flow around a sheet pile and the discretization of the flow field using the finite element method (triangular elements). It is considered that significant variations in piezometric heads occur in the vicinity of piles [13].

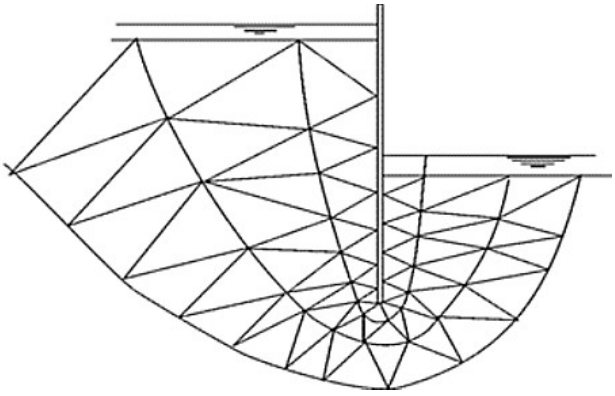

*Fig. 7 Example of a computational grid around sheet piles [13]*

Specifically, for the numerical model of the Tisza embankment, a grid of 51,890 elements with an average element size of 0.5 m was adopted. The adopted computational grid is presented in Figure 8 in the following subsection on boundary conditions.

## 4.2. BOUNDARY CONDITIONS

In the third step of the two-dimensional model, boundary conditions were defined and implemented. Within this study, four cases were considered.

- Case I: No protective measures were applied, and the upstream boundary was defined along the channel bed and floodplain as well as along the unprotected embankment slope, while the downstream boundary of the model was specified at the embankment–pier interface (Figure 8).

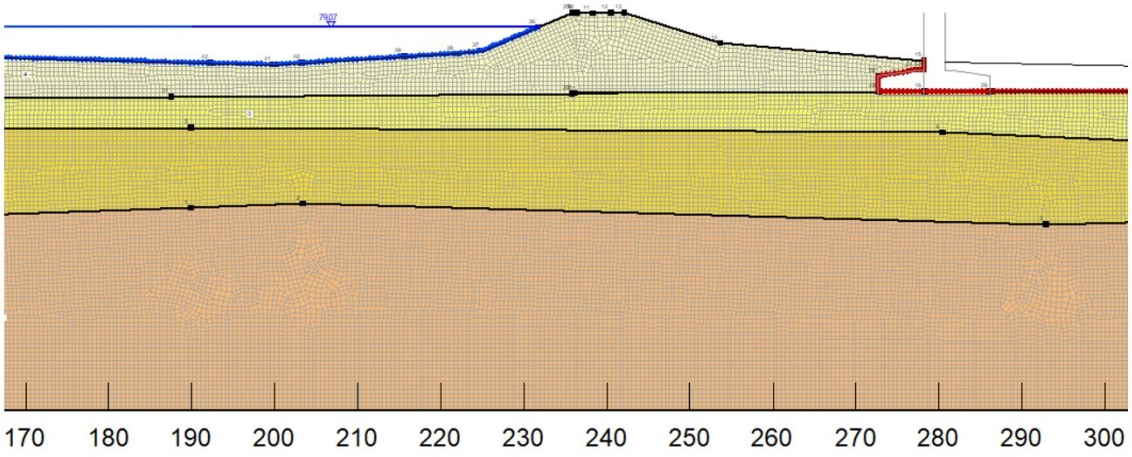


*Fig. 8 Adopted computational grid for Case I*

- Case II: A concrete slab revetment was applied on the embankment slope as a protective measure. The upstream boundary of the model was defined along the channel bed and floodplain up to the toe of the unprotected embankment slope, while the downstream boundary of the model was specified at the embankment–pier interface (Figure 9).

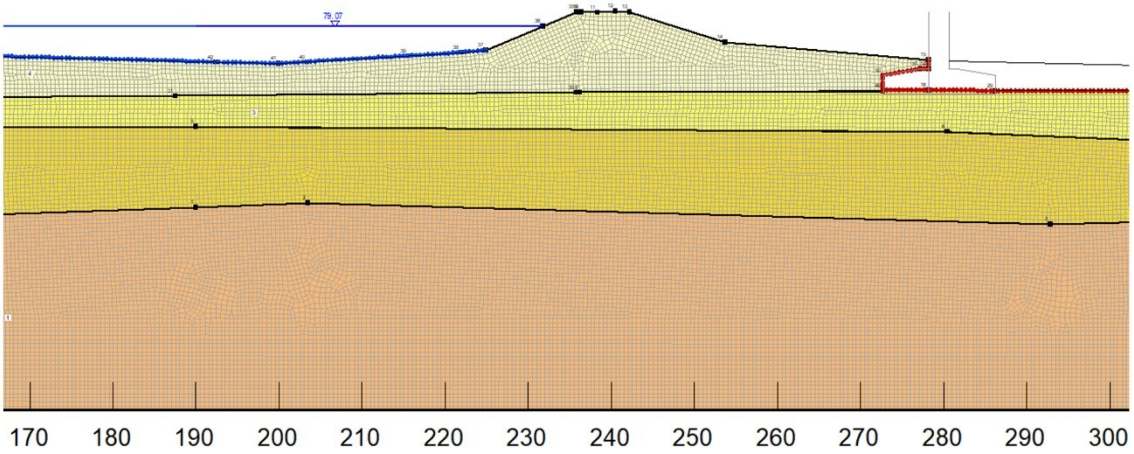


*Fig. 9 Adopted computational grid for Case II*

- Case III:
    a) A sheet pile cut-off wall installed at the embankment crest and a concrete slab revetment on the embankment slope were applied as protective measures. The upstream boundary of the model was defined along the channel bed and floodplain up to the toe of the unprotected embankment slope, while the downstream boundary was specified at the embankment–pier interface (Figure 10).
    b) A sheet pile cut-off wall installed at the toe of the unprotected embankment slope and a concrete slab revetment were applied as protective measures. The upstream boundary of the model was defined along the channel bed and floodplain up to the toe of the unprotected embankment slope, while the downstream boundary was specified at the embankment–pier interface (Figure 11).

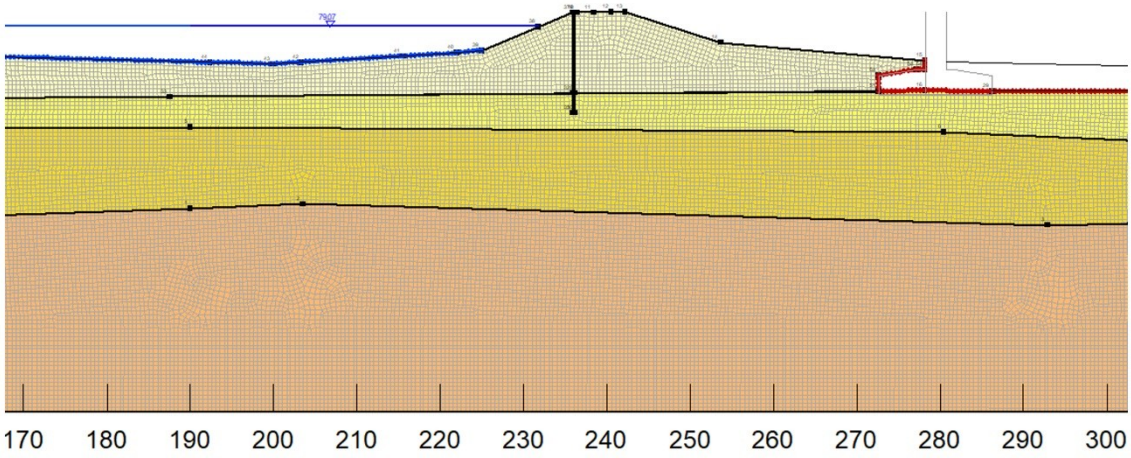


*Fig. 10 Adopted computational grid for Case III a)*

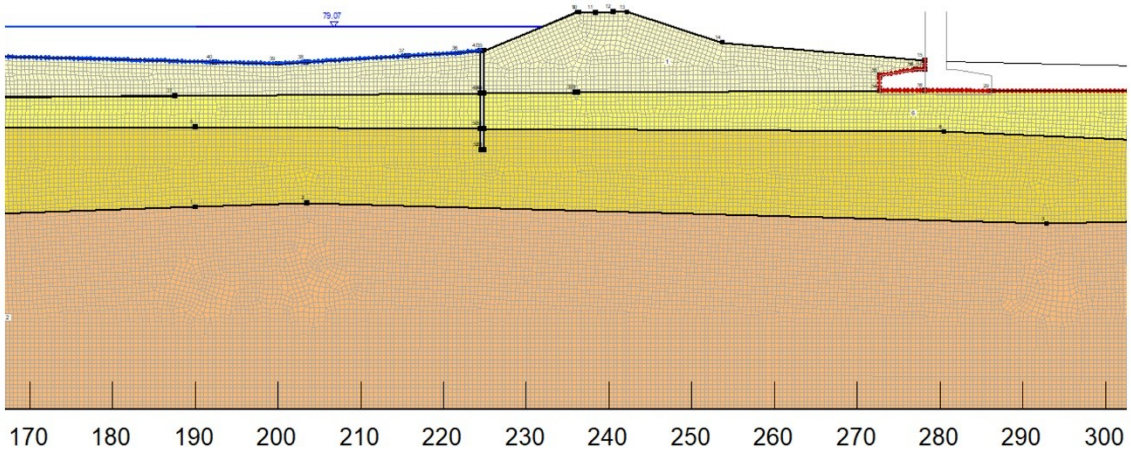


*Fig. 11 Adopted computational grid for Case III b)*

- Case IV: A sheet pile cut-off wall installed at the toe of the unprotected embankment slope, a concrete slab revetment, and an extended embankment were applied as protective measures. The upstream boundary of the model was defined along the channel bed and floodplain up to the toe of the unprotected embankment slope, while the downstream boundary was specified at the embankment–pier interface (Figure 12).

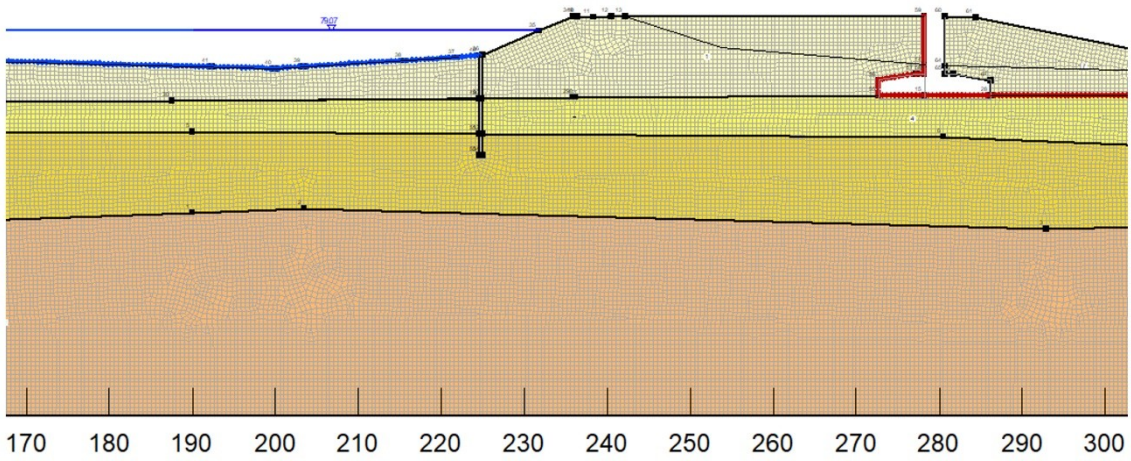


*Fig. 12 Adopted computational grid for Case IV*

The flood wave in the Tisza River is characterized by a prolonged duration, and therefore steady-state flow conditions corresponding to the design flood level were considered representative for the filtration stability analysis. Accordingly, the 1% annual exceedance probability (100-year return period) flood level obtained from [14], corresponding to a water surface elevation of 79.07 m a.s.l., was adopted as the upstream hydraulic boundary condition.

## 5. RESULTS AND DISCUSSION

After the model was established, a steady-state flow simulation was performed, and the results are presented in the following figures for all four cases as equipotential lines, flow lines, and gradient isolines.

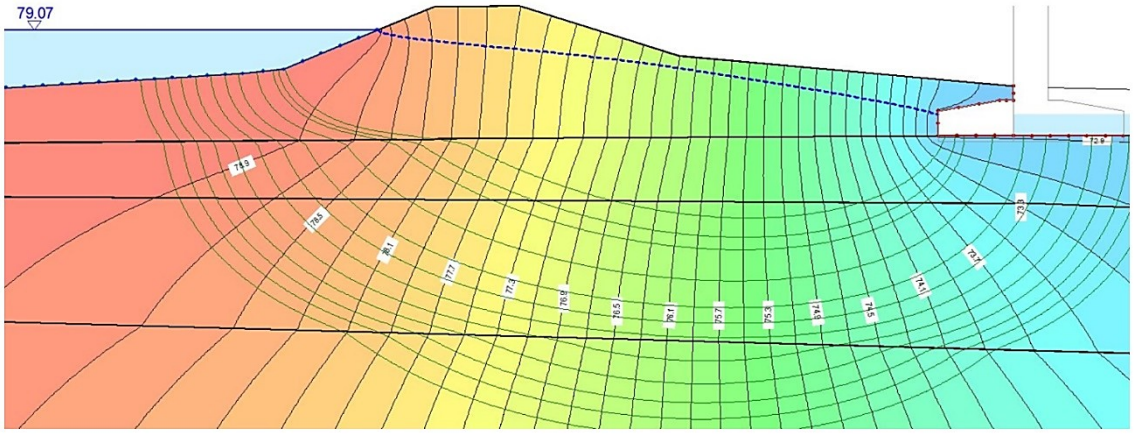


*Fig. 13 Piezometric head distribution for Case I*

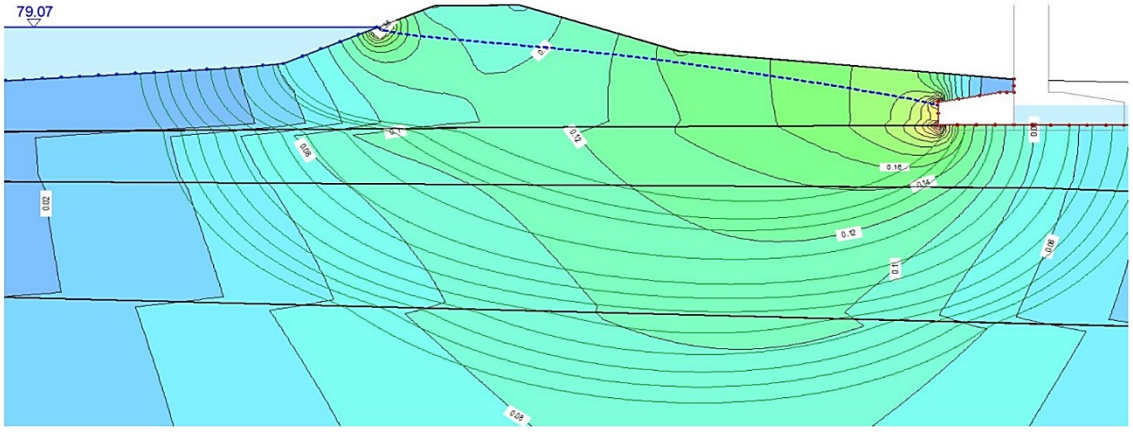


*Fig. 14 Gradient isolines for Case I*

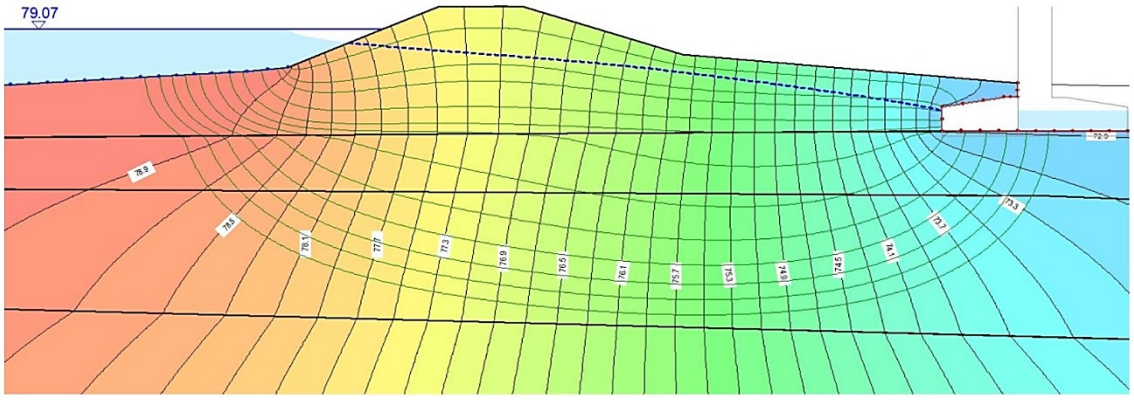


*Fig. 15 Piezometric head distribution for Case II*

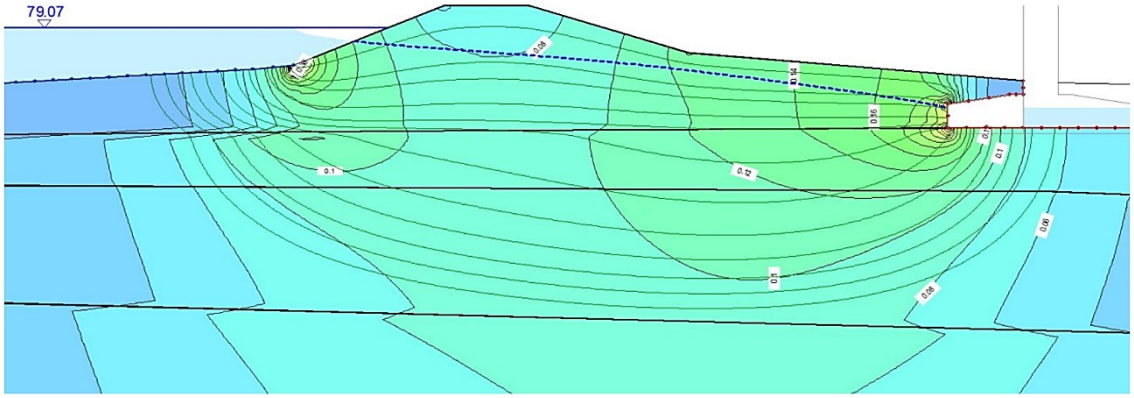


*Fig. 16 Gradient isolines for Case II*

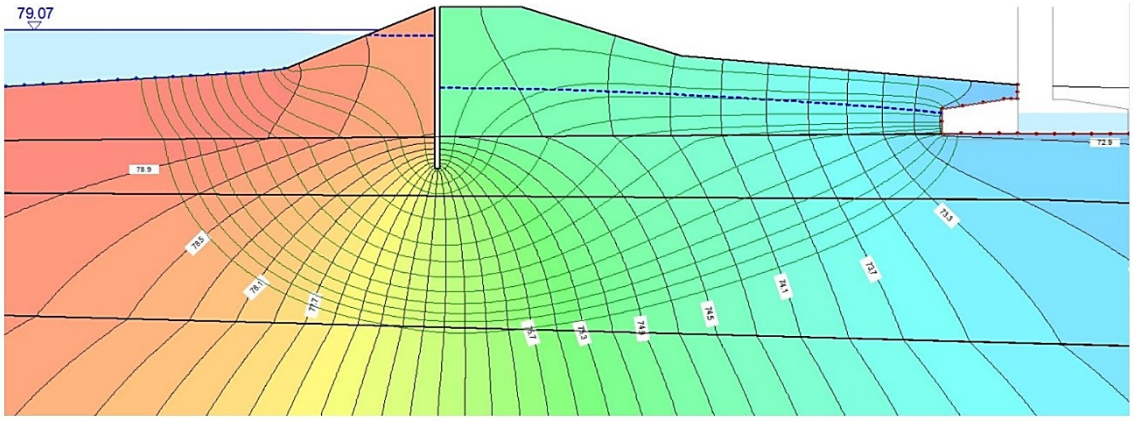


*Fig. 17 Piezometric head distribution for Case III a)*

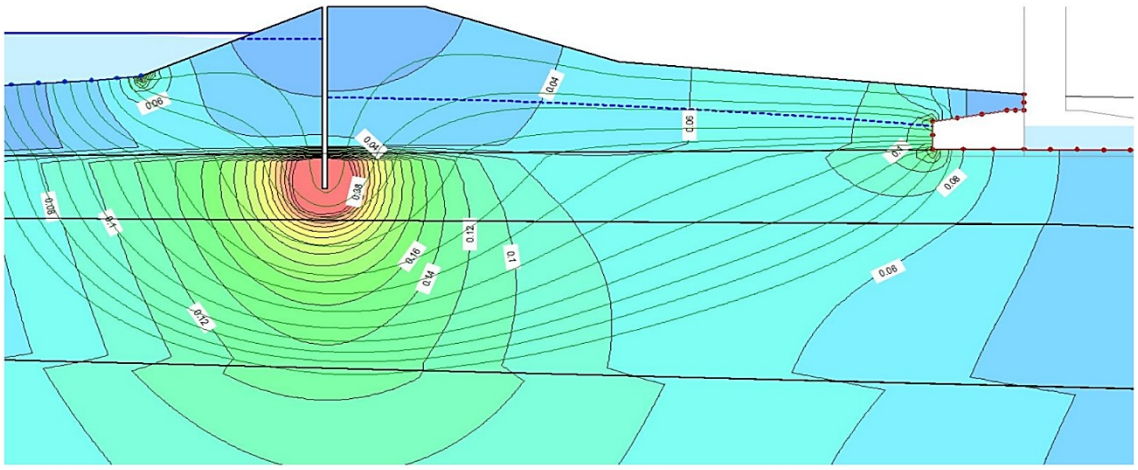

*Fig. 18 Gradient isolines for Case III a)*

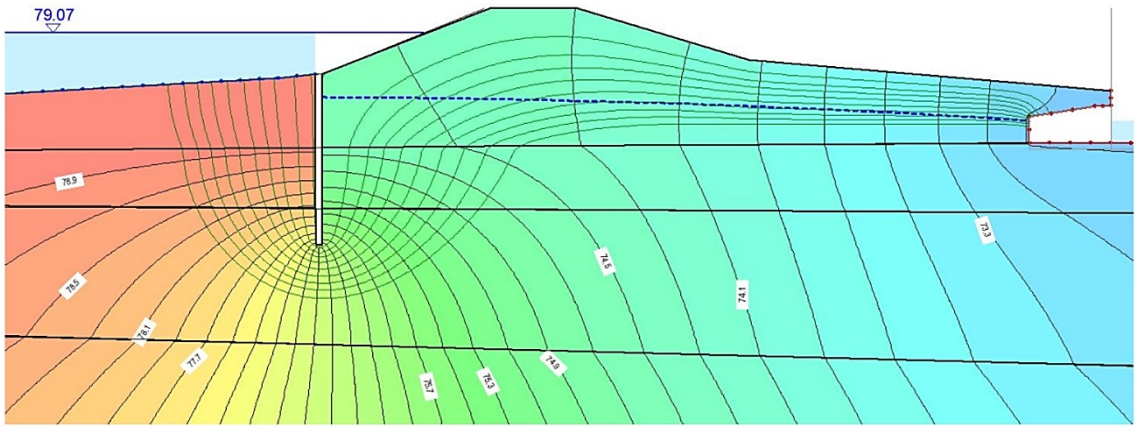

*Fig. 19 Piezometric head distribution for Case III b)*

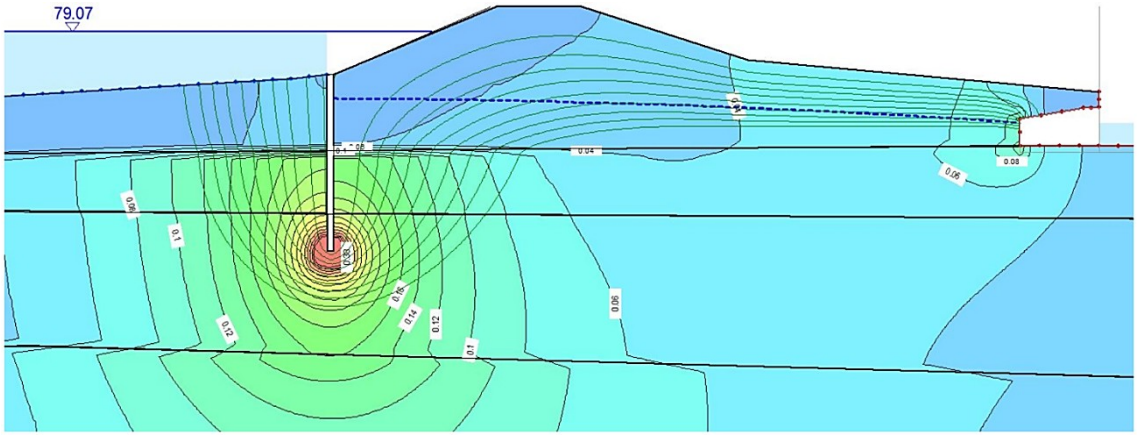


*Fig. 20 Gradient isolines for Case III b)*

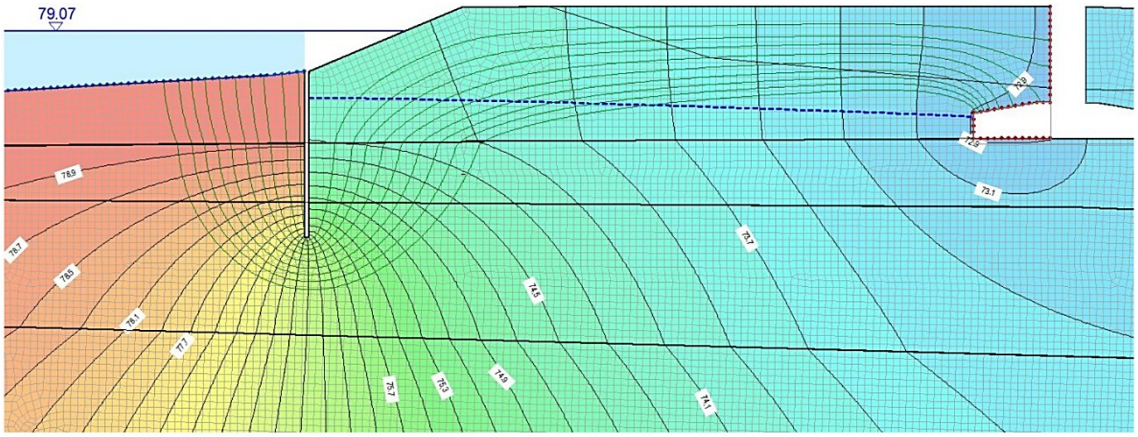


*Fig. 21 Piezometric head distribution for Case IV*

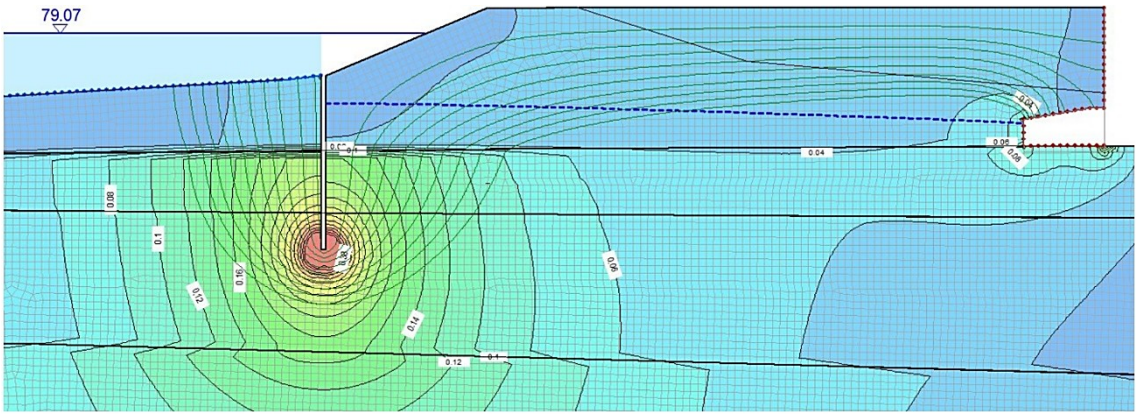


*Fig. 22 Gradient isolines for Case IV*

The results of the analysis indicate two potentially critical points at the embankment–bridge pier interface, based on the values of the exit gradient.

To assess the possibility of suffusion and fluidization at locations of maximum hydraulic gradients, the expression for calculating the critical filtration gradient was applied according to Lane's (Lane, 1935) recommendations (Table 3) [12].

*Tab. 3 Recommended safe exit gradient for Lane's weighted creep theory [12]*

| Material | Critical exit gradient (Ie) | Filtration coefficient K (m/s) |
|---|---|---|
| Very fine sand or silt | 1/8.5 | $10^{-3}$ – $10^{-4}$ |

| | | |
|---|---|---|
| Medium sand | 1/6.0 | $10^{-2} – 10^{-3}$ |
| Medium gravel | 1/3.5 | $10^{-1} – 10^{-2}$ |
| Boulders with some cobbles and gravel | 1/2.5 | $>10^{-1}$ |
| Soft clay | 1/3.0 | $10^{-6} – 10^{-8}$ |
| Hard clay | 1/1.8 | $<10^{-8}$ |

Case I: At the contact between the pier and the protected embankment slope, the exit gradient was 0.24, while the maximum exit gradient at the embankment–pier interface at the toe was 0.45 (Figure 23). To assess the possibility of suffusion and fluidization at locations of maximum hydraulic gradients, the expression for calculating the critical filtration gradient for suffusion was applied according to Lane's recommendations (Table 3), yielding a value of $I_{e,cr} = 0.12$ for silty sands.
Furthermore, given that the coefficient of uniformity $C_u$ ($d_{60}/d_{10}$) is 15.5 for the second layer and 5.1 for the first layer near the surface, Istomina's experimental investigations indicate that fluidization may occur. The critical gradient value ranges from $I_{cr} = 0.4–0.5$, and, according to the diagram $I_e = f(C_u)$ (Figure 1), this also indicates a potential risk of fluidization.

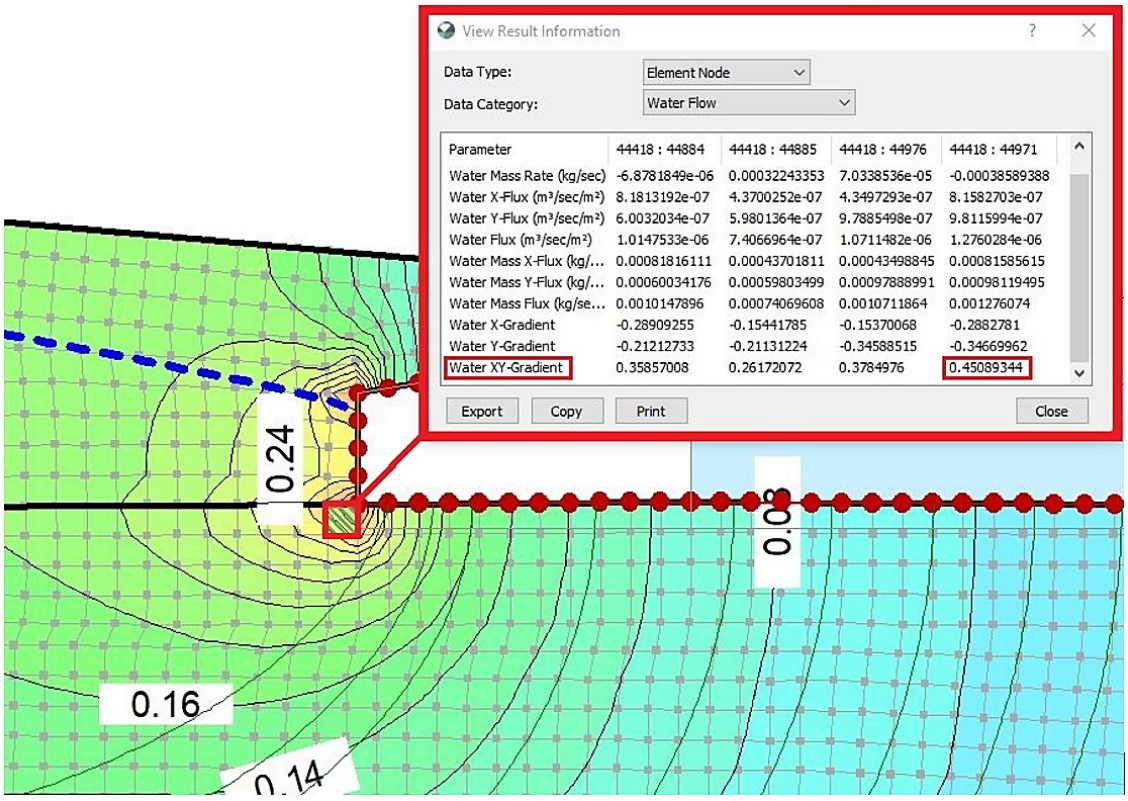


*Fig. 23 Maximum exit gradient for Case I*

Case II: At the contact between the pier and the protected embankment slope, the exit gradient was 0.22, while the maximum exit gradient at the embankment–pier interface at the toe was 0.33 (Figure 24). To assess the possibility of suffusion and fluidization at locations of maximum hydraulic gradients, the expression for calculating the critical filtration gradient for suffusion was applied according to Lane, yielding a value of $I_{e,cr} = 0.12$ for silty sands.

As described in Case I, based on Istomina's experimental investigations applied in practice, the critical gradient ranges from $I_{cr}$ = 0.4–0.5, indicating a lower risk of fluidization, as Istomina's recommended allowable exit gradient is $I_{e,perm}$ = 0.3.

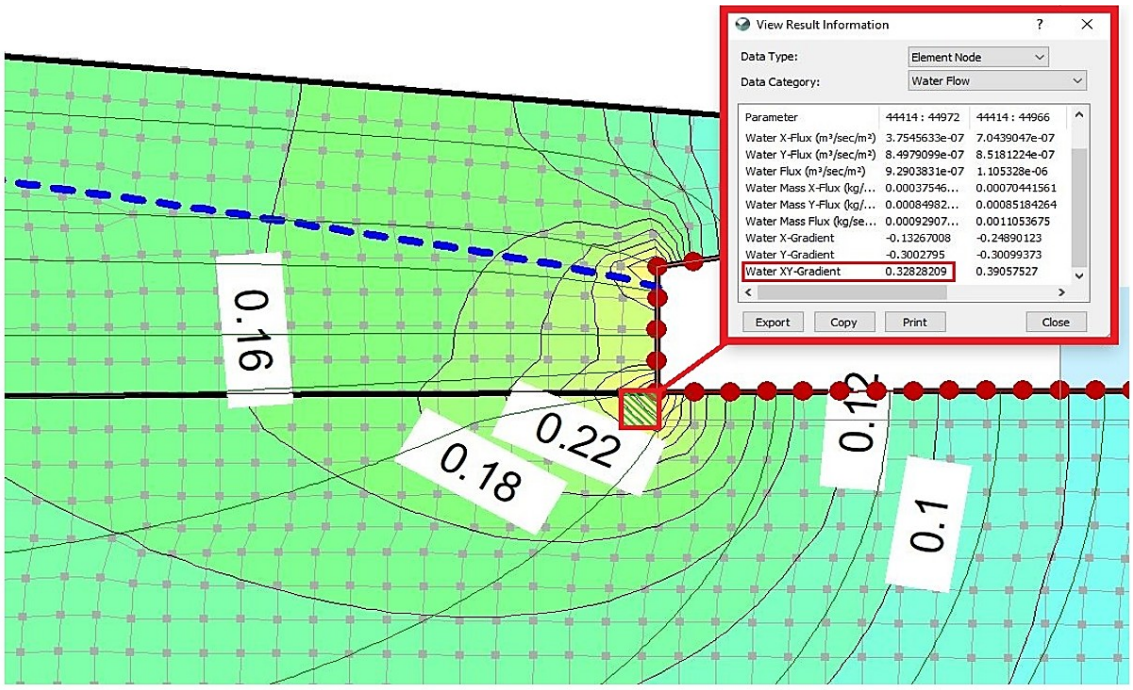


*Fig. 24 Maximum exit gradient for Case II*

Case III a): At the contact between the pier and the protected embankment slope, the exit gradient was 0.10, while the maximum exit gradient at the embankment–pier interface at the toe was 0.20 (Figure 25). To assess the possibility of suffusion and fluidization at locations of maximum hydraulic gradients, the expression recommended by Lane was applied, yielding a value of 0.12 for silty sands. According to Istomina's experimental investigations, there is no risk of fluidization.

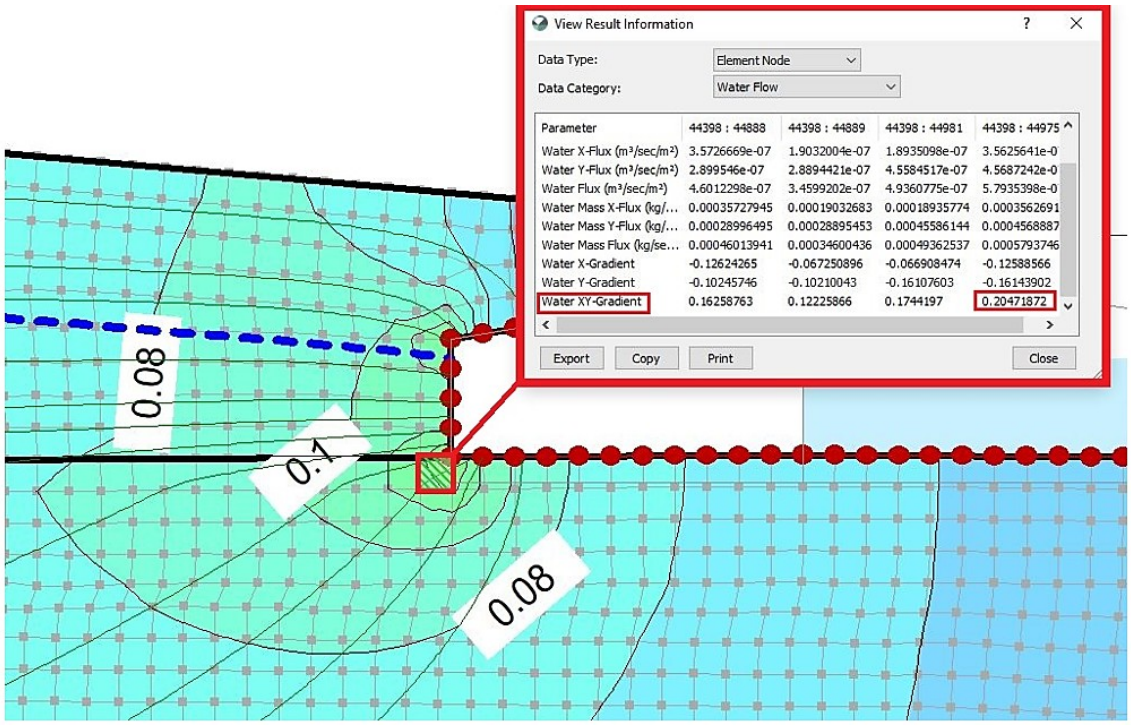


*Fig. 25 Maximum exit gradient for Case III a)*

Case III b): At the contact between the pier and the protected embankment slope, the exit gradient was 0.08, while the maximum exit gradient at the embankment–pier interface at the toe was 0.11 (Figure 26). To assess the possibility of suffusion and fluidization at locations of maximum hydraulic gradients, the expression recommended by Lane was applied, yielding a value of 0.12 for silty sands. According to Istomina's experimental investigations, there is no risk of fluidization.

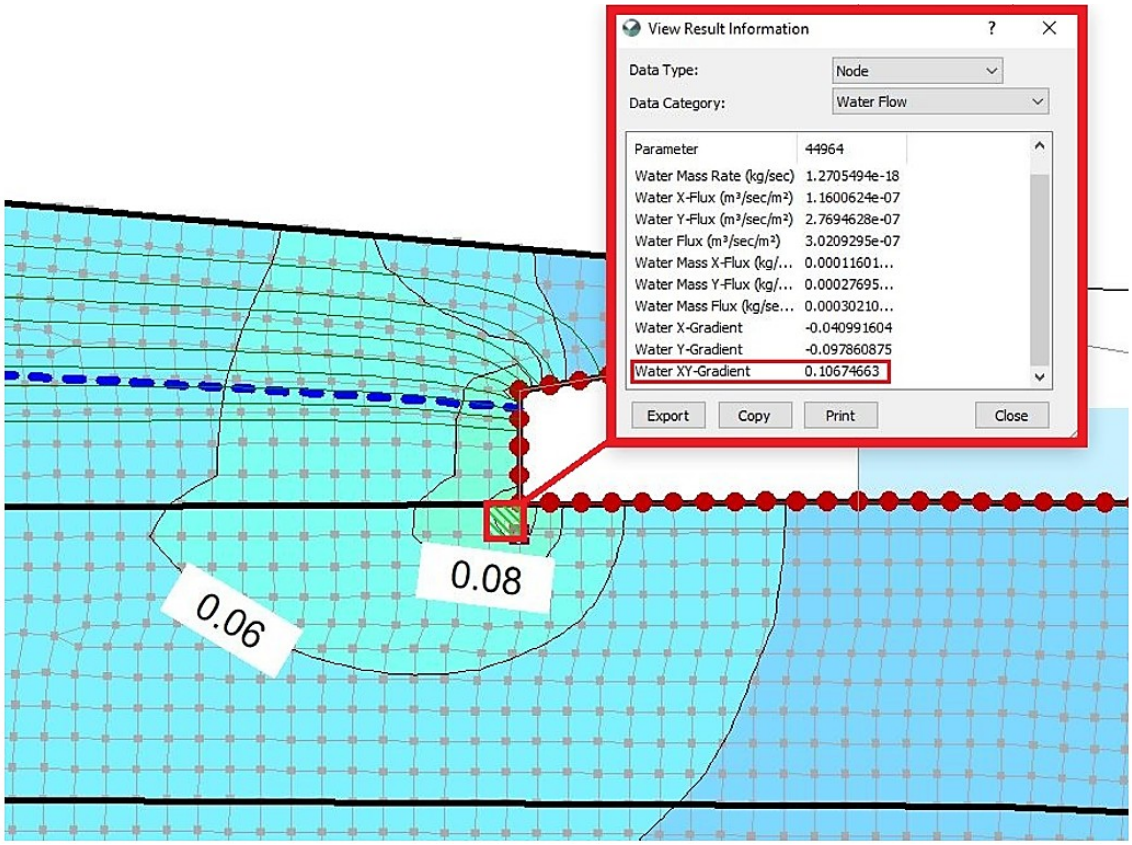


*Fig. 26 Maximum exit gradient for Case III b)*

In Case IV, the ballast is designed to extend above the 1% annual exceedance probability (100-year) flood level, up to the embankment crest. Consequently, material erosion at the interface between the bridge pier and the surrounding soil is not expected. The proposed stabilization measures include a concrete slab revetment on the upstream slope, a steel sheet-pile cutoff wall installed at the embankment crest, and a downstream sand ballast layer. The ballast is designed to extend to the crest elevation of the existing embankment, above both the Tisza River high-water level and the seepage line within the embankment body. As a result, the ground surface above the ballast remains unsaturated. Consequently, seepage emergence is not expected at this location, even under the extreme hydraulic conditions associated with the 1% annual exceedance probability (100-year) flood event.

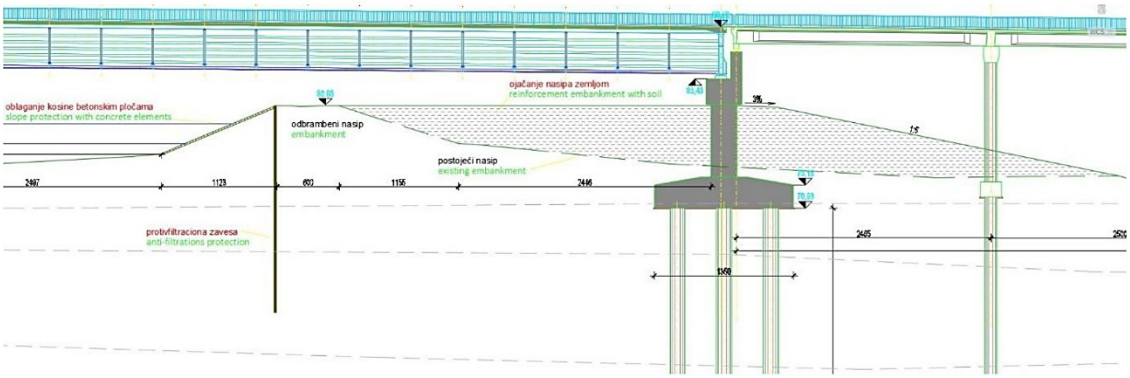


*Fig. 27 Applied measures for protection and seepage stability [7]*

## 6. CONCLUSION

Internal erosion resulting from groundwater seepage through embankments and their foundations is widely acknowledged as a primary cause of earth structure failures globally. Under unfavorable hydraulic conditions, seepage can initiate suffusion, piping, or fluidization, progressively degrading soil and diminishing structural stability. The introduction of bridge foundations within or near embankments further disrupts natural seepage patterns and locally elevates hydraulic gradients, thereby increasing vulnerability to internal erosion.

This study investigated the filtration stability of the right-bank Tisza embankment within the bridge influence zone using numerical seepage modeling. The analysis was performed using the two-dimensional (2D) module of the SEEP/W software package, which enables the development of numerical models for simulating water flow in porous media. The assessment focused on the distribution of hydraulic heads, seepage characteristics, and critical exit gradients under extreme hydraulic conditions.

Embankment geometry, bridge pier location, and lithological soil profile were defined to generate a finite element grid, with suitable initial and boundary conditions assigned. Four analysis scenarios were developed, each differing in boundary conditions determined by proposed protective measures aimed at mitigating suffusion and fluidization. All scenarios applied a uniform initial condition corresponding to the design 1% annual exceedance probability (100-year return period) flood level.

A steady-state seepage analysis was conducted using the SEEP/W model, with results for all scenarios presented as equipotential lines, flow lines, and hydraulic gradient isolines. The calculated exit gradients at the embankment–pier interface were compared with the critical and permissible values reported in the relevant literature.

Based on the results, protective measures were recommended to prevent suffusion and fluidization during extreme hydraulic conditions in the Tisza River associated with the 1% flood event. The proposed solution to ensure both seepage and structural stability involves a concrete slab revetment on the upstream slope, a steel sheet-pile cutoff wall installed at the embankment crest and a downstream embankment protection with a sand ballast layer extending to the crest elevation of the existing embankment. This approach intercepts the seepage line within the embankment body, preventing seepage from emerging at the surface. Under the analyzed extreme hydraulic conditions, no seepage outflow is anticipated at the ground surface at the site of interest.

**ACKNOWLEDGEMENT**

The research has been conducted within the project "Enhancement of teaching and scientific research capacities through the application of modern technologies in the fields of civil engineering, geodesy, and disaster risk management and fire safety", developed at the

Department of Civil Engineering and Geodesy, Faculty of Technical Sciences, University of Novi Sad, Serbia.

## REFERENCES

[1] Foster M., Fell R., Spannagle M. (2000). The statistics of embankment dam failures and accidents. *Canadian Geotechnical Journal*, Volume 37(5), pp. 1000–1024. https://doi.org/10.1139/t00-030

[2] Richards K.S., Reddy K.R. (2007). Critical appraisal of piping phenomena in earth dams. *Bulletin of Engineering Geology and the Environment*, Volume 66(4), pp. 381-402. https://doi.org/10.1007/S10064-007-0095-0

[3] Bonelli, S. (2013). *Erosion in Geomechanics Applied to Dams and Levees*. ISTE Ltd & John Wiley & Sons. ISBN: 978-1-84821-409-5

[4] Terzaghi K., Peck R.B., Mesri G. (1996). *Soil Mechanics in Engineering Practice*. 3rd Edition, Wiley. ISBN: 978-0-471-08658-1

[5] Skempton A.W., Brogan J.M. (1994). Experiments on piping in sandy gravels. *Géotechnique*, Volume 44(3), pp. 449–460. https://doi.org/10.1680/geot.1994.44.3.449

[6] GEO-SLOPE International Ltd. (2023). *SEEP/W Theory Manual*. Calgary, Canada.

[7] AG Institut. (2023). IDP Sveska 2/1.5. Autoput Beograd - Zrenjanin - Novi Sad - Deonica 2 – sektor 5: Zrenjanin - Novi Sad stacionaže km 67+662.47 – km 90+000.00

[8] Jovanović M. (2022). *Regulacija reka – radovi i građevine*. Univerzitet u Beogradu, Građevinski fakultet, Beograd. ISBN 978-86-7518-216-0

[9] Zhang Q., Chen Q., Wan L., Li X., Zhou Y., Cheng Q. (2024). Research Progress in Methods for the Analysis of the Internal Stability of Landslide Dam Soils. *Applied Sciences*, Volume 14(15), pp. 6702. https://doi.org/10.3390/app14156702

[10] Istomina V. S. (1957). *Filtration stability of soils*. Gostroizdat, Moscow, Leningrad, 15.

[11] AG Institut. (2023). IDP EL2.1.5. – Elaborat geotehničkih uslova izgradnje trase na sektoru K od km 67+662.47 do km 90+000.00

[12] Savić Lj. (2022). *Uvod u hidrotehničke građevine*. Univerzitet u Beogradu, Građevinski fakultet, Beograd. ISBN 978-86-7518-228-3

[13] Stipić M., Kolaković S. (2013). *Model strujanja vode kroz poroznu sredinu SEEP/W*. Fakultet tehničkih nauka, Novi Sad.

[14] AG Institut. (2022). IDR Hidrauličko-hidrološke studije uticaja mostova autoputa Beograd - Zrenjanin - Novi Sad na velike vode

https://doi.org/10.24867/INDIS-2026-EN-308

**INTERNATIONAL SCIENTIFIC CONFERENCE**
INTEGRATION, NOVELTY, DESIGN,
INTERDISCIPLINARITY, SUSTAINABILITY

iNDiS 2026

# CERTIFICATION OF RECYCLED CONCRETE AGGREGATES FOR APPLICATION IN STRUCTURAL CONCRETE

*Sofija Kekez-Baran*[1]

***Summary:***

Concrete waste is one of the largest waste streams in Europe, which makes the recycling of concrete waste crucial to achieving climate neutrality by 2050. Since concrete consists of around 70% of aggregates, application of recycled concrete aggregates to produce new concrete can significantly decrease environmental impact in terms of transport and landfilling of concrete waste, as well as mining of virgin materials. To achieve implementation of recycled concrete aggregates in concrete production, generated recycled concrete aggregates must be certified according to their intended use. This paper gives an overview of the pre-audit and certification procedure for recycled concrete aggregates for use in structural concrete. Special attention is given to concrete exposed to harsh marine environments.

*Keywords: CDW, secondary raw materials, recycled concrete aggregate, upcycling*

# SERTIFIKACIJA RECIKLIRANIH BETONSKIH AGREGATA ZA UPOTREBU U NOSEĆEM BETONU

***Rezime:***

Betonski otpad predstavlja jedan od najvećih tokova otpada u Evropi, što reciklažu betonskog otpada čini ključnom za postizanje klimatske neutralnosti do 2050. godine. S obzirom na to da beton sadrži oko 70% agregata, primena recikliranih betonskih agregata za proizvodnju novog betona može značajno smanjiti uticaj na životnu sredinu u pogledu transporta i odlaganja betonskog otpada, kao i eksploatacije prirodnih sirovina. Da bi se omogućila primena recikliranih betonskih agregata u proizvodnji betona, proizvedeni reciklirani betonski agregati moraju biti sertifikovani u skladu sa njihovom namenom. Ovaj rad daje pregled postupka pred-audita i sertifikacije recikliranih betonskih agregata za upotrebu u konstrukcijskom betonu. Posebna pažnja posvećena je betonu izloženom oštrim uslovima morske sredine.

*Ključne reči: GO, sekundarne sirovine, reciklirani betonski agregat, reciklaža*

[1] Researcher, Department of Building, Energy and Material Technology, UiT The Arctic University of Norway, Lodve Langes gate 2, Narvik, Norway, sofija.kekez@uit.no, ORCID **0000-0003-3879-2560**

## 1. INTRODUCTION

Concrete is second most used material in the world, and consequently, construction and demolition waste (CDW) is one of the largest waste streams. Only in Europe, waste generated by the construction sector in 2022 was 38% of the total waste. Adding to that the waste generated from mining and quarrying (23%), almost two thirds of the total waste generated in Europe was major mineral waste [1]. Eurostat statistics [2] show that in 2022 every country in Europe has produced from 1 to 12 kg per capita of CDW, see Fig. 1. Furthermore, with the aging buildings and current political climate, CDW generation is bound to increase in the next years.

The European Green Deal from 2020 has been implemented to achieve climate neutrality in the EU by 2050. Within this frame, CDW has been identified as one of the key pathways for the transition due to its high resource value and potential for recycling and reuse [1]. Even though average CDW recovery rate in Europe is 90%, countries show significant variation – from Netherlands with 100% recovery over Slovakia and Bulgaria with less than 60% to Montenegro with 0% in 2018 [3].

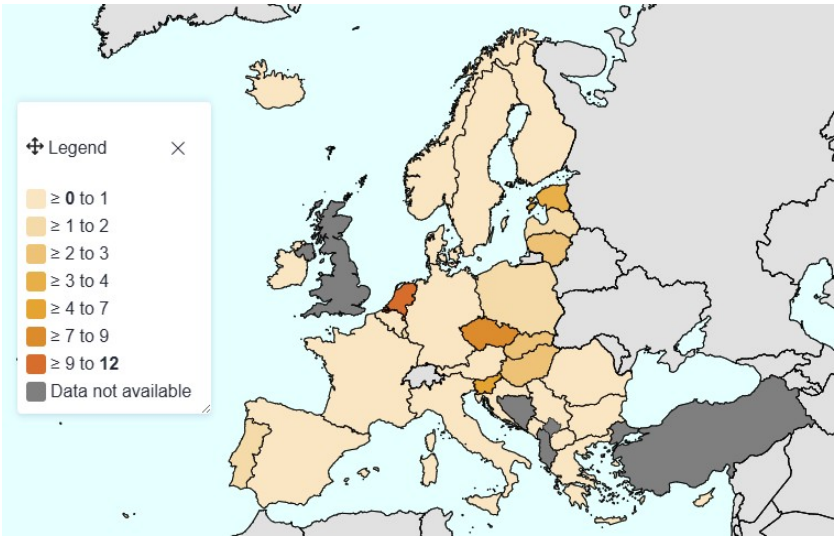


*Fig. 1 Generation of CDW in Europe in 2022 expressed in kilograms per capita [2]*

Concrete consists of approximately 70% of non-replenishable natural aggregates (NA), that are generated through emission-intensive mining or quarrying activities. Hence, recycling concrete waste into aggregates for production of new concrete decreases carbon emissions by lowering the need for mining and quarrying, and production and transportation of scarce NA. Moreover, less landfilling conserves natural land and marine environments and preserves biodiversity. This way, concrete waste becomes secondary raw material with broad range of civil engineering applications in road construction, land recultivation and landscaping, as well as in production of structural precast or ready-mix concrete.

This paper gives an overview of the pathway of transforming concrete from demolition waste into secondary raw material and summarizes the procedures involved in the production and certification of recycled concrete aggregates (RCA) for application in structural concrete.

# 2. END-OF-LIFE CONCRETE

## 2.1. PRE-AUDIT

Once a concrete structure is deemed for demolition, a pre-audit is required to establish the viability of concrete and its recyclability as secondary raw material. Detailed pre-audit procedure is regulated by national policy [4]. In addition to national legislation for building, environmental protection, and waste management, demolition projects must obide by municipal building regulations, environmental protection provisions and waste management regulations. These regulations impose requirements related to demolition, including content of plans, handling of demolition waste, and prevention of environmental harm. Additionally, demolition is generally subject to the same procedures for permit application, planning, implementation, and supervision as a construction project. Evenso, the main points of the pre-audit procedure are universal across European countries. Pre-audit report commonly includes environmental mapping and material mapping, and it must be submitted when applying for a demolition permit.

### 2.1.1. Environmental mapping

Environmental mapping is the initial stage of the pre-audit and involves a survey of hazardous substances that might be present in the structure. Environmental experts assess the structure and generate a list of all hazardous substances observed in structural elements and covers, such as lead, polychlorinated biphenyls (PCBs), asbestos, chlorinated paraffins, heavy shredding materials, electronic equipment (EE) waste, etc. Once these substances are revealed, the environmental remediation is defined. The remediation plan describes in detail the locations and the procedures of removing different hazardous materials from the structure that the demolition contractor must follow to perform carefull removal during the preparation stage of demolition.
Additionally, the environmental mapping gives information about possible contamination of the concrete. The presence of hazardous substances such as PCBs on the surface of concrete may affect its recyclability due to contamination. National regulation limits the presence of these substances in concrete. Hence, exposed concrete would have to go through additional process of cleaning (decontamination) before demolition to be eligible for use as secondary raw material. In case of doubt about the levels of hazardous materials, new concrete made from this RCA would necessitate additional leaching tests to ensure its safety. Therefore, the environmental mapping report presents also a starting point in the analysis of the viability of the concrete.

### 2.1.2. Material mapping

Material mapping involves assessing the structure in terms of materials and elements that may be recycled or reused, evaluating their condition, and estimating usable amounts. First step is reviewing available documentation and performing a visual inspection of the structure. The in-situ materials and their condition and geometry are compared to the design, and non-destructive tests are done on the concrete to give initial insight about the type, possible strength class, and usability. Then, the most promising locations in the structure are determined and concrete core samples are extracted for further testing to establish the viability of the old concrete for production of RCA. This is done by testing density and compressive strength of the concrete cores (cylinders), followed by crushing the cores into aggregates. The initial conditions that these aggregates should meet are favorable particle size distribution, water absorption, and density. Table 1 shows the basic Eurocode standard [5] for the properties of RCA that can be used in new concrete. Additional factors, such as shape index and fine particle

content, indicate the effects of RCA to the properties of new concrete, such as workability, pore structure, interfacial zone strength, etc.

*Tab. 1 European regulation for the use of RCA in new concrete.*

| Standard | Aggregate type | Allowed replacement of NA by RCA [weight %] | Filler in aggregates [%] | Concrete class | Bulk density [kg/m$^3$] | Water absorption [%] |
|---|---|---|---|---|---|---|
| EN 206 [5] | AN | ≤10% fine; ≤30% coarse; ≤20% coarse | unspecified | C25/30; C45/55 | ≥ 2100 | < 10 |
| | BN | ≤5% fine; ≤10% coarse | unspecified | C25/30 | ≥ 2000 | < 20 |

With the assessment of the structure and evaluation of the materials finished, material mapping report is generated. It estimates the amounts of non-contaminated concrete waste that can be recycled, shows the properties of the concrete, and gives recommendations for possible uses of future RCA. This report enables selective demolition and supports the organization and logistics of the works on the demolition site.

## 2.2. DEMOLITION AND RCA PRODUCTION

Traditional demolition rarely considers the management and sorting of CDW except for the regulated and prescribed final sorting for transport to the recycling facility [6]. Selective demolition is a more sustainable alternative because it leads towards the CDW reuse, thus, the demolition process is selective and carefully planned for most efficient removal of recyclable materials and elements of the structure. Pre-demolition activities include emptying the building and careful removal and sorting of hazardous elements. Then, the demolition starts in stages, to ensure proper dissasembly and preservation of all usable materials.

In this context, concrete is demolished and pre-sorted in terms of type and further processing. The contaminated concrete must be disposed off according to environmental remediation plan and removed from the site, while the non-contaminated concrete is prepared for further processing and production of RCA. Different in situ techniques can be employed to improve the waste quality, such as vibrating shovels that eliminate fines from the concrete waste. Since fine fraction of RCA is currently not applied in new concrete in most countries, using vibrating shovels ensures initial separation of unusable concrete waste. Therefore, instead of transporting concrete waste to the RCA production site and then transporting the fines to the recycling facility or landfill, fines are instantly disposed off from the demolition site. This presents a significant reduction of transportation emissions within the whole process since concrete contains around 60% of fine fraction.

Most common techniques for production of RCA are jaw or cone crushing that are types of compression crushing techniques, and impact crushing. While compression crushing is used for more hard and abrasive rock such as granite and basalt, the impact crushing is most convenient for soft and medium-hard rock like limestone. Hence, it is important to correlate the findings about the type and structure of concrete obtained during material mapping and the crushing technique that is applied for RCA production.

To minimize the carbon emissions of the whole process, production of RCA is often included in the demolition activites. If not planned properly, the demolition could involve transporting the materials several times, raising the footprint to the same level as new construction [6]. Production of RCA can be continuous, where the concrete waste is transported to a single location and continually processed, or it can be discontinuous, taking place directly at the demolition site using mobile crusher and sieve system. In many cases, continuous RCA production is not possible due to the lack of the concrete waste stream, however, discontinuous production exerts extensive amounts of dust and noise that require additional measures to avoid polluting immediate environment around the demolition site. Therefore, options and possibilities for RCA production should be reviewed before the demolition starts, and decisions should be made apriori, through collaboration between the demolition owner and contractor.

## 3. WASTE VALORIZATION OF RCA

### 3.1. CERTIFICATION

Once the RCA is produced and fractioned into fine and coarse fractions, the certification is an obligatory process that enables the structural use of RCA in new concrete. In Europe, this process is regulated by European Construction Products Regulation (CPR) [7] and EN 12620 [8] with additional provisions from national standards that define location-specific properties. Systems of attestation of conformity for aggregates can be defined for uses with high safety requirements (system 2+), or without high safety requirements (system 4). Under the European CPR, and specifically the Assessment and Verification of Constancy of Performance, system 2+ is the universal baseline standard for aggregates used in structural concrete, including also RCA. This system obliges the manufacturers to maintain factory production control system, which is assessed, surveilled, and certified by an independent approved body. As abovementioned, testing protocols are localized and depend on the country of origin of the RCA.

### 3.2. CASE STUDY: VESTERÅLEN PILOT

Vesterålen Pilot project within the Horizon Europe project “Circ-Boost: Boosting the uptake of circular integrated solutions in construction value chains” [9] demonstrates circular building process “from demolition to construction” in the Arctic region of Norway by deploying leading construction technologies and solutions for the region. The pilot follows the entire circular process, including selective demolition, production of RCA, and direct utilization of generated RCA in new construction. Initial stage was the selective demolition of an old slaughterhouse in Sortland, Norway. The building complex built in 1960 spread over 7300 $m^2$ surface area. After the demolition was completed, the waste reports showed that 99% of the concrete waste has been recycled in some way. Approximately 7445 t of non-contaminated concrete was extracted for upcycling or downcycling activities. Upcycling included 336 t of concrete waste sent to the local aggregate processing facility for production of RCA that will be used by the local concrete ready-mix producer. At the crushing site, the non-contaminated concrete waste was crushed and sorted into three fractions (0-4 mm, 4-8 mm, and 8-22 mm). The rest, approximatelly 7109 t of non-contaminated concrete waste, was downcycled at the demolition site for land recultivation and landscaping.

In Norway, certification of aggregates is regulated by Norwegian Public Roads Administration, Standard Norge, and the Directorate for Quality of Building, in accordance with [7, 8]. Norwegian national annex [8] defines aggregate properties that must be tested to acquire certification under the control system 2+. Therefore, RCA that

was crushed and sorted into fractions in Sortland must be CE-marked before the concrete producer can use it for production. Obligatory tests for RCA certification in Norway include:

- Geometrical properties: aggregate sizes, grading, flakiness index, shape index;
- Physical properties: particle density, water absorption;
- Mechanical properties: resistance to fragmentation of coarse aggregates,
- Durability: freeze-thaw resistance of coarse aggregates;
- Presence of unwanted elements: shell content of coarse aggregates, fines content, chlorides, acid-soluble sulfate, total sulfur content, constituents which alter the rate of setting and hardening of concrete, hazardous substances;
- Alkali-silica reaction of the aggregate blend (mortar).

Additional tests that could be requested for RCA in structural concrete include:

- Mechanical durability: resistance to surface wear, resistance to polishing, resistance to wear for coarse aggregates;
- Physical properties: volume stability – dehydration loss, influence on initial setting of cement (recycled aggregates);
- Presence of unwanted elements: content of water-soluble sulfate in recycled aggregates, carbonate content in fine aggregate for surface layers of concrete.

Since the planned utilization of RCA produced in Sortland includes building a concrete pier, new concrete will be grouped within the harshest exposure classes (XC2, XD3, XS3, XF4). Therefore, most properties require more rigorous examination. Most favorable RCA would show low water absorption (up to 2%) to avoid the workability issues, low fines content and presence of organic matter to ensure proper adherence between new and old residual mortar, high freeze-thaw resistance which implies minimal amounts of residual mortar in the RCA, low chloride and sulfur content, and low alkali-silica reaction.

Abovementioned obligatory and additional testing must be performed in a laboratory with certified and atested equipment and staff. If the RCA complies with the prescribed limitations, it is eligible for CE-marking which confirms that the processed RCA is no longer considered a waste, and commercial application is allowed. Certification presents the final step in the process of transforming waste into valuable construction material.

## 4. CONCLUSION

The increasing generation of CDW, particularly concrete waste, introduces significant environmental and resource challenges. This paper deals with the transformation of concrete waste into RCA, that presents a sustainable pathway to address these issues. By reducing the need for natural aggregate extraction, lowering carbon emissions, and minimizing landfill use, production of RCA aligns with the goals of the European Green Deal and broader global sustainability initiatives.

The process of recycling concrete waste, from pre-audit and selective demolition to RCA production and certification, demonstrates a comprehensive approach to circular construction. Pre-audit procedures, including environmental and material mapping, ensure the viability and safety of the recycled materials, while the selective demolition maximizes resource recovery. Furthermore, the certification process guarantees that RCA meets stringent quality and safety standards, enabling its commercial introduction on the market and its technical use in structural concrete.

The Vesterålen Pilot project exemplifies the practical implementation of these principles, achieving a remarkable 99% recycling rate for concrete waste. This project underscores the potential of RCA to support circular construction practices, even in challenging environments like the Arctic region with harsh climate and scarce population.

In conclusion, the adoption of RCA in structural concrete represents a critical step toward sustainable resource management and climate neutrality. Continued collaboration between policymakers, industry stakeholders, and researchers is essential to further optimize the second life cycle of “end-of-life” concrete, by improving the recycling process, enhancing material performance, and promoting the widespread use of RCA in the construction sector.

## ACKNOWLEDGEMENT

This paper is supported by Horizon Europe project Circ-Boost: Boosting the uptake of circular integrated solutions in construction value chains, grant agreement ID: 101082068, DOI: 10.3030/101082068.

## REFERENCES

[1] Moschen-Schimek J., Kasper T., Huber-Humer M. (2023). Critical review of the recovery rates of construction and demolition waste in the European Union – An analysis of influencing factors in selected EU countries. *Waste management*, Volume 167, pp. 150-164. https://doi.org/10.1016/j.wasman.2023.05.020

[2] https://ec.europa.eu/eurostat/, accessed on 27 April 2026.

[3] Zhang C., Hu M., Di Maio F., Sprecher B., Yang X., Tukker A. (2023). An overview of the waste hierarchy framework for analyzing the circularity in construction and demolition waste management in Europe. *Science of Total Environment*, Volume 803, pp. 149892. https://doi.org/10.1016/j.scitotenv.2021.149892

[4] Act relating to planning and the processing of building applications (Planning and Building Act). https://www.regjeringen.no/en/documents/planning-building-act/id570450/, accessed on 21 September 2026.

[5] NS-EN 206:2013+A2:2021+NA:2022. Concrete - Specification, performance, production and conformity, Standard Norge, 2022.

[6] Nováková I., Kekez-Baran S. (2026). Demonstration of a Circular Building Process at Large Scale: Circboost Pilot Project in Norway. In: Daoud, A., Balázs, G.L. (eds) *Concrete and Circular Economy. CCE 2025*. RILEM Bookseries, Volume 63, pp. 3-15. Springer, Cham. https://doi.org/10.1007/978-3-032-06802-6_1

[7] https://single-market-economy.ec.europa.eu/sectors/construction/construction-products-regulation-cpr_en, assessed on 5 May 2026.

[8] NS-EN 12620:2002+A1:2008+NA:2016. Aggregates for concrete. Standard Norge, 2016.

[9] https://circboostproject.eu/, accessed on 5 May 2026.

https://doi.org/10.24867/INDIS-2026-EN-315



# INDIVIDUAL AND COMBINED EFFECTS OF ZEOLITIC TUFF, FLY ASH AND LIMESTONE ON COMPRESSIVE STRENGTH OF REPAIR CEMENT-BASED MORTARS

*Tiana Milović*[1]

***Summary:***

The aim of this paper was to evaluate the individual and combined effects of replacing 20% of ordinary Portland cement with zeolite tuff and/or fly ash, as type II mineral additions, and combination of zeolitic tuff or fly ash with ground limestone, on the compressive strength of repair cement-based mortars, prepared with water-to-binder ratio of 0.5. Following the performance requirements given in SRPS EN 1504-3:2010, the 28-day compressive strength of the tested mortars was determined in accordance with SRPS EN 12190:2010. Based on the obtained results, it was concluded that all investigated mortars met the requirement for structural repair mortar class R4 according to SRPS EN 1504-3:2010 in a term of compressive strength. The use of fly ash alone or in combination with zeolitic tuff or ground limestone gave the highest compressive strengths of repair mortars, respectively. The use of zeolitic tuff alone led to a slight decrease in strength, while in combination with ground limestone the control value was reached.

*Keywords: zeolite, solid waste, mineral addition, filler, SRPS EN 1504-3:2010*

# INDIVIDUALNI I KOMBINOVANI UTICAJI ZEOLITSKOG TUFA, LETEĆEG PEPELA I KREČNJAKA NA ČVRSTOĆU PRI PRITISKU REPARATURNIH MALTERA NA BAZI CEMENTA

***Rezime:***

Cilj ovog rada je da se procene pojedinačni i kombinovani efekti zamene 20% Portland cementa zeolitskim tufom i/ili letećim pepelom, kao mineralnim dodacima tipa II, i kombinacijom zeolitskog tufa ili letećeg pepela sa mlevenim krečnjakom, na čvrstoću pri pritisku reparaturnih maltera na bazi cementa, spravljenih sa vodovezivnim faktorom 0,5. Prateći zahteve za performanse date u SRPS EN 1504-3:2010, čvrstoća pri pritisku ispitivanih maltera nakon 28 dana nege određena je u skladu sa SRPS EN 12190:2010. Na osnovu dobijenih rezultata zaključeno je da svi ispitani malteri ispunjavaju uslov za konstrukcijski reparaturni malter klase R4 prema SRPS EN 1504-3:2010 sa aspekta čvrstoće pri pritisku. Upotreba letećeg pepela samostalno ili u kombinaciji sa zeolitskim tufom ili mlevenim krečnjakom dala je najveće čvrstoće pri pritisku reparaturnih maltera, respektivno. Korišćenje samo zeolitskog tufa dovelo je do blagog smanjenja čvrstoće, dok je u kombinaciji sa mlevenim krečnjakom dostignuta kontrolna vrednost.

*Ključne reči: zeolit, čvrsti otpad, mineralni dodatak, filer, SRPS EN 1504-3:2010*

[1] Research Associate, University of Novi Sad, Faculty of Technical Sciences, Department of Civil Engineering and Geodesy, Novi Sad, Serbia, tiana.milovic@uns.ac.rs, ORCID 0000-0002-3905-7018

## 1. INTRODUCTION

During the 1960s and 1970s, a significant number of reinforced concrete (RC) structures were built across Europe [1]. Considering that notional design working life of building structures and other common structures (e.g. hospitals, schools) according to the SRPS EN 1990:2012 is 50 years, many of them have already reached that point. Therefore, there is a growing demand for innovative sustainable repair solutions that will comply with the following Sustainable Development Goals (SDGs) [2]:

- SDG 09: Industry, Innovation, and Infrastructure - Build resilient infrastructure, promote inclusive and sustainable industrialization and foster innovation,
- SDG 11: Sustainable Cities and Communities - Make cities and human settlements inclusive, safe, resilient and sustainable,
- SDG 12: Responsible Consumption and Production - Ensure sustainable consumption and production patterns as well as
- SDG 13: Climate Action - Take urgent action to combat climate change and its impacts.

To extend the service life of RC structures and infrastructure, different types of repair mortars can be used, such as cement-based mortars containing mineral additives of different origins, which, in addition to environmental advantages, can also have mechanical, physical and durability advantages. Fly ash (FA), a byproduct of coal combustion, acts as an artificial, pozzolanic supplementary cementitious material (SCM). The benefits of using FA as SCM in cement-based repair mortars, are certainly sustainable development, easy availability considering that 200 million tons of FA is deposited in Serbia in landfills with areas of a totally 1,500 hectares [3], and the existence of harmonized European standards for its application. On the other hand, zeolitic tuffs (ZTs) are widely abundant in the world and contain fine microcrystalline zeolite that binds nonzeolitic minerals like clay minerals, feldspars and glasses [4]. Natural zeolites, as volcanic or volcano-sediment materials, have a honeycomb-like structure with extremely small pores and channels that offers large total specific surface, which represents the base of their high pozzolanic reactivity [5]. In Serbia, the largest deposits of ZT, with a zeolite content of over 70%, are Beočin, Igroš, Jablanica 1, Toponica and Zlatokop [6]. Ground limestone (GL) is widely used in cement-based materials and reportedly, can influence their properties by filler, nucleation, dilution and chemical effects [7]. Therefore, this paper deals with the individual and combined effects of ZT and FA as type II mineral additions, and combination of ZT or FA with GL, on the 28-day compressive strength of repair cement-based mortars.

## 2. MATERIALS, MIXTURES AND METHODS

### 2.1. COMPONENT MATERIALS

In order to examine individual and combined effects of ZT and FA as SCMs, as well as mixture of ZT and GL and mixture of FA and GL, on the 28-day compressive strength of the repair cement-based mortars, the following component materials were used:

- Ordinary Portland cement (OPC) CEM I 42.5R (Lafarge-BFC Serbia),
- ZT with particle diameter size less than 125 μm, from the quarry "Igroš-Vidojevići", Fig. 1a (Brus, Serbia),
- FA from Thermal Power Plant "Nikola Tesla B", Fig. 1b (Obrenovac, Serbia),
- GL from "Jelen Do" quarry, Fig. 1c (Požega, Serbia),
- CEN standard sand, in accordance with SRPS EN 196-1:2017, and
- deionized water.



(a) (b) (c)

*Fig. 1 Quarry "Igroš-Vidojevići" [8] (a), TENT B landfill [9] (b) and "Jelen Do" quarry [10](c)*

True densities of OPC (3.126 g/cm$^3$), ZT (2.386 g/cm$^3$), FA (2.313 g/cm$^3$) and GL (2.587 g/cm$^3$) were determined in accordance with SRPS EN 1097-7:2023, while Blaine specific surfaces of OPC (4188.6 cm$^2$/g), ZT (8293.0 cm$^2$/g), FA (10212.5 cm$^2$/g) and GL (3182.2 cm$^2$/g) were obtained in accordance with the procedure specified in standard SRPS EN 196-6:2019. The activity index was determined in accordance with the standard SRPS EN 450-1:2014. After 28 days ZT and FA activity index values were 93% and 125% (> 75%), while after 90 days were 103% and 131% (> 85%), respectively, and therefore, both ZT and FA can be used as type II addition in accordance with SRPS EN 206:2021.

## 2.2. MIXTURES

Compositions of six repair cement/cement-based mortar mixtures are shown in Tab. 1. The first mixture is the control (reference), while in the other mixtures 20% of OPC was replaced by mass, i.e. in these mixtures, the amount of OPC remained constant (of 100% binder 80% is OPC). All mortar mixtures were prepared in accordance with the procedure described in SRPS EN 12190:2010, with water-to-binder ratio of 0.5.

*Tab. 1 Composition of the control and cement-based repair mortar mixtures*

| Component materials | C | ZT20 | FA20 | ZT10FA10 | ZT10GL10 | FA10GL10 |
|---|---|---|---|---|---|---|
| CEM I 42.5 R (g) | 450 | 360 | 360 | 360 | 360 | 360 |
| ZT (g) | - | 90 | - | 45 | 45 | - |
| FA (g) | - | - | 90 | 45 | - | 45 |
| GL (g) | - | - | - | - | 45 | 45 |
| CEN standard sand (g) | 1350 | 1350 | 1350 | 1350 | 1350 | 1350 |
| Deionized water (g) | 225 | 225 | 225 | 225 | 225 | 225 |

## 2.3. METHODS

### 2.3.1. Mineralogical characterization of zeolitic tuff and fly ash

Mineralogical compositions of ZT and FA were identified by XRD analysis (Philips PW1710 device) under the following experimental conditions: monochromatic Cu Kα radiation with 1.5418 Å wavelength in the 5–55° of 2θ range, scan rate 0.02° and 0.5s per step, at a voltage of 40 kV and a current of 30 mA.

### 2.3.2. Compressive strength of cement/cement-based repair mortars

The compressive strength of the mortars was determined according to the standard SRPS EN 12190:2010 using prism-shaped specimens with dimension of 40 × 40 × 160 mm$^3$, at

the age of 28 days, after recommended curing resume (covered with a plastic film to prevent moisture loss, demoulded after 24 h and cured under water at (21 ± 2)°C for 27 days). The mean strength values were determined based on six tests per repair mortar mixture. The load at failure was determined using a hydraulic press with a capacity of 150 kN.

## 3. RESULTS AND DISCUSSION

### 3.1. MINERALOGICAL CHARACTERIZATION OF ZEOLITIC TUFF AND FLY ASH

The X-ray diffractograms of ZT and FA used in the experimental work are shown in Fig. 2 and Fig. 3, respectively. According to the Fig. 2, the main mineral phase of ZT is clinoptilolite, one of the most common, widespread and abundant natural zeolites [11]. Other phases determined in the clinoptilolite-rich ZT are mica group minerals, feldspar, smectite (“swelling” clay mineral), quartz, analcime (a form of natural zeolite with irregular channels [12]) and amphibole.

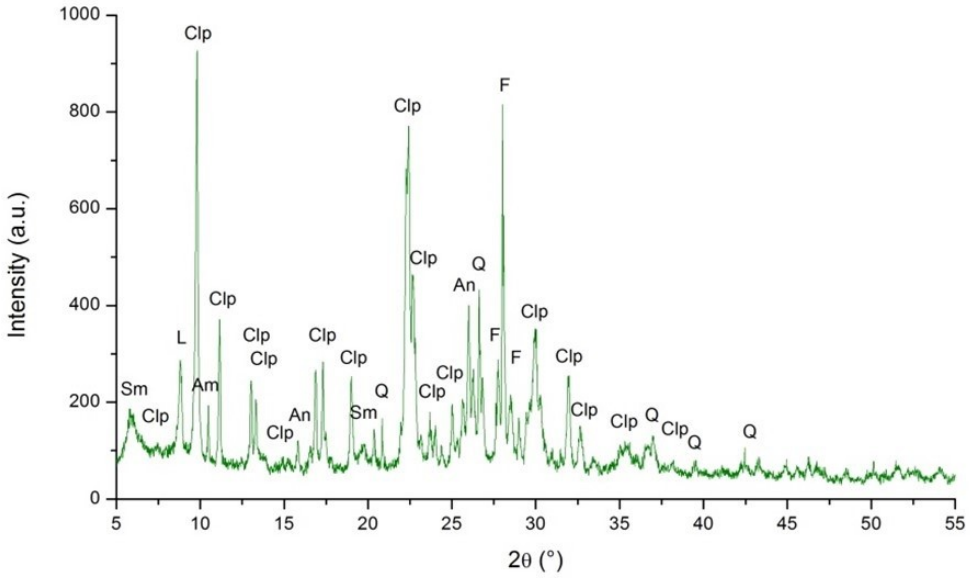


*Fig. 2 X-ray diffractogram of ZT (Clp – clinoptilolite, L – mica group minerals, F – feldspar, Sm – smectite, Q – quartz, An – analcime, Am – amphibole)*

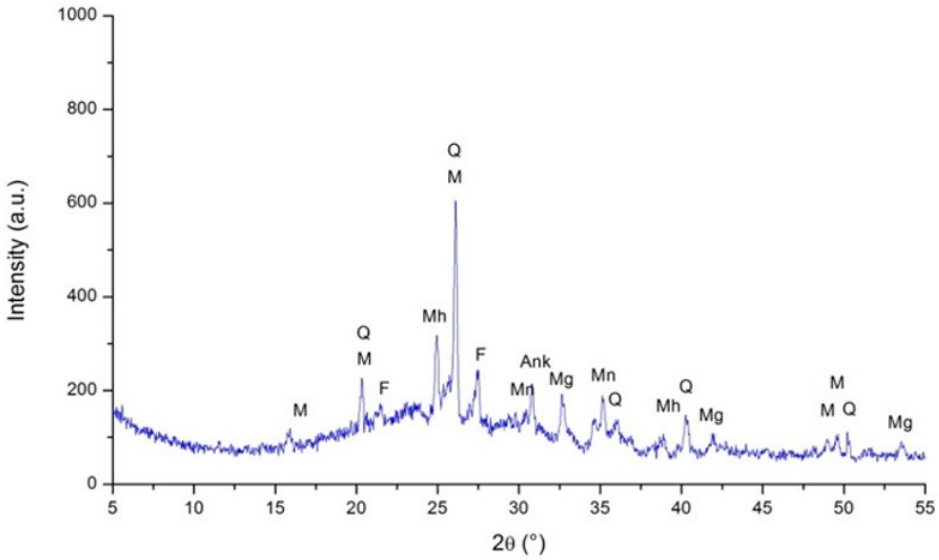


*Fig. 2 X-ray diffractogram of FA (Q – quartz, M – mullite, Mh – melilite, Mn – magnetite, Mg – magnesite, F – feldspar, Ank – ankerite)*

According to the XRD analysis results (Fig. 3) the following minerals are presented in FA sample: quartz, mullite, feldspar, melilite, magnesite, magnetite and ankerite.

## 3.2. COMPRESSIVE STRENGTH OF REPAIR CEMENT/CEMENT-BASED MORTARS

The 28-day compressive strengths of mortars, prepared with water-to-binder ratio of 0.5, containing 0% and 20% of ZT or FA as SCM, and combination of 10% ZT+10% FA, 10% ZT+10% GL, and 10% FA+10% GL, by cement mass, are shown in Fig. 4. Considering that obtained results were higher than 45 MPa, all examined mortars fulfilled the requirement for class R4 (the highest one) of structural repair mortars according to the standard SRPS EN 1504-3:2010 in term of compressive strength determined in accordance with SRPS EN 12190:2010.

The compressive strength range of tested mortars, at the age of 28 days, was from 48.96 MPa to 54.33 MPa. The highest value had mortar containing 20% FA (54.33 MPa), due to the high Blaine specific surface (over 10200 $cm^2/g$), the micro-filler effect of FA spherical particles, and consequently the high activity index value after only 28 days (125%), followed by combinations of 10% ZT+10% FA (53.96 MPa), and 10% FA+10% GL (53.70 MPa), respectively. Therefore, using 20% FA as SCM alone or in combination with ZT or GL gave the highest compressive strengths, respectively, i.e. up to 5% higher than the reference value.

Compared to the control mortar (51.72 MPa), only the mortar containing 20% ZT as SCM (48.96 MPa) had lower strength, by 5.3%. This slight decrease in the compressive strength of the repair mortar after 28 days at 20% OPC replacement level with ZT alone can be attributed to the dilution effect [13], but also to the ZT activity index which was 93% after 28 days.

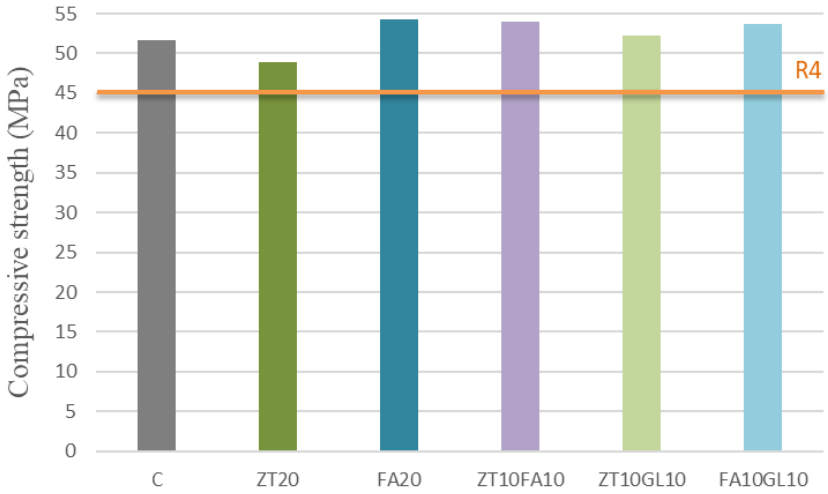


*Fig. 4 The 28-day compressive strength of control and cement-based repair mortars*

On the other hand, the combination of 10% ZT+10% GL reached the strength of the control mortar, which can be explained by the influence of GL on the early hydration rate, the filler effect, and by representing a nucleation site for hydration and pozzolanic reaction products [7], while the combination of 10% ZT+10% FA exceeded the control value by 4.3%.

## 4. CONCLUSION

Based on the obtained experimental results, the following can be concluded:

- The main mineral phase of ZT is clinoptilolite, one of the most abundant natural zeolites in the world. Other phases identified in this clinoptilolite-rich tuff are mica group minerals, feldspar, smectite, quartz, analcime and amphibole,
- FA consists of the following minerals: quartz, mullite, feldspar, melilite, magnesite, magnetite and ankerite,
- FA compared to ZT had a higher Blaine specific surface area and activity index,
- Considering that the range of the 28-day compressive strengths of tested mortars was from 48.96 MPa to 54.33 MPa (higher than 45 MPa), all examined mortars fulfilled the requirement for class R4 (the highest one) of structural repair mortars according to the standard SRPS EN 1504-3:2010 in term of compressive strength determined in accordance with SRPS EN 12190:2010,
- Using only FA as SCM in an amount of 20% led to the highest increase in strength, by ~5%, while using ZT in the same amount led to a decrease in strength by ~5% compared to the control value,
- Using FA as SCM alone or in combination with ZT or GL gave the highest compressive strengths of repair mortars, respectively,
- Although using 20% ZT as SCM alone led to a slight decrease in strength compared to the control value, ZT in combination with FA or GL had a positive effect on the strength, i.e. it increased by ~4% and ~1% (i.e. reached the strength of the control mortar), respectively.

**ACKNOWLEDGEMENT**

This research has been supported by the Ministry of Science, Technological Development and Innovation through Contract No. 451-03-33/2026-03/200156.

## REFERENCES

[1] Wittocx L., Buyle M., Audenaert A., Seuntjens O., Renne N., Craeye B. (2022). Revamping corrosion damaged reinforced concrete balconies: Life cycle assessment and life cycle cost of life-extending repair methods. *Journal of Building Engineering*, Volume 52, 104436, pp. 1-24. https://doi.org/10.1016/j.jobe.2022.104436

[2] United Nations: The 17 Goals. https://sdgs.un.org/goals , accessed on 28 February 2026.

[3] Dragaš J., Marinković S., Ignjatović I., Tošić N. (2014). Properties of high-volume fly ash concrete and its role in sustainable development. *Contemporary achievements in civil engineering*, Subotica, Serbia, pp. 849-858.

[4] Milović T., Rudić O., Furgan S., Radeka M., Malešev M., Radonjanin V., Baloš S., Laban M. (2021). Effects of soft water attack on Portland and natural zeolite blended cements. *Chemical Industry & Chemical Engineering Quarterly*, Volume 27(4), pp. 403-415. https://doi.org/10.2298/CICEQ201120009M

[5] Babak A., Shekarchi M. (2010). Use of Natural Zeolite as a Supplementary Cementitious Material. *Cement and Concrete Composites*, Volume 32(2), pp. 134-141. https://doi.org/10.1016/j.cemconcomp.2009.10.006

[6] Majkić T., Krstić P., Milović T. (2023). Effect of cement and zeolite compound on soil stabilization: A review. *Izgradnja*, Volume 77(5–8), pp. 96-105. UDK: 666.942:549.67

[7] Wang D., Shi C., Farzadnia N., Shi Z., Jia H., Ou Z. (2018). A review on use of limestone powder in cement-based materials: Mechanism, hydration and microstructures. *Construction and Building Materials*, Volume 181, pp. 659–672. https://doi.org/10.1016/j.conbuildmat.2018.06.075

[8] https://zeokop.co.rs/galerija77356/?lang=en , accessed on 23 May 2026.

[9] https://www.ekapija.com/news/4287975/potrebna-firma-za-istovar-uglja-iz-luke-konstanca-na-deponiju-tent-b , photographed by Zdravko Lončar, accessed on 23 May 2026.

[10] https://sr.wikipedia.org/sr-el/Јелен_До , accessed on 23 May 2026.

[11] Rodríguez-Iznaga I., Shelyapina M.G., Petranovskii V. (2022). Ion Exchange in Natural Clinoptilolite: Aspects Related to Its Structure and Applications. *Minerals*, Volume 12, 1628. https://doi.org/10.3390/min12121628

[12] https://www.sciencedirect.com/topics/materials-science/analcime, accessed on 23 May 2026.

[13] Milović T., Šupić S., Malešev M., Radonjanin V. (2022). The Effects of Natural Zeolite as Fly Ash Alternative on Frost Resistance and Shrinkage of Blended Cement Mortars. *Sustainability*, Volume 14, 2736. https://doi.org/10.3390/su14052736

https://doi.org/10.24867/INDIS-2026-EN-322



# AUTOGENOUS HEALING PROPERTY OF LOW-CLINKER CEMENT: THE MICROCRACKS REPAIR EFFICIENCY

*Tiana Milović[1], Olja Šovljanski[2], Miroslav Dramićanin[3], Marko Radenković[4], Ana Tomić[5]*

***Summary:***

To achieve carbon neutrality by 2050, one of the fastest and most effective methods is to reduce the clinker content in cement by replacing it with supplementary cementitious materials and other mineral additions. Besides the environmental, economic and usual performance advantages, these mineral additions are interesting from the aspect of autogenous healing of the cement-based composites. In that regard, this paper deals with the evaluation of autogenous healing efficiency of a cement matrix with a low clinker content, indirectly by testing the compressive strength of specimens after a healing period of 28 days. In addition, SEM-EDX analysis of the hydration and sealing products was performed.

*Keywords: self-healing, low-clinker cement, mineral additions, compressive strength recovery, SEM-EDX, ettringite*

# SVOJSTVO AUTOGENOG ZACELJENJA CEMENTA SA NISKIM SADRŽAJEM KLINKERA: EFIKASNOST SANACIJE PRSLINA

***Rezime:***

Da bi se postigla ugljenična neutralnost do 2050. godine, jedna od najbržih i najefikasnijih metoda je smanjenje sadržaja klinkera u cementu njegovom zamenom dodatnim cementnim materijalima i drugim mineralnim dodacima. Pored ekoloških, ekonomskih i uobičajenih prednosti u pogledu performansi, ovi mineralni dodaci su interesantni sa aspekta autogenog zaceljenja kompozita na bazi cementa. U tom smislu, ovaj rad se bavi procenom efikasnosti autogenog zaceljenja cementne matrice sa niskim sadržajem klinkera, indirektno preko ispitivanja čvrstoće pri pritisku uzoraka nakon perioda zaceljenja od 28 dana. Dodatno je urađena i SEM-EDX analiza produkata hidratacije i zaptivanja.

*Ključne reči:samozaceljenje, cement sa niskim sadržajem klinkera, mineralni dodaci, obnavljanje čvrstoće pri pritisku, SEM-EDX, etringit*

[1] Research Associate, Faculty of Technical Sciences, University of Novi Sad, Novi Sad, Serbia, tiana.milovic@uns.ac.rs, ORCID 0000-0002-3905-7018
[2] Research Associate, Faculty of Technology Novi Sad, University of Novi Sad, Novi Sad, Serbia, oljasovljanski@uns.ac.rs, ORCID 0000-0002-9118-4209
[3] Assistant Professor, Faculty of Technical Sciences, University of Novi Sad, Novi Sad, Serbia, dramicanin@uns.ac.rs, ORCID 0000-0002-9079-0864
[4] Research Assistant, BioSense Institute, University of Novi Sad, Novi Sad, Serbia, marko.radenkovic@dbe.uns.ac.rs, ORCID 0000-0002-0708-2454
[5] Assistant Professor, Faculty of Technology Novi Sad, University of Novi Sad, Novi Sad, Serbia, anav@uns.ac.rs, ORCID 0000-0002-6338-342X

## 1. INTRODUCTION

The cement industry causes 8% of all anthropogenic $CO_2$ emissions (Fig. 1), while the production of clinker alone accounts for approximately 90% of emissions from Ordinary Portland Cement (OPC) [1]. At the same time, according to the European Green Deal [2] the goal is to reduce emissions by at least 55% by 2030, while a 90% reduction is proposed for 2040, with a legally binding target of neutrality by 2050 through the European Climate Law [3]. Therefore, the development of low-carbon cement and low-clinker cement (LCC) is crucial according to the European Green Deal and global climate targets. LCC has reduced clinker content, and increased content of supplementary cementitious materials (SCMs) and other mineral additions. Ground granulated blast furnace slag, fly ash and ground limestone are most commonly used for this purpose. Schöler et al. [4] investigated the interactions between OPC, blast furnace slag, siliceous fly ash and limestone powder in quaternary cements with high clinker replacement level of 50 % by weight, and obtained that the types of hydrates presented in the quaternary blends were similar to those in OPC matrix. However, there were some differences in the volume of hydrates, less portlandite was present in blended OPC matrix, while more C-S-H gel and AFm phases were observed.

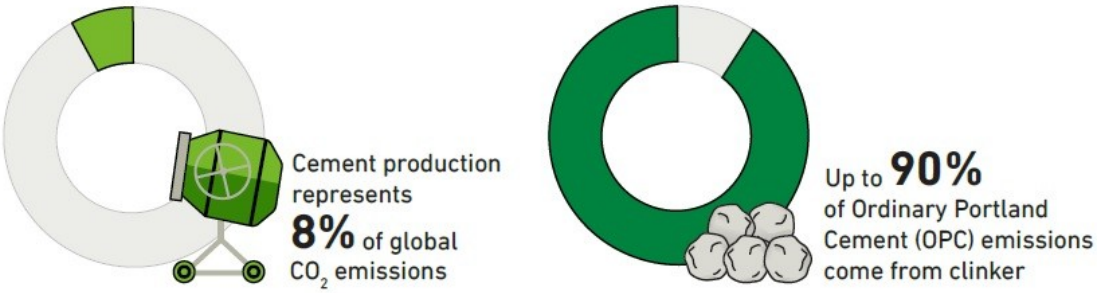


*Fig. 1 Highlights on $CO_2$ emission that comes from Ordinary Portland Cement production* [1]

On the other hand, extending the service life of reinforced concrete structures and infrastructure has become a priority. Given that LCC contains up to 50% alternative mineral additions, it has the prerequisites for autogenous healing of microcracks that occur for various reasons (i.e. plastic, autogenous and drying shrinkage, thermal stress, mechanical loading, differential settlement, and various other damage mechanisms [5]). Cracks represent a fundamental durability issue, because even microcracks can act as preferential pathways for water and aggressive ions, accelerating concrete degradation and reinforcement corrosion [6]. While cracks up to 970 μm in width can be autonomously healed [7] [8] [9], microcracks can also be autogenously healed. The mechanism of autogenous healing refers to recovery processes that rely on components naturally present in the cement-based composite, i.e. its own generic materials [10]. Autogenous healing methods include the application of the mineral additives, fibers, nanofillers and curing agents. Suleiman and Nehdi [5] investigated the influence of autogenous crack self-healing in Portland cement-based mortars, on its mechanical strength recovery under various exposure environments, and discovered that (i) the exposure condition plays a crucial role in the mechanical strength recovery process, (ii) the water submersion condition achieved the best strength recovery, particularly for specimens incorporating fly ash, and (iii) specimens incorporating limestone microfiller achieved the best crack healing ability in terms of crack filling and closing.
Therefore, the aim of the research presented in this paper was to evaluate the autogenous healing efficiency of the LCC matrix submerged in tap water, that is, to evaluate the

success of microcrack (through-crack) repair after a healing period of 28 days via compressive strength recovery, while scanning electron microscopy with energy dispersive X-ray spectroscopy (SEM–EDX) was used to determine the hydration and sealing products.

## 2. MATERIALS, SPECIMEN PREPARATION AND METHODOLOGY

### 2.1. COMPONENT MATERIALS

In order to evaluate the autogenous healing ability of LCC matrix, the following component materials were used to prepare the specimens:

- Low-clinker cement (LCC) from a manufacturer in Serbia, containing a mix of ground granulated blast furnace slag, fly ash and ground limestone as a clinker replacement up to 50% by mass,
- deionized water.

### 2.2. SPECIMEN PREPARATION

A batch of specimens were prepared in accordance with the procedure described in SRPS EN 196-1:2017 [11], using 450 g of LCC and 225 g of deionized water (water-to-cement ratio of 0.5). The mixing was performed in a mortar mixer. The homogenized LCC paste was cast into cube molds (measuring 10 mm on each side), which were then slightly vibrated for the removal of unwanted entrapped air from the fresh paste. The filled molds were covered with a plastic film to prevent moisture loss and left for 24 h to set in a moisture cabinet. After the initial 24 h, the specimens were de-molded and transferred to the containers for further curing underwater (tap water was used) at (20 ± 1) ˚C until the age of 90 days.

### 2.3. METHODOLOGY

For the purposes of the research presented in this paper, after 90 days of curing, a total of 16 LCC matrix specimens were removed from the water. The first 6 specimens were used for determination of the 90-day compressive strength. Each of them was placed between the platens of the Universal testing machine ZDM 5/91 (WPM, Leipzig, Germany) with a range of 25 kN, and tested.

The remaining 10 specimens were stored for 7 days in standard laboratory conditions, at a temperature of (21 ± 2) ˚C and a relative humidity of (60 ± 10) %, then they were cut in half using a sharp steel blade (placed in the middle of the upper base of the specimen) under the pressure. Furthermore, the specimens were assembled using silicone rubber bands, the crack (i.e. through-crack) widths were measured, and they were put in fresh tap water for autogenous healing during the next 28 days. To monitor the crack sealing, specimens were taken out of the water and photographed every 7 days. After 28 days of self-healing of the through-cracked LCC matrix specimens (SH CR LCC), all repaired specimens (i.e. specimens with the merged halves) were tested (the position of the specimen during testing is shown in Fig. 2) and the mean value of the compressive strength was determined.

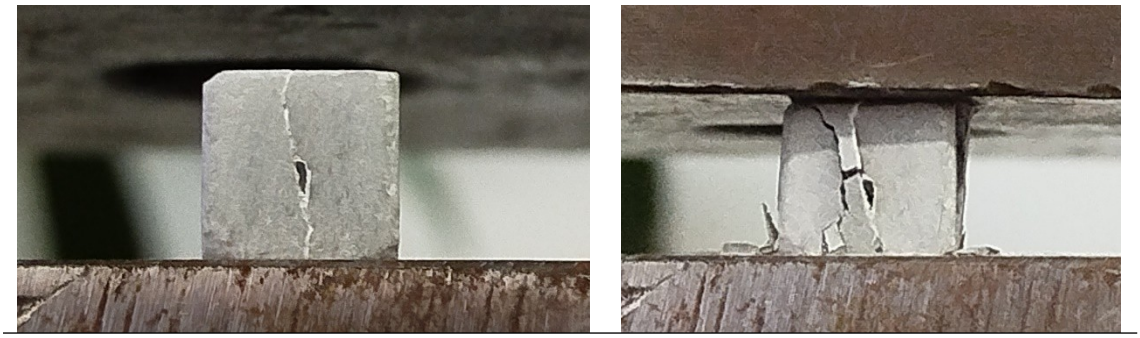

(a) (b)

*Fig. 2 SH CR LCC specimen before (a) and after (b) the compressive strength testing*

After the compressive strength testing, a sample containing both the self-healed part and the basic material was taken and further submitted for scanning electron microscopy with energy dispersive X-ray spectroscopy (SEM–EDX), using Apreo 2 C Scanning Electron Microscope equipped with ChemiSEM Technology (SEM, Thermo Fisher Scientific, Waltham, MA, USA), Fig. 3.



(a) (b)

*Fig. 3 Sample taken after the compressive strength testing of SH CR LCC (a) and submitted for SEM-EDX analysis (b)*

SEM imagine of the surface was taken at a beam acceleration of 5 kV, while an acceleration of 10 kV was used for EDX analysis which consisted of sample mapping and specific spot analysis.

## 3. RESULTS AND DISCUSSION

### 3.1. 90-DAY COMPRESSIVE STRENGTH OF LCC MATRIX

After 90 days of standard curing resume, the reference compressive strength of LCC matrix (the whole cube shape specimens with edge of 10 mm) was 41.39 ±2.54 MPa. Considering that this type of cement contains a large proportion of mineral additives, it was deliberately kept underwater up to 90 days, so that one of the resulting products of cement hydration, calcium hydroxide, could react with pozzolans and create additional amounts of C-S-H gel in order to get a more realistic picture of self-healing capacity of LCC matrix further on.

### 3.2. VISUAL OBSERVATIONS DURING 28 DAYS OF AUTOGENOUS HEALING OF MICROCRACKS

The initial crack widths of total of 10 CR LCC specimens were measured before they were put in fresh tap water for autogenous healing during the 28 days. Considering that all

cracks had widths less than 0.3 mm, they were classified as microcracks, although sometimes during the splitting of specimen, minor local surface damage also occurred (Fig. 4).

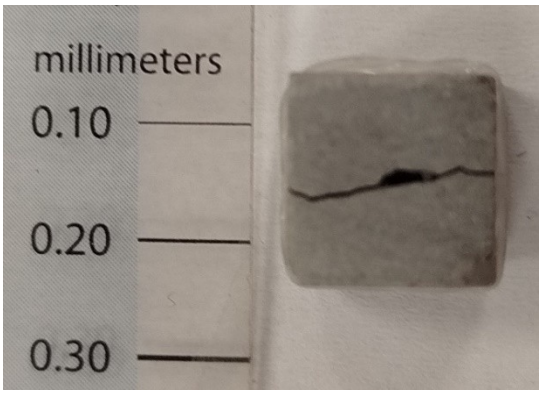


*Fig. 4 Measuring the width of the crack before starting the autogenous healing process*

To monitor the microcrack sealing, specimens were taken out of the water and photographed every 7 days (Fig. 5). As can be seen from Fig. 5a, significant microcrack filling has already occurred in the first seven days. The process of additional sealing of the microcrack was clearly visible for up to 14 days, after which minor shifts were visible based on the recorded images (Fig. 5c and Fig. 5d).

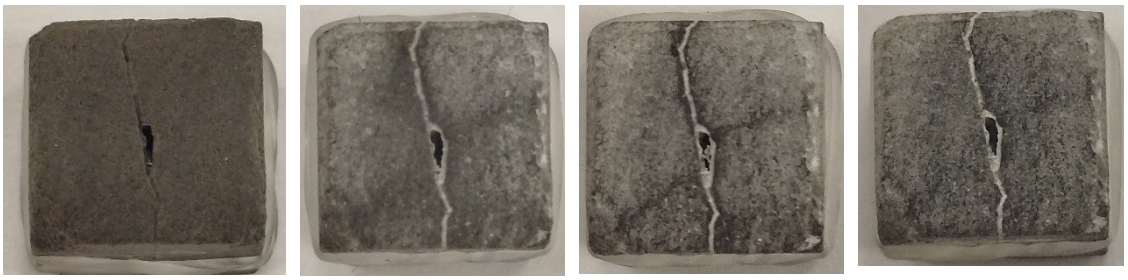

(a) (b) (c) (d)

*Fig. 5 Monitoring of the microcrack sealing progression in LCC matrix by camera after 7 (a), 14 (b), 21(c) and 28 (d) days of autogenous healing*

After 28 days of self-healing, the SH CR LCC matrix specimens were removed from the water, photographed, and then the silicone rubber bands were removed. In the case of all 10 specimens, the two halves were merged.

## 3.3. EFFICIENCY ASSESSMENT OF AUTOGENOUS HEALING OF MICROCRACKS VIA COMPRESSIVE STRENGTH RECOVERY

To evaluate the efficiency of autogenous healing of the through-cracked LCC matrix, the compressive strengths of all 10 SH CR LCC matrix specimens were determined. Given that the mean value was 30.63 ± 4.46 MPa, the recovery of the SH CR LCC matrix specimens after 28 days of self-healing was 74% compared to the reference 90-day compressive strength of the whole LCC matrix specimens (i.e. non-cracked ones). It can also be observed that the standard deviation was significantly higher in the case of self-repaired specimens, even though a larger number of specimens were examined (Fig. 6).

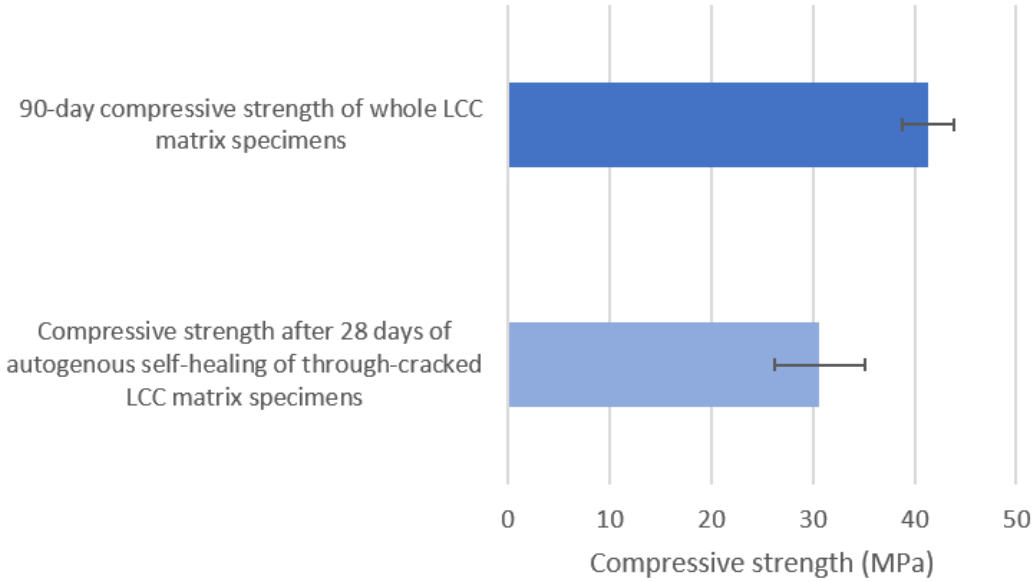


*Fig. 6 Compressive strengths of whole LCC matrix specimens after 90 days of curing, and SH CR LCC matrix specimens after 28 days of autogenous healing*

## 3.4. SEM-EDX OF AUTOGENOUSLY HEALED THROUGH-CRACKED LOW-CLINKER CEMENT MATRIX

After the compressive strength testing, a sample containing both the self-healed part and the basic material was taken and further submitted for SEM–EDX analysis, including ChemiSEM Technology (Fig. 7) to evaluate the microstructural morphology and elemental composition of mineral deposits inside repaired microcrack as well as in LCC matrix itself.

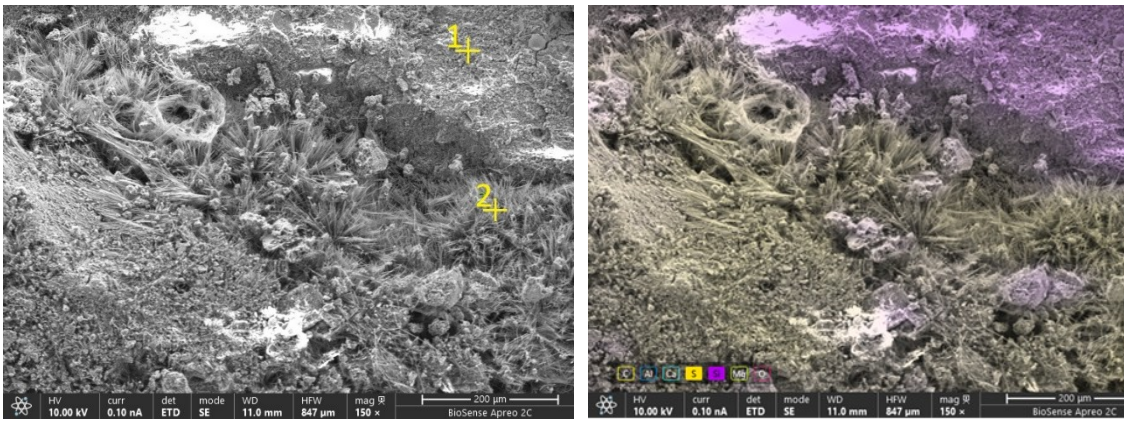


(a) (b)

*Fig. 7 SEM image with marked Points 1 (in basic material) and 2 (in the sealed-crack area) for EDX (a) and ChemiSEM image (b) of SH CR LCC matrix after compressive strength testing*

Based on the morphology of the crystals that sealed the microcrack (Fig. 7a), it can be assumed that this needle-like crystals are ettringite. According to the EDX analysis of Point 2, the present of sulfur is conformed (Tab. 1), while its distribution is in line with the sealed-crack area (marked in yellow at Fig. 7b).

*Tab. 1 Atomic percentages of elements in Points 1 and 2*

| Element | Atomic (%) | |
|---|---|---|
| | Point 1 | Point 2 |
| C | 5.8 | 3.2 |
| O | 69.6 | 70.3 |
| Mg | 0.1 | 0.0 |
| Al | 2.6 | 4.0 |
| Si | 6.8 | 0.4 |
| S | 0.3 | 5.2 |
| Ca | 14.8 | 16.9 |

On the other hand, the right upper half of Fig. 7a shows a denser, amorphous structure (C-S-H gel) from which border the ettringite crystals erupt into the initially cracked zone. Furthermore, the ChemiSEM image (Fig. 7b) highlights the dominant presence of silicon in that area, i.e. in LCC matrix, which is confirmed by the results of the EDX analysis in Point 1 (Tab. 1).

## 4. CONCLUSION

In this study, the effect of autogenous microcrack healing in low-clinker cement (LCC) matrix on its compressive strength recovery after 28 days of immersion in tap water was investigated. Based on the experimental findings and insights, the following concluding remarks can be drawn:

- The reference compressive strength of LCC matrix (the whole cube shape specimens with edge of 10 mm) was 41.39 ±2.54 MPa after 90 days of standard curing resume;
- The initial crack widths of total of 10 through-cracked LCC matrix specimens were less than 0.3 mm, and therefore they were classified as microcracks;
- A significant microcrack sealing has already occurred in the first seven days of the autogenous healing process;
- After 28 days of the self-healing of the through-cracked LCC matrix specimens, all repaired specimens (i.e. specimens with the merged halves) were tested and the mean value of the compressive strength was 30.63 ± 4.46 MPa;
- The recovery of the self-healed through-cracked LCC matrix specimens after 28 days was 74% compared to the reference 90-day compressive strength of the whole LCC matrix specimens. Moreover, the standard deviation was significantly higher in the case of self-repaired specimens, even though a larger number of specimens were examined;
- According to SEM-EDX analysis, the microcracks were mostly sealed by ettringite, while the LCC matrix had an amorphous structure (C-S-H gel) from whose boundary ettringite crystals begin to emerge into the initially cracked zone.

Based on the obtained results, LCC showed the potential for autogenous healing, but additional research is needed, especially regarding the influence of different exposure conditions on the efficiency of microcrack self-healing and the composition of the mineral deposits that fill the cracked zone.

## ACKNOWLEDGEMENT

This research has been supported by the Ministry of Science, Technological Development and Innovation (Contracts No. 451-03-33/2026-03/200156 (T.M.), 451-03-33/2026-03/200134 (O.Š.), 451-03-34/2026-03/200156 (M.D.), 451-03-33/2026-03/200358 (M.R.), and 451-03-34/2026-03/200134 (A.T.)) and the Faculty of Technical Sciences, University of Novi Sad through project "Scientific and Artistic Research Work of Researchers in Teaching and Associate Positions at the Faculty of Technical Sciences, University of Novi Sad 2026" (No. 01-3609/1).

## REFERENCES

[1] Decoding Industrial Decarbonization: Standards for Building a Low-Carbon and Low-Clinker Future. https://decarbonization.unido.org/wp-content/uploads/2025/09/lc3-explainer_final.pdf , accessed on 12 August 2026.

[2] The European Green Deal. https://commission.europa.eu/strategy-and-policy/priorities-2019-2024/european-green-deal_en , accessed on 12 August 2026.

[3] REGULATION (EU) 2021/1119 OF THE EUROPEAN PARLIAMENT AND OF THE COUNCIL of 30 June 2021 establishing the framework for achieving climate neutrality and amending Regulations (EC) No 401/2009 and (EU) 2018/1999 ('European Climate Law'). https://eur-lex.europa.eu/legal-content/EN/TXT/PDF/?uri=CELEX:32021R1119 , accessed on 12 August 2026.

[4] Schöler A., Lothenbach B., Winnefeld F., Zajac, M. (2015). Hydration of quaternary Portland cement blends containing blast-furnace slag, siliceous fly ash and limestone powder. *Cement & Concrete Composites*, Volume 55, pp. 374–382. http://dx.doi.org/10.1016/j.cemconcomp.2014.10.001

[5] Suleiman A.R., Nehdi M.L. (2021). Effect of autogenous crack self-healing on mechanical strength recovery of cement mortar under various environmental exposure. *Scientific Reports*, Volume 11, 7245. https://www.nature.com/articles/s41598-021-86596-2

[6] Mejić L., Šovljanski O., Pezo M., Pezo L., Milović T., Tomić A. (2026). Ready-to-Use or Ready-to-Adapt: Can the Self-Healing Potential of *Bacillus licheniformis* Be Modified? *Bioengineering*, Volume 13(5), 495. https://doi.org/10.3390/bioengineering13050495

[7] Wang J.Y., Soens H., Verstraete W., De Belie N. (2014). Self-healing concrete by use of microencapsulated bacterial spores. *Cement and Concrete Research*, Volume 56, pp. 139-152. https://doi.org/10.1016/j.cemconres.2013.11.009

[8] Milović T., Bulatović V., Pezo L., Dramićanin M., Tomić A., Pezo M., Šovljanski O. (2024). Enhancing Compressive Strength of Cement by Indigenous Individual and Co-Culture Bacillus Bacteria. *Materials*, Volume 17(20), 4975. https://doi.org/10.3390/ma17204975

[9] Šovljanski O., Pezo L., Milović T., Pezo M., Radenković M., Mejić L., Bulatović V., Dramićanin M., Tomić A. (2026). Bio-intelligent approach for rapid healing of cracks via artificial neural network-optimized urban bacterial consortium. *Journal of Building Engineering*, Volume 117, 114851. https://doi.org/10.1016/j.jobe.2025.114851

[10] Mirjanić J., Milović T., Bulatović V., Šovljanski O., Džolev I. (2025). Self-healing concrete: materials and mechanisms. *XXIX Congress DIMK and X Congress SIGP with International Symposium on Researching and Application of Contemporary Achievements in Civil Engineering in the Field of Materials and Structures*, Society for materials and structures testing of Serbia, Association of contemporary industry of clay products of Serbia, and Institute for materials testing -IMS institute, Sokobanja, Serbia, 21-23 May, pp. 156-167.

[11] SRPS EN 196-1:2017 - Methods of testing cement - Part 1: Determination of strength.

https://doi.org/10.24867/INDIS-2026-EN-330



# MIX DESIGN OF SLAG MORTARS ACTIVATED BY SUNFLOWER HUSK ASH AND SODIUM SILICATE FOR TARGET COMPRESSIVE STRENGTH

*Olivera Bedov[1], Suzana Draganić[2], Marijana Serdar[3]*

***Summary:***

Sunflower husk ash (SHA) is a waste material, rich in potassium, which is why it can be used as an alkali source instead of conventional chemicals for the production of alkali-activated materials. This paper presents the results of ground granulated blast furnace slag (GGBFS) activation with SHA and commercial sodium silicate solution at the mortar level, as a preliminary step towards developing mix designs for workable concrete in the target strength classes C30/37 and C35/45. Mortars with two silicate moduli, 0.22 and 0.42, were investigated at two water-to-binder ratios, 0.45 and 0.50, to address the workability limitations of the reference mixes, activated only with SHA. The incorporation of sodium silicate solution improved both the fresh-state and hardened properties of the mortar. The attained 28-day compressive strengths of 38.9-56.0 MPa support the development of concrete mix designs targeting strength classes C30/37 and C35/45.

*Keywords: alkali-activated materials, sunflower husk ash, alternative activator, valorisation, mix design, low-carbon concrete*

# PROJEKTOVANJE SASTAVA MALTERA NA BAZI ZGURE AKTIVIRANE PEPELOM SUNCOKRETOVE LJUSKE I NATRIJUM-SILIKATOM U FUNKCIJI CILJANE ČVRSTOĆE PRI PRITISKU

***Rezime:***

Pepeo suncokretove ljuske je otpad bogat kalijumom, zbog čega je pogodan kao zamena konvencionalnih hemikalijama za proizvodnju alkalno-aktiviranih materijala. U radu su prikazani rezultati ispitivanja granulisane zgure visokih peći (GGBFS) aktivirane pepelom suncokretove ljuske (SHA) i komercijalnim rastvorom natrijum-silikata na nivou maltera, kao preliminarni korak ka razvoju sastava mešavina obradivog betona ciljanih klasa čvrstoće C30/37 i C35/45. Ispitane su mešavine sa dva silikatna modula, 0,22 i 0,42, pri dva vodovezivna odnosa, 0,45 i 0,50, kako bi se prevazišla ograničena obradivost referentnih mešavina aktiviranih isključivo SHA. Uvođenje rastvora natrijum-silikata poboljšalo je svojstva maltera u svežem i očvrslom stanju. Ostvarene čvrstoće pri pritisku nakon 28 dana, u rasponu od 38,9 do 56,0 MPa, predstavljaju osnovu za razvoj sastava mešavina betona ciljanih klasa čvrstoće C30/37 i C35/45.

*Ključne reči: alkalno-aktivirani materijali, pepeo suncokretove ljuske, alternativni aktivator, valorizacija, projektovanje sastava, beton sa niskim ugljeničnim otiskom*

[1] Teaching Assistant, Ph.D., Faculty of Technical Sciences, University of Novi Sad, Trg Dositeja Obradovića 6, Novi Sad, Serbia, olivera.bukvic@uns.ac.rs, ORCID 0000-0001-8910-1630
[2] Asst. Professor, Faculty of Technical Sciences, University of Novi Sad, Trg Dositeja Obradovića 6, Novi Sad, Serbia, suzanav@uns.ac.rs, ORCID 0000-0003-3803-3484
[3] Assoc. Professor, Faculty of Civil Engineering, University of Zagreb, Fra Andrije Kačića-Miošića 26, Zagreb, Croatia, marijana.serdar@grad.unizg.hr, ORCID 0000-0001-8386-7272

## 1. INTRODUCTION

The cement industry is responsible for approximately 7% of global anthropogenic $CO_2$ emissions [1]. As increasing urbanisation worldwide results in a continuous rise in the demand for concrete [2], development of alternative binders with reduced cement clinker content is one of the priorities within emission reduction strategies up to 2050 [1].

Alkali-activated materials (AAMs) are binders synthesised through the reaction of aluminosilicate precursors with alkaline activators. Industrial by-products such as ground granulated blast furnace slag (GGBFS) and fly ash (FA) from coal-fired power plants, as well as metakaolin (MK), are usually used as precursors. Alkali activation reaction is initiated by the activators, alkali hydroxides, silicates, sulfates and/or carbonates. They catalyse the dissolution of silicon and aluminium from the precursor, enabling their polymerisation and the formation of the reaction products [3].

Depending on the dosage, chemical and physical properties of the precursor and activators, AAMs can exhibit comparable or superior performance to PC concrete, while having 40 to 60% lower $CO_2$ emissions as they do not contain cement [4].

The most widely used activators in both the literature and practice are sodium-based, because of their lower cost and wider availability, compared to potassium activators [5,6]. Hydroxide activators alone are rarely used in the practical preparation of AAM concretes - they are most often combined with silicates [5]. The combined activators result in better mechanical and durability properties. In addition to alkalis, they provide soluble $SiO_2$, which participates directly in the formation of the reaction products. Additionally, using silicate activators improves the workability of AAMs, since the reliable superplasticisers designed specifically for the high pH of the AAMs are not available in the market yet [20]. Besides alkali content, the most important mix design parameter for these AAMs is silicate modulus (Ms). It represents the molar ratio of silicon n($SiO_2$) to alkalis n ($Na_2O$ or $K_2O$) in the mixture. For basic slags, the literature proposes the use of Ms between 0.6 and 1.5, with Ms=1 being the optimum to attain satisfactory fresh and hardened-state properties [7].

However, the environmental advantage of AAMs is diminished precisely by the use of conventional chemical activators (NaOH, KOH, sodium silicate). Their production is energy-intensive and generates significant emissions [4,8]. Although alkali hydroxides typically account for only 1-5% and alkali silicates for 3-10% of AAM mass, their share of the total global warming potential of AAMs is 13-33% [9]. For this reason, the valorisation of waste materials as alternative alkali and silica sources has become one of the significant research directions in AAM technology [10–13].

Biomass ashes have been recognised as particularly suitable for this purpose, due to high content of potassium, calcium and silicon [14]. Biomass-fired power plants worldwide generate 480 million tonnes of ash annually [15], while it is estimated that biomass, as an alternative energy source, could replace 33-50% of global energy demand by 2050 [16]. Although a considerable share of this quantity is still landfilled, a growing body of research shows that biomass ashes can find valuable applications in a range of fields, as well as a sustainable material in the construction industry [16]. The literature to date has shown that AAMs activated with agricultural biomass ashes such as rice husk ash [17], olive ash [18–20], almond shell ash [21,22], hazelnut shell ash [23], coffee husk ash [24] can achieve strengths comparable to or higher than those activated with conventional hydroxides.

On the local level, in the Autonomous Province of Vojvodina, Serbia, approximately 196,759.0 tonnes of various agricultural biomass ashes are generated annually through

the combustion of biomass in power plants and in the processing industry [25]. Sunflower oil producers and the combined heat and power plant in Sremska Mitrovica use sunflower husks as fuel, thereby generating significant quantities of sunflower husk ash (SHA). According to data from the edible oil producer Victoria Oil from Šid and the combined heat and power plant in Sremska Mitrovica, 960 tonnes of SHA are landfilled annually [25].

SHA is highly rich in potassium [26] and it can be used in AAM technology as an alternative alkali source, instead of NaOH and KOH [17,27,28]. The use of SHA as a substitute for conventional hydroxide activators opens up the possibility of developing sustainable AAMs that are aligned with the principles of the circular economy - with no waste generation, short transport chains, and upscaling of local agricultural waste to a construction material [29].

The activation of GGBFS by locally available SHA has been established in the authors' previous work [26,30] on mortars with quartz sand. The binder was optimised by assessing the influence of the SHA content, the curing regime, and the mixing procedure on the hydration products, the workability, and the compressive strength [26]. The efficiency of SHA as an activator was compared to conventional hydroxides, where mortar samples reached a compressive strength of 55 MPa, compared to approximately 35 MPa for the samples activated with KOH and NaOH [30]. In these studies, SHA was used as the sole activator.

This paper presents the results of GGBFS activation with SHA and commercial sodium silicate solution at the mortar level, as a preliminary step towards developing mix designs for workable concrete in the target strength classes C30/37 and C35/45. Six mortar mixes containing crushed limestone aggregate (0-4 mm) were designed. The investigated parameters were the water-to-binder ratio (w/b; 0.45 and 0.50), activator type (SHA or a combination of SHA and sodium silicate), and activator content. In addition to the complete replacement of alkali hydroxides with SHA, the study proposes the use of substantially reduced sodium silicate contents, corresponding to Ms values of 0.42 and 0.22 rather than 1, to avoid compromising the sustainability of AAMs. The influence of these parameters was assessed by determining workability, compressive strength, and flexural strength after 7 and 28 days of curing.

## 2. EXPERIMENTAL PROGRAMME

### 2.1. MATERIALS

GGBFS provided by Lafarge Serbia was used as the precursor for the preparation of the mortar mixes. It was ground in a ball mill to a specific surface area of S = 517.8 m²/kg. The SHA was collected at Victoria Oil (Šid, Serbia) and used as an alkaline activator without any pre-treatment, with a specific surface area of S = 610 m²/kg. The chemical composition of the GGBFS and the SHA, determined by X-ray fluorescence spectroscopy (XRF), is presented in Tab. 1.

The commercial sodium silicate Geosil 34417 (Woellner, Germany) was used as the second component of the combined activator, with a molar ratio of 1.7 and a chemical composition of $Na_2O$ = 16.7%, $SiO_2$ = 27.5%, $H_2O$ = 55.8%.

The 0-4 mm fraction of crushed limestone aggregate produced by Iva Agrar (Ostreš quarry, Serbia) was used in all mixtures.

*Tab. 1 Chemical composition of GGBFS and SHA determined by XRF*

| Material | Oxide [%] | | | | | | | |
|---|---|---|---|---|---|---|---|---|
| | $SiO_2$ | CaO | $Al_2O_3$ | $Fe_2O_3$ | MgO | $SO_3$ | $K_2O$ | $Na_2O$ |
| GGBFS | 38.69 | 37.19 | 9.51 | 0.47 | 10.52 | 2.17 | 0.83 | 0.41 |
| SHA | 1.75 | 14.29 | 0.59 | 0.21 | 10.46 | 13.53 | 38.00 | 0.07 |

## 2.2. MIX DESIGN

Six mortar mixtures were designed, all with a constant GGBFS content of 400 g and a constant aggregate-to-binder ratio of 3. Their mix design is presented in Tab. 2.
The reference mix, denoted A, was activated with 25% of SHA by mass of GGBFS. This content was selected as an optimum for SHA-activated slag, based on the authors' previous work.
Sodium silicate was introduced as a second activator in two other mixes. The first one combined 25% of SHA with commercial sodium silicate solution to obtain Ms of 0.42 (mix B). The second mix was activated with 15% of SHA and had Ms of 0.22 (mix C). The two Ms were also selected based on the previous work of the authors on targeted compressive strength classes of alkali-activated slag concrete, activated with conventional activators, i.e., sodium hydroxide and sodium silicate [31].
Between the two dosages, both the ash and the silicate content change, and not in the same proportion, so the two mixtures represent two activator dosages with different silicate moduli rather than a single-variable series.
Each of the three described mixes, A, B, and C, was prepared at two w/b ratios, 0.45 and 0.50. The mixtures are designated by the letter of the activator system followed by the w/b ratio, e.g., A-0.45. The w/b ratio was calculated as the ratio of the total water to the total amount of binder, where the water comprises the water from the sodium silicate solution and the added water, and the binder comprises the sum of GGBFS and the solid component of the activator ($K_2O$ in SHA, and $Na_2O$ and $SiO_2$ in sodium silicate). The insoluble fraction of the ash was included in the total amount of aggregate.

*Tab. 2 Composition of the mortar mixtures (Geosil = sodium silicate Geosil 34417, Water = added water)*

| Mix | GGBFS [g] | SHA [g] | Geosil [g] | Water [g] | Agg. 0-4 [g] | Ms | w/b |
|---|---|---|---|---|---|---|---|
| **A-0.45** | 400 | 100 | - | 200 | 1281 | - | 0.45 |
| **A-0.50** | | 100 | - | 223 | 1281 | - | 0.50 |
| **B-0.45** | | 100 | 20.7 | 180 | 1308 | 0.42 | 0.45 |
| **B-0.50** | | 100 | 20.7 | 201 | 1308 | 0.42 | 0.50 |
| **C-0.45** | | 60 | 5.6 | 182 | 1256 | 0.22 | 0.45 |
| **C-0.50** | | 60 | 5.6 | 203 | 1256 | 0.22 | 0.50 |

## 2.3. MIXING PROCEDURE, SAMPLE CASTING AND CURING

The reference mortars activated with SHA were prepared by one-part alkali activation, in which the GGBFS and the SHA were first blended manually, followed by the addition of aggregate. The dry constituents were then added to the water, homogenised manually, and mixed in a mortar mixer for 5 minutes.
Mortars B and C were mixed as a combination of the one-part and two-part procedures. The GGBFS, SHA, and aggregate were manually homogenised, followed by the addition of water and mixing in a mortar mixer for 2 minutes. Sodium silicate was subsequently added, and mixing continued for a further 3 minutes, giving a total mixing time of 5 minutes.
All mortars were cast into metal moulds (40 × 40 × 160 mm), which were wrapped in polymeric film, and demoulded after 24 hours. The specimens were then rewrapped and cured at ambient temperature until testing.

## 2.4. TESTING METHODS

The consistency of the fresh mortar mixtures was determined by measuring the flow diameter in accordance with the standard SRPS EN 1015-3:2008 [32], using the flow table method.
The compressive and flexural strengths were determined after 7 and 28 days of curing, on three specimens each, in accordance with the standard SRPS EN 196-1:2017 [33].

# 3. RESULTS AND DISCUSSION

## 3.1. WORKABILITY

The measured flow diameters are presented in Fig. 1. The reference mixes activated with SHA are the stiffest of the series, with flow diameters of 119 mm at w/b = 0.45 and 133 mm at w/b = 0.50. Systems A and B provide the controlled comparison: they contain the same amount of ash and differ only by the addition of sodium silicate; the flow increases from 119 to 127 mm at w/b = 0.45 and from 133 to 160 mm at w/b = 0.50. The sodium silicate improved the workability of the fresh mortar, which was more pronounced at the higher water content. The same behaviour has been reported for alkali-activated systems with conventional activators [7] where the fluidifying effect of the sodium silicate is likewise more pronounced at higher w/b ratio. This suggests that replacing the alkali hydroxide with SHA does not change the mechanism by which the silicate affects the workability.
Mixtures B and C reached practically the same flow, 127 mm against 127 mm at w/b = 0.45 and 160 mm against 158 mm at w/b = 0.50. These results are consistent with the two contributions offsetting each other: the higher ash content of B increases the water demand of the mixture, while its higher silicate content acts in the opposite direction. The w/b ratio remains the dominant parameter, but the mixes respond to it differently. Increasing w/b ratio from 0.45 to 0.50 raised the flow of the reference mixture by only 14 mm, against 31 mm and 33 mm for the two combined-activator mixtures. In the SHA-only system, the added water is therefore less effective at increasing the flow. This is consistent with the high water demand of the insoluble fraction of the ash and of the crushed aggregate, and with the absence of the dissolved silicate anions, which have a plasticising effect in the mixtures that contain silicate [7]. An example of the mortar flow without and with the addition of sodium silicate is presented in Fig. 2.

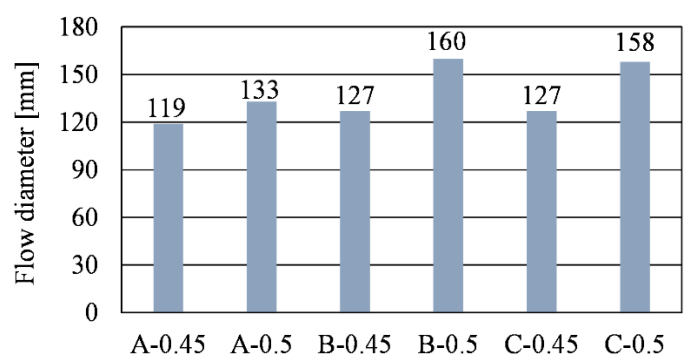


*Fig. 1. Flow diameter of the mortar mixtures (A - 25% SHA, no silicate; B - 25% SHA, Ms = 0.42; C - 15% SHA, Ms = 0.22)*

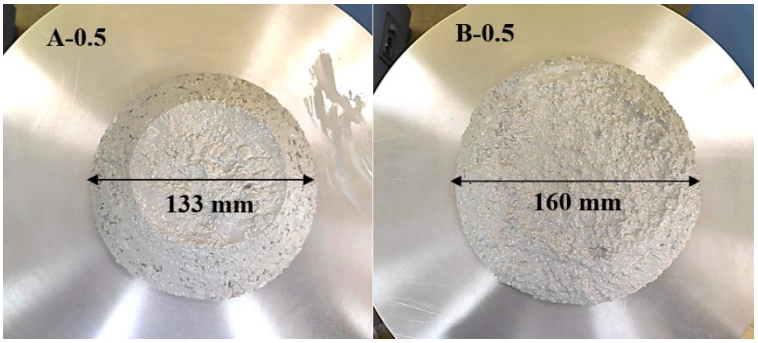


*Fig. 2. Mortar mixes A-0.5 and B-0.5 after flow table test*

## 3.2. COMPRESSIVE AND FLEXURAL STRENGTH

The compressive strengths after 7 and 28 days are presented in Fig. 3. The reference mixtures reached 36.5 MPa (w/b = 0.45) and 34.1 MPa (w/b = 0.50) after 28 days. At the same ash content and the same w/b ratio, the addition of the sodium silicate raised the 28-day strength to 56.0 MPa and 50.8 MPa, an increase of 53% and 49% respectively. The lower activator dosage, C, reached 44.5 MPa and 38.9 MPa, which is between the reference and the high dosage even though it contains less ash than the reference.

The effect is even more pronounced at an early age. After 7 days, the reference mixtures reached 21.4 MPa and 19.7 MPa, against 41.0 MPa and 36.6 MPa for the mixtures with the combined activator - an increase of 92% and 86%. Expressed as a share of the 28-day value, the reference mixtures developed 59% and 58% of their strength within 7 days, while the mixtures with the combined activator developed 73% and 72%.

The strength of the mixtures with the combined activator also increases with the silicate modulus. System B (Ms = 0.42) reached higher strengths than C at both w/b ratios, as a consequence of the higher alkali content and the higher silicate modulus. This is in agreement with the known mechanisms of the activation reaction, in which a higher alkali content results in a higher degree of slag activation, while a higher silicate modulus leads to the formation of a denser matrix and to slower slag hydration, which in turn results in a more uniform distribution of the reaction products and better mechanical properties [34]. Part of the strength of the SHA-activated systems is additionally attributed to the filler effect of the insoluble particles of the ash [35].

The influence of the w/b ratio was as expected in all three systems. Increasing the w/b ratio from 0.45 to 0.50 reduced the 28-day compressive strength by 7% in the reference mixtures, by 9% in B and by 13% in C. The strength loss is therefore small relative to the flow gain: raising the w/b ratio from 0.45 to 0.50 results in a 13% reduction in the 28-day strength but increases flow by about 30 mm in the mixtures with the combined

activator. The water content can therefore be used to adjust the consistency of these mixtures without a disproportionate loss of strength.

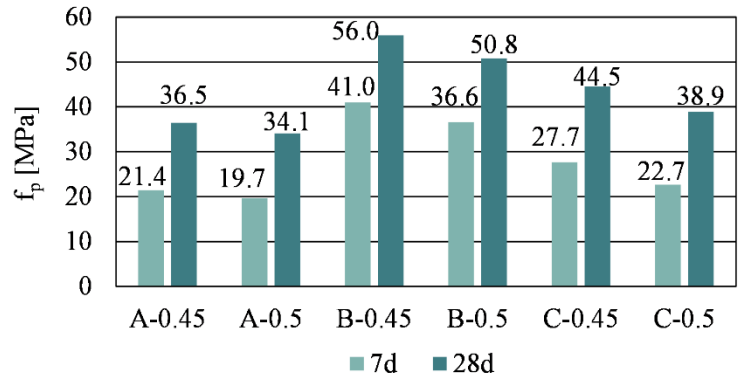


*Fig. 3 Compressive strength of the mortar mixtures after 7 and 28 days (A - 25% SHA, no silicate; B - 25% SHA, Ms = 0.42; C - 15% SHA, Ms = 0.22)*

The flexural strengths, presented in Fig. 4, follow the trend of the compressive strengths. The reference mixtures reached 6.6 MPa and 6.4 MPa after 28 days, B reached 8.7 MPa and 8.6 MPa, and C reached 8.0 MPa and 7.1 MPa. The increase in both SHA and sodium silicate content has led to higher flexural strength, as expected, due to the increase in alkali and silica content, i.e., formation of more hydration products [7,36].

The flexural strength of B is practically unaffected by the w/b, 8.7 MPa against 8.6 MPa, whereas in the other two systems it decreases by 3% and 11%.

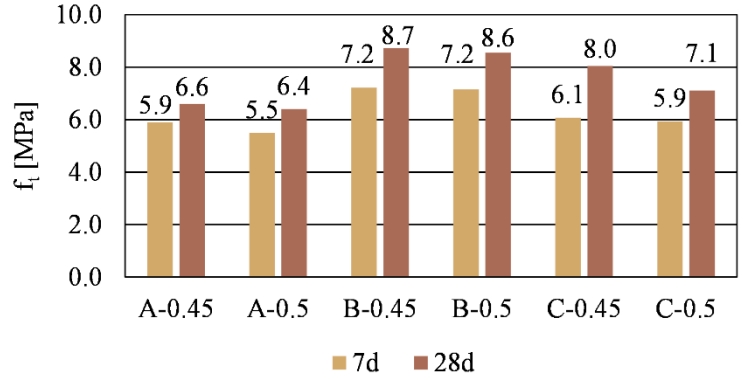


*Fig. 4 Flexural strength of the mortar mixtures after 7 and 28 days (A - 25% SHA, no silicate; B - 25% SHA, Ms = 0.42; C - 15% SHA, Ms = 0.22)*

### 3.3. SUITABILITY FOR THE TARGET CONCRETE STRENGTH CLASSES

The results show that the SHA-only system is not, on its own, a viable basis for concrete with the used aggregate: at w/b = 0.45 it produces the stiffest mixture in the series and the lowest strengths, and raising the water content improves workability only marginally while further reducing strength. The combined activator resolves both limitations at once, increasing flow and strength simultaneously rather than trading one for the other. Within the range investigated, sodium silicate makes compressive and flexural strengths less sensitive to increased water content, which is practical when the w/b ratio must be raised to obtain a placeable mixture.

The 28-day compressive strengths of 38.9 to 56.0 MPa obtained with the combined activator correspond to the ranges expected for the target concrete strength classes C30/37 and C35/45. The lower activator dosage, C, reaches the lower class with Ms of 0.22, against 0.42 for B. The proposed mix design improves the sustainability of AAMs

in two ways. First, the chemical alkali hydroxide is replaced entirely by locally available SHA. The second is that the remaining sodium silicate is kept as low as the target class allows, since the alkali silicate dominates the environmental footprint of the activator.

The mortar results indicated that composition B-0.5 could be used to target the C35/45 strength class. This assessment was subsequently confirmed on concrete specimens: concrete produced from composition B-0.5 reached a 28-day compressive strength of approximately 50 MPa, confirming the strength class estimated from the mortar results. These findings were obtained in the doctoral research of the first author [37], in which the effect of SHA was examined from the activation reaction in pastes, through the mortar composition, to the strength, shrinkage and durability of the alkali-activated concrete.

## 4. CONCLUSIONS

This paper presented a combined activator of SHA and sodium silicate for GGBFS-based alkali-activated mortars, prepared with crushed 0-4 mm aggregate, and the establishment of mix designs for development concretes of the target strength classes C30/37 and C35/45. The following conclusions can be drawn:

- at a constant SHA content, the introduction of sodium silicate improved both the fresh-state and the hardened properties of the mortar, consistent with the dissolved silicate acting simultaneously as a dispersing agent and as a source of reactive silica;
- the silicate further increased the rate of strength development, with a larger proportion of the 28-day compressive strength being attained within the first seven days; the flexural strength followed the same trend but to a lesser extent;
- the w/b ratio remained the governing parameter of consistency, although the three activator systems differed markedly in their response to it: in the SHA-only system, the additional water was considerably less effective, reflecting the high water demand of the insoluble ash fraction and of the crushed aggregate, whereas in the systems with the combined activator the associated loss of strength was small relative to the gain in flow, so that the water content may be adjusted to meet the required consistency without a disproportionate loss of strength;
- the two activator dosages reached 28-day compressive strengths of 38.9 to 56.0 MPa, consistent with the ranges expected for the target classes C30/37 and C35/45, the lower class being reached with approximately half the silicate content.

As a locally available waste material from edible oil production, SHA offers an alternative to conventional alkaline activators in AAM technology, contributing to the principles of the circular economy through the valorisation of agricultural waste within the construction sector. In the absence of superplasticisers that are reliably effective in alkali-activated systems, the combination of SHA and reduced content of commercial sodium silicate results in a mix design suitable for scaling up to concrete level.

**ACKNOWLEDGEMENT**

The research has been conducted within the project "Enhancement of teaching and scientific research capacities through the application of modern technologies in the fields of civil engineering, geodesy, and disaster risk management and fire safety", developed at the Department of Civil Engineering and Geodesy, Faculty of Technical Sciences, University of Novi Sad, Serbia.

## REFERENCES

[1] Habert G., Miller S.A., John V.M., Provis J.L., Favier A., Horvath A., Scrivener K.L. (2020). Environmental impacts and decarbonization strategies in the cement and concrete industries. *Nature Reviews Earth & Environment*, Volume 1, Issue 11, pp. 559–573. https://doi.org/10.1038/s43017-020-0093-3

[2] Marsh A., Dillon T., Bernal S. (2023). Cement and concrete decarbonisation roadmaps – a meta-analysis within the context of the United Kingdom. *RILEM Technical Letters*, Volume 8, pp. 94–105. https://doi.org/10.21809/rilemtechlett.2023.163

[3] Provis J.L. (2014). Geopolymers and other alkali activated materials: why, how, and what? *Materials and Structures*, Volume 47, Issue 1–2, pp. 11–25. https://doi.org/10.1617/s11527-013-0211-5

[4] Komkova A., Habert G. (2023). Optimal supply chain networks for waste materials used in alkali-activated concrete fostering circular economy. *Resources, Conservation and Recycling*, Volume 193, p. 106949. https://doi.org/10.1016/j.resconrec.2023.106949

[5] Garcia-Lodeiro I., Palomo A., Fernández-Jiménez A. (2015). Crucial insights on the mix design of alkali-activated cement-based binders. *Handbook of Alkali-Activated Cements, Mortars and Concretes*, Elsevier, pp. 49–73. https://doi.org/10.1533/9781782422884.1.49

[6] Koloušek D., Brus J., Urbanova M., Andertova J., Hulinsky V., Vorel J. (2007). Preparation, structure and hydrothermal stability of alternative (sodium silicate-free) geopolymers. *Journal of Materials Science*, Volume 42, Issue 22, pp. 9267–9275. https://doi.org/10.1007/s10853-007-1910-5

[7] Bondar D., Ma Q., Soutsos M., Basheer M., Provis J.L., Nanukuttan S. (2018). Alkali activated slag concretes designed for a desired slump, strength and chloride diffusivity. *Construction and Building Materials*, Volume 190, pp. 191–199. https://doi.org/10.1016/j.conbuildmat.2018.09.124

[8] Ramagiri K.K., Kar A. (2021). Environmental impact assessment of alkali-activated mortar with waste precursors and activators. *Journal of Building Engineering*, Volume 44, p. 103391. https://doi.org/10.1016/j.jobe.2021.103391

[9] Komkova A., Habert G. (2023). Environmental impact assessment of alkali-activated materials: Examining impacts of variability in constituent production processes and transportation. *Construction and Building Materials*, Volume 363, p. 129032. https://doi.org/10.1016/j.conbuildmat.2022.129032

[10] Alnahhal M.F., Kim T., Hajimohammadi A. (2021). Waste-derived activators for alkali-activated materials: A review. *Cement and Concrete Composites*, Volume 118, p. 103980. https://doi.org/10.1016/j.cemconcomp.2021.103980

[11] Mendes B.C., Pedroti L.G., Vieira C.M.F., Marvila M., Azevedo A.R.G., Franco De Carvalho J.M., Ribeiro J.C.L. (2021). Application of eco-friendly alternative activators in alkali-activated materials: A review. *Journal of Building Engineering*, Volume 35, p. 102010. https://doi.org/10.1016/j.jobe.2020.102010

[12] Mohapatra S.S., Mishra J., Nanda B., Patro S.K. (2022). A review on waste-derived alkali activators for preparation of geopolymer composite. *International Conference on Materials, Machines and Information Technology-2022*, Volume 56, pp. 440–446. https://doi.org/10.1016/j.matpr.2022.01.400

[13] Adesanya E., Perumal P., Luukkonen T., Yliniemi J., Ohenoja K., Kinnunen P., Illikainen M. (2021). Opportunities to improve sustainability of alkali-activated materials: A review of side-stream based activators. *Journal of Cleaner Production*, Volume 286, p. 125558. https://doi.org/10.1016/j.jclepro.2020.125558

[14] Vassilev S.V., Baxter D., Andersen L.K., Vassileva C.G. (2013). An overview of the composition and application of biomass ash. Part 1. Phase–mineral and chemical composition and classification. *Fuel*, Volume 105, pp. 40–76. https://doi.org/10.1016/j.fuel.2012.09.041

[15] Munawar M.A., Khoja A.H., Naqvi S.R., Mehran M.T., Hassan M., Liaquat R., Dawood U.F. (2021). Challenges and opportunities in biomass ash management and its utilization in novel applications. *Renewable and Sustainable Energy Reviews*, Volume 150, p. 111451. https://doi.org/https://doi.org/10.1016/j.rser.2021.111451

[16] Odzijewicz J.I., Wołejko E., Wydro U., Wasil M., Jabłońska-Trypuć A. (2022). Utilization of Ashes from Biomass Combustion. *Energies*, Volume 15, Issue 24, p. 9653. https://doi.org/10.3390/en15249653

[17] Zhu Z., Li X., Liu R., Wang Z., Zhang H., Zhao D., Bai J., Chen M., Li W. (2025). Workability and Environmental Evaluation of Using Sunflower Stalk Ash as an Alkali Activator with Blast Furnace Slag and Black Rice Hull Ash to Prepare Geopolymer Grouts. *Waste and Biomass Valorization*, Volume 16, Issue 4, pp. 1609–1626. https://doi.org/10.1007/s12649-024-02686-y

[18] Font A., Soriano L., Moraes J.C.B., Tashima M.M., Monzó J., Borrachero M.V., Payá J. (2017). A 100% waste-based alkali-activated material by using olive-stone biomass ash (OBA) and blast furnace slag (BFS). *Materials Letters*, Volume 203, pp. 46–49. https://doi.org/10.1016/j.matlet.2017.05.129

[19] Moraes J.C.B., Font A., Soriano L., Akasaki J.L., Tashima M.M., Monzó J., Borrachero M.V., Payá J. (2018). New use of sugar cane straw ash in alkali-activated materials: A silica source for the preparation of the alkaline activator. *Construction and Building Materials*, Volume 171, pp. 611–621. https://doi.org/10.1016/j.conbuildmat.2018.03.230

[20] Alonso M.M., Gascó C., Morales M.M., Suárez-Navarro J.A., Zamorano M., Puertas F. (2019). Olive biomass ash as an alternative activator in geopolymer formation: A study of strength, radiology and leaching behaviour. *Cement and Concrete Composites*, Volume 104, p. 103384. https://doi.org/10.1016/j.cemconcomp.2019.103384

[21] Soriano L., Font A., Tashima M.M., Monzó J., Borrachero M.V., Bonifácio T., Payá J. (2021). Almond-shell biomass ash (ABA): A greener alternative to the use of commercial alkaline reagents in alkali-activated cement. *Construction and Building Materials*, Volume 290, p. 123251. https://doi.org/10.1016/j.conbuildmat.2021.123251

[22] Soriano L., Font A., Tashima M.M., Monzó J., Borrachero M.V., Payá J. (2020). One-part blast furnace slag mortars activated with almond-shell biomass ash: A new 100% waste-based material. *Materials Letters*, Volume 272, p. 127882. https://doi.org/10.1016/j.matlet.2020.127882

[23] Omur T., Kanat D., Kabay N. (2024). Innovative use of hazelnut shell ash as an alkali activator: A comparative analysis with commercial activators. *Journal of Building Engineering*, Volume 90, p. 109466. https://doi.org/10.1016/j.jobe.2024.109466

[24] Lima F.S., Gomes T.C.F., Moraes J.C.B. (2023). Effect of coffee husk ash as alkaline activator in one-part alkali-activated binder. *Construction and Building Materials*, Volume 362, p. 129799. https://doi.org/10.1016/j.conbuildmat.2022.129799

[25] Draganić S., Šupić S., Laban M., Malešev M., Bulatović V., Lukić I., Bukvić O. (2023). Agricultural Biomass Ash as a Circular Building Material: Connecting Agriculture and Construction Industry. *Creating a Roadmap Towards Circularity in the Built Environment*, Springer, Cham., pp. 225–236. https://doi.org/10.1007/978-3-031-45980-1_19.

[26] Bedov O., Draganić S., Vučetić S., Serdar M. (2025). Optimisation of Sunflower Husk Ash-Activated Slag Binder. *Buildings*, Volume 15, Issue 23, p. 4210. https://doi.org/10.3390/buildings15234210

[27] Zhu Z., Xu X., Liu R., Liu P., Tang H., Gong Y., Zhang C., Li X., Liu Y., Bai J., Chen M. (2023). Feasibility study of highly alkaline biomass ash to activate alkali-activated grouts. *Construction and Building Materials*, Volume 393, p. 132067. https://doi.org/10.1016/j.conbuildmat.2023.132067

[28] Zhu Z., Zhang C., Liu R., Li S., Wang M. (2023). Sunflower straw ash as an alternative activator in alkali-activated grouts: A new 100% waste-based material. *Ceramics International*, Volume 49, Issue 19, pp. 32308–32312. https://doi.org/10.1016/j.ceramint.2023.06.306

[29] Bedov O., Andabaka A., Draganić S. (2025). Turning Agricultural Biomass Ash into a Valuable Resource in the Construction Industry—Exploring the Potential of Industrial Symbiosis. *Buildings*, Volume 15, Issue 2, p. 273. https://doi.org/10.3390/buildings15020273

[30] Bedov O., Draganić S., Serdar M., Malešev M. (2025). Compressive strength of alkali-activated mortars with conventional hydroxide activators and sunflower husk ash –

comparative analysis. *XXIX Congress DIMK and X Congress SIGP with international symposium on research and application of modern achievements in civil engineering in the field of materials and structures*, DIMK, Sokobanja, Serbia, 21 May, pp. 100–107.

[31] Bukvić O., Runci A., Serdar M. (2021). Critical parameters for the mix design of slag-based alkali-activated concrete. *15th International Conference iNDiS*, Novi Sad, Serbia, pp. 569–576.

[32] European Committee for Standardisation - CEN (1999). SRPS EN 1015-3_1999 - Methods of test for mortar for masonry. Determination of consistence of fresh mortar (by flow table).

[33] Institute for Standardization of Serbia (2017). SRPS EN 196-1: 2017 - Methods of testing cement - Part 1: Determination of strength. Belgrade.

[34] Wang S.-D., Scrivener K.L., Pratt P.L. (1994). Factors affecting the strength of alkali-activated slag. *Cement and Concrete Research*, Volume 24, Issue 6, pp. 1033–1043. https://doi.org/10.1016/0008-8846(94)90026-4

[35] de Moraes Pinheiro S.M., Font A., Soriano L., Tashima M.M., Monzó J., Borrachero M.V., Payá J. (2018). Olive-stone biomass ash (OBA): An alternative alkaline source for the blast furnace slag activation. *Construction and Building Materials*, Volume 178, pp. 327–338. https://doi.org/10.1016/j.conbuildmat.2018.05.157

[36] Taghvayi H., Behfarnia K., Khalili M. (2018). The Effect of Alkali Concentration and Sodium Silicate Modulus on the Properties of Alkali-Activated Slag Concrete. *Journal of Advanced Concrete Technology*, Volume 16, Issue 7, pp. 293–305. https://doi.org/10.3151/jact.16.293

[37] Bedov O. (2026). Possibilities of sunflower husk ash utilization as an alternative activator for slag-based alkali-activated materials. Doctoral thesis, University of Novi Sad, University of Zagreb. https://cris.uns.ac.rs/en/scientific-results/thesis/51336.

https://doi.org/10.24867/INDIS-2026-EN-341



# CONTEMPORARY REPAIR MORTARS: A REVIEW OF REQUIREMENTS, PROPERTIES AND DEVELOPMENT TRENDS

*Aleksandar Pujović[1], Tiana Milović[2], Anka Starčev-Ćurčin[3]*

***Summary:***

Repair mortars represent an important group of materials used for the rehabilitation and extension of the service life of concrete structures. This paper presents a review of contemporary repair mortars, with particular emphasis on the requirements and classification defined by EN 1504-3, the materials used for their production and modification, and the most commonly investigated properties. Particular attention is given to bond strength, mechanical and deformation properties, durability, and the use of alternative and waste materials. The reviewed studies indicate a development of repair systems aimed at simultaneously improving performance and sustainability, with increasing application of alternative binders, industrial by-products, fibres, and waste materials. Based on the literature review, further development of repair mortars should focus on achieving an appropriate balance between mechanical performance, bond strength, durability, compatibility, and sustainability.

*Keywords: repair mortars; concrete structure rehabilitation; EN 1504-3; bond strength; sustainable materials; alternative binders.*

# SAVREMENI REPARATURNI MALTERI: PREGLED ZAHTEVA, SVOJSTAVA I PRAVACA RAZVOJA

***Rezime:***

Reparaturni malteri predstavljaju značajnu grupu materijala za sanaciju i produženje eksploatacionog veka betonskih konstrukcija. U radu je prikazan pregled savremenih reparaturnih maltera, sa posebnim osvrtom na zahteve i klasifikaciju prema standardu EN 1504-3, materijale koji se koriste za njihovu proizvodnju i modifikaciju, kao i svojstva koja se najčešće ispituju. Posebna pažnja posvećena je prionljivosti, mehaničkim i deformacionim svojstvima, trajnosti i primeni alternativnih i otpadnih materijala. Analizirana istraživanja ukazuju na razvoj reparaturnih sistema usmerenih ka istovremenom unapređenju performansi i održivosti, uz sve veću primenu alternativnih veziva, industrijskih nusproizvoda, vlakana i otpadnih materijala. Na osnovu pregleda literature istaknuto je da dalji razvoj reparaturnih maltera treba usmeriti ka postizanju odgovarajuće ravnoteže između mehaničkih performansi, prionljivosti, trajnosti, kompatibilnosti i održivosti.

*Ključne reči: reparaturni malteri; sanacija betonskih konstrukcija; EN 1504-3; prionljivost; održivi materijali; alternativna veziva*

[1] Western Serbia Academy of applied studies, aleksandarpujovic@gmail.com
[2] Faculty of Technical Sciences, University of Novi Sad, tiana.milovic@uns.ac.rs
[3] Faculty of Technical Sciences, University of Novi Sad, astarcev@uns.ac.rs

## 1. INTRODUCTION

Concrete structures are susceptible to deterioration throughout their service life. Rehabilitation is therefore necessary to extend their service life [1]. Rehabilitation addresses problems resulting from inadequate concrete quality [2], construction defects, inappropriate design, and physical, mechanical, and chemical damage. These factors can lead to corrosion and deterioration of reinforcement and, consequently, to damage to the structure.

Exposure to these adverse effects creates a need for repair materials with enhanced durability, including repair mortars. A typical application of repair mortar for the rehabilitation of a damaged concrete substrate is shown in *Fig 1.*



*Fig 1. Application of repair mortar to a damaged concrete substrate, Source: IssueWire [3].*

Today, a wide range of cement-based materials incorporating various chemical and mineral admixtures, in the form of fibres [4] or powders, are used in the production of repair mortars. Approximately half of the annual construction budget in Europe has been allocated to the repair and rehabilitation of buildings [5].

The scale of rehabilitation required for existing concrete structures is also reflected in the substantial economic resources needed for their maintenance, repair, and extension of service life. According to available estimates, the value of the cement-based repair mortar market in the European Union was projected to reach approximately EUR 92 million in 2021, while costs associated with the premature deterioration of reinforced concrete elements were estimated at approximately EUR 1.1 billion [6,7]. Particularly significant investments are made in the United Kingdom, where annual expenditure on the maintenance and rehabilitation of the existing building stock exceeds EUR 57 billion [8,9]. A similar trend can be observed in the United States, where approximately EUR 18 billion is spent annually on the repair, protection, and strengthening of concrete structures, while economic losses associated with corrosion of steel reinforcement reach approximately EUR 110 billion per year [10].

In accordance with EN 1504-1:2005 [11], products and systems intended for the repair of concrete structures can be divided into two main categories: structural and non-structural repair materials. The primary criterion for this classification is their function after application. Non-structural products are primarily used to restore the shape and surface condition and to improve the appearance of concrete elements, whereas structural repair systems are intended to restore or improve the load-bearing capacity, functionality, and durability of a structure or its individual elements [1].

According to the requirements of EN 1504-3:2005 [12], repair products intended for structural and non-structural applications are evaluated based on relevant performance

characteristics. Their selection and application depend on the principles and methods of repair defined in EN 1504-9 [13].
The main performance requirements include compressive strength, chloride ion content, bond strength, and restrained shrinkage/expansion, while carbonation resistance and thermal compatibility are considered important durability-related requirements. Depending on the intended use and repair method, other properties may also be considered, including elastic modulus, resistance to slipping, coefficient of thermal expansion, and capillary absorption or water permeability. The standard does not require all of these properties to be assessed for every repair product; rather, their relevance depends on the specific repair principle and method and on the conditions under which the product will be applied [12].

These performance characteristics provide the basis for the further evaluation of repair products, while the specific requirements and limiting values for individual properties are defined in the subsequent provisions of the standard.
Repair mortar composites are used in repair procedures to restore damaged parts of concrete structures, both over surface areas and in locally confined zones [1,13]. Depending on their composition, particularly the type of binder and additives used, repair mortars can be classified into several main groups [1,14]:

- cement-based repair mortars;
- cement-based mortars with chemical admixtures;
- mineral-modified cement-based mortars;
- polymer-modified cement-based mortars;
- polymer mortars, including epoxy resin-based materials.

In addition to classification according to composition, repair mortars can also be classified according to their application technology. In this respect, three main groups can be distinguished [1,15]:

- hand/trowelled repair mortars;
- sprayed repair mortars;
- flow-applied repair mortars.

This paper focuses on a review of contemporary repair mortar materials, with particular emphasis on the requirements defined by EN 1504-3, the classification of repair mortars according to their performance, the materials used for their production and modification, and the properties most commonly investigated in recent research. Particular attention is given to bond strength, mechanical and deformation properties, durability, and the use of alternative and waste materials, with the aim of identifying current trends and future directions in the development of sustainable and reliable repair mortar systems.

## 2. REQUIREMENTS FOR REPAIR MORTARS ACCORDING TO EN 1504-3

According to EN 1504-3 [12], repair mortars are classified into four classes, R1, R2, R3 and R4, based on the required performance level and intended application. Classes R1 and R2 are intended for non-structural repair, whereas classes R3 and R4 are intended for structural repair. The classification of repair mortars is not based solely on compressive strength, but also considers a range of other properties relevant to achieving an adequate bond with the existing concrete, material compatibility, durability, and the performance of the repaired system during service.
The requirements for repair mortars include various mechanical, physical and durability-related properties, such as compressive strength, chloride ion content, tensile bond strength, restrained shrinkage and expansion, resistance to carbonation, elastic modulus, thermal compatibility, resistance to abrasion, coefficient of thermal expansion, and

capillary water absorption. The requirements for these properties vary depending on the repair mortar class and its intended application.
A particularly important requirement concerns the chloride ion content, which, according to EN 1504-3 [12], shall not exceed 0.05%. Limiting the chloride content is important for the durability of the repair system, as the presence of chloride ions may contribute to the depassivation of reinforcing steel and the initiation of corrosion. The requirement for chloride ion content applies to all four repair product classes, R1, R2, R3 and R4 [12], and testing is carried out in accordance with EN 1015-17 [16].

## 2.1. CLASSES R1 AND R2 – NON-STRUCTURAL REPAIR MORTARS

Repair mortars of classes R1 and R2 are intended for non-structural repair applications, in which the repair material does not have a primary role in restoring the load-bearing capacity or structural integrity of the element. Their use may include restoring the geometry and surface of concrete elements, filling local defects, and other interventions where the repair layer is not required to carry a significant portion of the structural load.
The minimum required compressive strength after 28 days is 10 MPa for class R1 and 15 MPa for class R2. For both classes, the required tensile bond strength is at least 0.8 MPa, highlighting the importance of achieving an adequate bond between the repair material and the existing concrete substrate [12].
No requirements for modulus of elasticity or resistance to carbonation are specified for classes R1 and R2. Requirements concerning behaviour under restrained shrinkage and expansion, as well as other properties, are applied in accordance with the criteria defined in the standard for the respective class and intended application [12].
For thermal compatibility testing, class R1 is assessed by visual inspection after the prescribed thermal cycles, whereas class R2 must achieve a minimum bond strength of 0.8 MPa after thermal exposure [12].
For class R2, a requirement is also specified for capillary water absorption, which must not exceed 0.5 $kg \cdot m^{-2} \cdot h^{-0.5}$, whereas no such requirement is specified for class R1. Limiting capillary water absorption is important for durability, as it reduces the potential ingress of water and dissolved harmful substances into the repair layer [12].

## 2.2. CLASSES R3 AND R4 – STRUCTURAL REPAIR MORTARS

Repair mortars of classes R3 and R4 are intended for structural repair, where the repair material contributes to restoring the structural integrity and adequate performance of the repaired element. Consequently, these classes are subject to more stringent requirements regarding mechanical properties, bond with the existing concrete, deformation behaviour, and durability.
The minimum required compressive strength after 28 days is 25 MPa for class R3 and 45 MPa for class R4, while the minimum tensile bond strength is 1.5 MPa for R3 and 2.0 MPa for R4. Unlike classes R1 and R2, classes R3 and R4 are also subject to requirements for the modulus of elasticity, with minimum values of 15 GPa for R3 and 20 GPa for R4 [12].
For testing behaviour under restrained shrinkage and expansion, classes R3 and R4 are required to achieve the specified tensile bond strength after testing, with minimum values of 1.5 MPa for R3 and 2.0 MPa for R4. This requirement is important because differential deformation between the existing concrete and the repair material may generate stresses at the interface [12].
Structural repair mortars are also subject to requirements concerning resistance to carbonation. Following the prescribed test procedure, the carbonation depth of the repair material must satisfy the criterion specified by the standard in relation to the reference

concrete. This requirement is important for protecting reinforcement and ensuring the long-term durability of the repaired element [12].
Particular attention is also given to thermal compatibility. Following exposure to different thermal cycles, including freeze-thaw cycles with immersion in de-icing salt solution, cycles involving temperature variations, and thunder-shower or dry cycles, the tensile bond strength must be at least 1.5 MPa for R3 and 2.0 MPa for R4. This requirement evaluates the ability of the repair system to maintain an adequate bond with the concrete substrate after thermal loading [12].
For repair mortars classified as R3 and R4, capillary water absorption is limited to a maximum value of 0.5 $kg \cdot m^{-2} \cdot h^{-0.5}$. This requirement contributes to the durability of the repair material by restricting moisture uptake and reducing the risk of water-related deterioration within the repair layer [12].

## 2.3. COMPARISON OF REQUIREMENTS FOR CLASSES R1–R4

The most pronounced differences between classes R1–R4 concern compressive strength and tensile bond strength. The performance requirements for repair mortar classes R1–R4 are compared in Tab. 1.

*Tab. 1 Comparison of performance requirements for repair mortar classes R1–R4 according to EN 1504-3, modified from [12]*

| Performance requirement | R1 | R2 | R3 | R4 |
|---|---|---|---|---|
| Intended application | Non-structural | Non-structural | Structural | Structural |
| Compressive strength after 28 days | ≥ 10 MPa | ≥ 15 MPa | ≥ 25 MPa | ≥ 45 MPa |
| Adhesive bond strength | ≥ 0.8 MPa* | ≥ 0.8 MPa* | ≥ 1.5 MPa | ≥ 2.0 MPa |
| Chloride ion content | ≤ 0.05% | ≤ 0.05% | ≤ 0.05% | ≤ 0.05% |
| Bond strength after restrained shrinkage/ expansion test** | No requirement | ≥ 0.8 MPa* | ≥ 1.5 MPa | ≥ 2.0 MPa |
| Carbonation resistance | No requirement | No requirement | $d_k \leq d_{k,control}$ for control concrete MC(0.45) | $d_k \leq d_{k,control}$ for control concrete MC(0.45) |
| Modulus of elasticity | No requirement | No requirement | ≥ 15 GPa | ≥ 20 GPa |
| Thermal compatibility after prescribed cycles | Visual inspection | ≥ 0.8 MPa* | ≥ 1.5 MPa | ≥ 2.0 MPa |
| Capillary water absorption | No requirement | ≤ 0.5 $kg \cdot m^{-2} \cdot h^{-0.5}$ | ≤ 0.5 $kg \cdot m^{-2} \cdot h^{-0.5}$ | ≤ 0.5 $kg \cdot m^{-2} \cdot h^{-0.5}$ |

* The 0.8 MPa requirement does not apply when cohesive failure occurs in the repair material; in this case, the minimum tensile strength is 0.5 MPa [12].
** The restrained shrinkage/expansion test is not required for repair method 3.3 or when thermal cycling is performed [12].
Note: The standard also specifies requirements for skid resistance, where relevant, and for the coefficient of thermal expansion when the prescribed thermal compatibility tests are not performed [12].

As shown in Tab. 1, the minimum compressive strength increases across classes R1–R4, while the required tensile bond strength is higher for structural classes R3 and R4. These classes are intended for structural repair.

In addition to these basic mechanical properties, the requirements address deformation behaviour, compatibility, and durability. Specific requirements for the modulus of elasticity and resistance to carbonation apply to classes R3 and R4, whereas no such requirements are specified for R1 and R2. Requirements for restrained shrinkage and expansion also differ between classes: no requirement is specified for R1, while the minimum required bond strength after testing is 0.8 MPa for R2, 1.5 MPa for R3, and 2.0 MPa for R4.

For class R1, thermal compatibility is assessed by visual inspection. For classes R2–R4, the minimum tensile bond strength after the prescribed cycles is 0.8 MPa, 1.5 MPa, and 2.0 MPa, respectively. Capillary water absorption is limited to 0.5 $kg \cdot m^{-2} \cdot h^{-0.5}$ for classes R2–R4, whereas no requirement is specified for R1.

Therefore, the selection of a repair mortar should take into account all the performance requirements specified in EN 1504-3, rather than compressive strength alone. The appropriate class (R1, R2, R3, or R4) is selected according to the requirements for the intended structural or non-structural repair application.

## 3. REVIEW OF CURRENT RESEARCH ON REPAIR MORTARS

### 3.1. MATERIALS USED IN MODERN REPAIR MORTAR

Recent research has increasingly focused on incorporating mineral additions and industrial by-products into repair mortar formulations. Fly ash, ground-granulated blast furnace slag, natural zeolite, and ceramic waste have been investigated as supplementary cementitious materials and as partial replacements for Portland cement in cement-based repair mortars [17-19]. These approaches aim to improve selected material properties, reduce cement consumption, and support the principles of a circular economy.

Wang et al. [20] investigated the effects of fly ash characteristics on the properties of alkali-activated FA/BFS repair mortars, with particular attention to mechanical strength, workability, and shrinkage. Related studies by Milović et al. [17-19] further examined cement-based repair mortars incorporating fly ash, ground-granulated blast furnace slag, and natural zeolite as partial replacements for Portland cement, with emphasis on their mechanical, physical, and deformation properties. Abadou et al. [21] investigated the effect of ceramic waste addition on the properties of dune-sand-based repair mortars and their interaction with the concrete substrate. Two types of ceramic waste were used-sanitary ceramics and ceramic tile waste-while bond strength and the stress state within the mortar layer were considered as indicators of repair system performance. The influence of substrate surface condition, degree of water saturation, porosity, type and content of ceramic waste, and curing conditions on bond strength was also examined. The results showed that bond strength was affected by the type and amount of ceramic waste as well as curing conditions, with optimum performance obtained at a ceramic waste content of approximately 30%.

Alkali-activated and geopolymer materials represent an important direction in the development of repair systems. Their application enables the use of industrial by-products, such as fly ash and slag, as binder components while reducing the consumption of Portland cement. Phoo-ngernkham et al. [22] developed a repair material based on alkali-activated high-calcium fly ash and calcium carbide residue (CCR), investigating setting time, strength development, microstructure, and bond strength to the concrete substrate.

The incorporation of fibres and polymers represents an important approach to modifying the mechanical and deformation properties of repair mortars. Various fibre types and combinations have been investigated, including steel, polyester, glass, natural, and waste-derived fibres, with studies focusing on mechanical performance, crack control, toughness, and durability-related properties. Alamian et al. [4] investigated repair mortars incorporating a combination of steel, polyester, and glass fibres, while Kenai et al. [23] examined the effects of natural Alfa fibres and date palm fibres on repair mortar properties.

Xu et al. [24] further investigated waste wood fibres combined with a vinyl acetate-ethylene (VAE) copolymer, with particular attention to crack control, toughness, and durability-related properties. Milović et al. [25] investigated the effects of hemp fibre conditions and chemical pre-treatments on the mechanical properties of fibre-reinforced repair cement mortars containing 1% hemp fibres. The 7-day and 28-day compressive and flexural strengths were determined for mortars containing untreated or pre-treated fibres, including fibres treated with $Ca(OH)_2$ and 1.6 M NaOH solutions. The mortars were also classified according to SRPS EN 1504-3 in term of their 28-day compressive strength. In a related study, Milović et al. [26] investigated the influence of hemp fibre condition and mixture design on the bulk density and 7-day flexural and compressive strengths of hemp fibre-reinforced repair cement mortars.

In addition to these materials, advanced repair ones with specific functional properties are being developed. Dabarera et al. [27] reviewed the use of magnesium potassium phosphate cement as a repair material, with particular emphasis on its fresh- and hardened-state properties, mechanical performance, and durability.

Litina and Al-Tabbaa [28] investigated self-healing cementitious repair materials incorporating polymeric microcapsules, aimed at reducing crack width and depth and restoring material impermeability. These systems represent an emerging direction in repair material development, focused on enhancing durability, controlling damage, and extending the service life of repaired structures.

The materials used and the properties investigated in the reviewed repair mortar studies are presented in Tab. 2.

*Tab. 2 Overview of materials and properties investigated in repair mortar research*

| Item number | Repair mortar | Materials used for production/modification | Tested properties | Reference |
|---|---|---|---|---|
| 1 | Repair mortar with hybrid fibres | Micro steel, polyester and glass fibres | Compressive, flexural and shear bond strength | [4] |
| 2 | Repair mortar modified with ceramic waste | Cement + dune sand + sanitary ceramic waste and ceramic tile waste | Mechanical strength, bond strength to concrete substrate, and durability-related performance | [21] |
| 3 | Repair mortar with natural fibres | Natural pozzolan, slag, Alfa fibres and date palm fibres | Compressive and flexural strength, total shrinkage, bond strength (slant-shear and pull-off), capillary water absorption | [23] |
| 4 | Cement-based repair material with microcapsules | Polymeric microcapsules containing liquid sodium silicate | Fresh properties, mechanical strength, crack-width and crack-depth reduction, and permeability | [28] |

| | | | | |
|---|---|---|---|---|
| | | | recovery | |
| 5 | Repair cement mortars modified with SCMs | Fly ash as a partial replacement for Portland cement | Restrained shrinkage | [17] |
| 6 | | Ground-granulated blast-furnace slag (GGBFS) as a partial replacement for Portland cement | Compressive and flexural strength, capillary water absorption, and unrestrained shrinkage | [18] |
| 7 | | Natural zeolite as a partial replacement for Portland cement | Mechanical, physical and deformation properties | [19] |
| 8 | Alkali-activated repair mortar | Fly ash + CCR; sodium silicate and sodium hydroxide | Setting time, strength, bond strength to concrete substrate, scanning electron microscopy (SEM) and X-ray diffraction (XRD) | [22] |
| 9 | Alkali-activated FA/BFS repair mortar | Fly ash + blast furnace slag (BFS) | Compressive, flexural and interfacial tensile-shear bond strength, workability and shrinkage | [20] |
| 10 | Magnesium phosphate repair material | Magnesium potassium phosphate cement (MKPC) | Fresh- and hardened-state properties and properties relevant to its application as a repair material | [27] |
| 11 | Repair mortar with waste fibres | Waste phloem wood fibres (WFP) + VAE copolymer | Workability, internal cracking, toughness, frost resistance, thermal stability and drying shrinkage | [24] |
| 12 | Hemp fibre-reinforced repair cement mortar | Hemp fibres; different fibre pre-treatment conditions | Compressive and flexural strengths | [25] |
| 13 | | Hemp fibres; optimization of mixture design | Mechanical properties and mixture-design parameters | [26] |

## 3.2. PROPERTIES OF REPAIR MORTARS INVESTIGATED IN RECENT RESEARCH

The literature review shows that the performance of repair mortars is evaluated through a range of mechanical, physical, deformation, and durability-related properties. As summarized in Tab. 2, the investigated properties include compressive and flexural strengths, bond strength, elastic modulus, capillary water absorption, shrinkage, fresh-state properties, and durability-related characteristics. Compressive and flexural strengths [4], [18-22], [25,26] are among the most frequently investigated mechanical properties, while considerable attention is also given to the interaction between the repair material and the concrete substrate, which is assessed using various test methods, including pull-off and slant-shear tests [4], [20,22]. Restrained shrinkage has also been investigated using a pull-off-based test method [17]. Other commonly investigated properties include elastic modulus and capillary water absorption [18,19], while restrained and unrestrained

shrinkage have also been investigated [17,18], [20], [24]. Several studies have specifically evaluated repair cement mortars according to the performance requirements specified in EN 1504-3 [17–19]. In particular, fly ash, ground-granulated blast furnace slag, and natural zeolite have been investigated as partial replacements for Portland cement [17-19]. The reported results showed that the investigated fly ash-modified mortars fulfilled the requirement for structural repair mortar class R4 with respect to restrained shrinkage [17]. Mortars containing natural zeolite fulfilled the requirements for class R4 in terms of compressive strength, capillary water absorption, and elastic modulus [19]. Similarly, repair cement mortars modified with ground-granulated blast-furnace slag fulfilled the R4 requirements for compressive strength and capillary water absorption, while flexural strength and unrestrained shrinkage were additionally investigated [18].

The quality of the bond between the repair material and the existing concrete substrate is one of the key factors determining the success of a repair. As highlighted by Luković et al. [2], the performance of a repaired system depends not only on high bond strength, but also on material compatibility, uniform stress distribution, and the achievement of behaviour as close as possible to that of a monolithic system. Consequently, recent research has increasingly focused on interface behaviour and the mechanisms that may lead to debonding of the repair layer from the concrete substrate.

The most commonly investigated deformation-related properties include shrinkage, modulus of elasticity, toughness, and crack initiation and control. In fibre-reinforced mortars, research is particularly focused on improving flexural behaviour, toughness, and crack control [4], [23,24], [25,26], whereas in alkali-activated systems, particular attention has been given to shrinkage and bond behaviour at the substrate interface [20], with other studies focusing on the development and performance of sustainable alkali-activated repair materials [22].

From a durability perspective, water and capillary absorption, permeability, resistance to environmental exposure, and other durability-related characteristics have been investigated depending on the type of repair material [21], [24], [27, 28]. These properties are important because water ingress and the penetration of harmful agents can significantly affect the long-term performance of repaired elements.

Microstructural analyses, including SEM and XRD techniques, are also used to provide insight into the material structure and the products of hydration or alkali activation [20]. Such analyses enable changes in microstructure to be related to the mechanical, and durability-related properties of repair mortars.

## 3.3. CONTEMPORARY TRENDS IN THE DEVELOPMENT AND RESEARCH OF REPAIR MORTARS

The reviewed literature indicates several major directions in the development of repair mortars. One of the most important is the development of more sustainable cement-based repair materials through the partial replacement of ordinary Portland cement with supplementary cementitious materials (SCMs) and other secondary raw materials. In this context, fly ash, ground-granulated blast furnace slag, and natural zeolite have been investigated as SCMs in cement-based repair mortars [17–19]. Ceramic powder waste has also been considered as a supplementary or modifying material in cement-based repair mortars, providing an opportunity for the valorization of construction and industrial waste [21]. Another research direction involves the development of alkali-activated repair mortars as an alternative to conventional cement-based systems. Alkali-activated materials based on fly ash and CCR, as well as systems incorporating fly ash and blast furnace slag, have been investigated as repair materials [20], [22].

Another important research direction concerns the improvement of mechanical and deformation-related properties through fibre reinforcement. Studies have investigated natural fibres, hybrid combinations of different fibre types, and fibres derived from waste wood biomass. Compressive and flexural strength, bond strength, shrinkage, toughness, workability, and freeze–thaw resistance have been examined, demonstrating a growing focus on the simultaneous improvement of multiple performance characteristics [4], [23,24], [25,26].

In addition to conventional cement-based and alkali-activated systems, alternative binders and advanced repair materials are also being investigated. Magnesium potassium phosphate cement (MKPC) has been considered as a binder in repair material, with research addressing its fresh- and hardened-state properties, as well as its potential and limitations for repair applications [27]. Alkali-activated and geopolymer materials likewise represent an important development direction [20], [22]. At the same time, self-healing systems are being developed, in which polymeric microcapsules containing sodium silicate are used to reduce crack width and depth and restore the impermeability of the repair material [28].

Overall, the reviewed studies indicate that the development of modern repair mortars is no longer focused solely on increasing strength, but increasingly on the simultaneous improvement of bond strength, deformation behaviour, durability, and sustainability. Particular attention is being given to alternative binders, secondary raw materials, and waste-derived materials, as well as to the development of systems with improved crack control and extended service life [17–28].

## 4. CONCLUSION

The review presented in this paper shows that the performance of repair mortars cannot be assessed on the basis of compressive strength alone. Successful repair requires an appropriate combination of mechanical performance, bond strength, deformation behaviour, durability, and compatibility with the existing concrete substrate. The requirements specified in EN 1504-3 provide a performance-based framework for the classification of repair products into classes R1–R4, with progressively increasing requirements for structural applications.

The reviewed studies demonstrate that bond strength and compatibility with the existing concrete are critical parameters for the long-term performance of repaired concrete elements. In addition to compressive and flexural strength, properties such as elastic modulus, shrinkage, capillary water absorption, thermal compatibility, and resistance to environmental actions play an important role in determining the suitability of a repair mortar for a particular application.

A clear trend identified in recent research is the development of more sustainable repair mortars through the incorporation of supplementary cementitious materials, industrial by-products, and waste-derived materials. Fly ash, ground-granulated blast-furnace slag, natural zeolite, and ceramic waste have been investigated as partial replacements or modifying materials in cement-based repair mortars. At the same time, alkali-activated systems based on fly ash and slag are being developed as alternatives to conventional Portland-cement-based repair materials.

Fibre reinforcement represents another important development direction, particularly for improving flexural behaviour, crack control, toughness, and deformation-related performance. Research on natural, hybrid, hemp, and waste-derived fibres indicates increasing interest in multifunctional repair mortars in which several performance characteristics are improved simultaneously. Alternative binders, such as magnesium potassium phosphate cement, and advanced systems incorporating self-healing

microcapsules further demonstrate the broadening range of materials being considered for repair applications.

Overall, contemporary research is moving from the development of repair mortars focused primarily on achieving high strength towards multifunctional and more sustainable repair systems. Future research should therefore focus on achieving an appropriate balance between mechanical performance, bond strength, deformation compatibility, durability, and environmental sustainability. Particular attention should also be given to the long-term behaviour of repair systems under realistic service conditions and to the relationship between laboratory-measured material properties and the actual performance of repaired concrete structures.

The development of repair mortars should ultimately be guided not only by the requirements for individual material properties, but by the performance of the complete repair system, including the repair material, the interface, and the existing concrete substrate.

## ACKNOWLEDGEMENT

This research has been supported by the Ministry of Science, Technological Development and Innovation (Contracts No. 451-03-33/2026-03/200156 and No. 451-03-34/2026-03/200156) and the Faculty of Technical Sciences, University of Novi Sad through project “Scientific and Artistic Research Work of Researchers in Teaching and Associate Positions at the Faculty of Technical Sciences, University of Novi Sad 2026” (No. 01-3609/1). (T.M. and A.S-Ć.)

## REFERENCES

[1] Milović, T. (2021). *Uticaj primene prirodnog zeolita na trajnost reparaturnih cementnih maltera* [Doktorska disertacija]. Fakultet tehničkih nauka, Univerzitet u Novom Sadu, Novi Sad.

[2] Luković M., Ye G., Dong H., Maekawa K., van Breugel K. (2017). Reliable concrete repair: A critical review. *Materials and Structures.* https://doi.org/10.1617/s11527-017-1082-y.

[3] IssueWire (2021). Everything you need to know about corrosion control and steel and concrete repair. *IssueWire*, 8 June 2021. https://www.issuewire.com/everything-you-need-to-know-about-corrosion-control-and-steel-and-concrete-repair-1702002426781467

[4] Alamian M., Asadollahi S., Dehestani M. (2024). Optimum mechanical properties of repair mortar containing hybrid fibers using the Taguchi method and analysis of variance. *Journal of Building Engineering*, Volume 98, 111049. https://doi.org/10.1016/j.jobe.2024.111049.

[5] Tilly, G. P. and J. Jacobs (2007). *Concrete repairs: Observations on performance in service and current practice*, CONREPNET Project Report, IHS BRE Press, Watford, UK.

[6] M.& Markets, *Concrete Repair Mortars Market - Global Forecast to 2021*, 2016. https://www.marketsandmarkets.com/Market-Reports/concrete-repairmortar- market-160103226.html.

[7] H. Davies, Repair and maintenance of corrosion damaged concrete: materials strategies, in: R.K. Dhir, M.R. Jones (Eds.), *Proceedings of the International Conference on Concrete Repair, Rehabilitation and Protection*, E & FN Spon, University of Dundee, UK, 1996: pp. 721–733.

[8] O. for N. Statistics, *Construction Statistics Annual Tables No 17, 2016 Edition, 2016.*

[9] ONS, *Construction output in Great Britain: May 2016,* (2016). https://www. ons.gov.uk/.

[10] International Concrete Repair Institute, *Vision 2020 A Vision for the Concrete Repair , Protection and Strengthening Industry, (2006)* 1–29.

[11] EN1504-1:2005 *"Products and systems for the protection and repair of concrete structures - Definitions, requirements, quality control and evaluation of conformity - Part 1: Definitions."*

[12] EN 1504-3:2005 *"Products and systems for the protection and repair of concrete structures — Definitions, requirements, quality control and evaluation of conformity — Part 3: Structural and non-structural repair"*, CEN, 2005, Clause 4, Table 1, p. 7–9.

[13] EN1504-9:2008 *"Products and systems for the protection and repair of concrete structures- Definitions, requirements, quality control and evaluation of conformity- Part 9: General principles for the use of products and systems."*

[14] Malešev, M., Radonjanin, V., Šupić, S.: *Malteri.* XV predavanje iz predmeta - Materijali u građevinarstvu 2., Departman za građevinarstvo i geodeziju, Univerzitet u Novom Sadu, 2020/2021.

[15] *Savremeni materijali i postupci sanacije građevinskih objekata*, izdavači: Udruženje inženjera građevinarstva, geotehnike, arhitekture i urbanista "Izgradnja", kao i Univerzitet u Beogradu, Građevinski fakultet, Beograd, 2013, 1-18. ISBN 978-86-82307-21-1

[16] EN 1015-17:2000+A1:2004 — *Methods of test for mortar for masonry — Part 17: Determination of water-soluble chloride content of fresh mortars.*

[17] Milović, T., Malešev, M., Radonjanin, V. (2022). Effect of Fly Ash as SCM on Restrained Shrinkage of Repair Cement Mortar. In: *Association of Structural Engineers of Serbia* - 16. Congress, Aranđelovac, Serbia, pp. 440-449, ISBN 978-86-7518-227-6

[18] Milović, T., Bulatović, V., Malešev, M., Marinković, M., Starčev-Ćurčin, A. (2023). Mechanical and Physical Properties of Repair Cement Mortars Modified with Slag. In: *SINARG 2023 Conference*, Niš, Serbia, pp. 316–323, ISBN 978-86-88601-80-1

[19] Milović, T., Malešev, M., Lukić, I., Bulatović, V., Radonjanin, V. (2023). Mechanical, physical and deformation properties of repair cement-based mortars containing zeolite. In: *International Symposium MASE,* Skopje, North Macedonia, MMT-8, pp. 1042-1051.

[20] Wang, J., Huang, T., Cheng, G., Liu, Z., Li, S., & Wang, D. (2019). Effects of fly ash on the properties and microstructure of alkali-activated FA/BFS repairing mortar. *Fuel*, 256, 115919. https://doi.org/10.1016/j.fuel.2019.115919.

[21] Abadou Y., Kettab R., Ghrieb A. (2018). Durability of a repaired dune sand mortar modified by ceramic waste. *Engineering Structures and Technologies*, Volume 10(1), pp. 1–9. https://doi.org/10.3846/2029882X.2018.1445038.

[22] Phoo-ngernkham, T., Phiangphimai, C., Intarabut, D., Hanjitsuwan, S., Damrongwiriyanupap, N., Li, L.-Y., & Chindaprasirt, P. (2020). Low cost and sustainable repair material made from alkali-activated high-calcium fly ash with calcium carbide residue. *Construction and Building Materials*, 247, 118543. https://doi.org/10.1016/j.conbuildmat.2020.118543.

[23] Kenai, A., Rezagui, M., Yahiaoui, W., Menadi, B., & Kenai, S. (2020). Performance of Repair Mortar with Natural Fibers. *MRS Advances*. https://doi.org/10.1557/adv.2020.178.

[24] Xu, C., Guo, Y., Li, Q., Kong, Z., & Shao, C. (2024). Advancing sustainable infrastructure: Leveraging forestry waste fibers to enhance crack resistance and durability in repair mortar. *Case Studies in Construction Materials*. https://doi.org/10.1016/j.cscm.2024.e04089.

[25] Milović, T., Šupić, S., Bulatović, V., Pantić, V. (2024). Effect of hemp fiber pre-treatment on repair cement mortar mechanical properties. In:*The First International Conference FUTURE-BME 2024*, Novi Sad, Serbia, pp. 1034- 1041, doi:10.24867/FUTURE-BME-2024-113

[26] Milović, T., Šupić, S., Pantić, V., Tomić, S. (2024). Optimization of the mixture design for hemp fiber-reinforced repair cement mortar. In: *The 2nd International Engineering Conference 2024*, Novi Sad, Serbia, pp. 415-420, ISBN 978-86-6022-692-3

[27] Dabarera, A., Fernández, R., & Provis, J. L. (2024). A systematic review of engineering properties of magnesium potassium phosphate cement as a repair material. *Frontiers in Materials*, 11, 1451079. https://doi.org/10.3389/fmats.2024.1451079.

[28] Litina C., Al-Tabbaa A. (2020). First generation microcapsule-based self-healing cementitious construction repair materials. *Construction and Building Materials*, Volume 255, 119389. https://doi.org/10.1016/j.conbuildmat.2020.119389.

https://doi.org/10.24867/INDIS-2026-EN-354



# EPA SWMM-BASED MODELING OF FLOODING PROCESSES IN RECLAIMED DRAINAGE AREAS: A CASE STUDY OF THE KNIĆANIN-ČENTA BASIN

*Tamara Pantić[1], Marijana Milić[2], Ljubomir Budinski[3], Goran Jeftenić[4], Danilo Stipić[5]*

***Summary:***

During May and June 2019, while the TurkStream gas pipeline was under construction, intense rainfall and flooding affected the Knićanin–Čenta basin. Prior to the pipeline construction, at the planned crossing points between the gas pipeline and the drainage canals, the canals were temporarily blocked, and culverts of various diameters and lengths were installed within these barriers. The objective of this study was to investigate the impact of the culverts on the occurrence and extent of flooding. Several hydrological-hydraulic models were developed using the EPA SWMM software package, and a statistical analysis of meteorological data was also performed. The results of the study showed that differences in flood extent were negligible, and that the culverts did not have a significant influence on the occurrence of flooding, with the primary cause identified as extreme precipitation.

*Keywords: melioration canals, pipe culverts, node flooding maps, EPA SWMM, HEC SSP, Knićanin–Čenta Basin*

# MODELIRANJE PROCESA PLAVLJENJA U MELIORACIONIM ODVODNIM PODRUČJIMA PRIMENOM EPA SWMM-A: STUDIJA SLUČAJA SLIVA KNIĆANIN-ČENTA

***Rezime:***

Tokom maja i juna 2019. godine, paralelno sa izgradnjom gasovoda Turski tok, obilne padavine i poplave pogodile su područje hidromelioracionog sistema Knićanin–Čenta. Pre izgradnje gasovoda, na mestima planiranog ukrštanja gasovoda i meliorativnih kanala, kanali su pregrađeni, a u pregrade su postavljena zacevljenja različitog prečnika i dužine. Cilj ovog rada bila je analiza uticaja zacevljenja na nastanak i obim poplava. Formirano je više hidrološko-hidrauličkih modela u softverskom paketu EPA SWMM I sprovedena je statistička analiza meteoroloških podataka. Rezultati studije su pokazali da su razlike u obimu plavljenja neznatne, te da zacevljenja nisu imala značajan uticaj na pojavu poplava, već se kao glavni uzrok navodi ekstremna količina padavina.

*Ključne reči: meliorativni kanali, cevni propusti, mape plavljenja, EPA SWMM, HEC SSP, sliv Knićanin-Čenta*

[1] Teach. Ass., Faculty of Technical Sciences, University of Novi Sad, Novi Sad, Serbia, tamara.pantic@uns.ac.rs, ORCID 0009-0003-6341-5692
[2] Teach. Ass., Faculty of Technical Sciences, University of Novi Sad, Novi Sad, Serbia, marijana.milic@uns.ac.rs, ORCID 0000-0003-1974-2461
[3] Full Prof., Faculty of Technical Sciences, University of Novi Sad, Novi Sad, Serbia, ljubab@uns.ac.rs, ORCID 0000-0001-7816-0889
[4] Assoc. Prof., Faculty of Technical Sciences, University of Novi Sad, Novi Sad, Serbia, goran.jeftenic@uns.ac.rs, ORCID 0000-0001-5639-4406
[5] Ass. Prof., Faculty of Technical Sciences, University of Novi Sad, Novi Sad, Serbia, danilostipic@uns.ac.rs, ORCID 0000-0001-6557-5997

## 1. INTRODUCTION

The study of floods caused by excess water in inland areas is crucial for Vojvodina, given the region's recurrent history of agricultural land inundation. At times, these floods reached devastating levels, impacting tens or even hundreds of thousands of hectares of arable land. Numerous researchers have examined this issue in their studies [1–6].

Given these historical challenges, water management in Vojvodina prioritizes removing excess surface and subsurface water to ensure favourable conditions for agriculture. The occurrence of harmful inland excess waters is predominantly associated with high precipitation amounts and their uneven temporal distribution. Due to the predominantly flat terrain and limited natural drainage capacity, drainage-related problems are particularly pronounced in shallow and poorly permeable soils, topographic depressions, and riverine areas during periods of high-water levels.

The Knićanin–Čenta area, located in the Central Banat region of Vojvodina, includes melioration and drainage systems situated between the settlements of Knićanin, Čenta, and Perlez, covering approximately 9,217 ha. The study area is bounded by the Begej River to the north, the Tisza River to the west, and the Danube River to the southwest, while the Karaš Canal forms its southern boundary. On the eastern side, the area is limited by the Zrenjanin loess terrace, which morphologically separates the lower alluvial plain from the surrounding elevated terrain. The area extends approximately 14 km north–south, whereas its shorter east–west dimension is about 7 km. According to the data from the main project [7], the terrain is geomorphologically characterized as a gently undulating plain with average elevations ranging from 71.5 to 74.0 m above sea level. The near-surface geological composition is dominated by sandy-clayey loam, yellow-gray clay, and fine-grained sand deposits. These soil materials are generally characterized by low to moderate permeability, which, together with the shallow relief and frequent occurrence of high groundwater levels, contributes to unfavorable drainage conditions and greater susceptibility to waterlogging and inland flooding.

A network of melioration canals has been established as an integral component of the DTD hydro system within the analyzed area. The drainage infrastructure spans the entire region, forming a hierarchically organized canal system comprising secondary and primary channels that discharge into a central main canal, with a pumping station located in the southern section. The drainage network was designed based on the area's topography, soil conditions, and land ownership patterns. Its primary objective is to ensure efficient collection and conveyance of excess surface and subsurface water from agricultural plots into the drainage system. The total length of the canal network is 74.7989 km [7].

The TurkStream gas pipeline represents a major international natural gas transmission corridor connecting the Russian and Turkish gas networks via a subsea route beneath the Black Sea. The pipeline system has an overall annual transport capacity of 31.5 billion $m^3$, distributed equally between two parallel transmission lines, each capable of conveying 15.75 billion $m^3$ of natural gas per year. Gas enters the system at the Russkaya compressor station, located near Anapa within the Russian Federation’s unified gas transmission network, where the required operating pressure is generated for transport through the offshore section extending more than 930 km to the receiving terminal near Midia on the Turkish coast.

Between March 2019 and the end of 2020, the Serbian section of the TurkStream gas pipeline was constructed over a route approximately 400 km long. Along certain sections, the pipeline corridor intersects the melioration and drainage canal network

within the Knićanin–Čenta catchment area. At these locations, the gas pipeline was installed below the canal beds, requiring temporary hydraulic regulation measures during construction. To enable pipeline installation and machinery crossing, the canals were temporarily closed by embankment structures constructed across their full cross-sections. To maintain water conveyance during the works, one or several culvert pipes of varying diameters were incorporated within the temporary barriers, allowing controlled passage of water through the affected canal sections. Figure 1 shows the Knićanin-Čenta basin together with the spatial distribution of melioration canals and the route of the TurkStream gas pipeline. The broader geographical location of the analyzed basin is shown in Fig. 1 in the upper left corner.

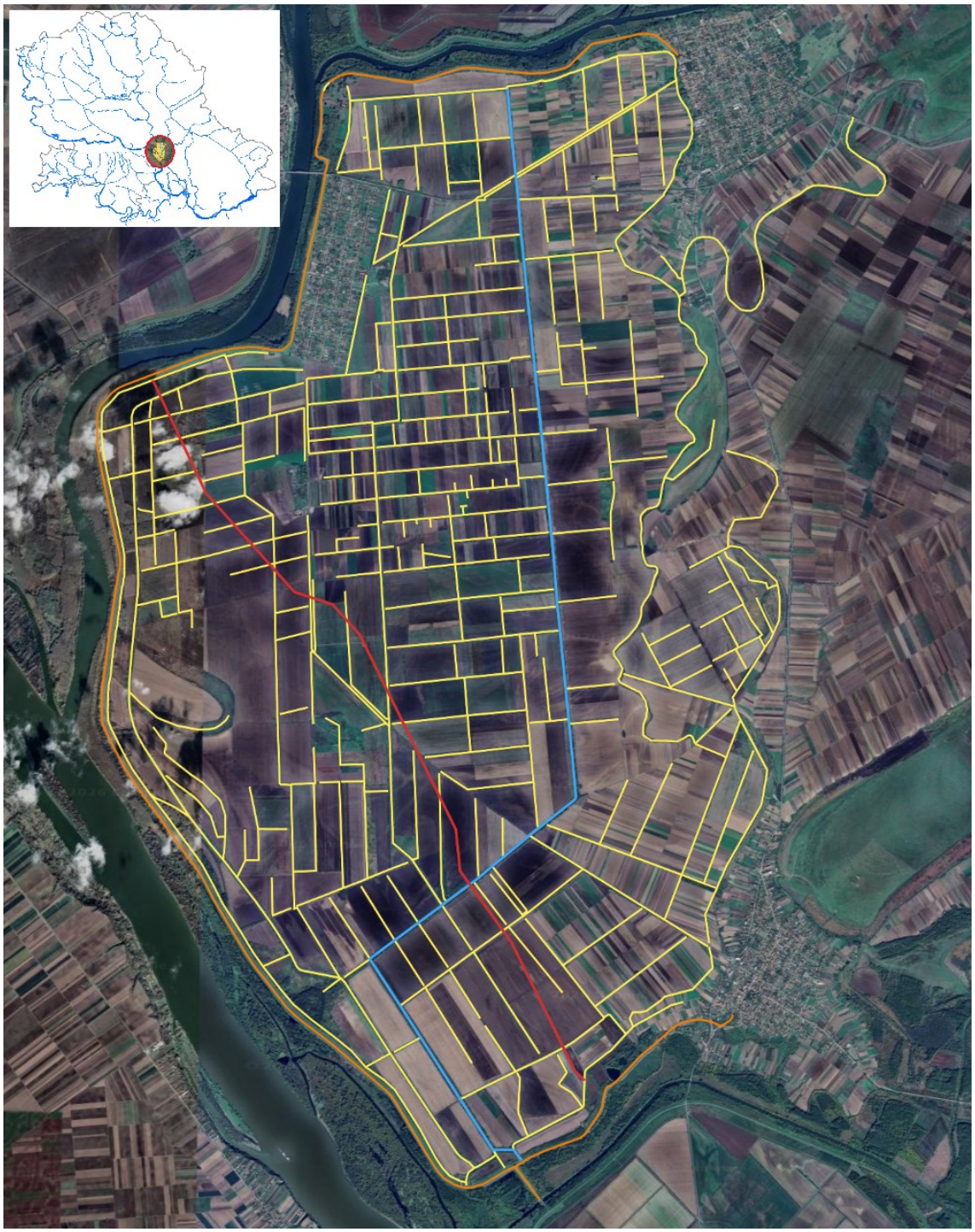

*Fig. 1 Display of the analyzed basin with melioration channels (secondary and primary channels – yellow, a central main canal – blue) and the gas pipeline (red) that intersects with them*

Following the completion of barrier construction and culvert installation in the canal, extensive rainfall occurred at the site during May and June 2019, resulting in floods that threatened approximately 3,225 hectares. This analysis aims to determine whether the flooding in the watershed was primarily caused by excessive precipitation or by channel clogging at intersections with the gas pipeline.

Hydraulic simulations and conceptual modeling in this study utilized the EPA SWMM software package. Developed by the United States Environmental Protection Agency (EPA), SWMM is a dynamic rainfall–runoff simulation model widely used for analyzing, planning, and designing stormwater drainage systems in both urban and rural settings [8]. Owing to its ability to simulate hydraulic and hydrological processes in open-channel and drainage networks, SWMM has been extensively applied worldwide in research on atmospheric water drainage, melioration systems, and combined sewer networks [9,10].

A comparative analysis was conducted using four distinct hydraulic model configurations to evaluate the effects of temporary canal obstructions and culvert installations on flow conditions within the drainage system:

- (1) A reference model representing the original canal system geometry without temporary barriers or culvert structures;
- (2) A model incorporating barriers and culverts, with the culvert invert elevation at the canal bed level;
- (3) A model including barriers and culverts, with the culvert invert elevation raised by 15 cm above the canal bottom;
- (4) A model with barriers and culverts, where the culvert invert elevations were elevated by 15 cm, 30 cm, or 50 cm above the canal bed, depending on local canal depth and hydraulic conditions.

To ensure consistency and comparability of results, all model scenarios were tested using an identical set of hydrological, hydraulic, and geometric input parameters.

## 2. HYDRAULIC CALCULATION

### 2.1. ESTABLISHMENT OF THE EPA SWMM MODEL

The hydraulic model was developed within the EPA SWMM environment by incorporating the geometric characteristics of the amelioration canal network in the analyzed catchment area, along with all relevant hydrological and hydraulic input parameters required for numerical simulation. The model setup represented canal cross-sections, hydraulic structures, flow connectivity, and boundary and initial conditions, enabling simulation of water movement throughout the drainage system under various operating scenarios.

A series of simulations was conducted using various combinations of input parameters to evaluate the system's hydraulic response under different conditions. Emphasis was placed on identifying parameter sets associated with the most unfavorable hydraulic behavior, characterized by the highest frequency and extent of canal overtopping and flooding. The parameter configuration selected for further analysis corresponds to the scenario that produced the most critical flow conditions within the system.

In the following sections, each defined model parameter is presented and discussed individually, with detailed explanations of its hydraulic significance, adopted values, and the grounds for its selection within the modeling procedure.

### 2.1.1. System geometry and significant coefficients

The geometric characteristics of the canal network in the analyzed catchment area were integrated into the hydraulic model using technical documentation from the main project [7]. The input dataset comprised key hydraulic and geometric parameters of the drainage system, including canal bottom widths, inter-nodal lengths, canal depths, longitudinal bed slopes, canal junction locations, and the positions and elevations of hydraulic cascades. One of the cross-sections of Canal X is shown in Figure 2.

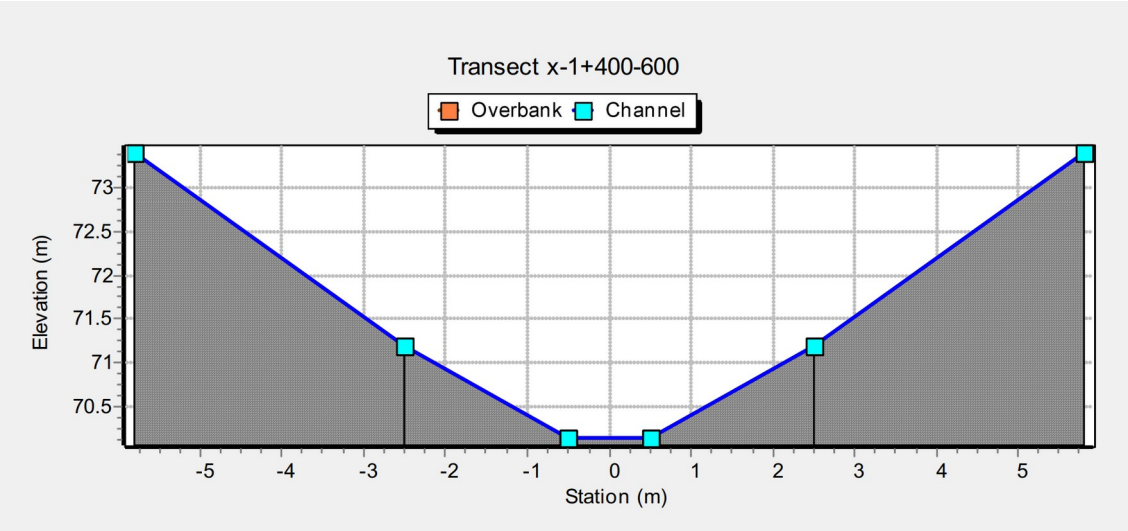


*Fig. 2 One of the cross-sections of Canal X*

In the hydraulic model, Manning's roughness coefficient for the channels was assigned based on recommended values reported in the relevant engineering literature [5] and standard modeling guidelines [8]. In defining this parameter, particular consideration was given to the observed in situ conditions of the canal surfaces, including vegetation presence, sedimentation, and general channel maintenance status, to ensure a realistic representation of flow resistance and water surface profiles.

For the final simulation scenario, a Manning's roughness coefficient of n = 0.0275 $s \cdot m^{-1/3}$ was adopted. This value represents the average hydraulic roughness of the existing canal network under field conditions and was applied uniformly across the modeled drainage system to maintain consistency in flow resistance assumptions.

Catchment delineation in the model was performed using a polygon-based approach, in which each subcatchment was hydraulically connected to its corresponding upstream node and routed through the downstream drainage network. Although this conceptualization does not fully capture the complexity of natural runoff processes, it was adopted as a conservative modeling approach to represent unfavorable hydraulic conditions and maximize the potential for canal overflow in the simulations. Each subcatchment was assigned standard hydrological parameters, including terrain slope, percentages of pervious and impervious surfaces, depression storage values, and infiltration characteristics, thereby enabling realistic simulation of runoff generation and flow routing processes within the drainage system.

A graphical representation of the canal network geometry and the corresponding subcatchment configuration within the analyzed area is presented in Figure 3. The elevation of the canal bed at the outlet section of the system is 66.88 m above sea level.

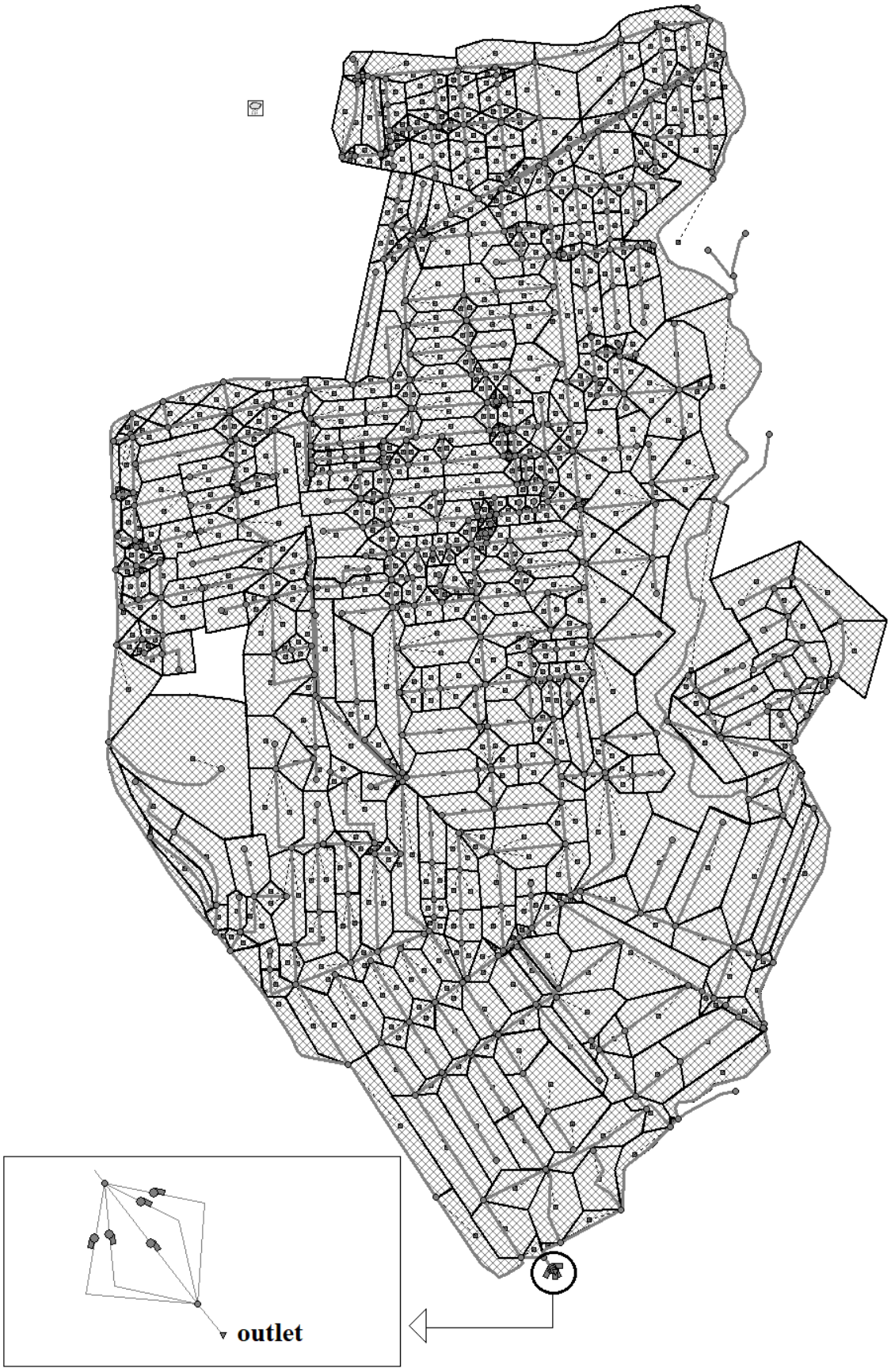


*Fig. 3 Graphical representation of channel geometry and associated subcatchment areas in the analyzed area*

Surface roughness coefficients, N-Imperv and N-Perv, quantify hydraulic resistance to overland flow resulting from friction between runoff and underlying impervious or pervious surfaces within subcatchments. These parameters significantly influence runoff velocity, flow retention, and the timing of surface water conveyance to the drainage network. Due to the absence of field measurements for surface roughness in the study area, coefficient values were selected based on recommendations from the EPA SWMM user manual [8], with consideration of the dominant soil characteristics and land cover within the catchment. These parameter values were deemed representative of the prevailing agricultural and semi-natural surfaces and were applied consistently throughout the simulation model.

Terrain slope within the subcatchments represents a significant parameter influencing runoff generation and flow routing in the hydraulic model. To evaluate potentially critical flooding conditions, two minimum slope values commonly cited in the literature for the lowland terrain of Vojvodina, 0.3% and 0.5%, were analyzed. Comparative simulations indicated only minor differences in hydraulic response and flooding extent between these two slope scenarios. Consequently, a slope value of 0.5% was selected for the final model configuration to provide a conservative and hydraulically realistic representation of terrain conditions in the investigated catchment.

### 2.1.2. Infiltration, Groundwater, Precipitation

The Horton infiltration method was applied in the EPA SWMM environment for hydrological modeling. Infiltration parameters were determined according to recommendations from technical documentation and software guidelines [8], while also accounting for the dominant soil types and pedological characteristics of the study area. This approach enabled simulation of temporal reductions in infiltration capacity during rainfall events, providing a realistic representation of runoff generation processes within the catchment.

Groundwater conditions in the study area are primarily determined by the hydrological regimes of the Tisza and Danube Rivers. Fluctuations in river water levels directly influence groundwater dynamics, resulting in significant seasonal changes in the groundwater table and affecting drainage efficiency within the melioration system.

Two distinct hydrological–hydraulic model configurations were analyzed using separate precipitation datasets. In the first simulation scenario, runoff generation and potential canal overflow were assessed using rainfall data from the Farkaždin meteorological station, designated by the Republic Hydrometeorological Service as the reference precipitation station for the Knićanin–Čenta catchment area. The second simulation scenario maintained identical hydraulic and hydrological model parameters, differing only in the spatial distribution of precipitation input data. In this case, daily precipitation records were applied separately to the cadastral municipalities of Knićanin, Čenta, and Perlez, allowing for spatial differentiation of rainfall across the study area.

A comparative assessment of simulation outputs from both model configurations showed that more severe flooding conditions, in terms of the spatial extent and frequency of canal overflow, occurred in the model using precipitation data from the Farkaždin station. Consequently, this precipitation scenario was selected as the representative critical case for further analysis. The cumulative precipitation curve for the selected rainfall station is presented in Figure 4.

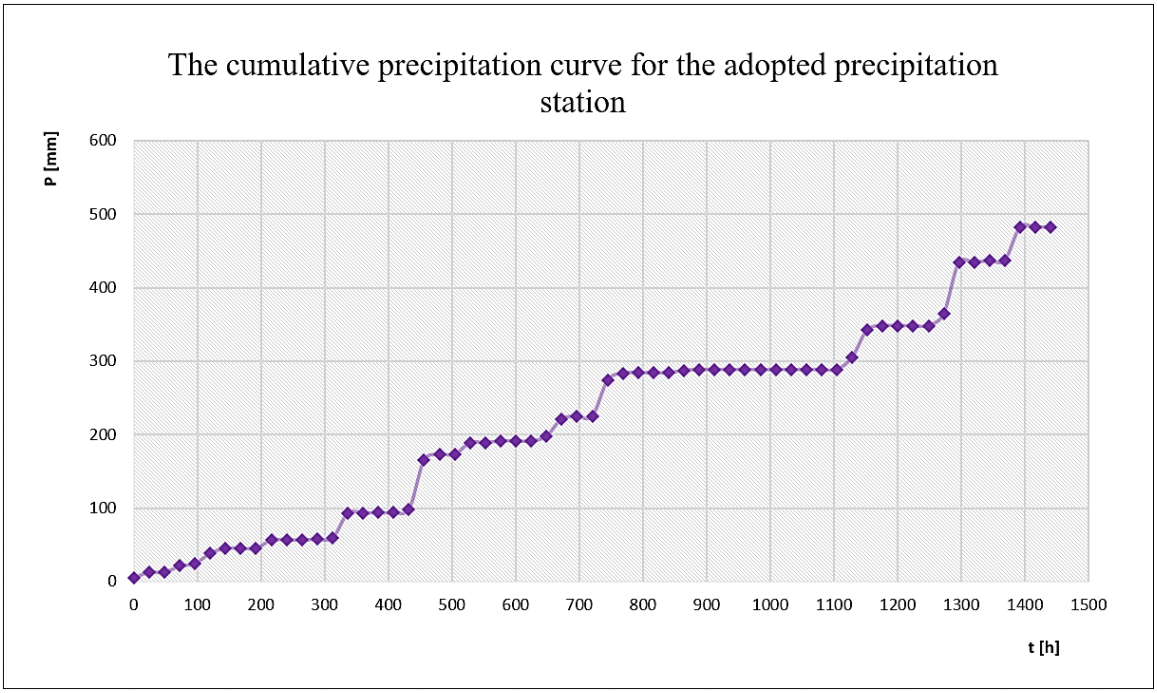


*Fig. 4 The cumulative precipitation curve for the adopted precipitation station*

Pump operation logs from May to June 2019 at PS Čenta, provided by VDP "Srednji Banat" d.o.o. Zrenjanin served as the basis for modeling the pumping station and analyzing pump unit operations during this timeframe. The Čenta pumping station transfers water over the embankment into the recipient, the Danube River.

A comprehensive set of simulations was performed using multiple combinations of input parameters to determine the most critical flooding scenario, defined as the configuration that produces the greatest extent of water overflow from the canal network. Table 1 presents all tested hydrological parameters and their respective value ranges, with the adopted values for the final simulation model emphasized in bold text. The adopted parameter set was subsequently applied in further simulations to evaluate the effects of temporary barriers and pipeline crossings on canal overflow and flooding dynamics within the study area.

*Tab. 1 Recapitulation of tested and adopted set of input data*

| Subcatchment Area Slope i [%] | Manning's Roughness Coefficient n [s*m$^{-1/3}$] | Infiltration f [mm/h] | Precipitation | Groundwater Level | Pumping Station Operation |
|---|---|---|---|---|---|
| 0.3 | **0.0275** | $f_0$ = 1.524<br>$f_c$ = 0.254<br>k = 4<br>t = 14 days | **Farkaždin** | 1.0 m below ground surface | According to PS Čenta operation logs |
| **0.5** | 0.033 | | Knićanin, Čenta, Perlez | | |

## 3. RUNOFF SIMULATION AND RESULTS

After entering the geometry of the basin and the channel network for the subject catchment, as well as all relevant hydraulic and hydrological parameters summarized in Table 1, a runoff simulation was performed for the analyzed catchment as a consequence of rainfall during the period of May–June 2019. The selected calculation model is based on the dynamic wave method, which enables the solution of the complete one-dimensional Saint-Venant equations for the entire network. This method allows for the simulation of all gradually varying parameters that can affect runoff. The simulation was conducted for the period from May 1, 2019 (start of the simulation) to June 30, 2019 (end of the simulation), with a time step of 30 minutes.

In this study, four scenarios were analyzed to assess the influence of culvert installation elevation relative to canal bed on both the volume of overflowed water and the spatial extent of flooding. The considered scenarios were as follows:

- (1) A model without installed barriers and without pipes in the barrier,
- (2) A model with installed barriers and pipes, where the invert elevation of the pipes is level with the canal bed,
- (3) A model with barriers and pipes where the invert elevation of the pipes is set 15 cm above the canal bed,
- (4) A model with barriers and pipes where the invert elevation of the pipes is set 15 cm, 30 cm, or 50 cm above the canal bed, depending on the canal depth.

Figure 5 shows the spatial distribution of nodes where water overflow was recorded—the maps display the maximum flooding for each of the four mentioned scenarios. The illustration corresponds to the moment when the model recorded the highest number of simultaneously active nodes with overflow (May 21, 2019, at 16:30). The color of each node indicates the intensity of water overflow at the observed moment: grey indicates no overflow, light blue signals mild overflow at the node location (25–50 LPS), while red indicates that, at that specific moment and location, overflow greater than 100 LPS occurred.

A simple visual comparison of the four maps reveals that there is no significant difference in the number of “active” nodes and the volume of overflowed water between the case without installed culverts and the cases with culverts (pay attention to the node color). Additionally, the results indicate that different installation heights of the culverts do not have a significant impact on the total amount of overflowed water. Moreover, a careful analysis of the numerical results shows that the presence of culverts has a positive effect on the distribution of overflow in this catchment area.

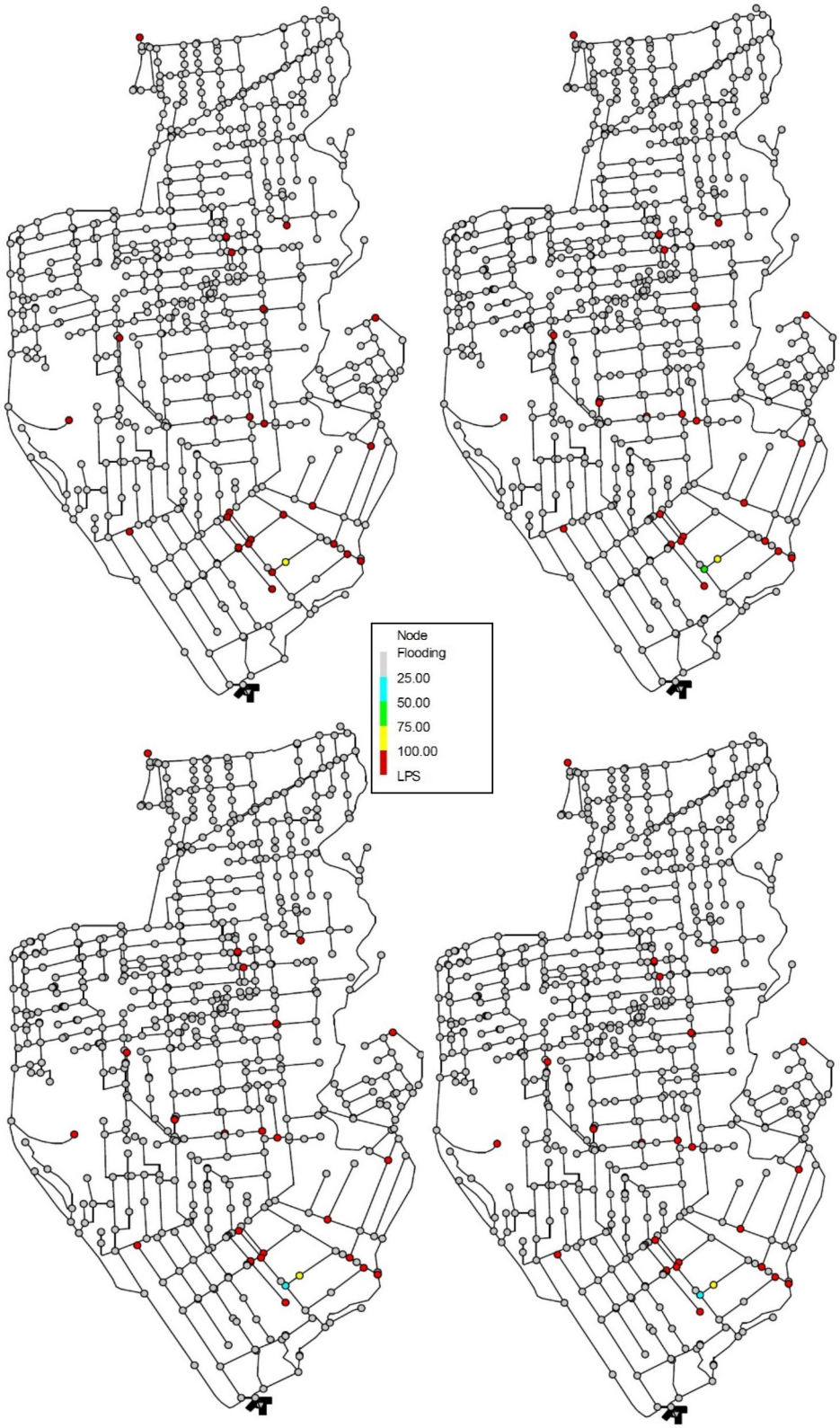


*Fig. 5 Map of maximum flooding*
*(1) for the model without installed culverts*
*(2) for the model with installed culverts, with the pipe invert set at the canal bed elevation*
*(3) for the model with installed culverts, with the pipe invert set 15 cm above the canal bed elevation*
*(4) for the model with installed culverts, with the pipe invert set 15 cm, 30 cm, or 50 cm above the canal bed elevation*

To conduct a detailed and quantitative analysis of the impact of installed culverts and the height of their installation on the volume of spilled water, the locations where flooding occurred (model nodes) and the corresponding flood volumes discharged from these nodes during the simulation were compared (see Table 2). The "Nodes" column presents the nodes that were activated in all four simulation scenarios, while the "Total Flood Volume" column shows the cumulative volume of water spilled from each node throughout the entire simulation period.

Analysis of the maximum flooding maps, together with monitoring the location and timing of flooding, showed that the comparison of the four models resulted in less than a 2% difference in flood volume. This indicates that the culverts were adequately sized, leading to the conclusion that the new gas pipeline did not have a significant impact on the volume of spilled water. Instead, the primary cause of the flooding was the large amount of rainfall that occurred in the area.

*Tab. 2 Recapitulation of tested and adopted set of input data*

| | **model (1)** | **model (2)** | **model (3)** | **model (4)** |
|---|---|---|---|---|
| |  | 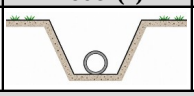 | 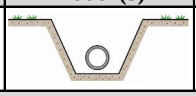 | 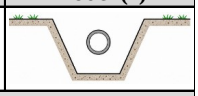 |
| **Node** | **Total Flood Volume (x10^6 ltr)** | | | |
| 156 | 0.034 | / | / | / |
| 161 | 46.968 | 49.155 | 48.833 | 48.821 |
| 211 | 1676.199 | 1865.041 | 1789.582 | 1781.845 |
| 212 | 1826.869 | 2048.51 | 1941.749 | 1927.62 |
| 275 | 193.937 | 240.902 | 236.342 | 235.641 |
| 277 | 496.231 | 423.095 | 416.961 | 416.139 |
| 290 | 136.558 | 147.659 | 146.64 | 146.436 |
| 299 | 83.439 | 46.915 | 45.855 | 45.53 |
| 400 | 282.581 | 283.375 | 283.31 | 284.82 |
| 436 | 159.774 | 159.783 | 159.187 | 159.063 |
| 469 | 39.674 | 39.207 | 39.142 | 39.142 |
| 481 | 243.169 | 269.551 | 252.568 | 250.422 |
| 483 | 136.914 | 157.548 | 154.238 | 153.049 |
| 491 | 130.395 | 106.514 | 104.88 | 104.491 |
| 498 | 52.459 | 1.141 | 1.011 | 1.031 |
| 464 | 335.25 | / | / | / |
| 474 | 58.593 | 59.674 | 58.891 | 58.633 |
| 475 | 94.058 | 77.106 | 75.925 | 75.655 |
| 476 | 198.189 | 184.354 | 174.576 | 173.38 |
| 503 | 3.725 | 3.592 | 3.523 | 3.522 |
| 504 | 75.71 | 2.736 | 2.236 | 2.245 |
| 505 | 300.316 | 282.272 | 265.993 | 263.943 |
| 518 | 579.391 | 604.587 | 567.995 | 563.936 |
| 521 | 2.978 | 2.978 | 2.978 | 2.978 |
| 529 | 492.999 | 619.605 | 593.812 | 590.894 |
| 550 | 2.928 | 2.931 | 2.93 | 2.931 |
| 554 | 1011.781 | 1138.95 | 1121.758 | 1120.172 |
| 555 | 39.021 | 39.079 | 39.058 | 39.058 |
| 557 | 1.879 | 1.88 | 1.88 | 1.881 |
| 560 | 551.214 | 451.411 | 444.689 | 443.14 |
| 562 | 482.426 | 511.645 | 496.999 | 494.155 |
| 567 | 49.416 | 47.539 | 46.877 | 47.054 |
| 1262 | / | 1.058 | / | / |
| 1274 | / | 144.922 | 142.813 | 141.993 |
| 1275 | / | 599.341 | 572.885 | 560.311 |
| 1261 | / | / | 0.207 | 0.213 |
| 1228 | / | / | / | 1.229 |

In addition to the analyses of maximum flooding and the total volume of spilled water during the two-month simulation period, changes in water levels were also monitored in channels of all categories within the observed catchment. This approach enabled a more detailed understanding of the hydraulic behavior of the system over time, as well as the identification of critical parts of the network. Figure 6 shows the longitudinal profile of the Main Channel at an arbitrarily selected moment during the simulation, with the culvert installed at the bottom of the channel.

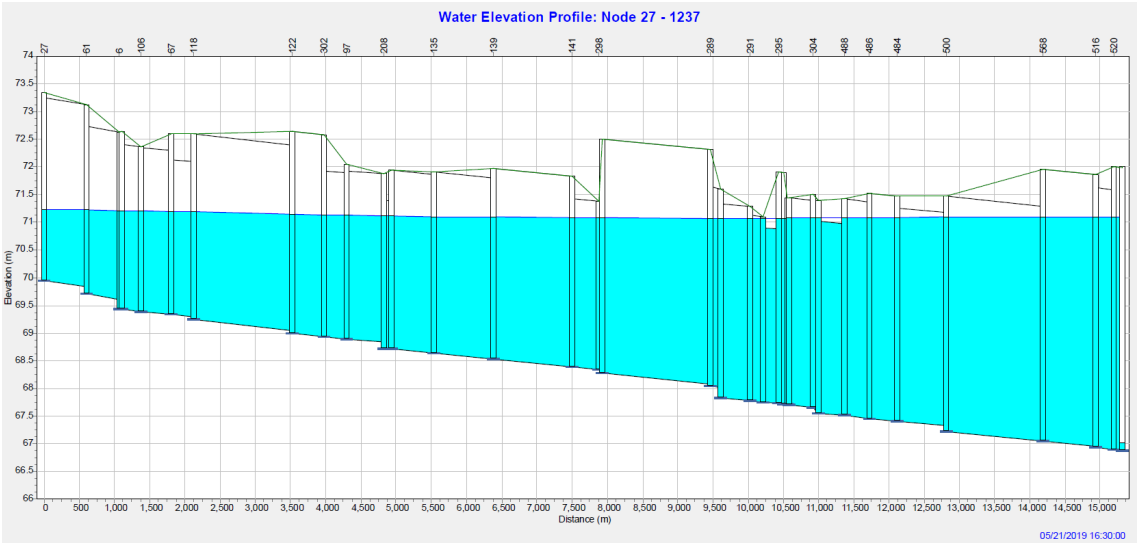


*Fig. 6 Longitudinal profile of the Main Channel at a selected simulation time*

## 4. STATISTICAL ANALYSIS OF PRECIPITATION DATA

In addition to the development of the hydrological-hydraulic model, a statistical analysis of meteorological data was also conducted to further validate the obtained results. The main objective of the analysis was to examine whether extreme precipitation events occurred in May and June 2019 at the study area, exceeding the design values for which the drainage canal system was originally dimensioned.

The analysis was based on the cumulative daily precipitation recorded during May and June at the Farkaždin meteorological station over a 36-year period. Before conducting the frequency analysis, the basic statistical assumptions of homogeneity and independence of the data series were tested. The results of the autocorrelation test showed that the observed series possesses the property of independence, while the Student's t-test confirmed its homogeneity. Based on the obtained results, it was concluded that the analyzed series is suitable for further statistical processing. All tests were conducted at a 5% significance level. The results of the homogeneity and independence tests are presented in Table 3.

*Tab. 3 Results of the homogeneity and independence testing*

| **Student's t-test** | | **Autocorrelation test** | |
|---|---|---|---|
| **Treshold values** | ∈(-1.685,1.658) | **Treshold values** | ∈(-0.335,0.335) |
| **t** | -0,56 | **r** | -0.080 |

It is important to note that the HEC-SSP software package was used to verify the calculated quantiles. This software package was developed by the U.S. Army Corps of Engineers and is used for the calculation of quantiles and probability analysis of hydrological variables based on measured data. The Weibull empirical distribution function was used, after which the quantiles were calculated using several theoretical distribution functions: normal, log-normal, Pearson III, and log-Pearson III distributions. The quantiles obtained from all four distributions are presented in Table 4.

*Tab. 4 Results of the homogeneity and independence testing*

| | | | **logPearson III** | **Pearson III** | **Normal** | **logNormal** |
|---|---|---|---|---|---|---|
| **Tp** | **p (X ≥ x)** | **p (%)** | **P [mm]** | **P [mm]** | **P [mm]** | **P [mm]** |
| 1.001 | 0.999 | 99.9 | 21.75 | 62.30 | -113.36 | 23.13 |
| 1.01 | 0.99 | 99 | 33.84 | 62.85 | -50.90 | 34.82 |
| 1.111 | 0.9 | 90 | 61.17 | 69.53 | 35.88 | 61.48 |
| 1.25 | 0.8 | 80 | 78.17 | 78.38 | 72.37 | 78.07 |
| 1.667 | 0.6 | 60 | 108.01 | 101.07 | 121.28 | 107.56 |
| 2 | 0.5 | 50 | 124.02 | 115.76 | 142.01 | 123.20 |
| 5 | 0.2 | 20 | 194.93 | 191.38 | 211.66 | 194.41 |
| 10 | 0.1 | 10 | 246.00 | 249.45 | 248.14 | 246.89 |
| 20 | 0.05 | 5 | 297.63 | 307.84 | 278.82 | 301.84 |
| 50 | 0.02 | 2 | 368.04 | 385.44 | 312.31 | 375.89 |
| 100 | 0.01 | 1 | 423.47 | 444.29 | 334.92 | 435.89 |
| 200 | 0.005 | 0.5 | 481.08 | 503.28 | 355.51 | 498.82 |
| 1000 | 0.001 | 0.1 | 624.17 | 640.54 | 397.38 | 656.23 |

Figure 7 provides a graphical representation of the empirical distribution and all four examined theoretical distribution functions. After the quantiles were calculated, the Kolmogorov test confirmed that, of the four distributions tested, the log-normal distribution showed the best agreement with the measured data.

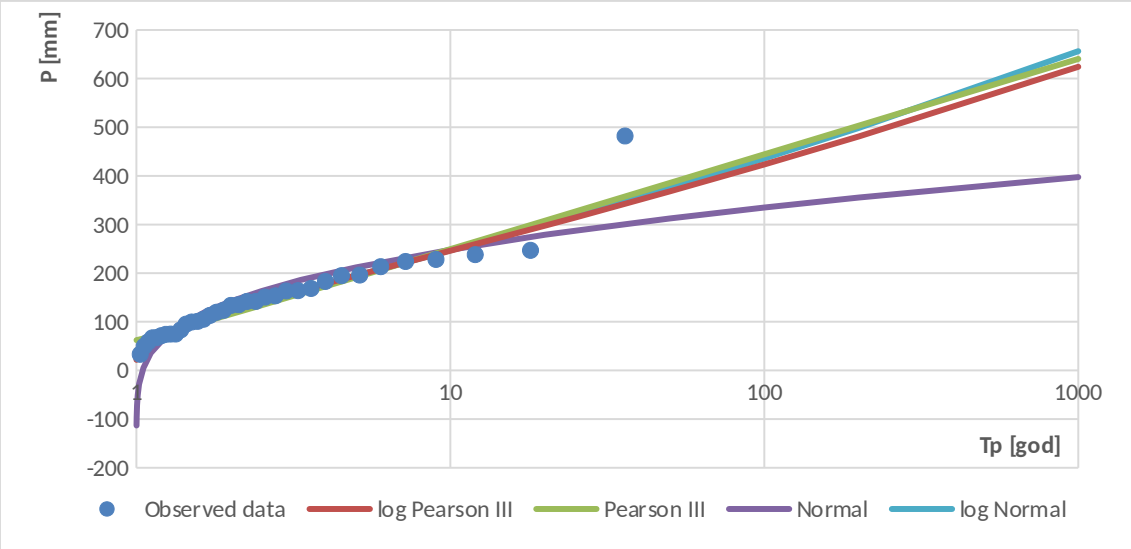


*Fig. 7 Empirical and considered theoretical distribution functions of total precipitation heights in May and June*

Based on the quantiles of the selected theoretical distribution function, it can be concluded that the return period for the total monthly precipitation recorded in May and June 2019 (which amounted to 482 mm in total) is 173 years. This leads to the conclusion that these were indeed extreme amounts of precipitation for which the reclamation canals in Vojvodina were not designed.

In the technical literature it can be found that the existing drainage systems in Vojvodina are designed to meet the requirements for the removal of the relevant excess water during the non-vegetation period, with a recurrence interval of 10 % and a return period of 10 years [11].

The drainage hydromodule represents the unit amount of water that needs to be removed from a unit area in a period of time. Its value characterizes the drainage needs of specific areas. According to the literature [7], the hydromodule for the area in question is q = 0.40 l/s/ha. If a relevant design month of 30 days is adopted, it follows that the excess water that the system can remove from the catchment areas during these 30 days is about 104 mm per hectare.

$$Q = q * A[m^3/s] \tag{1}$$

$$pv = \frac{Q * D * 86400}{A * 10000} * 1000[mm/month] \tag{2}$$

$$Q = 0.4\frac{\frac{l}{s}}{ha} * 1\,ha = 0.4\frac{l}{s} = 0.0004\,m^3/s$$

$$pv = \frac{0.0004 * 30 * 86400}{1 * 10000} * 1000 = 103.68\frac{mm}{month}$$

Where:

- D (days) number of days in the representative month; it is assumed that the representative month has 30 days,
- A (ha) area from which excess water is drained,
- q (l/s/ha) system hydromodule,
- pv (mm/month) excess water that can be removed from the observed area in one month

However, according to meteorological data measured during May and June of 2019, the cumulative precipitation values were significantly higher: in May, they amounted to 225 mm, and in June to 257 mm, totaling 482 mm. This also indicates hydrological overloading of the drainage system in the area.

## 5. CONCLUSION

The Knićanin – Čenta catchment area represents a region characterized by its distinctive geomorphological and hydrographic features. Due to its specific location, the basin is threatened by both external and internal waters. What further distinguishes it is the fact that a gas pipeline passes through the area, which at certain points intersects the network of existing drainage canals in the watershed. During May and June 2019, floods occurred in the subject basin that endangered part of the catchment area and caused significant material damage. The question naturally arose as to whether and to what extent the construction of the gas pipeline, the blocking of canals, and the installation of culverts at the crossing points of the gas pipeline with drainage canals, was related to the floods that occurred. A review of the literature preceding this work revealed that most studies and analyses addressing this issue examine the problem through hydromodulus analysis of the system.

The process of surface water runoff in hydrology is a complex phenomenon that depends on the interaction of a large number of parameters and therefore requires a comprehensive analysis. The factors determining whether, in what form, and in what quantity water from subcatchment areas will enter the drainage system (canal network) and lead to flooding are not limited to the amount and duration of precipitation. They also include the initial soil moisture, infiltration rate, the previous water level in canals, flow resistance coefficients on subcatchment surfaces and within canals (Manning's roughness coefficient), water loss dynamics from the canals, groundwater level, the operational regime of the canal network, as well as the dynamics of pump station operations. All these parameters are interdependent, and their combined effect is the fundamental cause of the complex runoff behavior from drainage areas.

The only appropriate approach to this problem is to perform an analysis using a suitable hydrological-hydraulic model that takes into account all previously selected parameters and their mutual interactions. For this purpose, four different simulations were conducted in order to perform a comparative analysis of the results and determine whether, and to what extent, the embankments and culverts influence flood extent. A comparative analysis of flood maps for the four different models showed that the difference in flood volume was less than 2%. This indicates that the culverts were adequately designed, leading to the conclusion that they did not have a significant impact on the volume of spilled water. Although fine-scale spatial prediction is uncertain, the comparison of the four constructed scenarios consistently shows that pipeline-related modifications did not increase flood extent or volume under the analyzed conditions.

After the hydrodynamic model was developed, a statistical analysis of cumulative daily precipitation recorded during May and June was also carried out using meteorological data measured at the Farkaždin meteorological station. The statistical analysis showed that the return period of the cumulative precipitation in May and June 2019 was 173 years, while drainage canals are typically designed to accommodate precipitation events with a return period of 10 years. Therefore, the extreme precipitation is identified as the main cause of the flooding.

## ACKNOWLEDGEMENT

The research has been conducted within the project "Enhancement of teaching and scientific research capacities through the application of modern technologies in the fields of civil engineering, geodesy, and disaster risk management and fire safety", developed at the Department of Civil Engineering and Geodesy, Faculty of Technical Sciences, University of Novi Sad, Serbia.

## REFERENCES

[1] Belić S., Conić J., Škorić M., Stojšić M., Šević Đ., Stojiljković D., Zdravić M., Nešković-Zdravić V. (1995). *Zaštita zemljišta od suvišnih unutrašnjih voda (odvodnjavanje), Hidrotehničke melioracije u Vojvodini*, str. 93-124, Poljoprivredni fakultet, Institut za uređenje voda, Novi Sad.

[2] Bezdan A., Vranešević M., Belić S. (2012). *Ugroženost površina poljoprivrednog zemljišta u različitim režimima pumpanja, Melioracije 12,* str. 30-36, Poljoprivredni fakultet, Novi Sad.

[3] Bezdan A. (2014). Procena rizika od suficita i deficita vode na melioracionom području. Doktorska disertacija, Univerzitet u Novom Sadu, Poljoprivredni faklutet, Novi Sad.

[4] Kolaković S. (2003). *Vode Vojvodine - neki aspekti funkcionalnosti sistema za zaštitu spoljnih i unutrašnjih voda na području Vojvodine*, Univerzitet u Novom Sadu, Fakultet tehničkih nauka, Novi Sad.

[5] Kolaković S., Trajković S. (2006). *Hidrotehničke melioracije – Odvodnjavanje*, Fakultet tehničkih nauka u Novom Sadu i Građevinsko-arhitektonski fakultet u Nišu.

[6] Kolaković S. (2006). The analysis of the pump station operations on the drainage systems in Vojvodina*"*, *BALWOIS 2006 Conference on Water, Climate and Environment*, Ohrid, R. Macedonia.

[7] Hidrozavod. (1975). Land Reclamation Development of the Čenta–Knićanin Area.

[8] Rossman L. A. (2015). *Storm Water Management Model User's Manual Version 5.1*, EPA/600/R-14/413b, U.S. Environmental Protection Agency, Cincinnati, OH.

[9] Ermalizar L. M., Junaidi A. (2018). Flood simulation using EPA SWMM on small subcatchment urban drainage system, *MATEC Web of Conferences 229(2):04022*, DOI:10.1051/matecconf/201822904022

[10] Yang Y., Sun L., Li R. et al. (2020). Linking a Storm Water Management Model to a Novel Two-Dimensional Model for Urban Pluvial Flood Modeling. *International Journal of Disaster Risk Science*, Volume 11, pp. 508–518. https://doi.org/10.1007/s13753-020-00278-7

[11] Vranešević M. (2015). Biotehničke mere kao mogućnost za povećanje efikasnosti sistema za odvodnjavanje. Doktorska disertacija, Univerzitet u Novom Sadu, Poljoprivredni faklutet, Novi Sad.

https://doi.org/10.24867/INDIS-2026-EN-370



# APPLICATION OF SPATIAL INTERPOLATION METHODS IN THE GREAT MORAVA RIVER BASIN

*Ivan Mesarović[1],Goran Jeftenić[2], Vladimir Mandić[3], Slobodan Kolaković[4]*

***Summary:***

The uneven spatial and temporal distribution of precipitation, intensified under climate change conditions, represents a significant challenge in hydrological analyses. This paper analyzes the application of spatial precipitation interpolation methods in the Great Morava River basin with the aim of determining the distribution of mean annual precipitation totals. Spatial interpolation, analysis, and comparison of results were performed using GIS tools through the application of the Thiessen polygon, Inverse Distance Weighted (IDW), and Spline interpolation methods. The results indicate that the differences between the mean annual precipitation totals derived from the analyzed methods are not significant, while considerable differences were observed in the representation of their spatial distribution. The research findings highlight the importance of selecting an appropriate interpolation method depending on the characteristics of the river basin area and the distribution of meteorological stations.

*Keywords: spatial interpolation,Thiessen, IDW, Spline, the Great Morava River*

# PRIMENA METODA PROSTORNE INTERPOLACIJE NA SLIVU REKE VELIKE MORAVE

***Rezime:***

Neravnomernost prostorne i vremenske raspodele padavina, izražena u uslovima klimatskih promena, predstavlja značajan izazov u hidrološkim analizama. U radu je analizirana primena metoda prostorne interpolacije padavina na slivu reke Velike Morave u cilju određivanja raspodele prosečne godišnje sume padavina. Prostorna interpolacija, analiza i poređenje rezultata izvršene su primenom GIS alata i korišćene su metodeThiessenovih poligona, Inverse Distance Weighted (IDW) i Spline interpolacije. Rezultati ukazuju da razlike između srednjih godišnjih suma padavina, dobijenih primenom analiziranih metoda, nisu značajne, dok su istovremeno uočeneznačajne razlike u prikazu njihove prostorne raspodele. Rezultati istraživanja ukazuju na značaj izbora odgovarajuće metode interpolacije u zavisnosti od karakteristika slivnog područja irasporeda mernih stanica.

*Ključne reči: prostorna interpolacija, Thiessen, IDW, Spline, reka Velika Morava*

[1]MSc, PhD student, Faculty of Technical Sciences, University of Novi Sad, Novi Sad, Serbia, ivanmesarovic@yahoo.com, ORCID 0009-0007-3319-8331
[2]PhD, Assoc. Prof., Faculty of Technical Sciences, University of Novi Sad, Novi Sad, Serbia, goran.jeftenic@uns.ac.rs, ORCID 0000-0001-5639-4406
[3]PhD, Asst. Prof., Faculty of Mechanical and Civil Engineering in Kraljevo, University of Kragujevac, Kraljevo, Serbia, mandic.v@mfkv.kg.ac.rs, ORCID 0000-0003-3529-171X
[4]PhD, Assoc. Prof., Faculty of Technical Sciences, University of Novi Sad, Novi Sad, Serbia, kolakovic.s@uns.ac.rs, ORCID 0000-0002-9859-9669

## 1. INTRODUCTION

Precipitation data represent an indispensable parameter in the study of river basins. The main challenge in the analysis and processing of meteorological data, such as precipitation, is their spatial distribution, considering that such data are measured only at specific locations of hydro-meteorological stations. The obtained precipitation data are therefore point-based, as they are linked to precisely defined locations of measurement stations within the observed river basin area [1].

The trend of climate change, which has become increasingly pronounced in recent decades, is reflected not only in the global temperature increase of approximately 0.8 ± 0.1°C [2], but also in the significant irregularity of the spatial and temporal distribution of precipitation. Precipitation variability is also evident in the prediction of the number of days with heavy rainfall [3]. The uneven distribution of precipitation significantly affects the availability of water resources, the occurrence of droughts and floods, as well as the overall management of river basin areas.

For the purpose of designing hydraulic structures, one of the most important parameters is the mean annual precipitation total [4]. Since precipitation data are collected at point locations, a large number of interpolation methods - ranging from classical to modern approaches - have been developed in order to determine their spatial distribution. Spatial interpolation methods enable the estimation of precipitation values at locations where direct measurements are not available [5].

The spatial variability of precipitation within a river basin, the insufficient number of measurement stations, and their irregular distribution represent additional challenges in the process of data interpolation. Additional sources of error include evaporation, wind effects, and insufficient precipitation capture by rain gauges, all of which may significantly influence the results of the analysis [6].

The importance of the problem of spatial interpolation of precipitation data is reflected in the development of a large number of different methods [7]. Traditional methods, such as Thiessen polygons, have long been widely used in engineering practice, primarily due to their simplicity of application and clarity of results. With the development of computer and GIS technologies, more advanced interpolation methods have been introduced. These methods are based on the assumption that spatially closer phenomena exhibit a higher degree of correlation than more distant phenomena, which represents the foundation of Tobler’s principle of spatial dependence [8].

Considering the importance of data on annual precipitation totals within a river basin, the selection of an appropriate spatial interpolation method is of crucial importance in order to obtain results that are as representative and accurate as possible for further analysis.

Previous studies have confirmed that there is no universally optimal method for the spatial interpolation of precipitation, but rather that the performance of individual methods depends on the characteristics of the study area, as well as the spatial distribution and density of measurement stations.

A study conducted in the Porsuk River basin in Turkey highlights the importance of the spatial distribution of measurement stations for interpolation results [9], while a study conducted in the Var River basin in France indicates that the selection of an appropriate method depends on the characteristics of the basin and the availability of data [10]. Furthermore, the density and spatial distribution of meteorological stations can significantly affect the quality of spatial precipitation estimates [11]. These studies indicate the need to select and compare different interpolation approaches in accordance with the characteristics of the specific basin area.

The aim of this paper is to analyze and compare the results of three spatial interpolation methods applied in the Great Morava River basin in order to determine the mean annual precipitation total and its spatial distribution. The obtained results, as well as their mutual comparison, may contribute to a better understanding of the applicability of different methods within the framework of spatial modeling of meteorological parameters.

## 2. MATERIALS AND METHODS

### 2.1. METHODS

With the development of computer technology, in addition to simpler spatial interpolation methods, numerous more advanced and sophisticated methods are now in use. The selection of an appropriate method depends on the characteristics of the study area, the spatial distribution of measurement stations, and the nature of the data being interpolated. For the purpose of evaluating, analyzing, and comparing the results of the spatial distribution of precipitation, three methods were applied in this paper: Thiessen polygons, Inverse Distance Weighted (IDW), and Spline interpolation.

Previous studies have shown that Thiessen polygons, the IDW method, and the Spline method can be applied to determine the spatial distribution of precipitation, with the choice of method potentially affecting the resulting spatial distribution [9][11]. The selection of these methods was based on the need to compare different approaches to the spatial interpolation of precipitation. Thiessen polygons represent a simple approach based on determining the areas of influence of individual measurement stations, the IDW method determines the spatial influence of stations based on their distance, while the Spline method generates a continuous and smooth interpolation surface. In this way, the selected methods encompass different approaches to representing the spatial variability of precipitation, ranging from a polygon-based approach to continuous interpolation surfaces. A similar selection of methods was applied in a study conducted in the Porsuk River basin [9].

The selected methods are based on different principles of spatial interpolation, which enables a comparison of their effects on the resulting spatial distribution of precipitation.

Thiessen polygons represent a simple and frequently used classical method in engineering practice, originally proposed by the American hydrologist Thiessen in 1911. The method is based on the assumption of a linear change in precipitation values between stations. Its fundamental principle is the division of the observed area into zones of influence around each meteorological station. The polygons are formed in order to define the area within which the point measurement from a particular station is considered representative [12].

The formation of Thiessen polygons is performed by connecting neighboring meteorological stations, thereby creating a network of triangles. Perpendicular bisectors are then constructed along the sides of the triangles, and their intersections define the polygons of influence. Based on the area of each polygon, a weighting factor is determined, proportional to the ratio of the polygon area to the total area of the analyzed river basin. The mean precipitation value for the observed area is calculated as the sum of the products of precipitation values measured at the stations and their corresponding weighting coefficients:

$$\overline{P} = \sum_{i=1}^{n} P_i \cdot w_i \tag{1}$$

Some of the advantages of the selected method are reflected in its simplicity of application, the possibility of use under conditions of irregularly distributed rain gauge stations, as well as in situations where there are no abrupt changes in terrain topography and pronounced meteorological factors.
However, a limitation of this method is that it assumes a constant precipitation value within each polygon and does not account for the gradual variation in precipitation values between measurement stations.
The Inverse Distance Weighted (IDW) method belongs to the group of more advanced interpolation methods and is based on the assumption that the influence of measurement stations on the estimation of values at a selected location decreases with increasing distance. The estimation of values at an unknown point is performed using weighted values from the known surrounding locations. Weighting factors are assigned to the measurement stations, inversely proportional to the distance between the selected location and the measurement station [13] [14]. Accordingly, the weighting coefficient ( $w_i$) or factor is defined as the inverse value of the distance of the measurement station ( $d_i$) from the selected location, raised to the power parameter p:

$$w_i = \frac{1}{d_i^p} \tag{2}$$

The value of the parameter p has a significant influence on the weighting coefficients and is determined based on cross-validation [15], thereby achieving optimal adjustment of the model to the spatial distribution of the data. Higher values of the parameter p result in a more rapid decrease in the influence of distant measurement points.
For a selected location s, which has m surrounding measurement points in its neighborhood, the interpolated value $Z_s$ is determined as the weighted average of the values Z of the surrounding points [16]:

$$Z_s = \sum_{i=1}^{m} w_i \cdot Z_i \tag{3}$$

The widespread application of this simple and computationally efficient method enables control over the number of input measurement points involved in the process [17].
A limitation of the method lies in its dependence on the spatial distribution of measurement stations and the choice of the power parameter *p*, which can significantly affect the resulting spatial distribution of precipitation.
The Spline method, which also belongs to the group of modern spatial interpolation techniques, is based on the construction of a smooth surface that either passes through the measurement points or approximates them. The idea is based on the application of a mathematical function in order to minimize the overall surface curvature, thereby achieving a continuous and smooth spatial distribution of the analyzed variable. The interpolant (spline) represents a piecewise polynomial function. The basic assumption of spline interpolation is the gradual change of values between measured points, without abrupt discontinuities. Instead of fitting a single high-degree polynomial to all observed data, spline interpolation uses lower-degree polynomials fitted in segments. For this reason, the method is particularly suitable for modeling natural phenomena that exhibit continuous spatial variability, such as precipitation. In contrast to the previously described methods, the spline method does not explicitly use weighting factors, but instead determines the interpolation surface by minimizing the overall curvature of the function. The advantage of the spline method lies in producing accurate results even when the available data are limited [17].

A limitation of the Spline method may be the occurrence of local extremes and the sensitivity of the results to the spatial distribution and values of the input measurement data.

## 2.2. EXPERIMENTAL BASIN

The Great Morava River is one of the largest rivers in the Republic of Serbia, with a basin area within the territory of the country of 36,638 *km²*. The Great Morava River basin can be divided into three hydrographic units, which differ from one another in terms of their specific characteristics and spatial extent [18]. The first hydrographic unit is the direct basin of the Great Morava, which includes the area from Stalać to the river's confluence with the Danube, while the second and third hydrographic units consist of the basins of the West Morava and South Morava rivers.

For the purpose of analyzing spatial interpolation methods, an experimental basin was selected, encompassing the direct basin of the Great Morava River. Within the analyzed area, three main relief units can be distinguished: the Veliko Pomoravlje region, as a broad valley of the Great Morava; part of Šumadija with low insular mountains; and part of Eastern Serbia belonging to the Carpathian-Balkan mountain range [18]. The direct basin of the Great Morava includes tributaries such as the Jasenica, Lepenica, Crnica, Ravanica, Belica, Rača, Resava rivers, as well as other smaller watercourses.

For the purpose of delineating the boundary of the direct basin of the Great Morava River, a digital terrain model (DTM) from the global ASTER project was used [19], while data on the locations of rain gauge stations and annual precipitation totals were obtained from the website of the Republic Hydrometeorological Service of Serbia [20].

For the application of spatial interpolation methods, 14 rain gauge stations were selected and analyzed, which mostly have continuous time series of annual precipitation data for the period from 1992 to 2022, with occasional gaps in certain years. Out of the 14 selected stations, three are located within the basin itself (Ćuprija, Kragujevac, and Smederevska Palanka), while the remaining 11 are situated in its immediate vicinity. Of the 19 rain gauge stations in the wider area of the analyzed catchment, data from five stations (Knjaževac, RC Bukulja, Rekovac, Sopot, and Vojska) could not be used in further analyses due to multi-year and significant interruptions in measurements, which prevented the formation of a continuous time series.

For the remaining stations, shorter interruptions in measurements were recorded in certain years. Missing values in these cases were estimated using the arithmetic mean method, thereby ensuring data continuity necessary for further analysis.

Spatial analysis, data processing, and application of spatial interpolation methods were performed using the ArcGIS software package, which enabled the development of spatial precipitation distribution models, as well as the visualization and analysis of the obtained results.

Figure 1 shows the extent of the direct basin of the Great Morava River along with the locations of the analyzed rain gauge stations.

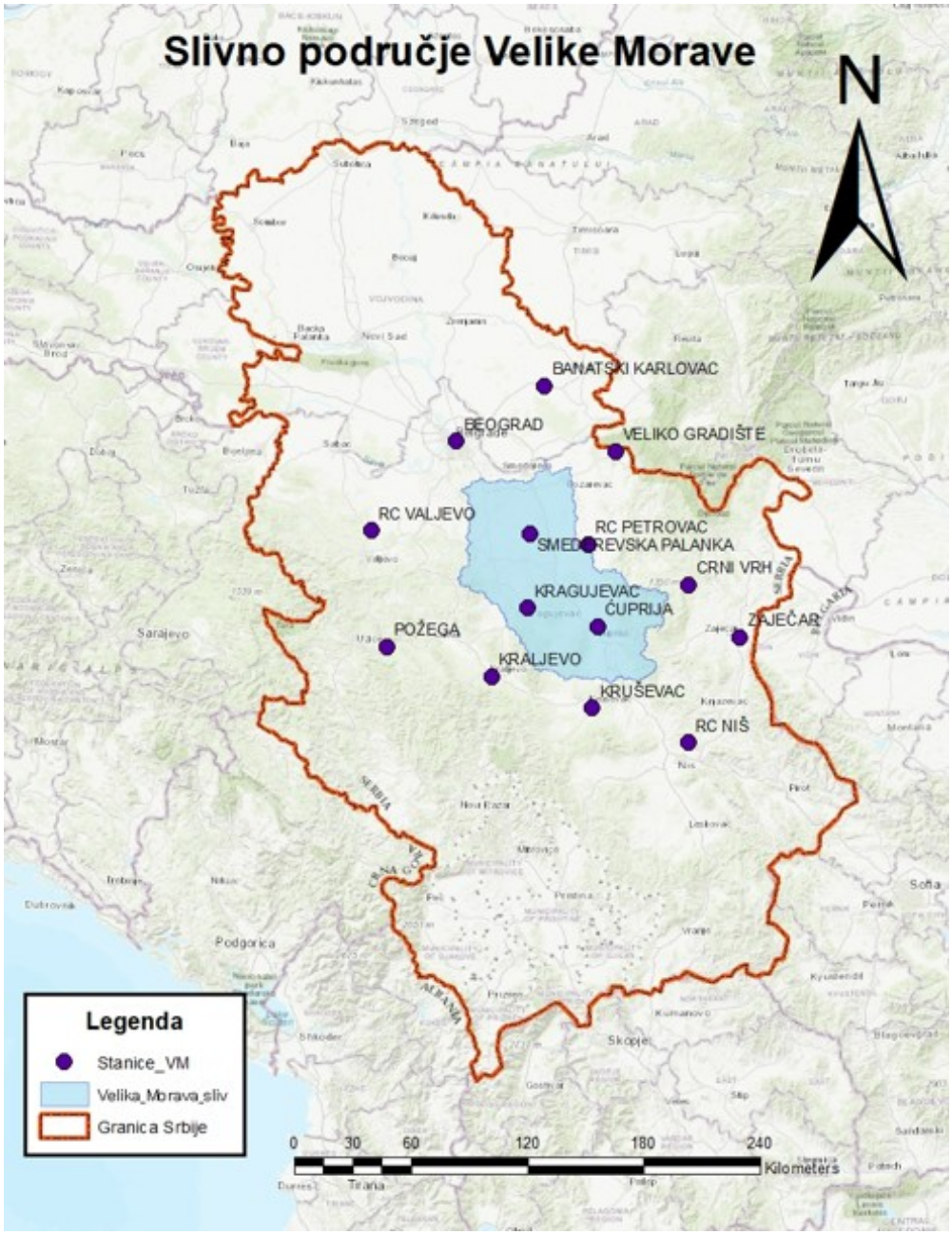


*Fig. 1 Direct basin of the Great Morava River with the location of rain gauge stations*

## 3. RESULTS AND DISCUSSION

Based on the analysis and processing of annual precipitation data from 14 selected measurement stations, it was determined that the stations Banatski Karlovac, Kraljevo, RC Petrovac, and RC Valjevo had interruptions in precipitation measurements in certain calendar years within the analyzed period. The estimation of missing data for these stations was performed using the arithmetic mean method, based on data from surrounding stations, in order to determine mean annual precipitation totals. The obtained values of mean annual precipitation for the period 1992-2022 ranged from 608.22 mm at the Zaječar station to 804.56 mm at the RC Valjevo station. Based on the processed and completed dataset, the selected spatial interpolation methods were applied to the mean annual precipitation over the area of the direct basin of the Great Morava River.

The results obtained using the Thiessen polygon method show that the weighting coefficients $w_i$ range from 0.01 to 0.32, where the experimental basin is divided into polygons according to the spatial position and influence of the measurement stations. Figure 2 shows the resulting Thiessen polygon network with the locations of the rain gauge stations and the corresponding weighting coefficients.

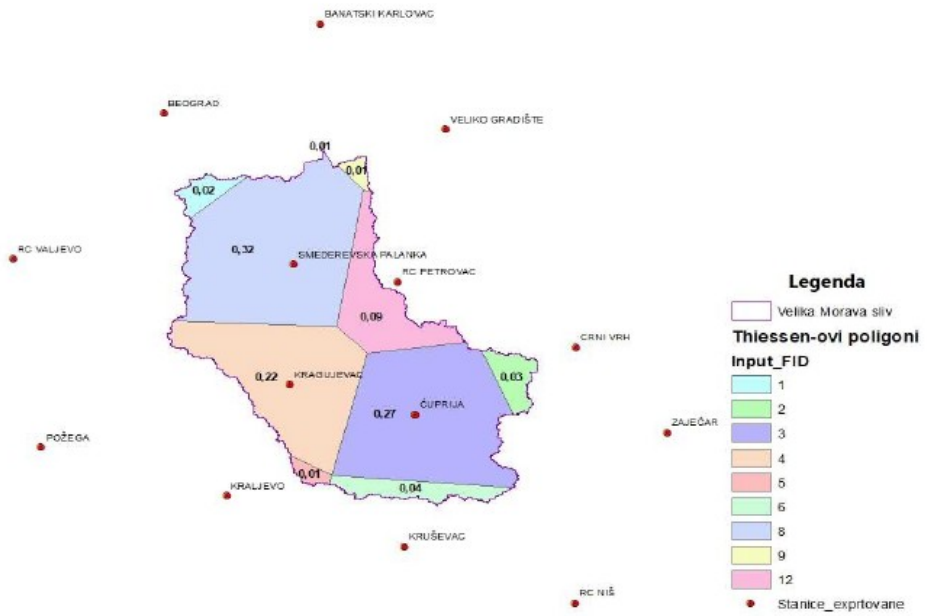


*Fig. 2 Thiessen polygon network with corresponding weighting coefficients*

Based on the obtained results, it can be concluded that higher weighting coefficients are associated with stations located within the basin itself (Ćuprija, Kragujevac, and Smederevska Palanka) compared to stations situated farther away from the analyzed basin. Rain gauge stations such as RC Niš, Zaječar, and Banatski Karlovac did not have a significant influence on the formation of the polygon network within the basin area. Based on the sum of the products of weighting coefficients and mean annual precipitation values for each measurement station, the mean annual precipitation P was obtained, amounting to 683.09 mm.

The application of the Inverse Distance Weighted (IDW) method produced results indicating a different spatial distribution and different values of mean annual precipitation. In the application of this method, a power parameter value of p=5 was adopted in accordance with recommendations from previous papers [16]. For this value of the power parameter, the influence of nearby measurement stations is emphasized, local variations are further highlighted, while more distant points have a reduced influence. Figure 3 shows the spatial distribution of annual precipitation totals obtained using the IDW method.

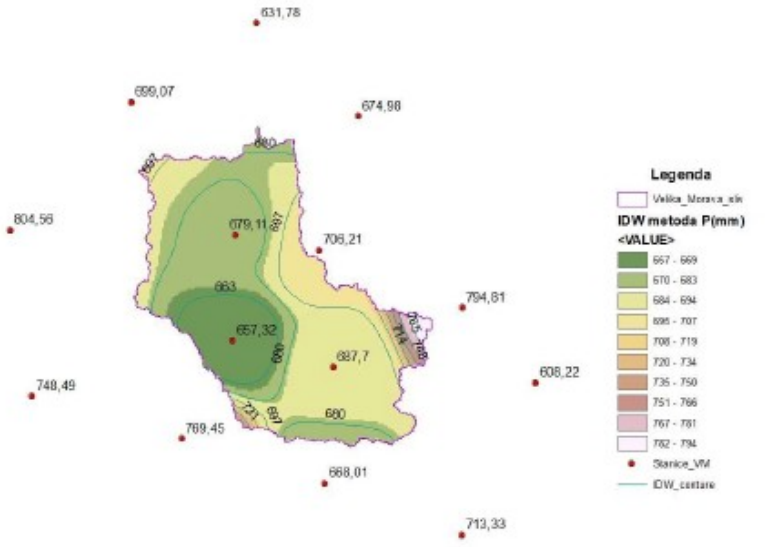


*Fig. 3 Spatial distribution of annual precipitation totals using the IDW method*

The influence of the values recorded at the measuring stations decreases inversely proportionally with the increase in distance from the analyzed basin area. Based on the obtained results, the mean annual precipitation total, P, was determined to be 684.46 mm.

The results obtained using the Spline method also indicate a different spatial distribution of average annual precipitation totals, with values ranging from 654 to 790 mm. The specific approach of this method, compared to the previous two, produced a range of values similar to that of the IDW method. Figure 4 shows the spatial distribution of annual precipitation totals obtained using the Spline method.

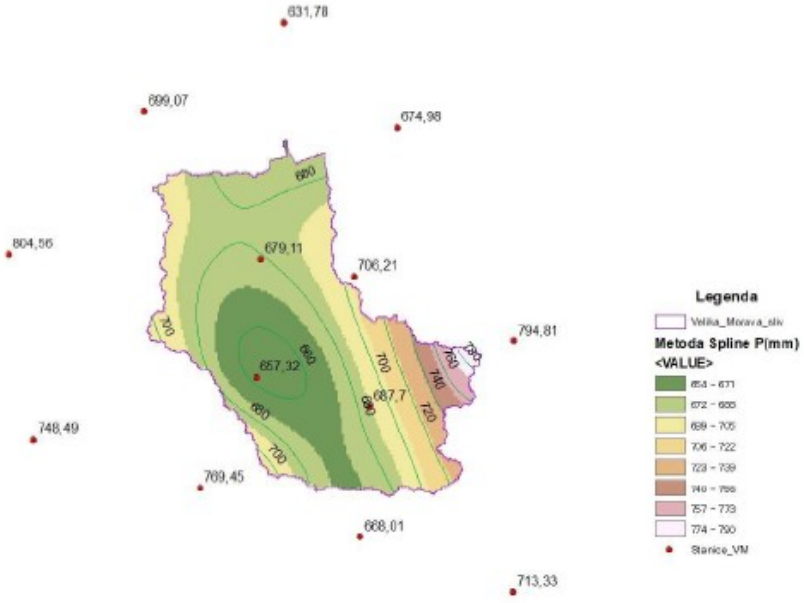


*Fig. 4 Spatial distribution of annual precipitation totals using the Spline method*

The mean annual precipitation total, P, obtained using the Spline method, is 686.88 mm. The results obtained using all selected spatial interpolation methods do not indicate significant deviations in the mean annual precipitation totals for the analyzed basin area of the Great Morava River. Table 1 presents a comparative overview of the results of the mean annual precipitation totals for the selected method.

*Tab. 1 Results of the mean annual precipitation totals*

| Input data | | | Thiessen method | IDW method | Spline method |
|---|---|---|---|---|---|
| Number of measuring stations N | Min. average annual precipitation total (mm) | Max. average annual precipitation total (mm) | Mean annual precipitation total(mm) | Mean annual precipitation total (mm) | Mean annual precipitation total (mm) |
| 14 | 608,22 | 804,56 | 683,09 | 684,46 | 686,88 |

The lowest mean value was obtained using the Thiessen method, while the highest value was obtained using the Spline method, with a total difference of 3.79 mm.
Although the results for the mean annual precipitation totals do not indicate significant deviations, it can be observed that, for the selected basin area, the Thiessen polygon method does not account for variations in precipitation between stations or the influence of topography. The IDW method is suitable for the analyzed area, given that 11 out of the 14 stations are located in the immediate vicinity of the basin, as their influence is determined based on distance; however, due to the uneven distribution of stations, the method is sensitive to the choice of the distance parameter. The Spline method enables a continuous representation of spatial variability, which is suitable for the heterogeneous basin area, but it is sensitive to local extreme values and the uneven distribution of stations.

## 4. CONCLUSION

Based on the conducted research and the application of precipitation spatial interpolation methods in the basin area of the Great Morava River (Thiessen, IDW, and Spline methods), it can be concluded that the choice of method does not significantly affect the mean precipitation value at the basin scale, but it plays an important role in the interpretation of their spatial distribution.
The Thiessen method provides a discontinuous distribution based on polygons of influence, while the IDW and Spline methods enable a continuous representation of the spatial variability of the data.
The results indicate that the greatest influence on interpolation is exerted by meteorological stations located within the basin area, as well as those in its immediate surroundings, while their influence decreases with increasing distance. In the case of the Thiessen method, certain stations located outside the basin do not have a direct influence on polygon formation, which is a consequence of the methodology itself.
It is also observed that a more uniform spatial distribution of measuring stations around the basin contributes to higher-quality interpolation and greater reliability of the obtained results.
Based on the conducted analysis, it can be recommended that in hydrological research the choice of method should be adapted to the objective of the analysis, where simpler methods may be sufficient for engineering assessments, while more complex methods enable detailed spatial analysis.The obtained results may be significant for further research in the fields of hydrological modeling, water resources management, and the assessment of climate change impacts on the spatial variability of precipitation.

**ACKNOWLEDGEMENT**

The research has been conducted within the project „Enhancement of teaching and scientific research capacities through the application of modern technologies in the fields of civil

engineering, geodesy, and disaster risk management and fire safety“, developed at the Department of Civil Engineering and Geodesy, Faculty of Technical Sciences, University of Novi Sad, Serbia.

## REFERENCES

[1] Michelon A., Benoit L., Beria H., Ceperley N., Schaefli B. (2021). Benefits from high-density rain gauge observations for hydrological response analysis in a small alpine catchment. *Hydrology and Earth System Sciences*, Volume 25, Issue 4, pp. 2301–2325. https://doi.org/10.5194/hess-25-2301-2021

[2] Bonacci O. (2010). Analiza nizova srednjih godišnjih temperatura zraka u Hrvatskoj. *Građevinar*, 62(9), pp. 781–791.

[3] Raković M., Jocković S., Pujević V., Obradović N. (2023). Klimatske promene i zemljani nasipi. In: Geotehnički aspekti građevinarstva i zemljotresno inženjerstvo, Savez građevinskih inženjera Srbije, Vrnjačka Banja, pp. 540–549.

[4] Mandić V., Kolaković S. (2021). Primena metoda prostorne interpolacije padavina na slivu reke Toplice. In: Voda 2021 – Zbornik radova 50. godišnje konferencije o aktuelnim problemima korišćenja i zaštite voda, Srpsko društvo za zaštitu voda, Beograd, pp. 57–66.

[5] Jeftenić G., Rašeta A., Kolaković S., Panić M., Mandić V. (2021). A methodology proposal for selecting the optimal location for small hydropower plants. *Tehnički vjesnik*, Volume 28, Issue 5, pp. 1462–1470. https://doi.org/10.17559/TV-20200408160557

[6] Mandić V., Kolaković S., Stojković M., Milošević B., Despotović I. (2023). Kriging interpolation of precipitation for Lake Ćelije catchment. In: XI International Conference “Heavy Machinery – HM 2023”, Faculty of Mechanical and Civil Engineering in Kraljevo, Vrnjačka Banja, pp. G.9–G.16.

[7] Ly S., Charles C., Degré A. (2013). Different methods for spatial interpolation of rainfall data for operational hydrology and hydrological modeling at watershed scale: a review. *Biotechnologie, Agronomie, Société et Environnement*, 17(2), pp. 392–406.

[8] Tobler W. R. (1970). A computer movie simulating urban growth in the Detroit region. *Economic Geography*, Volume 46, pp. 234–240. https://doi.org/10.2307/143141

[9] Bakış R., Bayazıt Y., Ahmady D. M., Çabuk S. N. (2021). Analysis and comparison of spatial rainfall distribution applying different interpolation methods in Porsuk River Basin, Turkey. Eskişehir Technical University Journal of Science and Technology B – Theoretical Sciences, Volume 9, Issue 1, pp. 1–14. https://doi.org/10.20290/estubtdb.726491

[10] Ma Q., Chang S., Lu G., Gourbesville P. (2024). Assessment of different interpolation algorithms for daily rainfall spatial distribution in the Var catchment, France. River, Volume 3, Issue 4, pp. 362–372. https://doi.org/10.1002/rvr2.106

[11] Liu Y., Zhuo L., Pregnolato M., Han D. (2022). An assessment of statistical interpolation methods suited for gridded rainfall datasets. International Journal of Climatology, Volume 42, Issue 5, pp. 2754–2772. https://doi.org/10.1002/joc.7389

[12] Mandić V., Despotović I., Šešlija M., Mihajlović S., Kolaković S. (2021). Efficiency analysis of two spatial interpolation methods of precipitation on the Kolubara river basin. In: X International Conference “Heavy Machinery – HM 2021”, Vrnjačka Banja, pp. G.43–G.50.

[13] Burrough P. A. (1986). Principles of Geographical Information Systems for Land Resources Assessment. Oxford, Clarendon Press.

[14] Watson D. F. (1992). Contouring: A Guide to the Analysis and Display of Spatial Data. Oxford, Pergamon.

[15] Mandić V., Šešlija M., Kolaković S., Kolaković S., Jeftenić G., Trajković S. (2021). *Mountain Road-Culvert Maintenance Algorithm*. Water, Volume 13, Article 471. https://doi.org/10.3390/w13040471

[16] Prohaska O., Plavšić J., Prohaska S., Todorović A. (2019). Kartiranje parametra metode Langbajna za proračun srednjih voda na neizučenim slivovima na teritoriji Srbije. *Vodoprivreda*, Volume 50, pp. 99–109.

[17] Arianti I., Soemarno, Hasyim A. W., Sulistyono R. (2018). Rainfall estimation by using Thiessen polygons, inverse distance weighted, spline, and kriging methods: a case study in Pontianak, West Kalimantan. *International Journal of Education and Research*, Volume 6, No. 11, pp. 301–310.

[18] Urošev M. (2016). Hidrološke suše u slivu Velike Morave. Doktorska disertacija, Prirodno-matematički fakultet, Univerzitet u Novom Sadu.

[19] NASA (2025). ASTER Data. Terra data portal. https://terra.nasa.gov/data/aster-data, accessed05.12.2025.

[20] Republički hidrometeorološki zavod Srbije (2025). Klimatološki godišnjaci – meteorološki podaci.https://www.hidmet.gov.rs/latin/meteorologija/klimatologija_godisnjaci.php, accessed:08.12.2025.

https://doi.org/10.24867/INDIS-2026-EN-381



# ASSESSMENT OF CLIMATE CHANGE IMPACTS ON HYDROLOGICAL AND CLIMATOLOGICAL VARIABLES: A CASE STUDY FROM THE SJENICA REGION, SERBIA

*Slobodan Kolaković[1], Vladimir Mandić[2], Marijana Milić[3], Ljubomir Budinski[4], Goran Jeftenić[5], Danilo Stipić[6], Tamara Pantić[7]*

***Summary:***

This study assesses climate change impacts on climatological and hydrological variables in a catchment in the Sjenica region, Serbia, using CMIP6 climate model outputs and an IPCC-recommended multi-model ensemble approach. Model performance was validated against observed data for the period 1990–2020, showing good agreement. Projections under future climate scenarios (SSP2-4.5 and SSP3-7.0) up to 2050 indicate an increase in mean annual air temperature of about 1°C, higher precipitation variability, and stronger contrasts between dry and wet years. IDF curves were adjusted using IPCC-based methods to represent future extreme rainfall conditions. The results emphasize the need to incorporate non-stationary climate conditions and ensemble-based climate projections into hydrological design and water resources management.

*Keywords: Climate change, IPCC, multi-model approach, SSP scenarios, IDF curves*

# PROCENA UTICAJA KLIMATSKIH PROMENA NA HIDROLOŠKE I KLIMATOLOŠKE POKAZATELJE: STUDIJA SLUČAJA PODRUČJA SJENICE, SRBIJA

***Rezime:***

U studiji je prikazana procena uticaja klimatskih promena na klimatološke i hidrološke veličine u slivu u području Sjenice, Srbija, korišćenjem izlaznih podataka klimatskih modela CMIP6 i multimodelskog pristupa, u skladu sa preporukama Međunarodnog panela o klimatskim promenama (IPCC). Model je verifikovan na osnovu osmotrenih podataka (srednja godišnja temperatura i suma godišnjih padavina) za period 1990–2020, pri čemu je uočena zadovoljavajuća vrednost koeficijenta korelacije. Projekcije budućih klimatskih scenarija (SSP2-4.5 i SSP3-7.0) do 2050. godine ukazuju na porast srednje godišnje temperature vazduha od oko 1°C, povećanu promenljivost padavina i izraženije razlike između sušnih i kišnih godina. Izvršena je transformacija postojećih ITP krivih na vrednosti intenziteta padavina za vremenski horizont do 2050. godine, prema preporukama IPCC. Rezultati ukazuju na potrebu uključivanja nestacionarnih klimatskih uslova i multimodelskih klimatskih projekcija u hidrološko projektovanje i upravljanje vodnim resursima u budućnosti.

[1] Assoc. Prof., Faculty of Technical Sciences (FTN), University of Novi Sad (UNS), Novi Sad, Serbia, kolakovic.s@uns.ac.rs, ORCID 0000-0002-9859-9669
[2] Ass. Prof., FMCE, UNKG, Kraljevo, Serbia, mandic.v@mfkv.kg.ac.rs, ORCID 0000-0003-3529-171X
[3] Teach. Ass., FTN, UNS, Novi Sad, Serbia, marijana.milic@uns.ac.rs, ORCID 0000-0003-1974-2461
[4] Full Prof., FTN, UNS, Novi Sad, Serbia, ljubab@uns.ac.rs, ORCID 0000-0001-7816-0889
[5] Assoc. Prof., FTN, UNS, Novi Sad, Serbia, goran.jeftenic@uns.ac.rs, ORCID 0000-0001-5639-4406
[6] Ass. Prof., FTN, UNS, Novi Sad, Serbia, danilostipic@uns.ac.rs, ORCID 0000-0001-6557-5997
[7] Teach. Ass., FTN, UNS, Novi Sad, Serbia, tamara.pantic@uns.ac.rs, ORCID 0009-0003-6341-5692

*Ključne reči: Klimatske promene, IPCC, multimodelski pristup, SSP scenariji, ITP krive*

## 1. INTRODUCTION

Climate change has become one of the most significant environmental challenges of the 21st century, affecting natural ecosystems, water resources, infrastructure, and socio-economic development worldwide. According to the Sixth Assessment Report of the Intergovernmental Panel on Climate Change (IPCC), global surface temperatures have already increased by approximately 1.1°C relative to the pre-industrial period (1850–1900), and further warming is expected in the coming decades under all greenhouse gas emission scenarios [1,2]. These changes are accompanied by modifications of the global hydrological cycle, including alterations in precipitation regimes, evapotranspiration, runoff generation, and the frequency and intensity of hydrological extremes such as floods and droughts [1,3].

Water resources are among the sectors most sensitive to both climate variability and long-term climate change. Even minor variations in air temperature and precipitation can substantially affect catchment hydrology by altering snow accumulation and melt, soil moisture, groundwater recharge, and river discharge [4,5]. As a result, reliable assessment of future climatological and hydrological conditions is essential for sustainable water resources management, infrastructure planning, and climate adaptation strategies. The traditional assumption of stationarity in hydrological processes is increasingly challenged under changing climatic conditions, requiring approaches that explicitly account for future climate variability [6].

Although mitigation measures aimed at reducing greenhouse gas emissions remain fundamental for limiting future warming, their effects are expected to become evident only over longer time scales. Consequently, adaptation has emerged as an equally important component of climate policy and water resources management. Scenario-based climate impact assessments provide an effective framework for evaluating possible future hydrological conditions under different emission pathways and for supporting long-term planning under increasing climatic uncertainty.

Europe has experienced warming at a rate exceeding the global average in recent decades, making it one of the fastest-warming continents [7]. Southeastern Europe is considered particularly vulnerable due to the increasing frequency of prolonged heat waves, irregular precipitation patterns, and more frequent hydrological extremes [7,8]. Recent observations indicate that Serbia has also experienced a significant rise in mean annual air temperature during the latter half of the twentieth century and the early twenty-first century, accompanied by notable changes in precipitation distribution and an increased frequency of extreme weather events [9]. These changes are expected to become even more pronounced over the coming decades, underscoring the need for regional and local-scale assessments to support adaptation planning.

While global and regional climate projections offer valuable insights, their spatial resolution is typically inadequate for direct application to individual catchment analyses. Local topography, land cover, and physiographic characteristics significantly influence climatological and hydrological responses, especially in mountainous regions where spatial variability is pronounced [10]. Consequently, site-specific studies are essential for understanding future changes in local hydrological conditions and for supporting engineering design and water management decisions. Reliable assessment at the local scale also requires careful analysis of historical climatological and hydrological observations, along with appropriate spatial interpolation techniques, to ensure representative input data for climate impact analyses.

Recent advances in climate modelling, particularly within the Coupled Model Intercomparison Project Phase 6 (CMIP6), have significantly enhanced the ability to

simulate future climate conditions under various Shared Socioeconomic Pathway (SSP) scenarios [11,12]. Coordinated under the World Climate Research Programme (WCRP), CMIP6 simulations constitute the scientific basis of the latest IPCC climate assessments. However, substantial uncertainties persist due to differences among individual climate models. To address these uncertainties, the IPCC recommends the use of multi-model ensemble approaches, in which projections from several climate models are combined to reduce uncertainties associated with any single model and to provide more robust estimates of future climate conditions [1,2]. As a result, ensemble-based methods have become standard practice in climate impact assessments and water resources studies worldwide. Among the available emission pathways, SSP2-4.5 represents an intermediate development scenario with stabilized emissions, whereas SSP3-7.0 reflects a future characterized by higher greenhouse gas emissions and stronger climate forcing.

Although research on climate change impacts on hydrological systems is expanding, few studies have specifically addressed small mountainous catchments in southwestern Serbia. The Sjenica region (Figure 1), characterized by high elevations, complex terrain, and pronounced continental climatic influences, is particularly sensitive to projected climatic changes. An improved understanding of future changes in climatological and hydrological variables in this region is therefore important for long-term water resources management, infrastructure planning, and climate adaptation.

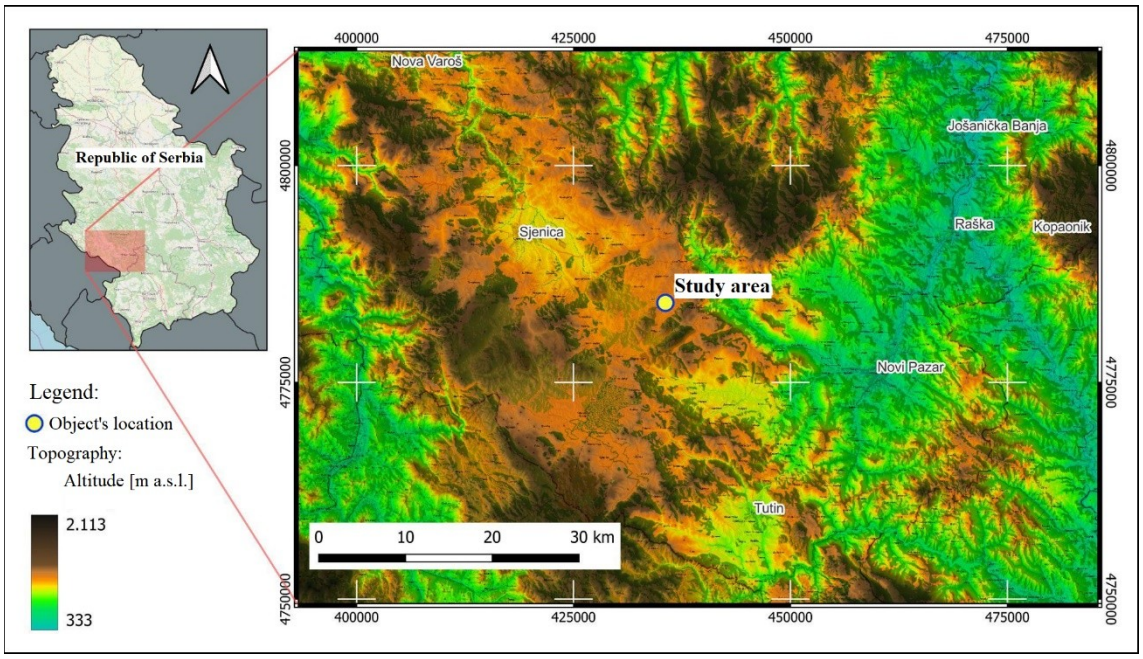


*Fig. 1 Topography of the Sjenica study area*

This study aims to assess the projected impacts of climate change on selected climatological and hydrological variables in the Sjenica region, Serbia, using historical observations and climate projections derived from a validated CMIP6 multi-model ensemble. Historical climatological and hydrological datasets were analysed, spatially interpolated, and used to evaluate the performance of selected CMIP6 models prior to their application for future climate projections. Future changes are analysed under the SSP2-4.5 and SSP3-7.0 emission scenarios up to the year 2050. The obtained results provide a scientific basis for evaluating future climatic conditions and their potential effects on catchment hydrology, contributing to more reliable adaptation planning and sustainable water resources management under changing climate conditions.

## 2. METHODOLOGY

The latest IPCC report (March 2023) indicates that global greenhouse gas emissions continue to rise, primarily due to unsustainable energy and land use, land-use change, and consumption and production patterns at multiple scales. The global hydrological cycle is projected to change unevenly throughout the 21st century. Precipitation contrasts between dry and wet regions, as well as between seasons, are expected to intensify, though regional exceptions may occur. Over the past 50 years, mean annual air temperatures in Europe have increased more rapidly than the global average, with particularly pronounced winter warming.

Observed mean annual air temperatures (Figure 2) over the past 50 years show a positive trend across almost the entire territory of Serbia (Figure 3). The largest increase in temperature has been recorded during the autumn season.

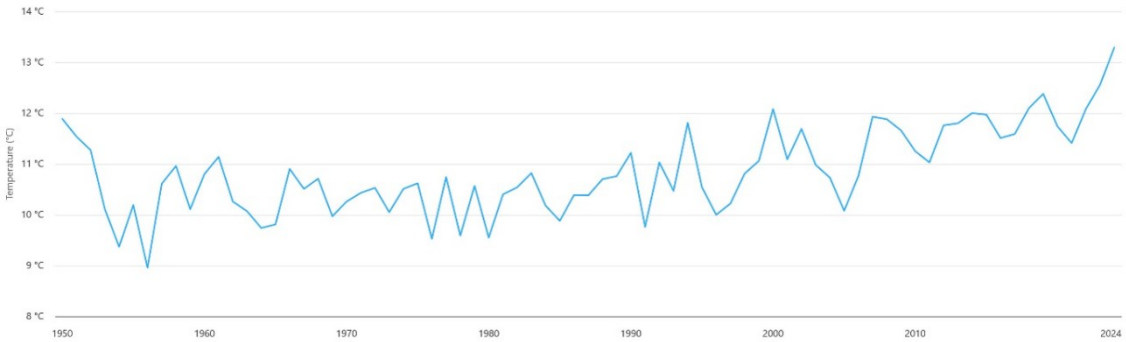


*Fig. 2 Mean annual air temperature in the Republic of Serbia (1950–2024) [13]*

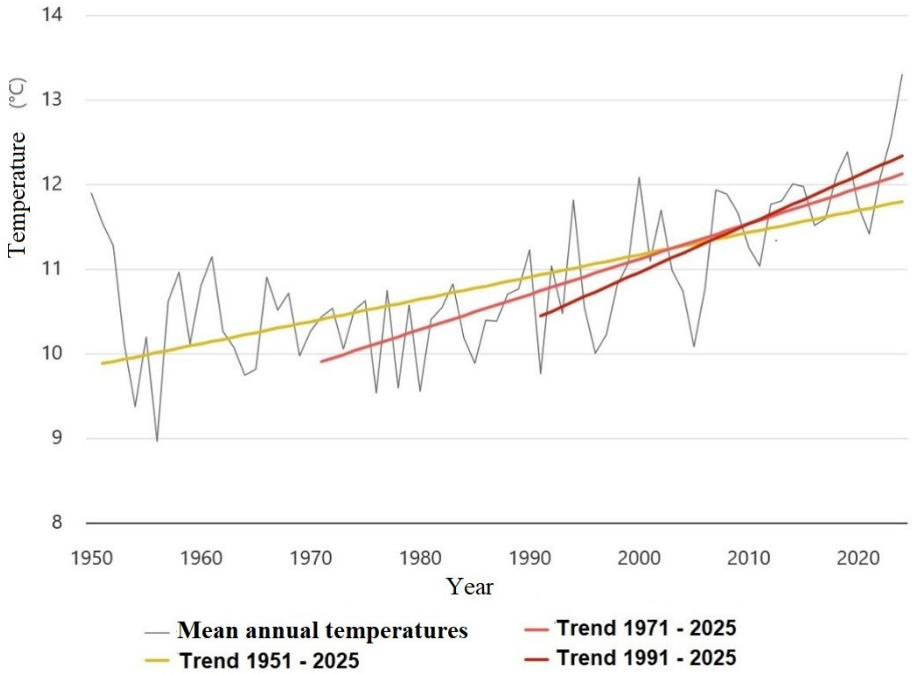


*Fig. 3 Trends in mean annual air temperature in the Republic of Serbia [13]*

Observed precipitation over the period 1950–2020 shows a positive trend across most of Serbia (Figure 4). This suggests that climatic variability in Serbia is influenced not only by natural climate factors but also by anthropogenic drivers. Based on these findings and IPCC recommendations for the study area, an assessment of future climate impacts on hydrological processes in the catchment was conducted using two highly likely climate scenarios: SSP2, an optimistic scenario, and SSP3, a pessimistic scenario.

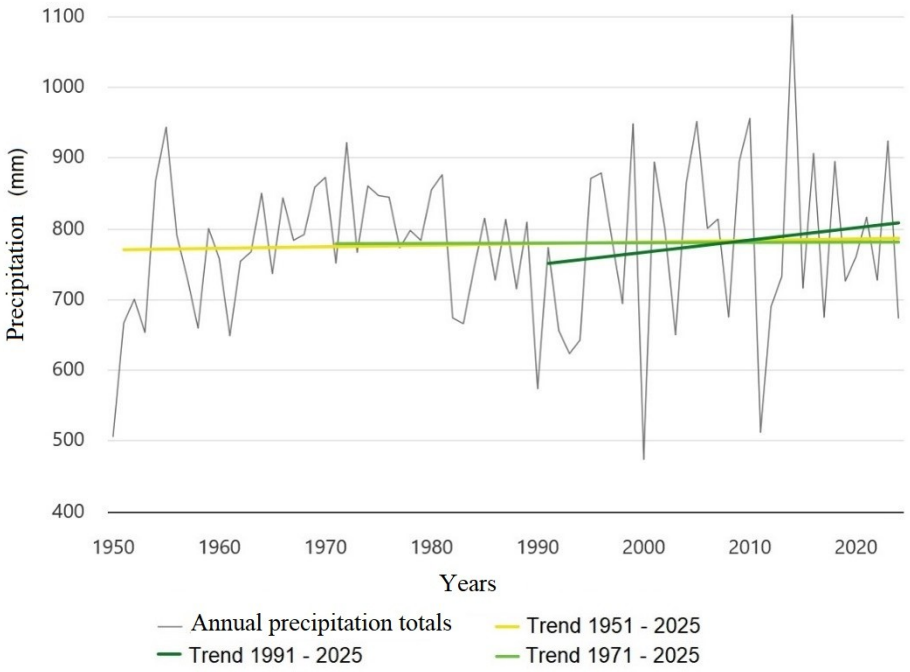


*Fig. 4 Trends in annual precipitation totals in the Republic of Serbia [13]*

## 2.1. CLIMATE MODEL SELECTION

A wide range of climate models is available globally for simulating future climate change scenarios. Current understanding of the climate system and its projected response to increasing atmospheric greenhouse gas concentrations relies on global climate models, powerful computational tools that simulate the physical processes governing the climate system. The World Climate Research Program, through the latest phase of the Coupled Model Intercomparison Project published in 2021 and 2022, provides the most recent projections based on simulations from 31 climate models developed by the international scientific community. Table 1 presents the climate models and the institutions responsible for their development.

*Tab. 1 Names of climate models and contributing institutions*

| item number | Climate models | Institution |
|---|---|---|
| 1 | AWI-CM-1-1-MR | Alfred Wegener Institute, Helmholtz Centre for Polar and Marine Research (AWI) |
| 2 | BCC-CSM2-MR | Beijing Climate Centre |
| 3 | CAMS-CSM1-0 | Chinese Academy of Meteorological Sciences |
| 4 | CanESM5 | Canadian Centre for Climate Modelling and Analysis, Environment and Climate Change Canada, Victoria, Canada |
| 5 | CAS-ESM2-0 | Chinese Academy of Sciences, Beijing, China |
| 6 | CESM2 | National Centre for Atmospheric Research (NCAR), Climate and Global Dynamics Laboratory, Boulder, USA |
| 7 | CESM2-WACCM | National Centre for Atmospheric Research (NCAR), Climate and Global Dynamics Laboratory, Boulder, USA |
| 8 | CIESM | Department of Earth System Science, Tsinghua University, Beijing, China |
| 9 | CMCC-CM2-SR5 | Fondazione Centro Euro-Mediterraneo sui Cambiamenti Climatici (CMCC), Lecce, Italy |
| 10 | CMCC-ESM2 | Fondazione Centro Euro-Mediterraneo sui Cambiamenti Climatici (CMCC), Lecce, Italy |

| | | |
|---|---|---|
| 11 | EC-Earth3 | EC-Earth consortium, Rossby Center, Swedish Meteorological and Hydrological Institute/SMHI, Norrkoping, Sweden |
| 12 | EC-Earth3-AerChem | EC-Earth consortium, Rossby Center, Swedish Meteorological and Hydrological Institute/SMHI, Norrkoping, Sweden |
| 13 | EC-Earth3-CC | EC-Earth consortium, Rossby Center, Swedish Meteorological and Hydrological Institute/SMHI, Norrkoping, Sweden |
| 14 | EC-Earth3-Veg | EC-Earth consortium, Rossby Center, Swedish Meteorological and Hydrological Institute/SMHI, Norrkoping, Sweden |
| 15 | EC-Earth3-Veg-LR | EC-Earth consortium, Rossby Center, Swedish Meteorological and Hydrological Institute/SMHI, Norrkoping, Sweden |
| 16 | FGOALS-f3-L | Chinese Academy of Sciences, Beijing, China |
| 17 | FGOALS-g3 | Chinese Academy of Sciences, Beijing, China |
| 18 | FIO-ESM-2-0 | First Institute of Oceanography (FIO) and Qingdao National Laboratory for Marine Science and Technology (QNLM), Qingdao, China |
| 19 | GFDL-CM4 | National Oceanic and Atmospheric Administration, Geophysical Fluid Dynamics Laboratory, Princeton, NJ, USA |
| 20 | GFDL-ESM4 | National Oceanic and Atmospheric Administration, Geophysical Fluid Dynamics Laboratory, Princeton, NJ, USA |
| 21 | INM-CM4-8 | Institute for Numerical Mathematics (INM), Russian Academy of Science, Moscow, Russia |
| 22 | INM-CM5-0 | Institute for Numerical Mathematics (INM), Russian Academy of Science, Moscow, Russia |
| 23 | IPSL-CM6A-LR | Institut Pierre Simon Laplace (IPSL), Paris, France |
| 24 | KACE-1-0-G | National Institute of Meteorological Sciences/Korea Meteorological Administration, Climate Research Division, Seoho-bukro 33, Seogwipo-si, Jejudo 63568, Republic of Korea (NIMS-KMA) |
| 25 | MIROC6 | Japan Agency for Marine-Earth Science and Technology (JAMSTEC), Kanagawa, Japan, Atmosphere and Ocean Research Institute (AORI), The University of Tokyo, Chiba, Japan, National Institute for Environmental Studies (NIES), Ibaraki, Japan, and RIKEN Center for Computational Science, Hyogo, Japan |
| 26 | MPI-ESM1-2-HR | Max Planck Institute for Meteorology (MPI-M), Hamburg, Germany |
| 27 | MPI-ESM1-2-LR | Max Planck Institute for Meteorology (MPI-M), Hamburg, Germany |
| 28 | MRI-ESM2-0 | Meteorological Research Institute (MRI), Tsukuba, Ibaraki, Japan |
| 29 | NESM3 | Nanjing University of Information Science and Technology (NUIST), Nanjing, China |
| 30 | NorESM2-LM | NorESM Climate modeling Consortium, Oslo, Norway |
| 31 | NorESM2-MM | NorESM Climate modeling Consortium, Oslo, Norway |

Possible climate scenarios serve as a tool for understanding the characteristics and magnitude of changes, thereby supporting decision-making processes. Relying solely on end-of-century climate model outcomes is not an adequate approach for assessing the usefulness of a given scenario. For societal decision-making purposes, shorter time horizons are more relevant. Table 2 provides an overview of the models included in the project and their range of applicability to temperature and precipitation under different climate scenarios.

*Tab. 2 Comparative overview of the applicability of climate models for simulating different climate change scenarios and historical data*

| # | Climate models | Historical | SSP1-1.9 | SSP1-2.6 | SSP2-4.5 | SSP3-7.0 | SSP4-6.0 | SSP5-8.5 |
|---|---|---|---|---|---|---|---|---|
| 1 | AWI-CM-1-1-MR | X | | X | X | X | | X |
| 2 | BCC-CSM2-MR | X | | X | X | X | | X |
| 3 | CAMS-CSM1-0 | X | X | X | X | X | | X |
| 4 | CanESM5 | X | X | X | X | X | X | X |

| | | | | | | | | |
|---|---|---|---|---|---|---|---|---|
| 5 | CAS-ESM2-0 | | | | | | | |
| 6 | CESM2 | X | | X | X | X | | X |
| 7 | CESM2-WACCM | X | | X | X | X | | X |
| 8 | CIESM | X | | X | X | | | X |
| 9 | CMCC-CM2-SR5 | X | | X | X | X | | X |
| 10 | CMCC-ESM2 | | | | | | | |
| 11 | EC-Earth3 | X | | X | X | X | | X |
| 12 | EC-Earth3-AerChem | | | | | | | |
| 13 | EC-Earth3-CC | | | | | | | |
| 14 | EC-Earth3-Veg | X | X | X | | X | | X |
| 15 | EC-Earth3-Veg-LR | | | | | | | |
| 16 | FGOALS-f3-L | X | | X | X | X | | X |
| 17 | FGOALS-g3 | X | X | | X | X | X | X |
| 18 | FIO-ESM-2-0 | X | | X | X | | | X |
| 19 | GFDL-CM4 | X | | X | X | X | | X |
| 20 | GFDL-ESM4 | X | X | X | X | X | | X |
| 21 | INM-CM4-8 | X | | | X | X | | X |
| 22 | INM-CM5-0 | X | | X | X | X | | X |
| 23 | IPSL-CM6A-LR | X | X | X | X | X | X | X |
| 24 | KACE-1-0-G | X | | X | X | X | | X |
| 25 | MIROC6 | X | X | X | X | X | X | X |
| 26 | MPI-ESM1-2-HR | X | | X | X | X | | X |
| 27 | MPI-ESM1-2-LR | X | | X | X | X | | X |
| 28 | MRI-ESM2-0 | X | X | X | X | X | X | X |
| 29 | NESM3 | X | | X | X | X | | X |
| 30 | NorESM2-LM | X | | X | X | X | | X |
| 31 | NorESM2-MM | X | | X | X | X | | X |

The data in the table indicate that certain models are not calibrated for specific scenarios. For the purposes of this study, simulations from models calibrated for the optimistic SSP2 and pessimistic SSP3 scenarios are considered relevant. For impact assessment, selecting an appropriate climate model is a key issue. Model selection is based on validation against observed historical data for a given region. Models whose outputs show good agreement with historical climate data are considered more suitable for planning purposes. This approach compares observed historical climate data over a defined period with model results to identify models that best reproduce observed conditions.

However, IPCC recommendations support an ensemble-based approach, suggesting that it is more appropriate to assess average temperature and precipitation anomalies by considering results from multiple models rather than relying on a single model. This approach uses the mean or median of all models to reduce the uncertainty associated with any individual model. Since climate models cannot simulate the exact sequence of future events, it is common practice to use multiple climate models for future projections. This allows estimation of the range within which changes can be expected. The more models that indicate a similar signal or comparable values, the higher the confidence that such a change is likely to occur in the future.

## 2.2. CLIMATE MODEL VALIDATION

For water resources, hydrological models are used, and according to IPCC recommendations for quantifying hydrological impacts of climate change, outputs from climate models are used as input data. However, a major limitation is the mismatch in spatial resolution between climate model outputs and the input requirements of hydrological models. Therefore, post-processing is necessary to improve the suitability of these large-scale global models for impact studies. Accordingly, a statistical downscaling method will be applied to meet this requirement. Figure 5 presents the climate models suitable for the territory of the Republic of Serbia and the multi-model ensemble approach.




*Fig. 5 List of climate models suitable for the territory of the Republic of Serbia and the multi-model ensemble approach*

The Intergovernmental Panel on Climate Change (IPCC) recommendations in its latest 2023 report state that using only a single one of the existing climate models may lead to subjective and unreliable results. Therefore, the IPCC recommends using multiple climate models based on their technical specifications, with the final results derived as the median (most frequently occurring value) of all model outputs. This methodology reduces the risk of obtaining unreliable results due to the subjective selection of a single climate model.

For further calculations of climate variables up to 2050, a multi-model ensemble approach was adopted, using the median of the previously mentioned 11 climate models. However, before applying any model, validation must be performed to assess its performance. The validation of the selected models was carried out using previously interpolated values of mean annual air temperature and annual precipitation totals for the period 1990–2020.

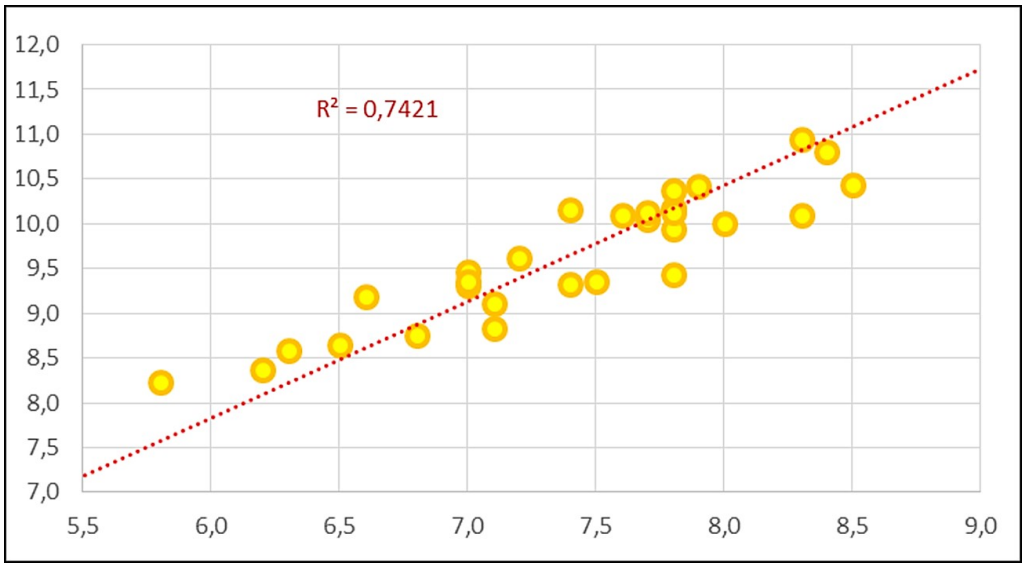


*Fig. 6 Comparison of observed mean annual air temperature and climate model results for the period 1990–2020*

Figure 6 compares observed mean annual air temperatures with those generated by the climate model. The results demonstrate a strong correlation between observed and modelled values. The coefficient of determination ($R^2$) for this dependence is 0.74, indicating substantial agreement between observed and modelled mean annual air temperatures.

In addition to air temperature, the selected model was validated for annual precipitation totals during the period 1990–2020. Figure 7 compares interpolated annual precipitation values at the study location with those produced by the climate model. The results indicate strong agreement between measured and modelled data, as demonstrated by a high correlation coefficient.

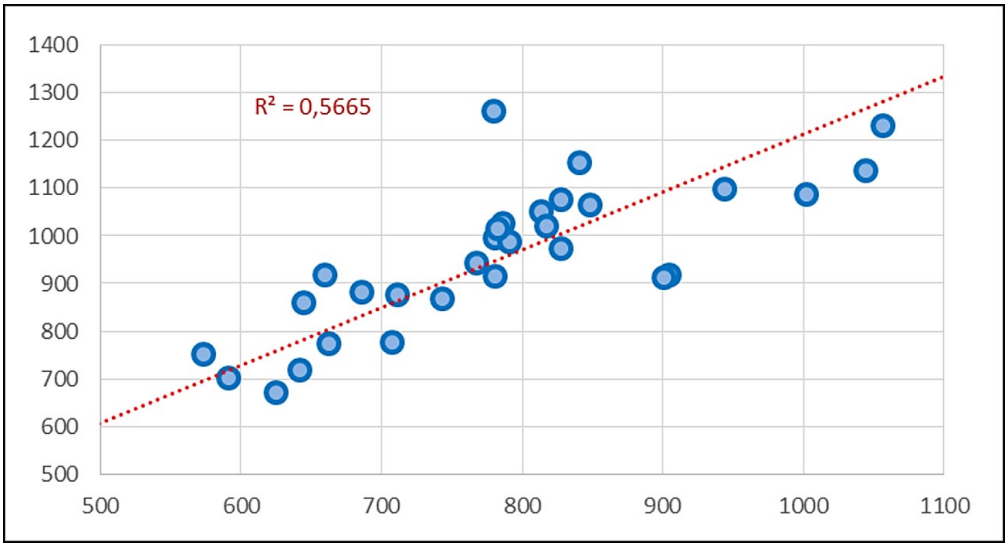


*Fig. 7 Comparison of observed annual precipitation totals and climate model results for the period 1990–2022*

Based on the above, it can be concluded that the multi-model ensemble approach for climate variable modeling provides satisfactory results when validated against historical data. Therefore, all subsequent calculations of climate variables for the future period from 2024 to 2050 will use the aforementioned multi-model ensemble approach, which will hereafter be referred to as the adopted climate model.

## 3. RESULTS AND DISCUSSION OF CLIMATE AND HYDROLOGICAL PROJECTIONS (UP TO 2050)

All climate models, including the model adopted in this study, yield varying results depending on the assumed future climate change scenario. The Intergovernmental Panel on Climate Change (IPCC) categorizes potential climate futures into five scenarios. Consequently, it is necessary to specify which future climate scenarios will be used for calculations prior to applying the climate model, as the results may differ substantially.
As shown in the following Figure 8, the results of climate model projections can vary significantly depending on the adopted scenario. All possible scenarios have been previously described, and two "highly likely" scenarios recommended by the IPCC were selected. In this study, calculations were performed for the SSP2-4.5 scenario, which assumes $CO_2$ emissions remain at approximately current levels by 2050, and the SSP3-7.0 scenario, which assumes $CO_2$ emissions double by 2050.

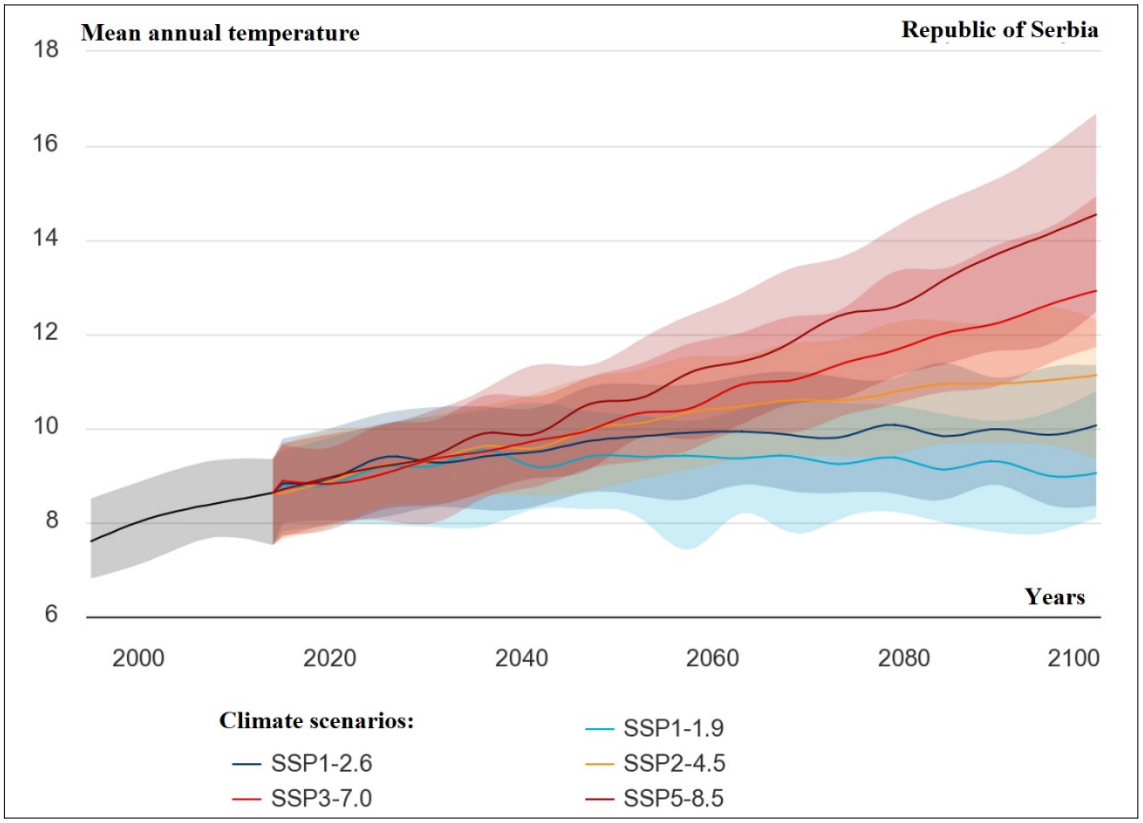


*Fig. 8 Results of applying different climate scenarios to mean annual air temperature projections for the Republic of Serbia [13]*

### 3.1. RESULTS OF CLIMATE MODEL PROJECTIONS

Using the adopted multi-model ensemble approach and the two selected climate change scenarios, mean annual air temperatures and annual precipitation totals were estimated for the study area in the Sjenica region up to the year 2050.

*Tab. 3 Climate model results*

| | SSP2-4.5 | | SSP3-7.0 | |
|---|---|---|---|---|
| Year: | $T_{mean,annual}$ [°C] | $P_{total,annual}$ [mm] | $T_{mean,annual}$ [°C] | $P_{total,annual}$ [mm] |
| 2024 | 9.2 | 928.1 | 9.1 | 882.4 |

| | | | | |
|---|---|---|---|---|
| 2025 | 9.2 | 877.3 | 8.8 | 836.9 |
| 2026 | 9.3 | 916.1 | 9.0 | 860.9 |
| 2027 | 9.2 | 890.4 | 9.1 | 891.9 |
| 2028 | 9.4 | 855.4 | 9.1 | 940.4 |
| 2029 | 9.3 | 830.4 | 9.2 | 871.4 |
| 2030 | 9.2 | 916.3 | 9.3 | 885.9 |
| 2031 | 9.4 | 866.7 | 9.4 | 898.8 |
| 2032 | 9.7 | 791.8 | 9.6 | 911.9 |
| 2033 | 9.3 | 866.0 | 9.3 | 947.8 |
| 2034 | 9.4 | 827.0 | 9.6 | 936.6 |
| 2035 | 9.6 | 859.9 | 9.3 | 858.4 |
| 2036 | 9.6 | 917.7 | 9.4 | 936.7 |
| 2037 | 9.6 | 885.8 | 9.5 | 913.0 |
| 2038 | 9.7 | 794.5 | 9.7 | 918.1 |
| 2039 | 9.6 | 938.5 | 9.7 | 899.1 |
| 2040 | 9.7 | 844.3 | 9.7 | 883.2 |
| 2041 | 9.5 | 853.1 | 9.9 | 876.9 |
| 2042 | 9.5 | 836.4 | 9.6 | 866.2 |
| 2043 | 9.8 | 855.1 | 9.8 | 903.0 |
| 2044 | 9.6 | 882.1 | 9.8 | 861.5 |
| 2045 | 9.9 | 864.6 | 9.9 | 861.8 |
| 2046 | 9.9 | 921.9 | 9.7 | 921.7 |
| 2047 | 10.0 | 857.8 | 10.1 | 888.0 |
| 2048 | 10.2 | 889.9 | 10.2 | 890.4 |
| 2049 | 10.0 | 837.1 | 10.3 | 886.9 |
| 2050 | 10.0 | 829.0 | 10.1 | 888.6 |

Although tabular presentation of climate model calculation results is highly useful, the following figures provide a graphical representation of the projected results of the adopted climate model for the two selected scenarios.

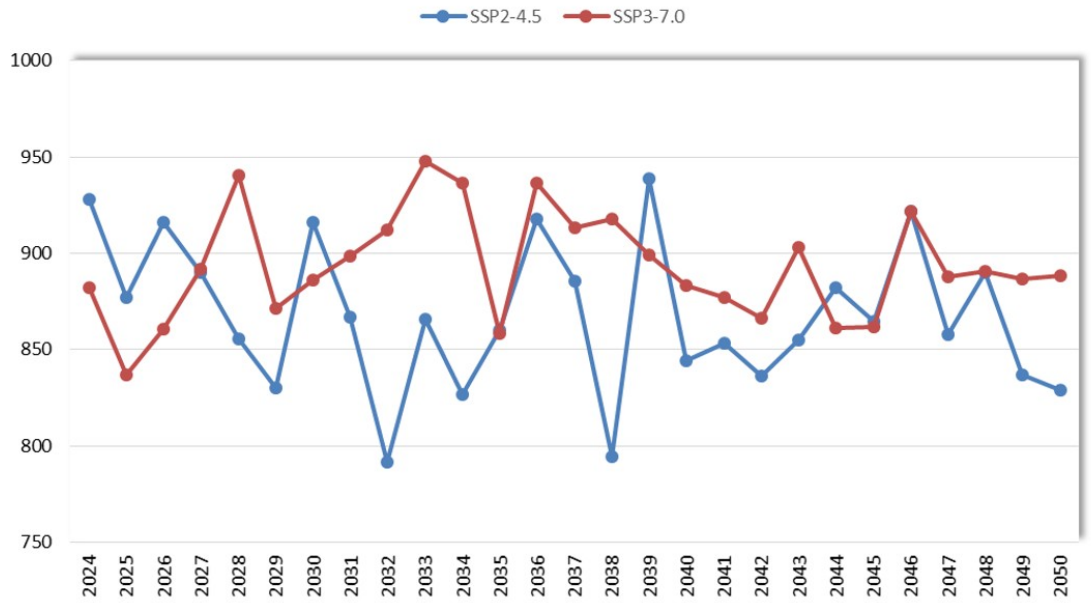


*Fig. 9 Projected annual precipitation totals from the adopted climate model up to 2050*

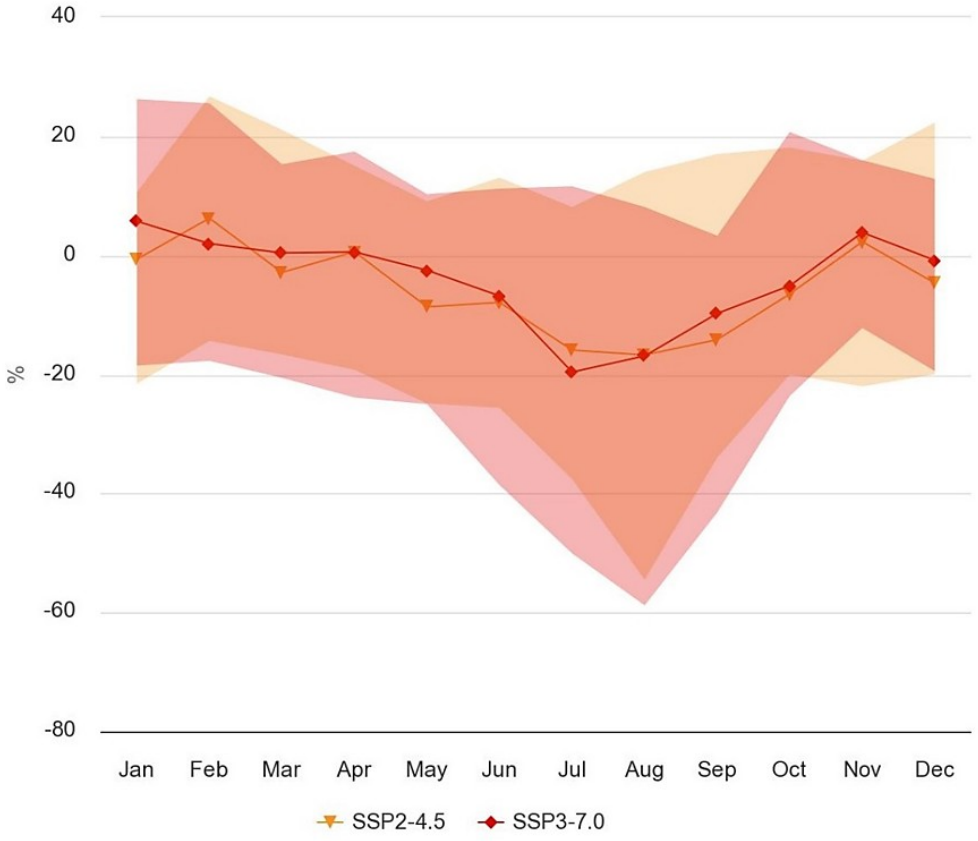


*Fig. 10 Projected monthly precipitation anomalies from the adopted climate model up to 2050, expressed in percentages [13]*

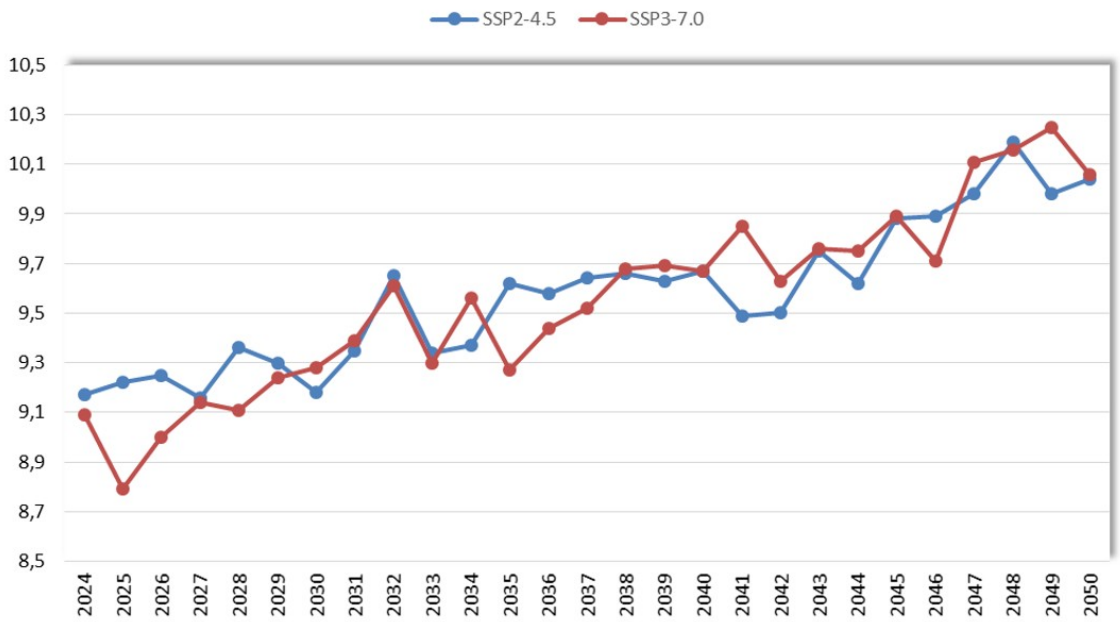


*Fig. 11 Projected mean annual air temperature from the adopted climate model up to 2050*

From the previous diagrams, it can be concluded that projections from the adopted multi-model ensemble approach indicate that mean annual air temperatures will continue to increase up to 2050 in both scenarios, resulting in an overall rise of approximately 1°C by 2050. This warming trend, according to the model results, is accompanied by a slight decrease in annual precipitation totals. In the diagram showing changes in annual precipitation totals up to 2050 (Figure 9), the decreasing trend is not particularly pronounced; however, a more significant feature is the increasingly pronounced contrast between dry and wet years, as illustrated by substantial interannual variability in precipitation.

## 3.2. RESULTS OF HYDROLOGICAL MODEL PROJECTIONS

For hydraulic analyses of flood events, this study estimated design rainfall depths for return periods of 5, 10, 20, 50, and 100 years. Since the study catchment is relatively small, its time of concentration was assumed to be less than 24 hours. Consequently, the estimation of runoff hydrographs required short-duration design rainfall events, specifically those lasting less than 24 hours.

The necessary Intensity–Duration–Frequency (IDF) curves for the Melaje rain gauge station, situated near the study area, were sourced from the Water Management Master Plan of the Republic of Serbia, prepared by the Jaroslav Černi Water Institute [14] and the Republic Hydrometeorological Service of Serbia [15]. Although the Melaje station has not been operational for approximately the past decade, historical IDF data were available in this documentation and were utilized in the present study. The relevant IDF data are presented in Table 4.

*Tab. 4 Intensity–Duration–Frequency (IDF) values: rainfall intensity (I, mm/min) as a function of rainfall duration (D, min) and exceedance probability (P, %) for GS Melaje*

| | D [min] | P [%] | | | | | | |
|---|---|---|---|---|---|---|---|---|
| I [mm/min] | | 0.1 | 1 | 2 | 5 | 10 | 20 | 50 |
| | 10 | 3.135 | 2.478 | 2.281 | 2.015 | 1.808 | 1.588 | 1.245 |
| | 20 | 1.981 | 1.566 | 1.442 | 1.274 | 1.143 | 1.004 | 0.787 |

| | | | | | | | | |
|---|---|---|---|---|---|---|---|---|
| | 30 | 1.479 | 1.169 | 1.076 | 0.951 | 0.853 | 0.749 | 0.588 |
| | 60 | 0.874 | 0.691 | 0.636 | 0.562 | 0.504 | 0.443 | 0.347 |
| | 120 | 0.506 | 0.400 | 0.368 | 0.325 | 0.292 | 0.256 | 0.201 |
| | 180 | 0.365 | 0.289 | 0.266 | 0.235 | 0.211 | 0.185 | 0.145 |
| | 360 | 0.209 | 0.165 | 0.152 | 0.134 | 0.120 | 0.106 | 0.083 |
| | 720 | 0.119 | 0.094 | 0.086 | 0.076 | 0.068 | 0.060 | 0.047 |
| | 1440 | 0.067 | 0.053 | 0.049 | 0.043 | 0.039 | 0.034 | 0.027 |

The data presented in Table 4 represent the IDF values derived from historical observations of short-duration rainfall events. An important question is whether these IDF relationships will remain unchanged under future climate conditions by 2050. The Intergovernmental Panel on Climate Change (IPCC), in its latest 2023 report, addresses this issue by providing recommendations for adjusting IDF curves for future time horizons according to the selected climate change scenario (Table 5).

*Tab. 5 Transformation of IDF return periods for the 2050-time horizon under the analyzed climate scenarios*

| Present Retrun Period | 5-years | 10-years | 20-years | 50-years | 100-years |
|---|---|---|---|---|---|
| Scenario | Future Retrun Period [years] | Future Retrun Period [years] | Future Retrun Period [years] | Future Retrun Period [years] | Future Retrun Period [years] |
| SSP1-1.9 | 3.94 | 7.2 | 14.78 | 35.64 | 69.44 |
| SSP1-2.6 | 3.66 | 6.98 | 13.22 | 30.85 | 58.66 |
| **SSP2-4.5** | **3.51** | **6.54** | **12.2** | **27.79** | **52.03** |
| **SSP3-7.0** | **3.37** | **6.24** | **11.54** | **26.13** | **48.92** |
| SSP5-8.5 | 3.27 | 5.99 | 11.04 | 24.65 | 45.35 |

Based on the IDF transformation methodology recommended by the IPCC, IDF curves for the SSP2-4.5 and SSP3-7.0 climate scenarios were derived for the 2050 time horizon for the purposes of this study (Tables 6 and 7).

*Tab. 6 IDF curves for the SSP2-4.5 scenario (2050-time horizon)*

| **Scenario: SSP2-4.5** | | P [%] | | | | |
|---|---|---|---|---|---|---|
| I [mm/min] | D [min] | 1 | 2 | 5 | 10 | 20 |
| | | Return Period [years] | | | | |
| | | 100 | 50 | 20 | 10 | 5 |
| | 10 | 2.700 | 2.472 | 2.170 | 1.942 | 1.714 |
| | 20 | 1.706 | 1.562 | 1.372 | 1.228 | 1.084 |
| | 30 | 1.274 | 1.166 | 1.024 | 0.916 | 0.808 |
| | 60 | 0.753 | 0.689 | 0.605 | 0.542 | 0.478 |
| | 120 | 0.436 | 0.399 | 0.350 | 0.313 | 0.277 |

| | | | | | | |
|---|---|---|---|---|---|---|
| | 180 | 0.315 | 0.288 | 0.253 | 0.226 | 0.200 |
| | 360 | 0.180 | 0.164 | 0.144 | 0.129 | 0.114 |
| | 720 | 0.102 | 0.094 | 0.082 | 0.073 | 0.065 |
| | 1440 | 0.058 | 0.053 | 0.046 | 0.042 | 0.037 |

*Tab. 7 IDF curves for the SSP3-7.0 scenario (2050-time horizon)*

| **Scenario: SSP3-7.0** | D [min] | P [%] | | | | |
|---|---|---|---|---|---|---|
| | | 1 | 2 | 5 | 10 | 20 |
| | | Return Period [years] | | | | |
| | | 100 | 50 | 20 | 10 | 5 |
| I [mm/min] | 10 | 2.723 | 2.493 | 2.189 | 1.959 | 1.729 |
| | 20 | 1.721 | 1.576 | 1.384 | 1.238 | 1.093 |
| | 30 | 1.285 | 1.176 | 1.033 | 0.924 | 0.816 |
| | 60 | 0.759 | 0.695 | 0.610 | 0.546 | 0.482 |
| | 120 | 0.439 | 0.402 | 0.353 | 0.316 | 0.279 |
| | 180 | 0.317 | 0.291 | 0.255 | 0.228 | 0.201 |
| | 360 | 0.181 | 0.166 | 0.146 | 0.130 | 0.115 |
| | 720 | 0.103 | 0.094 | 0.083 | 0.074 | 0.065 |
| | 1440 | 0.058 | 0.053 | 0.047 | 0.042 | 0.037 |

## 4. CONCLUSION

A climate change impact assessment of hydrological and climatological variables was conducted for the study area. The assessment is motivated by mounting evidence of ongoing and intensifying climate change, as emphasized in the IPCC Sixth Assessment Report, which confirms a continued rise in global temperatures and significant changes in the global hydrological cycle. Southeastern Europe and Serbia are identified as regions particularly vulnerable to rising temperature trends, precipitation variability, and more frequent hydrological extremes.

Several analyses were conducted in this study, resulting in the following key conclusions:

- An analysis of climate models recommended by the Intergovernmental Panel on Climate Change (IPCC) was conducted, including a comparative assessment of individual model performance and an overview of recommended future climate scenarios within the CMIP6 framework.
- A multi-model ensemble approach for climate variable modeling was implemented in line with IPCC recommendations. Validation using interpolated temperature and precipitation data from 1990 to 2020 demonstrated satisfactory agreement with observed records, confirming the reliability of this approach for future projections.
- The SSP2-4.5 and SSP3-7.0 scenarios were applied to estimate mean annual air temperature and annual precipitation totals for 2024 to 2050. Results indicate a persistent warming trend of approximately 1°C by mid-century, along with

increased interannual precipitation variability and more pronounced contrasts between dry and wet years.

- To assess extreme hydrological events, Intensity–Duration–Frequency (IDF) curves were adjusted to represent projected conditions for the 2050 time horizon using IPCC-based methodologies. The transformation was performed for both climate scenarios and for return periods of 5, 10, 20, 50, and 100 years. The results indicate an increase in short-duration rainfall intensities (less than 24 hours). Furthermore, rainfall events that currently correspond to a 100-year return period are projected to occur with a frequency approximately equivalent to a 50-year return period under future climate conditions. This trend indicates a substantial increase in the likelihood of extreme rainfall events and, consequently, an elevated risk of pluvial flooding.

Overall, this study provides a consistent methodological framework for integrating climate projections with hydrological analysis under non-stationary climate conditions. The results demonstrate that the assumption of climate stationarity is no longer valid and underscore the need to incorporate climate change impacts into hydrological design and water resources planning for future climate conditions up to 2050.

## ACKNOWLEDGEMENT

The research has been conducted within the project "Enhancement of teaching and scientific research capacities through the application of modern technologies in the fields of civil engineering, geodesy, and disaster risk management and fire safety", developed at the Department of Civil Engineering and Geodesy, Faculty of Technical Sciences, University of Novi Sad, Serbia.

## REFERENCES

[1] Intergovernmental Panel on Climate Change [IPCC]. (2023). *Climate Change 2023: AR6 Synthesis Report. Contribution of Working Groups I, II and III to the Sixth Assessment Report of the Intergovernmental Panel on Climate Change* [Core Writing Team, H. Lee and J. Romero (eds.)]. IPCC, Geneva, Switzerland, 184 pp. https://doi.org/10.59327/IPCC/AR6-9789291691647

[2] Intergovernmental Panel on Climate Change [IPCC]. (2021). *Climate Change 2021: The Physical Science Basis. Contribution of Working Group I to the Sixth Assessment Report of the Intergovernmental Panel on Climate Change*. Cambridge University Press.

[3] IPCC. (2021). *Climate Change 2021: The Physical Science Basis*, Chapter 8: Water Cycle Changes. In *Contribution of Working Group I to the Sixth Assessment Report of the Intergovernmental Panel on Climate Change*. Cambridge University Press.

[4] Arnell N.W. (1999). Climate change and global water resources. *Global Environmental Change*, Volume 9, pp. S31-S49. https://doi.org/10.1016/S0959-3780(99)00017-5

[5] Kundzewicz Z.W., et al. (2007). Freshwater resources and their management. In *Climate Change 2007: Impacts, Adaptation and Vulnerability* (pp. 173–210). Cambridge University Press.

[6] Milly P.C.D., et al. (2008). Stationarity Is Dead: Whither Water Management? *Science*, 319(5863), pp. 573–574. https://doi.org/10.1126/science.1151915

[7] European Environment Agency [EEA]. (2024). *European Climate Risk Assessment*. EEA Report No. 01/2024. Publications Office of the European Union. https://doi.org/10.2800/8671471

[8] Giorgi F., Lionello P. (2008). Climate change projections for the Mediterranean region. *Global and Planetary Change*, Volume 63(2–3), pp. 90–104. https://doi.org/10.1016/j.gloplacha.2007.09.005

[9] Đurđević S.V., et al. (2018). *Observed Climate Change and Future Climate Projections Based on Different Scenarios of Future Emission*. United Nations Development Programme (UNDP), Serbia.

[10] World Climate Research Programme [WCRP]. (2019). *Coupled Model Intercomparison Project Phase 6 (CMIP6): Experimental Design and Organization*.

[11] Eyring V., et al. (2016). Overview of the Coupled Model Intercomparison Project Phase 6 (CMIP6) experimental design and organization. *Geoscientific Model Development*, Volume 9(5), pp. 1937–1958. https://doi.org/10.5194/gmd-9-1937-2016

[12] O'Neill B. C., et al. (2016). The Scenario Model Intercomparison Project (ScenarioMIP) for CMIP6. *Geoscientific Model Development*, Volume 9(9), pp. 3461–3482. https://doi.org/10.5194/gmd-9-3461-2016

[13] World Bank. Climate Change Knowledge Portal. Available at: https://climateknowledgeportal.worldbank.org

[14] https://www.jcerni.rs/

[15] https://www.hidmet.gov.rs/

https://doi.org/10.24867/INDIS-2026-EN-399



# FLOW ANALYSIS IN A LABORATORY CHANNEL USING VIDEO PROCESSING AND HEC-RAS MODELLING

*Anica Milanović[1], Petar Praštalo[2]*

***Summary:***

This paper presents an analysis of flow in a laboratory channel equipped with a weir using experimental measurements and numerical modelling. Video processing techniques were applied to estimate discharge from surface velocities, which were determined using the Optical Flow (OF) method. The obtained discharge values were compared with values measured using a discharge measurement device, as well as with those estimated using the Froude based method. The water surface profile was determined through video processing and subsequently compared with the profile obtained using a one-dimensional hydraulic model in the HEC-RAS software. Based on the analysis of the water surface profile, the local energy head loss coefficient at the weir was estimated. The obtained results indicate the potential applicability of a combined approach involving video processing and hydraulic modelling for the investigation of flow in laboratory channels.

*Ključne reči: laboratory channel, discharge, Optical Flow, water surface profile, HEC-RAS, local head loss coefficient.*

# ANALIZA STRUJANJA U LABORATORIJSKOM KANALU PRIMJENOM OBRADE VIDEO SNIMKA I HEC-RAS MODELIRANJA

***Rezime:***

U radu je prikazana analiza strujanja u laboratorijskom kanalu sa prelivnim pragom primjenom eksperimentalnih mjerenja i numeričkog modeliranja. Za procjenu protoka na osnovu površinskih brzina primjenjena je tehnika obrade video snimka, pri čemu su površinske brzine određene metodom optičkog toka (OF). Na ovaj način dobijene vrijednosti protoka su upoređene sa vrijednostima izmjerenim pomoću uređaja za mjerenje protoka, kao i onim dobijenim primjenom metode zasnovane na Frudovom broju. Linija nivoa određena je obradom video snimka, a zatim je upoređena sa linijom nivoa dobijenom jednodimenzionalnim hidrauličkim modelom u programskom paketu HEC-RAS. Na osnovu analize linije nivoa izvršena je procjena koeficijenta lokalnog gubitka energije na prelivnom pragu. Dobijeni rezultati ukazuju na mogućnost primjene kombinovanog pristupa obrade video snimaka i hidrauličkog modeliranja u ispitivanju strujanja u laboratorijskim kanalima.

*Ključne reči: laboratorijski kanal, protok, optički tok, linija nivoa vode, HEC-RAS, koeficijent lokalnog gubitka.*

[1] Senior Teaching Assistant, Faculty of Architecture-Civil Engineering and Geodesy, University of Banja Luka, Banja Luka, Bosnia and Herzegovina, anica.milanovic@aggf.unibl.org, ORCID 0009-0005-5602-150X

[2] Senior Teaching Assistant, Faculty of Architecture-Civil Engineering and Geodesy, University of Banja Luka, Banja Luka, Bosnia and Herzegovina, petar.prastalo@aggf.unibl.org, ORCID 0009-0002-1238-1632

## 1. INTRODUCTION

Weirs are common hydraulic structures used in rivers and laboratory facilities. Their function is not limited to flow regulation or discharge measurement, but they also have a significant influence on the distribution of flow depths and velocities along the channel. Therefore, understanding the flow characteristics in the vicinity of a weir is of particular importance in the design of hydraulic structures.

Under laboratory conditions, flow analysis is commonly based on water depth measurements using point gauges and discharge determination using appropriate measuring devices. Although these methods can provide high measurement accuracy, their application often requires a time-consuming experimental procedure, while individual measurements may be difficult in zones with pronounced variations in flow depth and velocity [1], [2].

The development of digital cameras and image processing techniques has opened new possibilities for non-contact monitoring of hydraulic processes. In addition to determining surface velocities and estimating discharge, video recordings can be processed to obtain the water surface profile along the channel. Thus, a single set of recordings can provide substantially more information than can be obtained using conventional point measurements.

Furthermore, hydraulic modelling has become an indispensable tool for the analysis of open-channel flows. Among the most widely used software packages is HEC-RAS, which enables the simulation of steady and unsteady flow, determination of water surface profiles, as well as the distribution of flow velocities and energy characteristics. The reliability of the model largely depends on the proper definition of geometry, boundary conditions, and hydraulic parameters.

Several authors have investigated the applicability of HEC-RAS models for simulating flow over different types of weirs. Qasim (2013) compared laboratory measurements with HEC-RAS model results for a single-step broad-crested weir and showed that the model reproduced the water surface profile, hydraulic jump location, and loss–discharge relationship with satisfactory accuracy [3]. Similar results were reported by Mohammad Razi et al. (2020), who analysed flow characteristics over sharp-crested weirs and concluded that the model reliably describes changes in the water surface profile, with the largest discrepancies occurring in the immediate vicinity of the structure due to pronounced local three-dimensional effects [4]. Similarly, Ruslan (2015) indicated that the selection of the Manning roughness coefficient and appropriate cross-section discretization significantly affect the accuracy of simulation results in laboratory channels [5].

On the other hand, numerous studies have demonstrated that computational methods can provide a reliable alternative to conventional hydrometric measurements. Farnebäck (2003) developed a dense Optical Flow method, which has subsequently become one of the most widely used techniques for determining surface velocities from video recordings [6]. Later, Tauro et al. (2018) and Perks et al. (2020) demonstrated that video-based methods can provide reliable estimates of hydraulic parameters under both laboratory and field conditions, while requiring lower costs and offering simpler implementation compared with conventional measurements [7], [8].

The aim of this study is to present a combined approach to flow analysis in a laboratory channel using experimental measurements, video processing, and numerical modelling in HEC-RAS. For discharge estimation, the Optical Flow and Froude-based methods were applied, while particular attention was given to the comparison of experimentally and numerically determined water surface profiles, analysis of discrepancies between the obtained results, and estimation of the local energy head loss coefficient at the weir. In this

way, the applicability of a combined experimental–numerical approach to laboratory hydraulic investigations was assessed.

## 2. MATERIALS AND METHODS

### 2.1. LABORATORY SETUP

The experimental investigation was conducted in the Hydraulics Laboratory at the Faculty of Architecture, Civil Engineering and Geodesy, using a laboratory channel 1.30 m long with a rectangular cross-section 0.14 m wide. The channel bed is horizontal and made of glass, allowing visual observation of the flow. A wooden weir with a height of 3.54 cm was installed at a distance of X = 0.50 m from the downstream end of the channel. The weir has an isosceles right-triangular cross-section with side lengths of 5 cm.
The system is a closed recirculating system consisting of two reservoirs and a connecting pipeline, a pump, an inlet pipeline, a laboratory channel, and a discharge measurement device. The discharge was regulated using a ball valve installed on the inlet pipeline and measured using a calibrated device [9]. A schematic representation of the laboratory setup is shown in the following figure.

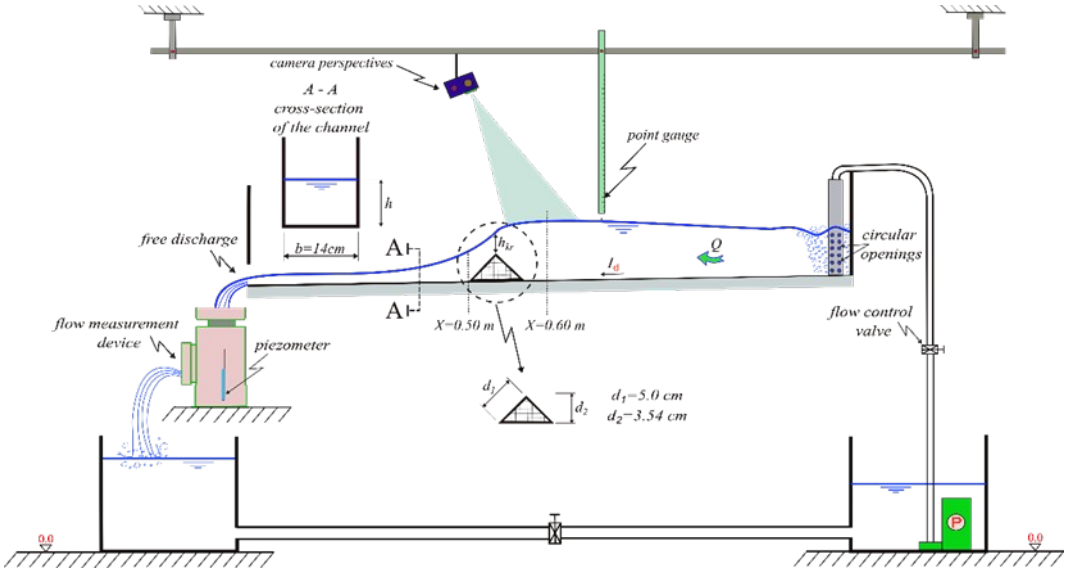


*Figure 1. Schematic representation of the laboratory setup [2]*

The experiments were conducted for a total of five discharge values, under conditions of free (unsubmerged) flow over the weir. For each considered case, video recordings were made for the determination of surface velocities and the water surface profile. In addition, discharge measurements were performed using the discharge measurement device, while point measurements of flow depth at the weir were carried out using a point gauge.
The video recordings were obtained using a Venture 5K Duo camera, which provides high-resolution video recording and high-megapixel still imaging. During the laboratory experiments, the camera was positioned at two fixed locations. One position, indicated in figure 1, was used for recording surface velocities, while the second position was used for recording the water surface profile.

## 2.2. DISCHARGE ESTIMATION TECHNIQUES

Discharge was estimated using three approaches:

- discharge measurement device;
- water depth measurement at the weir (Froude based method);
- video processing using the OF method.

The discharge values obtained using the discharge measurement device were adopted as reference values. The device was tested under laboratory conditions and verified under field conditions, as presented in the study by Praštalo et al. [9]. The geometric characteristics of the device and a detail of the weir are shown in the following figure.

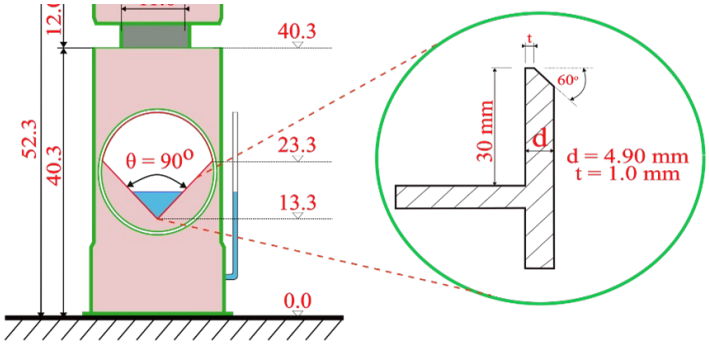


*Figure 2. Discharge measurement device [9]*

The discharge measurement device was constructed from DN 200/200 mm PVC sewer pipes arranged as a T-fitting. The lower part of the device is closed, while a 90° Thomson (V-notch) weir was installed on the lateral end cap. The water level is measured using a piezometer installed on the side of the device, corresponding to the water level at the weir. The discharge over the Thomson weir is determined using the following equation [10]:

$$Q = \frac{8}{15} C_d \sqrt{2g}\, h_p^{5/2} \tag{1}$$

Where $Q$ (m$^3$/s) is the discharge, $C_d$ (/) is the discharge coefficient, $g$ (m/s$^2$) is the gravitational acceleration, and $h_p$ (m) is the head over the weir, calculated as the difference between the water level in the piezometer and the weir crest elevation of 13.3 cm.

Following calibration of the weir, the discharge coefficient corresponds to Equation (model 3) proposed by Praštalo et al. [9]:

$$C_d = 0.6703 + 0.0161\left(h_p / P\right) \tag{2}$$

where $P$ (m) is the weir height, equal to 30 mm, as shown in Figure 2.

For the second approach, the Froude-based method was applied to estimate discharge using point measurements of water depth at the weir. Given the hydraulic conditions corresponding to free flow over the weir, the measured depth corresponds to the critical depth, $h_{cr}$. Thus, minimum specific energy is attained at the weir, for which the Froude number is equal to unity, i.e. [10]:

$$Fr = \frac{Q^2 B}{g A^3} = 1 \tag{3}$$

where $Fr$ (/) is the Froude number, $B$ (m) is the water surface width, which in this case is equal to the channel width $b$ of 14 cm, and $A$ ($m^2$) is the flow cross-sectional area. The flow cross-sectional area at the weir can be determined as $A = b \cdot h_{kr}$. Substituting this expression into Equation (3), the discharge can be expressed as:

$$Q = \sqrt{g \cdot h_{kr}^3 \cdot B^2} \tag{4}$$

The third approach for discharge estimation involved video processing, using different techniques to identify surface velocities from which discharge was subsequently determined. Several established video-processing methods are available for determining surface velocities, one of which is the OF method applied in this study. This method is based on analysing changes in pixel intensity between consecutive video frames. Originally developed by Farnebäck [6], the method enables the determination of displacement vectors for individual image pixels, thereby providing a dense surface-flow velocity field.

Video recordings were processed using the Optical Flow library in the Python programming language. Surface velocities were determined by analysing consecutive frames and subsequently spatially averaged across the channel width. Using the cross-sectional geometry and mean surface velocity, the discharge was estimated.

For comparison of the discharge values obtained from water depth measurements at the weir and video processing with the reference values from the discharge measurement device, the relative error was calculated as:

$$\varepsilon = \frac{\left| Q_{calc} - Q_m \right|}{Q_m} \cdot 100\,\% \tag{5}$$

where $\varepsilon$ (%) is the relative error, $Q_{calc}$ is the discharge value obtained using either the Froude based method or the OF method, and $Q_m$ is the measured discharge obtained using the discharge measurement device.

## 2.3. DETERMINATION OF THE WATER SURFACE PROFILEE

As previously stated, the water surface profile was determined using two approaches:

- video processing for water surface profile extraction;
- hydraulic modelling using HEC-RAS.

For the first approach, the camera was positioned perpendicular to the laboratory channel at a sufficient distance to capture its longitudinal profile within the video frame. To enable accurate digitization of the water surface profile, a reference station \(X = 0.50\) m, corresponding to the downstream face of the weir, was marked on the channel, while the downstream end of the channel was defined as \(X = 0.0\) m. The upstream face of the weir was located at station \(X = 0.5707\) m. For vertical calibration, a measuring scale with 5 cm divisions was attached to the side of the channel.

Video processing was performed by selecting a representative frame for each considered discharge. The water surface profile was digitized using the free online tool Plot Digitizer, after which the obtained coordinates were used for comparison with the numerical modelling results [11]. An example of a representative frame is shown in the following figure.

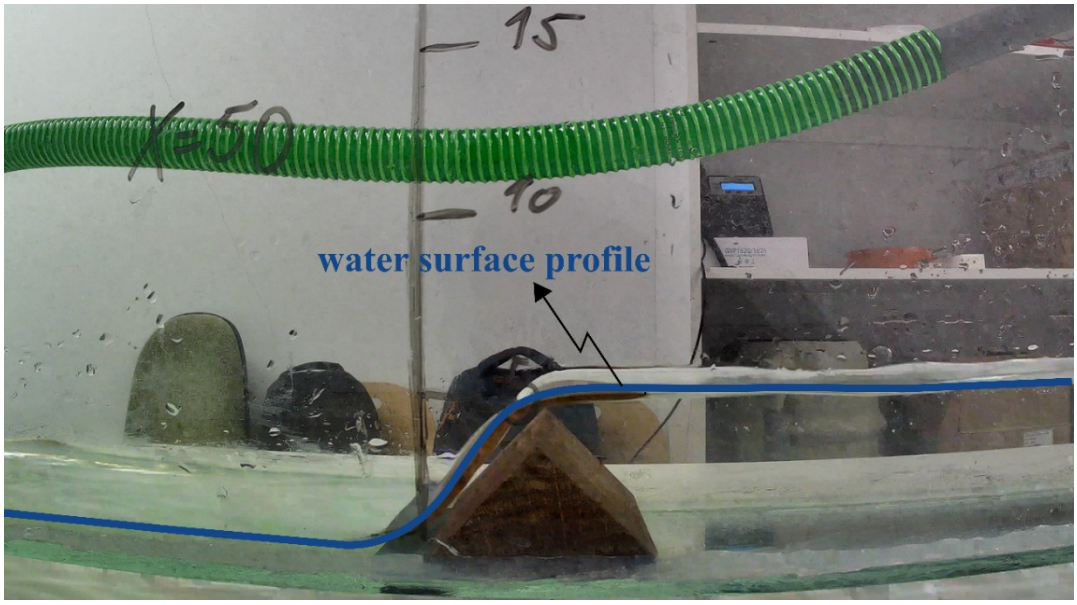


*Figure 3. Water surface profile in the laboratory channel*

The second approach involved a one-dimensional hydraulic model developed in the HEC-RAS software. The model geometry consisted of 13 cross-sections with a rectangular cross-section 0.14 m wide, corresponding to the geometry of the laboratory channel. Three characteristic cross-sections were defined in the vicinity of the weir: immediately upstream of the weir, at the weir crest, and immediately downstream of the weir. Downstream of the weir, the cross-sections were spaced at 0.10 m intervals, whereas upstream of the weir, from station \(X = 0.70\) m to the upstream end of the channel, the cross-sections were spaced at 0.20 m intervals. The channel bed slope was set to 0%, corresponding to the actual laboratory setup.

Flow resistance was represented by the Manning roughness coefficient. A value of n = 0.009 was adopted for the glass channel, while n = 0.011, was adopted for the wooden weir, in accordance with recommended values reported in the literature [12].

Steady-flow simulations were performed for five discharge values corresponding to the reference discharges obtained using the discharge measurement device. Considering the expected change in the flow regime in the vicinity of the weir, where subcritical flow upstream of the weir passes through critical depth at the crest and becomes supercritical downstream of the weir, the Mixed Flow Regime option was applied in HEC-RAS. The known discharge was specified as the upstream boundary condition, while Critical Depth was adopted as the downstream boundary condition, since free outflow was established at the downstream end of the channel.

The modelling results included not only the water surface profile but also the energy grade line and other relevant hydraulic parameters, enabling the estimation of energy losses at the weir and the corresponding local head loss coefficient $\xi$.

For comparison of the water surface profiles obtained using the two approaches, the difference Δh at selected cross-sections was used and can be expressed as:

$$\Delta h_i = WL_{video,i} - WL_{HEC-RAS,i} \tag{6}$$

where $WL_{video,i}$ (mm) is the water level at a given cross-section $i$ obtained from video processing, and $WL_{HEC-RAS,i}$ (mm) is the corresponding water level obtained from the HEC-RAS model. The relative error was also used for comparison and can be expressed as:

$$\varepsilon = \frac{WL_{video,i} - WL_{HEC-RAS,i}}{WL_{video,i}} \cdot 100\,\% \tag{7}$$

## 2.4. ESTIMATION OF THE LOCAL HEAD LOSS COEFFICIENT AT THE WEIR

Flow over a weir is accompanied by local energy losses resulting from abrupt changes in flow geometry and flow regime. Local head losses represent the difference in energy between two characteristic cross-sections and can be described using the Bernoulli equation with an energy-loss term [12], [13].
The Bernoulli equation for the cross-sections immediately upstream of the weir and at the weir crest is given by [10]:

$$E_{up} = E_{crest} + \Delta E_{up-crest} \tag{8}$$

where $E_{up}$ (m) is the energy per unit weight at the cross-section upstream of the weir, $E_{crest}$ (m) is the energy per unit weight at the weir crest, and $\Delta E_{up-crest}$ (m) is the energy loss between the two cross-sections. The energy at a given cross-section is defined as [10]:

$$E_i = z_{d,i} + h_i + \frac{v_i^2}{2g} \tag{9}$$

where $z_d$ (m) is the channel-bed elevation at the considered cross-section, $h_i$ (m) is the flow depth, $v_i$ (m/s) is the flow velocity, and $g$ (m/s$^2$) is the gravitational acceleration. If friction losses are neglected due to the short distance between the considered cross-sections, the energy loss from Equation (8) can be expressed as [10]:

$$\Delta E_{up-crest} = \xi_{up} \frac{v_{crest}^2}{2g} \tag{10}$$

where $\xi_{up}$ (-) is the local head loss coefficient at the weir, and $v_{pr}$ (m/s) is the flow velocity at the considered cross-section at the weir.
Using the above equations, the local head loss coefficient was estimated for all five considered discharge values, based on both the water surface profile obtained from video processing and the HEC-RAS model results.

# 3. RESULTS AND DISCUSSION

## 3.1. DISCHARGE ESTIMATION

The discharge estimates obtained using the previously described methods are presented in Table 1 and expressed in l/s.

*Table 1. Discharge values*

| Measured | Froude based method | Optical flow |
|---|---|---|
| 1.94 | 2.040 | 1.925 |
| 1.60 | 1.721 | 1.595 |
| 1.20 | 0.800 | 1.354 |
| 0.80 | 0.312 | 0.621 |
| 0.40 | 0.255 | 0.567 |

Both methods show good agreement with the measured discharge values for the higher discharges (1.60 l/s and 1.94 l/s), whereas larger discrepancies are observed at lower discharges. For the lower discharge values, the Froude-based method substantially underestimates the discharge, whereas the OF method underestimates the discharge only for the 0.80 l/s case. For discharges of 0.40 l/s and 1.20 l/s, the OF method overestimates the measured values. The results are illustrated in the following figure.

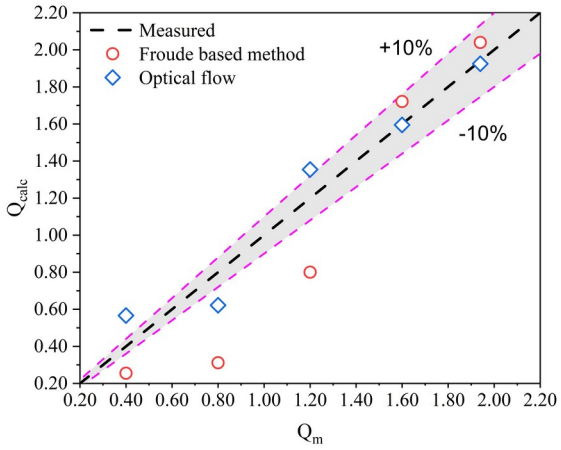


*Figure 4. Discharge estimation results [2]*

As shown in Figure 4, the method based on critical-depth measurement exhibits larger deviations from the measured discharge values. The main reason is the sensitivity of the discharge estimate to errors in reading the critical depth using the point gauge, which can have a significant effect on the calculated discharge. The OF method shows better agreement with the measured values over the entire investigated range, although larger deviations are still observed at lower discharges.

The smallest relative errors for both methods were obtained for discharges of 1.60 l/s and 1.94 l/s. For the OF method, the error was below 1%, while for the Froude-based method it was 7.5% and 5.14%, respectively. The largest relative error for the Froude-based method was recorded at a discharge of 0.80 l/s (-61.1%), whereas the largest deviation for the OF method was obtained at 0.40 l/s (41.6%).

## 3.2. COMPARISON OF WATER SURFACE PROFILES

The following figure presents a comparison of the water surface profiles obtained from video recordings and hydraulic modelling, with the value of Δh also shown for each considered discharge.

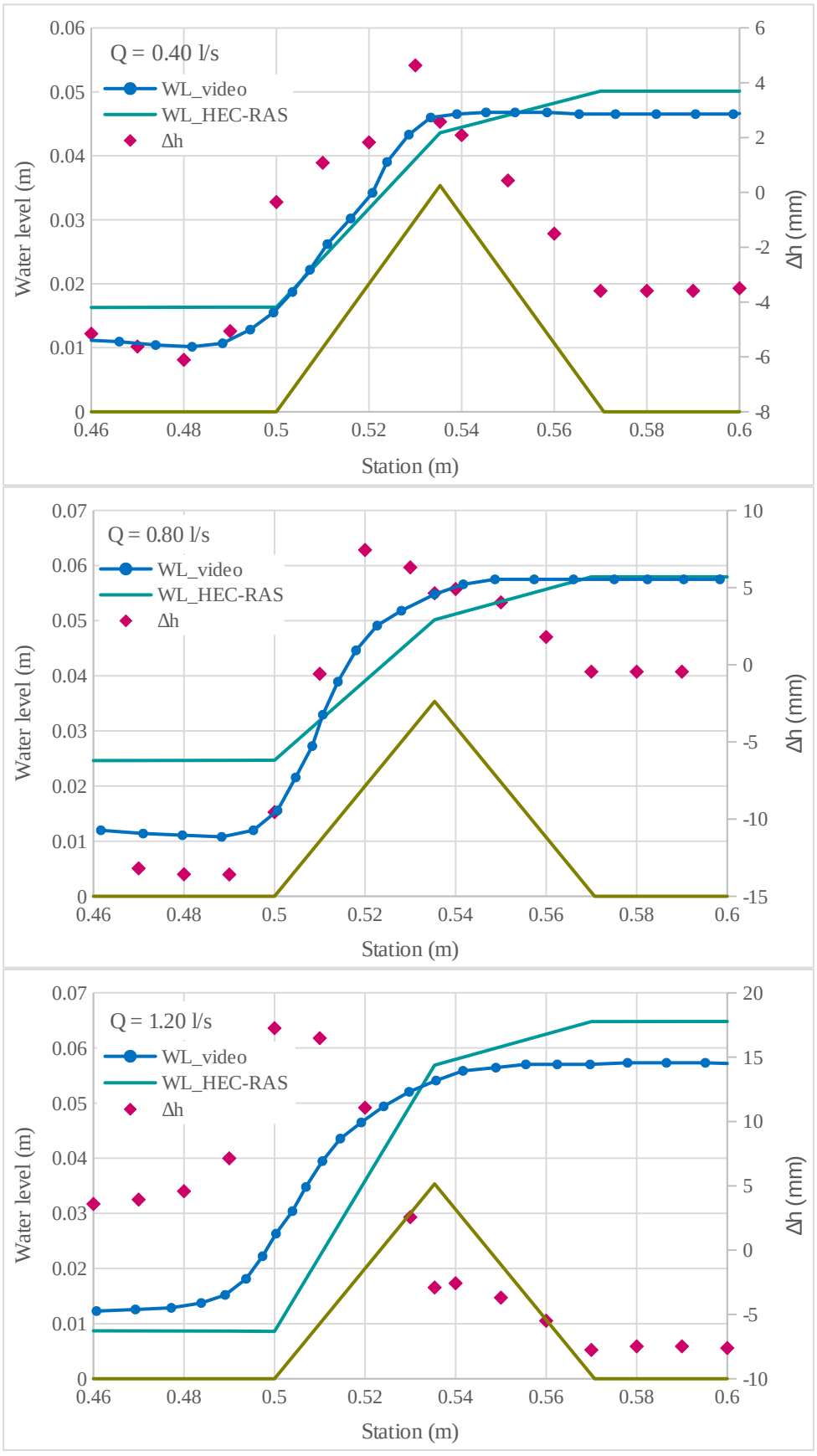
Q = 0.40 l/s
WL_video
WL_HEC-RAS
Δh
Water level (m)
Δh (mm)
Station (m)
Q = 0.80 l/s
WL_video
WL_HEC-RAS
Δh
Water level (m)
Δh (mm)
Station (m)
Q = 1.20 l/s
WL_video
WL_HEC-RAS
Δh
Water level (m)
Δh (mm)
Station (m)

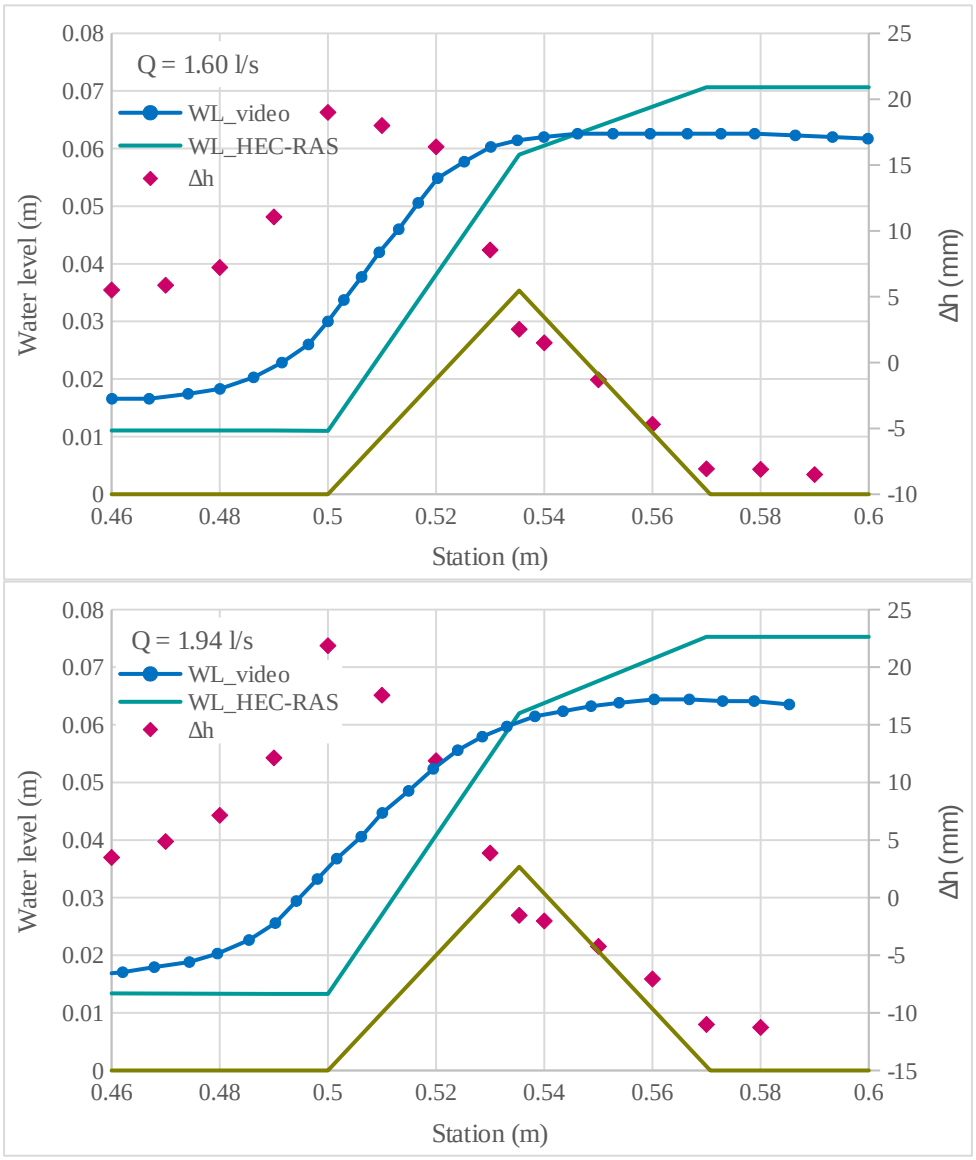


*Figure 5. Water surface profile analysis results*

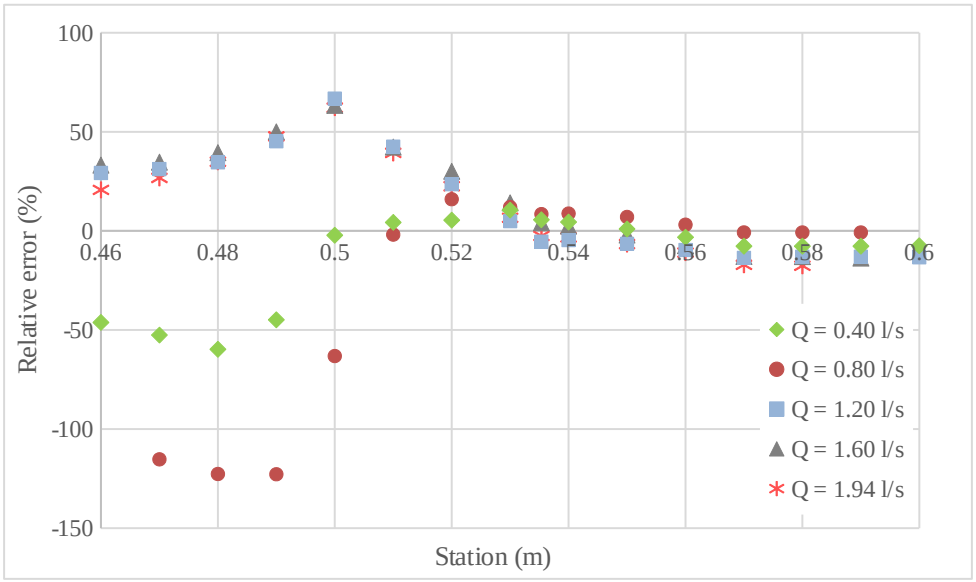


*Figure 6. Relative error*

The presented results show that the HEC-RAS model successfully reproduces the general shape of the water surface profile for all considered discharges. Subcritical flow occurs upstream of the weir, while the flow passes through critical depth at the weir crest and becomes supercritical downstream of the weir. A backwater effect caused by the weir is also evident. These results confirm that the one-dimensional model satisfactorily describes the dominant hydraulic processes in the laboratory channel.

However, differences between the experimentally determined and numerically obtained water surface profiles are present and are not uniformly distributed along the channel.

The Δh values show that the largest differences occur in the vicinity of the weir, i.e. in the part of the flow characterized by the most pronounced changes in depth, velocity, and specific energy. The maximum Δh values increase with increasing discharge, from 6.1 mm for the lowest discharge of 0.40 l/s to as much as 21.9 mm for a discharge of 1.94 l/s. It is also noteworthy that the maximum differences occur at station X = 0.48 m for discharges of 0.40 and 0.80 l/s, whereas for the remaining discharges the maximum difference occurs at X = 0.50 m. This indicates that the maximum differences occur downstream of the weir crest elevation. For discharges of 0.40 and 0.80 l/s, HEC-RAS predicts slightly greater depths than those obtained experimentally, whereas for the remaining discharges the model predicts lower depths. Further downstream of the weir, the differences gradually decrease and the water surface profiles become nearly parallel. Upstream of the weir, the differences are also less pronounced and the profiles exhibit a nearly parallel trend. This indicates that the model provides a relatively good description of the water surface profile upstream and downstream of the weir, while the greatest uncertainties are associated with the zone of local flow acceleration.

The differences between the experimental and modelled water surface profiles can be attributed to a combination of several factors. First, the experimental water surface profile was determined by digitalizing the video recording, and its accuracy depends on the recording quality, camera resolution, lighting conditions, and contrast between the water surface and channel wall. Minor geometric distortions of the image may also occur, particularly near the edges of the frame. In addition, the water surface is not completely stationary, but exhibits fluctuations that make it difficult to determine its representative position accurately. A further source of uncertainty is the digitalization procedure itself, which involves manually selecting characteristic points in the digitization software and may therefore introduce additional deviations. Although such errors are small, they can have a noticeable effect on the calculated depth because of the relatively small water depths in the channel.

On the other hand, the HEC-RAS model is one-dimensional and assumes a hydrostatic pressure distribution, while local three-dimensional effects in the vicinity of the weir are not explicitly represented. The accuracy of the results is additionally affected by the selection of the Manning roughness coefficient and the spacing of the cross-sections.

The relative error shown in the final diagram confirms that the largest deviations occur downstream of the weir, i.e. in the part of the channel where the water depth is smallest. Since the relative error is calculated with respect to the measured depth, the same absolute difference between the two water surface profiles results in a considerably larger percentage deviation at smaller depths than at greater water depths. Therefore, the relative error should be considered together with Δh, which provides a more realistic representation of the agreement between the results.

## 3.3. ESTIMATION OF THE LOCAL HEAD LOSS COEFFICIENT

The estimated local head loss coefficients for the different discharge values are presented in the following table.

*Table 2. Results of the local head loss coefficient estimation*

| Discharge (l/s) | Video | HEC-RAS |
|---|---|---|
| 0.4 | -0.850 | 0.099 |
| 0.8 | -0.274 | 0.097 |
| 1.2 | -0.586 | 0.093 |
| 1.6 | -0.755 | 0.094 |
| 1.94 | -0.618 | 0.093 |

A significant difference can be observed between the values obtained from the experimental water surface profile and those obtained from the HEC-RAS model. While the coefficients obtained from the model fall within a narrow range from 0.093 to 0.099, the values determined from the video-derived profile are negative, ranging from -0.274 to -0.850. The negative sign indicates that the energy relationship between the considered cross-sections does not yield a physically realistic energy loss.

It should be noted that the energy coefficient is determined indirectly from the difference in energy between the upstream cross-section and the cross-section at the weir. Under the considered laboratory conditions, the energy difference between these cross-sections is less than one centimetre, consequently, even a small error in determining the water level can result in a very large difference in the calculated energy loss. Since the calculation is also affected by the velocity head, i.e. the flow velocity in the considered cross-sections, measurement uncertainty introduces an additional error, particularly at lower discharges when the water depths are relatively small.

A particularly important observation is that the critical depth at the weir, determined from the experimental water surface profile, approximately corresponds to the theoretical critical depth. Therefore, it can be assumed that the main source of error in estimating the energy loss is not the determination of the depth at the weir itself, but rather the determination of the depth in the upstream cross-section. In this part of the channel, the free water surface is subject to more pronounced fluctuations, particularly at higher discharges, which makes it difficult to select a representative water surface position from the video recording.

To further examine this assumption, the following table presents the upstream depths obtained from the experimental water surface profile and the theoretical depths calculated for a local head loss coefficient of 0.1.

*Table 3. Experimental and theoretical depths in the cross-section upstream of the weir*

| Discharge (l/s) | $h_{uzv,video}$ (m) | $h_{uzv,teor}$ (m) | $\Delta h$ (mm) |
|---|---|---|---|
| 0.4 | 0.0465 | 0.0499 | 3.4 |
| 0.8 | 0.0575 | 0.0584 | 0.9 |
| 1.2 | 0.0573 | 0.0655 | 8.2 |
| 1.6 | 0.0621 | 0.0718 | 9.7 |
| 1.94 | 0.0640 | 0.0754 | 11.4 |

In all cases, the theoretical depth is greater than the depth determined from the video recording. The difference ranges from 0.9 to 11.4 mm and, except for the 0.8 l/s case, shows a tendency to increase with discharge. For the highest considered discharge, the difference reaches 11.4 mm, corresponding to approximately 18% of the experimentally determined depth.

This result is consistent with the comparison of the water surface profiles in Figure 5, where the HEC-RAS model also predicts greater upstream depths than those obtained from the experimental profile. In contrast, the critical depth at the weir obtained from the HEC-RAS model approximately corresponds to the theoretical value. This confirms that a relatively small difference in the determination of upstream depth can have a significant influence on the calculated energy loss, explaining the physically realistic coefficient values obtained from the model.

The coefficients obtained from the HEC-RAS model vary within a very narrow range, without a pronounced dependence on discharge. The obtained values are close to the adopted value of 0.1 and fall within the range of values reported in the literature for local losses at hydraulically well-shaped weir structures. However, the limitations of the one-dimensional HEC-RAS model, discussed previously, should also be considered, and some deviation between the actual and numerically simulated energy loss can therefore be expected. Nevertheless, the fact that the coefficient values remain within the expected range reported in the literature indicates that, under the considered conditions, the model successfully describes the changes in the water surface profile and the energy characteristics of the flow.

## 4. CONCLUSIONS

The paper presents a combined approach to flow analysis in a laboratory channel using experimental measurements, video processing, and a one-dimensional hydraulic model. Based on the conducted investigation, the following conclusions can be drawn:

- The Optical Flow method enables reliable discharge estimation at higher flow rates, while deviations from the reference values increase at lower discharges.
- The Froude-based method shows good agreement with the reference values at higher discharges, whereas significant underestimation occurs at lower discharges, with the accuracy depending on the ability to accurately measure the depth at the weir.
- Comparison of the experimentally determined and numerically simulated water surface profiles showed that HEC-RAS adequately reproduces the general shape of the water surface profile. The largest deviations were observed in the vicinity of the weir, which is expected due to abrupt changes in flow depth and the limitations associated with determining the water surface profile from video recordings.
- Estimation of the local head loss coefficient showed that the results obtained from the HEC-RAS model are consistent with the expected values reported in the literature. Physically unrealistic values were obtained from the video-derived water surface profile. This indicates the high sensitivity of the procedure to errors in determining the water surface profile and confirms that a more accurate extraction of the free surface from video recordings is required for reliable estimation of local energy losses.
- The results confirm that combining experimental measurements, video processing, and numerical modelling provides an effective tool for analysing hydraulic processes in laboratory channels. The proposed methodology may serve as a basis for further research focused on automated water surface profile detection, the application of two-dimensional hydraulic models, and more reliable estimation of local energy losses at hydraulic structures.

## REFERENCES

[1] G. Rak, M. Hočevar, S. Kolbl Repinc, L. Novak, and B. Bizjan, “A Review on Methods for Measurement of Free Water Surface,” Feb. 01, 2023, *MDPI*. doi: 10.3390/s23041842.

[2] D. Vučić *et al.*, “ESTIMATION OF DISCHARGE IN A LABORATORY CHANNEL USING VIDEO PROCESSING,” in *STEPGRAD XVII*, 2026. doi: 10.61892/STP202601020V.

[3] J. M. Qasim, “LABORATORY AND HEC-RAS SIMULATIONS OF A SINGLE-STEP WEIR,” *ARPN Journal of Engineering and Applied Sciences*, vol. 8, no. 12, 2013, [Online]. Available: www.arpnjournals.com

[4] A. Mohammad Razi, S. Adnan, S. N. Rahmat, M. Azlan, M. Yusoff, and H. Kasmin, “Characterization of Free Surface Hydraulics Flow Over Sharp-Crested Weir in a One-Dimensional HEC-RAS Model,” *INTERNATIONAL JOURNAL OF INTEGRATED ENGINEERING*, vol. 12, no. 4, pp. 319–327, 2020, doi: 10.30880/ijie.2020.12.04.031.

[5] B. A. R. Ruslan, “CALIBRATING A HEC-RAS MODEL OF V-NOTCH WEIR AS INLINE STRUCTURE USING OPEN CHANNEL FLUME FLOW METHOD AND ITS APPLICATION FOR SEDIMENT TRANSPORT,” 2015.

[6] G. Farnebäck, “Two-Frame Motion Estimation Based on Polynomial Expansion,” Linkoping, 2003. [Online]. Available: http://www.isy.liu.se/cvl/

[7] F. Tauro, F. Tosi, S. Mattoccia, E. Toth, R. Piscopia, and S. Grimaldi, “Optical tracking velocimetry (OTV): Leveraging optical flow and trajectory-based filtering for surface streamflow observations,” *Remote Sens. (Basel).*, vol. 10, no. 12, Dec. 2018, doi: 10.3390/rs10122010.

[8] M. T. Perks, “KLT-IV v1.0: Image velocimetry software for use with fixed and mobile platforms,” *Geosci. Model Dev.*, vol. 13, no. 12, pp. 6111–6130, Dec. 2020, doi: 10.5194/gmd-13-6111-2020.

[9] P. Praštalo and A. Milanović, “POSSIBILITIES FOR MEASURING SMALL DISCHARGES USING A SIMPLE WEIR CONSTRUCTION,” *Archives for Technical Sciences*, vol. 2, no. 33, pp. 165–175, Oct. 2025, doi: 10.70102/afts.2025.1833.165.

[10] R. Kapor, *Hidraulika*. Beograd: Grđevinski fakultet Univerziteta u Beogradu, 2011.

[11] “PlotDigitizer.” [Online]. Available: https://plotdigitizer.com/app

[12] V. Te Chow, *OPEN-CHANNEL HYDRAULICS*. New York: McGraw-Hill, 1959.

[13] F. M. Henderson, *Open Channel Flow*. New York: Macmillan Publishing Co., 1966.

https://doi.org/10.24867/INDIS-2026-EN-413



# STRUCTURAL FAILURE OF A REINFORCED CONCRETE RETAINING WALL

*Ivan Dolibašić[1], Željko Lebo[2], Jure Galić[3], Ivan Volarić[4]*

***Abstract:***

The paper presents the fundamental approach to data collection and analysis as part of a forensic investigation into the structural failure of a reinforced concrete retaining wall. The aim of this paper is to identify and analyse the causes and failure mechanism of the structure by comparing the design assumptions and available design documentation with the as-built conditions and the results of subsequent geotechnical analyses. The investigation includes verification of the technical characteristics specified in the design documentation, assessment of the sequence and stages of construction, and evaluation of the quality of the executed works. The paper presents a real case of a geotechnical failure involving the collapse of a retaining structure, which fortunately resulted in no injuries. In addition, the paper provides recommendations for future practice in the design and construction of geotechnical retaining structures in accordance with the applicable requirements and principles of Eurocode 7.

*Keywords: Failure of structures, geotechnical hazard, retaining wall, Eurocode 7*

# SLOM KONSTRUKCIJE ARMIRANO BETONSKOG POTPORNOG ZIDA

***Rezime:***

U radu su predstavljeni osnovni principi prikupljanja i obrade podataka tokom provedbe inspekcijskog postupka pronalaska uzroka sloma armirano betonskog potpornog zida. Cilj rada je utvrditi i analizirati glavne uzroke i mehanizme koji su doveli do sloma konstrukcije, usporedbom projektnih pretpostavki i dostupne projektne dokumentacije sa stvarno izvedenim stanjem te rezultatima naknadno provedenih geotehničkih analiza. Rad obuhvata proveru tehničkih karakteristika definisanih u projektnoj dokumentaciji, kao i redosled i faze izvođenja radova i proveru kvaliteta izvedenih radova. U radu je naveden realan primer hazarda i rizika kod geotehničkih konstrukcija, tj. urušavanja potporne konstrukcije u kojem, srećom, niko nije povređen. Rad dodatno naglašava smernice za buduće radove u vidu projektovanja i izvođenja geotehničkih potpornih konstrukcija u skladu sa trenutno važećim propisima kao deo Evrokoda 7.

*Ključne reči: Slom konstrukcije, geotehnički hazard, potporni zid, Eurokod 7*

[1] Lecturer, Tehničko veleučilište u Zagrebu, Zagreb, Hrvatska, ivan.dolibasic@tvz.hr
[2] College Professor, Tehničko veleučilište u Zagrebu, Zagreb, Hrvatska, zeljko.lebo@tvz.hr
[3] Senior Lecturer, Tehničko veleučilište u Zagrebu, Zagreb, Hrvatska, jure.galic@tvz.hr
[4] Senior Lecturer, Tehničko veleučilište u Zagrebu, Zagreb, Hrvatska, ivan.volaric@tvz.hr

## 1. INTRODUCTION

GENERAL SUPPORTING STRUCTURES

Retaining structures are massive or flexible, permanent or temporary structures designed to support vertical or steep cuts in natural ground or fill material. They may be constructed as independent structures or as integral parts of other structures and, since they primarily resist actions imposed by the ground, they are classified as geotechnical structures. This paper focuses on a reinforced concrete retaining wall; therefore, throughout the remainder of the paper, the term retaining structure refers to the retaining wall under consideration. Retaining walls often support fill material whose surface is at a higher elevation than the ground level in front of the wall. The material behind the wall constitutes the backfill, whose properties and geometry, together with the foundation conditions and wall geometry, influence the actions that the retaining structure must resist.

Retaining structures may be constructed using different materials and technologies and, depending on the type of material they support, may be classified as structures retaining cuts in natural ground or structures retaining embankments. This distinction determines the scope and type of geotechnical investigations required to obtain reliable parameters for the design and dimensioning of the retaining structure. When supporting a cut, appropriate geotechnical investigations are required to determine the composition and geotechnical properties of the natural ground, and the structure must be designed to resist the resulting actions. When supporting an embankment, the backfill material and its geotechnical properties can be specified, whereby the use of controlled fill material with more favourable properties may reduce the actions on the retaining structure and contribute to a more economical design.

Retaining structures may also be classified according to their structural system and the manner in which loads are transferred to the ground. According to Eurocode 7, they are divided into three main groups: gravity walls, embedded walls, and composite retaining structures. The subject of this paper is a cantilever reinforced concrete retaining wall, consisting of a vertical wall stem rigidly connected to a reinforced concrete base slab. The principal actions acting on this type of retaining structure are schematically presented in Figure 1.

The actions on the retaining structure are shown in Figure 1 and include external loads acting behind the wall (concentrated load P, line load P′, and uniformly distributed load q), the self-weight of the wall (G and Gt), active earth pressure from the backfill (Ea), passive earth resistance in front of the base slab (Ep), hydrostatic (Hw) and hydrodynamic (U) water pressures, ground reaction (N), and friction at the base–soil interface (T). Depending on the specific conditions, seismic actions, anchor forces (S), and additional external horizontal forces (V) should also be considered.

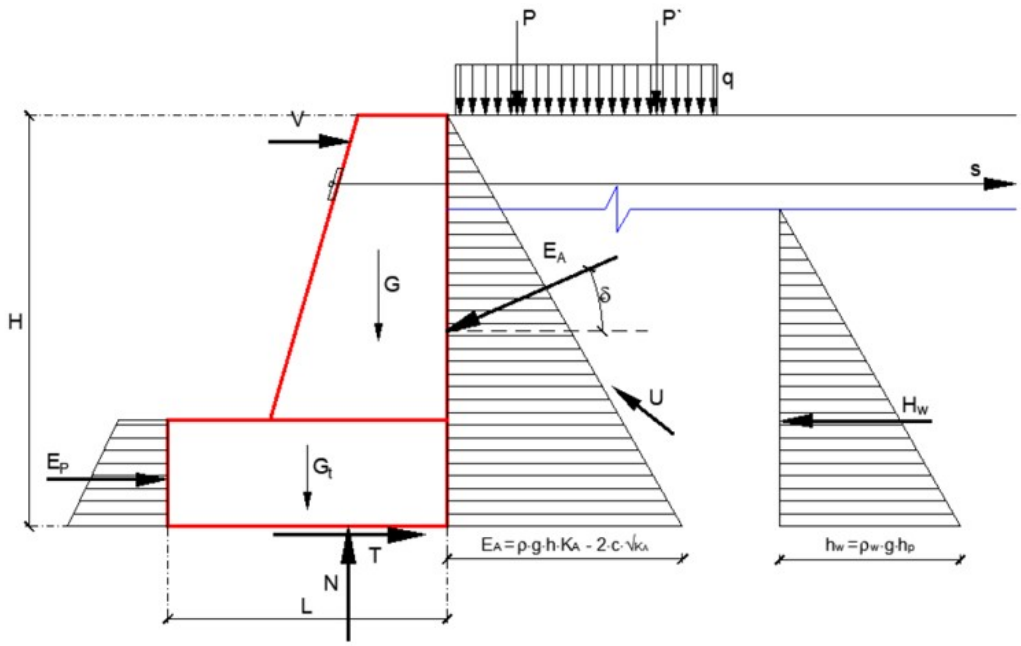


*Figure 1. Schematic representation of the action on the supporting structure (retaining wall)*

Considering the above actions, the design of retaining structures requires verification of stability against overturning (EQU/GEO) and sliding (GEO), structural resistance of critical sections (STR), bearing resistance of the foundation soil (GEO), settlement, and the overall stability of the wall and surrounding ground (GEO). Proper identification of the relevant actions and verification of the corresponding limit states form the basis for the safe design of geotechnical retaining structures.

## PROBLEM OF CONSTRUCTION FORENSICS

The aim of this section is to provide an overview of the procedure used to determine the causes and failure mechanism of the retaining wall in Pisarovina. The investigation aims to identify the failure mechanism of the retaining wall and assess the role of individual participants involved in its design and construction. The location of the retaining wall in question is in Pisarovina on cadastral plot no. 2429/1, cadastral plot Lijevo Središko.




*Figure 2. View of the location in question*

According to the information received from the investor, the retaining wall in question on the plot was constructed by the contractor in accordance with a valid building permit.

However, after a certain (only 4 months) period of exploitation, the reinforced concrete retaining wall structure collapsed in the central part of the length along the road around the building, as well as the backfill material behind the retaining wall collapsed.

The construction of the building as well as geotechnical structures around and next to the building itself is permitted in accordance with the issued building permit and in accordance with the main project, which is an integral part of the building permit. The main project contains 4 maps and one geotechnical study. The works began in November 2023 and were completed in July 2024. During the works, a construction log was kept with a total of 181 sheets. Upon completion of the works, a technical inspection was carried out and the Operating Permit was obtained at the end of September 2024. According to the investor's statement, the hazard, i.e. the collapse of the geotechnical structure of the retaining wall, occurred at the end of November 2024.

## 2. METHODS

The methods used in defining and developing the concept for defining the causes of structural failure presented below consist of (in-situ) site visits and data collection from the site, as well as collection of available project documentation and subsequent data elaboration and verification of the collected data.

### 2.1. CONSTRUCTION SITE TOUR - VISUAL INSPECTION

In-situ data collection included photographic documentation of the condition of the geotechnical structure immediately before and after the structural failure. The purpose of the site inspection was to identify existing damage, assess potential hazards, and detect indications of possible further failure or destabilization of both the retaining structure and the surrounding ground.

Inspection of the retaining structure immediately prior to the failure indicated that the backfill behind the wall was highly saturated (Figure 3, top left), suggesting inadequate performance of the drainage system. The saturated backfill, combined with the presence of cracks in the reinforced concrete structure, resulted in water seepage through the retaining wall itself (Figure 3, top right). Furthermore, no drainage openings (weep holes) were provided through the retaining wall. In combination with the inadequately constructed drainage system behind the wall, this resulted in progressive saturation of the backfill during periods of precipitation.

Under such conditions, saturation of the backfill may lead to the development of pore-water pressures over the retained height and consequently to a significant increase in hydrostatic pressure acting on the retaining wall. If these conditions persist and the retaining structure has not been designed to resist the resulting hydrostatic action, the additional lateral loading may become critical with respect to the relevant ultimate limit states and may ultimately contribute to structural failure.



*Figure 3. The situation of the retaining wall and the embankment behind the wall immediately after the 1st expansion hazard*

## 2.2. DOCUMENTING THE DAMAGE FOUND, NECESSARY MEASUREMENTS AND PHOTOGRAPHY

In-situ data collection involves photo-documenting the situation and the state of geotechnical structures before and immediately after the hazard itself, in order to confirm and observe potential threats and indications of possible new collapses and destabilization of both the structure and the terrain caused by the hazard.

After the outflow of the trapped water and after the dissipation of the pore pressure in the backfill behind the wall, the displacement of the wall in the crown (Figure 3 bottom left) is observed for min. 5-7 cm from the axis towards the road around the object, and additionally an activated passive part can be observed in front of the face/foot of the retaining wall (Figure 3 bottom right), which is also an indicator of destabilization of the wall in the form of displacement (translation) of the retaining wall, and later rotation. It can be seen that the situation in which the embankment behind the wall is completely submerged by water has reached the limit state of bearing capacity due to structural failure (STR).



*Figure 4. The situation of the retaining wall and the embankment behind the wall immediately after the hazard of the 1st and 2nd expansion*

Furthermore, upon visiting the location immediately after the hazard, it was observed that the embankment behind the supporting structure was still saturated, i.e. the drainage behind the wall was functioning very poorly, and the soil behind the wall was still soaked with water, and destabilization and wrinkling of the embankment behind the supporting structure were additionally observed.
Potential hazards were identified in the current situation and instructions were given to the investor for further action in order to reduce the risk of possible additional risks, with mandatory caution in order to preserve the evidence necessary to define the cause of the collapse of the structure.

A detailed inspection of the building and facilities is carried out by taking samples and carrying out the necessary measurements of the dimensions of the elements, reinforcement, etc. (Figure 5). The measurement determined the width of the foundation footing of the wall to be 160 cm and the width of the retaining wall body to be 30 cm, which is constant.



*Figure 5. Measurement and verification of reinforcement dimensions (diameter and spacing of reinforcing bars) of the retaining wall*

The reinforcement installed in the critical section of the wall, taking into account the diameter, is also in accordance with the detailed design, and the spacing of the installed reinforcement is greater than that provided for in the design (20 cm).

## 2.3. ANALYSIS OF AVAILABLE PROJECT DOCUMENTATION

Reviewing the available and submitted project documentation, the analysis reveals certain deviations in the geometry of the retaining wall between the Main Design and Detailed Design of the structure. The geotechnical parameters were selected in accordance with the instructions from the geotechnical study that preceded the creation of the project documentation. It can be seen that the calculation of the stability of the retaining wall was not made in accordance with Eurocode 7, HRN EN 1997 - Geotechnical design (with national supplements), and it is noted that not all forces acting on a retaining structure of this type were taken into account. Additionally, it was noticed that not all the checks that should be carried out when dimensioning the retaining wall were carried out.

### 2.3.1. Deviations between the main and detailed design documentation

By analyzing the design of the retaining wall from the main design of the structure, Figure 6, and by analyzing the design of the retaining wall defined in the detailed design of the structure, Figure 7, deviations are observed: In the main design, the width of the wall is 25 cm, and in the detailed design, the width of the wall is 30 cm. Furthermore, in the main design, the foundation footing is 200 cm wide, and in the detailed design, the foundation footing is 160 cm wide. Furthermore, in the main design, the static height of the foundation footing is 50 cm, and in the detailed design it is 70 cm, furthermore, the "heel" of the wall foundation, in the main design, is 25 cm wide, while in the detailed design the wall does not have a "heel".
The backfill behind the retaining wall is at the height of the wall crown, and this does not correspond to the actual situation on the ground.

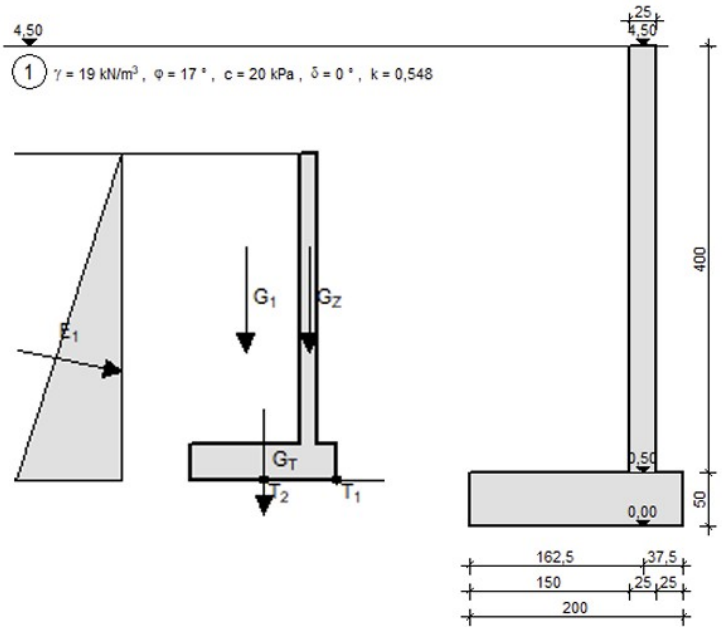


*Figure 6. Cross section of the retaining wall in question, Main design*

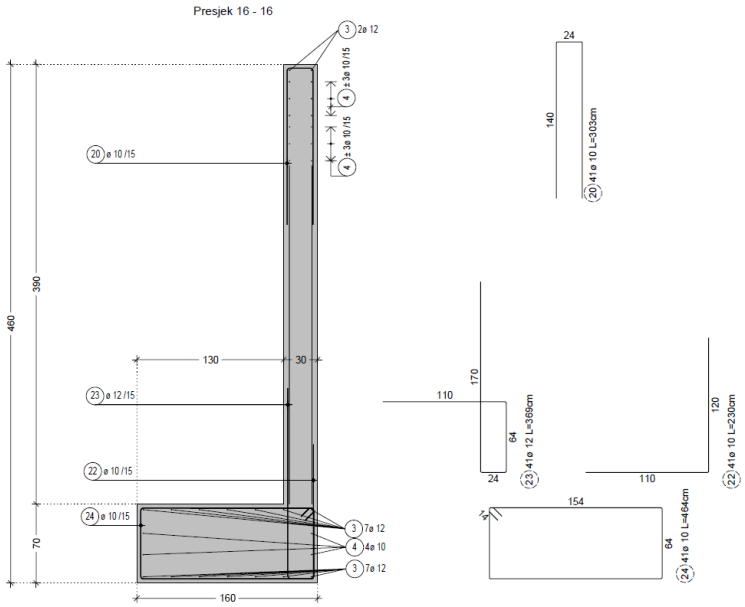


*Figure 7. Cross section of the retaining wall in question, Detailed design*

### 2.3.2. Analyzing the main and detailed design documentation

Based on the inspection, it can be definitively concluded that the retaining wall in question on the plot was constructed according to the Detailed Design of the structure. The reinforced concrete retaining wall in question is defined in the aforementioned project documentation in the recapitulation and reinforcement statement as "12. L604-2023-ARM-15-Retaining wall", and it has a total length of almost 80 m (79.77 m), and is shown in plan and cross-section (section 16 – 16) and additionally in elevation. Figure 7 shows a cross-section of the retaining wall that is the subject of the inspection.
After a detailed insight into the detailed design, the following dimensions of the retaining wall are observed: Width of the foundation footing 160 cm, width of the wall body 30 cm, height of the foundation footing 70 cm, height of the difference in level 390 cm, total height of the wall 460 cm.

According to the detailed design, reinforcement was installed in the retaining wall (for 1m' of the wall) as follows:
The foundation footing is reinforced with position 24, where 7 pcs Φ10mm with a total length L= 464 cm are defined. The wall body (towards the ground) is reinforced with position 23, where 7 pcs Φ12mm with a total length L= 369 cm are defined in connection with the foundation footing and with Q 524 reinforcement meshes in the remaining part of the body towards the top of the wall. The body of the wall (towards the hall) is reinforced with position 22, where 7 pieces of Φ10mm with a total length of L= 230 cm are defined in connection with the foundation footing and with a Q 335 reinforcement mesh in the remaining part of the body towards the top of the wall. The body of the wall at the top is reinforced with position 20, where 7 pieces of Φ10mm with a total length of L= 303 cm are defined. The specified amount of reinforcement is intended for 1m' of wall length. All reinforcing bars are of B500B reinforcing steel quality.



*Figure 8. View of the built-in drainage behind the retaining wall*

On the plot in question, after the collapse of the structure, it was observed and then confirmed that the drainage behind the wall was not carried out in accordance with the project documentation, which can be seen in Figure 8. A drainage filter made of stone material was not installed above the perforated drainage pipe, and no geotextile was installed, but the drainage pipe was installed at the bottom of the wall and "buried", that is, low-permeable soil material was laid over the drainage pipe, through which the trapped water flows very slowly and with great difficulty towards the drainage trench, which results in water retention within the fill.

Based on the analysis of the design documentation, comparison of the designed and as-built conditions, and the results of the conducted inspection, the following key deficiencies and deviations were identified:

- inconsistency in the retaining wall geometry between the Main Design and the Detailed Design;
- inconsistency between the designed backfill geometry and the actual site conditions;
- incomplete determination of the relevant actions on the retaining structure;
- incomplete verification in accordance with Eurocode 7;
- deviation of the installed reinforcement from the designed reinforcement arrangement;
- inadequate construction of the drainage system behind the retaining wall.

The identified deficiencies indicate incomplete consideration of the actual geometry and relevant actions, as well as insufficient coordination between the design documentation and the as-built conditions. Inadequate drainage behind the wall may result in water retention and additional hydrostatic pressure. The effects of these deficiencies on the resistance and stability of the retaining wall are quantified in Chapter 3.

## 3. RESULTS OF GEOTECHNICAL ANALYSES IN DETERMINING THE CAUSES OF STRUCTURAL FAILURE

The results of the geotechnical analyses are presented below, taking into account the available documentation and all available parameters after the collapse of the structure. When conducting geotechnical analyses (for static and seismic conditions), the parameters of the foundation soil and the backfill soil behind the supporting structure were taken, as well as the geometric dimensions, i.e. the geometry of the embankment

behind the supporting structure and the geometric dimensions of the supporting structure of the reinforced concrete retaining wall.

## 3.1. RESULTS OF THE GEOSTATIC STRESS-DEFORMATION ANALYSIS OF A RETAINING WALL – 2D

The following shows the stress-strain analysis of a retaining wall for 1m of wall, considering the actual conditions and the state on the ground (installed reinforcement).

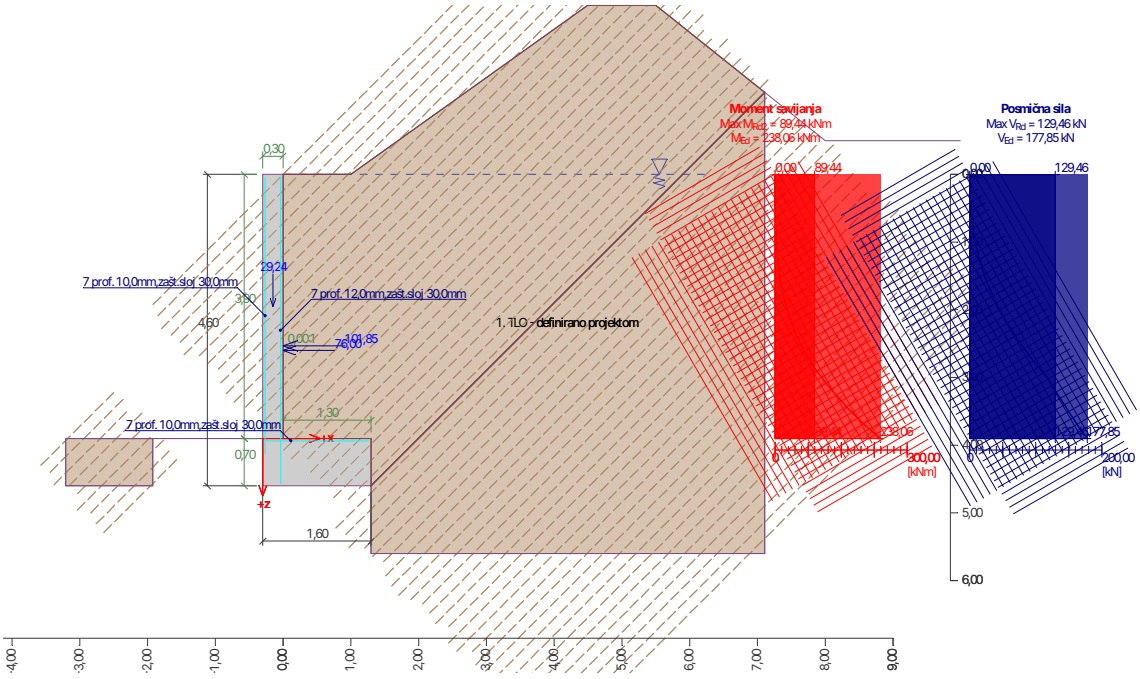


*Figure 9. Result - geostatic stress-deformation analysis of the retaining wall - 2D for 1m` of the wall*

*Table 1.Presentation of the results of the dimensioning of the AB element - 1 m` wall*

| **Stress check in the critical section at the junction of the body and the wall foot** | | **Stress check in the critical section at the junction of the body and the wall foot** | |
|---|---|---|---|
| **Installed reinforcement: 7pcs Φ12.0mm** | | **Installed reinforcement: 7pcs Φ10.0mm** | |
| Design bending resistance: | $M_{Rd}$ = 89.44 kNm | Design shear resistance: | $V_{Rd}$ = 129.46 kN/m |
| Design bending moment: | $M_{Ed}$ = 238.06 kNm | Design shear force: | $V_{Ed}$ = 177.85 kN/m |
| $M_{Ed} > M_{Rd}$<br>**Cross section NOT SATISFACTORY**<br>U = 266.17% | | $V_{Ed} > V_{Rd}$<br>**Cross section NOT SATISFACTORY**<br>U = 137.38% | |

After the geostatic analysis (Figure 9) and the presented design results (Table 1), it can be seen that the installed reinforcement of the retaining wall for a 1m' segment of the wall is not satisfactory. Also, it is observed that the calculated effect of the bending moment ($M_{Ed}$) in the critical section of the wall at the contact of the foundation footing and the wall body is $M_{Ed}$= 238.06 kNm, therefore we see that it is significantly higher than the

calculated bending moment resistance ($M_{Rd}$) which was realized by installing the reinforcement defined by the project for the same section which is $M_{Rd}$= 89.44 kNm.

## 3.2. RESULTS OF THE GEOSTATIC ANALYSIS FOR SLIDING AND OVERTURNING OF A RETAINING WALL

Taking into account the results obtained, which are not satisfactory regarding the minimum required reinforcement in the critical section of the reinforced concrete structure of the retaining wall, additional geostatic analyses were carried out, including checks for sliding (translation) and checks for overturning of the retaining wall in order to obtain a complete analysis of the stability of the retaining wall. The limit states of STR, GEO and EQU bearing capacity were checked. The results of the analyses on sliding and overturning of the retaining wall can be seen in Table 2.

*Table 2. Forces acting on the structure*

| Name | $F_x$ [kN/m] | $F_y$ [kN/m] | $d_x$ [m] | $d_y$ [m] |
|---|---|---|---|---|
| Weight – wall | 0.00 | 57.25 | 0.47 | -1.53 |
| FF front face resistance | 3.55 | 0.00 | 0.00 | -0.23 |
| Weight – earthen wedge | 0.00 | 96.94 | 0.95 | -2.66 |
| Active pressure | -99.16 | 19.61 | 1.60 | -1.87 |
| Water pressure | -105.80 | 0.00 | 1.60 | -1.53 |

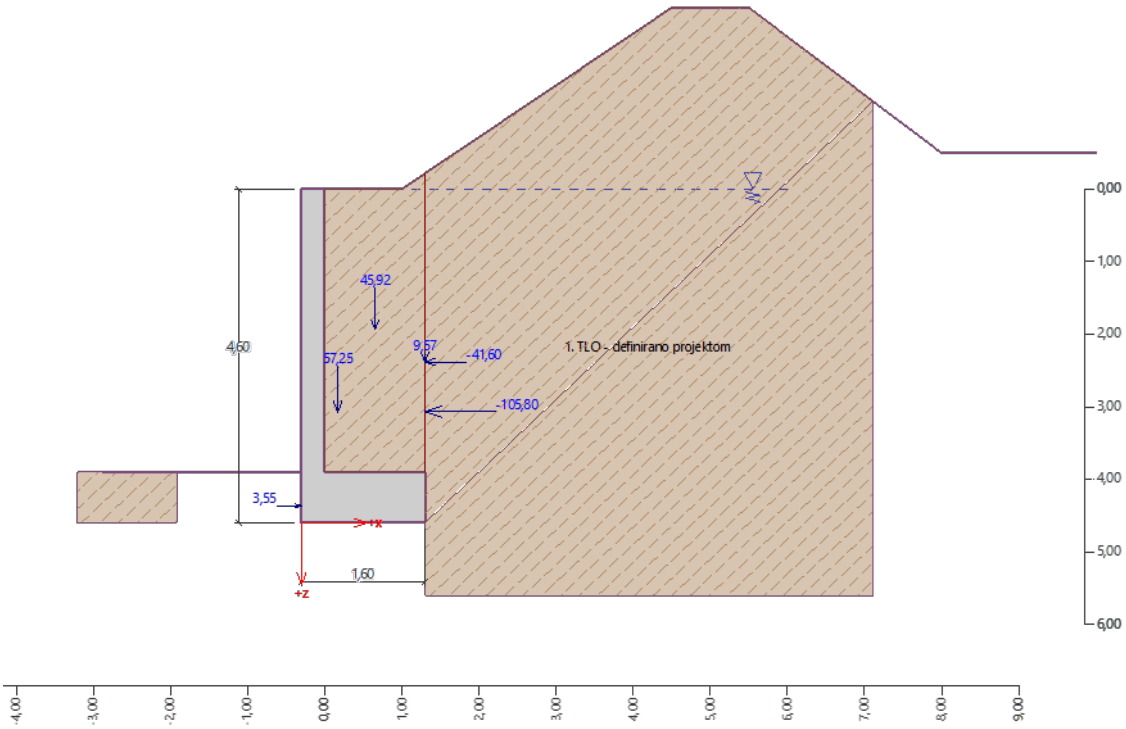


*Figure 10. Presentation of the analysis of the forces acting on the structure*

| **Overturning stability check** | | **Sliding stability check** | |
|---|---|---|---|
| Moment of resistance: | $M_{res}$ = 85.89 kNm/m | Horizontal resistance force: | $H_{res}$ = 27.58 kN/m |
| Overturning moment: | $M_{ovr}$ = 253.63 kNm/m | Active horizontal force: | $H_{act}$ = 143.86 kN/m |
| $M_{ovr} > M_{res}$<br>**Overturning check NOT SATISFACTORY**<br>U = 295.30% | | $H_{act} > H_{res}$<br>**Sliding check NOT SATISFACTORY**<br>U = 521.70% | |

After the overturning check of the retaining wall (Figure 10), it is observed that the calculated effect of the destabilizing overturning moment is $M_{ovr}$ = 253.63 kNm/m and as such is greater than the calculated resistance of the stabilizing overturning moment, which is $M_{res}$ = 85.89 kNm/m. It is observed that the overturning check is not satisfactory, since the degree of utilization is more than 290%. Furthermore, when performing the sliding check of the retaining wall (Figure 10), it can be observed that the calculated effect of the destabilizing active force is $H_{act}$ = 143.86 kN/m, while the calculated resistance of the stabilizing horizontal force is less intense and is $H_{res}$ = 27.58 kN/m. The sliding check of the retaining wall is not satisfied, since the degree of utilization is greater than 500%.
Since the retaining wall did not satisfy the required verifications under static conditions, no additional seismic analysis was performed.

The results of the subsequently performed analyses confirmed insufficient resistance and stability of the retaining wall for the analysed condition, with the following key results:

- Bending: $M_{Ed}$ = 238.06 kNm > $M_{Rd}$ = 89.44 kNm, with a utilization of 266.17 %;
- Shear: $V_{Ed}$ = 177.85 kN/m > $V_{Rd}$ = 129.46 kN/m, with a utilization of 137.38 %;
- Overturning: $M_{ovr}$ = 253.63 kNm/m > $M_{res}$ = 85.89 kNm/m, with a utilization of 295.30 %;
- Sliding: $H_{act}$ = 143.86 kN/m > $H_{res}$ = 27.58 kN/m, with a utilization of 521.70 %.

These results confirm the consequences of the deficiencies identified in Chapter 2, primarily the incomplete determination of relevant actions and the inconsistencies between the designed and as-built conditions. The analysed retaining wall does not satisfy the resistance requirements for bending and shear or the stability requirements for overturning and sliding, with the highest utilization obtained for the sliding verification.

## 4. CONCLUSION

Taking into account the design, construction, and as-built condition of the retaining structure, it can be concluded that the retaining wall was under-designed for the loads and actions that developed after construction.
The static calculations provided in the Main Design did not account for the actual backfill geometry above the wall crest or the pore-water pressure that developed within the backfill during periods of precipitation (rain and snow). These conditions resulted in an increase in the total horizontal action on the wall, adversely affecting its stability and ultimately contributing to its structural failure and collapse.

The retaining wall was not fully designed in accordance with the applicable requirements for geotechnical structures in the Republic of Croatia. In particular, the provisions of Eurocode 7, HRN EN 1997-1:2012 – Geotechnical design – Part 1: General rules (EN 1997-1:2004+AC:2009), were not fully applied.

The presented case demonstrates a comprehensive forensic approach to data collection and analysis for determining the causes of retaining structure failure. It also demonstrates that inadequate consideration of geotechnical conditions and actions in the design and construction of relatively simple structural systems, such as cantilever retaining walls, may result in excessive deformation and, ultimately, structural failure.
The subsequent analysis showed that the design bending moment in the critical section ($M_{Ed}$) was almost 2.6 times greater than the corresponding bending moment resistance, ($M_{Rd}$) provided by the installed reinforcement.

## REFERENCES

[1] Nonveiller E. (1979) Mehanika tla i temeljenje građevina. Zagreb: Školska knjiga

[2] Lebo Ž. i Dolibašić I. (2025) Geotehnika. Zagreb: Tehničko veleučilište u Zagrebu

[3] Lebo Ž. (2025) Nalaz i mišljenje sudskog vještaka. Zagreb: Geoplan d.o.o.

[4] Roje-Bonacci T. (2005) Potporne građevine i građevne jame. Split: Građevinsko - Arhitektonski fakultet sveučilišta u Splitu

[5] Zakon o gradnji, Narodne Novine 155/25 – Republika Hrvatska.

https://doi.org/10.24867/INDIS-2026-EN-426



# NUMERICAL ANALYSIS OF FIRE-INDUCED BUCKLING OF A COLD-FORMED STEEL COLUMN

*Igor Džolev[1], Vladimir Živaljević[2], Jelena Mirjanić[3], Petar Lazičić[4], Andrija Rašeta[5]*

***Summary:***

Fire-induced buckling of steel columns is governed by the combined effects of mechanical load, geometrical imperfections, and temperature-dependent material degradation. This paper presents a thermo-mechanical finite element procedure for evaluating instability problem using a fixed-ended thin-walled steel column as a case study. The analyses are performed in ANSYS using a material model defined according to EN 1993-1-2 advanced calculation method. The first eigenvalue buckling mode is introduced as the initial imperfection. Nonlinear analysis is conducted to calculate the buckling resistance, which is then used to define four fire load cases. Under ISO 834 exposure, failure times are calculated with respect to initial member utilization. Results demonstrate that the presented workflow can be used to support performance-based structural fire assessment of steel columns.

*Keywords: cold-formed steel column, fire resistance, nonlinear buckling, finite element analysis*

# NUMERIČKA ANALIZA IZVIJANJA PRI POŽARU HLADNO OBLIKOVANOG ČELIČNOG STUBA

***Rezime:***

Izvijanje čeličnih stubova pri dejstvu požara uslovljeno je kombinovanim uticajem opterećenja, geometrijskih imperfekcija i temperaturno zavisne degradacije materijala. U ovom radu je prikazan termo-mehanički postupak analize stabilnosti metodom konačnih elemenata, na primeru obostrano uklještenog tankozidnog čeličnog stuba. Analize su sprovedene u programu ANSYS korišćenjem materijalnog modela definisanog prema EN 1993-1-2 naprednoj računskoj metodi. Prvi svojstveni oblik izvijanja je uveden kao početna imperfekcija. Nelinearna analiza je sprovedena radi određivanja otpornosti na izvijanje, koja je zatim korišćena za definisanje četiri slučaja opterećenja u požaru. Pri izloženosti požaru prema ISO 834, vreme loma je sračunato prema stepenu iskorišćenja elementa. Rezultati pokazuju da prikazani postupak može da se koristi za strukturalnu požarnu procenu čeličnih stubova zasnovanu na ponašanju.

*Ključne reči: hladno oblikovani čelični stub, požarna otpornost, nelinearno izvijanje, metoda konačnih elemenata*

[1] Assoc. Prof., Faculty of Technical Sciences, University of Novi Sad, Novi Sad, Serbia, idzolev@uns.ac.rs, ORCID 0000-0002-7622-7936
[2] Asst. Prof., Faculty of Technical Sciences, University of Novi Sad, Novi Sad, Serbia, zivaljevic.vladimir@uns.ac.rs, ORCID 0000-0002-2808-2664
[3] Teach. Asst., Faculty of Technical Sciences, University of Novi Sad, Novi Sad, Serbia, jelena.mirjanic@uns.ac.rs, ORCID 0009-0006-6608-056X
[4] Teach. Assoc., Faculty of Technical Sciences, University of Novi Sad, Novi Sad, Serbia, petarlazicic@uns.ac.rs, ORCID 0009-0008-2589-7746
[5] Full Prof., Faculty of Technical Sciences, University of Novi Sad, Novi Sad, Serbia, araseta@uns.ac.rs, ORCID 0000-0002-4535-1379

## 1. INTRODUCTION

Steel members exposed to fire experience a progressive reduction of mechanical resistance due to temperature-dependent degradation of stiffness and strength. This is particularly important for compression members, where reduction of elastic modulus and yield strength may trigger instability. Considering that steel has high thermal conductivity, temperature increase can develop fast throughout the member, leading to a rapid loss of load-bearing capacity during fire exposure.

Cold-formed and thin-walled steel members are especially sensitive to instability phenomena. Their structural response is often governed not only by material yielding, but also by local, distortional, or global buckling modes. Previous studies on cold-formed steel members have shown that instability effects are central to their behaviour, and that member resistance can be strongly influenced by geometry, boundary conditions, imperfections, and loading configuration [1]. In fire conditions, this sensitivity becomes more pronounced since elevated temperatures simultaneously reduce stiffness, strength, and the ability of the column to resist second-order effects.

Advanced numerical analysis provides a suitable framework for assessing the fire resistance of structural members, particularly when experimental testing is expensive or difficult to perform for a wide range of geometries, load levels, and fire scenarios. Finite element software such as ANSYS has been widely used for structural fire analysis, allowing nonlinear thermal and mechanical properties to be considered [2,3]. A common modelling strategy is sequential thermal-structural analysis, where the transient thermal response is first calculated and then introduced into the structural model as time-dependent body temperatures. This procedure is consistent with the need to consider conduction, convection, and radiation during fire exposure, as well as temperature-dependent material properties.

The present paper investigates the fire-induced buckling response of a fixed-ended steel column with a C 250×80×40×5 cross-section and a length of 4.0 m. The column is made of S355 steel and is modelled using temperature-dependent multilinear isotropic hardening material properties defined according to EN 1993-1-2 [4]. The initial geometrical imperfection is introduced in the form of the first eigenvalue buckling mode, scaled according to the provisions referring to the use of advanced calculation models [4]. After determining the nonlinear buckling resistance of the imperfect column, four initial axial load levels are considered, corresponding to a range of utilization levels, in terms of the obtained nonlinear buckling force. The column is then subjected to ISO 834 standard fire exposure, and the failure time and corresponding steel temperature are evaluated for each load level.

The aim of the study is to establish the relationship between axial load utilization and fire resistance for the analysed steel column. Special attention is given to the numerical modelling procedure, including eigenvalue buckling analysis, imperfection scaling, nonlinear buckling analysis, transient thermal analysis, and subsequent structural analysis under increasing temperature. The results are intended to demonstrate how load level and temperature-dependent degradation of steel properties influence the onset of nonlinear buckling failure during fire exposure.

## 2. NUMERICAL MODEL

Numerical model is developed in ANSYS Workbench 16.0 [5] in order to simulate the mechanical response of the steel column at ambient and elevated temperatures. The modelling procedure consists of three main stages: definition of the column geometry

and boundary conditions, assignment of temperature-dependent nonlinear material properties, and generation of a finite element mesh suitable for nonlinear buckling and thermo-mechanical analysis.

## 2.1. GEOMETRY AND BOUNDARY CONDITIONS

The analysed member is a 4.0 m long steel column with a cold-formed channel cross-section C 250×80×40×5. The cross-section consists of a 250 mm web, two 80 mm flanges, and 40 mm edge lips, with a uniform plate thickness of 5 mm. The geometry is created by first defining the cross-sectional surface and then extruding it along the longitudinal axis of the column, resulting in a single three-dimensional solid body.
The column is modelled with fixed support conditions at both ends. At the upper end, displacement in the longitudinal direction of the column is free in order to allow axial deformation caused by mechanical compression and thermal effects. Remote points are introduced at the centroids of the upper and lower end sections. These remote points are used to apply boundary conditions and axial loading in a controlled and numerically stable manner (Fig. 1).
In the initial static analysis used for eigenvalue buckling, a compressive axial force of 1 N is applied. This load served only as a reference load for the subsequent linear buckling analysis, where the calculated load multiplier represents the elastic critical buckling force. In the nonlinear analyses, the imperfect geometry is used, and the axial action is introduced either through force or prescribed displacement, depending on the purpose of the analysis and convergence requirements.

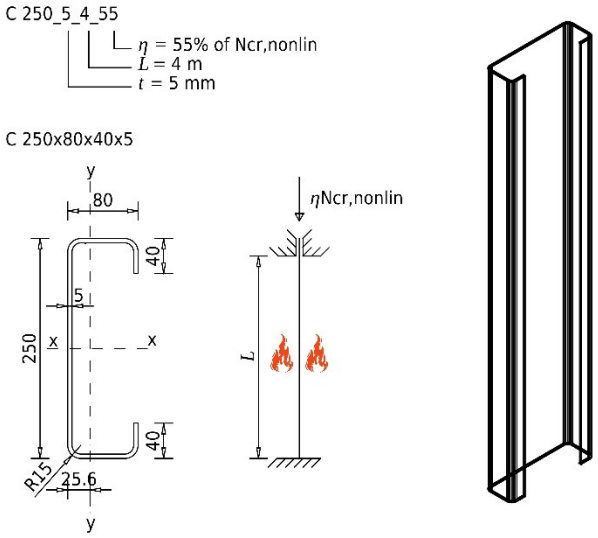


*Fig. 1 Geometry, cross-section and boundary conditions of the analysed column*

## 2.2. MATERIAL MODEL AT ELEVATED TEMPERATURES

The column is modelled as structural steel grade S355. A nonlinear material model is adopted in order to capture the degradation of mechanical properties and plastic response of steel at elevated temperatures. The material behaviour is defined using a multilinear isotropic hardening plasticity model.
Stress-strain relationships are calculated according to EN 1993-1-2 for a set of discrete temperatures covering both ambient and fire-exposed conditions (Fig. 2). For each temperature level, the corresponding reduction of yield strength, proportional limit, and

elastic modulus is taken into account. In this way, the model is able to represent the gradual loss of stiffness and resistance of steel during heating.
The temperature-dependent stress-strain curves are introduced into ANSYS as separate multilinear curves. During the structural fire analysis, the material properties are updated according to the imported body temperature field obtained from the preceding transient thermal analysis. This enables simulation of the reduction in load-bearing capacity as the temperature increases with time.
For thermal analysis, temperature-dependent thermal properties of steel are assigned also in accordance with the EN 1993-1-2 (Fig. 2). Heat transfer through the column is modelled by conduction within the steel body, while convection and radiation are applied on the exposed external surfaces.

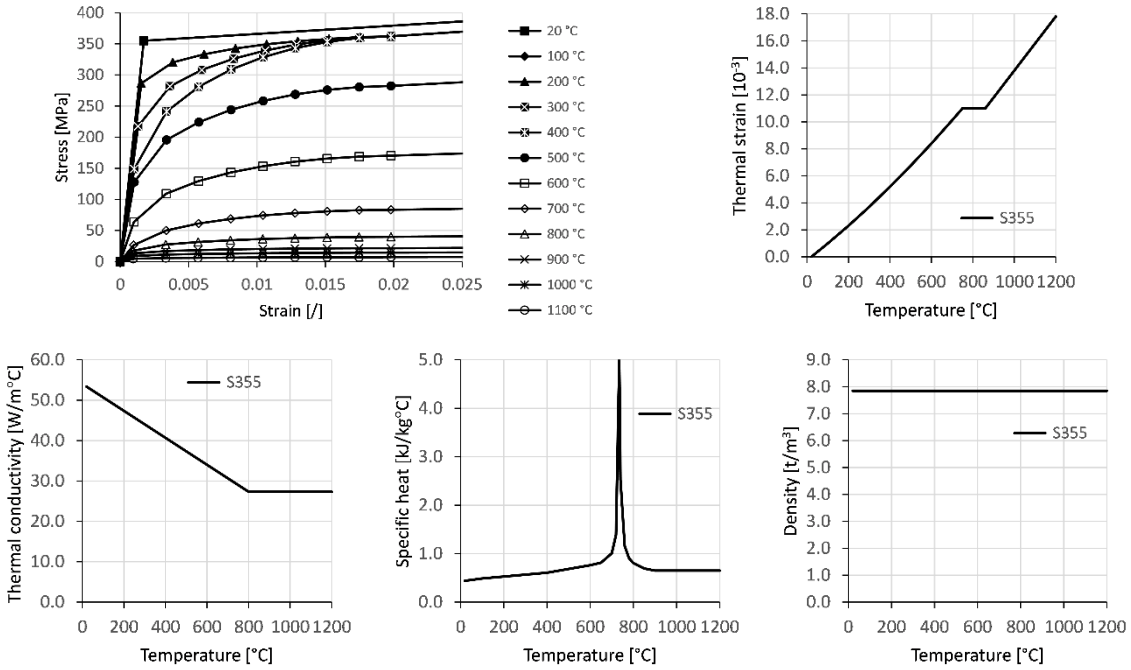


*Fig. 2 Temperature dependent properties of S355 steel*

## 2.3. MESH AND FINITE ELEMENTS

The finite element model is discretized using three-dimensional solid finite elements. The adopted element types are SOLID70 and SOLID185, for thermal and structural analysis, respectively. The same geometric model is used throughout the mechanical analyses in order to maintain consistency between the buckling, nonlinear structural, thermal, and structural fire simulations.
A fine mesh is generated to adequately describe the geometry of the thin-walled C-section and to capture the expected buckling deformation. Special attention is given to the discretization of the web, flanges, and edge lips, since these parts influence the global and local stiffness of the member.
The selected mesh density provides a sufficiently detailed representation of the cross-section and column length while remaining computationally feasible for nonlinear analysis. Since the failure mechanism is expected to be governed by instability and large lateral deformations, the mesh has to be fine enough to reproduce the first buckling mode and the subsequent nonlinear deformation pattern. The same mesh configuration is retained for the analyses involving the geometrically imperfect model, so that differences in response can be attributed to the introduced imperfection, load level, and temperature field rather than to changes in discretization.

A summary of the main finite element model parameters is given in Tab. 1.

*Tab. 1 Finite element model characteristics*

| Parameter | Value |
|---|---|
| Column length | 4000 mm |
| Cross-section | C 250×80×40×5 |
| Steel grade | S355 |
| Material plasticity model | Multilinear isotropic hardening |
| Temperature range | 20 – 1100 °C |
| Element type | SOLID70 / SOLID185 |
| Number of nodes | 138,831 |
| Number of elements | 91,200 |
| End conditions | Fixed-fixed, axial displacement released at top |

## 3. BUCKLING ANALYSIS AND INITIAL IMPERFECTION

Buckling resistance of the analysed column is determined in two stages. First, a linear eigenvalue buckling analysis is performed in order to obtain the elastic critical load and the corresponding buckling mode shape. In the second stage, the first buckling mode is used to introduce an initial geometrical imperfection into the model, after which nonlinear buckling analysis is carried out. This procedure enables a more realistic estimation of the column resistance, since geometrical imperfections and material nonlinearity are included.

### 3.1. LINEAR EIGENVALUE BUCKLING ANALYSIS

The first step consists of a static structural analysis of the perfect column geometry. The model includes the previously defined boundary conditions. A unit compressive force of 1 N is applied at the top end of the column in the direction of the longitudinal axis.
The solution of this static structural analysis is then connected to an eigenvalue buckling analysis system. In this way, the eigenvalue buckling analysis adopts the same geometry, boundary conditions, and loading configuration as the static model. Since the reference compressive force is equal to 1 N, the load multiplier obtained from the eigenvalue buckling analysis directly corresponds to the linear elastic critical buckling force $N_{cr,lin}$.
The first eigenvalue buckling mode is extracted as the governing global instability mode of the column (Fig. 3). This mode shape is then used as the basis for defining the initial geometrical imperfection. The linear elastic critical buckling force obtained from ANSYS was compared with the Euler critical force for an ideal fixed-ended column:

$$P_{cr} = \frac{\pi^2 EI}{(KL)^2} \tag{1}$$

where $E$ is the elastic modulus of steel (206 GPa), $I$ is the relevant area moment of inertia (195.51 cm$^4$), $L$ is the column length (4 m), and $K$ is the effective buckling length factor (0.5). The linear buckling force obtained from ANSYS is 911.07 kN. For comparison, the Euler critical force for an ideal fixed-ended column is calculated as

993.75 kN, which is 9.1% higher than the finite element result. This difference is considered acceptable, since the Euler expression represents an idealized beam-column solution, while the three-dimensional finite element model accounts for the actual open thin-walled C-section geometry, local cross-sectional flexibility, possible flexural–torsional coupling, and the numerical representation of end restraints through remote points. Therefore, the analytical calculation is used as an order-of-magnitude check, while the ANSYS eigenvalue result is adopted for subsequent imperfection scaling and nonlinear analysis.

Although the eigenvalue buckling analysis is useful for identifying the critical mode shape and estimating the elastic critical load, it does not account for geometrical imperfections, material yielding, or nonlinear second-order effects. Therefore, it is not used directly as the final column resistance, but only as an intermediate step in the development of the imperfect nonlinear model geometry.

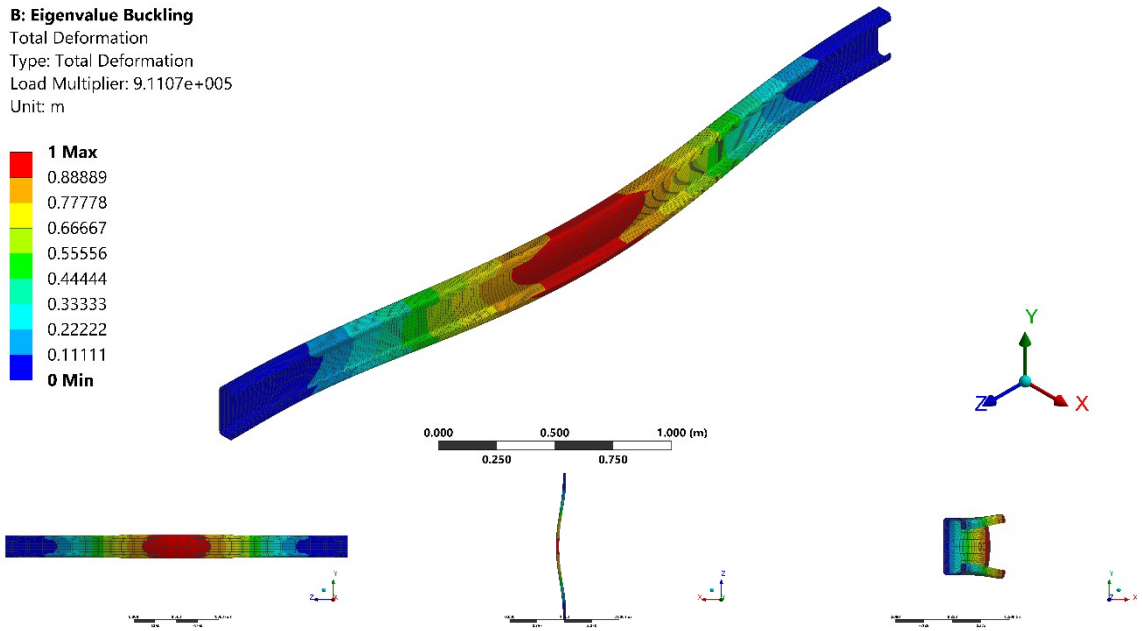


*Fig. 3 First eigenvalue buckling mode*

## 3.2. NONLINEAR BUCKLING ANALYSIS WITH GEOMETRIC IMPERFECTION

The first buckling mode obtained from the eigenvalue analysis is normalized to a maximum displacement of 1 m. This mode shape is then scaled so that the maximum lateral displacement at mid-height of the column corresponds to:

$$w_{0,max} = \frac{L}{1000} = 4\,mm \tag{2}$$

The deformed shape with the scaled imperfection is extracted using an APDL command procedure. The imperfect geometry is then transferred to the Finite Element Modeler [5] and used as the geometry for the subsequent nonlinear static analysis. In this way, the model includes an initial geometric imperfection consistent with the expected global buckling mode.

In contrast to the initial eigenvalue buckling model, the nonlinear buckling analysis includes geometrical nonlinearity and material nonlinearity. Axial compression is introduced through prescribed displacement at the upper end of the column instead of applied force, to provide better numerical stability in the post-critical range and reduce

convergence difficulties associated with force-controlled nonlinear buckling simulations.

The prescribed displacement is chosen to cause the axial strain of 0.15%. During the analysis, the axial reaction force and maximum lateral deformation of the column were monitored (Fig. 4). The maximum force reached in the nonlinear force-displacement response is taken as the nonlinear buckling resistance of the imperfect column.

The nonlinear buckling force $N_{cr,nonlin}$ is found to be equal to 599.52 kN or 65.8% of the linear buckling force:

$$N_{cr,nonlin} = 0.658\, N_{cr,lin} \tag{3}$$

The reduction relative to the ideal elastic buckling force is a consequence of the introduced geometrical imperfection, material and geometrical nonlinearity.

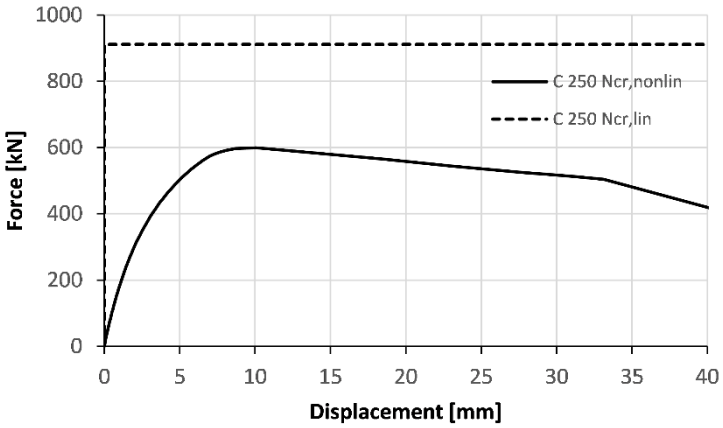


*Fig. 4 Force-displacement linear and nonlinear buckling*

The obtained nonlinear buckling resistance is then used as the reference resistance for the fire analysis. Four axial load levels were defined as fractions of this resistance:

$$N = \eta\, N_{cr,nonlin} \tag{4}$$

where $\eta$ is the load utilization factor. The considered values are 25%, 40%, 55%, and 70%, corresponding to $\eta$ = {0.25; 0.40; 0.55, 0.70}. These load levels are subsequently applied in the structural fire analysis in order to investigate the influence of mechanical utilization on the fire resistance of the column.

## 4. FIRE ANALYSIS PROCEDURE

The fire analysis is performed using a sequential thermo-mechanical procedure. First, a transient thermal analysis is carried out to determine the temperature development in the steel column during standard fire exposure. The calculated temperature field is then transferred to a structural model, where it is introduced as a time-dependent body temperature. This enabled simulation of the reduction of load-bearing capacity and the development of fire-induced buckling under constant axial load.

### 4.1. TRANSIENT THERMAL ANALYSIS

The transient thermal model is developed using the geometrically imperfect column model, the same as in the mechanical analysis. The aim of this analysis is to determine the time-dependent temperature distribution in the steel member during fire exposure.

The column is exposed to the ISO 834 standard fire curve [6], which defines the gas temperature as a function of time:

$$\theta_g = 20 + 345 \log_{10}(8t + 1) \tag{5}$$

where $\theta_g$ is the gas temperature in °C and $t$ is the fire exposure time in minutes.
All external surfaces of the column are assumed to be directly exposed to fire. Heat transfer from the surrounding hot gases to the steel surface is modelled by convection and radiation, while heat transfer within the steel body is modelled by conduction. The thermal boundary conditions are defined in accordance with EN 1991-1-2 [7].
Convective heat transfer is applied on the exposed steel surfaces using the appropriate heat transfer coefficient for fire-exposed members. Radiative heat transfer is considered through the Stefan-Boltzmann law, using the emissivity of the exposed steel surface and the temperature of the surrounding fire environment. The total heat flux acting on the exposed surfaces can be expressed as:

$$\dot{h}_{net} = \dot{h}_{net,c} + \dot{h}_{net,r} \tag{6}$$

where $\dot{h}_{net,c}$ is the convective component and $\dot{h}_{net,r}$ is the radiative component of the net heat flux.
The thermal analysis produces temperature fields for the full duration of fire exposure (Fig. 5). Since the column cross-section is relatively thin, the temperature increase in the steel is expected to be rapid. However, the use of a three-dimensional thermal model allows the temperature distribution over the web, flanges, lips, and along the member length to be captured. The calculated temperatures are stored at discrete time points and later transferred to the structural fire analysis as body temperatures.
The output of the transient thermal analysis is therefore not a failure criterion itself, but an input for the subsequent structural model. The relevant thermal results include the time-dependent steel temperature distribution and the average or representative steel temperature at the moment of structural failure.

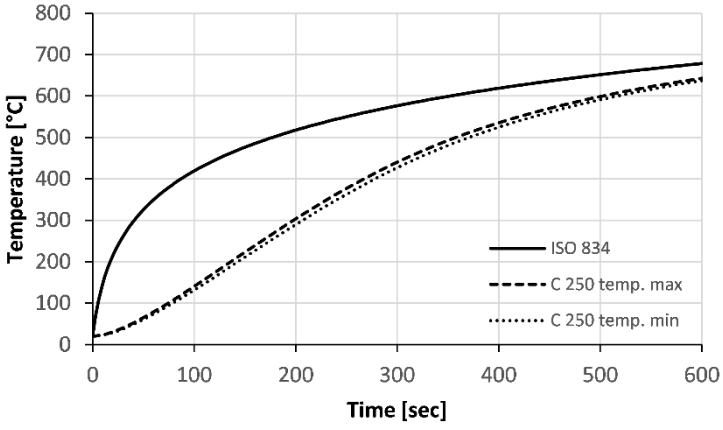


*Fig. 5 ISO 834 fire curve and calculated steel temperature development*

## 4.2. STRUCTURAL FIRE ANALYSIS

The same boundary conditions and nonlinear material model are adopted as in the nonlinear buckling analysis. The temperature-dependent stress-strain curves of S355 steel are assigned to the model, allowing degradation of stiffness and strength during heating. The analysis consists of two load steps. In the first load step, axial compression is applied to the column at ambient temperature. The compressive force is introduced

gradually at the upper end of the column until the required load level is reached (as described in 3.2). In the second load step, the axial force is kept constant, while the temperature fields obtained from the transient thermal analysis are introduced into the structural model as time-dependent body temperatures. Although the analysis is performed within a static structural system, the thermal loading varies with time according to the results of the preceding transient thermal simulation. This approach enables the progressive degradation of the material properties to be considered without performing a fully coupled transient thermo-mechanical analysis.

During heating, the column stiffness and strength decrease as the steel temperature increases. At the same time, the constant axial force produces increasing second-order effects due to the initial geometrical imperfection and lateral deformation of the member. Failure is identified by the occurrence of rapidly increasing lateral displacements and loss of numerical convergence associated with nonlinear buckling. The corresponding fire exposure time is taken as the failure time of the column.

For each load level, the following results are extracted:

- failure time,
- steel temperature at failure,
- axial displacement,
- lateral displacement development,
- deformed shape at failure.

The procedure is repeated for all four utilization levels. By comparing the obtained failure times and temperatures, the influence of axial load level on the fire resistance of the column is evaluated. The overall numerical analysis workflow is presented in Fig. 6.

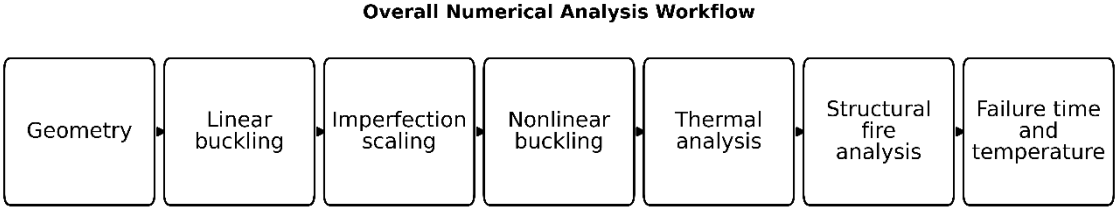


*Fig. 6 Numerical analysis workflow*

## 5. RESULTS AND DISCUSSION

The results are discussed in two parts. First, the nonlinear buckling response of the imperfect column at ambient temperature is presented. This result is then used as the reference resistance for defining the axial load levels in the fire analysis. Second, the fire resistance of the column is evaluated for four utilization levels, corresponding to 25%, 40%, 55%, and 70% of the nonlinear buckling resistance.

### 5.1. NONLINEAR BUCKLING RESISTANCE

The axial load is applied through displacement control, allowing the post-critical response to be traced after the maximum resistance is reached. The obtained force-displacement response is shown in Fig. 4. At the beginning of the analysis, the response is nearly linear, with a gradual increase in axial force and lateral displacement. As the load increases, geometrical nonlinearity becomes more pronounced and the lateral displacement grows at an increasing rate. The maximum reaction force is obtained at:

$$N_{cr,nonlin} = 599.52\,kN \tag{7}$$

with a corresponding maximum lateral displacement $u_{\text{lat}}$ as:

$$u_{lat} = 10.07\,mm \tag{8}$$

After this point, the column enters the post-critical range. Further increase in lateral displacement is accompanied by a reduction in axial resistance, confirming that the peak of the response represents the nonlinear buckling resistance of the imperfect column.
This reduction of 34.2% of the nonlinear buckling force compared to the Euler buckling force, confirms the importance of considering geometrical imperfections and nonlinear structural behaviour.

## 5.2. FIRE RESISTANCE FOR DIFFERENT LOAD LEVELS

Failure for each load level is identified by a rapid increase in lateral deformation and loss of stability.
The results show a clear reduction in fire resistance time with increasing load level. The longest fire resistance is obtained for the 25% utilization case, while the shortest resistance is obtained for the 70% utilization case (Tab. 2).

*Tab. 2 Failure times and temperatures*

| Load level | Applied force [kN] | Failure time [s] | Steel temperature at failure [°C] |
|---|---|---|---|
| 25% | 149.88 | 497.60 | 591.88 |
| 40% | 239.81 | 392.59 | 521.72 |
| 55% | 329.74 | 267.01 | 389.54 |
| 70% | 419.66 | 202.70 | 297.46 |

The fire resistance time decreases from 497.60 s at 25% utilization to 202.70 s at 70% utilization. The corresponding steel temperature at failure decreases from 591.88°C to 297.46°C. At low utilization, the column can sustain a larger reduction in stiffness and strength before instability occurs, and vice versa.
The results also confirm that the critical steel temperature is not a fixed material property, but depends strongly on the mechanical utilization level. For the 25% load case, the column remained stable until the steel temperature reached approximately 592°C. In contrast, for the 70% load case, failure occurred at approximately 297°C. This confirms that fire resistance of compression members cannot be assessed only through temperature development, but must account for the interaction between load level, imperfection, stiffness degradation, and second-order effects.

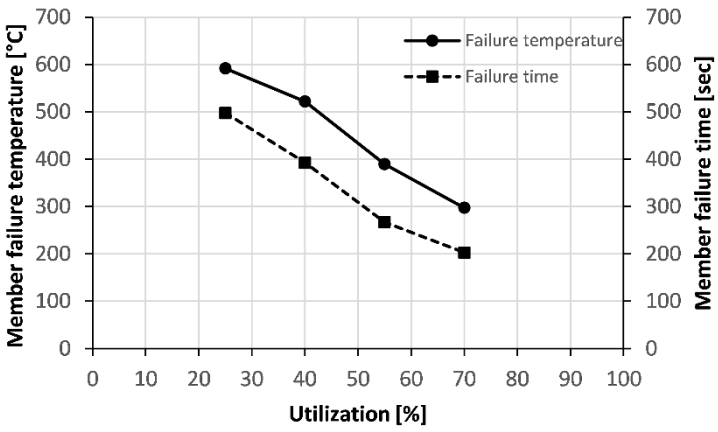

*Fig. 7 Member failure time and temperature as a function of load utilization level*

## 5.3. DEFORMATION AND FAILURE MODE

The axial displacement response shows two characteristic stages (Fig. 8). During the first load step, axial compression causes negative vertical displacement at the top of the column. After the thermal load is introduced, thermal expansion gradually dominates the axial response, and the displacement becomes positive for all load levels. Close to failure, a reduction or reversal of axial displacement is observed, corresponding to rapid lateral deformation and instability of the column.
The lateral displacement response is more directly related to the buckling failure. For all load levels, the lateral displacement initially increases slowly. This stage corresponds to stable behaviour under constant axial force and gradually increasing steel temperature. Near failure, however, lateral displacement increases rapidly, indicating the onset of nonlinear buckling (Fig. 9).

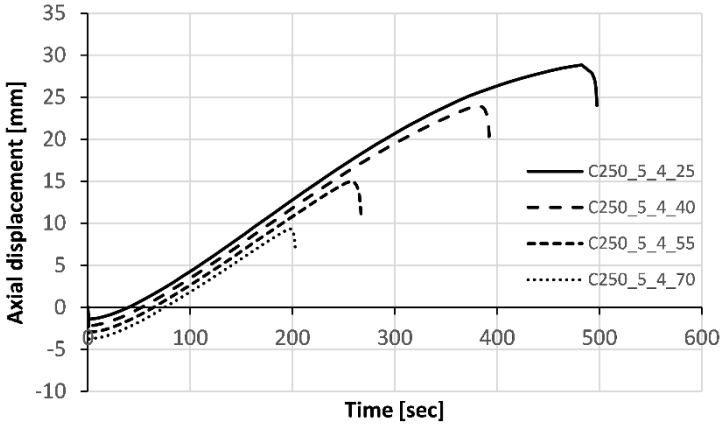


*Fig. 8 Axial displacement of the top section in time*

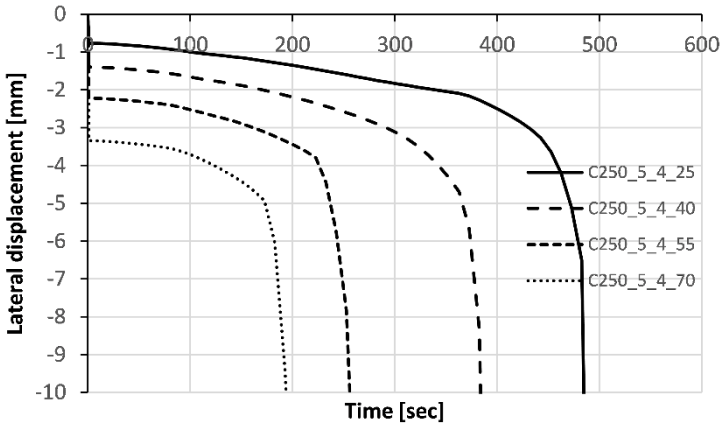


*Fig. 9 Lateral displacement of the mid-section in time*

The failure mode is governed by global flexural buckling, with the largest lateral displacement occurring approximately near the middle part of the column. Although the failure times and critical temperatures differ significantly, the deformation pattern remains similar, confirming that the initial imperfection based on the first eigenvalue buckling mode governs the instability shape during fire exposure (Fig. 10).

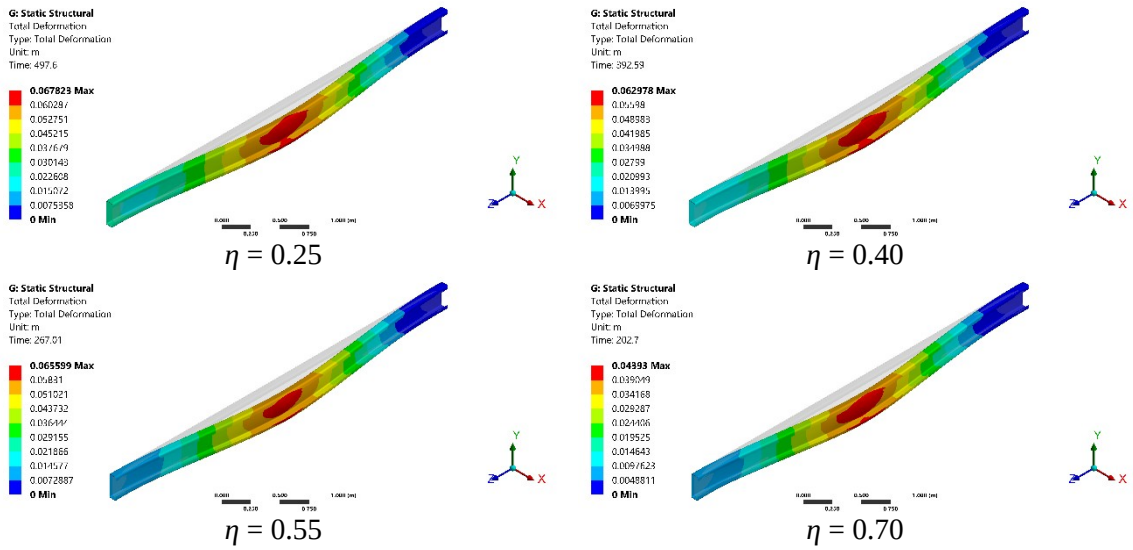


*Fig. 10 Deformed column shape at failure*

Overall, the results demonstrate that axial load utilization has a dominant influence on fire-induced buckling of the analysed steel column. Increasing the utilization level leads to shorter fire resistance time and lower steel temperature at failure. The adopted sequential thermo-mechanical model captures the progressive loss of stability caused by the combined effects of temperature-dependent material degradation, initial imperfection, and second-order deformation.

## 6. CONCLUSIONS

This paper presented a numerical investigation of the fire-induced buckling behaviour of a fixed-ended steel column with a C 250×80×40×5 cross-section and a length of 4.0 m. The column was modelled in ANSYS 16.0 using three-dimensional solid finite elements, temperature-dependent material properties for S355 steel, and a sequential thermal-structural analysis procedure. Based on the obtained results, the following conclusions can be drawn:

- The adopted modelling procedure enabled the complete numerical simulation of the column response, from the initial linear eigenvalue buckling analysis, through the introduction of geometrical imperfection, to nonlinear buckling and fire-induced instability. The first eigenvalue buckling mode was successfully used as the shape of the initial imperfection, scaled to a maximum lateral displacement of ($L$/1000), i.e. 4 mm.
- The nonlinear buckling resistance of the imperfect column was obtained as approximately 600 kN, which corresponds to 65.8% of the linear buckling force. This confirms that the ideal elastic buckling resistance may significantly overestimate the real resistance of compression members when geometrical imperfections and nonlinear effects are considered.
- The fire resistance of the column strongly depended on the applied axial load level. For load levels of 25%, 40%, 55%, and 70% of the nonlinear buckling resistance, the calculated failure times were 497.60 s, 392.59 s, 267.01 s, and 202.70 s, respectively. Increasing the utilization level from 25% to 70% reduced the fire resistance time by approximately 59%.
- The steel temperature at failure also decreased with increasing utilization level. The column failed at 591.88°C for 25% utilization, 521.72°C for 40% utilization, 389.54°C for 55% utilization, and 297.46°C for 70% utilization. This confirms that the critical temperature of a steel compression member is not a constant

value, but depends on the applied load, buckling resistance, initial imperfection, and second-order effects.

- The failure mode in all analysed cases was governed by global flexural buckling. The lateral displacement developed gradually during the early heating stage, followed by a rapid increase immediately before failure. This behaviour indicates progressive loss of stiffness and stability caused by the temperature-dependent degradation of steel properties under sustained axial compression.
- In all analysed cases, the unprotected cold-formed steel column failed before reaching R15, corresponding to 15 minutes of standard fire exposure, indicating that passive fire protection is required for this member to satisfy even the lowest fire-resistance class.
- The sequential thermal-structural procedure used in this study provides a practical numerical approach for evaluating fire-induced buckling of steel columns. However, further research should include comparison with experimental results, investigation of different imperfection amplitudes, and analyses of additional cross-sections, support conditions, and fire exposure scenarios.

## ACKNOWLEDGEMENT

The research has been conducted within the project "Enhancement of teaching and scientific research capacities through the application of modern technologies in the fields of civil engineering, geodesy, and disaster risk management and fire safety", developed at the Department of Civil Engineering and Geodesy, Faculty of Technical Sciences, University of Novi Sad, Serbia.

## REFERENCES

[1] Živaljević V., Jovanović Đ., Kovačević D., Džolev I. (2022). The Influence of Web Holes on the Behaviour of Cold-Formed Steel Members: A Review. *Buildings*, 2022 12(8):1091, pp. 1–33. https://doi.org/10.3390/buildings12081091

[2] Džolev I., Kekez-Baran S., Rašeta A. (2025). Fire Resistance of Steel Beams with Intumescent Coating Exposed to Fire Using ANSYS and Machine Learning. *Buildings*, 2025 15(13):2334, pp. 1–19, https://doi.org/10.3390/buildings15132334

[3] Džolev I., Cvetkovska M., Lađinović Đ., Radonjanin V. (2018). Numerical analysis on the behaviour of reinforced concrete frame structures in fire, *Computers and Concrete*, Vol. 21, No. 6, pp. 637–647, https://doi.org/10.12989/cac.2018.21.6.637

[4] EN 1993-1-2 (2012). *Eurocode 3: Design of Steel Structures, Part 1-2: General Rules, Structural Fire Design*, CEN—European Committee for Standardization (ISO), Geneve, Switzerland.

[5] ANSYS® Academic Teaching Mechanical (2015). *ANSYS Help Documentation*, Release 16.0, ANSYS, Inc., Canonsburg, PA, USA. https://ansys.synopsys.com/, accessed on 6 August 2026.

[6] ISO 834-1 (1999). *Fire-Resistance Tests—Elements of Building Construction—Part 1: General Requirements*, International Organization for Standardization (ISO), Geneve, Switzerland.

[7] EN 1991-1-2 (2012). *Eurocode 1: Actions on Structures: Part 1-2: General Actions—Actions on Structures Exposed to Fire*, CEN—European Committee for Standardization (ISO), Geneve, Switzerland.

https://doi.org/10.24867/INDIS-2026-EN-439



# ANALYSIS OF THE INFLUENCE OF PAVEMENT SURFACE MACROTEXTURE ON FRICTION USING THE MPD INDICATOR

*Sara Krsmanović[1], Miloš Šešlija[2], Panta Krstić[3]*

***Summary:***

Starting from the physical principles of friction, it can be observed that the value of the friction coefficient may be influenced by various parameters, one of which is the pavement surface texture, consisting of macrotexture and microtexture. This paper focuses on the theoretical principles of the friction coefficient, as well as on the measurement and analysis of data obtained from pavement macrotexture measurements expressed through the MPD parameter (Mean Profile Depth) along a section of State Road IIA-117, Novi Bečej–Banatsko Karađorđevo. The aim of the paper is to analyse the measured macrotexture values and to highlight the importance of MPD as a supplementary parameter in the assessment of pavement friction and driving safety.

***Keywords:*** *friction, macrotexture, microtexture, MPD, pavement*

# ANALIZA UTICAJA MAKROTEKSTURE KOLOVOZNE POVRŠINE NA TRENJE PRIMJENOM MPD POKAZATELJA

***Rezime:***

Polazeći od fizičkih osnova uviđamo da na vrijednost koeficijenta trenja mogu imati uticaj različiti parametri, dok je jedan od njih upravo tekstura kolovozne površine koju čine makrotekstura i mikrotekstura. Ovaj rad posvećen je teorijskim osnovama koeficijenta trenja kao i, mjerenju i analizi podataka dobijenih mjerenjem makroteksture izražene preko parametra MPD (srednje dubine profila), na dionici državnog puta IIA-117 Novi Bečej – Banatsko Karađorđevo. Cilj rada jeste analiza izmjerenih vrijednosti makroteksture i da se ukaže značaj vrijednosti MPD-a kao dopunskog parametra pri analizi trenja i bezbjednosti vožnje.

***Ključne riječi:*** trenje, makrotekstura, mikrotekstura, MPD, kolovoz

[1] Teaching Assistant, Department of Civil Engineering and Geodesy, Faculty of Technical Sciences, University of Novi Sad, sarakrsmanovic@uns.ac.rs, ORCID 0009-0006-5650-877X
[2] Associate Professor., Faculty of Technical Sciences, University of Novi Sad, Novi Sad, Serbia, sele@uns.ac.rs, ORCID 0000-0002-8857-8952
[3] Teaching Assistant, Department of Civil Engineering and Geodesy, Faculty of Technical Sciences, University of Novi Sad, panta.krstic@uns.ac.rs, ORCID 0000-0001-5519-391X

## 1. INTRODUCTION

Vehicle safety on roads is a fundamental requirement that must be ensured when designing road geometry. To a large extent, this safety depends precisely on friction and the ability of the tyres to grip the pavement surface. A reduced friction value significantly compromises vehicle stability on the road, especially on a wet pavement. The value of the friction coefficient can be influenced by numerous factors, one of which is the texture of the pavement surface. Microtexture affects the adhesion achieved between the tyre and the pavement, while macrotexture enables water to be expelled from the contact zone.

## 2. FRICTION BETWEEN TYRE AND PAVEMENT – PHYSICAL BASIS

One of the fundamental physical phenomena that enables the safe movement of vehicles is friction between the tyre and the pavement. Thanks to friction, a vehicle is able to accelerate, brake and change direction of travel. If the value of friction is reduced, this can lead to an increased stopping distance, reduced vehicle stability, or even an increased risk of skidding, which is especially pronounced on a wet pavement.

In standard general physics courses, it is usually stated that the sliding friction force acting between two bodies in contact — one of which is commonly regarded as the “upper” body resting on the “supporting surface” it presses against — is described by the phenomenological law:

$$F_{tr} = \mu * F_N$$

Where $F_N$ is the magnitude of the normal force (the reaction of the "supporting surface"), and μ is the coefficient of friction, whose value depends on the combination of materials in contact [1].

### 2.1. TYRE–PAVEMENT SURFACE CONTACT

When the tyre and the pavement surface come into contact, complex loading occurs due to deformation of the tread and the tyre carcass.

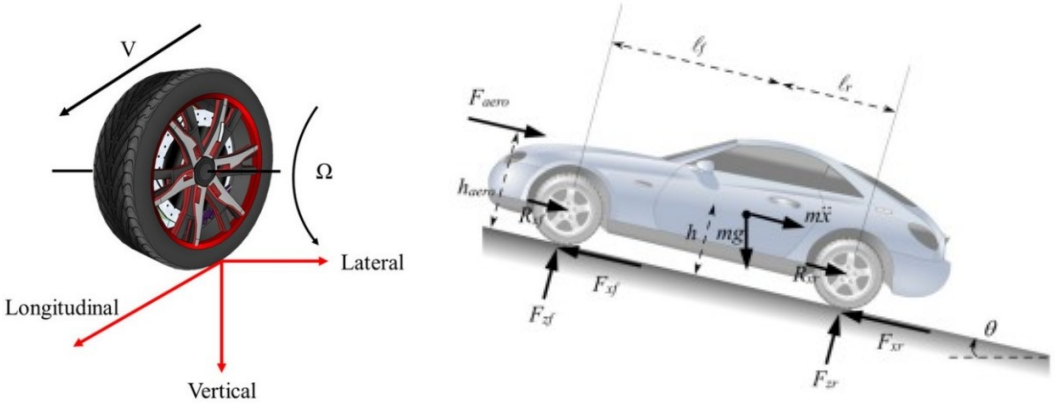


*Figure 1Schematic diagram of the forces in the contact zone [2]*

The vertical force acting on the tyre is called the normal load of the tyre [2]. It originates from the portion of the vehicle's weight that is transferred to the pavement surface through the tyre, and its value depends on the distribution of the vehicle's mass, the position of the centre of gravity, longitudinal acceleration, aerodynamic forces and the road gradient [2].

Pavement friction is the force that opposes the relative motion between the vehicle's tyre and the pavement surface. This resistive force arises when the tyre rolls or slides over the pavement surface [3]. Pavement friction plays a very important role in keeping the vehicle on the road, as it enables drivers to safely control and steer the vehicle, both longitudinally and laterally [3]. Friction is an important input parameter in the geometric design of roads, since it is used in determining the minimum stopping sight distance, the minimum radius of horizontal curves, the minimum radius of crest vertical curves, and the maximum superelevation on horizontal curves [3].

The resistive force, described by the dimensionless coefficient of friction μ, represents the ratio between the tangential friction force F, which arises between the tyre tread and the horizontal pavement surface, and the normal force, i.e. the vertical load Fw [3].

$$\mu = \frac{F}{F_w}$$

As a dimensionless quantity, the value of the friction coefficient further depends on the materials of the bodies in contact, while the coefficient values themselves generally range from 0 to 1 (with some exceptions) [4].

## 3. THE INFLUENCE OF MICROTEXTURE AND MACROTEXTURE ON FRICTION

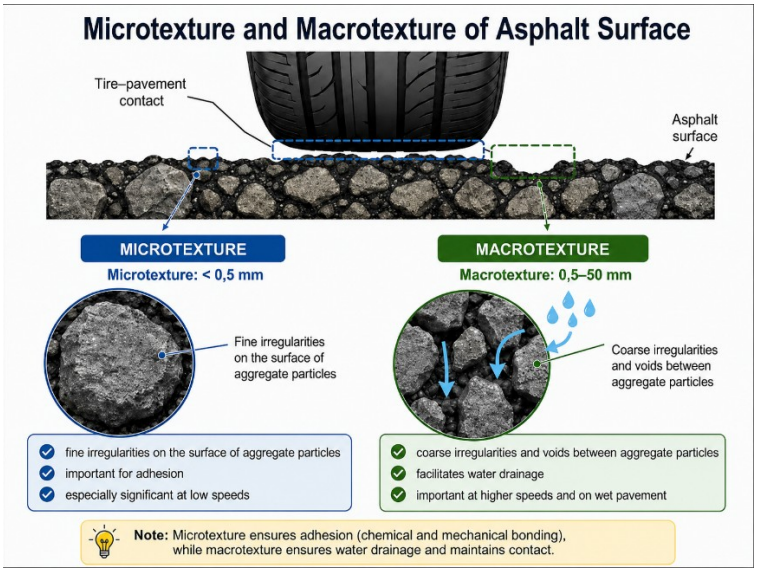


*Figure 2 Pavement microtexture and macrotexture*

Microtexture represents small-scale texture, smaller than 0.5 mm, found on the surface of the aggregate in asphalt or the sand in cement concrete, which comes into direct contact with the tyre rubber at the molecular level, providing adhesion [5]. It results from the mineral composition of the aggregate and the roughness of the aggregate grains themselves [6]. Microtexture is important for pavement friction on both wet and dry pavements, at all travel speeds, as it enables vehicles to manoeuvre and stop properly [5]. The parts of the pavement surface that come into contact with tyres become polished due to traffic action, so it is precisely the microtexture of the exposed aggregate surface in contact with the tyre that affects friction [7]. Depressions, i.e. the lower parts of the texture, are not exposed to polishing, so their contribution to the overall microtexture should not be taken into account when predicting friction [7]. Microtexture is most often not measured directly, but is instead assessed indirectly through skid resistance. In Serbia, the standard SRPS U.C4.018 was previously used to test the skid resistance of the wearing course of pavement structures. However, this standard was withdrawn in 2021, and the European standard SRPS EN 13036-4:2012, which defines the pendulum test method, is now applied for testing surface skid resistance.

Macrotexture represents larger-scale texture, from 0.5 mm to 50 mm, which forms on the pavement surface due to the presence of individual aggregate grains in the surface layer or due to grooves cut into the pavement surface [5]. It provides drainage channels through which water is expelled from the contact zone between the tyre and the pavement, thereby enabling better contact between the tyre and the pavement surface, increasing friction resistance and reducing the likelihood of hydroplaning, especially at higher speeds [5]. Unlike microtexture, macrotexture can be measured more directly. In modern practice it is determined profilometrically using laser devices, yielding the Mean Profile Depth – MPD. Macrotexture testing is carried out using the standard SRPS EN ISO 13473-1, which describes several methods for macrotexture testing, one of which is the CTM (Circular Texture Meter) method.

## 4. ANALYSIS OF PAVEMENT SURFACE CONDITION ON SECTION IIA-117 NOVI BEČEJ – BANATSKO KARAĐORĐEVO

On the analysed section, with a starting station of 0+000 km and an ending station of 35+754 km, field investigations were carried out to provide indicators of pavement condition. Particular attention was paid to the mean profile depth, i.e. the MPD indicator, which is used as the primary indicator of pavement surface macrotexture. In addition, other parameters were also considered on the same section, such as:

- IRI (International Roughness Index): the international pavement roughness index

Deviation from an ideally flat surface, with characteristic wavelength values that affect vehicle oscillations and ride comfort [8].

- Rutting: permanent longitudinal deformations

The occurrence of unevenness on the pavement surface due to the accumulation of permanent deformations under repeated loading [9].

### 4.1. MPD MEASUREMENT METHODOLOGY

MPD (Mean Profile Depth) is an indicator of pavement surface macrotexture. It is determined on the basis of the pavement surface, whereby the vertical deviation of the surface relative to the mean profile line is recorded. The measurement values for the tested section were obtained using mobile measuring equipment CFT – Continuous Friction Test, i.e. a towed measuring system that moves along the analysed road section during testing.




*Figure 3 CFT equipment*

The CFT is a device mounted on a trailer, which is connected to an appropriate towing vehicle and enables measurement of the pavement surface friction coefficient through continuous recording of friction and measurement of the side force, with the aim of reducing the risk of traffic accidents [10]. The device consists of a measuring trailer, an electronic control unit, a laptop computer and software. The trailer-type measuring equipment moves forward, towed by the corresponding vehicle. By sliding the test wheels — fitted with special smooth (non-treaded) tyres and set at a specific angle — a side force perpendicular to the direction of travel is generated. High-precision sensors measure and transmit the data to computer software for processing, after which tables and position curves on the pavement surface, as well as the friction coefficient, are displayed to users [10]. Although the original function of this device is to measure the friction coefficient via the side force, the measuring system is also equipped with a laser profilometer for determining pavement surface macrotexture, from which the MPD data for the tested section were obtained. As it moves, the laser sensor records the surface profile along the wheel paths, and the MPD is then calculated from the measured profiles through further software processing.

### 4.2. RESULTS OF MEASUREMENTS ON SECTION IIA-117 NOVI BEČEJ – BANATSKO KARAĐORĐEVO

Measurement of the MPD for the aforementioned section was carried out from the starting station 0+000 km to station 35+754 km. In this paper, due to the large volume

of data, the measurement results from station 0+000 km to station 1+000 km are presented for the left and right lanes.

*Tab. 1 Mean Profile Depth (MPD) values by measurement segment – right lane*

| ROAD | PKOD | SKOD | From | To | SZMERT | SZEK | SZEV | MPDL | MPDR | MPDmax |
|---|---|---|---|---|---|---|---|---|---|---|
| IIA-117 | 0 | 1 | 0+000 | 35+754 | 35755 | 0 | 25 | 0.85 | 0.83 | **0.85** |
| IIA-117 | 0 | 1 | 0+000 | 35+754 | 35755 | 25 | 50 | 0.78 | 0.81 | **0.81** |
| IIA-117 | 0 | 1 | 0+000 | 35+754 | 35755 | 50 | 75 | 0.79 | 0.75 | **0.79** |
| IIA-117 | 0 | 1 | 0+000 | 35+754 | 35755 | 75 | 100 | 1.32 | 1.26 | **1.32** |
| IIA-117 | 0 | 1 | 0+000 | 35+754 | 35755 | 100 | 125 | 1.08 | 1.25 | **1.25** |
| IIA-117 | 0 | 1 | 0+000 | 35+754 | 35755 | 125 | 150 | 1.15 | 1.17 | **1.17** |
| IIA-117 | 0 | 1 | 0+000 | 35+754 | 35755 | 150 | 175 | 1.08 | 1.14 | **1.14** |
| IIA-117 | 0 | 1 | 0+000 | 35+754 | 35755 | 175 | 200 | 1.19 | 1.56 | **1.56** |
| IIA-117 | 0 | 1 | 0+000 | 35+754 | 35755 | 200 | 225 | 1.09 | 1.09 | **1.09** |
| IIA-117 | 0 | 1 | 0+000 | 35+754 | 35755 | 225 | 250 | 1.07 | 1.21 | **1.21** |
| IIA-117 | 0 | 1 | 0+000 | 35+754 | 35755 | 250 | 275 | 1.15 | 1.26 | **1.26** |
| IIA-117 | 0 | 1 | 0+000 | 35+754 | 35755 | 275 | 300 | 1.02 | 1.35 | **1.35** |
| IIA-117 | 0 | 1 | 0+000 | 35+754 | 35755 | 300 | 325 | 1.05 | 1.13 | **1.13** |
| IIA-117 | 0 | 1 | 0+000 | 35+754 | 35755 | 325 | 350 | 1.03 | 1.14 | **1.14** |
| IIA-117 | 0 | 1 | 0+000 | 35+754 | 35755 | 350 | 375 | 1.10 | 1.41 | **1.41** |
| IIA-117 | 0 | 1 | 0+000 | 35+754 | 35755 | 375 | 400 | 1.26 | 1.03 | **1.26** |
| IIA-117 | 0 | 1 | 0+000 | 35+754 | 35755 | 400 | 425 | 0.99 | 0.84 | **0.99** |
| IIA-117 | 0 | 1 | 0+000 | 35+754 | 35755 | 425 | 450 | 1.08 | 1.25 | **1.25** |
| IIA-117 | 0 | 1 | 0+000 | 35+754 | 35755 | 450 | 475 | 1.12 | 1.06 | **1.12** |
| IIA-117 | 0 | 1 | 0+000 | 35+754 | 35755 | 475 | 500 | 0.86 | 1.24 | **1.24** |
| IIA-117 | 0 | 1 | 0+000 | 35+754 | 35755 | 500 | 525 | 0.95 | 1.02 | **1.02** |
| IIA-117 | 0 | 1 | 0+000 | 35+754 | 35755 | 525 | 550 | 1.07 | 1.26 | **1.26** |
| IIA-117 | 0 | 1 | 0+000 | 35+754 | 35755 | 550 | 575 | 1.07 | 1.39 | **1.39** |
| IIA-117 | 0 | 1 | 0+000 | 35+754 | 35755 | 575 | 600 | 0.92 | 0.91 | **0.92** |
| IIA-117 | 0 | 1 | 0+000 | 35+754 | 35755 | 600 | 625 | 1.21 | 0.91 | **1.21** |
| IIA-117 | 0 | 1 | 0+000 | 35+754 | 35755 | 625 | 650 | 1.05 | 0.91 | **1.05** |
| IIA-117 | 0 | 1 | 0+000 | 35+754 | 35755 | 650 | 675 | 1.12 | 1.04 | **1.12** |
| IIA-117 | 0 | 1 | 0+000 | 35+754 | 35755 | 675 | 700 | 1.18 | 0.93 | **1.18** |
| IIA-117 | 0 | 1 | 0+000 | 35+754 | 35755 | 700 | 725 | 1.08 | 1.04 | **1.08** |
| IIA-117 | 0 | 1 | 0+000 | 35+754 | 35755 | 725 | 750 | 1.20 | 1.22 | **1.22** |
| IIA-117 | 0 | 1 | 0+000 | 35+754 | 35755 | 750 | 775 | 0.94 | 0.90 | **0.94** |
| IIA-117 | 0 | 1 | 0+000 | 35+754 | 35755 | 775 | 800 | 1.00 | 0.91 | **1.00** |
| IIA-117 | 0 | 1 | 0+000 | 35+754 | 35755 | 800 | 825 | 1.03 | 0.89 | **1.03** |
| IIA-117 | 0 | 1 | 0+000 | 35+754 | 35755 | 825 | 850 | 1.20 | 1.23 | **1.23** |
| IIA-117 | 0 | 1 | 0+000 | 35+754 | 35755 | 850 | 875 | 1.31 | 1.43 | **1.43** |
| IIA-117 | 0 | 1 | 0+000 | 35+754 | 35755 | 875 | 900 | 1.36 | 1.54 | **1.54** |
| IIA-117 | 0 | 1 | 0+000 | 35+754 | 35755 | 900 | 925 | 1.36 | 1.61 | **1.61** |
| IIA-117 | 0 | 1 | 0+000 | 35+754 | 35755 | 925 | 950 | 1.39 | 1.65 | **1.65** |
| IIA-117 | 0 | 1 | 0+000 | 35+754 | 35755 | 950 | 975 | 1.45 | 1.68 | **1.68** |
| IIA-117 | 0 | 1 | 0+000 | 35+754 | 35755 | 975 | 1000 | 1.31 | 1.29 | **1.31** |

*Tab. 2 Mean Profile Depth (MPD) values by measurement segment – left lane*

| ROAD | PKOD | SKOD | From | To | SZMERT | SZEK | SZEV | MPDL | MPDR | MPDmax |
|---|---|---|---|---|---|---|---|---|---|---|
| IIA-117 | 0 | 2 | 35+754 | 0+000 | 35755 | 0 | 25 | 0.84 | 0.81 | **0.84** |
| IIA-117 | 0 | 2 | 35+754 | 0+000 | 35755 | 25 | 50 | 0.92 | 0.93 | **0.93** |
| IIA-117 | 0 | 2 | 35+754 | 0+000 | 35755 | 50 | 75 | 0.72 | 0.75 | **0.75** |
| IIA-117 | 0 | 2 | 35+754 | 0+000 | 35755 | 75 | 100 | 0.74 | 1.02 | **1.02** |
| IIA-117 | 0 | 2 | 35+754 | 0+000 | 35755 | 100 | 125 | 1.15 | 1.57 | **1.57** |

| | | | | | | | | | | |
|---|---|---|---|---|---|---|---|---|---|---|
| IIA-117 | 0 | 2 | 35+754 | 0+000 | 35755 | 125 | 150 | 1.35 | 1.17 | **1.35** |
| IIA-117 | 0 | 2 | 35+754 | 0+000 | 35755 | 150 | 175 | 1.55 | 1.22 | **1.55** |
| IIA-117 | 0 | 2 | 35+754 | 0+000 | 35755 | 175 | 200 | 1.53 | 1.58 | **1.58** |
| IIA-117 | 0 | 2 | 35+754 | 0+000 | 35755 | 200 | 225 | 1.57 | 1.77 | **1.77** |
| IIA-117 | 0 | 2 | 35+754 | 0+000 | 35755 | 225 | 250 | 1.66 | 1.93 | **1.93** |
| IIA-117 | 0 | 2 | 35+754 | 0+000 | 35755 | 250 | 275 | 1.60 | 1.85 | **1.85** |
| IIA-117 | 0 | 2 | 35+754 | 0+000 | 35755 | 275 | 300 | 1.39 | 1.58 | **1.58** |
| IIA-117 | 0 | 2 | 35+754 | 0+000 | 35755 | 300 | 325 | 1.29 | 1.33 | **1.33** |
| IIA-117 | 0 | 2 | 35+754 | 0+000 | 35755 | 325 | 350 | 1.64 | 1.71 | **1.71** |
| IIA-117 | 0 | 2 | 35+754 | 0+000 | 35755 | 350 | 375 | 1.57 | 1.56 | **1.57** |
| IIA-117 | 0 | 2 | 35+754 | 0+000 | 35755 | 375 | 400 | 1.29 | 1.25 | **1.29** |
| IIA-117 | 0 | 2 | 35+754 | 0+000 | 35755 | 400 | 425 | 1.26 | 1.16 | **1.26** |
| IIA-117 | 0 | 2 | 35+754 | 0+000 | 35755 | 425 | 450 | 1.29 | 1.19 | **1.29** |
| IIA-117 | 0 | 2 | 35+754 | 0+000 | 35755 | 450 | 475 | 1.17 | 1.15 | **1.17** |
| IIA-117 | 0 | 2 | 35+754 | 0+000 | 35755 | 475 | 500 | 1.22 | 1.21 | **1.22** |
| IIA-117 | 0 | 2 | 35+754 | 0+000 | 35755 | 500 | 525 | 1.20 | 0.99 | **1.20** |
| IIA-117 | 0 | 2 | 35+754 | 0+000 | 35755 | 525 | 550 | 1.44 | 1.18 | **1.44** |
| IIA-117 | 0 | 2 | 35+754 | 0+000 | 35755 | 550 | 575 | 1.46 | 1.26 | **1.46** |
| IIA-117 | 0 | 2 | 35+754 | 0+000 | 35755 | 575 | 600 | 1.19 | 1.20 | **1.20** |
| IIA-117 | 0 | 2 | 35+754 | 0+000 | 35755 | 600 | 625 | 0.98 | 1.03 | **1.03** |
| IIA-117 | 0 | 2 | 35+754 | 0+000 | 35755 | 625 | 650 | 1.12 | 1.01 | **1.12** |
| IIA-117 | 0 | 2 | 35+754 | 0+000 | 35755 | 650 | 675 | 1.18 | 0.88 | **1.18** |
| IIA-117 | 0 | 2 | 35+754 | 0+000 | 35755 | 675 | 700 | 1.25 | 0.97 | **1.25** |
| IIA-117 | 0 | 2 | 35+754 | 0+000 | 35755 | 700 | 725 | 1.22 | 0.86 | **1.22** |
| IIA-117 | 0 | 2 | 35+754 | 0+000 | 35755 | 725 | 750 | 1.18 | 0.98 | **1.18** |
| IIA-117 | 0 | 2 | 35+754 | 0+000 | 35755 | 750 | 775 | 1.33 | 0.89 | **1.33** |
| IIA-117 | 0 | 2 | 35+754 | 0+000 | 35755 | 775 | 800 | 1.04 | 0.77 | **1.04** |
| IIA-117 | 0 | 2 | 35+754 | 0+000 | 35755 | 800 | 825 | 1.14 | 0.87 | **1.14** |
| IIA-117 | 0 | 2 | 35+754 | 0+000 | 35755 | 825 | 850 | 0.97 | 0.83 | **0.97** |
| IIA-117 | 0 | 2 | 35+754 | 0+000 | 35755 | 850 | 875 | 1.00 | 0.81 | **1.00** |
| IIA-117 | 0 | 2 | 35+754 | 0+000 | 35755 | 875 | 900 | 1.00 | 0.87 | **1.00** |
| IIA-117 | 0 | 2 | 35+754 | 0+000 | 35755 | 900 | 925 | 0.99 | 0.72 | **0.99** |
| IIA-117 | 0 | 2 | 35+754 | 0+000 | 35755 | 925 | 950 | 0.95 | 0.77 | **0.95** |
| IIA-117 | 0 | 2 | 35+754 | 0+000 | 35755 | 950 | 975 | 1.25 | 0.84 | **1.25** |
| IIA-117 | 0 | 2 | 35+754 | 0+000 | 35755 | 975 | 1000 | 1.33 | 0.87 | **1.33** |

The measured MPD values are not used solely for individual assessment of pavement surface macrotexture; based on the measured values, homogeneous sections can also be formed, allowing the pavement surface to be analysed not only through individual measurements but also through spatially connected units with similar behaviour.

After the raw MPD value database was created, the data were processed in order to analyse the variation of macrotexture along the route and to identify homogeneous sections. Sections with approximately similar MPD values indicate a similar composition, structure and condition of the wearing course, while sudden changes in MPD values indicated a change in the type of pavement surfacing, a different degree of

wear, aggregate polishing, subsequent repairs, surface contamination, or other local texture changes.




*Figure 4 Macrotexture diagram (mm) – right lane*




*Figure 5 Macrotexture diagram (mm) – left lane*

## 5. ANALYSIS OF THE OBTAINED RESULTS

The MPD values on the first kilometre of the analysed section are not fully uniform across all segments. These variations may result from differing conditions of the wearing course, local wear, changes in surface structure, or previous interventions on the pavement.

Measurements of the section were carried out in 25 m long segments. Each row in the table represents one segment of the route for which the values of MPDL (mean profile depth at the left wheel path), MPDR (mean profile depth at the right wheel path) and

MPDmax (the more pronounced macrotexture value at either of the two wheel paths) were determined.

### 5.1. ANALYSIS OF THE OBTAINED RESULTS – RIGHT LANE

On the first kilometre of the analysed section, MPD values are lower, around 0.8 mm. These values indicate a more closed microtexture. In these zones, a weaker ability of the surface to expel water from the contact zone can be expected. This does not immediately indicate that the friction coefficient is low, but it can be concluded that, under wet pavement conditions, these segments would be less favourable in terms of available friction, particularly at higher speeds. Further along, MPD values generally increase, and in some segments exceed 1.5 mm. These values indicate a more open and pronounced macrotexture, which enables more efficient drainage and more favourable conditions for the development of friction on a wet pavement surface.

### 5.2. ANALYSIS OF THE OBTAINED RESULTS – LEFT LANE

The MPD values for the left lane range from 0.75 to 0.93 mm in the initial segments. This is followed by a sharp increase, with the highest values, reaching around 1.9 mm, occurring in the zone from approximately 0.2 to 0.28 km. Such values indicate a distinctly open pavement surface macrotexture. In the second half of the first kilometre, the MPD values gradually decrease and generally range from around 1.0 to 1.3 mm, indicating a moderately developed macrotexture, which can still have a positive effect on drainage of the contact zone but is less pronounced than in the zone of the local maximum in the first third of the analysed kilometre.

## 6. CONCLUSION

Based on the analysis of the measurement results, it can be concluded that both lanes have a well-developed macrotexture. The MPD values for the right lane increase gradually, while for the left lane there is a local maximum in the first third of the analysed kilometre.

If the same values are considered from the perspective of friction, segments with higher MPD values indicate a more open macrotexture and are considered more favourable under wet pavement conditions, as they enable better expulsion of water from the contact zone and thus provide better conditions for developing friction between the tyre

and the pavement. Segments with lower MPD values represent zones with a more closed microtexture, and these are the segments that require additional testing and measurement of the friction coefficient.

MPD values do not directly indicate the value of the friction coefficient. A final assessment of skid resistance requires direct measurement of the skid resistance coefficient.

## REFERENCES

[1] Nešić L., Prokić V. (2013). *Friction Force – From Fundamental Processes to Macroscopic Laws*. Online source, accessed 15 June 2026.
https://tesla.pmf.ni.ac.rs/people/nesiclj/predavanja/seminari/trenje-tekst2013.pdf

[2] Rajamani R. (2012). *Vehicle Dynamics and Control*. Springer, New York, USA..

[3] National Academies of Sciences, Engineering, and Medicine (2009). *Guide for Pavement Friction*. The National Academies Press, Washington, DC, USA..

[4] Liu B., Wang J., Zhao S., Qu C., Liu Y., Ma L., Zhang Z., Liu K., Zheng Q., Ma M. (2020). *Negative friction coefficient in microscale graphite/mica layered heterojunctions*. Science

Advances, Volume 6, Issue 16, Article eaaz6787. https://www.science.org/doi/10.1126/sciadv.aaz6787

[5] Tobias P., de León Izeppi E., Flintsch G., Katicha S., McCarthy R. (2023). Pavement Friction for Road Safety: Primer on Friction Measurement and Management Methods. Federal Highway Administration, Office of Safety, Washington, DC, USA

[6] Pranjić I., Deluka-Tibljaš A., Cuculić M., Šurdonja S. (2020). Influence of pavement surface macrotexture on pavement skid resistance. Transportation Research Procedia, Volume 45, pp. 747–754. https://doi.org/10.1016/j.trpro.2020.02.102

[7] Henry J. J. (2000). *Evaluation of Pavement Friction Characteristics. NCHRP Synthesis of Highway Practice 291*, Transportation Research Board, National Research Council, Washington, DC, USA.

[8] Mladenović G. (2024). *Recording the Functional Characteristics of Pavement Structure Surfaces: The Cumulative Difference Method*. Faculty of Civil Engineering, University of Belgrade, Belgrade, Serbia.

[9] Matić B. (n.d.). *Pavement Structures: Lecture Notes*. Faculty of Technical Sciences, University of Novi Sad, Novi Sad, Serbia.

[10] Tianpeng Instrument Manufacturing Co. (n.d.). *Continuous Friction Tester TPCFT-2*. https://www.testmould.com/test_on_site/continuous-friction-tester-tpcft-2, accessed 27 June 2026.

https://doi.org/10.24867/INDIS-2026-EN-451



# COMPARATIVE ANALYSIS OF MAIN TRUSS GIRDER CONFIGURATIONS FOR THE ROOF OF A LONG-SPAN SPORTS HALL

*Nikola Marjanović[1], Jelena Mirjanić[2], Aleksandra Radujković[3]*

***Summary:***

This paper investigates the optimisation of the previously designed main girder of a long-span sports hall in Subotica, Serbia, through the development and numerical analysis of alternative configurations of the main truss girder with a span of 65 m. Starting from the original truss girder, five alternative configurations were developed to assess the potential for reducing steel consumption while maintaining adequate load-bearing capacity and satisfying serviceability requirements. The numerical models were analysed for the ultimate and serviceability limit states, considering internal forces, cross-sectional utilisation ratios, deflections and steel mass. The results reveal significant differences in the structural efficiency of the proposed configurations and demonstrate that optimising an existing long-span roof structure through the systematic evaluation of alternative truss girder configurations can improve material efficiency while accounting for structural performance and architectural constraints.

*Keywords: truss girder, optimization, steel, long-span*

# UPOREDNA ANALIZA KONFIGURACIJA REŠETKASTIH GLAVNIH NOSAČA KROVA SPORTSKE HALE VELIKOG RASPONA

***Rezime:***

U radu se razmatra optimizacija prethodno projektovanog glavnog nosača sportske hale velikog raspona u Subotici kroz razvoj i numeričku analizu alternativnih konfiguracija glavnog rešetkastog nosača raspona 65 m. Polazeći od originalnog rešetkastog nosača, razvijeno je pet alternativnih konfiguracija kako bi se ispitao potencijal za smanjenje utroška čelika uz očuvanje odgovarajućih nosivih karakteristika i ispunjavanje zahteva upotrebljivosti. Numerički modeli analizirani su u graničnim stanjima nosivosti i upotrebljivosti, uz razmatranje unutrašnjih sila, stepena iskorišćenosti poprečnih preseka, deformacija i mase čelika. Rezultati pokazuju značajne razlike u konstruktivnoj efikasnosti predloženih konfiguracija, te da se optimizacijom postojeće krovne konstrukcije velikog raspona, zasnovanom na sistematskom ispitivanju alternativnih konfiguracija rešetkastih nosača, može postići efikasnija upotreba materijala uz istovremeno uvažavanje konstruktivnih performansi i arhitektonskih ograničenja.

*Ključne reči: rešetkasti nosač, optimizacija, čelik, veliki raspon*

[1] M.Sc. Student, Faculty of Technical Sciences, University of Novi Sad, Novi Sad, Serbia, marjanovic.g16.2025@uns.ac.rs
[2] Teach. Asst., Faculty of Technical Sciences, University of Novi Sad, Novi Sad, Serbia, jelena.mirjanic@uns.ac.rs, ORCID 0009-0006-6608-056X
[3] Assoc. Prof., Faculty of Technical Sciences, University of Novi Sad, Novi Sad, Serbia, leksa@uns.ac.rs, ORCID 0000-0003-4863-4486

## 1. INTRODUCTION

Truss girders represent efficient and rational engineering solutions for carrying loads across large spans, as solid-web girders become increasingly heavy and uneconomical under comparable conditions. Owing to the flexibility in terms of their structural form, number of chords, and web member configuration, truss girders are widely used in various types of structures, including industrial halls, bridges, and large-span sports and convention halls, where architectural requirements are often closely integrated with structural efficiency.

However, selecting a specific truss configuration is not a simple matter. The number of chords (two-, three-, or four-chord systems), the shape of chord members (straight or parabolic), and truss depth directly affect the distribution of internal forces, deflections and material consumption. Different combinations of these parameters can lead to significantly different solutions to the same structural problem, while selecting the most favourable configuration in practice involves a compromise between load-bearing capacity, serviceability, economic efficiency, and architectural requirements.

As a case study, this paper considers the main truss girder of a sports hall in Subotica, with a span of 65 m. The original conceptual design of the sports hall features a four-chord space truss girder with horizontal chord members [1]. The aim of this study is to analyse and compare alternative configurations of the main truss girder with respect to material consumption and deflections to identify the most suitable solution.

## 2. ANALYSIS OF TRUSS SHAPE BEHAVIOUR FOR MODEL SELECTION

Prior to the design of the main roof truss girder, a preliminary numerical study was conducted to examine how truss geometry and depth influence the distribution of internal forces and deformations under a uniformly distributed load. Three representative truss types were analysed:

- Model A: Pratt truss - a combination of vertical and diagonal members, with tension diagonals oriented towards the mid-span and compression verticals; the chords are parallel;
- Model B: Warren truss - diagonal members arranged in a zigzag pattern, alternately subjected to tension and compression; the truss is inherently stable through full triangulation;
- Model C: parabolic truss - the top chord follows a parabolic curve.

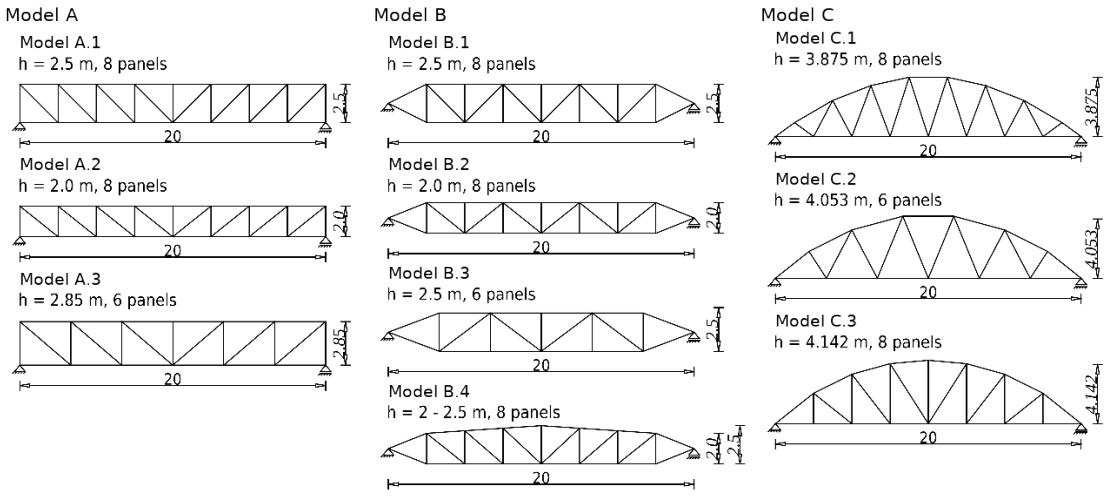


*Fig. 1 Truss girder models*

Each type was modelled in several variants, differing in depth and in the number and arrangement of web panels, resulting in a total of ten preliminary models (Fig. 1). Structural steel S355 was adopted as the material, with circular hollow sections: Ø 82.5 × 5.0 for the chord members and Ø 63.5 × 4.5 for the web members. The span of all models was fixed at L = 20 m to replicate the conditions of the main design problem, with a simply supported static system. A uniformly distributed line load of q = 8 kN/m was considered. In accordance with the principle that truss girders should be loaded at the nodes so that the members are subjected exclusively to axial forces, load was converted to concentrated nodal loads. The preliminary numerical analyses were carried out using the AxisVM X6 software [2]. The results are summarised in Tab. 1, where $S_{min}$ and $S_{max}$ are the minimum and maximum normal stresses in the members, and $e_z$ and $e_x$ are the maximum nodal displacements in the global Z and X directions, respectively, as obtained in AxisVM.

*Tab. 1 Overview of stress and deflection values for all models*

| Model | | h [m] | Panel length [m] | $S_{min}$ [N/mm$^2$] | $S_{max}$ [N/mm$^2$] | $e_z$ [mm] | $e_x$ [mm] |
|---|---|---|---|---|---|---|---|
| A | A.1 | 2.5 | 2.5 | -131.60 | 123.37 | -31.25 | -31.25 |
| | A.2 | 2.0 | 2.5 | -240.09 | 225.08 | -58.710 | -58.710 |
| | A.3 | 2.85 | 3.33 | -115.14 | 122.96 | -26.995 | -26.994 |
| B | B.1 | 2.5 | 2.5 | -131.60 | 123.37 | -26.61 | -26.61 |
| | B.2 | 2.0 | 2.5 | -164.50 | 154.22 | -39.38 | -39.38 |
| | B.3 | 2.5 | 3.33 | -131.58 | 116.96 | -27.58 | -27.58 |
| | B.4 | 2 – 2.5 | 2.5 | -132.48 | 132.19 | -29.64 | -29.64 |
| C | C.1 | 3.875 | 2.5 | -107.57 | 88.12 | -17.08 | -17.11 |
| | C.2 | 4.053 | 3.33 | -92.46 | 79.13 | -14.45 | -14.44 |
| | C.3 | 4.142 | 2.5 | -92.61 | 78.53 | -14.36 | -14.08 |

Based on the analysis of all ten preliminary models, a clear trend of decreasing maximum stresses and deflections with increasing truss depth was observed, consistent with theoretical expectations. Parabolic trusses (Model C) showed particularly favourable structural efficiency, with a more uniform stress distribution and the smallest deflections among all analysed types. This behaviour can be attributed to the fact that the parabolic truss geometry approximately follows the bending moment diagram. The results of the analysis can be summarised as follows:

- an increase in truss depth reduces deflection by approximately 40–50%;
- the most favourable span-to-depth ratio for the analysed models is approximately $L/h \approx 5$;
- the parabolic truss type provides the most favourable balance between stress levels, deflections, and material consumption.

On this basis, the parabolic truss is expected to represent the most rational structural solution for long spans.

# 3. NUMERICAL MODELS

## 3.1. VERIFICATION OF THE INITIAL MODEL

Considered structure represents the roof system of a sports hall in Subotica, consisting of nine main truss girders with a span of L = 65 m. The spacing between the truss girders is defined by two end spans of 9 m and six mid spans, each 10 m wide. The mid truss girders are designed as four-chord space trusses with an overall depth of h = 3.2 m, whereas the end trusses, due to lower loading and a different structural system, are designed as planar trusses with a depth of h = 2.0 m, while retaining the same adopted cross-sections. The depth of the main trusses is limited by the architectural constraints of the building, with the overall clear height of the hall being 14.5 m [1].
The numerical model of the roof structure was developed using the Tower 8 software [3]. The relevant loads were considered in accordance with the applicable parts of Eurocode 1: in addition to the self-weight of the structure, the analysis included an additional permanent load of 1.5 kN/m² and an imposed roof load of 1.5 kN/m² (category H) according to EN 1991-1-1 [4], a snow load of 1.0 kN/m² according to EN 1991-1-3 [5], and wind loads acting in the X and Y directions for the site location in Subotica according to EN 1991-1-4 [6]. The structure was assessed with respect to the ultimate limit states (ULS) and serviceability limit states (SLS) in accordance with EN 1993-1-1 [7], considering the internal forces and the corresponding deformations.

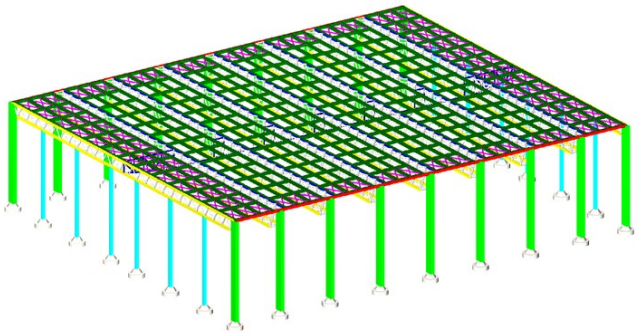

*Fig. 2 Three-dimensional view of the rendered roof structure model, Model 1*

To verify the correctness of the developed numerical model, Model 1 was compared with the baseline reference model (Model 0). Model 1 represents an isolated model of the sports hall roof structure, defined using the same geometric parameters, cross-sections, loads, and input data as the baseline model. This approach enabled the consistency of the structural system modelling, the correct application of loads, and the definition of support conditions simulating the interaction between the roof structure and the remainder of the building to be examined. By comparing the results obtained from both models, the reliability of the developed numerical model was assessed as a prerequisite for further analyses and for evaluating the behaviour of the truss girder.

## 3.2. VARIATIONS OF THE NUMERICAL MODELS

To investigate the influence of different structural configurations on the behaviour of the roof structure, four additional numerical models were developed. The models were compared in terms of internal forces, deformations, and cross-sectional utilisation ratios of the central truss girder, which was selected as the governing member for the analysis due to its position along the axis of symmetry and the governing loading conditions (Fig. 3). The four additional models, together with the baseline model, are presented in Fig. 4. Based on the results obtained, the suitability of each adopted truss type is discussed in the following sections, with the aim of identifying the most favourable structural solution.

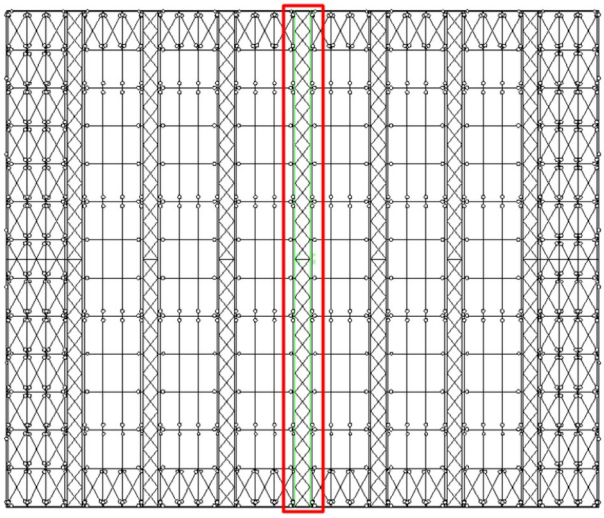

*Fig. 3 Structural Layout of the Analysed Truss Girder*

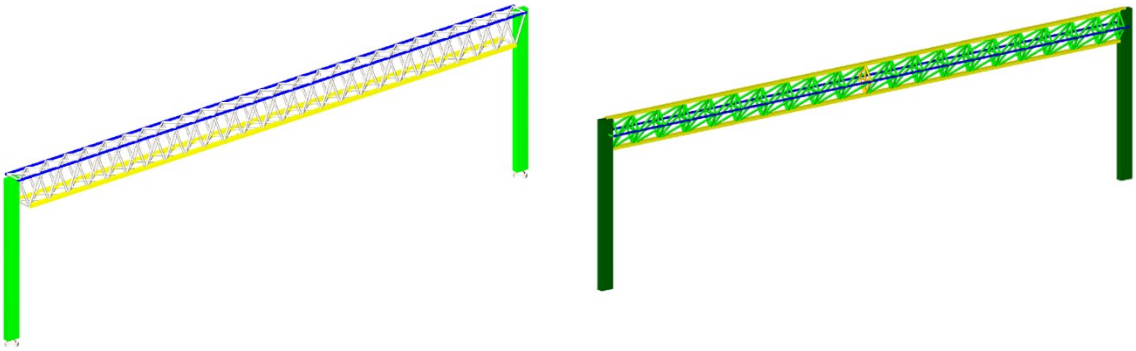

*Model 1 (0)* *Model 2*

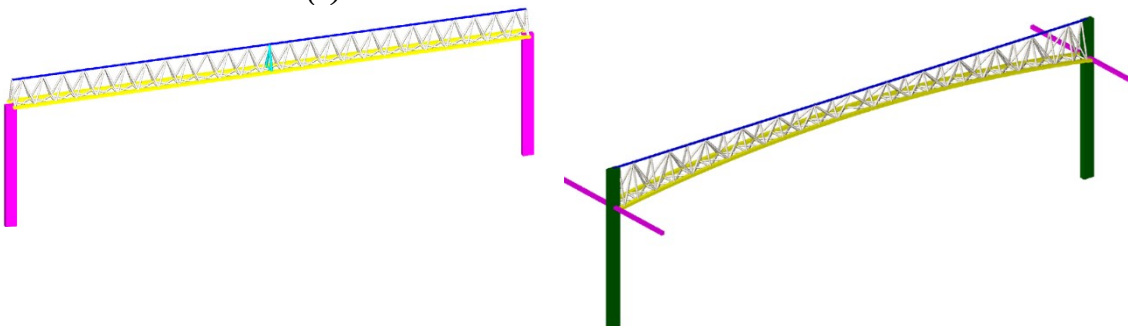

*Model 3* *Model 4*

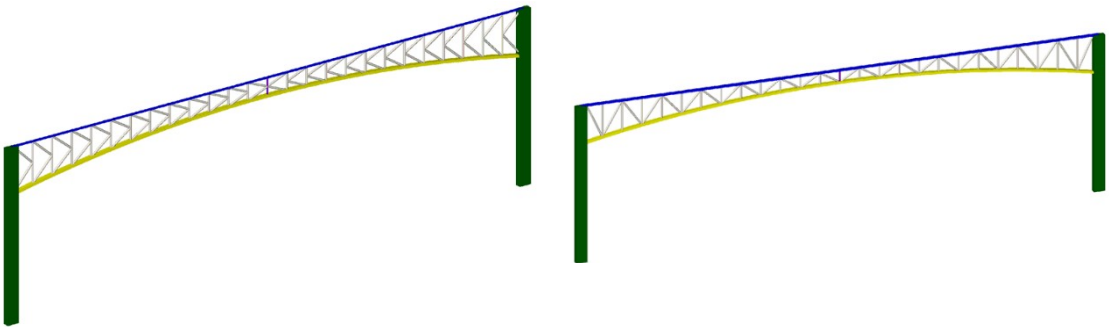

*Model 5* *Model 5.1*

*Fig. 4 Overview of the Numerical Models*

### 3.2.1. Model 1 – Initial Spatial Four-Chord Truss Girder

Model 1 represents the initial configuration of the roof truss girder and serves as the reference for subsequent modifications. The girder is designed as a spatial four-chord truss with horizontal upper and lower chords connected by a system of diagonal, vertical and horizontal web members. The configuration provides spatial stiffness and enables load transfer through the four-chord system. Its geometry, member arrangement and cross-sections establish the baseline for evaluating the effects of alternative truss configurations on structural performance and material consumption.

### 3.2.2. Model 2 – Spatial Four-Chord Rhombic Truss Girder

Model 2 retains the spatial four-chord concept but introduces a rhombic arrangement of the web members. The four main chords are interconnected by diagonal, horizontal and vertical members, providing an alternative load-transfer mechanism compared with Model 1. The revised arrangement aims to improve the distribution of internal forces and reduce the demand on individual members. To limit self-weight, the panel spacing is increased from 2.50 m to 3.25 m, and the cross-sections of selected web members are reduced. The lower chord cross-section is increased from RHS 500 × 300 × 16 to RHS 500 × 300 × 20 to accommodate the tensile forces. The truss has a depth of 3.20 m and a width of 2.00 m at the side-chord planes, with a configuration that is symmetric about the vertical axis. Attention is given to optimising the web members while maintaining adequate stiffness and satisfying strength and deformation requirements.

### 3.2.3. Model 3 – Spatial Three-Chord Truss Girder with Two Tension Chords

Model 3 adopts a spatial three-chord configuration with two lower tension chords and one upper chord, which primarily resists compression. The introduction of a second tension chord increases the available tensile-resisting area and provides an alternative to the four-chord configurations. Compared with Model 2, the arrangement reduces the number of main chords and is intended to achieve a lower self-weight, although with reduced spatial stiffness. The upper chord retains the RHS 250 × 150 × 10 cross-section, while the cross-sections of the lower chords are reduced from RHS 500 × 300 × 16 to RHS 500 × 300 × 12.5. The panel spacing is 2.50 m. The web system comprises diagonal members in the side planes and horizontal and diagonal members in the plane of the two lower chords. The girder is supported through the lower chords, allowing the support arrangement to be adapted to the overall roof system.

### 3.2.4. Model 4 – Spatial Three-Chord Truss Girder with Parabolic Lower Chords

Model 4 is derived from Model 3 by introducing parabolic lower chords to improve the geometric configuration and promote axial force transfer. The parabolic profile has a rise of f = 2.50 m, with the truss depth varying from 4.50 m at the supports to 2.00 m at midspan. This geometry provides greater clear height in the central part of the hall, offering an architectural advantage. The lower chord cross-section is RHS 500 × 300 × 12.5, while the web arrangement follows the concept adopted in Model 3, with diagonal member inclinations adjusted to the variable truss depth. The girder is supported at the columns through the upper chord and at the perimeter beam through the lower chords. Due to the modified geometry and associated stiffness characteristics, the vertical roof bracing requires larger cross-sections to ensure adequate load transfer and stability.

### 3.2.5. Model 5 – Planar Truss Girder with Parabolic Lower Chord

Model 5 introduces a planar two-chord truss with a horizontal upper chord and a parabolic lower chord, providing an alternative to the spatial configurations considered in the previous models. The parabolic rise is f = 3.25 m, while the truss depth varies from 5.25 m at the supports to 2.00 m at midspan. A K-shaped web arrangement is adopted to improve stability in the end panels compared with the initially considered triangular arrangement with vertical members. The girder is supported at the columns through both the upper and lower chords. The lower chord cross-section is increased to RHS 500 × 300 × 20, and the web members have a cross-section of Ø 219.1 × 12.5 mm. The cross-sections of the vertical roof bracing are also increased to provide adequate load-carrying capacity and stability. The planar configuration offers the potential for reduced material consumption; however, the relatively large depth at the supports represents an architectural limitation.

### 3.2.6. Model 5.1 – Modified Planar Truss Girder with Parabolic Lower Chord

Model 5.1 is a modification of Model 5 intended to improve architectural functionality by reducing the truss depth while retaining the parabolic configuration. The parabolic rise remains unchanged at f = 3.25 m, whereas the depth is reduced from 5.25 m to 4.80 m at the supports and from 2.00 m to 1.50 m at midspan. In addition to these geometric modifications, the cold-formed profiles of the main chords are replaced with welded box sections. The lower chord cross-section is changed from RHS 500 × 300 × 16 to 500 × 300 × 25, while the upper chord is changed from RHS 250 × 150 × 10 to 400 × 200 × 8. The web members retain the same cross-sections and arrangement as in Model 5. The modifications aim to achieve a more favourable balance between architectural requirements, structural performance and material consumption.

## 4. ANALYSIS RESULTS AND DISCUSSION

The results for all six models are summarised in Tab. 2 and Tab. 3. Tab. 2 gives the maximum axial force max N (tension positive, compression negative), the utilisation ratio η and the maximum vertical displacement $Z_p$ for the ultimate (ULS) and serviceability (SLS) limit states, and Tab. 3 gives the steel consumption.

*Tab. 2 Comparison of internal forces, utilisation ratios and vertical displacements of the analysed models*

| Model | Member group | max N [kN] | η [–] | ULS: max $Z_p$ [mm] | SLS: max $Z_p$ [mm] |
|---|---|---|---|---|---|
| Model 1 | Upper chord | −1140.12 | 0.61 | −338.95 | −241.63 |
| | Lower chord | 6763.69 | 0.88 | −338.92 | −241.61 |
| | Web members | 1436.93 | 0.68 | – | – |
| Model 2 | Upper chord | −3824.08 | 0.41 | −341.16 | −243.14 |
| | Lower chord | 9557.26 | 1.01 | −341.16 | −243.14 |
| | Web members | 1507.56 | 0.89 | – | – |
| Model 3 | Upper chord | −1529.30 | 0.74 | −403.79 | −287.17 |
| | Lower chord | 6046.00 | 0.98 | −402.16 | −286.62 |
| | Web members | 1441.87 | 0.86 | – | – |

| Model | Member group | max N [kN] | η [–] | ULS: max $Z_p$ [mm] | SLS: max $Z_p$ [mm] |
|---|---|---|---|---|---|
| Model 4 | Upper chord | −2602.53 | 0.87 | −513.37 | −365.53 |
| | Lower chord | 5556.04 | 0.91 | −513.44 | −365.58 |
| | Web members | −1253.00 | 0.97 | – | – |
| Model 5 | Upper chord | −1532.96 | 0.87 | −513.13 | −364.54 |
| | Lower chord | 9553.06 | 1.01 | −513.13 | −364.56 |
| | Web members | −1565.96 | 0.64 | – | – |
| Model 5.1 | Upper chord | −2057.62 | 0.85 | −603.60 | −429.12 |
| | Lower chord | 11684.75 | 0.97 | −603.55 | −429.10 |
| | Web members | −2372.61 | 0.95 | – | – |

Increasing the truss depth considerably reduces the stresses in the members and the deflections. The largest axial forces occur in the lower chords (from 5556.04 kN in Model 4 to 11684.75 kN in Model 5.1). The utilisation ratios range from 0.41 to 1.01; in Models 2 and 5 the lower chord marginally exceeds its resistance (η = 1.01). Since this exceedance is small and could be eliminated by a slightly larger lower chord cross-section without significantly affecting the comparison, it was accepted for the purposes of this comparative analysis.

The largest deflections were obtained for the parabolic girders (Models 4, 5 and 5.1), up to 429.12 mm at SLS in Model 5.1. In these girders the curved lower chord reduces the effective depth towards mid-span, where the bending moments are largest, which lowers the flexural stiffness; in addition, the smaller angles between the web members and the chords increase the axial forces and the elongation of the diagonals. This differs from the preliminary study (Section 2), where the parabolic Model C showed the smallest deflections because its depth was greatest at mid-span (Fig. 1). The deflections of the parabolic girders can be reduced by increasing the depth, adding bracing for spatial stability and optimising the web member angles, while for girders with straight chords a camber is a suitable solution.

*Tab. 3 Steel consumption of the analysed models*

| Model | Material | Consumption [kg/m$^2$] | m [t] |
|---|---|---|---|
| Model 1 | Steel | 110.98 | 1285 |
| Model 2 | Steel | 107.94 | 1170 |
| Model 3 | Steel | 106.27 | 1166 |
| Model 4 | Steel | 106.09 | 1181 |
| Model 5 | Steel | 124.74 | 1090 |
| Model 5.1 | Steel | 130.85 | 1174 |

Model 5 has the lowest total steel mass (1090 t, about 15% less than the initial model) because the required area is considerably smaller, although its consumption per unit area is higher; however, its deflections are pronounced and its large depth above the supports is problematic architecturally. Models 4 and 5.1 are the least economical when material consumption is compared with deflections, owing to the reduced effective depth at mid-span (Model 4) and the changed chord cross-sections (Model 5.1). Models

2 and 3 use about 9% less steel than Model 1 (1170 t and 1166 t). Model 2 has almost identical deflections but large tension in the lower chord and an unfavourable distribution of internal forces, whereas Model 3 has somewhat larger deflections but a favourable distribution of internal forces.
The allowable deflection was adopted as L/250 = 260 mm for the span L = 65 m, in line with usual recommendations for large-span roof girders without brittle finishes or suspended ceilings. Models 1 and 2 satisfy this limit (241.63 mm and 243.14 mm), whereas Model 3 (287.17 mm) and Models 4, 5 and 5.1 do not. For Model 3, the limit is exceeded by 27.17 mm, which could be compensated by a precamber. However, the camber was not designed in this study, so the serviceability verification remains to be carried out.

## 5. CONCLUSION

The comparative analysis showed that the configuration of the main truss girder considerably affects the internal forces, deflections and steel consumption of a long-span roof. Parabolic girders with a reduced depth at mid-span proved to be the most deformable, whereas the planar parabolic girder (Model 5) required the least steel but a large depth above the supports. Model 3, the three-chord truss, offers the best compromise between stiffness, distribution of internal forces and material consumption, reducing steel consumption by about 9% compared with the original design, provided that a camber is designed and the serviceability criteria are verified. Further work should therefore include the camber design and serviceability verification of Model 3, as well as the optimisation of the parabolic configurations with respect to deflections.

### ACKNOWLEDGEMENT

The research has been conducted within the project "Enhancement of teaching and scientific research capacities through the application of modern technologies in the fields of civil engineering, geodesy, and disaster risk management and fire safety", developed at the Department of Civil Engineering and Geodesy, Faculty of Technical Sciences, University of Novi Sad, Serbia.

## REFERENCES

[1] Behance (2023). Hala u Subotici. Behance.net, https://www.behance.net/gallery/196118053/Hala-u-Subotici, accessed on 10 September 2026.

[2] Inter-CAD Kft. (2025). AxisVM X6, User’s Manual. Inter-CAD Kft., Hungary.

[3] Radimpex (2019). Tower 8, Static and dynamic structural analysis software. Radimpex Software, Beograd, Serbia.

[4] CEN (2002). EN 1991-1-1, Eurocode 1: Actions on structures – Part 1-1: General actions – Densities, self-weight, imposed loads for buildings. European Committee for Standardization, Brussels, Belgium.

[5] CEN (2003). EN 1991-1-3, Eurocode 1: Actions on structures – Part 1-3: General actions – Snow loads. European Committee for Standardization, Brussels, Belgium.

[6] CEN (2005). EN 1991-1-4, Eurocode 1: Actions on structures – Part 1-4: General actions – Wind actions. European Committee for Standardization, Brussels, Belgium.

[7] CEN (2005). EN 1993-1-1, Eurocode 3: Design of steel structures – Part 1-1: General rules and rules for buildings, +AC:2009. European Committee for Standardization, Brussels, Belgium.

https://doi.org/10.24867/INDIS-2026-EN-460



# RESEARCH TRENDS IN THE APPLICATION OF ARTIFICIAL INTELLIGENCE FOR CONSTRUCTION COST ESTIMATION

*Dragana Stanojević[1], Vladimir Mučenski[2], Mirjana Terzić[3], Milena Senjak Pejić[4], Jovana Topalić[5],*

***Summary:***

This study is based on a structured literature review incorporating elements of the PRISMA guidelines. The search was conducted in the Web of Science database in July 2026. The aim of the study is to identify trends in scientific publishing, dominant research topics, methodological approaches, and areas of application of artificial intelligence and machine learning in construction cost estimation. The initial search identified 198 publications, and after applying inclusion and exclusion criteria, the final sample comprised 70 papers. The synthesis of results shows that neural networks and deep learning methods are the most prevalent, while total construction cost estimation is the dominant thematic area. Buildings are the most frequently studied category of structures. The analyzed papers indicate that reliable cost estimation requires adequate input data quality, as well as validation of models on independent projects.

*Keywords: literature review, machine learning, construction projects.*

# ISTRAŽIVAČKI TRENDOVI U PRIMENI VEŠTAČKE INTELIGENCIJE ZA PROCENU TROŠKOVA U GRAĐEVINARSTVU

***Rezime:***

Rad je zasnovan na strukturnom pregledu literature sa elementima PRISMA smernica. Pretraga je sprovedena u bazi podataka Web of Science u julu 2026. Cilj rada je identifikacija trendova u objavljivanju naučnih radova, dominantnih istraživačkih tema, metodoloških pristupa i oblasti primene veštačke inteligencije i mašinskog učenja u proceni troškova u građevinarstvu. Početnom pretragom identifikovano je 198 publikacija, dok je nakon primene kriterijuma uključivanja i isključivanja konačni uzorak obuhvatio 70 radova. Sinteza rezultata pokazuje da su neuronske mreže i metode dubokog učenja najzastupljenije, dok je procena ukupnog troška izgradnje dominantna tematska oblast. Zgrade su najčešće proučavana kategorija objekata. Analizirani radovi ukazuju na to da je za pouzdanu procenu troškova potreban adekvatan kvalitet ulaznih podataka, kao i validacija modela na nezavisnim projektima.

*Ključne reči: pregled literature, mašinsko učenje, građevinski projekti.*

[1] Teaching Assistant, Faculty of Technical Science, University of Novi Sad, Novi Sad, Serbia, dragana.stanojevic@uns.ac.rs, ORCID identifier 0000-0003-3471-5656
[2] Asst. Prof. PhD, Faculty of Technical Sciences, University of Novi Sad, Novi Sad, Serbia, mucenskiv@uns.ac.rs, ORCID 0000-0001-9830-4747
[3] Teaching Assistant, Faculty of Technical Science, University of Novi Sad, Novi Sad, Serbia, terzic.mirjana@uns.ac.rs, ORCID 0000-0002-8596-6562
[4] Teaching Assistant, Faculty of Technical Science, University of Novi Sad, Novi Sad, Serbia, senjakm@uns.ac.rs , ORCID 0000-0002-1036-1243
[5] Research Associate, Faculty of Technical Science, University of Novi Sad, Novi Sad, Serbia, jovanatopalic90@uns.ac.rs , ORCID 0000-0001-7854-3257

## 1. INTRODUCTION

Cost estimation is an important foundation for planning, project management, budgeting, and financial performance throughout the entire project life cycle [1], [2], [3]. The cost of constructing a facility depends on its size, purpose and structure, the quality and quantity of materials, location, the market, and various external and internal factors. The complexity of the industry and of the relationships among the elements within this system makes the estimation process difficult. Inaccurate cost estimation can lead to budget overruns and delays [3].

The development of computing technologies has led to the application of advanced artificial intelligence and machine learning methods, which enable pattern recognition and the modeling of nonlinear relationships between project characteristics and costs [4], [3]. Current research includes neural networks, support vector machines, ensembles, and hybrid models. Their development is accompanied by growing attention [1].

The aim of this paper is to, based on a structured review of the scientific literature and using the PRISMA guidelines, search for papers in the Web of Science database and identify publication trends, as well as dominant research topics, methodological approaches, and areas of application of cost estimation in construction using AI tools from 2018 to June 2026. The study analyzes changes in the number of published papers over the observed period, the most frequently used artificial intelligence (AI) and machine learning (ML) methods, the types of cost problems they are used to solve, and the phases of the construction project life cycle in which these models are applied.

## 2. METHODOLOGY

The study is based on a structured literature review with elements of the PRISMA approach. The search was conducted in July 2026. The database used as the search source is Web of Science, using the Topic field. The search was built by combining three groups of keywords; the groups are connected with the AND operator, and the terms within each group are connected with the OR operator. The full query is presented below: TS=(("cost estimation" OR "cost prediction" OR "cost forecasting") AND (construction OR building OR infrastructure) AND ("machine learning" OR "artificial intelligence" OR "neural network" OR "deep learning" OR "random forest" OR "XGBoost")). The keywords are presented in Table 1.

*Tab. 1 Keywords used in the literature search*

| Group | Operator | Keywords |
|---|---|---|
| Cost estimation | OR | "cost estimation", "cost prediction", "cost forecasting" |
| Construction sector | OR | construction, building, infrastructure |
| AI/ML method | OR | "machine learning", "artificial intelligence", "neural network", "deep learning", "random forest", "XGBoost" |

The search covered scientific articles and review papers published in English. The time frame covers the period from 2018 to June 2026. More detailed criteria for the inclusion and exclusion of papers are presented in Table 2.

The initial search yielded 198 publications. Screening of titles and abstracts led to the conclusion that 111 were irrelevant to the research topic, and of the remaining 87, 17

were not available in full text. The final sample comprised 70 papers. The flow of literature selection is shown in Figure 1.

*Tab. 2 Literature selection criteria*

| Type | Criteria |
|---|---|
| Included | Papers published in the period from 2018 to June 2026 |
| | Application of AI/ML methods for cost estimation in construction |
| | Original scientific articles and review papers (Article, Review) published in English |
| | Full text available |
| Excluded | Papers not related to the construction sector |
| | Papers in which AI/ML methods are not applied to cost estimation |
| | Papers that do not meet the criteria for publication type or full-text availability |

Each included paper was analyzed according to its year of publication, the AI method applied, the objective of cost estimation, and the type of construction project. Based on the data obtained, the papers were analyzed and synthesized.

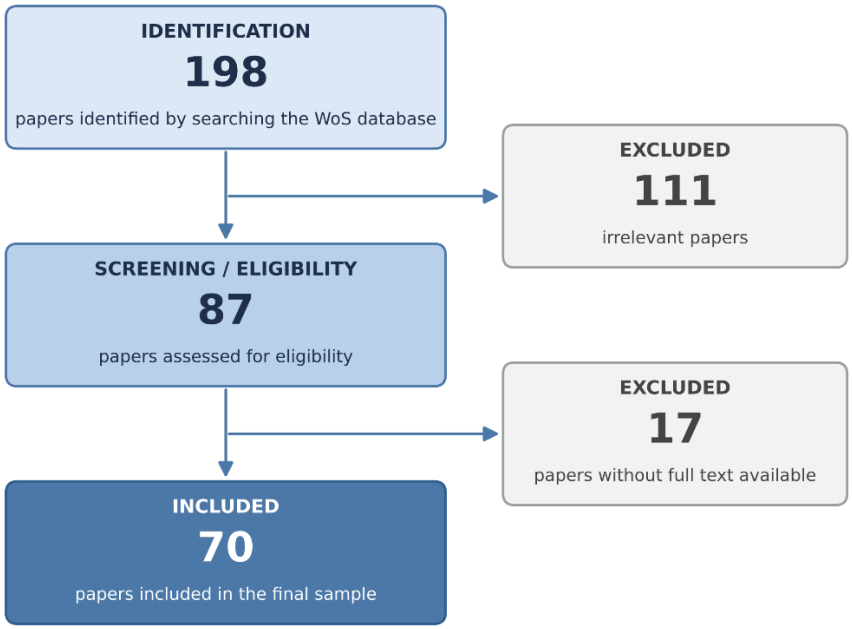


*Fig. 1 Flow of identification, screening, and selection of papers*

## 3. RESULTS

### 3.1. DISTRIBUTION OF STUDIES BY YEAR

The distribution of scientific papers by year is shown in Figure 2. The total number of publications is 70. The largest number of papers was recorded in 2024 (14 papers) and 2025 (20 papers). The data for 2026 should be interpreted with caution, because the search covers papers up to June of that year, and their number is 11.

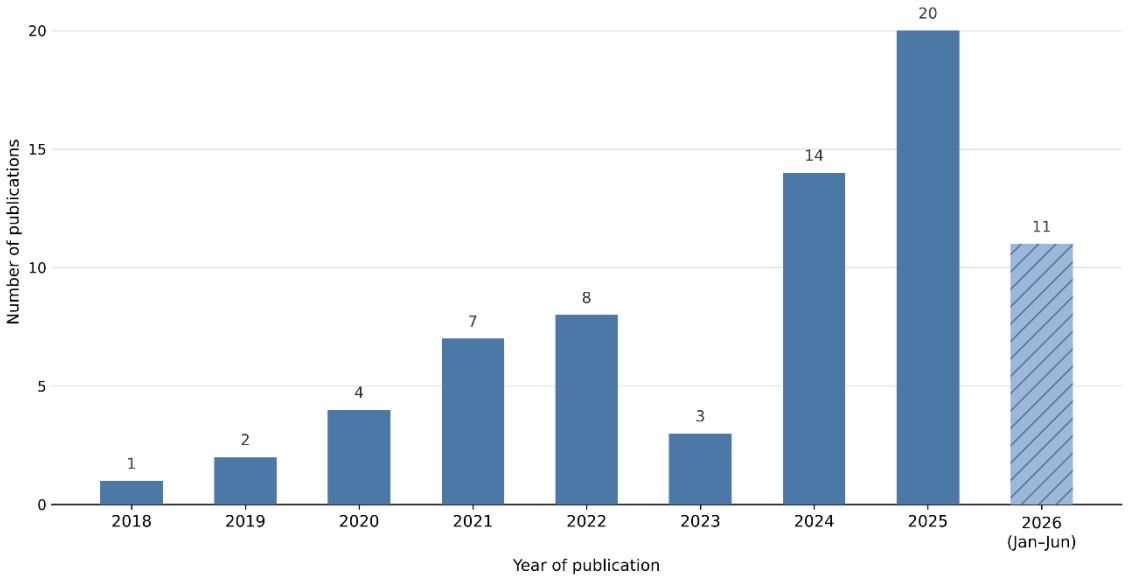


*Fig. 2 Distribution of papers by year*

## 3.2. DISTRIBUTION OF AI/ML METHODS

Each empirical paper was classified into one primary category based on the main proposed model, as can be seen in Table 3. Additionally, it was recorded whether the model is hybrid.

*Tab. 3 Prevalence of primary AI/ML methods in the analyzed papers*

| Primary AI/ML method | Number of papers | Share |
|---|---|---|
| Neural networks and deep learning | 38 | 54.30% |
| Trees and tree ensembles | 6 | 8.60% |
| Ensembles of multiple predictors | 6 | 8.60% |
| SVM/SVR methods | 5 | 7.10% |
| Regression and instance-based models | 2 | 2.90% |
| Large language model (LLM) | 1 | 1.40% |
| **Total** | **58** | **82.90%** |

Note: Percentages are calculated relative to the total sample of 70 papers.

Of the 70 papers analyzed, the primary AI/ML method could be identified in 58 papers, which accounts for 82.9% of the sample. The remaining 12 papers (Other* in Fig. 4) consist of seven review and systematic papers, two comparative papers, and three papers in which the primary method could not be determined.
Among the identified methods, neural networks and deep learning dominate, represented in 38 papers, which accounts for 54.3% of the sample. Trees and tree ensembles, as well as ensembles of multiple predictors, are each represented in six papers (8.6%), while support vector methods (SVM/SVR) appear in five papers (7.1%). It is worth noting that 29 of the 63 empirical papers use hybrid models that combine multiple methods, which indicates the prevalence of more complex approaches in construction cost estimation, as can be seen in Fig. 3.

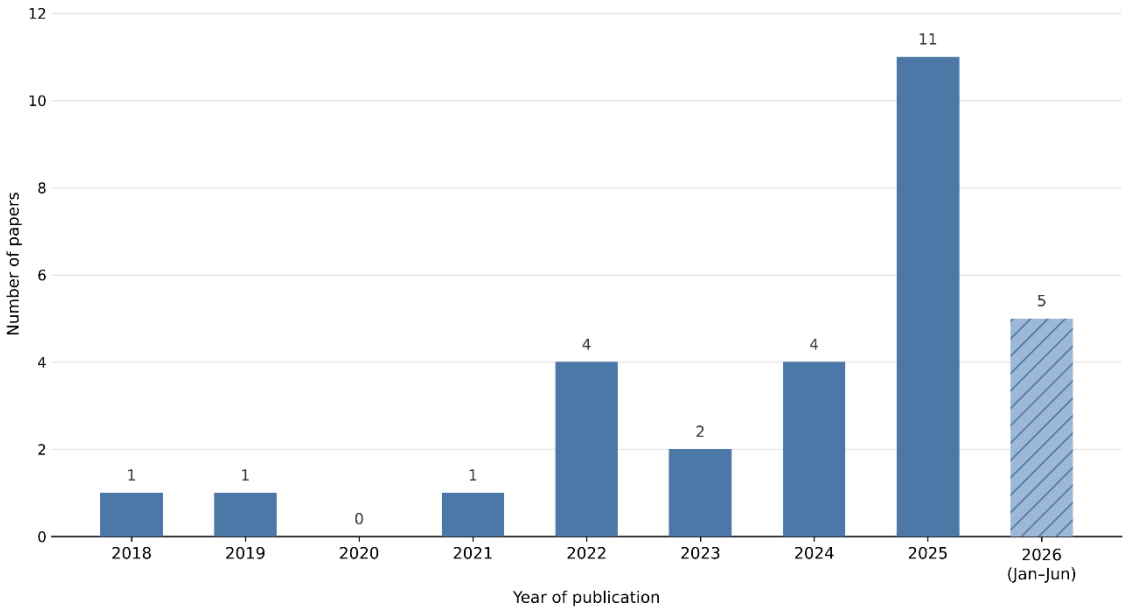


***Fig. 3 Distribution of papers using hybrid models by year of publication***

The analysis of papers by year of publication (Fig. 4) indicates a diversity in the application of AI methods. Before 2022, classical neural networks dominated. Since 2022, ensembles of multiple predictors have appeared. The expansion of hybrid models is most pronounced in the period 2025-2026. In the last two years, approaches that were not previously represented in the analysis have been identified, which points to a broadening of the range of applied methods and hybrid approaches.

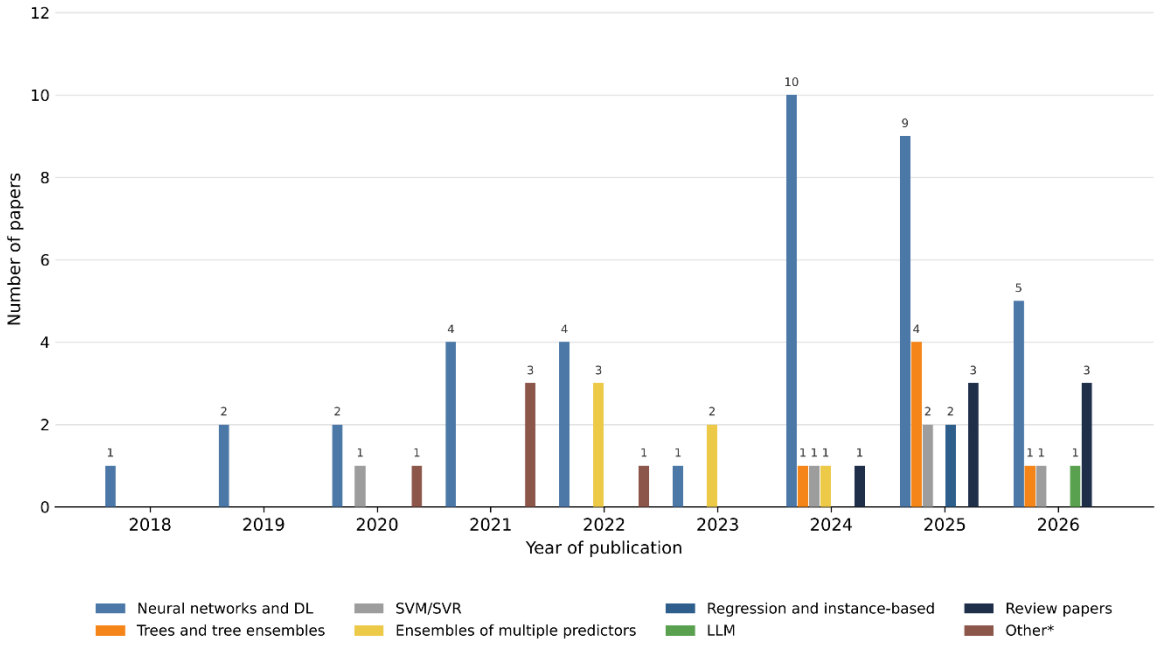


***Fig. 4** Distribution of primary AI/ML methods by publication year*

## 3.3. THEMATIC AREAS OF APPLICATION

The dominant thematic area is the estimation of total construction cost, which relates to the early, conceptual, preliminary, schematic, or detailed phase, as can be seen in Table 4. The share of this area in the overall sample is more than half and amounts to 57.1%.

Next in line is the cost estimation of individual elements, works, or structural systems, with a share of 10%, while five papers (7.1%) deal with the forecasting of construction cost indices.

*Tab. 4 Thematic areas of application of AI/ML methods in cost estimation*

| Thematic area | Number of papers | Share |
|---|---|---|
| Estimation of total construction cost | 40 | 57.10% |
| Estimation of the cost of individual elements, works, or structural systems | 7 | 10.00% |
| Forecasting of construction cost indices (CCI/HCCI) | 5 | 7.10% |
| Review papers (multiple application areas) | 5 | 7.10% |
| Prediction of estimate at completion and estimate to complete (EAC/ETC) | 3 | 4.30% |
| Estimation of final renovation cost | 3 | 4.30% |
| Improvement of data for cost estimation (imputation, augmentation) | 2 | 2.90% |
| Joint estimation of cost and duration | 1 | 1.40% |
| Simultaneous estimation of total and partial costs | 1 | 1.40% |
| Estimation of pre-construction and engineering services costs | 1 | 1.40% |
| Life cycle costs (LCCA) | 1 | 1.40% |
| Cannot be reliably determined | 1 | 1.40% |
| **Total** | **70** | **100%** |

Note: Seven review papers were identified in total. Five of them covered multiple application areas and are classified as ‘Review papers’, the remaining two focused on a single application area and are classified under the corresponding thematic area.

The dominant topic in the period up to 2022 was the early estimation of total cost. Systematic literature reviews become more prominent in 2025 and 2026: six of the seven review papers in total were published in that period.

## 3.4. DISTRIBUTION OF BUILDING TYPES AND PROJECTS

Buildings dominate as a subject of research and account for 58.6% of the sample, with residential buildings being the most represented, at 11 papers (15.7%). Road infrastructure is represented in 7.1% of papers. Other infrastructure facilities, such as bridges, sewerage, and irrigation systems, account for 8.6% of the sample. A separate category consists of papers that do not relate to a specific type of facility but to regional and national construction cost indices, represented in 7.1% of papers, as can be seen in Table 5.

*Tab. 5 Types of facilities and projects in the analyzed papers*

| Type of facility/project | Number of papers | Share |
|---|---|---|
| Residential buildings (new construction) | 11 | 15.70% |
| Buildings of various or unspecified purposes | 7 | 10.00% |
| Mixed building/infrastructure projects | 6 | 8.60% |
| Public/institutional buildings | 5 | 7.10% |
| Roads/highways/pavement rehabilitation | 5 | 7.10% |
| Regional/national index (not tied to a facility) | 5 | 7.10% |
| Reviews (multiple project types) | 5 | 7.10% |
| Green, prefabricated, and other special buildings | 4 | 5.70% |
| Educational institutions (schools) | 3 | 4.30% |
| Residential building renovation | 3 | 4.30% |
| Multi-story buildings, structural floor systems | 3 | 4.30% |
| Foundations and specific building systems (piles, excavation pits, electrical systems) | 3 | 4.30% |
| Bridges | 3 | 4.30% |
| Water, sewerage, and irrigation infrastructure | 3 | 4.30% |
| Office/commercial buildings | 2 | 2.90% |
| Energy facilities | 1 | 1.40% |
| Not specified | 1 | 1.40% |
| **Total** | **70** | **100%** |

Note: Two additional review papers focused on a single project type and are classified under that type.

Cost estimation of residential buildings is dominant in all periods, while papers on specific types of facilities, such as green and prefabricated buildings, are concentrated in 2025 and 2026 in this sample. Research on road infrastructure appears throughout all periods, without significant growth.

## 4. DISCUSSION

The analysis of the sample shows that the largest number of publications was recorded in 2024 and 2025, with a noticeable growth and development of the field and, at the same time, the presence of data availability problems [4]. The analysis cannot support the conclusion that error decreases with the year of publication, or that accuracy

depends solely on the name of the algorithm. Errors are related to data quality, sample size, project phase, the way of testing, and the prediction method itself. It is necessary to know on which projects the model was developed, what information is available to it, and how its ability to estimate new projects was verified [4]. An increasing prevalence of hybrid approaches has been observed, which indicates interest in modeling complex relationships between project characteristics and costs. Model performance depends on data preparation and model tuning, so the most frequently used method is not necessarily the best for all cost estimation tasks [5].

Papers are difficult to compare because they may investigate different tasks and use different data, while input variables change according to the phase and type of project, which further limits comparison [4]. A small overall error can conceal large individual errors, so model performance should be assessed not only on the basis of the overall estimate, but also on the basis of individual categories [6].

Also, more attention should be paid to updating data throughout the entire project life cycle. This means that the estimate should not remain the same while the project changes; rather, the system should be updated when design solutions or the scope of work change. At first, general data on area and purpose are known, then the amount of data grows to include technical characteristics and quantities, and subsequently actual quantities and work progress [4]. It is necessary to examine the applicability of models in everyday practice, which is not the same as performance on data from completed projects [7].

The analysis indicates that model performance depends on the data on which it was developed. Models developed on limited data may give good results within the observed sample, but their applicability to projects with different characteristics remains uncertain. Insufficient testing on independent projects and the limited geographic coverage of the data limit the assessment of their broader applicability [1], [4].

The limitations of this review arise from the use of only one database, the selected keywords, the inclusion of only English-language publications, and papers with available full text. Classifying papers by the applied method, topic, or type of facility further simplifies papers that encompass multiple approaches. For this reason, it should be emphasized that the presented results describe the identified sample and do not represent the entire literature in this field.

## 5. CONCLUSION

This paper presents a structured literature review with elements of the PRISMA guidelines for the period from 2018 to June 2026. The review indicates an increasing application of artificial intelligence and machine learning methods, with an emphasis on neural networks. The sample is dominated by total construction cost estimation and models based on building projects of various purposes. The prevalence of hybrid approaches is significant.

The analyzed papers confirm the possibility of improving cost estimation through model optimization and appropriate data processing, but do not indicate the existence of a single best, universal method. The value of a model depends on its performance on independent projects and its applicability in professional practice.

Further development should not focus only on reducing error, but also on improving the ability of models to successfully estimate the costs of projects that were not used in their development. Also, authors should transparently present the model validation procedure, so that the reader can see how credible the result is. Papers should place greater emphasis on uncertainty estimation, which would indicate the possible deviation from the estimate.

**ACKNOWLEDGEMENT (STYLE: ZAHVALNOST)**

This research has been supported by the Ministry of Science, Technological Development and Innovation (Contract No. 451-03-34/2026-03/200156) and the Faculty of Technical Sciences, University of Novi Sad through project “Scientific and Artistic Research Work of Researchers in Teaching and Associate Positions at the Faculty of Technical Sciences, University of Novi Sad 2026” (No. 01-3609/1).

## REFERENCES

[1] G. Chen, S. Zheng, X. He, X. Liang, and X. Liao, “Machine Learning-Based Cost Estimation Models for Office Buildings,” Buildings, vol. 15, no. 11, p. 1802, May 2025, doi: 10.3390/buildings15111802

[2] X. Ding and Q. Lu, “Construction cost management strategy based on BIM technology and neural network model,” Journal of Intelligent & Fuzzy Systems, vol. 40, no. 4, pp. 6669–6681, Apr. 2021, doi: 10.3233/jifs-189502

[3] Md. M. I. Shamim, A. B. b. A. Hamid, T. E. Nyamasvisva, and N. S. B. Rafi, “Advancement of Artificial Intelligence in Cost Estimation for Project Management Success: A Systematic Review of Machine Learning, Deep Learning, Regression, and Hybrid Models,” Modelling, vol. 6, no. 2, p. 35, Apr. 2025, doi: 10.3390/modelling6020035

[4] E. Sadikoglu and S. Demirkesen, “Mapping the state-of-the-art: bibliometric and systematic analysis of machine learning and AI-based cost and time prediction in construction,” Journal of Asian Architecture and Building Engineering, pp. 1–28, Mar. 2026, doi: 10.1080/13467581.2026.2641274.

[5] R. Wang, H. Salleh, K. Li, and Z. Abdul-Samad, “A conceptual cost estimation model for building construction projects by hybrid Back-Propagation Neural Network and Dung Beetle Optimizer algorithm,” Journal of Asian Architecture and Building Engineering, vol. 24, no. 6, pp. 5520–5542, Dec. 2024, doi: 10.1080/13467581.2024.2445596

[6] P. Jafary, D. Shojaei, A. Rajabifard, and T. Ngo, “AI-augmented construction cost estimation: an ensemble Natural Language Processing (NLP) model to align quantity take-offs with cost indexes,” International Journal of Construction Management, vol. 26, no. 8, pp. 1508–1526, Sep. 2025, doi: 10.1080/15623599.2025.2558070

[7] Y. Gao, M. F. Antwi-Afari, Y. Huang, Z.-S. Chen, and B. Manzoor, “Artificial Intelligence in Construction Project Management: A Systematic Literature Review of Cost, Time, and Safety Management,” Buildings, vol. 16, no. 5, p. 1061, Mar. 2026, doi: 10.3390/buildings16051061

https://doi.org/10.24867/INDIS-2026-EN-469



# BLOCKCHAIN - BASED FRAMEWORK FOR DAILY PROJECT INFORMATION SYNCHRONIZATION IN AEC PROJECTS

*Jelena M. Andrić*[1]

***Summary:***

The architecture, engineering and construction (AEC) projects are complex in nature and fragmented due to the large number of stakeholders and intensive information exchange throughout the project lifecycle. The existing applications of blockchains in the AEC industry are focused on separate processes, such as smart contracts, BIM, building permits, and others. This paper proposes a novel Blockchain-enabled Framework for Collaboration and Decision-making Support in AEC projects which is based on a multiple layer digital architecture: Blockchain collaboration layer, AEC project information management layer, visualization layer, and decision-making support layer and the concept of Daily Project Digital Synchronization (DPDS) algorithm is introduced to overcome the existing gaps. This approach automatically updates technical documentation, construction daily logs, actual costs, schedules, and resource utilization while detecting project deviations and generating recommendations.

*Keywords: Blockchain, AEC projects, Collaboration, Construction Daily Logs, Daily Project Digital Synchronization*

# OKVIR ZA SVAKODNEVNU SINHRONIZACIJU PROJEKTNIH INFORMACIJA U AEC PROJEKTIMA

***Rezime:***

Projekti u oblasti arhitekture, građevinarstva i građene sredine (AEC) složeni su i fragmentisani zbog velikog broja zainteresovanih strana i intenzivne razmene informacija tokom čitavog životnog ciklusa projekta. Postojeće primene blockchain tehnologija u AEC industriji uglavnom su usmerene na pojedinačne procese, kao što su pametni ugovori, BIM, građevinske dozvole i drugi procesi. Ovaj rad predlaže novi blockchain-om podržan okvir za saradnju i podršku donošenju odluka u AEC projektima, zasnovan na višeslojnoj digitalnoj arhitekturi koja obuhvata: sloj blockchain saradnje, sloj za upravljanje informacijama AEC projekta, sloj za vizuelizaciju i sloj za podršku donošenju odluka. U cilju prevazilaženja postojećih nedostataka uvodi se koncept algoritma za svakodnevnu digitalnu sinhronizaciju projekta (Daily Project Digital Synchronization – DPDS). Ovaj pristup omogućava automatsko ažuriranje tehničke dokumentacije, dnevnih građevinskih izveštaja, stvarnih troškova, rasporeda i korišćenja resursa, uz istovremeno detektovanje odstupanja u projektu i generisanje preporuka.

*Ključne reči: Blockchain, AEC projekti, Kolaboracija, Dnevni građevinski izveštaji, Dnevna Digitalna Sinhronizacija Projekta*

[1]University Lecturer, European University Cyprus, Nanjing University of Posts and Telecommunications, Nanjing, China, j.andric@external.euc.ac.cy, 0000-0002-5343-799X

## 1. INTRODUCTION

The architecture, engineering and construction (AEC) projects are complex in nature and fragmented due to the large number of stakeholders and intensive information exchange throughout the project lifecycle [1-3]. The challenges in the AEC projects are due to inefficient communication, lack of transparency, inconsistency and traceability across different project stakeholders [3]. Project information such as design revisions, request for information (RFI), construction site logs, supplier invoices, procurement records, plans, and technical documents are distributed across different platforms and different stakeholders. Project stakeholders are investors, design teams, professional institutions, local authorities, contractors, subcontractors, consultants, and others. As a result, project information is inconsistent, duplicates appear, hard to trace information and complex communication which lead to cost overruns, delays and insufficient quality. In order to successfully manage AEC projects till their completion, IT solutions in the construction industry and different software can aid project management.

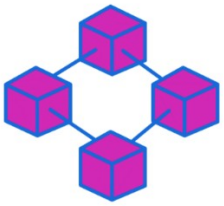

*Fig. 1 Chart of the comprehensive indicator system*

Blockchain technology emerged as promising technology which is capable to cope with existing challenges in AEC projects [1]. The initial concept of blockchain appeared in 2008 and it was introduced by Nakamoto as a technology related to bitcoin [4]. Generally, blockchain refers to a specific data structure that is similar as “a chain of blocks” (Figure 1). Blockchain is a decentralized distributed ledger technology which represents a system that contains history of all records of transactions and changes in the system state [5]. It allows peer-to-peer transactions without involving a third party. The data is structured as a continuing list of transaction information records shared between different computer network’s nodes. Further, these data are stored in blocks. Since it is a decentralized system, no single person or group has an impact on or control over transaction records. Compared to traditional centralized databases, blockchain provides trust, improved security, data integrity, transparency, speed, reduced cost, individual control of data, tokenization and traceability among all participants [6]. The other important aspect of blockchain is that stored data in blocks is immutable and irreversible. An essential role of blockchain is found in cryptocurrency systems for maintaining permanent records of transactions.

Within the AEC industry, the application of blockchain has attracted a lot of attention during the past decade. The application of blockchain technologies is in the management of AEC projects can be considered from the different project stakeholders’ perspectives. In the mostly studies, the focus is on the blockchain-enabled Building Information Modelling (BIM) [7, 8], enabling smart contracts for AEC contract administration [9], construction quality control [10], digital building permits [11], tracking activities, enabling more efficient data flow between stakeholders, and tracking subcontractors and suppliers in supply management [12]. The current literature emphases on single applications of blockchain addressing isolated project processes, instead of providing an integrated framework that allows collaboration between different parties, enable synchronization of project information, processes daily information and decision-making throughout the entire AEC project lifecycle.

The additional challenge in the AEC management consists on generation of daily project information such as construction daily logs, which are one of the most important sources of project information, documenting completed activities, resource utilization, labour allocation, equipment usage, material deliveries, weather conditions, inspections and unforeseen events occurring on site [13]. Generally, construction daily site logs are kept as separate documents from schedules, cost and time performance indicators and decision-making tools in real time. Consequently, project managers frequently make decisions without incomplete and updated information, making hard to determine early delays in projects, cost overruns and productivity deviations [14].

To address the current limitations, the aim of this paper is to develop a blockchain-based framework for collaboration and decision-making in the AEC projects with the multiple layers. The aim is to allow daily project digital synchronization and decision-making support for project managers and other stakeholders. The structure of proposed framework is multi layered consisting of four interconnected different layers, the first layer is the blockchain collaboration layer, followed by the AEC project information management layer, decision making support layer and the visualisation layer. The blockchain collaboration layer serves as trusted and immutable collaboration layer among project stakeholders storing all transaction. The second layer transforms validated blockchain transactions into synchronized project information. The decision-making support layer determines and evaluates the Key Performance Indicators (KPIs), identify deviations and propose recommendations accordingly. The final, visualization layer provides interactive digital representations of project information through dashboards, the Gantt charts, BIM models and others. The main contribution is the Daily Project Digital Synchronization (DPDS) concept which continuously synchronize executed blockchain transactions into updated representation of the AEC projects by validating construction daily logs. By daily synchronization, the framework automatically updates technical documents, construction daily logs, activity progress, track activities, cost, schedules, resource utilization, and evaluate performance. Based on the results, the decision-making support layer proposes a certain action to project managers to reduce the size of cost and time overruns.

## 2. LITERATURE REVIEW

The current literature review highlights existing applications of blockchain technology in the AEC industry, and Table 1 reviews relevant studies on use cases of blockchain technology in the AEC industry.

*Tab. 1 Literature review of blockchain within AEC industry*

| Num. | Field of blockchain application in AEC industry | Authors |
|---|---|---|
| 1 | BIM | [7, 8, 15, 16, 22] |
| 2 | Contract management | [9, 17, 18] |
| 3 | Supply chain | [12, 19, 20, 21] |
| 4 | Digital building permits | [11] |
| 5 | Construction waste | [23, 24, 25] |
| 6 | Prefabricated housing construction | [26, 27] |
| 7 | Quality control | [10, 28, 29] |

The initial application of the blockchain technology was with the BIM by improving data security, establishing trusted data ownership, improving data control, providing transparent modification tracking during the design phase and detecting clashes [15, 16, 22]. Since blockchain maintain undisrupted records of different version of BIM model it brings more responsibility and accountability between different stakeholders. Smart contracts are also part of the blockchain technology. From the perspective of AEC industry, the efficiency in the contracting process is increased with the use of smart contracts due to their trust and easy traceability and decreasing the disputes. The role of smart contracts is to automate contracting procedures, verification process of technical documentation, payment procedures between stakeholders, and contract execution [9, 17, 18]. Supply chain management is important part of the AEC industry, in which the blockchain can be integrated for tracking orders of construction materials and equipment, supplier coordination and circular supply chains [12, 19 - 21]. Particularly, blockchain technology track and trace information shared between suppliers and contractors. The recent trends show that the blockchain technology also found application toward digital building permits for verification of documents and obtaining approval [11]. Similarly, there are applications in the waste management [23 - 25], prefabricated construction where blockchain is integrated with IoT technologies [26 - 27]. The procedure for quality management can be done through the blockchain in order to ensure immutable quality inspection records, facilitate quality verification, and improve accountability during project execution [10, 28, 29].

The current literature shows different use cases of the blockchain technology through the AEC industry including integration with BIM, smart contracts, supply chain management, quality inspection, and construction site documentation. Particularly, all these studies are focus on single process rather than the multiple and continuous processes in the whole project lifecycle. The framework for integrating BIM with blockchain lacks of mechanism for continuously transforming verified transactions into synchronized information to support daily update [15, 19]. Likewise, the use of blockchain technologies for the construction daily logs is focused on documenting construction site activities without synchronizing the data and applying for project monitoring or updating KPI [30, 31]. The existing studies lack of integrating blockchain infrastructure with the synchronization of the construction daily log information, KPI monitoring, updating Gantt chart and costs, Digital Twins, visualization environments and support in decision making under one umbrella [30 – 33].

This research addresses all these limitation by proposing and developing Blockchain - enabled Framework for Collaboration and Decision-making support in the AEC projects based on the DPDS algorithm. The main idea is that the proposed framework simultaneously converts verified transaction into synchronized project information and updates project schedules, costs, and KPI in order to provide directions for decision making throughout of four-layer digital architecture.

## 3. METHODOLOGY

The proposed methodology for this study is based on the design science research approach since the aim is to develop and formalize a conceptual framework for blockchain-enabled collaboration and decision-making support for the AEC projects. Design science research approach is adopted since it supports problem-solving paradigm and creating innovative artifacts that are used in information systems or software engineering [34, 35]. Artifacts in a context present method, technique or algorithms designed, developed, maintained or used in software or information system [35]. In this case, a four-layer blockchain-enabled framework, the concept of DPDS and the DPDS algorithm is designed. A generic

architecture system consisting of four layers for supporting trusted information exchange, continuous synchronization of project information, and collaborative decision-making throughout the AEC project lifecycle is designed. The proposed methodology consists of five steps and it is shown in Figure 2.

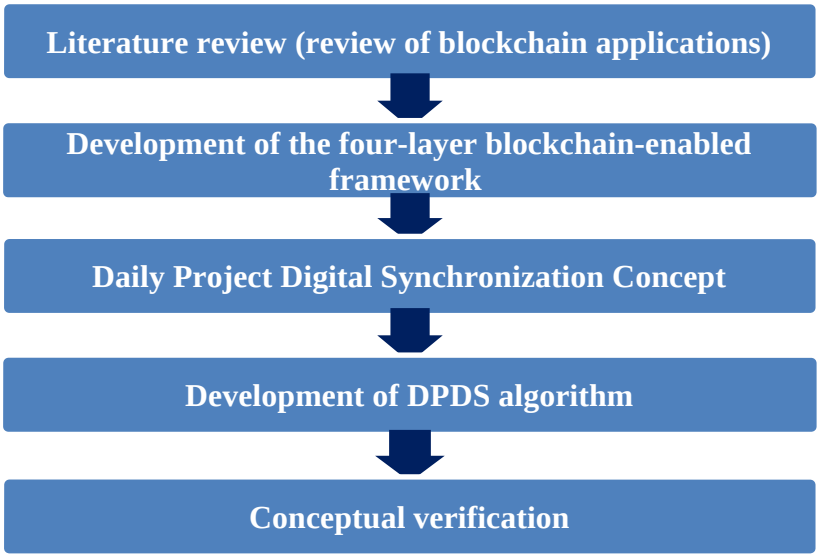


*Fig. 2 The proposed research methodology*

The initial process is a literature review on the applications of blockchain technologies in the AEC industry, which is completed in the Section 2. The detected limitation of the current research is integrating permanent daily site records, schedules, project documentation, monitoring the performance of project, and collaborative decision support within a single blockchain-enabled environment. Based on the identified research gaps, a conceptual blockchain-enabled framework is designed to cope the collaboration between different stakeholders and decision-making during the whole AEC project lifecycle. The framework is designed to contain four interoperable layers: 1.) Blockchain Collaboration Layer; 2.) AEC Project Information Management Layer; 3.) Decision-making support Layer; and 4.) Visualization Layer. A specific function is assigned to each layer and there is continuously information exchange between layers. The modular architecture has a purpose to support multiple stakeholders during the whole lifecycle of the AEC projects from planning and design, construction, commissioning, operation and maintenance period. For the designed modular architecture, the Daily Project Digital Synchronization (DPDS) concept is introduced. Compare to the traditional blockchain application where the primarily focus on static storing project transaction, this approach take into account each verified blockchain transaction as input to update information state of AEC project. After each change of some of project information such as design revisions, updates in BIM, RFIs, construction daily log inputs, inspection reports, quality reports, the delivery of materials, resource utilization, contract approvals, building permit approvals, invoices and schedule modifications, it is immutably recorded on the blockchain and further triggered synchronization in the subsequent project information management environment. The synchronization of data is performed immediately or upon daily synchronization interval depending on the project's nature. It enables that all stakeholders receive the latest version of project information and provides transparency, consistency and traceability during the whole project lifecycle. Following the DPDS concept, a corresponding synchronization algorithm is developed to enable flow of project information between users. The DPDS algorithm is triggered upon validated blockchain transaction and it continuously updates project information. The steps in the algorithm are shown in Figure 3.

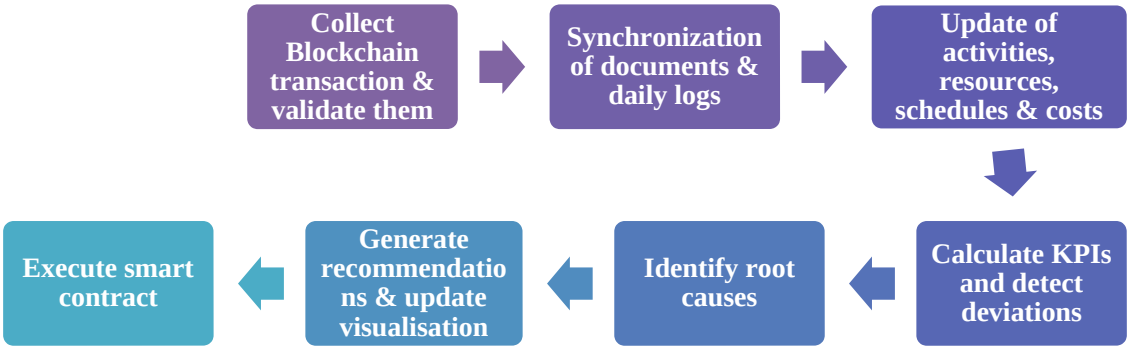


*Fig. 3 Steps in the DPDS algorithm*

## 4. BLOCKCHAIN-ENABLED FRAMEWORK FOR COLLABORATION AND DECISION-MAKING SUPPORT IN THE AEC PROJECTS

A proposed blockchain-enabled framework with four layers is capable to support secure collaboration, transparent project information sharing, visualization, and decision-making under a unified digital environment for the AEC projects during their whole lifecycle. It consists of four layers: 1.) Blockchain Collaboration Layer; 2.) AEC Project Information Management Layer; 3.) Visualization Layer; and 4.) Decision-making support Layer. Figure 4 illustrates all layers.

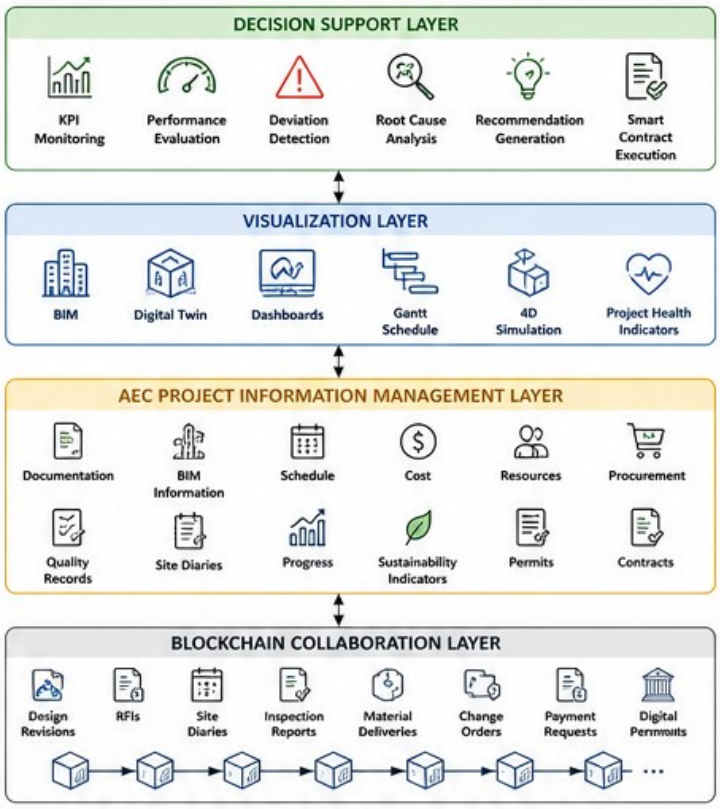


*Figure 4 Four Layer system*

The Blockchain Collaboration Layer is the underline layer that forms the foundation of the framework enabling transparent environment for stakeholders in the AEC projects. Since blockchain is a distributed and decentralized system, it would enable that every

project stakeholder has its own node and have equal access to documents and information in the blockchain system. All transactions are stored in a single database, and each project stakeholder stores a copy of the database on its node. Each project stakeholder has its own node, and nodes are the entry points for new data. The ledger is distributed as it is maintained on all the nodes in the network. The blockchain structure for collaboration between different project stakeholders in AEC is illustrated in Figure 5. The Blockchain Collaboration Layer records every significant project event as a blockchain transaction, including: design revisions; update of BIM models; RFIs; construction daily log entries; inspection reports; construction progress updates; delivery of materials; equipment utilization; quality control reports; meeting minutes; change orders; building permits; payment requests; contract approvals; and smart contract execution. Every project stakeholder can store and verify their information through transactions, which can be further used by other project stakeholders. All stakeholders are given access to all transaction records and project documents. Each transaction contains a timestamp, stakeholder identification, transaction metadata and cryptographic hash, creating a complete chronological history of the project. From the perspective of the design team, the designer is capable of uploading completed design solutions, technical specifications and documents, plans, and bill of quantity. Automatically, using the blockchain system, other parties in the system have full access to design documents at every moment. However, they are not capable of editing design documents; they have only permission to view the content. There is no need for separately sending documents to investors or contractors. The uploaded design documents are further processed for obtaining building permits. The local authorities that issue building permits have access to documents. The contractor and subcontractors need design specifications and technical documents for the construction process. Once the building permits for construction are obtained, they are stored in the system, and every stakeholder has access to them only for viewing the content. Also, the information regarding the progress of the construction process is stored in the system by the contractor. The blockchain technology enables transparency of project documents for each stakeholder and secures the integrity and reliability of information in the system. Further, smart contracts are used for the contract management of different stakeholders in the project: the contract between designer and investor, the contract between contractor and investor, the contract between contractor and subcontractors, and others.

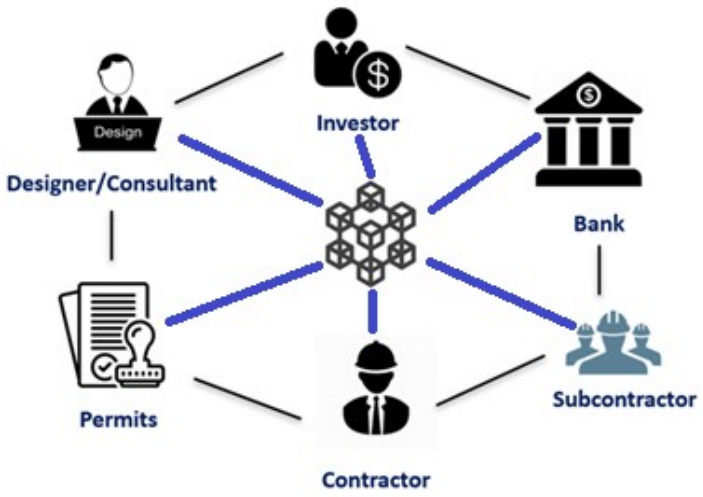


*Figure 5 Collaboration between project stakeholders using blockchain*

The AEC Project Information Management layer synchronizes validates blockchain transactions and transforms them to structured project information required for effective

project management. The task of this layer is to ensure that project information is updated, consistent and verified throughout project lifecycle. The key component of the layer is DPDS algorithm. The synchronized information includes: technical documentation, BIM models, schedules, construction progress, resource allocation, labour utilization, equipment utilization, procurement, cost, quality records, digital permits, contracts, and construction daily logs records.

Visualization layer enables transformation of synchronized project information into interactive visuals including BIM model, digital twin, the Gantt charts, 4D construction simulations, interactive dashboards. The main task of this layer is providing understanding and visual representation of the current project state depending on the blockchain transactions.

The highest layer is the Decision-making support Layer in the proposed framework. After the synchronized project information, a recommendations and decision-making throughout the AEC project lifecycle takes part. Based on the synchronized data by newly validated blockchain transaction, it triggers the project performance evaluation. In this step, the values for KPIs are estimated upon updating blockchain transactions. The following KPIs are monitored: Earned value, Planned Value, Actual Value, Schedule Performance Index (SPI), Cost Performance Index (CPI), track of completed works, labour productivity, procurement, quality control, and sustainability indicators [36]. Further, the KPIs values are compared with the planned values in order to detect deviation. Based on the results, the framework can detect cost overruns, schedule delays, failure to meet quality standards, procurement delays, and productivity reduction. The root causes for deviation are identified and analysed. Also, the algorithm proposes strategies how to overcome the potential deviations and improve performance.

## 4.1. DPDS ALGORITHM

The algorithm consists of the following steps:

- **Step 1:** Collect transactions & validate them: The validated transactions are collected after the synchronization period. Each transaction is verified for the integrity and authenticity.
- **Step 2:** Synchronization of technical documents & construction daily logs: Technical documents are added and updated in the project repository. Also, the daily logs are added and synchronized.
- **Step 3:** Update of activities, resources, schedules & costs: This steps updates activity progress, utilisation of labour, material and equipment, and project schedule and actual costs.
- **Step 4:** Calculate KPIs & detect deviations: Based on the updated information, new KPIs values are estimated. Further, a significant deviation from the baseline is detected.
- **Step 5:** Identify root cause: If there are significant deviations, the root causes are detected and analysed.
- **Step 6:** Generate recommendations & update visualisation: In case of deviations, recommendations to reduce them are proposed to decision-makers. Also, all visual representations of BIM models, digital twins, KPIs dashboard and the Gantt chart are updated and shown to stakeholders.
- **Step 7:** Execute smart contract: Smart contracts are trigger after the "*If*" conditions are fulfilled.

The synchronization process is a cycle process that can be described as a loop (Figure 6). After completing all steps in DPDS algorithm, the updated digital state becomes a new

base in for the AEC project. It is a loop process in which real time update is ensured between blockchain transactions and project management information.

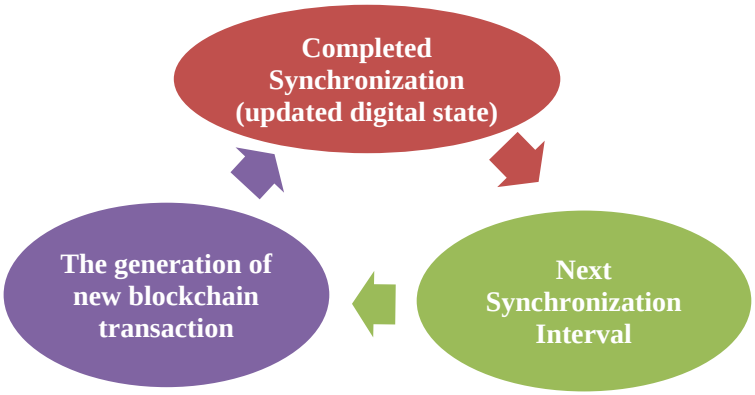


*Figure 6 Continues loop for synchronization process*

## 5. CONCLUSIONS

This paper proposed a Blockchain-enabled framework for collaboration and decision-making support in AEC projects, which extends existing blockchain applications by integrating reliable collaboration, project information management, visualization, and intelligent decision-making support within a unified digital environment. It provides holistic approach, compared to the previous studies by connecting multiple project management processes within a single blockchain-based architecture rather than addressing isolated applications. Furthermore, the proposed framework considers blockchain as the fundamental infrastructure for continuously synchronizing project information throughout the entire AEC project lifecycle.

In this paper, the key contribution is the introduction of the concept DPDS followed by synchronization algorithm. This concept supports that validated blockchain transactions automatically transforms to updated project information. It contributes to transparency, traceability, consistency, and information reliability

Future research will focus on implementing the proposed framework in a prototype software environment and validating the DPDS algorithm through real-world construction project case studies. Quantitative evaluation of synchronization efficiency, project performance, and decision-making effectiveness will provide further evidence of the framework's practical applicability and benefits for the AEC industry.

## REFERENCES

[1] Zhao, D., Duva, M., Mollaoglu, S., Frank, K., Garcia, A., & Tait, J. (2021). Integrative collaboration in fragmented project organizations: Network perspective. *Journal of Construction Engineering and Management*, *147*(10), 04021115.

[2] Wood, H., Piroozfar, P., & Farr, E. R. (2013, September). Understanding complexity in the AEC industry. In *Proceedings of the 29th Annual Conference of the Association of Researchers in Construction Management (ARCOM)* (pp. 859-869). ARCOM.

[3] Ali, F., & Haapasalo, H. (2023). Development levels of stakeholder relationships in collaborative projects: challenges and preconditions. *International Journal of Managing Projects in Business*, *16*(8), 58-76.

[4] Nakamoto, S. (2008). Bitcoin: A peer-to-peer electronic cash system.

[5] Tabatabaei, M. H., Vitenberg, R., & Veeraragavan, N. R. (2023). Understanding blockchain: Definitions, architecture, design, and system comparison. *Computer Science Review*, *50*, 100575.

[6] Bodkhe, U., Tanwar, S., Parekh, K., Khanpara, P., Tyagi, S., Kumar, N., & Alazab, M. (2020). Blockchain for industry 4.0: A comprehensive review. *Ieee Access*, *8*, 79764-79800.

[7] Nawari, N. O., & Ravindran, S. (2019, June). Blockchain technologies in BIM workflow environment. In *ASCE International Conference on Computing in Civil Engineering 2019* (pp. 343-352). Reston, VA: American Society of Civil Engineers.

[8] Turk, Ž., & Klinc, R. (2017). Potentials of blockchain technology for construction management. *Procedia engineering*, *196*, 638-645.

[9] Wang, J., Wu, P., Wang, X., & Shou, W. (2017). The outlook of blockchain technology for construction engineering management.

[10] Wu, H., Zhong, B., Li, H., Guo, J., & Wang, Y. (2021). On-site construction quality inspection using blockchain and smart contracts. *Journal of Management in Engineering*, *37*(6), 04021065.

[11] Gao, H., Zhong, B., & Ding, L. (2024). A blockchain-based engineering design review service trading scheme for digital building permits. *Automation in Construction*, *165*, 105496.

[12] Rodrigo, M. N., Perera, S., Senaratne, S., & Jin, X. (2018, November). Blockchain for construction supply chains: A literature synthesis. In *Proceedings of ICEC-PAQS Conference 2018*.

[13] Shiau, Y. C., & Wang, W. C. (2003). Daily report module for construction management information system. *ISARC2003 The Future Site*, *603*.

[14] Sanusi, B. O. (2024). The role of data-driven decision-making in reducing project delays and cost overruns in civil engineering projects. *SAMRIDDHI: A Journal of Physical Sciences, Engineering and Technology*, *16*(04), 182-192.

[15] Ni, Y., Sun, B., & Wang, Y. (2021). Blockchain-based BIM digital project management mechanism research. *IEEE access*, *9*, 161342-161351.

[16] Pradeep, A. S. E., Amor, R., & Yiu, T. W. (2020, March). Blockchain improving trust in BIM data exchange: a case study on BIMCHAIN. In *Construction Research Congress 2020* (pp. 1174-1183). Reston, VA: American Society of Civil Engineers.

[17] Das, M., Tao, X., Liu, Y., & Cheng, J. C. (2022). A blockchain-based integrated document management framework for construction applications. *Automation in Construction*, *133*, 104001.

[18] Kamel, M. A., Bakhoum, E. S., & Marzouk, M. M. (2023). A framework for smart construction contracts using BIM and blockchain. *Scientific Reports*, *13*(1), 10217.

[19] Li, X., Lu, W., Xue, F., Wu, L., Zhao, R., Lou, J., & Xu, J. (2022). Blockchain-enabled IoT-BIM platform for supply chain management in modular construction. *Journal of construction engineering and management*, *148*(2), 04021195.

[20] Yang, Y., Wei, Z., Zhang, Z., & Xie, H. (2025). Modeling the Enablers for Blockchain Technology Adoption in the Construction Supply Chain. *Journal of Construction Engineering and Management*, *151*(9), 04025113.

[21] Elghaish, F., Hosseini, M. R., Kocaturk, T., Arashpour, M., & Ledari, M. B. (2023). Digitalised circular construction supply chain: An integrated BIM-Blockchain solution. *Automation in Construction*, *148*, 104746.

[22] Zheng, R., Jiang, J., Hao, X., Ren, W., Xiong, F., & Ren, Y. (2019). bcBIM: a blockchain-based big data model for BIM modification audit and provenance in mobile cloud. *Mathematical problems in engineering*, *2019*(1), 5349538.

[23] Voorter, J., & Koolen, C. (2021). The traceability of construction and demolition waste in Flanders via blockchain technology: a match made in heaven?. *Journal for European Environmental & Planning Law*, *18*(4), 347-369.

[24] Lin, Y. H., Dai, J., Li, J., & Tao, X. (2026). Efficient Classification and Disposal Management of Construction Waste Using Blockchain Technology and System Dynamics. *Journal of Construction Engineering and Management*, *152*(2), 04025242.

[25] França, A. S. L., Neto, J. A., Gonçalves, R. F., & Almeida, C. M. V. B. (2020). Proposing the use of blockchain to improve the solid waste management in small municipalities. *Journal of Cleaner Production*, *244*, 118529.

[26] Li, C. Z., Chen, Z., Xue, F., Kong, X. T., Xiao, B., Lai, X., & Zhao, Y. (2021). A blockchain- and IoT-based smart product-service system for the sustainability of prefabricated housing construction. *Journal of Cleaner Production*, *286*, 125391.

[27] Wang, B., Geng, L., Dang, P., & Zhang, L. (2022). Developing a framework for dynamic organizational resilience analysis in prefabricated construction projects: a project life cycle perspective. *Journal of Construction Engineering and Management*, *148*(10), 04022110.

[28] Sheng, D., Ding, L., Zhong, B., Love, P. E., Luo, H., & Chen, J. (2020). Construction quality information management with blockchains. *Automation in construction*, *120*, 103373.

[29] Wu, H., Zhang, P., Li, H., Zhong, B., Guo, S., Fung, I. W., & Lee, Y. Y. (2024). Blockchain impact on construction quality management and its adoption analysis: A game theory–based method. *Journal of Construction Engineering and Management*, *150*(6), 04024039.

[30] Kang, K., Liu, X., Jiang, Y., Lee, K. K. H., Wan, S. K. W., Huang, G. Q., & Zhong, R. Y. (2023). Blockchain opportunities for construction industry in Hong Kong: a case study of RISC and site diary. *Construction Innovation*, *23*(2), 443-466.

[31] Zhang, Y., Wang, T., & Yuen, K. V. (2022). Construction site information decentralized management using blockchain and smart contracts. *Computer-Aided Civil and Infrastructure Engineering*, *37*(11), 1450-1467.

[32] Adel, K., Elhakeem, A., & Marzouk, M. (2023). Decentralized system for construction projects data management using blockchain and IPFS. *Journal of civil engineering and management*, *29*(4), 342-359.

[33] Olawumi, T. O., Ojo, S., Muftaudeen, S. T., Odeh, A. O., & Amoo, T. (2026). Assessing blockchain technology's technical utility in construction supply chains: A multi-KPI decision support approach via use cases. *Computers in Industry*, *175*, 104429.

[34] Vom Brocke, J., Hevner, A., & Maedche, A. (2020). Introduction to design science research. In *Design science research. Cases* (pp. 1-13). Cham: Springer International Publishing.

[35] Wieringa, R. (2014). Design science methodology for information systems and software engineering. Springer-Verlag Berlin Heidelberg.

[36] Fleming, Q. W., & Koppelman, J. M. (2016, December). Earned value project management. Project Management Institute.

https://doi.org/10.24867/INDIS-2026-EN-480



# FROM GREEN TO SUSTAINABILITY: AN INTEGRATED AHP AND AI FRAMEWORK FOR PRIORITISING SUSTAINABILITY INDICATORS

*Jelena M. Andrić*[1], *Hejing Feng*[2]

***Summary:***

The construction industry is among the highest consumers of global resources, energy, and water. This study prioritises sustainability indicators for shopping malls across social, environmental, and economic dimensions. Based on relevant domestic and international standards and previous research in green building and sustainability, 18 indicators are identified: 7 social, 8 environmental, and 3 economic. Data were collected from 50 professionals with expertise in public building projects, and the Analytical Hierarchy Process (AHP) was used to determine the priorities of indicators. A shopping mall project in Jiangsu Province, China, serves as a case study. The results show that cultural heritage ranks highest in the social dimension, land use in the environmental dimension, and cost in the economic dimension. These findings support decision-making in shopping mall projects based on sustainability performance.

*Keywords: Sustainability, Social dimension, Economic dimension, Environmental dimension, Public Buildings, AHP*

# OD ZELENOG PREMA ODRŽIVOM RAZVOJU: INTEGRISANI OKVIR ZA AHP I AI ZA ODREĐIVANJE PRIORITETNIH INDIKATORA ODRŽIVOG RAZVOJA

***Rezime:***

Građevinska industrija je među najvećim potrošačima globalnih resurasa, energije i vode. Ova studija vrši prioritizaciju indikatora održivosti za tržne centre po društvenoj, ekomomskoj i ekološkoj dimenziji. Na osnovu domaćih i internacionalnih standarda i ranijih istraživanja u zeleno gradnji i održivosti, 18 indikatora je detektovano: 7 društvenih, 8 ekoloških i 3 ekonomska. Podaci su prikupljeni od 50 profesionalaca koji su eksperti u izgradnji javnih zgrada, i AHP za određivanje prioritetnih indikatora. Tržni centar u Jiangsu provinciji u Kini je izabran kao studija slučaja. Rezultati pokazuju da kulturno nasleđe je najviše rangiran u društvenoj dimenziji, upotreba zemlje u ekološkoj dimenziji, i troškovi u ekonomskoj dimenziji. Ovi rezultati pokazuju da podržavaju donošenje odluka za projekte tržnih centara na osnovu performansi održivosti.

*Ključne reči: Održivost, Društvena dimenzija, Ekonomska dimenzija, Ekološka dimenzija, Javne zgrade, AHP*

[1] University Lecturer, European University Cyprus, Nanjing University of Posts and Telecommunications, Nanjing, China, j.andric@external.euc.ac.cy, 0000-0002-5343-799X
[2] MSc Civil Engineer, Department of Civil Engineering, Xi'an Jiaotong-Liverpool University, Suzhou, China, Hejing.Feng22@alumni.xjtlu.edu.cn

## 1. INTRODUCTION

The construction industry is characterised as one of the highest consumption industries regarding natural resources, energy and water consumption worldwide. Overall, 40% of the energy consumption annually worldwide is consumed by the building sector during the whole building's life cycle, including processing and manufacturing materials, transportation, construction phase, operation & maintenance phase of the building, and demolition phase, ranking the building sector in the first place compared to other industries [1]. The sector also places considerable pressure on water resources and raw materials and is responsible for a significant proportion of global greenhouse gas emissions and construction waste [1–3]. Consequently, the environmental impacts associated with the construction industry have become an important concern in the context of global warming, climate change and resource consumption. The challenges caused to move beyond traditional building approaches to the development of sustainable strategies. The sustainability in the construction industry refers to protecting environment, reducing energy, resources and water consumption, and enable the cohesion of nature and the built environment [4]. Sustainable development refers to a development approach that meets current needs without compromising the ability of future generations to meet their needs [5, 6]. The basis idea of sustainability is to combine three different aspects: 1) environmental; 2) economic; and 3) social[7].

The aim of this study is to rank the importance of sustainability indicators in building projects in Jiangsu province in the People’s Republic of China. For this purpose, the Analytical Hierarchy Process (AHP) method is applied to rank the importance of the sustainability index in each dimension of sustainability. There are a lot of methods to study sustainability evaluation. Practically, the AHP method provides a hierarchical and structural arrangement of sustainability indicators and analysis that combines qualitative and quantitative methods. AHP was proposed and developed by Saaty [8]. This study provides an effective method for assessing the importance of sustainability indicators in large buildings and provides a theoretical basis and practical guidance for realising sustainable large public buildings with energy-saving and healthy characteristics in the Jiangsu region.

## 2. LITERATURE REVIEW

The construction of public buildings is closely related to social development, with large investments, long construction period, many stakeholders, and long operation cycle [9]. The role of the government is obvious, as well as a wide range of service impacts, etc., and it also has a benchmarking demonstration role for other projects. The sustainability of large-scale public buildings is an important part of their performance, and this attribute reflects the interaction between large-scale public buildings and external economic, environmental, social and other systems, their intrinsic economic and resource utilisation performance, as well as their own manageability, renewability, maintainability and ability to cope with emergencies such as disasters. China's Agenda 21 clearly states that all sectors and regions of China should realise the path of sustainable development [10]. Currently, there are many studies on sustainable development and sustainability, but most of them focus on the development of the country, region or industry, and the evaluation and improvement of the sustainability of the most important and most basic carrier of human economic construction activities - large-scale public buildings - is still relatively weak [11].

The research on sustainable building issues started earlier and has recognised evaluation standards and tools. In the 1980s, the international building energy efficiency system had

taken shape and was widely used in developed countries such as Britain, France, and Germany. In October 2000, the "Sustainable Building 2000" (GBC2000) conference was held, whose main goal was to pay attention to the dynamics of sustainable development and emphasise the establishment of the contents and methods of environmental evaluation of buildings, so as to promote the development of building evaluation technology. As a result, the evaluation of sustainable buildings has become an indispensable part [12].

Over the past years, with the continuous development and popularisation of sustainable building theories and technologies, a series of evaluation standards, evaluation systems and tools related to sustainable building have appeared in the international arena, and although they are all in the stage of suggestion and trial, their influence is also getting bigger and bigger. These include: Building Research Establishment Environment Assessment Method (BREEAM) in the United Kingdom, Leadership in Energy & Environmental Design Building Ratings System (LEED) in the United States, Canada's Green Building Tool (GBTOOL), Comprehensive Assessment System for Building Environmental Efficiency (CASBEE) in Japan, Chinese standards for green building/energy efficient building assessment or design codes developed by GOBAS-Group (2003), GAQSIQ (2006), MEP (2007), and others. However, the Chinese standards for green building, design codes or energy-efficient building assessment are not translated into English yet [13].

BREEAM is the first and most widely used and authoritative international standard for describing the performance of the built environment. The assessment system adopts the core concept of "balancing benefits with local conditions", and the assessment includes core performance factors, design and implementation, management and operation, and the weighting system is established by soliciting the opinions of government decision makers, building engineering professionals, experts and scholars, material manufacturers, developers and environmental organisations, etc. The evaluation results are graded as pass, good, very good and excellent [14].

LEED is an evaluation standard for the market requirements, and is also a legally mandatory standard in some U.S. states and some countries, which evaluates the environmental performance of the building as a whole from the whole life cycle of the building, and comprehensively analyses the building site, water resource utilization, building energy efficiency and atmosphere, energy and resources, and indoor environmental quality, etc., and evaluates the results of the evaluation for the "certified, silver, gold, and platinum levels" [15].

The evaluation index system of GB Tool favours the overall evaluation of the whole life cycle of the building. Its evaluation includes seven aspects, including environmental sustainability indicators, resource consumption, economy, operation management, environmental load, maintainability, and indoor air quality, and the evaluation results are scored on a 0 - 5 scale [16].

CASBEE proposed the concept of "*Building Environmental Efficiency*" from the viewpoint of sustainability, and evaluated a total of about 160 entries of "*Building Environmental Quality and Performance*" and "*External Environmental Load on Buildings*" in a comprehensive manner, with the results of excellent (S), very good (A), good (B+), relatively poor (B-), and poor (C) [17].

Figure 1 shows the flow chart of indicator establishment. The preliminary indicators are firstly determined based on the information of China's current and recommended technical standards and codes for building energy efficiency, domestic and international building energy efficiency and environmental evaluation methods, and foreign green building and environmental assessment methods, including BREEAM, LEED and others. Further, the indicators are repeatedly screened and refined to obtain the final evaluation indicator system [18, 19].

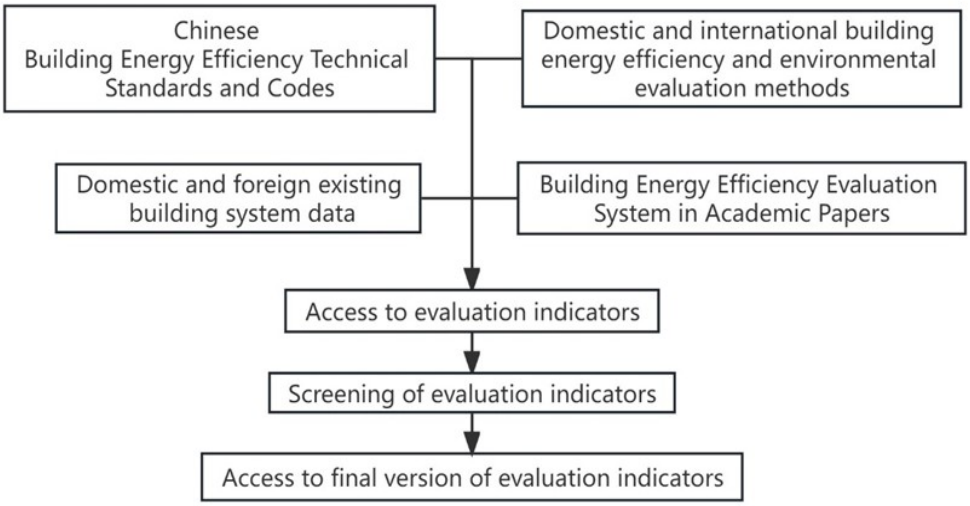


*Fig. 1 Chart of the comprehensive indicator system*

Sustainability indicators that are selected in this study are listed in Table 1. In total, 18 sustainability indicators are extracted from the previous studies and considered in this study for evaluating the importance of sustainability indicators in building projects. Each sustainability indicator is assigned to one of three sustainability dimensions: social (7 indicators), environmental (8 indicators) and economic (3 indicators).

*Tab. 1 Sustainability indicators from the literature*

| Num. | Dimension | Factors | Sources |
|---|---|---|---|
| 1 | Social | Cultural heritage | [20, 26] |
| 2 | | Public access | [21, 24] |
| 3 | | Public participation | [22, 27] |
| 4 | | Safety & Health | [20] |
| 5 | | Public utility | [20] |
| 6 | | Social integration | [23, 27] |
| 7 | | Responsibility (Sustainable awareness) | [24, 25] |
| 8 | Environmental | Land use | [22, 24] |
| 9 | | Water consumption | [21, 22, 26] |
| 10 | | Air emissions | [21, 22, 24, 25] |
| 11 | | Biodiversity | [26, 27] |
| 12 | | Visual impact | [24] |
| 13 | | Resources consumptions | [24, 27] |
| 14 | | Waste management | [20, 21, 22, 24] |
| 15 | | Energy consumption | [21, 25, 26, 27] |
| 16 | Economic | Cost | [20, 21, 22, 24, 27] |
| 17 | | Technical requirements | [26] |

| | | | |
|---|---|---|---|
| 18 | | Bureaucracy | [27] |

## 3. METHODOLOGY

Figure 2 shows the proposed framework. Firstly, a Breakdown Structure of Sustainability Indicators (BSSI) is formed based on the list of sustainability indicators from Table 1. The second step is to establish an evaluation indicator set, to decide the scale for comparison matrices in the AHP method. Based on the established set, a questionnaire is designed for collecting data. The questionnaire survey is conducted, and data are collected from the experts in the field of construction engineering and management. The participants are engaged in the building projects. When data is collected, the AHP method is applied to determine the importance of the sustainability factors within each dimension. The sustainability evaluation is the expression of the degree of influence of the same-level indicators on the upper-level indicators. This paper uses AHP to determine the weights of the evaluation indicators. The AHP method is used to judge the relative importance of factors on the same level since it combines qualitative and quantitative analysis, which improves the nature of evaluation. In the next step, AI-based scenario and sensitivity analysis is used to determine the robustness of the indicator weights under different scenarios and to identify the key indicators. When the new values are determine, intelligent sustainability decision-making system proposes the strategies how to improve sustainability performance of the critical indicators and overall sustainability.

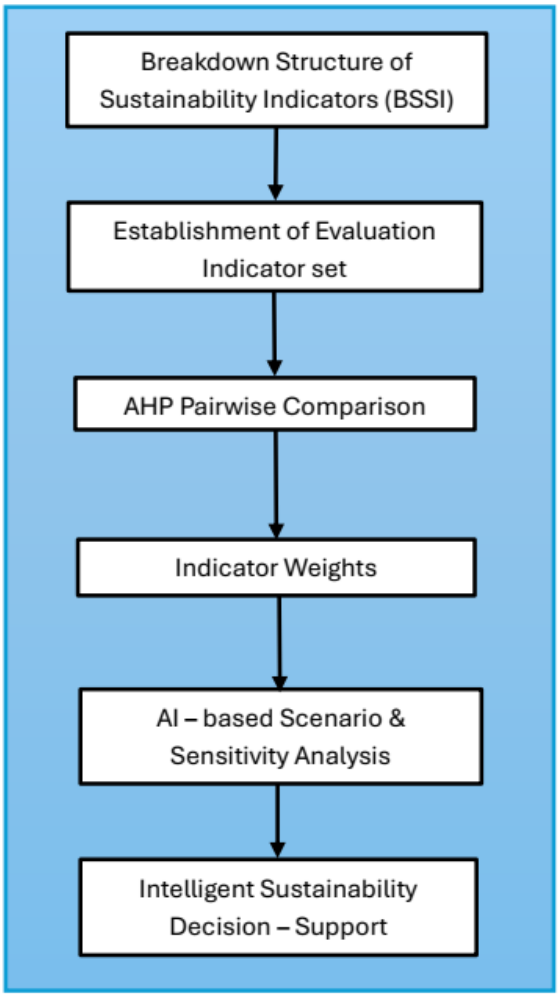


*Fig. 2 The proposed methodology*

Based on the above principles combined with the questionnaire survey, this paper mainly constructs the BSSI consisting of three levels: the overall level is sustainability, the second level is sustainability dimensions, and the third level is indicators for each dimension. In total, 18 factors are the guideline layer, and then a detailed analysis is carried out for each guideline to get the specific indicator system, as shown in Figure 3.

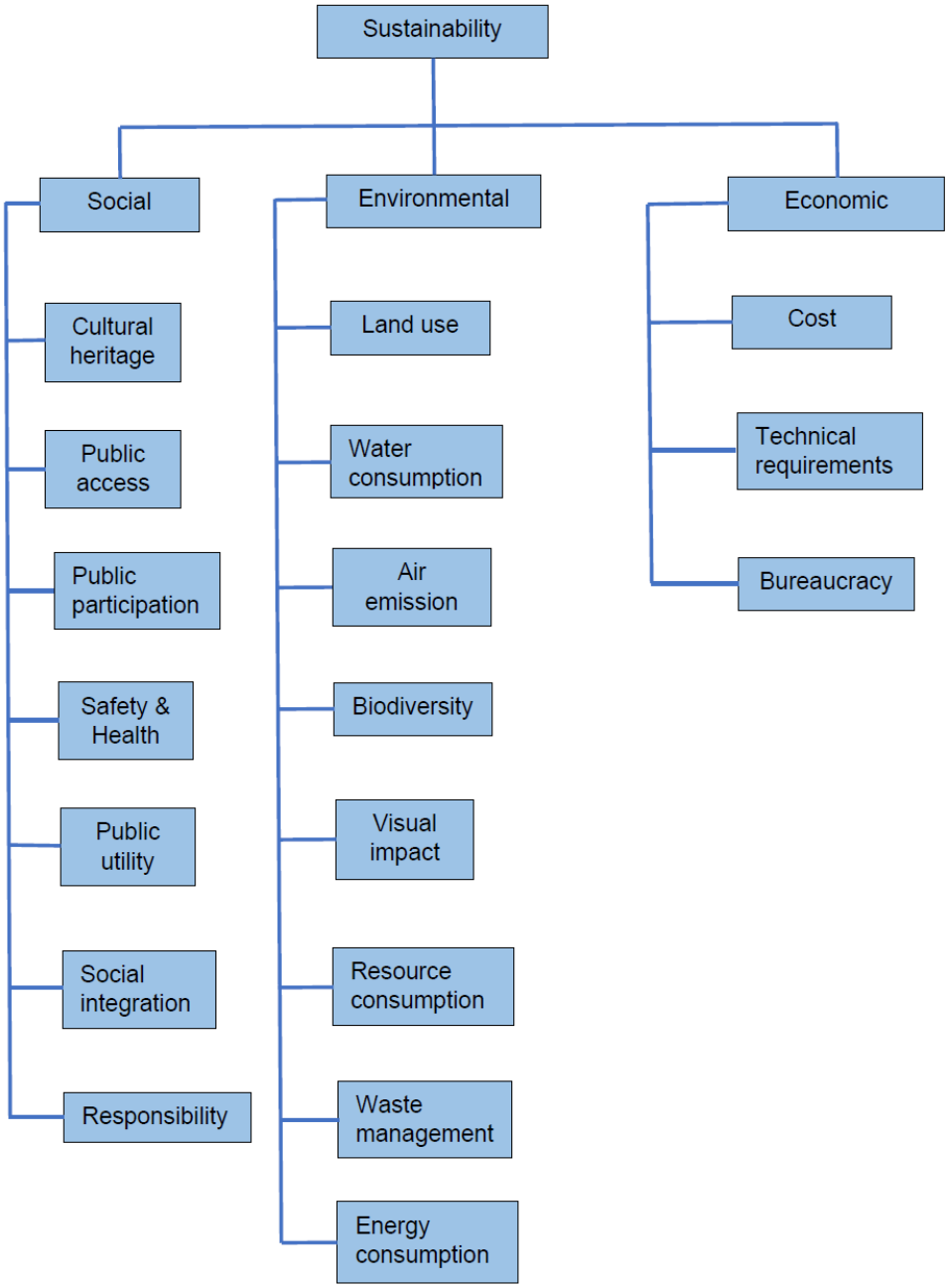


*Fig. 3 BSSI*

The relationship between indicators is analysed using the AHP principle to establish a recursive hierarchical structure of the system [28]. That is, under this structure, the complex problem consists of a number of indicators, which in turn are divided into groups according to their properties, forming different levels. Indicators at the same level act as guidelines governing certain indicators at the next level, and at the same time are governed by indicators at the previous level.

Weighting is a measure of the relative importance of an indicator, and different weights often lead to significant differences in evaluation results. A questionnaire survey is an

effective method for determining the weights, in which the survey factors are formulated in advance by the surveyor and relevant professionals (designers, engineers, etc.), who express their opinions on the importance of each factor [29]. However, this method cannot avoid the influence of personal subjective factors and has certain limitations. The AHP method is a combination of qualitative and quantitative decision analysis methods proposed by Satty TL, an American operations researcher, in the 1970s [30]. Also, the AHP method is a quantitative method which can be accurately calculated through mathematical models for decision-making, thus better solving complex decision-making problems. It is suitable for the analysis of multi-criteria, multi-objective and complex problems, and it is able to establish a quantifiable channel between personal subjective judgments and mathematical logical rigour. Therefore, the weights are determined using a combination of questionnaire survey and AHP.

The basic idea is to decompose the complex decision-making problem into multiple levels, gradually carry out hierarchical analysis from the level of objectives to the level of specific measures, combine subjective and objective factors, and determine the weight of each factor in decision-making according to the relationship between the factors.

When using the AHP method, it is first necessary to determine the decision-making objectives and evaluation indicators, and then these objectives and indicators are hierarchically decomposed to form a hierarchical structure diagram. By comparing the factors of each level two by two, a judgment matrix is constructed, so as to calculate the weight of each factor. In addition, the AHP method can be used for consistency testing of judgment matrices to ensure the reasonableness of decision-making results. The collective steps are as follows [8]:

**Step 1:** Constructing a judgment matrix:

In total, there are *n* decision objectives, which need to be compared with each other to construct a judgment matrix $A = (a_{ij})$. A judgment matrix is shown below:

$$A=\begin{bmatrix} a_{11} & \cdots & a_{1n} \\ \vdots & \ddots & \vdots \\ a_{n1} & \cdots & a_{nn} \end{bmatrix} \tag{1}$$

Where $a_{ij}$ represents the importance of the *i-th* goal relative to the *j-th* goal, satisfying the following conditions:

$a_{ij} = 1$, which indicates that a goal's comparison with itself results in 1;

$a_{ij} = 1/a_{ji}$, which indicates that the comparison between two goals is reciprocal;

For any three goals i, j, and k, if $a_{ij}$ and $a_{jk}$ are known, $a_{ik}$ can be determined by transitivity.

**Step 2:** Calculate the feature vector

By eigenvalue decomposition of the judgment matrix, the largest eigenvalue $\lambda_{max}$ and the corresponding eigenvector $W= (w_1, w_2, ... w_n)$. Where the eigenvector w represents the weight of each target in the overall decision, i.e., the weight of the *i-th* target is $w_i$.

**Step 3:** Calculation of coherence indicators

The consistency of the judgment matrix can be tested by calculating the consistency index CI and consistency ratio CR. The consistency ratio is calculated by Equation (2):

$$CR=\frac{CI}{RI} \tag{2}$$

Where RI is the random consistency index of the judgment matrix, and CI is the consistency index is calculated as in equation (3):

$$CI=\frac{\lambda_{max}-1}{n-1} \tag{3}$$

If CR is less than 0.1, the judgment matrix is considered to have acceptable consistency. The random consistency index RI is the consistency index value of a randomly generated matrix. Saaty [8] used scales 1/9, 1/8, ..., 1, ..., 8, 9 to generate random inverse matrices, and the average values of the random consistency index for 500 randomly generated matrices with different values of n are shown in Table 2.

*Tab. 2 Random Consistency Index*

| N | RI |
|---|---|
| 1 | 0 |
| 2 | 0 |
| 3 | 0.58 |
| 4 | 0.90 |
| 5 | 1.12 |
| 6 | 1.24 |
| 7 | 1.32 |
| 8 | 1.41 |
| 9 | 1.45 |
| 10 | 1.49 |
| 11 | 1.51 |

The relationship between goals and factors, and factors and sub-factors in the traditional AHP method, is established by a judgment matrix or pairwise comparison matrix X, constructed as factors on the same level. The elements in rows *i* and *j* represent the judgment values of attribute *i* on attribute *j*. Verbal judgment values in matrix X in traditional AHP is represented as clear numerical values. The meaning of a 9-point scale is given in Table 3.

*Tab. 3 Criteria for proportionality and relative importance*

| Scale | Meaning |
|---|---|
| 1 | When comparing two factors, they are equally important |
| 3 | When comparing two factors, the former factor is slightly more important than the latter factor |
| 5 | When comparing the two factors, the former factor is significantly more important than the latter factor |
| 7 | When comparing the two factors, the former factor is more strongly important than the latter factor |
| 9 | When comparing the two factors, the former factor is extremely more important than the latter factor |
| The inverse of the above value | The inverse of the two factors is the inverse of the value of the original comparison |

The AHP method has been widely used in engineering, management, economics and other fields. It can help decision makers accurately assess the importance of each factor, better solve the problem of subjectivity and complexity, and is a more reliable multi-factor

decision-making method [31]. At the same time, the AHP method has its limitations, which require decision makers to have a deeper understanding and grasp of the problem, as well as a clear quantitative method and data support for each evaluation index.

## 4. RESULTS AND DISCUSSIONS

### 4.1. THE IMPORTANCE OF SUSTAINABILITY INDICATORS

The obtained results for each dimension separately are given in Tables 4 – 6. According to the results, the most important sustainability indicator in the social dimension is cultural heritage, which is followed by public access and public participation. From the social point of view, Jiangsu province has many scenic gardens, which are valuable cultural heritage. So, the large-scale public building architecture in Jiangsu province should definitely have elements of them as well. The second important sustainability indicator is public access. From the social aspect, it is important to enable uninterrupted access to buildings, pathways and parks around buildings, and the building services systems inside the building. The least important indicator is sustainability awareness, which means that the strategies to increase awareness of sustainability for participants in the construction industry should be developed and applied.

*Tab. 4 The values of importance factors for social dimension*

| Num. | Dimension | Factors | Values |
|---|---|---|---|
| 1 | Social | Cultural heritage | 0.31 |
| 2 | | Public access | 0.22 |
| 3 | | Public participation | 0.15 |
| 4 | | Safety & Health | 0.12 |
| 5 | | Public utility | 0.08 |
| 6 | | Social integration | 0.07 |
| 7 | | Responsibility (Sustainable awareness) | 0.04 |

*Tab. 5 The values of importance factors for environmental dimension*

| Num. | Dimension | Factors | Values |
|---|---|---|---|
| 8 | Environmental | Land use | 0.27 |
| 9 | | Water consumption | 0.21 |
| 10 | | Air emissions | 0.16 |
| 11 | | Biodiversity | 0.11 |
| 12 | | Visual impact | 0.09 |
| 13 | | Resources consumptions | 0.08 |
| 14 | | Waste management | 0.05 |
| 15 | | Energy consumption | 0.04 |

From the environmental perspective, the most significant indicator is land use. This signifies that it is important to make efficient urban plans for future buildings and plan the landscape and access paths to the buildings. Water consumption is ranked in the second place. Since the construction industry is a high-consumption industry, it is important to make strategies for how to optimally use water for building projects. Energy consumption is the least important indicator for the environmental dimension. This is due to the fact that many strategies for energy efficiency and reducing energy consumption have been implemented in the past and applied to building projects.
According to the results from Table 6, the most important economic factor is cost. Cost includes direct and indirect costs on the project, as well as construction cost, maintenance & operation cost, and the whole lifecycle cost. This factor is more important compared to the other two factors together.
Different scenarios are not considered in this case.

*Tab. 6 The values of importance factors for economic dimension*

| Num. | Dimension | Factors | Values |
|---|---|---|---|
| 16 | Economic | Cost | 0.51 |
| 17 | | Technical requirements | 0.36 |
| 18 | | Bureaucracy | 0.13 |

## 4.2. DISCUSSIONS

Urban development is dynamic, there are many uncertain factors affecting its development, the uncertainty of urban development will further affect the uncertainty of the operation of large-scale public building projects, that is, the uncertainty of its sustainability if the sustainability of the project cannot meet the standards or belong to the unsustainable project, will not be able to meet the demand for urban development, affecting the life cycle; on the contrary, if the project sustainability If the sustainability of the project exceeds its requirements, then it will cause a certain amount of waste, affecting the operational efficiency of large-scale public buildings and the performance of their functions. The sustainable development of cities is a broad and complex subject, and the development of sustainable buildings to create an eco-city requires the concerted efforts of many relevant parties to put sustainable programs into practice.
Through the development of sustainable buildings, it promotes the construction and development of sustainable materials, energy-saving and water-saving products, environmentally friendly enterprises and renewable energy enterprises, as well as related enterprises, fosters more bases for the production, development and application of sustainable building materials, focuses on the development of solar energy, bio-energy, and geothermal energy, and promotes the large-scale development of new types of industries, reduces the unemployment rate of the urban population, and promotes the development of a harmonious society.
Strengthen capacity-building for the sustainable evaluation of large-scale public buildings, establish a nationally unique system of technologies, products and services, and train specialised sustainable building evaluation agencies responsible for relevant design, consultation, contracting, product testing and evaluation. Establish a professional qualification system for the evaluation of sustainable buildings, strengthen the training of complex talents in sustainable building design, planning, testing and evaluation, and promote the coordinated development of cities, human life and sustainable buildings.

## 5. CONCLUSIONS

Based on the existing research results, standards and domestic and international building evaluation systems, this paper investigates the sustainability evaluation system of large public buildings in Jiangsu province, mainly the sustainability evaluation during the operation stage. The main work of this paper includes:

1) Reviewing and summarising rich domestic and international scientific research data, consulting experts in related fields to establish a three-tier sustainability evaluation system for large public buildings, including the three pillars of sustainable development: social, economic and environmental aspects. For the social pillar, cultural heritage, public access, public participation, safety & health, public utility, social integration, and sustainability awareness are considered. The economic pillar includes cost, technical requirements and bureaucracy. Under the environmental pillar, land use, water consumption, air emissions, biodiversity, visual impact, resource consumption, waste management, and energy consumption are evaluated.

2) Through the questionnaire survey, the weights of the indicators were determined by using the hierarchical analysis method. Two weights were polynomially calculated to obtain the final weights of the indicators and were scored. The weights overcame the shortcomings of the hierarchical analysis method, which is too much influenced by the subjectivity of experts, and finally formed a complete sustainability evaluation model of large shopping malls in the Jiangsu region.

The results show that the most important factors in the social aspect are cultural heritage and public access, while the most important aspects in the case of the environmental dimension are land use and water consumption, and cost is the most important aspect from the economics' perspective.

Work that needs further research and improvement:

1) This paper only focuses on the establishment of a sustainability evaluation system for the operation phase of public buildings in the Jiangsu region, and in further research, the evaluation of the design and construction phases can be added, and the geographical expansion of the evaluation can also be considered.

2) In this paper, there are a total of 18 sustainability indicators, including 8 sustainability indicators in the environmental aspect, 3 sustainability indicators in the economic aspect, and 7 sustainability indicators in the social aspect. The ratio of indicators in these three aspects is about 3:1:3, which is not particularly evenly distributed. The accuracy of the model would be further improved if a few more sustainability indicators on economic aspects were added for evaluation.

3) The various stages of the article have been completed, but have not been developed into an integrated software, and in future research, consideration could be given to integrating the various parts into the same software.

## REFERENCES

[1] Dixit, M. K., Culp, C. H., Fernández-Solís, J. L.: System boundary for embodied energy in buildings: A conceptual model for definition. *Renewable and Sustainable Energy Reviews, 21* (2013), pp. 153-164, doi: 10.1016/j.rser.2012.12.037

[2] Lu, K., Wang, H.: Estimation of building's life cycle carbon emissions based on life cycle assessment and building information modeling: A case study of a hospital building in China. *Journal of Geoscience and Environment Protection, 7* (2019) 6, pp. 147-165, doi: 10.4236/gep.2019.76013

[3] Hussain, M., Zheng, B., Chi, H. L., Hsu, S. C., Chen, J. H.: Automated and continuous BIM-based life cycle carbon assessment for infrastructure design projects. *Resources, Conservation and Recycling, 190* (2023), pp. 106848, doi: 10.1016/j.resconrec.2022.106848

[4] Clements-Croome, D.: Sustainable intelligent buildings for people: A review. *Intelligent Buildings International*, *3* (2011) 2, pp. 67-86, doi: 10.1080/17508975.2011.582313

[5] Mat Aron, N. S., Khoo, K. S., Chew, K. W., Show, P. L., Chen, W. H., Nguyen, T. H. P.: Sustainability of the four generations of biofuels–a review. *International Journal of Energy Research*, *44* (2020) 12, pp. 9266-9282, doi: 10.1002/er.5557

[6] YANG Hongxiong, LIU Yiying, WANG Yunpeng: Analysis of sustainable development direction of assembly building based on lean construction. *Construction Economy*, 44 (2023) 04, pp. 89-96, doi: 10.14181/j.cnki.1002-851x.202304089

[7] Alhaddi, H.: Triple bottom line and sustainability: A literature review. *Business and Management studies*, *1* (2015) 2, pp. 6-10, doi: 10.11114/bms.v1i2.752

[8] Saaty, T. L.: Decision making with the analytic hierarchy process. *International Journal of Services Sciences*, *1* (2008) 1, pp. 83-98.

[9] Wu, S., Clements-Croome, D.: Understanding the indoor environment through mining sensory data—A case study. *Energy and Buildings*, *39* (2007) 11, pp. 1183-1191, doi: 10.1016/j.enbuild.2006.07.011

[10] HOU Xiangzhao, LIN Zhiyan, HUANG Zhonghui.: On the mode of public works project financing in lieu of construction. *Journal of Chongqing Architecture University*, 25 (2003) 3, pp.78-81.

[11] ZHAO Guojie, LAN Guoliang.: A preliminary study on sustainability measurement of urban development. *Journal of Tianjin University: Social Science Edition*, 7 (2003).

[12] Shin, Q.-Y.: Research on Green Construction Theory and Construction Environmental Load Evaluation. Wuhan: Huazhong University of Science and Technology. (2007).

[13] Geng, Y., Dong, H., Xue, B., Fu, J.: An overview of Chinese green building standards. *Sustainable Development*, *20* (2012) 3, pp. 211-221, doi: 10.1002/sd.1537

[14] Papadopoulos, A. M., Giama, E.: Rating systems for counting buildings' environmental performance. *International Journal of Sustainable Energy*, *28* (2009) 1-3, pp. 29-43, doi: 10.1080/14786450802452423

[15] Kubba, S. LEED practices, certification, and accreditation handbook. Butterworth-Heinemann. 2009.

[16] Sanya, T.: Sustainable architecture evaluation method in an African context: transgressing discipline boundaries with a systems approach. *Sustainability Science*, *7* (2012) 1, pp. 55-65, doi: 10.1007/s11625-011-0137-1

[17] Sasatani, D., Bowers, T., Ganguly, I., Eastin, I. L.: Adoption of CASBEE by Japanese house builders. *Journal of Green Building*, *10* (2015) 1, pp. 186-201, doi: 10.3992/jgb.10.1.186

[18] Qin, Y., Lin, B., Zhu, Y.: Research on Green Building Assessment System in China. *Journal of Ecological Building*, (2007), pp. 68-71.

[19] Clements-Croome, D.: Sustainable intelligent buildings for people: A review. *Intelligent Buildings International*, *3* (2011) 2, pp. 67-86, doi: 10.1080/17508975.2011.582313

[20] Kamali, M., Hewage, K.: Performance indicators for sustainability assessment of buildings, International Construction Specialty Conference (5th: 2015: Vancouver, B. C.): Canadian Society for Civil Engineering. Canada. 2015.

[21] Kajjoba, D., Wesonga, R., Olupot, P. W., Kirabira, J. B., Lwanyaga, J. D., Kasedde, H.: Prioritizing sustainability indicators for Uganda's built environment: Expert perspectives using the Delphi technique. *Results in Engineering*, *24* (2024), pp. 103182, doi: 10.1016/j.rineng.2024.103182

[22] Sharifi Orkomy, A., Sharbatdar, M. K.: Identifying effective sustainable development indicators for airport construction projects: Zahedan international airport in iran as case study. *Iranian Journal of Science and Technology, Transactions of Civil Engineering*, *45* (2021) 1, pp. 241-252, doi: 10.1007/s40996-020-00478-7

[23] Passoni, C., Marini, A., Belleri, A., Menna, C.: Redefining the concept of sustainable renovation of buildings: State of the art and an LCT-based design framework. *Sustainable Cities and Society*, *64* (2021), pp. 102519, doi: 10.1016/j.scs.2020.102519

[24] Akhanova, G., Nadeem, A., Kim, J. R., Azhar, S.: A multi-criteria decision-making framework for building sustainability assessment in Kazakhstan. *Sustainable Cities and Society*, *52* (2020), pp. 101842, doi: 10.1016/j.scs.2019.101842

[25] Yang, Y., Ren, J., Solgaard, H. S., Xu, D., Nguyen, T. T. Using multi-criteria analysis to prioritize renewable energy home heating technologies. *Sustainable Energy Technologies and Assessments*, *29* (2018), pp. 36-43, doi: 10.1016/j.seta.2018.06.005

[26] Alyami, S. H., Rezgui, Y., Kwan, A.: Developing sustainable building assessment scheme for Saudi Arabia: Delphi consultation approach. *Renewable and Sustainable Energy Reviews*, *27* (2013), pp. 43-54, doi: 10.1016/j.rser.2013.06.011

[27] Stanitsas, M., Kirytopoulos, K., Leopoulos, V.: Integrating sustainability indicators into project management: The case of construction industry. *Journal of Cleaner Production*, *279* (2021), pp. 123774, doi: 10.1016/j.jclepro.2020.123774

[28] Alwaer, H., Clements-Croome, D. J.: Key performance indicators (KPIs) and priority setting in using the multi-attribute approach for assessing sustainable intelligent buildings. *Building and environment*, *45* (2010) 4, pp. 799-807, doi: 10.1016/j.buildenv.2009.08.019

[29] Radziszewska–Zielina, E.: Survey studies in construction project engineering. In *IOP Conference Series: Materials Science and Engineering*, Vol. 960, No. 4, pp. 042035. IOP Publishing. 2020.

[30] Teng, C. C., Horng, J. S., Hu, M. L. M., Chien, L. H., Shen, Y. C.: Developing energy conservation and carbon reduction indicators for the hotel industry in Taiwan. *International Journal of Hospitality Management*, *31* (2012) 1, pp. 199-208, doi: 10.1016/j.ijhm.2011.06.006

[31] Caceoğlu, E., Yildiz, H. K., Oğuz, E., Huvaj, N., Guerrero, J. M.: Offshore wind power plant site selection using Analytical Hierarchy Process for Northwest Turkey. *Ocean engineering*, *252* (2022), pp. 111178, doi: 10.1016/j.oceaneng.2022.111178

https://doi.org/10.24867/INDIS-2026-EN-493



# INFLUENCE OF LIME BINDER PROPORTION ON STRENGTH DEVELOPMENT OF STABILIZED RIVER SEDIMENT

*Panta Krstić[1], Miloš Šešlija[2], Dragana Tomašević Pilipović[3], Nikolina Ćirić[4], Sara Krsmanović[5]*

***Summary:***

This paper presents a continuation of research on the stabilization of river sediment from the Begej River using the lime-based binder ViaCalco 90 at varying proportions. The paper presents the results of unconfined compressive strength (UCS) testing after 7 days and California Bearing Ratio (CBR) for mixtures with 3% and 9% binder content, along with additional UCS and indirect tensile strength (ITS) testing after 28 days for mixtures with 3, 5, 7, and 9% binder content. The results indicate a continuous increase in CBR values with higher binder content, with mixtures stabilized at 5% and above classified as excellent quality subgrade material. UCS results confirmed the slower but continuous strength development of the stabilized samples, with values ranging from 0.13 to 0.40 MPa after 28 days of curing. The ITS/UCS ratio of the samples is in line with typical values reported for lime-stabilized fine-grained soils.

*Keywords: dredged sediment, lime stabilization, road construction, sustainability*

# UTICAJ PROCENTUALNOG UDELA KREČNOG VEZIVA NA RAZVOJ ČVRSTOĆE STABILIZOVANOG REČNOG SEDIMENTA

***Rezime:***

U okviru ovog rada prikazan je nastavak istraživanja stabilizacije rečnog sedimenta poreklom iz reke Begej krečnim vezivom ViaCalco 90 u različitim procentualnim udelima. U radu su prikazani rezultati istraživanja jednoaksijalne pritisne čvrstoća (UCS) nakon 7 dana i Kalifornijskog indeksa nosivosti (CBR) za mešavine sa 3 i 9% udela veziva, te dodatna ispitivanja UCS i indirektne zatezne čvrstoće (ITS) nakon 28 dana za mešavine sedimenta i 3, 5, 7 i 9% veziva. Rezultati ukazuju na kontinuiran porast CBR vrednosti sa povećanjem udela veziva, pri čemu su mešavine stabilizovane sa 5% i više veziva karakterisane kao posteljica odličnog kvaliteta. Rezultati UCS ispitivanja potvrdili su sporiji ali kontinuiran razvoj čvrstoće uzoraka, sa vrednostima između 0.13 do 0.40 MPa nakon 28 dana. Odnos ITS i UCS uzoraka je u skladu sa tipičnim vrednostima za krečom stabilizovana sitnozrna tla.

*Ključne reči: izmuljeni sediment, stabilizacija krečom, izgradnja puteva, održivost*

[1] Teaching Assistant, Department of Civil Engineering and Geodesy – Faculty of Technical Sciences, University of Novi Sad, Serbia, panta.krstic@uns.ac.rs , ORCID 0000-0001-5519-391X
[2] Associate Professor, Department of Civil Engineering and Geodesy – Faculty of Technical Sciences, University of Novi Sad, Serbia, sele@uns.ac.rs, ORCID 0000-0002-8857-8952
[3] Full Professor, Department of Chemistry, Biochemistry and Environmental Protection, Faculty of Sciences, University of Novi Sad, Serbia, dragana.tomasevic@dh.uns.ac.rs, ORCID 0000-0002-8275-3297
[4] Teaching Assistant, Department of Civil Engineering and Geodesy – Faculty of Technical Sciences, University of Novi Sad, Serbia, nikolina.ciric@uns.ac.rs, ORCID 0000-0001-5740-0986
[5] Teaching Assistant, Department of Civil Engineering and Geodesy – Faculty of Technical Sciences, University of Novi Sad, Serbia, sarakrsmanovic@uns.ac.rs, ORCID N/A

## 1. INTRODUCTION

Dredged sediment (further referred to as *sediment*) is a material formed by the deposition of fine clay, sand, and silt particles at the bottom of rivers, lakes, or canals. In general, deposited sediment is characterized as a fine-grained material with low strength and bearing capacity [1,2]. The physical and mechanical properties of sediment largely depend on the specific location of its formation, including geological processes such as deposition conditions, mineralogical composition, and organic matter content. Therefore, sediments can exhibit significant variability in their composition depending on the sampling location.

The formation of sediment in rivers or canals is associated with the erosion of riverbanks or surrounding soil, and the transport of material by water flow. In addition to these natural processes, sediment formation can also be linked to various human activities, such as the discharge of wastewater or industrial and agricultural waste. In such cases, the sediment may be heavily contaminated, with elevated concentrations of heavy metals, organic, and other pollutants [3,4]. A significant content of contaminants in sediment can represent an obstacle to its reuse due to the potential leaching of harmful substances into the environment.

Stabilization of sediment can simultaneously improve its initially poor geotechnical properties while immobilizing heavy metals and other contaminants, thereby opening the possibility for the reuse of this waste material in construction [5]. Previous research has indicated the potential for using stabilized sediment in bearing layers or the subgrade of road pavements, where significant improvements in geotechnical properties can be achieved to meet the technical criteria for incorporation into pavement layers or road embankments [2,6]. Typical binders used for sediment stabilization include Portland cement, lime, fly ash, other industrial by-products, and their combinations.

This paper presents a continuation of a study conducted in 2025, in which a geotechnical characterization of sediment from the Begej River near Zrenjanin was performed [7]. Following the basic geotechnical characterization, the sediment was stabilized using the commercial lime-based binder ViaCalco 90, based on CaO, at proportions of 5% and 7% by dry sample mass (mixtures VC90-5 and VC90-7). The mechanical properties of the stabilized material were evaluated through unconfined compressive strength (UCS) testing after 7 days of curing and the California Bearing Ratio (CBR). Although a significant increase in sample strength was recorded, the mixtures did not meet the requirements for application in a stabilized subgrade or bearing layer.

This paper is conceived as an extension of the previous study, applying the same binder over a wider range of proportions to better monitor strength development (binder additions of 3% and 9% by dry sample mass). Given that lime-based binders typically exhibit a slower rate of strength gain compared to cement-based binders, this study additionally includes the determination of UCS after 28 days of curing, indirect tensile strength (ITS) after 28 days for all formed mixtures, as well as additional CBR test results for the remaining mixtures.

## 2. MATERIALS AND METHODS

### 2.1. GEOTECHNICAL PROPERTIES OF RIVER SEDIMENT

As previously mentioned, the basic geotechnical characterization was conducted as part of a previous study [7]. Sediment sampling was performed at a sediment disposal site

formed following a dredging campaign of the Begej River, carried out in 2021. The experimental part of the characterization included standard laboratory tests for soil identification and classification, such as particle size distribution analysis [8], bulk density and natural moisture content determination [9,10], Atterberg consistency limits [11], and maximum dry density ($\rho_{d,max}$) at optimum moisture content ($w_{opt}$) using the standard Proctor compaction test [12]. Finally, the material was classified according to the Unified Soil Classification System (USCS) in accordance with ASTM D2487-17 [13]. A summary of the engineering properties of the sediment determined in the previous study is presented in *Table 1*. The results of the standard Proctor test are presented in *Table 2*.

*Tab. 1 Basic geotehnical properties of river sediment based on previous research* [7]

| Property | Unit | Value | Standard |
|---|---|---|---|
| Granulometric composition<br>*Clay (<0.002 mm)*<br>*Silt (0.002 - 0.06 mm)*<br>*Sand (0.06 - 2 mm)*<br>*Gravel (2 - 6 mm)*<br>*Boulder (>60mm)* | % | <br>22.55<br>41.40<br>32.55<br>3.50<br>0 | SRPS EN ISO 17892-4:2017 |
| Initial moisture content | % | 1.98 | SRPS EN ISO 17892-1:2015 |
| $\rho_d$ | Mg/m$^3$ | 1.34 | SRPS EN ISO 17892-2:2015 |
| Liquid limit (%) | % | 27.44 | SRPS EN ISO 17892-12:2018 |
| Plasticity limit (%) | % | 17.32 | |
| Plasticity index (%) | % | 10.12 | |
| Soil classification (according to USCS) | - | CL | ASTM D2487 − 17 |

*Tab. 2 Proctor compaction test for river sediment based on previous research* [7]

| Property | Unit | Value | Standard |
|---|---|---|---|
| $\rho_{d,max}$ | Mg/m$^3$ | 1.62 | SRPS EN 13286-2:2012 |
| $w_{opt}$ | % | 12.50 | |

Additionally, the organic matter content of the river sediment was determined by the ignition method at a temperature of 650°C, in accordance with standard SRPS U.B1.024:1968 [14]. A relatively low organic matter content of 2.61% was recorded, indicating the suitability of the material for stabilization and further use.

Basic chemical characterization of the sediment was performed using X-ray fluorescence analysis (XRF). The chemical composition of the samples was determined using a SPECTRO XEPOS energy dispersive X-ray fluorescence spectrometer (Germany). The samples were dried prior to analysis, after which 5 g of each sample was mixed with 1 g of micro powder C (CEREOX BM-0002-1), homogenized, and pressed under 1 t into a pellet with a diameter of 32 mm.

A summary of the chemical composition of the sediment is presented in Table 3. The chemical composition indicates that the material is predominantly composed of $SiO_2$

and $Al_2O_3$ oxides, characteristic of sediments with a significant proportion of clay and sand, alongside a low sulfate content ($SO_3$).

*Tab. 3 Chemical composition of sediment determined by XRF*

| Sample | Chemical composition (%) | | | | | | | | |
|---|---|---|---|---|---|---|---|---|---|
| | $Na_2O$ | MgO | $Al_2O_3$ | $SiO_2$ | $P_2O_5$ | $SO_3$ | $K_2O$ | CaO | Other |
| Sediment | 0.36 | 1.85 | 13.11 | 43.89 | 0.41 | 0.53 | 1.82 | 1.17 | 36.92 |

## 2.2. BINDER PROPERTIES

For the stabilization of sediment, a commercial lime-based binder ViaCalco 90, produced by Carmeuse, was used at proportions of 3, 5, 7, and 9% by dry sample mass. According to the manufacturer's specifications, the binder contains more than 80% CaO, with the remainder consisting of limestone filler [15]. XRF analysis for the determination of the chemical composition of the binder was conducted following the same procedure as for the sediment. The results of the chemical composition of the binder are presented in Table 4.

*Tab. 4 Chemical composition of ViaCalco binder determined by XRF*

| Sample | Chemical composition (%) | | | | | | | | |
|---|---|---|---|---|---|---|---|---|---|
| | $Na_2O$ | MgO | $Al_2O_3$ | $SiO_2$ | $P_2O_5$ | $SO_3$ | $K_2O$ | CaO | Other |
| ViaCalco 90 | 0.003 | 0.73 | 0.097 | 0.101 | 0.0005 | 0.27 | 0.011 | 73.89 | 24.85 |

## 2.3. SAMPLE PREPARATION AND TESTING METHODS

The standard Proctor compaction test was additionally conducted for the remaining mixtures stabilized with 3% and 9% binder by dry sample mass. Samples were prepared in the form of cylinders with a diameter of Ø100 mm and height H=120 mm, with a compaction energy of 600 kN/m³ applied. These results were subsequently compared with those obtained for mixtures stabilized with 5% and 7% of the same binder in the previous study [7]. The sample preparation process is shown in *Figure 1*.

Additional UCS testing after 7 and 28 days, as well as ITS testing after 28 days, was conducted in accordance with standards SRPS EN ISO 17892-7:2018 and SRPS EN 13286-42:2012 [16,17]. For UCS and ITS testing, cylindrical samples with a height of H=120 mm and diameter of Ø100 mm were prepared, with the sediment and binder material, at the added optimum moisture content, compacted in three layers. The test results represent the arithmetic mean of three consecutively tested cylinders for each mixture. UCS testing was performed using a standard hydraulic press, with the maximum force at sample failure recorded. ITS was determined using the Brazilian test, in which cylindrical samples were placed in special steel loading plates and loaded diametrally until failure. The ITS value was calculated according to the formula provided in the referenced standard.

Additional CBR testing for mixtures VC90-3 and VC90-9 was conducted following the standard procedure in accordance with SRPS EN 13286-47 [18]. For CBR testing of stabilized mixtures, cylindrical samples with a height of H=214 mm and diameter of Ø200 mm were prepared and submerged in water for 96 hours to monitor linear swelling. The CBR test procedure is shown in *Figure 2*.



*Fig. 1 ViaCalco 90 binder (left), binder and sediment (center) and stabilized sample preparation (right)*



*Fig.2 CBR sample preparation (left) and immersion in water procedure (right)*

## 3. RESULTS AND DISCUSSION

### 3.1. COMPACTION CHARACTERISTICS

The Proctor test results from the previous study (mixtures VC90-5 and VC90-7) indicated an increase in both $w_{opt}$ and $\rho_{d,max}$ with higher binder content. For samples stabilized with 5% binder by dry sample mass, a $\rho_{d,max}$ of 1.70 Mg/m³ and $w_{opt}$ of 16.9% were obtained. When 7% binder was added, a $\rho_{d,max}$ of 1.73 Mg/m³ and $w_{opt}$ of 19.4% were recorded.

The Proctor compaction curves for mixtures VC90-3 and VC90-9 are presented in *Figure 3*. The expected trend of increasing $\rho_{d,max}$ and $w_{opt}$ was confirmed for mixtures VC90-3 and VC90-9 as well. Given the high CaO content in the binder, an increase in $w_{opt}$ was anticipated, reaching 20.7% for the mixture with 9% binder addition. This can be explained with the hydration of CaO, which requires additional moisture from the sample. Furthermore, the increase in $\rho_{d,max}$ with higher binder content can be explained by the filling of pores between sediment particles with binder, as well as the higher specific surface area of the lime-based binder.

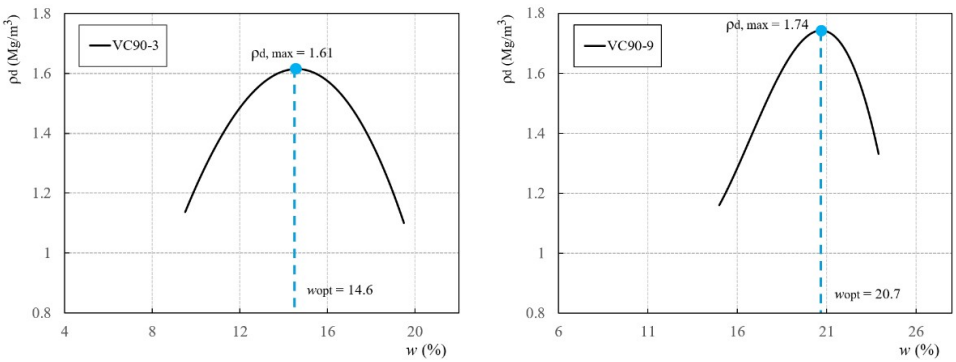


*Fig.3 Proctor compaction curves for stabilized mixtures: VC90-3 (left) and VC90-9 (right)*

## 3.2. UNCONFINED COMPRESSIVE STRENGTH

The combined UCS test results after 7 and 28 days of curing are presented in *Figure 4*.
The UCS value after 7 days could not be determined for mixture VC90-3 due to sample failure on the loading machine, which was also the case for mixture VC90-5 in the previous study. It can therefore be concluded that the minimum binder proportion for UCS testing after 7 days is 7% by dry sample mass. For mixture VC90-9, a compressive strength value of 0.23 MPa was recorded, representing a slight increase compared to the mixture with 7% binder content.
Considering the UCS results after 28 days of curing, a noticeable increase in strength compared to the 7-day values was observed. Strength values ranged from 0.13 to 0.40 MPa, with a clear trend of increasing strength with higher binder content. The highest strength value was recorded for mixture VC90-9. However, despite the increase in strength with higher binder content, none of the mixtures met the minimum requirement of 0.5 MPa after 7 days for application in a stabilized subgrade, as prescribed by the referent Technical Conditions [19].

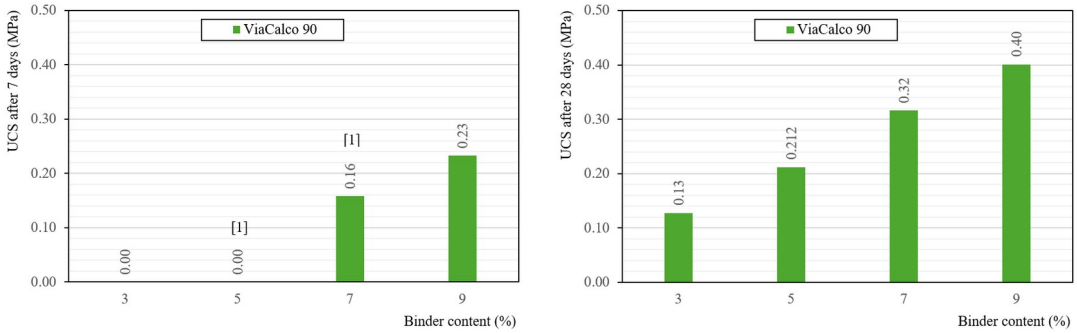


*Fig.4 UCS after 7 days (left) and 28 days (right) for all stabilized mixtures*

## 3.3. INDIRECT TENSILE STRENGTH

The ITS values after 28 days of curing for all mixtures are presented in Figure 5.
The ITS values for mixtures VC90-3 and VC90-5 could not be determined due to sample failure on the loading machine, indicating insufficient material cohesion. For mixtures VC90-7 and VC90-9, indirect tensile strength values of 0.05 and 0.07 MPa were recorded, respectively. A slight increase in indirect tensile strength with higher binder content was observed, consistent with the UCS results after 28 days of curing.
The ITS/UCS ratio for the tested mixtures was 0.156 for VC90-7 and 0.175 for VC90-9, which is in line with values typically reported in the literature for lime-stabilized fine-grained soils [20]. This result indicates a uniform development of both compressive and tensile strength of the material with increasing binder content.

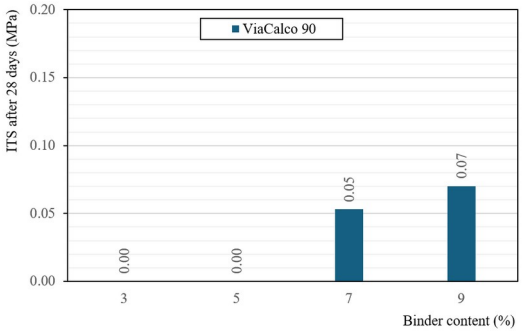


*Fig.5 ITS after 28 days for all stabilized mixtures*

### 3.4. CBR INDEX

The recorded CBR index values for all stabilized samples are presented in *Figure 6*. The non-stabilized sediment (data from the previous study) achieved a CBR value of 9.70%, indicating satisfactory bearing capacity even without stabilization, primarily for use as embankment fill or road subgrade. Regarding the stabilized samples, a continuous increase in CBR values with higher binder content was observed. The addition of 3% ViaCalco 90 binder resulted in only a minor change in the CBR value of the sample. However, at binder additions of 5% and 7% by dry sample mass, a more pronounced increase in CBR was recorded. When the binder content was increased from 7% to 9%, the CBR further increased by 6.57%, indicating that higher binder proportions do not necessarily lead to a significant improvement in CBR. Nevertheless, considering the achieved values, the application of 3% binder yields a medium quality subgrade (CBR = 8–20%), while higher binder proportions result in an excellent quality subgrade (CBR > 30%) [21].

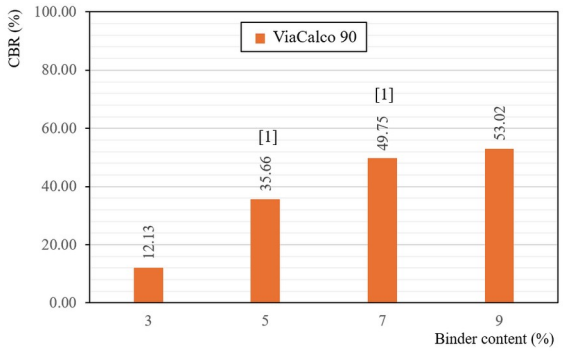


*Fig.6 CBR values for all stabilized mixtures*

## 4. CONCLUSIONS

Within this study, the influence of varying the content of the commercial lime-based binder ViaCalco 90, based on CaO, on the improvement of the physical and mechanical properties of sediment from the Begej River was investigated. Additional CBR and UCS testing after 7 days (for mixtures VC90-3 and VC90-9), as well as UCS and ITS testing after 28 days for mixtures with 3, 5, 7, and 9% binder content, were conducted. Based on the laboratory investigation, the following conclusions were drawn:

1. When conducting the Proctor compaction test, the expected increase in $w_{opt}$ and $\rho_{d,max}$ with higher binder content was confirmed. The increase in $w_{opt}$ is most likely due to the hydration of CaO in the binder, while the increase in $\rho_{d,max}$ is most likely from filling of pores in the sediment with binder particles;
2. An increase in CBR index was observed with higher lime binder content, with a more pronounced increase at lower binder additions (from 3% to 5%). At higher binder proportions (7% and 9%), values of 49.75% and 53.02% were achieved, respectively, with a decelerating trend in CBR increase between these two mixtures, similar to the trend observed for $\rho_{d,max}$. Stabilization of the sediment led to subgrade material of medium (for 3% of binder added) and excellent bearing capacity for higher binder contents;
3. UCS testing after 28 days indicated strength development over time. Furthermore, the UCS and ITS results confirmed an improvement in mechanical properties with increasing binder content. However, despite satisfactory CBR

values, none of the mixtures met the minimum strength requirement of 0.5 MPa for application in a stabilized subgrade, even after 28 days of curing;

4. The ITS/UCS ratio for mixtures VC90-7 and VC90-9 was 0.156 and 0.175, respectively, which is in line with typical values reported for fine-grained soils stabilized with lime.

Based on the obtained results, it can be concluded that stabilized sediment with a binder content of 5% and above significantly improves subgrade bearing capacity, as confirmed by the achieved CBR values. Future research should include mechanical testing after 56 days of curing, to provide a more comprehensive assessment of the long-term strength development of lime-stabilized sediment.

## ACKNOWLEDGEMENT

This research has been supported by the Ministry of Science, Technological Development and Innovation (Contract No. 451-03-34/2026-03/200156) and the Faculty of Technical Sciences, University of Novi Sad through project “Scientific and Artistic Research Work of Researchers in Teaching and Associate Positions at the Faculty of Technical Sciences, University of Novi Sad 2026” (No. 01-3609/1).

## REFERENCES

[1] Balkaya M. (2019). Beneficial Use of Dredged Material in Geotechnical Engineering. Environmental Science and Engineering, pp. 21–38. https://doi.org/10.1007/978-3-319-95888-0_3.

[2] Yoobanpot N., Jamsawang P., Simarat P., Jongpradist P., Likitlersuang S. (2020). Sustainable reuse of dredged sediments as pavement materials by cement and fly ash stabilization. Journal of Soils and Sediments, Volume 20, pp. 3807–3823. https://doi.org/10.1007/s11368-020-02635-x.

[3] Amar M., Benzerzour M., Kleib J., Abriak N.E. (2021). From dredged sediment to supplementary cementitious material: characterization, treatment, and reuse. International Journal of Sediment Research, Volume 36, pp. 92–109. https://doi.org/10.1016/j.ijsrc.2020.06.002.

[4] Kumar N., Kumar R. (2024). Geotechnical Properties of Lime-Stabilized Dredged Soil for Sustainable Construction Applications. National Academy Science Letters. https://doi.org/10.1007/s40009-024-01572-4.

[5] Rađenović D., Kerkez Đ., Tomašević Pilipović D., Dubovina M., Šešlija M., Tenodi S., Peško I. (2024). The beneficial reuse of contaminated sediment: Long-term assessment of fly ash and lime-based mixtures. Case Studies in Construction Materials, Volume 20. https://doi.org/10.1016/j.cscm.2023.e02711.

[6] Jamsawang P., Charoensil S., Namjan T., Jongpradist P., Likitlersuang S. (2021). Mechanical and microstructural properties of dredged sediments treated with cement and fly ash for use as road materials. Road Materials and Pavement Design, Volume 22, pp. 2498–2522. https://doi.org/10.1080/14680629.2020.1772349.

[7] Krstić P., Šešlija M., Ćirić N., Krsmanović S. (2025). Geotechnical properties of dredged sediment from Vojvodina for use in road construction. International Conference Synergy of Architecture and Civil Engineering, Faculty of Civil Engineering and Architecture, Niš, Serbia, pp. 489–499. https://doi.org/10.62683/SINARG2025.063.

[8] Institut za standardizaciju Srbije. (2018). SRPS EN ISO 17892-4:2017 Geotehničko istraživanje i ispitivanje - Laboratorijsko ispitivanje tla - Deo 4: Određivanje granulometrijskog sastava. Beograd.

[9] Institut za standardizaciju Srbije. (2015). SRPS EN ISO 17892-2:2015 Geotehničko istraživanje i ispitivanje - Laboratorijsko ispitivanje tla - Deo 2: Određivanje zapreminske mase. Beograd.

[10] Institut za standardizaciju Srbije. (2015). SRPS EN ISO 17892-1:2015 Geotehničko istraživanje i ispitivanje - Laboratorijsko ispitivanje tla - Deo 1: Određivanje vlažnosti. Beograd.

[11] Institut za standardizaciju Srbije. (2018). SRPS EN ISO 17892-12:2018 Geotehničko istraživanje i ispitivanje - Laboratorijsko ispitivanje tla - Deo 12: Određivanje tečenja i plastičnosti tla. Beograd.

[12] Institut za standardizaciju Srbije. (2012). SRPS EN 13286-2:2012 Nevezane i hidrauličkim vezivom vezane mešavine — Deo 2: Metode ispitivanja za laboratorijsku referentnu zapreminsku masu i sadržaj vode — Zbijanje po Proktoru. Beograd.

[13] ASTM International. (2017). D2487-17 Classification of Soils for Engineering Purposes (Unified Soil Classification System). ASTM International, West Conshohocken, PA. https://doi.org/10.1520/D2487-17E01.

[14] Institut za standardizaciju Srbije. (1968). SRPS U.B1.024:1968 Geomehanička ispitivanja - Određivanje sadržaja sagorljivih i organskih materija tla. Beograd.

[15] Carmeuse. (2025). Vezivo za puteve ViaCalco. https://www.carmeuse.com/rs-rs/proizvodi/gradevinarstvo/viacalco (accessed April 24, 2025).

[16] Institut za standardizaciju Srbije. (2012). SRPS EN 13286-42:2012 Nevezane i hidrauličkim vezivom vezane mešavine – Deo 42: Metoda ispitivanja za određivanje čvrstoće pri indirektnom zatezanju mešavina vezanih hidrauličkim vezivom. Beograd.

[17] Institut za standardizaciju Srbije. (2018). SRPS EN ISO 17892-7:2018 Geotehničko istraživanje i ispitivanje – Laboratorijsko ispitivanje tla – Deo 7: Ispitivanje jednoaksijalne čvrstoće pri pritisku. Beograd.

[18] Institut za standardizaciju Srbije. (2022). SRPS EN 13286-47:2022 Nevezane i hidrauličkim vezivom vezane mešavine – Deo 47: Metode ispitivanja za određivanje kalifornijskog indeksa nosivosti, neposrednog indeksa nosivosti i linearnog bubrenja. Beograd.

[19] JP Putevi Srbije. (2012). Priručnik za projektovanje puteva u Republici Srbiji; 8. Konstruktivni elementi puta; 8.2 Kolovozne konstrukcije. Beograd.

[20] Baldovino J.A., Moreira E.B., Izzo R.L.S., Rose J.L. (2018). Empirical Relationships with Unconfined Compressive Strength and Split Tensile Strength for the Long Term of a Lime-Treated Silty Soil. Journal of Materials in Civil Engineering, Volume 30, No. 8. https://doi.org/10.1061/(ASCE)MT.1943-5533.0002378

[21] Mladenović G. (2018). Predavanja iz predmeta Kolovozne konstrukcije. Građevinski fakultet u Beogradu, Beograd.

https://doi.org/10.24867/INDIS-2026-EN-502



# WELCOMING THE SECOND GENERATION OF EUROCODE 7 – RETAINING WALLS' ADDRESSING

*Aleksandar Andonov Sarev[1], Jovan Br. Papić[2], Kemal Edip[3], Viktorija Velinska[4], Miloš Šešlija[5] and Marjan Matić[6]*

***Summary:***

After years of extensive development and harmonization efforts, the new generation of Eurocodes (EC) entered into force in 2025. Although a transitional period allowing parallel application with the existing EC will remain in place until 2028, Member States have already initiated the process of adapting to the revised provisions and emerging design requirements. Among these developments, EC7 has undergone significant revisions that are also reflected in related standards. In contrast to its previous structure, EC7 is now presented in three separate parts, marking a substantial change in its organization and overall design framework. As part of the paper, a brief overview of the innovations in EC7 2025 will be given, while attention would be devoted to analyses of retaining walls and giving recommendations for them for the National Annex, in order to maintain the continuity of the experience that designers gained using EC7, both from the aspect of the calculation method and from the aspect of the achieved dimensions.

*Keywords: Eurocode 7 2025, National Annex, retaining walls, verification cases*

# DOBRODOŠLICA DRUGOJ GENERACIJI EVROKODA 7 – OBRAĆANJE POTPORNIH ZIDOVA

***Rezime:***

Nakon nekoliko godina opsežnog razvoja i usklađivanja, nova generacija evrokodova (EC) stupila je na snagu 2025. god. Iako će period tranzicije, koji omogućava paralelnu primenu sa postojećim EC, ostati na snazi do 2028., države članice su već započele proces prilagođavanja revidiranim odredbama i novim zahtevima za projektovanje. Među ovim promenama, EC7 je prošao kroz značajne revizije koje su takođe reflektovane u povezanim standardima. Za razliku od svoje prethodne strukture, EC7 je sada predstavljen u tri knjige, što predstavlja značajnu promenu u njegovoj organizaciji i opštem okviru projektovanja. Kao deo rada, biće dat kratak pregled novina u EC7 2025, dok će posebna pažnja biti posvećena analizama potpornih zidova i davanju preporuka za njih za Nacionalni aneks, kako bi se održao kontinuitet iskustava koje su projektanti stekli koristeći EC7, kako sa aspekta proračuna, tako i dimenzionisanja.

*Ključne reči: Evrokod 7 2025, Nacionalni aneks, potporni zidovi, verifikacioni slučajevi*

[1] MSc, GCM, Skopje, N. Macedonia, sarev@gcm.com.mk, ORCID 0009-0004-1533-684X
[2] Prof., Ss. Cyril and Methodius University in Skopje, Faculty of Civil Engineering, Skopje, N. Macedonia, papic@gf.ukim.edu.mk, ORCID 0000-0002-2952-302X
[3] Prof., Ss. Cyril and Methodius University in Skopje, IZIIS, Skopje, N. Macedonia, kemal@iziis.ukim.edu.mk, ORCID 0000-0003-3394-510X
[4] BSc, Ss. Cyril and Methodius University in Skopje, Faculty of Civil Engineering, Skopje, N. Macedonia, viki.velinska@gmail.com
[5] Prof., University of Novi Sad, Faculty of Technical Sciences, Novi Sad, Serbia, sele@uns.ac.rs, ORCID 0000-0002-8857-8952
[6] MSc, MHM Projekt, Novi Sad, Serbia, marjangrmatic@gmail.com

## 1. INTRODUCTION

The period following the introduction of Eurocode 7 (EC7) in 2010 has enabled the execution of numerous analyses and practical design applications, some of which have revealed certain limitations, including partially complex design procedures and challenges associated with the application of Design Approaches (DA). In response to these observations, the development of a new generation of Eurocodes was initiated in 2012, aiming to achieve greater harmonization of National Annexes (NA), introduce new chapters (e.g., groundwater, rock engineering, reinforced soil, ground improvement, numerical methods etc.), simplify design procedures, improve reliability management, and refine the definition of geotechnical categories. The current EC7 framework is primarily based on limit equilibrium methods and the use of partial factors (PF); accordingly, the second generation of Eurocode 7 (EC7 2025) introduces a restructured format consisting of three separate parts (Franzen, Batali and Burlon, 2026).

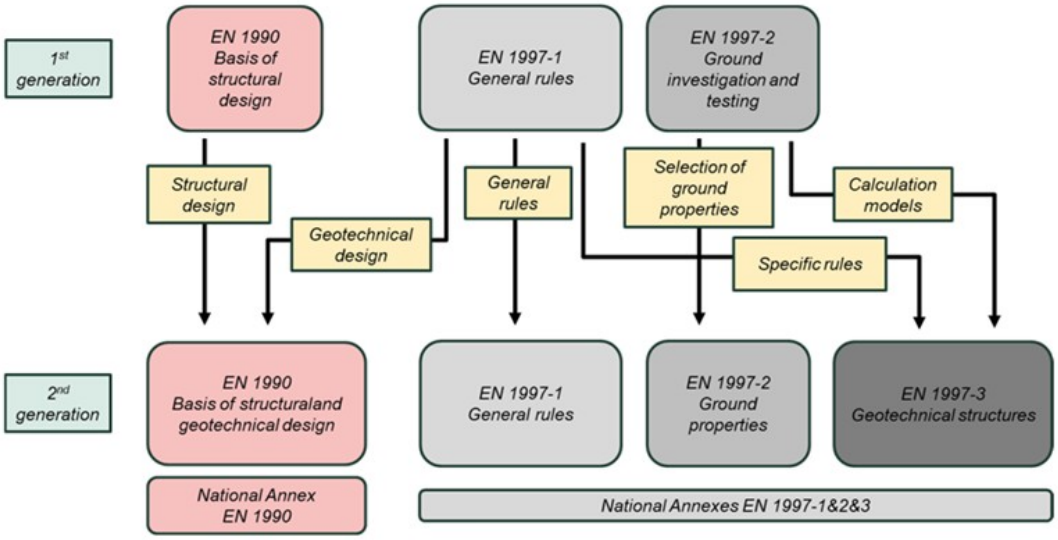


*Fig. 1 Reorganization of Eurocode 7 and Eurocode 0 in the second generation of Eurocodes*

As can be seen from Fig.1, one of the key changes is the transfer of the term “geotechnical design” from Book 1 of EC7 into the scope and title of the new generation of Eurocode 0 (EC0 2025). This shift also entails modifications to the fundamental verification format, facilitating a clearer distinction between the effects of actions and resistances in geotechnical structures. Significant updates are introduced in Book 3 of EC7 2025, which includes dedicated sections for the application of design methods tailored to specific types of geotechnical structures. Accordingly, a series of informative annexes have been introduced to provide additional guidance, such as Annex D for retaining walls (RW). At the same time, EC7 2025 advances the framework for the selection of design calculations and the definition of Nationally Determined Parameters (NDPs), with the aim of reducing inconsistencies and improving reliability in practical design (Bond et al., 2019).

## 2. CALCULATION METHODS IN EUROCODE 7 2025

Eurocode 7 has undergone several significant changes in order to address the perceived shortcomings of the first-generation code. One of the main changes is the replacement of separate verifications for ultimate limit states STR, EQU, GEO, UPL, and HYD with a unified verification based on the equations $E_d \leq R_d$ and $E_d \leq C_{d,ULS}$, where $E_d$ is the design effect of actions; $R_d$ is the design resistance to that effect; and $C_{d,ULS}$ is the design value of

deformation that causes an ultimate limit state to be exceeded in a supported structure. Another significant change is the replacement of DA with Verification Cases (VC) 1-4 (for determining effects of actions, $E_d$) and the Material and Resistance Factor Approaches, MFA and RFA (for determining resistance, $R_d$). In the EC7 2025, the design of retaining structures is addressed in Clause 7 of EC 7-3. There, retaining structure is defined as a structure that provides lateral support to the ground or that resists pressure from a mass of other material, which includes:

- gravity walls – retaining structures of stone or plain or reinforced concrete having a base spread foundation with or without a heel, ledge or buttress;
- embedded walls – relatively thin retaining structures of steel, reinforced concrete, or timber that is supported by anchors, struts and/or passive earth pressure;
- composite retaining structures – retaining structures composed of elements of gravity and embedded walls (Bond, Dietz and Jeanmarie, 2026).

In EC0 2025, a verification table A.1.8 is introduced defining the four VCs. These are prescribed for structural verification (VC1), static equilibrium and uplift (VC2), and geotechnical design (VC3 and VC4), thereby enabling a more streamlined application and reducing the number of required design combinations. Moreover, VC1 can also be used for geotechnical design, VC3 is typically used for design of slopes, embankments, spread foundations and gravity RW, while VC4 Is typically used for the design of transversally loaded piles and embedded RW and (in some countries) gravity RW.

| Action or effect | | | | Partial factors $\gamma_F$ and $\gamma_E$ for verification cases | | | | |
|---|---|---|---|---|---|---|---|---|
| Type | Group | Symbol | Resulting effect | Structural resistance[a] | Static equilibrium and uplift[b] | | Geotechnical design | |
| Verification case | | | | VC1[a] | VC2(a)[b] | VC2(b)[b] | VC3[c] | VC4[d] |
| Permanent action ($G_k$) | All[f] | $\gamma_G$ | unfavourable /destabilizing | 1,35$k_F$ | 1,35$k_F$ | 1,0 | 1,0 | $G_k$ is not factored |
| | Water[l] | $\gamma_{Gw}$ | | 1,2$k_F$ | 1,2$k_F$ | 1,0 | 1,0 | |
| | All[f] | $\gamma_{G,stb}$ | stabilizing[g] | not used | 1,15[e] | 1,0 | not used | |
| | Water[l] | $\gamma_{Gw,stb}$ | | | 1,0[e] | 1,0 | | |
| | All | $\gamma_{G,fav}$ | favourable[h] | 1,0 | 1,0 | 1,0 | 1,0 | |
| Prestressing ($P_k$) | | $\gamma_P$[k] | | | | | | |
| Variable action ($Q_k$) | All[f] | $\gamma_Q$ | unfavourable | 1,5$k_F$ | 1,5$k_F$ | 1,5$k_F$ | 1,3 | $\gamma_{Q,red}$[j] |
| | Water[l] | $\gamma_{Qw}$ | | 1,35$k_F$ | 1,35$k_F$ | 1,35$k_F$ | 1,15 | 1,0 |
| | All | $\gamma_{Q,fav}$ | favourable | 0 | | | | |
| Effects of actions ($E$) | | $\gamma_E$ | unfavourable | $\gamma_E$ is not applied | | | | 1,35$k_F$ |
| | | $\gamma_{E,fav}$ | favourable | | | | | 1,0 |

*Fig. 2 Partial factors for actions and action effects in Verification Cases*

Within the VC, both the Material Factor Approach (MFA) and the Resistance Factor Approach (RFA) are adopted, with their respective combinations specified in Book 3 for different types of geotechnical structures (e.g., slopes, shallow foundations, RW) (Figure 3). PF for materials and resistances are again defined through NDPs and NA, now aligned with the structure of the new Book 3. In this context, PF values continue to be derived from the established sets M1 and M2, including parameters such as $\tan\varphi$, $c$, and $c_u$, for persistent, transient, and accidental design situations. At first glance, EC7 2025 appears to retain the same basic values for PF for actions, resistance and shear strength parameters as in the previous edition which is very important initial step towards introducing the EC 2025 (e.g., M1 set has value of 1,00 for all parameters, while 1,25 for set M2); however, the updated M2 set is extended to include parameters such as residual strength and rock mass strength!

A significant advancement is the introduction of modification factors K applied to PF: K for actions; $K_M$ if MFA is applied; $K_R$ – for RFA. The values of K are selected based on consequence classes (CC), reflecting the consequences associated with the structure, as defined in EC7-1 2025. Recommended values of K=0,9/1,0/1,1 are respectively provided for CC1 (low) / CC2 (normal) / CC3 (high consequences) although individual countries may adjust them within NA, as illustrated in Papić, Andonov-Sarev, and Maraš (2023). EC7 2025 also gives examples for different CC: RW and foundations supporting buildings with low occupancy, slopes in areas where a failure will have low impact, minor road/railway embankments not vital for society etc. are in CC1; in CC3 are RW and foundations supporting public buildings, slopes and retaining structures with high exposure, major road/railway embankments, bridge foundations that can cause severe interruption of service in emergency situations, flood barrier protecting a large number of people, underground constructions with large occupancy etc., while in CC2 are all geotechnical structures not classified as CC0 (not applicable for geotechnical structures), CC1, CC3 and CC4 (geotechnical structures whose integrity is of vital importance for civil protection or in areas with significant landslide hazards).

| Material Factor Approach (MFA) | Resistance Factor Approach (RFA) |
|---|---|
| **Overall Stability:** EN 1997-3, Clause 4 | |
| **Bearing/sliding resistance of gravity walls:** EN 1997-3 §7.6.9, Table 7.2 (NDP) | |
| (a): VC4 ($\gamma_E$) + M1 ($\gamma_M$=1) and (b): VC3 ($\gamma_F$) + M2 ($\gamma_M$) or (c): VC1 ($\gamma_F$) + M2 ($\gamma_M$) | (d): VC1 ($\gamma_F$) + ($\gamma_{RN}$) or ($\gamma_{RT}$) for bearing or sliding<br>(e): VC4 ($\gamma_E$) + ($\gamma_{RN}$) or ($\gamma_{RT}$) for bearing or sliding |
| **Bearing/rotational resistance of embedded walls:** EN 1997-3 §7.6.9, Table 7.2 (NDP) | |
| (a): VC4 ($\gamma_E$) + M1 ($\gamma_M$=1) and (b): VC3 ($\gamma_F$) + M2 ($\gamma_M$)<br>(c): not used | (d): VC1 ($\gamma_F$) + ($\gamma_{Re}$)<br>(e): VC4 ($\gamma_E$) + ($\gamma_{Re}$) |
| **Basal Heave:** EN 1997-3 §7.6.9, Table 7.2 (NDP), Annex D | |
| (a): VC4 ($\gamma_E$) + M1 ($\gamma_M$=1) and (b): VC3 ($\gamma_F$) + M2 ($\gamma_M$)<br>(c): not used | (d): VC1 ($\gamma_F$) + ($\gamma_R$)<br>(e): VC4 ($\gamma_E$) + ($\gamma_R$) |

| Verification of | Partial factor on | Symbol | Material Factor Approach (both (a) and (b) or only (c)) (a) | (b) | (c) | Resistance Factor Approach (d) | (e) |
|---|---|---|---|---|---|---|---|
| Overall stability Gravity walls | Based on Clause 4 (Slopes, cuttings, and embankments) | | | | | | |
| | Actions, Effects of actions | $\gamma_F$, $\gamma_E$ | VC4 | VC3 | VC1 | VC1 | VC4 |
| | Ground properties | $\gamma_M$ | M1 | M2 | M2 | Not factored | |
| | Bearing resistance | $\gamma_{RN}$ | Not factored | | | 1,4 | |
| | Sliding resistance | $\gamma_{RT}$ | | | | 1,1 | |
| Embedded walls | Actions, Effects of actions | $\gamma_F$, $\gamma_E$ | VC4 | VC3 | Not used | VC1 | VC4 |
| | Ground properties | $\gamma_M$ | M1 | M2 | | Not factored | |
| | Vertical resistance, basal heave | $\gamma_R$ | Not factored | | | 1,4 | |
| | Passive earth resistance | $\gamma_{Re}$ | | | | 1,4 | |

*Fig. 3 Basic design situations for retaining structures*

Table 1 shows comparison of the parameters as given below.

*Tab. 1 Comparison of partial factors in set M2 between the current EC7 and the EC7 2025*

| Material | Parameters | Set M2 | |
|---|---|---|---|
| | | EC7 | EC7 2025 |
| Soil | Shear strength under effective stresses ($\tau$) | 1,25 | 1,25 $K_M$ |
| | Peak angle of shear strength (tan $\varphi'_{peak}$) | 1,25 | 1,25 $K_M$ |
| | Peak effective cohesion ($c'_{peak}$) | 1,25 | 1,25 $K_M$ |
| | Critical state friction angle (tan $\varphi'_{cv}$) | 1,25 | 1,1 $K_M$ |
| | Residual friction angle (tan $\varphi'_{res}$) | / | 1,1 $K_M$ |
| | Residual effective cohesion ($c'_r$) | / | 1,1 $K_M$ |

| | | | |
|---|---|---|---|
| | | | |
| | Shear strength under effective stresses ($c_u$),<br>Uniaxial compressive strength ($q_u$) | 1,4 | 1,4 $K_M$ |
| Rock – masive | Shear strength ($\tau$) | / | 1,25 $K_M$ |
| | Uniaxial compressive strength ($q_u$) | | |
| Rock – discontinuity | Shear strength ($\tau_{dis}$) | / | 1,25 $K_M$ |
| | Angle of residual friction (tan $\varphi'_{dis}$) | / | 1,1 $K_M$ |
| Contact | Interface friction between soil and structure (tan $\delta$) | / | 1,25 $K_M$ |

## 3. CALCULATION COMPARISON

The first step in the verification is checking the condition $Ed \leq Rd$ where the design effects of actions should be less than or equal to the design resistances. The design effects have so far been determined using an equation valid for linear systems, where the factorization of actions is applied directly. However, it does not recognize that some actions, such as soil pressure, also depend on material properties. This is especially true for RW where bending moments induced by the soil occur. Accordingly, there are cases where the PF is applied to the load and the increase in action $\gamma_F \cdot Fk$ can cause an increase in the effect greater than the factor $\gamma_F$ itself, i.e. a superlinear structural response. The opposite also applies, where the effect increases with a value smaller than $\gamma_F$, for the same increase in action as before (Bond et al., 2019). Extending the expression in EC7 2025 by the term $X_{Rd}$ which emphasizes that the action depends on the characteristics of the design material used in assessing the resistance, the formula can be smoothly applied when checking VC1, VC2, and VC3, and when nonlinearity is expected, the VC4 procedure is recommended, where PF are directly assigned to the effects of actions. Also, in EC7 2025, according to the "single source" concept, all actions are treated as single if they generate effects that are related or correlated with each other, even if they act on different parts of the structure. In most cases, the resistances of geotechnical structures depend on material characteristics entered as design values $X_d$ in the analysis. Thus, according to EC0 2025, the resistance values $R_d$ when applying RFA will be obtained using the formula:

$$R_{Td} = \frac{N'_d \tan \delta_{rep}}{\gamma_{RT}} \tag{1}$$

where $\delta_{rep}$ represents the shear resistance angle between the soil and the structure, which for concrete cast directly on the ground in this particular case is taken as $2/3\varphi$, as a precaution measure, although $\varphi$ would be in accordance with recommendations given in EC7 (table 2). The new regulations require that the effective angle of resistance, when checking base sliding, should always be taken in the critical state ($\varphi_{cv}'$), and if the Mohr–Coulomb approach is used, the value of effective cohesion $c'$ at the foundation base should be taken as zero.

*Table 2. Recommended interface factors and interface friction angles for foundation sliding verification according to EC7 2025*

| ***Interface condition*** | $k_{interface}$ | Recommended value $\delta$ |
|---|---|---|
| *Concrete cast directly against soil* | 1.0 | $\varphi_{cv}'$ |
| *Roughened interface* | 1.0 | $\varphi_{cv}'$ |

| | | |
|---|---|---|
| *Smooth precast concrete* | 2/3 | 2/3 $\varphi_{cv}'$ |

The values presented in Table 2 illustrate that EC7 2025 distinguishes interface behaviour according to surface roughness rather than the structural material itself. Consequently, concrete cast directly against the soil is treated as a rough interface ($k_{interface}$), whereas smooth precast concrete interfaces are assigned a reduction factor of 2/3. Compared with the first generation of EC7, where recommendations on interface friction were distributed throughout different clauses, EC7 2025 introduces a unified framework based on interface factors. This provides a more transparent and consistent treatment of soil–structure interaction while preserving the underlying design philosophy.

For comparison of the calculation approaches between the current EC7, where DA2 / DA2* are dominantly proposed for RW design in the region, and the EC7 2025, a parametric analysis was performed and the achieved safety factors were compared (Andonov Sarev et al., 2025). Figure 4 illustrates the geometry of the analysed reinforced concrete RW, which was verified with respect to bearing capacity, sliding resistance and overturning stability. For the sake of simplicity, only results from RFA are given, as it is the same approach applied in DA2. The results show that VC1 using the M1 set within the RFA represents the closest equivalent to the so far implemented DA, which is similar to the recommendations of Bogusz (2024). The adopted geometry, material properties and loading conditions are summarized in Table 3, while the corresponding PF considered in the analyses are presented in Table 4. To further confirm the correspondence between DA2* and VC1 (RFA), a parametric study was carried out considering a RW with identical geometric characteristics subjected to constant loading conditions. The verification results obtained for all considered approaches are summarized in Table 5.

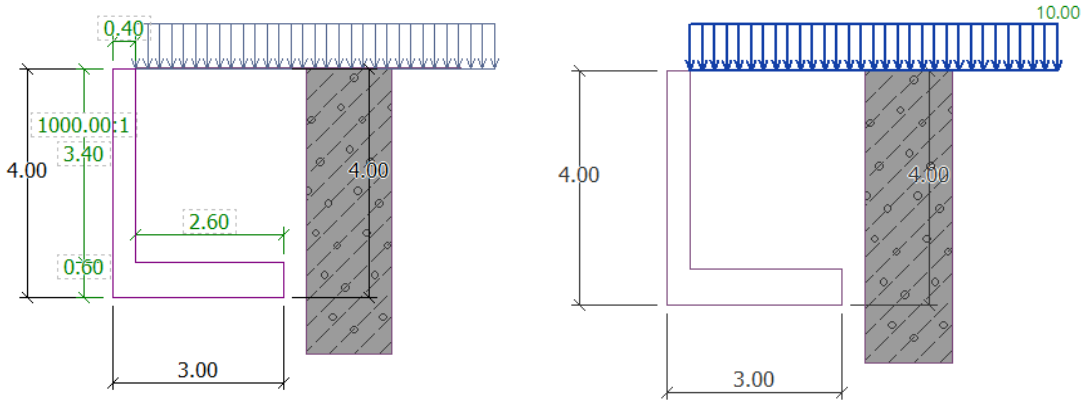


*Fig. 4 Cross-section of the analyzed reinforced concrete retaining wall*

*Table 3. Geometry, material properties and loading conditions adopted in the analyses*

| Parameter | Symbol | Value | Unit |
|---|---|---|---|
| Retaining wall height | H | 4.0 | m |
| Foundation width | B | 3.0 | m |
| Foundation length | L | 1.0 | m |
| Foundation embedment depth | $D_f$ | 0.6 | m |
| Soil unit weight | γ | 20 | kN/m³ |
| Concrete unit weight | $\gamma_c$ | 25 | kN/m³ |
| Effective cohesion | c′ | 5 | kPa |
| Effective friction angle | φ′ | 28 | ° |

| | | | |
|---|---|---|---|
| Uniform surcharge | q | 10 | kPa |

*Table 4. Partial safety factors adopted for the considered verification cases*

| Partial factor | DA2 / DA2* | VC1 (RFA) | VC4 (RFA) |
|---|---|---|---|
| $\gamma_{G,unf}$ | 1.35 | 1.35 | 1.00 |
| $\gamma_{G,fav}$ | 1.00 | 1.00 | 1.00 |
| $\gamma_{Q,unf}$ | 1.50 | 1.50 | 1.11 |
| $\gamma_{E,unf}$ | 1.00 | 1.00 | 1.35 |
| $\gamma_{E,fav}$ | 1.00 | 1.00 | 1.00 |
| $\gamma_{\varphi}$ | 1.00 | 1.00 | 1.00 |
| $\gamma_{c}$ | 1.00 | 1.00 | 1.00 |
| $\gamma_{Rv}$ | 1.40 | 1.40 | 1.40 |
| $\gamma_{Rh}$ | 1.10 | 1.10 | 1.10 |

*Table 5. Ultimate limit state verification results for the analysed design approaches*

| Verification | Quantity | DA2* | VC1 (RFA) | VC4 (RFA) |
|---|---|---|---|---|
| Bearing capacity | Design action, Nd (kN) | 199.80 | 199.80 | 148.00 |
| | Design resistance, Rd (kN) | 265.99 | 241.41 | 241.41 |
| | Factor of Safety | 1.33 | 1.21 | 1.63 |
| | Utilization (%) | 75.12 | 82.76 | 61.31 |
| Sliding | Driving force, Td (kN) | 65.03 | 65.03 | 48.17 |
| | Sliding resistance, RT,d (kN) | 71.54 | 71.54 | 71.54 |
| | Factor of Safety | 1.10 | 1.10 | 1.49 |
| | Utilization (%) | 90.90 | 90.90 | 67.34 |
| Overturning | Stabilizing moment, Mstb (kNm) | 167.87 | 167.87 | 167.87 |
| | Destabilizing moment, Mdst (kNm) | 78.08 | 78.08 | 78.08 |
| | Net resisting moment, Mres (kNm) | 89.79 | 89.79 | 89.79 |
| | Factor of Safety | 2.15 | 2.15 | 2.15 |
| | Utilization (%) | 46.51 | 46.51 | 46.51 |

Although table A.1.8 describes that VC4 is typically used for design of embedded RW, the results demonstrate a very good agreement between DA2* and VC1 (RFA), particularly with respect to the sliding verification. This similarity is expected because both approaches (DA2 / DA2* and VC1) are based on essentially the same resistance-based design philosophy and employ identical PF, at least for CC2. But, VC4 (RFA) produces progressively higher safety margins, resulting in a nonlinear increase in the calculated sliding safety factor that becomes more pronounced as the effective friction angle increases, partly due to the different PF. The obtained results are consistent with the findings reported by Andonov Sarev et al. (2025), who demonstrated that the factors of safety obtained using VC1 (RFA) closely correspond to those calculated using DA2* for different loading conditions and RW configurations, including gravity retaining walls.

Similar trends have also been observed for RW of different height supporting both coarse-grained (cohesionless) and fine-grained (cohesive) soils (Velinska, 2026). This agreement confirms that, for structures belonging to CC2, the 1st and 2nd generation EC7 provide essentially equivalent safety levels when equivalent calculation procedures and corresponding PF are adopted. Consequently, the transition from the current DA2-based design methodology to the new verification framework based on RFA can be implemented for RW without significant changes in the design tradition, resulting reliability and structural dimensions.

## 4. CONCLUSIONS

This paper briefly outlines key innovations introduced by the new generation of EC, which entered into force in 2025, including renaming the EC0 2025 into "Basics of structural and geotechnical design", the restructuring of EC7 into three parts, some new chapters, the revision of VC, and the introduction of CC-dependent PFs. This aspect has been studied in the paper for the need of RW, which are also described in the informative Annex D. Particular attention is given to the implications for the future NA of EC7 2025, with the aim of preserving continuity with the design experience gained so far with EC7. Important first step is that the basic values of PF are kept the same as in the previous generation of EC7. So, respecting that DA2/DA2*, as resistance reduction based approach, has been adopted for RW design in the region, the VC1 with RFA is acceptable for introducing, since VC4 slightly differs, at least for sliding stability, while some attention could also be paid for selecting an appropriate K, as its value is CC-dependent.

## REFERENCES

[1] Andonov Sarev A., Papić Br. J., Josifovski J., Maraš M. (2025). Transgeneracijska stabilnost proračuna potpornih zidova. *Geotehnički aspekti građevinarstva i zemljotresno inženjerstvo*, Vrnj. Banja, Srbija, 15-17 oktobar, pp. 93-102, https://doi.org/10.46793/GEOAG25.093AS

[2] Bogusz W. (2024). Eurocode 7 – Second Generation: Retaining structures – Looking beyond the partial factors for safety in design. *Proceedings of the XVIII ECSMGE*, Lisbon, Portugal, august 2024, pp. 1475-1480, https://doi.org/10.1201/9781003431749-271

[3] Bond A., Dietz K., Jeanmarie T. (2026). 2nd generation of Eurocode 7 – Retaining structures and anchors. *Proceedings of the 21st ICSMGE*, Vienna, Austria, 14-19 June 2026, pp. 6793-6798, https://doi.org/10.53243/ICSMGE2026-781

[4] Bond A., Janner C., Moormann C. (2019). Tomorrow's geotechnical toolbox: EN 1997-3:202x Geotechnical structures. *Proceedings of the XVII ECSMGE*, Reykjavik, Iceland, september 2019

[5] EN 1990-1:2023. Eurocode – Basis of structural and geotechnical design

[6] EN 1997-1:2025. Eurocode 7: Geotechnical design – Part 1: General rules

[7] EN 1997-3:2025. Eurocode 7: Geotechnical design – Part 3: Geotechnical structures

[8] Franzen G., Batali L., Burlon S. (2026). 2nd Generation of Eurocode 7 – Overview. *Proceedings of the 21st ICSMGE*, Vienna, Austria, 14-19 June 2026, pp. 6817-6822, https://doi.org/10.53243/ICSMGE2026-769

[9] Papić J. Br., Andonov-Sarev A., Maraš M. (2023). Evrokod 7 202x i JUS 1990: tako daleko, a nikad bliži. *Geotehnički aspekti građevinarstva i zemljotresno inženjerstvo*, Vrnjačka Banja, Srbija, 1-3. novembar, pp. 299-308.

[10] Velinska V. (2026). Designing of retaining wall in urban area according to the first generation of eurocodes and with EC7 2025. Diploma thesis (in Macedonian). Ss. Cyril and Methodius University in Skopje, Faculty of Civil Engineering, N. Macedonia

https://doi.org/10.24867/INDIS-2026-EN-510



# THE INFLUENCE OF SEDIMENT-DERIVED MINERAL ADMIXTURES ON BITUMEN-FILLER INTERACTION AND THE PERFORMANCE OF ASPHALT MIXTURES: A SYSTEMATIC REVIEW OF THE LITERATURE

*Branko Ranković[1], Miloš Šešlija[2], Milan Draganović[3], Nikola Grubić[4]*

***Summary:***

This paper provides an overview of the possibility of using sedimentary materials as a substitute for part of the mineral filler in asphalt mixtures. Research shows that sediments with high organic matter content and large Rigden voids increase the need for binder and adversely affect compaction and mechanical properties. Heat treatment and a limited degree of filler replacement can improve stiffness, rutting resistance and moisture resistance. NMR and FTIR analyzes indicate that the increase in stiffness is a consequence of the physical stiffening of the filler-bitumen system, and not a change in the molecular structure of the bitumen. The flow curves show that the appropriate proportion of filler reduces the irreversible deformation and increases the resistance to permanent flow. It is concluded that sedimentary materials are a promising and sustainable alternative to traditional fillers, with property control, pre-treatment and optimization of binder content.

*Keywords:* ***Sediment, filler, asphalt mastic, sustainable materials.***

# UTICAJ SEDIMENTNIH MINERALNIH PRIMESA NA INTERAKCIJU BITUMEN-FILER I PERFORMANSE ASFALTNIH MEŠAVINA: SISTEMATSKI PREGLED LITERATURE

***Rezime:***

Ovaj rad daje pregled mogućnosti primene sedimentnih materijala kao zamene za deo mineralnog filera u asfaltnim mešavinama. Istraživanja pokazuju da sedimenti sa visokim sadržajem organske materije i velikim Rigdenovim šupljinama povećavaju potrebu za vezivom i nepovoljno utiču na zbijanje i mehaničke karakteristike. Termička obrada i ograničen stepen zamene filera mogu poboljšati krutost, otpornost na kolotraženje i otpornost na vlagu. NMR i FTIR analize ukazuju da je povećanje krutosti posledica fizičkog ukrućivanja sistema filer-bitumen, a ne promene molekularne strukture bitumena. Krive tečenja pokazuju da odgovarajući udeo sedimednta kao filera smanjuje nepovratnu deformaciju i povećava otpornost na trajno tečenje. Zaključuje se da su sedimentni materijali perspektivna i održiva alternativa tradicionalnim filerima, uz kontrolu svojstava, prethodnu obradu i optimizaciju sadržaja veziva.

*Ključne reči:* ***Sediment, filer, asfaltni mastiks, održivi materijali***.

[1] MSc (Master of Engineering) Civil Engineering, Teaching Assistant (Assistant in Teaching), Faculty of Civil Engineering and Architecture, University of Niš, Niš, Serbia, branko.rankovic@gaf.ni.ac.rs, ORCID 0009-0001-7358-3038
[2] Associate Professor, Faculty of Technical Sciences, University of Novi Sad, Novi Sad, Serbia, sele@uns.ac.rs, ORCID 0000-0002-8857-8952
[3] MSc (Master of Engineering) Civil Engineering, Assistant, Faculty of Civil Engineering and Architecture, University of Niš, Niš, Serbia, ORCID 0009-0001-5907-9388
[4] BEng (Bachelor of Engineering) Civil Engineering, Teaching Assistant (Assistant in Teaching), Faculty of Civil Engineering and Architecture, University of Niš, Niš, Serbia

## 1. INTRODUCTION

Increased road traffic load, along with changes in climate conditions that include more frequent periods of high temperatures and more intense moisture effects, impose the need to develop asphalt mixes that are more resistant to rutting and have a longer service life. For this purpose, various material modifications, such as polymers or synthetic reinforcing components, are introduced into the asphalt structure. In addition, it is possible to use waste material such as fly ash and others. This affects the behavior under repeated loads and weather-related degradation. As one of the most significant examples of the application of waste material to improve the characteristics of asphalt, the addition of sedimentary admixtures can be mentioned [1,4,5].

Filler, that is, a very small mineral fraction, is one of the key factors that shape the geological and mechanical properties of asphalt mixtures. It complements the granulometric composition, contributes to the compaction and formation of mastic, more precisely to the formation of the asphalt-filler system. It is also characterized by the role of binding, but also of transmitting voltage at the micro level. The literature clearly indicates that the filler is not only a "gap filler", its effect includes volume filling, but also particle structuralization and physico-chemical interactions with bitumen [1,7,10]. Accordingly, the granulometry of the filler, its specific surface area, mineralogical composition and chemical activity can significantly affect the stiffness of the mastic, the resistance to damage and the behavior of the mixture at different temperatures [7,10].

Although limestone powder has traditionally been the most common filler, rising costs and sustainability requirements are encouraging the consideration of waste materials as an alternative. In addition, in support of this idea, there is a need to reduce the amount of waste for landfilling, savings in the exploitation of mineral resources, and therefore the overall impact of the production of asphalt mixtures on the environment [1,9]. The possibilities of application of these materials largely depend on their physical and chemical properties and the way of pre-treatment. Sediments, which include deposited material in waterways and waste silite (silicon oxide), are becoming particularly important in recent research. They often have a porous structure, increased specific surface area and variable content of organic matter. These characteristics can lead to higher bitumen absorption, changing the bitumen-filler ratio, leading to an increased optimum binder content [5].

Investigations of waste silite show that in the case of application of the original material, there may be a limited or even unfavorable influence on the stiffness of the asphalt mixture. However, if calcination is applied, i.e. heating of the material at high temperatures, the structure of the silite can be significantly improved and the sensitivity of the mixture to actual moisture can be reduced. In research [3] thermally treated silite showed an increase in stiffness and rutting resistance, while the use of untreated material led to a decrease in stiffness. Also, calcination led to an increase in the indirect tensile strength of the asphalt mixture after the action of water, indicating improved moisture resistance.

Research has shown that the behavior of sediment filler depends on its share in the mixture. By increasing the amount of fine and porous particles, there is an increased need for bitumen and an increase in the content of air voids, which is reflected in workability, sensitivity to moisture and resistance to rutting [4,5]. For these reasons, the sediment cannot be evaluated only on the basis of one property, but it is necessary to simultaneously analyze its influence on stiffness, permanent deformations, fatigue and degradation caused by moisture [1,7,10].

This paper provides an overview of the application of sedimentary materials, with an emphasis on the application of sediment deposited in waterways. The influence of the

type of sedimentary materials, its properties and the influence of the pretreatment of this material on the characteristics of the asphalt mixture was analyzed. The results of the research that deal with the problem of resistance to rutting, the effect of moisture, as well as the fatigue of asphalt mixtures are presented.

## 2. CHARACTERISTICS AND INFLUENCE OF SEDIMENTARY ADMIXTURES ON ASPHALT MASTIC AND PROPERTIES OF ASPHALT MIXTURES

### 2.1. CHARACTERISTICS OF FILLER AND SEDIMENTAL IMPURITIES

The quality and behavior of asphalt mixtures, apart from aggregates and bitumen, depend to a great extent on the properties of the mineral filler. Sediment admixtures (fine fractions from waterways/sediment landfills) can be introduced as a filler replacement, or as an additional fraction in the asphalt-bitumen system. It is known that filler acts on the volumetric filling of voids, mastic structuring and physical-chemical interaction of particles and bitumen [7,9,10].

When sedimentary admixtures are used instead of or together with traditional filler, it is a complex material, whose changes in mineralogy, porosity and morphology can lead to different degrees of adhesion/cohesion. In addition, there may be potential impacts on the moisture resistance and durability of the asphalt mixture. In addition, if the sediments contain contaminants, there may be ecological aspects (e.g. leaching of contaminants), which have been highlighted in the literature [5,11].

Research has shown that the performance of an asphalt mixture with sediment/waste fillers is not determined only by the amount of additives, but also by the complex physical, chemical and microstructural properties of the fillers. This primarily refers to the formation of the mastic (asphalt-filler system), the degree of interaction with the bitumen and the ability of the material to "hold" stability and resistance to rutting and moisture-related damage [5,7].

Porous sediments rich in organic matter may require a higher amount of binder, (by 4.6% to 6.3%), which represents approximately 24-37% relative increase in the optimum bitumen content [2,4].

Research has shown that the physical properties of fillers from deposited waste materials affect compaction and durability by changing the viscoelastic characteristics of the mastic [8,9]. In the works, it is emphasized that it is necessary to choose and control the fineness and monitor the distribution of particles, because this changes the porosity and the spatial contact with the bitumen [5]. Also, the role of granulometry as a mechanism for filling voids and structuring mastic is emphasized [2,7,8].

It is concluded that if the sediment has appropriate properties and is properly prepared beforehand, it can be used as a substitute for traditional filler, but with the control of its influence on bitumen consumption and asphalt mixture durability.

## 3. THE INFLUENCE OF SEDIMENTAL ADMIXTURES ON ASPHALT MASTIC AND THE PROPERTIES OF ASPHALT MIXTURES

The application of sedimentary, or mineral fillers, in the formation of asphalt mastic, is not limited only to volume filling of cavities. Its application depends to a significant extent on intergranular voids (Rigden Voids, RV), specific surface area, acidity/alkalinity, content of organic matter and filler/bitumen mass ratio (F/A) [5,7].

Fouad Belalayli et al. [5] investigated untreated and thermally treated waste sludge in comparison with limestone filler. River sediments (ASL, ARS, MEL, NSL) were compared with limestone filler in mastic-asphalt. They showed that raw sediment can only replace up to about 20% of the filler. They concluded that MEL and NSL are of limited use due to high organic matter content and high RV, which increases binder absorption and leads to excessive bitumen consumption. They also showed that calcination at 550ºC removed organic matter more effectively than treatment with 3% calcium oxide (CaO). In the research of Abbas Solouki et al. [4], it was concluded that mastic with calcined NSL (NSLC) gives up to 80% better mechanical performance compared to the mixture with raw sediment. By using a softer bitumen (50/70 instead of 35/50), it is possible to substitute up to 23% of filler while reducing the amount of bitumen up to 19% [5]. Figure 1 shows the influence of organic compounds on bitumen absorption.

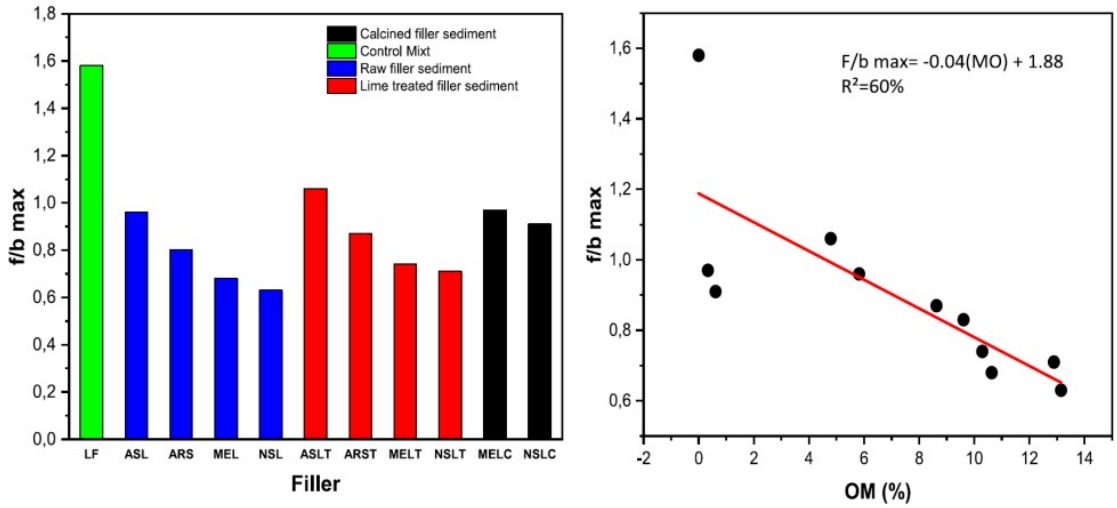


*Figure 1 The influence of organic compounds on the absorption of bitumen [5].*

Wenyi Xu et al. [7] explain this dependence by saying that at a low filler content, the mastic behaves like a diluted suspension, while around a volume fraction of filler of about 40%, the particles are connected in a network and the stiffness increases sharply. FTIR does not show absorption peaks, so the interaction is mainly physical, ie absorption of polar fractions of bitumen and dispersion of waxy crystals. The specific surface mostly determines the ability to interact, and the filler/binder mass ratio should be kept below 1.5 [7]. Aboelkasim Diab and Mahmoud Enieb confirm this by NMR. They concluded that the changes in penetration, softening point and penetration index are not the result of a change in the molecular structure of bitumen, but rather a physical strengthening that depends on the type and concentration of the filler. The static flow and recovery curves shown in Figure 2 additionally show that an increase in the proportion of filler reduces the total and especially irreversible deformation after unloading, i.e. increases the mastic's resistance to permanent flow. At the same time, the differences between the fillers used confirm that the performance is not only affected by their quantity, but also by the type, i.e. the ability to form a stiffer mastic structure [10].

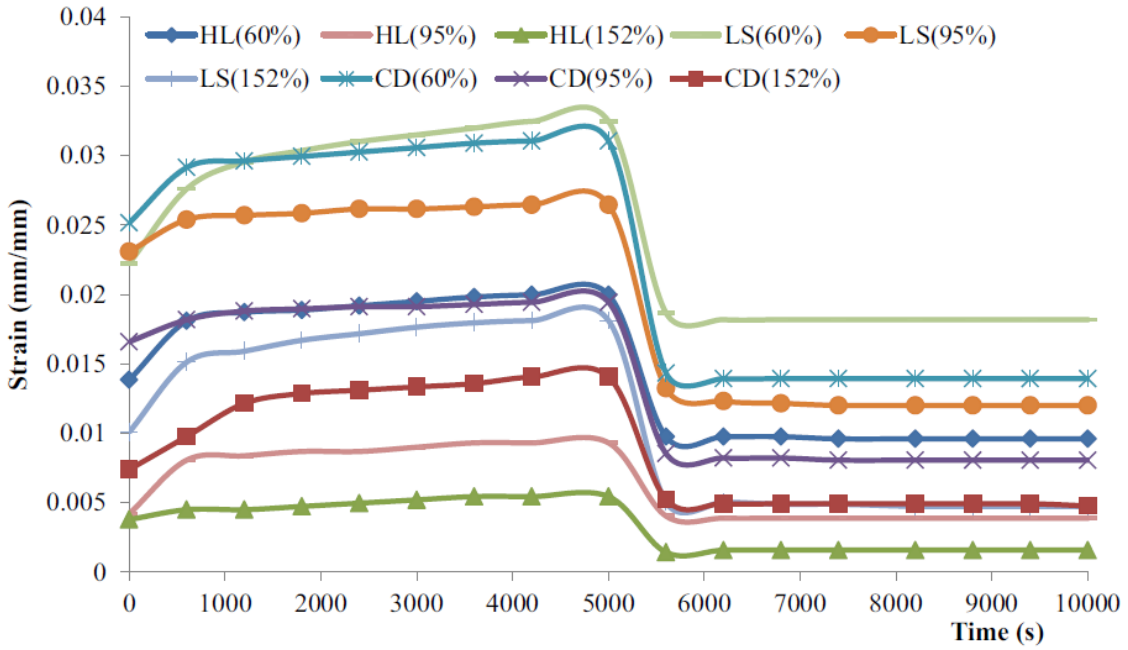


*Figure 2 Flow curve of different asphalt mixtures at 25°C [10].*

Hasan Al-Mosawe et al. [12] showed that the type and proportion of fillers significantly influence MSCR[1], LAS[2] and adhesion strength on limestone dust, portland cement and hydrated lime at F/A = 0.6-1.2 (approximately 20-45% filler replacement). Hydrated lime increases the resistance to rutting and athesia the most, but at higher dosages it excessively stiffens the mastic and shortens its service life. Portland cement at F/A=0.8 stands out as a compromise as the optimal formulation, as it provided the most balanced relationship between low permanent deformation, satisfactory fatigue resistance and good adhesion strength.

Solouki et al. [4] investigated the same problem with waste sludge from water treatment, because sludge is a sedimentary fraction with a higher fineness and a greater ability to absorb water and binders than limestone filler.

According to ASTM D1559 and the Asphalt Institute gradation for the wearing course, Noman Khan and colleagues [13] completely replaced the fine fraction and filler with stone dust, natural sand, brick dust (surkhi) and ash (cinder). The optimum binder content was 4.40% for stone dust, 4.1% for natural sand, 6.57% for cinder and 6.64% for surkhi. They concluded that the angle of internal friction decreased respectively for surkhi 35°, natural sand 33.7°, stone dust 32° and cinder 28.4°. The Wheel-tracking test confirms the same order: the mixture with surkhi has the highest resistance to rutting, and the mixture with cinder has the lowest. The direct drop shows that a higher angle of internal friction is associated with higher anti-rutting stability, so fineness alone is not sufficient if the particles are poorly compacted.

## 4. DISCUSSION

The problem of applying sediment admixtures, as a replacement for part of natural stone fillers, which is also an integral element of asphalt mixes, is a current and insufficiently researched area. Published works have shown that the physical properties of the sediment, primarily porosity, density and bitumen absorption, determine its influence on compaction, volumetric ratios and mastic stiffness.

[1] **MSCR** (Multiple Stress Creep Recovery) is a rheological test that measures the resistance of mastic or bitumen to permanent deformation, i.e., rutting.
[2] **LAS** (Linear Amplitude Sweep) is a fatigue resistance test.

Compared to limestone filler, raw sediments often have higher porosity and specific surface area, which is why they absorb a larger amount of bitumen. This can lead to an increase in the optimum binder content, difficult workability and changes in the volumetric characteristics of the asphalt mixture. Therefore, the application of raw sediment is usually limited to a smaller percentage of filler replacement. A special problem is the presence of organic matter, which further increases the absorption of bitumen and can adversely affect its durability and resistance to moisture.

Pretreatment of sediment can significantly improve its characteristics. The results of the analyzed research show that calcination removes organic matter and reduces the unfavorable absorption of the binder, which greatly improves the stiffness and mechanical characteristics of the mastic. However, the application of calcination requires additional energy, so its application must be justified through the achieved technical and environmental benefits.

Increasing the proportion of filler in the mastic generally increases stiffness and reduces irreversible deformations, i.e. improves resistance to permanent flow. However, excessive filler content must cause excessive stiffening and reduced fatigue resistance as well as temperature changes. Therefore, the optimal content cannot be determined only by the amount of added material, but it is necessary to observe its ability to form a stable mastic structure.

Investigations of different waste mineral fillers have confirmed that fineness alone is not sufficient to evaluate the behavior of an asphalt mixture. Resistance to rutting is also influenced by particle shape, intergranular friction, compaction ability, porosity and interaction with bitumen. A similar conclusion is drawn when it comes to sedimentary admixtures. A material with a large specific surface may have a favorable effect on stiffness, but at the same time require a larger amount of binder and show a lower resistance to moisture if proper compaction is not provided.

## 5. CONCLUSION

The number of works published in the field of the application of sedimentary or mineral fillers in the production of asphalt mixtures is relatively scarce and provides a significant opportunity for further research. Previous findings from this field have shown that the application of sedimentary admixtures is possible and justified from an engineering, economic and ecological point of view, especially due to the reduction of the amount of waste and the consumption of natural mineral resources.

The conclusion that can be drawn is that a high RV and an increase in organic admixtures increase the amount of bitumen required. By calcining, limiting sediment replacement (about 20-23%) and choosing a softer binder, the mastic can be returned to the range where the filler strengthens the system, increases stiffness and provides better rutting resistance. However, the optimal proportion of sediment depends on its properties and cannot be defined in advance for all types and origins of material. Therefore, before application, it is necessary to examine its composition, bitumen absorption, impact on compaction and other mechanical properties of the asphalt mixture.

## LITERATURE

[1] Jwaida, Z., Al Quraishy, Q. A., Almuhanna, R. R. A., Dulaimi, A., Bernardo, L. F. A., & Andrade, J. M. A. (2024). The use of waste fillers in asphalt mixtures: A comprehensive review. *CivilEng*, Volume 5, No. 4, 801–826. https://doi.org/10.3390/civileng5040042

[2] Kahveci, T. E., & Özen, H. (2024). Utilisation of waste sludge from drinking water treatment as a filler material in hot mix asphalt. *Materials*, Volume 17, No. 7, Article 1528. https://doi.org/10.3390/ma17071528

[3] Barraj, F., Mahfouz, S., Kassem, H., Khatib, J., Goulias, D., & Elkordi, A. (2023). Investigation of using crushed glass waste as filler replacement in hot asphalt mixtures. *Sustainability*, Volume 15, No. 3, Article 2241. https://doi.org/10.3390/su15032241

[4] Solouki, A., Tataranni, P., Tarsi, G., & Sangiorgi, C. (2023). Waste silt as filler in hot mix asphalt: A laboratory characterization. *Applied Sciences*, Volume 13, No. 6, Article 3473. https://doi.org/10.3390/app13063473

[5] Belayali, F., Maherzi, W., Benzerzour, M., & Abriak, N.-E. (2023). Influence of the physical and chemical characteristics of sediment fillers on the properties of mastic asphalt. *Powder Technology*, Volume 421, Article 118393. https://doi.org/10.1016/j.powtec.2023.118393

[6] Tošković, Đ., Jovanović, P., Tatić, U., & Pap, I. (2018). The influence of synthetic fibers on the base of aramide and polyolefines on physical-mechanical and dynamic characteristics of asphalt mixtures. *Put i saobraćaj*. Volume 60, No. 2, pp. 65 – 70, (in Serbian) https://www.putisaobracaj.rs/index.php/PiS/article/download/19/18/

[7] Xu, W., Qiu, X., Xiao, S., Hong, H., Wang, F., & Yuan, J. (2020). Characteristics and mechanisms of asphalt–filler interactions from a multi-scale perspective. *Materials*, Volume 13, No. 12, Article 2744. https://doi.org/10.3390/ma13122744

[8] Zhang, J., Liu, S., Yao, Z., Wu, S., Jiang, H., Liang, M., & Qiao, Y. (2018). Environmental aspects and pavement properties of red mud waste as the replacement of mineral filler in asphalt mixture. *Construction and Building Materials*, Volume 180, pp. 605–613. https://doi.org/10.1016/j.conbuildmat.2018.05.268

[9] Dimulescu, C., & Burlacu, A. (2021). Industrial waste materials as alternative fillers in asphalt mixtures. *Sustainability*, Volume 13, No. 14, Article 8068. https://doi.org/10.3390/su13148068

[10] Diab, A., & Enieb, M. (2018). Investigating influence of mineral filler at asphalt mixture and mastic scales. *International Journal of Pavement Research and Technology*, Volume 11, No. 3, pp. 213–224. https://doi.org/10.1016/j.ijprt.2017.10.008

[11] Asadi Azadgoleh, M., Mohammadi, M. M., Ghodrati, A., Sharifi, S. S., Palizban, S. M. M., Ahmadi, A., Vahidi, E., & Ayar, P. (2022). Characterization of contaminant leaching from asphalt pavements: A critical review of measurement methods, reclaimed asphalt pavement, porous asphalt, and waste-modified asphalt mixtures. *Water Research*, Volume 219, pp. 1-24, Article 118584. https://doi.org/10.1016/j.watres.2022.118584

[12] Al-Mosawe, H., Mohammad, H. K., Albayati, A. H., & Al-Kheetan, M. J. (2026). Role of mineral filler type and ratio in the rheological, fatigue, and adhesive performance of asphalt mastics. *Results in Engineering*, Volume 30, pp. 1-12, Article 109500. https://doi.org/10.1016/j.rineng.2026.109500

[13] Khan, N., Karim, F., Qureshi, Q. B. A. I. L., Mufti, S. A., Rabbani, M. B. A., Khan, M. S., & Khan, D. (2023). Effect of fine aggregates and mineral fillers on the permanent deformation of hot mix asphalt. *Sustainability*, Volume 15, No. 13, Article 10646. https://doi.org/10.3390/su151310646

https://doi.org/10.24867/INDIS-2026-EN-517



# INTEGRATION OF TECTONIC AND SEISMOLOGICAL DATA OF THE WIDER KOSMAJ MOUNTAIN AREA: A REGIONAL APPROACH TO GEOHAZARD ASSESSMENT

*Nikolina Ćirić Avramović [1, 2], Panta Krstić[3], Sara Krsmanović[4]*

***Summary:***

This study examines the seismicity of the wider Kosmaj Mountain area in relation to its regional tectonic setting. Tectonic data from previous studies were combined with the homogenized earthquake catalog of the Seismological Survey of Serbia. The analysis included selected earthquakes, their magnitudes, hypocentral depths and macroseismic intensities. The 1922 (Mw 5.7) and 1927 (Mw 5.8) events stand out in the analyzed record. These magnitudes are higher than those given for the inner southern Pannonian Basin and closer to those reported for its southern margin. Although the events cannot be linked to individual faults, the historical record contributes to understanding seismic activity and geohazard in the wider Kosmaj area.

*Keywords: Kosmaj Mountain, seismicity, tectonics, geohazard*

# INTEGRACIJA TEKTONSKIH I SEIZMOLOŠKIH PODATAKA ŠIREG PODRUČJA PLANINE KOSMAJ: REGIONALNI PRISTUP SAGLEDAVANJU GEOHAZARDA

***Rezime:***

U ovom radu razmatrana je seizmičnost šireg područja planine Kosmaj u odnosu na njegov regionalni tektonski položaj. Tektonski podaci iz prethodnih istraživanja objedinjeni su sa podacima iz homogenizovanog kataloga zemljotresa Republičkog seizmološkog zavoda Srbije. Analizirani su odabrani zemljotresi, njihove magnitude, hipocentralne dubine i makroseizmički intenziteti. U analiziranom zapisu posebno se izdvajaju događaji iz 1922. (Mw 5,7) i 1927. godine (Mw 5,8). Ove magnitude su više od vrednosti koje se navode za unutrašnji deo južnog Panonskog basena i bliže su onima koje se navode za njegov južni obod. Iako se ovi događaji ne mogu povezati sa pojedinačnim rasedima, istorijski seizmički zapis doprinosi sagledavanju seizmičke aktivnosti i geohazarda šireg područja Kosmaja.

*Ključne reči: planina Kosmaj, seizmičnost, tektonika, geohazard*

[1]Teaching Assistant, Department of Civil Engineering and Geodesy – Faculty of Technical Sciences, University of Novi Sad, Serbia: nikolina.ciric@uns.ac.rs, ORCID 0000-0001-5740-0986
[2]PhD student, Faculty of Mining and Geology, University of Belgrade, Belgrade, Serbia
[3]Teaching Assistant, Department of Civil Engineering and Geodesy – Faculty of Technical Sciences, University of Novi Sad, Serbia, panta.krstic@uns.ac.rs , ORCID 0000-0001-5519-391X
[4]Teaching Assistant, Department of Civil Engineering and Geodesy – Faculty of Technical Sciences, University of Novi Sad, Serbia, sarakrsmanovic@uns.ac.rs, ORCID N/A

## 1. INTRODUCTION

Earthquake occurrence is related to recent tectonic activity and crustal deformation. The spatial distribution of earthquakes may differ from the pattern of faults recognized by geological mapping. Comparison of seismic records with geological and structural data can help to characterize tectonically complex areas and their associated geohazards.

The territory of Serbia has a complex tectonic framework resulting from a multiphase geodynamic evolution. The southern margin of the Pannonian Basin is a significant area for neotectonic activity. Marović et al. (2002) [1] note differences in the Quaternary tectonic evolution of the basin's internal and marginal parts, with numerous fault structures activated along its southern boundary zone and accompanied by moderate seismic activity. At the same time, the irregular spatial distribution of earthquake epicenters makes it difficult to directly associate individual seismic events with specific tectonic structures.

Within this regional framework, the wider Kosmaj Mountain area is structurally complex and lies in central Serbia. Previous investigations indicate a multiphase deformation history and fault-related structures of different scales, with differences between regional structures identified by photogeological analysis and local structures documented through field investigations [2]. These characteristics provide a basis for reviewing the area within a more extensive neotectonic and seismological context.

This study considers the spatial relationship between tectonic structures and recorded seismicity in the wider Kosmaj Mountain area as a regional geohazard issue. It focuses on the joint consideration of the tectonic framework and the spatial distribution of seismicity, without assuming a direct genetic relationship between them. In this way, the study considers the value of an integrated approach that unites geological and seismological datasets for regional geohazard analysis.

## 2. GEOLOGICAL AND TECTONIC SETTING

The wider Kosmaj Mountain area lies within a complex regional tectonic framework shaped by several stages of deformation. Regionally, it lies along the southern margin of the Serbian part of the Pannonian Basin, where basin and peri-basin structures extend southward between the Dinaridic and Carpatho-Balkanidic morphostructures [1]. The pre-existing Alpine tectonic fabric strongly influenced the geometry and development of the Neogene structures in this region.

Within this regional pattern, the Neogene structural pattern of the southern Pannonian margin consists of a series of basins, troughs, horsts, and major faults. Marović et al. (2002) [1] distinguish the Avala–Kosmaj Horst (AKH) as one of the main uplifted structures. Its geometry was strongly influenced by older fault systems, which were subsequently affected by Plio-Quaternary and Quaternary tectonic activity. In the Quaternary, the inner parts of the Pannonian Basin were predominantly subsiding, whereas its marginal areas underwent uplift and fault reactivation.

The geology of Kosmaj Mountain is characterized by rocks of different ages and origins. In its central part, Jurassic serpentinites and Cretaceous sedimentary rocks are in tectonic contact [2]. Structural investigations of the central part of Kosmaj indicate several phases of deformation, including compressional deformation associated with

reverse faulting, folding, and later gravitational faulting. A comparison of faults identified by photogeological analysis with those measured in the field showed differences in dominant orientations. The photogeologically identified faults predominantly have an E–W orientation and represent regional-scale structures, whereas the faults documented in the field predominantly trend NW–SE and are interpreted as local structures [2].

The occurrence of structures at different scales, together with Kosmaj's position within the broader Avala–Kosmaj structural domain, provides the geological and tectonic framework for comparing the regional seismicity presented in this study with the local structural setting. This framework also helps relate the observed seismicity to the structural pattern described above, clarifying how seismicity is linked to the identified structures.

## 3. DATA AND METHODOLOGY

The study integrates existing tectonic and seismological data for the wider Kosmaj Mountain area. The analysis was carried out at a regional scale to compare recorded seismicity with the known local and regional tectonic characteristics of the area, without assuming a direct relationship between individual seismic events and mapped fault structures.

Tectonic data were obtained from previous geological and structural studies. The local structural setting of Kosmaj Mountain was considered based on geological mapping, photogeological analysis, and field structural measurements presented by Ćirić [2]. The regional tectonic framework was based on Marović et al. [1], with particular attention to the position of the Avala–Kosmaj Horst, the neotectonic evolution of the southern margin of the Pannonian Basin and the regional distribution of seismic activity. In this way, tectonic data at different spatial scales were included in the analysis.

Seismological data were obtained from the homogenized *Earthquake Catalog Mw ≥ 3.5 of the Republic of Serbia*, published by the Seismological Survey of Serbia (RSZ) [3]. For the analyzed events, the date of occurrence, epicentral coordinates, hypocentral depth, macroseismic intensity, and homogenized moment magnitude (Mw) were used [3]. The lower Mw limit of 3.5 was not defined in this study but corresponds to the criterion of the catalog used as the data source. This value is therefore not considered a uniform completeness magnitude for the entire time period covered by the catalog.
The integration of tectonic and seismological data was performed by comparing several parameters. First, characteristic seismic events and earthquake sequences recorded in the immediate and wider surroundings of Kosmaj were selected. Their location, magnitude, hypocentral depth, macroseismic intensity, and temporal distribution were considered. The resulting pattern was then compared with the regional position of the Avala–Kosmaj Horst and the seismotectonic characteristics of the southern margin of the Pannonian Basin described by Marović et al. [1], as well as with the local and regional structural characteristics of Kosmaj reported by Ćirić [2].

Particular attention was paid to comparing the magnitudes of the selected events with the ranges of maximum expected magnitudes reported by Marović et al. [1] for different parts of the southern Pannonian Basin and its peri-Pannonian margin. In this way, the seismological data were considered not only descriptively, but also in relation to the existing regional seismotectonic model.

For selected seismic events, the epicentral distance from Kosmaj was also considered, using the geographic coordinates of the epicenters from the RSZ catalog [3] and a reference point on Kosmaj Mountain. This parameter was used only to distinguish events occurring in the immediate and wider surroundings of the mountain and was not used to assign individual events to specific faults.

Possible spatial similarities between seismic events and known tectonic structures were treated as indicative. Due to the different spatial scales of the structural datasets used, as well as the lack of detailed information on the geometry of potentially active faults and their focal mechanisms, individual earthquakes could not be directly linked to specific fault structures.

## 4. RESULTS AND DISCUSSION

Data from the homogenized RSZ catalog [3] show that earthquakes of different magnitudes and hypocentral depths have been recorded in the wider surroundings of Kosmaj. Within the catalog used in this study, a group of stronger events is particularly evident during the 1920s, especially between 1922 and 1927. This concentration refers to the events in the catalog. It should not be interpreted as an absolute maximum of seismic activity, given changes in the availability and quality of seismological data over time.

Among the selected events, the earthquake of 24 March 1922 stands out, with a homogenized magnitude of Mw 5.7, a hypocentral depth of 24 km and a macroseismic intensity of VIII. The earthquake of 19 May 1926 had Mw 5.2, a depth of 20 km and an intensity of V, while the strongest of the considered events occurred on 15 May 1927, with Mw 5.8, a depth of 20 km and an intensity of VIII [3]. The high macroseismic intensities of the strongest historical events indicate pronounced surface effects, which is also relevant from a geohazard perspective.

*Tab. 1 Selected earthquakes with Mw ≥ 3.5 recorded in the wider surroundings of Kosmaj Mountain according to the homogenized earthquake catalogue [3]*

| Date | Lat. (°N) | Lon. (°E) | Depth (km) | Mw | I |
|---|---|---|---|---|---|
| 24.03.1922 | 44.412 | 20.295 | 24 | 5.7 | VIII |
| 25.03.1922 | 44.401 | 20.563 | 12 | 4.5 | — |
| 19.05.1926 | 44.401 | 20.528 | 20 | 5.2 | V |
| 15.05.1927 | 44.168 | 20.529 | 20 | 5.8 | VIII |
| 15.05.1927 | 44.450 | 20.570 | 10 | 4.5 | — |
| 17.05.1927 | 44.100 | 20.400 | 25 | 5.2 | — |
| 19.07.1929 | 44.291 | 20.567 | 10 | 4.6 | — |
| 22.09.1932 | 44.247 | 20.461 | 11 | 4.4 | — |
| 28.03.1938 | 44.134 | 20.301 | 7 | 4.4 | — |
| 30.08.1974 | 44.430 | 20.700 | 5 | 4.5 | — |
| 23.12.1981 | 44.094 | 20.609 | 13 | 4.3 | — |
| 08.11.1986 | 44.084 | 20.246 | 25 | 4.3 | — |
| 29.06.2012 | 44.294 | 21.006 | 3.4 | 3.8 | — |

*Note: Table 1 presents selected events and not the complete set of earthquakes contained in the RSZ catalogue [3]. Macroseismic intensity (I) is shown only for the strongest selected events from 1922 and 1927, while for the remaining events this parameter was not analysed in detail in the present study.*

In the latter part of the catalog record, earthquakes with Mw ≥ 3.5 are still present in the wider surroundings of Kosmaj, although the selected events are lower in magnitude. These include, among others, earthquakes recorded in 1974 (Mw 4.5), 1981 (Mw 4.3), 1986 (Mw 4.3) and 2012 (Mw 3.8) [3]. Therefore, 1974 does not represent the end of seismic activity or the end of the analyzed record. At the same time, among the selected events from the later period, there are no earthquakes with magnitudes comparable to the Mw 5.7 event of 1922 and the Mw 5.8 event of 1927. The absence of events of similar magnitude does not indicate the cessation of tectonic activity but represents a characteristic of the catalog record considered here.

The obtained results can be further considered in relation to the regional seismotectonic model proposed by Marović et al. [1]. These authors distinguish between the inner part of the southern Pannonian Basin and its peri-Pannonian margin. The inner part of the basin is characterized by relatively low seismicity, with maximum expected magnitudes generally below 4.5. In contrast, for the inner southern margin of the Pannonian Basin (SPPB), which is one of the most seismically active zones in Serbia, earthquakes with magnitudes up to M = 5.5–6 may be expected [1].

The 1922 and 1927 earthquakes had magnitudes of Mw 5.7 and Mw 5.8, respectively. These values are higher than those given by Marović et al. [1] for the inner part of the southern Pannonian Basin and are within the range reported for its more active southern margin. The recorded magnitudes therefore correspond better to the seismic characteristics of the basin margin than to those of its inner part.

This comparison, however, does not provide evidence that the 1922 and 1927 events were related to the Avala–Kosmaj Horst or to any particular fault. Marović et al. [1] point to the irregular spatial distribution of epicenters and the difficulty of identifying seismically active faults solely from seismological data. The agreement between the recorded magnitudes and the values characteristic of the peri-Pannonian margin should therefore be regarded as regional seismotectonic consistency rather than evidence for the activity of a specific tectonic structure.

Additional complexity arises from the presence of tectonic structures at different scales. Ćirić [2] showed that the dominant orientations of regional structures identified by photogeological analysis differ from those of local faults recorded in the field. The regional structures predominantly trend E–W, whereas the locally recorded faults mainly trend NW–SE [2]. This difference shows that the structural pattern depends on the spatial scale of observation and represents an additional limitation when attempting to relate regional seismicity directly to mapped surface faults.

From a geohazard perspective, historical events with magnitudes greater than Mw 5 are particularly important, including the Mw 5.7 and Mw 5.8 earthquakes, which reached macroseismic intensity VIII [3]. Their occurrence indicates that the seismic hazard of this area should not be assessed solely on the more recent instrumental period, in which lower-magnitude events dominate among those analyzed, but should also take the historical seismic record into account.

Macroseismic intensity VIII was recorded for the strongest events [3]. This refers to the effects observed during these earthquakes and does not represent the intensity at Kosmaj. The effects at a particular location depend, among other factors, on its distance from the source and local geological conditions.

The integration of tectonic and seismological data therefore indicates that the Kosmaj area lies within a regional setting in which historically significant earthquakes have been documented. Their magnitude range shows greater agreement with the characteristics of the more seismically active peri-Pannonian margin than with the inner part of the southern Pannonian Basin [1]. At the same time, the available data are not sufficient to identify individual seismogenic faults.

A detailed seismic hazard assessment, including the determination of expected peak ground acceleration (PGA), design seismic parameters and possible effects on the built environment, would require the use of official seismic hazard maps, local geological and geotechnical conditions, and a more detailed characterization of potential seismogenic sources. The results of this study therefore represent a regional-level assessment of geohazard and provide a basis for more detailed seismotectonic analyses.

## 5. CONCLUSION

The analysis of available tectonic and seismological data shows that the seismicity of the wider Kosmaj area should be considered within the regional tectonic setting of the southern margin of the Pannonian Basin. In the analyzed seismic record, the events of 1922 and 1927, with magnitudes of Mw 5.7 and Mw 5.8, respectively, stand out [3].
The magnitudes of the 1922 and 1927 earthquakes are higher than those reported by Marović et al. [1] for the inner part of the southern Pannonian Basin and are closer to the values given for its more active southern margin. This suggests that the recorded seismicity should be considered in relation to Kosmaj's regional tectonic setting.
At the same time, the available data do not allow individual earthquakes to be directly related to the Avala–Kosmaj Horst or to specific mapped faults. Differences between regional and local structural trends further show that such correlations would require more detailed data on the geometry and activity of potential seismogenic structures [1, 2].
From a geohazard perspective, the historical Mw 5.7 and Mw 5.8 events, both associated with a macroseismic intensity of VIII, are particularly important [3]. The seismic hazard of the wider Kosmaj area should therefore not be assessed solely on more recent instrumentally recorded activity; the historical seismic record also needs to be taken into account.
The results provide a basis for further seismotectonic studies. At the same time, a more detailed seismic hazard assessment would require data on potential seismogenic sources, local geological and geotechnical conditions, and relevant seismic hazard parameters. In this way, the study provides an example of a regional, integrative approach to geohazard assessment based on the combined analysis of available tectonic and seismological data from diverse sources and at different spatial scales.

### ACKNOWLEDGEMENT

The research has been conducted within the project "Enhancement of teaching and scientific research capacities through the application of modern technologies in the fields of civil engineering, geodesy, and disaster risk management and fire safety", developed at the Department of Civil Engineering and Geodesy, Faculty of Technical Sciences, University of Novi Sad, Serbia.

## REFERENCES

[1] Marović M., Djoković I., Pešić L., Radovanović S., Toljić M., Gerzina N. (2002). Neotectonics and seismicity of the southern margin of the Pannonian Basin in Serbia. *Stephan Mueller Special Publication Series*, Volume 3, pp. 277–295.

[2] Ćirić N. (2017). Geološki razvoj centralnog dela planine Kosmaj. *Petničke sveske*, Volume 76, Part II, pp. 450–458.

[3] Radovanović S., Kovačević S., Dragičević B., Knežević V., Petrović M., Veselinović B. (2013). Đurđević S. *Katalog zemljotresa Mw ≥ 3.5 Republike Srbije*. Republički seizmološki zavod, Beograd, Srbija.

# ARCHITECTURE AND URBAN PLANNING

iNDiS 2026

https://doi.org/10.24867/INDIS-2026-EN-525



# TENDENCIES AND URBAN DEVELOPMENT UNDER MODERN TRAFFIC CONDITIONS: THE CASE OF NOVI SAD

*Željko Jakšić[1], Milan Trivunić[2], Dušanka Plazina-Pevač[3]*

***Summary:***

Technological progress and rapid urbanization have introduced urban challenges that frequently generate a new set of complex problems. With the evolution of transport and the mass adoption of private automobiles—initially introduced to provide individual mobility and elevate the urban quality of life—the conflict between vehicular traffic and residential living has become increasingly pronounced. Modern cities are progressively dimensioned and traffic-oriented to meet the immediate demands of automobile usage. Consequently, there is a growing trend toward minimizing the role of individual vehicles in urban development, making the so-called "urban transformation" a pressing reality. European cities are actively restricting automobile traffic as a standard practice. Although each city pursues a distinct strategic path, they share a common guiding principle: less cars – more space for living. This paper provides a comprehensive review and analysis of well-known European urban transformations and explores the feasibility of implementing similar structural changes in the city of Novi Sad, considering that this constitutes a long-term and capital-intensive process.

*Keywords:* ***individual transport, urban transformation, superblock, 15-minute and multi-minute cities***

# TENDENCIJE I RAZVOJ GRADOVA U USLOVIMA SAVREMENOG SAOBRAĆAJA NA PRIMERU NOVOG SADA

***Rezime:***

Tehnološkim napretkom i urbanizacijom gradova, nastali problemi su zahtevali rešenja koja su često proizvodila set novih problema. Razvojem transporta, masovne uvođenjem automobila, kao oblik individualnog prevoza i višeg kvaliteta života u gradu, sve je izraženiji konflik između saobraćaja i stanovanja. Gradovi su sve više dimenzionisani i saobraćajno orijentisani prema trenutnim zahtevima upotrebe automobila. Sve je izraženija tendencija minimizacije uloge individualnih vozila u razvoju grada, a tzv. urbana transformacija grada postaje realnost. Evropski gradovi aktivno ograničavaju automobilski saobraćaj, kao obrazac ili standard, iako je svaki od njih krenuo drugačijim putem, sa zajedničko idejom vodiljom: manje automobila – više prostora za život. U radu su izvršeni pregled i analiza poznatih transformacija evropskih gradova i moguće transformacije na nivou grada Novog Sada, s obzirom na to da je reč o dugotrajnom, a istovremeno, skupom procesu.

*Ključne reči: individualni transpor, urbana transformacija, superblok, 15-to i višeminutni gradovi*

[1] Assiss. prof., Faculty of Technical Sciences, University of Novi Sad, Novi Sad, Serbia, alt96@uns.ac.rs, ORCID 0000-0003-3512-1227)
[2] Full. prof., Fakultet tehničkih nauka, Univerzitet u Novom Sadu, Novi Sad, Srbija, trule@uns.ac.rs, ORCID 0000-0002-6611-4524
[3] Head of Engineering Department, IEE Consult s.e. d.o.o., Mičurinova street no.8, Novi Sad, Republic of Serbia, dusanka.plazina@iee.rs

## 1. INTRODUCTION

The First Industrial Revolution marked a critical turning point in urban housing due to its long-lasting socio-spatial consequences, which continue to manifest today. The massive influx of the rural labor force during the First Industrial Revolution led to severe urban overcrowding, resulting in rapid, unplanned urbanization. The industrial city transformed into an "industrial backyard" [1], which was only gradually humanized through state interventionism [2] in the latter half of the 19th century, when governments began introducing the first public health and urban planning legislation. The state exerted a more intensive influence on urban development following the Second Industrial Revolution, which triggered spatial expansion, advanced manufacturing processes, and revolutionized communication and transport infrastructure. These socio-urban shifts led to the emergence of modern metropolises characterized by tram networks, underground railways, street lighting, and the earliest skyscrapers. Ultimately, urban development became intrinsically conditioned by the evolution of traffic and transport systems.

Current projections estimate that by 2050, approximately 70% of the global population will reside in urban areas. This demographic shift will inevitably reshape transport systems and their surrounding environments. [3] In the majority of contemporary cities, public space has been fundamentally designed to facilitate the efficient movement of motorized vehicles. This traditional design paradigm reduces the urban space available for sustainable transport alternatives, negatively impacting both the environment and public health. As living standards gradually rose, cities became increasingly dimensioned and traffic-oriented to accommodate current automobile demands rather than actual transport necessities. [4] Prominent examples of European urban transformations illustrate a shift in perspective, where the private automobile is increasingly viewed as a source of spatial conflict rather than a means of enhancing urban quality of life.

## 2. PLANNED RESIDENTIAL DEVELOPMENT

As a direct response to the escalating tension between vehicular traffic and residential zones, the concept of "green housing" emerged at the end of the 20th century. A key example of green engineering successfully implemented in major European cities—such as Barcelona, Paris, and Copenhagen—is the "superblock" concept. The core principle of this model relies on redefining the organization and priorities within the traffic-urban layout of basic neighborhood units (blocks). The objective is to prioritize active mobility, non-motorized transport, and social interaction within these designated zones. Every layer of traffic—including motorized transit, stationary traffic, cycling, e-scooters, and pedestrian movement—contributes uniquely to the functionality, user satisfaction, and overall quality of life within an urban neighborhood.

### 2.1. TRANSFORMATION OF A BLOCK INTO A SUPERBLOCK

Whether traffic is entirely displaced from a block or permitted under strictly programmed conditions, these variations represent different approaches to mitigating urban conflict. By relocating motorized traffic from the interior of the block to its perimeter (the superblock model), the internal space is liberated. This structural shift enhances the spatial quality and safety for its users (Fig. 1):

- Increased safety for vulnerable users (particularly the elderly and children) by eliminating physical contact with motorized vehicles (primarily cars and motorcycles).
- Mitigation of localized environmental pollution (air and noise pollution).
- Promotion of social interaction.
- Creation of well-designed, dynamic spaces for social activities, moving away from the conventional monotony of isolated green patches.

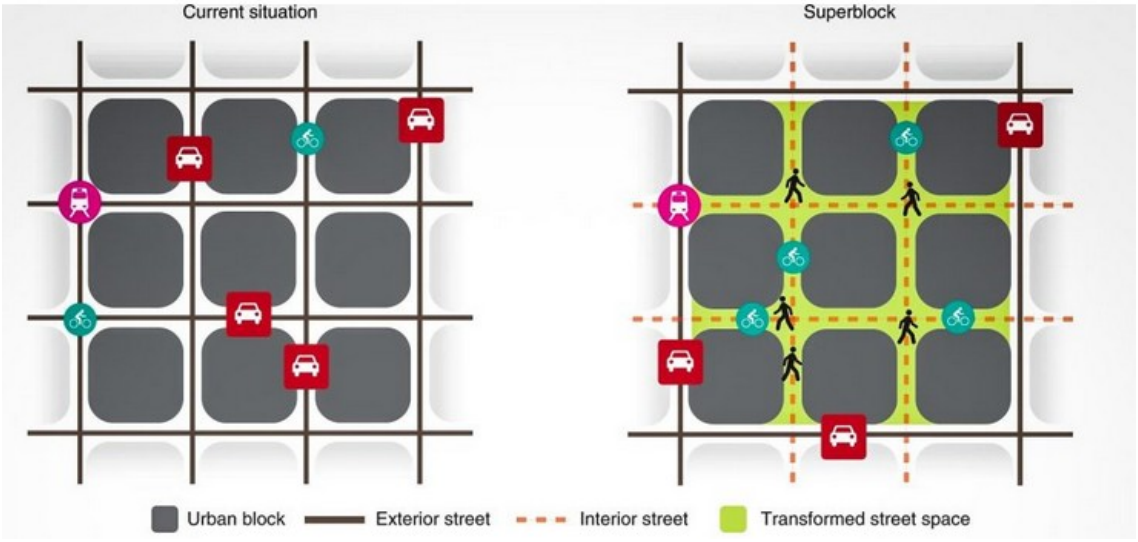


*Fig. 1 Barcelona – Transformation of blocks into a superblock [5]*

Conversely, perimeter roads catering to motorized traffic run the risk of becoming overloaded bottlenecks, potentially leading to traffic congestion. Such scenarios can effectively "entrap" the internal blocks by obstructing inbound and outbound access. These outcomes risk creating new urban hot spots for noise and air pollution.

Traffic engineering analyses [6] suggest technical solutions through traffic regulation and the design of smart corridors. These include: 1) establishing optimal speed limits via electronic information systems, and 2) preventing frequent lane changes by deploying wireless sensors in each lane. These sensors optimize vehicle flow via dynamic traffic light signaling, controlling intersections to maximize throughput. However, resolving bottlenecks through these methods remains highly complex due to several uncontrollable parameters: a) driver behavior, b) general vehicle maintenance (brakes, tires), and c) road surface conditions (wet, dry/dusty, icy).

Adapting to new functional conditions within a block relative to motorized traffic requires the implementation of temporary, "soft" urban measures. These measures involve temporary pavement painting, single-day street closures for community events, the installation of parklets (urban furniture) on designated parking spaces, and the deployment of temporary greenery via large planters. [3]

## 2.2. THE PROBLEM OF STATIONARY TRAFFIC IN THE SUPERBLOCK

The superblock is an urban planning model that aggregates several traditional city blocks into a larger unified unit. Within this structure, interior streets are closed or strictly restricted to transit motorized traffic, while the reclaimed space is dedicated to pedestrians, cyclists, and urban greenery. Automobile traffic is re-routed to the external, peripheral streets of the superblock. Thus, the term "superblock" reflects the elevated

quality of life provided to its users, even though its physical dimensions are significantly larger than a standard block.

This concept, most famously implemented in Barcelona (*Catalan: superilles*), continues to generate extensive debate among public and professional circles. Table 1 outlines the rational, technical, and empirical arguments for and against this model.

*Tab. 1. Arguments for and against the implementation of the "Superblock" model*

| Implementacija SUPERBOK modela | |
|---|---|
| Pro | Contra |
| Reduction of air and noise pollution within the block. | "Traffic spillover" effect: Closing interior streets does not eliminate cars from the city; it merely reroutes them. |
| Increased safety for pedestrians and children. | Risk of gentrification (escalating real estate prices). |
| Revitalization of the local economy. | Logistics and delivery challenges. |
| Increased green areas and mitigation of "urban heat islands". | Deficit of available parking spaces. |
| Promotion of a healthier lifestyle. | Dependence on public transit systems. |
| | Geometric incompatibility: The superblock concept is ideally tailored for cities with a regular, orthogonal street grid (such as Barcelona). In cities with irregular, historical, or organically developed street networks, implementation is technically highly complex and costly. |

The benefits achieved through superblock organization are consistently hindered by the issue of stationary traffic. Data indicates that private automobiles spend 92% to 95% of their operational lifespan parked, thereby consuming a disproportionate share of valuable urban space. The contemporary paradigm of urban development dictates that *"a city designed for cars is not a city designed for people"*. From this perspective, the superblock model addresses stationary traffic by relocating parking spaces to peripheral, transit streets or into underground parking structures, leaving only a minimal number of spaces within the block for specialized needs [8].

Urban development research demonstrates that executing new urban paradigms represents the primary barrier to implementation, as it constitutes a protracted process—a reality well-illustrated by Copenhagen. Strategic investment in cycling infrastructure began in the early 2000s, guided by measurable targets and systematic evaluations. Today, Copenhagen boasts 350 kilometers of segregated bike lanes, and 45% of the city's workforce and student population commutes via bicycle. The city's first bike lane was constructed in 1892, expanding to 50 kilometers of cycling tracks by 1912. This underscores that the transformation was not instantaneous, but rather a multi-decadal political commitment to systematically supporting active mobility. The key takeaway is that residents did not choose bicycles solely due to environmental awareness; they chose them because the city's design made cycling faster, more comfortable, and cheaper than driving a car [9].

## 3. THE SUPERBLOCK: A PATHWAY TO THE 15-MINUTE AND MULTI-MINUTE CITY

The concept of the 15-minute city was developed by Professor Carlos Moreno [10], inspired by the seminal work of Jane Jacobs [11]. It outlines an urban framework where all residents can fulfill their essential daily needs within the span of a short walk or bicycle ride.

The superblock model serves as one of the primary urban planning tools for operationalizing the 15-minute city (with corresponding neighborhood analyses also extending to 20-minute city frameworks [12]). The structural differences between the two concepts are categorized as follows:

- **Superblock (Micro-level / Module):** Focuses on the spatial reorganization of streets within a localized cluster, typically comprising 9 traditional blocks (roughly 400x400 meters). Its objectives center on reducing noise, mitigating pollution, and reclaiming public space.
- **15-Minute and Multi-Minute City (Macro-level / Vision):** Represents a comprehensive urban master plan encompassing the entire city (e.g., Novi Sad). Its goal ensures that no resident, regardless of their neighborhood, needs to travel longer than 15 minutes (via walking or cycling) to reach work, education, retail, or healthcare services.

Regarding stationary traffic, the 15-minute city framework resolves parking issues through structural urban development embedded in national legislation. This approach aims to fundamentally lower the necessity for private car ownership and usage. When all vital services are accessible via walking or cycling, the demand for residential parking spaces naturally declines.



*Fig.2: A striking before and after of Paris' riverbank highway closure in 2016 [13]*



*Fig.3: Since Paris started this broader project about two decades ago, car ownership has fallen from 60% to 35%.[13]*

Following the removal of parking spaces in Paris [13], automobiles were not merely displaced to adjacent corridors; instead, the reduction of parking availability triggered a behavioral shift among citizens. Several realized scenarios emerged:

- A significant portion of private vehicles was sold (66% of Paris residents currently do not own a car). This occurred because parking became restrictive while the city provided high-quality alternatives, including massive cycling infrastructure expansion, public transit growth, and car-sharing networks.
- Paris utilizes an extensive, highly developed network of underground parking garages located beneath residential buildings, public squares, and commercial facilities.
- Economic drivers play a critical role, as high rates for on-street parking made long-term space leases in underground garages more financially stable and attractive for local residents.
- The "Park and Ride" system was expanded, allowing commuters to park at large peripheral terminals and continue their journeys to the city center via the metro system or rapid tramways.
- By introducing "Limited Traffic Zones" (ZTL), Paris legally banned transit traffic through its historic center, successfully diverting these vehicular flows to outer ring roads.

In practice, reducing physical space allocated for automobiles led to a drop in the total number of cars within the city—a phenomenon known as "induced traffic reduction" (reducing space for cars directly reduces their utility and usage).

## 4. URBANIZATION OF NOVI SAD AND POTENTIAL DIRECTIONS OF DEVELOPMENT

Incipient phases of serious urban development in Novi Sad occurred between 1930 and 1940 [14]. However, the period between 1960 and 1980 (Phase II) is widely recognized as the "golden age" of Novi Sad urban planning. This era was guided by the modernist visions of architect Juraj Neidhardt and the General Urban Plan of the 1950s, which adhered strictly to the principles of the Athens Charter. The construction of wide boulevards during this time represents one of the most significant urban planning achievements in the city's history. The third, contemporary phase began in 2000 and continues today, marked by the execution of major capital boulevards on the western and northern perimeters of the city, though without introducing significant traffic stratification compared to previous eras.

*Tab 2. Comparative Analysis: Limani vs. Novo Naselje regarding Superblock Model Transformation*

| **Superblock Evaluation Criteria** | **Liman 1-4** | **Novo naselje (Bistrica)** |
|---|---|---|
| Current Baseline State | Severe deficit of spatial capacity; automobiles systematically encroach upon green areas and pedestrian sidewalks. | Abundant spatial capacity, though inefficiently utilized, with a growing trend of vehicular saturation. |
| Constraints & Barriers | High water table (proximity to the Danube River) significantly escalates construction costs for underground parking structures. | Extensive spatial footprint requires rigid delineation between pedestrian and vehicular zones to preserve connectivity. |
| Urban Planning | Development of peripheral | Implementation of modular |

| | | |
|---|---|---|
| Solutions | (perimetrical) multi-storey parking garages along major boulevards + clearing vehicles from interior sidewalks. | courtyard/neighborhood "green" garages + introduction of one-way traffic loops. |
| Socio-Spatial Benefits | Concentration of ground-level public space with socially active infrastructure + curated landscaping and preservation of green areas. | Reclaiming wide street corridors to establish linear parks and high-speed cycling highways. |

Unlike many historical European cities characterized by radial (circular) street networks surrounding an old core, Novi Sad was systematically developed on an orthogonal (rectangular) grid featuring wide, straight boulevards [14]. These boulevards transformed Novi Sad into a spacious and traffic-permeable city compared to other Balkan cities of similar size. These broad corridors were not reserved solely for motorized traffic; from their inception, they were designed with integrated green belts (tree lines) that provide acoustic and environmental insulation, alongside spacious sidewalks. This layout later enabled Novi Sad to position itself as a regional leader in cycling traffic.

Novi Sad holds a unique urban planning position in Serbia, as it features two large residential neighborhoods structurally designed according to the principles of modernism—Limani (sections 1, 2, 3, and 4) and Novo Naselje (Bistrica). These neighborhoods represent the only sectors of Novi Sad where the superblock model could be implemented at a significant scale.

As detailed in Table 2, while both residential areas share the chronic issue of being overloaded by stationary traffic, Limani and Novo Naselje necessitate fundamentally distinct approaches to superblock implementation due to their specific spatial morphologies.




*Fig. 4: A) High parking saturation in the Liman district caused by unregulated vehicle accumulation; B) Residential block courtyard featuring neglected greenery (Photo: Authors)*

The case of Liman 1 and 2—which presents a spatially tighter block layout compared to the open expanses of Bistrica (Novo Naselje)—contains early indicators of urban transformation. It highlights viable directions for resolving the chronic issue of stationary traffic within the city's realistic financial constraints.



*Fig. 5: Residential block courtyard featuring neglected greenery and social interaction amenities originally designed around 1965 (Photo: Authors)*

## 4.1. RESOURCES OF URBAN TRANSFORMATION OF LIMAN 1 & 2

The spatial layout (Fig. 6) of Liman 1 and 2 highlights specific sites where: 1) the model of displacing vehicular traffic from block interiors has already been deployed, or 2) existing infrastructure can be repurposefully adapted to optimize parking capacity.

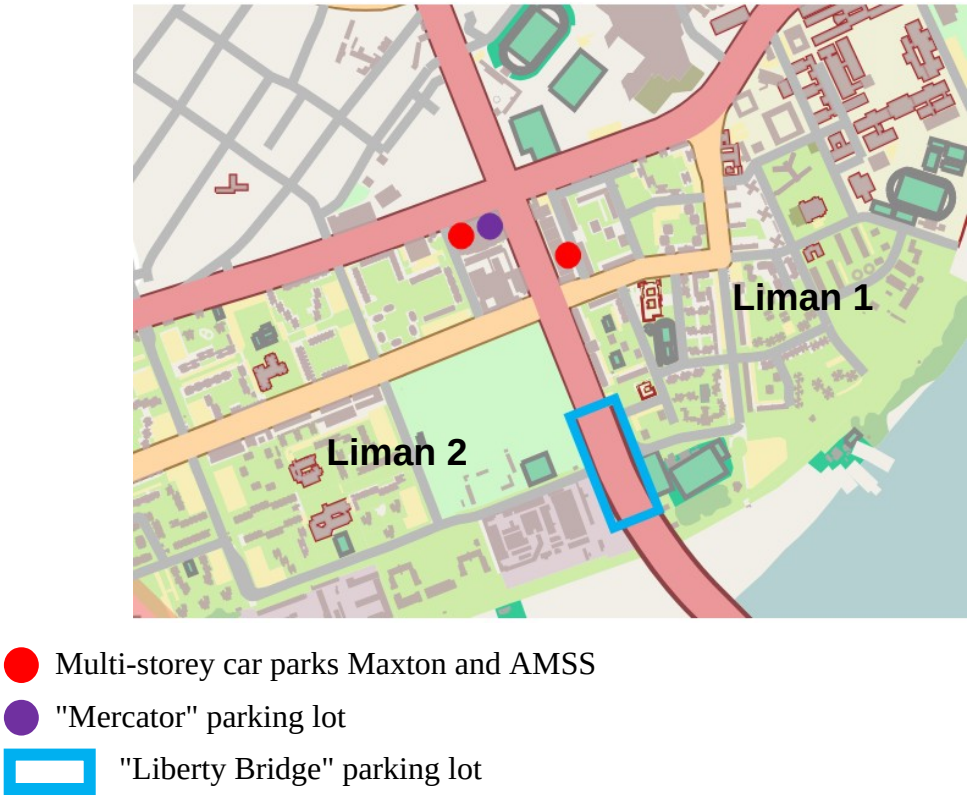


*Fig. 6: Elements of urban transformation – consolidated parking areas (Image: Authors)*

1. A prime example is the space beneath the Liberty Bridge (Most slobode), which has been successfully transformed into a high-capacity parking lot. Its construction significantly relieved vehicular pressure within the courtyards of surrounding residential blocks. This demonstrates a viable path for adapting underutilized urban spaces for multi-functional use (e.g., sheltered parking structures featuring roof-integrated solar/photovoltaic panels).



*Fig. 7: An example of an effective stationary traffic solution (Photo: Authors)*

2. The second approach utilizes existing infrastructure, such as the multi-storey public parking garages "Maxton" and AMSS, alongside the two-level parking facility within the "Mercator" shopping center. These cases demonstrate the feasibility of integrating multi-storey parking garages with mixed-use commercial and administrative functions (banks, retail, offices). Mirroring this model, modular, multi-storey "green" parking garages could be strategically positioned at the primary access points leading into the residential blocks.



*Fig. 8: Example of a prefabricated multi-storey car park with roof-integrated photovoltaic panels [15]*

## 5. CONCLUSION

Urban transformation represents the resolution of conflicts between vehicular traffic and urban residents, particularly within residential areas. It constitutes a protracted implementation process aimed at embedding new solutions into established behavioral patterns of the citizens. A prime example of this is Copenhagen, where cultivating the habit of utilizing bicycles as a primary mode of transport—rather than merely for recreation—has spanned nearly a century. Furthermore, numerous examples of "successful" transformations in European cities (such as Barcelona, Paris, and Amsterdam) demonstrate that this is a highly capital-intensive process, requiring a fundamental overhaul of the entire transport infrastructure network. In the case of Novi Sad, it has been demonstrated that the modernist block matrix designed in accordance with the principles of the Athens Charter yields a distinct advantage. Developed much earlier than in many major European metropolises, this spatial layout offers the capacity to resolve traffic issues—specifically stationary traffic—relatively simply and at manageable costs within the financial and economic capabilities of the City of Novi Sad.

## ACKNOWLEDGEMENT

This research has been supported by the Ministry of Science, Technological Development and Innovation (Contract No. 451-03-34/2026-03/200156) and the Faculty of Technical Sciences, University of Novi Sad through project “Scientific and Artistic Research Work of Researchers in Teaching and Associate Positions at the Faculty of Technical Sciences, University of Novi Sad 2026” (No. 01-3609/1).

## REFERENCES

[1] Mumford, L. (2006).*The City in History: Its Origins, Its Transformations, and Its Prospects*. Book and Marso, Belgrade. (in Serbian) ISBN: 978-86-7748-047-9

[2] Blau E. (1998). *The Architecture of Red Vienna 1919-1934*. The MIT Press, Cambridge Massachusetts, London, England.

[3] Damnjanović N., Jevremović S., Trpković A., Gajić R. (2024). Superblock: *The modern urban traffic concept of sustainable city development*. Ecological Engineering - Place and Role, Status and Future Development (16), Aspects of Spatial Protection, (in Serbian), pp. 194-206. DOI: 10.5937/EKO-ENG24015D.

[4] Atmodiwirjo P., Yatmo Y.A. (2015). Architecture as machine; Towards an architectural system for human well-being, Le Corbusier, 50 years later, International Congress, Valencia 18th-20th November 2015. DOI: http://dx.doi.org/10.4995/LC2015.2015.679

[5] https://www.researchgate.net/figure/Schematic-of-superblock-design-a-Barcelona-superblock-adopted-from-the-urban-mobility_fig1_358986970

[6] Kabrane, M., Krit, S., Elmaimuoni, L. (2018). Reducing traffic congestion in modern cities: A challenge based on physico-mathematical theories and wireless sensor network. Journal IJMPERD, Vol. 8, Issue 1, ISSN (E): 2249-8001.

[7] MacArthur, E. (2015). *Growth within - A circular economy vision for a competitive Eeurope*. Ellen MacArthur Foundation, Growth within: A circular economy vision for a competitive Europe.

[8] Morillo, E. (2021) How Barcelona is claiming its streets back from cars. https://www.datawrapper.de/blog/barcelona-urban-planning-superblocks

[9] Danish Road Directorate (2023). *Road engineering measures for cyclists: effects on safety and perceived safety*. Vejdirektoratet, ISBN (digital version): 978-87-7595-035-5

[10] Morena K. (2024). The 15-Minute City: A Solution to Saving Our Time and Our Planet (2024). Wiley.

[11] Jacobs, J. (1992). *The Death and Life of Great American Cities*. Vintage Books, A Division Random House, INC, New York.

[12] Capasso Da Silva, D., King, D.A., Lemar, S. (2020). *Accessibility in practice: 20-minute city as a sustainability planning goal.* Magazine Sustainability. 2020, 12, 129. doi:10.3390/su12010129.

[13] Peter, Y. (2022). *Cars Are Vanishing from Paris*. Reasons to be cheerful, Web magazine, https://reasonstobecheerful.world/cars-are-vanishing-from-paris/

[14] Dragosavljević-Savin, LJ. (2022). Novi Sad Neighbourhoods as Centres of Culture. District. *https://visitdistrikt.rs/en/2022/09/12/novi-sad-neighbourhoods-as-centres-of-culture/*

[15] Parking network (2023). Astron Buildings: Eco-Designed Multi-Storey Car Park https://www.parking.net/parking-news/astron-buildings/eco-designed-multi-storey-car-park

https://doi.org/10.24867/INDIS-2026-EN-536



# EDUCATIONAL MODELS AND THE TRANSFORMATION OF PRIMARY SCHOOL ARCHITECTURAL PROGRAMS: THE INFLUENCE OF THE MONTESSORI METHOD

*Marijana Divljak[1], Milena Krklješ[2], Dejana Nedučin[3]*

***Summary:***

The paper explores the relationship between educational models and the organization of architectural space in which pedagogical principles are implemented. It assumes that the successful design of educational institutions requires an understanding of contemporary educational models and their spatial implications. As educational approaches evolve, architecture plays a key role in shaping environments that support new modes of learning. The research examines the impact of the Montessori educational method on the reorganization of primary school programs and the transformation of their spatial and functional characteristics. Through a comparative analysis of Montessori schools and schools based on the traditional ex cathedra teaching model, the study identifies key changes in spatial organization, programmatic structure, and relationships between educational activities. The findings emphasize the importance of space as an active factor in learning and educational processes, while highlighting the growing pedagogical interest in its design and organization.

*Keywords: education, architectural program, schools, architectural typology.*

# OBRAZOVNI MODELI I TRANSFORMACIJA ARHITEKTONSKOG PROGRAMA OSNOVNIH ŠKOLA: UTICAJ MONTESSORI METODE

***Rezime:***

Rad istražuje odnos između obrazovnih modela i organizacije arhitektonskog prostora u kojem se pedagoški principi primenjuju u praksi. Polazi se od pretpostavke da uspešno projektovanje obrazovnih institucija zahteva razumevanje savremenih obrazovnih modela i njihovih prostornih implikacija. Kako se obrazovni pristupi kontinuirano razvijaju, arhitektura ima značajnu ulogu u oblikovanju prostora koji podržavaju nove načine učenja. Istraživanje analizira uticaj Montessori obrazovne metode na reorganizaciju programskog sklopa osnovnih škola i transformaciju njihovih prostornih i funkcionalnih karakteristika. Kroz uporednu analizu Montessori škola i škola zasnovanih na tradicionalnom ex cathedra modelu nastave identifikuju se ključne promene u organizaciji prostora, programskoj strukturi i odnosima između različitih obrazovnih aktivnosti. Rezultati ukazuju na značaj prostora kao aktivnog faktora u procesima učenja i vaspitanja, kao i na rastući interes pedagogije za njegovo oblikovanje i organizaciju.

*Ključne reči: obrazovni model, arhitektonski program, škole, arhitektonska tipologija.*

[1] MSc, Radio Television of Vojvodina, Novi Sad, Serbia, marijana.divljak@rtv.rs
[2] PhD, Full professor, University of Novi Sad, Faculty of Technical Sciences, Novi Sad, Serbia, mkrkljes@uns.ac.rs, ORCID 0000-0003-4252-258X
[3] PhD, Full professor, University of Novi Sad, Faculty of Technical Sciences, Novi Sad, Serbia, d.neducin@uns.ac.rs, ORCID 0000-0002-9828-072X

## 1. INTRODUCTION

The contemporary context of architectural theory and practice is defined by constant shifts and the introduction of new tendencies. Architecture at the beginning of the twenty-first century is characterized as integrated and interdisciplinary, open, multiple, and indeterminate [1]. The complexity of contemporary social conditions is particularly evident in the field of education. Since education is inherently oriented towards the future, changes within the educational sphere directly reflect both the current state of society and its anticipated directions of development. As contemporary society exists in a constant state of transformation, rigid forms are losing significance, affecting spatial determinants at both urban and architectural levels.

Within architectural practice, this process is reflected in the continuous transformation of established typologies. In the planning and design of educational institutions, the Montessori pedagogical approach has had a particularly significant influence. In less than half a century, the Montessori approach evolved from an alternative and experimental method into one of the most influential models within contemporary educational systems, particularly in developed and democratic countries. Its principles have also been incorporated into guidelines for the design, organization, and furnishing of educational spaces.

The impact of the Montessori educational model is recognized not only in a pedagogical sense but also in the reorganization of primary school architectural programs. Grounded in principles of interaction, independent learning, and self-reflection, this educational approach has significantly influenced the transformation of school environments and their spatial organization. The programmatic reconfiguration associated with the Montessori model has led to notable changes in the formal characteristics, scale, and spatial relationships within school buildings, particularly in the integration of interior and exterior learning environments.

## 2. ARCHITECTURE AND THE PHENOMENON OF PROGRAMMATIC VARIABILITY

The phenomena commonly described in everyday and architectural discourse as changes of use, programmatic variability, or spatial multifunctionality imply a pronounced architectural spatial adaptability, or a significant degree of variability within architectural space itself [2]. The phenomenon of programmatic variability emerges from the interaction of complex, dynamic, and active relationships between a limited spatial framework and the forms or modes of its use. On a broader interpretative level, programmatic variability refers to the relationship between the formally defined spatial structure and the set of activities occurring within that space, which are inherently dynamic, changeable, or interchangeable.

In this context, an architectural program represents a synopsis (a set of instructions or an outline of content) of events intended to take place within a given space over time. According to Milenković [2], an event may be understood as any specific form of activity through which the function of a space is constructed within the framework of a programmatic concept. Depending on its position and role within the thematic structure of the spatial program, an event may also function as a key element in defining potential spatial possibilities. These possibilities are based on abstract principles necessary for the structured organization of selected programmatic components. In this sense, the architectural program determines the set of events according to their type, while the process of spatial structuring defines their functionality, which only at the level of

primary spatial elements becomes applicable to actual practice and activity within architectural space.

Spatial variability is based on the capacity of space to organize elements of programmatic variability within its structure in accordance with the events assigned, anticipated, or introduced into it. Everyday life, particularly within a fluid society, is characterized by unpredictability and constant change; consequently, the event emerges as a potential factor influencing the ability of space to reformulate its programmatic organization. Multifunctional or multipurpose spaces inherently involve complex situations in which events of different functional orientations are brought into spatial relationships. In this regard, the architectural program may be understood as content contained within a spatial framework that defines explicit while simultaneously enabling potential combinations of events organized through time.

The concept of multifunctionality presupposes function as the fundamental basis for understanding the complex unity of form and function in architecture. A certain degree of independence between these elements undoubtedly exists. However, an exclusive focus on either form or function inevitably produces a contradiction in relation to the initial premise of their interdependence. Multifunctionality therefore assumes function as the primary framework through which the relationship between form and use is articulated. Starting from usability and utility as essential components of architectural function, it becomes possible to define the field in which the phenomenon of spatial variability is introduced as part of the architectural program.

Multifunctionality, or multiple use as a programmatic requirement, incorporates various elements of both closed and open spatial concepts. On a theoretical level, the criteria established for determining the relationships among elements that carry multiple spatial contents acquire multifunctional definitions through the accumulation, overlap, or combination of different spatial events and experiences [2]. Such a model of spatial organization is implemented as a direct response to the pedagogical framework and educational principles that define Montessori schools (see Figure 1).

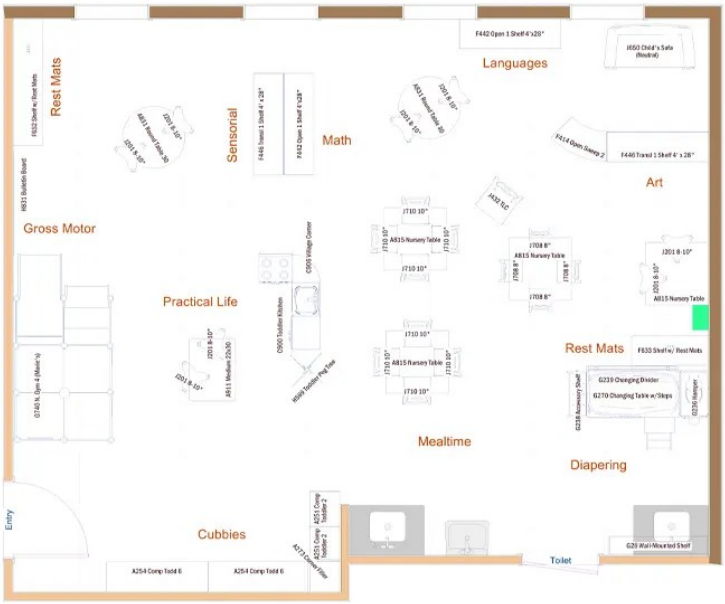


***Fig. 1 Montessori Classroom Layout Example (https://xihakidz.com/montessori-classroom-layout/, April 2026)***

## 2.1. STANDARDIZED PRIMARY SCHOOL TYPES AND THE MONOTYPY OF PROGRAMMATIC ORGANIZATION

The main attributes of primary school architectural programs, developed in accordance with the minimum standards required for their educational function, are directed toward identifying fundamental models of spatial organization, particularly through the overlap, integration, and separation of primary activities. The core programmatic structure typically includes administrative offices, art studios, cafeterias and dining areas, subject-specific classrooms, common spaces and courtyards, exercise and sports facilities, health service rooms, entrance lobbies, media centers, multifunctional spaces, music classrooms, storage areas, and science laboratories. This programmatic framework serves as a basic organizational structure and does not predetermine the final architectural form of the building. Instead, it provides the conditions for diverse spatial and formal interpretations in response to specific pedagogical, functional, and contextual requirements [3, 4].

The classroom constitutes the fundamental building unit of standardized primary school types. Within it, the educational process is most commonly organized through the model of oral instruction, based on the transmission of knowledge and information within a particular academic subject. Although classrooms may vary in form and dimensions, their multiplication on both horizontal and vertical levels represents the primary principle of spatial organization and construction (see Figure 2). The relationship between individual elements and the overall structure, between the micro-unit and the macro-composition, is the determining factor shaping the architecture of the standard primary school, both in terms of formal organization and spatial planning [5].

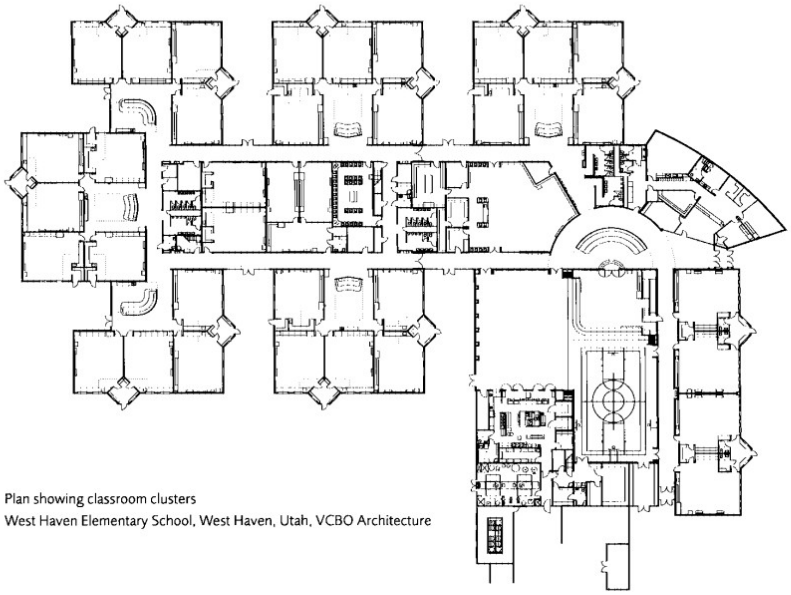


***Fig. 2 West Haven Elementary School, West Haven, Utah, VCBO Architecture (Mark, D. Schools and Kindergardens: A Design Manual. Basel, Boston, Berlin: Brikhauser, 2007)***

The segregation of content according to principles of similarity represents an important characteristic of standardized primary school types. Activities within the school are divided into groups of related functions, such as administration, artistic activities, and scientific laboratories. The separation of subjects within the curriculum is clearly reflected in the organization of the school itself, which is layered, divided, and segregated. Such a programmatic structure reveals principles of functional segregation

characteristic of the modernist and technocratic approach, one of whose principal advocates was Le Corbusier. The efficiency of the educational process is based on the separation of unrelated subjects and activities, connected through simplified systems of corridors and halls that, in addition to their circulation role, functioned as shared gathering spaces. Economic considerations also influenced programmatic organization, limiting opportunities for increasing spatial capacities or spatial experimentation [6].
Monofunctionality represents another defining characteristic of standardized primary school types designed according to minimum requirements. Within such systems, each subject is assigned a dedicated space according to the principle of one subject or one class - one room. This functionalist approach is clearly reflected in the architectural program of primary schools. The architectural program occupies a central position in the design of these buildings. However, this program is most often organized according to a monofunctional principle, in which each activity is assigned its own spatial unit. All activities are fragmented and organized according to principles of segregation and separation. Programmatic overlap, multifunctional spaces, and multivalent spatial configurations are generally absent. When such spaces do exist, they are reduced to a minimum and appear more as exceptions than as standard organizational principles [7].

## 3. MONTESSORI PRIMARY SCHOOLS AND THE COMPLEXITY OF PROGRAMMATIC ORGANIZATION

Considered from the perspective of contemporary developmental theories, the Montessori educational method represents an optimized approach to working with children from birth to the age of twenty-four. It is based on group, individual, and reflective work, while emphasizing the child’s natural potential for development, intrinsic motivation, active learning, emotional maturation, rational reasoning, and the acquisition of functional knowledge and skills. The founder of this educational method was Maria Montessori (1870–1952), who devoted her professional career to studying child development, examining existing educational approaches, and continuously improving them. Through observation and inductive reasoning, Montessori identified fundamental principles of child and adolescent development, forming the basis of the Montessori educational method, which later initiated an educational reform of global significance. Although its practical implementation began modestly during the early decades of the twentieth century, today it is recognized as one of the most influential pedagogical methods worldwide [8].

### 3.1. MONTESSORI EDUCATIONAL METHOD – FOUNDATIONS AND PRINCIPLES

The Montessori educational method is grounded in the belief in children’s creative potential, their natural motivation to learn, and the importance of treating each child as an individual. Beyond intellectual development, Montessori pedagogy fosters attention, concentration, physical development, and motor coordination through continuous engagement with meaningful activities. Within the Montessori environment, children develop positive social behavior through interaction with peers and the independent resolution of social situations. The aim of the Montessori educational program extends beyond the traditional objective of developing intelligence. Its focus on preparing children for everyday life, together with balancing freedom and responsibility, represents a distinctive characteristic of the Montessori model. Education is therefore understood not merely as the transfer of knowledge, but as the development of complete and well-rounded human beings [9].

The Montessori educational model requires a specific organizational framework and specialized didactic materials adapted to the interests and developmental needs of each child, situated within an environment of appropriate spatial qualities and design characteristics. The transformation of conventional school models, together with the development of new forms of programmatic organization, represents an important challenge for contemporary architectural practice. The integration and spatial-temporal overlap of activities, learning processes, and didactic tools constitute the foundation of the Montessori approach to education. This educational model is based on a spatial organization characterized by openness, multifunctionality, diversity, flexibility, and interaction. Rather than separating activities into rigid functional categories, Montessori schools encourage integration, overlap, and interconnection among different forms of learning and everyday experiences. The creation of an environment that is simultaneously open and flexible, yet structured and clearly articulated, constitutes one of the fundamental principles of Montessori schools. Within this framework, space becomes an active participant in the learning process, supporting interaction between children and teachers, among children themselves, and through individual reflective practices. In this sense, the physical environment functions as an educational instrument rather than as a fixed and predetermined framework. For this reason, Montessori schools seek to establish a balance between openness and enclosure, structure and freedom, privacy and publicity, as well as collective and individual experience, while architectural environment must adapt to the educational philosophy and pedagogical principles of the Montessori method [10].

## 3.2. THE INFLUENCE OF THE MONTESSORI EDUCATIONAL MODEL ON THE PROGRAMMATIC ORGANIZATION OF PRIMARY SCHOOLS

The reorganization of the programmatic structure of primary schools represents a complex phenomenon. In its most direct form, it is manifested through several key spatial characteristics, including multifunctionality, programmatic complexity, programmatic variability, and programmatic permeability.

### 3.2.1. Multiple Use - Multifunctionality

The phenomenon of multiple use, or multifunctionality, is essential for understanding the influence of the Montessori educational model on the reorganization of primary school programs. The variability of architectural space becomes a key element in establishing both actual and potential relationships between activities and time within the spatial framework defined by the architectural structure [2]. In this context, the capacity for multiple uses implies variability as an inherent spatial quality, enabling the substitution and transformation of different programmatic functions over time. The potential for programmatic change is therefore determined not by fixed formal characteristics, but by the degree of freedom embedded within the spatial structure itself. Within environments of identical dimensions and organizational frameworks, a wide range of activities may occur with minimal or no alteration of their primary spatial attributes. As a result, multifunctionality can operate both as a guiding principle in the design of new educational environments and as a framework for reinterpreting and adapting existing ones. The emphasis on potentiality rather than formal or functional completion is particularly significant for understanding the spatial characteristics of contemporary educational institutions. In this sense, architectural space is conceived not as a static container of predetermined functions, but as an adaptable system capable of accommodating changing educational practices, diverse forms of interaction, and evolving pedagogical requirements.

### 3.2.2. Programmatic Complexity

A tendency toward the increasing complexity of activities within the internal structure of school buildings has been observed, accompanied by a simultaneous reduction in the number of spatial determinants that define them. The decreasing differentiation between individual spaces expands the possibilities for overlap, integration, and interaction among diverse programmatic contents. Since the Montessori educational method rejects standardized hierarchies of functions and activities, its principles of spatial organization differ significantly from those of traditional school models. The conventional axial arrangement of functions along corridors, together with their mutual segregation, is replaced by a network of potential relationships connecting different activities, contents, and domains of learning. In its most developed form, this network may extend toward the complete integration of programmatic elements. Consequently, spatial complexity is defined not through the accumulation of functions, but through the orientation, distribution, and interconnection of activities within the educational environment. Such complexity generates focal points of interaction and learning within the school building, establishing centers of activity alongside more peripheral zones of reduced intensity. Rather than emphasizing separation and confrontation between spatial domains, the Montessori model promotes their coordination and mutual dependence. As a result, the internal programmatic structure of the school is transformed into a complex, dynamic, and interconnected organism capable of supporting diverse educational processes and forms of social interaction.

### 3.2.3. Programmatic Variability

One of the defining characteristics of school architecture is the progressive opening of the internal spatial structure through the reduction of rigid functional determinants.Accordingly, the purpose of a space is no longer regarded as its defining characteristic. Instead, spaces, both individually and collectively, are understood through their primary spatial qualities, their relationship to the surrounding environment, and the spatial accents that shape their identity. The highest degree of programmatic variability and adaptability is generally concentrated within common areas, while individual spaces remain partially determined by their position within the overall organizational framework of the building. Flexibility may also be achieved through the liberation of space as an autonomous architectural component, enabling it to function as a platform for a broad spectrum of activities and events. Similar to multifunctionality, variability may be interpreted through two complementary approaches. The first is based on the liberation of space, where internal organization is not determined through fixed and predefined functions, but through spatial dimensions, possibilities for secondary subdivision, orientation toward the surrounding environment, and patterns of circulation and movement. The second approach is defined through the variable character of space itself, that is, through the organization of partially determined environments. In this case, the programmatic structure inherently contains the potential for transformation, incompleteness, and adaptation within its formal configuration. From these considerations, two fundamental characteristics of the contemporary concept of primary school organization designed to support the Montessori educational method can be identified. The first involves providing numerous combinations of activities and programmatic contents together with elastic and adaptable patterns of movement and interaction. This requirement stems from the fact that the Montessori method functions as a framework for action rather than as a rigid system of instructions to be mechanically implemented. The second characteristic concerns the creation of spaces whose primary qualities can accommodate diverse

contents, flexible programmatic structures, and continuously changing educational activities. The aspiration toward freedom as a pedagogical principle generates a new model of spatial organization within school interiors, shifting from the domain of simple modification toward the domain of open action and continuous transformation. In such an environment, architectural space supports the harmonized development of the child, the educational institution, the immediate surroundings, and all participants involved in the learning process, establishing a dynamic relationship between pedagogy, architecture, and everyday experience.

### 3.2.4. Programmatic Permeability

The fixed nature of school programs represents one of the fundamental characteristics of standardized primary school typologies. Through the introduction of new educational contents and the spatial expansion of existing ones, permeability emerges as one of the key principles through which the Montessori educational model influences the reorganization of primary school programs. It encourages the interpenetration of individual and collective environments, as well as served and service spaces, while contemporary educational buildings often extend this principle through the dynamic relationship between open and enclosed spatial structures. Programmatic permeability is conditioned by both complexity and variability, corresponding to a high degree of integration and the flexible character of internal spatial organization. Within this framework, gradation or the gradual transition between different spatial conditions becomes a fundamental architectural parameter through which permeability is physically manifested.

As such, permeability establishes direct relationships between different spatial domains. It connects interior and exterior environments while organizing the interaction between open and enclosed areas within the school and determining the degree of their overlap. In this way, rigid divisions are replaced by transitional conditions in which space may simultaneously function as open and enclosed, individual and collective, depending on the immediate needs of users, the subject of learning, or the educational project being developed. Through this process of spatial diffusion, traditional organizational models of primary schools are adapted to the principles of the Montessori educational method, generating new standards, requirements, and spatial-programmatic relationships.

Programmatic permeability may therefore be understood as a condition of spatial diffusion, a principle according to which events, activities, and interactions intertwined within the educational environment. These relationships range from spontaneity and improvisation to guidance and planning, creating a framework in which free action remains unrestricted while the creative potential of learning can develop to their fullest extent. Diffusion may also be interpreted as a design principle, a model of spatial and programmatic organization that provides flexibility, openness, and controlled unpredictability. Although such an environment allows for spontaneous interaction and exploration, it remains guided and supervised by educational staff rather than being left to pure chance.

Within the Montessori framework, permeability thus becomes more than a spatial characteristic; it functions as an educational principle translated into architectural form. Through the continuous negotiation between openness and control, freedom and guidance, the school environment evolves into a dynamic and interconnected system capable of supporting diverse learning processes, social interactions, and forms of individual development.

## 4. CONCLUSION

Primary schools are institutions in which the first forms of formal education take place over an extended period of time, making them an architectural typology of considerable social significance. For this reason, particular attention has traditionally been directed toward the development of regulations, standards, and design principles governing the construction of educational facilities, including preschool, primary, and secondary schools. At the same time, transformations within the contemporary economy, the emergence of digital technologies and media, the growing importance of creative industries, the decline of industrial production in developed countries, and numerous other social and cultural processes have significantly influenced the nature, methods, and objectives of contemporary education. Changes occurring at the conceptual and methodological levels of educational practice have consequently affected the development of school architecture through both the adaptation of existing building stock and the construction of facilities with contemporary spatial characteristics.

It can be concluded that the application of the Montessori educational approach significantly influences the reorganization of primary school programs in multiple ways. Although the transformation of school programmatic structures represents a complex phenomenon that cannot be fully systematized within the scope of a single study, several key spatial characteristics can be identified as their most direct manifestations: multifunctionality, programmatic complexity, variability, and permeability. Each of these categories derives its theoretical foundation and operational logic from the fundamental pedagogical principles of the Montessori method. Furthermore, the implementation of Montessori principles at the level of architectural standards and design strategies contributes to greater programmatic diversity and openness within educational institutions. It enhances the multifunctionality and multivalence of interior environments, promotes the openness of overall spatial structures, reduces the dominance of the classroom as the primary organizational unit of the school, encourages smaller-scale and more intimate learning environments, and strengthens the relationship between activities occurring in interior and exterior spaces. As a result, the influence of the Montessori educational model extends beyond pedagogy itself and becomes visible in the development of new design approaches.

The implementation of the Montessori educational method has introduced substantial changes in the conceptualization, design, and construction of educational facilities at all levels, particularly within primary education, where children are especially sensitive to environmental influences. These changes are reflected in the transformation of school programmatic structures and in the reorganization of individual spatial elements toward their integration across both space and time. Multifunctionality, complexity, variability, and permeability may therefore be understood as the principal mechanisms through which the Montessori educational model influences the architectural organization of primary schools, from the earliest stages of design to the everyday realities of educational practice. Ultimately, the significance of the Montessori approach lies not only in its pedagogical framework but also in its capacity to redefine the relationship between architecture and education. By promoting openness, adaptability, interaction, and spatial diversity, it establishes a model in which educational environments become active participants in the learning process. In this sense, architecture is no longer understood merely as a physical container for educational activities, but as a dynamic and transformative medium through which pedagogical values are translated into everyday spatial experience.

## ACKNOWLEDGEMENT

This paper is the result of the project “Innovative approaches to integrating contemporary scientific research and artistic practices into educational processes in the fields of architecture, urbanism, and scene design, with the aim of advancing knowledge and disseminating results” conducted by the Department of Architecture and Urban Planning, Faculty of Technical Sciences, University of Novi Sad, 2026.

## REFERENCES

[1] Tschumi, B. & Cheng, I. (2004). *The State of Architecture at the Beginning of the 21st Century*, The Monacelli Press, Columbia.

[2] Milenković, V. (2004). *Arhitektonska forma i multifunkcija*, Zadužbina Andrejević, Beograd.

[3] Auf Franić, H. (2004). *Osnovne škole: Programiranje, planiranje i projektovanje*, Golden marketing, Zagreb.

[4] Anđelković, M. (1995). *Školske zgrade*, Građevinska knjiga, Niš.

[5] Crosbie, M. (2001). *Class Architecture*, Images Publishing, Mulgrave.

[6] Mark, D. (2007). *Schools and Kindergardens: A Design Manual*, Brikhauser, Basel, Boston, Berlin.

[7] Curtis, E. (2003). *School Buildings*, Wiley-Academy, Chichester.

[8] Montesori, M. (2002). *Otkriće deteta*, CRS, Beograd.

[9] Röhrs, H. (1994). *Maria Montessori*, UNESCO: International Bureau of Education, Education: A Reference Handbook (Contemporary Education Issues), ABC-CLIO, New York.

[10] De Jesus, R. (1987). Design Guidelines for Montessori Schools. Milwaukee: University of Wisconsin.

https://doi.org/10.24867/INDIS-2026-EN-546



# FROM REGIONAL RESOURCE TO SPATIAL STRATEGY: A NEW CONTEXTUAL READING OF DTD CANAL

*Dragana Konstantinović[1], Slobodan Jović[2], Boško Ristić[3]*

***Summary:***

This paper presents strategic design as an integrated paradigm within architectural education, with a focus on the Master Studio Course at the University of Novi Sad. Using the vast territorial, ecological, and infrastructural system of the Danube-Tisa-Danube (DTD) hydro system as a case study, the task connects territories, settlements, and individual built structures into a single strategy. Through design-based research and regional contextual analysis, students developed prototypical spatial solutions and strategic scenarios. The outcomes demonstrate how addressing complex, multilateral challenges and reclaiming marginalised infrastructure shift architectural pedagogy from static object-making toward dynamic, socially justified spatial agency.

*Keywords: strategic design; contextual reading; design-studio; territory; prototyping; hydro system Danube-Tisa-Danube*

# OD REGIONALNOG RESURSA, DO PROSTORNE STRATEGIJE: NOVO KONTEKSTUALNO ČITANJE KANALA DTD

***Rezime:***

Ovaj rad predstavlja strateško projektovanje kao paradigmu primenjenu u edukaciji arhitekata, fokusirajući se na master projektantski studio na Univerzitetu u Novom Sadu. Koristeći kompleksni prostorni, ekološki i infrastrukturni potencijal hidrosistema Dunav-Tisa-Dunav (DTD) kao studiju slučaja, zadatak upostavlja veze između teritorija, naselja i pojedinačnih građenih struktura, kroz kreiranje strategije. Kroz istraživanje zasnovano na projektovanju i sveobuhvatnu analizu konteksta, studenti su razvili prototipska rešenja i razvojne scenarije. Rezultati pokazuju kako suočavanje sa složenim prostornim izazovima i aktivacija zanemarene infrastrukture pomera arhitektonsku pedagogiju sa projektovanja pojedinačnog objekta ka dinamičnom društvenom delovanju.

*Ključne reči: strateško projektovanje; projektantski studio; teritorija; prototipovi; hidro sistem Dunav-Tisa-Dunav*

[1] Professor, Faculty of Technical Sciences, University of Novi Sad, Novi Sad, Serbia, konstan_d@uns.ac.r.s, ORCID 0000-0003-3971-0678
[2] Teaching Assistant, Faculty of Technical Sciences, University of Novi Sad, Novi Sad, Serbia, slobodan.jovic@uns.ac.rs, ORCID 0000-0003-2584-5010
[3] Teaching Assistant, Faculty of Technical Sciences, University of Novi Sad, Novi Sad, Serbia, ristic.bosko@gmail.com

## 1. STRATEGIC DESIGN

Strategic design is an integrated process that connects architectural practice with broader social, economic, environmental, and political systems and settings. It views the built structure not as an isolated aesthetic or functional artifact, but as a spatial instrument that drives change, resolves complex conflicting situations, and creates long-term value in the built environment. Explaining the importance of strategic design in times of crisis, Dan Hill emphasizes that it is an approach “focused on the systemic redesign of cultures of decision-making at the individual and institutional levels, and particularly as applied to what we can think of as the primary problems of the 21st century — healthcare, education, social services, the broader notion of the welfare state, climate change, sustainability and resilience, steady state economic development, fiscal policy, income equality and poverty, social mobility and equality, immigration and diversity, democratic representation and so on.”[1]
Compared to the standard approach to architectural design, strategic design introduces following

- Expanding the problem framework: In contrast to the standard design process, which begins with a project brief or task, through strategic design, the architect actively participates in creating the brief itself.
- Concentrating on the processes that affect the architectural work, rather than just the outcome of the design process: While the focus of standard design is on form, materiality, and construction, the strategic approach focuses on processes and scenarios. The object is not viewed as a final product, but as a dynamic system with its own life cycle.
- Understanding social and urban challenges: The process accounts for complex urban and social challenges involving numerous stakeholders with conflicting interests. Strategic design seeks to absorb social tensions and ensure that the intervention is widely accepted and socially justified.
- A comprehensive understanding of context: The focus shifts from the micro-location (the plot) to macro-systems. A strategically designed object consciously connects with the elements of its surroundings, both physically and socially.

Strategic design relies on important theoretical foundations that remain relevant today: the problem of problem-definition (wicked problems), which was highlighted back in 1973 by Horst Rittel and Melvin Webber, pointing out the underdeveloped capacities of correlating fields to support the planning process, because these problems do not have an unambiguous solution; instead, every solution changes the very nature of the problem.[2] As Hill states, this situation has not changed much to date, so wicked problems remain an important standpoint of contemporary urban and architectural theory. Another important dimension of strategic design relies on Lefebvre's theory of the production of space, which highlights the social dimension of practice and "lived space" in contrast to the conceived one.[3] Till also emphasises the social dimension of architectural work.[4] Architectural action (agency) lies in setting a network of relationships into motion. In this sense, strategic design is the operationalisation of spatial agency: it deals with pre-project phases, negotiations, long-term management, and the transformation of the existing built environment.
Researching and applying this design methodology is significant in the final years of architectural studies, serving as both a synthesis of design knowledge and its expansion. For this reason, this approach has become the backbone of the course Architectural Design – Complex Programs during the winter semester of the master’s studies program, spanning several generations of students.

## 2. THE MASTER'S COURSE AS A TESTING GROUND FOR STRATEGIC THINKING

The nearly invisible infrastructure of the Danube-Tisa-Danube hydro system became a platform for processes of research, reinvention, and strategic rethinking of its future. The final year of studies provided an adequate environment to introduce innovative working methodologies: design-based research, the formulation of prototypical solutions, strategic planning, and design.

The execution during 2024/2025 and 2025/2026 ranged from data collection and initial infrastructure research (its dimensions, structures, topographical features, connections, overlaps with other characteristic networks, environmental qualities, and ecological status) to uncovering the multifaceted values on which its future would be built. During this process, spaces, landscapes, settlements, and structures directly connected to or in the immediate vicinity of the canal network were explored: industrial complexes (both active and abandoned), settlements and the typology of their contact with the water surface, numerous hydro-technical structures, as well as landscapes that challenge our understanding of natural and artificial environments.

The working methodology addressed the space of this region in its entirety, blurring the boundaries between the natural and man-made landscapes, as well as between the scales of the spaces themselves, thereby dissolving the divisions between spatial planning, urbanism, and architectural design. In this manner, a platform was created for specific strategies that put the spaces and the canal network into the service of conceptualising contemporary development scenarios, which were further contextualised by the project brief. The outcomes of this phase include prototypical solutions, spatial situations, infrastructural interventions, the conceptualisation of new landscapes, new programmatic connections, and the reinvention of urban and rural environments. Throughout the process, new technologies provided support for both research and the testing of potentials and solutions.[5]

## 3. THE DTD CANAL: A STRATEGIC NETWORK

Although little known, the construction of the Danube-Tisa-Danube canal system represents the largest infrastructural project in the territory of the former Yugoslavia. Based on the regulation project for the floodplains of the southern Pannonian provinces of the Austro-Hungarian Empire, the project took on a new dimension within the framework of the infrastructural and industrial development of Vojvodina during the second half of the twentieth century. Guided by the vision of engineer Nikola Mirkov – an eccentric, unconventional social figure of that time – this project altered the spatial, social, economic, and cultural landscape of Vojvodina.

The scale of the project is most evident in its spatial dimension, the characteristics of the canal network, and the area of its direct and indirect impact. The Danube-Tisa-Danube hydro system project represents a complex water management project covering an area of approximately 2,100,000 hectares. This includes drainage and irrigation processes, water supply, and navigation capabilities. The hydro system project also encompasses all auxiliary structures: bridges, sluice gates, canal locks, pumping stations, docks, and other civil, technical, and hydro-technical structures. The 960-kilometer-long canal network, together with the Danube and Tisa rivers, connects the largest cities and municipalities in Vojvodina, forming the foundation for industrial and agricultural development.

The end of the twentieth and the beginning of the twenty-first century, characterized by the dissolution of the former state and a transitional crisis, cast a shadow over this decades-long project. However, although the role and potential of the canal network have fallen into obscurity, its fragments remain significant touchpoints in the lives of the local population, who continue to recognise its spaces as venues for various activities. The project thus remains trapped between the grand ambitions of the state in the past century and its neglect during the current one – between the great dream of its creator and changed social circumstances that have restricted the realisation of its full potential.

The initial contemplation of the canal network in the territory of present-day Vojvodina was shaped by a long-term interplay between natural processes and human intervention. The spatial dimension of the network relies on multi-millennial geological and hydrological shifts in the Pannonian Basin, as well as historical traces of water regulation from the Roman and Austro-Hungarian Empire periods. The existing lowland landscape of Bačka, Banat, and Srem was shaped by sediment deposition and the formation of wide floodplains, which, for centuries, limited settlement of the region and hindered agricultural production.[6]

Observed traces of irrigation and drainage from the Roman period, alongside the development of the canal network in the nineteenth century, testify to the necessity of taming this vast area of the Pannonian plain and transforming floodplains into agricultural land, thereby facilitating settlement. The construction of the Danube-Tisa-Danube (DTD) hydro system relies heavily on its predecessors – the Great Bačka Canal and the Begej Canal – connecting and integrating these existing channels into a hydrosystem spanning over six hundred kilometres.

The end of World War II brought a new social order to the peoples of the Yugoslav space, whose war-exhausted economy entered a new phase of reconstruction and development. The social circumstances surrounding the establishment of the new political and economic system stimulated economic, cultural, artistic, and technical-technological development. Social transition and the need for strategic spatial planning provided fertile ground for initiating and executing the largest infrastructural project in the former Yugoslavia – the Danube-Tisa-Danube Hydrosystem. The conceptual creator of this project, engineer Nikola Mirkov, frequently emphasised that the canal was not merely a technical endeavour of water regulation, but also an instrument for the planned shaping of territory, balanced regional development, and the long-term stabilisation of agricultural production in one of the country's largest granaries:

“The Great Canal will swiftly change the face of not just one province, but the entire country. History has never recorded a scenario where, alongside the planning of a new water regime, a new province is planned, a new agriculture, a new economy, a new industry, and a new transport network – rail, road, and even air – new towns and villages, new industrial centres, and new working-class settlements. Only in this way can the Great Canal be utilised to its full extent.” [7]

The value of this project is reflected in its significance for Vojvodina today. The DTD canal represents a network of primary and secondary channels with a multi-faceted role and vital importance for irrigation, water supply, fishing, transport, tourism, industry, flood control and more. The importance of this network is most clearly read through its key numerical indicators.[8] *(Tab. 1)*

*Tab. 1 Numerical indicators for DTD Canal*

| Parameter / Indicator | Value |
|---|---|
| Drained territory | 1,060,000 ha |
| Irrigated territory | 510,000 ha |
| Total length of the canal network | 960 km |
| Navigable length of the network | 600 km |
| Number of connected settlements | 80 |
| Vojvodina population gravitating toward the canal | 50% |
| Number of hydro-technical structures (locks, gates, etc.) | 53 |

The monumentality, scale, and significance of the canal network for life in Vojvodina today constitute the primary reason for the need for strategic planning across the entire territory gravitating toward the DTD hydro system. The historical continuity of establishing a more favourable agricultural position, settlement patterns, and the perpetual need for land management provides a further foundation for continuing and developing plans and projects dedicated to the maintenance, development, and transformation of the network.

## 4. THEMATIC STRANDS: STRUCTURING RESEARCH AND DESIGN RESPONSES

The historical and current significance of the canal network highlights the imperative of its future. The foundation for theoretical research and the further development of projects and conceptual designs is deeply rooted in interdisciplinarity and strategic planning. Research and design work in the academic years 2024/25 and 2025/26 can be defined through several distinct approaches:

A) **The first group of outcomes** highlights research processes generated during the 2024/25 academic year, featuring clearly defined topics that can be methodologically and typologically classified into several categories:
   - Interdisciplinary research work – aimed at uncovering motifs and potentials of the network within the fields of agriculture, transport, industry, tourism, etc.;
   - Research work in the field of construction and architectural heritage – focusing on the technical, technological, and morphological significance of hydro-technical and other structures, also including the issues of architectural and industrial heritage preservation and reuse;
   - Research work addressing environmental pollution, ecological issues, as well as ecological chains and systems living in the vicinity of the canal;
   - Research work mapping the entire hydro-network and comparing it with other network systems, such as transport, energy, or telecommunication networks. The nods and sections of the networks are particularly addressed.

B) **The second group comprises planning and design outcomes** generated during the 2025/26 academic year. Methodologically and typologically, these works are clustered around several major themes defined during the preparatory phase of the studio work:
   - **Landscape:** This theme examines spatial categories grouped around shared characteristics of the natural environment and its inherent processes. Within the broader consideration of the DTD hydrosystem, this topic is particularly significant as it blurs the boundaries between the natural and artificial

landscapes of the Pannonian plain, placing this precise new quality at the core of redefining the regional landscape. *(Fig.1)*

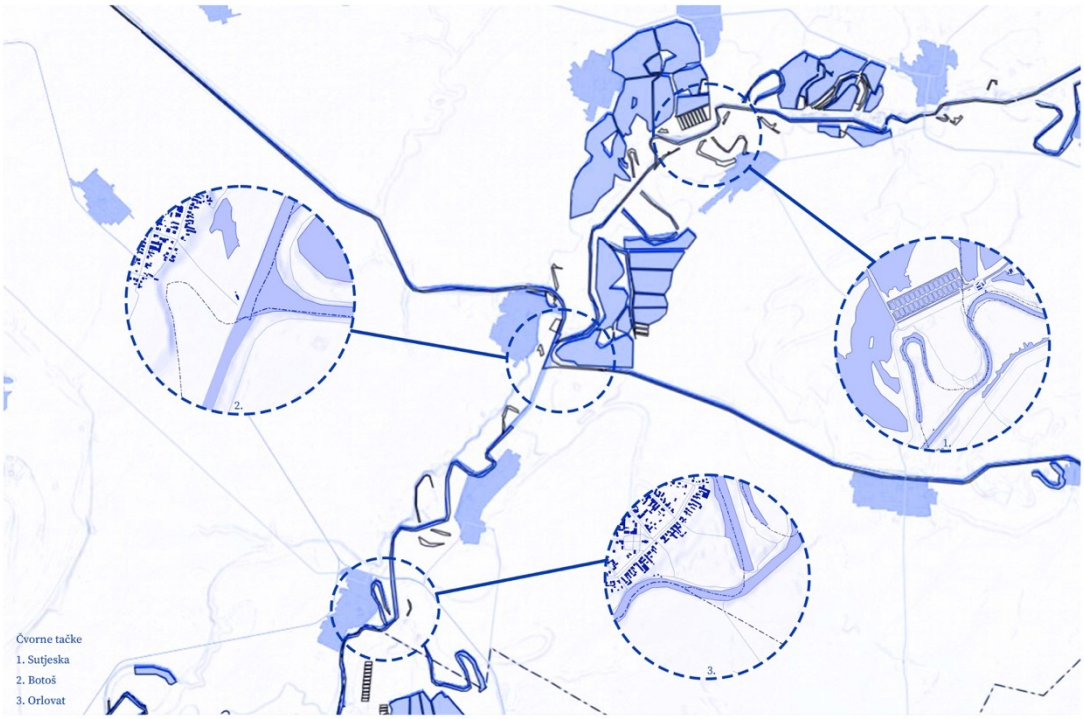


*Fig. 1 Landscapes of the Banat flooding region: Sutjeska, Botoš, Orlovat (Author: Dušica Piperski)*

**Connections / Networks.** The existing infrastructure of the DTD canal has been marginalised by the further development of transport systems, recently accelerated by railway upgrades and, particularly, by the expansion of telecommunications infrastructure. Settlement connections that were logical and efficient during the hydrosystem's peak operating period are being re-examined in light of new forms of water transport and infrastructure that create new connections and programmatic possibilities. *(Fig. 2)*

**New Centres of Social Life and Work.** Projections for the region's further development rely on emerging forms of living and working through which new urbanisation strategies are implemented. *(Fig. 3)*

Regional resources and contemporary lifestyles – supported by information infrastructure – can serve as a foundation for exploring new typologies centred around novel programs and forms that supports new ways of living and working. Whether involving digital-era occupations or information-supported smart agriculture, these frameworks harbour new qualities of life at the thresholds of natural landscape and water. *(Fig. 4)*

**Ecology.** Contemporary environmental pressures are particularly evident along the DTD canal system. In certain segments of the network, these processes have generated severe ecological issues, resulting in a definitive alienation from the water bodies, which are now, almost paradoxically, viewed exclusively as sources of pollution. How to reclaim the water landscape, what processes occur on-site, how they manifest, and how to re-establish the ecosystem are among the core questions that occupied the studio’s work. *(Fig. 5)*

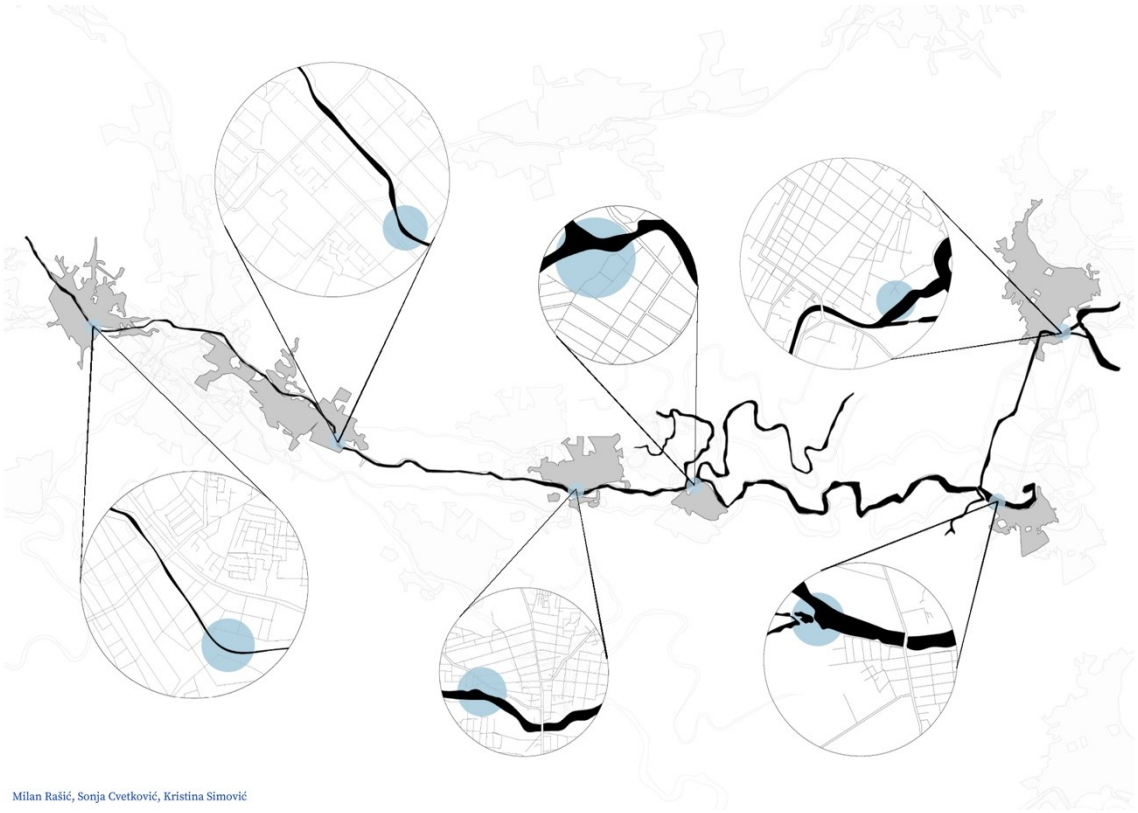


*Fig. 2 Creating Connections: Water system traffic infrastructure Kula-Bečej*
*(Authors: Milan Rašić, Kristina Simović, Sonja Cvetković)*




*Fig. 3 Connecting Waterfronts: Srbobran*
*(Authors: Ivana Knežević, Nina Jovanović, Mia Jovanović)*

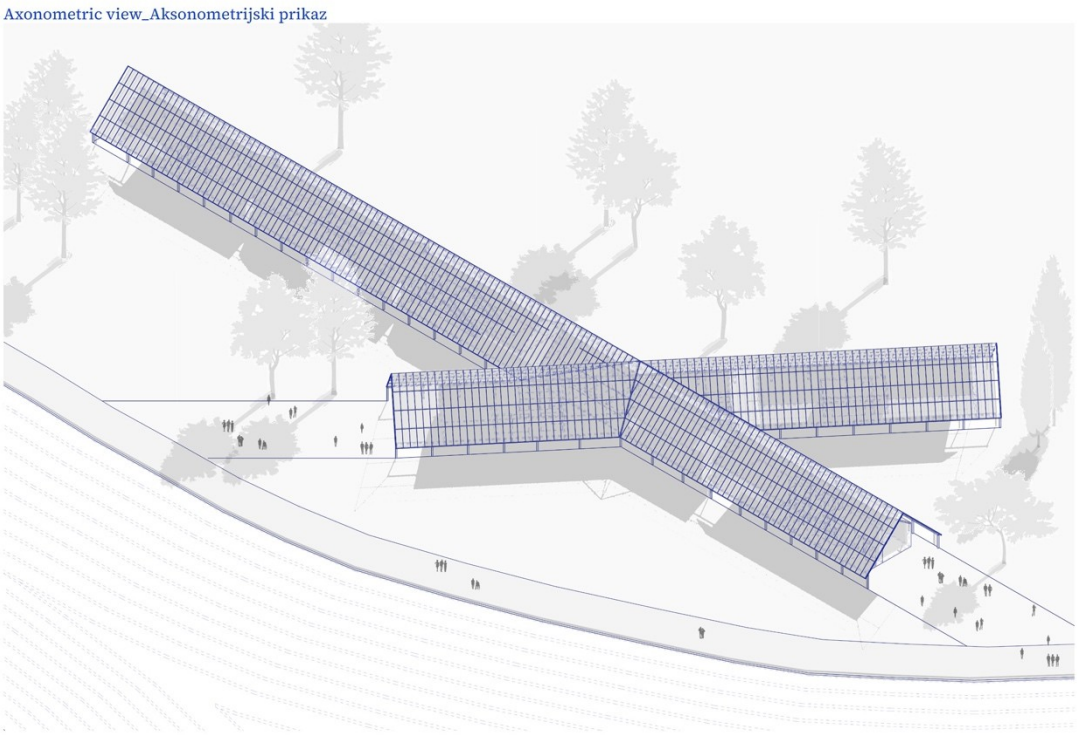


*Fig. 4 Pocket City – New Community Hub*
*(Authors: Tamara Mitrović, Tatjana Zamaklar, Ivana Ivančić)*

*Fig. 5 Research Center for Monitoring Waterbird Return and Habitat Reclamation*
*(Authors: Tijana Kovačević, Aleksandra Ćirić)*

## 5. STRATEGIC DESIGN AS AN EVOLVING PEDAGOGICAL FRAMEWORK

The historical, cultural, and economic significance of the canal network – as the foundation for the strategic planning of the region surrounding the Danube-Tisa-Danube Hydro system – lies at the core of a new rethinking of the hydrosystem and its impact on contemporary urbanisation patterns. The established working methodology is rooted in a comprehensive, contextual reading of the architectural project. Consequently, spatial strategy constitutes the framework for defining the project – its thematic backbone, program, and all necessary decisions in the execution of the architectural work.

The significance of this approach raises new questions regarding architectural education at the master's level: deepening the understanding of the importance of spatial and regional resources, which are very often overlooked; the complexity of impacts that are read, interpreted, and determined through the architectural work; and the development of strategic thinking at the intersection of architectural and urban themes, alongside understanding the complex relationships between space, society, economy, and ecology. The outcomes of this work offer perspectives for further research and practice. The diversity of challenges, the spatial scope, and the vast number of newly discovered situations provide an exceptional incentive for this process to continue and further evolve.

### ACKNOWLEDGEMENT

This research has been supported by the Ministry of Science, Technological Development and Innovation (Contract No. 451-03-34/2026-03/200156) and the Faculty of Technical Sciences, University of Novi Sad through the project "Scientific and Artistic Research Work of Researchers in Teaching and Associate Positions at the Faculty of Technical Sciences, University of Novi Sad 2026" (No. 01-3609/1).

### REFERENCES

[1] Hill, D. (2012). Dark Matter and Trojan Horses: A Strategic Design Manifesto. Strelka Press, p.8

[2] Rittel, H. W., & Webber, M. M. (1973). Dilemmas in a general theory of planning. Policy Sciences, 4(2), 155–169.

[3] Lefebvre, H. (1991) The Production of Space. Lefebvre, H. (1991) The Production of Space.

[4] Awan, N., Schneider, T., & Till, J. (2011). Spatial Agency: Other Ways of Doing Architecture. Routledge.

[5] Konstantinović, D., Jović, S., Ristić, B. (2026) The Great Dream of the Great Canal. Fakultet tehničkih nauka & BAZA-Platforma za prostorne prakse, Novi Sad (in print)

[6] Milovanov, D. (1972) Hidrosistem Dunav-Tisa-Dunav. Vodoprivredno preduzece DTD, Novi Sad

[7] Mirkov, N. (1947), Veliki kanal Dunav-Tisa-Dunav. Letopis Matice Srpske, novembar 1947.

[8] Hidrosistem Dunav-Tisa-Dunav. Vode Vojvodine. https://www.vodevojvodine.com/o-nama/vodni-resursi/hidrosistem-dunav-tisa-dunav/, accessed on 21 May 2026)

https://doi.org/10.24867/INDIS-2026-EN-555

**INTERNATIONAL SCIENTIFIC CONFERENCE**
INTEGRATION, NOVELTY, DESIGN,
INTERDISCIPLINARITY, SUSTAINABILITY

iNDiS 2026

# HOW DOES ARCHITECTURE REMEMBER? NARRATIVE ARTICULATION IN MEMORIAL SITES WITHIN TRANSFORMING URBAN LANDSCAPES

*Petar Mitrović[1], Višnja Žugić[2]*

***Summary:***

Continuous transformations of the urban landscape destabilize the relationship between memorial architecture and the city. This paper argues that successful reintegration depends not on the degree of physical survival of original structures, but on how architecture consciously articulates the narrative that persists within the transforming urban fabric. A dual-axis framework positions three World War II memorial sites across two independent dimensions: degree of physical destruction and degree of deliberate architectural reintegration, examining Auschwitz I, Sachsenhausen, and the Topography of Terror, defining them as absorbed, contested, and articulated narrative, respectively. The analysis reveals a consistent inverse relationship: as physical evidence recedes, architecture assumes an increasingly active and irreplaceable narrative role. The need for narrative articulation in architecture, therefore, emerges directly from the transformation of urban landscapes.

*Keywords: narrative architecture, narrative articulation, memorial architecture, urban landscape transformation, collective memory*

# KAKO ARHITEKTURA PAMTI? NARATIVNA ARTIKULACIJA MEMORIJALNIH PROSTORA U URBANIM PEJZAŽIMA U TRANSFORMACIJI

***Rezime:***

Kontinuirane transformacije urbanog pejzaža destabilizuju odnos između memorijalne arhitekture i grada. Ovaj rad polazi od pretpostavke da uspešna reintegracija ne zavisi od stepena fizičkog očuvanja originalnih objekata, već od načina na koji arhitektura svesno artikuliše narativ koji opstaje unutar transformišućeg urbanog tkiva. Kroz dvodimenzionalni analitički okvir analiziraju se tri memorijalna prostora iz Drugog svetskog rata prema dve nezavisne dimenzije: stepenu fizičke destrukcije i stepenu svesne arhitektonske reintegracije. Analizom lokaliteta Aušvic I, Zaksenhauzen i Topografija terora definišu se tri narativna stanja: apsorbovani, osporeni i artikulisani narativ. Analiza ukazuje na dosledan inverzni odnos: kako fizički tragovi nestaju, arhitektura preuzima sve aktivniju i nezamenljivu narativnu ulogu. Potreba za narativnom artikulacijom u arhitekturi, stoga, neposredno proizlazi iz transformacije urbanih pejzaža.

*Ključne reči: narativna arhitektura, narativna artikulacija, memorijalna arhitektura, transformacija urbanog pejzaža, kolektivna memorija*

[1] Jr. Res. Asst., Faculty of Technical Sciences, University of Novi Sad, Novi Sad, Serbia, petarmitrovic@uns.ac.rs, ORCID 0009-0002-1291-6924
[2] Assoc. Prof., Faculty of Technical Sciences, University of Novi Sad, Novi Sad, Serbia, zugic.visnja@uns.ac.rs, ORCID 0000-0002-4677-7355

## 1. INTRODUCTION

Urban landscapes are active, dynamic, and continuously transforming. They combine historical and spatial layers that accumulate and overlap over time. Within this process, memorial spaces face a unique and persistent challenge. They hold narratives of traumatic events that resist erasure yet simultaneously contend with redevelopment pressures and evolving urban needs. The result, particularly in post-socialist and transitional contexts, is the formation of fragmented “islands of memory”, spaces that still exist but remain isolated from the transforming urban landscape around them (Elsaesser 2009).

The prevailing assumption in both heritage practice and urban planning holds that the fate of these spaces is determined by the degree to which their physical fabric survives transformation. What remains standing, it is assumed, determines what can be remembered. This paper argues the opposite. Drawing on the understanding that memory "is related to history, but is not history, it is relational and implicated with meaning production and identity construction" and that "remembering a past, we are actually projecting a future" (Hong 2020: 251), the paper proposes that narrative persists regarding physical destruction. Therefore, architecture, rather than merely preserving what remains, actively articulates that narrative within the transforming urban landscape.

Understanding how architecture performs this function requires moving beyond urban and architectural analysis toward the narrative and phenomenological dimensions of spatial experience. As Benjamin observed, buildings are appropriated "by use and by perception, or rather, by touch and sight" (Benjamin 2007: 240), pointing toward the experiential layers through which users engage with memorial spaces across their entire historical depth. It is precisely these dimensions, not the material condition of surviving fabric, that determine whether a memorial space successfully reintegrates into the city around it. Architectural narrative articulation is therefore not a response to destruction. It is a response to transformation.

This paper develops a dual-axis analytical framework positioning memorial sites across two independent dimensions, the degree of physical destruction of original structures and the degree of deliberate architectural reintegration into the transforming urban landscape. The framework is examined with three World War II memorial sites as illustrative examples: Auschwitz I in Oświęcim, Poland; Sachsenhausen in Oranienburg, Germany; and the Topography of Terror Documentation Centre in Berlin, Germany. Through these three examples, the paper demonstrates that as urban landscape transformation intensifies and physical evidence within memorial sites recedes, architecture assumes an increasingly active, visible, and irreplaceable role as the primary narrative articulator.

## 2. THEORETICAL FRAMEWORK: ARCHITECTURE, NARRATIVE, AND MEMORY

Cities are layered systems in which memorial spaces play a central role in shaping collective memory and identity (Sonkoly 2017). Yet they are frequently marginalized within contemporary urban processes, losing both spatial presence and narrative capacity. Architecture not only contains stories but also actively transmits them, and users construct meaning through their engagement with spatial forms (Ryan et al. 2016). In addition, from a semiotic perspective, meanings are not preserved but continuously reconstructed (Eco 1975). The critical question, therefore, is not how narratives in

memorial architecture are transmitted, but how narratives can be (re)articulated once their original frameworks have collapsed. Memorial spaces thus function through ongoing processes of reinterpretation, in which architecture provides the conditions under which narratives can be articulated and then read and remembered.

In memorial architecture, space is the primary medium through which narrative is delivered. At sites where the landscape can be perceived as the open museum, this logic becomes structural: the building, the terrain, and the story are inseparable, each giving the others meaning. The arrangement of texts, objects, and circulation paths determines not only what visitors encounter but also the order and rhythm in which they encounter it. Designing the space with sequential trajectory logic blurs the line between landscape and museum narratives (Ryan et al. 2016: 180). Narrative, in other words, does not inhabit the space—it produces it, and this production is never passive. Vujanović (2018) develops the concept of landscape dramaturgy in contemporary performance to describe how spatial arrangements structure experience rather than deliver fixed meanings where audiences are invited to move through and co-produce the work, rather than follow a prescribed trajectory. Vujanović further draws a direct parallel between this mode of attending and the experience of moving through a gallery or museum, where attention is free, non-linear, and shaped by the spatial conditions of the encounter. Applied to memorial space, this logic suggests that the dramaturgical force lies not in any single text or object, but in the overall organization of movement and perception through the site.

This makes the post-Yugoslav case particularly revealing. Jagdhuhn (2022) observes that World War II memorial sites across the former Yugoslavia now exist as “metamuseums”, defining them as institutions in form but not in function. Ideological frameworks that once organized meanings have collapsed, yet the spatial and material structures that carried those meanings remain. What survives is narrative without an author: stories embedded in landscape and architecture, persisting after the institutions that shaped them have disappeared.

What connects these conditions is that narrative does not require architecture to survive, but does require space to be communicated. When buildings are destroyed or ideological frameworks collapse, the narrative is not lost; what is lost is the spatial structure through which it was organized and made legible. Architecture's role, then, is not to preserve what remains but to actively articulate what survives, to provide a new spatial framework that consciously responds to enduring narrative content, and to further reintegrate it into the living tissue of the city. It is this capacity for articulation, rather than preservation, that this paper identifies as the determining factor of successful memorial space (re)integration within evolving urban landscapes.

## 3. TOWARD A FRAMEWORK FOR NARRATIVE ARTICULATION

This paper selects examples for their ability to illustrate a theoretical argument, not for their representativeness. The example sites occupy distinct and logically necessary positions within the dual-axis analytical framework proposed here. Three selection criteria were applied consistently: a direct historical connection to World War II, ensuring thematic coherence; meaningfully different degrees of physical destruction ranging from largely intact fabric through partial destruction to total erasure; and a dominant commemorative function within an urban context, allowing analysis of integration into the transforming urban landscape. Auschwitz I, Sachsenhausen, and the Topography of Terror Documentation Centre function as illustrative examples through which the framework is demonstrated. Each is analysed through a consistent sequence addressing overall historical context, landscape transformation, urban integration,

landscape dramaturgy, and narrative articulation. The paper acknowledges that three illustrative examples constitute a preliminary typology. The dual-axis framework requires broader empirical testing before its claims can be generalized and should be understood as a theoretical proposition inviting further research that could apply to contested heritage sites.

### 3.1. ABSORBED NARRATIVE: AUSCHWITZ I

*We arrived on a morning in January 1943. The doors of the cattle cars were pushed open, revealing the edge of an icy plain. It was a place from before geography. Where were we? We were to find out—later, at least two months hence; we, that is those of us who were still alive two months later—that this place was called Auschwitz. We couldn't have given it a name.* (Delbo, 2014:167).

The camp was established in 1940 on the site of former Polish military barracks in Oświęcim, Poland, and functioned as a site of extermination and forced labour until its liberation by Soviet troops on 27 January 1945, a date later designated as International Holocaust Remembrance Day. During its five years of operation, more than one million people were killed at the Auschwitz complex, over 90% of whom were Jewish (Philpott 2016: 157). The Auschwitz concentration camp complex consisted of three main parts: Auschwitz I (main camp), Auschwitz II-Birkenau (extermination camp), and Auschwitz III-Monowitz (labor camp), along with roughly 50 satellite subcamps (Holocaust Encyclopedia). The camp was preserved as a museum and memorial shortly after the war, opening in 1947 with a permanent exhibition established in 1955. Its significance was formally recognized in 1979 when UNESCO inscribed Auschwitz on the World Heritage List.



*Fig. 1: Contemporary urban fabric of Oświęcim, Poland, showing the spatial extent of Auschwitz I integrated into the surrounding city. The absence of a clearly defined boundary between the musealized site and urban tissue illustrates the passive and unresolved mode of reintegration.*

The integration of the Auschwitz complex, particularly the buildings in Auschwitz I (Fig. 1) that will be further analysed, into the transforming urban landscape of Oświęcim represents an example of the unintentional absorption of narrative into everyday urban life. The city's residents have continuously confronted the stigma of the

camp in both semantic and material terms, raising the fundamental question of where the former camp ends and normal life begins. (Rawecki 2016: 88). Today, the memorial and the city are fully intertwined where the museum of Auschwitz I sits close to the city centre across the Soła river, while Birkenau is located approximately three kilometres to the west near the village of Brzezinka. Crucially, the remains of the Holocaust extend well beyond these two musealized locations, dispersed throughout the city and beyond the boundaries of formally protected and controlled memorial space (Van De Putte 2025). The preservation of these material traces ensures that the historical significance of the camp is not lost as the space integrates into everyday life.

This condition illustrates the first typological position of the proposed framework. Where physical fabric survives largely intact, architectural narrative articulation remains invisible, where the ruins speak autonomously, and reintegration into the urban landscape occurs without conscious design intervention. Every surviving trace, including warehouses, workshops, and infrastructure elements such as bridges and roads, constitutes what Rawecki (2016: 81) describes as “corpus delicti”, where material evidence of the mechanisms of crime is irreplaceable in reconstructing the full memorial narrative. Even elements that appear secondary contribute to understanding how the site functioned and must therefore be understood as active narrative carriers within the urban landscape.

### 3.2. CONTESTED NARRATIVE: SACHSENHAUSEN

Founded in 1936, the Sachsenhausen concentration camp in Oranienburg, Germany, was designed to reflect SS ideology and had a powerful influence on the urban landscape. Over time, postwar reconstruction and the loss of surrounding historical fabric led to the disappearance of much of the original camp structure. What remained became subject to successive waves of politically motivated transformation, making Sachsenhausen the clearest example of contested narrative through competing acts of architectural reauthoring.

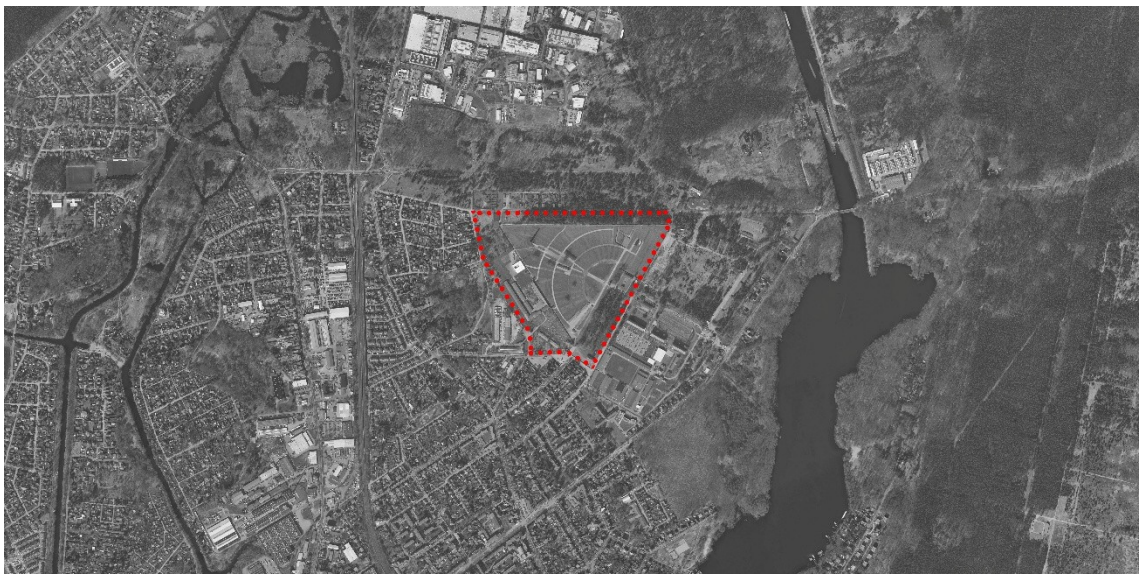

*Fig. 2: Contemporary urban fabric of Oranienburg, Germany, showing the spatial extent of the Sachsenhausen memorial complex. A buffer zone demarcates the northern and eastern border of the camp, yet the boundary between the memorial site and the urban development remains spatially ambiguous.*

Following the war, Soviet authorities assumed control of the site and almost entirely erased its original spatial structure. Original buildings were removed, and the space was reshaped with new architectural elements, replacing what had been described as the geometry of total terror with a narrative of triumph over fascism, culminating in a forty-meter obelisk with red triangles at its peak. This intervention consciously negated the original spatial logic of the camp and imposed a new ideological framework. After 1993, a comprehensive reconstruction began, which focused on preserving remaining Nazi-era structures. The previous look of the camp from the German Democratic Republic was partially dismantled, and different historical layers were critically reevaluated and placed in dialogue. Of the original sixty-eight barracks, only a handful survived, and the rest were marked by concrete plates set into the ground, spatial imprints suggesting their former presence.

Memorial spaces must be understood as palimpsests, layered with their history and successive transformation, and any future intervention requires awareness of their previous spatial changes (Massey 2005). At Sachsenhausen, curatorial decisions extended beyond museum spaces to the management and shaping of the broader landscape (Pastor and Kent 2021), exposing the ethical dimensions of architectural narrative agency. This condition illustrates the second typological position of the framework. Where destruction is partial, architecture becomes visible as a narrative medium, instrumentalized by successive political regimes to contest and reauthor the memorial narrative. The ruins no longer speak autonomously; competing agents have already intervened, making architecture's narrative role visible precisely through the conflict over who controls it.

### 3.3. ARTICULATED NARRATIVE: TOPOGRAPHY OF TERROR

The Prinz-Albrecht complex, former headquarters of the Gestapo, SS, and Reich Main Security Office, represented the organizational core of Nazi terror and repression in Berlin. Originally a school of applied arts, the building was converted in 1933 into the seat of the Third Reich's principal repressive institutions, becoming a symbol of the mechanisms responsible for the majority of the regime's war crimes (Philpott 2016: 72). The complex was almost entirely destroyed during Allied bombing and subsequently cleared, leaving only fragmentary ruins within a postwar urban void.



*Fig. 3: Contemporary urban fabric of the former Prinz-Albrecht complex, Berlin (now Niederkirchnerstraße), now housing the Topography of Terror Foundation and Documentation*

*Centre, excavated cellar ruins, a preserved section of the Berlin Wall, and surrounding institutional and open space.*

Recognition of the site's historical significance re-emerged in the late 1970s (Rürup 1989). With support from institutions and civic associations, a temporary exhibition titled Topography of Terror opened in 1987 and was extended due to public interest. A commission in 1989 recommended establishing a permanent documentation centre while preserving existing ruins. Two architectural competitions followed in 1983 and 1992, which were never fully realised. The third competition in 2005 was won by Ursula Wilms and Heinz W. Hallmann, whose documentation centre was realised and opened in 2010. The building contains four exhibition spaces alongside preserved remains of the original buildings, prison cells, and a section of the Berlin Wall, emphasizing the site itself as the primary historical artifact. The winning design enables what competition documents describe as varied and changeable views across the Topography of Terror (Topography of Terror 2025).

The Topography of Terror illustrates the third typological position of the framework. Where physical destruction is total, architecture can no longer defer to material evidence and must assume sole responsibility for narrative articulation. The documentation centre does not reconstruct what was lost—it creates a precise architectural frame through which the void itself becomes legible as historical evidence. Through minimal intervention, the site preserves what remains of the Third Reich's physical traces while providing a structure for interpretation and collective reflection (Walton, 2024). The site functions as its own primary historical artifact, while new architectural elements amplify its value and enable visitors to actively engage with the landscape, making architecture the product of shared experience and complex urban narration (Al-Bayati 2021). Here, the architecture's narrative role has been made fully and undeniably visible because almost nothing else remained to transmit narrative in its place.

## 4. DISCUSSION

Urban landscape transformation is not a neutral background process but an active force that continuously destabilizes the relationship between memorial spaces and the city. Physical destruction is only one manifestation of this destabilization; equally significant are the organic growth of the city through surviving fabric, the political reauthoring of spatial relationships, and the creation of urban voids that demand conscious resolution. What varies across the three typological positions examined in this paper is therefore not simply the degree of physical survival, but the manner in which landscape transformation reshaped each memorial space's relationship with its urban context over time. All three sites operate as palimpsests, but at fundamentally different degrees of legibility: at Auschwitz I the accumulated layers are absorbed into everyday urban life without conscious reading, while at the Topography of Terror, architecture makes every surviving and absent layer deliberately legible. Table 1 synthesizes these three positions across the two analytical axes.

*Tab. 1 Typological matrix positioning three World War II memorial sites across two analytical axes, revealing the inverse relationship between physical survival and architecture's role as active narrative articulator.*

| | Degree of Physical Destruction | Mode of (Re)integration into Urban Landscape | Role of Architecture as Narrative Articulator |
|---|---|---|---|
| Auschwitz I (Absorbed Narrative) | Low; fabric largely intact | Passive; integration happened organically, never consciously resolved | Invisible; ruins speak independently, architecture remains narratively passive |
| Sachsenhausen (Contested Narrative) | Partial; surviving elements alongside erasure | Contested; repeatedly overwritten by successive political regimes | Instrumental; architecture becomes visible as narrative agent through political conflict |
| Topography of Terror (Articulated Narrative) | Total; original structures completely destroyed | Deliberate; consciously designed reintegration into urban fabric | Primary; architecture carries entire narrative weight, fully exposed as active articulator |

The analytical matrix demonstrates a single argument read diagonally. As physical destruction increases across the three illustrative examples, the deliberateness of architectural reintegration increases proportionally, constituting the analytical basis for the main hypothesis of this paper: that architectural narrative articulation is the determining variable of successful memorial space reintegration into the transforming urban landscape. Where physical fabric survives largely intact, architectural narrative articulation remains invisible, where material remnants carry narrative autonomously, and reintegration occurs without conscious design intervention, appropriated through use rather than conscious perception. Where destruction is partial, architectural narrative articulation becomes visible and contested, instrumentalized by successive political regimes to reauthor the memorial narrative within the urban fabric. Where destruction is total, architectural narrative articulation becomes primary and sole, assuming full responsibility for reintegration and demanding active perceptual engagement from those who encounter it, precisely because there is nothing left to appropriate through use alone.

These findings indicate that the presence, visibility, and agency of architectural narrative articulation are not consequences of what physically survived but of how consciously architecture responded to the persistent narrative within the transforming urban landscape. In this sense, memorial spaces function as Austin's narrative environments through spaces that transmit stories with their material, spatial, and sensory qualities and as Vujanović's landscape dramaturgy, staging the encounter between historical memory and contemporary urban life through the very organization of movement and perception. Architectural narrative articulation is therefore not a response to destruction—it is a response to transformation, and the determining instrument through which memorial spaces negotiate a new coherent relationship within a continuously changing urban fabric.

## 5. CONCLUSION

This paper has argued that the determining factor of successful memorial space reintegration is not the degree of physical survival of original structures but the degree to which architecture consciously articulates the narrative that persists within the transforming urban fabric. Through a dual-axis analytical framework and three illustrative examples, the analysis demonstrates a consistent inverse relationship: as landscape transformation intensifies and physical evidence recedes, architecture assumes an increasingly active, visible, and irreplaceable narrative role. Of the three positions examined, the Topography of Terror represents the most complex reintegration precisely because total destruction forced the need for narrative articulation. Auschwitz I proves that physical survival without conscious architectural intervention leaves the relationship between memorial space and urban fabric permanently unresolved. Sachsenhausen reveals both the power and the danger of instrumentalizing architecture as a narrative agent, raising critical questions about whose narrative is being articulated.

At the landscape (macro) scale, the boundary between memorial space and urban fabric is not a physical condition but a narrative one, determined less by what survives materially than by how consciously the urban landscape acknowledges the contested narratives it carries. At the architectural (micro) scale, the primary function of memorial architecture is not preservation but articulation—the active spatial organization of narrative for those who inhabit, visit, and pass through these spaces. The preliminary typological framework proposed here invites empirical testing across a broader set of memorial sites, including the experiences of residents and tourists who encounter these narratives.

### ACKNOWLEDGEMENT

This research has been supported by the Ministry of Science, Technological Development and Innovation through Contract No. 451-03-33/2026-03/200156 and the Faculty of Technical Sciences, University of Novi Sad through project “Innovative approaches to integrating contemporary scientific research and artistic practices into educational processes in the fields of architecture, urbanism, and scene design, with the aim of advancing knowledge and disseminating results”.

## REFERENCES

[1] Benjamin, W. (2007) The Work of Art in the Age of Mechanical Reproduction. In H. Arendt (Ed.) Illuminations, pp. 217–251, Schocken Books, New York, United States of America.

[2] Hong, G. (2020) Islands of memory, islands of trauma: The case of Dongzhou, Hengyang, China. Island Studies Journal, Volume 15(2), pp. 237–254. https://doi.org/10.24043/isj.131

[3] Elsaesser, T. (2009). Sonnen-Insulaner: On a Berlin Island of Memory. In U. Staiger, H. Steiner, A. Webber (Eds.) Memory Culture and the Contemporary City, pp. 32–51, Palgrave Macmillan, Basingstoke, Great Britain.

[4] Eco, U. (1975) A Theory of Semiotics, Indiana University Press, Bloomington, United States of America.

[5] Jagdhuhn, N. (2022) Post-Yugoslav metamuseums: Reframing Second World War heritage in postconflict Croatia, Bosnia and Herzegovina, and Serbia, Palgrave Macmillan, London, Great Britain. https://doi.org/10.1007/978-3-031-10228-8

[6] Ryan, M. L., Foote, K., Azaryahu, M. (2016) Narrating Space/Spatializing Narrative: Where Narrative Theory and Geography Meet, The Ohio State University Press, Columbus, United States of America.

[7] Sonkoly, G. (2017) Historical Urban Landscape, Springer, Cham, Germany.

[8] Vujanović, A. (2018) Landscape dramaturgy: Space after perspective. In I. Midgard Fiksdal (Ed.) Thinking Alongside, pp. 159–170, The Oslo National Academy of the Arts, Oslo.

[9] Delbo, C. (2014) Auschwitz and After, Yale University Press, New Heaven, United States of America.

[10] Philpott, C. (2016) Relics of the Reich – The Buildings the Nazis left behind, Pen and Sword Military, Barnsley, Great Britain.

[11] Van De Putte, T. (2025) Auschwitz and its locale. In S. M. Cushman, J. Pettitt, D. Williams (Eds.) The Routledge Handbook to Auschwitz-Birkenau, pp. 61–70. Routledge, Abingdon, Great Britain. https://doi.org/10.4324/9781003262848-7

[12] Rawecki, M. (2016) Niechciany Auschwitz [The Unwanted Auschwitz]. Zarzadzanie w Kulturze, Volume 17(1), pp. 77–89. doi:10.4467/20843976ZK.16.006.4480

[13] Pastor, D., & Kent, A. J. (2020). Transformative landscapes: liminality and visitors' emotional experiences at German memorial sites. Tourism Geographies, Volume 22(2), pp. 250–272. https://doi.org/10.1080/14616688.2020.1725617

[14] Massey, D. (2005) For Space. Sage Publications Ltd, London, Great Britain.

[15] Topography of Terror. Available at: https://www.topographie.de/ (accessed 20 April 2025).

[16] Reinhard, R. (1989) Topography of Terror: Gestapo, SS and Reichssicherheitshauptamt on the „Prinz-Albrecht-Terrain": A Documentation. Berliner Festspiele GmbH, Berlin, Germany.

[17] Al-Bayati, S. (2021) Berlin: Post-War Reconstruction (or Destruction). Available at: https://sah.org/2021/10/04/berlin-post-war-reconstruction-or-destruction/ (accessed 22 April 2025).

[18] Walton, J. (2024) The Case for (Counter)Preservation: How Should Relics of Nazi Architecture be Dealt with in Contemporary Berlin? Available at: https://www.anthropologyofarchitecture.com/the-case-for-counterpreservation-how-should-relics-of-nazi-architecture-be-dealt-with (accessed 22 April 2026).

[19] Holocaust Encyclopedia. *Auschwitz environs, summer 1944.* Available at: https://encyclopedia.ushmm.org/content/en/map/auschwitz-environs-summer-1944 (accessed 29 April 2026).

https://doi.org/10.24867/INDIS-2026-EN-565



# BETWEEN BUILDING DENSITY AND HOUSING QUALITY: A COMPARATIVE ANALYSIS OF RESIDENTIAL BLOCKS OF BISTRICA AND PODBARA

*Mia Stantić*[1]

***Summary:***

This paper examines the relationship between urban planning parameters and the quality of the immediate residential environment through a comparative analysis of residential blocks in Bistrica and Podbara, Novi Sad. The aim is to assess whether development intensity indicators can be used to evaluate residential environmental quality. The study compares site coverage ratios, floor area ratios, building heights, and estimated gross floor areas, alongside a qualitative assessment of green spaces, traffic areas, and public and semi-public spaces. Despite similar site coverage ratios, the blocks differ in the organisation and use of open spaces. Despite the higher floor area ratio, the block in Bistrica has a more connected and functionally diverse inner-block space, while in Podbara, unbuilt areas are fragmented and predominantly used for parking. The analysis shows that a lower development intensity does not necessarily imply a higher residential block quality, as the organisation of the unbuilt spaces also plays a significant role.

*Keywords: urban planning parameters, housing quality, floor area ratio, unbuilt space*

# IZMEĐU IZGRAĐENOSTI I KVALITETA STANOVANJA: KOMPARATIVNA ANALIZA BLOKOVA BISTRICE I PODBARE

***Rezime:***

Rad ispituje odnos urbanističkih parametara i kvaliteta neposrednog stambenog okruženja na primeru blokova Bistrice i Podbare u Novom Sadu. Cilj je da se utvrdi u kojoj meri urbanistički parametri, kao pokazatelji intenziteta gradnje, mogu poslužiti i povezati se pri proceni kvaliteta neposrednog stambenog okruženja. Primenjena je komparativna analiza indeksa zauzetosti i izgrađenosti, spratnosti, procenjene bruto razvijene građevinske površine, uz kvalitativnu analizu zelenih, saobraćajnih, javnih i polujavnih površina. Iako imaju isti indeks zauzetosti, analizirani blokovi se razlikuju po organizaciji i načinu korišćenja javnih površina. Bistrica, i pored većeg indeksa izgrađenosti, ima povezaniji i sadržajniji unutarblokovski prostor, dok su na Podbari neizgrađene površine fragmentisane i pretežno namenjene parkiranju. Analiza pokazuje da niži stepen izgrađenosti ne podrazumeva nužno kvalitetniji stambeni blok, već da značajnu ulogu ima i način na koji su neizgrađeni prostori oblikovani.

*Ključne reči: urbanistički parametri, kvalitet stanovanja, indeks izgrađenosti, neizgrađene površine*

[1] Junior Research Assistant, Faculty of Technical Sciences, University of Novi Sad, Novi Sad, Serbia, stantic.dc2.2025@uns.ac.rs, ORCID 0009-0008-8309-2612

# 1. INTRODUCTION

The issue of housing quality is particularly important today in the context of the contemporary housing crisis, growing demand for housing and increasing development intensity. Under such circumstances, it is essential to consider not only how much is being built but also the quality of housing, which depends not solely on the characteristics of individual dwelling units. It also results from the organisation of the immediate surroundings, the relationship between built and unbuilt areas, and the quality of unbuilt spaces. This paper examines one aspect of housing quality: the quality of the immediate residential environment, considered through the spatial organisation and use of built and unbuilt areas within a residential block.

Urban planning parameters—site coverage ratio, floor area ratio and building height—provide a quantitative assessment of development intensity, but their values alone reveal little about how space is organised and used. Blocks with similar or identical planning parameters can have entirely different spatial configurations and, consequently, different levels of quality in their immediate residential environments.

This paper presents a comparative analysis of two residential blocks in Novi Sad, one in Bistrica and the other in Podbara. These blocks represent different models of urban development and spatial organisation. The aim is to investigate whether, and to what extent, urban planning parameters can be used to assess housing quality at the residential-block scale.

# 2. URBAN PLANNING PARAMETERS AND HOUSING QUALITY

## 2.1. URBAN PLANNING PARAMETERS AS INDICATORS OF DEVELOPMENT INTENSITY

Housing quality cannot be analysed solely through criteria relating to the dwelling unit or its internal layout; the analysis must also consider the block, public spaces, greenery and privacy. Professor Ljiljana Vukajlov also emphasises the significance of the block for housing quality, viewing it not simply as a physical area bounded by streets but as a spatial, functional and morphological whole. In her interpretation, block quality also depends on the organisation of buildings, circulation areas, open spaces and green areas, since these functions determine how the block operates and “lives” on a daily basis [1].

Urban planning parameters primarily indicate development intensity. The site coverage ratio shows what proportion of a block is occupied by building footprints. Building height complements this indicator by allowing development intensity to be assessed vertically. The floor area ratio expresses the relationship between total gross floor area and block area. Nevertheless, a high floor area ratio is not inherently negative if accompanied by high-quality, carefully designed public spaces, greenery and sound overall organisation of the plot or block.

## 2.2. ORGANISATION OF UNBUILT AREAS AND QUALITY OF THE RESIDENTIAL ENVIRONMENT

The quality of a plot or block depends not only on how much of its area is built up, but also on how the remaining space is treated. Unbuilt space may consist of greenery, public areas, pedestrian paths or parking, but it may also be an unmaintained residual area. In addition to the amount of unbuilt space, its function, design and accessibility therefore need to be considered. This understanding of space can be linked to Ranko

Radović's view of urban form not as a single physical structure, but as a relationship between spaces, environments and the ways of life unfolding within them [2].
In multifamily housing, green areas are especially important because they form part of the shared space available to residents. Parking and service areas serve important functions, but their dominance may reduce the availability of greenery, pedestrian paths and places for social interaction. Jane Jacobs also highlights the significance of everyday encounters in public space. In The Death and Life of Great American Cities, she emphasises the role of sidewalks, encounters and activities in creating a vibrant urban environment [3]. Jan Gehl likewise stresses the importance of spaces between buildings as settings for everyday encounters, activities and movement [4]. Recent research by Kleeman et al. [5] suggests the importnaceof the design and organisation of communal open spaces in apartment developments. Their findings indicate that the implementation of comprehensive design guidelines is positively associated with residents' use of shared outdoor spaces, highlighting the significance of spatial quality and the organisation of open spaces.

## 3. METHODOLOGY

### 3.1. SELECTION OF THE ANALYSED BLOCKS AND DATA SOURCES

Two residential blocks in Novi Sad were selected for analysis: one in Bistrica and another in Podbara. From architectural and urban planning perspectives, they represent different models of spatial organisation.
The first block is located in Bistrica, a planned neighbourhood of Novi Sad.
The second block is located in Podbara, an older part of Novi Sad's urban fabric that is currently undergoing transformation.
These two blocks were selected as markedly different examples of urban planning models, allowing the relationship between planning parameters, the organisation of unbuilt spaces and the quality of the immediate residential environment to be examined.
The analysis was based on available graphic materials, satellite imagery from the GeoSrbija and Google Maps platforms, and photographs of the analysed blocks.

### 3.2. QUANTITATIVE AND QUALITATIVE ANALYSIS PROCEDURE

The analysis combined a quantitative comparison of urban planning parameters with a qualitative assessment of unbuilt spaces. The quantitative component covered block area, building footprint area, site coverage ratio, building height, estimated gross floor area (GFA) and floor area ratio.
Block areas were measured approximately through graphic analysis of the available base maps. Block boundaries were defined by the regulation lines of the surrounding streets, while building footprint area was calculated as the sum of the footprints of individual buildings. The site coverage ratio was calculated as the percentage of total block area occupied by building footprints.

$$I_z = \frac{area\ under\ buildings}{total\ area\ block}\ x\ 100\,\%$$

Building heights were determined from available photographs and site imagery. GFA was estimated from building footprint areas and the number of above-ground storeys, and was subsequently used to calculate the floor area ratio.
Estimated GFA represents the sum of the products of each individual building footprint and its number of above-ground storeys.

$$GFA = area\ footprint\ building\ x\ number\ of\ storeys$$

The floor area ratio was calculated by dividing the estimated GFA by the total block area.

$$I_i = \frac{GFA}{area\,block}$$

The qualitative analysis examined the organisation and use of unbuilt spaces, with particular attention to greenery, parking and service areas, pedestrian and vehicular circulation, and the character of public and semi-public spaces. Their spatial connectivity, accessibility and functions within the block were assessed.
To ensure a consistent qalitative comparison, four criteria were applied to both residential blocks: spatial connectivity of the block, accessibility, functionality and spatial quality. Each criteria was examined through observable scaharacteristics of the unbuilt areas. The assessment was descriptive, based on available graphic materials, satellite imagery, and photographs, without calculating numerical scores.

| Criteria | Indicators used in the assessment |
|---|---|
| Spatial connectivity | Continuity of open spaces, pedestrian connections, spatial fragmentation |
| Accessibility | Access points, physical barriers, accessibility of shared areas |
| Functionality | Presence of greenery, recreational and social spaces, parking and circulation functions |
| Spatial quality | Vegetation, spatial coherence, relationship between pedestrian and vehicular areas |

*Table 1 Criteria and indicators used in the qualitative assessment of unbuilt spaces*

## 3.3. RESEARCH LIMITATIONS

The calculations derived from this analysis are intended primarily for comparative purposes rather than as an official urban planning assessment of the blocks. Given the methodology, the primary objective is not absolute numerical accuracy but a comparison of the relationships between parameters and the analysed blocks.
Data obtained from graphic analysis of satellite imagery may differ from official figures; therefore, all numerical results presented should be interpreted as estimates.
This study does not investigate the satisfaction of residents in the analysed blocks; instead, it is based on an analysis of the blocks' spatial characteristics. Consequently, its conclusions relate to the quality of the immediate residential environment rather than overall housing quality.

# 4. ANALYSIS OF THE BLOCK IN BISTRICA

## 4.1. LOCATION AND GENERAL CHARACTERISTICS OF THE BLOCK

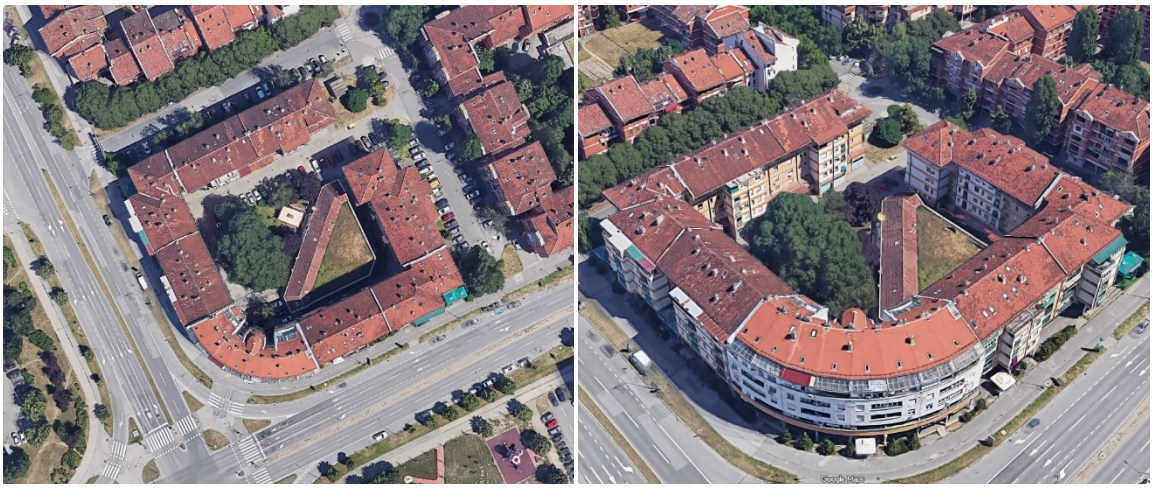

*Figure 1 Bird's-eye view of the block. Source: https://www.google.rs/maps*

The block under analysis is bounded by Radomira Raše Radujkova Street, Slobodana Jovanovića Boulevard and Todora Toze Jovanovića Street, which extends in two directions and is commonly known as Tozin sokak.

## 4.2. MORPHOLOGY AND BUILT STRUCTURE

The buildings in the analysed block are predominantly situated around its perimeter, with the exception of a single-storey building that extends diagonally across the block. Their positioning partly shields the inner-block space from noise and pollution, contributing to a more pleasant internal environment. Apart from the single-storey building at the centre, the surrounding buildings have a consistent number of storeys.

## 4.3. QUANTITATIVE ANALYSIS OF URBAN PLANNING PARAMETERS

| Parameter | Value |
|---|---|
| Block area | 7440 m² |
| Building footprint area | 3900 m² |
| Site coverage ratio | 52% |
| Range of building heights | G – G+4+A |
| Average building height | 5.17 above-ground storeys |
| Estimated GFA | 19 646 m² |
| Floor area ratio | 2.64 |

*Table 2 Urban planning parameters of the analysed block in Bistrica*

## 4.4. QUALITATIVE ANALYSIS OF OPEN SPACE

The block contains greenery that contributes to its environmental quality, including low, medium-height and tall vegetation. It is also worth noting that the single-storey building within the block has a green roof.
Parking areas occupy a substantial amount of space but are not dominant, since the access road runs around the perimeter of the inner courtyard.

Pedestrian and vehicular circulation is well organised: the interior of the block is not entirely subordinated to cars. Vehicular access roads are present but do not compromise the environment or the character of the space, precisely because of their peripheral position. Pedestrian routes within the block are clearly defined.
The interior has a semi-public character, as it is neither fully enclosed nor intended exclusively for residents. Access is provided through open passages in the buildings and via the access road. At the same time, its separation from the main roads and its particular atmosphere mean that it does not function as an entirely public space.
In addition to the sheltered setting, which encourages residents to socialise, public-facing commercial uses, such as a café or restaurant with outdoor seating, play an important role in encouraging social interaction and use of the block courtyard.

## 5. ANALYSIS OF THE BLOCK IN PODBARA

### 5.1. LOCATION AND GENERAL CHARACTERISTICS OF THE BLOCK



*Figure 2 Bird's-eye view of the block. Source: https://www.google.rs/maps*

The block under analysis is bounded by Pavla Stamatovića Street to the south, Filipa Višnjića Street to the east, Kosovska Street to the west and Save Vukosavljeva Square to the north. The block has a heterogeneous structure, currently containing both single-family and multifamily residential buildings.

### 5.2. MORPHOLOGY AND BUILT STRUCTURE

Buildings are distributed along the perimeter and within the block, without a uniform spatial arrangement. New development tends to be positioned around the block perimeter; however, the inner-block space has not been clearly defined through urban design. The presence of taller buildings within the block affects views, privacy and the quality of open space.

### 5.3. QUANTITATIVE ANALYSIS OF URBAN PLANNING PARAMETERS

| Parameter | Value |
|---|---|
| Block area | 8340 m² |
| Building footprint area | 4306 m² |
| Site coverage ratio | 52% |
| Range of building heights | G – G+4+A |

| | |
|---|---|
| Average building height | 3.96 above-ground storeys |
| Estimated GFA | 17 034 m² |
| Floor area ratio | 2.04 |

*Table 3 Urban planning parameters of the analysed block in Podbara*

## 5.4. QUALITATIVE ANALYSIS OF OPEN SPACE

The block is divided into numerous individual plots that are physically separated from one another, so the interior is not perceived as a unified spatial whole. As a result, there is no shared inner-block area that could more effectively accommodate outdoor activities, social interaction and greenery.
Greenery within the block is very limited and occurs only on plots containing single-storey, single-family houses. Newly constructed buildings have no tall, medium-height or low vegetation, and there is no coherent system of green spaces within the block. Parking areas dominate the interior and effectively take over the role of shared space, significantly reducing its environmental quality.
Vehicular circulation within the block primarily provides access to parking. Pedestrian paths, on the other hand, are largely absent; instead, parking areas and paved forecourts are used for access to parking and buildings.

# 6. COMPARATIVE ANALYSIS

## 6.1. COMPARISON OF URBAN PLANNING PARAMETERS

| Parameter | Bistrica | Podbara |
|---|---|---|
| Block area | 7440 m² | 8340 m² |
| Building footprint area | 3900 m² | 4306 m² |
| Site coverage ratio | 52% | 52% |
| Range of building heights | G – G+4+A | G – G+4+A |
| Average building height | 5.17 above-ground storeys | 3.96 above-ground storeys |
| Estimated GFA | 19 646 m² | 17 034 m² |
| Floor area ratio | 2.64 | 2.04 |

*Table 3 Comparison of urban planning parameters of the analysed blocks*

The site coverage ratio is approximately the same in both analysed blocks. The average building height is 5.17 above-ground storeys in Bistrica and 3.96 in Podbara.
The difference results from the greater number of single-storey buildings within the Podbara block. Thus, although Bistrica has a similar site coverage ratio to Podbara, it has a larger GFA and a higher floor area ratio.

## 6.2. ORGANISATION OF BUILT AND UNBUILT SPACE

The main difference between the blocks lies in the organisation of unbuilt space. In Bistrica, it forms a more connected whole, whereas in Podbara it is fragmented as a consequence of plot subdivision and the dispersed arrangement of buildings.
Because circulation and parking areas in the Bistrica block are organised around the perimeter, the central area remains available for green spaces that contribute to spatial quality. In Podbara, greenery is far less prevalent and is mainly associated with plots

containing single-storey buildings. There is no clear system of green areas associated with the more prevalent newer multifamily housing. Parking and access roads dominate the block, serving everyday circulation and servicing needs, while spaces for residents to spend time outdoors, recreate or socialise are absent.
The difference is also evident in the organisation of circulation: in Bistrica, pedestrian routes are deliberately planned and connected to green spaces, whereas in Podbara movement within the block mainly takes place across parking and access areas.

## 6.3. DISCUSSION OF RESULTS

Although both blocks have approximately the same site coverage ratio, their spatial organisation differs considerably. In this case, Bistrica's higher floor area ratio is not associated with a less favourable organisation of unbuilt spaces than in Podbara.
This relationship can be explained by the morphology of the analysed blocks. In Bistrica, the characteristic perimeter arrangement of buildings allows a more connected internal space to develop, whereas the dispersed arrangement of buildings and subdivision into individual plots in Podbara limit opportunities to create shared open spaces.
These differences also show contrasting patterns of urban development and land subdivision. In Bistrica, the planned arrangement of buildings enables the inner-block area to function as a relatively continuous space, accommodating grenery, pedestrian movement, and shared activities. In contrast with that, in Podbara, the division of land into individual plots, combined with succesive building interventions, has produced a lot more fragmented spatial structure. Consequently, the provision of open space is largely determined at the plot level, rather through a coordinated approach to the block as a whole. This comparison suggests that the quality of the immediate residential environment depends not only on development intensity, but also on the relationship between land subdivision, building arrangement, and the organisation of the open spaces.

## 7. CONCLUSION

The study has shown that urban planning parameters alone are insufficient to assess the quality of the immediate residential environment. The findings indicate that lower development intensity does not necessarily result in a better residential environment. Urban planning parameters should therefore not be treated exclusively as numerical indicators but interpreted in relation to the functions and organisation of unbuilt spaces.
Future research could include a larger number of residential blocks with different urban planning characteristics, as well as a quantitative analysis of green, pedestrian and public spaces. Incorporating residents' experiences would also make it possible to develop a more comprehensive understanding of the relationship between development intensity, spatial organisation and housing quality.

## REFERENCES

[1] L. Vukajlov, The Role of Urban and Rural Blocks in Shaping the Structure and Identity of Settlements in Vojvodina [in Serbian], University of Novi Sad, Faculty of Technical Sciences, Department of Architecture and Urban Planning, 2010.

[2] R. Radović, Urban Form: Foundations, Theory and Practice [in Serbian], Belgrade: Građevinska knjiga, 2009.

[3] J. Jacobs, The Death and Life of Great American Cities, Mediterran Publishing (Serbian edition), 2011.

[4] J. Gehl, *Life Between Buildings: Using Public Space*, Urban Planning Institute of Belgrade (Serbian edition), 2010.

[5] A. Kleeman, P. Hooper, N. Edwards, J. Bolleter and S. Foster, Research note: Associations between the implementation of communal open space design guidelines and residents, Landscape and Ubran Planning, 2023.

https://doi.org/10.24867/INDIS-2026-EN-574



# BUILT STRUCTURE AND FUNCTIONAL TRANSFORMATION IN THE ADAPTIVE REUSE OF THERMAL POWER STATION "SNAGA I SVETLOST" IN BELGRADE

*Jovana Đurovski[1] and Miljana Zeković[2]*

***Summary:***

Post-industrial complexes represent specific spatial systems in which the existing architectural structures establish the framework for the introduction of new functions. Within the process of transformation, the relationship between the existing built structure and new programmatic requirements becomes a key factor that directly affects the possibilities of adaptive reuse. The aim of this paper is to examine how the existing built structure conditions the introduction of new functions and how this relationship is manifested in the spatial organization of the complex. The paper addresses the case of the "Snaga i svetlost" ("Power and Light") Thermal Power Station in Belgrade through an analysis of its spatial, structural, and programmatic characteristics. By examining the existing condition and potential transformation scenarios, the key relationships between built structure and function are identified. The results indicate that adaptive regeneration requires the alignment of structural capacities and programmatic demands, whereby this relationship determines both the scope and the character of the transformation.

*Keywords: industrial heritage, adaptive regeneration, post-industrial complexes, adaptive reuse*

# FIZIČKA STRUKTURA I FUNKCIONALNA TRANSFORMACIJA PRI ADAPTIVNOJ PRENAMENI TERMOELEKTRANE „SNAGA I SVETLOST" U BEOGRADU

***Rezime:***

Postindustrijski kompleksi predstavljaju specifične prostorne sisteme u kojima postojeće arhitektonske strukture postavljaju okvir za uvođenje novih funkcija. U procesu transformacije, odnos između postojeće fizičke strukture i novih programskih zahteva postaje ključni faktor koji direktno utiče na mogućnosti ponovne upotrebe kroz adaptaciju. Cilj rada je da ispita na koji način postojeća fizička struktura uslovljava uvođenje novih funkcija i kako se taj odnos manifestuje u prostornoj organizaciji kompleksa. Rad se bavi slučajem Termoelektrane „Snaga i svetlost" u Beogradu, kroz analizu njenih prostornih, konstrukcijskih i programskih karakteristika. Kroz sagledavanje postojećeg stanja i potencijalnih scenarija transformacije, identifikuju se ključni odnosi fizičke strukture i funkcije. Rezultati ukazuju da adaptivna regeneracija zahteva usklađivanje konstrukcijskih mogućnosti i programskih potreba, pri čemu taj odnos određuje domete i karakter transformacije.

*Ključne reči: industrijsko nasleđe, adaptivna regeneracija, postindustrijski kompleksi, reutilizacija*

[1] PhD student, Faculty of Technical Sciences, University of Novi Sad, Serbia, djurovski.dc1.2024@uns.ac.rs, ORCID 0009-0005-7635-0802
[2] Full. Prof., Faculty of Technical Sciences, University of Novi Sad, Novi Sad, Serbia, miljana_z@uns.ac.rs, ORCID 0000-0002-1327-7063

## 1. INTRODUCTION

Post-industrial complexes represent a significant layer of the contemporary city in which architectural structure, historical traces, and collective memory are interconnected with the contemporary needs of urban development. Former industrial facilities, although they have lost their original production function, retain a strong spatial and identity potential, which positions them as important resources within processes of urban renewal and adaptive regeneration. Their value today extends beyond purely technical and historical significance and opens the possibility for the formation of new forms of public and urban life.

The transformation of such spaces implies more than the physical restoration of existing structures. It requires a careful understanding of the existing architecture, its spatial organization, structural logic, morphology, and capacity to accommodate new programmatic contents while preserving its own identity. Within this process, the relationship between the existing structure and the new function represents one of the key questions of architectural intervention. The spatial structure simultaneously establishes limitations and reveals the potentials of future use, while precisely within this relationship lies the basis for the sustainable and meaningful transformation of post-industrial complexes.

This paper is based on the examination of the relationship between the existing architectural structure and the possibilities for introducing new functions within the process of adaptive reuse of post-industrial complexes. Particular attention is directed toward the manner in which the spatial and structural logic of the existing building determines the scope of transformation and the character of future architectural intervention, as well as toward the possibility for the existing structure to become a carrier of new urban value.

The “Snaga i svetlost” Thermal Power Station in Belgrade was selected as the case study, representing one of the significant examples of industrial heritage whose spatial potential remains insufficiently utilized even today. Its position within the riverfront zone, historical significance in the industrialization of the city, and clearly defined architectural and structural organization make it a suitable example for the analysis of possible transformation models. The paper is based on the theoretical consideration of adaptive regeneration and the analysis of a specific case study through the examination of the historical development of the complex, its spatial organization, degree of preservation, and diagrammatic presentation of potential adaptive reuse scenarios.

## 2. CASE STUDY: THE “SNAGA I SVETLOST” THERMAL POWER STATION

### 2.1. HISTORICAL AND URBAN CONTEXT

The “Snaga i svetlost” Thermal Power Station represents one of the more significant examples of industrial heritage in Belgrade and an important segment in the development of the city’s infrastructure during the first half of the twentieth century. It was constructed between 1930 and 1932 as the third thermal power station in Belgrade, and subsequently operated operating at full capacity from 1934 until 1969 [1]. Its construction is associated with a period of intensive modernization of the city, when population growth, industrial development, and the demands of urban life required new capacities for the production and distribution of electrical energy. Once the capacity of the old Dorćol power plant could no longer meet the needs of the city, the Swiss Society

for Electrification and Transport from Basel obtained a concession in 1929 for the construction of a new thermal power station and for the supply of electrical energy to Belgrade over the following twenty-five years [1].

The selection of the site on the right bank of the Danube, within the area of present-day Marina Dorćol, was not accidental. Its riverside position enabled access to the technical water necessary for the operation of the facility, as well as the transportation of coal by river and railway, which at the time represented the most rational solution from an economic and logistical perspective [1]. At the same time, the proximity of the railway infrastructure provided additional connectivity with the urban and regional supply system. As the largest facility of its kind in interwar Belgrade, the Thermal Power Station became the principal component of the city's electrical power system and replaced the old Dorćol power plant [3].

The Dorćol riverfront, as a zone situated between the city centre and the river edge, long represented an area in which infrastructural, industrial, and transportation systems intersected. The industrial complexes located along this stretch formed a specific urban landscape in which the architecture of production became an important part of the city's collective memory. Within this context, the "Snaga i svetlost" Thermal Power Station, beyond its primary technical and utilitarian role, also symbolized industrialization, modernization, and the European orientation of Belgrade at a time when electrification signified integration into contemporary civilizational trends.

Today, after decades of disuse, the complex remains a space positioned between neglect and significant development potential. Its location on one of the most valuable urban sites in Belgrade, in immediate proximity to the city centre and the Danube riverfront, makes it the subject of various urban and architectural considerations. Planning documentation recognizes the "Snaga i svetlost" Thermal Power Station complex and its accompanying crane as structures of historical and architectural value within the framework of industrial heritage, with recommendations for their preservation and integration into contemporary urban programs [2]. It is precisely this attractiveness of the location that raises the question of the relationship between the protection of industrial heritage and contemporary development pressures, making this complex particularly significant for the analysis of possible models of adaptive regeneration.

## 2.2. SPATIAL AND STRUCTURAL CHARACTERISTICS

The "Snaga i svetlost" Thermal Power Station was conceived as a complex whose organization directly emerged from the technological requirements of electricity production. The spatial structure of the facility was based on a clearly defined functional division between the main machine hall, the boiler room, auxiliary technical spaces, and the supporting infrastructure necessary for the operation of the plant. A particularly significant role was assigned to the transport bridge with its loading crane, which enabled the delivery of coal by river and its direct transfer into the boiler system, making the functional relationship between the river and the facility a fundamental principle in the organization of the complex [1].

The main building is characterized by large spans, high interior spaces, and a strongly articulated structural logic typical of industrial architecture of the first half of the twentieth century. The machine hall was designed to accommodate large-scale technical equipment, ensure the uninterrupted functioning of the production process, and facilitate system maintenance. It is precisely this spatial generosity that today represents one of the most significant potentials for future adaptive reuse, as it enables the introduction of various new functions without radically compromising the existing architectural structure.

The structural system of the complex is based on a robust and rational arrangement of load-bearing elements, while the overhead traveling crane consists of a large bridge-type riveted steel truss structure, with a load capacity of 6.8 tons and a total travel span of 108 m. Such technical solutions ensured the durability and stability of the complex even after the cessation of its original function. Unlike many contemporary buildings characterized by short life cycles, industrial structures of this type possess a high degree of adaptability precisely because of their spatial clarity and structural resilience.

A particular value of the complex lies in its architectural expression, in which technical function and the aesthetics of industrial modernism intertwine to form a unified spatial identity. The vertical emphasis of the main tower, the rhythm of façade openings, extensive glazed surfaces, and the clear legibility of the internal organization expressed through the external form give the building a recognizable character that surpasses its exclusively infrastructural role. The use of glass as a dominant material reflected contemporary European principles of modern architecture, in which the wall, beyond its protective function, also became a membrane between the interior and the exterior.

The spatial organization and structural logic of the “Snaga i svetlost” Thermal Power Station demonstrate that the value of such complexes lies precisely in their capacity to accommodate new programs without losing their own identity. This provides the basis for considering possible scenarios of adaptive reuse, in which the structure becomes the carrier of future functions and an active element of contemporary spatial transformation.

## 2.3. EXISTING CONDITION AND DEGREE OF PRESERVATION

Today, the “Snaga i svetlost” Thermal Power Station exists in a state of long-term neglect, which significantly affects both its built structure and the way in which this space is perceived within the contemporary city. Although the complex has lost its original function, its architectural, spatial, and urban value remains clearly recognizable. The complex is located within the Marina Dorćol area, on an exceptionally valuable site along the Danube riverfront. Such a position provides considerable development potential, while simultaneously raising questions about contemporary development pressures and the possibility of inappropriate adaptive reuse. Planning documentation recognizes the “Snaga i svetlost” Thermal Power Station and its accompanying crane as structures of historical and architectural value within the framework of industrial heritage, with recommendations for their preservation and integration into contemporary urban programs [2]. Precisely because of the attractiveness of the location, the risk of losing the authenticity of this space becomes even more pronounced.

The physical condition of the complex indicates decades of a lack of systematic maintenance. Certain structural and façade elements have deteriorated, while some segments of the complex have lost their original functional integrity. Secondary elements, roof structures, and portions of the façade cladding are particularly affected, whereas the basic spatial organization of the main building remains clearly legible. Nevertheless, the primary spatial structure and recognizable architectural character of the complex have been preserved, providing an important foundation for future regeneration.

The analytical diagram of the existing condition (Figure 1) illustrates the clear spatial hierarchy of the complex, in which the main building of the Thermal Power Station and the transport bridge represent key elements defining spatial identity complex. At the same time, the deteriorated sections of the structure, the open plateau, and the direct contact with the Danube indicate significant potential for future regeneration and the establishment of new urban connections between the complex, the city, and the riverfront.

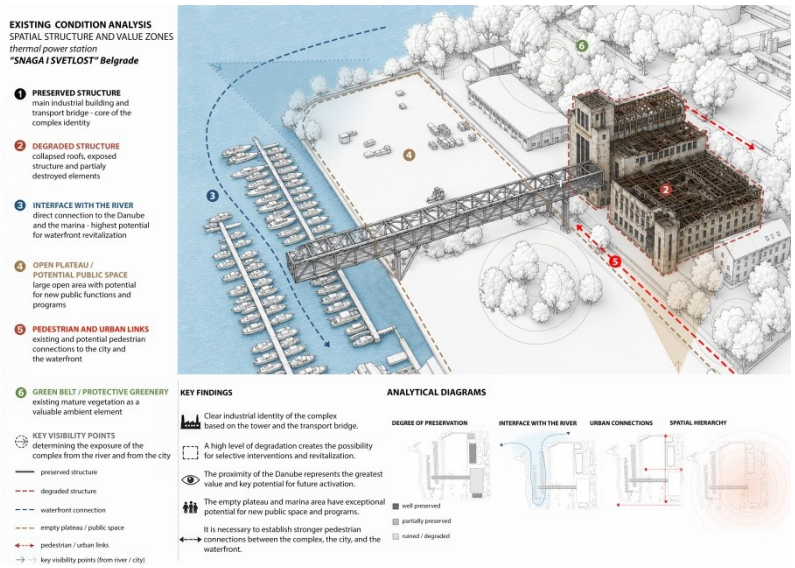


*Fig. 1 Existing condition analysis (author's illustration)*

A particular issue lies in the fact that industrial complexes of this type are frequently perceived primarily as development land with high investment potential, rather than as carriers of the cultural and spatial memory of the city. Within such an approach, the value of heritage is often subordinated to new development, resulting in the loss of place identity and the disruption of the continuity of urban memory.

The preservation of the "Snaga i svetlost" Thermal Power Station is therefore considered not only through the degree of physical protection, but also through the possibility of preserving its spatial logic, historical significance, and urban role. It is precisely this relationship between the material condition of the complex and its symbolic value that provides the basis for considering its future transformation and defining the boundary between preservation and architectural intervention.

## 3. TRANSFORMATION POTENTIAL: THE RELATIONSHIP BETWEEN BUILT STRUCTURE AND FUNCTION

### 3.1. SPATIAL LIMITATIONS AND POSSIBILITIES OF ADAPTIVE REUSE

The transformation process of the "Snaga i svetlost" Thermal Power Station is primarily conditioned by the relationship between the existing spatial structure and the requirements of new functions. This relationship defines the boundaries of intervention and the possibilities of adaptive reuse, since an industrial complex of this type requires the careful introduction of new programs while preserving its own identity.

One of the most significant spatial limitations derives from the structural logic of the complex itself. Large spans, high floor-to-floor heights, and the specific organization of technical spaces emerged as a response to the requirements of the production process, forming a spatial system that today requires careful integration with contemporary public and commercial use. This means that every new function must be carefully aligned with the existing structure, with the current construction system representing both the basis of the design decision and the starting point for future transformation [4].

On the other hand, these very characteristics also represent the greatest potential for adaptive reuse. Spatial continuity of large halls, flexible volumes, and a clearly defined structural grid enable the introduction of cultural, educational, exhibition, and hybrid public programs that require spatial openness and adaptability. Such functions emerge more naturally from the existing structure than conventional residential or

administrative models, as they respect the logic of industrial space and its spatial generosity.

An additional potential lies in the position of the complex along the riverfront. The proximity to the city centre and the direct connection with the waterfront enable the new function to extend beyond the framework of an individual building and become part of a broader process of urban regeneration. The activation of the open plateau, the connection with the marina, and the establishment of new pedestrian flows create the possibility for the adaptive reuse of the Thermal Power Station to become a catalyst for the reactivation of the wider Dorćol area and an important element of contemporary urban transformation.

The diagram of architectural intervention points (Figure 2) illustrates the key spatial relationships between the main hall, the transport bridge, the riverfront, the open plateau, and newly established pedestrian flows. The analysis is focused on identifying points of preservation, transformation, and spatial activation, as well as on the possibilities of connecting the complex with the river, the marina, and the surrounding urban fabric. Through the preservation of key structural elements and the careful introduction of new functional layers, a balance is established between industrial heritage and the contemporary use of space.

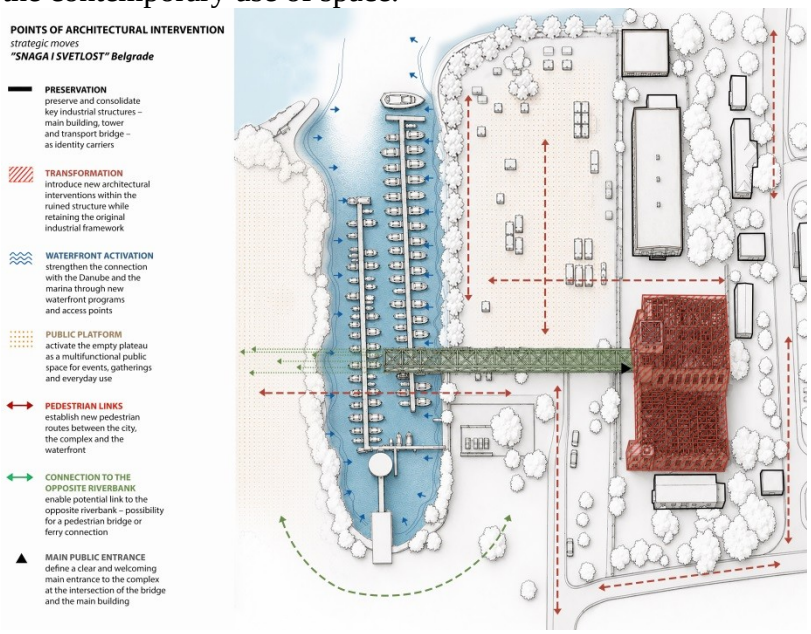


*Fig. 2 Points of architectural intervention (author's illustration)*

Therefore, the limitations and potentials of this space are understood as a unified system. A successful transformation depends on the degree of compatibility between the new function and the existing structure, as well as on the capacity of the new program to emerge naturally from the inherited spatial framework. Within this relationship lies the essence of adaptive regeneration: the establishment of a balance between preservation and contemporary use.

## 3.2. SPATIAL LIMITATIONS AND POSSIBILITIES OF ADAPTIVE REUSE

The transformation of the "Snaga i svetlost" Thermal Power Station requires an approach that considers the existing structure as the primary carrier of future functions. Architectural intervention is directed toward the recognition and activation of key points within the complex, where a balance is established between heritage preservation and the introduction of new programs. Such an approach corresponds to the principles of

adaptive regeneration, in which the existing structure becomes both the basis of the design decision and the starting point for future development [4].

The first and most significant intervention point relates to the main building. Its height and structural openness enable the introduction of public programs that require flexible space, such as exhibition spaces, cultural centres, multifunctional halls, or public gathering programs. The preservation of the primary spatial structure allows the industrial character of the building to remain legible, while the new function activates its contemporary urban significance.

The second intervention zone concerns the relationship between the complex and the riverfront. Today, the Thermal Power Station functions as an isolated and enclosed entity, while its riverside position offers the possibility of forming a new urban public frontage. Opening the complex toward the waterfront, introducing pedestrian flows, and connecting it to the broader network of public spaces enable the complex to become an active part of contemporary urban life and a generator of new urban dynamics.

The third intervention point refers to the relationship between old and new within the architectural structure itself. New elements establish a dialogue with the existing architecture through a clear distinction of the contemporary layer and the preservation of recognizable industrial elements. Through a controlled process of hybridization, based on the legibility of the new layer and the preservation of the existing structural identity, an architectural continuity is established that preserves the identity of the place while enabling its contemporary interpretation.

Architectural intervention is therefore understood as a system of carefully defined spatial operations that enable the gradual regeneration of the complex. The main hall, the transport bridge, the open plateau, and the interface with the river represent the key spatial carriers of future adaptive reuse, while their interconnection determines the character of the overall transformation and the manner in which the complex is integrated into contemporary urban life. In this way, the intervention represents a new reading of the existing space. The complex is understood both as a carrier of memory and as a structure that directs future use. Through these critical points, the foundation is established for the further consideration of the relationship between structure and function, which ultimately determines the scope of the entire transformation process.

## 3.3. DIAGRAMMATIC REPRESENTATION OF POSSIBLE TRANSFORMATION SCENARIOS

Diagrammatic representations within the processes of analysis and design enable a clearer understanding of the relationship between the existing structure and possible models of its transformation. In the case of industrial complexes, particularly those characterized by a pronounced spatial and structural logic, the diagram represents a tool for reading architecture and defining intervention strategies [5]. Through a diagrammatic approach, it is possible to understand more precisely the boundary between the preservation of the existing structure and the introduction of new functional layers.

The first diagrammatic level refers to the analysis of the relationship between structure and function through the identification of key spatial elements of the complex and their potential for adaptive regeneration. The analysis includes the spatial organization of the existing buildings, their structural characteristics, the relationship between enclosed and open spaces, the connection of the complex to the river, as well as the possibilities for integration into future urban flows and public programs. Particular attention is directed toward elements that possess spatial, identity-related, and functional potential for the introduction of new programs.

The main industrial hall was analysed through its capacity to retain a large open interior space suitable for cultural, exhibition, and public functions. The tower was considered as a dominant vertical landmark and a potential point of visual orientation and public use. The transport bridge was analysed as an element of both physical and symbolic connection linking the complex to the river and future pedestrian flows, while the open plateaus and the interface with the waterfront were considered potential spaces for public activation and the formation of new urban programs. Auxiliary buildings were examined through the possibility of selective adaptation and the introduction of educational, research, and working programs.

The "Structure–Function Relationship" diagram (Figure 3) illustrates the manner in which the existing built structure is transformed through strategies of preservation, activation, adaptive reuse, reintegration, and selective intervention. The diagram establishes a relationship between the existing elements of the complex, methods of transformation, and new functional scenarios, demonstrating that the new function emerges from the spatial, structural, and urban characteristics of the inherited system. In this way, the existing structure becomes a generator of new public, cultural, and urban activities while preserving the industrial identity and collective memory of the space.

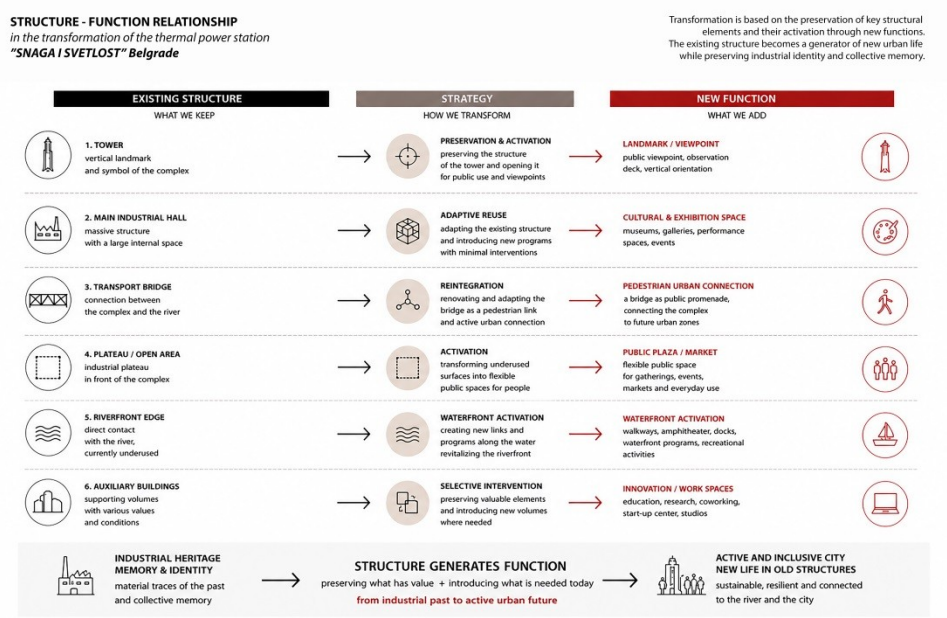


*Fig. 3 Structure-function relationship (author's illustration)*

The second diagrammatic level refers to the definition of the programmatic model for the future use of the complex through the analysis of functional relationships between different programs and their integration within a unified urban system. The analysis is directed toward the formation of a hybrid programmatic model that integrates cultural, educational, research, recreational, and public functions, while simultaneously activating the waterfront and reconnecting the complex to the city and the river. The programmatic model builds upon the previously defined spatial and structural potentials of the complex, whereby future programs emerge from the spatial characteristics and adaptive regeneration capacities of the existing system.

The programmatic diagram (Figure 4) illustrates the organization of future programmatic units and their interrelationships through several primary thematic layers. The first layer addresses the preservation and interpretation of industrial and power generation heritage through cultural and exhibition programs. The second layer encompasses working, research, and educational programs, including coworking spaces, research centres, and spaces for knowledge exchange. The third layer is oriented toward

public and social functions, such as gathering spaces, events, hospitality programs, and everyday user activities.

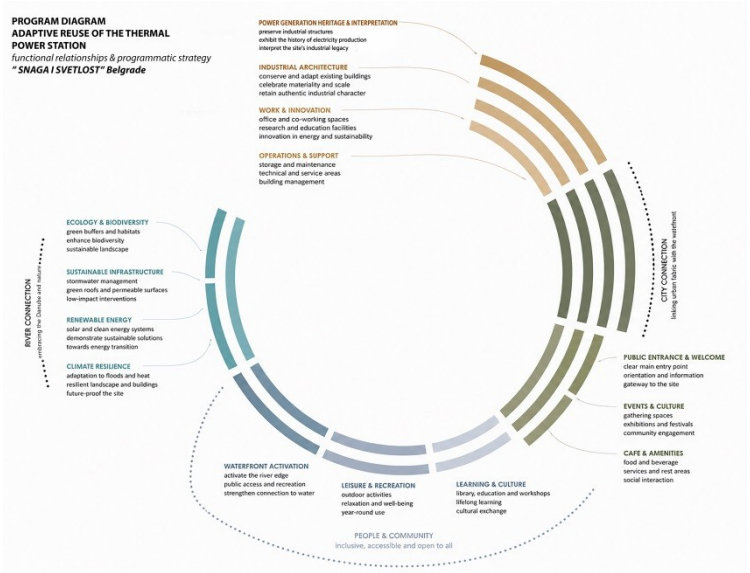


*Fig. 4 Program diagram, adaptive reuseof the thermal power station (author's illustration)*

A particular segment of the diagram addresses the activation of the riverfront through recreational, landscape, and ecological programs, including public access to the water, green infrastructure, renewable energy sources, and climate resilience strategies. In this way, the complex is understood as an open and adaptable urban system that connects industrial heritage, the contemporary needs of the city, and sustainable models of future development.

The third diagrammatic level refers to the definition of a temporal strategy for transforming the complex through phases of gradual revitalization and adaptive regeneration. The analysis is directed toward understanding the possibilities of transformation through a continuous temporal process that encompasses the preservation of existing values, the introduction of new spatial layers, and the gradual activation of the complex in accordance with the urban, functional, and economic capacities of the site.

The transformation phases diagram (Figure 5) illustrates the development of the complex through five interconnected stages. The first stage relates to the understanding of the existing condition of the complex as an urban scar, characterized by degradation, loss of function, and physical deterioration of the structure. The second stage focuses on the stabilization and preservation of key elements of industrial identity, including structural rehabilitation, protection of the primary structures, and preservation of the characteristic spatial elements of the complex. The third stage involves selective interventions and the introduction of new spatial and functional layers through adaptive reuse, the formation of public spaces, the activation of the waterfront, and the establishment of new pedestrian connections. The fourth stage refers to the formation of a hybrid urban model integrating cultural, educational, research, and public programs, while reconnecting the complex to the city and the river. The final stage presents the transformation of the complex into a model of the contemporary city of the future, grounded in sustainability, inclusiveness, collective memory of place, and the creation of a new urban identity.

The analysis indicates that the phased transformation model enables the gradual and adaptable regeneration of the complex, with each stage representing a logical continuation of the previous phase of development. Such an approach enables the

alignment of spatial, functional, and economic aspects of transformation while preserving continuity between industrial heritage and contemporary urban needs.

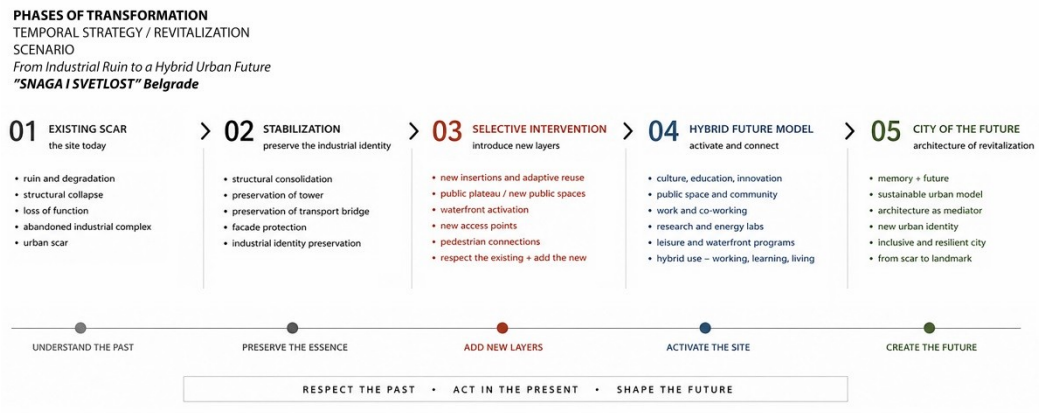


*Fig. 5 Phases of transformation, temporal strategy /revitalization scenario (author's illustration)*

The diagrammatic approach demonstrates that adaptive regeneration depends on the manner in which relationships are established between the existing structure, new programmatic layers, and phases of transformation. Through the analysis of spatial relationships, functional connections, and the temporal strategy of development, a model of gradual and sustainable transformation is formed, in which industrial heritage becomes an active component of the contemporary city and a generator of new urban, cultural, and social values.

## 4. CONCLUSION

The transformation of post-industrial complexes represents one of the key issues of contemporary architecture and urban development, particularly in cities where industrial heritage occupies significant and spatially valuable urban locations. The "Snaga i svetlost" Thermal Power Station in Belgrade represents an example of a space in which historical value, spatial potential, and the need for contemporary regeneration are closely intertwined. The analysis indicates that the existing architectural structure of this complex represents a primary resource for the formation of new functional and urban models of future adaptive reuse. Large spans, spatial openness, structural stability, and the interface with the riverfront create conditions for the introduction of hybrid programs capable of integrating cultural, public, educational, and contemporary urban functions.

The particular significance of this research lies in the consideration of the relationship between built structure and function as a key criterion of adaptive regeneration. The capacity of a new function to emerge from the existing spatial logic determines the quality and sustainability of future transformation. Architectural intervention thus becomes a process of reinterpretation and careful integration of new programs, while the preservation of spatial identity remains the fundamental principle of the design approach.

The diagrammatic analysis encompassed the existing condition of the complex, spatial and functional relationships, the interface with the riverfront, possibilities for programmatic reorganization, and phases of gradual spatial transformation. Through the analysis of the existing condition, the significance of the main building of the Thermal Power Station and the transport bridge were identified as key carriers of spatial identity, together with the potential of the open plateau, marina, and waterfront for the

establishment of new urban and public programs. The examination of the relationship between structure and function confirmed the possibility of aligning new programs with the existing spatial logic of the complex, while the programmatic transformation model defined the potential for the formation of a hybrid system connecting culture, education, working environments, public functions, and riverfront-related activities. The temporal transformation strategy established the possibility of gradual regeneration through phases of stabilization, selective intervention, spatial activation, and the formation of a sustainable urban model for the future.

The research results indicate that the regeneration potential lies in carefully defined intervention points, the waterfront interface, and the possibility of establishing new spatial and functional connections between the complex, the city, and the river. Such an approach enables industrial heritage to become an active component of the contemporary city and a carrier of new spatial, cultural, and social values.

The “Snaga i svetlost” Thermal Power Station may therefore be understood as a model for a broader approach to the revitalization of post-industrial spaces in Belgrade, in which architecture assumes the role of a mediator between the memory of place, contemporary urban needs, and future urban scenarios. Within this balance between preservation and transformation lies the possibility of creating a sustainable and identity-conscious city of the future.

Further research may be directed toward the development of more specific design models and application scenarios of adaptive regeneration for similar post-industrial complexes, thereby further strengthening the connection between the theoretical framework and contemporary urban development practice.

## REFERENCES

[1] Knežević N. Revitalizacija termoelektrane „Snaga i svetlost” u Beogradu. *Spomeničko nasleđe*, Beograd.

[2] Nikolić M., Vukmirović M. (2020). Industrijsko nasleđe duž beogradskog priobalja u planskim dokumentima. *Arhitektura i urbanizam*, br. 51.

[3] Erić D. Prva javna termoelektrična centrala u Beogradu. *Spomeničko nasleđe*, Beograd.

[4] Douglas J. (2006). *Building Adaptation*. Oxford: Butterworth-Heinemann.

[5] Allen S. (1998). Diagrams Matter. ANY: *Architecture New York*, No. 23, pp. 16–19.

https://doi.org/10.24867/INDIS-2026-EN-585



# TYPOLOGY OF DAMAGE TO ORTHODOX SACRED BUILDINGS DURING THE SECOND WORLD WAR: A CASE STUDY OF THE MUNICIPALITY OF PEĆINCI

*Una Radivojević [1], Mirjana Sladić Todorov [2]*

***Summary***

The paper examines the typology of architectural damage to Orthodox sacred buildings sustained during the Second World War in the territory of the Municipality of Pećinci. The aim is to determine the nature and extent of wartime damage and establish a typology based on the degree of physical loss and its impact on the architectural integrity of the buildings. The analysis of available documentation, archival sources and photographs identified four types of damage, ranging from localized damage to complete destruction. The results show a pronounced prevalence of damage to bell towers, the most frequently affected architectural elements. Greater physical damage results in greater alteration of the original architectural integrity, directly affecting the nature and complexity of subsequent interventions. The proposed typology enables systematic comparison of wartime destruction and provides a basis for assessing the needs and possibilities for restoring sacred architectural heritage.

***Keywords:*** *Orthodox churches, wartime damage, architectural typology, cultural heritage, Second World War, Srem.*

# TIPOLOGIJA OŠTEĆENJA PRAVOSLAVNIH SAKRALNIH OBJEKATA STRADALIH TOKOM DRUGOG SVETSKOG RATA: STUDIJA SLUČAJA OPŠTINE PEĆINCI

***Rezime:***

Rad se bavi tipologijom arhitektonskih oštećenja pravoslavnih sakralnih objekata stradalih tokom Drugog svetskog rata na teritoriji opštine Pećinci. Cilj istraživanja je utvrđivanje karaktera i stepena ratnih oštećenja i formiranje tipologije zasnovane na obimu fizičkog gubitka i posledicama po arhitektonsku celinu objekta. Analizom dostupne dokumentacije, arhivske građe i fotografija crkava, izdvojena su četiri tipa oštećenja, od lokalizovanih oštećenja do potpunog uništenja. Rezultati pokazuju izraženu zastupljenost oštećenja zvonika, koji predstavljaju najčešće zahvaćene arhitektonske elemente. Utvrđeno je da se sa povećanjem obima oštećenja povećava i stepen promene prvobitne arhitektonske celine, što neposredno utiče na karakter i složenost kasnijih intervencija. Formirana tipologija omogućava sistematičnije poređenje posledica ratnih razaranja i predstavlja osnovu za preciznije sagledavanje potreba i mogućnosti obnove sakralnog graditeljskog nasleđa.

**Ključne reči:** pravoslavne crkve, ratna oštećenja, arhitektonska tipologija, kulturno nasleđe, Drugi svetski rat, Srem

[1] Faculty of Technical Sciences, University of Novi Sad, Novi Sad, Serbia, unaradivojevic11@gmail.com, ORCID 0009-0007-1819-0251
[2] Associate Professor, Faculty of Technical Sciences, University of Novi Sad, Novi Sad, Serbia, ORCID 0000-0003-3666-8865

## 1. INTRODUCTION

Orthodox sacred buildings represent a significant part of Serbia's immovable cultural heritage, encompassing historical, architectural, artistic, and spiritual values accumulated over different historical periods. In addition to their primary religious function, churches serve as spatial expressions of the collective identity of local communities and as testimonies to the historical and cultural development of particular areas. Therefore, the preservation and restoration of sacred architectural heritage constitute complex processes that require prior assessment of the state of preservation, the nature of damage, and the possibilities for applying appropriate conservation and restoration measures.

A particular challenge in the protection of cultural heritage is posed by buildings that suffered damage during armed conflicts as a result of demolition, deliberate explosive destruction and/or arson, when the consequences of wartime destruction are often multi-layered and encompass different levels of loss, ranging from damage to individual architectural elements to the complete destruction of a building. International approaches to condition assessment of immovable cultural heritage indicate the need for systematic recording and classification of damage in order to enable the comparison of buildings, the establishment of priorities, and the planning of appropriate conservation and restoration measures. The EN 16096:2012 standard particularly emphasizes the importance of documenting the existing condition and systematically assessing the physical condition of built cultural heritage as a basis for decision-making regarding further interventions.[1]

During the Second World War, Orthodox sacred heritage in the Srem region suffered significant wartime destruction. Numerous churches and monasteries were exposed to various forms of devastation, including demolition, arson, damage to architectural elements, and the loss of parts of their historic and artistic contents. In his research on the destruction of Serbian monasteries and churches within the Eparchy of Srem, Dinko Davidov documents the scale of destruction affecting sacred buildings during the period 1941–1945, emphasizing that the consequences of these events represent a significant loss of the cultural heritage of this area.[2]

Contemporary research on war-induced damage to cultural heritage indicates that assessing the consequences of destruction requires a clear classification of different forms of physical loss and damage. Studies focusing on the restoration of historic buildings following armed conflicts, particularly in the Middle East, have developed approaches that distinguish types of damage according to their nature, extent, and consequences for the structural system and architectural integrity of the building. Such models demonstrate the importance of systematically recording and classifying damage as an initial step in the process of restoration and cultural heritage management.[3] Furthermore, research into the effects of Second World War bombing on architectural heritage demonstrates the long-term effects of warfare on materials, structural systems, and the authenticity of historic buildings, as well as the need for a precise understanding of the different mechanisms of damage.[4]

Although various approaches to cultural heritage condition assessment exist, previous research on the Orthodox sacred heritage of Srem has predominantly documented individual cases and the extent of wartime destruction, while the typological classification

[1] EN 16096:2012, Conservation of cultural property – Condition survey and report of built cultural heritage, European Committee for Standardization, 2012.
[2] D. Davidov, *Zlodela i gresi: Uništavanje srpskih manastira i crkava, Sremska eparhija 1941–1945–1950*, Beograd: Sremska eparhija, 1990.
[3] A. Dilsiz, S. Haj Ismail, "Documentation and assessment of war induced damage on historic buildings in Aleppo," *Journal of Architectural Conservation*, Vol. 26, Issue 3, 2020, pp. 291–308.
[4] X. Wang, L. Mol, M. Tucker et al., "Impacts of WWII bomb explosions on weathering damage of architectural heritage: Bath, England," *Heritage Science*, Vol. 12, 2024, Article 157.

of architectural damage according to the extent of physical loss and its consequences for the architectural integrity of the building remains insufficiently developed. Damage is most often described using general categories such as partial or complete destruction, without a more detailed consideration of the architectural elements lost, the degree to which spatial and structural integrity has been compromised, or the implications of such damage for the nature and complexity of subsequent restoration interventions.

This study examines Orthodox sacred buildings in the territory of the Municipality of Pećinci that suffered damage during the Second World War. The aim of the research is to establish a typology of architectural damage based on an analysis of the entire corpus of affected buildings in the study area and to identify characteristic patterns of destruction. The typology is based on the extent of physical loss, the type of architectural elements affected, and the degree of disruption to the original architectural integrity of the building. The analysis seeks to establish a classification system that enables a more precise assessment of the degree of damage and provides a basis for understanding the complexity of subsequent restoration interventions involving Orthodox sacred heritage.

## 2. METHODOLOGY

The research corpus comprises a total of 12 Orthodox sacred buildings located in the Municipality of Pećinci. The corpus was defined according to two main criteria: location within the present-day administrative territory of the Municipality of Pećinci and documented evidence of damage sustained during the Second World War. It includes the following Orthodox sacred buildings:

- Ašanja - Church of the Holy Archangel Gabriel
- Deč - Church of the Ascension of Christ
- Donji Tovarnik - Church of the Holy Apostles Peter and Paul
- Kupinovo - Church of the Annunciation
- Kupinovo - Church of the Holy Spirit
- Ogar - Church of St. Nicholas
- Pećinci - Church of St. Nicholas
- Popinci - Church of St. Nicholas
- Prhovo - Church of St. Nicholas
- Sremski Mihaljevci - Church of St. John the Theologian
- Subotište - Church of the Nativity of St. John the Baptist
- Šimanovci - Church of St. Nicholas

The research is based on an analysis of Orthodox sacred buildings in the Municipality of Pećinci, selected as a spatially defined case study for examining the consequences of wartime destruction of Orthodox sacred heritage in the Srem region. Although numerous sacred buildings in the Srem region suffered various forms of devastation during the Second World War, focusing on a clearly defined geographical area allows for an analysis of the entire local corpus of affected buildings and a comparison of different forms and degrees of architectural loss. The research includes Orthodox sacred buildings in the Municipality of Pećinci for which wartime damage sustained during the period 1941–1945 could be confirmed on the basis of available historical sources and documentation.

Historical and archival sources, existing technical and conservation documentation, historical photographs, relevant literature, and data on subsequent interventions were used to determine the nature and extent of the damage. Data obtained from different sources were cross-referenced in order to reconstruct the type and extent of wartime damage as reliably as possible. Where historical photographs documenting the post-damage condition were not available, the extent and characteristics of damage were determined from written archival records, historical descriptions, conservation documentation, and other relevant documentary sources.

For each building analyzed, the following aspects were considered: its condition prior to wartime destruction; the type and extent of documented damage; the architectural and structural elements affected; the degree to which the original architectural integrity was preserved; and the nature of subsequent interventions, where relevant data were available. The criteria for the analysis of architectural damage were defined according to the extent of physical loss and the type of architectural elements affected. The following were considered: (1) damage or loss of elements defining the spatial and volumetric organization of the building; (2) loss or damage to vertical architectural elements (bell towers, and their terminations); (3) disruption of the structural system (walls, vaults, roof structures, and other load-bearing elements); and (4) loss of decorative and artistic elements that constitute an integral part of the architectural and cultural significance of the building. Based on a combination of these indicators, the degree of alteration of the original architectural integrity of each building was assessed.

Using these criteria, a comparative analysis of all 12 buildings was conducted according to the nature and extent of the damage sustained. The typology was not predetermined, but was derived inductively from the analyzed corpus through the identification and comparison of recurring patterns of damage. In this way, four types of damage were identified ranging from localized damage to individual architectural elements to the complete physical destruction of the building. This procedure enables the systematic classification of buildings according to the extent of physical loss and the degree of alteration of their original architectural integrity, as well as the comparison of the consequences of different forms of wartime destruction.

It should be noted that some of the historical, archival, and other documentary material was destroyed or lost as a result of wartime destruction, including records relating to individual sacred buildings. The incomplete preservation of the documentary record constitutes one of the main limitations of the study, particularly in cases where it was not possible to reliably reconstruct the original condition of the building, precisely determine the extent of the damage sustained, or trace individual phases of its post-war restoration. In such cases, conclusions were drawn by cross-referencing available archival sources, historical photographs, literature, and preserved documentation, while only aspects of the documented damage that could be reliably verified were included in the typological analysis.

## 3. RESULTS

### 3.1. SPATIAL AND HISTORICAL CONTEXT

Srem is located in the northern part of the Republic of Serbia, within the Autonomous Province of Vojvodina, between the Danube to the north and the Sava to the south. Its geographical position, at the intersection of different regional and cultural spheres, has historically played a significant role in shaping its specific cultural characteristics.[1] The position of Srem as a border region further influenced its historical development. Since the Middle Ages, the territory of Srem has been situated between major political and cultural centar, including the Frankish Empire, the Kingdom of Hungary and the Byzantine Empire.[2] Over the centuries, it therefore developed as a contact zone in which different religious, cultural, and social influences intersected, contributing to the formation of its specific identity. The complex historical and geographical position of

[1] B. Đerčan, D. Bjelajac, M. Bubalo-Živković, T. Lukić, D. Gatarić, "Exploring the contemporary spatial and temporary dynamics of the settlement hierarchy and system in Serbia's Srem Region," Geographica Pannonica, Vol. 28, Issue 4, 2024, pp. 271–283.

[2] M. Imerovski, "O Sremu – kao vojnoj krajini nastaloj još u vreme Franaka," Kultura polisa, Vol. 9, No. 17, 2012, pp. 167–188.

Srem was also reflected in the development of its cultural and sacred heritage. The interaction of different cultural influences was manifested not only in social and political relations but also in the architectural transformation of the region and the development of its sacred architecture. At the same time, the position of Srem as an area exposed to different historical and political circumstances also increased its exposure to the consequences of armed conflicts.

The destruction of the cultural and sacred heritage of Srem was evident during different periods of armed conflict, but reached particularly significant proportions during the Second World War. From 1941 to 1945, numerous Serbian monasteries and churches within the Eparchy of Srem were subjected to systematic destruction, devastation and various forms of damage by the German occupying forces, the communist authorities, and the armed forces of the Independent State of Croatia (NDH).[3] The consequences of these events were reflected not only in the complete destruction of individual buildings, but also in the loss or alteration of individual architectural elements, resulting in lasting changes to the architectural integrity and authenticity of parts of Srem's sacred heritage. However, the destruction of the sacred heritage did not end with the conclusion of the war. In the post-war period, the attitude of the communist authorities towards the Serbian Orthodox Church led to new forms of pressure, which, in addition to their direct impact on the church organization and property, also affected the condition of individual sacred buildings.[4] A transition in the nature of threats to this heritage can therefore be observed, from direct wartime destruction to post-war neglect, alterations, and gradual deterioration of buildings. This historical continuity of different forms of threat is important for understanding the present condition of sacred buildings and provides a basis for further consideration of specific architectural damage within the research corpus.

It is precisely the diversity of the consequences of wartime destruction that constitutes an important issue in the study of this heritage. Wartime destruction cannot be considered exclusively in terms of whether a building was destroyed or preserved, since between these two extreme outcomes there is a whole spectrum of different degrees and forms of architectural damage. Therefore, in order to understand the consequences of wartime destruction, it is necessary to determine which architectural elements were damaged or lost, to what extent, and how these losses affected the architectural integrity of the building. Such an approach provides the basis for further systematization and typological classification of damage to Orthodox sacred buildings, which is presented in the following sections.

## 3.2. ANALYZED SACRED BUILDINGS

The research corpus comprises twelve Orthodox sacred buildings located in the Municipality of Pećinci. The analysis of the available archival, photographic, historical, and parish records provided information on the period of construction of the buildings, their original architectural form, the nature and extent of their destruction, and subsequent interventions. Different forms and degrees of wartime destruction were identified within the analyzed corpus.

Some of the buildings were completely destroyed during the Second World War. Such a case was recorded in Ašanja, where the masonry church built in 1838 was completely destroyed during the war.[5] A similar fate befell the church in Donji Tovarnik, built in 1807, which was destroyed during the war, while a new building was constructed on its

[3] D. Davidov, Zlodela i gresi, 1990.
[4] S. B. Jović, Utamničena crkva: stradanje sveštenstva Srpske pravoslavne crkve od 1945. do 1985. godine, Beograd: Književno društvo „Sveti Sava", 2007.
[5] Provincial Institute for the Protection of Cultural Monuments of Vojvodina, archival documentation on the church in Ašanja, Novi Sad.

site in 1967.[6] The church in Donji Tovarnik was destroyed with explosives in 1943.[7] The same method of destruction was recorded in Ogar, where the church, built in 1747, was damaged with explosives in 1943.[8] [9] Complete destruction during the war was also recorded in the case of the Church of the Annunciation in Kupinovo, whose development is associated with an older wooden church. Following its wartime destruction, a new church was constructed in 2007 based on the architectural model of the former building.[10] In some buildings, the destruction did not affect the entire architectural structure of the building but rather individual architectural elements. In several cases, bell towers were particularly affected, altering the character and vertical composition of the existing churches. In Deč, a section of the bell tower above the western part of the church was destroyed in 1944 as a result of an explosive attack[11] , while in Pećinci, the bell tower was demolished during the war, after which the church was shortened on its western side.[12] In Subotište, the attached bell tower was destroyed and was not reconstructed until the 2000s.[13] A similar pattern can be observed in Popinci, where the church sustained explosive damage during the war, while the bell tower was restored after the war, but in a shortened form.[14] [15] [16] In Prhovo, the church bell tower was partly demolished, according to available data because it had been used as an observation post.[17] In Šimanovci, the church bell tower was demolished during the war in 1943, after which the building was restored.[18] [19] These examples indicate a pronounced prevalence of damage to vertical elements within the research corpus, which will be further considered in the subsequent classification.

In addition to demolition and explosive destruction, other forms of wartime destruction were also recorded. The Church of the Holy Spirit in Kupinovo, built in 1814, was damage by fire during the Second World War and subsequently restored.[20] The Church of St. John the Theologian in Sremski Mihaljevci, which underwent several phases of construction and extension throughout its history, also suffered damage during the war.[21] A particular case is the Chapel of St. Petka in Brestač. Unlike the previously mentioned buildings, the chapel did not suffer during the war itself, but immediately after the end of the Second World War, when it was demolished by the communist authorities in order to

[6] Institute for the Protection of Cultural Monuments of Sremska Mitrovica, archival documentation on the church in Donji Tovarnik, Sremska Mitrovica.
[7] D. Davidov, *Zlodela i gresi*, 1990.
[8] D. Davidov, *Zlodela i gresi*, 1990.
[9] *Crkveni letopis*, 20th century, manuscript, archive of the parish of Ogar.
[10] P. Puzić, B. Mijanović, *Kupinovački relikvijari*, Pećinci: National Library, 2023.
[11] Institute for the Protection of Cultural Monuments of Sremska Mitrovica, archival documentation on the church in Deč, Sremska Mitrovica.
[12] Institute for the Protection of Cultural Monuments of Sremska Mitrovica, archival documentation on the church in Pećinci, Sremska Mitrovica.
[13] Institute for the Protection of Cultural Monuments of Sremska Mitrovica, archival documentation on the church in Subotište, Sremska Mitrovica.
[14] D. Davidov, *Zlodela i gresi*, 1990.
[15] Provincial Institute for the Protection of Cultural Monuments of Vojvodina, archival documentation on the church in Popinci, Novi Sad.
[16] Institute for the Protection of Cultural Monuments of Sremska Mitrovica, archival documentation on the church in Popinci, Sremska Mitrovica.
[17] Institute for the Protection of Cultural Monuments of Sremska Mitrovica, archival documentation on the church in Prhovo, Sremska Mitrovica.
[18] Institute for the Protection of Cultural Monuments of Sremska Mitrovica, archival documentation on the church in Šimanovci, Sremska Mitrovica.
[19] *Crkveni letopis*, unpublished manuscript, archive of the parish of Šimanovci.
[20] Institute for the Protection of Cultural Monuments of Sremska Mitrovica, archival documentation on the Church of the Holy Spirit in Kupinovo, Sremska Mitrovica.
[21] Provincial Institute for the Protection of Cultural Monuments of Vojvodina, archival documentation on the church in Sremski Mihaljevci, Novi Sad.

construct a cooperative centre on its site.[22] [23] Although it is not included in the research corpus, its case is significant for the broader context of the research, considering its immediate temporal proximity to the wartime events and the ideological and social circumstances that followed the war and influenced the subsequent destruction of the sacred architectural heritage.

The documented cases demonstrate considerable variation in the extent and character of wartime damage, ranging from the loss of individual architectural elements to the destruction of the entire building. Representative examples of these conditions are presented in Figures 1 and 2, illustrating different degrees of physical loss and their impact on the architectural integrity of the buildings. These visual examples support the distinction between the damage types established through the analysis of the complete corpus.



*Figure 1.* ***Kupinovo - Church of the Holy Spirit. Remains of the church following damage sustained during the Second World War.***[24]

[22] *Crkveni letopis*, 19th century, manuscript, archive of the parish of Brestač.

[23] U. Radivojević, "Processing of non-existent architectural heritage for AI visualization, a case study of the Chapel of Saint Petka in Brestač," *Proceedings of STEPGRAD 2026*, Banja Luka, 2026. https://doi.org/10.61892/STP202601017R

[24] Institute for the Protection of Cultural Monuments of Sremska Mitrovica, archival documentation on the Church of the Holy Spirit in Kupinovo, Sremska Mitrovica.



*Figure 2.* ***Subotište - Church of the Nativity of Saint John the Baptist. Remains of the church following damage sustained during the Second World War.***[25]

The analyzed buildings demonstrate a wide range of consequences of wartime destruction, from the complete destruction of a building, through the demolition of individual architectural elements, particularly bell towers, to localized damage. These differences provide the basis for their further systematization and the formation of a typology of architectural damage.

Based on the analyzed data, it can be observed that wartime destruction within the research corpus can be characterized by a range of different forms and degrees of architectural loss. These include the complete destruction of buildings, the explosive destruction or demolition of bell towers, alterations to the original volume of buildings, fire damage, and other forms of localized damage. These differences provide the basis for their further comparison and systematization according to the character and nature of architectural damage.

## 3.3. TYPOLOGY OF ARCHITECTURAL DAMAGE

Based on the previously conducted analysis of historical and archival sources concerning twelve Orthodox sacred buildings, a comparative analysis of the character and extent of their wartime damage was carried out. The classification adopted the principle of systematic documentation and condition assessment of built cultural heritage defined by the EN 16096:2012 standard as a professional framework. The standard provides for the documentation of the condition of a building, its individual components, and identified changes, allowing for a comparative approach to a group of buildings.[26] However, given the specific subject of this research, the classification was not adopted from the existing standard but was developed based on the characteristics of wartime damage identified

[25] Institute for the Protection of Cultural Monuments of Sremska Mitrovica, archival documentation on the in Subotište, Sremska Mitrovica.
[26] EN 16096:2012.

within the analyzed corpus. The primary criteria considered were the type of damaged architectural element, the extent of its loss, and the consequences of the damage for the integrity of the building. In this way, characteristic patterns of destruction were identified, enabling the comparison of buildings and their grouping according to the degree and character of architectural loss. The classification was established according to the extent of physical loss and the degree to which the damage affected the architectural whole, with particular emphasis placed on vertical elements, the structural system, and the basic volume of the building.

- Type I – localized damage to an individual architectural element comprises cases in which wartime destruction affected one clearly defined architectural element or part thereof, while the basic volume, structural system, and other key elements of the building remained predominantly preserved.
- Type II – damage to multiple architectural elements with preservation of the basic volume comprises cases in which several architectural elements, such as the bell tower, roof, or their associated components, were simultaneously affected by the destruction, while the basic volume and the majority of the structural system remained preserved. This category may also include the complete loss of an individual element, such as a bell tower, provided that its destruction was not accompanied by significant damage to other parts of the building.
- Type III – severe damage to the architectural whole comprises cases in which the destruction, in addition to individual architectural elements and the roof, also affected walls, vaults, or other parts of the primary structural system. Such a degree of physical loss results in significant alteration of the original volume and architectural integrity of the building.
- Type IV – complete destruction of the original building comprises cases in which the entire or almost entire original building structure was lost as a result of wartime destruction, resulting in the complete loss of the original architectural whole. A subsequent building may have been constructed on the same site, but such a replacement is not considered a preservation of the original building within this classification.

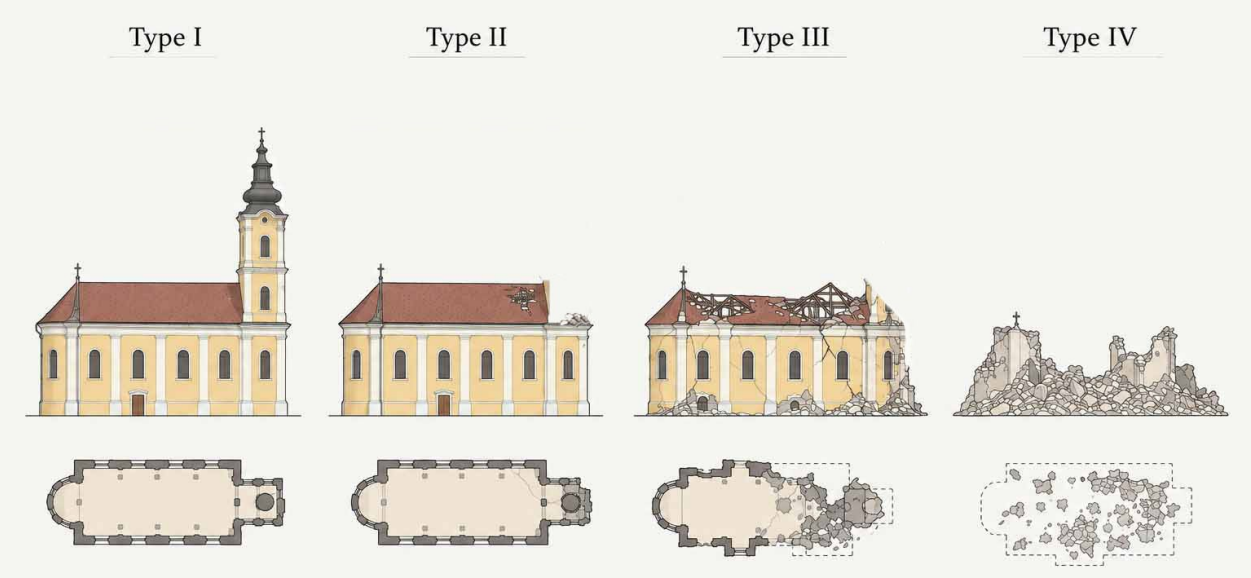


*Figure 3.* ***Typology of Damage to Orthodox Sacred Buildings during the Second World War in the Municipality of Pećinci***[27]

[27] Source: Author, 2026.

## 4. DISCUSSION OF RESULTS

### 4.1. ANALYSIS OF PATTERNS OF ARCHITECTURAL DAMAGE

The results of the analysis show that the wartime destruction of Orthodox sacred buildings in the Municipality of Pećinci did not have a uniform form, but ranged from damage to individual architectural elements to the complete destruction of buildings. The high frequency of damage to bell towers is particularly pronounced, as these elements were demolished or severely damaged in several of the analyzed churches.

This prevalence indicates that damage to vertical elements represents one of the characteristic patterns of wartime destruction within the analyzed corpus. However, the reasons for their frequent occurrence cannot be determined unequivocally based on the available documentation, as in some cases the damage resulted from planned demolition by explosives, while in other cases the circumstances of their occurrence are insufficiently documented. A comparison of the analyzed buildings also shows that, as the extent of physical loss increases, the degree of alteration of the original architectural integrity increases. In buildings where an individual element was damaged, interventions were generally focused on its restoration, whereas in cases of more severe destruction, the consequences were more long-lasting and involved changes in volume, loss of parts of the building, or its complete replacement.

In this respect, the established typology does not represent merely a classification according to the amount of lost building structure, but also indicates different degrees of change to the architectural integrity of the building. The transition from Types I and II to Types III and IV represents a transition from localized loss to the alteration, and ultimately the complete loss, of the original architectural integrity.

| Location / Church | Type / Level of Damage | Affected Architectural Elements | Condition Before Damage | Condition After Damage | Current Condition |
|---|---|---|---|---|---|
| Ašanja - Church of the Holy Archangel Gabriel | Type IV – complete destruction | Entire church | 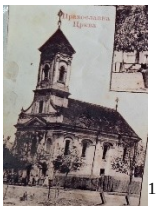 [1] | / | A new church was built |
| Deč – Church of the Ascension of Christ | Type I – localized damage | Part of the bell tower |  | / |  |

[1] Source: *Church Chronicle of Ašanja*.
[2] Source: Institute for the Protection of Cultural Monuments of Sremska Mitrovica, archival documentation on the church in Deč, Sremska Mitrovica.
[3] Source: Author, 2026.

| | | | | | |
|---|---|---|---|---|---|
| Donji Tovarnik – Church of the Holy Apostles Peter and Paul | Type IV – complete destruction | Entire church | / | / | A new church was built |
| Kupinovo – Church of the Annunciation | Type IV – complete destruction | Entire church | / | / | A new church was built |
| Kupinovo – Church of the Holy Spirit | Type III – severe damage | Bell tower, roof and walls | / |  [4] | 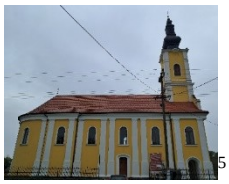 [5] |
| Ogar – Church of Saint Nicholas | Type III – severe damage | Bell tower, roof and walls | / | / |  |
| Pećinci – Church of Saint Nicholas | Type II – significant damage to part of the architectural whole | Bell tower and roof | / | / |  [7] |
| Popinci – Church of Saint Nicholas | Type I – localized damage | Part of the bell tower | / |  |  |
| Prhovo – Church of Saint Nicholas | Type I – localized damage | Part of the bell tower | / |  |  |

[4] Source: Institute for the Protection of Cultural Monuments of Sremska Mitrovica, archival documentation on the Church of the Holy Spirit in Kupinovo, Sremska Mitrovica.
[5] Source: Author, 2026.
[6] Source: Author, 2026.
[7] Source: Author, 2026.
[8] Source: Institute for the Protection of Cultural Monuments of Sremska Mitrovica, archival documentation on the church in Popinci, Sremska Mitrovica.
[9] Source: Author, 2026.

| | | | | | |
|---|---|---|---|---|---|
| Sremski Mihaljevci – Church of Saint John the Theologian | Type II – significant damage to part of the architectural whole | Bell tower and roof | / | 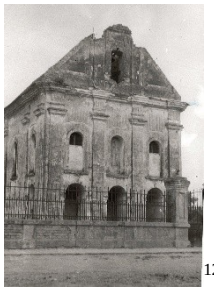 12 |  13 |
| Subotište – Church of the Nativity of Saint John the Baptist | Type II – significant damage to part of the architectural whole | Bell tower | / |  14 |  |
| Šimanovci – Church of Saint Nicholas | Type II – significant damage to part of the architectural whole | Bell tower | / |  16 |  |

*Table. 1* ***Classification of Damage***

## 4.2. REPRESENTATION OF DAMAGE TYPES AND ELEMENTS

Based on the analysis of the research corpus, a relatively even distribution of all four types of damage can be observed. Particularly notable is the frequency of damage to vertical architectural elements, namely bell towers, which were destroyed in nine of the twelve analyzed buildings, and partly damage in three cases. Roof elements were damaged in seven cases, while walls were recorded as damaged in five buildings where the destruction affected a broader architectural whole. This distribution indicates that wartime destruction did not manifest exclusively through the complete destruction of buildings, but in a significant number of cases affected individual architectural elements while preserving a larger part of the building structure. The particularly pronounced prevalence of damage to bell towers represents one of the most evident patterns within the analyzed corpus.

Their damage was of particular significance for the architectural integrity of the churches, since the loss of a dominant vertical element represented not only the physical loss of one

[10] Source: Institute for the Protection of Cultural Monuments of Sremska Mitrovica, archival documentation on the church in Prhovo, Sremska Mitrovica.
[11] Source: Author, 2026.
[12] Source: Institute for the Protection of Cultural Monuments of Sremska Mitrovica, archival documentation on the church in Sremski Mihaljevci, Sremska Mitrovica.
[13] Source: Author, 2026.
[14] Source: Institute for the Protection of Cultural Monuments of Sremska Mitrovica, archival documentation on the church in Subotište, Sremska Mitrovica.
[15] Source: Author, 2026.
[16] Source: Institute for the Protection of Cultural Monuments of Sremska Mitrovica, archival documentation on the church in Šimanovci, Sremska Mitrovica.
[17] Source: Author, 2026.

part of the building, but also altered the volumetric composition and silhouette of the building.

At the same time, the prevalence of individual damaged elements should be interpreted independently of the distribution of damage types, since a single building may simultaneously have a damaged bell tower, roof, and walls. The types therefore express the overall degree of architectural loss at the building level, while the analysis of individual elements enables the identification of building components that most frequently occur in the documented patterns of wartime destruction.

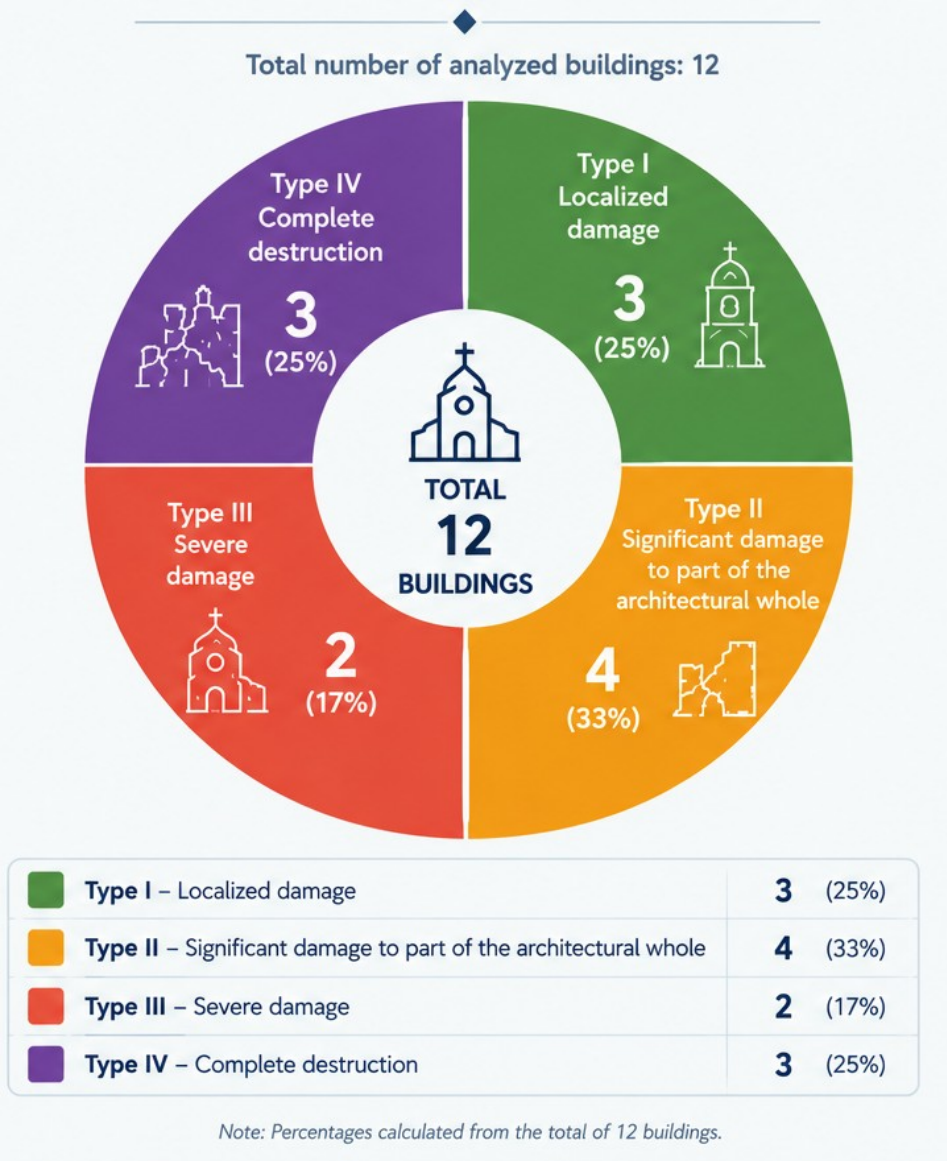


*Figure 4.* ***Number of Buildings by Damage Type*** [18]

[18] Source: Author, 2026.

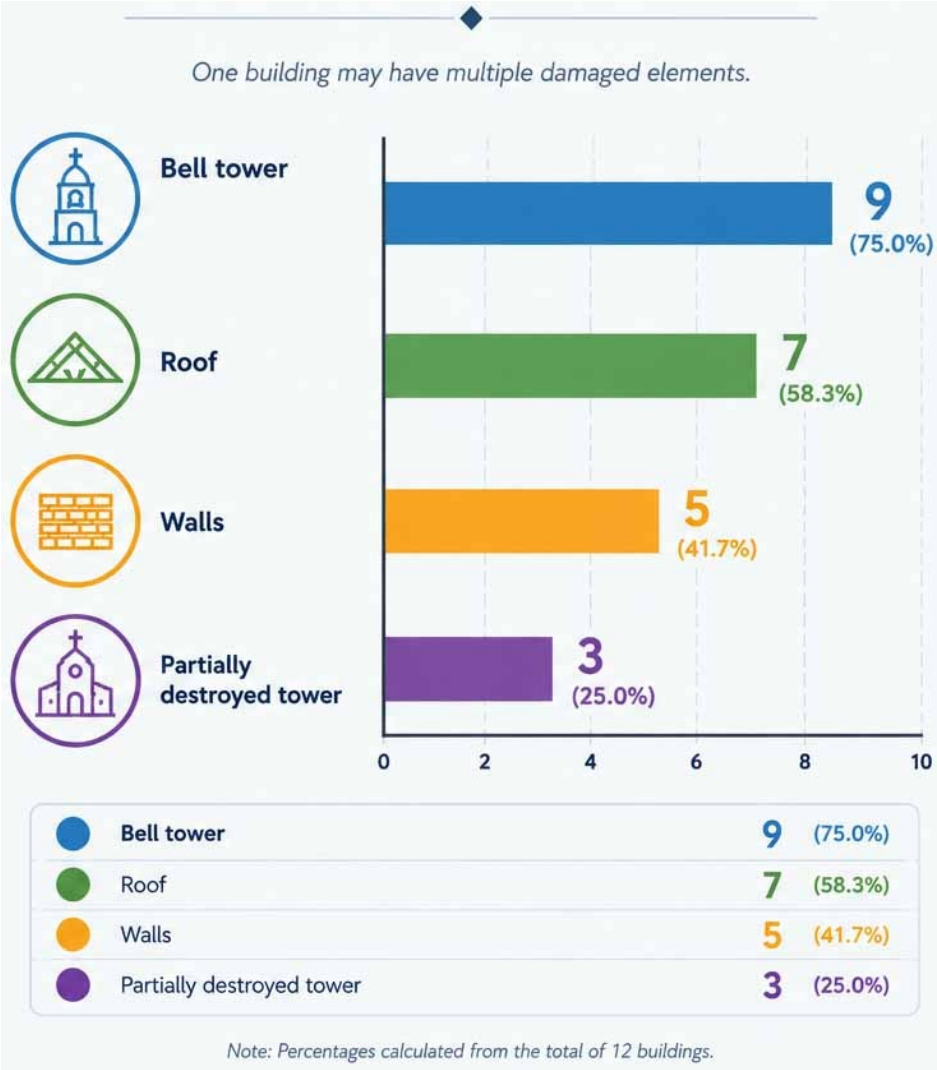


*Figure 5.* ***Frequency of Damage by Architectural Elements*** [19]

## 5. CONCLUSION

The study demonstrates that the wartime destruction of Orthodox sacred buildings in the Municipality of Pećinci encompassed different forms and degrees of architectural damage, ranging from localized damage to individual architectural elements to the complete destruction of buildings. Based on the analysis of twelve buildings, a typology comprising four types of damage was established based on the extent of physical loss and the degree of alteration of the original architectural integrity. The resulting gradation reflects a progression from localized loss, through damage affecting multiple architectural elements and the structural system, to the complete loss of the original architectural integrity.

The results show that bell towers were the architectural elements most frequently recorded as damaged within the analyzed corpus, while in cases of more severe destruction, damage extended to roofs, walls, and other components of the structural system, ultimately resulting in the complete loss of the original building. The significance of damage to vertical elements lies in the fact that their loss affected not only the physical fabric of the churches but also their volumetric composition and characteristic silhouette. The established typology enables a clearer comparison of the analyzed buildings and a

[19] Source: Author, 2026.

more precise understanding of the consequences of wartime destruction for the architectural integrity of the buildings.

The contribution of the proposed typology lies in the systematic classification of different forms of wartime damage according to architectural criteria, moving beyond general categories of partial and complete destruction. This classification can provide a basis for assessing the degree of alteration of architectural integrity and understanding different conservation and restoration requirements, particularly in terms of the extent of required interventions and the possibilities for preserving authentic architectural elements.

The research results should be considered in light of the limitations associated with the incomplete preservation of historical, archival, and other documentary material, as well as the geographically limited scope of the research corpus. The proposed model therefore represents a corpus-derived typology whose broader applicability requires further testing on a larger sample of Orthodox sacred buildings across the Srem region. Such an extension of the research would enable the validation of the identified damage types, the recognition of potential additional patterns, and a more comprehensive understanding of wartime damage to Orthodox sacred architectural heritage in Srem.

## ACKNOWLEDGEMENTS

This research has been supported by the Ministry of Science, Technological Development and Innovation (Contract No. 451-03-34/2026-03/200156) and the Faculty of Technical Sciences, University of Novi Sad through project “Scientific and Artistic Research Work of Researchers in Teaching and Associate Positions at the Faculty of Technical Sciences, University of Novi Sad 2026” (No. 01-3609/1).

## REFERENCES

[1] EN 16096:2012. *Conservation of Cultural Property – Condition Survey and Report of Built Cultural Heritage*. Brussels: European Committee for Standardization.

[2] Davidov, D. (1990). *Zlodela i gresi: Uništavanje srpskih manastira i crkava, Sremska eparhija 1941–1945–1950*. Belgrade: Diocese of Srem.

[3] Dilsiz, A., Haj Ismail, S. (2020). Documentation and assessment of war induced damage on historic buildings in Aleppo. *Journal of Architectural Conservation*, 26(3), 291–308. https://doi.org/10.1080/13556207.2020.1804734

[4] Wang, X., Mol, L., Tucker, M., Blenkinsop, T., Gilbert, O., Campbell, O. (2024). Impacts of WWII bomb explosions on weathering damage of architectural heritage: Bath, England. *Heritage Science*, 12, 157. https://doi.org/10.1186/s40494-024-01262-w

[5] Đerčan, B., Bjelajac, D., Bubalo-Živković, M., Lukić, T., Gatarić, D., Pogrmić, Z. (2024). Exploring the contemporary spatial and temporary dynamics of the settlement hierarchy and system in Serbia's Srem Region. *Geographica Pannonica*, 28(4), 271–283. https://doi.org/10.5937/gp28-51736

[6] Imerovski, M. (2012). O Sremu – kao vojnoj krajini nastaloj još u vreme Franaka. *Kultura polisa*, 9(17), 167–188.

[7] Jović, S. B. (2007). *Utamničena crkva: stradanje sveštenstva Srpske pravoslavne crkve od 1945. do 1985. godine*. Belgrade: Literary Society “Saint Sava”.

[8] Provincial Institute for the Protection of Cultural Monuments of Vojvodina. Archival documentation on the church in Ašanja. Novi Sad.

[9] Institute for the Protection of Cultural Monuments of Sremska Mitrovica. Archival documentation on the church in Donji Tovarnik. Sremska Mitrovica.

[10] Puzić, P., Mijanović, B. (2023). *Kupinovački relikvijari*. Pećinci: National Library.

[11] Institute for the Protection of Cultural Monuments of Sremska Mitrovica. Archival documentation on the church in Deč. Sremska Mitrovica.

[12] Institute for the Protection of Cultural Monuments of Sremska Mitrovica. Archival documentation on the church in Pećinci. Sremska Mitrovica.

[13] Institute for the Protection of Cultural Monuments of Sremska Mitrovica. Archival documentation on the church in Subotište. Sremska Mitrovica.

[14] Provincial Institute for the Protection of Cultural Monuments of Vojvodina. Archival documentation on the church in Popinci. Novi Sad.

[15] Institute for the Protection of Cultural Monuments of Sremska Mitrovica. Archival documentation on the church in Prhovo. Sremska Mitrovica.

[16] Provincial Institute for the Protection of Cultural Monuments of Vojvodina. Archival documentation on the church in Sremski Mihaljevci. Novi Sad.

[17] Institute for the Protection of Cultural Monuments of Sremska Mitrovica. Archival documentation on the church in Šimanovci. Sremska Mitrovica.

[18] Institute for the Protection of Cultural Monuments of Sremska Mitrovica. Archival documentation on the Church of the Holy Spirit in Kupinovo. Sremska Mitrovica.

[19] *Crkveni letopis Brestač*. 19th century. Manuscript, archive of the Brestač parish.

[20] Radivojević, U. (2026). Processing of non-existent architectural heritage for AI visualization, a case study of the Chapel of Saint Petka in Brestač. *Proceedings of STEPGRAD 2026*. Banja Luka. https://doi.org/10.61892/STP202601017R

[21] *Crkveni letopis Ašanja*. 20th century. Manuscript, archive of the Ašanja parish.

[22] *Crkveni letopis Šimanovci*. Unpublished manuscript, archive of the Šimanovci parish.

https://doi.org/10.24867/INDIS-2026-EN-601

**INTERNATIONAL SCIENTIFIC CONFERENCE**
INTEGRATION, NOVELTY, DESIGN,
INTERDISCIPLINARITY, SUSTAINABILITY

iNDiS 2026

# THE ROOF AS ACTIVE URBAN INFRASTRUCTURE: TOWARDS THE REINTEGRATION OF TECTONICS, PROGRAM, AND SUSTAINABILITY

*Miralem Bećić*[1]

***Summary:***

This paper examines the contemporary crisis of architectural roofs and argues that modern architecture has reduced the roof to a passive technical barrier, weakening the connection between construction, spatial experience, and cultural meaning. By combining tectonic theory, phenomenological interpretation, and contemporary sustainable design approaches, the paper proposes a framework for understanding roofs as active architectural and urban elements that simultaneously support identity, program, and environmental performance. The research shows that successful roof design depends on balancing three interconnected dimensions: identity, programmatic use, and tectonic expression. The paper concludes that the future of urban architecture depends on redefining the roof not only as a protective layer, but also as a generator of urban space capable of responding to climate change, biodiversity loss, and social fragmentation through integrated design strategies.

*Keywords: roof architecture, critical tectonics, parametric design, green infrastructure, urban sustainability, cultural identity.*

# KROV KAO AKTIVNA URBANA INFRASTRUKTURA: KA REINTEGRACIJI TEKTONIKE, PROGRAMA I ODRŽIVOSTI

***Rezime:***

Ovaj rad ispituje savremenu krizu arhitektonskih krovova, tvrdeći da je moderna arhitektura svela krov na pasivnu tehničku barijeru, čime je prekinuta suštinska veza između konstrukcijskog izraza i prostornog iskustva. Kroz sintezu tektonske teorije, fenomenološke analize i savremenih praksi održivog dizajna, predlažemo okvir za razumevanje krovova kao aktivnih topoloških entiteta koji istovremeno služe funkcijama identiteta, programa i ekoloških performansi. Istraživanje otkriva da uspešan dizajn krova zahteva balansiranje tri komplementarne dimenzije: dimenzije identiteta, programske dimenzije i tektonske dimenzije. Zaključujemo da budućnost urbane arhitekture zavisi od prepoznavanja krovova ne samo kao zaštitnih elemenata, već kao kritičnih generatora savremenog urbanog prostora, sposobnih da odgovore na klimatske promene, gubitak biodiverziteta i društvenu otuđenost kroz integrisane strategije dizajna.

*Ključne reči: arhitektura krovova, kritička tektonika, parametrijski dizajn, zelena infrastruktura, urbana održivost, kulturni identitet.*

[1] PhD student, Faculty of Technical Sciences, University of Novi Sad, Novi Sad, Serbia, miralem.arch@gmail.com, ORCID 0009-0000-2301-0621

## 1. INTRODUCTION

Architecture has historically been organized around fundamental questions of shelter, form, context, climate, and human experience. Among all architectural elements, the roof holds a unique position because it directly mediates the relationship between people and the sky. Historically, roofs were not only protective structures but also carriers of cultural identity, constructional logic, and spatial meaning. In contemporary architectural practice, however, the roof has gradually lost much of this significance.
Modern construction methods, standardized building systems, and increasingly strict energy regulations have transformed roofs into highly technical systems focused primarily on insulation, waterproofing, thermal control, and efficiency. As a result, the roof is often treated as a neutral technical surface rather than an architectural element capable of shaping spatial experience and urban identity. This transformation has contributed to the loss of tectonic expression and to the weakening of the relationship between construction and perception.

The problem is not merely aesthetic or philosophical; it reflects a fundamental rupture in architectural thinking. Traditional architectural cultures maintained a clear connection between roof form, structural logic, climate, and social life [1]. Medieval pitched roofs expressed gravity and structural forces through visible timber construction. Venetian altanas transformed rooftops into collective social spaces, while Parisian mansards enabled the occupation of previously unused spaces beneath the roof. In each case, the roof was more than protection from weather; it became a meaningful part of everyday life and urban culture.

Contemporary architecture often replaces these spatial and cultural qualities with standardized multilayer roof systems that prioritize thermal performance and technical optimization while simultaneously concealing constructional logic, structural relationships, and material expression. Roofs become visually silent surfaces that no longer communicate how they work or how they relate to the surrounding environment. They neither shape meaningful spatial experiences nor contribute to a deeper understanding of dwelling.

At the same time, contemporary cities face unprecedented environmental and social challenges, including climate change, biodiversity loss, urban heat island effects, excessive resource consumption, and growing forms of social isolation and spatial alienation. In this context, roofs represent an enormous but insufficiently explored urban resource. Green roof technologies, renewable energy systems, parametric design methods, and ecological infrastructure now allow roofs to perform multiple functions simultaneously. They can support biodiversity, collect rainwater, produce energy, and create new social spaces.

Despite these possibilities, many contemporary roof strategies remain disconnected from broader architectural questions related to tectonics, cultural identity, phenomenological experience, and spatial meaning. This paper argues for a conceptual reframing: understanding the roof not as a technical component but as an active topological entity capable of reintegrating architecture's fragmented contemporary concerns. Rather than treating the roof as a purely technical component, it should be understood as an active architectural and urban element capable of reconnecting environmental performance, social use, and tectonic expression.

The proposed framework is organized around three complementary dimensions: identity, program, and tectonics. Through theoretical discussion and contemporary case studies, the paper demonstrates how the integration of these dimensions can contribute to more sustainable, meaningful, and spatially expressive urban environments.

## 2. THE CRISIS OF CONTEMPORARY ROOF ARCHITECTURE

### 2.1. THE LOSS OF TECTONIC EXPRESSION

Tectonics, as developed through the work of theorists like Kenneth Frampton and others, emphasizes the expressive potential of construction itself. A tectonic approach recognizes that the way materials are joined, the manner in which loads are transmitted, and the visible organization of structural systems constitute legitimate artistic expression. The essence of architecture lies not only in the aesthetics of form, but also in the aesthetics of construction [2]. In this sense, the roof can be considered the pinnacle of tectonic thought. Understanding this concept requires insight into two complementary terms: techne and poiesis. While techne represents the rational basis (knowledge of materials, statics, and structural joints), poiesis is what elevates the technical solution into the realm of art, transforming the roof from a mere protective element into a work of architecture.

Historically, the roof represented one of the clearest manifestations of tectonic thinking because it revealed the relationship between gravity, structure, material, and shelter. Traditional roofs openly communicated how they worked. Timber structures, rafters, joints, and construction details were often visible and understandable to inhabitants.
Contemporary roof construction has largely eliminated this visibility. Standard roof systems today are usually composed of multiple layers of insulation, waterproof membranes, vapor barriers, and technical installations that conceal the logic of construction. From the interior, suspended ceilings hide the structural system, while from the exterior, roofs often appear as neutral surfaces without material or structural expression. As a result, the roof becomes functionally efficient but architecturally silent. It performs technically, yet it no longer communicates the forces it resists or the way it shelters human life.

This issue also has important phenomenological implications. Martin Heidegger argued that authentic dwelling requires the establishment of equilibrium between earth, sky, mortals, and divinities. He poses a key thesis: we do not dwell because we have built, but we build because we are beings who dwell [3]. The contemporary roof often weakens this relationship by reducing the sky to a technical and climatic condition rather than an existential and spatial presence. Inhabitants no longer perceive shelter as a meaningful human construction, but primarily as an invisible technical system.

### 2.2. THE MARGINALIZATION OF ROOF-BASED HABITATION

Historical architectural traditions frequently treated roofs as inhabitable spaces with distinct social and spatial qualities. In Balkan architecture, attic creates zones of intimate withdrawal and personal refuge beneath pitched roofs. In his phenomenological reflections, Gaston Bachelard explores the poetic dimension of space, describing the attic as the most intimate and secure sanctuary. For him, sloped roofs generate a space where imagination and subjectivity are nurtured [4]. Parisian mansards, despite their initial marginalization, developed into spaces of artistic creativity and social mixing.

Venetian altanas functioned as crucial points of social interaction and collective identity formation.

Contemporary urban development has significantly reduced these roof-based habitation patterns. Flat roofs are often preferred because they maximize usable building volume and simplify technical construction. Energy regulations and standardized envelopes further contribute to the disappearance of spatial diversity beneath and above roofs. When roofs are inhabited today, they are usually transformed into exclusive penthouses or luxury terraces disconnected from the broader social and tectonic logic of the building. Rather than functioning as integral spatial elements, they often become isolated commercial amenities.

The disappearance of meaningful roof spaces has consequences beyond aesthetics. Research in environmental psychology shows that diverse and legible spatial configurations contribute to psychological well-being, social interaction, and a stronger sense of belonging [5]. Monotonous and standardized environments can produce feelings of alienation, stress, and social detachment.

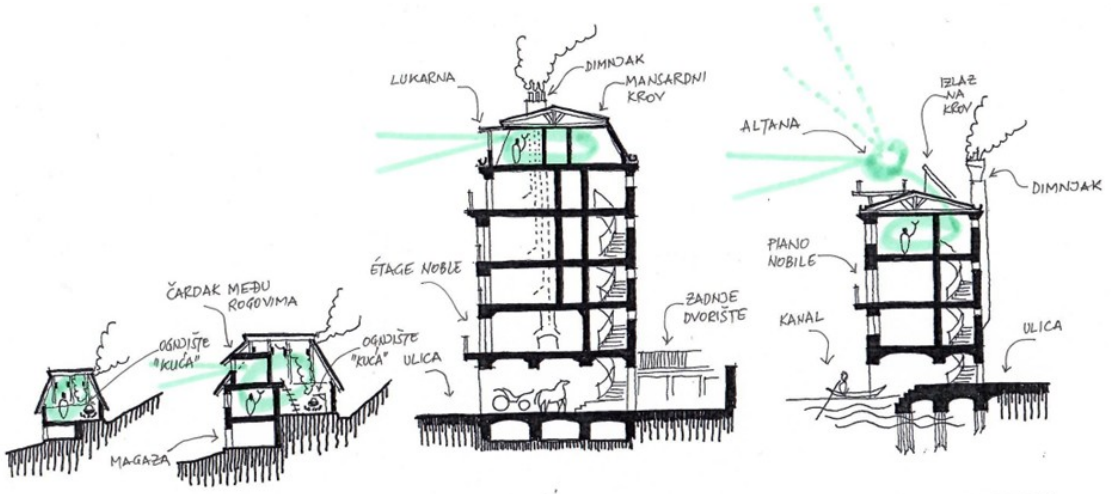


*Fig. 1 diversity beneath and above roof: a) Balkan shelter-Katun; b) Balkan traditional house; c) Parisian mulyistorey residential building; d) Venetian multystorey residential building; illustration by Author*

## 2.3. THE SEPARATION OF ENERGY PERFORMANCE AND SPATIAL EXPERIENCE

Contemporary building regulations have made energy efficiency a central concern of architectural design. Although this development is necessary in environmental terms, it has often produced a separation between technical performance and spatial quality. Roofs optimized primarily through thermal calculations can result in spatially poor solutions that neglect natural ventilation, daylight access, and coherent interior experiences. In many cases, environmental performance becomes an isolated technical objective rather than part of a broader architectural strategy.

Green roofs illustrate this contradiction clearly. While green roof systems can provide important ecological benefits, they are sometimes implemented superficially as

symbolic environmental gestures. Vegetation may be added without fundamentally transforming the architecture itself or its relationship to urban ecology.

This tendency creates what can be described as “green aesthetics” or environmental symbolism without deeper ecological integration. The challenge is therefore not only to make roofs technically sustainable, but also to rethink how architecture can genuinely participate in environmental and social transformation.

## 3. METHODOLOGY

This research applies a qualitative interdisciplinary methodology that combines architectural theory, phenomenological interpretation, historical-typological analysis, and contemporary case-study evaluation. The study investigates the transformation of roof architecture through three analytical dimensions: identity, programmatic activation, and tectonic articulation.

Historical examples of vernacular and urban roof typologies are compared with contemporary architectural practices in order to examine changing relationships between dwelling, ecology, and spatial infrastructure. The Nieuw Bergen project by MVRDV is selected as a representative contemporary case study because of its integration of environmental performance, urban density, roof geometry, and architectural expression.

## 4. THEORETICAL FRAMEWORK: TOWARDS A MULTIDIMENSIONAL UNDERSTANDING OF ROOFS

### 4.1. THE IDENTITY DIMENSION: ROOFS AS CULTURAL SYMBOLS

Architecture has always been closely related to place, local culture, climate, and collective identity. Cultural identity in architectural form is communicated through material tradition, geometric order, spatial organization, and relationships to landscape and climate [6]. The roof, as the most visually prominent element in the urban silhouette, functions as a primary carrier of cultural meaning.

Gottfried Semper argued that roof forms are not merely technical responses to climate, but also cultural expressions that reveal how societies understand nature, community, and everyday life. Along with the hearth, the roof stands out as one of the four basic elements of the architectural art [1].

Mediterranean flat roofs reflected openness to collective urban life and climate conditions, while steep Alpine or Balkan mountain roofs expressed adaptation to snow, weather, and family-based dwelling traditions. These roof forms emerged gradually through local building knowledge and environmental adaptation. They were not arbitrary stylistic decisions, but material expressions of culture and climate [7].

Contemporary architecture faces the challenge of preserving this cultural dimension while responding to new environmental, economic, and technological conditions. The question is not whether contemporary roofs should imitate historical forms, but how they can continue to communicate identity and belonging within present-day contexts. Projects such as Nieuw Bergen demonstrate that contemporary architecture can

integrate advanced environmental technologies while still maintaining recognizable spatial and cultural qualities.

### 4.2. THE PROGRAMMATIC DIMENSION: FROM PASSIVE PROTECTION TO ACTIVE INFRASTRUCTURE

The second dimension considers the roof as an active topological field rather than a passive protective surface. This requires moving beyond the conventional binary of habitable/inhabitable space toward understanding of the roof as a zone of multiple simultaneous programs. Venetian altanas functioned as spaces for domestic labor (vegetable gardens and herbal cultivation), drying textiles, and social gathering. Parisian mansards evolved through different social and economic uses (from servant chambres to artistic studios to luxury appartements) over time while maintaining coherent spatial identities.

These examples suggest that roofs can support overlapping and flexible forms of occupation. Rather than separating technical systems from everyday life, roofs can become spaces where ecological, social, and spatial functions intersect.

Contemporary sustainable design increasingly recognizes roofs as important ecological infrastructure. Green roofs contribute to stormwater retention, biodiversity support, temperature reduction, and urban cooling [8,9]. Solar roofs produce renewable energy, while blue roofs help manage increasing flood risks through water retention systems. The most advanced contemporary approaches integrate several functions simultaneously. Multifunctional roof systems can combine ecological performance, recreation, energy production, and social interaction within a single architectural element. Research also shows that ecologically diverse green roofs provide stronger environmental performance than simplified monoculture systems. This highlights the importance of designing roofs as living ecosystems rather than purely technical installations.

### 4.3. THE TECTONIC DIMENSION: MATERIAL AND STRUCTURAL EXPRESSION

The third dimension focuses on tectonic expression and the visible communication of structural and material logic. Tectonics concerns the way architecture reveals how it is assembled and how it resists forces.

This tectonic dimension distinguishes between stereotomy (the expression of mass and weight) and tectonics proper (the logic of how elements are assembled and forces transmitted). Contemporary roofs often prioritize invisible technical performance over visible constructional clarity. Thermal insulation, waterproofing systems, and mechanical installations dominate the design process, while the structural and material logic remains hidden [10].

Architects such as Renzo Piano, Alvar Aalto, Santiago Calatrava and Pier-Luigi Nervi demonstrate alternative possibilities by designing roofs that visibly express structural systems, light modulation, ventilation strategies, and material behavior. In these projects, the roof becomes an architectural narrative that communicates the relationship between gravity, protection, technology, and human occupation.

Parametric design methods and topology optimization further expand these possibilities. Computational systems can generate forms that simultaneously minimize material use, improve structural efficiency, optimize solar exposure, and create expressive geometries. Importantly, these forms are not arbitrary visual experiments. They emerge from measurable physical and environmental conditions, making structural and environmental performance visible through architectural form.

## 5. CASE STUDY: NIEUW BERGEN, EINDHOVEN

The Nieuw Bergen project by MVRDV in Eindhoven represents an important contemporary example of integrated roof design. In this project, the roof is not treated as a secondary technical layer, but as a primary generator of urban identity, environmental performance, and spatial organization. The development uses pitched roofs with a geometry derived partly from solar considerations. Their angular forms allow improved daylight access to surrounding buildings and public spaces while also creating a dynamic urban silhouette.

These roof forms help reduce the visual monotony often associated with dense urban development. At the same time, they establish a stronger relationship between architecture, skyline, and human perception. The roofs also function as ecological infrastructure. Large areas support vegetation that improves biodiversity, reduces urban heat, and contributes to rainwater management. Other sections incorporate photovoltaic systems for renewable energy production.



*Fig. 2 Nieuw Bergen project, panoramic views; source: https://www.mvrdv.com/projects/290/nieuw-bergen*

Rather than adding ecological systems as isolated technical layers, the project integrates environmental performance directly into the architectural composition. Roof geometry, ecological infrastructure, and urban identity become part of a unified design strategy. Nieuw Bergen demonstrates that contemporary roofs can simultaneously operate as

environmental devices, spatial generators, tectonic expressions, and carriers of urban identity.

## 6. SUSTAINABLE FUTURES: INTEGRATION OF TECHNOLOGY AND MEANING

### 6.1. GREEN INFRASTRUCTURE AND ECOSYSTEM SERVICES

Research over the past two decades has confirmed the environmental benefits of green roofs. These systems can reduce urban temperatures, retain stormwater, improve air quality, support biodiversity, and contribute to psychological well-being.

Recent studies increasingly emphasize the importance of adapting green roof systems to local ecological conditions. Roofs designed according to local plant communities and climatic conditions tend to provide stronger ecological performance than generic green surfaces [8,9]. This ecological specificity also strengthens cultural identity because locally adapted roofs reconnect urban environments with regional landscapes and environmental traditions.

### 6.2. PARAMETRIC DESIGN AND TOPOLOGICAL OPTIMIZATION

Contemporary computational design methods allow architects to optimize roof forms according to multiple performance criteria simultaneously. Topology optimization can reduce material consumption while improving structural efficiency, solar performance, ventilation, and environmental responsiveness.

The process begins by defining design constraints and performance objectives. Computational systems then generate optimized solutions that balance competing requirements. When used critically, these methods can support tectonic clarity rather than undermine it. Optimized forms can visibly express how structural forces flow through the building and how environmental conditions influence geometry. Instead of producing arbitrary formal complexity, computational design can therefore become a tool for revealing structural and environmental logic.

### 6.3. PARAMETRIC URBANISM AND THE FIFTH FAÇADE

In contemporary cities, roofs increasingly function as the “fifth façade” because they are highly visible from surrounding buildings and aerial perspectives. As urban density increases, roof design becomes central to the visual and environmental quality of the city.

Recent research examines how parametric design can optimize roof forms for multiple urban-scale performance criteria simultaneously: visual coherence with surrounding context, optimization of solar and wind conditions, facilitation of pedestrian movement and gathering, and support for ecological networks

Henri Lefebvre bases his theory of rhythmanalysis on the idea that everyday life and urban space can be understood through the analysis of the rhythms that permeate them. The city is not static; it pulses through the movement of people and the alternation of light and darkness. For Lefebvre, rhythm is not reduced merely to space and time, but arises from the interaction of space and time within the energy that is spent or accumulated [11].

This perspective expands the role of the roof beyond the individual building. Roofs become interconnected elements of larger urban ecological and spatial systems.

## 7. CHALLENGES AND CRITICAL PERSPECTIVES

### 7.1. THE RISK OF "GREENWASHING"

The growing popularity of green roofs also creates the risk of superficial environmental strategies. In some cases, vegetation is used primarily as a marketing tool rather than as part of a deeper ecological transformation. Green roofs alone cannot resolve environmental problems if broader questions related to embodied carbon, material extraction, social inequality, and urban consumption patterns remain unaddressed. Avoiding greenwashing requires an integrated understanding of sustainability in which environmental performance is inseparable from spatial quality, social inclusion, and cultural meaning. A roof that technically performs well but remains disconnected from human experience and urban life cannot be considered fully sustainable.

### 7.2. THE LIMITATIONS OF TECHNICAL OPTIMIZATION

Although computational optimization offers important possibilities, it also has limitations. Excessive dependence on numerical performance criteria can produce formally complex but spatially uncomfortable environments. A roof optimized only for energy efficiency may neglect natural ventilation, daylight quality, or human comfort. Similarly, highly complex computational forms may become difficult to construct, maintain, or socially appropriate.

For this reason, sustainable architecture requires balanced judgment rather than purely technical optimization. Quantitative analysis must remain connected to qualitative concerns related to atmosphere, spatial experience, and cultural meaning.

### 7.3. SOCIAL EQUITY AND ACCESSIBILITY

Another important issue concerns the unequal distribution of ecological infrastructure within cities. Green roofs are often concentrated in expensive private developments where they function primarily as exclusive amenities. Meanwhile, neighborhoods experiencing the greatest environmental stress frequently receive limited investment in green infrastructure. Addressing this imbalance requires policy changes and design strategies that treat roofs as collective urban resources. Public accessibility, equitable investment, and community-oriented roof programs are essential for creating socially sustainable urban environments.

## 8. DISCUSSION AND FUTURE DIRECTIONS

### 8.1. THE NEED OF MULTIDISCIPLINARY INTEGRATION

The framework proposed in this paper requires genuine collaboration between multiple disciplines. Architects, engineers, ecologists, planners, and social scientists must work together from the earliest stages of design. Ecological systems, structural systems, spatial organization, and social programs cannot be treated as separate layers added sequentially to a finished design. Instead, they must develop simultaneously through integrated design processes. Such collaboration enables roofs to operate as multifunctional systems that combine environmental performance, spatial quality, and social value.

## 8.2. POLICY INNOVATION

Architectural and technological innovation must be accompanied by supportive policy frameworks. Building regulations could encourage more diverse roof typologies by rewarding ecological performance and public accessibility. Urban planning policies could support collective roof infrastructure networks that contribute to cooling, biodiversity, and stormwater management across entire cities. Treating roofs as forms of urban infrastructure rather than isolated private surfaces may become essential for addressing contemporary environmental challenges.

## 8.3. FUTURE RESEARCH

Future research should focus on understanding how diverse roof strategies perform under actual environmental conditions in varied geographic and cultural contexts. While research on individual technologies—green roofs, blue roofs, solar roofs—is extensive, integrated research examining how diverse roof strategies function together within urban ecosystems remains limited.

Equally important is documentation of how contemporary roof design influences human experience and behavior. Psychological and sociological research could examine whether access to legible roof structures, participation in designing roof programs, or even simple visual contact with transformed roof landscapes influences psychological well-being, social cohesion, and environmental consciousness.

# 9. CONCLUSION

This paper has argued that reducing the roof to a purely technical problem requiring only instrumental and engineering-based solutions represents a major conceptual limitation within contemporary architectural thinking and practice. The roof should instead be understood as a critical architectural frontier where environmental performance, tectonic expression, cultural identity, and social life intersect.

Contemporary technologies such as green infrastructure systems, renewable energy integration, parametric design, and advanced materials provide new opportunities for redefining the role of the roof within architecture and urbanism. However, these technologies become meaningful only when they are integrated into broader architectural intentions related to human experience, ecological responsibility, cultural continuity, and spatial quality.

The future of sustainable urban architecture depends on recognizing roofs as active contributors to urban life, environmental resilience, cultural continuity, and spatial identity rather than merely passive technical barriers or neutral constructional surfaces. Roofs can generate ecological value, support social interaction, communicate structural logic, and reinforce cultural identity simultaneously.

A roof that once again expresses its construction, supports diverse forms of occupation, and contributes to environmental resilience can become far more than a technical enclosure. It can become a meaningful architectural and urban element capable of responding to some of the most urgent challenges of contemporary society.

## REFERENCES

[1] Semper, G. (1989). *The four elements of architecture and other writings*, Cambridge University Press, Cambridge, United Kingdom.

[2] Frampton, K. (1995). *Studies in tectonic culture*, MIT Press, Cambridge, Massachusetts, United States.

[3] Heidegger, M. (1975). *Poetry, language, thought*, Harper & Row, New York, New York, United States.

[4] Bachelard, G. (1961). *La poétique de l'espace*, Presses universitaires de France, Paris, France.

[5] Pallasmaa, J. (2009). *The thinking hand: Existential and embodied wisdom in architecture*, John Wiley & Sons, Chichester, United Kingdom.

[6] Starzyk, A., Cortiços, N. D., Duarte, C. C., & Łacek, P. (2025). Timber architecture for sustainable futures: A critical review of design and research challenges in the era of environmental and social transition. *Buildings*, 15(8), 2774. https://doi.org/10.3390/buildings15152774

[7] Stevanović, S. (2021). Tipološki modeli arhitektonske kolibe kroz pisanu istoriju i teoriju arhitekture. Doctoral thesis (in Serbian), University of Novi Sad, Serbia. https://nardus.mpn.gov.rs/handle/123456789/18917, accessed on 10 February 2026.

[8] Sang, Å. O., Thorpert, P., & Fransson, A. M. (2022). Planning, designing, and managing green roofs and green walls for public health – An ecosystem services approach. *Frontiers in Ecology and Evolution*, 10, 804500. https://doi.org/10.3389/fevo.2022.804500

[9] van Oorschot, J., Slootweg, M., Remme, R., Sprecher, B., & van der Voet, E. (2024). Optimizing green and gray infrastructure planning for sustainable urban development. *Communications Earth & Environment*, 5(1), 178. https://doi.org/10.21203/rs.3.rs-3896888/v1

[10] Kostić, M. S. (2021). Arhitektonski detalj u savremenoj tektoničkoj praksi: Metodološko-interpretativni model. Doctoral thesis (in Serbian), University of Beograd, Serbia. https://eteze.bg.ac.rs/application/showtheses?thesesId=8386, accessed on 10 Febrary 2026.

[11] Lefebvre, H. (1992). *Éléments de rythmanalyse*, Syllepse, Paris, France.

https://doi.org/10.24867/INDIS-2026-EN-612



# REINTERPRETING MARGINAL URBAN SPACES: FROM THE HISTORICAL TO THE SUBCULTURAL GHETTO

Vladimir Savić[1]

***Abstract:***

The traditional concept of the *ghetto* refers to urban districts that have undergone institutional segregation, initially inhabited by Jewish communities in early modern Europe, and later by the African American population in the U.S. during the 20th century. However, in contemporary socio-cultural discourse, the term extends beyond its original institutional framework. Thus, the ghetto becomes a broader spatial phenomenon associated with marginality, resistance and alternative subcultural identities. The paper analyses the transformation of the ghetto from a historically defined form of urban segregation into a symbolic space appropriated by contemporary urban subcultures. Drawing on conventional theories of the interaction between space and society, the study examines how young people appropriate marginal urban spaces such as residential blocks and infrastructural voids, transforming them into territories of subcultural identity, or micro-units referred to in the paper as the *subcultural ghetto*.

*Keywords: ghetto, subcultural ghetto, marginal space, boundaries, identity*

# REINTERPRETACIJA URBANIH PROSTORA MARGINE: OD ISTORIJSKOG DO SUPKULTURNOG GETA

***Rezime:***

Tradicionalni pojam *geto* odnosi se na gradske četvrti koje su pretrpele institucionalnu segregaciju, prvobitno naseljavane jevrejskim zajednicama u Evropi ranog novog doba, a zatim i afroameričkim žiteljima Amerike tokom 20. veka. Međutim, u savremenom društveno-kulturološkom diskursu značenje ovog pojma proširuje se izvan njegovog prvobitnog institucionalnog okvira. Tako geto postaje šire shvaćen prostorni fenomen koji biva povezan sa marginalnošću, otporom i alternativnim supkulturnim identitetima. Rad analizira transformaciju geta iz istorijski definisanog oblika urbane segregacije u simbolički prostor koji prisvajaju savremene urbane potkulture. Polazeći od konvencionalnih teorija interakcije prostora i društva, istraživanje razmatra na koji način mladi prisvajaju marginalne gradske prostore, poput stambenih blokova i infrastrukturnih praznina, pretvarajući ih u teritorije supkulturnog identiteta, odnosno mikroceline koje se u radu označavaju kao *supkulturni geto*.

*Ključne reči: geto, supkulturni geto, prostor margine, granice, identitet*

[1]PhD student and Teaching Assistant, Faculty of Technical Sciences, Novi Sad, Serbia, savicvladimir88@uns.ac.rs, ORCID 0000-0003-2195-0438

## 1. INTRODUCTION—TOWARD A SUBCULTURAL GHETTO

Understanding the reciprocal relationship between society and space represents one of the fundamental principles for interpreting urban structures. Urban sociologist Robert Park defines the city as “man’s most consistent and on the whole, his most successful attempt to remake the world he lives in more after his heart’s desire. But, if the city is the world which man created, it is the world in which he is henceforth condemned to live. Thus, indirectly, and without any clear sense of the nature of his task, in making the city man has remade himself” [1]. This claim is further elaborated by David Harvey, who argues that “the question of what kind of city we want cannot be divorced from the question of what kind of people we want to be, what kinds of social relations we seek, what relations to nature we cherish, what style of life we desire, what aesthetic values we hold. The right to the city is, therefore, far more than a right of individual or group access to the resources that the city embodies: it is a right to change and reinvent the city more after our hearts' desire” [2]. In this sense, the structure of the city can be understood as the result of the interaction between social relations, cultural practices, and space as a primary resource.

Within such a relationship between society and space, various forms of urban marginalization also emerge. One of the most recognizable manifestations of spatial segregation is the ghetto. In the contemporary globalized world, the term ghetto is often used loosely, without a substantive understanding of semantics, etymology, and the key characteristics of this urban phenomenon in practice. This is largely due to the complexity of defining the term with precision, above all as a result of its heterogeneous nature and origin. In other words, “‘ghetto’ hardly ever means one thing” [3]. In regard to the complex nature of the ghetto, Daniel Schwartz highlights that the term “depending on how it is used and who is using it, can suggest both danger and security, weakness and toughness, social pathology and communal solidarity, a prison and a fortress; a descriptive sociological concept that is hardly value free; and a keyword of both the Jewish and African American imaginaries—the ghetto, historically, has been all of the above” [4].

In the contemporary social and cultural context, the term has come to denote a broader, symbolic urban phenomenon. This transformation is noted by French sociologist Loïc Wacquant, who argues that in contemporary social and media discourse, the term ghetto is increasingly used as a metaphor for urban marginality, thus expanding and transposing its traditional historical and institutional meaning into new cultural contexts [5]. Through popular culture, music, film, and the media, the term ghetto is recognized within urban subcultures, where it is used to denote specific forms of space, identity, and belonging. In other words, marginal spaces in the contemporary city are not only institutional in character, as was the case with the historical ghetto, but are also recognized and articulated within broader social processes in which subcultures play a significant role.

As emphasized by media theorist and sociologist Dick Hebdige, subcultures can be understood as forms of symbolic resistance that, through style, space, and everyday practices, reshape the meaning of the urban environment [6]. Similarly, ethnographer Sarah Thornton, in her analysis of youth in the United Kingdom, notes that subcultural groups often gather around specific urban places such as clubs, pubs, streets or neighborhoods, which function as nodes of subcultural capital and social exchange [7]. Such territories represent places where young people gather, socialize, play, create, perform their rituals and, in a predominantly symbolic way, resolve their problems [8]. In this context, contemporary subcultural discourse increasingly employs the term ghetto as a metaphor for symbolically enclosed urban micro-environments. In this

context, the contemporary subcultural narrative increasingly uses the term ghetto as a metaphor for symbolically enclosed urban micro-environments.
In this paper, the key aspects of the ghetto as a constituent of urban structure will be analytically outlined within a traditional historical discourse, alongside related forms of spatial segregation in urban environments. The paper then addresses the contemporary social trend in which youth subcultures appropriate and articulate marginalized fragments of urban structure, transforming them into symbolically enclosed units—*subcultural ghettos*.

## 2. RESEARCH METHODOLOGY

The research is based on a qualitative and interpretative approach, aimed at analysing the transformation of the concept of the ghetto from a historically and institutionally defined form of urban segregation, into a contemporary symbolic and subcultural phenomenon. The methodological framework of the paper is based on the analysis of relevant historical, sociological, urban planning, and architectural-theoretical literature, as well as on a comparative and conceptual interpretation of the relationship between space, society, marginalisation, and collective identity.
The first phase of the research examines theoretical approaches to the relationship between society and urban space, with particular emphasis on space as a product of social relations, as well as on the processes of its social, cultural, and symbolic production. This theoretical framework provides the basis for further examination of marginal spaces and processes of urban marginalisation.
The second phase consists of a historical-comparative analysis of the phenomenon of the ghetto. Its characteristic forms and socio-spatial functions are examined across different historical and geographical contexts, with particular attention given to Jewish ghettos in Europe, Nazi ghettos, and African American ghettos in the United States. At the same time, examples of other forms of spatial segregation, including French *banlieues* and Brazilian favelas, are considered in order to establish the limits of applicability of the concept of the ghetto and to identify its specific characteristics.
The third phase of the research focuses on analysing the transformation of the meaning of the term ghetto within contemporary social and cultural discourse. Particular attention is given to the influence of popular culture, the media, and urban subcultures on the dissemination and reinterpretation of the concept, whereby the historical and institutional character of the ghetto is examined in relation to contemporary forms of symbolic and informal spatial marginalisation.
In the final phase, the results of the preceding analyses are synthesised through the identification of common spatial, social, and symbolic characteristics of the historical ghetto and contemporary subcultural marginal spaces. Based on this comparative analysis, the concept of the *subcultural ghetto* is proposed as an analytical category for describing specific micro-territories that emerge through processes of informal spatial appropriation, territorialisation, visual marking, the formation of collective identity, and the establishment of a distinctive function of place.
The aim of this methodological approach is not to equate subcultural spaces with the historical ghetto, but rather to examine their structural and functional similarities, as well as their key differences. In this way, the concept of the subcultural ghetto represents the result of a theoretical synthesis of the previously analysed phenomena, rather than a direct transposition of the historical model of the ghetto onto contemporary urban spaces.

## 3. THE CITY AS A RESULT OF SOCIAL RELATIONS

The introduction pointed to the specific nature of the city, which is not merely a material structure, but is defined by complex processes of interaction between society and space. The physical structure of the city is an expression of the totality of its social community over time, comprising a broad spectrum of different forms of urban life, including economic and social relations, tradition, politics, technology, and natural factors [9]. In other words, the urban structure of the city should be understood as a dynamic system within which the community, through its actions, produces, uses, and symbolically marks space as its habitat.

One of the first to develop an understanding of the city as an institutionalized form of social relations was urban sociologist Robert Park, who argued that the city is a psychophysical mechanism in which private and political interests find their collective expression, that is, that the city is a developmental process and the product of the lives and actions of successive generations of people within it [10]. This suggests that urban space is not exclusively a physical structure, but a living environment within which specific collective relations are formed. Park further argues that human habits and customs constitute the moral and physical organization of the city, each acting upon and shaping the other [10]. Spatial structure is, therefore, closely linked to the social relations that develop within it, just as those relations shape the city's spatial development. These relations are further elaborated by sociologist and, among other things, one of the first critics of everyday life, Henri Lefebvre, who understands space as an active product of social relations. Moreover, for Lefebvre, space is the foundation of social relations, arguing that they have no real existence except in and through space [11]. Urban space can therefore be understood as a construct of the political, economic, and cultural patterns that unfold within it. In defining a relational understanding of space, Professor Martina Löw emphasizes that space emerges as a relational arrangement of social, i.e., material goods and people in a given place, where place may be viewed as both as the result of social activities and as the framework within which these activities unfold [12]. The positions of Park, Lefebvre, and Löw indicate a shared perspective, according to which the space of the city is not a passive instance, but the result of dynamic social relations within economic, political, and cultural frameworks, which manifest themselves in concrete spatial structures.

Analyzing the process of urbanization in the context of capitalist society, David Harvey notes that urban space can be understood through the dynamics of capital accumulation and class relations that affect the spatial organization of the city [13]. The city is not therefore a homogeneous structure, but rather a complex network of diverse macro and micro territories that reflect the economic, cultural, and social differences among its population. As Harvey emphasizes, the capitalist urban process entails the formation of different elements of the built environment that serve the specific functions of production, circulation, and consumption, leading to the spatial differentiation of urban structures [13]. A consequence of this practice is reflected in the development of different forms of inequality among the population. It is precisely within these processes that marginal urban spaces emerge—parts of the city situated at the periphery of social and economic flows, among which the ghetto stands out as the most recognizable typology of urban segregation. In observing contemporary forms of this phenomenon, Wacquant identifies a trend of "advanced marginality, i.e., the novel regime of sociospaial relegation and exclusionary closure" [5], arising as a result of economic and political forces that further marginalize the space and inhabitants of the ghetto (and similar typologies). These marginalized spaces are typically characterized by a concentration of poverty, institutional isolation, and social stigmatization. By contrast, Sharon Zukin views culture as a powerful means of controlling cities, one that

symbolizes social and spatial belonging [14]. The introduction of symbolic narratives into urban space, including marginal spaces, is therefore crucial to processes of their formation and reinterpretation, as they enable different social groups to articulate their presence in the city. In this way, marginal spaces become conducive to the development of new cultural practices and forms of collective identity.

The complex relations between society and space, as broadly outlined above, constitute the starting point for understanding the topic of marginal spaces, including the phenomenon of the ghetto. The following section presents the historical genesis of this urban typology as one of the most dramatic and representative examples of marginalization and segregation, whose meaning has been redefined and expanded over time, particularly in the contemporary world.

## 4. THE ORIGIN AND HISTORICAL SIGNIFICANCE OF THE GHETTO

The emergence and development of the ghetto is a five-century-long, complex process that is difficult to consider in its entirety, particularly given that it evolved simultaneously across two continents, in different historical periods and social contexts. However, examining the history of this phenomenon is essential for understanding its contemporary reinterpretation and transformation.

In 1516, the government of the Republic of Venice ordered that Venetian Jews be confined to a small island at the northern edge of the city called Ghetto Nuovo (New Ghetto), which was known for its copper foundries. The verb gettare means to cast (referring precisely to the casting of metal). Thus, the word ghetto was already in use before the settlement of Jews on this island and did not originally refer to compulsory, enclosed, and segregated Jewish quarters [3]. The Venetian ghetto represents an early example of racial segregation in urban space [3], and similar measures were subsequently adopted in other Italian cities. Particularly significant was the ghetto in Rome. In 1555, Pope Paul IV issued a decree stipulating that all Jews were required to reside in an enclosed area with one entrance and one exit [4]. While the ghetto in Venice represented a compromise between Christian religious ideals and the practical (economic) interests of the Venetian government, the one in Rome sought to impose physical and economic restrictions on the Jewish population, something that had not previously been recorded. In other words, the papal ghetto was considered a form of punishment for the Jewish population [4]. From a spatial perspective, two types of Italian ghetto can be distinguished. The first, more commonly applied approach involved transforming existing Jewish quarters by adding walls and gates, while the second entailed relocating Jews to a new, enclosed area, most often at the periphery of the city [4].

At the end of the eighteenth century, Napoleon abolished the ghetto, civil rights were granted to Jews and other minorities, and the gates of Italian ghettos were removed and symbolically burned, marking the beginning of the modern era [3].

During this period, the ghetto no longer had an institutional function. Instead, it was romanticized, particularly in the works of Jewish writers, journalists, and activists of the time, who wrote about the lives of their ancestors in the ghetto [15]. Historian Salo Baron notes that, despite their hardships and spatial confinement, the Jewish community in fact continued to develop in isolation [16]. However, in early modern Europe, antisemitism intensified, compelling Jews from Poland, Czechia, France, Germany, and especially Imperial Russia (from 1881 to 1884 and again from 1903 to 1906) to emigrate, first to England and then to the United States [15]. From that point onward, the phenomenon of the ghetto developed simultaneously, yet entirely separately, in Europe and in America.

The European ghetto was revived in the twentieth century by Nazi Germany; it retained its basic utilitarian function as a space of segregation, marginalization, and stigmatization of the Jewish population, but in an entirely different form. The question of the establishment of ghettos as an urban spatial typology for the segregation of Jews was revised only after the invasion of Poland, when, in successive waves between 1939 and 1944, more than a thousand ghettos were created, the largest of which were in Łódź and Warsaw [4]. The concept of the ghetto in Nazi Germany developed and changed over time, but sociologist Mitchell Duneier underscores five characteristics that distinguish it from the medieval ghetto: "First, the Nazi ghetto illustrated that it was now possible to control a segregated population with absolute efficiency. These ghettos' walls or other boundaries were put in place virtually overnight rather than over several years, as had been the case in Rome (...) Second, this efficiency made it possible for the Nazi ghettos to introduce as complete a segregation as the world had ever seen. While the earlier ghettos had allowed relatively easy passage of people and merchandise during the daytime, many of the Nazi ghettos fenced in their inhabitants day and night. (...) Third, in earlier centuries religion had justified the segregation of Jews. A defining component of Nazi ghetto logic was, by contrast, race. (...) Fourth, (...) Both qualified German physicians and ideological Nazis claimed that the Jews were carriers of disease who required quarantine. (...) The purported probability that they would spread the illness was an important reason to have them ghettoized. (...) Fifth, the Nazi ghettos were sites of continuous violence and brutality. Residents were forced to watch their fellow citizens die in mass executions..." In addition to shaping the future identity of the Jewish people, the symbol of the Nazi ghetto, particularly the Warsaw ghetto, would exert a strong influence on the one that was simultaneously emerging in America. "For many blacks after World War II, the Nazi ghetto provided a powerful metaphor for their own experience." [17].

Jewish emigration brought the term ghetto to America. However, it is not possible to determine with certainty when emerging non-white enclaves began to be referred to as ghettos [17]. The term existed only as an idea and a metaphor. Since the beginning of the twentieth century, the ghetto as an urban, social, and political phenomenon has become increasingly associated with African Americans in the United States—a connection that persists to this day. In other words, "the only long-standing ghetto in the United States is the 'Negro' or 'black' or 'African-American' ghetto (depending on the era)" [3]. African American populations settled in the central areas of major metropolitan cities, most notably in Chicago and New York City. A key factor in the development of the black ghetto was state-led housing investment in central ghettoized neighborhoods. The aim of this process was to prevent the black population from settling in white neighborhoods at the peripheries of large cities [18]. Douglas Massey and Nancy Denton identify five spatial and social measures that characterize racial segregation in the USA.

Unevenness: African Americans may be distributed so that they are overrepresented in some areas and underrepresented in other areas.

Isolation: African Americans may be distributed so that they have little interaction with other groups.

Clustered: Black neighborhoods may be tightly clustered to form one contiguous enclave, or they may be scattered about in checkerboard fashion.

Concentrated: Black neighborhoods may be concentrated within a very small area, or they may be settled sparsely throughout the urban environment.

Centralized: Black neighborhoods may be spatially centralized around the urban core or spread out along the periphery [19].

Therefore, the ghetto as a defined and enclosed territory became a key component of the structure of American metropolises, as well as of African American identity.

In the 1990s, conditions changed dramatically, transforming the image of the ghetto as African Americans were legally permitted to purchase property outside central urban areas. This led to the outflow of precisely the social stratum that had sustained the ghetto's institutional structure. As a result, many buildings were left vacant and a surplus of available space emerged, opening the way for the gentrification of the ghetto,[1] which drastically altered the demographic as well as spatial and structural characteristics of the historical ghetto in the USA [19].

## 4.1. THE DIFFERENCE BETWEEN THE GHETTO AND OTHER FORMS OF SEGREGATION

The historical overview of the development of the ghetto as an urban typology reveals the heterogeneous nature of its manifestations, meanings, and perceptions, both among its inhabitants and among those observing it from the outside. This layered complexity, together with a general indeterminacy arising from numerous (primarily subjective) interpretations, makes the phenomenon difficult to precisely define. Today, there is a widespread tendency, both in colloquial usage and in academic discourse, to use the term *ghetto* to identify other forms of spatial segregation. Researchers in the social sciences have further complicated the use of the term by employing it as a universal synonym for poverty, segregation, and social organization, both in African American communities and in minority communities worldwide [16]. In many of his works, Loïc Wacquant addresses the question of properly articulating the ghetto as a socio-spatial mechanism of ethnic/racial enclosure, highlighting the structural and functional differences between ghettos and ethnic neighborhoods [20]. He notes three arguments in support of distinguishing the ghetto from other forms of urban segregation: "1. Poverty is a derivative and variable characteristic of ghettos. (...) 2. All ghettos are segregated, but not all segregated areas are ghettos. (...) 3. Ghettos and ethnic neighborhoods sport divergent structures and serve opposite functions" [20].

Parisian suburbs, known as *banlieues* (densely populated areas with significant immigrant populations and serious socio-economic difficulties), are often equated with the ghetto (particularly the American ghetto). Didier Lapeyronnie notes that the term ghetto belongs to the everyday vocabulary of the *banlieue* [lower-class periphery], where it is used to denote adverse social or personal situations, including psychological states marked by chaos, poverty, or violence, without necessarily implying urban segregation or territorial enclosure [21]. Wacquant criticizes this claim by Lapeyronnie, arguing that he did not analyze the overlap between these phenomena in his study, and instead "uses the word *ghetto* as a loose synonym for declining lower-class estates branded as such by journalists and by some of their residents (who themselves have learned the label from the media). The notion then inexplicably devolves into a subjective concept pertaining to lifestyle, self-conception, and 'the shared feeling of having been betrayed' by dominant institutions" [20]. That the ghetto as a form of spatial segregation does not align with French institutional principles is also indicated by the fact that official policymakers, "terrified about the possible development of ghettos and immigrant enclaves, are quick to deny any similarity with places in French territory and quick to attack any ethnic mobilizations in the *banlieues*" [21]. In his study of ghettos and anti-ghettos, Loïc Wacquant notes five characteristics that an urban district must meet in order to become a ghetto, which the *banlieues* in France do not meet: "(1) growing ethnic homogeneity, (2) increased encompassment of the target population, (3) rising organizational density, (4) the production and adoption of a collective identity, and (5) impermeable boundaries" [22].

[1] The gentrification of the ghetto is a specific and distinct urban process that will not be examined in detail in this paper.

Sociologist Ernesto Castañeda argues that the concept of the *ghetto* cannot be applied in France because it has no historical equivalent to the African American population in the United States, further noting that the term ghetto may generate more polemical misunderstandings than it offers clear explanations. Instead, Castañeda proposes the use of the term *places of stigma*, "to designate the different spaces that result from the same categorical processes of creation and reproduction of social inequality (stigmatization, constraint, confinement, marginalization, underemployment) that become inscribed in flesh and stone" [23].

By contrast, favelas in Brazil are also urban settlements frequently associated with the ghetto, but often inaccurately so. "The assumption that one can apply what has been learned from studies of the U.S. ghetto to social and historical contexts as different as the megaslums of Mumbai and Nairobi or the favelas of Rio has turned out to be fraught with unexamined complexities" [17]. Bruce D. Haynes and Ray Hutchison observe that, in general, favelas "arose as a marginal space where economically and socially excluded individuals were collected because of the rapid migration from rural areas during the period of industrial growth. The ethnic composition of favelas has always diversified, and segregation has its roots in economic marginality" [16]. American scholar Alan Gilbert identifies as many as seven reasons why the concept of the *ghetto* is not applicable to Latin America, among which the most significant are the following: from an ethnic perspective, there are relatively few Jewish communities in Latin America, while a large proportion of the population is of African descent; spatial segregation is less pronounced, as Latin American settlements are more heterogeneous than those in the USA; leaving the favela and relocation to another area is possible, unlike the American ghetto; and the urban poor constitute the majority of the population in Latin American cities [24].

Upon considering these two examples, it becomes clear that the term *ghetto* must be used with caution, whether as an epithet or as a spatial designation. Although its exact attributes are difficult to define—aside from its exclusive historical association with the fates of Jewish and African American populations—it is important to emphasize the responsibility involved in using this term when categorizing forms of spatial segregation within an urban structure.

## 4.2. THE GHETTO AS A CULTURAL METAPHOR

Presenting the development of the historical ghetto and its equivalents is important for highlighting the traditional understanding of this urban typology, that is, its fundamental spatial and social characteristics. However, mass media, particularly the film industry and popular music, have played a key role in the reinterpretation of the term ghetto into a more broadly understood socio-spatial phenomenon. The glorification of life in the ghetto in Hollywood films, particularly with the rise of hip-hop culture since the 1970s, has further contributed to the globalization of the term. Today, the ghetto no longer refers exclusively to urban districts for the institutional segregation of Jews and African Americans, but also to a wide range of other universally understood and symbolically characterized marginal spaces [3, 4, 25].

In this way, the term ghetto becomes part of a global cultural vocabulary, finding application in diverse urban contexts worldwide. Stuart Hall, in his studies on the production and circulation of meaning through language, notes that the meaning of a term is variable, depending on context, use, and historical conditions. In other words, it is never fixed, but rather contingent and subject to modification and adaptation to new situations [26]. Similarly, through his concept of mediascapes, anthropologist Arjun Appadurai notes that electronic media enable the rapid transnational circulation of terms, transforming local meanings into global ones that are often metaphorical, chimerical, and aestheticized [27]. If these two discourses are applied to the context of

the ghetto, which was originally closely linked to the cultural frameworks of Jewish and African American communities but later became part of a global cultural phenomenon (most notably hip-hop culture), its meaning is altered, modified, and subject to multiple interpretations depending on context. In other words, the ghetto becomes a flexible symbol within global cultural currents.

It is precisely these global cultural processes that have led to the term ghetto being applied to a range of marginal spaces within urban structures. These spaces are often occupied by members of different subcultures, who identify with the inhabitants of the historical ghetto on a metaphorical level. In this way, specific spatial formations of belonging and identity emerge, which will be examined in detail in the following sections of the paper.

## 5. SUBCULTURES AND THE APPROPRIATION OF MARGINAL URBAN SPACES

The appropriation of marginal urban spaces by subcultural groups can be understood as an informal, symbolic, often illegal, and at times guerrilla practice. Young people frequently detect and appropriate spaces that are meaningful to them, but are often neglected and excluded from dominant political, economic, and cultural currents. As already noted in this paper, there is a certain dichotomy in the relationship between space and social processes, in that space represents both an active resource of production and an active stage for the manifestation of complex social relations. Subcultures, therefore, not only use space but also transform it through their active presence and participation in its existence.

However, the fundamental precondition for the formation of subcultural territories is the existence of marginal spaces. Architect Aleksandra Pešterac introduces the concept of *desolate space*, referring to spaces that, as a result of both intentional and unintentional external factors, have undergone various forms of degradation and are therefore perceived as insignificant parts of the urban context, whose potential is largely overlooked [28]. Architect and theorist Ignasi de Solà-Morales notes that the contemporary city abounds in vacant spaces, such as abandoned industrial zones, railway stations or residential areas, excluded from the urban system and everyday use, which he defines as *terrain vague*. He further argues that architects are unable to engage with these spaces other than through acts of violent transformation, the introduction of boundaries, order, and form, whereas their essential nature lies in their capacity to provide refuge for diverse social groups, “precisely when the city offers them an abusive identity, a crushing homogeneity, a freedom under control” [29]. Regarding liberation from imposed frameworks and platforms, Rem Koolhaas, in his study of the *Generic City*, argues that the periphery must free itself from the identity imposed on it by the dominant center, making urban space more flexible and open to diverse forms of use [30]. This flexibility is crucial, as it enables the appropriation and reinterpretation of marginal spaces.

The way in which subcultures carry out this process should be considered through the combined operation of the following mechanisms:[1]

**Informal appropriation of space (place-making)**. Members of subcultures identify abandoned spaces and physically occupy them, transforming them into places of gathering, dwelling, and action. The process of informal appropriation aims to transform neglected and underused spaces into places, becoming centers of social interaction, cultural expression, and cohesion for the (subcultural) community [31]. These initiatives reflect a fundamental human need to foster a sense of belonging to and

[1] These mechanisms require further elaboration and presentation. This paper outlines the main ideas and principles.

ownership of space [29]. In other words, place emerges when individuals enter into a dialogue with space—when the interaction between the internal world of living beings and the influence of the environment generates new codes, meanings, and values in the relationship between people and space [32]. In this way, abandoned hangars become rave clubs or gallery spaces for graffiti artists; old residential buildings become squats, while unused fragments of housing blocks are transformed into gathering places for local youth.

**Establishing spatial boundaries (territorialization)**. Subcultures are typically closed communities. Their spaces may be physically open, but they are socially selective. Territorial belonging, understood as ownership over a particular space, is highly significant in the subcultural world, as subcultural groups tend neither to claim others' territory nor to welcome members of different groups [8]. This approach to spatial belonging is not exclusive to delinquent subcultures, such as football supporters, but is also characteristic of peaceful groups, such as ravers. Access to parties is often denied to those outside the rave community, due to the need for isolation and distancing from others [7].

**Marking of space**. Marking represents the final stage of the physical appropriation of marginal space. Dick Hebdige highlights that subcultural style communicates through signs, symbols, and codes with subversive meanings, challenging traditional interpretations and principles [6]. Graffiti, murals, and other forms of visual coding of space serve as territorial markers. They are a form of conscious and intentional form of action in public space, that is, a non-institutional and informal mode of communication among individuals and groups, both internally and with the wider social environment [33].

**Establishing the function of place**. Ranko Radović argues that the city expresses life [9]. Following the same analogy, it may be said that the micro-units of the urban fabric, as the primary topic of this paper, should express the attributes of subcultural life. In other words, the primary function of subcultural spaces is to establish a relationship with these attributes and to correspond with them. One of the main characteristics underlying the existence of subcultures is ideology. Regarding the ideological function of space, Radivoje Dinulović highlights that it reflects (at least in its potential): a refusal to consciously participate in a world that offers no sense of trust, a resistance to adaptation and compliance with various centers of power, and an active subversion of constructed and imposed systems of values [34]. In addition to their ideological function, these spaces also fulfill utilitarian, ambiental, demarcational, ethical, narrative, political, progressive, scenic, symbolic, and other functions.

Through the informal establishment of ownership, *terrain vague*, urban clusters, abandoned and forgotten spaces are transformed into active places of subcultural life. In this way, the positions of Robert Park and David Harvey regarding the inseparable relationship between urban space and humankind, in which each entity transforms the other, are affirmed.

## 6. THE CONCEPT OF THE SUBCULTURAL GHETTO

After outlining the primary characteristics of the historical ghetto and subcultural micro-units, it is necessary to establish a link between these two urban phenomena in order to formulate the concept of the *subcultural ghetto*. Despite the fact that the historical ghetto and subcultural marginal spaces emerged in different periods and under different socio-political conditions, a number of structural and functional parallels can nevertheless be drawn between them. It is precisely this shared interstitial space that provides the platform for conceptualizing the *subcultural ghetto* as a specific urban typology, which, unlike the historical ghetto, is not based on institutional isolation and

stigmatization, but on symbolic and cultural self-segregation and self-isolation, treating space as a socially produced category [12, 13].

As previously noted, the historical ghetto represents an administrative instrument of ethnic and racial segregation, characterized by clearly (forcibly) established physical boundaries, a high degree of social isolation, as well as the strongly developed collective identity of its inhabitants [3, 4, 20]. By contrast, subcultural spaces emerge as the result of informal, non-institutional appropriation of marginal spaces, characterized by the symbolic establishment of territorial boundaries, specific forms of visual demarcation, and social coherence grounded in shared ideological affiliation, corresponding to Hebdige's understanding of subcultural style as a driver of social resistance [6]. Although the *subcultural ghetto* does not meet the criteria of ethnic and racial coercion or institutional segregation, it metaphorically reproduces certain mechanisms of enclosure and exclusion, limiting access to those who do not belong to the subculture. In other words, unlike the historical ghetto, where enclosure was imposed externally through coercion, the boundaries of the *subcultural ghetto* are produced internally. Regarding permanence, the historical ghetto was a structurally defined, stable, and enduring space. This led to the development of a specific form of community life over time, closely linked to the formation of an autochthonous collective identity and culture. By contrast, the *subcultural ghetto* is often ephemeral, fluid, and subject to transformation. Such changes may arise through processes of urbanization (such as gentrification) or shifts within the subculture itself. However, as previously discussed, the function of these spaces lies in the articulation of identity, alternative social relations, and modes of life different from those outside their boundaries. This characteristic of the *subcultural ghetto* is another important metaphorical reflection of the historical ghetto.

Finally, the *subcultural ghetto* may be understood as a spatial micro-territory within the urban fabric, characterized by: (1) the appropriation and transformation of space into place; (2) the establishment of symbolic, territorial boundaries; (3) the use of distinctive visual codes and signs; (4) a strong collective identity closed to the outside world; (5) ideological affiliation.

The conception of a contemporary typology of marginal space provides an opportunity to reposition the concept of the ghetto outside of its institutional and historical framework, without degrading or negating its traditional meaning. Rather than relying on the problematic colloquial use of the term arising from its media-driven dissemination, this paper introduces a more analytically precise formulation that retains the main attributes of the historical ghetto: boundary, cohesion, and identity, recognized in contemporary forms of urban spatiality. In this way, the concept of the *subcultural ghetto* becomes a useful tool for understanding and identifying the mechanisms through which subcultures (and youth in general) establish their own spaces within the existing structure of the city.

## 7. CONCLUSION

The concept of the *subcultural ghetto* is positioned in this paper as a platform for further, more detailed, and more comprehensive research through which its key aspects and manifestations may be identified. The significance of defining this phenomenon lies in its potential to expand both the practical and theoretical frameworks of architecture and urbanism, which have traditionally relied on formal and institutionally regulated aspects of the spatial planning of cities. In this way, informal, ephemeral, and subcultural practices are either neglected or treated as anomalies that should be eliminated. However, the *subcultural ghetto*, if recognized as a legitimate urban typology, has the potential to demonstrate the validity of these specific spatial micro-

units, which emerge as products of the everyday practices of a social group, rather than of planned interventions. This concept therefore enables architects and urban planners to reconsider the dominant (institutional) models of spatial analysis, planning, and treatment, and instead to consider and apply more flexible and inclusive approaches to theory and practice. In light of Solà-Morales's observation regarding the inability of architects to fully grasp all the potentials of *terrain vague*, the concept of the *subcultural ghetto* would facilitate the identification and use of such spaces primarily as key resources for the development of alternative cultural practices. Finally, the *subcultural ghetto* functions not only as an analytical category, but also as a critical tool that allows for the possibility of redefining the relationship between the planned and the unplanned, the permanent and the ephemeral, the formal and the informal, the institutional and the non-institutional in contemporary cities.

## REFERENCES

[1] Park, R. (1967). On Social Control and Collective Behavior, Chicago University Press, Chicago, United States of America.

[2] Harvey, D. (2012). Rebel cities : from the right to the city to the urban revolution, Verso, London, Great Britain.

[3] Cheyettem, B. (2020). The Ghetto: A Very Short Introduction, Oxford University Press, Oxford, Great Britain.

[4] Schwartz, D. (2019). Ghetto: The History of a Word, Harvard University Press, Cambridge, Massachusetts.

[5] Wacquant, L. (2008). Urban Outcasts: A Comparative Sociology of Advanced Marginality, Polity Press, Cambridge, Massachusetts.

[6] Hebdige, D. (1979). Subculture: The Meaning of Style, Routledge, London, Great Britain.

[7] Thornton, S. (1995). Club Cultures: Music, Media and Subcultural Capital, Polity Press, Cambridge, Massachusetts.

[8] Božović, N. (2012). Potkulturni bumerang: između tolerancije i nasilja, Obrazovanje i savremeni univerzitet, ur. Dimitrijević, B., Filozofski fakultet, Niš, Srbija, str. 579–594.

[9] Radović, R. (2009). Forma grada: osnove, teorija i praksa, Građevinska knjiga, Beograd, Srbija.

[10] Park, R. (1915). The City: Suggestions for the Investigation of Human Behavior in the City Environment, American Journal of Sociology, Chicago University Press, Chicago, United States of America, Volume 20, No. 5, March, pp. 577–612.

[11] Lefebvre, H. (1991). The Production of Space. Basil Blackwell Ltd, Oxford, Great Britain.

[12] Löw, M. (2016). The Sociology of Space: Materiality, Social Structures, and Action. Palgrave Macmillan, New York, United States of America.

[13] Harvey, D. (1985). The Urbanization of Capital, Basil Blackwell Ltd, Oxford, Great Britain.

[14] Zukin, S. (1995). The Cultures of Cities, Basil Blackwell Ltd, Oxford, Great Britain.

[15] Hutchison, R., Haynes, B. (2010).Introduction, The ghetto : contemporary global issues and controversies. Ed. Ray Hutchison, Bruce D. Haynes, Westview Press, Boulder, Colorado, pp. VII–XXXVIII.

[16] Salo, B. (1928). Ghetto and Emancipation: Shall We Revise the Traditional View?, Menorah Journal, Volume 14, No. 6, New York, pp. 515–524.

[17] Duneier, M. (2016). Ghetto: the invention of a place, the history of an idea, Farrar, Straus and Giroux, New York, United States of America.

[18] Gottdiener, M., Hutchison, R. (2010). The new urban sociology, Westview Press, Boulder, Colorado.

[19] Douglas, M., Denton, N. (1993). Urban Apartheid: Segregation and the Making of the Underclass. Harvard University Press Cambridge, Massachusetts.

[20] Wacquant, L. (2010). A Janus-Faced Institution of Ethnoracial Closure: A Sociological Specification of the Ghetto, The ghetto : contemporary global issues and controversies. Ed. Ray Hutchison, Bruce D. Haynes, Westview Press, Boulder, Colorado, pp. 1–33.

[21] Lapeyronnie, D. (2007). Ghetto urbain. Ségrégation, violence, pauvreté en France aujourd'hui, Robert Laffont, Paris, France.

[22] Wacquant, L. (2008). Ghettos and Anti-Ghettos: An Anatomy of the New Urban Poverty, Thesis Eleven, Volume 94, No. 1, August, pp. 113–118. DOI: 10.1177/0725513608093280

[23] Castañeda, E. (2010). Places of Stigma: Ghettos, Barrios, and Banlieues, The ghetto : contemporary global issues and controversies. Ed. Ray Hutchison, Bruce D. Haynes, Westview Press, Boulder, Colorado, pp. 159–190.

[24] Gilbert, A. (2010). On the Absence of Ghettos in Latin American Cities, The ghetto : contemporary global issues and controversies. Ed. Ray Hutchison, Bruce D. Haynes, Westview Press, Boulder, Colorado, pp.197–224.

[25] Rose, T. (1994). Black Noise: Rap Music and Black Culture in Contemporary America. Wesleyan University Press, Hanover, Germany.

[26] Hall, S. (1997). Representation: Cultural Representations and Signifying Practices. Sage, London, Great Britain.

[27] Appadurai, A. (1996). Modernity at Large: Cultural Dimensions of Globalization. University of Minnesota Press, Minneapolis, Minnesota.

[28] Pešterac, A., Dimitrovska, D., Stojšić, M. (2014). The Aestetics of Disolate Spaces, Places and Technologies, Arhitektonski fakultet, Beograd, Srbija,str. 565–569.

[29] Solà-Morales, I. de. (1995). Terrain vague. In Cynthia Davidson, Anyplace, MIT Press, Cambridge, Massachusetts, pp. 118–123.

[30] Koolhaas, R., Mau, B. (1995). S, M, L, XL, Monacelli Press, New York, United States of America.

[31] Erek, A., Krasznahorkai, K. (2024). Informal placemaking: social activism and practices of art and culture, Journal of Urbanism: International Research on Placemaking and Urban Sustainability, Volume 17, pp. 165–168 https://doi.org/10.1080/17549175.2024.2354284

[32] Pešterac, A. (2017). Transformacija prostora u mesto: stalnosti i promene poetičkog dejstva mesta, Doktorska disertacija, Fakultet tehničkih nauka, Novi Sad, Srbija.

[33] Lalić, D., Leburić, A., Bulat, N. (1991). Najsmo luđi. Grafiti i subkultura. Alinea, Zagreb, Hrvatska.

[34] Dinulović, R. (2012). Ideološka funkcija arhitekture u društvu spektakla, Međunarodna konferencija Arhitektura i ideologija, ULUPUDS, Beograd, Srbija.

https://doi.org/10.24867/INDIS-2026-EN-625



# TENNIS COURT AS A TYPOLOGY IN SCENE ARCHITECTURE – SPATIAL TRANSFORMATIONS IN THE CULTURAL AND SOCIAL CONTEXT OF THE 18TH CENTURY

*Darko Sekulić*[1]

***Summary:***

*Building on Professor R. Dinulović's understanding of architecture as constituted by multiple functions, this paper examines the tennis court as a historical spatial type relevant to the genealogy of theatre space. It compares documented uses and transformations of tennis courts with later stage-auditorium configurations, focusing on the elongated plan, perimeter galleries, adaptable central field, and spectators positioned on opposing sides. Historical sources confirm that tennis courts were adapted for theatrical and other collective events. The proposed relationship to the two-sided transversal stage is therefore treated as a typological interpretation based on spatial similarities and continuity, not as a proven direct derivation. The paper asks whether tennis-court morphology can be considered one of several spatial precedents that contributed to ideas about theatre space in the seventeenth and eighteenth centuries.*

*Keywords: cultural function, scene architecture, tennis court theatre, typology, theatre, transversal stage*

# TENISKA DVORANA KAO TIPOLOGIJA SCENSKE ARHITEKTURE – PROSTORNE TRANSFORMACIJE U KULTURNOM I DRUŠTVENOM KONTEKSTU XVIII VEKA

***Rezime:***

Oslanjajući se na istraživanje profesora R. Dinulovića, prema kome arhitekturu čini skup funkcija koje je konstituišu, rad razmatra tenisku dvoranu kao istorijski prostorni tip relevantan za genealogiju pozorišnog prostora. Porede se dokumentovani načini upotrebe i transformacije teniskih dvorana sa kasnijim scensko-gledališnim konfiguracijama, uz fokus na izduženu osnovu, obodne galerije, prilagodljivo centralno polje i publiku raspoređenu na suprotnim stranama. Istorijski izvori potvrđuju da su teniske dvorane prilagođavane za pozorišne i druge kolektivne događaje. Veza sa dvostrano orijentisanom transferzalnom pozornicom zato se razmatra kao tipološka interpretacija zasnovana na prostornim sličnostima i kontinuitetu, a ne kao dokazana direktna geneza. Rad ispituje da li se morfologija teniske dvorane može posmatrati kao jedan od prostornih presedana koji su doprineli razvoju ideja o pozorišnom prostoru u XVII i XVIII veku.

*Ključne reči: kulturalna funkcija, scenska arhitektura, teniska dvorana, tipologija, pozorište, transferzalna pozornica*

[1]Teaching Associate, Sub-department for Art and Design, Department for Architecture and Urban Planning, Faculty of Technical Scicences, University of Novi Sad, darkosekulic@uns.ac.rs, ORCID id. No.: https://orcid.org/0009-0002-1750-2085

## 1. INTRODUCTION

Connections between sport, ritual, spectacle and performance can be traced through different historical periods. Ancient festivals such as the Olympic and Dionysian games provide a broad cultural background (Young, 2004; Crane, 2025) for the coexistence of athletic, ritual and performative practices, but they are not treated here as a direct genealogy of the theatre spaces examined in this paper. The research instead focuses on the early modern game of real tennis (fr. *Jeu de Paume*), the architecture developed for it, and the documented adaptation of tennis courts for theatrical and other collective uses. The central research question is whether the spatial characteristics of these courts can be understood as one of the precedents relevant to the later development of a two-sided, transversal stage-auditorium configuration. Methodologically, the paper distinguishes between historical evidence and typological interpretation. Documentary evidence is used to establish the construction, use and adaptation of particular spaces; similarities in plan, proportion, galleries and audience-action relationships are then examined comparatively. Spatial similarity alone is not taken as proof of direct historical transmission. Sections 2-4 provide the historical and theoretical context, while Sections 5 and 6 form the principal analysis of the relationship between tennis-court morphology and theatre-space typology.

## 2. TENNIS - THE STORY OF THE ORIGIN OF THE GAME

The term tennis (fr. *Jeu de Paum*) appears for the first time in literature in the Middle Ages (circa 1200), and the place from which it originates has connections with a very dark and sinister establishment - hell. The first records of tennis date back to medieval Paris. It is a record of the memory of a young priest from holy orders, whose associates ridiculed him for his extremely short-term memory. One day, the devil spoke to the priest and showed him a magical stone, saying: "As long as you possess this stone, you will know everything." (Gillmeister, 2017, p. 18) The priest accepted the stone as a gift and soon became an excellent scholar. However, not long after accepting the gift, the priest became deathly ill (or so people thought). A gang of demons grabbed the priest's soul and hurried off into a valley filled with sulfur fumes. Here the gang split into two teams, one team standing opposite the other, on opposite sides of this valley. They began the game, striking the priest's soul from one side of the valley to the other: "Those who stood on one side struck his soul, in the manner of a game with a ball, while the others caught it in mid-flight with their bare hands." (Gillmeister, 2017, p. 18) The whole situation was certainly not made any better by the fact that the demons had claws as sharp as nails, thus tormenting the priest's soul more than any martyrdom he could experience. There are several other similar medieval records of the game of tennis in literature, all of which concern the clergy who were ridiculed for their idleness, and branded as idiots for an innocuous thing that would become a central theme of human existence during the 19th century - the theme of leisure. However, perhaps for the modern context, the society of the spectacle, the society in which only the strongest survive, the most prominent legend about the genesis of this game happened a whole century before Tennis emerged from Lucifer's empire. If the legend *Ystoire de Appollonius roy de Thir is to be believed* (Gillmeister, 2017, p. 19), the world's first tennis match was played in North Africa. The first champion, of course, was not a European, but a man from the Orient, Apollonius of *Tyre*, a citizen of Lebanon. According to this legend, Apollonius is the oldest recorded tennis champion, however,

judging by all the available facts, he is still a fictitious champion. The message that this legend conveys is actually in focus here, and that message is that the story of a man who came from nothing and created a life for himself, has always been received well among the populous. In the Middle Ages, the most successful method of achieving this goal was to marry a princess. Apollonius did exactly that, except for the fact that he played tennis. In an attempt to escape from his oppressor of his homeland, King Antichus, Apollonius was shipwrecked and stranded on the coast of North Africa, near the city of *Cyrene*. At that time, the city was ruled by Archistrates, a ruler who is known for his fondness for holding spectacular games that were like the games in ancient Greece - the Olympics. The important difference between Archistrates' games and the Olympics is that at Archistrates' event, a ball game was played, the so-called tennis. The event took place on the main city square. Apollonius had nothing but a robe given to him by a charitable fisherman, after which Apollonius decided to compete. Apollonius impressed everyone present, including the ruler, but also his daughter. Apollonius responded to the ruler's invitation to play a match against him and he made a decisive victory. However, after the match, Apollonius could not resist the charm of Archistratus' daughter. He married her immediately after the match. (Gillmeister, 2017, p. 20) Despite the opinion that such stories are clichés, platitudes, or just empty words, the author's claim stands that precisely such stories form the essence of theater - the conflict around which the plot develops. For sport, a conflict has always been necessary, a conflict between two opponents who will reach the goal through honorable struggle, perseverance and persistence. That goal is not only and exclusively victory over the opponent. On the way to that goal, it is important to understand why we decided to set out on that path in the first place. In some ways we could agree this represents the essence of any kind of sport, and the stories remain behind us as a legacy for the generations that will succeed us. This is precisely why culture and its development through various social, political, and economic events was at the center of the development of sports and theater, that is, spectacles in general. We can agree with this statement because the spectacle is a part of people's everyday life, it always has been and will certainly remain so for some time to come. It is in human nature to crave new, unpredictable outcomes of various events that we witness almost daily.

## 3. HISTORICAL DEVELOPMENT OF TENNIS AS A SPORT

Traditionally, tennis as a sport is known to the narrow community that practices this sport under the name tennis on grass, and the sport is played with the help of rackets. This sport was invented in Edgbaston, a neighborhood of Birmingham in England, and is a direct successor of the game that we call today real tennis or royal tennis (eng. *Royal Tennis*, fr. *Jeu de Paume*). This sport is still played today, however, on slightly different grounds, and the rules of the game are somewhat more complex. Most of the rules of the game come from the forerunner of tennis, that is, most experts today consider tennis and real tennis to be a variation of one and the same game. The majority of modern historians have reached a consensus that tennis as a game originates from the Middle Ages, from monastery cloisters in northern France (*circa* XII century). The first historical records record that people played tennis only with the help of their hands, that is, they hit the ball with their fists. This is where the name *Jeu de Paume* (fist game) (Gillmeister, 2017) comes from. It was only in the 16th century that the racket appeared, came into regular use, and the technology of making tennis equipment began to develop, when the name of the sport that we all know today was popularized. This sport was first popular in the Kingdom of France, also in England. King Henry VIII of England was the foremost enthusiast of the game at the time. It is significant to note that

the variation of the same game played by King Henry VIII has today developed into the variation we call "real tennis". (Crego, 2003) Many of the venues where tennis was originally played in the United Kingdom have survived to this day. Some of the most important spaces are the courts in Oxford, Cambridge, Falkland Palace in Scotland, where Mary Queen of Scots regularly played tennis, as well as the royal hall in Hampton Court Palace. However, in France, the situation is somewhat different - many spaces where the game of tennis was originally played have changed their purpose or completely lost their function and remained abandoned. The main reason for this was the ruling order's fear of the return of the strength, will and initiative of the French Revolution in 1789. Oath on the tennis court (fr. *Serment du Jeu de Paume, Eng. Tennis Court Oath*) is an event of key importance primarily for the wider social context of France in the 18$^{th}$ century, but also for tennis as a sport in general. The first days of the revolution were marked by this event, when 576 out of a total of 577 members of the third estate signed the oath at the general assembly of all estates held on June 20, 1789 in Versailles at the royal court, which divided power equally among all three estates, that is, the common people took control of the election of the executive authorities after this event. Several significant events for the development of tennis followed much later, only in the second half of the 19th century. The rules of lawn tennis were finally established in 1875, with minor and occasional changes. This set of rules was applied all over the world, but it was most significantly applied in the All England Lawn Tennis and Croquet Club at the same time when the oldest and today's most prestigious tennis competition, *The Championship,* was formed at Wimbledon in 1877. It is important to mention the Davis Cup, an international championship in men's competition that was formed in 1900, the same year that the Universal Exhibition (fr. *Exposition Universelle*, abr. *EXPO*) was held in Paris. Analogous to the Davis Cup, the international women's (International Tennis Federation ITF, 2025) competition Fed Cup (*Federation Cup, abr. Fed Cup)* was formed in 1963 to celebrate the 50th anniversary of the International Tennis Federation (*abr. ITF*). Probably the most significant moment in the history of tennis as a sport is the event that took place in 1968, known as the beginning of the Open Era *of* tennis. Due to the enormous pressures of the commercialization of sports, the distinction that previously existed between amateur and professional players was abolished. From this moment on, all players could play in all tournaments, the Association of Professional Players (*ATP*) and the Women's Tennis Association (*WTA*) were established, which united all professional players and provided better conditions at tournaments, fought for the rights of athletes and, as associations, began to earn money from the sale of rights for television broadcasts of tournaments around the world. From this moment, tennis as a sport got rid of all the prejudices it had before - that the sport is played exclusively by the upper and middle class of the Western world. There are still exceptions, but generally speaking, this statement has become widely accepted as fact. (Henderson, 2006)

## 4. FUNCTIONS OF SCENE ARCHITECTURE

In the context of the modern era, the moment in which architecture changed the paradigm, or the angle of observing the profession as such, but also the way in which people treat construction, stands out very clearly. The 20th century was permanently marked by the greats of the modern movement in Architecture with a new paradigm that set and then strongly dictated the direction in which architecture would develop. Of course, we are talking about the triple morpheme function-form-construction that establishes a cause-and-effect relationship between the other triple morpheme: utilitas-firmitas-venustas known today as the Vitruvian values or the Vitruvian triad. The

paradigmatic reversal of the observation of architecture through the prism of the triple morpheme function-form-construction meant a total and comprehensive reversal in the understanding of space, and initiated new theoretical researches, many of which are very significant today. Relying on Professor Dinulović's research, I would first of all like to consider the concept of architectural form. "If we accept the understanding of form as a perceptual structure, configuration, or discursive composition of elements" (Dinulović, 2025, p. 3), we must accept as a fact that form itself is not and never can be a distinct attribute. Form is by implication the only outcome of every creative activity of an architect, "regardless of whether we are talking about realized, real, physical objects, temporary or virtual structures, graphic fantasies, or theoretical, artistic and literary utopias" (Dinulović, 2025, p. 3). Since we have established the meaning of the term form, the next logical question in the series is what is the form for, that is, what are its functions? The way in which the question was asked suggests that it is possible to view architecture as a set of a plurality of several different functions, so not only the most basic utilitarian ones that exclusively answer the question of what a space should serve, that is, how the space will be used. In this way, the architect increases his own modeling abilities. On the basis of this conclusion, it is possible to derive a whole set of functions of the architecture, by which we would more closely define its program. However, there is another important fact that needs to be noted beforehand. Classical definitions of architecture, as we all know well, centuries ago were usually triadic and based on the establishment of cause-and-effect relationships between utilitas-firmitas-venustas (Vitruvius, 2014). However, it is extremely important to form a definition like we could find in an encyclopedia, a definition that answers three key questions: "What is it for? What is it made of? And, where is it?". In this connection, we can define architecture as a systematized and organized field of human action that has its origin in the articulation of existential space. Analogously, we can see the stage in architecture as a systematized and organized area of human activity that has its origin in the articulation of the stage space using stage means. Stage means represent a set of devices and techniques with which the author's team led by the director articulates the space of the stage, i.e. devices and techniques with which stage reality is built. Further, by analogy, we come to the conclusion that the functions of scene architecture really make up the same set of functions that any other architecture has. From the discursive position established in this way, we can agree that the set of functions of architecture is arbitrary, that is, that the designer is a person who redefines that set every time. For the purposes of this research, particular attention is given to the cultural and social functions of scene architecture, understood as analytical categories rather than deterministic causes of formal change. The chronological development of tennis and of the tennis court demonstrates that these spaces accommodated sporting activity as well as theatrical and other collective events. This documented multiplicity of use provides the historical basis for a typological comparison. It does not, by itself, demonstrate that the social and political circumstances of the sixteenth, seventeenth and eighteenth centuries directly caused a particular theatre-space configuration. The argument developed in the following sections is therefore narrower: repeated adaptation of tennis courts, together with their proportions and galleries, created spatial conditions that could be appropriated by theatre practitioners. Eighteenth-century criticism of existing theatre spaces, including the positions associated with Voltaire and Diderot discussed below, is used as evidence of dissatisfaction with particular arrangements and adaptation practices, not as proof of a single causal path from social change to architectural form.

## 5. PREREQUISITES FOR THE DEVELOPMENT OF THEATER SPACE IDEAS IN THE AGE OF ENLIGHTENMENT

Debates concerning theatre space in eighteenth-century France developed within the broader intellectual and artistic context of the Enlightenment and the renewed interest in classical principles. Ledoux's theatre in Besançon, opened in 1784, as an important example of this reform discourse, but it should not be understood as the direct architectural consequence of a single social or cultural transformation. For the present argument, the more relevant evidence is the condition and use of existing performance spaces. Pannill Camp documents that, at the beginning of the eighteenth century, theatrical performances in France frequently took place in adapted buildings, including tennis courts. Their elongated proportions, relatively modest scale and existing galleries made them practical spaces for conversion, even when those same conditions imposed limitations on scenery, sightlines and circulation (Camp, 2014, p. 41). The common length-to-width ratios of approximately 5:2 or 3:1 are therefore significant as spatial characteristics that made adaptation possible. Comparisons between converted tennis-court interiors and purpose-built theatres, such as the theatre at Sabbioneta, can reveal formal similarities in the relation between an elongated central area, parterre and surrounding galleries; however, such similarities should be read as typological parallels unless a direct historical influence is documented. Criticism attributed to Voltaire and Diderot provides evidence that contemporary theatre practitioners and writers were dissatisfied with aspects of existing French theatre spaces (Camp, 2014, p. 46). In this sense, the eighteenth century can be understood as a period in which inherited and adapted spatial arrangements were increasingly questioned. The relevance of the tennis court lies not in being a sufficient cause of later theatre reform, but in providing a recurring, already available spatial model against which new stage-auditorium relationships could be tested and reconsidered.

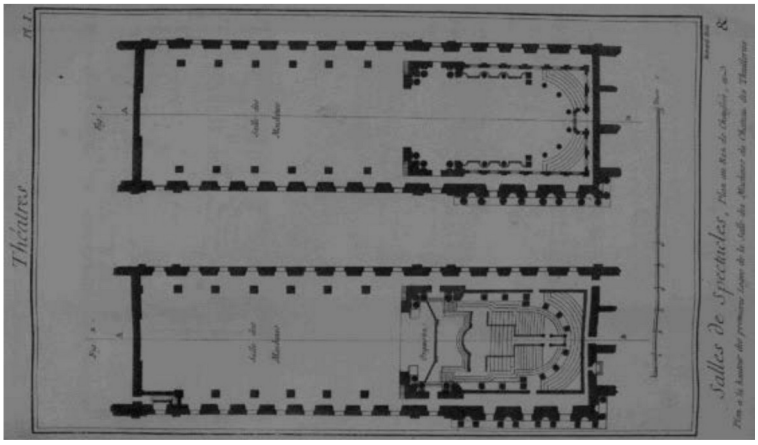


***Figure 1*** *"Theatre, horizontal plan of the ground floor and plan of the first level of the box in the Engine Room of the Palace of Tuileries," Engraving by Robert Bernard for Diderot and D'Alembert's Encyclopédie, collection of plates (1762-72).*

## 6. TENNIS AND SCENE ARCHITECTURE – TENNIS-COURT MORPHOLOGY AND THE TWO-SIDED STAGE-AUDITORIUM CONFIGURATION

Building on Dinulović's typological research and Helen and Richard Leacroft's historical survey, this section examines whether the morphology of the real-tennis court can be understood as a relevant spatial precedent for the two-sided stage-auditorium configuration. The Leacrofts' chapter 'French tennis courts, parterres and amphitheatres' is particularly useful because its plans and structural reconstructions document the spatial organization of courts and their relationship to spectators (Leacroft & Leacroft, 1988, p. 49). The Royal Tennis Court at Hampton Court Palace is used here as a comparative case because the preserved court clearly shows an elongated central playing field framed by galleries and spectator positions. These characteristics are historical evidence of the organization of a tennis court. Their relationship to later theatre typologies is a second, interpretive step: the comparison tests morphological continuity, but it does not assume that the Hampton Court example itself was transformed into, or directly generated, a transversal theatre.

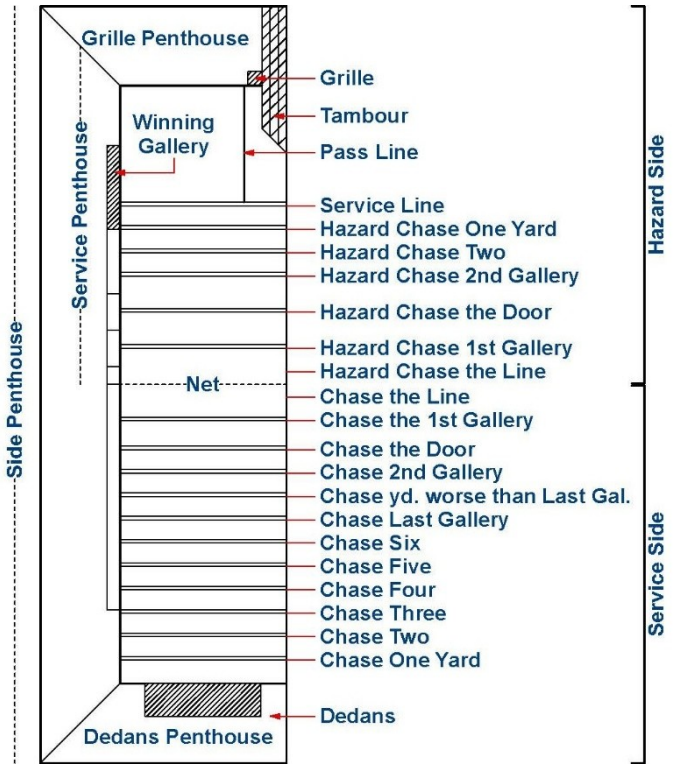


*Figure 2 – reconstruction of a schematic representation of the horizontal plan of the tennis court in the Royal Tennis Court in Hampton Royal Court, source: (The Royal Tennis Court Club, Hampton Court Palace, 2025)* [https://tinyurl.com/mupsb3eb](https://tinyurl.com/mupsb3eb)

In the schematic plan, the elongated playing field occupies the center of the court while spectator positions are distributed along its perimeter, including positions on opposing sides. This organization shares an important formal characteristic with what later theatre terminology describes as a transversal, longitudinal, runway or tennis-court stage: an elongated central zone of action placed between audience groups. The comparison makes it possible to propose a typological relationship, but the available material does not establish a documented sequence in which this particular court, or a single identifiable tennis court, was converted step by step into the later two-sided theatre type.

Nor is there a clear historical consensus assigning the invention of this configuration to one person or one date. Stephen Joseph's twentieth-century work is significant for the modern development and advocacy of flexible and non-proscenium forms, yet the spatial logic of opposing spectators and a central action zone has earlier precedents. For this reason, the tennis court is better understood as one element within a broader genealogy of theatre-space ideas. Its relevance lies in a group of recurring spatial features: the elongated central field, close proximity between action and spectators, galleries or perimeter viewing positions, and the possibility of organizing spectators on more than one side. When appropriated for performance, these features could support greater proximity between actors and spectators and intensify visual relationships across the central space. Such effects describe the spatial affordances of the type; they do not demonstrate that a change in social or cultural function directly produced the later theatre configuration.



*Figure 3 - Photograph of the exterior of the Royal Tennis Court, Hampton Royal Court, source: https://tinyurl.com/mupsb3eb*

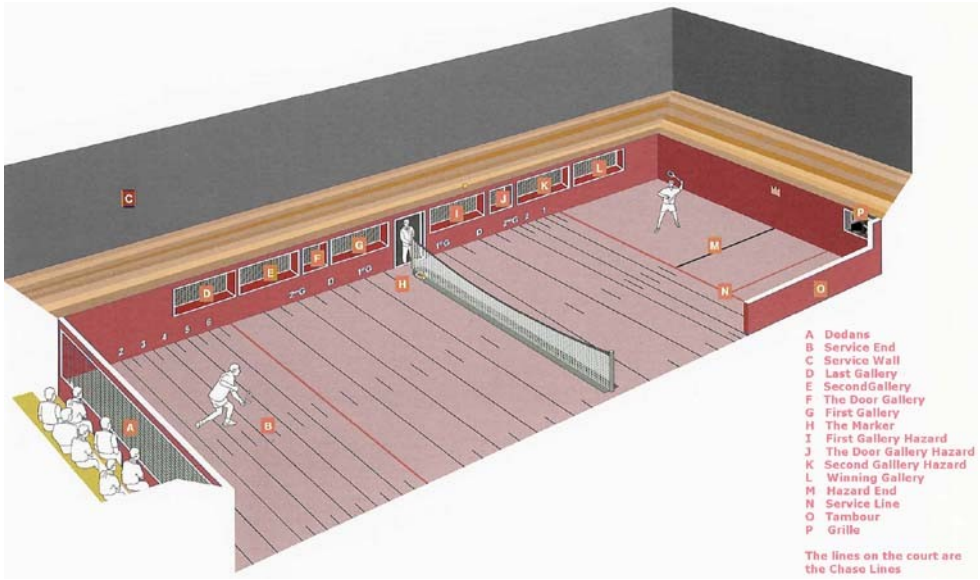


*Figure 4 - schematic representation of the interior of the Royal Tennis Court in Hampton (Hampton Royal Court), source: (Petworth House Tennis Court, 2026) https://tinyurl.com/3a7j8d6t*

Real tennis developed in both France and England, and courts were constructed in royal and urban contexts in each country. For the present study, the important point is not to

explain the circulation of the type through political rivalry, but to note that comparable elongated halls with galleries existed in several contexts and could accommodate changing forms of use. In France, the popularity of jeu de paume led to the construction of numerous courts, many of which were subsequently adapted, abandoned or assigned new functions. The Royal Tennis Court at Versailles (fr. *Jeu de Paume royal du château de Versailles*) is a particularly important surviving example because its later history records a shift from sporting use to a major collective political event and, eventually, to museum use (Figure 5). This continuity of the building, despite changes of program, is relevant to the paper's argument about spatial adaptability.

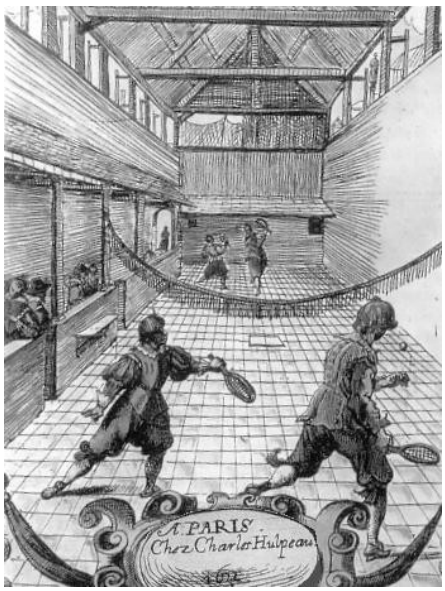


*Figure 5 - "Je de paume", copy of the engraving from the book "Le Jeu royal de la paume", Charles Hulpeau (fr. Charles Hulpeau) (Hulpeau, 1632), unknown author of the engraving*

At the French court the game was known as *jeu de paume* or real tennis. The engraving reproduced in Figure 5 documents characteristic features of the court type: an elongated central playing area and viewing positions arranged along the perimeter. These features recur in other examples discussed in the paper and provide a basis for morphological comparison. The Royal Tennis Court at Versailles also acquired a non-sporting role in 1789, when it became the site of the Tennis Court Oath. Jacques-Louis David's later representation of the event (Figure 6) should therefore be read primarily as visual evidence of the political and collective occupation of a space designed for another purpose. Its relevance to scene architecture lies in demonstrating the capacity of the court's central field and surrounding edges to accommodate a dense assembly and a concentrated focus of attention.



*Figure 6 - painting "The oath on the tennis court" (fr. Le Serment du Jeu de paume)), oil on canvas, Jacques-Louis David; source: https://tinyurl.com/mwj8apbx*

David's image should not be treated as documentary evidence that a later theatre morphology was already present, nor as a direct prediction of the transversal stage. What the composition makes visible is a spatial condition that is also evident in the architecture itself: a large central field can be occupied by a collective event while observers and participants are distributed around it and along the galleries. The centrally emphasized figure and the surrounding crowd create a visual analogy with the relation between a performance focus and spectators, but this analogy remains interpretive. It supports the argument that the tennis court could accommodate non-sporting modes of assembly and spectatorship; it does not establish that the political event of 1789 caused, or directly anticipated, a specific later stage-auditorium type.



*Figure 7 - photo of the interior of the Royal Tennis Court in Versailles after reconstruction in 2022; photo author: Didier Saulnier; source: https://en.chateauversailles.fr/discover/estate/royal-tennis-court*

Today the Royal Tennis Court at Versailles functions as a museum, demonstrating another stage in the adaptive history of the building. The persistence of its characteristic proportions and perimeter elements makes the space useful for examining how a stable architectural envelope can receive different programs over time. Within the history of theatre space, the later emergence and renewed use of two-sided stage-auditorium arrangements cannot be derived from the tennis court through a single linear sequence. Dinulović's discussion of courtyard theatres is relevant here because it points to other historical forms in which spectators surround or flank a central area of action (Dinulović, 2005, p. 13). Considered together, tennis courts, courtyard theatres and later transversal configurations reveal a recurring spatial logic rather than a single line of descent: an elongated or centralized zone of action, close audience proximity, and viewing positions located on more than one side. The evidence examined in this paper therefore supports a limited claim. Tennis-court architecture can reasonably be included among the spatial precedents that contributed to the repertoire of arrangements available to theatre practice, especially because courts were demonstrably adapted for performance. What remains unproven is a direct causal chain from tennis, or from wider political and social transformations, to the formation of the transversal stage. Cultural and social circumstances are consequently treated as the context in which spaces were used, reassigned and interpreted, while the principal argument remains historical and typological.

## 7. CONCLUSION

This paper examined whether the tennis court can be considered a relevant spatial precedent in the genealogy of the two-sided transversal stage-auditorium configuration. The historical and typological analysis supports three main findings. First, real-tennis

courts were not exclusively sporting spaces: historical sources record their adaptation for theatrical performances and other forms of collective use. Second, the recurrent morphology of these courts - an elongated central field, perimeter galleries and spectator positions capable of flanking the central area - provides spatial characteristics that are comparable to later two-sided stage-auditorium arrangements. Third, eighteenth-century criticism of adapted and existing theatre spaces shows that these inherited spatial conditions were both useful and restrictive, and formed part of a broader period of reconsideration of theatre architecture. The evidence does not demonstrate that the transversal stage originated from one tennis court, nor that social and political changes directly caused this theatre typology. The more defensible conclusion is that the tennis court constituted one of several historical spatial models whose proportions, adaptability and audience-action relationships could contribute to later experiments with non-frontal theatre space. Its importance for scene architecture is therefore typological rather than deterministic: the tennis court helps identify a recurring spatial relationship between a central zone of action and spectators positioned in close proximity on more than one side. Further research based on documented conversions of individual courts and chronological comparison with courtyard and other non-frontal theatre types could test this proposed genealogy in greater detail.

## 8. ACKNOWLEDGMENT

This research is supported by the Ministry of Science, Technological Development and Innovation (contract number: 451-03-137/2025-03/200156) and the Faculty of Technical Sciences of the University of Novi Sad through the project "Scientific and artistic research work of researchers in teaching and associate positions at the Faculty of Technical Sciences of the University of Novi Sad 2025" (number: 01-50/295).

## 9. LITERATURE

[1] **Bojanić dr Petar and Đokić dr Vladan** Luis Mamford [Lewis Mumford]: Šta je Grad? [Journal] // Zbornik radova: Misliti grad. - Beograd : Univerzitet u Beogradu, Arhitektonski fakultet, 2011. - pp. 15-20. - 9788679240538.

[2] **Camp Pannill** The First Frame: theatre space in Enlightement France [Book]. - St. Louis : Cambridge University Press, 2014. - Hardback. - 978-1-107-07916-8.

[3] **Crane Gregory R.** Pausanias = Pausanias, Description of Greece. - Medford : Tufts University, 2025.

[4] **Crego Robert** Sports and Games of the 18th and 19th Centuries [Book]. - London : Bloomsbury Academic, 2003. - 2nd Illustrated Edition : p. 274. - 9780313316104.

[5] **Dinulović Radivoje** Ideološka funkcija arhitekture u društvu spektakla [Online] // SCEN - Odsek za umetnost i dizajn. - 2025. - 2 9 2025. - https://scen.uns.ac.rs/h-content/uploads/2023/09/Ideoloska-funkcija-arhitekture-u-drustvu-spektakla-sa-prologom-scen.pdf.

[6] **Dinulović Radivoje** TIPOLOGIJE POZORIŠNOG PROSTORA: Klasifikacije tipova i modela scensko-gledališnog prostora u teoriji i istoriji pozorišta XX veka [Journal] // Zbornik radova fakulteta dramskih umetnosti / ed. Jevtović dr Vladimir and Rapajić Svetozar. - Beograd : Fakultet dramskih umetnosti, Januar 2005.. - Vols. VIII-IX. - pp. 1-35.

[7] **Gillmeister Heiner** Tennis: a cultural history [Book]. - Sheffield : Equinox Publishing Ltd., 2017. - Second Edition.

[8] **Henderson Jon** Middle-class heroes can lift our game = Sportblog, Tennis. - London : Guardian Media Group, 11 12 2006.

[9] **Hulpeau Charles** Le Jeu royal de la paume [Book]. - Paris : chez Charles Hulpeau, 1632.

[10] **International Tennis Federation ITF** Davis Cup History [Online] // Davis Cup | The World Cup of Tennis. - 2025. - 17 9 2025. - https://www.daviscup.com/en/organisation/davis-cup-history.aspx.

[11] **Leacroft Richard and Leacroft Helen** Theatre and Playhouse: An illustrated survey of theatre building from Ancient Greece to the present day [Book]. - London : Methuen Drama, 1988. - 1st paperback reprint, 1988. - 0413529401.

[12] **Petworth House Tennis Court** Petworth House Tennis Court [Online] // Petworth House Tennis Court. - 2026. - 1 November 2026. - https://petworthrealtennis.com/the-game-2/the-court/.

[13] **The Royal Tennis Court Club, Hampton Court Palace** The Game [Online] // The Royal Tennis Court. - 2025. - 18 Spetember 2025. - https://www.royaltenniscourt.com/the-game.

[14] **Vitruvije Polion Marko** Deset knjiga o arhitekturi [Book] / ed. Kovačević Dragorad and Jadrešin-Milić Renata / trans. Lopac Matija. - Beograd : Orion Art, 2014. - Obnovljeno izdanje sa predgovorom Ranka Radovića : p. 273. - 9788663890145.

[15] **Young David C.** The Beginnings: A Brief History of the Olympic Games [Book]. - London : Wiley-Blackwell, 2004.

https://doi.org/10.24867/INDIS-2026-EN-638



# CENTRALITY OF SUBURBAN SETTLEMENTS UNDER URBAN EXPANSION: THE CASE STUDY OF VETERNIK

*Ranka Medenica Todorović*[1], *Milica Vračarić*[2], *Marina Carević Tomić*[3]

***Summary:***

Contemporary processes of urban expansion and the transformation of city regions are altering the role of suburban settlements in the broader urban framework, creating the need to examine their centrality. The aim of this paper is to analyse centrality of the suburban settlement of Veternik within the Novi Sad city region. The research is based on a survey and field observation, with a focus on the perception of the centre and the spatial distribution of urban functions and amenities. The results show that Veternik possesses a pronounced functional centrality, predominantly of linear and transit-oriented character, with limited capacity for more intensive social interactions. Although the need for social encounters is partially accommodated through various urban functions that do not primarily serve a social purpose, the planned design of high-quality public spaces and the development of diverse urban amenities is required.

*Keywords: centrality, suburban settlements, urban expansion, Veternik, public space*

# CENTRALITET PRIGRADSKIH NASELJA U USLOVIMA URBANOG ŠIRENJA: STUDIJA SLUČAJA VETERNIKA

***Rezime:***

Savremeni procesi urbanog širenja i transformacije gradskih regiona menjaju ulogu prigradskih naselja u okvirima urbanih sistema, namećući potrebu za sagledavanjem njihovog centraliteta. Cilj rada je analiza centraliteta prigradskog naselja Veternika u okviru gradskog regiona Novog Sada. Istraživanje se zasniva na anketnom ispitivanju i terenskoj opservaciji, sa fokusom na percepciju centra i prostornu distribuciju urbanih funkcija i sadržaja. Rezultati pokazuju da Veternik poseduje izražen funkcionalni centralitet, pretežno linearnog i tranzitnog karaktera, sa ograničenim kapacitetom za intenzivnije društvene interakcije. Iako se potrebe za susretima delimično ostvaruju kroz različite urbane funkcije koje nemaju dominantno društvenu namenu, neophodno je plansko oblikovanje kvalitetnih javnih prostora i razvoj raznovrsnih urbanih sadržaja.

*Ključne reči: centralitet, prigradska naselja, urbano širenje, Veternik, javni prostor*

[1] Msc, Faculty of Technical Sciences, University of Novi Sad, Novi Sad, Serbia, ranka.medenica@uns.ac.rs, ORCID 0000-0003-1734-6772
[2] Prof., Faculty of Technical Sciences, University of Novi Sad, Novi Sad, Serbia, kostresm@uns.ac.rs, ORCID 0000-0002-2120-8738
[3] Assoc. Prof., Faculty of Technical Sciences, University of Novi Sad, Novi Sad, Serbia, marinac@uns.ac.rs, ORCID 0000-0003-0209-5747

## 1. INTRODUCTION

Contemporary processes of urban expansion and transformation of city regions lead to changes in the spatial and functional organisation of settlements, particularly in suburban areas, which are becoming an increasingly important segment of urban systems [1]. Understanding their socio-spatial transformations are of particular importance in terms of the impact that physical structure and the distribution of urban functions have on quality of life, economic growth, social equality, and sustainable urban development [2]. The intensive suburbanisation and functional integration of settlements contribute to the redefinition of their roles, highlighting the need to examine centrality as a key characteristic of the quality of urban space and everyday life of suburban areas.

The aim of this paper is to reconsider centrality of suburban settlements based on the case study of Veternik, as part of the settlement network of the City of Novi Sad urban region. The empirical research is designed to better understand the dynamics of peri-urban areas, which are often insufficiently regulated and shaped through spontaneous and informal patterns of use. It focuses on examining the relationship between urban functions and the perception of the centre, in order to identify key characteristics of central space within expanding urban regions.

The paper is based on the assumption that the presence of urban amenities may partially fulfill the function of the urban centre by creating opportunities for encounters and everyday interactions; however, its development and enhancement depend on the planned spatial organisation and design of high-quality open public spaces. In this sense, the analysis of Veternik as a suburban settlement provides insight into specific patterns of centrality formation in the context of contemporary suburban settlements.

## 2. URBAN EXPANSION AND CENTRALITY IN CONTEMPORARY CITY REGIONS

Urban growth encompasses transformation of the functional dynamics of urban centres and their interrelations within a broader regional context. The emergence of local centres in suburban and peripheral areas, driven by decentralisation processes and the rise of polycentric urban forms, reflects changes of the functions, priorities, and role of centrality in contemporary urban development [3]. While suburbanisation represents one of the most prominent phenomena of contemporary spatial transformation [4], the expansion of urban functions beyond the boundaries of the compact city increasingly exhibits characteristics of urban sprawl, accompanied by controversial ecological, economic, and social consequences [5].

Despite the growing number of urban functions and amenities, suburban settlements often face the problem of insufficiently developed or inadequately structured central areas. Although mixed-use development has been widely accepted as a principle of contemporary urban planning [6], suburbanisation often results in low-density suburban environments lacking adequate public amenities and spaces, particularly the active settlement centres capable of supporting social interaction and collective community life [7]. In this sense, urban centrality is understood as a node of activities — spatial points where the concentration of public functions and movement generates urban life, social encounters, and community identity [8]. Such an approach provides a human-scale and immediate living environment perspective [9], opening up the space for understanding centrality through the prism of activities and everyday practices. Therefore, centrality is not reflected solely through the concentration of urban functions, but also through the way space is used, perceived, and valued by its users.

## 3. CENTRALITY OF VENETRNIK SUBURBAN SETTLEMENT

The study was carried out through a case study of the settlement of Veternik, a settlement within the urban region of the City of Novi Sad. The territory of the region is defined by the Spatial plan of the City of Novi Sad [10], comprising a network of suburban settlements clustered around Novi Sad, Petrovaradin, and Sremska Kamenica. Veternik was selected as a case study due to pronounced processes of urban expansion and transformation from a predominantly rural to an urban settlement.

### 3.1. METHODOLOGY

The empirical research was conducted using a combination of survey research, field observation, contextual analysis, and reviews of planning documents. Data on patterns of spatial use were collected through a survey questionnaire conducted among settlement residents, with the aim of identifying users' perceptions of the centre. A total of 140 responses were collected. In addition, field observation was carried out to identify and map existing urban amenities. The methodological approach is further grounded in the mapping and spatial analysis of the obtained data. The analysis of the collected data enabled an examination of the relationship between the functional structure of space and users' activity patterns.

### 3.2. SPATIO-FUNCTIONAL DEVELOPMENT OF VETERNIK

Veternik is one of the youngest and most dynamically transformed suburban settlements within the urban region of the City of Novi Sad, with a population of 18,849 inhabitants [11]. Veternik simultaneously exhibits both suburban and peri-urban characteristics, with spatial proximity to Novi Sad (less than 10 km) and almost complete physical integration into the urban fabric of the city. Its large overall population and the relatively small share of agricultural population reflect its urban character, while its lower building density, spatial structure characteristics, and the evident mismatch between existing and required capacities of public facilities contribute to its rural character [12].

Until the early 1990s, Veternik was characterized by a relatively coherent spatial structure. However, in the period of accelerated growth, particularly after the 1990s and the large influx of refugees from war-affected regions of the former SFR Yugoslavia, Veternik underwent intensive morphological and demographic changes over the following decades. Merging of the built-up areas of Novi Sad, Veternik, and Futog, formed a unified Novi Sad urban agglomeration in accordance with UN-Habitat definitions [10]. Uncontrolled and illegal construction initially formed a new linear development zone along the entrance corridor connecting Veternik with the inner urban area of Novi Sad, while the subsequent phase of urban growth involved the occupation of surrounding agricultural land through the illegal construction of numerous family housing units, followed by contemporary construction of multi-family residential complexes. Its favourable position along an important transport corridor, population size, and immediate proximity to Novi Sad make Veternik an attractive location for the development of non-residential functions intended both to satisfy the needs of the population and to support the decentralisation of certain functions from the urban core of Novi Sad. The lack of central functions has been accompanied by the absence of regulated public spaces and a clearly articulated centre, representing one of the settlement's major challenges [12].

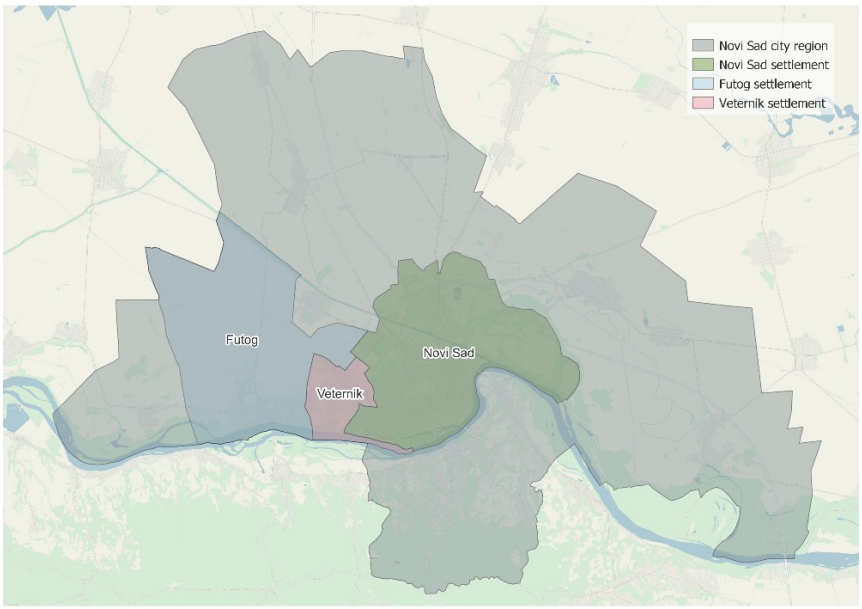


*Fig. 1 Administrative boundaries of the settlements of Novi Sad, Veternik and Futog, and their spatial relationship within the continuously urbanized area of the Novi Sad agglomeration (Novi Sad city region).*

Accordingly, the planning framework envisions the future development of Veternik as oriented toward strengthening its urban characteristics through the enhancement of its functional structure, public amenities, and its role within the wider urban agglomeration [13]. The development of Veternik also aims to strengthen central functions and to establish a settlement centre that is both functionally and socially recognizable. The central zone includes key public, educational, cultural, communal, and market-related facilities, with a pronounced social role as a place of gathering, interaction, and strengthening of local community identity, conceived as a spatially unified yet functionally diverse urban entity. The centre of Veternik primarily aims to satisfy the everyday and occasional needs of residents through facilities that contribute to improved housing quality and the effective functioning of the local community. The centre is conceived as a potential driver for the decentralisation of certain functions from the urban core of Novi Sad, while simultaneously strengthening spatial cohesion, connecting parts of the settlement north and south of the road to Bačka Palanka, and contributing to the integration of the settlement as a whole [14].

## 3.3. SPATIAL DETERMINANTS OF THE CENTRE OF VETERNIK

The questionnaire examines respondents' perception regarding the existence of a centre of the settlement in which they live, namely Veternik. Figure 2 presents the distribution of respondents' views related to the question whether Veternik possesses a center. The majority of respondents (51%) believe that there is a part of the settlement that, in some way, performs a function similar to that of a centre. A total of 31% stated that a centre exists in their settlement, while 11% believe that no centre exists. The remaining 6% were uncertain about the existence of a centre in their settlement. Taken together, a high proportion of respondents (82%) recognise, to some extent, the existence of a centre in Veternik. Either as a clearly defined spatial entity or as a part of the settlement with pronounced central functions, it indicates the presence of a perception of centrality in the collective image of respondents, although one that remains morphologically insufficiently articulated.

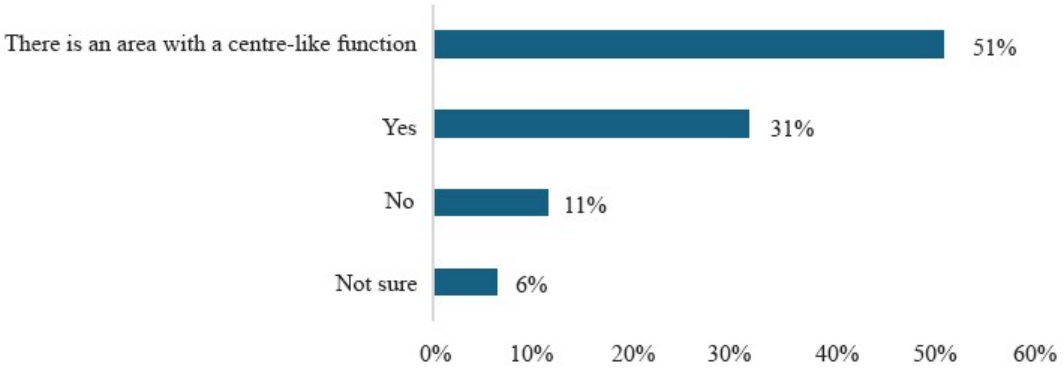


*Figure 2. Distribution of respondents' perceptions regarding the existence of a centre in Veternik.*

The survey also included an open-ended question enabling respondents to identify particular buildings, streets, squares, open spaces, or other elements regarded as constituting the centre of Veternik. All responses referring to commercial and service amenities (e.g. bakery, supermarket, cafés, pharmacies, flower shops, kiosks, boutiques, shops), without a clear indication linking them to a specific facility and its precise location within Veternik, were grouped into the category of commercial and service amenities (Figure 3), representing a non-spatial determinant of centrality. Although such responses do not indicate a precise spatial location, their frequency and content enable an interpretation of how respondents perceive the settlement centre. Figure 3 illustrates the distribution of responses. The data show that respondents predominantly perceive commercial and service facilities (28.5%), as a non-spatial determinant, as the element shaping the centre of Veternik. Such a perception of centrality indicates a functionally rather than morphologically defined settlement centre.




*Figure 3. Spatial representation of non-spatial determinants of centrality in Veternik. The locations of non-spatial determinants were approximated based on the spatial concentration of corresponding categories of urban amenities within the settlement.*

Further analysis of responses and their spatial contextualisation suggests that the majority of these commercial and service facilities are located along Kralja Petra I and Novosadski put streets, which represent the main entry and exit routes of Veternik. These major transport corridors account for a total share of 37.14% responses, specifically Kralja Petra I Street (10%), Novosadski put (7.86%), and the roundabout (19.29%) from which these linear axes extend (Figure 4). Altogether, they indicate a pronounced linear centrality, which characterizes suburban settlements with an insufficiently developed traditional central square or public space.

These transport corridors function as the primary carriers of central functions within the settlement, as commercial, service, and retail activities are concentrated along them, together with other facilities that contribute to the collective image of the centre among residents. The findings further show that, in addition to commercial and service facilities and transport corridors, the local community center (10.71%), the cultural centre (7.86%), and the church (6.43%) are also identified as elements of centrality, while other facilities are represented to a lesser extent (i.e. market, bakery, supermarket, or the monument at the roundabout). Their spatial configuration and relatively lower share in responses suggest that they do not yet function as dominant landmarks in the collective perception of the centre, but rather operate as complementary elements within a broader, linearly organised central space.

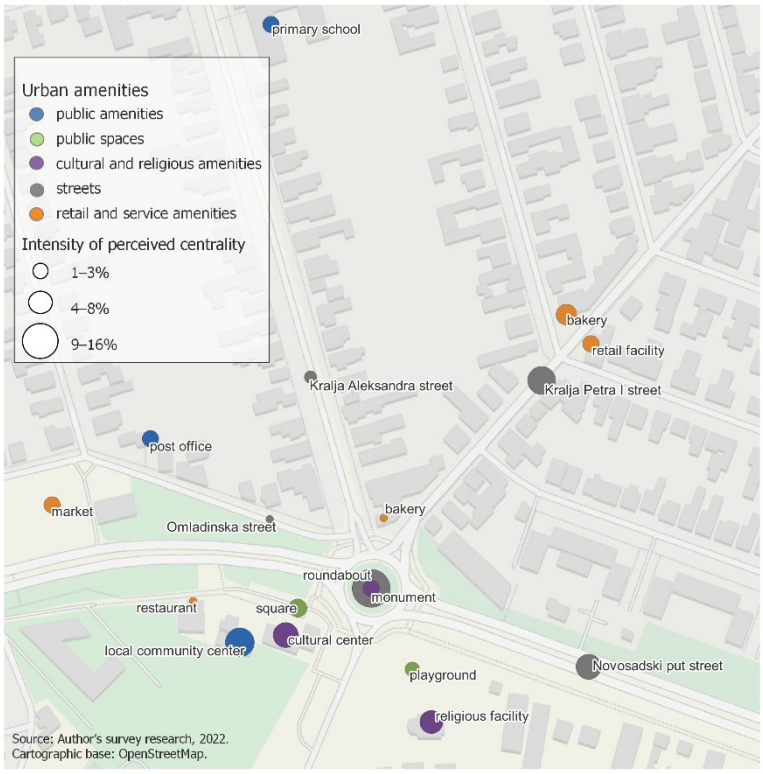


*Figure 4. Spatial distribution of urban amenities identified as determinants of centrality in Veternik. The map illustrates the concentration of public, cultural, commercial, and traffic-related functions within the perceived central area of the settlement.*

## 3.4. INFERRED FUNCTIONAL AND LINEAR CENTRALITY

According to the results of the study, the central space of Veternik is perceived along the main transport corridors, shaping its linear and transit-oriented character (Figure 5).

Dominant landmarks include commercial and service amenities, as well as certain public institutions, cultural and religious amenities. The research findings indicate that Veternik possesses a pronounced functional centrality, primarily based on the everyday activities of residents, such as shopping, services, and administrative needs.

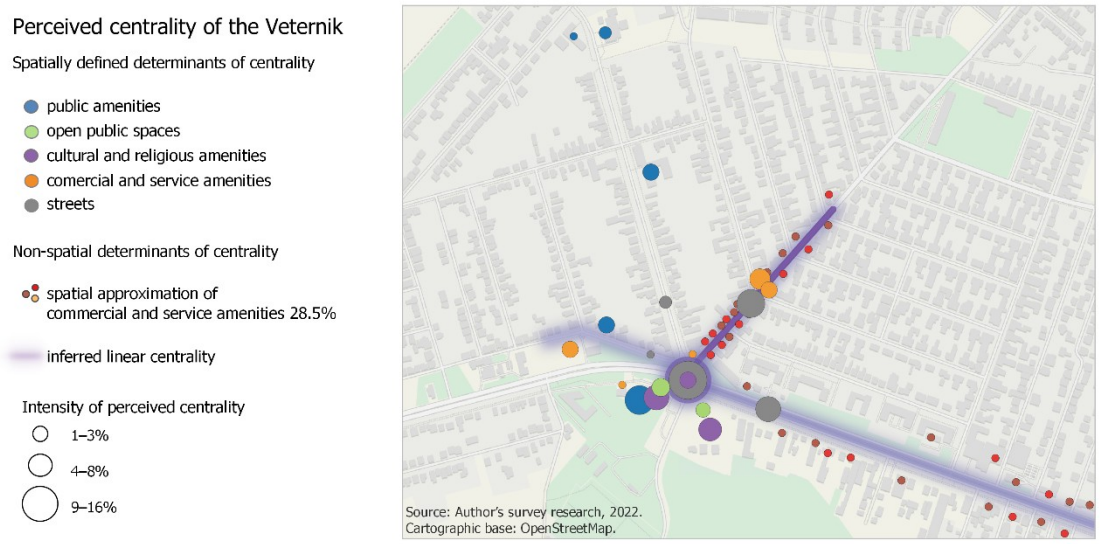


*Figure 5. Inferred functional and linear centrality of the settlement.*

The analysis of the respondents' frequency of visits to the centre of Veternik according to different purposes indicates a strong functional orientation of the centre, primarily in relation to the everyday needs of residents. The highest levels of frequency are associated with activities such as shopping in stores and supermarkets (e.g., 48.57% of respondents frequently engage in this activity), shopping at the market, visiting a bank or post office, as well as going to work or school (e.g., 41.43% of respondents frequently engage in this activity). These findings confirm that, in residents' perceptions, the centre of Veternik is primarily used as a space of everyday functional gravitation, where basic service, commercial, and administrative activities are concentrated.

In contrast to functional centrality, activities involving social interaction, such as spending time in public space, socialising, or recreation, are present to a lesser extent and are not spatially clearly defined. The lack of adequately designed public spaces further limits the development of social life. The square in front of the cultural centre represents one of the few spatial elements in Veternik that formally concentrates the functional and social dimensions of centrality. At the same time, places of social gathering are often identified along Kralja Petra I Street, where the majority of commercial and service amenities are concentrated, such as the bakery or the supermarket, indicating that everyday functional spaces partially assume the role of informal social meeting points. In addition, the church, together with the playground located within its premises, represents one of the recognised places of socialisation, particularly as a space for informal encounters and everyday community interaction.

Although the centre of Veternik is to some extent recognised as a place of social interaction and a potential gathering space, it still lacks sufficiently developed spatial and programmatic characteristics that would encourage more intensive and continuous use by residents. Such a pattern further confirms that the centre of this settlement primarily functions as a linear and transit-oriented space, while the social aspects of centrality are present but less pronounced and largely occasional. This creates potential for further planning interventions aimed at strengthening and transforming it into a more active

social centre of the settlement. Therefore, a careful approach to the planning of well-positioned, comfortable, and adequately equipped public spaces, together with a locally specific approach to urban design, is more than necessary in future planning interventions within the suburban settlement of Veternik.

## 4. CONCLUDING REMARKS

Urban vitality of local centres, particularly in suburban contexts, is determined not only by the presence of functional amenities, but also by the co-location of diverse socio-cultural activities. Such an expanded range of functions enables a higher frequency of visits, prolonged stays, and a greater number of opportunities for social encounters. However, the long-term vitality and sustainability of smaller and suburban centres depend not only on the diversity of programmatic content, but also on the existence of well-designed, accessible, and attractive open public spaces that can support everyday social interaction, encourage longer stays, and strengthen the sense of place and community identity. It is the interaction between functional diversity and the quality of public space that contributes to the long-term sustainability of smaller and suburban centres.

The analysis indicates that the centrality of the suburban settlement Veternik is predominantly functional in character, with limited social capacity. The centre is primarily used for the performance of everyday activities, while activities that encourage longer stays and social interaction are less represented. Although processes of urban expansion, growth, and the increasing integration of Veternik with Novi Sad, have contributed to the decentralisation of certain central functions, the social dimension of centrality remains underdeveloped, while remaining equally essential. The research findings indicate that residents' needs for centrality and social interaction are expressed through various urban functions and amenities that do not primarily serve a social purpose, but temporarily assume the role of spaces for encounters and social exchange. However, their spatial and functional capacities to support more intensive and continuous social interactions remain limited. The findings further suggest that the formation and enhancement of centrality require the planned design of high-quality public spaces, as well as the development of diverse urban amenities capable of fostering socialisation, recognisability, and the identity-forming role of the settlement centre.

### ACKNOWLEDGEMENT

This research has been supported by the Ministry of Science, Technological Development and Innovation (Contract No. 451-03-34/2026-03/200156) and the Faculty of Technical Sciences, University of Novi Sad through project "Scientific and Artistic Research Work of Researchers in Teaching and Associate Positions at the Faculty of Technical Sciences, University of Novi Sad 2026" (No. 01-3609/1).

## REFERENCES (STYLE: LITERATURA)

[1] A. Münter and K. Volgmann, "Polycentric regions: Proposals for a new typology and terminology," *Urban Stud.*, vol. 58, no. 4, pp. 677–695, Mar. 2021, doi: 10.1177/0042098020931695.

[2] C. Zhong, M. Schläpfer, S. Müller Arisona, M. Batty, C. Ratti, and G. Schmitt, "Revealing centrality in the spatial structure of cities from human activity patterns," *Urban Stud.*, vol. 54, no. 2, pp. 437–455, 2017, doi: 10.1177/0042098015601599.

[3] R. J. Rogerson and B. Giddings, "The future of the city centre: Urbanisation, transformation and resilience-a tale of two Newcastle cities," *Urban Stud. J. Ltd.*, vol. 58, no. 10, pp. 1967–1982, 2021, doi: 10.1177/0042098020936498.

[4] T. Szabó, B. Szabó, and Z. Kovács, “Polycentric urban development in post-socialist context: the case of the Budapest Metropolitan Region,” *Hungarian Geogr. Bull.*, vol. 63, no. 3, pp. 287–301, 2014, doi: 10.15201/hungeobull.63.3.4.

[5] L. Sýkora and K. Stanilov, “The Challenge of Postsocialist Suburbanization,” in *Confronting Suburbanization: Urban Decentralization in Postsocialist Central and Eastern Europe*, K. Stanilov and L. Sýkora, Eds. John Wiley & Sons, Ltd., 2014, pp. 1–32.

[6] M. Carević, “Mešovite namene – ključni parameter planiraja savremenih gradova,” Fakultet tehničkih nauka Univerziteta u Novom Sadu, 2017.

[7] M. Dinić, “Restruktuiranje centara suburbanih naselja - mogućnosti unapređenja modela od funkcionalnog zoniranja ka mešovitim funkcijama,” Građevinsko-arhitektonski fakultet Univerziteta u Nišu, 2015.

[8] C. Alexander, S. Ishikawa, and M. Silverstein, *A Pattern Language - Towns, Buildings, Construction*. New York: Oxford University Press, 1977.

[9] L. Yu, W. Zheng, T. Yu, and Y. Wu, “How to identify urban centers/subcenters in metropolises? An analytical review,” *Habitat Int.*, vol. 115, no. 102397, pp. 1–10, 2021, doi: 10.1016/j.habitatint.2021.102397.

[10] JP Urbanizam, “Prostorni plan Grada Novog Sada,” Službeni list Grada Novog Sada, 2012.

[11] Republički zavod za statistiku, “Popis stanovništva, domaćinstava i stanova 2022: Starost i pol (Knjiga 2),” Beograd, 2023.

[12] M. Kostreš, “Urbano-ruralne veze i odnosi između naselja,” Fakultet tehničkih nauka Univerziteta u Novom Sadu, 2012.

[13] JP Urbanizam, “Plan generalne regulacije naseljenog mesta Veternik,” Novi Sad, 2015.

[14] JP Urbanizam, “Plan generalne regulacije centra u Veterniku,” Novi Sad, 2021.

https://doi.org/10.24867/INDIS-2026-EN-647



# SUSTAINABILITY OF CULTURAL HERITAGE OF KOTOR REGION ON THE WORLD HERITAGE LIST

*Ilija Lalošević*[1]

***Summary:***

The paper is dealing with conservation and structural consoliodation of historic buildings in the old urban core of medieval town of Kotor, and its region, inserted on the World Heritage List after Montenegro earthquake 1979. Kotor case study proved that all historic buildings are not weak simply because they are old and made of stone masonry. Some historic buildings, like some modern buildings, are weak because they were poorly and unskillfully built, they were inadequately altered during their history, or because they were bad maintained. Some historic buildings are stable due to good materials used, the quality of workmanship, design and overall disposition. In the paper sustainability of traditional buildings are discussed, focusing on the most important Kotor historic buildings and their seismic response. Recommendations for improving conservation procedures and choosing appropriate contemporary strengthening techniques are made.

*Keywords: conservation, structural consolidation, sustainability, cultural heritage, Kotor, seismic resistance*

## ODRŽIVOST KULTURNOG NASLJEĐA PODRUČJA KOTORA NA LISTI SVJETSKE BAŠTINE

***Rezime:***

Rad se bavi konzervacijom i sanacijom istorijskih građevina gradskog jezgra srednjovjekovnog Kotora i njegovog područja na Listi svjetske baštine poslije Crnogorskog zemljotresa 1979. godine. Primjer Kotora dokazuje da građevine same po sebi nisu slabe jer su stare i građene kao zidane strukture. Neke stare građevine, poput nekih savremenih, su slabe, jer su loše i nestručno građene, neadekvatno prepravljane, ili loše održavane. Neke stare građevine su stabilne zahvaljujući dobrom materijalu, kvalitetu izvođenja, projektu i opštoj dispoziciji. U radu se razmatra održivost tradicionalnih konstrukcija, s posebnom pažnjom na najznačajnije građevine Kotora i njihovo ponašanje u zemljotresima. Date su preporuke za poboljšanje konzervatorskih procedura i izbora adekvatnih savremenih tehnika ojačanja.

*Ključne riječi: konzervacija, statička sanacija, održivost, kulturna baština, Kotor, seizmička otpornost*

[1] Full Professor, Faculty of Architecture, University of Montenegro, Podgorica, Montenergo, ilalos@t-com.me

## 1. INTRODUCTION

When dealing with structural consolidation and conservation of historic buildings, the extremely variable quality of building materials and construction systems is evident. Except for timber buildings, most historic structures are unframed masonry buildings, made of unburned earth, brick, or stone, connected with binding mediums. Each of these materials varies widely in form and mechanical and other properties.

Masonry structures generally are considered to be less resistant to earthquakes. Masonry materials, both mortar and stone/brick are stiff and brittle, have quite high compressive, but low tensile and shear strength. Masonry constructions have a high mass, hence their high inertial response to the earthquakes, they are rigid and have low ductility and low capacity for redistribution of stress.

However, the resistance of historic buildings can vary between quite good and poor, depending on the conditions of the building affected. The 1979 Montenegro earthquake brought to light, among disadvantages, numerous advantages and qualities of the traditional way of constructing historic buildings, especially in the Kotor region, included in the UNESCO's World Heritage List. Due to the conditions after the earthquake and treats of destructions, especially having in mind high concentration of the cultural heritage, the old urban core of Kotor within the medieval walls was also inserted in the World Heritage in Danger List. After successfully preservation and reconstruction works the town was withdrawn from the World Heritage in Danger List in 2003.

By exploring the previous earthquake history, by analyzing relevant data, dates of occurrences, intensities, magnitudes etc., and by "in situ" investigations, continuity and interruptions in the "local seismic culture" could be better understood and followed. The shorter the return periods are, the most widespread seismic culture is. Due to the numerous earthquakes (dates and intensities of the stronger earthquakes: 1559-IX, 1563-X, 1608-X, 1632-IX, 1639-IX, 1667-X, 1750-VIII, 1780-IX, 1979-X), [1], 15-17, good building tradition, and economic prosperity during Byzantine, Serbian and Venetian role, in the Kotor region there are evidences of the appropriate construction technical procedures.

## 2. DISPOSITION AND DESIGN

### 2.1. LOCATION

One of the most significant issues to be analyzed regarding settlements, ensembles and individual buildings, is their location. The part of the old town of Kotor on the foot of San John Hill, funded on the rock, suffered slight damage during the earthquakes, and still have preserved the highest concentration of the oldest buildings from XII and XIII century. From the other hand, one of the reasons of collapse of the belfries and western facade of St. Tryphon's Cathedral in the 1667 earthquake, was different movement of the two parts of the building, due to the kind of soil (rock-send).

Settlements built on the rock (Perast, Drazin Vrt) suffered less damage than those funded on the mealy ground (Risan, Prcanj, Dobrota), even with identical or very similar design and quality of structures. It is interesting to point out the example of the churches built on the monolithic stone (St. George, Orahovac) and islands (St. George Monastery, Perast), that suffered less damage than other similar relevant cases (Our Lady of the Rock Church on the artificial island etc.).

## 2.2. DESIGN

Although criteria for earthquake resistant design have been established for the new buildings, [2], they can be usefully applied to the existing ones, both before the earthquake, to assess their vulnerability, and "post festum", to explain their behavior during the seismic events.

The building configuration, structural form, and design, have significant effects on the relevant behavior during an earthquake. The Montenegro 1979 earthquake, like many others, demonstrated that the simplest structures have the greatest chance of survival. ***Simple*** buildings are sustainable, can easily be built, maintained and repaired. On the other hand, their response to the earthquake can relatively easily be analyzed and determined.

It has been also recognized that the building plan in general is ***symmetrical***. Symmetry simplifies construction and improves response to earthquakes. On the contrary, lack of symmetry, which is rather rare case with historic buildings, produces torsion effects, which can be very destructive. For the most number of the relevant historic buildings their overall shape is ***compact*** and ***not too elongated.*** Otherwise, there are more chances of different earthquake movements being applied to the terminals. Elongated plan (60 x 6 m), beside sand soil, and lot of changes during building history, has been the main reason for the collapse of the central part of the Prince's Palace at Kotor during the 1979 earthquake (fig 1). Fortunately, the cases with extreme discrepancy between horizontal dimensions in traditional architecture are rather rare.




*Fig. 1. Kotor, Pince's Palace, ("Palazzo del Provveditore") XVIc, 15.04.1979.*

Although the excitement and the damage of the building depend upon the relationship between its natural frequency and the frequency of the earthquake, general recommendation is: the building ***should not be too high***. Actually, usual height of a historic building in the relevant region doesn't exceed its fourfold shorter horizontal dimension, recommended for the modern buildings [2], 82. That's why overturning effects are rather rare in the case of historic buildings.

Of course the exceptions are belfries. For instance, as already mentioned, in the occasion of severe 1667 earthquake two belfries of the Romanesque St. Tryphon Cathedral (fig. 2.) collapsed at all. The influence of that earthquake on the local seismic culture, can be seen in the fact that the belfries built after 1667 had no damage at all during the recent 1979 earthquake.

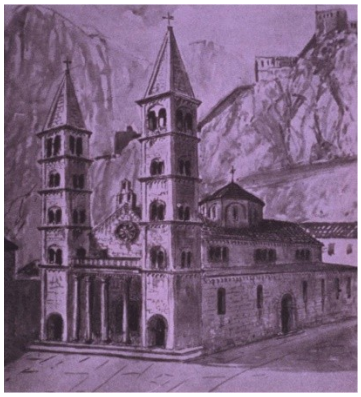

*Fig. 2. S. Tryphon Cathedral, Kotor, Ideal reconstruction, XII c.*

It is also important that the building ***vertical cross-section is regular***, setbacks and especially reverse setbacks, i.e. enlargements in the building upper region should be avoided. Still, in some cases, functional reasons dictated exactly like irregular vertical cross section, for example at belfries. It is well known that St. Luke's Church belfry collapsed and was rebuilt a several times during 800 years of the building history [3], 59.

The most representative palaces in the Kotor Bay, built under the influence of Venetian architecture, have the main facades with added central upper part which form loft (Italian: "belvedere"). Although originally there were attempts to connect this part with the rest of the building (with iron ties and wooden beams), during an earthquake the high stress concentration occurs at the region of discontinuity, producing cracks, partial, or even total collapse of the central part (fig 3).



*Fig. 3. Tripkovic Palace, Dobrota-Kotor, XVIII c., 15.04.1979.*

Irregularity is appearing in dome churches cross section too. However, these constructions vary radically in their seismic response, depending on their size, shape and overall construction system of upper parts of the building. For instance, at the primary dome of St. Tryphon's Cathedral, (fig. 2.), which was collapsed in 1667 earthquake, appeared problem of discontinuity of construction, and self-standing pillars, non-adequate elements carrying the heavy dome, and suffering from extreme seismic vibrations (effect of so called "soft ground-floor").

The St. Mary of the River Church's (fig 4,5.) and St. Luke Church's domes have been conceived and built more adequately; their narrowing and discontinuity are less expressed. They have been carried by strong pilasters and transversal and attached arches, which are in monolith connection with walls and vaults. In the base of the dome, there is a ring made of long slates of excellent stone which successfully accepts forces and gathers all arches.

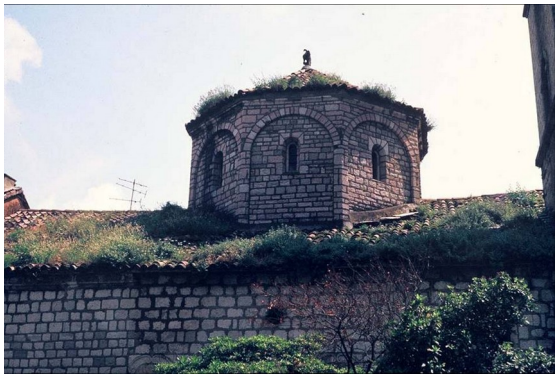



*Fig. 4. S. Marry of the River Church Fig. 5. S. Marry of the River Church, interior*

At St. Luke's Church, above the mentioned ring there are two additional rows of long (45-55 cm) and low (13, 10 cm) very precisely dressed slates of the same stone (fig 6, fig 7). This certain collar, made completely reconcile with contemporary theories, [4], 171, 180, had a crucial role in reception tensile forces in the base of the dome, and had a significant contribution in stability of whole building [5], 58. Such a way of constructing a circular tie in the bottom of the dome is already known from the much older Byzantine

buildings, where were some cases with stone blocks connected with iron anchors, so they can behave as a kind of a chain [6], 50. In order to improve overall, and in the same time seismic stability, upper part of the dome very often was made of lightweight stone, tuff (fig. 7).

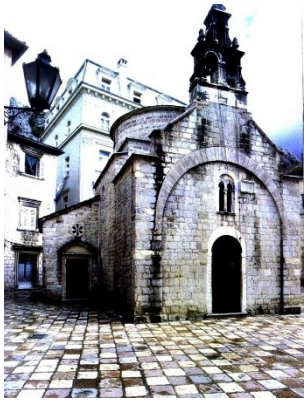

*Fig. 6. S. Luke Church, Kotor*

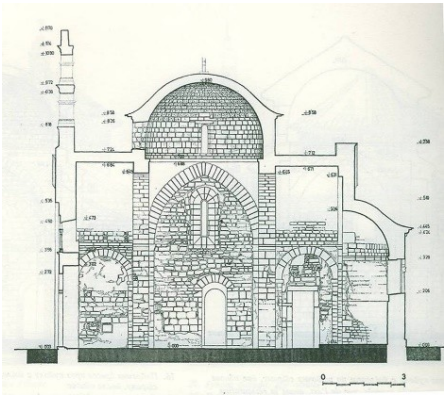

*Fig. 7. S. Luke Church, Kotor, cross section*

Historic earthquake–proof buildings have quite ***uniform and continuous distribution of strength*.** Their load bearing elements are uniformly distributed, continuous and without changing section suddenly. Should be noted similarity of St. Luke's Church, the most successful seismic-proof historic building in Kotor, with the prescriptions of the much later Piro Ligurio's manuscript manual (fig 8.).[1]

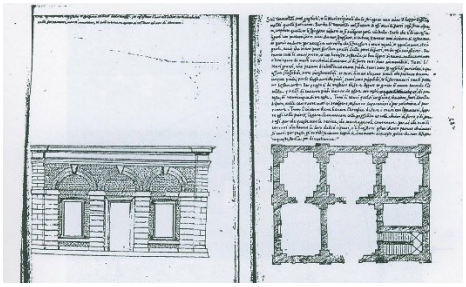

*Fig. 8. Pirro Ligorio: Delli rimedi contra I terremoti per la sicurezza degli edifici, vol.XVIII, State Archive Torino*

## 3. ELEMENTS AND TECHNIQUES

Reasonable resistance of the historic buildings can be often explained by the evidence of suitable traditional techniques. Study of old techniques and elements is essential in the process of repair and strengthening of historic buildings, whatever traditional or modern techniques being applied.

[1] Proposal of an earthquake-proof house ("casa antisismica") in manuscript: Pirro Ligorio, Delli rimedi contra I terremoti per la sicurezza degli edifici, vol. XVIII, State Archive Torino, Published in: Costruire in Laterizio, 16/90, Interventi in zone sismiche, II, Milano, 1990, 249

The ***walls*** of the historic buildings in the Boka Kotorska Bay were made of the local limestone, as binding medium always was used lime mortar. The local limestone is too hard and non-adequate for the elements of more remarkable dimensions, that's why for the doors and windows frames, consoles, balconies, stairs etc., have been used limestone from Korčula island, near Dubrovnik.

It is interesting to point out that the way of wall construction was almost the same from XIV to the end of XIX century. There are two stone faces of the wall: external and internal; in the middle there is mixture of smaller pieces of stone and lime mortar. It wasn't practiced to connect two faces of the wall by bond headers, even this should be the case. Despite of this fact, evidence of detachment of the two faces of the wall is rather rare, due extremely good quality of ***mortar*** used. Wall mortar is one of the main reasons for the survival of masonry structures during earthquakes in the long building history of Boka Kotorska region.

Walls strengthen with ***pilasters***, especially in churches, contribute to the raise of inertial moment of the building and to its overall stability. Those elements were suggested by mentioned old manuals for the improvement of the building earthquake resistance.[1]

Walls with similar elements, ***buttresses*** and ***escarpments***, used for various purposes, for example fortifications, of course, have also good seismic response, being conceived and designed to be strong enough to accept artillery shots.

***Vaults*** and ***arches*** are very often used constructive elements, playing crucial role in the earthquake stability of the buildings. Not adequately executed arches, especially vaults, usually cause strong damage and even collapse of the whole structure. On the other hand, some of them, especially pointed arches precisely cut out from the good limestone, with extremely thin joints, are seismic proof constructions, what was proved by their stability through numerous earthquakes, including the last one occurred 1979. Of course, iron ties have been very important additional, sometimes crucial element for their stability (fig 9).

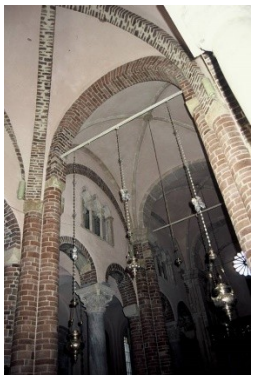

*Fig. 9. S. Tryphon Cathedral, Kotor, interior*

In buildings with unconnected walls and wooden ***floor structures***, they will separate, and cracks will develop along vertical joints, usually in the openings region. If the walls are connected properly with the floors, they have to oscillate harmoniously, and the behavior

[1] Proposal of an earthquake-proof house ("casa antisismica") in manuscript: Pirro Ligorio, op. cit.

and earthquake response is much better. In the traditional workmanship in Boka Kotorska Bay, walls have been usually connected by ties, be iron, or wooden beams of the floor structure with iron terminals, “keys” (italian: “capochiave”) on the opposite facades (fig 10).



*Fig. 10. Gregorina Palace, Maritime museum, Kotor, XVIII c.*

Taking into account the nature of the earthquake movements and the seismic behavior of the buildings, it is evident that the level of the most desirable connection is in the top of the structure, under the roof (fig 11). Otherwise, roof timber rafters or vaults push and disintegrate the walls.



*Fig. 11. Radimiri Palace, Dobrota-Kotor, XVII c.*

Almost all buildings originally properly tied suffered no, or very little, acceptable damage. In these cases introducing numerous reinforced concrete elements was useless, even contra productive, not only for the building authenticity but also for the overall building stability. That’s why reinforced concrete slabs, wall jackets, vertical internal or external pillars, sometimes destroying the very strong building corners, and especially heavy concrete roofs, should be avoided. The best practice would be: proper tying and connecting, rebuilding of collapsed parts, grouting, and only eventually, minimum, and wise introducing reinforced concrete elements when necessary.

It is important to point out attention paid by the old masons to the ***openings***. The vaults and arches have been constructed over the openings, in order not to load stone lintels of the doors/windows frames, but to distribute weight to the piers. That’s because the fact that the lintels can crack even due to the static load. Moreover, due to dynamic seismic forces, lintels broke and walls crack around the openings, being weakened in those places.

## 4. CONCLUSIONS AND RECOMMENDATIONS

Despite of widespread presumption that historic buildings, especially masonry structures in seismic prone regions are weak, it is a fact that sometimes they are very resistant. This is proved by the evidence of their existence so long time in those areas. In the region of Boka Kotorska Bay there is evidence of the numerous sustainable constructions and techniques, due to simultaneous strong seismic activity, economic prosperity and cultural links within wide Mediterranean region from Venice to Constantinople.

The most recent earthquake in the region, like in other similar cases, has demonstrated that we can usually rely on the most existing constructive elements: foundations, walls, vaults, floors etc. Although, there are evident attempts to tie the structure, generally insufficient anchorage and particularly inadequate interlocking between rafters, beams and walls, in the roof and floor levels, are often serious disadvantages.

However, it is important not to ignore entire traditional buildings or their parts, because some of them are weak. Contrary, solution for the strengthening and repair must be based on the actual resistance and capacity, structural conditions, and sustainability. From the historic preservation point of view, it is necessary to consider, analyze, assess and preserve and retrofit those elements relevant for structural stability of the traditional structures. For the successful preservation of an old structure, a team work of experts from different profiles is needed.

The main question in this process is how far we should go as to the level of safety and the extent of the interventions. Methods and techniques for repair and strengthening have to provide economically justified and technically consistent structural safety, as well as acceptable damage level in the future earthquakes. If structural interventions doesn’t go beyond obtaining reasonable security, preserving human lives and building integrity, preventing sudden collapse, but not damage at all, original structural system usually can be satisfactory preserved.

In order to improve, not degradate authentic structural system, being the important value of historic building, a special approach in consolidation methodology must be developed taking into account the most important principles of historic preservation. Consolidation of these buildings cannot be performed using design codes for modern structures, and should consider traditional materials and techniques. Of course, modern technology can be used, but always having in mind that basic problem in structural consolidation of these buildings is compatibility of the introduced techniques and materials with old ones. Introduction of new elements for repair and strengthening should be minimum, possibly reversible, and must assure sustainability and authenticity preservation.

## REFERENCES

[1] Mihailović, J., Seizmički karakter i trusne katastrofe našeg južnog primorja (Seismic Character and Earthquake Catastrophes of Our South Adriatic Coast), Beograd, SANU, 1947

[2] Dowrick, D.J, Earthquake Resistant Design, A Manual for Engineers and Architects, John Wiley&Sons, London, 1977

[3] Lalošević, I, Aseizmičke karakteristike crkve Sv. Luke u Kotoru (Seismic proof Characteristics of the St. Luke's Church in Kotor), Simpozijum: Crkva Sv. Luke kroz vjekove (Symposium: Church of St. Luke's through the Ages), Kotor, 1997

[4] Tahirović, I, Otpornost zidane kupole na djelovanje zemljotresa, uzroci za pojavu pukotina i njihov pravac i područja rasprostiranja, (Resistance of the Masonry Domes…) Kulturna bastina Balkana i seizmički problemi (The Balkan Cultural Heritage and Seismic Problems), CANU, Titograd , 1983

[5] Čanak Medić, M, St. Luke in the New Theory, Matica Srpska, Zbornik za likovne umetnosti 21, Novi Sad 1985

[6] Repair and Strengthening of Historic Monuments and Buildings in Urban Nuclei, Buildings Constructions in the Balkan Region, vol. 6, UNDP, Vienna, 1984

https://doi.org/10.24867/INDIS-2026-EN-867



# VERTICAL ARCHITECTURE AS AN EXPRESSION OF INVESTMENT SYSTEMS: THE TRANSFORMATION OF BELGRADE SKYLINE

*Sandra Šlegl[1], Đuro Krnić[2]*

***Summary:***

This paper investigates the transformation of Belgrade's skyline through different investment systems and their influence on vertical architecture. In the context of contemporary investment flows, vertical architecture represents a spatial expression of development processes through the construction of high-rise buildings that transform the urban silhouette. The objective of the research is to analyze how state, transitional, private and hybrid investment models shape architectural form, public space and urban identity. The methodology combines theoretical analysis of urban political economy and spatial production with comparative case studies of representative high-rise buildings in Belgrade. The results indicate that each investment model generates distinct spatial and aesthetic patterns, directly influencing the morphology of the contemporary city profile. The paper concludes that vertical architecture represents a spatial manifestation of capital and broader socio-economic transformations within the city.

*Keywords: vertical architecture, investment systems, skyline, urban transformation, capital, public space*

# VERTIKALNA ARHITEKTURA KAO IZRAZ INVESTICIONIH SISTEMA: TRANSFORMACIJA URBANE SILUETE BEOGRADA

***Rezime:***

Rad istražuje transformaciju urbane siluete Beograda kroz različite investicione sisteme i njihov uticaj na vertikalnu arhitekturu. U kontekstu savremenih investicionih tokova, vertikalna arhitektura predstavlja prostorni izraz razvojnih procesa kroz izgradnju visokih objekata koji transformišu urbanu siluetu grada. Cilj istraživanja jeste analiza načina na koji državni, tranzicioni, privatni i hibridni investicioni modeli oblikuju arhitektonsku formu, javni prostor i urbani identitet. Metodologija kombinuje teorijsku analizu urbane političke ekonomije i teorije produkcije prostora sa komparativnim studijama slučaja reprezentativnih visokih objekata u Beogradu. Rezultati ukazuju da svaki investicioni model proizvodi specifične prostorne i estetske obrasce, koji direktno utiču na morfologiju savremenog profila grada. Rad potvrđuje da vertikalna arhitektura predstavlja prostornu manifestaciju kapitala i širih društveno-ekonomskih transformacija grada.

*Ključne reči: vertikalna arhitektura, investicioni sistemi, urbana silueta, urbana transformacija, kapital, javni prostor*

[1] PhD Student, MSc, Faculty of Technical Sciences, University of Novi Sad, Novi Sad, Serbia, slegl.dc4.2024@uns.ac.rs, ORCID ID: 0009-0009-3037-1084
[2] Teaching assistant., MSc, Faculty of Technical Sciences, University of Novi Sad, Novi Sad, Serbia, djuro.geo@uns.ac.rs, ORCID ID: 0000-0003-4481-3209

## 1. INTRODUCTION

Contemporary urban development is increasingly conditioned by the interaction between capital flows, governance structures and investment mechanisms that directly influence the production of urban space. A skyline is the distinctive visual silhouette of a city, formed by the arrangement, height and shape of its buildings, particularly high-rise structures, as seen against the horizon. Within contemporary neoliberal urbanization processes, architecture can no longer be interpreted solely as an autonomous artistic or technical discipline, but rather as a spatial and institutional outcome of broader political-economic relations. In this context, vertical architecture occupies a particularly significant position because high-rise structures represent some of the most visible indicators of urban transformation, investment concentration and symbolic power within the contemporary city [1].

The relationship between architecture and capital has become increasingly significant within theories of urban political economy and spatial production. Lefebvre argues that urban space is socially produced through systems of power, organization and economic relations rather than passively occupied by society [2]. Harvey further interprets urbanization as a mechanism of capital accumulation, emphasizing that architectural and urban transformations are directly conditioned by investment cycles, financial systems and market restructuring [3]. Contemporary urbanization is therefore increasingly shaped by processes of privatization, commercialization and financialization of urban space, where architecture functions simultaneously as built environment, investment asset and instrument of symbolic representation [4].

Within such conditions, vertical architecture reflects not only technological development and formal ambition, but also the organizational logic of contemporary investment systems. Skyscrapers emerge as highly capital-intensive structures requiring concentrated financial resources, long-term investment coordination and institutional support. Consequently, the vertical profile increasingly operates as a visual indicator of economic power, urban competitiveness and capital distribution within globalized urban systems [5].

The transformation of Belgrade’s skyline clearly illustrates these processes. Unlike cities developed through coherent long-term planning strategies, Belgrade evolved through successive political and economic transitions that generated heterogeneous forms of vertical urbanization. During the socialist period, high-rise structures were primarily produced through centralized state planning, functioning as symbols of collective identity, institutional stability and modernist progress. Buildings such as Genex Tower represented monumental expressions of state-controlled urban development and ideological representation [6].

Following the collapse of socialism and the transition toward market-oriented urbanism, new investment systems introduced fragmented privatization processes, speculative construction and commercially driven development models. Contemporary projects such as West 65 Tower, Belgrade Tower and Skyline Complex increasingly reflect hybrid forms of investment combining global capital, private development and public regulation. In this context, architecture becomes progressively embedded within market-oriented strategies of branding, exclusivity and real-estate valorization [7].

The urban silhouette therefore becomes more than a visual composition of tall buildings. It can be interpreted as a spatial indicator of successive political-economic transformations and investment regimes. Each vertical structure embodies the financial and organizational logic of the system that produced it, influencing architectural aesthetics, public accessibility and urban identity. The morphology of contemporary Belgrade reveals the gradual transition from centrally planned urbanism toward

investment-driven spatial production, where architectural form increasingly emerges from profitability calculations, market positioning and investment strategies rather than comprehensive urban planning principles [8].

The objective of this research is to investigate how different investment systems influence the production of vertical architecture and the transformation of Belgrade's skyline. The paper examines the relationship between investment structures, architectural articulation and public space through comparative analysis of representative high-rise developments from different historical and economic periods. Particular attention is given to the relationship between capital, monumentality, skyline integration and transformation of public space.

The paper starts from the hypothesis that contemporary vertical architecture in Belgrade does not emerge from a unified urban vision, but rather represents a fragmented spatial expression of changing investment systems and capital flows. Consequently, the skyline can be interpreted as a morphological diagram of broader economic and social transformations within the contemporary city.

## 2. CAPITAL, SPACE AND VERTICAL URBANIZATION

The relationship between capital and architecture represents one of the defining characteristics of contemporary urban development. Within neoliberal urbanization processes, cities increasingly operate as platforms for investment accumulation, while architecture functions simultaneously as spatial infrastructure, financial asset and symbolic representation of economic power [3].

Theories of spatial production emphasize that architecture cannot be separated from the economic and political structures that generate it. Lefebvre argues that urban space is socially produced through relations of power, organization and capital [2]. Harvey identifies urbanization as a mechanism through which surplus capital is absorbed and reproduced, directly connecting architecture with processes of investment accumulation and spatial restructuring [4]. Similarly, Smith interprets uneven urban development as a consequence of capitalist spatial organization and differentiated investment cycles [5].

Contemporary vertical urbanization is closely connected to the financialization of urban space, where architecture increasingly functions not only as built environment, but also as an investment asset integrated into global capital circulation [1]. High-rise buildings therefore emerge as instruments of economic visibility and urban competitiveness. This process is closely related to broader neoliberal restructuring and the increasing role of cities within global economic competition [11,12]. Their construction requires concentrated financial investment, institutional coordination and long-term market forecasting. Consequently, skyscrapers reflect the logic of capital organization as much as technological advancement or architectural innovation.

The growing influence of real-estate development further transformed the relationship between architecture and capital. Developers increasingly function as dominant actors in shaping urban form, influencing decisions related to density, spatial hierarchy, public accessibility and urban identity. Investment indicators such as profitability, market value and return expectations directly affect architectural articulation and program distribution [7]. Such processes correspond to broader forms of neoliberal urban restructuring observed across contemporary cities, where urban development is increasingly shaped by market-oriented governance and investment priorities [12].

As a consequence, many contemporary skyscrapers prioritize iconicity, visibility and commercial differentiation, often producing fragmented urban environments characterized by privatized public spaces and selective accessibility.

Within transitional cities such as Belgrade, these processes become particularly visible because different economic systems coexist within the urban fabric. Socialist modernism, post-socialist privatization and global investment urbanism each produced distinct forms of vertical architecture reflecting specific political and financial conditions. The skyline therefore represents a layered spatial record of changing investment regimes and economic transformations. Through the analysis of representative high-rise developments, it becomes possible to identify how capital shapes not only urban growth, but also architectural aesthetics, public space and collective urban identity. The main relationships identified through the theoretical framework and comparative case-study analysis are summarized in Tab. 1.

*Tab. 1 Investment Systems and Their Spatial Effects*

| Investment system | Dominant economic logic | Architectural consequence | Spatial organization | Type of public space |
|---|---|---|---|---|
| Socialist state model | Collective modernization | Monumentality and permanence | Centralized planning | Public and collective |
| Transitional model | Fragmented privatization | Spatial inconsistency | Weak institutional control | Degraded public space |
| Private investment model | Market profitability | Exclusivity and luxury | Selective accessibility | Commercialized public space |
| Hybrid investment model | Public-private partnership and global capital | Iconicity and branding | Managed urban environments | Semi-public / regulated |

## 3. INVESTMENT SYSTEMS AND THE TRANSFORMATION OF BELGRADE SKYLINE

The contemporary skyline of Belgrade reflects successive transformations of political economy and investment organization that have shaped the city throughout different historical periods. Unlike cities developed through coherent urban strategies, Belgrade evolved through discontinuous economic transitions that produced fragmented forms of vertical urbanization. High-rise architecture in Belgrade therefore represents a spatial consequence of changing investment systems and governance models rather than a unified architectural language.

During the socialist period, vertical architecture primarily emerged through centralized state planning and socially owned development structures. High-rise buildings were conceived as symbols of modernization, technological progress and collective identity. Projects such as Genex Tower embodied the ideological ambitions of socialist Yugoslavia, combining monumentality, infrastructural integration and institutional representation [6]. Architecture functioned within a system where urban development was directed through long-term planning strategies rather than market profitability. Public space, collective accessibility and infrastructural coherence therefore occupied a central role within the production of vertical architecture.

The collapse of socialism and the transition toward market-oriented urbanism introduced radically different spatial dynamics. During the 1990s and early 2000s, deregulated privatization processes, economic instability and speculative investment significantly

transformed urban development practices. Vertical construction increasingly became associated with fragmented planning, private capital and market-driven spatial organization [9].

Contemporary high-rise developments in Belgrade increasingly reflect hybrid forms of investment combining domestic private capital, international financing and public-private partnerships. Projects such as West 65 Tower, Belgrade Tower and Skyline Complex demonstrate the growing influence of global investment logic on architectural production. Their architectural language emphasizes exclusivity, visibility, luxury and market positioning, while urban space increasingly becomes commercially structured and selectively accessible. In such developments, the skyline functions not only as an urban composition, but also as an instrument of branding, economic representation and symbolic competition between investment systems [9].

These transformations reveal how different forms of capital generate distinct architectural and spatial consequences. State-controlled urbanism produced monumental and infrastructurally integrated forms of verticality, while contemporary investment urbanism prioritizes market visibility, financial efficiency and privatized urban experience. The morphology of Belgrade's skyline therefore represents a spatial archive of changing economic systems and organizational models, while a conceptual interpretation of these transformations is presented in Fig. 1.

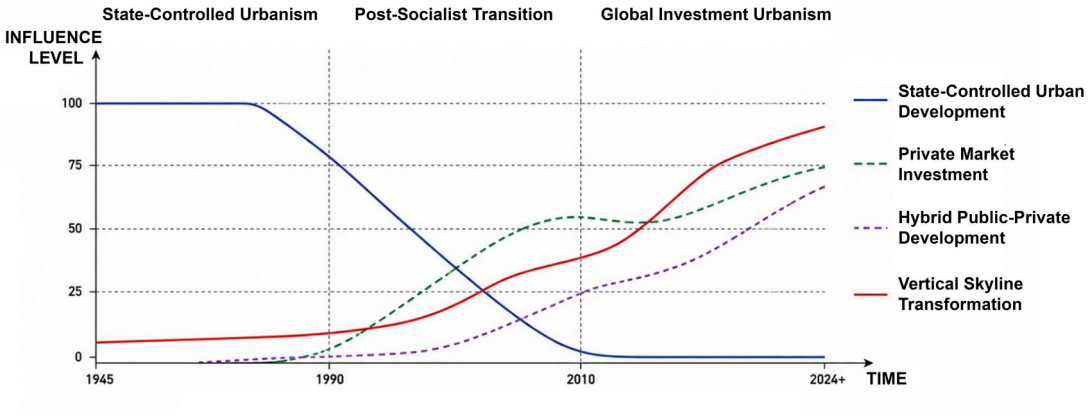


*Fig. 1 Transformation of Belgrade Skyline Through Changing Investment Systems*

The diagram presents an interpretative comparative model of the transformation of Belgrade's city profile through successive investment systems and urban development regimes. It illustrates the changing influence of state-controlled urbanism, private market investment and hybrid public-private development on the production of vertical architecture from the socialist period to contemporary global investment urbanism. The graph does not represent quantitative statistical data, but a theoretical interpretation of dominant spatial and economic processes that shaped the morphology and intensity of vertical urban development in Belgrade over time. It serves as a conceptual model developed by the authors.

## 4. METHODOLOGY

This research is based on an interdisciplinary methodological framework that combines architectural analysis, urban political economy, spatial theory and comparative case-study research. The methodological approach is developed in accordance with the central hypothesis of the paper: that vertical architecture in Belgrade represents a spatial and aesthetic expression of changing investment systems, governance structures and capital flows.

The first methodological level is theoretical. It establishes the conceptual relationship between capital, space and architectural form through theories of spatial production and urban political economy [2,3]. Within this framework, architecture is interpreted as a material and spatial outcome of broader economic and institutional structures. The second methodological level is historical and contextual. It identifies four dominant investment regimes that shaped the development of vertical architecture in Belgrade:

- the socialist state-controlled model,
- the transitional fragmented market model,
- the private investment model and
- the hybrid public-private investment model.

Each system is examined in relation to financing mechanisms, ownership structures, planning organization, governance models and approaches to public-space production.

The third methodological level is comparative case-study analysis. Five representative high-rise developments were selected: Genex Tower, Rudo Complex, West 65 Tower, Belgrade Tower and Skyline Complex. The cases were selected according to three criteria: historical representativeness, diversity of investment structures and visibility within the contemporary skyline of Belgrade.

The selected case studies represent different historical periods and investment configurations associated with the development of vertical architecture in Belgrade. To ensure methodological consistency and comparability, the same analytical framework was applied to each case study. The framework examines eight common criteria: investment model, historical context, ownership and governance, building function, skyline effect, architectural expression, relationship to public space and urban context, as summarized in Tab. 2. These criteria establish a common basis for examining how investment structures are reflected in architectural, spatial and urban characteristics. Their application to the selected cases is presented in Tab. 3.

*Tab. 2 Analytical Framework for Comparative Evaluation of High-Rise Developments*

| Criterion | Analytical focus |
|---|---|
| Investment model | State-planned, transitional, private or hybrid investment structure |
| Historical context | Period of construction and socio-economic conditions of development |
| Ownership and governance | Financing structure, ownership model and management system |
| Building function | Residential, office, hotel, mixed-use or commercial program |
| Skyline effect | Landmark, background structure, compositional, cluster or symbolic urban marker |
| Architectural expression | Monumentality, materiality, transparency, luxury and iconicity |
| Relationship to public space | Degree of openness, accessibility, control and commercialization |
| Urban context | Planned development, fragmentation, megaproject or integrated urban composition |

The analysis combines qualitative architectural interpretation, comparative urban morphology and examination of investment and governance structures. The fourth methodological level is interpretative synthesis, through which the findings obtained from

the common analytical criteria are compared across the selected cases. This enables the identification of recurring relationships between investment systems, architectural expression, skyline role, public-space conditions and urban context, without assuming a direct or deterministic relationship between investment structure and architectural form.

## 5. CASE STUDIES

The selected case studies constitute a comparative analytical framework through which the relationship between investment systems and vertical architectural production in Belgrade can be examined. Rather than being interpreted as isolated architectural objects, the analyzed high-rise developments are understood as spatial manifestations of specific political-economic conditions, governance structures and capital organization models. The comparative approach enables the identification of recurring morphological, spatial and aesthetic patterns associated with different investment regimes, ranging from socialist state planning to contemporary private and hybrid investment urbanism. The comparative application of the analytical criteria defined in Tab. 2 is presented in Tab. 3.

*Tab. 3 Comparative Evaluation of Representative High-Rise Developments in Belgrade*

| Criteria | Genex Tower | Rudo Complex | West 65 Tower | Belgrade Tower | Skyline Complex |
|---|---|---|---|---|---|
| Investment model | State-planned socialist model | State-planned; fragmented | Private | Hybrid / global capital | Hybrid / private |
| Historical context | 1980; socialist modernization | 1976; socialist collective housing | 2021; post-transitional market-oriented | 2024; megaproject | 2022; mixed-use development |
| Ownership and governance | State-controlled | State / collective | Private; commercial | Public regulation | Private; commercial |
| Building function | Mixed-use: residential and office | Residential | Mixed-use: residential, commercial and services | Mixed-use: residential, hotel and commercial | Mixed-use: residential, office and commercial |
| Skyline effect | Symbolic gateway; major landmark | Residential landmark | Residential landmark | Dominant landmark | Compositional cluster |
| Architectural expression | Monumental twin towers | Repetitive towers | Transparent luxury-oriented | Iconic; vertical | Coherent multi-tower |
| Relationship to public space | Collective; restricted access | Collective; weakened management | Accessible; commercial selectively controlled | Visually open; regulated | Shared; regulated |
| Urban context | Planned New Belgrade | Planned New Belgrade | Transforming New Belgrade | Belgrade Waterfront | Central urban fabric |

The application of the same analytical criteria demonstrates the differences between the selected cases while maintaining a common methodological basis for comparison. The cases differ not only in investment model, but also in historical conditions, governance structures, functional organization, skyline role, architectural expression, public-space

conditions and urban context. Their comparison therefore enables the transformation of Belgrade's skyline to be interpreted as a multidimensional process rather than as a simple succession of building heights or architectural styles.

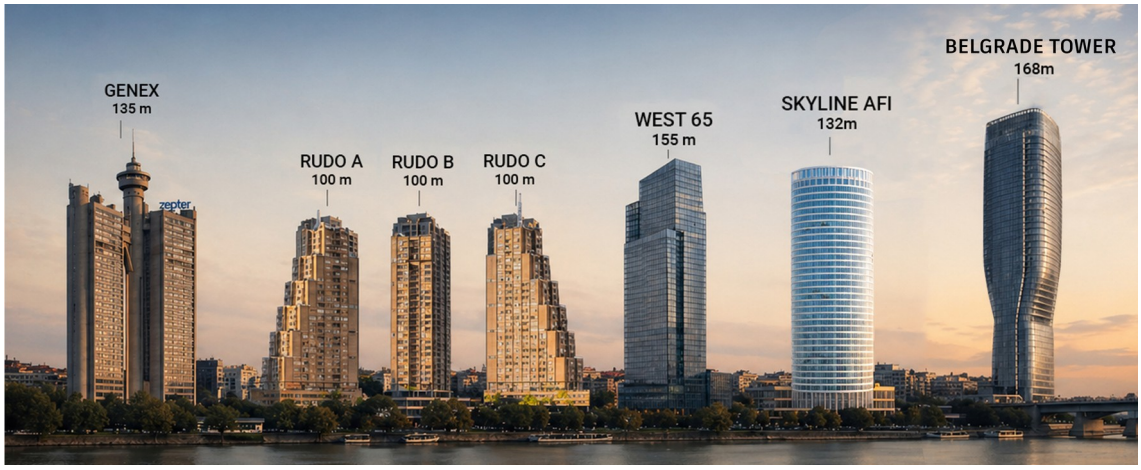


*Fig. 2 The Skyline of Belgrade*

## 5.1. GENEX TOWER, 1980: STATE CAPITAL AND INSTITUTIONAL MONUMENTALITY

Genex Tower represents one of the most significant examples of socialist vertical architecture in Belgrade. Developed within a state-controlled investment and planning system, the complex combines residential and office functions and occupies a strategic position at the western entrance to New Belgrade. Its construction reflected the broader objectives of socialist modernization, technological progress and institutional representation. The architectural expression of the building is characterized by monumentality, exposed concrete materiality and a distinctive twin-tower composition connected by a bridge structure. Unlike contemporary market-oriented towers that emphasize transparency, luxury and commercial branding, Genex Tower communicates permanence, collective identity and state authority through its scale and formal presence. As one of the most recognizable landmarks in Belgrade, the building plays a dominant role within the city’s skyline and functions as a symbolic urban gateway. Although highly visible and integrated into the collective urban image, its internal spaces are not fully publicly accessible, reflecting a mixed relationship between public visibility and functional restriction. The case demonstrates how socialist investment systems generated vertical architecture as an expression of institutional power, collective modernity and long-term urban planning objectives rather than market profitability.

## 5.2. RUDO COMPLEX, 1976: SOCIALIST HOUSING MONUMENTALITY AND POST-SOCIALIST MAINTENANCE FRAGMENTATION

The Rudo Complex was originally developed within the socialist state-planned housing system and therefore belongs to the socialist investment model in terms of its production. Designed as a large-scale residential development, the complex reflected the principles of collective housing provision and modernist urban planning that characterized the period of its construction. Architecturally, the complex is defined by repetitive residential towers, standardized construction methods and a strong visual presence within the eastern vertical profile of Belgrade. As one of the city’s most recognizable residential high-rise ensembles, it remains an important component of the urban silhouette despite the challenges that emerged during the post-socialist period. Its later evolution reveals the

consequences of fragmented ownership structures, weakened governance mechanisms and insufficient maintenance practices. Following the collapse of centralized management systems, collective spaces and building infrastructure gradually deteriorated, exposing the long-term vulnerabilities of large-scale housing developments operating without coordinated institutional support. The case illustrates that the success of vertical architecture depends not only on its original design and construction, but also on the continuity of governance, maintenance and financial management throughout its life cycle.

### 5.3. WEST 65 TOWER, 2021: PRIVATE CAPITAL AND SELECTIVE LUXURY

West 65 Tower represents the logic of private real-estate development in post-transitional Belgrade. Completed in 2021 as part of a large-scale private development in New Belgrade, the project combines residential, commercial and service functions within a market-oriented investment framework focused on profitability and real-estate value creation. Its architectural expression is shaped by transparency, contemporary façade design, luxury housing standards and visual differentiation within the competitive real-estate market. The tower's height, material treatment and formal articulation are directly connected to the production of market visibility and investment attractiveness. Within the contemporary skyline of Belgrade, West 65 functions as a prominent residential landmark and a visible symbol of private investment urbanism. Public space surrounding the development is formally accessible, yet functionally controlled through commercial programming, private management and selective use patterns. The project demonstrates how private investment systems transform vertical architecture into an instrument of lifestyle production, status representation and market differentiation, where architectural value is closely linked to economic performance and investment logic.

### 5.4. BELGRADE TOWER, 2024: HYBRID INVESTMENT AND THE SPECTACLE OF GLOBAL CAPITAL

Belgrade Tower represents a hybrid investment model in which public regulation, private development and global capital intersect. Completed in 2024 and rising to 168 meters, Belgrade Tower is currently the tallest building in Serbia and the dominant landmark of Belgrade's contemporary urban horizon. The tower forms the central element of the Belgrade Waterfront megaproject, one of the largest urban development initiatives in Southeast Europe. Such megaprojects are frequently interpreted as instruments of entrepreneurial urban governance and city-branding strategies within contemporary globalization processes [10,12]. The project combines residential, hotel and commercial functions within a highly visible architectural structure designed to operate simultaneously as real-estate product, urban landmark and branding mechanism. Its architectural expression is characterized by iconicity, vertical dominance, advanced facade technologies and strong visual presence along the Sava riverfront. Unlike earlier state-planned forms of vertical urbanization, Belgrade Tower emerged through a hybrid investment structure involving public authorities and foreign private capital. Public space within the surrounding development is carefully designed and visually accessible, yet largely regulated through commercial programming and private management practices. The case demonstrates how contemporary global investment systems utilize vertical architecture not only as built infrastructure, but also as a tool of urban branding, economic representation and international city positioning.

### 5.5. SKYLINE COMPLEX, 2022: INTEGRATED CONTEMPORARY MODEL

Skyline Complex represents a contemporary mixed-use development model that combines residential, office and commercial functions within an integrated high-rise composition. Developed through a hybrid investment structure, the project illustrates the growing tendency toward coordinated urban clusters rather than isolated vertical landmarks. Architecturally, the complex is characterized by a coherent composition of towers, contemporary material expression and an emphasis on spatial integration between different programs and building volumes. Unlike singular iconic towers, Skyline operates through the interaction of multiple structures that collectively shape the surrounding urban environment. Within Belgrade's skyline, the project functions as a compositional cluster that contributes to the diversification of the city's vertical profile. The surrounding open spaces, pedestrian areas and shared amenities improve spatial continuity; however, their operation remains largely dependent on private management and commercially regulated access. The project demonstrates a contemporary approach to vertical urbanization in which integration, mixed-use development and spatial coherence coexist with the investment logic of optimization, controlled accessibility and managed urban experience.

## 6. RESULTS AND DISCUSSION

The Results and Discussion section synthesizes the findings obtained through the comparative analysis of selected case studies and interprets them within the broader theoretical framework of urban political economy and spatial production. The analysis demonstrates that vertical architecture in Belgrade cannot be understood solely through formal or technological criteria, but must be interpreted as a spatial outcome of specific investment systems, governance structures and capital flows. By comparing different historical and economic models of urban development, the research identifies recurring relationships between investment logic, architectural articulation, public-space transformation and skyline morphology. The discussion therefore positions the contemporary skyline of Belgrade as a material and symbolic record of successive socio-economic transformations that have redefined the production of urban space, as synthesized in Tab. 4.

*Tab. 4 Comparative Synthesis of Investment Systems and Skyline Transformation*

| Building | Model | Key finding |
|---|---|---|
| Genex | Socialist state | Verticality as state modernization |
| Rudo | Socialist + post-socialist management | Maintenance fragmentation |
| West 65 | Private | Verticality as market product |
| Belgrade Tower | Hybrid / global | City branding |
| Skyline | Hybrid / private | Integration and control |

### 6.1. INVESTMENT SYSTEMS, ARCHITECTURAL FORM AND SKYLINE TRANSFORMATION

The analysis confirms that different investment systems generate distinct architectural expressions and directly influence the transformation of Belgrade's skyline. State-controlled investment produced monumental, massive and institutionally symbolic

architecture intended to represent collective modernization and political stability. Transitional fragmentation generated unstable and poorly maintained spatial systems characterized by weakened institutional coordination and inconsistent urban development. Contemporary private capital introduced exclusivity, market visibility and typological differentiation, while hybrid investment models produced spectacle, branding and controlled urban environments.

These findings demonstrate that architectural form is not autonomous or neutral. Instead, it reflects the priorities of the economic and organizational system that produces it: stability, profitability, visibility, exclusivity or spatial control. Vertical architecture therefore operates as a material translation of broader political-economic structures.

The skyline of Belgrade consequently does not function as a coherent urban composition, but rather as a fragmented spatial record of successive investment cycles and socio-economic transformations. Each analyzed case corresponds to a specific historical and economic phase, collectively illustrating the transition from state-planned urbanism to contemporary investment-driven development. The contemporary skyline can therefore be interpreted as a morphological diagram of changing political-economic systems in which vertical architecture simultaneously functions as infrastructure, symbolic representation and spatial manifestation of capital accumulation.

The research further demonstrates that architectural aesthetics increasingly functions as a visible expression of investment logic. Socialist architecture communicates permanence, collective identity and institutional authority through monumentality and material mass. Contemporary private developments communicate luxury, transparency and lifestyle through glass facades, reflective surfaces and controlled interiors. Hybrid global projects communicate economic power and visibility through height, illumination and iconicity. Consequently, facade articulation, materialization, monumentality and vertical dominance operate as visual indicators of investment systems and broader economic organization. Architecture increasingly functions as a representational mechanism through which contemporary capital materializes symbolic power and spatial control within the urban environment.

## 6.2. PUBLIC SPACE AND CONTROLLED URBAN EXPERIENCE

One of the central findings concerns the transformation of public space within different investment systems. In the socialist model, public space was conceived as part of collective urban infrastructure and integrated planning strategy. During the transitional period, these spaces frequently became neglected, fragmented and institutionally weakened due to unclear ownership structures and insufficient maintenance systems. In contemporary private and hybrid developments, public space is increasingly redesigned as a controlled and commercially programmed environment. Similar processes have been identified in numerous post-socialist cities, where public accessibility is increasingly mediated through private governance and market-oriented development strategies [13,14].

This transformation demonstrates that public space is no longer defined exclusively through physical openness, but also through governance structures, accessibility regimes and programmed use. Questions of accessibility, social equity and public benefit therefore become increasingly important within contemporary investment-driven urban development [11]. Spaces surrounding contemporary high-rise developments may appear publicly accessible while simultaneously functioning through private management, surveillance systems, commercial programming and selective accessibility. Similar tendencies toward privatization and controlled accessibility have been documented across numerous post-socialist urban environments [13]. The research therefore confirms the transition from public space as collective urban right toward public space as an

investment-managed spatial product [7]. From a human-centered urban perspective, the quality and accessibility of public space remain essential indicators of sustainable urban development [14].

The analysis additionally indicates a significant transformation in the role of architecture and the architect within investment-driven urbanism. Contemporary architects no longer operate exclusively as autonomous authors of form, but increasingly function as mediators between financial feasibility, investor expectations, urban regulations and spatial quality. Architectural decisions are progressively conditioned by profitability, market positioning, construction efficiency and operational sustainability.

However, this does not imply the disappearance of architectural agency. On the contrary, understanding investment systems enables architects to negotiate more effectively between economic viability and public spatial value. The critical role of architecture therefore lies not in ignoring capital, but in understanding how economic systems shape urban space and in strategically intervening within those processes.

## 6.3. DISCUSSION SYNTHESIS: VERTICAL ARCHITECTURE AS A SPATIAL MANIFESTATION OF CAPITAL

The comparative analysis confirms that different investment systems generate distinct spatial and architectural outcomes that directly influence the morphology of Belgrade's skyline. The examined case studies reveal a gradual transformation from state-planned and collectively oriented forms of vertical urbanization toward market-driven and hybrid development models characterized by branding, investment visibility and controlled urban environments. A recurring pattern identified across the analyzed projects is the shift from monumentality as an expression of institutional authority toward iconicity as a mechanism of market differentiation and city branding. At the same time, the role of public space changes from collectively planned urban infrastructure to increasingly managed, commercially programmed and selectively accessible environments. The findings further indicate that skyline transformation cannot be understood solely through architectural form or building height. Rather, it reflects broader changes in governance structures, ownership relations and investment organization. The contemporary urban profile of Belgrade therefore functions as a layered spatial record of successive political-economic regimes and changing modes of urban production. Through the interaction of architecture, investment and governance, vertical urbanization emerges as a visible expression of contemporary urban development processes and the evolving relationship between capital, public space and urban identity. Contemporary verticality therefore functions simultaneously as an architectural, economic and symbolic system of urban representation [15].

## 7. CONSIDERATIONS AND CONCLUSIONS

The research is based on qualitative and interpretative analysis; therefore, it does not include quantitative skyline measurements or empirical user-space accessibility surveys. Nevertheless, the findings demonstrate that vertical architecture in Belgrade represents a spatial manifestation of changing investment systems and broader socio-economic transformations. Through the comparative analysis of representative high-rise developments, it was demonstrated that different models of investment and governance generate distinct architectural expressions, spatial organizations and approaches to public space. The findings indicate a clear shift from state-planned forms of vertical urbanization, characterized by monumentality, collective functions and institutional representation, toward contemporary private and hybrid development models oriented toward market visibility, branding and investment attractiveness. At the same time, the

transformation of public space reflects changing governance structures, moving from collectively planned urban infrastructure toward increasingly managed and commercially regulated urban environments.

The comparative evaluation of Genex Tower, Rudo Complex, West 65 Tower, Belgrade Tower and Skyline Complex reveals that skyline transformation is not determined solely by technological progress or architectural innovation. Rather, it is closely connected to changes in ownership structures, capital flows and development strategies that shape the production of urban space. The scientific contribution of the study lies in the establishment of an analytical framework linking investment systems, architectural production and skyline morphology. The proposed framework may serve as a transferable analytical tool for examining the relationship between capital, vertical urbanization and skyline transformation in other post-socialist urban contexts. This approach enables a broader interpretation of vertical architecture as both a physical and socio-economic phenomenon and provides a basis for understanding contemporary urban transformation in post-socialist cities.

The contemporary skyline of Belgrade can therefore be interpreted as a layered spatial record of successive political-economic regimes, where architecture functions not only as built form but also as an expression of investment logic, governance structures and urban development priorities. Future research may further develop this approach through quantitative skyline analysis and comparative studies of other post-socialist urban contexts.

**ACKNOWLEDGEMENT**

This research was conducted within the broader framework of doctoral studies in Architecture and Urbanism at the Faculty of Technical Sciences, University of Novi Sad. The authors acknowledge the academic and research environment provided by the Department of Architecture and Urbanism.

## REFERENCES

[1] Sassen S. (2001). *The Global City: New York, London, Tokyo*. Princeton University Press, Princeton, USA.

[2] Lefebvre H. (1991). *The Production of Space*. Blackwell Publishing, Oxford, Great Britain.

[3] Harvey D. (1985). *The Urbanization of Capital*. Johns Hopkins University Press, Baltimore, USA.

[4] Harvey D. (2001). *Spaces of Capital: Towards a Critical Geography*. Routledge, New York, USA.

[5] Smith N. (2008). *Uneven Development: Nature, Capital and the Production of Space*. University of Georgia Press, Athens, USA.

[6] Blagojević Lj. (2007). *Strategije modernizma u planiranju i projektovanju urbane strukture i arhitekture Novog Beograda*. Arhitektonski fakultet Univerziteta u Beogradu, Beograd, Srbija.

[7] Zukin S. (1995). *The Cultures of Cities*. Blackwell Publishing, Oxford, Great Britain.

[8] Castells M. (1996). *The Rise of the Network Society*. Blackwell Publishing, Oxford, Great Britain.

[9] Stanilov K. (Ed.) (2007). *The Post-Socialist City: Urban Form and Space Transformations in Central and Eastern Europe after Socialism*. Springer, Dordrecht, Netherlands.

[10] Grubbauer M., Čamprag N. (2019). Urban Megaprojects, nation-state politics and regulatory capitalism in Central and Eastern Europe: The Belgrade Waterfront project. *Urban Studies*, 56(4), 649-671. https://doi.org/10.1177/0042098018757663.

[11] Fainstein S. (2010). *The Just City*. Cornell University Press, Ithaca, USA.

[12] Brenner N., Theodore N. (2002). Cities and the Geographies of Actually Existing Neoliberalism. *Antipode*, 34(3), 349-379. https://doi.org/10.1111/1467-8330.00246.

[13] Hirt S. (2012). *Iron Curtains: Gates, Suburbs and Privatization of Space in the Post- Socialist City*. Wiley-Blackwell, Oxford.

[14] Gehl J. (2010). *Cities for People*. Island Press, Washington D.C., USA.

[15] Graham S. (2016). *Vertical: The City from Satellites to Bunkers*. Verso, London, Great Britain.

# GEODESY AND GEOINFORMATICS

iNDiS 2026

https://doi.org/10.24867/INDIS-2026-EN-658



# SCAN-TO-BIM FOR CULTURAL HERITAGE PRESERVATION: DIGITAL RECONSTRUCTION AND BIM MODELING OF A HISTORICAL CHURCH IN RAMSEL, BELGIUM

*Vesko Đorđević[1], Vladan Komatović[2], Dejan Pavlović[3]*

***Summary:***

Scan-to-BIM is a useful method for documenting cultural heritage buildings. Many old buildings have no complete design records, and their shape is often irregular. This paper presents a Scan-to-BIM workflow for a historic parish church in Ramsel, Herselt (Belgium). The church has a long nave, a transept, and a tall bell tower with a spire, which makes it a demanding case for digital modeling. A terrestrial laser scan was used as the main reference for BIM modeling, carried out level by level, from the ground floor to the roof and tower. The result is a full set of documentation: floor plans, a roof plan, elevations, sections, and 3D views. The paper also discusses how such models can support future work on conservation and building management.
***Keywords:*** *Scan-to-BIM, cultural heritage, HBIM, point cloud, terrestrial laser scanning, digital documentation*

# SCAN-TO-BIM ZA OČUVANJE KULTURNOG NASLEĐA: DIGITALNA REKONSTRUKCIJA I BIM MODELIRANJE ISTORIJSKE CRKVE U RAMSELU, BELGIJA

***Rezime:***

Scan-to-BIM je koristan metod za dokumentovanje objekata kulturnog nasleđa. Mnoge stare zgrade nemaju kompletnu projektnu dokumentaciju, a njihov oblik je često nepravilan. Ovaj rad prikazuje Scan-to-BIM proces modelovanja parohijske crkve u Ramselu, opština Herselt (Belgija). Crkva ima dugačak brod, transept i visok zvonik sa šiljatim krovom, što je čini zahtevnim primerom za digitalno modelovanje. Terestričko lasersko skeniranje korišćeno je kao osnovna referenca za BIM modelovanje, sprovedeno sprat po sprat, od prizemlja do krova i zvonika. Rezultat je kompletan set dokumentacije: osnove, plan krova, fasade, preseci i 3D prikazi. Rad takođe razmatra kako ovakvi modeli mogu podržati budući rad na konzervaciji i upravljanju objektom.

***Ključne reči:*** *Scan-to-BIM, kulturno nasleđe, HBIM, oblak tačaka, terestričko lasersko skeniranje, digitalna dokumentac*

[1] Chief Executive Officer, MSc Geodetic Engineer, DT Mapping, Kraljevo, Serbia, vdjordjevic@dtmapping.com, ORCID 0009-0007-7524-683X
[2] Civil Engineering Technician, DT Mapping, Kraljevo, Serbia, vkomatovic@dtmapping.com
[3] Geodetic Engineer, DT Mapping, Kraljevo, Serbia, dpavlovic@dtmapping.com

## 1. INTRODUCTION

Building Information Modeling (BIM) is a digital way to describe buildings. A BIM model does not just show shapes, but it also holds rich information about the building, covering its whole life, from design and construction to later use and maintenance [1].
Normal design workflows work well for new buildings, but not always for old ones. Many historic buildings have incomplete, outdated, or missing design records. In such cases, data-driven approaches based on direct spatial measurement offer a more objective alternative, as they capture the building's as-built condition rather than its idealized design intent. Advances in terrestrial laser scanning and photogrammetric data acquisition have made it possible to generate dense spatial datasets in the form of point clouds, which serve as the primary source for digital reconstruction and BIM modeling processes [2], [3]. In general, this process has three steps: data collection, data cleaning (removing noise and joining scans into one system), and building the 3D model [4].
When BIM is used for buildings with historical or cultural value, it is often called Heritage BIM, or HBIM. HBIM adds more than geometry to the model and also stores information about the building's condition, its history, and its materials [5], [6]. HBIM can support conservation work, structural checks, and the mapping of damage directly onto the 3D model [7]. A recent review of HBIM research groups existing studies into three main topics: collecting and modeling geometry, managing information such as material and condition data, and using augmented or virtual reality. The review found that information management is still less developed than geometric modeling [6].
Even with these advances, Scan-to-BIM and HBIM still face problems with complex, irregular buildings. Old churches with towers, spires, and walls that are not straight or flat are a good example. This kind of geometry makes both automatic detection and manual modeling harder. Reviews of Scan-to-BIM research point out that missing data caused by occlusion, together with weak planning of scan positions, are among the biggest problems in this field [4]. This is related to the so-called next-best-view problem in scan planning: choosing scan positions that cover as much of the object as possible, even when the object's own shape blocks part of the view [4].
Heritage buildings bring extra difficulties. Most BIM software comes with ready-made building parts, called families, for modern, standard construction. These libraries often lack parts for older, irregular, or historic elements [5]. Case studies on old churches [8] show that once the standard families are used up, most special heritage elements must be built by hand, directly from the point cloud. This takes more time, but it keeps the real shape of the building instead of simplifying it. Checking the accuracy of a Scan-to-BIM model usually means comparing the model with control points measured by a total station. Some studies report models with an overall accuracy better than about ±1 cm compared with these control points [9].
These results support the use of Scan-to-BIM, and HBIM in particular, not only to visualise a building but also to provide real dimensions for restoration planning, structural checks, and long-term building management [5]. This paper presents a Scan-to-BIM case study of a historic parish church in Ramsel, part of the municipality of Herselt in Belgium. The church has a long nave, a transept, and a tall bell tower with a spire. This makes it a demanding example for studying how Scan-to-BIM works for heritage buildings, and how it can support the wider goal of documenting and protecting cultural heritage.

## 2. STUDY AREA AND DATASET

The church studied here stands at Gustaaf Vandenheuvelstraat 4, in Ramsel, part of the municipality of Herselt, in the Belgian province of Antwerp (Fig. 1). It was chosen as a case study because of its complex shape and because it is a typical example of the historic churches often studied in Scan-to-BIM heritage projects.

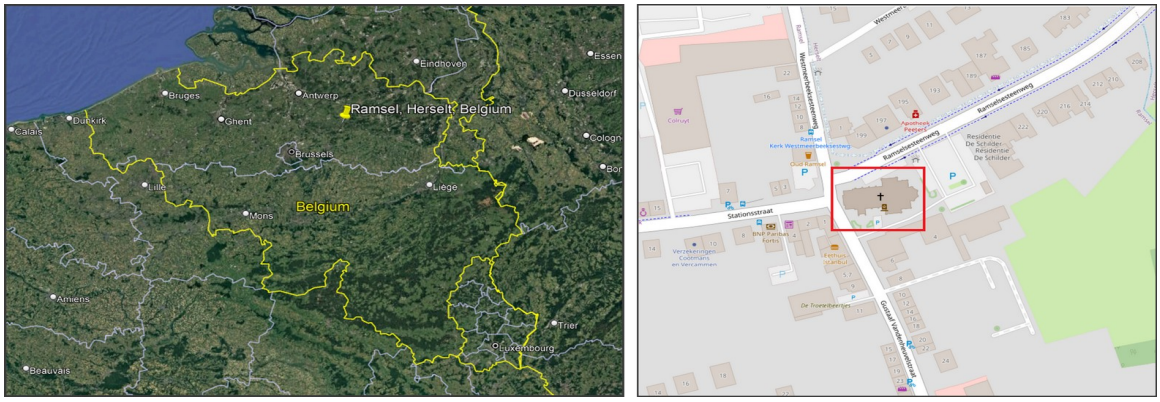


*Fig. 1 Location of the church within Ramsel, Herselt, Belgium*

The building has one long nave on an east–west axis, a transept that forms a cross-shaped plan, a polygonal apse, and a tall bell tower with an octagonal spire above the crossing. The building has a ground floor and five more levels above it: first, second, third, fifth, and attic. There is no separate fourth floor, because the main roof of the nave sits at this height instead. Reference heights run from 0.00 m at the ground floor to about 37 m at the top of the tower and spire. This tall, narrow shape, together with the curved and sloped roof around the crossing, makes the building a demanding case for heritage documentation.

The dataset used in this study is a three-dimensional point cloud made with terrestrial laser scanning. It covers the outside of the building (facades, roof slopes, and the tower with its spire) and the inside layout on every level. Scan positions were placed with enough overlap to support registration. This point cloud is the main geometric reference for all the modeling and documentation work described in the next section. No separate control survey, such as a total station network, was collected to check accuracy. So, in this study, the point cloud is treated only as the geometric source, not as a benchmark for measuring model accuracy.

## 3. POINT CLOUD-BASED BIM MODELING

After data collection, the individual scans were registered into one unify point cloud. Noise was removed before the data was used for modeling, while points from surrounding elements such as plants, trees, and street furniture was kept, since these were also modeled as part of the site context around the church. This cleaning step matters, because several factors can lower the quality of a point cloud or the final model, such as noise, scanner limits, small errors during registration, occlusion from nearby objects, or the limits of the parametric parts used for modeling [9], [10]. Because of this, careful registration and cleaning are needed before the point cloud can serve as a reliable reference for modeling.

The point cloud gave a clear picture of the church: the layout of the nave and transept on each floor, the stepped structure inside the bell tower, and the timber roof frame visible in the sections. The tower and spire needed extra care. Their narrow, steep, and

partly self-blocking surfaces meant fewer points were captured, and some upper parts were hard to reach from the ground. This matches a well-known problem in the scan-planning literature: choosing enough scan positions to cover a complex object, even when its own shape blocks part of it [4].

Modeling was done in a BIM environment, using Autodesk Revit, with each element built by referencing the point cloud. Walls, floor slabs, window and door openings, and roof surfaces were modeled level by level, from the ground floor to the roof, following the levels described above. Each part of the model was given a level of detail suited to its role: simple shapes for the general roof, and more detail for window and door openings on the façades. In the modeling process, ready-made system parts were used where possible. But the tower's octagonal spire, its timber bell frame, and the steel spire frame have sloped and layered shapes that standard parts cannot follow. These were built as separate custom objects, shaped directly from the point cloud. Two examples of these hand-built parts are given in Fig. 2: the timber bell frame inside the tower, and the brick and stonework at the top of the spire.

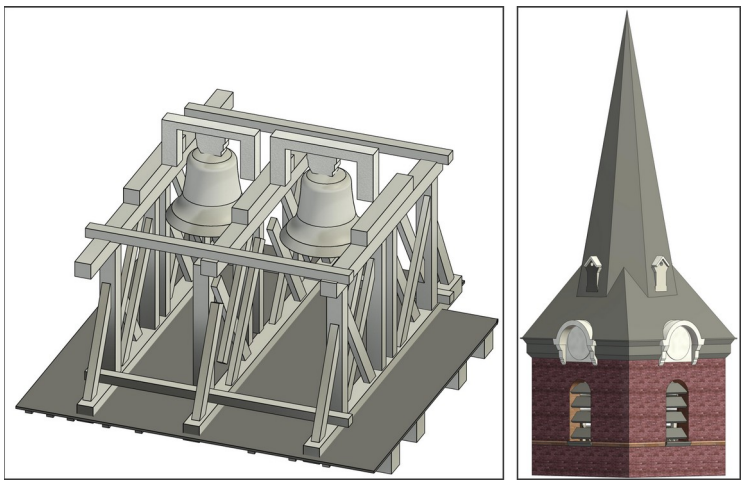

*Fig. 2 Examples of custom-modeled elements not covered by standard parametric families: the timber bell frame (left) and the top of the tower spire (right)*

Beyond these individual elements, the overall fit between the model and the source data can also be checked at the scale of the whole building.



*Fig. 3 Comparison between the acquired point cloud and the resulting BIM model of the church exterior*

A side-by-side view of the point cloud and the matching model geometry is shown in Fig. 3. It shows how closely the model follows the shape of the real building.

This hand-built, point-cloud-based approach matches what other Scan-to-BIM studies of heritage churches have found: most special architectural features, such as pillars, vaults,

openings, and decorative details, also had to be built as custom parts instead of standard ones [5], [8]. After the building envelope and inside walls were modeled, the BIM model was used to create all the two-dimensional drawings: floor plans for the ground floor and the first, second, third, fifth, and attic levels, a separate roof plan, four elevations (north, south, east, west), and four sections through the nave, transept, and tower. Because all these drawings come from the same 3D model, they always match each other in geometry and height. This is one of the practical benefits of working in BIM instead of drawing each sheet separately.

## 4. RESULTS AND DISCUSSION

The Scan-to-BIM process used for the Ramsel church produced a full, matching set of technical drawings and 3D views, covering the building's shape, layout, and modeled information. The set includes floor plans for the ground floor and five more levels, a roof plan, four elevations, and four sections.
The floor plans show the church's cross-shaped layout. The nave and transept meet at a central crossing under the tower, with smaller rooms and a sacristy next to the apse.



*Fig. 4 3D perspective view of the church generated from the BIM model*

Fig. 4 shows a 3D view of the finished model, giving an overall sense of the building's shape and its bell tower. A wider view of the church together with its surroundings is shown in Fig. 5.



*Fig. 5 Aerial view of the church and its surroundings, derived from the BIM/site model*

The roof plan records the layout of the hipped and gabled roof sections that meet at the crossing, together with the tented roof at the base of the spire. Roof pitches range from about 37° over the side aisles to steep angles of around 80° on the faces close to the tower base. This roof plan is shown in Fig. 6.

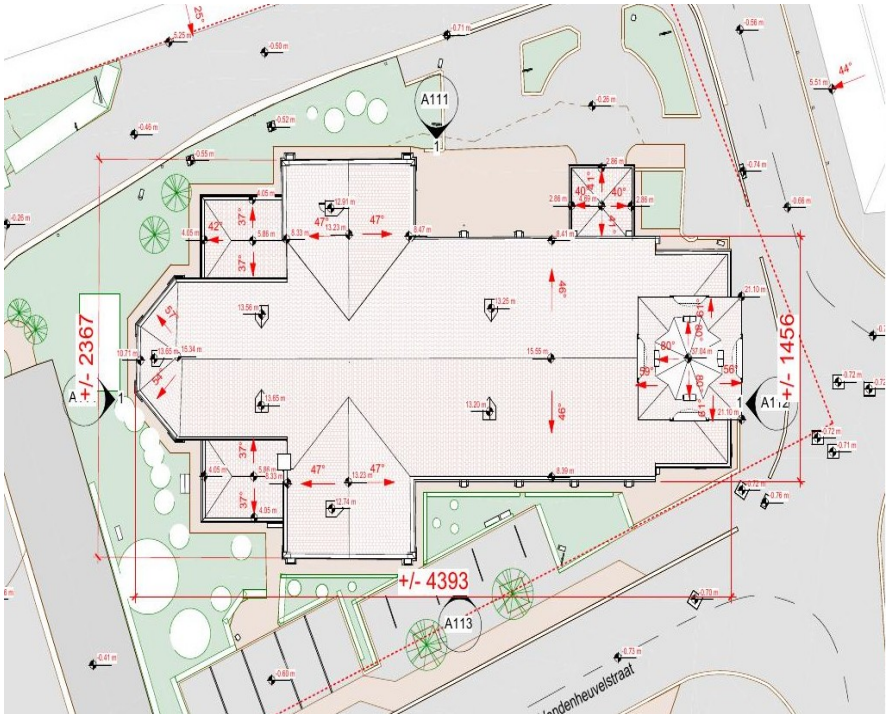


*Fig. 6 Site plan showing the roof layout and surrounding context*

Other Scan-to-BIM [9] studies of simpler buildings report model accuracy better than about ±1 cm compared with independent control measurements. No independent control survey was carried out for the Ramsel case study, so no matching accuracy value is

given here. Instead, the extra complexity from the tower, spire, and several roof planes meeting together is discussed only in general terms: it needed more manual modeling work than a simple rectangular building would. This fits with the general idea that automatic Scan-to-BIM methods work best for flat, straight elements such as walls, while irregular, strongly three-dimensional shapes still depend heavily on the modeler working directly with the point cloud [4].

As an internal check, rather than an independent accuracy test, the finished model was compared with the point cloud directly inside the modeling software, similar to the Cloud-to-Model (C2M) comparisons used in other Scan-to-BIM case studies [10] to check how well a model fits its source point cloud. Local differences between the model and the point cloud stayed under 1 cm across most of the building. Fig. 7 shows deviation between model and point cloud in one section of the building. This is only a general indicator that the model fits the point cloud well and it does not replace a proper accuracy check based on separate control points.

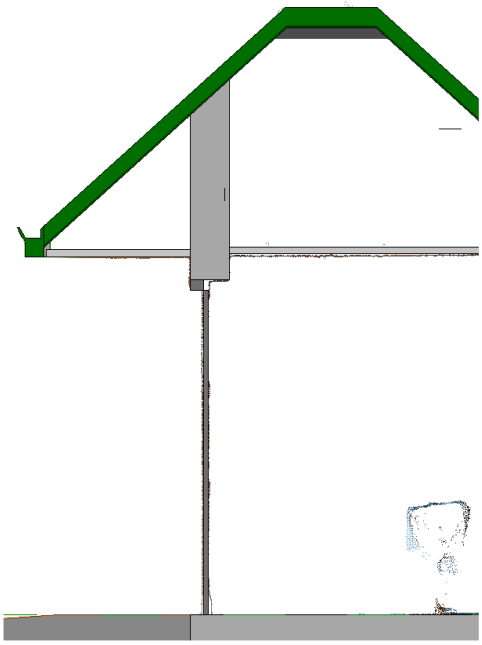

*Fig. 7 Example of local deviation between the BIM model and the reference point cloud (informational only); deviations across most of the model remain below 1 cm*

Beyond its role as a geometric record, the BIM model also shows the kind of digital tool that HBIM literature connects to heritage management. Because the floor plans, elevations, and sections all come from the same point cloud and the same model, this documentation set could, in future, work as a shared reference for restoration planning, structural checks, and ongoing condition monitoring. Other Scan-to-BIM heritage studies [5], [7], [6] have used similar models to store damage maps, material data, and other conservation information. Whether the Ramsel model is extended this way is a question for future work, not a claim made in this study. An example of the resulting ground floor plan is shown in Fig. 8.

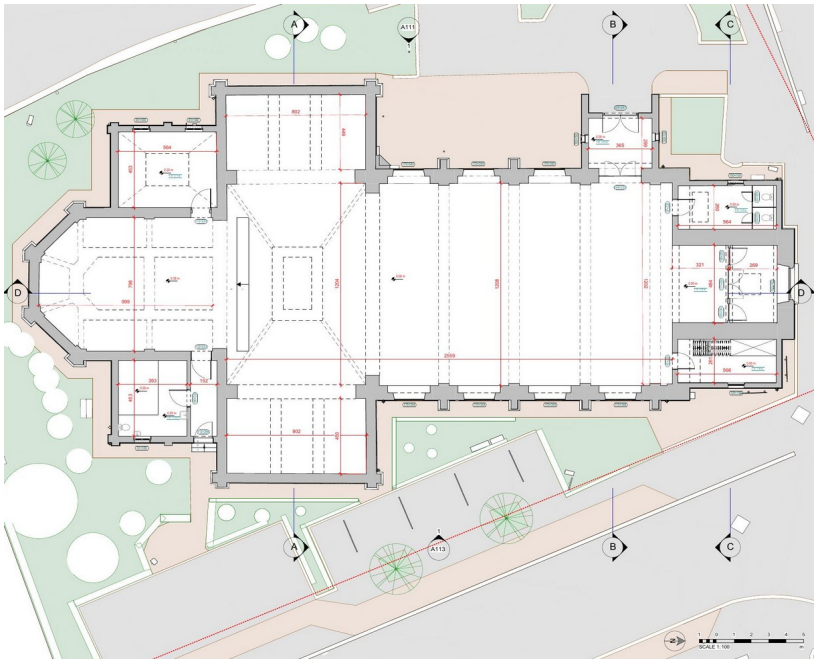

*Fig. 8 Ground floor plan derived from the point cloud, showing the nave, transept, tower base, and adjoining rooms*

The same model was also used to produce the building's elevations. The west elevation, which best shows the tower and spire, is given in Fig. 9.




*Fig. 9 West elevation, showing the tower, spire, and nave roofline with reference floor levels*

A vertical section through the same model, cutting through the nave and tower, is shown in Fig. 10.




*Fig. 10 Section A-A through the nave and tower, illustrating the internal vertical structure and the timber roof framing*

## 5. CONCLUSION

This case study shows one way to apply the Scan-to-BIM method to a complex historic building. Using the parish church in Ramsel, Herselt, as a case study, the workflow turned a terrestrial laser scan into a multi-level BIM model and a full set of matching drawings: floor plans, a roof plan, elevations, sections, and 3D views.

The case suggests that Scan-to-BIM can turn raw scan data into structured digital models, even when the building's shape is far from simple and rectangular, as with this church's tower, spire, and crossing roofs. The literature shows that automatic feature detection still works best for flat and straight elements [4]. This case study points to hand-built, point-cloud-based modeling as a working way to reconstruct irregular parts of a building. Because no independent control survey was carried out, this is offered as a general description of the modeling process, not as a checked accuracy result.

For heritage buildings, the value of this kind of workflow is not only the 3D model itself. It is also its possible role in a longer conservation process. Broader reviews of HBIM show that similar models have been used to store damage maps, material and condition data, and restoration planning information, turning a one-time survey into a living reference for building management [5], [7], [6]. Looking at the Ramsel model this way, instead of only as a visual exercise, fits with how Scan-to-BIM is developing in the heritage field. It also supports long-term digital storage, future updates, and links to restoration or facility management work.

Wider reviews of the field point to a few directions for future work: combining data from several sensor types, better scan planning, standard parametric libraries for historic building parts, and shared benchmark datasets, all aimed at reducing the manual work still needed in heritage Scan-to-BIM projects [7], [6]. Adding conservation information

to the Ramsel model, such as a damage map or a simple condition record, following examples from other HBIM case studies, is suggested here as a direction for future work rather than part of the present study.

## REFERENCES

[1] Antova G., Kunchev I., Mickrenska-Cherneva C. (2016). Point clouds in BIM. IOP Conference Series: Earth and Environmental Science, Volume 44, 042034. https://doi.org/10.1088/1755-1315/44/4/042034

[2] Dobelis M., Kalinka M., Borodinecs A. (2016). The Capture of BIM Compatible 3D Building Model from Laser Scanner Data. Proceedings of the 17th International Conference on Geometry and Graphics (ISGG), Beijing, China, Paper 81.

[3] Klinc R., Jotanović U., Kregar K. (2021). Point clouds for use in building information models (BIM). Geodetski vestnik, Volume 65, Issue 4, pp. 594–613. https://doi.org/10.15292/geodetski-vestnik.2021.04.594-613

[4] Abreu N., Pinto A., Matos A., Pires M. (2023). Procedural Point Cloud Modelling in Scan-to-BIM and Scan-vs-BIM Applications: A Review. ISPRS International Journal of Geo-Information, Volume 12, Issue 7, 260. https://doi.org/10.3390/ijgi12070260

[5] Rocha G., Mateus L., Fernández J., Ferreira V. (2020). A Scan-to-BIM Methodology Applied to Heritage Buildings. Heritage, Volume 3, Issue 1, pp. 47–67. https://doi.org/10.3390/heritage3010004

[6] Lovell L.J., Davies R.J., Hunt D.V.L. (2023). The application of Historic Building Information Modelling (HBIM) to Cultural Heritage: A review. Heritage, Volume 6, Issue 10, pp. 6691–6717. https://doi.org/10.3390/heritage6100350

[7] Aricò M., Ferro C., La Guardia M., Lo Brutto M., Taranto G., Ventimiglia G.M. (2024). Scan-to-BIM Process and Architectural Conservation: Towards an Effective Tool for the Thematic Mapping of Decay and Alteration Phenomena. Heritage, Volume 7, Issue 11, pp. 6257–6281. https://doi.org/10.3390/heritage7110294

[8] Aricò M., Lo Brutto M., Maltese A. (2023). A Scan-to-BIM Approach for the Management of Two Arab-Norman Churches in Palermo (Italy). Heritage, Volume 6, Issue 2, pp. 1622–1644. https://doi.org/10.3390/heritage6020087

[9] Skrzypczak I., Oleniacz G., Leśniak A., Zima K., Mrówczyńska M., Kazak J.K. (2022). Scan-to-BIM method in construction: assessment of the 3D buildings model accuracy in terms of inventory measurements. Building Research & Information, Volume 50, Issue 8, pp. 859–880. https://doi.org/10.1080/09613218.2021.2011703

[10] Gavrilović M., Ruskovski I., Šarkanović Bugarinović M., Jovanović D., Govedarica M. (2026). Accuracy Assessment of a Scan to BIM Model: A Case Study of the Building of the Department of Civil Engineering and Geodesy. Proceedings of the International Conference on Contemporary Theory and Practice in Construction XVII, Banja Luka, pp. 1022–1038. https://doi.org/10.61892/STP202601073G

https://doi.org/10.24867/INDIS-2026-EN-668



# EXPROPRIATION FOR THE PURPOSE OF INFRASTRUCTURE DEVELOPMENT

*Gordana Nataroš[1], Mirjana Bajić[2], Marina Davidović Manojlović[3]*

***Summary:***

This paper deals with expropriation as an important procedure for the implementation of infrastructure and other projects of public interest. The objective of the paper is to present the concept, aim, purpose, and need for conducting expropriation, as well as the basic steps of the procedure, from establishing public interest to the transfer of rights over immovable property. Special emphasis is placed on the importance of the geodetic profession, particularly in the identification of parcels, preparation of technical documentation, harmonization of cadastral data, and ensuring legal certainty. The practical part of the paper includes selected case studies, through which the application of expropriation in specific infrastructure projects is presented. The case studies indicate that properly conducted geodetic and cadastral activities have an important role in ensuring the efficient, accurate, and legally secure implementation of expropriation procedures.

*Keywords: expropriation, geodetic works, land consolidation, infrastructure projects*

# EKSPROPRIJACIJA U FUNKCIJI INFRASTRUKTURNOG RAZVOJA

***Rezime:***

U radu je obrađena tema eksproprijacije kao važnog postupka za realizaciju infrastrukturnih i drugih projekata od javnog interesa. Cilj rada je da se prikažu pojam, cilj, svrha i potreba sprovođenja eksproprijacije, kao i osnovni koraci koji prate ovaj postupak, od utvrđivanja javnog interesa do prenosa prava na nepokretnostima. Poseban akcenat stavljen je na značaj geodetske struke, naročito u dijelu identifikacije parcela, izrade tehničke dokumentacije, usklađivanja katastarskih podataka i obezbjeđivanja pravne sigurnosti. U praktičnom dijelu rada date su odabrane studije slučaja, kroz koje je prikazana primjena eksproprijacije u konkretnim infrastrukturnim projektima. Studije slučaja ukazuju na to da pravilno sprovedene geodetske i katastarske aktivnosti imaju važnu ulogu u obezbjeđivanju efikasnog, tačnog i pravno sigurnog sprovođenja postupka eksproprijacije.

*Ključne reči: eksproprijacija, geodetski radovi, komasacija, infrastrukturni projekti*

[1] Real estate consultant, Novi Sad, Republic of Serbia, jeja023@gmail.com
[2] Head of the Real Estate Cadastre Office, Zrenjanin, mirjana.bajic@rgz.gov.rs
[3] Research Associate, Faculty of Technical Sciences, University of Novi Sad, Novi Sad, Serbia, marina.davidovic@uns.ac.rs, ORCID 0000-0001-6736-0615

## 1. INTRODUCTION

Expropriation is the forced transfer of real estate (land, buildings) from private to public ownership for the purpose of achieving public interest (construction of infrastructure, schools, hospitals), with fair compensation that cannot be lower than the market price. The procedure is based on the Law on Expropriation and the Law on Special Procedures for the Implementation of Projects for the Construction of Linear Infrastructure.

A closer historical analysis of expropriation can show that it is not a legal institution originating from socialist law, but that it started in earlier legal and social orders. In comparison, it can be said that the 3 legal institutions, nationalization, confiscation and sequestration, are new legal institutions related to socialist revolutions, while expropriation is a "classical", traditional institution that gets its constitutional origin and character in civil society, and has its roots in the distant past [1].

In this paper, a special focus is placed on the expropriation role in the process of road infrastructure construction. First, a brief theoretical overview of the concept of expropriation, its significance, legal framework and basic stages of the procedure is given. After that, specific examples from practice were analyzed through case studies, namely the Belgrade-Zrenjanin-Novi Sad highway under construction, as well as the infrastructure projects Corridor 10 and Corridor 11. In this way, it was shown how the expropriation procedure is carried out within the large transport projects and the role it plays in creating the necessary conditions for their implementation.

## 2. EXPROPRIATION - THEORETICAL BASIS

Our legislation treats two types of expropriation: complete and incomplete expropriation. Complete expropriation transfers real estate from an owner to the ownership of the beneficiary of expropriation. It includes, besides land, buildings and other structures located on it. Incomplete expropriation involves the establishment of an easement over land and objects, as well as a lease of land for a certain period of time.

The determination of public interest is the basis for initiating the expropriation process. Public interest in expropriation may be determined if, in accordance with the Law, an appropriate planning act has been adopted, unless otherwise defined by the Law. The parties in the expropriation procedure are the beneficiary of the expropriation and the owner of the real estate being expropriated [2].

A proposal for determining public interest may be submitted by a person who, according to the provisions of this Law, may act as the beneficiary of expropriation, while the proposal for expropriation itself may be submitted by the beneficiary only after public interest has been established in accordance with the Law. On behalf of the Republic of Serbia, the proposal shall be submitted by the Republic Public Attorney. On behalf of an autonomous province, city, or municipality, it shall be submitted by the competent public attorney, or another person representing the autonomous province, city, or municipality. The proposal for expropriation shall be submitted to the municipal administration of the municipality on whose territory the real estate is located, within one year from the date of determination of public interest [2]. The decision on the expropriation implementation is issued by the City and Municipal Administration Service competent for property and legal affairs of the municipality on whose territory the real estate proposed for expropriation is located. According to the principles of the Law on General Administrative Procedure, the first-instance authority in the expropriation procedure is always the competent municipal authority. The appeal against the first-instance decision issued on the proposal for expropriation is decided by

the Ministry competent for financial affairs. According to the new Law, the procedure of non-acceptance of the offer does not postpone the expropriation, because the expropriation beneficiary has the right, despite the rejection of the offer, to continue with the works. Dissatisfied owners can seek their rights through the Court.
The amount of compensation in money, i.e., fair compensation for expropriated agricultural land and construction land, is determined according to the market price, which is assessed by the authority responsible for determining the tax on the transfer of absolute rights to real estate. It is also important to mention real estate valuation, which represents a separate topic and is carried out by experts of various profiles, depending on the purpose for which it is performed [3].
The expropriation process itself lasts from 6 to 8 months, and in some cases even longer. Negotiations with real estate owners are the longest process, as they last from two to three months. In the case of unresolved property-legal relations, the procedures can last up to a year or longer.

## 2.1. GEODETIC-TECHNICAL WORKS IN THE EXPROPRIATION PROCESS

Geodetic-technical works in the expropriation process represent the key technical basis for changing ownership rights and implementing infrastructure projects. These works primarily focus on the precise identification of real estate and marking the boundaries of the affected area. Main phases and activities are:

- Preparation of the geodetic work study for expropriation: this is the basic and key document containing data on real estate
- Setting out the boundary lines: this phase involves calculating the required setting-out elements for transferring the designed expropriation zone to the field. The boundary points of the expropriation zone are then marked and permanently stabilized on site.
- Surveying the changes: detailed surveying of all changes such as division of plots, etc.
- Registration of changes in the cadastre: a digital terrain model is prepared to serve as a basis for design activities, while changes related to ownership rights are simultaneously recorded in the cadastral register.
- Technical control and supervision: checking the compliance of the carried out works with the main geodetic project, adhering to applicable regulations

All these phases of geodetic works, preparatory works, design, implementation and registration, are carried out in accordance with the following laws:

- Law on Expropriation: the basic law that regulates the procedure and compensation for expropriated real estate [2]
- Law on the Procedure for Registration in the Real Estate and Utilities Cadastre: according to this law, the expropriation, i.e., the change of ownership rights, is recorded in the cadastre [4]
- Law on State Survey and Cadastre: it is necessary to record the technical aspects of the change in cadastral data [5]

## 2.2. RELATIONSHIP BETWEEN EXPROPRIATION AND LAND CONSOLIDATION

Author Bogdanović in his professional literature [6] treats land consolidation and expropriation as two different, but complementary legal and geodetic instruments for

land territory regulation and resolving property-legal relations. Namely, although both relate to land regulation, they have different goals, methods and effects. The only clear connection between them is the primacy in the domain of efficiency and spatial planning [6].

Land consolidation can be seen as a possible alternative to the expropriation process - instead of the state paying money for confiscated plots where the owner would lose the property with financial compensation, the owners are allocated new, enlarged plots elsewhere within the land consolidation area. In this case, land consolidation aims to group scattered plots into a single unit for easier cultivation, thereby increasing the value and usability of the land that the owner retains.

In the case where a large infrastructure project (highway, railway, drainage systems, etc.) should be implemented, which construction disintegrates the territory of a cadastral municipality, the "Land consolidation as part of an investment project" model is applied (Figure 1) [1]. This is an example where land consolidation can completely replace expropriation. Land acquisition can be carried out through a reduction coefficient with fair compensation, as in the case of expropriation for a larger number of participants in a wider area.

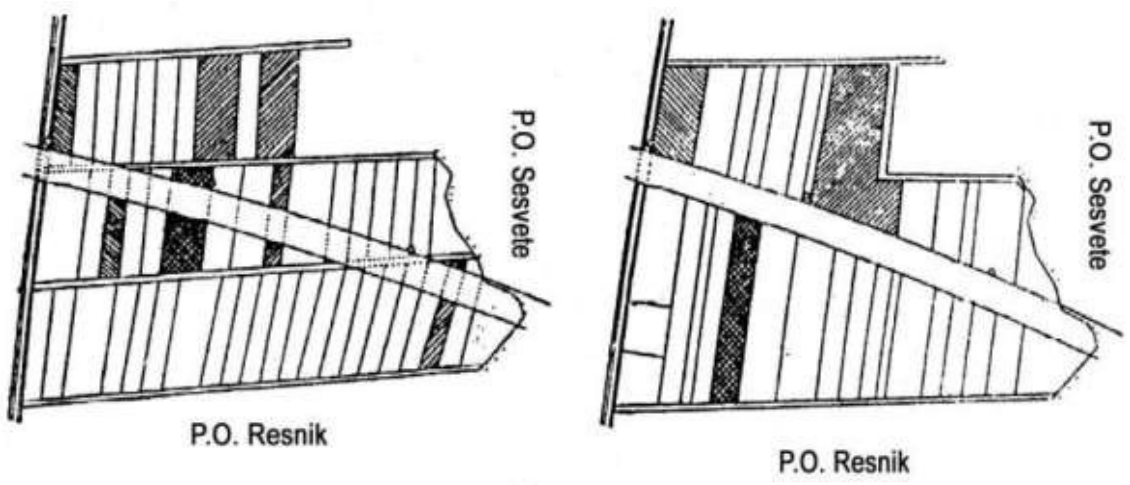


*Fig. 1 Condition before and after land consolidation along the highway Beograd-Zagreb [1]*

In the case of the Belgrade-Požega highway, it was necessary to first carry out expropriation (exclude land), then define the land consolidation area and carry out land consolidation. Figure 2 shows the expropriation boundary of the designed Belgrade-Požega highway corridor (the "Miloš Veliki" highway).

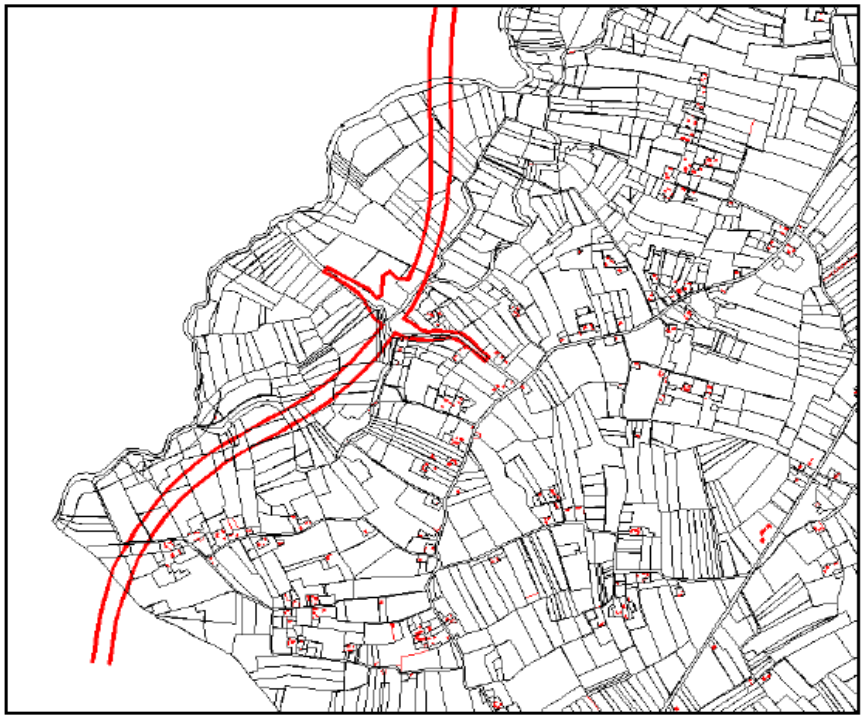

*Fig. 2 Expropriation boundary of the designed Belgrade-Požega highway*

## 3. ANALYSIS OF THE IMPLEMENTATION OF THE EXPROPRIATION PROCEDURE ON PRACTICAL EXAMPLES

In order to see the practical application of the expropriation procedure, selected examples from the implementation of infrastructure projects are analyzed below. The case studies were selected in a targeted manner, based on their relevance to the topic of the paper and the availability of sufficiently complete documentation for the analysis of the key stages of the expropriation procedure. Additionally, the selected examples were chosen to reflect the significant infrastructure projects and to enable the presentation of various practical aspects of expropriation implementation.

### 3.1. CASE STUDY: HIGHWAY UNDER CONSTRUCTION BELGRADE-ZRENJANIN-NOVI SAD

This highway, also called the Banat Corridor, has a total length of 105.4 km. It consists of two sections: Belgrade–Zrenjanin, 67.7 km long, and Zrenjanin–Novi Sad, 37.7 km long. The works are currently being carried out from two directions, from Belgrade and from the Zrenjanin area, in order to accelerate the implementation of the project. Based on the Decision of the Government of the Republic of Serbia, at first, public interest has been established (Figure 3 shows part of the aforementioned decision).

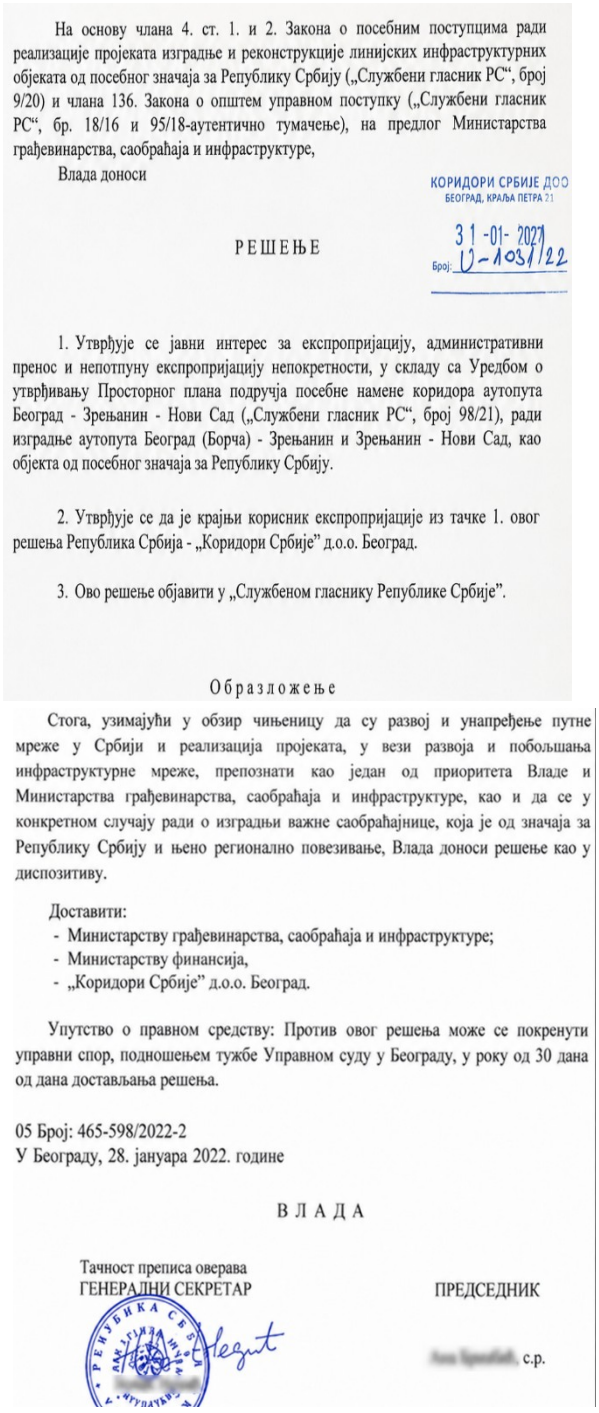

На основу члана 4. ст. 1. и 2. Закона о посебним поступцима ради реализације пројеката изградње и реконструкције линијских инфраструктурних објеката од посебног значаја за Републику Србију („Службени гласник РС“, број 9/20) и члана 136. Закона о општем управном поступку („Службени гласник РС“, бр. 18/16 и 95/18-аутентично тумачење), на предлог Министарства грађевинарства, саобраћаја и инфраструктуре,

Влада доноси

КОРИДОРИ СРБИЈЕ ДОО
БЕОГРАД, КРАЉА ПЕТРА 21
31-01-2022
Број: ЈЈ-1031/22

РЕШЕЊЕ

1. Утврђује се јавни интерес за експропријацију, административни пренос и непотпуну експропријацију непокретности, у складу са Уредбом о утврђивању Просторног плана подручја посебне намене коридора аутопута Београд - Зрењанин - Нови Сад („Службени гласник РС“, број 98/21), ради изградње аутопута Београд (Борча) - Зрењанин и Зрењанин - Нови Сад, као објекта од посебног значаја за Републику Србију.

2. Утврђује се да је крајњи корисник експропријације из тачке 1. овог решења Република Србија - „Коридори Србије” д.о.о. Београд.

3. Ово решење објавити у „Службеном гласнику Републике Србије”.

Образложење

Стога, узимајући у обзир чињеницу да су развој и унапређење путне мреже у Србији и реализација пројеката, у вези развоја и побољшања инфраструктурне мреже, препознати као један од приоритета Владе и Министарства грађевинарства, саобраћаја и инфраструктуре, као и да се у конкретном случају ради о изградњи важне саобраћајнице, која је од значаја за Републику Србију и њено регионално повезивање, Влада доноси решење као у диспозитиву.

Доставити:
- Министарству грађевинарства, саобраћаја и инфраструктуре;
- Министарству финансија,
- „Коридори Србије” д.о.о. Београд.

Упутство о правном средству: Против овог решења може се покренути управни спор, подношењем тужбе Управном суду у Београду, у року од 30 дана од дана достављања решења.

05 Број: 465-598/2022-2
У Београду, 28. јануара 2022. године

В Л А Д А

Тачност преписа оверава
ГЕНЕРАЛНИ СЕКРЕТАР

ПРЕДСЕДНИК

с.р.

*Fig. 3 Decision of the Government of the Republic of Serbia on determining public interest*

After determining the public interest and initiating the expropriation, a geodetic works report was prepared and implemented. The division of cadastral plots defined the future boundaries of the expropriation. Figures 4 and 5 show part of the report number 952-06-116-94/2024 dated 22.07.2024, with a selected real estate certificate with the shown status before and after this procedure.

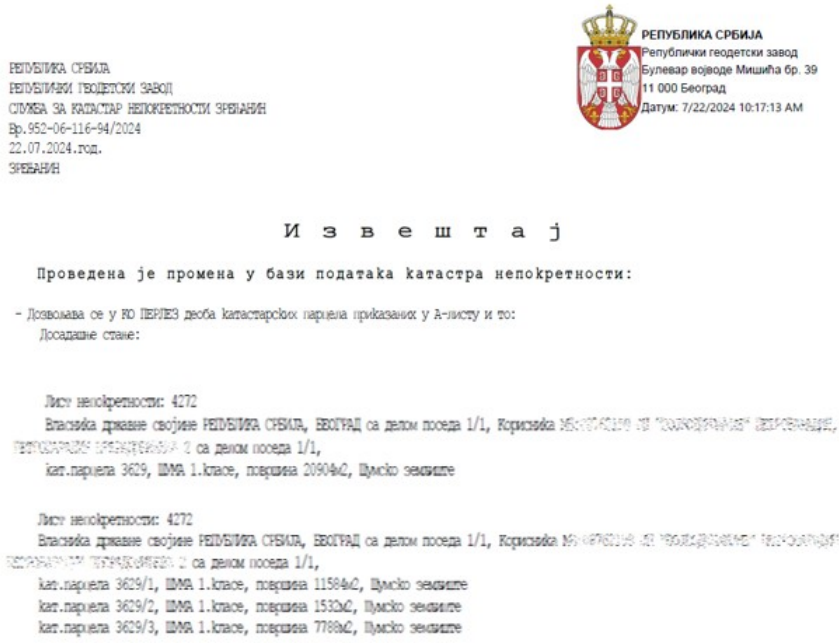

РЕПУБЛИКА СРБИЈА
РЕПУБЛИЧКИ ГЕОДЕТСКИ ЗАВОД
СЛУЖБА ЗА КАТАСТАР НЕПОКРЕТНОСТИ ЗРЕЊАНИН
Бр.952-06-116-94/2024
22.07.2024.год.
ЗРЕЊАНИН

РЕПУБЛИКА СРБИЈА
Републички геодетски завод
Булевар војводе Мишића бр. 39
11 000 Београд
Датум: 7/22/2024 10:17:13 AM

И з в е ш т а ј

Проведена је промена у бази података катастра непокретности:

- Дозвољава се у КО ПЕРЛЕЗ деоба катастарских парцела приказаних у А-листу и то:
Досадашње стање:

Лист непокретности: 4272
Власништво државне својине РЕПУБЛИКА СРБИЈА, БЕОГРАД са делом поседа 1/1, Корисник
са делом поседа 1/1,
кат.парцела 3629, ШУМА 1.класе, површина 20904м2, Шумско земиште

Лист непокретности: 4272
Власништво државне својине РЕПУБЛИКА СРБИЈА, БЕОГРАД са делом поседа 1/1, Корисник
са делом поседа 1/1,
кат.парцела 3629/1, ШУМА 1.класе, површина 11584м2, Шумско земиште
кат.парцела 3629/2, ШУМА 1.класе, површина 1532м2, Шумско земиште
кат.парцела 3629/3, ШУМА 1.класе, површина 7788м2, Шумско земиште

*Fig. 4 Part of the Republic Geodetic Authority Report on the plot division (example for Real Estate List 4272 - status before)*



- Лист непокретности број 4272 КО ПЕРЛЕЗ

Упис: УКЊИЖЕНО ЈЕ ЗАЛОЖНО ПРАВО У ИЗНОСУ ОД 7.000,00 ДИН
И СЛОВИМА СЕДАМХИЉАДА ДИН. У КОРИСТ:
на непокретности означеној у А-листу и то:
кат.парцела 3629/1, ШУМА 1.класе, површина 11584м2, Шумско земиште

Упис: УКЊИЖЕНО ЈЕ ЗАЛОЖНО ПРАВО У ИЗНОСУ ОД 7.000,00 ДИН
И СЛОВИМА СЕДАМХИЉАДА ДИН. У КОРИСТ:
на непокретности означеној у А-листу и то:
кат.парцела 3629/2, ШУМА 1.класе, површина 1532м2, Шумско земиште

Упис: УКЊИЖЕНО ЈЕ ЗАЛОЖНО ПРАВО У ИЗНОСУ ОД 7.000,00 ДИН
И СЛОВИМА СЕДАМХИЉАДА ДИН. У КОРИСТ:
на непокретности означеној у А-листу и то:
кат.парцела 3629/3, ШУМА 1.класе, површина 7788м2, Шумско земиште

Упис: УКЊИЖЕНО ЈЕ ЗАЛОЖНО ПРАВО У ИЗНОСУ ОД 120.000,00 ДИН.
И СЛОВИМА СТОДВАДЕСЕТХИЉАДА ДИН.У КОРИСТ:
на непокретности означеној у А-листу и то:
кат.парцела 3629/1, ШУМА 1.класе, површина 11584м2, Шумско земиште

Упис: УКЊИЖЕНО ЈЕ ЗАЛОЖНО ПРАВО У ИЗНОСУ ОД 120.000,00 ДИН.
И СЛОВИМА СТОДВАДЕСЕТХИЉАДА ДИН.У КОРИСТ:
на непокретности означеној у А-листу и то:
кат.парцела 3629/2, ШУМА 1.класе, површина 1532м2, Шумско земиште

Упис: УКЊИЖЕНО ЈЕ ЗАЛОЖНО ПРАВО У ИЗНОСУ ОД 120.000,00 ДИН.
И СЛОВИМА СТОДВАДЕСЕТХИЉАДА ДИН.У КОРИСТ:
на непокретности означеној у А-листу и то:
кат.парцела 3629/3, ШУМА 1.класе, површина 7788м2, Шумско земиште

*Fig. 5 Part of the Republic Geodetic Authority Report on the plot division (example for Real Estate List 4272 - status after)*

Based on proposal No. 03-465-875/2025, dated 22.10.2025 of Corridor of Serbia Ltd. Belgrade, the property and legal service of the Zrenjanin city issues a decision on

complete expropriation, with compensation on the Perlez administrative district (Figure 6).

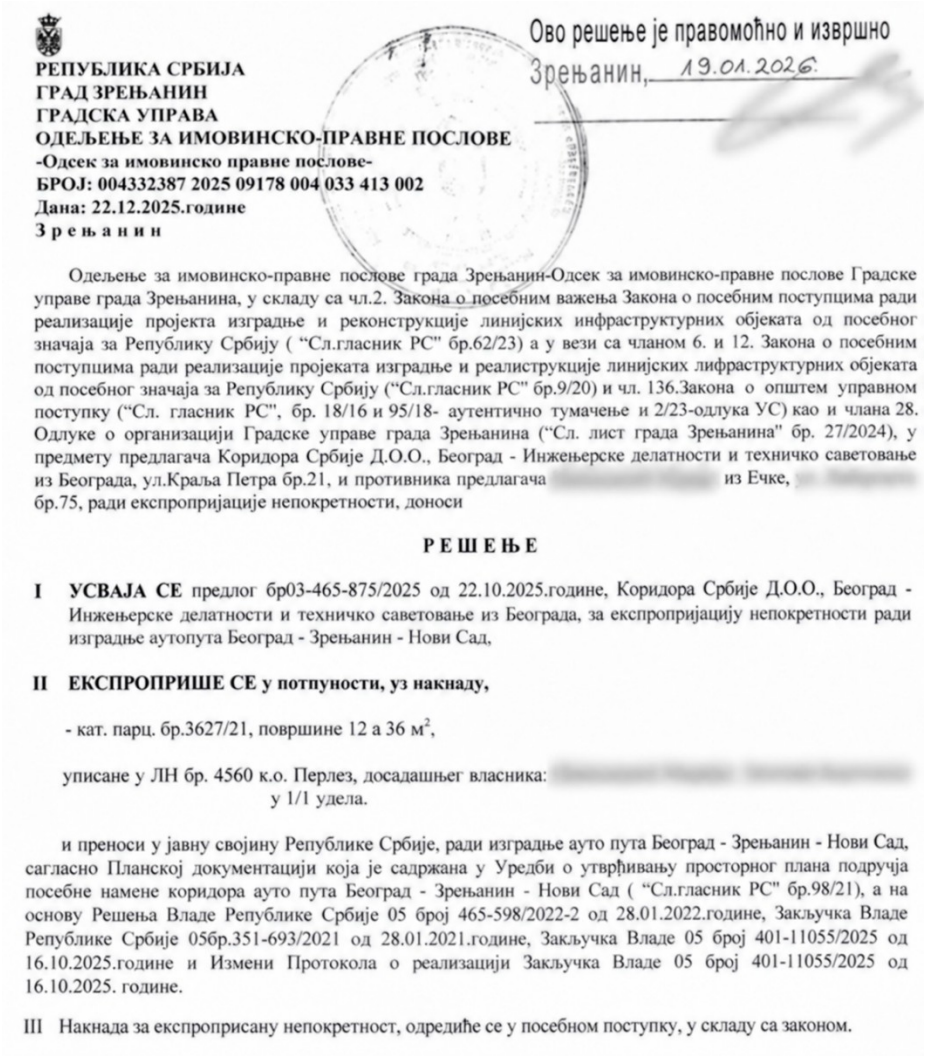

**РЕПУБЛИКА СРБИЈА**
**ГРАД ЗРЕЊАНИН**
**ГРАДСКА УПРАВА**
**ОДЕЉЕЊЕ ЗА ИМОВИНСКО-ПРАВНЕ ПОСЛОВЕ**
**-Одсек за имовинско правне послове-**
**БРОЈ: 004332387 2025 09178 004 033 413 002**
**Дана: 22.12.2025.године**
**З р е њ а н и н**

Ово решење је правомоћно и извршно
Зрењанин, 19.01.2026.

Одељење за имовинско-правне послове града Зрењанин-Одсек за имовинско-правне послове Градске управе града Зрењанина, у складу са чл.2. Закона о посебним важења Закона о посебним поступцима ради реализације пројекта изградње и реконструкције линијских инфраструктурних објеката од посебног значаја за Републику Србију ( "Сл.гласник РС" бр.62/23) а у вези са чланом 6. и 12. Закона о посебним поступцима ради реализације пројеката изградње и реалиструкције линијских лифраструктурних објеката од посебног значаја за Републику Србију ("Сл.гласник РС" бр.9/20) и чл. 136.Закона о општем управном поступку ("Сл. гласник РС", бр. 18/16 и 95/18- аутентично тумачење и 2/23-одлука УС) као и члана 28. Одлуке о организацији Градске управе града Зрењанина ("Сл. лист града Зрењанина" бр. 27/2024), у предмету предлагача Коридора Србије Д.О.О., Београд - Инжењерске делатности и техничко саветовање из Београда, ул.Краља Петра бр.21, и противника предлагача [redacted] из Ечке, [redacted] бр.75, ради експропријације непокретности, доноси

**Р Е Ш Е Њ Е**

I **УСВАЈА СЕ** предлог бр03-465-875/2025 од 22.10.2025.године, Коридора Србије Д.О.О., Београд - Инжењерске делатности и техничко саветовање из Београда, за експропријацију непокретности ради изградње аутопута Београд - Зрењанин - Нови Сад,

II **ЕКСПРОПРИШЕ СЕ у потпуности, уз накнаду,**

- кат. парц. бр.3627/21, површине 12 а 36 м$^2$,

уписане у ЛН бр. 4560 к.о. Перлез, досадашњег власника: [redacted] у 1/1 удела.

и преноси у јавну својину Републике Србије, ради изградње ауто пута Београд - Зрењанин - Нови Сад, сагласно Планској документацији која је садржана у Уредби о утврђивању просторног плана подручја посебне намене коридора ауто пута Београд - Зрењанин - Нови Сад ( "Сл.гласник РС" бр.98/21), а на основу Решења Владе Републике Србије 05 број 465-598/2022-2 од 28.01.2022.године, Закључка Владе Републике Србије 05бр.351-693/2021 од 28.01.2021.године, Закључка Владе 05 број 401-11055/2025 од 16.10.2025.године и Измени Протокола о реализацији Закључка Владе 05 број 401-11055/2025 од 16.10.2025. године.

III Накнада за експроприсану непокретност, одредиће се у посебном поступку, у складу са законом.

*Fig. 6 Excerpt from the expropriation decision for the Belgrade–Zrenjanin–Novi Sad highway project*

## 3.2. CASE STUDY: CORRIDORS 10 AND 11

### 3.2.1. Corridor 10

Corridor 10 is one of the most important pan-European transport corridors, connecting Austria, Hungary, Slovenia, Croatia, Serbia, Bulgaria, North Macedonia and Greece. Corridor 10 is 2300 km long, with 4 branches, and was added to the list of European corridors (Figure 7) at the Helsinki conference in 1997, as the main connection of north-western Europe with southern and southeastern Europe.




*Fig. 7 Map of Corridor 10*

The expropriation process for the needs of Corridor 10 in Serbia directly involved more than 30 cities and municipalities. The Corridor has 3 key directions: northern, southern and eastern. For the northern branch (E-75), expropriation was carried out on the territories of cities and municipalities such as: Subotica, Kanjiža, Mali Iđoš, Vrbas, Novi Sad, Inđija and Stara Pazova. Regarding the southern branch (E-75), expropriation was carried out on the territories of cities and municipalities such as: Leskovac, Vladičin Han, Vranje, Bujanovac and Preševo. Finally, there is the eastern branch (E – 80) which includes the areas from Niš to the Bulgarian border, with a focus on Niš, Bela Palanka, Pirot and Dimitrovgrad. Here it is necessary to add the bypass around Belgrade, which is Zemun (Batajnica), Surčin (Dobanovci) and Čukarice. The full highway profile on the entire Corridor 10 in Serbia has been operational since 2019.

### 3.2.2. Corridor 11

Corridor 11 is also a pan-European corridor, which is not yet fully completed, but most of the route through Serbia is functional. The goal of Corridor 11 and the continuation of these works is to complete the entire road connecting the Adriatic and the Danube. Corridor 11 (Figure 8) represents not only a connection between Serbia and Montenegro, but in a broader context connects Romania, Serbia, Montenegro and Italy. Corridor 11 connects everything from Timisoara, via Vršac, Belgrade, Čačak, Požega, Podgorica - all the way to Bar, from where it will be connected by sea across the Adriatic to Bari in Italy. The total length of the basic route Belgrade - Bar is about 400 km, of which about 170 km is planned in Montenegro, and about 240 km in Serbia.
The "Miloš Veliki" highway (A2) is a key part, i.e. the backbone of Corridor 11 in Serbia. This is the most important part through Central Serbia. A good example of efficient implementation of the expropriation procedure is the municipality of Lajkovac, where in about 95% of cases the procedure was concluded by issuing a decision, based on a compensation agreement, while approximately 5% of cases were in the appeal procedure, which have been resolved to date [1].

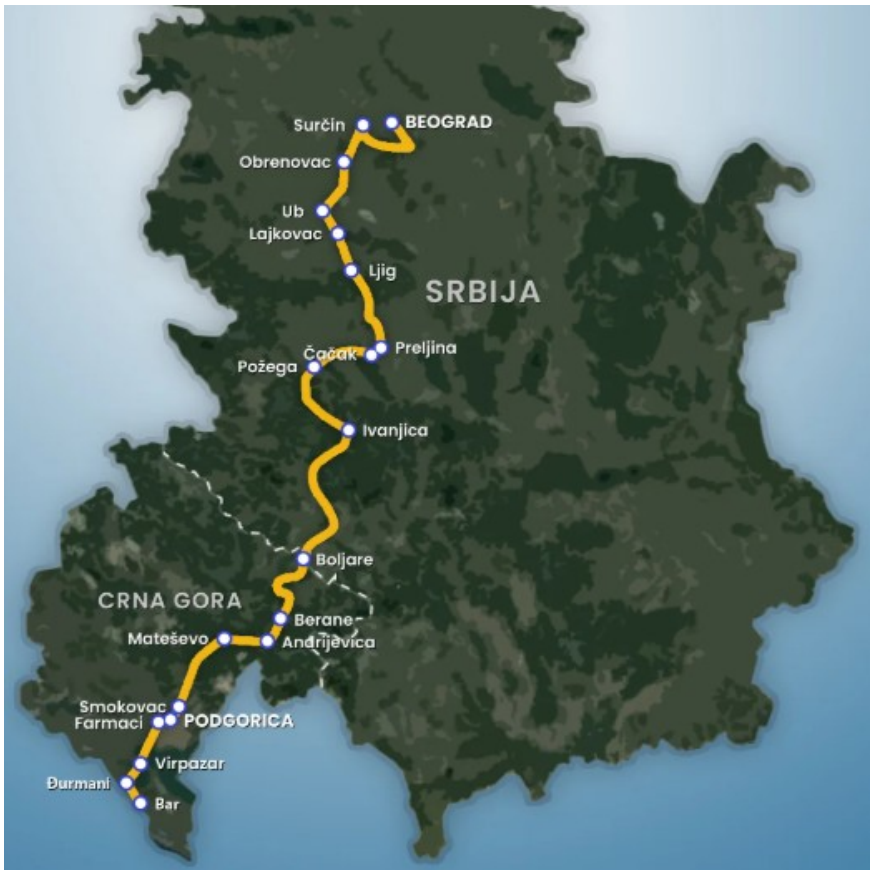


*Fig. 8 Map of Corridor 11*

## 4. CONCLUSION

In the expropriation process, the geodetic profession plays an irreplaceable role, both private geodetic organizations and the Republic Geodetic Authority (RGA). A pilot project has been developed for years, and today there are modern software solutions based on geographic information system technologies. Therefore, the cooperation between the aforementioned private geodetic organizations and the RGA has been raised to a higher level, in the form of urgency and efficient resolution of the expropriation process.

The use of modern GIS software can further improve the expropriation process through the integration of cadastral, ownership and project data, spatial identification of plots covered by expropriation, visualization of corridors of infrastructure facilities, as well as more efficient monitoring of the status of individual plots during the entire procedure. In this way, faster access to relevant information is enabled, simpler exchange of data between competent institutions and greater efficiency in decision-making.

Based on all the above, as well as the analysis of the specific examples, it can be concluded that the expropriation procedure is a complex and time-consuming process. This assessment stems, first of all, from the fact that a large number of institutions participate in its implementation, including the Government of the Republic of Serbia, the Ministry of Finance, the Serbian Land Survey, municipal administrations, geodetic organizations, public enterprises and other competent entities. Given the large number of participants and the phasing of the procedure itself, good institutional coordination, promptness in the procedure, quality preparation of documentation, as well as the

possibility of reaching an agreement on compensation are of particular importance, which can greatly affect the speed and efficiency of expropriation.
This paper provides a theoretical overview of the concept of expropriation, its division, the relationship between land consolidation and expropriation, as well as the role of the geodetic profession. An analysis of the implementation of the expropriation procedure on the Belgrade-Zrenjanin-Novi Sad highway is presented, as well as the changes caused by the construction of Corridors 10 and 11.

**ACKNOWLEDGEMENT**

The research has been conducted within the project "Enhancement of teaching and scientific research capacities through the application of modern technologies in the fields of civil engineering, geodesy, and disaster risk management and fire safety", developed at the Department of Civil Engineering and Geodesy, Faculty of Technical Sciences, University of Novi Sad, Serbia.

## REFERENCES

[1] Bajić M. (2010). Eksproprijacija nepokretnosti. Master's thesis, University of Novi Sad, Republic of Serbia.

[2] Zakon o eksproprijaciji ("Sl. glasnik RS", br. 53/95, "Sl. list SRJ", br. 16/2001 - odluka SUS i "Sl. glasnik RS", br. 20/2009, 55/2013 - odluka US i 106/2016 - autentično tumačenje)

[3] Marinković G., Trifković M., Nestorović Ž. (2013). Eksproprijacija – uzroci i posledice. Zbornik radova Građevinskog fakulteta Subotica, br. 22, str. 185–198. DOI: 10.14415/zbornikGFS22.017.

[4] Zakon o postupku upisa u katastar nepokretnosti i katastar infrastrukture ("Sl. glasnik RS", br. 41/2018, 95/2018, 31/2019, 15/2020 i 92/2023)

[5] Zakon o državnom premeru i katastru ("Sl. glasnik RS", br. 72/2009, 18/2010, 65/2013, 15/2015 - odluka US, 96/2015, 47/2017 - autentično tumačenje, 113/2017 - dr. zakon, 27/2018 - dr. zakon, 41/2018 - dr. zakon, 9/2020 - dr. zakon, 92/2023 i 91/2025)

[6] Bogdanović B. (1979). Komasacija i eksproprijacija. Beograd: Republički zavod za javnu upravu.

https://doi.org/10.24867/INDIS-2026-EN-679



# "SMART PARCEL" SYSTEM – A FOUNDATION FOR DIGITAL LAND MANAGEMENT IN SERBIA

*Jelena Tatalović[1], Bogdan Bojović[2], Milica Malešić Petković[3]*

***Summary:***

The digital transformation of land administration represents one of the key directions in the development of modern cadastral systems. Traditional real property registration models are no longer sufficient to meet the demands of efficient land management, urban development, investment processes, and natural resource protection. In this context, the "Smart Parcel" system, developed by the Republic Geodetic Authority of Serbia, represents an innovative solution based on the integration of spatial, legal, and planning data into a unified digital framework. This paper analyzes the concept, functionalities, and significance of this system as a foundation for the modernization of the cadastre and the improvement of land administration in the Republic of Serbia. The research findings indicate that the "Smart Parcel" system constitutes a significant step toward establishing an efficient, transparent, and sustainable model of land management.

*Keywords: Smart Parcel, Cadastre, Land Administration, Land Management*

# SISTEM „PAMETNA PARCELA" - OSNOV ZA DIGITALNO UPRAVLJANJE ZEMLJIŠTEM U SRBIJI

***Rezime:***

Digitalna transformacija zemljišne administracije predstavlja jedan od ključnih pravaca razvoja savremenih katastarskih sistema. Tradicionalni modeli evidencije nepokretnosti više nisu dovoljni da odgovore na zahteve efikasnog upravljanja zemljištem, urbanog razvoja, investicionih procesa i zaštite prirodnih resursa. U tom kontekstu, sistem „Pametna parcela", koji razvija Republički geodetski zavod, predstavlja inovativno rešenje zasnovano na integraciji prostornih, pravnih i planskih podataka u jedinstveni digitalni okvir. Rad analizira koncept, funkcionalnosti i značaj ovog sistema kao osnove za modernizaciju katastra i unapređenje zemljišne administracije u Republici Srbiji. Rezultati istraživanja ukazuju na to da sistem „Pametna parcela" predstavlja značajan korak ka uspostavljanju efikasnog, transparentnog i održivog modela upravljanja zemljištem.

*Ključne reči: pametna parcela, katastar, zemljišna administracija, upravljanje zemljištem*

[1] Assistant Professor, Faculty of Civil Engineering Subotica, University of Novi Sad, Subotica, Serbia, lazicjelena@uns.ac.rs, ORCID: 0000-0001-7280-919X
[2] M.Sc. Eng. in Geodesy, Faculty of Civil Engineering Subotica, University of Novi Sad, Subotica, Serbia, bojovic@gf.uns.ac.rs
[3] M.Sc. Eng. in Geodesy, Republic Geodetic Authority, Belgrade, Serbia, milica.malesic@gmail.com

## 1. INTRODUCTION

Modern land management increasingly relies on digital systems that integrate spatial and legal data into a single functional framework. The traditional cadastre, based mainly on records of boundaries and property rights, can no longer fully respond to the demands of the dynamic real estate market, urban development, protection of natural resources, and increasingly complex investment processes. The speed of societal change, urban growth, and the need for transparent and legally secure data have imposed the need for new models of digital transformation in the field of land administration.

In this context, the Republic Geodetic Authority is developing the "Smart Parcel" system as a platform that represents the foundation for digital land management in Serbia. This system enables each cadastral parcel to receive its own digital profile with clearly defined spatial, legal, and planning attributes. In this way, not only is faster and more reliable access to data enabled, but also support is provided for planning processes, investments, and public policy decision-making.

The main idea of this paper is to present the importance of the "Smart Parcel" as a tool that improves the quality of land management, contributes to sustainable development, and integrates Serbia into European and global trends in the digital transformation of cadastral systems.

The subject of this research is the concept and development of the "Smart Parcel" system as a modern model of digital land management in the Republic of Serbia. The research includes an analysis of the functional, technical, legal, and institutional aspects of this system, with special emphasis on the integration of spatial, legal, and planning data into a unified digital framework. It also examines the role of the "Smart Parcel" system in modernizing the cadastre, improving land administration, and aligning it with contemporary European and global trends in digital transformation.

The aim of the research is to determine the significance and potential of the "Smart Parcel" system as a basis for efficient, transparent, and sustainable land management in Serbia. The paper aims to show how the digital profile of a cadastral parcel contributes to improving legal security, data accessibility and reliability, more efficient spatial planning, support for investment processes, and public policy decision-making. In addition, the aim is to analyze the possibilities of interoperability of this system with other information systems and its contribution to further digitalization of the cadastre and land administration in the Republic of Serbia.

### 1.1. PREVIOUS RESEARCH

The rapid development of modern society, changes in the way the economy operates, and technological advances have placed new demands on real property registration systems. The need for faster access to reliable geospatial data, as well as the protection and security of registered rights, has created a need for reforms of traditional cadastral systems [1].

The modernization of land administration and cadastral systems has been a subject of continuous interest for international organizations, land administration authorities, and researchers. The United Nations, the International Federation of Surveyors (FIG), and the World Bank have addressed the need for modern land administration systems in various documents and at numerous conferences [2]. In this context, various organizations and researchers have proposed a number of frameworks and models for improving land administration and cadastral systems [3, 4, 5, 6, 7].

In the Republic of Serbia, long-standing public records - cadastre, land registers, and title deeds - primarily served legal and fiscal purposes. However, the growth of the real estate market and the requirements of modern spatial management call for a broader range of services, including digital accessibility, integrated spatial and legal data, faster updating,

and transparent information exchange. In recent years, cadastral records in Serbia have faced numerous challenges, including: the existence of different institutions responsible for managing land and real property data; simultaneous storage of data in multiple locations; storage of data in analogue form; inconsistencies between recorded data and the actual situation in the field; separation of alphanumeric and spatial data; a complex structure of records resulting from the integration of data from different sources; poor performance in searching, retrieving, and updating data; and the lack of a standardized data exchange format. Some of these issues have been addressed in recent years, while many still remain. Such problems can lead to data redundancy, duplication of development efforts for the same functionalities, and deterioration of data accuracy. In an environment where rapid processing of changes in records and efficient provision of geospatial and other information on the legal status of real property are expected, reforms must include both legal and technical measures: simplification of procedures, clearly defined responsibilities, standards for digitization and data exchange, as well as mechanisms for long-term data maintenance and quality control.

In the contemporary period, modern cadastral systems worldwide have ceased to be merely static records of boundaries and ownership and have evolved into integrated digital systems that form the backbone of national spatial infrastructures [8, 9]. Countries regarded as leading examples of modernization, such as the Netherlands, Finland, Estonia, the United Kingdom, and Australia, have gone beyond technical digitization. They have harmonized their legal frameworks, introduced standardized data modelling, established service-oriented architectures for data exchange and public access, and developed institutional support for continuous maintenance and quality control [8, 10, 11, 12]. Unlike traditional approaches, in which the cadastre primarily served legal and fiscal purposes, modern systems also support spatial planning, resource management, and the real estate market, with interoperability, transparency, and data accessibility becoming key principles.

Through its reform activities, the Republic Geodetic Authority (RGA) of Serbia follows these global principles. The introduction of geoportals, digitization of cadastral data, establishment of permanent GNSS stations, and integration with the information systems of other public services demonstrate a clear orientation towards INSPIRE standards and the Land Administration Domain Model (LADM) concept.

## 1.2. METHODOLOGY

The research presented in this paper is based on a case study approach, with the “Smart Parcel” system in the Republic of Serbia serving as the primary subject of analysis. The methodological framework combines an analysis of the system concept and functional architecture with an examination of the data integration and validation procedures applied during the pilot implementation.

The research was conducted through four main methodological steps. The first step involved identifying the main data domains relevant to parcel-level land management, including cadastral, planning, legal, and institutional data. The second step focused on analysing the procedures used to transform heterogeneous source data into standardized geospatial datasets suitable for integration into the “Smart Parcel” environment. The third step was aimed at analysing the relationships between cadastral parcels and the associated planning documents, legal acts, land-use categories, and holders of public authority. The fourth step involved analysing selected indicators from the pilot implementation and the reduction of technical errors following data validation.

Data quality was assessed by identifying technical inconsistencies, including unclosed polygons, overlaps, gaps, and inconsistencies in the datasets.

The methodological framework also considers interoperability as an important characteristic of the system. The "Smart Parcel" concept is therefore analysed in relation to the Framework for Effective Land Administration (FELA), the Land Administration Domain Model (LADM), and the principles of the INSPIRE Directive relating to spatial data interoperability. These frameworks are not treated as identical standards, but rather as complementary reference frameworks for analysing the functional, conceptual, and interoperability aspects of the system.

The relationship between the "Smart Parcel" system and the Land Administration Domain Model (LADM) can primarily be considered at the conceptual level. The cadastral parcel corresponds to the spatial component of land administration, while information on rights, restrictions, and responsibilities provides the legal and administrative dimension of the system.

Within the "Smart Parcel" concept, the parcel is not considered merely as a geometric object. It represents a spatial reference through which information on land use, planning restrictions, and legal acts can be linked. This approach is consistent with the fundamental principle of LADM, according to which spatial units are associated with parties involved in land administration and their rights, restrictions, and responsibilities.

The "Smart Parcel" system therefore extends the parcel-based cadastral perspective by linking cadastral information with planning and spatial information. FELA provides a broader land administration perspective and is used to assess whether the "Smart Parcel" concept supports integrated and effective land administration. LADM provides a conceptual basis for structuring relationships between spatial units, parties, and rights, restrictions, and responsibilities. INSPIRE, on the other hand, addresses the interoperability and harmonisation of spatial information and services.

FELA provides the strategic and functional framework, LADM provides the conceptual modelling perspective, while INSPIRE defines principles and technical requirements relevant to spatial data interoperability.

## 1.3. DEVELOPMENT OF THE INFORMATION SYSTEM OF THE REPUBLIC GEODETIC AUTHORITY: FROM THE ESTABLISHMENT OF THE REAL ESTATE CADASTRE TO THE PRESENT

History of cadastre in the territory of present-day Serbia is long and complex, with a legacy that is reflected in the current structure and function of real estate records. The beginnings can be traced back to the period of the Ottoman Empire, when land surveys were conducted. Their main purpose was to determine tax obligations and maintain records of land ownership in accordance with the tax system of that time. Although these surveys were not a cadastre in the modern sense, they laid the foundations for the systematic tracking of land.

Before the establishment of the real estate cadastre, two parallel records of immovable property existed in our country: on one side, land registers or title deed records as records of property rights, and on the other side, the land cadastre as a record of land and buildings on the land. In some regions, only the land cadastre existed, while land registers or title deed books were never established, or were destroyed during wars. Where dual records existed, the data in land registers and title deed books were in some areas disorganized, and often these records were not mutually harmonized with the land cadastre data.

Another issue was that different authorities were responsible for maintaining these records—land registers were under the jurisdiction of municipal courts, while the land cadastre was under the jurisdiction of the Republic Geodetic Authority. Gradually, the idea emerged that these two records should be unified into a single system that would include both data on immovable property and data on property rights, and that would be managed by a single institution. In 1988, the adoption of laws in the field of real estate

cadastre began. Today, this register is called the Real Estate Cadastre and is under the jurisdiction of the Republic Geodetic Authority.

During this period, the transition process and alignment with European standards initiated intensive modernization efforts: establishing the Republic Geodetic Authority as the central institution for cadastre management, introducing geographic information systems, digitization of cadastral maps and attributes, and the application of GNSS technologies and permanent reference stations that improve the accuracy and reliability of spatial data. Modern trends include further integration of the cadastre with other databases, development of geoportals and public services, as well as harmonization of the legal framework to make records faster, more accessible, and legally more secure. This historical legacy and ongoing reform activities form the basis for further steps in cadastre modernization: it is necessary to continue technical improvements while simultaneously working on legal, organizational, and human resource solutions in order to ensure a comprehensive and sustainable system transformation.

Table 1 presents the key activities in the development of the real estate cadastre in the Republic of Serbia.

*Tab. 1 Key Activities in the Development of the Cadastre in the Republic of Serbia [13,14]*

| Period | Key Activities |
|---|---|
| Late 1980s – 1990s | Institutional start, initial records, early digital data |
| 1990s – early 2000s | Pilot projects, trial digitization, software testing |
| 2004–2012 | Mass conversion (World Bank project, etc.), registry integration |
| 2011–2012 | Formal confirmation of cadastre in most municipalities (4,322 cadastral municipalities ≈ 95.6%) |
| 2013–present | Database centralization, GeoSrbija, e-services, standards and ISO integration |

In the contemporary period, modern cadastres worldwide have ceased to be merely static records of boundaries and ownership—they have become integrated digital systems that form the backbone of national spatial infrastructures. Countries considered leading examples of modernization (e.g., the Netherlands, Finland, Estonia, the United Kingdom, and Australia) have done more than simply digitize data: they have harmonized their legal frameworks, introduced standardized data modeling, established service-oriented architectures for data exchange and public access, and developed institutional frameworks for continuous maintenance and quality control.

Unlike traditional approaches, where the cadastre primarily had a legal and fiscal role, modern systems also support spatial planning, resource management, and real estate markets—where interoperability, transparency, and data accessibility become key values. The Republic Geodetic Authority, through its reform activities, follows these global principles: the introduction of geoportals, digitization of cadastral data, establishment of permanent GNSS stations, and integration with information systems of other public services clearly demonstrate alignment with INSPIRE standards and the Land Administration Domain Model (LADM) concept.

## 2. SMART PARCEL: A MODEL FOR DIGITAL LAND ADMINISTRATION AND MANAGEMENT IN SERBIA

The role of the cadastral parcel in the 21st century is changing dramatically—from a static legal-geometric entity, it is becoming a dynamic unit of spatial management, economic

analysis, and development planning. Contemporary challenges such as urban growth, climate change, digital transformation of public administration, and an increasing demand for transparency require new approaches to land use and land administration. It is precisely in this context that the "Smart Parcel" initiative emerges—as a systemic response to the need for integrated, reliable, and accessible cadastral parcel data in Serbia. The "Smart Parcel" system is an initiative of the Republic Geodetic Authority (RGA) aimed at the digital transformation of spatial and urban planning and the modernization of land administration in Serbia. It is part of the National Spatial Data Infrastructure (NSDI) and is aligned with the guidelines of the Framework for Effective Land Administration (FELA), adopted by UN-GGIM (United Nations Committee of Experts on Global Geospatial Information Management).

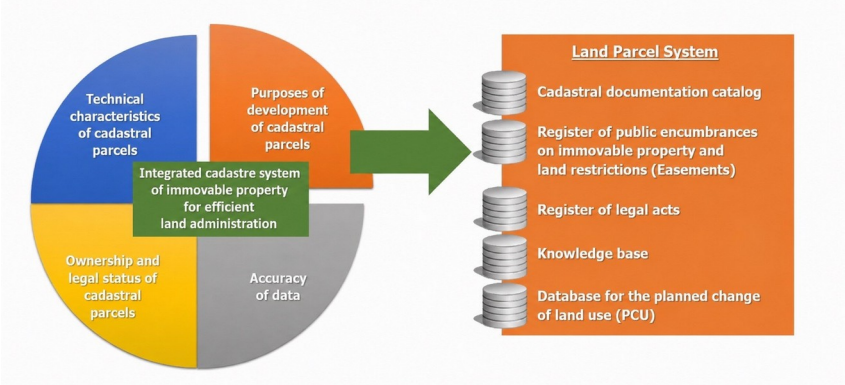


*Fig. 1 Transformation of the Real Estate Cadastre into the Smart Parcel System as the Basis for Digital Land Governance [3]*

The concept of the system is based on the idea that each cadastral parcel in Serbia has a digital profile that integrates all spatial, legal, and planning data in one place. Instead of users searching through dozens of sources and institutions, all information will be available through a single platform—from the technical characteristics of the parcel, to ownership data, to legal restrictions and designated land use (Figure 1).

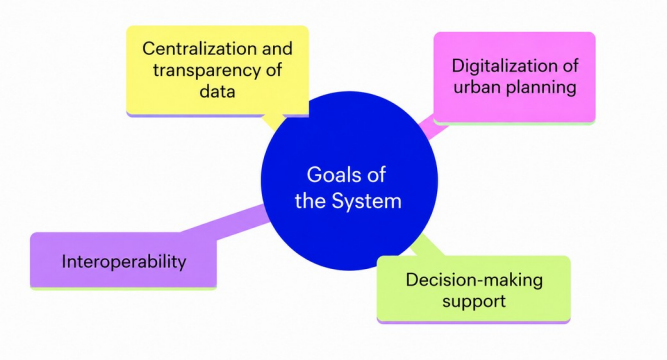


*Fig. 2 Objectives of the Smart Parcel System*

The objectives of the system are (Figure 2):
1. Centralization and transparency of data: The system enables data that were previously scattered (in paper documents, local databases, municipal archives) to be centralized and digitized. Users can identify the legal, planning, and regulatory status of land through a simple spatial query.
2. Decision-making support: Investors, planners, government institutions, and citizens gain the ability to make decisions based on comprehensive, up-to-date, and official data.
3. Interoperability: Compliance with the INSPIRE Directive and FELA guidelines enables the integration of Serbia's system with European spatial data infrastructure (SDI) solutions, as well as the potential for cross-border cooperation and projects.

4. Foundation for the digitalization of urban planning: The Smart Parcel serves as a bridge toward digital planning documents—preparing the ground for a new generation of standardized and technically validated digital urban plans.

## 2.1. SMART PARCEL AND FELA: THE FOUR PILLARS OF MODERN CADASTRE

FELA defines four core data sets (so-called "pillars") that together form the functional profile of each cadastral parcel. The Smart Parcel system is based precisely on this structure, where each of the pillars relies on existing or newly established data sources within the Republic Geodetic Authority.

*Tab. 2 The Four Information Pillars according to the FELA Framework*

| No. | Title and Description | Data Source |
|---|---|---|
| 1. | **Technical characteristics of the parcel** - location, shape, and area of the parcel | ISKN - Real Estate Cadastre Information System |
| 2. | **Legal status and ownership** - rights holders, annotations, encumbrances | ISKN, legal registers of the Republic Geodetic Authority (RGZ) |
| 3. | **Property value** - market and assessed value | Real Estate Price Register (RPR), mass appraisal system |
| 4. | **Planned and functional land use** - possibilities for land utilization | Parcel memory: catalogs, legal acts, spatial plans |

While the first three pillars already exist within the official registers and systems of the Republic Geodetic Authority (RGA), the fourth pillar represents a key innovation introduced by the Smart Parcel system (Tab. 2). Its purpose is to provide, for each parcel, information on what activities are permitted on that land, under which conditions, and which authorities are responsible for issuing permits and approvals.

### 2.1.1. Components of the Fourth "Pillar": A Functional Framework for Assessing the Development Potential of a Parcel

The fourth "pillar" integrates planning, regulatory, and institutional information that together describe the functional usability of a cadastral parcel.
Within this pillar, four components have been developed:
1. Catalogue of planning documents – contains all spatial and urban plans with the possibility of linking them to specific parcels. The catalogue systematizes all relevant spatial and urban plans with their geographic extents and metadata. Each document is geolocated and connected to both textual and graphical parts, so that for any parcel it is immediately possible to determine the set of applicable plans.
2. Catalogue of holders of public authority (HPA) – information on institutions that influence land use (e.g., Institute for Nature Protection). This database includes institutions responsible for issuing special land-use conditions (e.g., nature protection, water resources, infrastructure, cultural heritage). For each institution, its area of competence is defined as a geospatial layer, enabling automatic identification of which authority issues conditions for a specific parcel and based on which regulation. The role model in the system (editor/supervisor) ensures data quality: a local editor first enters or updates the data, and then a supervisor reviews and publishes it. This addresses an identified organizational challenge: the need for two-person verification before publication, thereby reducing errors and increasing data reliability.
3. Catalogue of legal acts – a link between legal regulations and planning bases for individual parcels. This catalogue connects the legal framework (laws, regulations, decisions) with planning documents and the institutions issuing them. Each act has a

status, type, reference source, and a link to the spatial domain to which it applies. At the user experience level, data entry is simplified and standardized through guided forms and instructions, reducing the risk of vague inputs and ensuring that searches return consistent results instead of depending on free-text naming.

4. Land Use Planning Database (LUPD) – a consolidated land-use classification (construction land, agricultural land, etc.) derived from valid plans.

The LUPD serves as a national-level generalized layer intended for quick orientation, consisting of five basic categories (construction, agricultural, forest, water, and other land) as well as information on special conditions. Its purpose is not to replace detailed regulations—which remain within planning documents—but to provide an immediate and consistent overview of the planning regime for each parcel. Methodologically, the LUPD is created by converting heterogeneous source files (often AutoCAD-based) into topologically correct polygons with INSPIRE-compliant attributes.

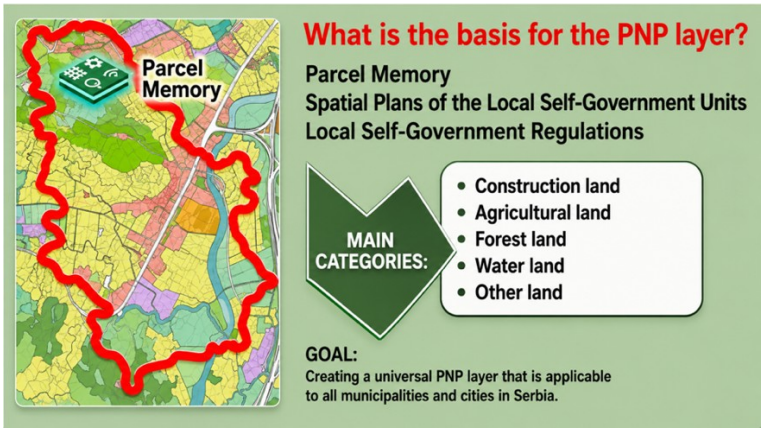


*Fig. 3 Presentation of the Land Use Planning Database*

These components are interconnected and enable the user, through a simple search by parcel number, to obtain all necessary information on the rights, restrictions, and development potential of a given parcel (Figure 3). The integration of the mentioned components allows the user, through a simple spatial query (e.g., by clicking on a parcel), to receive a clear answer: what is permitted on the given parcel, which plans are applicable, what restrictions exist, and which authority is responsible for issuing conditions.

## 3. RESULTS OF SYSTEM IMPLEMENTATION

The results of the implemented activities within the Smart Parcel project demonstrate that the system has significantly improved the way spatial data is managed in Serbia. Even in the pilot phase, which included 18 local self-government units, it was shown that the integration of planning documents, legal acts, and cadastral data into a single digital framework enables more efficient and reliable use of information.

Instead of users having to navigate multiple disconnected sources, the system provided a consolidated view, which in practice resulted in time savings, a reduced risk of errors, and greater transparency.

A particularly significant technical outcome relates to the coverage of the Land Use Planning Database (LUPD). During the first six quarters, coverage increased from 22% to over 80% in the included municipalities (Figure 4). This figure illustrates that the system successfully accelerated and simplified the process of digitizing planning documents, even though most of them were previously available only in analog form or as incomplete digital records.

The fact that more than three-quarters of standardized data were made available in less than two years demonstrates the system's strong potential for nationwide implementation.

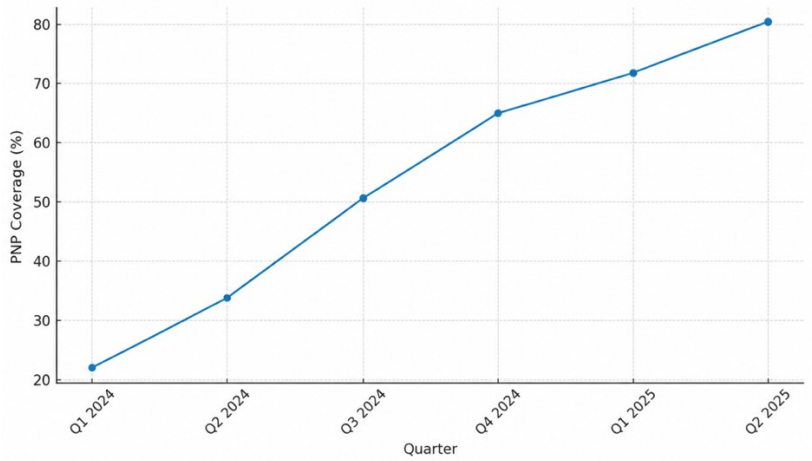


*Fig. 4 Coverage of Planned Land Use in Pilot Municipalities Over Time*

In addition to quantitative progress, a qualitative improvement has also been observed in terms of data accuracy. With the introduction of automated topological checks and manual corrections in cooperation with local self-government units, the number of errors such as unclosed polygons, overlaps, or gaps was reduced by more than 80%.
Furthermore, the standardization of coordinate reference systems and the introduction of controlled code lists ensured consistency in data that was previously unreliable.
Table 3 shows that the introduction of automated topological validation, data standardization, and verification processes directly leads to a significant reduction in technical errors. The greatest improvement was achieved in the harmonization of coordinate reference systems (−96%), which was crucial for the correct visualization and integration of different spatial layers.
In this way, the system ensures that digital plans become a reliable foundation for analysis, planning, and decision-making.

*Tab. 3 Reduction of errors in planning documents after validation (per 100 documents)*

| Type of error | Before check (% of documents) | After check (%) | Changes |
|---|---|---|---|
| Non-closure of the polygon | 12.5 | 1.9 | –85% |
| Overlap | 8.3 | 1.7 | –80% |
| Gap | 6.1 | 1.2 | –80% |
| CRS not defined | 12.2 | 0.6 | –95% |

From a legal and institutional perspective, the Smart Parcel system has demonstrated that establishing a single canonical record per document (with a clearly defined status, issuing authority, and source file) significantly increases legal certainty. Institutions gained the ability to track the entire chain—from the legal act, through the planning document and its spatial extent, to the specific parcel. This level of data connectivity was previously missing, and its introduction enables users to obtain a complete overview of rights and restrictions on a parcel without additional interpretation.
From the perspective of user experience, the benefits are multiple. For citizens, the system provides a simple single access point through which they can check what is permitted on their parcel, which plans are in force, and which institution is responsible for issuing

conditions. Urban planners and spatial designers gain a reliable tool that links textual and geospatial components of documents, while investors are able to perform a "quick due diligence" of a location within minutes and assess regulatory risks. Institutions, on the other hand, benefit from improved control through editor and supervisor roles, data replication mechanisms, and clear audit trails of changes.

The analysis of results shows that technical, legal, and social aspects of the system are directly intertwined. Technical machine readability and data standards ensure that each legal act or plan is predictably linked to a specific parcel. Institutional quality control mechanisms, such as role-based workflows and the "four-eyes" principle, have proven to be the most effective means for stable system operation. At the same time, response speed and data transparency influence user behavior, enabling the system to be used in real time during discussions with citizens or investors.

## 3.1. LIMITATIONS IN THE IMPLEMENTATION OF THE SMART PARCEL SYSTEM

Although the Smart Parcel system has delivered significant results in the pilot phase, certain shortcomings have also been identified that slow down its full-scale implementation. The biggest challenge is the heterogeneity of source data: many spatial plans still exist in DWG formats without topological correctness, with undefined or insufficiently described layers. Such deficiencies significantly slow down the digitization process and require additional time for conversion and quality control.

A second issue relates to the varying capacities of local self-government units. While some municipalities have the staff and equipment necessary for efficient implementation, others lag behind, resulting in uneven data quality.

In addition, frequent changes in laws and secondary legislation require continuous legal support and adaptation of data models.

For the stable development of the system, it is necessary to address these limitations. First, it is essential to adopt a unified standard for the delivery of digital plans, which would include topological integrity, controlled code lists, and a unified coordinate reference system. This would allow new plans to be integrated into the system immediately, without additional conversion or correction steps.

## 3.2. SIGNIFICANCE OF THE IMPLEMENTATION OF THE SMART PARCEL SYSTEM

### 3.2.1. Significance for Land Management

The Smart Parcel system represents an operational bridge between cadastral data, planning documents, legal acts, and the competences of holders of public authority. By linking these sources into a unified, machine-readable, and standardized framework, the system raises the quality of land management at the national level: citizens and the economy receive clear and fast answers, planning professionals gain a reliable working platform, and institutions obtain tools for quality control, legal certainty, and transparency.

For citizens, the "Smart Parcel" system means simpler and more transparent access to information about their own or any other parcel. Instead of visiting different institutions or searching multiple sources, they can now, with a single parcel number entry, address search, or map click, obtain a complete overview of the situation—what the land use designation is, which plans are in force, whether any restrictions exist, and which authority is responsible for issuing conditions. This is a "single source of truth" that eliminates confusion and saves time. In addition, citizens remain informed through news,

announcements of events, notification systems, and a contact form that enables direct communication with institutions.

For urban planners and spatial designers, the system offers a completely new dimension of work. All inputs undergo topological and content validation, and data are entered according to unified code lists and reference systems. This ensures that the results of their work are reliable and compliant with standards. Textual and geospatial parts of documents are logically connected, making search and analysis easier. The system also enables collaboration among multiple experts through editor and supervisor roles, where each entry is reviewed before becoming official. In this way, data quality is preserved, and every change can be tracked through historical records.

Investors gain a significantly more reliable basis for decision-making. All valid plans and restrictions for a selected location are visible in one place, along with clearly indicated institutions responsible for issuing land-use conditions. This transparency reduces regulatory risk and enables better investment planning. Investors can quickly verify whether their project complies with the designated land use and protection requirements, such as water or natural resources, cultural heritage, or infrastructure. An additional advantage is that, through API services, they can directly integrate their internal systems and automatically retrieve data for multiple locations, significantly accelerating portfolio analysis.

For institutions, the Smart Parcel system represents a platform that ensures a high level of data control and integrity. Each user logs in through a unified system with clearly defined permissions and access rights. Data entries are regularly replicated and distributed, ensuring that public viewers always display the most up-to-date state. The use of harmonized metadata and standards facilitates data exchange with other registers and systems, while reports on data completeness and quality enable better monitoring and governance. In this way, public administration gains a tool that simultaneously increases efficiency and transparency [15, 16, 17].

### 3.2.2. Contribution to Sustainable Development

The Smart Parcel system has a direct impact on improving sustainable development in Serbia. It enables more efficient land use, better resource protection, and decision-making based on high-quality and standardized data. The consolidated land use database guides development toward locations that are already infrastructure-ready, thereby preventing the expansion of uncontrolled construction and the formation of unplanned settlements.

In addition, the system enables the integration of data with zones of environmental protection, water resources, and cultural heritage, which allows for early identification of conflict areas. In this way, development conditions can be adjusted in advance and defined so as to minimize risks.

An important component is the use of standardized code lists and machine-readable formats, which enable systematic analysis and monitoring of indicators. This allows public authorities and decision-makers to plan development based on evidence and in line with sustainable urbanization policies.

The system also reduces administrative costs and burdens by eliminating the need for paper-based documents and duplicate data entry. Finally, it increases transparency and data accessibility for the public. In this way, citizens and institutions can actively participate in planning processes, thereby increasing trust and enabling a fairer and more efficient model of land governance.

## 4. CONCLUDING REMARKS

The Smart Parcel system represents a significant step in the modernization of land administration in Serbia and in the introduction of digital transformation in the fields of cadastre and urban planning. This study has shown that traditional, fragmented, and analog approaches are no longer capable of addressing contemporary challenges such as rapid urban growth, the need for transparency, data integration, and improved legal certainty. Through the introduction of a new model based on the FELA concept and the standards of the National Spatial Data Infrastructure, the cadastral parcel is transformed from a purely legal-geometric unit into a functional node within the spatial management system.

The results of the pilot implementation demonstrate that integrating cadastral, planning, and legal data into a single platform brings direct benefits to all user groups. Citizens gain fast and clear access to information about their parcels, urban planners work with harmonized and topologically correct data, investors have reliable foundations for decision-making, while institutions are provided with tools for quality control and monitoring of legal validity of documents. In this way, significant progress has been achieved in legal certainty, procedural transparency, and administrative efficiency.

From a technical perspective, the system has shown that it is possible to significantly reduce long-standing issues such as DWG-based plans without topology, undefined coordinate reference systems, or non-machine-readable PDF documents. Through the introduction of standardized code lists, metadata, and topological validation, data have been transformed into usable formats that enable automated analysis and interoperability with other systems. At the same time, organizational workflows based on the “four-eyes principle” ensure data quality and reliability.

From a socio-economic perspective, the greatest value of the system lies in equal access to information for citizens and investors and in the speed of obtaining reliable data. The system is not only a tool for technical data processing, but also a mechanism that increases trust in institutions, reduces space for interpretative disputes, and enables better development planning. A particular contribution is made to sustainable development: system data enable more efficient land use, protection of natural and cultural resources, and the directing of investments toward planned and infrastructure-equipped locations.

Although significant results have been achieved, several challenges remain to be addressed in future phases - primarily the heterogeneity of source data, varying capacities of local self-government units, and the need for continuous alignment with regulatory changes. These challenges represent directions for further work: standardization of plan formats, improvement of training, and further introduction of digital tools in administration.

Overall, the Smart Parcel system represents the foundation for a new generation of digital land administration in Serbia. It unifies legal, technical, and social aspects into a single functional system that contributes to legal certainty, transparency, and sustainable development. This model may serve as a best practice example not only in Serbia but also in a broader regional and European context, as a basis for more efficient and equitable spatial governance.

## REFERENCES

[1] Williamson, I., & Ting, L. (2001). *Land administration and cadastral trends — a framework for re-engineering*. Computers, Environment and Urban Systems, 25(4–5), 339–366.

[2] Jahani Chehrehbargh, F.; Rajabifard, A.; Atazadeh, B.; Steudler, D. Identifying global parameters for advancing Land Administration Systems. Land Use Policy 2024, 136, 106973.

[3] International Federation of Surveyors (FIG). Statement of the Cadastre; FIG Publication No 11; FIG: Copenhagen, Denmark, 1995; Available online: https://www.fig.net/resources/publications/figpub/pub11/figpub11.asp(accessed on 22 June 2024).

[4] Kaufmann, J.; Steudler, D. Cadastre 2014 Vision. International Federation of Surveyors (FIG), 1998. Available online: https://www.fig.net/resources/publications/figpub/pub11/FIG%20Statement%20on%20the%20Cadastre.pdf(accessed on 22 June 2024).

[5] Intergovernmental Committee on Surveying and Mapping (ICSM). Cadastre 2034 Powering Land & Real Property: Cadastral Reform and Innovation for Australia—A National Strategy. Canberra, Australia, 2020. Available online: https://www.icsm.gov.au/cadastre-2034(accessed on 13 July 2024).

[6] Jahani Chehrehbargh, F.; Rajabifard, A.; Kalantari Soltanieh, M.; Steudler, D. Advancing Land Administration System—Implications of Recent International Trends. In Proceedings of the FIG Congress: Volunteering for the Future-Geospatial Excellence for a Better Living, Warsaw, Poland, 11–15 September 2022.

[7] Govedarica, M., Radulović, A., et al. (2021). Designing and implementing a LADM-based cadastral information system in Serbia, Montenegro and Republic of Srpska. Land Use Policy, 109, 105732.

[8] Uşak, B., Çağdaş, V., & Kara, A. (2024). *Current Cadastral Trends—A Literature Review of the Last Decade*. Land, 13(12), 2100. https://doi.org/10.3390/land13122100

[9] Lemmen, C., et al. (2024). *Design of the new structure and capabilities of LADM edition II including 3D aspects*. Land Use Policy, 137, 107003.

[10] van Oosterom, P., et al. (2022). *The new, LADM inspired, data model of the Dutch cadastral map*. Land Use Policy.

[11] Krigsholm, P., Riekkinen, K., & Ståhle, P. (2018). *The changing uses of cadastral information: A user-driven case study*. Land Use Policy, 77, 329–337.

[12] Atazadeh, B., Rajabifard, A., & Olfat, H. (2023). Rad o modernizaciji 3D digitalnog katastra. Land Use Policy, 131.

[13] Valda Rajić, I. A., Radulović, A. (2016). Unapređenje katastarskog informacionog sistema u Republici Srbiji = Improvement of Cadastral Information System in the Republic of Serbia. Zbornik radova FTN, Novi Sad. DOI: https://doi.org/10.24867/03KO02Valda

[14] Zakon o državnom premeru i katastru (Sl. glasnik RS, br. 72/2009)

[15] Grilc, M., Gruevski, G., Vučetić, D., Matiić Varenica, J., Šimunić, V., Živković, Lj., Matiić Mičić, J., Glogovac, M. (2025). Sistem Pametna parcela – temelj digitalnog prostora. Naučno-stručna konferencija sa međunarodnim učešćem „Urbanizam i održivi razvoj“. DOI: 10.46793/Urbanizam25.129G

[16] SmartParcel - including Web Page, Data Collection Tool and API Services, REF NO. LM2024/056984, *Detailed System Specification (Version 1.0)*, Brezovica pri Ljubljani, December 30, 2024.

[17] Republički geodetski zavod, vebinar na temu “Uspostavljanje sistema Pametna Parcela”, 2025: https://www.youtube.com/watch?v=cf2vHBPNXCQ

https://doi.org/10.24867/INDIS-2026-EN-692



# INTEGRATION OF BIM AND GIS IN GEODESY: TECHNOLOGICAL PERSPECTIVES AND THE NEED FOR EDUCATIONAL CURRICULUM REFORM

*Radovan Đurović[1], Marija Delić[2], Gojko Nikolić[3], Andrea Buntić[4], Zoran Sušić[5]*

***Abstract*:**

Modern construction engineering and geodesy increasingly rely on three-dimensional (3D) data and advanced digital modeling methods. The aim of this paper is to explain the fundamental types of 3D data, present the concept of Building Information Modeling (BIM) technology, and analyze its potential applications in geodetic practice, with particular emphasis on its integration with Geographic Information Systems (GIS). The paper first describes the main forms of 3D data, it then provides a comprehensive overview of BIM technology, the differences between BIM and the traditional Computer-Aided Design (CAD) approach, the significance of BIM objects, and the Levels of Development (LOD) concept used to define model maturity. Special attention is given to openBIM standards and the integration of BIM and GIS as a key prerequisite for efficient data exchange and interoperability. ArcGIS GeoBIM is presented as an example of a software platform supporting the integration of BIM-related project information with geographic context. The final section discusses the need to integrate BIM- and GIS-related topics into the curricula of geodesy and civil engineering programs.

*Keywords: 3D data, BIM, GIS, LOD, 3D cadastre, educational curriculum*

***Rezime:***

Savremeno građevinarstvo i geodezija sve se više oslanjaju na trodimenzionalne podatke i napredne metode digitalnog modelovanja. Cilj ovog rada je da objasni osnovne tipove 3D podataka, prikaže koncept BIM (Building Information Modeling) tehnologije i analizira mogućnosti njene primjene u geodetskoj praksi, sa posebnim naglaskom na integraciju sa GIS-om. U radu su najprije objašnjeni oblici 3D podataka, zatim je detaljno obrađena BIM tehnologija, razlike u odnosu na tradicionalni CAD pristup, značaj BIM objekata, te nivoi razvoja modela kroz LOD koncept. Posebna pažnja posvećena je openBIM standardima i integraciji BIM-a i GIS-a, kao ključnom preduslovu za razmjenu podataka. Kao primjer praktične primjene integracije BIM-a i GIS-a predstavljena je platforma ArcGIS GeoBIM. Završni dio rada bavi se analizom potrebe za integracijom sadržaja o BIM-u i GIS-u u obrazovne kurikulume geodetskih i građevinskih studija.

*Ključne riječi: 3D podaci, BIM, GIS, LOD, 3D katastar, obrazovni kurikulumi*

[1] Associate Professor, University of Montenegro, Faculty of Civil Engineering, Podgorica, e-mail: radovandj@ucg.ac.me
[2] M.Sc. in Geodesy, Agencija za projektovanje i planiranje LLC, Nikšić, Montenegro, kosticmarija51@gmail.com
[3] University of Montenegro, Department of Geography, Nikšić, Montenegro e-mail: gojkorn@t-com.me ORCID: https://orcid.org/0000-0001-8703-2184
[4] Department of Geodesy and Geoinformatics, Faculty of Technical Sciences, University of Novi Sad, Serbia, andrea.buntic@gmail.com
[5] Full Professor, Faculty of Technical Sciences, University of Novi Sad, Serbia, zsusic@uns.ac.rs

## 1. INTRODUCTION

In the era of digital transformation, the construction industry and related disciplines are undergoing significant changes. Traditional two-dimensional (2D) drawings and project documentation are increasingly being replaced by advanced three-dimensional (3D) information-rich models that enable more efficient planning, construction, and maintenance of built assets. At the same time, the field of geodesy is experiencing a technological revolution through the application of modern spatial data acquisition technologies, such as laser scanning and Unmanned Aerial Systems (UAS).
However, collecting data on the existing conditions of terrain and structures and integrating them into digital models remains a complex task. Generating a point cloud alone is not sufficient; these data must be transformed into intelligent information by linking them with attributes that describe their function, properties, and relationships. This is where the synergy between geodesy, as the science of measuring and positioning in space, and Building Information Modeling (BIM), as a methodology for creating and managing information throughout the entire life cycle of a facility, becomes particularly significant.
The subject of this paper is 3D data, BIM technology, and its integration with Geographic Information Systems (GIS), with a particular focus on applications in geodetic practice. The objectives of the paper are fourfold: first, to present and explain the fundamental types of 3D data; second, to provide a detailed overview of the BIM concept, its standards, and Levels of Development (LOD); third, to illustrate the practical implementation of BIM–GIS integration using the ArcGIS GeoBIM platform; and fourth, to investigate the potential applications of BIM in geodesy, with particular emphasis on BIM–GIS integration and the development of the 3D cadastre.
In addition to its technical aspects, this paper addresses an equally important issue—education and the ongoing accreditation process at the University of Montenegro. Regardless of how advanced technology becomes, its successful implementation in professional practice depends on the availability of adequately trained specialists. This raises an important question: are the curricula of geodesy and civil engineering programs aligned with the demands of the labor market and the rapid development of technologies such as BIM and GIS? Accordingly, this paper also highlights the need to reform educational curricula in order to equip students with the knowledge and skills required to work effectively in an integrated BIM–GIS environment.

## 2. 3D DATA SETS AND TECHNOLOGIES FOR THEIR ACQUISITION

To understand the application of Building Information Modeling (BIM) in geodesy, it is first necessary to clarify the fundamental concepts related to 3D data, which form the basis for the creation of any information model. Within modern computer-based systems, 3D data sets exist in various forms that differ in both their structure and their characteristics [1].

### 2.1. POINT CLOUD AND 3D MODELS

The fundamental forms of 3D data are **point clouds** and **3D models**. A **point cloud** is a collection of points defined within a three-dimensional coordinate system. Each point is spatially referenced by its **x, y, and z** coordinates and often represents the geometry and surface characteristics of an object or its surrounding environment. Point clouds are most commonly acquired using technologies such as **LiDAR** (Figure 1), **photogrammetry** (Figure 2), and **mobile mapping**.

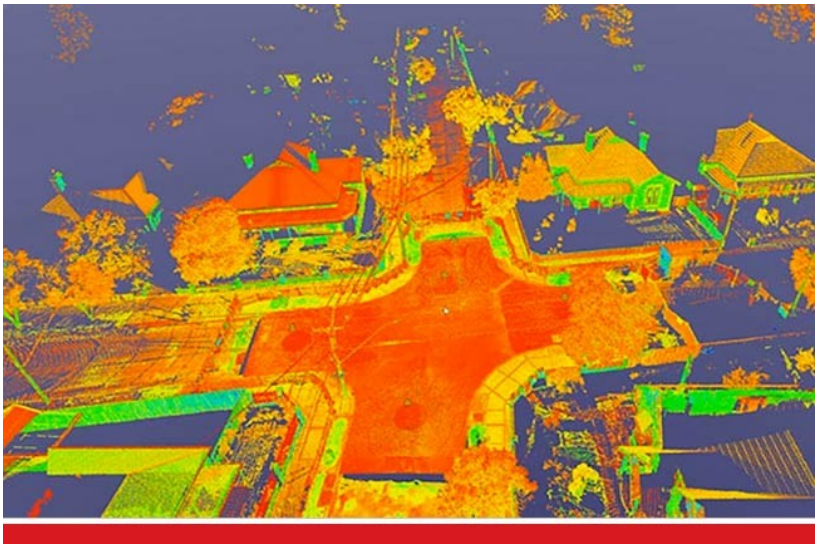

*Figure 1. Point cloud generated by laser scanning. [F1]*

Photogrammetry is a technology for acquiring reliable 3D information about physical objects and the environment through the process of capturing, measuring, and interpreting photographic images. The aim of photogrammetry is the accurate reconstruction of the captured 3D space. From photographs, it is possible to derive real-world coordinates of points on the observed objects, maps and plans, orthorectified images, digital terrain models, and digital 3D models of objects.



*Figure 2. Point cloud generated in 2014 using photogrammetric methods [F2]*

Both photogrammetry and LiDAR can generate three-dimensional point clouds. Their coverage, density, and accuracy depend on the acquisition platform, sensor configuration, viewing geometry, and processing workflow. A 2.5D representation describes a surface with a single elevation value for each horizontal position, rather than an inherent limitation of LiDAR.

A 3D model is a digital representation of an object composed of geometric elements such as surfaces, polygons, meshes, or BIM objects. Nearly all 3D models can be classified into three categories:

- **Surface models**: These models define the boundary of the represented object. Surface models are most commonly used in engineering and medical simulations.
- **Parametric models (CAD – Computer-Aided Design)** are suitable for leveraging computational capabilities to model component attributes in order to replicate the real world. These models use a combination of solid and surface modeling approaches to enable model manipulation. Parametric models (Figure 3) allow the definition of a wide range of shape classes. This process is particularly important for object detection and infrastructure extraction from point cloud data. Additionally, such parametric models can be derived by combining 2D CAD drawings that interpolate the shape of point clouds. Although these models are often demanding to create, they provide the highest value when working with 3D point cloud data.
- **Depth maps**: These are raster-based representations of point clouds. A depth map is a metric 2D structure in which each pixel represents the distance of a 3D point from the scanner, typically encoded in grayscale values. This type of representation is used in 3D data processing for surface reconstruction and visualization of spatial relationships between objects [1].

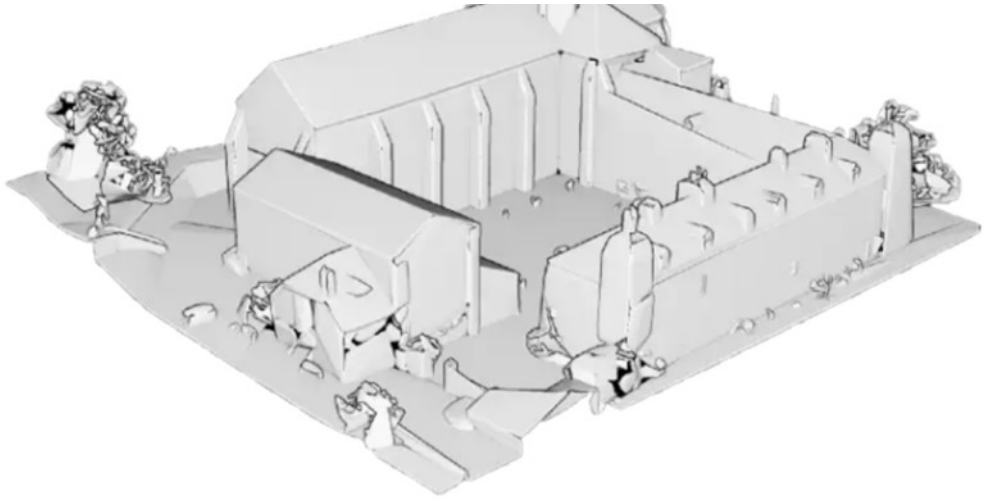

*Figure 3. Automatically generated CAD model [F3]*

## 3. BIM TECHNOLOGY

### 3.1. INTRODUCTION TO BIM TECHNOLOGY

Building Information Modeling (BIM) technology represents a revolution in the way structures are designed, constructed, and managed. According to the U.S. National Standard, BIM is defined as a “digital representation of the physical and functional characteristics of a facility,” emphasizing that it is not limited to geometry alone, but rather encompasses a comprehensive set of information. It is a process in which information and technology are combined to create a digital representation of a project. This methodology is applied in numerous projects within the construction sector, infrastructure development, as well as geodesy.

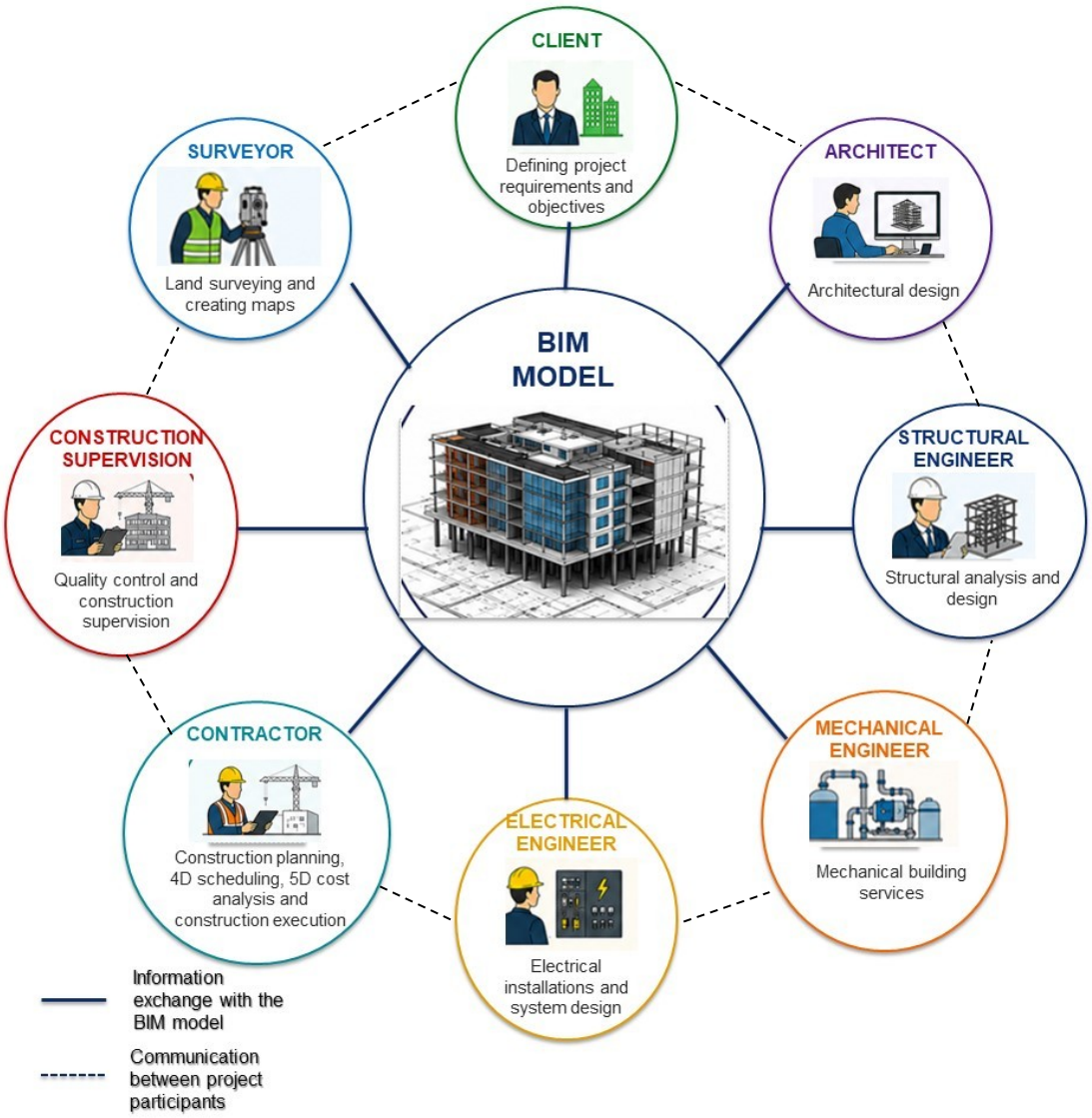


*Figure 4. Information flow in BIM [F4]*

The true value of BIM lies in the information integrated into the process and transparently exchanged among all parties involved. In traditional workflows, documents and drawings are communicated between project stakeholders by creating a new file each time information is shared. In BIM, the model serves as a central database in which information is stored and from which data can be extracted as needed, as shown in Figure 4.

## 3.2. DIFFERENCE BETWEEN BIM AND CAD

The original concept of CAD tools was to enable fast drawing of lines, replacing traditional manual drafting methods. Technological advancements later made it possible to organize different lines into layers, which opened the path toward three-dimensional design. When architects began using surfaces instead of two-dimensional lines, BIM emerged. This step forward allowed designers not only to consider the appearance of an element but also to understand what that element actually represents.

A window, which initially represented only a set of lines, has now become an independent component. It contains information about each part of the assembly, how that assembly behaves as a whole, and even what it represents in relation to adjacent components. When

a window is placed in a wall, the wall “understands” that an opening must be created, while the window “understands” that it must be placed vertically, just like the wall.
Building Information Modeling enables the assignment of attributes to each component created within the model. These attributes may include dimensions, material properties, or any other information describing the component. This technology allows reuse of model elements without the need to redraw them for each project. Instead of drawing different doors for different dimensions, the same door object is assigned different attributes.
The real value of BIM lies in its ability to analyze data. Even low-cost CAD software can support project visualization through multiple views based on a single model; however, this is not a new concept. What CAD cannot do is distinguish between, for example, a floor and a roof unless explicit information is assigned to define their differences. CAD carries only graphical information, and although it allows basic organization of lines and minimal definitions, it cannot understand the relationships between components—only their spatial positions [2].
Therefore, the key difference is that CAD (even in 3D form) operates primarily with geometry—lines, surfaces, and solids. BIM, on the other hand, operates with intelligent objects that, in addition to geometry, also contain data about materials, cost, manufacturers, energy performance, and their relationships with other objects [2].

### 3.3. BIM OBJECTS AND THE LOD CONCEPT

Objects (Figure 5) represent components of a project that can exist independently and do not need to rely on other elements in order to be understood. They must contain all the information necessary for design; they locate, analyze, and define a given product. To this end, additional information is assigned to describe the material and the components of the object.
For a window, such additional information may include the type of glass and its color, grilles, the material of the window frame, or any other information related to the functionality of the window.

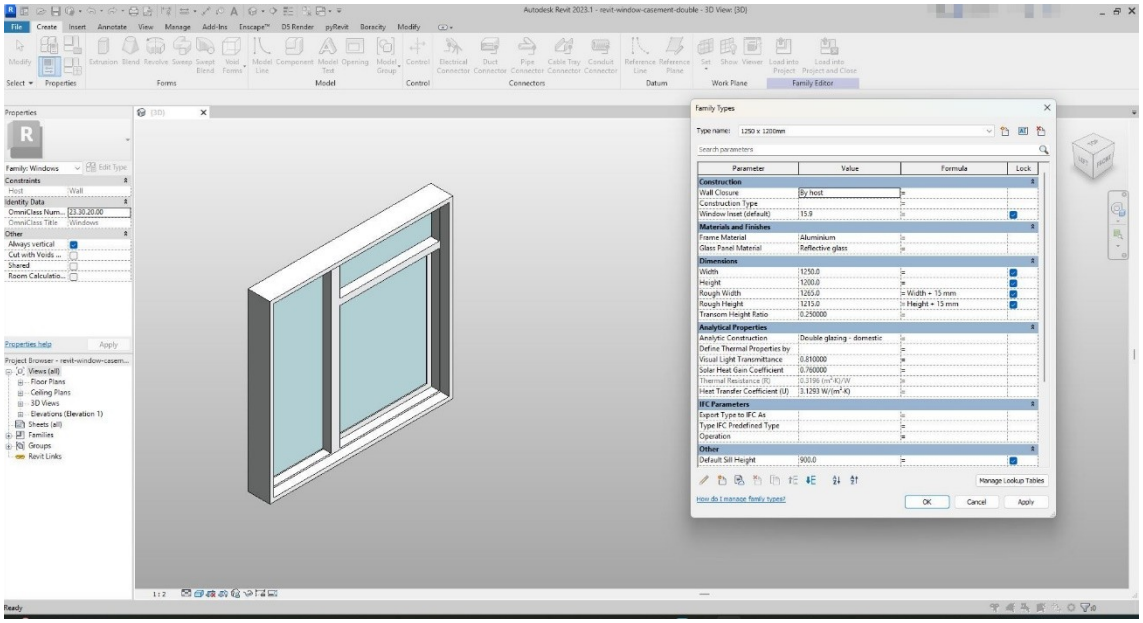


*Figure 5. BIM object [F5]*

Certain objects can only be placed in specific orientations and locations. Windows and doors are always installed in walls, recessed lighting is always placed in ceilings, and

skylights are always mounted on roofs. Thinking about objects in terms of their real-world applications can help in developing components that perform only their intended function, thereby preventing users from placing components incorrectly [3].

The American Institute of Architects has published Document E202, or the Building Information Modeling Protocol Exhibit, which is used to establish BIM protocols and prevent unauthorized use of the model. There are five Levels of Development (LOD): LOD 100 (Level of Development), LOD 200, LOD 300, LOD 400, and LOD 500. Each level of development corresponds to specific requirements and purposes of the model.

- LOD 100 (Figure 6) is essentially a massing study of the overall project used to determine areas, heights, volumes, location, and orientation. At this level of development, the BIM model does not consider detailed content but focuses only on overall masses. It is typically used for preliminary project planning, feasibility studies, and early cost estimation. At this stage, there is limited information available, consisting mainly of gross dimensions and basic geometrical representations such as approximate area, enclosed volume, and general shape.
- LOD 200 (Figure 6) includes model elements represented as generalized systems or assemblies with approximate quantities, size, shape, location, and orientation. At this level, non-graphical attributes may also be assigned to model components. LOD 200 is used to define spatial requirements and overall project size rather than detailed aspects of individual components or assemblies.
- LOD 300 (Figure 6) provides more accurate representation in terms of quantity, size, shape, location, and orientation. Most BIM development work is carried out around LOD 300, making it a solid starting point for design and coordination processes.
- The primary difference between LOD 300 and LOD 400 (Figure 6) lies in the level of information contained within the object, as well as the extent of detailed information that is either embedded in or directly linked to the component.
- LOD 500 (Figure 6) describes model elements representing existing or as-constructed conditions, based on observation and field verification, with their accuracy explicitly documented. It does not indicate a higher degree of geometric detail than LOD 400 and should not be interpreted as a level intended primarily for high-resolution visualization.

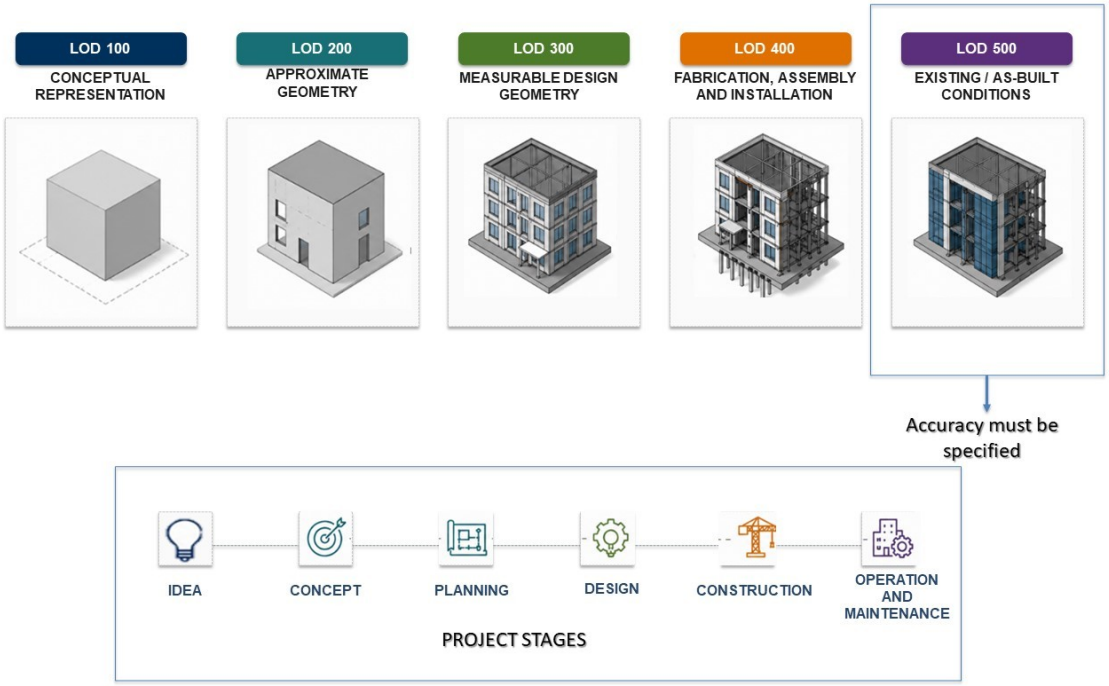


*Figure 6. Levels of Development (LOD) [F6]*

For geodetic surveying and the documentation of existing conditions, model requirements should be defined according to the intended use, required information, and specified accuracy. Survey data can support the creation and verification of as-built BIM elements. LOD 500 refers to the representation of existing conditions, whereas the required geometric detail and measurement accuracy must be specified separately [4].

### 3.4. OPENBIM STANDARDS

BuildingSMART International is a non-profit organization that develops and promotes open standards and services for information exchange in the built environment. OpenBIM is an approach to collaborative working based on open standards, enabling participants to exchange information across different software platforms. The standards, specifications, and services discussed here include Industry Foundation Classes (IFC), Information Delivery Manual (IDM), Model View Definitions (MVD), BIM Collaboration Format (BCF), and buildingSMART Data Dictionary (bSDD).

- **IFC** ISO 16739-1 is used to describe the data of a building information model, with the aim of establishing a standard method for representing and storing data so that all types of building information can be imported and exported in this format.
- **IDM** ISO 29481 is a method for specifying the entire process and information flow throughout the building life cycle, with the aim of ensuring the exchange of relevant data in a manner that can be interpreted by the recipient's software. IDM is a plan defining who sends and receives which information and when—it represents the communication schedule within a project.
- **MVD** is a set of rules that defines which data from an IFC model must, may, or should not be exchanged for a specific purpose (e.g., architecture, structural engineering, quantity takeoff, or coordination). Essentially, an MVD is a subset of the building database created for a specific purpose.
- **BCF** is a simplified and open XML (Extensible Markup Language) format used for encoding information and enabling communication between different BIM software applications.

- **bSDD** is an online service for publishing and accessing classifications, properties, and definitions describing the built environment. It supports consistent terminology and implements concepts from ISO 12006-3 and ISO 23386 (Figure 7).

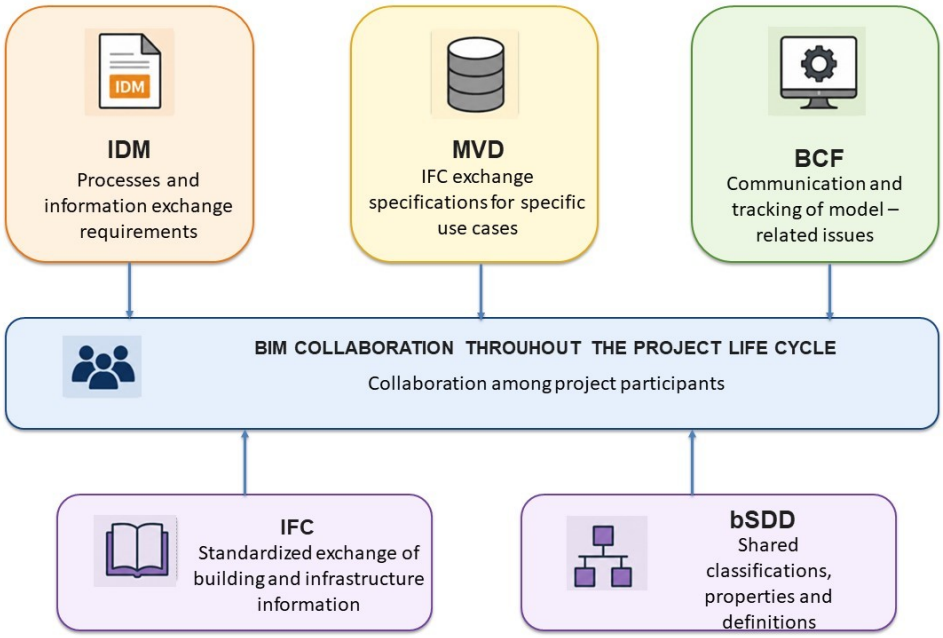


*Figure 7. Roles of selected openBIM standards, specifications and services in project collaboration [F7]*

OpenBIM covers a broad range of industrial information, such as information related to building components. However, in certain fields, such as roads and bridges, OpenBIM is still not sufficient to support specific applications. Therefore, it is necessary to extend the information model to encompass and satisfy all requirements.
The OpenBIM standard can also be used to extend attribute information. In addition to extending domain and attribute information, OpenBIM also makes a significant contribution to the semantic extension of information. For example, the lack of semantic clarity in the mapping of entities, attributes, and relationships leads to multiple representations of the same information.
Information integration refers to the process in which data from different sources, systems, or disciplines are combined into a single, consistent, and usable information system. OpenBIM provides a general standard for data exchange within this process.
The significance of the OpenBIM standard, particularly the IFC format, lies in enabling interoperability between different software platforms. This is especially important in geodesy, where data collected from field surveying equipment must be seamlessly imported into BIM tools without any loss of information [5].

## 3.5. BIM DIMENSIONS

Structural engineers and project managers use BIM for design coordination at the production level and quality control; for planning, scheduling, and designing the construction process; for quantity takeoff, cost estimation, budgeting, and procurement; for construction control; and for delivering as-built information. In the context of BIM, the terms 3D, 4D, and 5D BIM are used to refer to 3D digital visualization, time and scheduling, and cost estimation, respectively. A wide range of software tools is available to construction professionals to support all of these BIM functionalities.

The benefits of 4D CAD tools enable contractors to simulate and evaluate planned construction sequences and share them with other members of the project team. If the model is developed by the architect or contractor while the building is still in the design phase, the contractor can provide rapid feedback regarding constructability, construction sequencing, and estimated construction costs.
5D BIM represents an extension of the BIM model in which 3D geometry and 4D scheduling are linked with cost information. This enables integrated management of quantities, cost estimation, and financial control throughout the project life cycle.
The dimensions of BIM are important because they enable the integrated management of building information across space, time, and cost, thereby improving coordination, reducing errors, and supporting more accurate decision-making throughout the entire project life cycle [6].

## 4. APPLICATION OF BIM IN GEODETIC PRACTICE

### 4.1. INTEGRATION OF BIM AND GIS

GIS (Geographic Information System) and BIM are two distinct domains used to interpret 3D models from different perspectives. GIS focuses on geographic information related to buildings and their components from various viewpoints, whereas BIM focuses on the detailed components of a building and project-related information [7].
BIM and GIS were developed for different purposes, but they complement each other through data exchange. BIM provides detailed geometric and semantic information about buildings and infrastructure, and IFC supports georeferencing. GIS provides tools for relating these models to terrain, cadastral parcels, infrastructure networks, and other geographic features. Their integration supports site planning, environmental assessment, spatial analysis and information management throughout the project life cycle, as illustrated in Figure 8.
The integration of GIS and BIM enables efficient information management throughout the various phases of a project's life cycle, including planning, design, construction, operation, and maintenance. In such a system, information can be accessed at any spatial and temporal point. Effective management of diverse information provides essential support for decision-making based on multiple data sources. The integration of GIS and BIM is an important tool in the development of smart and sustainable cities due to its capabilities in technology, data integration, urban management, and quantitative analysis.




*Figure 8. Schematic Representation of the GeoBIM Building Model [F8]*

### 4.1.1. Data-Level Integration and the ArcGIS GeoBIM Platform

Data-level integration simply represents interoperability between BIM and GIS. This integration serves as a key bridge between the single-object level addressed by BIM and the city or regional level addressed by GIS. For surveyors, this is of essential importance because it enables accurately measured objects to be placed within a broader spatial context and linked to cadastral data. Data formats must always be considered, as different formats exist for storing 3D geometry. GIS and BIM data schemas have different concepts, development purposes, and structures, which makes data integration challenging unless specific criteria are defined.

The two most commonly used data exchange formats are CityGML and IFC. CityGML is an open standard for storing 3D city models in XML format, while IFC is used to describe building information model data [8].

Modern software tools increasingly enable practical implementation of BIM and GIS integration through user-oriented solutions. One notable example is ArcGIS GeoBIM, a platform that enables the linking of BIM models with geographic context for the analysis of design, site characteristics, risks, costs, and schedules. ArcGIS GeoBIM enables the integration and visualization of GIS data with engineering documentation from the Autodesk Construction Cloud (ACC) environment, thereby facilitating coordinated and collaborative decision-making among project teams.

Key functionalities of ArcGIS GeoBIM include automatic georeferencing of BIM documents and projects into hosted feature layers, maps, and scenes, as well as the ability to ingest simplified 3D models from Revit and IFC formats. The platform enables rendering of ACC files in Autodesk Viewer, while simultaneously analyzing map or scene content through a side-by-side comparison. Such integration allows surveyors and other professionals to visualize a project in its full spatial context, analyze environmental impacts, and monitor changes over time, which is particularly important for field-based project management through integration with ArcGIS Field Maps applications [9].

## 4.2. APPLICATION OF BIM IN GEODETIC WORK AND 3D CADASTRE

Designing three-dimensional objects has always presented difficulties in their visual representation through images, plans, and diagrams. A special form of visualization is physical modeling and the arrangement of designed objects. The creation of models and layouts in construction and architecture is an extremely complex and time-consuming process. Every designer and construction professional would like to continuously refer to their model in order to achieve better and more efficient execution of work. Such capability is provided to all participants in the creation of objects throughout their entire lifecycle through Building Information Modeling (BIM).

Designers must have a topographic base for linking each object—a Digital Terrain Model (DTM). Such a model should represent a combination of spatial terrain representation, geological soil structures beneath the object, hydrological data, and other relevant information. Modern geodetic and cartographic technologies are actively developing and enabling the creation of highly accurate digital models that can meet BIM requirements. The construction objects being designed are placed on the physical surface of the Earth. This is the first and unavoidable step in integrating BIM systems with databases created through geodetic and topographic surveying. BIM technology must be adopted and connected with standard technologies for creating Digital Terrain Models.

In current conditions, many objects are undergoing legalization, a process carried out by geodetic organizations. During legalization, inconsistencies are continuously identified between objects and design documentation that arise during construction, reconstruction, repair, or restoration. Often, design modifications are made without approval, and such changes remain permanent and are incorporated into the technological process. The use of laser technology enables the creation of digital models of objects and the monitoring of all structural changes resulting from deformations or installation and other works. During legalization, surveyors create a spatial model of the existing object, and from the moment of its creation, BIM technology can be introduced as further information support. Thus, a second necessary phase of merging the interests of construction and geodesy is achieved: geodetic and topographic survey data enable continuous monitoring of the object's geometry throughout its entire lifecycle. There is an urgent need to introduce BIM technology, in combination with other software, into surveying and the creation of digital terrain models. This task can be achieved through the joint efforts of professionals in construction and geodesy [7].

Urbanization over the last hundred years has brought significant changes to the environment and has most often resulted in densely populated urban areas. As a result, space above and below the ground surface is increasingly used for the construction of buildings and complex structures. These changes have increased the importance of property ownership. Traditional cadastral systems face many challenges in representing complex structures on 2D plans, as well as situations where property rights are intertwined across multiple levels. Therefore, 2D cadastral plans cannot serve as a basis for registering such situations. A system is needed that enables simple registration and representation of all possible situations in 3D space. Based on these issues, it can be concluded that it is necessary to extend the existing 2D cadastre toward a 3D cadastre of real estate in order to enable efficient registration and representation of data and real rights in 3D space. Such an extended system would not be exclusively tied to a cadastral parcel represented in a 2D plane, as is currently the case.

Implementing the BIM concept and developing a 3D cadastre by adding information about buildings and constructed areas is a way to improve the usability and visualization capabilities of cadastral systems. BIM has evolved within the construction domain, while 3D property modeling has evolved within the legal cadastral domain. BIM is

characterized by a clear and logical structure of spatial building objects that enables spatial analysis, not only visualization of the building and its elements. BIM can contribute to improving processes of property creation, registration, and visualization. However, BIM faces various challenges in representing information required for a complete 3D cadastre. Its limitation is that it cannot provide a city-scale overview. For this purpose, a city model is required. This is analogous to the 2D cadastre, where detailed cadastral maps are complemented by cadastral index maps. For example, in Sweden, developers provide computer-aided (CAD) 3D drawings that include 3D property boundaries. The representation of a complex 3D cadastre with BIM-based 3D aspects can be classified into four groups: legal, technical, registry, and organizational. The legal aspect defines property boundaries, areas of calculation, and property content; technical aspects concern how 3D properties can be visualized, geometrically represented, managed, and extracted in technical applications.

In the first step, legal information should be embedded into BIM data and 3D property boundaries should be defined. Parcel boundaries surrounding a building, as well as property boundaries within the structure, are identified and represented with a high level of positional accuracy in an extended BIM model. The question arises whether the 3D cadastre should be integrated into 3D physical space models needed for the integration of cadastral data with BIM and city models. This issue is addressed by integrating legal information with IFC, after which the integrated IFC is transformed into CityGML. The next step involves linking it with the city model [10]. Figure 9 illustrates this BIM-based process.

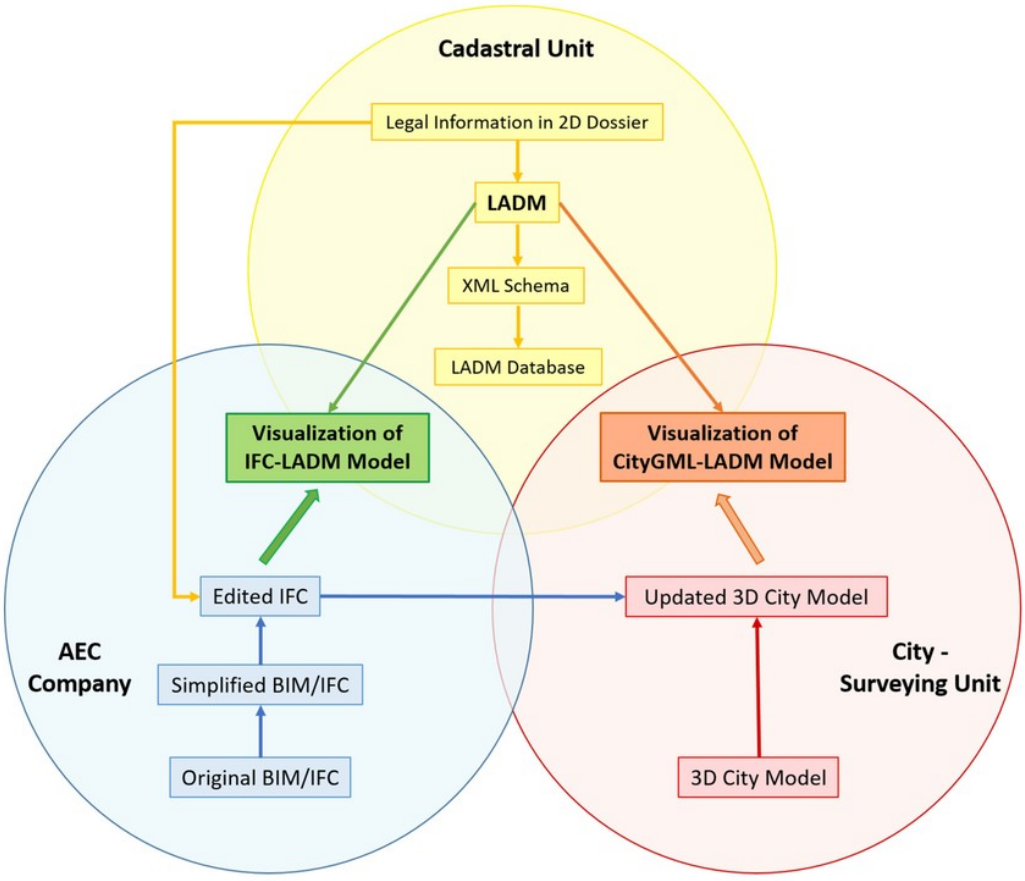


*Figure 9. The general framework for integrating cadastre with building information model (BIM) and geographic information system (GIS). [F9]*

A 3D cadastre should represent the geometries of cadastral objects and manage their spatial relationships. BIM provides a useful framework for 3D modeling, but it is not suitable for visualization and analysis of a 3D cadastre at the city level. Since 3D GIS is designed for spatial analysis and decision-making, its use in a 3D cadastre is justified for spatial queries related to cadastral property. BIM could provide information on 3D cadastral data for each element or an entire building; however, it still does not meet the requirements for modeling a complete 3D cadastre [4].

## 5. THE IMPORTANCE OF BIM AND GIS INTEGRATION FOR THE EDUCATION OF SURVEYORS

The modern surveying engineer is no longer just a "field measurer." Today, they are expected to be a professional capable of managing complex spatial data, using advanced software tools, and collaborating with architects, civil engineers, and urban planners in a digital environment. These changes impose the need for fundamental reforms in the educational curricula of surveying and construction disciplines.

### 5.1. CURRENT STATE OF EDUCATION

Regardless of how advanced technology may be, its full application in practice is only possible if there is a workforce trained to use it. A modern surveying engineer must possess a combination of traditional skills and new digital competencies. However, traditional curricula at surveying faculties are often still focused on classical measurement methods and data processing in a 2D environment. Although this knowledge remains relevant, practice in the construction and geodetic industries has changed significantly—BIM and GIS have become the standard rather than the exception. Students often encounter these technologies only in elective courses, which is not sufficient for acquiring systematic knowledge.

In order to prepare students for work in a modern BIM-GIS environment, it is necessary to integrate these topics into core courses. A modern surveying curriculum should include the basics of BIM methodology and the LOD concept, GIS technologies and spatial analysis, point cloud and LiDAR data processing in a GIS environment, principles of BIM and GIS interoperability through the use of IFC and CityGML formats, HBIM and its application in cultural heritage documentation [11], practical work with software tools, as well as an introduction to the concept of a 3D cadastre. There are examples of good practice worldwide, such as the Technical University of Varna, where students engage in practical training using Blender software.

### 5.2. RECOMMENDATIONS FOR IMPROVING TEACHING

Studies have emphasized the importance of integrating BIM into surveying education, through practical and case-based teaching approaches that connect theoretical knowledge with real-world project applications [12]. Based on the literature analysis, the following recommendations can be identified:

- introduce a mandatory course in BIM technologies at undergraduate studies
- integrate GIS content across multiple courses
- organize practical workshops in cooperation with industry
- introduce interdisciplinary teaching-joint projects for students of surveying, civil engineering, and architecture; simulation of complete infrastructure projects from geodetic surveying to BIM and GIS analysis
- train teaching staff to work with modern BIM and GIS tools
- develop lifelong learning modules for practicing engineers

These recommendations are of great importance for Montenegro, where in recent years activities have intensified regarding the introduction of BIM standards in the construction sector, including initiatives for the integration of BIM and GIS technologies.

## 6. DISCUSSION

The topics examined in this paper point to a common educational requirement: surveyors need to understand how spatial data move between geodetic workflows, BIM models, and GIS environments. Point clouds document existing conditions, BIM organizes information about individual structures, and GIS relates those structures to their wider spatial and cadastral context. The examples of IFC and CityGML integration and 3D cadastre show why data exchange, coordinate reference systems, and data quality should be addressed together in practical teaching. A project-based exercise following data from field acquisition to BIM modeling and GIS analysis would allow students to apply these skills within one workflow.

Implementing this approach in teaching requires training for academic staff, access to suitable software and spatial data, and cooperation between geodesy, civil engineering, and architecture programs. These practical requirements should be considered when curricula are updated.

In addition to technical challenges, the issue of human resources also arises. A modern surveying engineer must possess a combination of traditional skills and new digital competencies. Without adequate training at universities, it is difficult to expect that practice will fully exploit the potential of integrated BIM-GIS systems.

The example of the Bay of Kotor [13] demonstrates how important it is to train professionals in the application of modern technologies in the protection of cultural heritage. Only through the integration of geodetic knowledge, BIM methodology, and GIS tools is it possible to create efficient systems for monitoring and preserving such valuable sites.

## 7. CONCLUSION

This paper provides an overview of the basic types of 3D data, a detailed presentation of BIM technology and its integration with GIS, with a focus on applications in geodetic practice. It has been shown that BIM is not only a software tool, but a comprehensive process that integrates information about an object throughout its entire life cycle. The importance of the LOD concept and openBIM standards for interoperability has been particularly emphasized. The integration of BIM and GIS is presented as a key prerequisite for linking information about individual objects with a broader spatial context, alongside the presentation of specific software solutions such as the ArcGIS GeoBIM platform.

The example of ArcGIS GeoBIM illustrates how engineering documentation and GIS data can be accessed within a shared geographic context to support project coordination and making decisions.

Finally, the paper highlights the necessity of reforming educational curricula in surveying and civil engineering studies. It is not sufficient for students to acquire only theoretical knowledge of BIM and GIS; they must also be trained in practical work with modern software tools and in understanding the principles of interoperability. Only in this way can the education system keep pace with the dynamic development of technology and prepare professionals for the challenges of digitized construction. The integration of BIM and GIS is not only a technical issue, but also an educational matter of strategic importance [14].

## 8. LITERATURE

[1] F. Poux, "How to Represent 3D Data," *Towards Data Science*, 2020. [Online]. Available: https://towardsdatascience.com/how-to-represent-3d-data-66a0f6376afb

[2] R. S. Weygant, *BIM Content Development: Standards, Strategies, and Best Practices*. John Wiley & Sons, 2011.

[3] K. Kensek and D. Noble, *Building Information Modeling: BIM in Current and Future Practice*. Wiley, 2014.

[4] J. Oldfield, P. van Oosterom, W. Quak, J. van der Veen, and J. Beetz, "Can Data from BIMs be Used as Input for a 3D Cadastre?," in *Proc. 5th International FIG 3D Cadastre Workshop*, Athens, Greece, Oct. 18–20, 2016, pp. 199–214.

[5] S. Jiang, L. Jiang, Y. Han, Z. Wu, and N. Wang, "OpenBIM: An Enabling Solution for Information Interoperability," *Applied Sciences*, vol. 9, no. 24, Art. no. 5358, 2019, doi: 10.3390/app9245358.

[6] R. Sacks, C. Eastman, G. Lee, and P. Teicholz, *BIM Handbook: A Guide to Building Information Modeling for Owners, Designers, Engineers, Contractors, and Facility Managers*, 3rd ed. Hoboken, NJ, USA: John Wiley & Sons, 2018.

[7] N. Arsenieva, "Features of BIM Technologies in Geodetic Works," *Scientific Collection InterConf*, no. 113, pp. 486–492, 2022, doi: 10.51582/interconf.19-20.06.2022.052.

[8] M. J. Sani and A. Abdul Rahman, "GIS and BIM Integration at Data Level: A Review," *The International Archives of the Photogrammetry, Remote Sensing and Spatial Information Sciences* vol. XLII-4/W9, pp. 299–306, 2018, doi: 10.5194/isprs-archives-XLII-4-W9-299-2018.

[9] Esri, "Introduction to ArcGIS GeoBIM," *ArcGIS Online Documentation*. [Online]. Available: https://doc.arcgis.com/en/geobim/latest/get-started/an-introduction-to-arcgis-geobim.htm

[10] J. Sun, S. Mi, P.-O. Olsson, J. Paulsson, and L. Harrie, "Utilizing BIM and GIS for Representation and Visualization of 3D Cadastre," *ISPRS International Journal of Geo-Information*, vol. 8, no. 11, Art. no. 503, 2019, doi: 10.3390/ijgi8110503.

[11] P. Clini, R. Nespeca, R. Angeloni, and U. Ferretti, "Above-Ground and Underground Architectural Heritage Documentation: A Scan-to-HBIM-to-XR Approach for Historic Centres," *The International Archives of the Photogrammetry, Remote Sensing and Spatial Information Sciences*, vol. XLVIII-M-9-2025, pp. 345–351, 2025, doi: 10.5194/isprs-archives-XLVIII-M-9-2025-345-2025.

[12] Y. Liu and S. Li, "BIM Teaching Strategy for Surveying Students in China," in *Proc. International Conference on Education Technology and Management Science (ICETMS 2013)*, Atlantis Press, 2013, pp. 540-543.

[13] Government of Montenegro, Ministry of Culture, *Heritage Impact Assessment (HIA) – Natural and Culturo-Historic Region of Kotor*. Podgorica, Montenegro, 2018. [Online]. Available: https://whc.unesco.org/document/197460

[14] Faculty of Civil Engineering, University of Montenegro, *Feasibility Study for the Implementation of a Lifelong Learning Program – "BIM and GIS in Construction"*. Podgorica, Montenegro, 2026.

## 9. FIGURES

[F1] Source: Leica Geosystems. [Online]. Available: https://leica-geosystems.com/industries/pure-surveying/get-inspired-to-grow-your-business/laser-scanning

[F2] Source: F. Poux, "How to Represent 3D Data," *Towards Data Science*, 2020. [Online]. Available: https://towardsdatascience.com/how-to-represent-3d-data-66a0f6376afb

[F3] Source: F. Poux, "How to Represent 3D Data," *Towards Data Science*, 2020. [Online]. Available: https://towardsdatascience.com/how-to-represent-3d-data-66a0f6376afb

[F4] Author's own elaboration and graphical representation

[F5] Source: Boracity. [Online]. Available: https://www.boracity.com/revit/windows/white-double-casement-window-ii

[F6] Author's own elaboration and graphical representation

[F7] Author's own elaboration and graphical representation

[F8] Author's own elaboration and graphical representation

[F9] Source: J. Sun, S. Mi, P.-O. Olsson, J. Paulsson, and L. Harrie, "Utilizing BIM and GIS for Representation and Visualization of 3D Cadastre," *ISPRS International Journal of Geo-Information*, vol. 8, no. 11, Art. no. 503, 2019, doi: 10.3390/ijgi8110503.

https://doi.org/10.24867/INDIS-2026-EN-709



# DIGITAL DOCUMENTATION AND CRACK MAPPING OF A HISTORIC FORTIFICATION USING PHOTOGRAMMETRY: A CASE STUDY OF THE KRONACH WALL

*Erta Kushta[1], Arli Llabani[2], Marin Allaraj[3], Fation Kurti[4]*

***Summary***

Historic masonry fortifications require accurate and non-invasive documentation for condition assessment, conservation planning, and long-term monitoring. This study examines the use of UAV(Unmanned Aerial Vehicle) photogrammetry for the digital documentation and crack mapping of the historic Kronach city wall in Bavaria, Germany. A total of 2,460 high-resolution images were processed using Structure-from-Motion and dense image matching to generate a point cloud, a textured 3D model, and orthophotos. The reconstruction achieved an RMSE of approximately 2 cm and a GSD of 0.5–1 mm/pixel. A representative orthophoto was used for the visual identification, mapping, and metric documentation of visible surface discontinuities and localized deterioration. The results demonstrate the potential of UAV photogrammetry for detailed heritage documentation and future monitoring.

*Keywords: Structure-from-Motion; UAV; Heritage documentation; Visual Crack mapping; Point cloud; Digital preservation*

# DIGITALNA DOKUMENTACIJA I DETEKCIJA PUKOTINA NA ISTORIJSKOM UTVRĐENJU PRIMENOM FOTOGRAMETRIJE: STUDIJA SLUČAJA GRADSKIH ZIDINA KRONACH

***Rezime***

Istorijska zidana utvrđenja zahtevaju preciznu i nedestruktivnu dokumentaciju radi procene stanja, planiranja konzervacije i dugoročnog praćenja. Ovo istraživanje razmatra primenu UAV fotogrametrije za digitalno dokumentovanje i mapiranje pukotina na istorijskim gradskim zidinama Kronaha u Bavarskoj, Nemačka. Ukupno 2.460 snimaka visoke rezolucije obrađeno je primenom metode Structure-from-Motion i gustog uparivanja slika radi generisanja oblaka tačaka, teksturisanog 3D modela i ortofoto snimaka. Rekonstrukcija je postigla RMSE od približno 2 cm i GSD od 0,5–1 mm/piksel. Reprezentativni ortofoto korišćen je za vizuelnu identifikaciju, mapiranje i metričku dokumentaciju vidljivih površinskih diskontinuiteta i lokalizovanih oštećenja. Rezultati pokazuju potencijal UAV fotogrametrije za detaljnu dokumentaciju kulturnog nasleđa i buduće praćenje.

*Ključne reči: Struktura iz pokreta; UAV; dokumentovanje kulturnog nasleđa; vizuelno mapiranje pukotina; oblak tačaka; digitalno očuvanje*

[1] Msc, Phd Student, Faculty of Civil Engineering, Polytechnic University of Tirana, Albania, erta.kushta@fin.edu.al , ORCID 0009-0002-3957-002X
[2] Dr. Faculty of Civil Engineering, Polytechnic University of Tirana, Albania, arli.llabani@fin.edu.al,
[3] Msc, Phd Student, Faculty of Civil Engineering, Polytechnic University of Tirana, Albania, marin.allaraj@fin.edu.al
[24] SRP Albanian Engineering, St. Tom Plezha, Tirana 1049, Albania, info@srp.al

## 1. INTRODUCTION

Historic masonry fortifications are exposed to progressive deterioration caused by material ageing, moisture, thermal variations, biological growth, weathering, and limited maintenance. Cracks are among the most relevant visible indicators because their position, orientation, continuity, and spatial distribution can support preliminary condition assessment and the identification of areas requiring detailed inspection. Reliable documentation is therefore essential for conservation planning, periodic monitoring, and the establishment of a measurable record of the existing condition [1].

Conventional surveys generally rely on direct visual inspection, manual measurements, and terrestrial photography. Although these methods remain necessary, their application to extensive and geometrically complex structures can be time-consuming, difficult, and potentially unsafe. Tall walls, towers, changes in elevation, restricted access, vegetation, and adjacent buildings may prevent continuous documentation of the masonry surfaces. Visual assessment may also depend on the experience of the operator and may not provide a spatially consistent record for subsequent comparison [2].

Close-range UAV photogrammetry provides a non-contact method for acquiring high-resolution imagery of inaccessible and geometrically complex structures. Structure-from-Motion estimates camera positions and reconstructs scene geometry from overlapping photographs [3]. Dense image-matching or Multi-View Stereo procedures subsequently generate detailed three-dimensional point clouds from the oriented image block [4]. These datasets can be used to produce textured three-dimensional models and geometrically corrected orthophotos for architectural documentation and condition assessment [5]. The selection of an appropriate photogrammetric workflow depends on the scale, geometry, accessibility, documentation objectives, and available resources associated with the heritage asset [6].

Orthophotos are particularly valuable for masonry inspection because they reduce perspective distortion and provide a consistent image scale for locating and mapping visible surface discontinuities. Close-range UAV photogrammetry has been applied to manual crack identification and façade inspection [7]. Photogrammetric surveys have also been used for the condition assessment and digital documentation of historic buildings [8]. UAV-based documentation has also been used in the conservation of historic places to record architectural geometry and inaccessible surfaces [9]. UAV oblique photogrammetry has additionally been applied to the identification of surface defects in historic city walls, demonstrating its relevance to extensive masonry structures [10]. Nevertheless, interpretation depends on image resolution, acquisition geometry, lighting conditions, surface visibility, and the ability to distinguish cracks from mortar joints, stone boundaries, shadows, stains, and vegetation.

Recent research has extended image-based heritage inspection through automated or semi-automated deterioration detection and the integration of photogrammetric information with digital models. UAV photogrammetry has been incorporated into broader digital documentation workflows combining survey data, three-dimensional reconstruction, and heritage interpretation [11]. Photogrammetry-based digital-twin frameworks can organize geometric and deterioration information for the monitoring of historic structures [12]. Crack-detection methods linked to UAV photogrammetry-based digital twins further demonstrate the potential of integrating visible defects with spatial three-dimensional records [13]. Semi-automatic analysis of UAV-derived data can assist the identification of damaged surfaces, although classification errors and the need for specialist verification remain important limitations [14]. Automated crack-detection

methods based on drone orthophotos also demonstrate the growing potential of image-processing techniques for infrastructure inspection [15].

Most previous applications have focused on individual façades, isolated monuments, or specific damaged areas. Fewer studies address the combined large-scale reconstruction and detailed surface mapping of an extensive historic fortification characterized by long wall sections, towers, gates, variable elevations, vegetation, and constrained urban surroundings. This study addresses this gap by integrating large-scale digital documentation of the fortification with representative orthophoto-based visual mapping and metric documentation of visible surface discontinuities and localized deterioration.

The objective is to evaluate the suitability of UAV photogrammetry for the digital documentation of an extensive masonry fortification and for the production of high-resolution orthophotos supporting visual crack mapping. The study focuses on the generation of a dense three-dimensional representation of the wall system, the production of geometrically corrected orthophotos, and the visual identification, mapping, and metric documentation of selected surface discontinuities on a representative wall section.

## 2. STUDY AREA

The case study is the historic city wall of Kronach, located in Upper Franconia, Bavaria, Germany. The fortification forms a continuous defensive system around the historic urban core and represents a significant component of the architectural heritage of the old town. The oldest surviving sections date to the thirteenth century, while later extensions and modifications reflect the progressive development of the city's defensive infrastructure. The complete system, including the walls, towers, and gates, is protected as a historic monument and forms part of the listed ensemble of Kronach's old town.

The principal wall circuit has an approximate length of 836 m and an average height of approximately 8 m. An additional 548 m of masonry walls enclose the outer Zwinger gardens located in front of the main defensive line. The structure is predominantly composed of sandstone ashlar masonry and includes continuous wall sections, towers, gates, stairways, pedestrian accesses, and partially preserved timber wall walks.

The documented fortification includes the Stadtturm, Storchenturm, Rosenturm, Mäuseturm, and Hexenturm, together with the Pförtchen, Anna Chapel, and Bamberger Tor. For survey organization and data management, the wall circuit was divided into seven sections following the project overview plan:

- Stadtturm–Storchenturm;
- Storchenturm–Am Pförtchen;
- Am Pförtchen–Bamberger Tor;
- Bamberger Tor–Rosenturm;
- Rosenturm–Mäuseturm;
- Mäuseturm–Hexenturm;
- Hexenturm–Stadtturm.

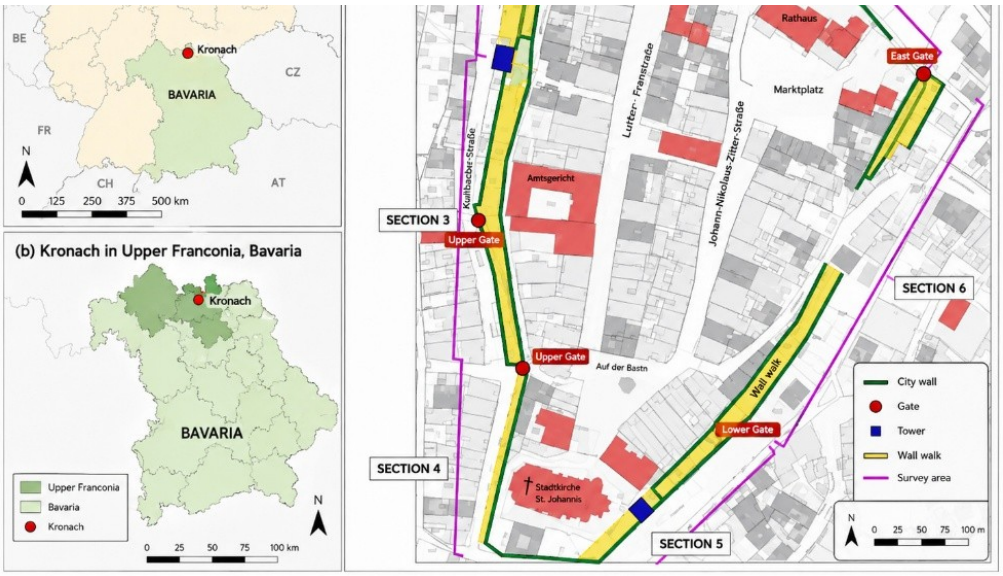


*Fig. 1 Overview of the historic city wall of Kronach into seven survey sections*

This segmentation provided a consistent spatial framework for image acquisition, control-point distribution, photogrammetric processing, and the organization of the generated products.

The fortification presents considerable geometric and environmental variability. Long rectilinear walls alternate with towers, gates, curved transitions, changes in elevation, narrow passages, and sections located close to adjacent buildings. Vegetation, private gardens, restricted access, and irregular terrain further limit direct visibility of several wall surfaces. The photographic documentation also indicates variations in surface condition, including weathered masonry, biological growth, moisture staining, vegetation cover, and localized material loss.

These conditions make the Kronach city wall an appropriate case study for UAV-based documentation. Its scale, vertical development, complex geometry require a survey method capable of recording both the complete fortification system and detailed surface information from multiple viewpoints.

## 3. MATERIALS AND METHODS

### 3.1. METHODOLOGICAL WORKFLOW

The adopted methodology combined field control, close-range UAV image acquisition, photogrammetric reconstruction, and orthophoto-based surface inspection. The workflow consisted of six principal stages: survey planning, establishment of the control network, UAV image acquisition, image orientation and dense reconstruction, generation of photogrammetric products, and manual mapping and documentation of visible surface discontinuities.

The image block was processed using a Structure-from-Motion and dense image-matching approach [3]. Ground control points were incorporated during bundle adjustment to constrain the reconstruction within the survey reference system [16]. The resulting point cloud, textured three-dimensional model, and orthophotos provided

complementary datasets for documenting the geometry and visible surface condition of the fortification [5].

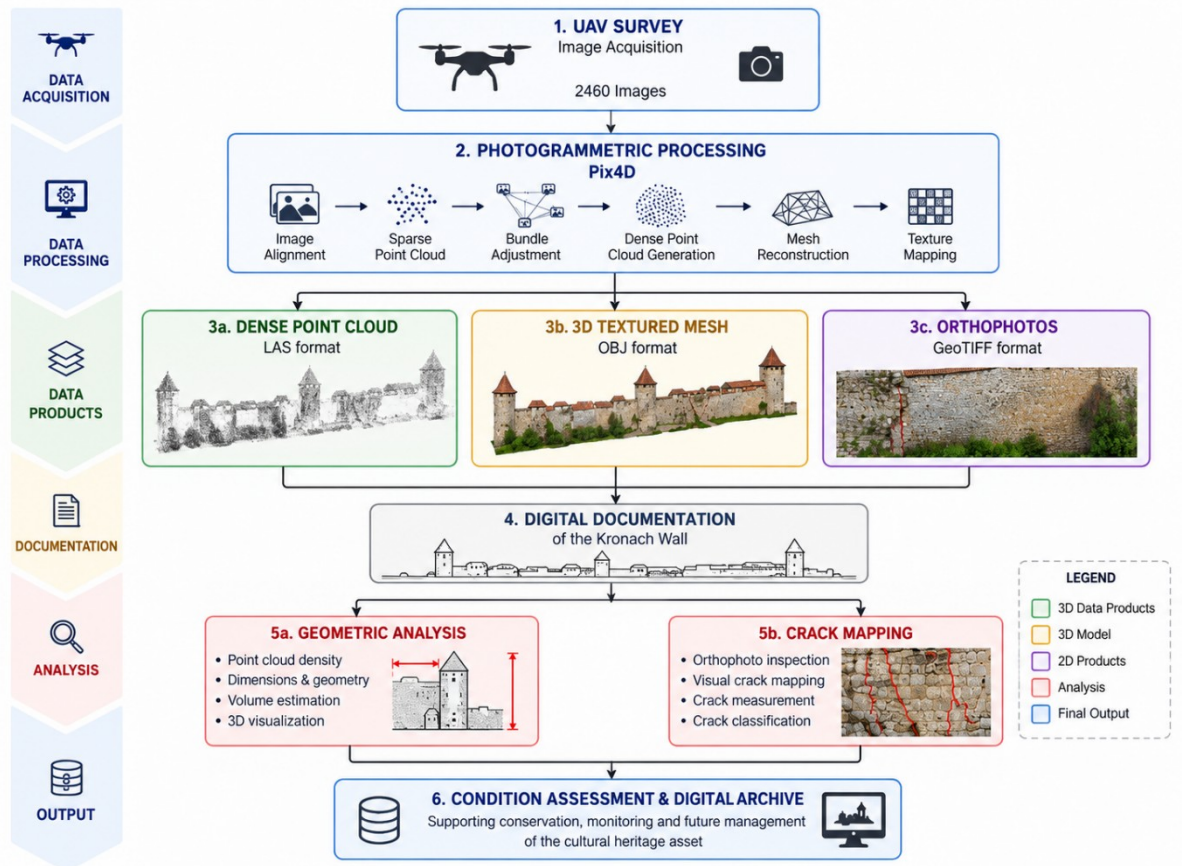


*Fig. 2 Methodological workflow for field control, UAV image acquisition, photogrammetric reconstruction, digital product generation, and manual mapping*

## 3.2. UAV IMAGE ACQUISITION

The aerial survey was carried out using an Intel Falcon 8+ octocopter equipped with a Sony Alpha 7R full-frame camera and a Sony FE 35 mm fixed focal-length lens. The camera produced images of 7360 × 4912 pixels, supporting the recording of masonry textures, joints, architectural elements, and visible surface discontinuities.

The Falcon 8+ incorporates a triple-redundant Trinity inertial measurement system, in which gyroscopic and barometric observations support platform orientation and flight stabilization. Its onboard GNSS(Global Navigation Satellite System) receiver provides initial image-position metadata, while a two-axis camera compensator maintains the viewing direction selected by the operator and limits the influence of platform rotation during close-range acquisition.

The compact multi-rotor configuration was suitable for the constrained urban setting of the Kronach fortification, where wall height, towers, vegetation, adjacent buildings, and changes in terrain required controlled flight paths and variable camera-to-object distances. A total of 2,460 images were acquired using façade-oriented, oblique, and convergent views. The average image overlap was 75-80%, with coverage around towers, gates, corners, and changes in wall direction.

## 3.3. GROUND CONTROL AND GEOREFERENCING

A survey-control network comprising 25 ground control points (GCPs) was distributed across the seven wall sections. The points were measured using GNSS(Global Navigation Satellite System) RTK and included locations along external access routes as well as selected positions close to the masonry surfaces. The distribution was designed to provide control throughout the fortification, with particular attention to towers, corners, changes in elevation, and changes in wall direction. The GCPs were introduced during image orientation and bundle adjustment to constrain the position, scale, and geometry of the photogrammetric block.Their spatial distribution contributed to strengthening the geometric configuration of the reconstruction across the extensive wall circuit [16,17].




*Fig. 3 Distribution of ground control points across the Kronach city wall*

## 3.4. PHOTOGRAMMETRIC PROCESSING

The UAV images were processed in Pix4D using a Structure-from-Motion and dense image-matching workflow. The processing sequence included image import, feature extraction, automatic tie-point matching, camera calibration, bundle adjustment using ground control points, dense point-cloud generation, textured mesh reconstruction, and orthomosaic production.

Façade-oriented, oblique, and convergent imagery supported the reconstruction of vertical surfaces, towers, wall junctions, and changes in direction. Similar multi-view acquisition strategies are commonly applied in UAV-based heritage documentation to improve the reconstruction of complex architectural geometry [9].

The processing achieved 100% image calibration, with a mean reprojection error of approximately 0.15 pixels and a GCP-based RMSE of approximately 2 cm. The resulting orthophotos achieved a ground sampling distance (GSD) of approximately 0.5–1 mm/pixel.

The reconstructed dense point cloud was exported in LAS format, while the textured three-dimensional model was generated in OBJ format. Geometrically corrected orthophotos were exported as GeoTIFF files. These products provided complementary datasets for geometric documentation, visualization, and orthophoto-based mapping of visible surface discontinuities.

The generated three-dimensional datasets may also provide a basis for subsequent integration with heritage information systems. Photogrammetric surface models have been used as geometric sources for HBIM-oriented knowledge representation [18], while HBIM environments can support the organization of geometric, condition, and conservation information for built heritage [19].

### 3.5. MANUAL ORTHOPHOTO-BASED SURFACE MAPPING AND METRIC ANALYSIS

A representative orthophoto of the perimeter wall was selected for manual mapping and metric visible surface analysis. Linear discontinuities interpreted as visible or possible cracks were manually digitized as polylines, while localized surface alterations were represented as polygons.

The mapped linear features were measured according to their length, while the extent of localized surface alterations was quantified by calculating their surface area. Particular attention was given to distinguishing potential cracks from mortar joints, stone boundaries, shadows, vegetation, staining, and irregular masonry textures.

The analysis was intended as a representative demonstration of the potential of UAV-derived orthophotos for visual identification, mapping, and metric documentation of surface discontinuities rather than as a structural assessment of the masonry. Based on the generated orthophoto, visible cracks were manually identified and mapped, following approaches in which UAV-derived orthomosaics are used for visual crack detection on building façades [7].

## 4. RESULTS

### 4.1. PHOTOGRAMMETRIC RECONSTRUCTION

The processing of 2,460 UAV images generated a dense point cloud, a textured three-dimensional model, and geometrically corrected orthophotos exported in GeoTIFF format.The reconstruction provided extensive coverage of the principal wall sections, towers, gates, changes in elevation, and adjacent architectural elements.

The dense point cloud preserved the overall geometry of the fortification, while the textured model supported the visual interpretation of masonry surfaces and architectural details.

The photogrammetric processing achieved 100% image calibration, with a mean reprojection error of approximately 0.15 pixels. The ground control adjustment resulted in an RMSE of approximately 2 cm. The generated orthophotos achieved a ground sampling distance of approximately 0.5–1 mm/pixel.

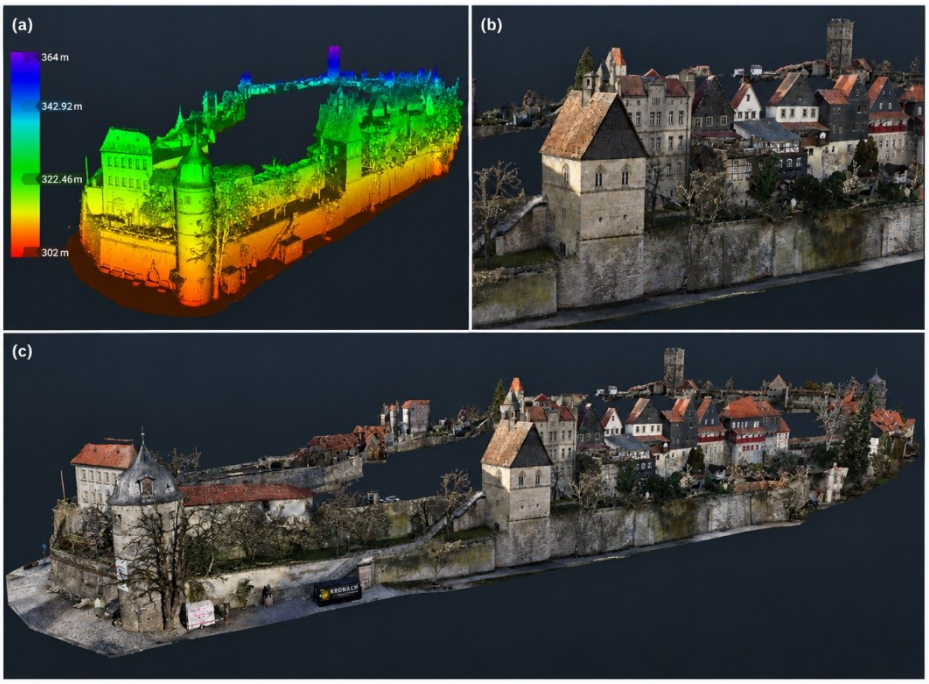


*Fig. 4 Dense point-cloud representation of the Kronach city wall: (a) Elevation view, (b) RGB Oblique view, (c) Panoramic RGB view of the fortification*

## 4.2. ORTHOPHOTO-BASED MAPPING AND METRIC ANALYSIS

A representative section from orthophoto RightExport1.10 was selected for detailed manual interpretation. The selected area contained sufficiently visible masonry texture and several distinguishable surface discontinuities.

Four linear features were mapped as visible or possible cracks. Three short cracks were predominantly vertical and isolated, while a longer crack in the lower-right part of the selected wall section followed a slightly diagonal direction and showed greater continuity. Two irregular areas were mapped as localized surface deterioration because they presented altered texture, discontinuous masonry appearance, and possible material loss or previous repair.

The mapped features were simply classified according to orientation, morphology, continuity, position, relationship with the masonry, and visibility. The orthophoto supported preliminary remote mapping of visible surface features and the selection of areas requiring subsequent field verification.

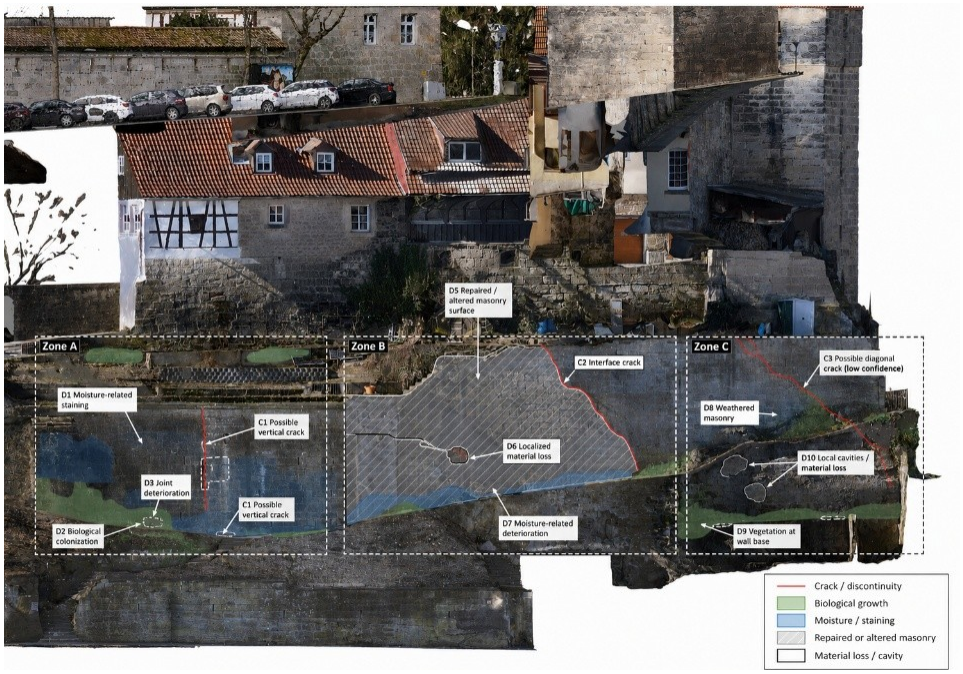


*Fig. 5 Orthophoto and manually interpreted map of the selected wall section*

*Tab. 1 Inventory of visible cracks and localized deterioration features identified on the selected orthophoto*

| ID | Feature type | Orientation / form | Continuity | Position | Relationship with masonry | Visibility |
|---|---|---|---|---|---|---|
| C1 | Visible crack | Vertical, linear | Isolated | Left wall area | Mainly follows mortar joints | Clear |
| C2 | Visible crack | Vertical, linear | Isolated | Left wall area | Mainly follows mortar joints | Clear |
| C3 | Possible crack | Vertical, linear | Isolated | Left-central wall area | Mixed path through joints and masonry units | Moderate |
| C4 | Visible crack | Slightly diagonal, linear | Continuous | Lower-right wall area | Mixed path | Clear |
| D1 | Localized surface deterioration | Irregular area | — | Lower-central wall area | Altered masonry texture | Clear |
| D2 | Localized surface deterioration | Irregular area | — | Lower-central/right wall area | Possible material loss or previous repair | Clear |

In addition to qualitative interpretation, the orthophoto allowed direct metric measurements of selected visible discontinuities. The example shown in Fig. 6 demonstrates that UAV-derived orthophotos can support direct metric measurements of visible surface features, complementing visual mapping with basic quantitative documentation.




*Fig. 6 Example of direct metric measurements performed on the orthophoto*

## 5. DISCUSSION

The results demonstrate that close-range UAV photogrammetry can support the documentation of an extensive and geometrically complex historic fortification. The integration of a dense point cloud, a textured three-dimensional model, and high-resolution orthophotos enabled the Kronach city wall to be examined at both architectural and surface-detail scales. Similar UAV workflows have been used to document historic places where complex geometry and restricted access limit conventional survey procedures [9]. Integrated approaches combining UAV photogrammetry with broader digital reconstruction and heritage-interpretation processes have also demonstrated the value of linking survey products with subsequent documentation and visualization activities [11].

The visibility of surface discontinuities depends on image resolution, contrast, lighting, focus, viewing geometry, and surface characteristics. Automated orthophoto-based crack studies similarly identify image resolution and surface appearance as important factors affecting detection reliability [15]. In the present study, the orthophoto provided a suitable basis for visual identification, mapping, and direct metric measurement of selected visible discontinuities.

Manual interpretation was retained because the objective was visual mapping and metric documentation rather than automated defect classification. Similar close-range UAV photogrammetric approaches have used orthomosaics for visual crack identification on building façades [7]. Semi-automatic and automatic approaches can support the screening of larger datasets, but heterogeneous masonry surfaces may still lead to false classifications and require expert verification [14,15]. These approaches should therefore be considered complementary to manual interpretation rather than a replacement for it.

The Kronach case involved a long and heterogeneous fortification system characterized by variable elevations, towers, vegetation, adjacent buildings, and restricted access. Detailed mapping and metric measurements were demonstrated only on a representative orthophoto section and therefore do not constitute a complete condition assessment of the entire fortification. The measurements should be interpreted as photogrammetric documentation of visible surface features rather than as a structural assessment of the masonry.

Future work should extend the analysis to additional orthophotos and repeated surveys to evaluate changes in mapped features over time. UAV-based repeated imaging has previously been investigated as a basis for long-term crack-pattern monitoring in historic structures [20]. Photogrammetry-based digital-twin frameworks may also support the organization of future survey epochs and deterioration records [12]. The generated surface models could subsequently support HBIM-oriented organization of geometric and semantic data [18], while heritage information models may facilitate the management of condition and intervention records [19].

## 6. CONCLUSIONS

This study demonstrated the applicability of UAV photogrammetry for the digital documentation of the historic Kronach city wall and for the visual mapping of surface discontinuities. A total of 2,460 images were successfully processed, achieving 100% image calibration, a mean reprojection error of approximately 0.15 pixels, and a GCP-based RMSE of approximately 2 cm. The generated orthophotos reached a GSD of approximately 0.5–1 mm/pixel, providing detailed spatial information for the documentation of masonry surfaces.

The resulting dense point cloud, textured three-dimensional model, and orthophotos documented the geometry of the fortification at different levels of detail. Visual mapping on a representative orthophoto demonstrated that visible linear discontinuities and localized surface alterations could be identified, spatially documented, and directly measured. This illustrates the potential of UAV-derived orthophotos to complement conventional heritage documentation with quantitative information.

The detailed surface analysis was limited to a representative wall section and does not constitute a complete condition or structural assessment of the fortification. Future work should extend the mapping to additional wall sections, repeat the surveys for temporal comparison, and investigate semi-automatic approaches as a complementary tool for screening larger datasets

## REFERENCES

[1] Rossi M., et al. (2023). Structural health monitoring and management of cultural heritage structures: A State-of-the-Art Review. Applied Sciences, Volume 13, Issue 11, 6450. DOI: 10.3390/app13116450.

[2] Stepinac M., et al. (2020). A review of emerging technologies for an assessment of safety and seismic vulnerability and damage detection of existing masonry structures. Applied Sciences, Volume 10, Issue 15, 5060. DOI: 10.3390/app10155060.

[3] Westoby M.J., Brasington J., Glasser N.F., Hambrey M.J., Reynolds J.M. (2012). “Structure-from-Motion” photogrammetry: A low-cost, effective tool for geoscience applications. Geomorphology, Volume 179, pp. 300–314. DOI: 10.1016/j.geomorph.2012.08.021.

[4] Smith M.W., Carrivick J.L., Quincey D.J. (2016). Structure from motion photogrammetry in physical geography. Progress in Physical Geography, Volume 40, Issue 2, pp. 247–275. DOI: 10.1177/0309133315615805.

[5] Remondino, F. (2011). Heritage Recording and 3D Modeling with Photogrammetry and 3D Scanning. *Remote Sensing*, 3(6), 1104–1138. DOI: 10.3390/rs3061104.

[6] Rahaman, H., Champion, E. (2019). To 3D or Not 3D: Choosing a Photogrammetry Workflow for Cultural Heritage Groups. *Heritage*, 2(3), 1835–1851. DOI: 10.3390/heritage2030112.

[7] Santrač N., Batilović M., Marković M., Govedarica M., Benka P. (2024). Application of close-range UAV photogrammetry in the detection of cracks on facade. Proceedings of the International Conference on Contemporary Theory and Practice in Construction XVI, pp. 611–620. DOI: 10.61892/stp202401028S.

[8] De Fino M., et al. (2023). Condition assessment of heritage buildings via photogrammetry: A Scoping Review from the Perspective of Decision Makers: Heritage, Volume 6, Issue 11. DOI: 10.3390/heritage6110367.

[9] Federman, A., Shrestha, S., Quintero, M.S., Mezzino, D., Gregg, J., Kretz, S., Ouimet, C. (2018). Unmanned Aerial Vehicles Photogrammetry in the Conservation of Historic Places: Carleton Immersive Media Studio Case Studies. *Drones*, 2(2), 18. DOI: 10.3390/drones2020018.

[10] Wu J., Shi Y., Wa H., We Y., Du Y., (2023). Surface defect detection of Nanjing City Wall based on UAV Oblique Photogrammetry and TLS, Volume 15, Issue 8, 2089. DOI: 10.3390/rs15082089.

[11] Stanga, C., Banfi, F., Roascio, S. (2023). Enhancing Building Archaeology: Drawing, UAV Photogrammetry and Scan-to-BIM-to-VR Process of Ancient Roman Ruins. *Drones*, 7(8), 521. DOI: 10.3390/drones7080521.

[12] Kong, X., Hucks, R.G. (2023). Preserving Our Heritage: A Photogrammetry-Based Digital Twin Framework for Monitoring Deteriorations of Historic Structures. *Automation in Construction*, 152, 104928. DOI: 10.1016/j.autcon.2023.104928.

[13] Yiğit A.Y., M.U., (2025). Detection of cracks in cultural heritage buildings using UAV photogrammetry-based digital twin. Journal on Computing and Cultural Heritage, Volume 18, Issue 1. DOI: 10.1145/3703634.

[14] Caciora, T., Ilieș, A., Herman, G.V., Berdenov, Z., Safarov, B., Bilalov, B., Ilieș, D.C., Baias, Ș., Hassan, T.H. (2024). Advanced Semi-Automatic Approach for Identifying Damaged Surfaces in Cultural Heritage Sites: Integrating UAVs, Photogrammetry, and 3D Data Analysis. *Remote Sensing*, 16(16), 3061. DOI: 10.3390/rs16163061.

[15] Komi, D., Yoshida, D., Kameyama, T. (2025). Development of an Automated Crack Detection System for Port Quay Walls Using a Small General-Purpose Drone and Orthophotos. *Sensors*, 25(14), 4325. DOI: 10.3390/s25144325.

[16] Sanz-Ablanedo E., Chandler J.H., Rodríguez-Pérez J.R., Ordóñez C. (2018). Accuracy of unmanned aerial vehicle photogrammetry as a function of the number and location of ground control points. Remote Sensing, Volume 10, Issue 10, 1606. DOI: 10.3390/rs10101606.

[17] Türk T., Tunalioglu N., Erdogan B., Ocalan T., Gurturk M. (2022). Accuracy assessment of UAV-PPK and UAV photogrammetry with ground control points. Environmental Monitoring and Assessment, Volume 194, Issue 7. DOI: 10.1007/s10661-022-10170-0.

[18] Yang, X., Lu, Y.-C., Murtiyoso, A., Koehl, M., Grussenmeyer, P. (2019). HBIM Modeling from the Surface Mesh and Its Extended Capability of Knowledge Representation. *ISPRS International Journal of Geo-Information*, 8(7), 301. DOI: 10.3390/ijgi8070301.

[19] Alshawabkeh, Y., Baik, A., Miky, Y. (2024). HBIM for Conservation of Built Heritage. *ISPRS International Journal of Geo-Information*, 13(7), 231. DOI: 10.3390/ijgi13070231.

[20] Germanese, D., Leone, G.R., Moroni, D., Pascali, M.A., Tampucci, M. (2018). Long-Term Monitoring of Crack Patterns in Historic Structures Using UAVs and Planar Markers: A Preliminary Study. *Journal of Imaging*, 4(8), 99. DOI: 10.3390/jimaging4080099.

https://doi.org/10.24867/INDIS-2026-EN-722



# BUILDINGS FOOTPRINT EXTRACTIONS USING SEGMENT ANYTHING MODEL

*Nikola Santrač[1], Mehmed Batilović[2], Pavel Benka[3], Marko Marković[4], Željko Bugarinović[5]*

***Summary:***

Building footprint extraction is one of the most extensively researched problems across fields such as architecture, GIS, civil engineering, urban planning, disaster management, and environmental monitoring. Automating this process with high accuracy is its most demanding aspect, and many approaches have been attempted. This paper applies the Segment Anything Model to open-source satellite imagery to extract building footprints. Building footprints were labeled and normalized, after which detection was performed using the text prompt "house," generating a bounding box and segmentation for each image. The results were compared with the ground truth and building footprints were detected in 96.42% of the images, with an average IoU of 86.97, a dice similarity coefficient of 93.03%, a precision of 96.80%, and a recall of 89.55%. This approach and level of accuracy demonstrate that the method can be applied in most cases and across various fields, with satisfactory results to be expected.

*Keywords: Buildings footprint, SAM, GeoAI, GIS*

# DETEKCIJA KONTURA OBJEKATA POMOĆU SEGMENT ANYTHING MODELA

***Rezime:***

Detekcija konture objekata predstavlja jedan od najčešće istraživanih problema u arhitekturi, GIS, građevinarstvu, urbanom planiranju, upravljanju katastrofama i životnoj sredini. Automatizacija ovog procesa uz ostvarivanje visoke tačnosti je najzahtevniji zadatak, zbog čega su primenjivani brojni pristupi. U ovom radu primenjuje se model Segment Anything na besplatnim satelitskim snimcima radi detekcije kontura objekata. Na slikama su iscrtane konture objekata, zatim je urađena normalizacija, nakon čega je izvršena detekcija korišćenjem tekstualnog prompta „house“, čime su za svaku sliku generisani okvir i segmentacija. Rezultati su upoređeni sa tačnim podacima, pri čemu je okvir za konture objekata detektovan na 96,42% slika, uz prosečan IoU od 86,97, Dice koeficijent od 93,03%, preciznost od 96,80% i osetljivost od 89,55%. Ovakav pristup i

1 Teaching asistant, University of Novi Sad, Faculty of Agriculture, Novi Sad, Serbia, nikola.santrac@polj.uns.ac.rs, https://orcid.org/0000-0001-7183-8511

2 Associate professor, University of Novi Sad, Faculty of Technical Sciences, Novi Sad, Serbia, mehmed@uns.ac.rs, https://orcid.org/0000-0001-5605-1112

3 Full Profesor, University of Novi Sad, Faculty of Agriculture, Novi Sad, Serbia, pavel.benka@polj.uns.ac.rs, https://orcid.org/0000-0001-6229-5180

4 Associate professor, University of Novi Sad, Faculty of Technical Sciences, Novi Sad, Serbia, marko_m@uns.ac.rs, https://orcid.org/0000-0003-3666-6325

5 Assistant professor, University of Novi Sad, Faculty of Technical Sciences, Novi Sad, Serbia, zeljkob@uns.ac.rs, https://orcid.org/0000-0002-7237-5130

postignuti nivo tačnosti pokazuju da se metoda može primeniti u većini potreba, kao i u različitim oblastima, uz očekivanje zadovoljavajućih rezultata.

*Ključne reči: Konture objekata, SAM, GeoAI, GIS*

## 1. INTRODUCTION

One of the most useful types of information in spatial analysis is the building footprint. Its widely used in architecture, GIS, civil engineering, urban planning, disaster management, and environmental monitoring [1-4]. They can be obtained in several ways, including detection from orthophotos and direct field surveying using classical measurement methods. The first approach is much faster, while the second is more precise. However, for most of the listed applications, detecting all building footprints over a selected area is often more important than achieving very high positional accuracy.
Manual digitization of objects from satellite and aerial images has been a common practice for many years. With the increasing use of AI (*Artificial Intelligence*), this approach is becoming less dominant. Datasets containing accurately and manually delineated objects are now commonly used as ground truth data for training and validating AI models. These datasets help models learn how to detect the same types of objects in new images. One of the main challenges in building footprint extraction is creating a model that can correctly recognize buildings under different conditions, such as varying illumination, shadows, different roof types, object sizes, image noise, image resolution, and other visual limitations [5].

AI based object detection can identify an object using a bounding box, which indicates that the object is located within a rectangular area. Each detected bounding box is assigned a confidence score, which represents the certainty of the model prediction. This approach is commonly used for object counting or rough estimation of object positions in an image. It is especially useful for objects with simple shapes and for tasks where exact object boundaries are not required.

In contrast, segmentation provides a more detailed representation of an object by identifying the exact pixels that belong to it. This makes segmentation a more precise, but also more demanding, form of object recognition [6,7]. Deep learning models, such as U-Net, a CNN (*Convolutional Neural Network*) architecture with an encoder-decoder structure and skip connections, have shown strong performance in building segmentation by learning hierarchical features from labeled datasets [8]. However, these models usually require large amounts of labeled training data, which limits their scalability across different environments.

The development of foundation models, such as the SAM (*Segment Anything Model*) [9], has created new opportunities for automating geospatial tasks. SAM is based on a vision transformer architecture. Unlike CNN, which mainly focus on local spatial patterns through convolutional filters, SAM uses self-attention mechanisms to model global relationships within an image. This allows the model to generalize across different domains with minimal input prompts. SAM can process different types of prompts without additional training samples, while maintaining good efficiency and accuracy in different scenarios. Since it was pretrained on a very large image dataset, SAM has shown strong zero-shot segmentation capabilities for general objects.

As the first vision foundation model designed specifically for image segmentation, SAM has strong zero-shot generalization ability and high potential for use in many downstream tasks. However, SAM also has limitations when applied to remote sensing image segmentation [10,11]. Its performance in specialized environments remains insufficiently explored, especially in areas where buildings are affected by shadows, vegetation,

spectral similarity, and complex roof structures. These conditions can reduce segmentation accuracy because buildings and surrounding objects often have similar texture and color characteristics.

Recent studies, such as Ošep et al. [12] and Yarroudh [13], have explored the use of SAM in automatic and unsupervised LiDAR based segmentation. Their results indicate that SAM has strong potential for improving segmentation accuracy in complex environments, including building footprint extraction.

This study focuses on building footprint detection and segmentation from open source aerial imagery using SAM.

## 2. MATERIALS AND METHODS

For this analyses, a dataset of 1,341 images was collected from an open-source satellite platform [14]. The images were then manually labeled by delineating the building footprints, which served as the ground truth data. The text prompt was defined within the SAM workflow, and inference was performed on all RGB images, with the results stored as bounding boxes and segmentation masks. For this step, the image inference function recommended in the official SAM repository [15] was used. The function was applied to each image from the dataset by changing only the input image path, while the text prompt was “house”. The model was used in a zero-shot manner, without any additional training, fine-tuning, or dataset-specific parameter adjustment. The generated segmentation masks and bounding boxes were then stored and compared with the manually annotated building footprints. The final step was the validation of these results, evaluated both by object detection performance and by per-pixel accuracy and precision. The complete workflow described above is illustrated in Figure 1.

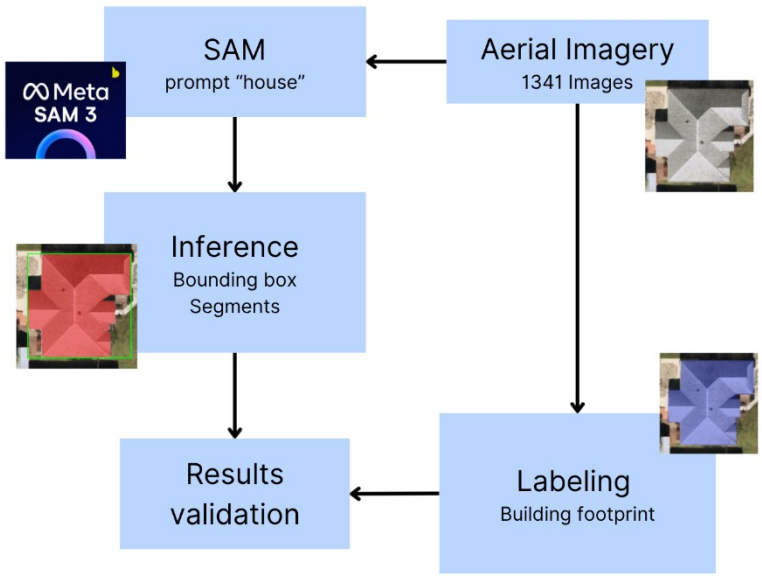


*Figure 1 Workflow*

## 2.1. DATASET

Pixel labeling tasks are among the most common remote sensing tasks. For the purposes of this experiment, a dataset of 1,341 image screenshots was collected as RGB screenshots from imagery displayed on Google Maps [14]. The images were resized to 256 × 256 pixels to standardize the input image dimensions for processing and inference. Each image contains only RGB bands. The images depict residential houses randomly selected from across the United States and Europe. The dataset includes a wide range of building types. Different roof complexity are represented, including simple roofs with 2 to 4 roof planes, easy roofs with 5 to 8 roof planes, and simple-complex roofs with more than 8 roof planes and multiple dormers. The spatial resolution of the source imagery varied across locations and depended primarily on the imagery available through Google Maps. Within the selected dataset, urban scenes generally showed finer spatial detail than rural scenes. The level of detail retained in the screenshots also depended on the viewing scale and subsequent image resizing. Therefore, although all images were resized to 256 × 256 pixels, this standardization did not imply a uniform ground sampling distance across the dataset. The native ground sampling distance was not available for individual screenshots; therefore, differences in spatial detail were assessed qualitatively. The dataset contains a larger number of buildings from urban areas, mainly because these areas have a higher building density compared to rural fields.

Manual annotation was performed by labeling only the central building footprint in each image. Each image was created for one target building that was fully visible, while in some cases other buildings were partially visible at the image edges. These partially visible buildings were not annotated and were excluded from the ground truth data. Each footprint was manually drawn as a polygon following the roof or building boundary visible in the RGB image. Therefore, each ground truth image contained a single annotated object, which was used for evaluating the segmentation results. Figures 2 and 4 show examples of RGB images, while Figures 3 and 5 show the building footprint ground truth overlaid on the corresponding RGB images.



*Figure 2 RGB Example*



*Figure 3 Building footprint - ground truth*



*Figure 4 RGB Example*



*Figure 5 Building footprint - ground truth*

## 2.2. SEGMENT ANYTHING MODEL-SAM

SAM consists of an image encoder, a prompt encoder, and a compact mask decoder. SAM operates around a robust image encoder that transforms the image into a high-dimensional feature space, producing a 256-dimensional image embedding. It is designed to accept different types of prompts, including sparse options such as points, boxes, and text, as well as dense prompts known as mask prompts. The main role of the prompt encoder is to convert these prompts into feature embeddings. In the mask decoder, SAM provides two modes for segmentation: interactive segmentation mode and automatic segmentation mode. In interactive segmentation mode, SAM produces segmentation results that reflect the user's interests based on the prompts they supply. In automatic segmentation mode, by contrast, SAM generates a grid of point prompts over the image and segments the entire input image based on those prompts. In this study, SAM was used in automatic segmentation mode driven by a text prompt. The detailed procedure and the SAM3 architecture workflow are shown in Figure 6.

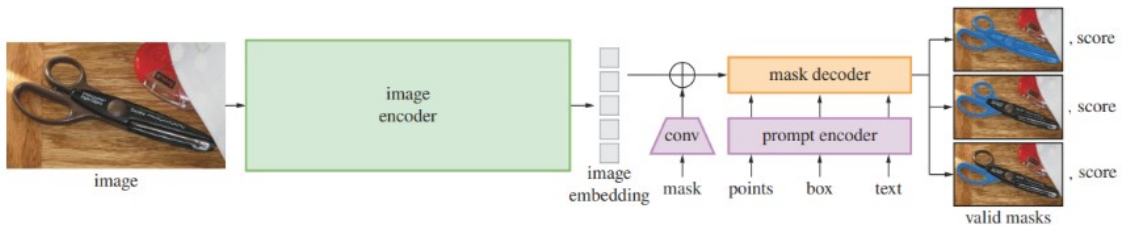


*Figure 6 SAM overview [9].*

AI models have a complex and computationally demanding architecture, and detecting and segmenting objects across a large number of images requires a workstation equipped with a sufficiently powerful GPU. The specifications of the computer used for this experiment are provided in Table 1.

*Table 1 Computer specifications*

| item number | Hardware Component | Model and Performance |
|---|---|---|
| 1 | CPU | Ryzen 9 9950X 16-Core |
| 2 | RAM | 96GB |
| 3 | GPU | NVIDIA GeForce RTX 5070 Ti |
| 4 | VRAM | 16 GB |

### 2.3. VALIDATION METRICES

The first parameter examined was object detection in the images, represented by the bounding box. The percentage of images in which an building was detected, was measured and compared with the actual number of building present in the images. This metric is expressed as a percentage.

The second evaluated parameter was the global_dice_coefficient, also known as the DSC (*Dice Similarity Coefficient*). The DSC, also called the Sørensen-Dice index, corresponds to the F1-score. It is calculated as twice the intersection between S (*predicted segmentation*) and GT (*ground truth*) divided by the sum of their areas, as shown in the equation 1 and Figure 7.

$$DSC = \frac{2|\mathrm{GT} \cap S|}{|\mathrm{GT}| + |S|} \tag{1}$$

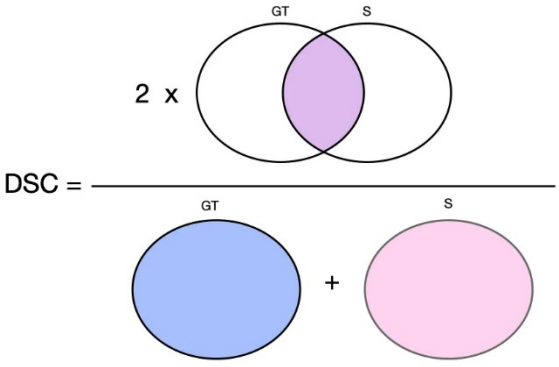


*Figure 7 DSC*

The third evaluated parameter was the IoU (*Intersection over Union*) or the Jaccard Index. IoU measures the overlap between the S and the GT, as shown in the equation 2 and Figure 8.

$$IoU = \frac{|\mathrm{GT} \cap S|}{|\mathrm{GT} \cup S|} \tag{2}$$

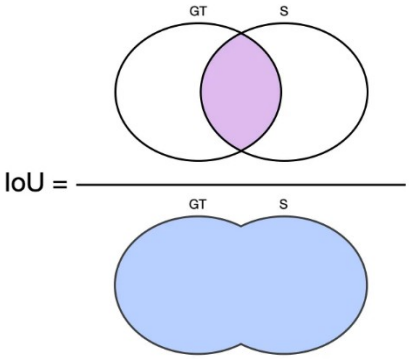


*Figure 8 IoU*

The fourth evaluated parameter was Recall, Sensitivity, or the True Positive Rate. Recall measures the ability of the model to detect all actual positive regions or pixels. A high recall value indicates a low number of missed objects or regions in the segmentation, as shown in the formula below.

The fifth evaluated parameter was Precision or Positive Predictive Value. Precision measures the accuracy of the model's positive predictions. It shows how many predicted positive regions or pixels actually belong to the object of interest. A high precision value indicates a low number of false positive errors in the segmentation, as shown in the formula below.

Figure 9 shows a confusion matrix that illustrates the relationship between predicted labels and real labels. It presents the four possible outcomes of a classification model: TP (*true positive*), FP (*false positive*), FN (*false negative*), and TN (*true negative*). A TP represents a correctly predicted positive sample, while a TN represents a correctly predicted negative sample. A FP occurs when the model incorrectly predicts a positive sample, and a FN occurs when the model fails to detect an actual positive sample. Based on these values, evaluation metrics such as precision, recall, and accuracy can be calculated.

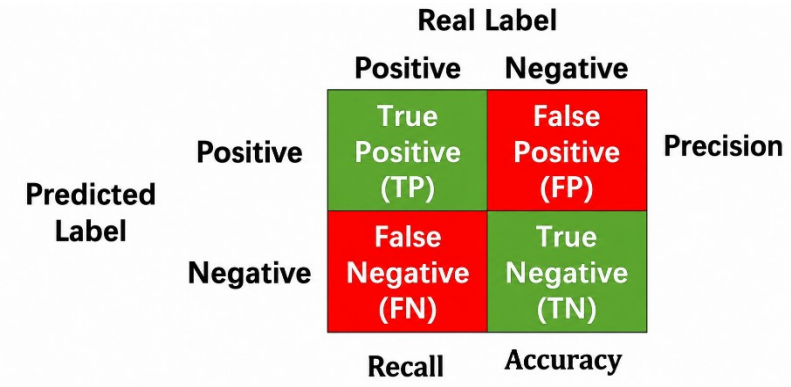


*Figure 9 Precision, Recall and Accuracy*

## 3. RESULTS AND DISCUSSES

Since multiple objects were detected in some images, only the mask closest to the image center was selected, while the remaining masks were ignored. This approach was applied because only one house was annotated in the ground truth images. Therefore, this

selection step was used only to ensure a fair comparison between the detected result and ground truth annotation, and should not be interpreted as a limitation of the algorithm in cases where multiple objects are present in a single image. Also, if the detected masks overlap by more than 70%, they can be considered to refer to the same object and can be discarded.

The SAM3 model showed very good performance in building footprint detection and segmentation. The average IoU value was 86.97%, while the average DSC value was 93.03%. Precision reached 96.80%, and recall reached 89.55%, which indicates a high level of segmentation accuracy. The high precision value shows that the model produced a low number of false positive predictions, while the high recall value indicates that most building footprints present in the images were successfully detected.

The object detection rate was 96.42%. Out of a total of 1341 images, a building footprint bounding box was detected in 1293 images, while in 48 images the building footprint was not detected, although it was present. Figure 10 shows the bounding box detection results. The graph compares the number of images in which a building footprint bounding box was detected with the number of images in which no bounding box was detected. The much higher number of detected bounding boxes confirms that the model successfully detected building footprints in most validation images

Figure 11 shows the validation metrics for IoU, DSC, precision, and recall. The graph clearly shows that all evaluated parameters achieved high values. Precision had the highest value, indicating that most predicted building footprint regions correctly matched the ground truth. DSC also reached a very high value, showing strong similarity between the predicted segmentation masks and the ground truth masks. IoU and recall were slightly lower, but still indicate reliable segmentation and detection performance.

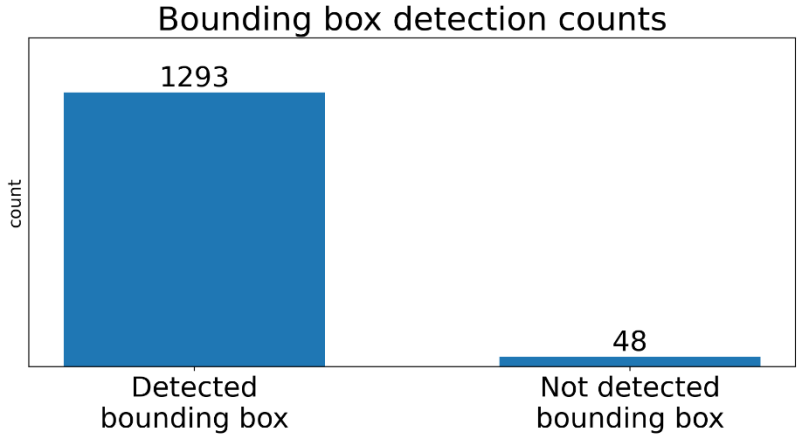


*Figure 10 Bounding box detection counts*

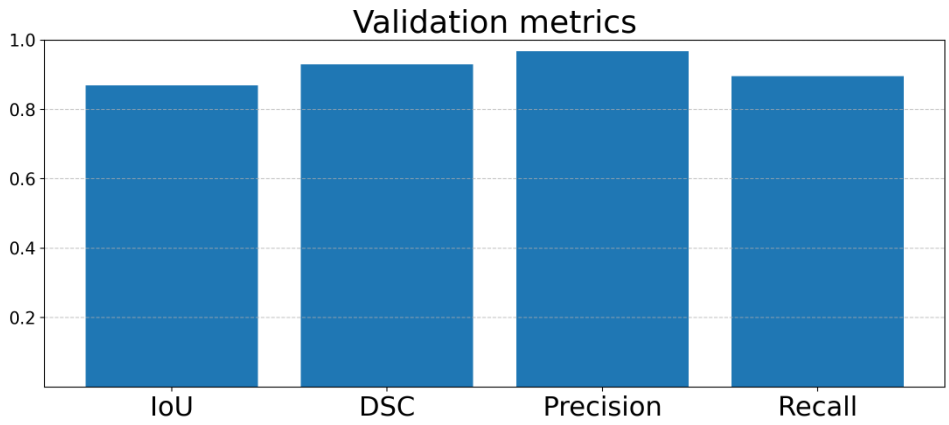


*Figure 11 Validation metrics*

Recent studies have also reported strong results for building footprint extraction. Ji et al. [16] proposed a SAM-based workflow that combines LiDAR data and very-high-resolution imagery, where LiDAR-derived information was used for approximate footprint detection and automatic prompt generation for SAM. Zhong et al. [17] proposed a zero-shot SAM-based framework for building footprint extraction and regularization from 3D mesh data, achieving 78.31% AP50 on the Vaihingen dataset. Hattula et al. [18] also investigated SAM for building segmentation in forest areas using true orthophotos and LiDAR-derived DSM, and compared its performance with U-Net. Recent supervised approaches also show high performance, but they usually require model training and more complex input data. Hakim and Tsai [1] used Mask R-CNN with geometric regularization for building footprint extraction from very-high-resolution satellite imagery, reporting 97.6% precision, 91.6% recall, and 94.5% F1-score. Haghighi Gashti et al. [19] evaluated different U-Net architectures for building footprint extraction using Google Maps imagery and OSM data, with the best model achieving 73.73% IoU, 88.65% accuracy, and 88.53% F1-score. NourEldeen and Wahed [20] used Mask R-CNN with PointRend for building footprint extraction from low-resolution satellite imagery and reported an F1-score of 85.71%.

The contribution of this study lies in evaluating a simple, text-prompted SAM 3 workflow for residential building delineation using RGB aerial images. Several related SAM-based approaches incorporate LiDAR-derived information or 3D mesh data [16–18], whereas the evaluated workflow requires only RGB imagery and a textual prompt. Furthermore, it avoids the task-specific training required by the supervised approaches discussed in [1, 19, 20]. The evaluation on 1,341 manually annotated images provides evidence of the performance and limitations of this approach under varying building characteristics and image conditions. From a practical perspective, these characteristics could facilitate initial building delineation where training annotations or elevation data are unavailable. The predicted outlines could serve as a starting point for operator-assisted mapping and updating incomplete building inventories. Nevertheless, the reported results do not establish superiority over existing methods, since the datasets, annotation protocols, and evaluation metrics differ. The evaluation also focuses on one centrally located building per image, so its findings cannot be directly extended to the extraction of all buildings across larger scenes. Further experiments comparing alternative prompts and reference methods on a common test dataset would help establish the conditions under which the workflow offers practical advantages.

Although the SAM model achieved high overall performance, several typical failure cases were observed, as shown in Figures 12 and 13. Most missed or inaccurate detections occurred in images where the target building was partially occluded by trees, affected by strong shadows, or covered by visually dominant roof elements such as solar panels, dormers, chimneys, or other artificial obstacles. Errors were also more frequent in images with different roof colors, made the building boundary less clear. Another source of error was related to image resolution and object visibility. In some rural images, the lower spatial resolution reduced the visual separation between the building and the surrounding background. These examples show that the main limitations are related to visual ambiguity, and image quality, rather than to the general ability of the model to detect buildings.

It is important to note that the segmentation confidence threshold, was set to 0.3, while the bounding box detection threshold was set to 0.1. These values are relatively low. However, they were selected because most images had lower resolution, so a lower confidence level was considered more appropriate for this dataset.

Examples of ground truth data overlaid with RGB images are shown in Figures 14, 16, 18, 20, and 22. The corresponding detection and segmentation results are shown in Figures 15, 17, 19, 21, and 23. These examples allow a direct visual comparison between the manually annotated building footprints and the results produced by the model. Based on these examples, it can be concluded that the main segmentation problems are similar to those observed in bounding box detection. The most common sources of error include shadows, trees, roof extensions with different colors compared to the rest of the roof, edge inaccuracies, complex roof structures, and other objects that reduce the visibility of the building footprint.



*Figure 12 Example of undetected building footprints.*



*Figure 13 Example of undetected building footprints.*



*Figure 14 Ground truth data - overlay with RGB*



*Figure 15 Detection and segmentation results*



*Figure 16 Ground truth data - overlay with RGB*



*Figure 17 Detection and segmentation results*

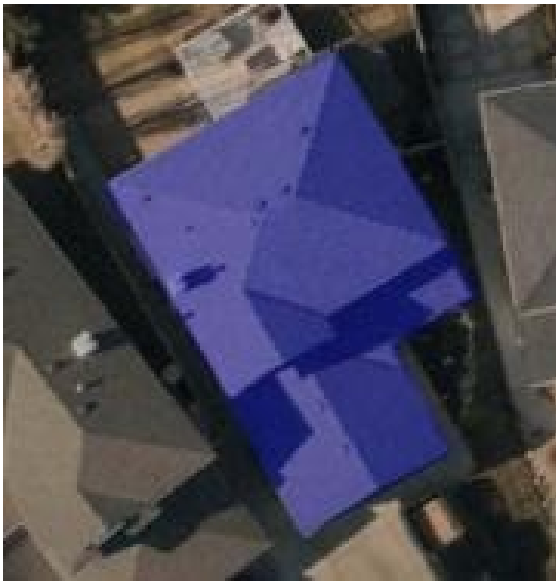

*Figure 18 Ground truth data - overlay with RGB*



*Figure 19 Detection and segmentation results*

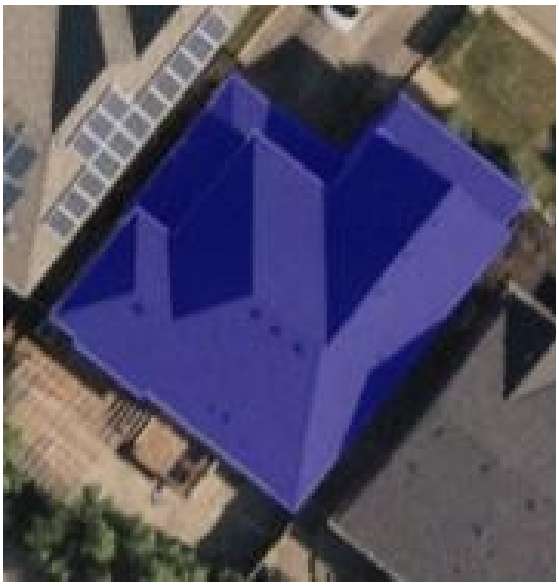

*Figure 20 Ground truth data - overlay with RGB*



*Figure 21 Detection and segmentation results*



*Figure 22 Ground truth data - overlay with RGB*



*Figure 23 Detection and segmentation results*

On the computer whose specifications are shown in Table 1, the detection of masks and segments took 351.29 seconds in total, while the validation of the results took 3.29 seconds in total.

From a practical perspective, the predicted masks could provide initial building outlines in unmapped areas, reducing the need for manual digitization. After georeferencing, vectorization, and quality checks, these outlines could support GIS database updates and spatial planning. Comparing spatially aligned imagery from different time series could help monitor construction activity and changes in urban and rural areas. Combined with official records, detected changes could also help identify potentially unauthorized construction for further inspection.

## 4. CONCLUSION

In this study, building footprint extraction was performed using the SAM. A total of 1341 manually annotated RGB images were used as ground truth data for result validation. The SAM model was applied for building footprint detection and segmentation, using the prompt “house”.

The results showed very high performance. The average IoU value was 86.97%, while the average DSC value was 93.03%. Precision reached 96.80%, and recall reached 89.55%. The object detection rate was 96.42%, which confirms that the model successfully detected building footprints in most images.

These results indicate that this approach achieves high accuracy across all evaluated parameters and is suitable for use in most cases. In addition to the short processing time, an important advantage of this method is the practical application of the SAM algorithm, which has strong potential for automatic object detection and segmentation.

It can be concluded that SAM and similar models are useful even with limited prior knowledge in this field. They provide good results for recognizing basic and clearly visible objects in images. However, for more complex and less common cases, such as objects affected by shadows, trees, roof obstacles, or unclear boundaries, the accuracy decreases.

Future work should include DSM data, higher resolution images, and drone based imagery. Additional steps should also include polygon regularization, orthogonalization methods, changes in the prompt, adjustment of the confidence level, and the use of a larger dataset. The results should also be compared with other models, such as Mask2Former, YOLO, U-Net, Detectron2, and similar approaches.

**ACKNOWLEDGEMENT**

The research funds were provided by the Ministry of Science, Technological Development and Innovation under Contracts No. 451-03-34/2026-03/200117 and 451-03-34/2026-03/200156, Provincial Secretariat for Higher Education and Scientific Research of AP Vojvodina, Republic of Serbia, (contract no. 003876050 2025 09418 003 000 000 001 04 003) and the Faculty of Technical Sciences, University of Novi Sad through project “Scientific and Artistic Research Work of Researchers in Teaching and Associate Positions at the Faculty of Technical Sciences, University of Novi Sad 2026” (No. 01-3609/1).

**REFERENCES**

[1] Hakim, Y. F., & Tsai, F. (2026). Building Footprint Extraction for Large-Scale Basemaps Using Very-High-Resolution Satellite Imagery. Buildings, 16(3), 675–675. https://doi.org/10.3390/buildings16030675

[2] Li, Q., Shi, Y., Huang, X., & Xiao Xiang Zhu. (2020). Building Footprint Generation by Integrating Convolution Neural Network With Feature Pairwise Conditional Random Field (FPCRF). IEEE Transactions on Geoscience and Remote Sensing, 58(11), 7502–7519. https://doi.org/10.1109/tgrs.2020.2973720

[3] Biljecki, F., Zheng, L., Milojevic-Dupont, N., & Creutzig, F. (2021). Open government geospatial data on buildings for planning sustainable and resilient cities. https://doi.org/10.48550/arXiv.2107.04023

[4] Somanath, S., Naserentin, V., Eleftheriou, O., Sjölie, D., Wästberg, B. S., & Logg, A. (2023). On procedural urban digital twin generation and visualization of large scale data. https://doi.org/10.48550/arXiv.2305.02242

[5] Zhang, Y., Ryu, D., & Zheng, D. (2021). Using Remote Sensing Techniques to Improve Hydrological Predictions in a Rapidly Changing World. Remote Sensing, 13(19), 3865. https://doi.org/10.3390/rs13193865

[6] He, K., Gkioxari, G., Dollár, P., & Girshick, R. (2018, January 24). Mask R-CNN. ArXiv.org. https://doi.org/10.48550/arXiv.1703.06870

[7] Liu, W., Anguelov, D., Erhan, D., Szegedy, C., Reed, S., Fu, C.-Y., & Berg, A. C. (2016). SSD: Single Shot MultiBox Detector. Computer Vision – ECCV 2016, 9905(5), 21–37. https://doi.org/10.1007/978-3-319-46448-0_2

[8] Ronneberger, O., Fischer, P., & Brox, T. (2015). U-Net: Convolutional Networks for Biomedical Image Segmentation. Lecture Notes in Computer Science, 9351, 234–241. https://doi.org/10.1007/978-3-319-24574-4_28

[9] Kirillov, A., Mintun, E., Ravi, N., Mao, H., Rolland, C., Gustafson, L., Xiao, T., Whitehead, S., Berg, A. C., Lo, W.-Y., Dollár, P., & Girshick, R. (2023). Segment Anything. ArXiv (Cornell University). https://doi.org/10.48550/arxiv.2304.02643

[10] Ding, L.; Zhu, K.; Peng, D.; Tang, H.; Yang, K.; Bruzzone, L. Adapting Segment Anything Model for Change Detection in VHR Remote Sensing Images. IEEE Trans. Geosci. Remote Sens. 2024, 62, 1–11. https://doi.org/10.1109/TGRS.2024.3368168

[11] Chen, T.; Zhu, L.; Ding, C.; Cao, R.; Wang, Y.; Zhang, S.; Li, Z.; Sun, L.; Zang, Y.; Mao, P. SAM-Adapter: Adapting Segment Anything in Underperformed Scenes. In Proceedings of the 2023 IEEE/CVF International Conference on Computer Vision Workshops (ICCVW), Paris, France, 2–6 October 2023; pp. 3359–3367. 37. https://doi.org/10.48550/arXiv.2304.09148

[12] Ošep, A., Meinhardt, T., Ferroni, F., Peri, N., Ramanan, D., & Leal-Taixé, L. (2024). Better Call SAL: Towards Learning to Segment Anything in Lidar. https://doi.org/10.48550/arXiv.2403.13129

[13] Yarroudh, A. (2023). LiDAR Automatic Unsupervised Segmentation using Segment-Anything Model (SAM) from Meta AI [GitHub repository]. https://github.com/Yarroudh/segment-lidar

[14] Google. (2026). Google Maps. Retrieved April 20, 2026, from https://maps.google.com

[15] Github (2026). SAM3 repository. Retrieved April 20, 2026, from https://github.com/facebookresearch/sam3

[16] Ji, Y., Wu, W., Wan, G., Zhao, Y., Wang, W., Yin, H., Tian, Z., & Liu, S. (2024). Segment Anything Model-Based Building Footprint Extraction for Residential Complex Spatial Assessment Using LiDAR Data and Very High-Resolution Imagery. *Remote Sensing*, *16*(14), 2661–2661. https://doi.org/10.3390/rs16142661

[17] Zhong, J., Zhang, Y., Liu, X., Zhang, J., Fei, L., Xia, W., Zhang, B., Fan, W., & Yue, D. (2025). Zero-shot building footprint extraction and regularization based on Segment Anything model with Mesh Model. *The International Archives of the Photogrammetry, Remote Sensing and Spatial Information Sciences*, *XLVIII-G-2025*, 1777–1783. https://doi.org/10.5194/isprs-archives-xlviii-g-2025-1777-2025

[18] Hattula, E., Raninen, J., & Zhu, L. (2025). Segment Anything Model with LiDAR based images for building segmentation in forest areas. *the International Archives of the Photogrammetry, Remote Sensing and Spatial Information Sciences/International Archives of the Photogrammetry, Remote Sensing and Spatial Information Sciences*, *XLVIII-M-7-2025*, 13–19. https://doi.org/10.5194/isprs-archives-xlviii-m-7-2025-13-2025

[19] Ehsan Haghighi Gashti, Mahmoud Reza Delavar, Guan, H., & Li, J. (2024). Semantic Segmentation Uncertainty Assessment of Different U-net Architectures for Extracting Building Footprints. *ISPRS Annals of the Photogrammetry, Remote Sensing and Spatial Information Sciences*, *X-4-2024*, 141–148. https://doi.org/10.5194/isprs-annals-x-4-2024-141-2024

[20] NourEldeen, A., & E. Wahed, M. (2024). Enhanced building footprint extraction from satellite imagery using Mask R-CNN and PointRend. *Bulletin of Electrical Engineering and Informatics*, *13*(5), 3601–3608. https://doi.org/10.11591/eei.v13i5.7443

https://doi.org/10.24867/INDIS-2026-EN-738



# UAV-BASED DOCUMENTATION OF CULTURAL HERITAGE SITES: A CASE STUDY OF KRUJA CASTLE

*Arli Llabani[1], Bledar Sina[2], Eduart Blloshmi[3], Radovan Đurović[4], Marko Z. Marković[5]*

***Summary:***

This study presents a UAV-based photogrammetric approach for the high-resolution digital documentation of Kruja Castle, an important cultural heritage monument in Albania characterized by complex topography and significant historical value. The objective is to evaluate the effectiveness of UAV photogrammetry for accurate spatial documentation of heritage sites in challenging terrain conditions.

Data acquisition was conducted using a DJI Phantom 4 RTK UAV following a pre-planned flight mission at an average altitude of approximately 60 meters above ground level. A total of 257 high-resolution images were captured with high forward and side overlap to ensure complete and redundant coverage of the study area.

The imagery was processed using Pix4D software based on Structure-from-Motion (SfM) and Multi-View Stereo (MVS) methods, including image alignment, camera calibration, dense point cloud generation, and orthomosaic production. All data were georeferenced within the ETRS89 / Albania TM 2010 coordinate system.

The photogrammetric results demonstrate high geometric reliability and spatial detail. The dataset was georeferenced using the onboard RTK positioning of the DJI Phantom 4 RTK, with real-time corrections provided through the Albanian Permanent GNSS Network (ALBCORS). Based on the RTK-supported georeferencing and photogrammetric adjustment, an estimated positional RMSE of approximately 2–3 cm was obtained. Since no independent Ground Control Points (GCPs) or Check Points (CPs) were established, this value represents an estimate of the georeferencing and adjustment consistency rather than an independently validated absolute positional accuracy.

The study confirms that UAV photogrammetry is a highly efficient, accurate, and cost-effective method for the digital preservation of complex cultural heritage sites. The produced geospatial outputs support conservation planning, monitoring, and long-term digital archiving applications.

*Keywords: UAV Photogrammetry, Cultural Heritage Documentation, 3D Reconstruction, Structure from Motion (SfM)*

[1] PhD, Lecturer, Faculty of Civil Engineering, Polytechnic University of Tirana, Tirana, Albania, arli.llabani@fin.edu.al, ORCID 0009-0003-6726-0106
[2] PhD, Lecturer, Faculty of Civil Engineering, Polytechnic University of Tirana, Tirana, Albania, bledar.sina@fin.edu.al
[3] PhD, Lecturer, Faculty of Civil Engineering, Polytechnic University of Tirana, Tirana, Albania, eduart.blloshmi@fin.edu.al
[4] Associate Professor, Faculty of Civil Engineering, University of Montenegro, Podgorica, Montenegro, zlatko1979@yahoo.com
[5] Associate Professor, Faculty of Technical Sciences, University of Novi Sad, Novi Sad, Serbia, marko_m@uns.ac.rs

## 1. INTRODUCTION

The documentation and preservation of cultural heritage sites has become an increasingly important field in recent decades due to rapid urban development, environmental impacts, and the natural deterioration of historical monuments over time. Cultural heritage structures represent not only architectural and historical value but also serve as key elements of national identity and collective memory. Therefore, their accurate documentation is essential for conservation, restoration, monitoring, and digital archiving purposes. Traditional surveying techniques, although widely used in geodetic and architectural documentation, often present limitations when applied to complex cultural heritage structures. These methods can be time-consuming, require direct access to difficult or unsafe areas, and may not fully capture the geometric complexity of irregular surfaces such as walls, towers, and fortification systems. In contrast, modern remote sensing technologies have introduced more efficient and comprehensive approaches for spatial data acquisition [1].

Among these technologies, UAV (Unmanned Aerial Vehicle) photogrammetry has emerged as one of the most effective tools for high-resolution spatial documentation. UAV systems enable flexible data acquisition from different altitudes and perspectives, allowing for the capture of dense and overlapping imagery. When combined with Structure-from-Motion (SfM) and Multi-View Stereo (MVS) techniques, UAV imagery can be processed into accurate georeferenced spatial products, including dense point clouds, orthomosaics, and digital surface models. The advantages of UAV-based photogrammetry include high spatial resolution, reduced field time, lower operational costs compared to traditional methods, and the ability to document inaccessible or hazardous areas. These characteristics make UAV photogrammetry particularly suitable for cultural heritage applications, where precision and non-invasive methods are critical requirements [2] [3].

Kruja Castle, located in northern Albania, is one of the most significant historical and cultural monuments in the country. Situated on a steep hill at approximately 600 meters above sea level, the site features complex topography, irregular terrain, and a dense concentration of historical architectural elements. Its strategic location and historical importance, particularly during the resistance against the Ottoman Empire, make it a valuable case study for the application of UAV-based documentation techniques. Due to its morphological complexity and elevation differences, Kruja Castle presents several challenges for conventional surveying methods, including limited accessibility, occlusions, and difficulty in achieving complete spatial coverage. These conditions make it an ideal environment for testing the effectiveness of UAV photogrammetry in capturing detailed and accurate spatial information [4] [5].

This study aims to apply UAV-based photogrammetric methods for the high-resolution documentation of Kruja Castle and to evaluate the quality and reliability of the generated spatial data. The focus is on demonstrating the capability of UAV imagery to produce accurate geospatial outputs suitable for cultural heritage preservation and analysis. The contribution of this work lies in providing a practical case study that highlights the integration of UAV technology and photogrammetric processing for cultural heritage documentation in complex terrain conditions, offering a scalable approach that can be applied to other similar sites in the region [6].

## 2. STUDY AREA

Kruja Castle is one of the most important cultural and historical monuments in Albania, located in the northern part of the country within the city of Kruja. The castle is positioned on a steep hill at an approximate elevation of 600 meters above sea level, which provides a dominant visual and strategic overview of the surrounding landscape. Its geographical coordinates are approximately 41.517° N latitude and 19.947° E longitude. The site is characterized by a complex topographic environment with significant elevation variations, steep slopes, and rugged terrain. This morphological complexity is a result of long-term geological processes, including tectonic activity and erosion, which have shaped the surrounding hills and valleys. The terrain conditions have historically contributed to the defensive advantages of the castle, making it a strategically important fortification during different historical periods.

The area surrounding Kruja Castle is dominated by Mediterranean vegetation, including shrubs, low forested areas, and rocky surfaces. The environmental conditions, combined with the elevation of the site, create a visually rich but technically challenging environment for spatial data acquisition. These factors significantly influence the visibility, accessibility, and imaging conditions during UAV-based surveys, especially due to shadowing effects and occlusions caused by terrain irregularities. The geographical location of Kruja Castle within Albania is presented in Fig. 1.




*Fig. 1 Geographic location of Kruja Castle*

Hydrologically, the region is influenced by the Erzen River, which flows through the valley below the castle. This river has played an important role in shaping the local geomorphology and supporting human settlement in the area. The surrounding landscape includes a combination of natural and anthropogenic features, including pathways, fortification walls, residential structures, and tourism-related infrastructure. From a cultural heritage perspective, Kruja Castle represents a key historical landmark closely associated with Albanian national identity and the resistance led by Gjergj Kastrioti Skanderbeg during the 15th century. Today, the site functions as both a protected monument and a major tourist attraction, receiving a high number of visitors throughout the year. Due to its elevation, complex geometry, and mixed natural–built environment, Kruja Castle presents a challenging case for traditional surveying techniques. Limited accessibility in certain parts of the site and the need for non-

invasive documentation methods make it particularly suitable for UAV-based photogrammetric surveying techniques.

The UAV survey covered an area of approximately 8.5 ha, including the castle complex, surrounding fortification walls, internal roads, and adjacent open spaces. The elevation within the surveyed area ranges from approximately 570 m to 630 m above sea level, resulting in a vertical difference of nearly 60 m. The combination of steep slopes, irregular terrain, historical masonry structures, narrow pathways, and vegetation creates a morphologically complex environment that presents significant challenges for UAV photogrammetric data acquisition and 3D reconstruction

## 3. DATA ACQUISITION

UAV data acquisition for Kruja Castle was conducted using a DJI Phantom 4 RTK unmanned aerial system, which integrates high-precision GNSS positioning with a stabilized gimbal camera system. The objective of the survey was to acquire high-resolution, georeferenced aerial imagery suitable for photogrammetric processing and accurate 3D spatial reconstruction [7].
The flight campaign was designed to ensure full spatial coverage of the study area, considering the complex topography, elevation differences, and structural density of the castle environment. The data acquisition process was divided into three main subsections: flight planning, flight execution, and image dataset characteristics.

### 3.1. FLIGHT PLANNING AND MISSION DESIGN

The flight planning phase was carried out prior to field data acquisition using predefined mission parameters. The UAV flight path was generated to ensure systematic coverage of the entire castle area, minimizing occlusions and maximizing image overlap for reliable photogrammetric reconstruction. The mission was configured at an average flight altitude of approximately 60 meters above ground level (AGL). This altitude was selected as a compromise between spatial resolution and coverage efficiency, ensuring sufficient Ground Sampling Distance (GSD) for detailed heritage documentation [8]. The planned UAV flight mission, including the flight path and image acquisition geometry, is illustrated in Fig. 2.

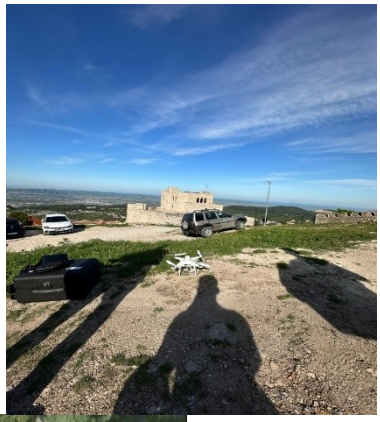

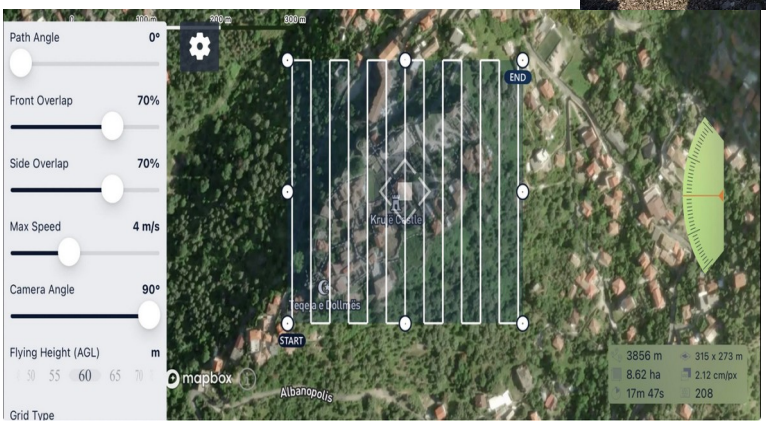


*Fig. 2 Flight mission in the Castle of Kruja*

The principal flight parameters adopted during the UAV survey are summarized in Table 1.

*Tab. 1 Flight mission parameters*

| Parameter | Value |
|---|---|
| UAV Platform | DJI Phantom 4 RTK |
| Flight altitude | 60 m AGL |
| Image overlap (forward) | 70% |
| Image overlap (side) | 70% |
| Flight mode | Automated grid mission |
| Coordinate system | ETRS89 / Albania TM 2010 |
| Weather conditions | The UAV survey was conducted under clear sky conditions with cloud cover below approximately 10% and wind speeds below 3 m/s, ensuring stable flight conditions and minimizing image blur caused by platform movement |

The overlap parameters were set to ensure redundancy in image coverage, which is critical for dense point cloud generation and geometric stability of the block adjustment. The flight path followed a grid-based pattern adapted to the irregular shape of the terrain, with additional attention given to steep and shadowed areas of the site [9].

The UAV mission was flown at an average speed of approximately 4 m/s with the camera fixed in a nadir orientation (90°). Automatic exposure mode was applied, maintaining an ISO value between 100–200 and shutter speeds faster than 1/800 s to minimize motion blur. The complete survey required approximately 18 minutes and was completed using one DJI Phantom 4 RTK battery.

## 3.2. DATA ACQUISITION AND IMAGE CAPTURE

The aerial imagery was collected using a high-resolution RGB camera integrated into the UAV system. The sensor captured nadir-oriented images with consistent exposure settings to ensure radiometric stability across the dataset.
A total of 257 images were acquired during the flight campaign. The high image redundancy was intentionally planned to improve photogrammetric robustness and to ensure sufficient overlap between adjacent image footprints. The UAV maintained a constant flight speed to avoid motion blur and to guarantee uniform image spacing along flight lines. The acquisition process was performed under stable meteorological conditions, with minimal wind influence and consistent lighting, reducing shadow variability and improving feature matching during processing [10].
Each image was automatically geotagged using onboard GNSS/RTK positioning, which significantly improved the initial alignment phase during photogrammetric processing. The dataset provided full spatial coverage of the castle area, including steep slopes, walls, and interior structural elements. The collected imagery was later used as the primary input for Structure-from-Motion (SfM) and Multi-View Stereo (MVS) processing [11].
The imported UAV images used for photogrammetric processing are shown in Fig. 3.



*Fig. 3 UAV aerial capture view*

## 3.3. DATASET CHARACTERISTICS AND GEOREFERENCING

The acquired dataset consists of high-resolution RGB images with consistent spatial resolution and sufficient overlap for photogrammetric reconstruction. The average image resolution is approximately 5472 × 3648 pixels, enabling fine-scale representation of architectural and topographic details.
The integration of RTK positioning data improved the absolute georeferencing accuracy of the model, reducing the need for extensive ground control points (GCPs) and enhancing the reliability of spatial outputs [12] [13].

The Ground Sampling Distance (GSD) achieved in this study is approximately 2.7–3.0 cm/pixel, which is suitable for high-resolution cultural heritage documentation and structural analysis.

No Ground Control Points (GCPs) or independent Check Points (CPs) were established during the survey. Instead, absolute georeferencing was supported by the onboard RTK capabilities of the DJI Phantom 4 RTK. The UAV received real-time positioning corrections through the Albanian Permanent GNSS Network (ALBCORS), providing centimeter-level positioning information for the camera exposure locations. These RTK-derived coordinates were incorporated into the photogrammetric block adjustment and were used to establish the spatial reference of the generated products. The resulting georeferencing quality was assessed from the RTK-supported photogrammetric adjustment and associated residuals.

## 4. METHODOLOGY

The methodology adopted in this study is based on a standard UAV photogrammetric pipeline integrating Structure-from-Motion (SfM) and Multi-View Stereo (MVS) techniques. The main objective is to transform overlapping UAV imagery into accurate georeferenced spatial products, including a dense point cloud and an orthomosaic of Kruja Castle.
The processing workflow consists of four main stages: image preprocessing and import, camera alignment and SfM reconstruction, dense point cloud generation, and orthomosaic production. All processing was performed using Pix4D software, which provides automated photogrammetric computation and geospatial output generation [14].

### 4.1. IMAGE PREPROCESSING AND PROJECT SETUP

The first step of the methodology involved the creation of a new photogrammetric project in Pix4D software. The UAV images acquired during the flight campaign (257 images) were imported into the system without manual alteration.
Each image contained embedded GNSS/RTK metadata, which was used to initialize the georeferencing process. The project coordinate system was defined as ETRS89 / Albania TM 2010, ensuring compatibility with national geospatial standards.
The image dataset was checked for completeness, consistency, and overlap adequacy before processing. No images were removed due to the high quality and stability of the dataset [15] [16].
The overall workflow adopted in this study, from mission planning to the generation of the final geospatial products, is illustrated in Fig. 4.

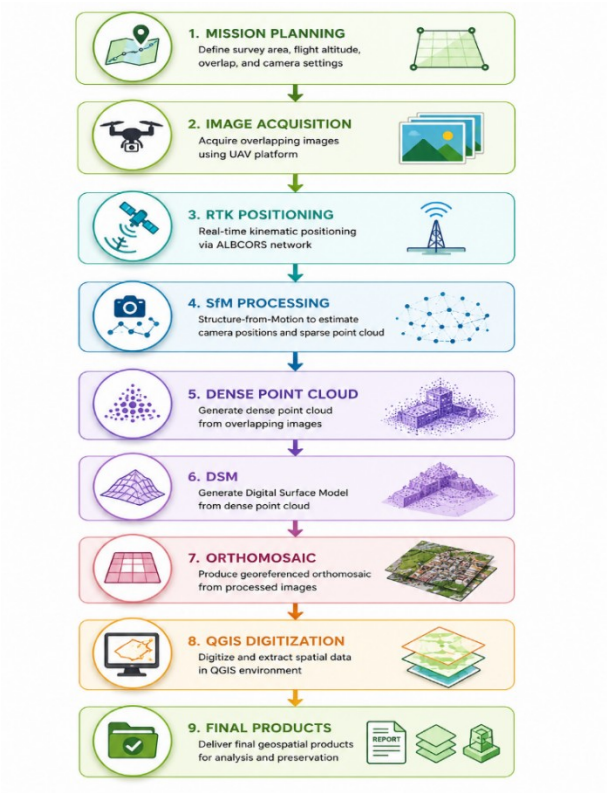


*Fig. 4 Workflow of the UAV-based photogrammetric methodology adopted for the documentation of Kruja Castle*

## 4.2. STRUCTURE-FROM-MOTION (SFM) AND CAMERA ALIGNMENT

In this stage, the Structure-from-Motion (SfM) algorithm was applied to estimate the internal and external camera parameters. The process involved automatic feature extraction, feature matching between overlapping images, and bundle adjustment optimization [17].
Keypoints were detected across multiple images and matched using robust feature descriptors, allowing the reconstruction of camera positions and orientations in a three-dimensional coordinate space.
The alignment process resulted in a globally consistent sparse point cloud, which represents the initial geometric structure of the study area. The quality of alignment was verified through reprojection error analysis, ensuring geometric reliability of the model.

The full image set achieved successful calibration (100%), indicating strong overlap and high-quality image acquisition conditions. The resulting ray cloud, showing camera positions and image connectivity after bundle adjustment, is presented in Fig. 5.

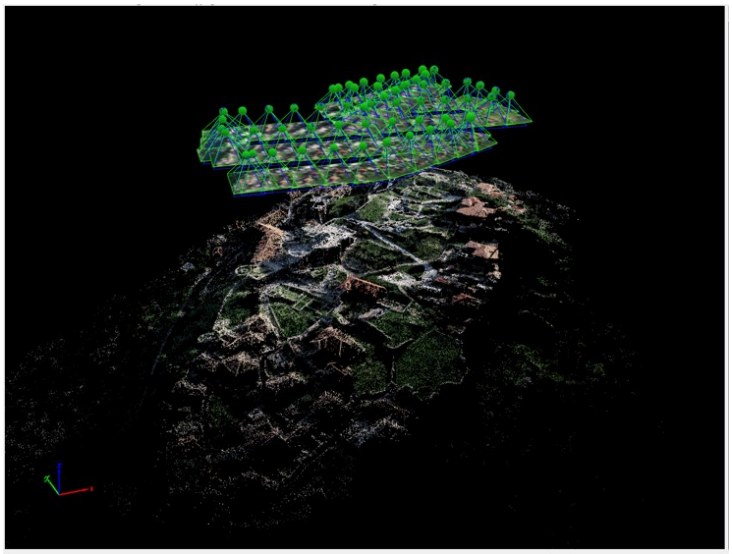

*Fig. 5 Camera positions preview in Pix4DMapper*

The main photogrammetric processing settings and quality parameters used in Pix4D are summarized in Table 2.

*Tab. 2 SfM processing parameters*

| Parameter | Value |
|---|---|
| Feature extraction method | Automatic |
| Matching strategy | Multi-view |
| Bundle adjustment | Yes |
| Image calibration success | 100% |
| Mean reprojection error | ~0.15 pixels |

## 4.3. DENSE POINT CLOUD GENERATION

Following successful SfM reconstruction, a dense point cloud was generated using Multi-View Stereo (MVS) algorithms. This step significantly increases the number of reconstructed points by estimating depth information for each image pixel.
The resulting dense point cloud provides a highly detailed representation of the terrain and architectural structures of Kruja Castle. The density of the point cloud allows for precise geometric interpretation of walls, slopes, and structural elements [18].
Noise filtering and outlier removal were applied to improve the quality of the final dataset, ensuring a clean and geometrically consistent 3D representation. The dense point cloud generated from the UAV imagery is presented in Fig. 6.

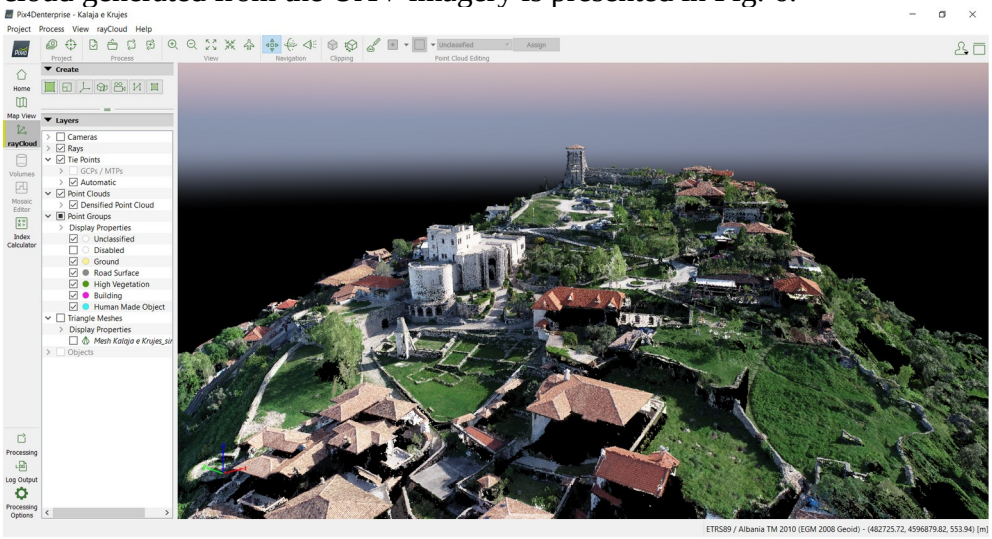


*Fig. 6 Dense point cloud of Kruja Castle*

## 4.4. ORTHOMOSAIC GENERATION

The final stage of processing involved the generation of a geometrically corrected orthomosaic and additional geospatial outputs. The orthomosaic represents a high-resolution, scale-accurate image of the study area, free from perspective distortions.
The orthomosaic was generated using the reconstructed 3D geometry and ground control information derived from RTK positioning. This ensures high positional accuracy and allows the product to be used for mapping and spatial analysis [19].
The final Ground Sampling Distance (GSD) achieved in this study is 2.77 cm/pixel, providing sufficient spatial resolution for detailed cultural heritage documentation. The final high-resolution orthomosaic generated from the processed UAV imagery is shown in Fig. 7.



*Fig. 7 High-resolution orthomosaic of Kruja Castle*

## 4.5. GEOSPATIAL DATA PROCESSING AND DIGITALIZATION IN QGIS

The high-resolution orthomosaic generated in Pix4D was exported in GeoTIFF format and used as the primary spatial reference layer for further geospatial analysis and vector data extraction. The orthomosaic, being geometrically corrected and georeferenced in the ETRS89 / Albania TM 2010 coordinate system, provided a reliable base for detailed mapping and digital reconstruction of the Kruja Castle area.
Geospatial processing and digitization were performed using QGIS (Quantum GIS), an open-source GIS platform widely used for spatial data management, vector digitization, and cartographic analysis [20].

### 4.5.1. Vector Layer Creation

Based on visual interpretation of the orthomosaic, multiple vector layers were created to represent the main structural and functional elements of the study area. A total of seven feature classes were defined:

- Castle boundary (Polygon)
- Buildings (Polygon)
- Roads (Line)
- Stairs (Line)
- Defensive walls (Polygon/Line)
- Historical structures (Polygon)
- Surrounding area (Polygon)

Each layer was created using the “New Shapefile Layer” tool, defining geometry type and attribute fields such as object name, category, and structural characteristics.

### 4.5.2. Digitization Process

The digitization process was performed manually by on-screen vectorization over the orthomosaic. Editing mode was activated for each layer, and features were digitized using polygon and polyline tools following visible structural outlines.
To ensure geometric accuracy, snapping tools, vertex editing, and zoom-based refinement were applied. The completeness of the digitized features was checked

systematically by comparing the vector layers with the underlying high-resolution orthomosaic across the entire surveyed area. Particular attention was given to the continuity and spatial alignment of defensive walls, buildings, roads, and stairs, while misplaced vertices, overlaps, and other visible inconsistencies were corrected during the editing process. A final visual and geometric quality-control check was performed at different map scales to verify that the digitized features followed the visible structural boundaries represented in the orthomosaic. The manual digitization process performed in QGIS is illustrated in Fig. 8.

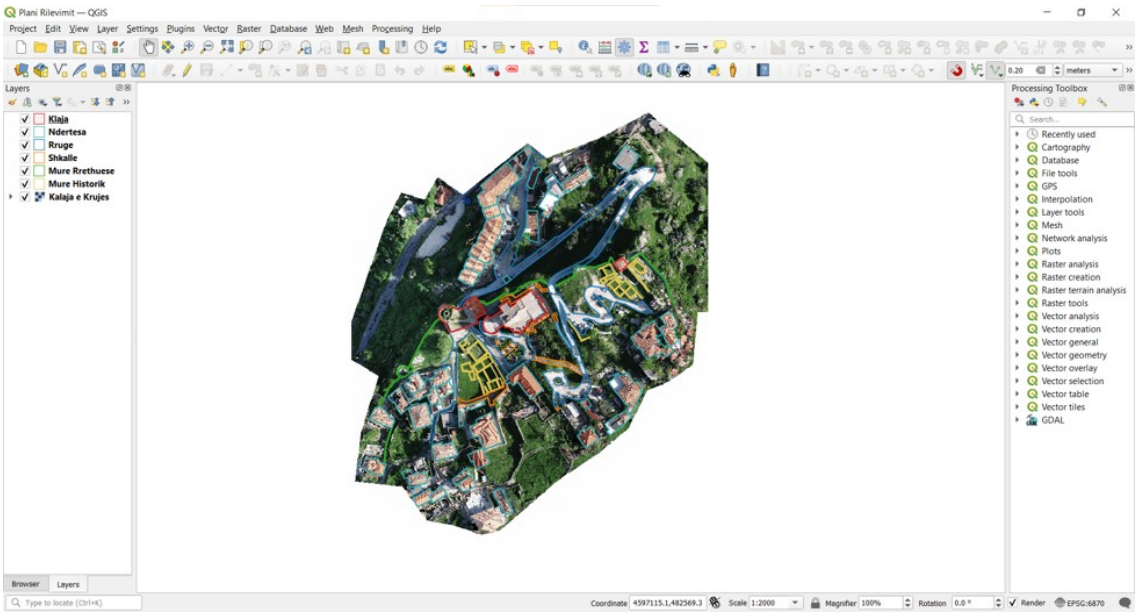


*Fig. 8 Digitization process in QGIS*

### 4.5.3. Cartographic Styling and Visualization

After digitization, layers were symbolized to improve interpretability. Different colors and line styles were assigned based on feature type. Defensive walls and historical structures were emphasized using thicker and darker symbology, while roads and access paths were represented using differentiated line patterns.
A complete map layout was then prepared including legend, scale bar, and coordinate grid for spatial reference.

### 4.5.4. Data Export and Outputs

The final GIS project was exported in multiple formats including QGIS project file (.qgz), GeoPDF, and shapefiles for interoperability with other GIS platforms. These outputs provide a structured geospatial dataset suitable for heritage documentation, spatial analysis, and future conservation planning. The completed GIS map layout produced after digitization is presented in Fig. 9.

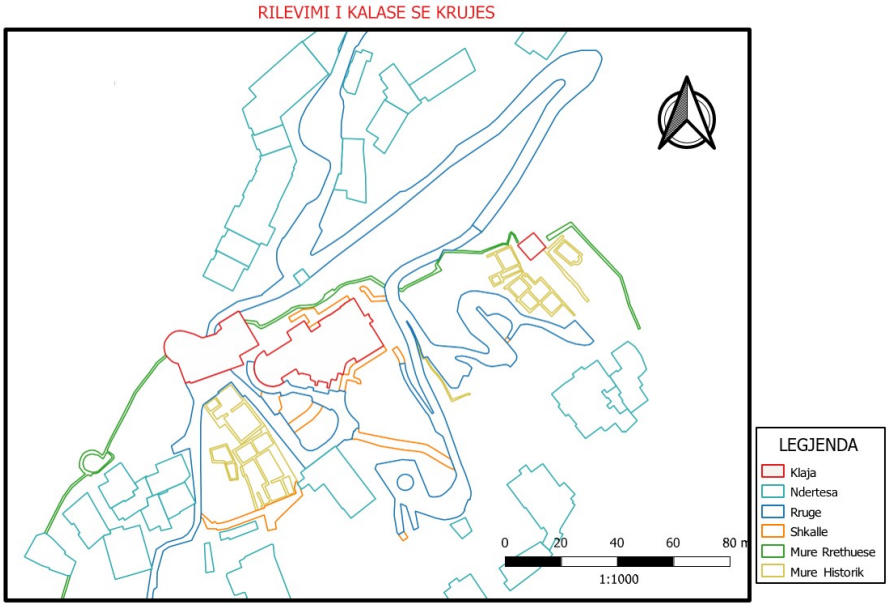


*Fig. 9 Final GIS map layout*

The GIS vector layers created from the orthomosaic are summarized in Table 3.

*Tab. 3 Vector dataset structure*

| Layer | Geometry | Description |
|---|---|---|
| Buildings | Polygon | Built structures |
| Roads | Line | Access paths |
| Walls | Polygon | Defensive structures |
| Stairs | Line | Vertical access elements |

## 5. RESULTS AND DISCUSSION

The implemented UAV photogrammetric workflow resulted in the successful generation of high-resolution geospatial products for Kruja Castle, including a dense point cloud, a geometrically corrected orthomosaic, and a detailed GIS-based vector map. The integration of UAV imagery with photogrammetric processing and GIS-based digitization enabled a multi-scale representation of the cultural heritage site, suitable for both documentation and spatial analysis [21].
The obtained results demonstrate that UAV-based photogrammetry is an efficient and highly accurate method for cultural heritage documentation, particularly in complex topographic environments such as Kruja Castle.

### 5.1. PHOTOGRAMMETRIC RECONSTRUCTION RESULTS

The Structure-from-Motion (SfM) and Multi-View Stereo (MVS) processing workflow successfully reconstructed the three-dimensional geometry of the Kruja Castle study area from a total of 257 UAV images, achieving a 100% image calibration success rate. The complete photogrammetric processing was completed in approximately 2 hours and 20 minutes using Pix4DMapper on a workstation equipped with a multi-core processor and a dedicated GPU.
During the initial SfM stage, approximately 1.85 million sparse points were generated, providing a robust geometric framework for the subsequent dense reconstruction.
The MVS process produced a dense point cloud containing approximately 82 million points, accurately representing both the terrain morphology and the architectural features of the castle, as illustrated in Fig. 6.
The average reprojection error of approximately 0.15 pixels confirms the high internal geometric consistency of the photogrammetric model.
The RTK-derived camera positions, corrected through the ALBCORS network, provided the georeferencing basis for the photogrammetric block. The estimated RMSE of approximately 2–3 cm reflects the consistency of the RTK-supported georeferencing and bundle adjustment. Because no independent GCPs or CPs were available, the reported value is not considered an independent external accuracy validation.

### 5.2. ORTHOMOSAIC ACCURACY AND SPATIAL QUALITY

The final orthomosaic provides a geometrically corrected, high-resolution representation of the Kruja Castle study area, enabling accurate spatial measurements, detailed mapping, and reliable visualization of the site's structural features. Produced in the ETRS89 / Albania TM 2010 coordinate system, the orthomosaic is fully compatible with the Albanian national geospatial reference framework.
The final product (Fig. 7) has approximate dimensions of 15,800 × 14,300 pixels and covers an area of approximately 8.5 ha, encompassing both the castle complex and the surrounding terrain.
The positional quality of the photogrammetric dataset was assessed based on the RTK-derived camera positions and the residuals obtained during photogrammetric block adjustment. The UAV was continuously supported by RTK corrections from the ALBCORS network, providing centimeter-level positioning information during image acquisition. The resulting adjustment indicated an estimated RMSE of approximately 2–3 cm. As no independent Ground Control Points (GCPs) or Check Points (CPs) were used, this RMSE should be interpreted as an estimate of the georeferencing and photogrammetric adjustment consistency rather than as an independently verified absolute positional accuracy.

## 5.3. GIS-BASED SPATIAL ANALYSIS RESULTS

The orthomosaic was further processed in QGIS to extract vector-based spatial information. A total of seven feature classes were created, representing the main structural components of the castle environment.

The digitized GIS dataset enabled the transformation of raster-based photogrammetric outputs into structured spatial information, allowing further analysis of spatial relationships within the site.
The resulting vector map clearly distinguishes between:

- defensive structures (walls and fortifications)
- access infrastructure (roads and stairs)
- built environment (buildings)
- surrounding terrain

The final GIS map shown in Fig. 10 demonstrates the successful extraction and classification of the main spatial features from the orthomosaic.
This classification provides a structured spatial understanding of the site, which is essential for heritage management and conservation planning.
The main quantitative results obtained from the UAV survey and photogrammetric processing are summarized in Table 4.

*Tab. 4 Summary of final results*

| Parameter | Value |
|---|---|
| Number of images | 257 |
| GSD | ~2.7–3.0 cm/pixel |
| Reprojection error | ~0.15 pixels |
| RMSE accuracy | ~2–3 cm |
| Calibration success | 100% |
| Coordinate system | ETRS89 / Albania TM 2010 |

## 5.4. DISCUSSION

The results demonstrate that UAV-based photogrammetry integrated with GIS-based digitization provides an efficient and reliable framework for the documentation of cultural heritage sites. The estimated RMSE of approximately 2–3 cm, obtained from the RTK-supported photogrammetric adjustment, together with a GSD of 2.77 cm/pixel, demonstrates the high geometric consistency and spatial resolution of the generated dataset. However, because independent GCPs or Check Points were not used, the RMSE should be considered an estimate of georeferencing and adjustment consistency rather than an independently validated absolute positional accuracy.

Compared with conventional terrestrial surveying and GCP-based photogrammetric workflows, the RTK-enabled UAV approach significantly reduces fieldwork duration by eliminating the need to establish and measure numerous Ground Control Points. In this study, real-time positioning corrections were obtained through the Albanian Active GNSS Network (ALBCORS), allowing efficient georeferencing while maintaining the positional accuracy required for high-resolution cultural heritage documentation.

Despite these advantages, several limitations were observed during the survey. Dense vegetation, steep terrain, and cast shadows locally reduced image texture and introduced minor occlusions, affecting the completeness of the reconstructed model in some areas. The exclusive use of nadir imagery also limited the reconstruction of vertical façades and other complex architectural features.

Future studies could address these limitations by integrating oblique image acquisition with terrestrial laser scanning (TLS) or UAV-mounted LiDAR sensors, thereby improving façade reconstruction, reducing occlusions, and increasing the completeness and geometric accuracy of the final 3D model. The proposed methodology is readily transferable to other castles, archaeological sites, monasteries, and historical monuments with similar topographic and architectural characteristics, providing a practical framework for large-scale digital heritage documentation and long-term preservation initiatives.

The proposed workflow also offers a cost-effective alternative to conventional surveying techniques, particularly for large or difficult-to-access cultural heritage sites where rapid and non-invasive documentation is required.

## 6. CONCLUSION

This study demonstrated that UAV-based photogrammetry combined with GIS-based digitization is an effective approach for the high-resolution documentation of cultural heritage sites, using Kruja Castle as a case study. The integration of UAV image acquisition, Structure-from-Motion processing, and geospatial analysis enabled the generation of accurate and detailed spatial datasets suitable for mapping, visualization, and heritage documentation purposes.

The results demonstrated a high level of internal geometric consistency, with a full image calibration rate of 100% and a mean reprojection error of approximately 0.15 pixels. The RTK-supported photogrammetric adjustment, based on camera positioning corrected through the ALBCORS network, resulted in an estimated RMSE of approximately 2–3 cm. Since no independent Ground Control Points or Check Points were used, this value represents an estimate of the georeferencing and adjustment consistency rather than an independently validated absolute positional accuracy.

The final orthomosaic and GIS-based vector dataset provide a comprehensive digital representation of the site, allowing clear identification and classification of structural and environmental features of Kruja Castle. The transformation of UAV imagery into structured geospatial information highlights the strength of integrating photogrammetry with GIS technologies in modern surveying workflows.

The study also confirms that UAV-based methods offer a cost-effective, efficient, and scalable solution for cultural heritage documentation, significantly reducing field time while increasing spatial resolution and coverage compared to traditional surveying techniques. Despite these advantages, the methodology remains sensitive to environmental conditions such as lighting and occlusions, which may affect data quality in complex areas.

Overall, the proposed approach provides a robust framework that can be applied to other cultural heritage sites, supporting their documentation, monitoring, and long-term preservation through accurate and up-to-date geospatial data.

## REFERENCES

[1] Balázsik V, Tóth Z, Abdurahmanov I (2021) Analysis of Data Acquisition Accuracy with UAV. International Journal of Geoinformatics, Vol. 17 Issue 1, p1-10. 10p. https://doi.org/10.52939/ijg.v17i1.1697

[2] Mulakala J (2019) Measurement Accuracy of the DJI Phantom 4 RTK & Photogrammetry. https://iopscience.iop.org/article/10.1088/1755-1315/1123/1/012015/pdf

[3] Akgul M, Yurtseven H, Gulci S, Akay A.E (2018) Evaluation of UAV and GNSS-Based DEMs for Earthwork Volume. Arab. J. Sci. Eng., 43, 1893–1909. https://doi.org/10.1007/s13369-017-2811-9

[4] Mohammadi M, Rashidi M, Mousavi V, Karami A, Yu Y, Samali B (2021) Quality evaluation of digital twins generated based on UAV photogrammetry and TLS: bridge case study. Remote Sens. https://doi.org/10.3390/rs13173499

[5] Guo M, Sun M, Pan D, Wang G, Zhou Y, Yan B, Fu Z (2023) High-precision deformation analysis of yingxian wooden pagoda based on UAV image and terrestrial LiDAR point cloud. Herit Sci.;11(1):1. https://doi.org/10.1186/s40494-022-00833-z

[6] Llabani, A., Abazaj, F. (2024). 3D documentation of cultural heritage using terrestrial laser scanning. Journal of Applied Engineering Science, 22(2), 267-271. https://doi.org/10.5937/jaes0-50414

[7] Llabani, A., Lubonja, O. (2024). Integrating UAV Photogrammetry and Terrestrial Laser Scanning for the 3D surveying of the Fortress of Bashtova. WSEAS Transactions on Environment and Development. 20:306-315. https://doi.org/10.37394/232015.2024.20.30

[8] Llabani, A., Abazaj, F. (2024). A comparative analysis between personal and terrestrial laser scanning for the documentation of heritage sites. Civil Engineering Journal, 33(2), 199-214. https://doi.org/10.14311/CEJ.2024.02.0014

[9] Llabani, A., Abazaj, F. (2024). Comparison of UAV-LIDAR and aerial photogrammetry in rural areas with high vegetation. Int. J. Sci. Eng. Sci, 8, 46-51

[10] Remondino F (2011) Heritage recording and 3D modeling with photogrammetry and 3D scanning. Remote Sens.;3(6):1104–38. https://doi.org/10.3390/rs3061104

[11] Logothetis S, Delinasiou A, Stylianidis E (2015) Building information modelling for cultural heritage: a review. ISPRS Ann Photogramm Remote Sens Spatial Inf Sci.; II-5/W3:177–83. https://doi.org/10.5194/isprsannals-II-5-W3-177-2015

[12] Yastikli N (2007) Documentation of cultural heritage using digital photogrammetry and laser scanning. J Cult Herit.;8(4):423–7. https://doi.org/10.1016/j.culher.2007.06.003

[13] Kwoczynska B, Piech I, Polewany P, Gora K (2018) Modeling of sacral objects made on the basis of aerial and terrestrial laser scanning. In: 2018 Baltic geodetic congress (BGC Geomatics) p. 275–82. https://doi.org/10.1109/BGC-Geomatics.2018.00059

[14] Hassan, A.T.; Fritsch, D. Integration of Laser Scanning and Photogrammetry in 3D/4D Cultural Heritage Preservation—A Review. Int. J. Appl. Sci. Technol. 2019, 9, 16. https://doi.org/10.30845/ijast.v9n4p9

[15] Aicardi, I.; Chiabrando, F.; Lingua, A.M.; Noardo, F. Recent trends in cultural heritage 3D survey: The photogrammetric computer vision approach. J. Cult. Herit. 2018, 32, 257–266. https://doi.org/10.1016/j.culher.2017.11.006

[16] Erdelyi, J.; Kopacik, A.; Kyrinovic, P. Construction control and documentation of facade elements using terrestrial laser scanning. Appl. Geomat. 2018, 10, 113–121. https://doi.org/10.1007/s12518-018-0208-4

[17] Wang, Y.; Chen, Q.; Zhu, L.; Liu, L.; Zheng, L. A Survey of Mobile Laser Scanning Applications and Key Techniques over Urban Areas. Remote Sens. 2019, 11, 1540. https://doi.org/10.3390/rs11131540

[18] Haala, N.; Alshawabkeh, Y. Combining Laser Scanning and Photogrammetry—A Hybrid Approach for Heritage Documentation, Proceedings of the 7th International conference on Virtual Reality,

[19] Jaafar, H.A.; Meng, X.; Sowter, A.; Bryan, P. New approach for monitoring historic and heritage buildings: Using terrestrial laser scanning and generalised Procrustes analysis. Struct. Control. Heal. Monit. 2017, 24, e1987. https://doi.org/10.1002/stc.1987

[20] Pritchard, D.; Sperner, J.; Hoepner, S.; Tenschert, R. Terrestrial laser scanning for heritage conservation: The Cologne Cathedral documentation project. ISPRS Ann. Photogramm. Remote Sens. Spat. Inf. Sci. 2017, 2, 213–220. https://doi.org/10.5194/isprs-annals-IV-2-W2-213-2017

[21] Rodríguez-Gonzálvez, P.; Jiménez Fernández-Palacios, B.; Muñoz-Nieto, Á.L.; Arias-Sanchez, P.; Gonzalez-Aguilera, D. Mobile LiDAR System: New Possibilities for the Documentation and Dissemination of Large Cultural Heritage Sites. Remote Sens. 2017, 9, 189 https://doi.org/10.3390/rs9030189

[22] Pavelka, K.; Šedina, J.; Pavelka, K., Jr. Knud Rasmussen Glacier Status Analysis Based on Historical Data and Moving Detection Using RPAS. Appl. Sci. 2021, 11, 754. https://doi.org/10.3390/app11020754

[23] Bouček, T.; Stará, L.; Pavelka, K.; Pavelka, K., Jr. Monitoring of the Rehabilitation of the Historic World War II US Air Force Base in Greenland. Remote Sens. 2023, 15, 4323. https://doi.org/10.3390/rs15174323

https://doi.org/10.24867/INDIS-2026-EN-757



# EVOLUTION OF THE UTILITY CADASTRE IN THE REPUBLIC OF SRPSKA: FROM LEGISLATION TO INTEROPERABILITY

*Mladen Amović[1], Gordana Jakovljević[2], Miro Govedarica[3], Miloš Tutnjević[4]*

***Summary:***

Utility cadastres are becoming an increasingly important component of national land administration systems as urbanisation accelerates and underground infrastructure networks continue to expand. This paper traces the development of the utility cadastre of the Republic of Srpska from a technical infrastructure register through three legislative reforms (2014, 2021, 2026) and two generations of its conceptual data model. Particular attention is given to the three-tier database architecture introduced by the 2026 amendments to the Rulebook, which separate technical acquisition, provisional verification and official registration into the Technical, Temporary and Official Utility Cadastre Databases. The current model of utility cadastre (KVDB) is checked against the INSPIRE Utility Networks profile, ISO 19152 (LADM Edition II) and OGC and the remaining compliance gaps are identified.

***Keywords:*** *utility cadastre, land administration, LADM, INSPIRE, information model*

# EVOLUCIJA KATASTRA VODOVA U REPUBLICI SRPSKOJ: OD ZAKONODAVSTVA DO INTEROPERABILNOSTI

***Rezime:***

Katastar vodova postaje sve značajnija komponenta nacionalnih sistema upravljanja zemljištem kako se urbanizacija ubrzava, a mreže podzemne komunalne infrastrukture kontinuirano šire. Ovaj rad prikazuje razvoj katastra vodova Republike Srpske, od registra tehničke infrastrukture do savremenog sistema kroz tri zakonodavne reforme (2014, 2021. i 2026. godine) i dvije generacije njegovog konceptualnog modela podataka. Posebna pažnja posvećena je troslojnoj arhitekturi baze podataka uvedenoj izmjenama Pravilnika iz 2026. godine, kojom su tehničko prikupljanje podataka, privremena verifikacija i zvanična registracija razdvojeni u Tehničku bazu podataka katastra vodova, Privremenu bazu podataka katastra vodova i Zvaničnu bazu podataka katastra vodova (KVDB). Aktuelni model katastra vodova (KVDB) analiziran je u odnosu na INSPIRE specifikaciju Utility Networks, ISO 19152 (LADM Edition II) i OGC standarde, pri čemu su identifikovani preostali nedostaci u pogledu usklađenosti.

***Ključne reči:*** *katastar vodova, upravljanje zemljištem, LADM, INSPIRE, informacioni model*

[1] Assistant Professor, Faculty of Architecture-Civil Engineering-Geodesy, University of Banja Luka, Banja Luka, BiH, mladen.amovic@aggf.unibl.org, ORCID https://orcid.org/0000-0002-5464-0148
[2] Associate Professor, Faculty of Architecture-Civil Engineering-Geodesy, University of Banja Luka, Banja Luka, BiH, gordana.jakovljevic@aggf.unibl.org, ORCID https://orcid.org/0000-0003-2784-8370
[3] Full Professor, Faculty of Technical Sciences, University of Novi Sad, Serbia, miro@uns.ac.rs, ORCID https://orcid.org/0000-0003-1698-0800
[4] Assistant, Faculty of Architecture-Civil Engineering-Geodesy, University of Banja Luka, Banja Luka, BiH, milos.tutnjevic@aggf.unibl.org, ORCID https://orcid.org/0009-0000-7698-143X

## 1. INTRODUCTION

Reliable, up-to-date records of underground utility infrastructure have become a basic requirement for spatial planning, infrastructure management and public safety. As cities grow denser and the number of buried networks increases, utility cadastres are expected to give more information than just record of the position of pipes and cables. They should support land administration decisions, emergency response and infrastructure investment planning. Unlike land cadastres, utility cadastres deal with assets that are technically heterogeneous, owned by several different operators, and constantly extended or replaced, which makes long-term data governance considerably harder [1, 2].

Over the last two decades a number of international frameworks have shaped how such data is modelled and exchanged. The INSPIRE Directive set a common legal and technical basis for spatial data infrastructures in Europe [3], the ISO 19100 family of standards defined how geographic application schemas should be built, and the Land Administration Domain Model (LADM) introduced a shared conceptual structure for land administration data [4]. The ongoing revision of LADM into a multi-part Edition II extends this structure toward domains beyond classical land registration, including, in principle, utility infrastructure [5–7].

Most published work on utility cadastre, however, looks at one layer of the problem at a time: conceptual modelling (Yan et al. [1]; Radulović et al. [8]), legal registration (Roić & Dželalija [9]), INSPIRE harmonisation (Cetl et al. [10]), three-dimensional representation (Bieda et al. [11]; Saeidian et al. [12]), or data-acquisition technology (Hansen et al. [13]). Comparative European overviews of the Utility Cadastre by the countries is published (Hansen [14]). Recent reviews list technical infrastructure cadastres among emerging research topics (Uşak et al. [2]), but studies that follow a single national system through successive legal reforms and the matching changes in its data model are scarce. Table 1 positions the present study against this background.

*Tab. 1 Selected related work and the position of this study*

| Reference(s) | Research focus | Where this study differs |
|---|---|---|
| Yan et al. [1]; Radulović et al. [8] | LADM-based conceptual modelling of utility/underground networks | Follows one national model through two legislative cycles rather than a single snapshot |
| Cetl et al. [10]; Hansen [14] | INSPIRE harmonisation; comparative European overview | Examines one jurisdiction's complete legal-to-technical transition instead of a cross-country survey |
| Roić & Dželalija [9] | Legal registration of public utility infrastructure | Links specific legal provisions directly to individual classes and attributes of the data model |
| Bieda et al. [11]; Saeidian et al. [12] | 3D / underground cadastral representation | Out of scope here; noted in the Discussion as a future extension |
| Hansen et al. [13] | Mobile and reality-capture data acquisition for utilities | Addresses the database and legal side of the same data lifecycle |
| Kara et al. [5] | Requirement-based redesign of LADM Edition II | Method adapted here to evaluate a national utility cadastre rather than the standard itself |

The utility cadastre of the Republic of Srpska offers a useful case for closing that gap. Between 1978 and 2026 the system moved from an analogue technical register, through a first wave of legal digitalisation, a dedicated conceptual-modelling project, and finally a 2026 reform that split the database into three interconnected tiers. This paper reconstructs that sequence, examines how the legal text and the underlying UML application schema changed together. Resulting model is checked, referred as KVDB, against INSPIRE, ISO 19152 and OGC. The intention of this paper is not to propose another conceptual model for utility infrastructure, but to show, through a concrete national example, how legislation and conceptual modelling can be developed as a single process rather than two separate tracks.

## 2. HISTORICAL AND LEGISLATIVE DEVELOPMENT OF THE UTILITY CADASTRE

The development of the utility cadastre in the Republic of Srpska is better read as four overlapping phases than as a list of isolated amendments (Figure 1). Each phase changed both what the regulation required and how the underlying data were structured.

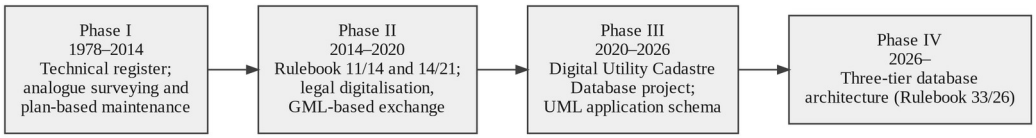


*Fig. 1 Development phases of the utility cadastre in the Republic of Srpska, 1978–2026.*

### 2.1. PHASE I – THE TECHNICAL REGISTER (1978–2014)

In its first phase the utility cadastre functioned as a technical register for the spatial position of underground infrastructure. Data collection relied on conventional geodetic surveying, and maintenance was carried out through analogue plans and survey documentation. The register served its purpose, documenting where infrastructure had been built and supporting further construction. Information exchange between institutions was limited and updating was essentially manual.

### 2.2. PHASE II – LEGAL DIGITALISATION (2014–2020)

The second phase began with the 2014 Rulebook on the Establishment and Maintenance of the Utility Cadastre, issued under the Law on Survey and Cadastre of Republika Srpska [17]. It gave the system its first unified legal basis [16]. It defined the content of survey reports, required digital data submission, and set procedures for maintaining the database (Article 3). The 2021 amendment went a step further by requiring that every survey report include a digital file in GML format, structured according to the ISO 19100 conceptual model (Article 7, Annex 10) and by extending the database definition to cover geometry, attributes and metadata together with a public topographic key in SLD format (Article 3, Annex 9). This is the point at which the utility cadastre acquired a genuine, feature catalogue.

### 2.3. PHASE III – THE CONCEPTUAL MODEL (2020–2026)

The third phase was the Digital Utility Cadastre Database project, completed in 2020. Rather than digitalising the existing database structure, the project produced a formal UML application schema – internally referred to as Model KV [18] – that defines utility lines, utility objects, survey points, code lists, administrative entities and the topological

relationships between them within one application schema. This was the first time the content of the utility cadastre was described independently of any particular software implementation, which is what later made it possible to check the model against INSPIRE, LADM and OGC rather than against a database schema alone.

## 2.4. PHASE IV – THE THREE-TIER ARCHITECTURE (2026–)

The fourth and most far-reaching phase began with the 2026 amendments to the Rulebook, which replace the single operational database with three sequentially linked databases – the Technical, the Temporary and the Official Utility Cadastre Database. It introduce explicit recording of data source and quality.

*Tab. 2 Successive amendments to the utility cadastre Rulebook and their effect on the data model*

| Rulebook | Key legal change | Consequence for the data model |
|---|---|---|
| Official Gazette of RS 11/14 | The database holds geospatial and other data on the lines and on the rights holders (Art. 3); entries are based on survey reports, with no prescribed digital exchange format. | An implicit, informal model – essentially a CAD/GIS layer with attributes; no application schema or feature catalogue. |
| Official Gazette of RS 14/21 | The database is redefined as geometric, attribute and metadata content with a topographic key (Art. 3); survey reports must include a digital GML file built on the ISO 19100 model (Art. 7, Annex 10). | First formal GML application schema (RS_xx_Tacka / Vod / Objekat / Dokument feature types, CL_xx code lists) – the basis of the Model KV network package. |
| Official Gazette of RS 33/26 | A Technical Utility Database is introduced, recording source and quality of data (Art. 1); the line sheet gains source/quality fields (Art. 5); Annex 8 is removed and Annex 11 added. | The database splits into provisional and official tiers and gains explicit provenance/quality attributes, aligning with ISO 19157 and the LA_Source pattern in LADM. |

Read together, the three amendments show a system that did not simply add fields to an existing table: each legal reform corresponds to a specific, identifiable change in the conceptual model, from an undefined CAD layer, to a documented GML feature catalogue, to a model that distinguishes data by its verification status (Table 2). The next section looks more closely at the last and most structurally significant of these changes.

## 3. THE 2026 THREE-TIER INFORMATION ARCHITECTURE

Until 2026 the Rulebook operated with a single utility cadastre database, into which survey data was entered after a relatively informal check of completeness and accuracy. The 2026 amendments (Official Gazette of RS 33/26) [16] replace this with three explicitly named, sequentially linked databases: the Technical Utility Database, the Temporary Utility Cadastre Database and the Official Utility Cadastre Database (Figure 2).

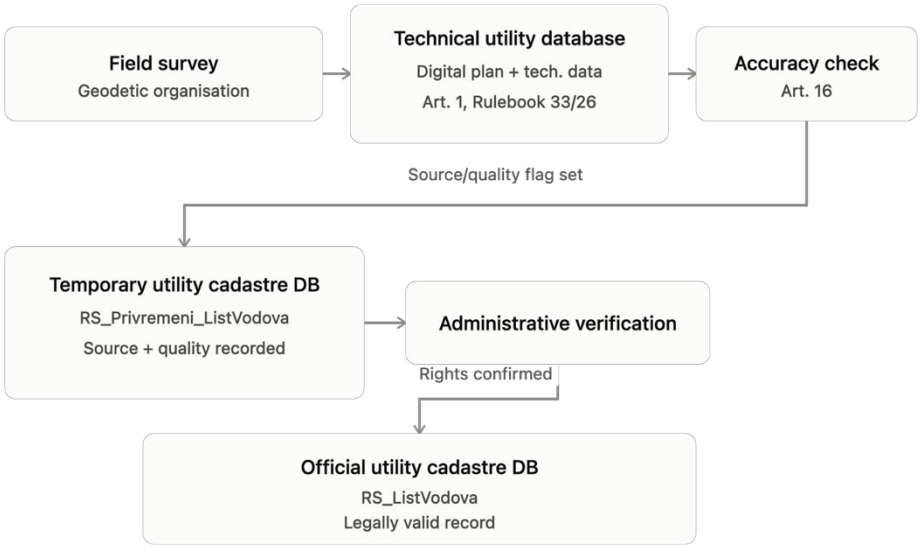


*Fig. 2 The three-tier database architecture introduced by the 2026 amendments to the Rulebook.*

The Technical Utility Database is the entry point: it holds the digital cadastral plan, divided and labelled into detail sheets, together with the technical data prescribed in Article 3(2) – geometry, descriptive attributes, symbolisation according to the topographic key, and metadata. Whether a survey qualifies for the next tier depends on the accuracy thresholds already set out in Article 16 of the original Rulebook: a horizontal standard deviation below 10 cm in built-up areas (20 cm elsewhere) and a vertical standard deviation below 5 cm for sewer networks (10 cm for all other networks). Data that falls short of these thresholds is not discarded, as it would have been under the pre-2026 wording of Article 8, but is kept and explicitly tagged with its source and quality, which is closer to a graded-quality approach in the spirit of ISO 19157 than to a binary accept/reject rule.

The quality of geodetic survey data is assessed before a record is transferred from one database level to the next. At the level of the Technical Utility Database, the submitted GML file is first validated against the XSD schemas of the application schema, which checks its structure and the use of prescribed code-list values. The data are then checked for completeness and for logical and topological consistency, e.g. whether every line is connected to its survey points, whether objects are correctly related to the lines they contain and whether mandatory attributes are filled in. Positional accuracy is verified on the basis of the survey report, which documents the survey method, instruments, reference points and the computed standard deviations, and can additionally be confirmed by control measurements on a sample of identical points. The results of these checks, expressed through the ISO 19157 data quality elements of completeness, logical consistency and positional accuracy, are recorded in the source and quality attributes introduced in 2026. Only records whose survey report has been accepted are transferred to the Temporary Utility Cadastre Database, while the transfer to the Official Utility Cadastre Database does not involve a new geometric verification but depends on the legal confirmation of the rights holder.

Once tagged, a record moves into the Temporary Utility Cadastre Database. This tier is not simply a procedural waiting room. It corresponds to its own feature type in the application schema, RS_Privremeni_ListVodova, which exists in Model KV alongside the regular line sheet class, RS_ListVodova, and is likewise associated with RS_KomunalniUredjaj. In other words, the distinction between provisional and officially

registered utility lines was already present at the class level before the 2026 amendments made it a formal procedural requirement. The legal reform sharpened a separation the conceptual model had anticipated rather than inventing one from scratch. A record only reaches the Official Utility Cadastre Database, and the class RS_ListVodova proper. Once the rights holder has been administratively confirmed under the same provisions that have governed ownership determination since 2014 (Articles 33–43 of the Rulebook). At that point the entry becomes legally valid cadastral data. Until then it remains technical or provisional information that can still be corrected, re-surveyed or contested without affecting any registered right. The practical effect is a clearer division of responsibility. Geodetic organisations acquire and submit data, the Republic Administration for Geodetic and Property Affairs verifies and registers it, and neither role has to double as the other. Compared with the earlier regime, in which data that failed the accuracy check simply sat outside the database "for future re-survey" with no formal status, the three-tier model gives every record a traceable state – technical, temporary or official. This is a governance change as much as a technical one, and it is the main reason the data model needed a corresponding extension rather than a simple field addition.

## 4. COMPLIANCE WITH INTERNATIONAL STANDARDS

The "Utility Cadastre" package in Model KV is declared as an «ApplicationSchema», which commits it to the ISO 19109 rules for application schemas. Its relationship to the other reference frameworks is modelled explicitly as a set of UML «dependency» links to ISO/TC 211, OGC, the INSPIRE Utility Networks profile and ISO 19152 (Figure 3). This is broadly the same logic Kara et al. [5] apply when revising LADM Edition II. Classes and requirements are tied explicitly to other standards rather than treated as self-contained, which later makes conformance easier to check against an abstract test suite.

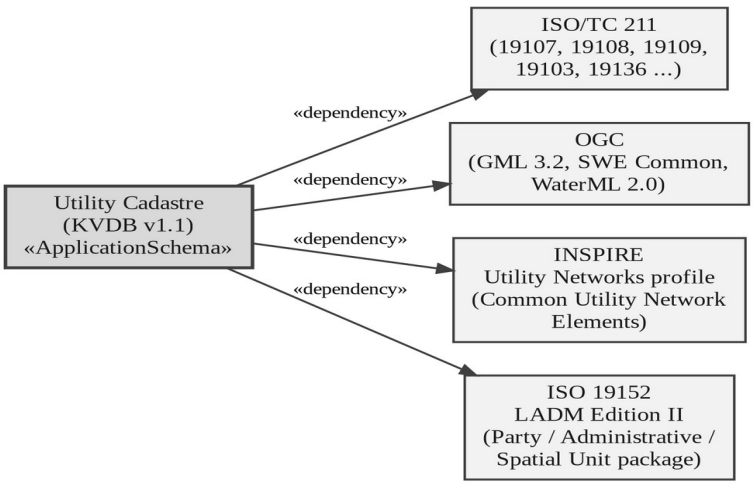


*Fig. 3 Dependencies of the Utility Cadastre application schema) on the reference frameworks.*

The level of compliance reported in this section and summarised in Table 4 was assessed qualitatively, by mapping each requirement of the reference frameworks to the elements of the application schema and of the Rulebook that implement it. Two sources of evidence were considered for every requirement: (i) the UML application schema (Model KV), i.e. the presence of a corresponding class, attribute, association or code list, and (ii) the legal text, i.e. whether the Rulebook makes the corresponding content mandatory. A requirement is classified as fully met ("yes") when it is implemented in the application schema and explicitly supported by the Rulebook; as partially met ("partial") when only

some of its elements are modelled, or when it is present in the application schema but not required by the legal text (or vice versa); and as not met ("no") when neither the application schema nor the Rulebook contains a corresponding element. For LADM, the requirement identifiers defined by Kara et al. [5] were used as the checklist; for INSPIRE, the attributes and associations of the Common Utility Network Elements package; and for OGC, the encoding and service specifications listed as dependencies in Model KV. The assessment is therefore a documentary conformance check rather than an executable test, a limitation that is returned to in the Discussion.

## 4.1. COMPLIANCE WITH THE INSPIRE UTILITY NETWORKS PROFILE

The network model of the utility cadastre generalises the INSPIRE Common Utility Network Elements package, part of the Utility Networks profile under the theme Utility and Government Services (Annex IV). The abstract class RS_KomunalniUredjaj generalises the INSPIRE class UtilityNetworkElement, and its concrete subclasses take on the corresponding geometric roles. RS_Tacka maps to UtilityNode (survey points of devices and installations), RS_Vod to UtilityLinkSet (the line itself), and RS_Objekat to UtilityNodeContainer (structures housing one or more nodes). The node–link–container pattern of the cadastre therefore lines up with INSPIRE's node-and-edge network topology. That alignment, however, is mostly structural, topology and geometric. A number of the optional («voidable») attributes of the INSPIRE specification currentStatus, governmentalServiceReference, utilityFacilityReference, among others are not yet mirrored by any RS_ attribute in KVDB. Also no inspireId has been defined for a national identifier. This is the most obvious place where further work is still needed.

## 4.2. COMPLIANCE WITH ISO 19152 (LADM EDITION II)

At its core, the utility cadastre model follows the LADM "triplet" pattern – Requirement 1-2, "Triplet Structure Present", in Kara et al. [5] in which the relationship between a person and land, or here a utility line is organised around LA_Party, LA_RRR and LA_BAUnit/LA_SpatialUnit. KVDB implements this through RS_NosilacPrava (generalising LA_Party), RS_PravoSvojine and RS_DrugoStvarnoPravo (both generalising LA_RRR), RS_ListVodova (generalising LA_BAUnit), and RS_KomunalniUredjaj with its subclasses (generalising LA_SpatialUnit), summarised in Table 3 and Figure 4.

*Tab. 3 Class mapping: ISO 19152 (LADM) ↔ INSPIRE (Utility Networks) ↔ KVDB*

| ISO 19152 (LADM Ed. II) | INSPIRE (Common Utility Network Elements) | KVDB (class) | Role in the model |
|---|---|---|---|
| LA_Party | — | RS_NosilacPrava | holder of rights over the utility line |
| LA_RRR | — | RS_PravoSvojine, RS_DrugoStvarnoPravo | ownership and other rights in rem / annotations |
| LA_BAUnit | — | RS_ListVodova | administrative unit of the utility line |
| LA_SpatialUnit | UtilityNetworkElement | RS_KomunalniUredjaj (abstract) | common superclass of all spatial utility-network features |
| — | UtilityNode | RS_Tacka | survey point of a |

| | | | |
|---|---|---|---|
| | | | device or installation |
| — | UtilityLinkSet | RS_Vod | the utility line itself |
| — | UtilityNodeContainer | RS_Objekat | structures housing one or more nodes |

Beyond this structural match, the datumOd/datumDo and aktivnost attributes carried by RS_KomunalniUredjaj correspond to the LA_VersionedObject pattern, Requirement 1-4, “Versioned Objects”. The source and quality fields are added by the 2026 amendment play the role of LA_Source and Requirement 1-6, “Source Document Present”. It is not only the UML model but the legislation itself that has been moving, in terminology as well as in structure, toward LADM Edition II.

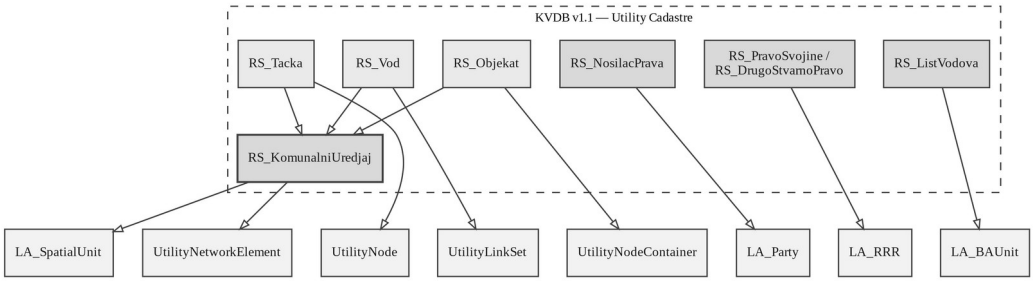


*Fig. 4 Generalisation of the KVDB v1.1 classes towards the LADM core and the INSPIRE Common Utility Network Elements package.*

## 4.3. COMPLIANCE WITH OGC SPECIFICATIONS

The requirement to exchange data in GML format, introduced by the 2021 amendment, is given concrete form through a set of XSD schemas like vodovodnamreza.XSD, elektroenergetskamreza.XSD, kodneliste.XSD and others built on the gml:AbstractFeatureType namespace (GML 3.2 / ISO 19136 [15]). Also for storing the rendering styles of features is used (SLD). In Model KV, the OGC package lists ISO 19136, SWE Common 2.0 and WaterML 2.0 as dependencies of the Utility Cadastre application schema, which positions the model for eventual service-based (WFS/SOS) data exchange, although the WaterML 2.0 classes are not yet put to operational use.

*Tab. 4 Compliance of the conceptual model with selected requirements, 2020 versus 2026*

| Requirement | KVDB 2020 | KVDB 2026 |
|---|---|---|
| Formal UML application schema (ISO 19109) | partial | yes |
| (Bi-)temporal versioning of objects | partial | yes |
| Source and quality metadata | partial | yes |
| Three-tier data lifecycle | no | yes |
| GML exchange format (ISO 19136) | yes | yes |
| INSPIRE voidable attributes / national inspireId | no | no |
| OGC web services (WFS / SOS) | no | no |

The comparison in Table 4 is deliberately conservative. It credits the 2026 model with what the legal text and the application schema actually specify, not with what could plausibly be added later. On that basis, the largest gains between 2020 and 2026 are in

versioning, provenance and lifecycle management. Exactly the areas the legislative changes targeted, while INSPIRE national identifiers and OGC web services remain open items regardless of which model version is considered.

## 5. DISCUSSION

The results indicate that the modernisation of the utility cadastre in the Republic of Srpska was not a single database redesign but a sequence of legal changes, each of which required, a matching change in the conceptual model. This is visible most clearly in the three-tier architecture: the legal separation of technical, provisional and official data which is mirrored by a corresponding separation of feature types in Model KV, down to the existence of a distinct provisional line-sheet class. The relationship runs in both directions – the 2020 conceptual model already contained the seed of that separation, and the 2026 legislation then formalised it as a procedural requirement.

From the standards perspective, the model is closer to LADM Edition II and to the INSPIRE Utility Networks profile than its predecessor, but the remaining gaps are specific rather than general. A handful of INSPIRE voidable attributes, a national inspireId, and the operational use of OGC web services are set for improvment. None of these require restructuring the application schema; they are extensions of classes that already exist, which suggests the next round of development can be incremental rather than a further redesign.

The source and quality attributes also provide a natural entry point for data obtained by non-invasive detection methods, such as ground-penetrating radar (GPR) and electromagnetic locators, which are increasingly used to map existing networks that were never surveyed in an open trench. Such data differ from conventional geodetic surveys because the position of a line is inferred from a geophysical signal rather than observed directly, and their horizontal and, in particular, vertical accuracy depend on soil conditions, depth and the material of the line. In the proposed model these data can be incorporated without structural changes: the survey or detection method can be recorded as a code-list value of the source attribute (e.g. direct geodetic survey, GPR, electromagnetic location, digitisation of existing plans), while the positional accuracy or confidence can be expressed either as an estimated standard deviation or as a quality level analogous to those defined in ASCE 38-22 [19] and PAS 128 [20]. Since detection-based positions will often not meet the accuracy thresholds of Article 16, such records would remain in the Technical or Temporary database, explicitly tagged with their source and quality, until confirmed by a direct geodetic survey. This is precisely the graded treatment of data quality that the three-tier architecture was designed to support.

A limitation of this analysis is that it relies on the legal text and the UML application schema as evidence of compliance, rather than on a running implementation or an automated conformance test of the kind LADM Edition II envisages through its Abstract Test Suite. Building such a test suite for the utility cadastre, and using it to check the database in operation rather than the schema on paper, is a natural next step. Extending the model toward three-dimensional representation of underground infrastructure, BIM exchange or digital twin platforms is a further direction.

## 6. CONCLUSION

The utility cadastre of the Republic of Srpska illustrates how a national infrastructure register can be modernised in stages, with legislation and conceptual modelling advancing together rather than one waiting for the other. Four phases – an analogue technical register, a first wave of legal digitalisation, a dedicated UML application schema, and a

2026 reform introducing a three-tier database architecture took the system from an undocumented CAD layer to a model that separates technical acquisition, provisional verification and legally valid registration into distinct, traceable stages.
Checked against INSPIRE, ISO 19152 (LADM Edition II) and OGC, the current model (KVDB) already reproduces the LADM party–RRR–spatial/administrative unit pattern and the INSPIRE node–link–container network topology and exchanges data through a GML application schema consistent with ISO 19136 [15]. Still remaines INSPIRE voidable attributes, a national identifier, and operational OGC web services which are specific, bounded extensions rather than open design questions. The Republic of Srpska case suggests that this kind of staged, legally anchored modernisation is a workable path for other utility cadastre systems facing similar interoperability requirements.

## 7. REFERENCES

[1] Yan, J., Jaw, S. W., Soon, K. H., Wieser, A., Schrotter, G. (2019). Towards an Underground Utilities 3D Data Model for Land Administration. *Remote Sensing*, 11(17), 1957. https://doi.org/10.3390/rs11171957

[2] Uşak, B., Çağdaş, V., Kara, A. (2024). Current Cadastral Trends – A Literature Review of the Last Decade. *Land*, 13(12), 2100. https://doi.org/10.3390/land13122100

[3] European Parliament and Council (2007). Directive 2007/2/EC establishing an Infrastructure for Spatial Information in the European Community (INSPIRE). *Official Journal of the European Union*, L108, 25 April 2007, pp. 1–14.

[4] International Organization for Standardization (2024). ISO 19152-1:2024, Geographic information – Land Administration Domain Model (LADM) – Part 1: Generic Conceptual Model. Geneva, Switzerland: ISO.

[5] Kara, A., Lemmen, C., Kalogianni, E., Van Oosterom, P. (2023). Requirements Based Design of the LADM Edition II. *11th International FIG LADM/3D Land Administration Workshop*, Gävle, Sweden, 11–13 October 2023, pp. 181–194.

[6] International Organization for Standardization (2025). ISO 19152-2:2025, Geographic information – Land Administration Domain Model (LADM) – Part 2: Land Registration. Geneva, Switzerland: ISO.

[7] International Organization for Standardization (2025). ISO 19152-5:2025, Geographic information – Land Administration Domain Model (LADM) – Part 5: Spatial Plan Information. Geneva, Switzerland: ISO.

[8] Radulović, A., Sladić, D., Govedarica, M., Ristić, A., Jovanović, D. (2019). LADM Based Utility Network Cadastre in Serbia. *ISPRS International Journal of Geo-Information*, 8(5), 206. https://doi.org/10.3390/ijgi8050206

[9] Roić, M., Dželalija, G. (2024). Registration of the Legal Status of Public Utilities. *Land*, 13(2), 209. https://doi.org/10.3390/land13020209

[10] Cetl, V., Šamanović, S., Bjelotomić Oršulić, O., Lisec, A. (2023). Building a Cadastral Map of Europe through the INSPIRE and Other Related Initiatives. *Land*, 12(7), 1462. https://doi.org/10.3390/land12071462

[11] Bieda, A., Bydłosz, J., Warchoł, A., Balawejder, M. (2020). Historical Underground Structures as 3D Cadastral Objects. *Remote Sensing*, 12(10), 1547. https://doi.org/10.3390/rs12101547

[12] Saeidian, B., Rajabifard, A., Atazadeh, B., Kalantari, M. (2022). Extending CityGML 3.0 to Support 3D Underground Land Administration. *Int. Arch. Photogramm. Remote Sens. Spatial Inf. Sci.*, XLVIII-4/W4-2022, pp. 125–132. https://doi.org/10.5194/isprs-archives-XLVIII-4-W4-2022-125-2022

[13] Hansen, L. H., Mandahl Pedersen, T., Kjems, E., Wyke, S. (2021). Smartphone-Based Reality Capture for Subsurface Utilities: Experiences from Water Utility Companies in Denmark. *Int.*

*Arch. Photogramm. Remote Sens. Spatial Inf. Sci.*, XLVI-4/W4-2021, pp. 25–31. https://doi.org/10.5194/isprs-archives-XLVI-4-W4-2021-25-2021

[14] Hansen, L. H. (2024). *Utility Cadastre Systems: Paving the Way to Smart Society*. The Council of European Geodetic Surveyors (CLGE).

[15] International Organization for Standardization (2020). ISO 19136-1:2020, Geographic information – Geography Markup Language (GML) – Part 1: Fundamentals. Geneva, Switzerland: ISO.

[16] Republic Administration for Geodetic and Property Affairs of Republika Srpska (2014, 2021, 2026). Rulebook on the Establishment and Maintenance of the Utility Cadastre. *Official Gazette of Republika Srpska*, no. 11/14, 14/21 and 33/26.

[17] National Assembly of Republika Srpska (2012). Law on Survey and Cadastre of Republika Srpska. *Official Gazette of Republika Srpska*, no. 6/12 and subsequent amendments.

[18] Class Model – Utility Cadastre (Model KV) (2026). UML application schema, Enterprise Architect, v.1.0 (internal project documentation).

[19] American Society of Civil Engineers (2022). Standard Guideline for Investigating and Documenting Existing Utilities (ASCE/UESI/CI 38-22). Reston, VA, USA: ASCE.

[20] British Standards Institution (2022). PAS 128:2022, Underground utility detection, verification and location – Specification. London, UK: BSI.

https://doi.org/10.24867/INDIS-2026-EN-768



# SPATIALLY-ENRICHED HOUSING PRICE MODELING: ASSESSING THE ROLE OF LANDSCAPE METRICS AND LAND COVER ATTRIBUTES

*Vasilije Ilić[1], Milutin Pejović[2],*

***Summary:***

This study presents a spatially-aware machine learning framework for housing price prediction using the Ames Housing dataset extended with geospatial variables. The research focuses on improving predictive performance while investigating the influence and interpretability of spatial variables within machine learning models. A hypothesis-driven approach was used to systematically evaluate distance-based and multi-scale spatial features through Linear Regression, SVM, and XGBoost models. Only spatial variables with meaningful contribution were included in the final model. The results show that spatial information improves predictive performance, particularly in linear models, while also enabling better interpretation of nonlinear models. The study demonstrates that spatial effects are nonlinear and scale-dependent, highlighting the potential of hypothesis-driven spatial feature engineering for more interpretable and efficient real estate modeling.

*Keywords: Spatial modeling; Machine learning; Model interpretability; Landscape metrics; Land cover attributes.*

# MODELOVANJE CENA NEKRETNINA KORIŠĆENJEM PROSTORNIH PODATAKA

***Rezime:***

Ova studija predstavlja prostorno-orijentisan okvir mašinskog učenja za predikciju cena nekretnina korišćenjem Ames Housing skupa podataka proširenog geoprostornim atributima. Istraživanje je usmereno na unapređenje prediktivnih performansi, uz istovremeno ispitivanje uticaja i interpretabilnosti prostornih promenljivih unutar modela mašinskog učenja. Pristup zasnovan na hipotezama korišćen je za sistematsku evaluaciju prostornih atributa zasnovanih na udaljenostima i višeskalnim karakteristikama pokrivenosti zemljišta primenom Linearne regresije, SVM i XGBoost modela. U finalni model uključene su samo prostorne promenljive sa značajnim doprinosom. Rezultati pokazuju da prostorne informacije unapređuju prediktivne performanse, posebno kod linearnih modela, dok istovremeno omogućavaju bolju interpretaciju nelinearnih modela. Studija pokazuje potencijal uključivanja prostornih atributa zasnovanog na hipotezama za interpretabilnije i efikasnije modelovanje tržišta.

*Ključne reči: Predikcija cena nekretnina; ML; Prostorni atributi; Analiza značajnosti atributa;*

[1] Teaching Assistant, Dept. of Geodesy & Geoinformatics, Faculty of Civil Engineering Belgrade, vailic@grf.bg.ac.rs
[2] Assistant Professor, Dept. of Geodesy & Geoinformatics, Faculty of Civil Engineering Belgrade, mpejovic@grf.bg.ac.rs

## 1. INTRODUCTION

The prediction of housing prices represents a fundamental problem in both economics and urban studies, with significant implications for market analysis, urban planning, and investment decision-making. Accurate estimation of property prices is inherently complex, as prices are influenced by a wide range of structural, locational, and environmental factors. Traditionally, housing price prediction has been addressed using statistical approaches such as hedonic pricing models, which aim to quantify the contribution of individual property attributes to overall value [1]. In recent years, the increasing availability of data and computational power has led to the widespread adoption of machine learning techniques in real estate analysis. Compared to classical linear models, machine learning approaches are capable of capturing complex, nonlinear relationships between predictors and housing prices, resulting in improved predictive performance [2]. Studies have shown that models such as Support Vector Machines, Random Forests, and Gradient Boosting significantly outperform traditional regression methods in this domain [3].

Recent studies have shown that housing prices are influenced not only by intrinsic property characteristics, but also by the spatial context in which properties are located. Spatial attributes such as proximity to services, environmental quality, and land use composition play a significant role in shaping property prices [4]. The integration of such information into predictive models has been shown to improve both model accuracy and interpretability. In recent years, considerable attention has been given to combining geospatial data with machine learning approaches for housing price prediction. Previous studies demonstrated that spatial features, including distance-based variables, land cover characteristics, and neighborhood descriptors, can substantially enhance predictive performance [5–7]. In particular, multi-scale spatial features have emerged as an important component, since the influence of urban and environmental factors often depends on the spatial scale at which they are observed.

The main objective of this study is to identify significant spatial attributes through a hypothesis-driven feature engineering approach based on prior assumptions and domain knowledge about spatial influences on housing prices. Rather than relying on the inclusion of all available spatial variables, the study aims to systematically evaluate groups of spatial features in order to construct a final model that achieves improved predictive performance, compared to both the baseline feature set and models extended with all spatial attributes.

In addition to improving predictive accuracy, the study focuses on increasing model interpretability by analyzing the contribution and behavior of individual spatial variables within different machine learning models. Such an approach enables a clearer understanding of how spatial characteristics influence housing prices and provides a transferable framework for applying interpretable spatial feature engineering to other housing price prediction datasets and real estate markets.

## 2. MATERIALS AND METHODS

The empirical analysis in this study is based on the well-known Ames Housing Dataset, one of the most widely used benchmark datasets in real estate price prediction and applied data science. The dataset contains 2930 residential property observations from Ames, Iowa, together with a rich set of structural, locational, and qualitative property attributes. In its original form, the dataset includes nominal, ordinal, discrete, and continuous variables describing different property characteristics. Due to its quality,

completeness, and interpretability, the Ames dataset has become a standard benchmark in both machine learning and economics, and has been described as “a modern alternative to the Boston Housing dataset for data science education” [8].

Despite its richness, the original dataset lacks explicit information about the surrounding environment and spatial context, which are known to play an important role in housing market dynamics. Property prices are influenced not only by intrinsic housing characteristics, but also by urban structure, environmental conditions, accessibility, and land-use composition in the surrounding area. To address this limitation, this study employs an extended version of the dataset introduced by David Barbour and Michail Fragkias, where additional spatial variables are generated through the integration of land cover information from the National Land Cover Database (NLCD).

A total of 80 spatial variables were generated for each housing observation using buffer zones with radii of 300 m, 600 m, and 1000 m. This multi-scale approach enables the analysis of spatial effects at different neighborhood levels, from immediate surroundings to broader environmental context. The generated variables describe both the composition and spatial structure of the surrounding environment. The first group includes variables representing the proportional presence of different land cover classes within each buffer zone, while the second group consists of landscape metrics such as patch counts, aggregation indices, and diversity measures (e.g., Shannon’s and Simpson’s indices). These metrics provide additional information about spatial organization, fragmentation, and environmental heterogeneity around each property.

The spatial variables were generated through a geospatial workflow implemented in the R programming environment using the *landmetrics package* and raster-based NLCD data with a spatial resolution of 30 m. Land cover information was extracted for each buffer zone after reprojection into a common coordinate system (NAD83 / Conus Albers, EPSG:5070). Temporal consistency was maintained by matching each property observation with the corresponding land cover dataset based on the year of sale. Figure 1 presents the spatial distribution of housing units with generated spatial attributes within a 600 m buffer zone.

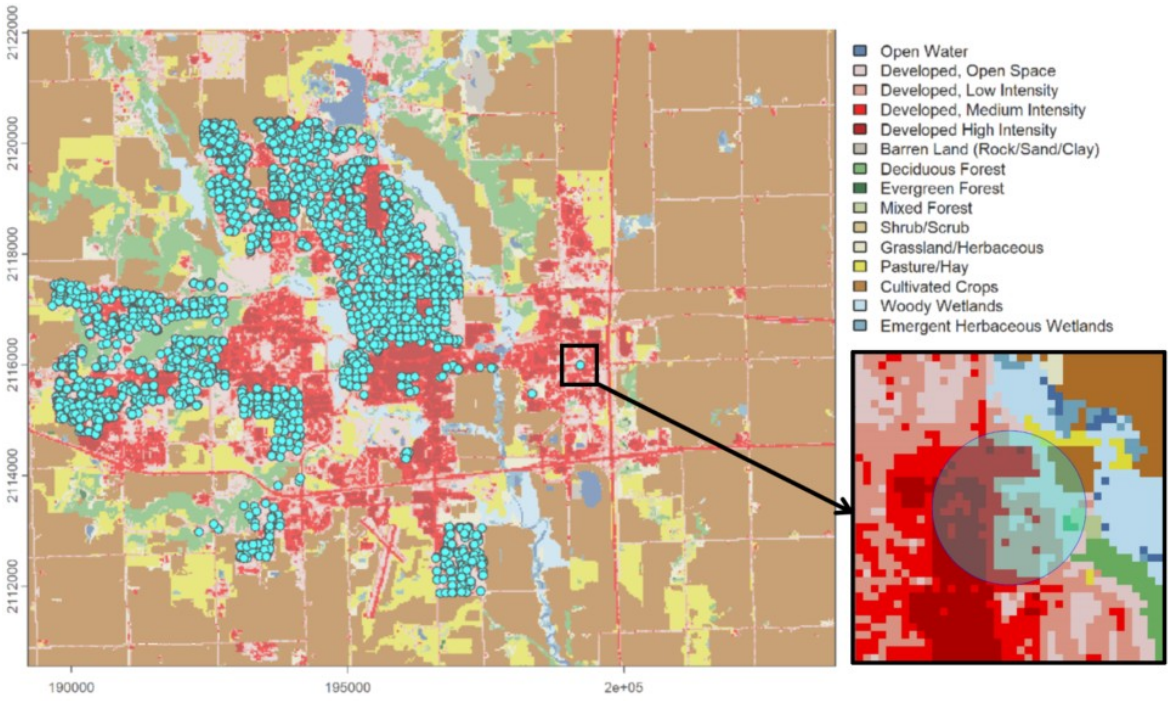


*Fig. 1 Spatial distribution of housing units with extracted land cover attributes [9]*

## 3. EXPERIMENTAL DESIGN

The experimental design was developed to assess the influence of spatial attributes on housing price prediction while preserving model interpretability. A baseline model was first constructed using only the original Ames Housing attributes. After standard preprocessing and hyperparameter tuning, the dataset was divided into training and test subsets using a 70/30 split. OLS, SVM, and XGBoost models were then applied. A hypothesis-driven spatial feature engineering approach was used to evaluate groups of spatial variables related to urban, environmental, and landscape characteristics. Since several metrics were calculated at 300, 600, and 1000 m scales, correlation analysis and the Variance Inflation Factor (VIF) were used to assess potential multicollinearity and reduce redundancy among predictors. Each spatial feature group was compared with the baseline model using test-set RMSE. Spatial variables showing relevant influence in at least two of the three models were retained for the final feature set. The final model therefore combines the original Ames Housing attributes with spatial variables selected through hypothesis-based analysis. The random train/test split does not explicitly account for spatial dependence between nearby observations and may therefore introduce spatial information leakage and optimistic performance estimates. Spatial cross-validation or geographically constrained splitting should consequently be considered in future validation. The complete methodological workflow is presented in Figure 2.

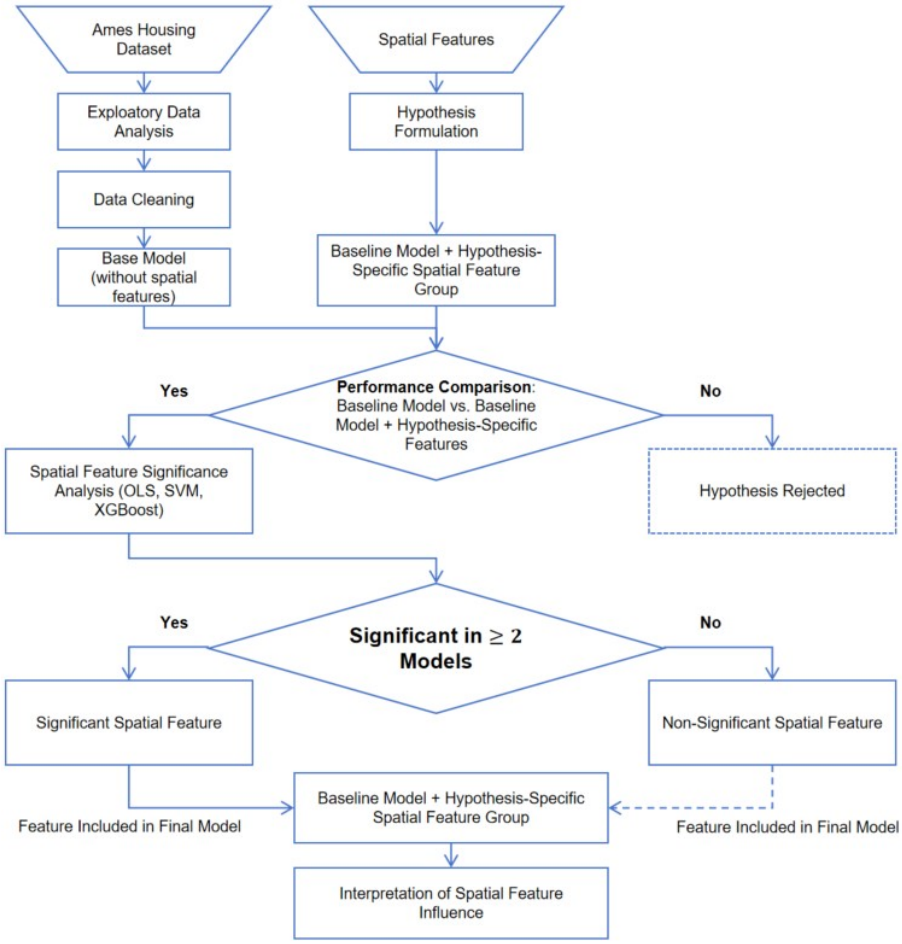


*Fig. 2 Workflow of the proposed hypothesis-driven spatial feature engineering framework*

## 3.1. HYPOTHESIS FORMULATION

Spatial and environmental factors represent a complex system characterized by multiple interdependencies, interactions, and scale-dependent effects. Such complexity implies that property prices are influenced not only by intrinsic characteristics of real estate, but also by the structure and organization of the surrounding space. The influence of spatial context may vary depending on urban density, land-use composition, accessibility, and environmental quality, making these relationships nonlinear and difficult to interpret. In addition, spatial variables may produce both positive and negative effects depending on their spatial extent and local context. For example, urban development may improve accessibility and economic attractiveness, while excessive urban intensity in the immediate surroundings may negatively affect residential quality. Similarly, natural areas may contribute positively to housing value, although their influence depends on proximity, distribution, and fragmentation.The following hypotheses are formulated to examine and clarify these effects. Specifically, they address the role of (1) urban development, (2) natural environment, (3) interaction between urban and natural features, (4) spatial fragmentation, (5) spatial diversity, and (6) accessibility. These aspects are commonly recognized in urban studies as important determinants of real estate prices, but their combined and scale-dependent effects require further empirical validation. The hypotheses are presented in Table 1.

*Tab. 1 Hypotheses on the influence of spatial and environmental factors on real estate prices*

| **Hypothesis** | **Description** | $H_0$ | $H_A$ |
|---|---|---|---|
| **H1**: Urban Development | Urbanized areas provide better access to infrastructure, services, and economic opportunities, increasing residential attractiveness. | Urban development has no significant impact on property prices. | The level of urban development significantly influences property prices. |
| **H2**: Natural Environment | Natural land cover affects environmental quality, visual attractiveness, and overall perception of residential areas. | Natural environment variables have no significant impact on property prices. | Natural environment characteristics significantly influence property prices. |
| **H3**: Urban–Natural Interaction | The interaction between urban and natural features may produce combined effects different from individual influences. | No significant interaction effect exists between urban and natural features. | Interaction between urban and natural features significantly influences property prices. |
| **H4**: Spatial Fragmentation | Fragmentation describes landscape configuration and spatial structure, affecting connectivity and organization. | Spatial fragmentation has no significant impact on property prices. | Spatial fragmentation significantly influences property prices. |
| **H5**: Spatial Homogeneity & Diversity | Homogeneity and diversity reflect dominance and variability of land cover types in the environment. | Homogeneity and diversity indices have no significant impact. | Homogeneity and diversity significantly influence property prices. |
| **H6**: Accessibility (Distance to Schools) | Distance to schools represents an important accessibility factor influencing location attractiveness. | Distance to schools has no significant impact on property prices. | Distance to schools significantly influences property prices. |

## 3.2. HYPOTHESIS EVALUATION

For each hypothesis, only the group of spatial attributes related to the examined hypothesis is added to the baseline model. This enables the isolated evaluation of specific spatial feature groups and their influence on housing price prediction. The resulting models are compared with the baseline model to assess whether the inclusion of spatial variables improves predictive performance, evaluated through RMSE. If performance improvement is observed, the significance of the introduced spatial attributes is further analyzed. Feature significance is evaluated using Linear Regression, SVM, and XGBoost. Linear Regression provides an interpretable and statistically grounded framework, while SVM and XGBoost capture complex nonlinear relationships and interactions between variables. It should be noted that the feature-importance measures obtained from the three approaches are not directly comparable numerically, as they represent different concepts: regression coefficients in Linear Regression, performance decrease after feature permutation in SVM, and gain-based importance in XGBoost. Therefore, the comparison focuses on the consistency of feature relevance across models rather than on the absolute magnitude of the importance values. By combining results from different modeling approaches, the analysis reduces dependence on a single method and enables a more robust assessment of spatial feature relevance. Spatial attributes identified as significant in at least two of the three models are incorporated into the final model.

### 3.2.1. Feature Importance Analysis - Linear Regression Model

Within the framework of Linear Regression, the assessment of feature importance is grounded in the estimation and statistical inference of model coefficients, which quantify the relationship between explanatory variables and the target variable. The starting point is the multiple linear regression model:

$$y = X\beta + \varepsilon \tag{1}$$

where $y \in R^n$ is the response vector, $x \in R^{n \times p}$ is the design matrix of predictions, $\beta \in R^p$ is the vector of unknown parameters, and $\varepsilon$ is a random error term with $var[\varepsilon] = \sigma^2 I$.

The ordinary least squares (*OLS*) estimator is obtained by minimizing the sum of squared residuals, yielding with its precision [10]:

$$\hat{\beta} = (X^T X)^{-1} X^T y \;\; ; \;\; \sigma_{\beta_i} = \sigma \cdot \sqrt{(X^T X)^{-1}_{ii}} \tag{2}$$

In practical applications, predictors are measured in different units (e.g., meters, percentages, indices), making the magnitudes of regression coefficients not directly comparable. To overcome this limitation, both predictors and the response variable are standardized prior to analysis. As a result, the standardized coefficients represent dimensionless effect sizes, enabling direct comparison of predictor importance. Their sign indicates the direction of the relationship, while the absolute value reflects the relative strength of influence, with larger magnitudes corresponding to stronger effects [10],[11].

To assess whether a predictor has a statistically significant effect, the following hypothesis is tested [12]:

$$H_0 : \beta_i = 0 \quad vs \quad H_a : \beta_i \neq 0 \tag{3}$$

The test statistic is:

$$t_i = \frac{\hat{\beta}_i}{\sigma_{\beta_i}} \tag{4}$$

Under the null hypothesis, $t_i$ follows a Student's t distribution with $n-p$ degrees of freedom. The corresponding *p-value* is computed as:

$$p = 2 \cdot P\left(T_{n-p} > |t_i|\right) \tag{5}$$

### 3.2.2. Feature Importance Analysis - Support Vector Machine

Within the framework of Support Vector Machine (SVM), the relationship between explanatory variables and the target variable is modeled through an optimization-based approach that allows capturing complex and nonlinear dependencies. In contrast to Linear Regression, SVM does not provide directly interpretable coefficients; therefore, feature importance must be assessed using alternative, model-agnostic methods [13]. For regression tasks, the SVM model is formulated as the following optimization problem:

$$\min_{\omega, b, \xi, \xi^*} \frac{1}{2}\|\omega\|^2 + C\sum_{i=1}^{n}\left(\xi + \xi^*\right),$$

*where*:

$$y_i - \left(\omega^T \phi\left(x_i\right) + b\right) \le \varepsilon + \xi_i \tag{6}$$

$$\left(\omega^T \phi\left(x_i\right) + b\right) - y_i \le \varepsilon + \xi^*{}_i$$

$$\xi_i, \xi^*{}_i \ge 0$$

where $\omega$ is the weight vector, $b$ is the bias term, $\phi\left(x_i\right)$ represents the mapping into a higher-dimensional feature space, $C$ is the regularization parameter controlling the trade-off between model complexity and training error, $\varepsilon$ defines the width of the insensitive loss region (ε-tube), and $\xi_i, \xi^*{}_i$ are slack variables allowing deviations beyond this margin [14].

Instead of explicitly computing the mapping $\phi\left(x_i\right)$, SVM employs the kernel function:

$$K\left(x_i, x_j\right) = \phi\left(x_i\right)^T \phi\left(x_j\right) \tag{7}$$

which enables efficient modeling of nonlinear relationships and interactions between variables [14]. However, due to the use of kernel functions, the model does not yield explicit coefficients associated with individual predictors, and thus direct interpretation of feature effects is not possible. Consequently, feature importance must be evaluated using model-agnostic approaches [15]. To overcome this limitation, feature importance is evaluated using permutation-based methods. For a trained model $f$ and a chosen performance metric $M$ (*RMSE*), the permutation importance of feature $i$ is defined as:

$$PI_i = M\left(f, X, y\right) - M\left(f, X_{perm(i)}, y\right) \tag{8}$$

where $X_{perm(i)}$ denotes the dataset in which the values of feature i are randomly permuted, thereby destroying its relationship with the target variable [15].

In practical implementation, each feature is permuted multiple times in order to obtain a stable estimate. In this study, each predictor is permuted $K$ times, and the importance is

computed on a subset of the test dataset consisting of up to *N* number of samples, selected to reduce computational cost while preserving representativeness. The final importance value is obtained as the average degradation in model performance:

$$PI_i = \frac{1}{K}\sum_{k=1}^{K}\left[M\left(f, X, y\right) - M\left(f, X_{perm(i)}, y\right)\right] \tag{9}$$

while the corresponding standard deviation is calculated as:

$$\sigma_{PI_i} = \sqrt{\frac{1}{K-1}\sum_{k=1}^{K}\left[PI_i^{\,k} - \overline{PI}_i^{(k)}\right]} \tag{10}$$

Standardized importance score can be defined as:

$$Z_i = \frac{PI_i}{\sigma_{PI_i}} \tag{11}$$

where larger values of $Z_i$indicate higher confidence in the relevance of the feature. Features with low importance relative to their standard deviation (i.e., $PI_i \approx 0$ or $Z_i$ close to zero) are considered non-informative, as their contribution to model performance is unstable or negligible. This approach provides an empirical criterion for distinguishing meaningful predictors from noise, analogous to significance testing in parametric models.

Permutation importance can be interpreted as a measure of the dependence between the target variable and a given predictor. By randomly permuting a feature, the statistical relationship $x_i \not\vdash y$ is artificially broken, and the resulting increase in prediction error reflects how strongly the model relies on that feature. Features associated with larger performance degradation are therefore considered more important [15],[16]. It should be noted that this method does not provide information about the direction of influence (i.e., positive or negative effect), but rather quantifies the overall contribution of a predictor to model accuracy.

### 3.2.3. Feature Importance Analysis - XGBoost Model

Within the framework of gradient boosting decision trees, the relationship between explanatory variables and the target variable is modeled through an ensemble of sequentially constructed trees, where each subsequent tree aims to correct the errors of the previous ones. This approach enables the modeling of complex nonlinear relationships and interactions between predictors. Unlike Linear Regression, XGBoost does not provide directly interpretable coefficients, but instead evaluates feature importance based on their contribution to the reduction of the objective function during tree construction [17].

As iteration *t*, the model prediction is updated as:

$$\hat{y}_i^{(t)} = \hat{y}_i^{(t-1)} + f_t\left(x_i\right) \tag{12}$$

where $f_t$ represents the newly added decision tree. The model is trained by minimizing the regularized objective function:

$$L^{(t)} = \sum_{i=1}^{n} l\left(y_i, \hat{y}_i^{(t)}\right) + \sum_{k=1}^{t} \Omega\left(f_k\right) \tag{13}$$

Where $l\left(y_i, \hat{y}_i^{(t)}\right)$is a differentiable loss function and $\Omega\left(f_k\right)$is a regularization term controlling model complexity.

Using a second-order Taylor expansion, the objective function can be approximated as:

$$L^{(t)} \approx \sum_{i=1}^{n}\left[g_i f_t\left(x_i\right) + \frac{1}{2}h_i f_t\left(x_i\right)^2\right] + \Omega\left(f_k\right) \tag{14}$$

where $g_i$ and $h_i$ denote the first and second derivatives of the loss function with respect to the predictions.

During tree construction, the algorithm evaluates candidate splits and selects those that maximize the reduction in the objective function. For a given split, the corresponding gain is defined as:

$$Gain = \frac{1}{2}\left( \frac{G_L^2}{H_L + \lambda} + \frac{G_R^2}{H_R + \lambda} - \frac{(G_L + G_R)^2}{H_L + H_R + \lambda} \right) + \gamma \tag{15}$$

where $G_L$,$G_R$ and $H_L$, $H_R$ are the sums of gradients and second-order gradients for the left and right nodes, respectively, while $\lambda$ and $\gamma$ are regularization parameters controlling model complexity [26].

The gain quantifies the improvement in model performance achieved by splitting the data according to a given feature. Feature importance is then defined as the cumulative contribution of a feature across all splits in all trees:

$$FI_i = \sum_{splits\ on\ i} Gain_i \tag{16}$$

In contrast to permutation-based methods, gain importance is computed internally during the training process and does not require additional model evaluations, making it computationally efficient [17]. However, this measure does not provide information about the direction of influence (i.e., whether a feature increases or decreases the target variable), but only quantifies its contribution to predictive performance.

In order to identify the most relevant predictors, a threshold-based selection strategy is adopted. Specifically, features are ranked according to their gain values, and the top five features are selected under the additional condition that their gain exceeds the average gain across all features:

$$FI_i > \frac{1}{p}\sum_{k=1}^{p} FI_k \tag{17}$$

This criterion ensures that only features with above-average contribution to error reduction are considered significant, while also limiting the selection to the most influential predictors. Such an approach provides a practical and interpretable way of distinguishing relevant variables in the absence of formal statistical significance tests.

## 4. RESULTS AND DISCUSSION

This chapter presents the results of the proposed hypothesis-driven spatial modeling framework and evaluates the influence of spatial attributes on housing price prediction. The analysis is organized in three stages corresponding to the methodology presented in Figure 2. First, the predictive performance of models extended with hypothesis-specific spatial feature groups is compared against the baseline model constructed only from the original Ames Housing attributes. The objective of this stage is to examine whether the inclusion of spatial variables related to a particular hypothesis leads to improved predictive performance, evaluated through RMSE on the test dataset.
Second, for hypothesis-specific feature groups that demonstrate performance improvement, a detailed feature significance analysis is performed using OLS, SVM, and XGBoost. This stage aims to identify spatial attributes with meaningful and

consistent influence across different modeling approaches, while also improving the interpretability of spatial effects in housing price prediction.
Finally, a final model is constructed by combining the original baseline attributes with spatial features identified as significant in at least two of the three modeling approaches. The predictive performance of the final model is then compared with the original baseline model in order to evaluate the overall contribution of the selected spatial attributes.

## 4.1. COMPARATIVE PERFORMANCE ANALYSIS OF SPATIAL HYPOTHESES

The results presented in Table 2 indicate that all hypothesis-specific spatial feature groups improved predictive performance relative to the baseline model across all three machine learning approaches. Consequently, none of the proposed hypotheses were rejected, and all spatial feature groups were retained for further feature significance analysis.

*Table 2. Percentage improvement in RMSE relative to the baseline model after the inclusion of hypothesis-specific spatial feature groups.*

| Method | RMSE Imp H1 | RMSE Imp H2 | RMSE Imp H3 | RMSE Imp H4 | RMSE Imp H5 | RMSE Imp H6 |
|---|---|---|---|---|---|---|
| **Linear Regression** | 12.78% | 13.28% | 16.46% | 12.01% | 10.00% | 9.50% |
| **SVM Regressor** | 37.20% | 44.55% | 44.77% | 37.74% | 29.85% | 32.91% |
| **XGBoost Regressor** | 18.03% | 15.00% | 17.02% | 18.67% | 12.22% | 18.90% |
| **Average** | *22.67%* | *24.28%* | *26.08%* | *22.81%* | *17.36%* | *20.44%* |

The results indicate that all hypothesis-specific spatial feature groups improved predictive performance relative to the baseline model across all three machine learning approaches. Consequently, none of the proposed hypotheses were rejected, and all spatial feature groups were retained for further feature significance analysis.
Among the evaluated models, SVM achieved the largest performance improvements after the inclusion of spatial attributes, indicating that nonlinear models particularly benefit from spatial and environmental information. This suggests that spatial effects on housing prices are highly nonlinear and involve complex interactions between variables.
The highest average improvement was obtained for Hypothesis 3, which combines urban and natural spatial characteristics. This result indicates that the interaction between built and natural environments has the strongest influence on housing price prediction. Hypotheses related exclusively to urban development and natural environment also produced substantial improvements, confirming the importance of spatial context in real estate valuation. In contrast, Hypothesis 5, related to spatial homogeneity and diversity, produced the smallest overall improvement. This may indicate that landscape diversity metrics are more difficult to interpret and model due to their abstract spatial meaning and indirect relationship with housing prices.

## 4.2. INTERPRETATION OF SPATIAL HYPOTHESES

The **Hypothesis 1** examines whether the level of urban development in the surrounding area significantly influences property prices, based on the assumption that more urbanized environments provide better access to infrastructure and services. Figure 3 presents the importance of urban development variables obtained from Linear Regression (LR), SVM, and XGBoost models.

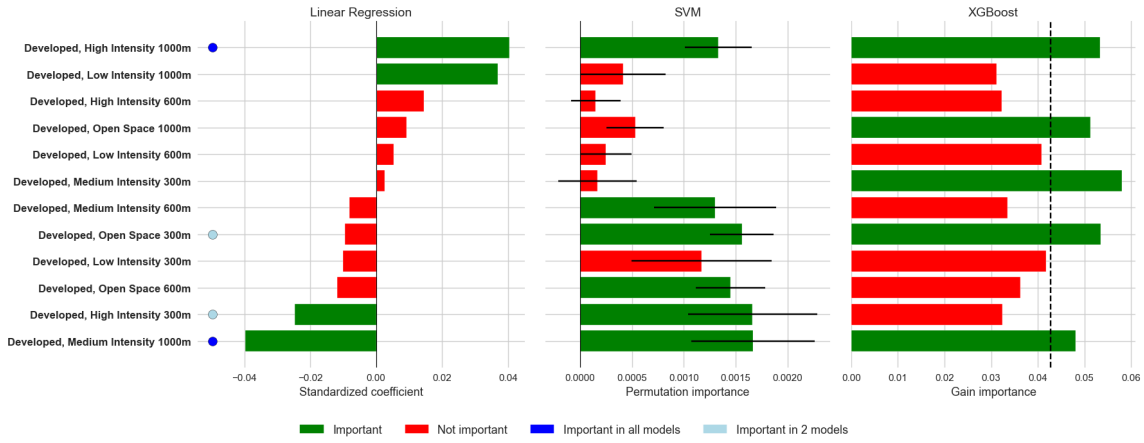


*Fig.3. Feature importance of urban development attributes*

LR analysis reveals a significant but heterogeneous impact of urban development on housing prices. Developed High Intensity 1000m and Developed Low Intensity 1000m show positive effects, while Developed High Intensity 300m and Developed Medium Intensity 1000m exhibit negative influences. SVM and XGBoost further confirm the importance of urban development variables, particularly at 300 m and 1000 m scales, indicating nonlinear and scale-dependent spatial effects. Accordingly, the final model retains urban development features at 300 m and 1000 m scales, while the 600 m scale showed limited additional contribution.

The **Hypothesis 2** examines whether natural land cover characteristics in the surrounding area significantly influence property prices, based on the assumption that natural environments improve environmental quality, visual attractiveness, and overall residential perception. Figure 4 presents the importance of natural land cover variables obtained from Linear Regression (LR), SVM, and XGBoost models.

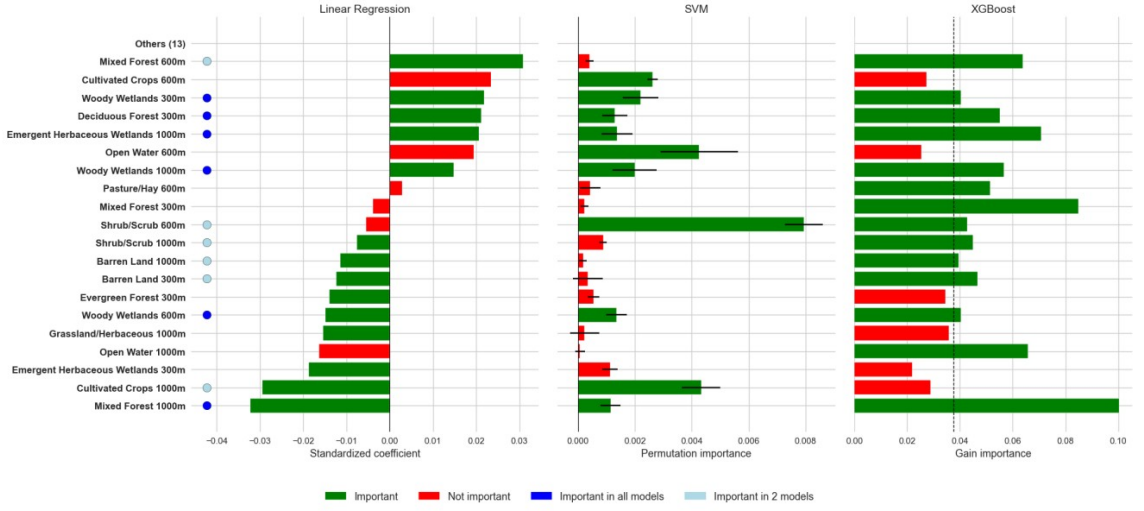


*Fig. 4. Feature importance of natural attributes across LR, SVM, and XGBoost models.*

The LR analysis reveals a significant but heterogeneous impact of natural environment variables on housing prices. Features such as Mixed Forest 600m, Woody Wetlands, Deciduous Forest 300m, and Emergent Herbaceous Wetlands 1000m show positive effects, while variables including Cultivated Crops, Grassland, Barren Land, and Evergreen Forest exhibit negative influences. SVM and XGBoost further confirm the importance of these natural land cover variables across multiple spatial scales. The results indicate that the influence of natural environments is nonlinear and strongly scale-dependent. Forests and wetlands can positively affect property prices in the immediate surroundings, while larger proportions of undeveloped land at broader scales often correspond to lower urbanization and accessibility, leading to lower property values. Therefore, the hypothesis is accepted in a modified form, confirming a significant and context-dependent influence of natural environment variables on housing prices.

The **Hypothesis 3** examines whether the interaction between urban development and natural land cover significantly influences property prices. The underlying assumption is that the combined effect of urban and natural features may differ from their individual effects, since urban areas provide accessibility and infrastructure, while natural land cover contributes to environmental quality, visual attractiveness, and residential perception. To test this hypothesis, several interaction variables were constructed. The “green_premium_forest” and “green_premium_water” variables were introduced to capture whether natural features provide additional value when combined with urban accessibility. Variables such as “low1000_grass300”, “low1000_crops300”, “medium1000_woody1000”, and “high1000_evergreen300” were designed to examine how different levels of urbanization interact with nearby natural land cover. In addition, “urban_pressure_forest” and “urban_pressure_wetlands” were included to represent potential pressure of urban development on natural environments, while “urban_noise_crops” and “urban_noise_barren” were used to capture possible negative effects of less attractive land cover types within urban surroundings. Finally, variables such as “low_near_far_water” and “high_near_far_forest” were introduced to analyse whether the spatial contrast between near and distant natural features affects property values. Figure 5 presents the importance of urban–natural interaction variables obtained from Linear Regression, SVM, and XGBoost models.

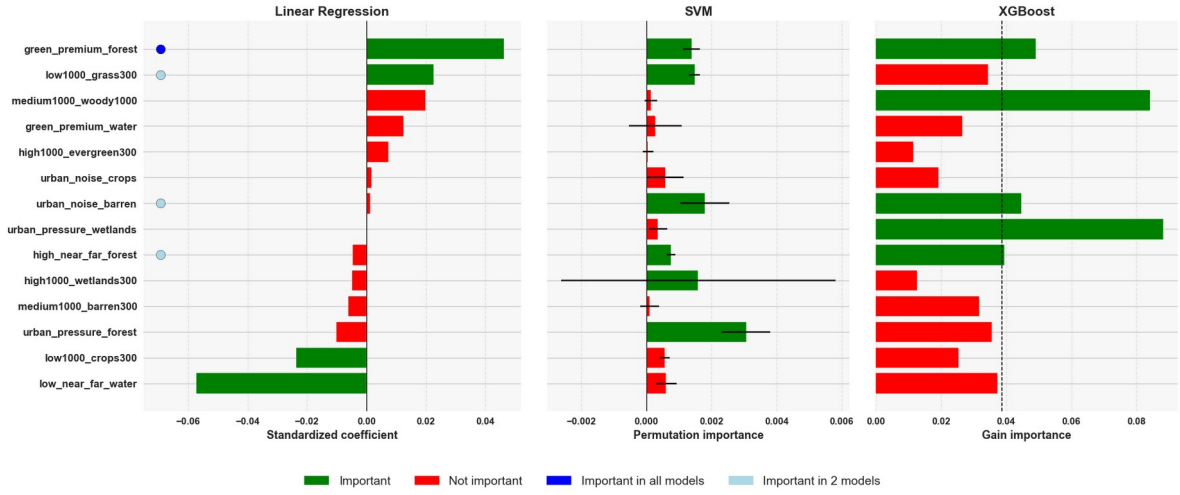


*Fig. 5. Feature importance of urban–natural interaction attributes across LR, SVM, and XGBoost models.*

The LR results indicate that only a limited number of interaction variables are statistically significant. The strongest positive effect is observed for “green_premium_forest”, suggesting that the combination of urban accessibility and forest proximity increases property prices. A positive and significant effect is also identified for “low1000_grass300”, indicating that low urbanization combined with nearby grassland or open natural space may represent an attractive suburban environment. In contrast, “low1000_crops300” and “low_near_far_water” show significant negative effects, suggesting that agricultural surroundings and certain spatial configurations of water bodies may reduce property values. The SVM results confirm the importance of several interaction variables, particularly “urban_pressure_forest”, “urban_noise_barren”, “high1000_wetlands300”, “low1000_grass300”, and “green_premium_forest”. XGBoost further highlights the relevance of nonlinear interaction effects, especially “medium1000_woody1000”, “low1000_grass300”, “medium1000_barren300”, and “low1000_crops300”. These results indicate that **some interaction effects are not fully captured by the linear model, but become more important in nonlinear modelling approaches**. Overall, the results show that the interaction between urban and natural features has a significant but selective influence on property prices. The hypothesis is therefore partially accepted. The most consistent positive evidence is found for the green premium effect, where forest proximity combined with urban accessibility increases property value. However, not all natural–urban combinations are beneficial. Interactions involving agricultural land, barren land, wetlands, or specific water configurations may have neutral or negative effects depending on spatial context and model type. Therefore, the effect of urban–natural interactions is nonlinear, context-dependent, and strongly influenced by the type of land cover and the level of surrounding urbanization.

The **Hypothesis 4** examines whether spatial fragmentation characteristics significantly influence property prices. The results indicate a significant but heterogeneous impact of fragmentation variables. Fragmentation of urban land cover negatively affects property prices, while fragmentation metrics related to natural land cover types may exhibit positive or neutral effects. The findings further show that compact urban areas generally increase property value, whereas aggregation of certain natural land cover types may negatively affect prices. Overall, the results indicate that spatial fragmentation has a significant, nonlinear, and context-dependent influence on housing prices.

The **Hypothesis 5** examines whether spatial homogeneity and diversity indices significantly influence property prices. The results indicate that SHDI, SHEI, SIDI, and SIEI do not show a significant or consistent impact across models. While XGBoost detects a weak signal, their contribution remains limited compared to other spatial attributes. Overall, the hypothesis is rejected, suggesting that land cover type and spatial context are more important than aggregated diversity measures.

The **Hypothesis 6** examines whether distance to schools significantly influences property prices. The results indicate a significant but heterogeneous impact of distance-to-school variables. Proximity to certain schools positively affects property prices, while the effect is not consistent across all schools. SVM and XGBoost confirm the importance of distance-related features, suggesting that accessibility to educational facilities influences housing prices in a context-dependent manner. Therefore, the

hypothesis is accepted in a modified sense. The summary of all hypothesis evaluation results is presented in Table 3.

*Tab. 3 Summary of Hypoyhesis Evaluation Results*

| Hypothesis | Main Conclusion | Accepted / Rejected | Final Feature Engineering Decision | Features Retained in Final Model |
|---|---|---|---|---|
| **H1 – Urban Development** | Urban effects are nonlinear and scale-dependent. Immediate high-intensity urbanization may negatively affect prices, while broader urban context contributes positively. | Accepted (modified sense) | Retain only the most informative urban-development scales. Remove redundant intermediate scales. | Urban development variables at 300 m and 1000 m scales |
| **H2 – Natural Land Cover** | Natural features have heterogeneous effects depending on land-cover type and spatial scale. Forests/wetlands may increase value locally, while large-scale undeveloped areas may reduce accessibility. | Rejected in simple form, accepted in modified sense | Retain only natural features with stable and significant effects across models and scales. | Mixed Forest, Woody Wetlands, Emergent Herbaceous Wetlands, Barren Land, Shrub/Scrub, selected forest and water-related variables |
| **H3 – Urban–Natural Interactions** | Interaction effects are selective and strongly nonlinear. Green premium effects are important, while some agricultural and barren interactions reduce value. | Partially accepted | Retain only interaction variables consistently identified across LR, SVM, and XGBoost. | *green_premium_forest*, *low1000_grass30*, *medium1000_woody1000*, selected urban-pressure and urban-noise variables |
| **H4 – Spatial Fragmentation** | Fragmentation effects depend on land-cover type and aggregation structure. Urban fragmentation is mostly negative, while some natural fragmentation patterns may be neutral or positive. | Rejected in simple form, accepted in modified sense | Retain fragmentation metrics only where model importance is stable and interpretable. | Selected fragmentation metrics for Developed Low Intensity, Mixed Forest, Grassland, Open Water |
| **H5 – Homogeneity & Diversity Indices** | SHDI, SHEI, SIDI, and SIEI show weak, unstable, and inconsistent effects. | Rejected | Exclude from final model | None |
| **H6 – Distance to Schools** | School accessibility influences prices, but effects depend on school location and local context. | Accepted in modified sense | Retain only statistically and predictively relevant school-distance variables. | Selected distance-to-school variables with stable importance |

## 4.3. FINALE MODEL EVALUATION

In the final stage of the methodology, all spatial attributes identified as significant through the hypothesis-driven analysis were incorporated into the baseline models. The objective was to evaluate whether the selected spatial variables collectively improve predictive performance while preserving model interpretability. Unlike the fully extended spatial models, the final models include only spatial features that demonstrated meaningful and consistent influence across the hypothesis evaluation process. Consequently, the proposed framework produces machine learning models that are not only more accurate, but also interpretable, since the contribution of each spatial feature group is analytically justified. Table 4 presents the final model evaluation results.

Table 4. Imrpovement of performance between Baseline and final model

| Method | Baseline RMSE | Baseline Relative RMSE | Final RMSE | Final Relative RMSE | Relative RMSE Improvement |
|---|---|---|---|---|---|
| **Linear Regression** | 32011.75 | 16.88 % | 26220.02 | 13.97 % | 17.21 % |
| **SVM Regressor** | 37427.32 | 19.73 % | 19656.65 | 10.36 % | 47.48 % |
| **XGBoost Regressor** | 25776.98 | 13.59 % | 21375.72 | 11.27 % | 17.08 % |

The results indicate that the inclusion of hypothesis-selected spatial attributes improved the predictive performance of all models. Linear Regression achieved improvement, reducing the test RMSE from 32011.75 to 26220.02, corresponding to a decrease in relative RMSE from 16.88% to 13.97%. This represents an improvement of approximately 17.21% relative to the baseline model. The SVM Regressor showed the largest improvement. The RMSE decreased from 37427.32 to 19656.65, while the relative RMSE was reduced from 19.73% to 10.36%. This corresponds to the largest relative performance gain among all evaluated models, with an improvement of approximately 47.48%. XGBoost Regressor achieved a moderate but consistent improvement. The RMSE decreased from 25776.98 to 21375.72, whereas the relative RMSE dropped from 13.59% to 11.27%, corresponding to an improvement of approximately 17.08%.

Overall, the results confirm that hypothesis-driven spatial feature selection improves predictive accuracy while simultaneously increasing model interpretability. Although nonlinear models achieved the best absolute predictive performance, the most significant relative improvement was observed for the SVM model, indicating that carefully selected spatial attributes are particularly beneficial for nonlinear learning approaches.

## 5. CONCLUSION

The conducted experiment was successfully implemented and demonstrated that spatial data significantly enrich the classical Ames Housing dataset and improve the performance of housing price prediction models. The integration of spatial attributes enabled the models to capture environmental and locational influences that cannot be represented through traditional structural housing variables alone. The obtained results confirmed that nonlinear machine learning models outperform linear approaches in predictive accuracy. However, linear models remain substantially more interpretable. For this reason, the proposed methodology introduced a hypothesis-driven framework that improves the interpretability of nonlinear models by systematically analyzing and selecting spatial variables with meaningful influence on housing prices. In addition to improving predictive performance, the study enabled deeper understanding of the influence of space and surrounding environment on property values. Through six defined hypotheses, the research investigated the effects of urban development, natural environment, accessibility, and multi-scale spatial context. The results further indicate that these effects are not only spatially dependent, but also scale-dependent and model-dependent. The relevance of individual spatial attributes varies across the analyzed buffer distances and differs between linear and nonlinear modeling approaches, emphasizing the importance of considering both spatial scale and model structure when interpreting feature influence. The proposed framework therefore provides not only more accurate predictions, but also valuable spatial insights into real estate dynamics. Furthermore, the hypothesis structure can easily be extended in future research by introducing additional spatial concepts and new groups of variables. An important contribution of this work is that the final models are fully interpretable. The inclusion of spatial attributes is not arbitrary, but analytically justified through hypothesis evaluation and comparison across multiple machine learning approaches. Consequently, the proposed workflow combines predictive capability with scientific interpretability, which is essential for practical applications and decision-making processes. The methodology is also highly transferable. Using spatial datasets together with the *LandMetrics* package, the same workflow can be applied to other cities, regions, and real estate markets. Although different environments may produce different outcomes and lead to different conclusions regarding the hypotheses, the overall methodological framework remains applicable and reproducible across various spatial contexts.

## REFERENCES

[1] Rosen, S. (1974). Hedonic prices and implicit markets: Product differentiation in pure competition. Journal of Political Economy, 82(1), 34–55.

[2] Mullainathan, S., & Spiess, J. (2017). Machine learning: An applied econometric approach. Journal of Economic Perspectives, 31(2), 87–106.

[3] Park, B., & Bae, J. K. (2015). Using machine learning algorithms for housing price prediction: The case of Fairfax County, Virginia housing data. Expert Systems with Applications, 42(6), 2928–2934.

[4] Can, A. (1992). Specification and estimation of hedonic housing price models. Regional Science and Urban Economics, 22(3), 453–474.

[5] Li, W., Saphores, J. D., & Gillespie, T. W. (2015). A comparison of the economic benefits of urban green spaces estimated with NDVI and with high-resolution land cover data. Landscape and Urban Planning, 133, 105–117.

[6] Law, S., Paige, B., & Russell, C. (2019). Take a look around: Using street view and satellite images to estimate house prices. ACM Transactions on Intelligent Systems and Technology, 10(5), 1–19.

[7] Zhu, X., & Ferreira, J. (2014). Data-driven model for predicting real estate prices using machine learning and geospatial features. Computers, Environment and Urban Systems, 45, 29–42.

[8] De Cock, D. (2011). Ames, Iowa: Alternative to the Boston Housing Data Set. Journal of Statistics Education, 19(3).

[9] Barbour, D., & Fragkias, M. (2024). Spatializing Ames: Complementing the Ames, IA housing dataset for spatial social-ecological analysis. Data in Brief.

[10] Bring, J. (1994). How to standardize regression coefficients. The American Statistician, 48(3), 209–213.

[11] Schielzeth, H. (2010). Simple means to improve the interpretability of regression coefficients. Methods in Ecology and Evolution, 1(2), 103–113.

[12] Kutner, M. H., Nachtsheim, C. J., Neter, J., & Li, W. (2005). Applied Linear Statistical Models (5th ed.). McGraw-Hill.

[13] Smola, A. J., & Schölkopf, B. (2004). A tutorial on support vector regression. Statistics and Computing, 14(3), 199–222. https://doi.org/10.1023/B:STCO.0000035301.49549.88

[14] Cortes, C., & Vapnik, V. (1995). Support-vector networks. Machine Learning, 20(3), 273–297. https://doi.org/10.1007/BF00994018

[15] Breiman, L. (2001). Random forests. Machine Learning, 45(1), 5–32. https://doi.org/10.1023/A:1010933404324

[16] Molnar, C., Lundberg, S. M., & Lee, S.-I. (2020). Interpretable machine learning: A unified approach to interpreting model predictions. arXiv preprint arXiv:2003.04792. https://arxiv.org/abs/2003.04792

[17] Chen, T., & Guestrin, C. (2016). XGBoost: A scalable tree boosting system. Proceedings of the 22nd ACM SIGKDD International Conference on Knowledge Discovery and Data Mining, 785–794. https://doi.org/10.1145/2939672.2939785

https://doi.org/10.24867/INDIS-2026-EN-785



# THE ACCURACY FLOOR IN LEGACY-TO-ETRS89 DATUM TRANSFORMATION: RESIDUAL DISTORTION MODELLING FOR THE REPUBLIC OF SRPSKA

*Oleg Odalović[1], Dejan Vasić[2], Dušan Petković[3], Slavko Vasiljević[4], Miljana Todorović-Drakul[5]*

***Summary:***

A legacy-to-ETRS89 (European Terrestrial Reference System 1989) datum transformation for the Republic of Srpska was modelled by combining a seven-parameter Helmert transformation with a distortion grid representing spatially correlated residuals of the classical network. Twenty variants from four interpolation families were evaluated using 3977 control points. The numerically stable variants converge to approximately 10 cm horizontal RMS (root mean square) at the observed point density and 15 cm to 16 cm under block validation. This level is not materially improved by the interpolation method or by excluding locally inconsistent points, and is therefore interpreted as the effective empirical accuracy floor of the available control dataset.

*Keywords: datum; transformation; distortions; accuracy; NTv2*

# PRAG TAČNOSTI PRI TRANSFORMACIJI IZ NASLEĐENOG DRŽAVNOG DATUMA U ETRS89: MODELOVANJE REZIDUALNIH DISTORZIJA ZA REPUBLIKU SRPSKU

***Rezime:***

Transformacija iz nasleđenog državnog datuma u ETRS89 (Evropski terestrički referentni sistem 1989) za Republiku Srpsku modelovana je kombinovanjem Helmertove transformacije sa sedam parametara i korekcionog grida koji predstavlja prostorno korelisane reziduale klasične mreže. Dvadeset varijanti iz četiri familije interpolacionih metoda ocenjeno je na osnovu 3977 kontrolnih tačaka. Numerički stabilne varijante konvergiraju ka približno 10 cm horizontalnog RMS-a (koren srednjeg kvadratnog odstupanja) pri gustini posmatranih tačaka i 15 cm do 16 cm pri blokovskoj validaciji. Taj nivo se bitno ne poboljšava ni izborom interpolacione metode ni isključivanjem lokalno nekonzistentnih tačaka, pa se tumači kao efektivni empirijski prag tačnosti kontrolnog skupa.

*Ključne reči: datum; transformacija; distorzije; tačnost; NTv2*

[1] Assoc. Prof., Faculty of Civil Engineering, University of Belgrade, Belgrade, Serbia, odalovic@grf.bg.ac.rs, ORCID 0000-0001-6004-824X
[2] Assist. Prof., Faculty of Architecture, Civil Engineering and Geodesy, University of Banja Luka, Banja Luka, Republic of Srpska, Bosnia and Herzegovina, dejan.vasic@aggf.unibl.org, ORCID 0009-0006-9586-729X
[3] Assist. Prof., Faculty of Civil Engineering, University of Belgrade, Belgrade, Serbia, dpetkovic@grf.bg.ac.rs, ORCID 0000-0002-8285-9710
[4] Assist. Prof., Faculty of Architecture, Civil Engineering and Geodesy, University of Banja Luka, Banja Luka, Republic of Srpska, Bosnia and Herzegovina, slavko.vasiljevic@aggf.unibl.org, ORCID 0009-0003-2636-841X
[5] Assist. Prof., Faculty of Civil Engineering, University of Belgrade, Belgrade, Serbia, mtodorovic@grf.bg.ac.rs, ORCID 0000-0002-8782-0890

## 1. INTRODUCTION

National geodetic reference frames across Europe are in transition from legacy datums, realised throughout the nineteenth and twentieth centuries by classical triangulation, to modern realisations of ETRS89 established by Global Navigation Satellite Systems (GNSS). In the Republic of Srpska (Bosnia and Herzegovina), as in the wider region, the legacy datum is realised on the Bessel 1841 ellipsoid with coordinates expressed in the Gauss–Krüger projection, while the spatial data infrastructure is migrating to ETRS89 with the Universal Transverse Mercator (UTM) projection. The transformation between the two frames must serve a large body of existing spatial data (cadastral plans, utility registers, topographic products) and must therefore be unique, simple to apply, and accompanied by a realistic accuracy statement.

A similarity (Helmert) transformation alone cannot satisfy these requirements, because classical networks are affected by distortions: spatially correlated coordinate errors accumulated through decades of triangulation measurements, adjustments in chains and blocks, and successive computational campaigns, as well as through crustal motion over the long time span of the observations. The established remedy, pioneered for the North American and Australian datum modernisations, is a two-step model in which a conformal transformation removes the datum difference and an interpolated correction surface (a distortion grid) absorbs the spatially coherent residuals [1, 2]. The grid is distributed in a standard binary format such as NTv2 (National Transformation Version 2) [3], which commercial geographic information system (GIS) and GNSS tools apply transparently. The Australian national grids, built by least-squares collocation (LSC), remain a reference implementation of the workflow [4]; least-squares prediction was applied to horizontal coordinate distortions even earlier in Canada [5]. The interpolation step itself has attracted systematic study, often aimed at identifying the most suitable predictor for a given network [6], while distortion-grid transformations continue to be produced for national datums elsewhere, such as the recent CS42-to-WGS84 transition in Uzbekistan [7].

A question of practical importance has, however, received less systematic attention: *what limits the accuracy of the final transformation?* When a distortion grid is validated on independent points, the residual error is routinely attributed to the interpolation method, and effort is invested in increasingly sophisticated predictors. The present paper offers evidence for a different interpretation: it does not seek to identify a universally best interpolator, but asks whether the residual validation level is method-controlled or data-controlled. Unlike previous studies focused on constructing a particular transformation grid, it treats the convergence of methodologically distinct interpolation families as diagnostic evidence for the accuracy floor of the available control data. In this paper, the *accuracy floor* denotes the empirical validation-error level reached by all numerically stable interpolation methods under the given control-point density, validation geometry and transformation architecture; it is not a theoretical lower bound, but an observed limit of predictability of the available common-control dataset. Using a dense national control set and identical validation protocols, we compare twenty configurations of four interpolation families and show that: (i) all numerically stable configurations converge to the same holdout accuracy level of approximately 10 cm at the available control density; (ii) this level is insensitive to the removal of locally inconsistent points; and (iii) under the tested architecture and validation protocols, the common level is therefore best interpreted as a property of the control dataset (with the legacy network as the most plausible major contributor) rather than as a property of any algorithm.

The paper offers: (1) a systematic benchmark of distortion-modelling methods on the Republic of Srpska dataset under repeated, cross-validated and spatially blocked protocols; (2) the interpretation of the common holdout level as the effective empirical accuracy floor of the available control dataset; (3) a demonstration that conventional outlier tests must not be applied directly to distortion fields, with a robust spatial alternative; and (4) a documented scale-compatibility result for the hole-effect covariance in cell-local collocation.
The paper is organised as follows: Section 2 presents the methodology. Section 3 presents the case study and the benchmark results. Section 4 discusses the interpretation and the practical consequences of the accuracy floor, and Section 5 concludes.

## 2. METHODOLOGY

This section summarises the functional model, the diagnostic statistics, the interpolation methods and the validation protocol used in the remainder of the paper. The methodology is organised to distinguish between the deterministic part of the datum relationship and the residual distortion that remains after the global transformation has been applied. This distinction provides the basis for comparing interpolation methods, identifying numerically unstable variants and evaluating whether the observed residual level reflects model limitations or the intrinsic accuracy of the available control dataset.

### 2.1. HELMERT TRANSFORMATION AND RESIDUAL DIAGNOSTICS

The datum relationship is modelled by the seven-parameter similarity transformation in the position-vector convention. For a point with Earth-centred, Earth-fixed (ECEF) Cartesian coordinates, $\mathbf{X}_S$ in the source frame and $\mathbf{X}_T$ in the target frame:

$$X_T = t + (1+\mu)\, R(\varepsilon_x, \varepsilon_y, \varepsilon_z)\, X_S \tag{1}$$

where $\mathbf{t} = (t_x, t_y, t_z)^T$ is the translation vector, μ the scale parameter and **R** the rotation matrix linearised for small angles $\varepsilon_x$, $\varepsilon_y$, $\varepsilon_z$. In the numerical implementation, μ is dimensionless (reported in ppm in Tab. 1), and the rotations are converted from arcseconds to radians when forming the linearised matrix **R**. Geodetic coordinates on the Bessel 1841 and GRS80 (Geodetic Reference System 1980) ellipsoids are converted to and from ECEF analytically, so that the estimation is carried out entirely in Cartesian space. With $n$ control points known in both frames ($n \geq 3$, not all collinear), the linearised observation equations are reduced to the centroid to decorrelate translations from rotations and scale, and the normal equations are solved by Cholesky factorisation. The a posteriori variance factor follows from the $3n - 7$ redundancy:

$$\hat{\sigma}_0^2 = \frac{v^T v}{3n - 7} \tag{2}$$

with **v** the residual vector under unit weighting. For every point, the residual is expressed in the local east–north–up (ENU) frame; for each coordinate component, the redundancy number $r_i$ is the corresponding diagonal element of the residual cofactor matrix $Q_{vv} = I - AN^{-1}A^T$ expressed in the ENU frame ($r_i = 1 - h_{ii}$, with $h_{ii}$ the diagonal of the hat matrix), yielding the component-wise standardised residuals:

$$w_i = \frac{v_i}{\sigma_0 \cdot \sqrt{r_i}} \tag{3}$$

used by the conventional outlier tests, with $\sigma_0$ chosen according to the particular test: known a priori for Baarda's data snooping, and replaced by the a posteriori estimate $\hat{\sigma}_0$ for Pope's test [8–9].

Whether the residual field contains spatially coherent signal, i.e. whether a distortion model is justified at all, is quantified by Moran's $I$ statistic of spatial autocorrelation [10]:

$$I = \frac{n}{S_0} \cdot \frac{\Sigma_i \Sigma_j w_{ij} z_i z_j}{\Sigma_i z_i^2}, \quad z_i = v_i - \bar{v} \tag{4}$$

computed separately for the east and north residual components, where $z_i$ is the residual component $v_i$ centred on its mean $\bar{v}$, with symmetric $k = 8$ nearest-neighbour weights $w_{ij}$ in the projection plane and $S_0 = \Sigma_{ij} w_{ij}$. As a practical diagnostic in this study, values of $I$ close to zero were treated as weakly autocorrelated at the scale of this diagnostic, while clearly elevated values (such as the 0.65–0.95 levels observed in Section 3) indicate a coherent residual structure worth modelling.

## 2.2. DETECTION OF LOCALLY INCONSISTENT POINTS

A point of methodological importance is that the tests built on statistic (3) are not operationally informative when applied directly to the residuals of the deliberately rigid Helmert model. Baarda's and Pope's procedures assume that the functional model is complete, so that residuals contain only random noise. In a datum transformation, the opposite holds by design: the similarity transformation is deliberately too rigid to absorb network distortions, so the residuals retain precisely the distortion signal that is subsequently modelled. For the dataset described in Section 3, the residuals after the Helmert fit have a horizontal RMS value of about 0.55 m, which is an order of magnitude larger than the adopted observation noise. When applied with a realistic a priori sigma of 0.05 m, Baarda's test flags approximately 96 % of all points, making it operationally uninformative for screening local blunders. This does not indicate a failure of Baarda's or Pope's tests themselves; it indicates that their assumptions are violated when the deliberately rigid Helmert model is used before distortion modelling.

Locally inconsistent points must instead be sought as *spatial* anomalies: points whose residual disagrees with the residuals of their immediate neighbours, rather than with a global noise model. For each point i, the residual predicted from its $k$ nearest neighbours (excluding i) by inverse-distance weighting (IDW) is denoted $\hat{\mathbf{v}}_i$, and the deviation $\delta_i = \|\mathbf{v}_i - \hat{\mathbf{v}}_i\|$ is tested against a robust threshold derived from the median absolute deviation of all deviations, $\mathrm{MAD}(\delta) = \mathrm{med}(|\delta_i - \mathrm{med}(\delta)|)$:

$$\delta_i > \mathrm{med}(\delta) + 3 \cdot 1.4826 \cdot \mathrm{MAD}(\delta) \tag{5}$$

In all detection runs, $k = 12$ neighbours (a compromise between locality and the robustness of the prediction) were selected by horizontal distance, the prediction used inverse-squared-distance weights, $\delta_i$ was the 3D norm of the misfit, and the criterion was applied iteratively with re-fitting of the Helmert parameters. The procedure flagged 227 points over five passes (extending the iteration to convergence flags 232 points and changes the representative repeated-holdout RMS by less than 1 mm). The factor 1.4826 in (5) is a robust scale normalisation, not a formal Gaussian test for the non-negative norm $\delta_i$. A horizontal-only (east–north) control flags a partly different set of points but leads to the same common accuracy floor. A point exceeding the threshold is treated as a candidate blunder or a point requiring geodetic inspection, whereas a smoothly varying residual, even a large one, is retained as genuine distortion; the 3D-screened (cleaned) set serves only as a diagnostic configuration for comparing methods,

while the production statement of Section 4 rests on the raw behaviour, because all operational legacy points must be transformed. In production, no points are discarded: every legacy point is transformed, and the flagged ones are only marked for inspection.

## 2.3. INTERPOLATION METHODS

Four families of interpolation methods, in twenty configurations, were compared under identical conditions: four IDW variants, five ordinary-kriging variants, three triangulated-irregular-network fallback variants and eight LSC variants. All operate per component on the Helmert residuals in a single computational plane, the east–north plane of the local ENU frame anchored at the target-network centroid, used as the working projection plane throughout; the production grid nodes, defined in ETRS89 / UTM zone 34, are converted to this plane for evaluation. The up component is modelled alongside east and north for completeness and diagnostic purposes; the production grid and all primary metrics in this paper are horizontal (Section 2.5).

**Inverse distance weighting** [11] predicts the value at $P$ as a normalised weighted sum of the $k$ nearest data points, with weights $a_i = d_i^{-p}$:

$$\hat{s}(P) = \frac{\Sigma_i a_i s_i}{\Sigma_i a_i}, \quad a_i = d_i^{-p} \tag{6}$$

Four selected configurations with representative combinations of $k$ and $p$ were tested (IDW(8, 2), IDW(12, 2), IDW(20, 3) and IDW(30, 2)), with neighbour search performed on a k-d tree. If $P$ coincides with a data point, the observed residual at that point is used directly.

**Ordinary kriging (OK)** predicts by solving the kriging system with Lagrange constraint over the $k$ = 32 nearest neighbours. Spherical, exponential, Gaussian and Matérn ($\nu$ = 3/2) variogram models were fitted automatically to the empirical variogram (15 distance bins, weighted by the number of point pairs per bin) by the derivative-free bounded BOBYQA algorithm [12]; all three parameters (range, sill, nugget) are estimated within data-driven bounds, the range within 0.1 to 4 times the empirical lag span, the sill within $10^{-3}$ to 10 times the empirical maximum, and the nugget between zero and the sill (estimated, not fixed at zero), independently for each residual component, and a failed fit falls back to a manual seed (5 km range, 0.01 m² sill, zero nugget). A variant with geometric anisotropy of the spherical model was included. In this local-neighbourhood setting, the very smooth Gaussian and Matérn covariances combined with automatic fitting produced nearly singular systems (Section 3.2) and are reported for completeness only; these variants are therefore not interpreted as evidence against kriging in general, but as unsafe automatic configurations under the adopted local fitting protocol.

**Triangulated irregular network (TIN) piecewise-affine interpolation** triangulates the control points by Delaunay triangulation and applies, within each triangle, the affine function determined by its three vertices; the interpolant is exact at the data points. Outside the convex hull three fallback strategies were tested: local IDW, nearest-edge affine extrapolation, and zero correction.

**Least-squares collocation** [13, 14] predicts the signal at $P$ from the vector $\ell$ of the residuals at the neighbouring data points as:

$$\hat{s}_P = \hat{m} + c_P^{\mathrm{T}} (C + \sigma_n^2 I)^{-1} (\ell - \hat{m} \cdot 1) \tag{7}$$

where $\mathbf{C}$ is the signal covariance matrix among the data points, $\mathbf{c}_P$ the covariance vector between $P$ and the data, $\sigma_n$ the noise standard deviation and $\hat{m}$ the (removed and restored) mean level; the prediction is solved independently per residual component,

with the mean removed and restored per component. Following the Australian practice [4] and the local-neighbourhood formulation of [15], the collocation is solved cell-locally over the $k$ = 12 nearest points; on this dataset the median radius of that neighbourhood is about 3.6 km (90th percentile 8.4 km), which, with a non-zero noise term, keeps the system well conditioned for thousands of points. Covariance functions derived from the four monotone variogram models were tested alongside the hole-effect model of Reilly [16], adopted for the Australian grids [4]:

$$C(d) = C_0\left(1 - \tfrac{1}{2}(d/d_0)^2\right)e^{-\frac{1}{2}(d/d_0)^2} \tag{8}$$

which changes sign at $d = \sqrt{2}\cdot d_0$ and attains a minimum of $-C_0\cdot e^{-2} \approx -0.135\cdot C_0$ at $d = 2\cdot d_0$, a feature that no monotone covariance can represent. The parameters ($C_0$, $d_0$) were fitted to the empirical, mean-removed covariance of the data. For the monotone covariance models the benchmark uses $\sigma_n$ = 0.10 m; the Reilly model was additionally tested with $\sigma_n \in \{0, 0.05, 0.10, 0.20\}$ m.
In addition, a natural-neighbour (Sibson) interpolator [17] was benchmarked in a supplementary configuration (Section 3.2).

## 2.4. MULTI-SCALE CASCADE AND SPECTRAL DIAGNOSTICS

The implementation supports a cascaded, multi-scale decomposition of the residual field. With $r_0$ the Helmert residuals at the control points, level $k$ fits an interpolated surface $g_k$ on a grid of step $L_k$ ($L_1 > L_2 > \ldots$) and passes the remaining point residuals to the next level:

$$r_k = r_{k-1} - g_k, \quad G = \Sigma_k g_k \tag{9}$$

so that the final correction grid $G$ is the sum of the level surfaces. Throughout this paper, the *distortion grid* denotes the surface storing the correction added to the Helmert-transformed coordinates. Level scales are chosen from the radially averaged power spectrum of the gridded residual field (two-dimensional fast Fourier transform), and Moran's $I$ recomputed on $r_k$ after each level indicates when the remaining residuals become only weakly autocorrelated under this diagnostic. As Section 3.3 shows, this machinery acts in practice as a *diagnostic* that tells the analyst when a single interpolation pass is already sufficient.

## 2.5. VALIDATION PROTOCOLS AND IMPLEMENTATION

Two kinds of residuals must be kept apart: the *Helmert residuals* (≈ 0.55 m horizontal RMS here), which are the input signal to distortion modelling, and the *validation residuals* after the grid correction (≈ 0.10 m), which measure the final transformation. All accuracy metrics refer to the latter. The horizontal and spatial errors are reported as:

$$RMS_{2D} = \sqrt{\left(\frac{1}{n}\Sigma_i\left(dE_i^2 + dN_i^2\right)\right)} \tag{10}$$

and analogously $RMS_{3D}$ with the dU component included. Since the purpose of the paper is the horizontal transformation, all primary conclusions are based on $RMS_{2D}$; the 3D quantities are used only to monitor the full Helmert residual behaviour and numerical stability.
The stability indicator max |grid| denotes the maximum absolute value of either horizontal correction component over all valid nodes of the grid used for NTv2 export (the up grid is monitored separately and yields the same classification); a variant is classified as unstable or unsafe when it exceeds 30 m, variants below the threshold are referred to as production-safe (numerically safe for production use), far beyond any

plausible datum distortion in the dataset (the largest horizontal Helmert residual in the cleaned set is 1.21 m) and certain to create catastrophic extrapolation artefacts in a production grid. A mild exceedance of the input residual range is not itself instability; the excluded variants exhibit gross overshoot by orders of magnitude. The 30 m threshold is not a tuned statistical limit but a production-safety guard: the retained variants reach at most 1.44 m and the excluded ones at least 54 m, so any threshold between these extremes would yield the same classification.

The benchmark of Section 3.2 uses a single final-pass grid with 500 m step, limited to the national boundary polygon, a 20 % holdout sample drawn once (uniform random, fixed seed) and reused for every variant, and the same cleaned point set. To quantify the sampling noise of that single split, three additional protocols were run for four representative stable methods as point-prediction experiments (the interpolator is fitted on the training subset and evaluated directly at the validation points): (i) the 20 % random holdout repeated with ten different seeds; (ii) 5-fold cross-validation (CV); and (iii) a spatial block holdout, in which the points are aggregated on a fixed projected 20 km square grid, the blocks are assigned pseudo-randomly to five groups, and in each fold all points of the withheld blocks are excluded from training, so that predictions are made in blocks without local training points, i.e. with reduced local support compared with random holdout. No buffer was imposed around the withheld blocks; the protocol therefore measures reduced local support, not complete extrapolation across a 20 km gap. These protocols compare the relative behaviour of the methods at and away from the sampled density; they do not include the 500 m gridding step of the production pipeline and are not intended as an exact simulation of NTv2 production. All splits apply to the residual interpolation step: the seven Helmert parameters are estimated once per configuration and are not re-estimated per split; a control experiment with per-split re-estimation reproduced the reported values within 0.1 mm (random and CV) and 1 mm (block), so this conditioning is immaterial. In every experiment the withheld points were excluded from the residual interpolation and from the construction of the grid used to predict their corrections; they entered only the final accuracy evaluation. In short, the cleaned set serves the diagnostic method comparison and the raw set the operational statement. Repeated holdout and CV characterise behaviour at the sampled density, the block protocol behaviour under reduced local support, while the grid benchmark represents the production scenario and the point-prediction runs the relative behaviour of the methods.

The residual-correction grids, used as the second step after the Helmert transformation, are exported in the NTv2 format [3], which stores latitude and longitude shifts in arcseconds on a regular geographic grid, the de facto standard also for current national transformations [18]. The projected east/north residuals are first transformed to the target geographic frame, and the corresponding latitude/longitude shifts are written in NTv2 arcseconds. The sign convention is that of the NTv2 source-to-target shift file, i.e. the grid shift is added to the Helmert-transformed coordinates:

$$\varphi_{ETRS89} = \varphi_{Helmert} + \Delta\varphi_{\text{grid}}, \quad \lambda_{ETRS89} = \lambda_{Helmert} + \Delta\lambda_{\text{grid}} \tag{11}$$

where $\varphi_{\text{ETRS89}}$ and $\lambda_{\text{ETRS89}}$ are the target ETRS89 latitude and longitude, $\varphi_{\text{Helmert}}$ and $\lambda_{\text{Helmert}}$ the corresponding values after the Helmert step, and $\Delta\varphi_{\text{grid}}$ and $\Delta\lambda_{\text{grid}}$ the latitude and longitude shifts interpolated from the distortion grid.

The export conventions were verified independently with PROJ (version 9.5.1) [19] on one fixed 20 % withheld split of the cleaned set (750 points), not used for grid construction. With the correct convention, the grid applied to the Helmert-transformed coordinates reproduces the reference ETRS89 coordinates at the holdout accuracy level (RMS 0.107 m, against 0.104 m for direct point prediction), whereas a reversed sign

approximately doubles the residual (RMS 1.09 m). Cells outside the boundary polygon receive the nearest valid value at export, a format requirement that must not be interpreted as extending the validity of the transformation outside the national boundary.

## 3. CASE STUDY: THE REPUBLIC OF SRPSKA

This section applies the methodology of Section 2 to a dense territory-wide control set for the Republic of Srpska. The aim of the case study is to determine how much of the post-Helmert residual field can be modelled as a spatially correlated distortion and how much represents an effective accuracy limit of the available control data. The analysis therefore combines interpolation benchmarking with independent block validation, cascade and spectral diagnostics, and hole-effect covariance modelling.
The section presents the data and the Helmert solution, the benchmark of the interpolation methods, the cascade and spectral diagnostics, and the hole-effect covariance analysis.

### 3.1. DATA AND HELMERT SOLUTION

The dataset comprises 3977 control points with coordinates in both frames, covering the territory of the Republic of Srpska (Fig. 1). The source coordinates are given in the legacy state datum: Bessel 1841 ellipsoid, Gauss–Krüger projection, zone 6 (central meridian 18°, scale factor 0.9999, false easting 6 500 000 m), in metres, accompanied by the official heights of the legacy survey. Since true ellipsoidal heights in the legacy frame are not available, the supplied heights serve only as an auxiliary coordinate for the 3D Cartesian conversion, not as a physical height model. Sensitivity tests bound this convention: constant ±50 m shifts change the horizontal residual RMS by less than 0.5 mm and the post-grid holdout RMS by less than 0.1 mm, while a deliberately adverse spatial perturbation (±30 m, ≈ 150 km wavelength) raises the Helmert residual RMS by 5.5 cm yet changes the post-grid holdout RMS by at most 1.3 mm, with the convergence and ranking of the stable methods unchanged; the horizontal floor is therefore not an artefact of the height convention. The vertical component is treated as a diagnostic quantity, and all production conclusions are horizontal.

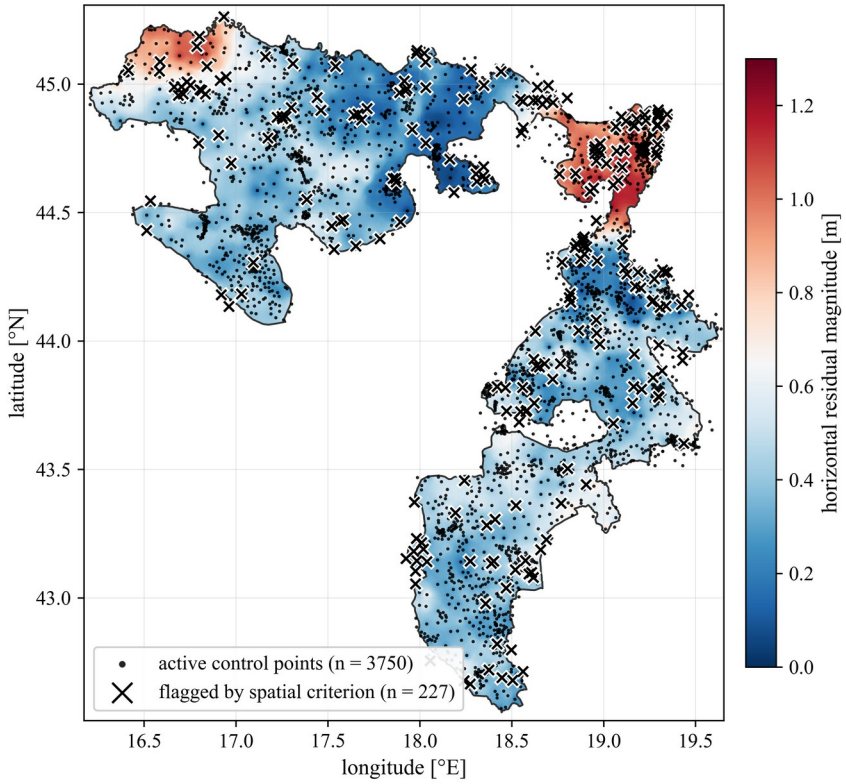


*Fig. 1 Control points and boundary of the Republic of Srpska; the colour surface is the magnitude of the horizontal Helmert residual field (cleaned set; IDW, k = 12, p = 2; colour encodes magnitude only); black crosses mark the 227 points flagged by criterion (5)*

Throughout the paper, ETRS89 denotes the target reference system, realised by the supplied ETRF2000 coordinates at epoch 2011.307 [20]: the target coordinates are GNSS-derived Cartesian (ECEF) coordinates provided by the geodetic authority; no evidence in the present validation results suggests that the difference between this reference epoch and the epochs of the underlying GNSS observations dominates the decimetre-level floor discussed below. The control points are not spatially uniform, the mean distance to the nearest neighbour is 1.3 km (median distance to the 12th neighbour 3.6 km), with denser urban clusters and sparser mountainous areas visible in Fig. 1.

After conversion to ECEF, the seven parameters of model (1) were estimated; the solution summary is given in Tab. 1. For the full set, $\hat{\sigma}_0$ = 0.683 m; after removing the 227 locally inconsistent points (5.7 %) flagged by criterion (5), the cleaned (3D-screened) set used for the diagnostic method comparison, $\hat{\sigma}_0$ = 0.676 m, a first indication that the dataset is dominated by genuine distortion rather than by isolated errors. The residual field has a horizontal RMS of approximately 0.55 m with pronounced spatial structure (Fig. 1, shown as the interpolated magnitude surface): large coherent patches of consistent direction and magnitude, confirmed by very strong Moran's *I* autocorrelation of both horizontal components ($I$ = 0.965 for ΔE and 0.951 for ΔN). The field therefore clearly justifies the use of a distortion model.

*Tab. 1 Helmert (position-vector) solution for the Republic of Srpska (cleaned set, 3750 of 3977 points)*

| Parameter | Value | Std. dev. |
|---|---|---|
| $t_x$ [m] | 525.933 | ± 0.967 |
| $t_y$ [m] | 162.620 | ± 1.028 |
| $t_z$ [m] | 490.658 | ± 0.866 |
| $\varepsilon_x$ [″] | 5.4607 | ± 0.0277 |
| $\varepsilon_y$ [″] | 2.8904 | ± 0.0344 |
| $\varepsilon_z$ [″] | −11.9785 | ± 0.0305 |
| μ [ppm] | 2.543 | ± 0.111 |
| $\hat{\sigma}_0$ [m] | 0.676 | – |
| Redundancy 3n − 7 | 11 243 | – |
| Moran's *I* (ΔE; ΔN) | 0.965; 0.951 | – |

## 3.2. BENCHMARK RESULTS: THE COMMON ACCURACY FLOOR

Tab. 2 summarises the production-safe (stable) benchmark variants on the cleaned dataset, ranked by holdout 2D RMS, and Tab. 3 lists the variants excluded by the stability rule of Section 2.5. The $RMS_{3D}$ values of the stable variants (including the up component) follow the same ordering. Tab. 2 is not a cleaned-data production accuracy claim: it is a diagnostic comparison of the methods under a controlled cleaned configuration, and the rank order within the leading group has no operational significance; the operational accuracy statement is based on the raw repeated-holdout behaviour (Section 4). Three observations follow.

*Tab. 2 Production-safe benchmark variants ranked by holdout 2D RMS (cleaned diagnostic set; identical fixed-seed 20 % holdout); training RMS is evaluated through the 500 m gridded surface, not at the interpolator's own data points. Abbreviations: IDW(k, p); OK = ordinary kriging (variogram model); LSC (covariance model, $\sigma_n$ [m]); TIN+fallback*

| # | Variant | Hold 2D [m] | Train 2D [m] | max \|grid\| [m] |
|---|---|---|---|---|
| 1 | LSC-exp, $\sigma_n$ = 0.10 | 0.1026 | 0.0521 | 1.15 |
| 2 | LSC-sph, $\sigma_n$ = 0.10 | 0.1046 | 0.0663 | 1.13 |
| 3 | TIN+IDW | 0.1047 | 0.0302 | 1.17 |
| 4 | OK-exp | 0.1049 | 0.0569 | 1.23 |
| 5 | IDW(8, 2) | 0.1058 | 0.0298 | 1.16 |
| 6 | IDW(12, 2) | 0.1060 | 0.0312 | 1.16 |
| 7 | IDW(20, 3) | 0.1061 | 0.0259 | 1.18 |
| 8 | LSC-Mat, $\sigma_n$ = 0.10 | 0.1088 | 0.0858 | 1.30 |
| 9 | OK-sph | 0.1088 | 0.0699 | 1.24 |
| 10 | IDW(30, 2) | 0.1092 | 0.0342 | 1.16 |

| # | Variant | Hold 2D [m] | Train 2D [m] | max \|grid\| [m] |
|---|---|---|---|---|
| 11 | LSC-Rei, $\sigma_n$ = 0.05 | 0.1124 | 0.0922 | 1.44 |
| 12 | LSC-Gau, $\sigma_n$ = 0.10 | 0.1133 | 0.0937 | 1.22 |
| 13 | OK-sph, aniso. | 0.1135 | 0.0710 | 1.22 |
| 14 | LSC-Rei, $\sigma_n$ = 0.10 | 0.1155 | 0.0959 | 1.12 |
| 15 | TIN+zero | 0.1183 | 0.0485 | 1.17 |
| 16 | LSC-Rei, $\sigma_n$ = 0.20 | 0.1192 | 0.0992 | 1.08 |

*Tab. 3 Variants excluded by the stability rule (horizontal max |grid| > 30 m); abbreviations as in Tab. 2*

| Variant | Hold 2D [m] | Train 2D [m] | max \|grid\| [m] | Failure mode |
|---|---|---|---|---|
| TIN+edge | 0.1306 | 0.0306 | 54.2 | unsafe extrapolation |
| LSC-Rei, $\sigma_n$ = 0 | 0.3740 | 0.0427 | 161 | ill-conditioned exact collocation |
| OK-Mat (auto-fit) | 1.1179 | 0.3513 | $1.12 \cdot 10^5$ | degenerate auto-fit |
| OK-Gau (auto-fit) | 204.53 | 5.977 | $4.99 \cdot 10^6$ | degenerate auto-fit |

First, **all production-safe variants cluster around a common accuracy level**: the sixteen retained configurations span 0.1026 m to 0.1192 m holdout 2D RMS in the fixed-seed split (a band of 10 cm to 12 cm) and the leading ten lie within less than 1 cm of one another (Fig. 2). Tab. 4 quantifies the split noise: across ten repeated random holdouts the four representative methods give mean 2D RMS between 0.098 m and 0.101 m with standard deviations of about 2 mm, and 5-fold cross-validation reproduces the same values, so the ranking among the stable methods is within the noise of the validation split. A supplementary run including the natural-neighbour interpolator on the raw configuration confirms the picture (0.0971 m against a raw fixed-split level of approximately 0.099 m). An idealised point-wise best selection (choosing at each holdout point the variant with the smallest actual error) would improve the RMS by only about 1.7 cm (≈ 18 %); since the method errors are mutually correlated ($r \approx 0.86$), no realisable selector can approach even that upper bound; the remaining errors are largely shared rather than method-specific. The choice among stable interpolation methods is, for this dataset, a second-order decision.

*Tab. 4 Validation protocols for four representative stable methods (point-prediction experiments, cleaned set, ≈ 750 validation points per split or fold): holdout 2D RMS, mean ± standard deviation [m]*

| Method | Repeated 20 % holdout (10 seeds) | 5-fold CV | Spatial 20 km block holdout |
|---|---|---|---|
| IDW(12, 2) | 0.1007 ± 0.0019 | 0.1026 ± 0.0029 | 0.164 ± 0.021 |
| TIN+IDW | 0.1013 ± 0.0017 | 0.1023 ± 0.0038 | 0.165 ± 0.024 |
| OK-exp | 0.0995 ± 0.0018 | 0.1010 ± 0.0031 | 0.148 ± 0.015 |
| LSC-exp, $\sigma_n$ = 0.10 | 0.0979 ± 0.0015 | 0.0989 ± 0.0033 | 0.158 ± 0.013 |

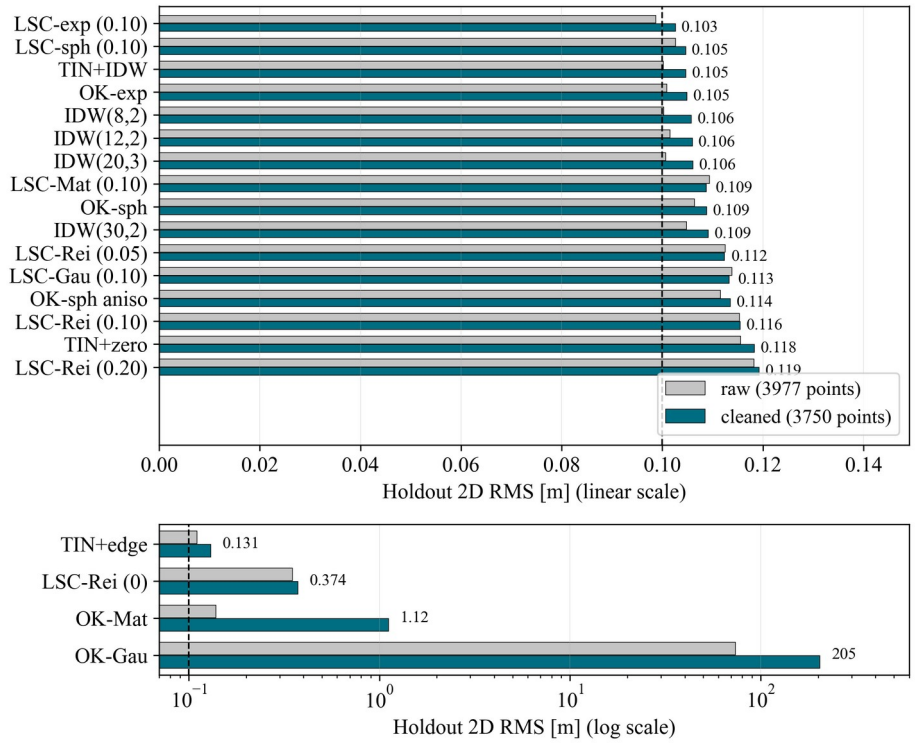


*Fig. 2 Holdout 2D RMS per variant, raw versus cleaned dataset (fixed-seed splits): stable variants on a linear scale (top), excluded variants on a logarithmic scale (bottom); dashed line: the 10 cm level*

The spatial block protocol in Tab. 4 adds an important qualification: when entire 20 km blocks are withheld, the error grows to 0.15 m to 0.16 m for all methods. The ≈ 10 cm floor therefore applies *at the available control density*; predictions with reduced local support degrade by roughly one half, which any production accuracy statement should acknowledge.

Second, **the common level is insensitive to the removal of locally inconsistent points**. Four train/test combinations were evaluated with a common fixed raw holdout (Tab. 5). In every combination the level stays at 10.0 cm to 10.7 cm; the flagged points are locally harder (RMS ≈ 0.19 m), but they neither create the floor nor can their removal lower it. Combination (c) against (a) isolates the local contribution of the flagged points; (d) against (b) shows that training on the cleaned set does not resolve the raw test points; and row (e) confirms that the flagged points are locally harder yet too few to generate the floor. Operationally, the raw repeated-holdout statistics (ten-seed

protocol of Tab. 4 on the raw set) are the relevant production figures: for the four representative methods the mean 2D RMS is 0.102 m to 0.106 m and the pooled P95 (the 95th percentile of the horizontal 2D point error) is 0.198 m to 0.204 m. These raw values, rather than the cleaned diagnostic benchmark, form the basis of the production accuracy statement in Section 4.

*Tab. 5 Raw/cleaned train–test combinations (fixed raw 20 % holdout): holdout 2D RMS [m]*

| Train / test combination | IDW(12, 2) | TIN+IDW |
|---|---|---|
| (a) train raw, test raw holdout ($n$ = 795) | 0.1048 | 0.1045 |
| (b) train cleaned, test cleaned holdout ($n$ = 755) | 0.1006 | 0.0999 |
| (c) train raw, test raw holdout ∩ cleaned set ($n$ = 755) | 0.1002 | 0.0998 |
| (d) train cleaned, test full raw holdout ($n$ = 795) | 0.1070 | 0.1054 |
| (e) flagged points only ($n$ = 40) | 0.1906 | 0.1803 |

Third, **numerical stability, not accuracy, separates the methods** (Tab. 3). Auto-fitted Gaussian and Matérn kriging produced horizontal grids overshooting to $10^5$ m to $10^6$ m, and collocation with $\sigma_n = 0$ (exact interpolation) overshot to hundreds of metres; these configurations are unusable in production even where their training RMS looks acceptable. The TIN nearest-edge variant is excluded for a different reason: not because of its interpolation inside the convex hull, which is sound, but because its extrapolation behaviour outside the hull is numerically unsafe (max |grid| = 54 m); holdout points rarely sample the dangerous cells outside the hull, so holdout RMS alone is an insufficient criterion; hence the grid-based indicator.

Tab. 6 gives the distribution of the holdout errors, pooled over the ten repeated splits. The best variants reproduce the smoothly correlated part of the field, while the remaining error is spread over the validation points (roughly one third fall below 5 cm and two thirds below 10 cm) and is concentrated in a set of locally difficult points with errors up to about 0.55 m. A spatial diagnostic confirms the floor interpretation: over the same ten splits, Moran's $I$ of the validation errors at the withheld points drops from 0.94/0.90 (input ΔE/ΔN residuals) to 0.03–0.07 for all four representative methods ($k$ = 8 neighbour weights), so the post-grid error is only weakly spatially autocorrelated at the sampled scale.

*Tab. 6 Distribution of holdout 2D errors, pooled over ten repeated 20 % holdouts (cleaned set; configurations of Tab. 4)*

| Method | RMS [m] | ≤ 5 cm | ≤ 10 cm | ≤ 15 cm | ≤ 20 cm | P95 [m] | max [m] |
|---|---|---|---|---|---|---|---|
| IDW(12, 2) | 0.1007 | 32.3 % | 67.9 % | 87.5 % | 95.7 % | 0.193 | 0.58 |
| TIN+IDW | 0.1013 | 31.3 % | 67.5 % | 87.4 % | 95.8 % | 0.192 | 0.56 |
| OK-exp | 0.0996 | 31.8 % | 68.9 % | 87.7 % | 96.0 % | 0.192 | 0.52 |
| LSC-exp | 0.0979 | 32.3 % | 69.1 % | 88.7 % | 96.4 % | 0.187 | 0.55 |

Tab. 7 documents the auto-fitted parameters per residual component on the full cleaned set. The exponential and spherical kriging ranges repeatedly reach the upper bound of the fitting interval (reported as ≥ 643 km), which is harmless for variograms that are non-smooth at the origin; for the very smooth Gaussian and Matérn models the long fitted ranges combined with near-zero nuggets make the local kriging matrices nearly singular, the mechanism behind the degenerate entries of Tab. 3. The monotone LSC correlation lengths (25 km to 124 km) far exceed the 3.6 km median neighbourhood radius; the cell-local system stays well conditioned only through the noise term $\sigma_n$, which enters the prediction separately from the fitted nugget.

*Tab. 7 Auto-fitted variogram (OK) and covariance (LSC, $\sigma_n$ = 0.10 m) parameters per residual component (cell format E; N; U), full cleaned set; ≥ 643 km = upper bound of the fitting interval; OK-sph, aniso.: major/minor axis; LSC-Rei: range = $d_0$*

| Variant | Range a / $d_0$ [km] | Sill $C_0$ [m²] | Nugget [m²] |
|---|---|---|---|
| OK-sph | 168; ≥643; 146 | 0.266; 0.379; 1.462 | 0.000; 0.018; 0.000 |
| OK-exp | ≥643; ≥643; 406 | 0.538; 0.268; 2.287 | 0.000; 0.007; 0.000 |
| OK-Gau | 132; 203; 123 | 0.269; 0.166; 1.523 | 0.000; 0.034; 0.000 |
| OK-Mat | 73; 111; 65 | 0.308; 0.192; 1.676 | 0.000; 0.027; 0.000 |
| OK-sph, aniso. | 331/118; ≥643/300; 265/108 | 0.267; 0.253; 1.462 | 0.000; 0.014; 0.000 |
| LSC-exp | 66; 108; 71 | 0.435; 0.146; 1.901 | 0; 0; 0 |
| LSC-sph | 78; 124; 87 | 0.318; 0.111; 1.419 | 0; 0; 0 |
| LSC-Gau | 64; 99; 73 | 0.279; 0.099; 1.234 | 0; 0; 0 |
| LSC-Mat | 25; 39; 27 | 0.331; 0.115; 1.448 | 0; 0; 0 |
| LSC-Rei | 55; 73; 54 | 0.227; 0.091; 1.226 | – |

## 3.3. CASCADE AND SPECTRAL DIAGNOSTICS

The cascade machinery of Section 2.4 was evaluated by an A/B experiment with the TIN interpolator: a single final pass against a four-level cascade (30 km / 10 km / 5 km / 1 km), at a 1 km final step with a stratified holdout; the conclusion concerns the mechanism, not the particular step. The cascade improved the training RMS (4.47 cm against 4.88 cm) but *worsened* the holdout RMS (10.73 cm against 10.42 cm, Tab. 8): with an interpolant that is exact at the data points, the residuals passed to deeper levels

are dominated by sampling noise; multi-scale refinement overfits. Moran's $I$ per level makes the mechanism visible (Tab. 8): the original field is very strongly autocorrelated ($I \approx 0.96$), substantial structure remains after the 30 km level ($I \approx 0.65$–$0.72$), while the residuals entering the final level are only weakly autocorrelated under this diagnostic ($I \approx 0.02$ and $-0.02$). For exact or near-exact interpolators a single final pass is therefore the correct default; for sparser networks or stronger long-wavelength distortions a cascaded or remove–restore approach may still be useful.

*Tab. 8 Single-pass versus cascaded TIN modelling and associated Moran's I diagnostics per cascade stage*

| **Configuration** | **Train 2D [cm]** | **Holdout 2D [cm]** |
|---|---|---|
| Single final pass (1 km grid) | 4.88 | 10.42 |
| Four-level cascade (30/10/5/1 km) | 4.47 | 10.73 |
| **Cascade stage** | **Moran's *I* (ΔE)** | **Moran's *I* (ΔN)** |
| Original Helmert residual field (input) | 0.965 | 0.951 |
| Residuals after level 1 (30 km) | 0.65 | 0.72 |
| Residuals entering final level (1 km) | 0.018 | −0.015 |

## 3.4. THE HOLE-EFFECT COVARIANCE: A SCALE-COMPATIBILITY RESULT

The empirical covariance of the Republic of Srpska residual field exhibits the hole effect: the mean-removed empirical covariance dips below zero in all three components (Fig. 3), which is precisely the feature that motivated the Reilly model (8) in the Australian workflow [4, 16]. The fitted hole scale, however, lies at $d_0 \approx 54$ km to 73 km per component (Tab. 7), with the zero crossing at $\sqrt{2} \cdot d_0 \approx 76$ km to 103 km, a country-scale feature. Cell-local collocation over twelve nearest neighbours operates entirely inside the positive part of the covariance function: the median neighbourhood radius of 3.6 km (P90 8.4 km) is more than an order of magnitude below the zero crossing, so the negative lobe is never exploited. The Reilly variants (holdout 0.1124 m to 0.1192 m) therefore do not outperform the monotone covariances (best 0.1026 m), even on the cleaned set. This result is therefore not a rejection of the Reilly covariance model but a scale-compatibility result: the theoretical justification is confirmed by the data, while its practical advantage is absent under a local-neighbourhood solver; exploiting country-scale structure would require global collocation or remove–restore trend removal.

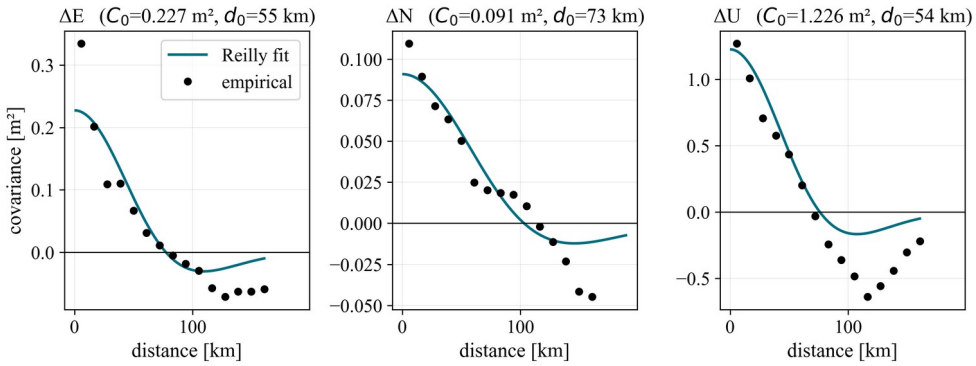


*Fig. 3 Mean-removed empirical covariance of the residual components with the per-component Reilly fit (variant LSC Reilly, $\sigma_n$ = 0.10, cleaned set); the negative lobe (hole effect) appears beyond ≈ 80 km to 100 km*

## 4. DISCUSSION: THE COMMON LEVEL AS THE ACCURACY FLOOR OF THE CONTROL DATASET

The results of Section 3 admit one consistent interpretation. The two-step transformation (Helmert plus interpolated grid) aims to remove the datum offset and the smoothly correlated part of the residual field; the remaining validation error is dominated by the component that is not predictable at the available sampling scale: no method, however sophisticated, can model what does not correlate across the sampled scales. The common holdout level therefore primarily measures the effective empirical accuracy floor of the available common-control dataset under the tested two-step architecture, control-point density and validation protocols, most plausibly reflecting the unpredictable component of the legacy network together with target-frame coordinate noise, point-identification uncertainty and monument-related effects. For the Republic of Srpska control set this floor is approximately 10 cm horizontally.

The physical origin of such a weakly correlated component is plausible from the way classical coordinates were produced: the horizontal position derives from triangulation observations adjusted in chains and blocks over decades, with scale and orientation introduced at discrete baselines and astronomical stations, while heights stem from separate height-determination procedures. Substantial parts of the error budget (observation errors, centring, identification of monuments, partitioning of the adjustment) accumulate in a locally erratic way rather than as a smooth field. The smooth component is what the grid is designed to model; the erratic component is what the accuracy floor reveals.

Four practical consequences follow.

1. *Method choice is secondary.* All stable interpolators deliver the common floor; selection should be driven by numerical robustness, behaviour outside the convex hull, and implementation simplicity, not by chasing millimetres of holdout RMS that are within split noise (Tab. 4). Conversely, configurations from the exclusion list must be screened out by the stability indicator.

2. *The practical lever for lowering the floor is the data.* At fixed control density, and for the stable local methods tested here, densifying and spatially homogenising the control set, re-observing suspect points or improving the identification of monuments can lower the floor, whereas further tuning of the interpolator cannot. Investment should be directed accordingly.

3. *Accuracy statements must be transparent and two-level.* The published accuracy should not be a single number: the raw holdout statistics support about 10 cm horizontal

RMS with a P95 of about 20 cm at the observed control density, and about 15 cm to 16 cm RMS in block-validation areas with reduced local support. Such a statement should not imply GNSS-level accuracy: an arbitrary user point behaves like a holdout point, training residuals are not an operational measure, and a cleaned holdout is a survivorship-biased statistic; for cadastral use the raw figure is the operationally relevant one.

The cleaned-set distribution of Tab. 6 (P95 ≈ 19 cm) serves the method comparison, not the production statement, consistent with the practice of the Australian grids [4, 18].

4. *The tested architecture is sufficient.* For the tested control density and distortion spectrum, the classical 7-parameter-plus-grid architecture at the tested 500 m to 1 km grid steps reaches the observed accuracy floor. Once the grid step is sufficiently smaller than the control-point spacing and the dominant distortion wavelength, further refinement mainly increases the file size and is not expected to lower the validation floor.

Several limitations bound these conclusions. The floor value is specific to the network, the control density and the validation geometry, and must be re-estimated, by the same protocols, for every national case. The control points are not spatially uniform; the height convention is controlled by sensitivity tests but remains a convention; no full decomposition of the error budget by physical source was attempted; and the hole-effect model was not tested in a global collocation setting. Finally, the spatial criterion (5) deliberately flags *locally inconsistent* points, which is not synonymous with blunders; in cadastral production such points must still be transformed, flagged, and where possible re-surveyed.

## 5. CONCLUSIONS

A systematic benchmark of twenty distortion-modelling configurations on 3977 control points in the Republic of Srpska leads to the following conclusions:

1. All production-safe variants of the four primary interpolation families (IDW, kriging with monotone variograms, TIN piecewise-affine interpolation and LSC) cluster around a common holdout accuracy level of approximately 10 cm horizontal RMS at the available control density (repeated holdout 0.098 m to 0.101 m), but 15 cm to 16 cm when predicting in withheld 20 km blocks; a supplementary natural-neighbour run confirmed the same behaviour. The leading variants differ by millimetres to about one centimetre, within or close to the sampling noise of the validation splits.

2. The common level is insensitive to the removal of locally inconsistent points in all four train/test combinations and is interpreted, under the tested architecture and validation protocols, as the effective empirical accuracy floor of the available common-control dataset, primarily reflecting its unpredictable component, with the legacy network as the most plausible major contributor alongside target-frame coordinate noise, point-identification uncertainty and monument-related effects. Once a stable method has reached this floor, further validation primarily reflects the local accuracy and spatial unpredictability of the control dataset rather than the particular interpolation algorithm.

3. Conventional outlier tests (Baarda, Pope) are not operationally informative for distortion fields, where the Helmert residual is signal rather than noise; the robust spatial nearest-neighbour criterion provides a more appropriate screening of local spatial inconsistencies.

4. The secondary diagnostics behave consistently: multi-scale cascading brings no accuracy gain for exact interpolators (it overfits sampling noise) but objectively shows when a single pass is sufficient, and the country-scale hole effect in Reilly's covariance

($d_0$ ≈ 54 km to 73 km) brings no advantage under the tested cell-local collocation setting; exploiting it would require global collocation or trend removal.
5. For production, a 7-parameter-plus-NTv2-grid architecture at the tested 500 m to 1 km grid steps, built with any stable method and screened by the numerical-stability indicator, is sufficient to reach the observed accuracy floor; the published accuracy statement should be based on the raw holdout validation statistics and report both RMS and a high percentile.
The result is therefore a defensible production accuracy statement rather than a ranking of interpolation methods: about 10 cm horizontal RMS with a raw 95th-percentile horizontal error of about 20 cm at the observed control density, and about 15 cm to 16 cm RMS under block validation. These values describe the available control dataset under the reported protocols (not the nominal precision of GNSS, nor of the interpolation method, nor a universal property of the NTv2 architecture) and should not be transferred to another country or dataset without repeating the validation.
All results were produced with a single consistent computational workflow; the approach itself can be applied directly to other national datasets.

**ACKNOWLEDGEMENT**

The authors acknowledge the control point data made available by the Republic Administration for Geodetic and Property Affairs of the Republic of Srpska.

## REFERENCES

[1] Collier P.A., Argeseanu V.S., Leahy F.J. (1998). Distortion Modelling and the Transition to GDA94. The Australian Surveyor, Volume 43, No. 1, pp. 29–40. https://doi.org/10.1080/00050347.1998.10558718

[2] Dewhurst W.T. (1990). NADCON – The Application of Minimum-Curvature-Derived Surfaces in the Transformation of Positional Data from the North American Datum of 1927 to the North American Datum of 1983. NOAA Technical Memorandum NOS NGS-50, 30 pp.

[3] Junkins D.R., Farley S.A. (1995). NTv2 National Transformation Version 2 – Developer's Guide. Geodetic Survey Division, Geomatics Canada, 27 pp.

[4] Collier P. (2002). Development of Australia's National GDA94 Transformation Grids. Consultant's Report to the Intergovernmental Committee on Surveying and Mapping, Department of Geomatics, University of Melbourne, February 2002, 36 pp.

[5] Lachapelle G., Mainville A. (1982). Least Squares Prediction of Horizontal Coordinate Distortions in Canada. Bulletin Géodésique, Volume 56, pp. 242–257.

[6] Grgić M., Varga M., Bašić T. (2016). Empirical Research of Interpolation Methods in Distortion Modeling for the Coordinate Transformation between Local and Global Geodetic Datums. Journal of Surveying Engineering, Volume 142, No. 2, 05015004. https://doi.org/10.1061/(ASCE)SU.1943-5428.0000154

[7] Fazilova D. (2022). Uzbekistan's Coordinate System Transformation from CS42 to WGS84 Using Distortion Grid Model. Geodesy and Geodynamics, Volume 13, No. 1, pp. 24–30. https://doi.org/10.1016/j.geog.2021.10.001

[8] Baarda W. (1968). A Testing Procedure for Use in Geodetic Networks. Netherlands Geodetic Commission, Publications on Geodesy, New Series, Volume 2, No. 5, Delft.

[9] Pope A.J. (1976). The Statistics of Residuals and the Detection of Outliers. NOAA Technical Report NOS 65 NGS 1, Rockville, Maryland, 133 pp.

[10] Moran P.A.P. (1950). Notes on Continuous Stochastic Phenomena. Biometrika, Volume 37, No. 1/2, pp. 17–23. https://doi.org/10.1093/biomet/37.1-2.17

[11] Shepard D. (1968). A Two-Dimensional Interpolation Function for Irregularly-Spaced Data. Proceedings of the 1968 23rd ACM National Conference, pp. 517–524. https://doi.org/10.1145/800186.810616

[12] Powell M.J.D. (2009). The BOBYQA Algorithm for Bound Constrained Optimization without Derivatives. Report DAMTP 2009/NA06, Department of Applied Mathematics and Theoretical Physics, University of Cambridge.

[13] Krarup T. (1969). A Contribution to the Mathematical Foundation of Physical Geodesy. Meddelelse No. 44, Geodætisk Institut, Copenhagen.

[14] Moritz H. (1980). Advanced Physical Geodesy. Herbert Wichmann Verlag, Karlsruhe, 500 pp.

[15] Darbeheshti N., Featherstone W.E. (2009). Non-stationary Covariance Function Modelling in 2D Least-Squares Collocation. Journal of Geodesy, Volume 83, No. 6, pp. 495–508. https://doi.org/10.1007/s00190-008-0267-0

[16] Reilly W.I. (1979). Mapping the Local Geometry of the Earth's Gravity Field. Report No. 143, Geophysics Division, Department of Scientific and Industrial Research, Wellington, New Zealand, 56 pp.

[17] Sibson R. (1981). A Brief Description of Natural Neighbour Interpolation. In: Barnett V. (ed.), Interpreting Multivariate Data, John Wiley & Sons, Chichester, pp. 21–36.

[18] ICSM (2024). Geocentric Datum of Australia 2020 Technical Manual, Version 1.8. Intergovernmental Committee on Surveying and Mapping, April 2024. https://www.icsm.gov.au/publications/gda2020-technical-manual-v18

[19] PROJ contributors (2024). PROJ Coordinate Transformation Software Library, Version 9.5.1. Open Source Geospatial Foundation. https://doi.org/10.5281/zenodo.5884394

[20] Altamimi Z. (2024). EUREF Technical Note 1: Relationship and Transformation between the International and the European Terrestrial Reference Systems, Version of 4 March 2024. EUREF. http://etrs89.ensg.ign.fr/pub/EUREF-TN-1-Mar-04-2024.pdf

https://doi.org/10.24867/INDIS-2026-EN-804



# A PRELIMINARY COMPLETE BOUGUER ANOMALY MAP OF THE REPUBLIC OF SRPSKA

*Oleg Odalović[1], Marko Stanković[2], Dejan Vasić[3], Sanja Grekulović[4], Stefan Krstić[5]*

***Summary:***

A modern Bouguer anomaly map based on new gravimetric measurements has so far been unavailable for the territory of the Republic of Srpska. This paper presents a preliminary map derived from 3589 gravity points (the detailed survey and the NVT3 levelling benchmarks, 2020), tied to the fundamental gravimetric network and four absolute stations. The full workflow is described: transformation from the state system (Gauss–Krüger zone 6, Bessel 1841) to ETRS89, orthometric heights, gravity reduction, computation of the complete Bouguer anomaly, and gross-error elimination (SRTM comparison and a spatial-consistency test). After quality control 3478 points are retained; the complete Bouguer anomaly ranges from −83 to +40 mGal and is interpolated by ordinary kriging. The results show a strong negative anomaly over the high Dinarides and positive values in the north-western lowlands and locally in the southernmost part of the territory, around Trebinje.

*Keywords: Bouguer anomaly; gravimetry; Republic of Srpska; ETRS89 transformation; quasigeoid; gross-error elimination*

# PRELIMINARNA KARTA KOMPLETNIH BUGEROVIH ANOMALIJA ZA TERITORIJU REPUBLIKE SRPSKE

***Rezime:***

Za teritoriju Republike Srpske do sada nije postojala savremena karta Bugerovih anomalija zasnovana na novim gravimetrijskim merenjima. U radu se predstavlja preliminarna karta dobijena iz 3589 tačaka sa izravnatim vrednostima ubrzanja sile teže (detaljni premer i reperi nivelmana NVT3, 2020), oslonjenih na osnovnu gravimetrijsku mrežu i četiri apsolutne stanice. Opisan je kompletan postupak: transformacija iz državnog sistema (Gaus-Kriger zona 6, Bessel 1841) u ETRS89, određivanje ortometrijskih visina, redukcija ubrzanja i računanje kompletne Bugerove anomalije, te eliminacija grubih grešaka (poređenje sa SRTM i test prostorne saglasnosti). Posle kontrole kvaliteta zadržano je 3478 tačaka; kompletna Bugerova anomalija kreće se od −83 do +40 mGal i interpolovana je metodom običnog kriginga. Rezultati pokazuju jaku negativnu anomaliju nad visokim Dinaridima i pozitivne vrednosti u severozapadnim nizijama, kao i lokalno na krajnjem jugu (oblast Trebinja).

*Ključne reči: Bugerove anomalije; gravimetrija; Republika Srpska; ETRS89 transformacija; kvazigeoid; eliminacija grešaka*

[1] Assoc. Prof. Dr, University of Belgrade, Faculty of Civil Engineering, Department of Geodesy and Geoinformatics, Belgrade, Serbia, odalovic@grf.bg.ac.rs, ORCID 0000-0001-6004-824X
[2] Research Associate, PhD, University of Belgrade, Faculty of Civil Engineering, Department of Geodesy and Geoinformatics, Belgrade, Serbia, stankovic.d.marko@gmail.com, ORCID 0000-0003-2471-0026
[3] Assist. Prof. Dr, University of Banja Luka, Faculty of Architecture, Civil Engineering and Geodesy, Geodesy Study Programme, Banja Luka, Republic of Srpska, Bosnia and Herzegovina, dejan.vasic@aggf.unibl.org, ORCID 0009-0006-9586-729X
[4] Assist. Prof. Dr, University of Belgrade, Faculty of Civil Engineering, Department of Geodesy and Geoinformatics, Belgrade, Serbia, sanjag@grf.bg.ac.rs, ORCID 0000-0002-2533-1100
[5] Teaching Assistant, MSc, University of Belgrade, Faculty of Civil Engineering, Department of Geodesy and Geoinformatics, Belgrade, Serbia, skrstic@grf.bg.ac.rs, ORCID 0009-0000-2513-7386

## 1. INTRODUCTION

The Earth's gravity field reflects the distribution of masses within the planet, and its measurement and careful reduction is a cornerstone of both geodesy and applied geophysics. Among the quantities derived from gravity observations, the Bouguer anomaly is one of the most widely used, because it isolates the gravitational signal of subsurface density variations from the much larger and well-understood effects of geographic latitude, station elevation and the surrounding topography. A map of the Bouguer anomaly therefore provides a direct, although non-unique, image of the density structure of the crust and upper mantle, and is at the same time an essential intermediate product in regional gravity-field and (quasi)geoid modelling.

The Bouguer anomaly is formed by subtracting the normal (theoretical) gravity of a reference ellipsoid from the observed gravity and applying a sequence of corrections that account for the position of the station and the masses around it. The atmospheric correction removes the attraction of the air masses; the free-air correction accounts for the elevation of the station above the reference surface; the Bouguer-plate correction removes the attraction of the slab of rock between the station and that surface, evaluated for a standard crustal density of 2670 kg $m^{-3}$; and the terrain correction accounts for the departure of the real topography from the idealised plate. When only the terrain correction is omitted, the result is the simple Bouguer anomaly; when the terrain correction, including the effect of the surrounding relief, is added as well, the result is the complete Bouguer anomaly, which is the quantity of primary geophysical interest [1,2].

Because the dominant latitude, elevation and topographic effects have been removed, the complete Bouguer anomaly reflects lateral variations of density at depth. Broad negative anomalies are characteristically associated with thickened, low-density crust beneath mountain belts (crustal roots) and with thick, low-density sedimentary fills, whereas positive anomalies indicate denser or shallower basement, crustal thinning, or near-surface mafic bodies. Bouguer anomaly maps are accordingly a primary tool for regional geological and tectonic interpretation, for studies of crustal thickness and isostasy, and for sedimentary-basin and mineral exploration; a recent regional example is the recalculation of the Bouguer anomaly map of neighbouring Slovenia from modern data [3].

For the territory of the Republic of Srpska (Bosnia and Herzegovina) a contemporary Bouguer anomaly map based on modern gravimetric data has not been available; existing regional depictions rely on older surveys of the former Yugoslavia. In the period 2013–2020 a coherent set of campaigns established an absolute gravity datum, a fundamental gravimetric network and a dense detailed survey, providing for the first time the data required to compute such a map [4,5,6].

The methodology follows recent unified standards for gravity reduction [1]; the processing strategy is comparable to the recent recalculation for neighbouring Slovenia [3], but the present study is based on an independent data set for the Republic of Srpska. The paper documents the full processing chain – coordinate transformation, orthometric heights, gravity reduction and gross-error elimination, summarised in a workflow diagram (Fig. 4) – and presents the resulting complete Bouguer anomaly map.

## 2. MATHEMATICAL BACKGROUND

The processing chain rests on a small set of standard relations of physical geodesy, which are recalled in this section before their application to the data of the Republic of Srpska, with the estimated parameters and adopted thresholds, is described in Section 4.

The starting point is the coordinate transformation, since the gravity reduction must be referred to the geodetic latitude on the GRS80 ellipsoid.
The archived plane coordinates (Gauss–Krüger zone 6, Bessel 1841; central meridian 18°E, k0 = 0.9999, false easting 6 500 000 m) are inverse-projected to Bessel geodetic coordinates, converted to Cartesian coordinates and transformed to ETRS89 (GRS80) by a seven-parameter Helmert transformation (Position Vector convention), Eq. (1):

$$\begin{aligned} X_T &= t_x + (1+ds)(X - r_z Y + r_y Z), \\ Y_T &= t_y + (1+ds)(r_z X + Y - r_x Z), \\ Z_T &= t_z + (1+ds)(-r_y X + r_x Y + Z), \end{aligned} \tag{1}$$

where $(X, Y, Z)$ and $(X_T, Y_T, Z_T)$ are the Cartesian coordinates of a point on the Bessel and on the ETRS89 (GRS80) datum, respectively; $t_x$, $t_y$, $t_z$ are the three translations (m); $r_x$, $r_y$, $r_z$ the three rotation angles (rad); and $ds$ the scale difference (dimensionless). The estimation and application of the transformation are described in Section 4.
The Bouguer reduction refers gravity to physical (orthometric) heights; the orthometric height is obtained from the ellipsoidal height and the geoid undulation, Eq. (2):

$$H = h - N, \tag{2}$$

where $H$ is the orthometric height (m), $h$ the ellipsoidal height in ETRS89 (m), and $N$ the geoid undulation (m). In the following, $H \equiv H^O$ denotes the orthometric height, $H^N$ the normal height and $\zeta$ the height anomaly; the determination of $N$ (and of $\zeta$) from the available models is described in Section 4.
Normal gravity on the GRS80 ellipsoid is computed by the Somigliana formula, Eq. (3):

$$\gamma = \gamma_e \frac{1 + k \sin^2\varphi}{\sqrt{1 - e^2 \sin^2\varphi}}, \tag{3}$$

where $\gamma$ is normal gravity on the ellipsoid (mGal), $\gamma_e$ = 978032.67715 mGal normal gravity at the equator, $k$ = 0.00193185 the Somigliana gravity-flattening constant, $e^2$ = 0.00669438 the squared first eccentricity of GRS80, and $\varphi$ the geodetic latitude. The measured gravity is then reduced by the atmospheric, second-order free-air and simple-Bouguer corrections, Eqs (4)–(6):

$$\delta g_{ATM} = 0.874 - 9.9 \times 10^{-5} H + 3.56 \times 10^{-9} H^2, \tag{4}$$

$$\delta g_{FA} = (0.3087691 - 0.0004398 \sin^2\varphi) H - 7.2125 \times 10^{-8} H^2, \tag{5}$$

$$\delta g_B = 2\pi G \rho H, \tag{6}$$

where $\delta g_{ATM}$, $\delta g_{FA}$ and $\delta g_B$ are the atmospheric, free-air and simple-Bouguer (infinite-plate) corrections (mGal); $H$ is the orthometric height (m); $\varphi$ the geodetic latitude; $G$ the Newtonian gravitational constant; and $\rho$ = 2670 kg m$^{-3}$ the standard reduction density [1], for which the plate factor is $2\pi G\rho$ = 0.11196 mGal m$^{-1}$. The simple

Bouguer anomaly and, with the terrain correction, the complete Bouguer anomaly follow from Eqs (7) and (8):

$$\Delta g_{SB} = g - \gamma + \delta g_{ATM} + \delta g_{FA} - \delta g_{B}, \tag{7}$$

$$\Delta g_{CB} = \Delta g_{SB} + TC, \tag{8}$$

where $\Delta g_{SB}$ and $\Delta g_{CB}$ are the simple and complete Bouguer anomalies (mGal), $g$ the observed gravity (mGal), $\gamma$ the normal gravity of Eq. (3), and $TC$ the terrain correction (mGal). Here $TC$ denotes the total terrain correction, including the near, intermediate and distant topographic effects computed as described in Section 4.

## 3. AVAILABLE DATA

The study area is the territory of the Republic of Srpska, situated in the transition zone between the Pannonian Basin in the north and the high Dinarides in the south. This setting spans a broad range of crustal thicknesses and surface elevations, and therefore of gravity values, which is precisely what makes a homogeneous Bouguer anomaly map informative here. All archived coordinates are given in the State (national) Coordinate System (DKS), a Gauss–Krüger projection (zone 6, central meridian 18°E) on the Bessel 1841 ellipsoid; in the field the points were positioned by RTK-GNSS, yielding three-dimensional coordinates in ETRS89, which were transformed to Bessel 1841 and archived in the DKS as projected horizontal coordinates together with the Bessel ellipsoidal height; for this study the complete three-dimensional positions, including the ellipsoidal heights, are recovered and transformed back to ETRS89 (Section 4). Gravity is expressed in the IGSN71 system [7].

The gravimetric basis was established between 2013 and 2020 in a coherent sequence of campaigns that, for the first time, replaced the older Potsdam-based gravity level (affected by a systematic error of the order of 14 mGal) with a modern absolute realisation. The absolute level is fixed by four absolute stations (Banja Luka/Gomionica and Bijeljina/Tavna in the Republic of Srpska, and Sarajevo and Mostar in the Federation), observed in 2013 with a Micro-g LaCoste FG5 #233 ballistic gravimeter. The adopted standard uncertainties are 2 μGal to 4 μGal, and the solid-Earth tide, ocean loading, polar motion and atmospheric effects were removed with the standard models during processing [4].

Relative to these absolute stations, the fundamental gravimetric network (OGM) of Bosnia and Herzegovina was established in 2014. It comprises 60 points, of which 30 lie in the Republic of Srpska, observed with a Scintrex CG-5 relative gravimeter as a system of 45 closed loops and adjusted by least squares; the adjustment achieved a standard deviation of unit weight of 0.009 mGal, corresponding to a per-point standard error of about 0.011 mGal [5]. The network is consistent with the IGSN71 system to within its uncertainty and constitutes the reference frame to which the subsequent detailed survey is tied.

The detailed gravimetric survey carried out in 2020 densified this framework over the third-order high-precision levelling benchmarks (NVT3) and the spatial reference points (DGP). Two Scintrex CG-5 gravimeters were employed, each point being positioned by RTK-GNSS. The relative observations on the NVT3 benchmarks were adjusted by least squares, tied to the OGM and to the border NVT3 benchmarks of the Federation, while the gravity of the DGP points was transferred from points with adjusted gravity values; the mean errors of the resulting gravity remain below about 50 μGal for 90 % of the points [6]. This survey provides the bulk of the data used here: the initial set comprises

3589 points with gravity values, 2319 of them on NVT3 benchmarks and 1270 on DGP points [6]. After the quality control described in Section 4, 3478 points remain (2261 NVT3 and 1217 DGP); their distribution, which largely follows the national levelling and reference networks and covers the territory with a density adequate for a regional map, is shown in Fig. 1.

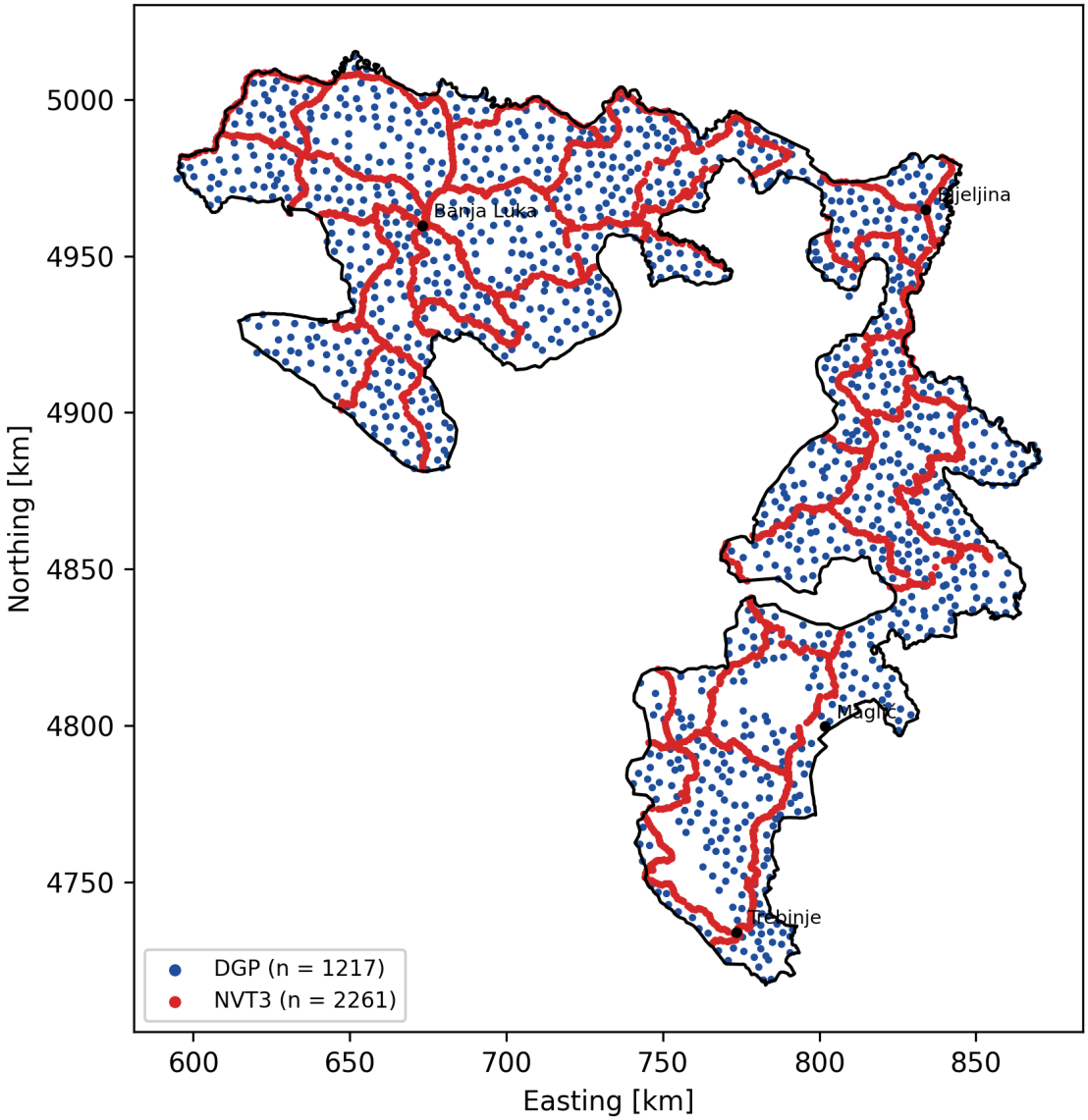


*Fig. 1 Distribution of the 3478 quality-controlled gravimetric points, ETRS89 / UTM zone 33N: the red points are the NVT3 levelling benchmarks (2261), which follow the levelling routes, and the remaining points are the DGP stations (1217); the black line is the boundary of the Republic of Srpska.*

## 4. METHODS

This section applies the relations of Section 2 to the data of Section 3. First, the seven-parameter transformation of Eq. (1) was applied in the Position Vector convention; its parameters were estimated by least squares from 3977 identical (trigonometric and polygonometric) points, with an a posteriori standard deviation of unit weight of $\sigma_0$ = 0.68 m. This value most likely reflects, at least in part, non-modelled local distortions of the older network rather than only observational noise, and is small enough that its effect on the gravity reduction is negligible. At an independent control point the result

agrees, at the centimetre level, with the official EPSG transformation 'MGI 1901 → ETRS89' for the Balkans [8], which provides an additional independent check of the transformation accuracy for the present regional purpose.

The ellipsoidal heights (ETRS89) so obtained were then reduced to physical heights, both height systems being determined. The height anomaly $\zeta$ was interpolated bilinearly from the EGG2015 quasigeoid [9] ($\zeta$ = 41.4 m to 47.2 m, mean 45.7 m), giving the normal height $H^N = h - \zeta$. The orthometric height $H = h - N$ was obtained from the geoid undulation $N = \zeta + (N - \zeta)$, the geoid–quasigeoid separation $N - \zeta$ (up to 13.5 cm in the high Dinarides) being taken from the EGG97 geoid and quasigeoid models [10] (supplementary procedure); the determination of both heights is summarised in Fig. 2. This combination of the EGG2015 height anomaly with the EGG97 geoid–quasigeoid separation is a pragmatic procedure adopted for the present preliminary map; it is not a substitute for an official national (quasi)geoid and official levelling heights, but is justified here because its effect on the complete Bouguer anomaly is negligible relative to both the anomaly signal and the interpolation error (Section 6).

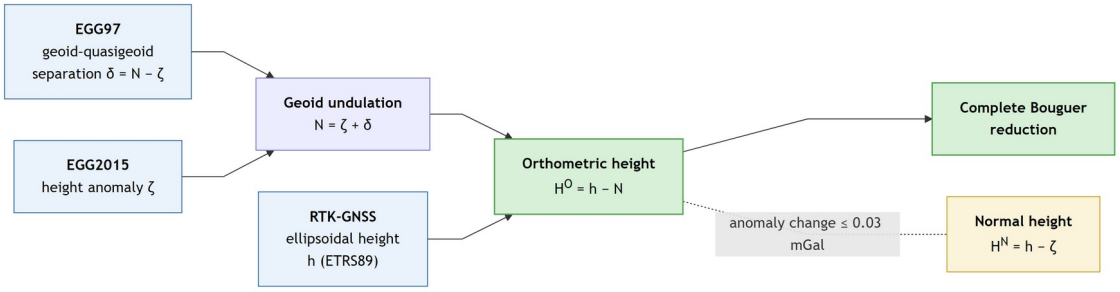


*Fig. 2 Determination of the orthometric height (and, for comparison, the normal height) used in the Bouguer reduction.*

The complete Bouguer anomaly is referred to the orthometric height; using the normal height instead changes it by at most 0.03 mGal (Section 6). The 3D fit of the transformation, with no evident geoid-like systematic component in the residuals, supports the interpretation that the input heights are ellipsoidal.

The measured gravity was then reduced with Eqs (3)–(8). The terrain correction was computed from the void-filled SRTM 1-arc-second (≈ 30 m) digital elevation model [11] (a reflective-surface model whose heights are referred to the EGM96 geoid and which is not corrected for vegetation or buildings) by rectangular-prism integration [12], using the same reduction density $\rho$ = 2670 kg m$^{-3}$ as the Bouguer plate. The near and intermediate relief was integrated out to 20 km and the distant relief out to a radius of 167 km; relief beyond the national boundary was included, so that the correction is not truncated at the border. The effect of the distant topographic masses was evaluated with an exact closed-form formula that accounts for the Earth's curvature [13]. The resulting anomaly is therefore the complete Bouguer anomaly. The same SRTM model was also used below for the height-based quality control, where it does not constitute an independent height reference.

Two complementary gross-error procedures were then applied. First, the orthometric height of each point was compared with the SRTM digital elevation model through the difference of Eq. (9):

$$d\,h = H - H_{SRTM}, \tag{9}$$

where $d\,h$ is the height difference (m), $H$ the orthometric height of the gravimetric point and $H_{SRTM}$ the SRTM height at the same location (obtained by bilinear interpolation);

points with $|dh|$ > 30 m were rejected as gross errors, the comparison serving only as a coarse blunder check rather than an absolute validation of the heights. It must be emphasised that the comparison was made against SRTM, whose own reliability is a source of disagreement: its absolute vertical accuracy is of the order of several metres and is degraded over steep slopes and under vegetation (a reflective-surface model). Hence $dh$ combines errors of the gravimetric point and of the SRTM surface, and the 30 m threshold is deliberately loose.
Second, gross errors in the measured gravity itself are detected by a robust spatial-consistency test based on the residual of Eq. (10) and the robust scale of Eq. (11):

$$r_i = \Delta g_{CB,i} - median_{j \in K_i} \Delta g_{CB,j}, \tag{10}$$

$$\hat{\sigma}_{MAD} = 1.4826 \cdot median\left|r_i - median(r)\right|, \tag{11}$$

where $r_i$ is the residual of point $i$ (mGal), $\Delta g_{CB,i}$ its complete Bouguer anomaly, and the median is taken over the set $K_i$ of its $K$ = 10 nearest neighbours; $\hat{\sigma}_{MAD}$ is the robust scale estimate from the median absolute deviation, the factor 1.4826 rendering it consistent with the standard deviation of a normal distribution. A $3\sigma$ cut would remove the signal over the high Dinarides; the natural break in the $|r_i|$ distribution supports the threshold $|r_i|$ > 25 mGal, which flagged 15 isolated points. In all, the SRTM height test rejected 86 points and the spatial-consistency test a further 15; together with 10 points discarded in the preliminary screening (missing, non-positive or out-of-range heights), the initial 3589 points were reduced to the final 3478. The 15 points rejected by the spatial-consistency test are isolated by construction; the points rejected by the SRTM height test tend to lie in more rugged, higher terrain, as indicated by their higher mean elevation (643 m) relative to the retained set (510 m). The coherent regional anomaly field is thus preserved. The main steps of the processing chain are summarised in Fig. 4.

## 5. RESULTS

For the spatial representations all coordinates (points, grid and the national boundary) were projected to ETRS89 / UTM zone 33N (EPSG:25833). The 3478 complete-Bouguer-anomaly values were interpolated by ordinary kriging [14] (spherical variogram; partial sill ≈ 644 mGal², range ≈ 126 km, nugget 0) onto a 2.5 km grid and clipped to the official boundary of the Republic of Srpska (Fig. 3). For the present preliminary regional map a zero-nugget variogram was retained as a first approximation; its limitation with respect to prediction uncertainty is discussed below. The basic statistics of the reduced field are summarised in Tab. 1. A 10-fold cross-validation of the interpolation gives a negligible mean error (−0.1 mGal), a mean absolute error of 1.3 mGal and a root-mean-square error of 2.3 mGal, about one tenth of the anomaly standard deviation; because neighbouring gravity points are strongly correlated, this value should be read as a measure of the internal stability of the interpolation rather than as a fully independent external validation. The standardized residuals, however, indicate that the zero-nugget variogram substantially underestimates the prediction uncertainty, and a non-zero nugget will be tested in future work (Section 6).

*Tab. 1 Statistics of the complete and simple Bouguer anomalies and the terrain correction over the 3478 points (mGal).*

| Quantity | min | max | mean | std |
|---|---|---|---|---|
| Complete Bouguer anomaly | −83.2 | +39.7 | −16.2 | 23.1 |

| | | | | |
|---|---|---|---|---|
| Simple Bouguer anomaly | −109.8 | +35.3 | −19.5 | 25.0 |
| Terrain correction | 0.0 | +29.9 | 3.3 | 3.3 |

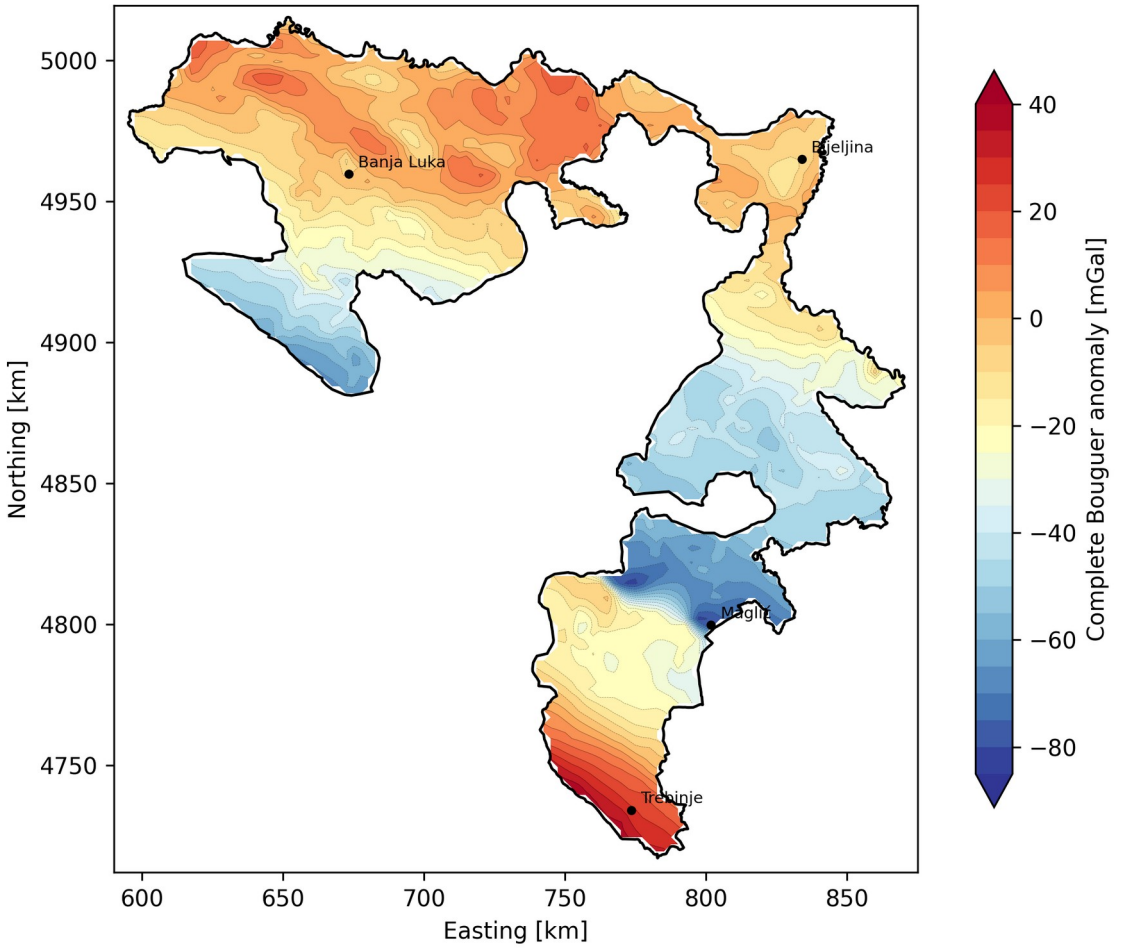


*Fig. 3 Complete Bouguer anomaly map of the Republic of Srpska (ordinary kriging; ETRS89 / UTM zone 33N).*

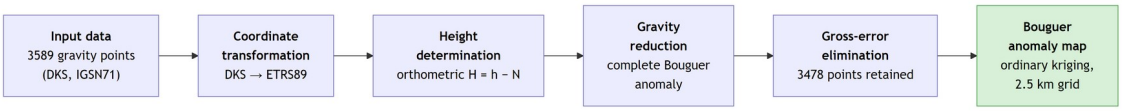


*Fig. 4 Main steps of the processing chain.*

The map shows a pronounced negative anomaly (down to about −80 mGal) over the high Dinarides in the south-east (Maglić/Sutjeska), and positive values in the north-western lowlands as well as a distinct positive zone in the southernmost part of the territory, around Trebinje (the overall maximum, about +40 mGal). The strong negative level over the central-southern mountains is consistent with thickened crust beneath the Dinarides.

## 6. DISCUSSION

To the authors' knowledge this is the first complete Bouguer anomaly map of the Republic of Srpska based on modern gravimetric data, modern reduction standards and a homogeneous, quality-controlled data set. The resulting field is geophysically coherent and reflects the first-order crustal structure of the area. The pronounced negative anomaly over the high Dinarides in the south-east, reaching about −80 mGal, is consistent with a thickened, low-density crustal root that isostatically compensates the

topography of the orogen, in line with the deep crust–mantle boundary inferred for the Dinaric belt [15]. Towards the north-west the anomaly rises to positive values (up to about +35 mGal) over the lowlands, where the positive regional field is compatible with thinner crust and a shallower mantle at the margin of the Pannonian Basin, although the sedimentary fill may locally reduce the anomaly. A second, more local positive zone is visible in the far south, around Trebinje (where the overall maximum, about +40 mGal, is reached); it is compatible with crustal thinning towards the Adriatic and with the high-density carbonates of the external Dinarides, but the sparse data coverage there warrants caution in its interpretation. The smooth, regionally consistent gradient between the main domains suggests that the data set is internally homogeneous and does not show obvious large datum offsets between the contributing campaigns.

Several methodological aspects nevertheless deserve comment. A single reduction density of 2670 kg $m^{-3}$ was adopted throughout, following the unified standards [1]; although appropriate for a regional first approximation, it does not capture the lateral and vertical density variations of the heterogeneous Dinaric and Pannonian geology, and in high, rugged terrain an unrepresentative density can introduce a spurious correlation between the anomaly and elevation. A regionally adjusted or Nettleton-type reduction density is left to future work.

The reliability of the SRTM model, used both for the terrain correction and for the height-based quality control, is a further limitation. Because SRTM is a global reflective-surface model with a vertical accuracy of several metres that degrades in mountainous, vegetated terrain, part of the observed height differences originates from the model rather than from the gravimetric points; the height comparison is therefore used only to flag coarse blunders, not to correct heights. Moreover, SRTM is not an independent national height control, so it cannot validate the gravimetric heights in an absolute sense but only reveal gross inconsistencies, which weakens the height-based quality control precisely in the mountainous, forested terrain where the map is least constrained. A national bare-earth digital terrain model is recommended for future work, for both the terrain correction and the height check.

The height reduction relies on the public EGG2015 quasigeoid (10′×15′), which is coarse; because the (quasi)geoid is smooth, however, its effect on the derived heights is small ($\lesssim 0.04$ mGal in the anomaly), and a higher-resolution or national model would be preferable mainly for completeness. The Bouguer anomaly is classically referred to orthometric heights (geoid undulation $N$), as adopted here; the corresponding normal heights (quasigeoid height anomaly $\zeta$) were also determined, and, assessed independently from the EGG97 geoid–quasigeoid separation, the two height surfaces differ by up to 13.5 cm (mean 3 cm) in the high Dinarides, changing the complete Bouguer anomaly by at most 0.03 mGal (mean 0.006 mGal) – negligible relative to the data accuracy and the anomaly signal.

It is useful to summarise the error budget. The observed gravity is the most accurate component: the absolute stations carry uncertainties of 2 µGal to 4 µGal, the adjustment of the OGM a standard deviation of unit weight of 0.009 mGal, and the gravity of the detailed-survey points is accurate to about 0.05 mGal, so the gravimetric contribution to the anomaly remains negligible compared with the terrain-correction and interpolation errors. The height enters through the combined free-air and plate gradient of 0.1967 mGal $m^{-1}$; with RTK-GNSS ellipsoidal heights (centimetre level) and the EGG2015 height anomaly (decimetre level) the height-induced error stays below about 0.05 mGal, and the geoid–quasigeoid choice adds at most 0.03 mGal. By far the largest point-level contribution is the terrain correction: derived from the reflective-surface SRTM model, its error grows with slope and vegetation and may reach one to a few mGal in the rugged high Dinarides, while remaining sub-mGal in the lowlands. At the level of the interpolated map the dominant uncertainty is the interpolation, with a cross-validation

RMSE of 2.3 mGal. At the regional scale resolved by the available data, the interpolated field is therefore expected to be accurate at the level of approximately 2 mGal to 3 mGal, whereas larger local and systematic errors may occur in the steep, forested south-eastern terrain because of the SRTM-based terrain correction.

In the quality control, the spatial-consistency test was deliberately tuned to separate isolated blunders from the coherent strong-negative anomaly of the high Dinarides, which is retained as a coherent regional signal consistent with a crustal-root interpretation, rather than discarded as an outlier pattern. Finally, the map is an interpolated product: ordinary kriging with a single global variogram was applied, so the reliability of the surface decreases where the data are sparse, notably in the highest, least accessible parts of the Dinarides and along the state border, where edge effects are unavoidable. The 2.5 km grid resolves the regional field but not short-wavelength, near-surface sources; a denser interpolation with a locally adapted variogram would sharpen the map where the data permit. The cross-validation root-mean-square error (2.3 mGal) quantifies the interpolation error, whereas the standardized residuals show that the zero-nugget assumption is over-optimistic for the prediction variance; a non-zero nugget, absorbing the measurement, height and terrain-correction errors, should be adopted in future work.

## 7. CONCLUSION

A preliminary complete Bouguer anomaly map of the Republic of Srpska has been produced from a homogeneous, modern data set of 3478 quality-controlled points, drawn from the absolute, fundamental and detailed gravimetric campaigns of 2013–2020. The full processing chain – coordinate transformation, orthometric heights, gravity reduction and a two-stage gross-error elimination – was documented and summarised in a workflow diagram.

The resulting complete Bouguer anomaly ranges from about −83 to +40 mGal and is geophysically consistent: it shows a strong negative anomaly over the high Dinarides, consistent with a thickened crustal root beneath the Dinaric orogen, and positive values over the north-western lowlands at the margin of the Pannonian Basin as well as locally in the far south, around Trebinje. To the authors' knowledge it is the first such map for the territory based on modern data and unified reduction standards, and it provides a coherent regional reference both for geological and tectonic interpretation and as an intermediate product for future gravity-field and (quasi)geoid modelling. Detailed local interpretation, however, should await a denser terrain model, a verification of the reduction density and a locally adapted interpolation.

Being preliminary, the map is intended as the basis for a subsequent detailed study. Future work will refine the terrain correction with a higher-resolution national bare-earth digital terrain model, adopt a higher-resolution or national (quasi)geoid together with official levelling heights, re-examine the reduction density (a regionally adjusted or Nettleton-type value), and extend the analysis to ellipsoidal gravity anomalies and the indirect effect, with a denser, locally adapted interpolation. A quantitative comparison with neighbouring regional data sets is also envisaged.

**ACKNOWLEDGEMENT**

The authors acknowledge the gravimetric data made available by the Republic Administration for Geodetic and Property Affairs of Republika Srpska (RGURS), and the contribution of the CILAP project.

## 8. REFERENCES

[1] Hinze W.J., Aiken C., Brozena J. et al. (2005). New standards for reducing gravity data: the North American gravity database. Geophysics 70(4), J25–J32. https://doi.org/10.1190/1.1988183

[2] Hackney R.I., Featherstone W.E. (2003). Geodetic versus geophysical perspectives of the 'gravity anomaly'. Geophysical Journal International 154(1), 35–43. https://doi.org/10.1046/j.1365-246X.2003.01941.x

[3] Medved K., Odalović O., Koler B. (2021). New Bouguer Anomaly Map for the Territory of the Slovenia. Remote Sensing 13(22), 4510. https://doi.org/10.3390/rs13224510

[4] Engfeldt A., Ågren J., Zimić S. (2013). Absolute gravity campaign in Bosnia and Herzegovina (CILAP), Report BAL1-4-2, Lantmäteriet, Sweden.

[5] Starčević M. (2014). Fundamental gravimetric network of the Republic of Srpska and FBiH – final report, Report BAL1_4-4.

[6] Starčević M. (2021). Corrected final report on gravimetric measurements in the Republic of Srpska, VEKOM Geo, Belgrade.

[7] Morelli C., Gantar C., Honkasalo T. et al. (1974). The International Gravity Standardization Net 1971 (IGSN71). International Association of Geodesy, Special Publication No. 4, Paris.

[8] IOGP (2024). EPSG Geodetic Parameter Dataset. International Association of Oil & Gas Producers, Geomatics Committee. https://epsg.org

[9] Denker H. (2015). A new European gravimetric (quasi)geoid EGG2015. XXVI IUGG General Assembly, Prague; Institut für Erdmessung, Leibniz University Hannover.

[10] Denker H., Torge W. (1998). The European Gravimetric Quasigeoid EGG97 – An IAG Supported Continental Enterprise. In: Forsberg R., Feissel M., Dietrich R. (eds), Geodesy on the Move, IAG Symposia vol. 119, Springer, Berlin. https://doi.org/10.1007/978-3-642-72245-5_36

[11] Farr T.G., Rosen P.A., Caro E. et al. (2007). The Shuttle Radar Topography Mission. Reviews of Geophysics 45, RG2004. https://doi.org/10.1029/2005RG000183

[12] Forsberg R. (1984). A Study of Terrain Reductions, Density Anomalies and Geophysical Inversion Methods in Gravity Field Modelling. Report No. 355, Department of Geodetic Science and Surveying, Ohio State University, Columbus.

[13] Mikuška J., Pašteka R., Marušiak I. (2006). Estimation of distant relief effect in gravimetry. Geophysics 71(6), J59–J69. https://doi.org/10.1190/1.2338333

[14] Oliver M.A., Webster R. (1990). Kriging: a method of interpolation for geographical information systems. International Journal of Geographical Information Systems 4(3), 313–332. https://doi.org/10.1080/02693799008941549

[15] Grad M., Tiira T., ESC Working Group (2009). The Moho depth map of the European Plate. Geophysical Journal International 176(1), 279–292. https://doi.org/10.1111/j.1365-246X.2008.03919.x

https://doi.org/10.24867/INDIS-2026-EN-815



# MULTI-SOURCE ASSESSMENT OF CADASTRAL PARCEL POSITIONAL ACCURACY USING GNSS SURVEYS AND ORTHOPHOTO DATA: A CASE STUDY FROM HIMARA, ALBANIA

*Eduart Blloshmi*[1], *Bledar Sina*[2], *Arli Llabani*[3]

***Summary:***

Reliable cadastral information forms the foundation of effective land administration, supporting property registration, spatial planning, infrastructure development, and legal security. The positional quality of cadastral boundaries directly influences the reliability of land-related decisions and the efficiency of cadastral management systems. This study evaluates the positional consistency of cadastral parcel boundaries in the municipality of Himara, Albania, through the comparison of three independent geospatial data sources: official cadastral records provided by the State Cadastre Agency (ASHK), orthophotos acquired in 2007 and 2015, and high-precision GNSS field observations.

GNSS measurements collected using the ALBCORS permanent reference station network were considered as the reference dataset for the analysis. Coordinates extracted from cadastral datasets and orthophoto imagery were compared with the field observations to quantify positional deviations and evaluate their spatial agreement. Statistical indicators, including coordinate differences in the northing and easting components together with horizontal positional discrepancies, were computed for all surveyed parcel corner points.

The obtained results demonstrate that GNSS observations provide the highest positional reliability, while noticeable differences exist between official cadastral data and historical orthophoto datasets. The 2015 orthophoto exhibits substantially better agreement with the field measurements than the 2007 imagery, reflecting improvements in data acquisition and processing techniques. The analysis also reveals that although the official cadastral database provides an adequate representation for many land administration tasks, centimetre-level boundary definition should rely on direct geodetic surveys.

The findings contribute to the evaluation of cadastral data quality in Albania and provide practical recommendations for improving future cadastral updating procedures through the integration of modern GNSS surveying techniques with geospatial reference datasets.

*Keywords: Cadastral Accuracy, GNSS Surveying, ALBCORS, Orthophoto, Spatial Quality Assessment*

[1] PhD, Lecturer, Faculty of Civil Engineering, Polytechnic University of Tirana, Tirana, Albania, eduart.blloshmi@fin.edu.al
[2] PhD, Lecturer, Faculty of Civil Engineering, Polytechnic University of Tirana, Tirana, Albania, bledar.sina@fin.edu.al
[3] PhD, Lecturer, Faculty of Civil Engineering, Polytechnic University of Tirana, Tirana, Albania, arli.llabani@fin.edu.al

# VIŠEIZVORNA PROCENA TAČNOSTI POLOŽAJA KATASTARSKIH PARCELA KORIŠĆENJEM GNSS MERENJA I ORTOFOTO PODATAKA: STUDIJA SLUČAJA IZ HIMARE, ALBANIJA

***Rezime:***

Pouzdane katastarske informacije čine osnovu efikasne administracije zemljišta, podržavajući registraciju imovine, prostorno planiranje, razvoj infrastrukture i pravnu sigurnost. Položajni kvalitet katastarskih granica direktno utiče na pouzdanost odluka vezanih za zemljište i efikasnost sistema katastarskog upravljanja. Ova studija procenjuje položajnu konzistentnost granica katastarskih parcela u opštini Himara, Albanija, kroz poređenje tri nezavisna geoprostorna izvora podataka: zvaničnih katastarskih evidencija koje je obezbedila Državna katastarska agencija (ASHK), ortofoto snimaka dobijenih 2007. i 2015. godine i terenskih visokopreciznih GNSS merenja. GNSS merenja prikupljena korišćenjem mreže permanentnih stanica ALBCORS razmatrana su kao referentni skup podataka za analizu. Koordinate dobijene iz katastarskih skupova podataka i ortofoto snimaka upoređene su sa terenskim merenjima kako bi se kvantifikovala položajna odstupanja i ocenila njihova prostorna saglasnost. Statistički indikatori, uključujući razlike položajnih koordinata, sračunati su za sve snimljene ugaone tačke parcela. Dobijeni rezultati pokazuju da GNSS merenja pružaju najveću položajnu pouzdanost, dok postoje primetne razlike između zvaničnih katastarskih podataka i istorijskih ortofoto skupova podataka. Ortofoto iz 2015. godine pokazuje znatno bolje slaganje sa terenskim merenjima nego snimci iz 2007. godine, što odražava poboljšanja u tehnikama prikupljanja i obrade podataka. Analiza takođe otkriva da, iako zvanična katastarska baza podataka pruža adekvatnu prezentaciju za mnoge zadatke upravljanja zemljištem, definicija granica na centimetarskom nivou treba da se oslanja na direktna geodetska merenja. Istraživanja doprinose proceni kvaliteta katastarskih podataka u Albaniji i pružaju praktične preporuke za poboljšanje budućih procedura ažuriranja katastarskog stanja kroz integraciju modernih GNSS tehnika merenja sa geoprostornim referentnim skupovima podataka.

*Ključne reči: Katastarska tačnost, GNSS premer, ALBCORS, ortofoto, procena prostornog kvaliteta*

## 1. INTRODUCTION

Accurate geospatial information represents one of the fundamental components of modern land administration systems. Reliable cadastral data support a wide range of activities, including property registration, taxation, urban planning, infrastructure development, environmental management, and legal protection of ownership rights. As countries continue their transition toward digital cadastres and integrated land information systems, the positional accuracy of cadastral boundaries has become increasingly important for ensuring the credibility and long-term sustainability of cadastral databases.

In recent decades, rapid developments in geospatial technologies have significantly improved the methods available for cadastral surveying and mapping. High-precision Global Navigation Satellite Systems (GNSS), continuously operating reference station (CORS) networks, digital orthophotos, unmanned aerial systems (UAS), terrestrial laser scanning, and Geographic Information Systems (GIS) have transformed the way cadastral information is collected, validated, and updated. These technologies provide opportunities not only to acquire more accurate spatial data but also to assess the quality of existing cadastral records that were produced using older surveying techniques.

Although official cadastral databases remain the primary legal source of property boundary information, many cadastral maps have been compiled over different periods using various surveying standards, coordinate systems, and mapping methodologies. Consequently, differences may occur between archived cadastral records and present-day field measurements. Such discrepancies become particularly evident in areas experiencing intensive urban expansion, infrastructure development, or historical modifications of parcel boundaries. Evaluating these positional inconsistencies is therefore essential for improving cadastral quality and supporting future updating processes.

Orthophoto imagery has become an indispensable geospatial product for land administration because it provides geometrically corrected aerial photographs that accurately represent ground features within a defined coordinate reference system. Historical orthophotos additionally enable the investigation of temporal changes in land use and parcel configuration, allowing cadastral information to be evaluated across different acquisition periods. Nevertheless, despite their high spatial resolution, orthophotos should not be considered a substitute for direct geodetic observations when centimetre-level positional accuracy is required.

GNSS surveying currently represents one of the most reliable techniques for determining precise coordinates of cadastral boundary points. The availability of permanent reference station networks such as the Albanian Active Geodetic Reference Network (ALBCORS) enables surveyors to perform centimetre-level positioning through Real-Time Kinematic (RTK) observations and post-processing methods. These capabilities make GNSS measurements an appropriate reference for validating the positional quality of existing cadastral datasets and detecting potential geometric inconsistencies.

The municipality of Himara, located along the southern Albanian coastline, represents an appropriate study area due to its complex topography, increasing tourism-related development, and growing demand for accurate cadastral information. Continuous investment in residential construction, transportation infrastructure, and land management activities requires cadastral datasets that accurately reflect the real position of property boundaries. Consequently, evaluating the positional agreement between official cadastral records and modern geospatial observations is of considerable practical importance.

The present research investigates the positional accuracy of cadastral parcel boundaries by integrating information derived from official cadastral records maintained by the State Cadastre Agency (ASHK), orthophoto datasets produced in 2007 and 2015, and high-precision GNSS observations acquired in the field. Coordinate differences between these datasets are quantified through comparative statistical analysis in order to determine their level of spatial agreement and identify potential positional deviations.

Unlike studies that focus exclusively on a single source of geospatial information, this research adopts a multi-source validation approach in which independent datasets are evaluated simultaneously against precise GNSS observations. This methodology provides a comprehensive understanding of the positional quality of cadastral information and highlights the relative performance of each dataset.

The outcomes of this study provide useful information for cadastral authorities, surveyors, urban planners, and land administration professionals involved in maintaining and modernising cadastral databases. Furthermore, the obtained results contribute to ongoing efforts aimed at improving the spatial quality of Albania's cadastral system and support future initiatives related to digital cadastre, spatial data infrastructure, and sustainable land management.

## 2. MATERIALS AND METHODS

### 2.1. STUDY AREA

The investigation was carried out in the municipality of Himara, situated along the southern Adriatic-Ionian coastline of Albania within Vlora County. The area has experienced continuous urban expansion and increasing tourism-related development during the last two decades, creating a growing demand for reliable cadastral information and accurate property boundary definition.



*Fig. 1 Aerial photography of the selected urban area*

The selected test site contains residential, commercial and public parcels that represent different cadastral configurations and land-use characteristics. Its diverse topography, combined with the existence of historical cadastral records and multi-temporal orthophoto datasets, makes Himara an appropriate location for evaluating the positional consistency of cadastral information derived from different geospatial sources.

A total of twenty cadastral boundary points distributed throughout the study area were selected for detailed analysis. These points were chosen because they could be clearly identified in all available datasets, allowing direct coordinate comparison.

## 2.2. GEOSPATIAL DATASETS

The positional assessment was based on four independent datasets representing different periods and surveying methodologies:

- Official cadastral information maintained by the Albanian State Cadastre Agency (ASHK);
- Orthophoto imagery produced in 2007;
- Orthophoto imagery produced in 2015;
- High-precision GNSS observations collected during field surveys.

Each dataset represents a different stage in the evolution of cadastral information and provides valuable insight into the positional quality of cadastral parcel boundaries. Their integration enables a comprehensive evaluation of spatial consistency.

## 2.3. GNSS SURVEY AND EQUIPMENT

Field observations were performed using a Sokkia GRX2 dual-frequency GNSS receiver, capable of centimetre-level positioning under both real-time and post-processing surveying modes [1].

The receiver was employed to determine the precise coordinates of selected cadastral corner points, which were considered the reference observations throughout the analysis. Appropriate satellite visibility and favourable observation conditions were ensured during the survey campaign in order to minimise positioning errors.

The resulting GNSS coordinates constitute the benchmark against which all remaining datasets were evaluated.



*Fig. 2 GNSS Sokkia GRX2*

## 2.4. ALBCORS REFERENCE NETWORK

Positioning was referenced to the Albanian Active Geodetic Reference Network (ALBCORS), the national Continuously Operating Reference Station (CORS) infrastructure established within the European Terrestrial Reference System 1989 (ETRS89).
ALBCORS provides nationwide geodetic coverage through a network of permanent stations and enables both RTK positioning and static GNSS post-processing. Under favourable observation conditions, the network provides horizontal accuracies of approximately ±2 cm for RTK surveys and approximately ±1 cm when post-processing techniques are applied [2].
The availability of this infrastructure ensures homogeneous positioning throughout Albania and guarantees compatibility with the national geodetic reference framework.




*Fig. 3 State Active Global Positioning Network, ALBCORS*

## 2.5. PROCESSING OF GNSS OBSERVATIONS

Raw satellite observations were processed using Trimble Business Center (TBC) version 5.2. Data from the nearest ALBCORS reference stations, including Vlora, Himara and Saranda, were incorporated during post-processing to maximise positional reliability.
Following quality control procedures, adjusted coordinates were generated for each surveyed point. These coordinates served as the reference dataset for all subsequent comparisons performed in this study [3].

## 2.6. COORDINATE REFERENCE SYSTEM

To ensure direct comparison among all available datasets, every coordinate was transformed into a common mapping reference system.

The adopted projection parameters were:

- Projection: Universal Transverse Mercator (UTM);
- Zone: 34 North;
- Reference ellipsoid: WGS84;
- Linear unit: metre;
- Scale factor: 0.9996;
- Central meridian: 21°E;
- False Easting: 500000 m;
- False Northing: 0 m.

Coordinate transformation parameters correspond to the official national transformation adopted for geodetic applications in Albania, enabling compatibility between historical cadastral information, GNSS observations and orthophoto datasets.

## 2.7. COMPARATIVE ACCURACY ASSESSMENT

The positional evaluation was carried out by comparing the coordinates obtained from the different geospatial datasets. For every selected cadastral point, coordinate differences in the northing (dN) and easting (dE) components were computed, together with the resulting horizontal positional difference (dL) [4].

Several comparative analyses were performed, including:

- GNSS observations versus ALBCORS-derived coordinates;
- GNSS observations versus Orthophoto 2007;
- GNSS observations versus HTR cadastral records;
- HTR cadastral records versus Orthophoto 2007;
- GNSS observations versus Orthophoto 2015;
- Orthophoto 2015 versus Orthophoto 2007;
- HTR cadastral records versus Orthophoto 2015.

The calculated coordinate differences were subsequently analysed using descriptive statistical indicators, allowing the positional agreement and spatial consistency of each dataset to be quantified. The resulting statistics provide an objective basis for evaluating the reliability of the available cadastral information and identifying datasets that are more suitable for cadastral updating and land administration applications.

*Tab. 1 Coordinates of the transformed base*

| Point | Albcors | | Transformed State Geodetic Network | | Differences | |
|---|---|---|---|---|---|---|
| | N | E | N | E | dN | dE |
| BM-Himara | 4439836.280 | 392322.619 | 4439834.367 | 392323.043 | 0.01914 | -0.0424 |
| BM-Himara | 4439836.28 | 392322.619 | 4439836.347 | 392322.686 | -0.06641 | -0.06703 |
| BM-Himara | 4439836.323 | 392322.658 | 4439836.347 | 392322.686 | -0.0244 | -0.028 |
| BM-Himara | 4439836.323 | 392322.658 | 4439836.28 | 392322.619 | 0.043 | 0.039 |

## 3. RESULTS AND DISCUSSION

The positional quality assessment was performed using coordinate observations obtained from twenty selected cadastral boundary points distributed throughout the study area. The comparison involved independent geospatial datasets representing different acquisition periods and surveying techniques, allowing a comprehensive evaluation of positional consistency among official cadastral records, historical orthophotos and high-precision GNSS observations.

### 3.1. COMPARISON BETWEEN GNSS MEASUREMENTS AND ALBCORS COORDINATES

The first analysis evaluated the agreement between the GNSS observations and the coordinates derived from the ALBCORS reference network. As expected, the comparison revealed the highest level of positional consistency among all analysed datasets.
The coordinate differences remained below 0.15 m for every surveyed point, with maximum discrepancies of 0.096 m in the northing component, 0.135 m in the easting component and 0.149 m for the resulting horizontal distance. The calculated mean deviations ($\sigma N = 0.054$ m and $\sigma E = 0.066$ m) confirm the excellent performance of the national CORS infrastructure [5].
These findings demonstrate that ALBCORS provides a reliable geodetic reference for cadastral surveying and represents an appropriate positioning framework for centimetre-level land administration applications.

### 3.2. COMPARISON BETWEEN GNSS OBSERVATIONS AND ORTHOPHOTO 2007

The comparison with the 2007 orthophoto produced noticeably larger positional discrepancies than those observed for the ALBCORS dataset.
Horizontal differences varied considerably among the investigated points, reaching maximum values of 0.474 m in the northing direction and 0.487 m in the easting direction, while the maximum planar positional difference reached 0.770 m.
The average coordinate deviations ($\sigma N = 0.249$ m and $\sigma E = 0.540$ m) indicate that although the orthophoto provides a valuable visual representation of parcel boundaries, its positional quality is insufficient for applications requiring centimetre-level cadastral accuracy [6].
The observed discrepancies are likely associated with image rectification errors, ground control quality, image resolution and the surveying standards available at the time of orthophoto production.

### 3.3. COMPARISON BETWEEN GNSS OBSERVATIONS AND HTR CADASTRAL RECORDS

The evaluation of the HTR cadastral dataset revealed greater positional variation than both the ALBCORS and Orthophoto 2015 datasets.
Maximum coordinate differences reached 0.712 m in the northing direction and 1.413 m in the easting direction, while the largest horizontal displacement exceeded one metre (1.149 m).
These results suggest that historical cadastral information may contain local geometric inconsistencies resulting from older surveying methodologies, analogue map digitisation procedures or transformations between coordinate reference systems [7].

Despite these deviations, the majority of parcel boundaries remain reasonably consistent for general cadastral representation.

### 3.4. COMPARISON BETWEEN HTR DATA AND ORTHOPHOTO 2007

A direct comparison between the historical cadastral dataset and the 2007 orthophoto demonstrated moderate positional agreement.
Although several parcel corners coincided well, other locations exhibited horizontal discrepancies approaching 1.15 m. Such differences indicate that positional inconsistencies originate not only from the orthophoto itself but also from historical cadastral information [8].
This comparison illustrates the cumulative influence of different mapping technologies and production methods employed over several decades.

### 3.5. COMPARISON BETWEEN GNSS OBSERVATIONS AND ORTHOPHOTO 2015

Among all image-based datasets, the orthophoto produced in 2015 showed the highest positional agreement with the GNSS measurements.
Maximum coordinate differences were limited to 0.198 m in the northing component and 0.258 m in the easting component, while the maximum horizontal discrepancy reached only 0.367 m.
The corresponding average deviations ($\sigma N = 0.165$ m and $\sigma E = 0.137$ m) demonstrate a considerable improvement compared with the 2007 orthophoto [9].
These results reflect advances in aerial image acquisition, camera calibration, photogrammetric processing and georeferencing techniques that became available between the two orthophoto production campaigns.

### 3.6. COMPARISON BETWEEN ORTHOPHOTO 2007 AND ORTHOPHOTO 2015

The comparison between the two orthophoto datasets provides valuable information regarding positional consistency over time.
The maximum coordinate differences reached 0.608 m in the northing direction and 1.555 m in the easting direction, confirming that significant geometric differences exist between the two image products.
These variations may be attributed to improvements in photogrammetric processing, differences in image orientation procedures, control point distribution and data acquisition technologies rather than actual changes in parcel geometry.

### 3.7. COMPARISON BETWEEN HTR RECORDS AND ORTHOPHOTO 2015

The final comparison involved the historical cadastral records and the more recent orthophoto dataset.
Although several parcel corners presented good positional agreement, larger discrepancies were observed for individual locations, with maximum coordinate differences reaching 0.779 m and 1.040 m in the northing and easting components, respectively.
The comparison confirms that modern orthophotography provides a more accurate geometric representation of ground features than many historical cadastral datasets. Nevertheless, image-based products alone cannot replace direct geodetic measurements when legally defining parcel boundaries.

## 4. CONCLUSIONS

This study investigated the positional quality of cadastral parcel boundaries in the municipality of Himara by comparing official cadastral information with GNSS field observations and orthophoto datasets acquired in 2007 and 2015. The comparative analysis provided a comprehensive assessment of the spatial consistency among the available geospatial datasets and highlighted their suitability for cadastral applications.

The comparison between GNSS observations and ALBCORS coordinates produced the smallest positional discrepancies, confirming the high accuracy and reliability of the Albanian permanent GNSS reference network. The maximum observed differences were limited to 0.096 m in the northing component, 0.135 m in the easting component and 0.149 m in horizontal position, while the corresponding mean deviations were 0.054 m and 0.066 m, respectively. These values demonstrate that the ALBCORS infrastructure satisfies the accuracy requirements for high-precision cadastral surveying.

The analysis involving the 2007 orthophoto revealed significantly larger positional deviations. Maximum differences reached 0.474 m in northing, 0.487 m in easting and 0.770 m in horizontal displacement, with average deviations of 0.249 m and 0.540 m. These findings indicate that the older orthophoto dataset should primarily be considered a reference source for visualization and general spatial analysis rather than for precise boundary determination.

A comparison between GNSS observations and the HTR cadastral records identified the largest discrepancies among all evaluated datasets. Maximum coordinate differences of 0.712 m in northing, 1.413 m in easting and 1.149 m in horizontal distance suggest that historical cadastral information may contain geometric inconsistencies associated with older surveying methods, legacy mapping techniques and coordinate transformations.

The positional agreement between the HTR dataset and the 2007 orthophoto was found to be moderate, confirming that deviations originate from both historical cadastral documentation and the geometric quality of the orthophoto itself.

The 2015 orthophoto demonstrated substantially better agreement with the GNSS measurements than the 2007 imagery. Maximum coordinate differences were limited to 0.198 m in northing, 0.258 m in easting and 0.367 m in horizontal position, with average deviations of 0.165 m and 0.137 m. These results reflect the improvements achieved through advances in photogrammetric processing and georeferencing techniques.

The comparison between the two orthophoto datasets showed that positional differences remain evident between successive image acquisition campaigns, reaching maximum values of 0.608 m in northing and 1.555 m in easting. These variations emphasize the importance of continuously updating geospatial reference data used in cadastral activities.

Finally, the comparison between the HTR records and the 2015 orthophoto confirmed that more recent geospatial products provide improved positional representation of cadastral features, although direct geodetic observations remain indispensable whenever legal boundary definition requires centimetre-level accuracy.

## 5. RECOMMENDATIONS

Based on the obtained results, several recommendations can be proposed to improve the quality and long-term reliability of cadastral information in Albania.

First, cadastral boundary determination should increasingly rely on high-precision GNSS surveying methods supported by the ALBCORS permanent reference station network. The centimetre-level accuracy achieved through RTK observations and post-processing techniques provides a reliable basis for legal property boundary definition and cadastral updating.

Second, all future cadastral modifications, including parcel subdivision, parcel amalgamation and boundary reconstruction, should be established using accurately surveyed coordinates referenced to the national geodetic framework. Coordinate-based boundary definition reduces ambiguity and ensures greater consistency within digital cadastral databases.

Third, although digital orthophotos represent valuable geospatial products for visualization, land-use interpretation and preliminary planning, they should not be used as the primary source for determining legal parcel boundaries without supporting field surveys. Orthophotos are affected by image resolution, acquisition geometry and processing limitations that may introduce positional uncertainties.

Furthermore, continued investment in the modernization of the national cadastral system should prioritize periodic updating of geospatial datasets, integration of contemporary surveying technologies and systematic quality control procedures. Combining GNSS observations with modern photogrammetric products can significantly improve the positional integrity of cadastral records.

Finally, future cadastral development in Albania should focus on strengthening the integration between geodetic control networks, digital orthophoto databases, cadastral information systems and Geographic Information Systems (GIS). Such an integrated spatial framework would support more efficient land administration, improve data interoperability and facilitate evidence-based decision-making for sustainable territorial development.

## REFERENCES

[1] Land Research Institute's Archive, Tirana, 1996: Bulletin No. 6.

[2] Geofoto SRL, 2007: Final technical report of aerial photography.

[3] Trimble Navigation Limited, September 2003; Real Time Kinematic Surveying, Training Guide, Part Number 33142 40.

[4] Nurçe B., Thesis, 2013: Study of the development of coordinative references of Albania.

[5] Standard on Digital Cadastral Maps and Parcel Identifiers, 2015; International Association of Assessing Officers (IAAO), https://www.iaao.org/media/standards/Standard_Digital_Cadastral_Maps_2015.pdf

[6] Tamrakar, Rabindra Man, (2013), Potential Use of GPS Technology For Cadastral Surveys in Nepal, Nepalese Journal on Geoinformatics, -12, 2070 (2013AD).

[7] Veersema, Adam, (2004), RTK-GPS for Cadastral Boundary Surveying in NSW, School of Surveying and Spatial Information Systems, The university of New South Wales.

[8] Lee, I. and Ge, L., (2006), The performance of RTK-GPS for surveying under challenging environmental conditions, Earth Planets Space.

[9] Öcalan, T. and Tunalioglu, N., (2010), Data communication for real-time positioning and navigation in global navigation satellite systems (GNSS)/continuously operating reference stations (CORS) networks, Scientific Research and Essays Vol. 5(18).

https://doi.org/10.24867/INDIS-2026-EN-827



# DEVELOPMENT OF THE LOCAL GEODETIC REFERENCE NETWORK FOR THE CITY OF GRAMSH BASED ON GNSS MEASUREMENTS

*Bledar Sina*[1], *Eduart Blloshmi*[2], *Arli Llabani*[3]

***Summary:***

The establishment of a reliable local geodetic reference framework is essential for accurate spatial data acquisition, cadastral surveying, engineering applications, and urban development. This study presents the establishment and quality assessment of a local GNSS-based geodetic reference network for the city of Gramsh, Albania. The network consists of 9 newly materialized control points connected to the Albanian national geodetic reference framework through observations to five permanent ALBCORS stations located at Berat, Çorovodë, Fier, Lushnje, and Gramsh.

GNSS observations were conducted using the fast-static technique with three receivers operating simultaneously, with observation sessions ranging from 30 to 45 minutes and a recording interval of 5 seconds. The collected observations were processed using Trimble Business Center, and the network was adjusted using a weighted least-squares approach. Quality assessment included baseline processing, redundancy analysis, network adjustment statistics, repeated observations, and independent verification measurements.

The network adjustment results indicate that the estimated horizontal coordinate precision was generally at the few-millimetre level, while the estimated ellipsoidal-height precision was generally within the millimetre-to-centimetre range. The reported adjustment solutions passed the global Chi-square test at the 95% confidence level, with reference factors close to unity. Repeated observations of selected network points and comparisons involving existing geodetic points were used to assess the consistency of the available coordinate solutions. The interpretation of these comparisons as independent accuracy checks depends on whether the corresponding observations were excluded from the adjustment.

The results demonstrate the feasibility of establishing a reliable local geodetic reference framework in Gramsh using GNSS observations connected to the ALBCORS network. The resulting infrastructure can provide a homogeneous spatial reference for cadastral surveying, engineering works, GIS applications, infrastructure development, and future urban planning activities.

*Keywords: GNSS, geodetic control network, positioning, geospatial data, urban surveying*

[1] PhD, Lecturer, Faculty of Civil Engineering, Polytechnic University of Tirana, Tirana, Albania, bledar.sina@fin.edu.al
[2] PhD, Lecturer, Faculty of Civil Engineering, Polytechnic University of Tirana, Tirana, Albania, eduart.blloshmi@fin.edu.al
[3] PhD, Lecturer, Faculty of Civil Engineering, Polytechnic University of Tirana, Tirana, Albania, arli.llabani@fin.edu.al

## 1. INTRODUCTION

The increasing demand for accurate and homogeneous spatial information has made geodetic reference networks an essential component of modern surveying, land administration, infrastructure development, and urban planning. A properly established geodetic framework provides the spatial basis for the integration of surveying measurements, cadastral information, geographic information systems (GIS), engineering projects, and other geospatial datasets.

The availability of reliable local geodetic control is particularly important in urban areas where surveying activities are continuously required for cadastral updating, infrastructure development, construction projects, utility management, and territorial planning. In the absence of a sufficiently dense and homogeneous local reference framework, individual surveying projects may rely on different control sources, potentially resulting in inconsistencies between datasets and difficulties in integrating spatial information.

The municipality of Gramsh, located in central Albania within Elbasan County, represents an area where reliable geodetic reference information is required to support ongoing and future surveying, cadastral, engineering, and urban development activities. Although the national geodetic infrastructure provides a fundamental reference framework, the spatial distribution of control points within an urban area may not always be sufficient for efficient local surveying operations. The establishment of an appropriately distributed local network can therefore improve access to geodetic control and facilitate the practical implementation of high-precision surveying techniques.

The development of Global Navigation Satellite System (GNSS) technology has substantially changed the establishment and maintenance of geodetic control networks. Modern multi-constellation GNSS receivers allow precise three-dimensional positioning and provide an efficient alternative to conventional terrestrial methods. Fast-static GNSS observations, combined with differential processing and rigorous network adjustment, can provide millimetre- to centimetre-level coordinate precision when appropriate observation procedures, reference stations, and quality-control methods are applied.

An important aspect of a local GNSS network is its connection to an existing national reference framework. In Albania, the ALBCORS permanent GNSS network provides continuously operating reference stations that can be used to establish a consistent relationship between local surveying networks and the national geodetic reference system. The use of multiple reference stations also provides redundancy and allows the consistency of the local network to be evaluated during baseline processing and network adjustment.

In this context, the present study focuses on the establishment of a local geodetic reference network for the city of Gramsh using GNSS observations connected to five ALBCORS permanent reference stations. Nine new control points were selected, materialized, and observed using fast-static GNSS techniques. The observations were subsequently processed and adjusted using Trimble Business Center.

Particular attention is given to the quality assessment of the resulting network. In addition to the processing of GNSS baselines, the study considers redundant observations, repeated occupations of selected points, network adjustment statistics, and independent measurements at existing geodetic reference points. These procedures are intended to provide an objective assessment of the consistency and precision of the resulting coordinates rather than relying solely on the nominal accuracy of the GNSS equipment or observation methodology.

## 2. MATERIALS AND METHODS

### 2.1. STUDY AREA

The study was conducted in the municipality of Gramsh, located in the central part of Albania within Elbasan County. The municipality extends from Qafa e Shënkolli and Lleshan in the north to Siman (Sqimar) in the south, while its western and eastern boundaries are defined by Sarasel and the Valamara mountain range near Lenie, respectively. Covering an area of approximately 695 km², Gramsh consists of one municipality, nine administrative units, and ninety-five villages.

The municipality is characterized by a diverse topography shaped primarily by the Devoll and Tomorrica river valleys. These river systems divide the territory into three main geographical regions: Vërca, Sulova, and Tomorrica. While the valleys contain the most productive agricultural land and the majority of the settlements, the surrounding mountainous terrain creates significant variations in elevation and accessibility.

According to available demographic statistics, Gramsh has a population of approximately 42,600 inhabitants. The municipality has experienced gradual urban expansion accompanied by increasing demands for infrastructure development, land administration, engineering projects, and environmental management. These developments require accurate and reliable geospatial information to support planning and decision-making processes.

From a geodetic perspective, the municipality presents favorable conditions for the establishment of a local control network. The urban area contains numerous stable locations suitable for monumentation, while the surrounding terrain allows the creation of a well-distributed network capable of supporting cadastral, engineering, and GIS applications. Nevertheless, careful planning is required to minimize the influence of natural obstacles and to ensure optimal satellite visibility during GNSS observations.

For these reasons, Gramsh was selected as an appropriate case study for the implementation of a modern GNSS-based geodetic control network. The resulting network provides a precise spatial reference framework that supports future surveying activities and contributes to the sustainable development of the municipality [1].

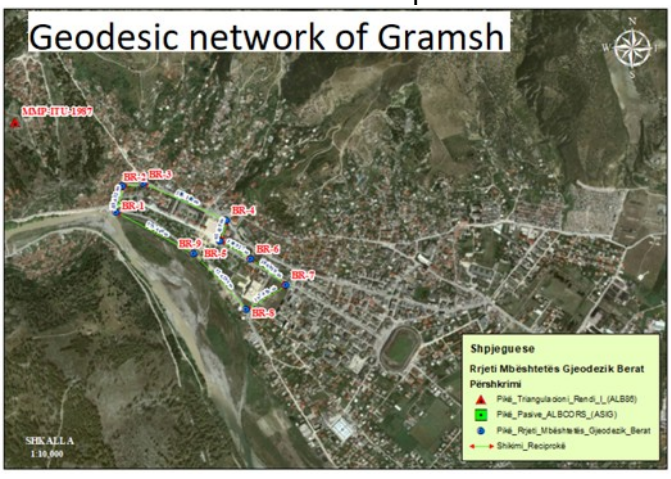


*Fig. 1 Geodesic network of Gramsh*

## 2.2. PLANNING AND DESIGN OF GNSS MEASUREMENTS

The preliminary determination of the points forming the local geodetic support network of Gramsh was carried out based on several fundamental cartographic and technical documents. These materials were used to define the approximate location and spatial distribution of the points before conducting field reconnaissance activities [2].
The main reference documents used during the initial design phase included:
Topographic maps at a scale of 1:25,000, produced by the Geographical and Military Infrastructure Institute (former ITU) during the period 1959–1985 (Figure 2).

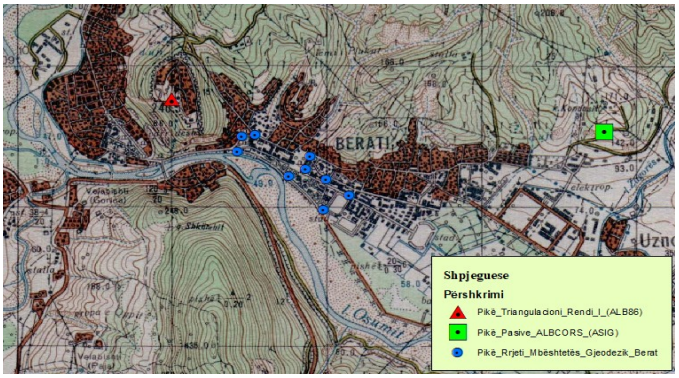


*Fig. 2 Topographic map of scale 1:25000*

During the selection process of the GNSS point locations, several important criteria were considered to ensure the quality and reliability of satellite observations:
The selected locations had to provide an unobstructed view of the sky, avoiding obstacles above the elevation angle of 20° in order to minimize satellite signal interruptions.
Areas with reflective surfaces that could generate multipath effects and degrade GNSS signal quality were avoided [3].
The new points were established in stable and permanent locations, such as natural rock formations, concrete structures, stone blocks, GRidges, and other stable constructions.
Locations near high-voltage electrical lines, temporary structures, unstable objects, and areas subject to future development were excluded.

The selected sites had to provide suitable conditions for safe and efficient GNSS observation procedures.
The preliminary design of the network configuration was performed in collaboration with specialists from the Urban Planning Department of the Municipality of Gramsh. Through joint field assessments, it was ensured that the distribution of the geodetic points would provide complete coverage of the urban area and meet the requirements for a local geodetic support network [4].

## 2.3. MONUMENTATION AND MATERIALIZATION OF THE LOCAL GEODETIC SUPPORT NETWORK POINTS IN GRAMSH

After completing the field reconnaissance phase and defining the final positions of the points according to the established GNSS network design criteria, the next stage consisted of the physical realization and stabilization of the geodetic points in the field.
The materialization of the local geodetic support network points was mainly carried out along sidewalks and in locations that were considered stable and unaffected by future urban development activities, in accordance with the urban planning conditions of the Municipality of Gramsh.
The contribution of the technical specialists from the Municipality of Gramsh was particularly important during this phase, as their detailed knowledge of the territory helped in selecting suitable locations and ensuring the long-term preservation of the points [5].
The selected locations were generally positioned outside areas affected by construction activities, maintaining distances between approximately 20–100 m from possible development zones. The physical realization of the points was performed using metallic concrete markers, consisting of a central mark used for GNSS antenna positioning. The markers had a length of 150 mm and a diameter of 10 mm.



*Fig. 3 Materialized center of the geodetic point*

Before installation, each metallic marker was prepared by creating a small central hole with a diameter of 3–4 mm. This modification allowed the precise placement of the GNSS antenna thread directly over the point center, improving the accuracy of the measurements.
The main equipment and materials used during the point installation process included:

- battery-powered drilling equipment;
- a two-component high-strength fixing compound used as an alternative to traditional concrete mortar;
- hammer and other necessary field tools.

The use of permanent markers and stable locations ensured the durability of the network points and allowed their future utilization for geodetic, topographic, GIS, and engineering applications [6].

## 2.4. GNSS OBSERVATION CAMPAIGN AND MEASUREMENT STRATEGY

The GNSS observation campaign for the establishment of the Gramsh local geodetic reference network was conducted on 22 May 2021. Three Trimble R8 GNSS receivers were used simultaneously at different points of the network [7].

The observation strategy was based on the fast-static GNSS technique. Depending on the observation session and field conditions, individual occupations lasted approximately 30–45 minutes. GNSS observations were recorded at a 5-second interval. The observation configuration was designed to provide both sufficient network geometry and redundancy. During the campaign, observations from the newly established Gramsh points were combined with observations to permanent ALBCORS reference stations, allowing the local network to be connected to the national geodetic reference framework.

Five ALBCORS stations were used:

- ALBCORS Berat;
- ALBCORS Çorovodë (Skrapar);
- ALBCORS Fier;
- ALBCORS Lushnje;
- ALBCORS Gramsh.

In addition to the observations involving the new network points, repeated observations were performed at selected points for quality assessment. The classical geodetic point MMP-ITU-1987 was reoccupied, while the newly established points GR-1 and GR-7 were measured on more than one occasion. An additional 60-minute observation was performed at the passive KRGJSH point D29HaHpVG.
These observations were introduced into the project for two complementary purposes: observations used in the network adjustment contributed to the determination of the final coordinates, whereas observations retained as independent checks were used to evaluate the consistency of the adjusted solution.
The GNSS observations were processed using a weighted least-squares adjustment in Trimble Business Center (TBC). The local network was connected to five ALBCORS reference stations, namely Berat, Çorovodë, Fier, Lushnje, and Gramsh. These stations were treated as fixed reference control in the processing configuration described in this study, thereby constraining the local network to the adopted reference framework. The adjustment procedure included the evaluation of convergence, reference factors, global Chi-square test results, coordinate precision estimates, and observation residuals. These parameters provide complementary information on the internal consistency of the adjusted network. However, the interpretation of the final coordinate quality also depends on the reliability of the fixed reference coordinates and on the availability of independent checks.

## 2.5. GNSS FIELD SURVEY PROCEDURE AND DATA COLLECTION

The field survey was conducted by a team of three surveyors distributed among the observation points. The first observation session commenced at approximately 09:30, with the GNSS receivers operated simultaneously according to the predefined observation schedule [8].
During the field campaign, particular attention was given to the correct installation and levelling of the GNSS antennas. The antenna poles were maintained in a vertical position using bipod supports, while the circular bubbles were checked throughout the observations.
Potential sources of multipath and signal obstruction were also controlled. Vehicles and other reflective objects were kept away from the antenna positions whenever possible, with a minimum separation of approximately 10 m adopted during the observations.

For each of the 9 newly established points, field documentation was completed according to the applicable GNSS surveying requirements. The field records included point identification, observation time, antenna information, receiver information, and other parameters required for subsequent processing.
Additional information concerning the satellite geometry was also recorded, including the number of tracked satellites and GDOP/PDOP indicators. These parameters were considered during the subsequent assessment of observation quality.
The field data were subsequently transferred to the processing environment for baseline determination, quality control, and network adjustment.

## 2.6. GNSS DATA PROCESSING AND NETWORK ADJUSTMENT

The processing and adjustment of GNSS observations were performed using the software package Trimble Business Center (TBC). The final coordinates of the measured points belonging to the Gramsh local geodetic support network were determined based on observations from five permanent reference stations of the ALBCORS GNSS network [9].
The network adjustment procedure in TBC is defined as the solution of a system of simultaneous equations designed to close the fast-static observation network by applying the weighted least squares method. This approach allows the minimization of observation residuals and provides the most probable values for the unknown coordinates.

The GNSS processing workflow consisted of several main stages:

- Importing raw GNSS observation files obtained from field measurements;
- Defining the reference stations of the ALBCORS network as control points;
- Processing GNSS baselines between the measured points and reference stations;
- Performing quality control and eliminating observations affected by errors;
- Conducting network adjustment and determining final coordinates.

The five permanent ALBCORS stations used as reference points were:

- Berat;
- Çorovodë (Skrapar);
- Fier;
- Lushnje;
- Gramsh.

Before baseline processing, the main parameters in the TBC environment were configured according to the field observation conditions:

- GNSS data recording interval: 5 seconds;
- Satellite systems used: GPS and GLONASS;
- Elevation mask angle: 20°;
- Coordinate estimation method: Weighted Mean of All Observations.

Since GNSS baseline processing determines the spatial vector between simultaneously observed stations, the initial processing step focused on selecting the appropriate baselines generated during each observation session.
For the first observation session, the activated baselines corresponded to the simultaneous observations performed between the local network points and the ALBCORS reference stations.

Session I:

Observation time: 09:30 – 10:30

Observed points:

- MMP-ITU-1987;
- GR-2;
- GR-3;
- Five ALBCORS reference stations.

Therefore, only the baselines generated during this session were activated for the initial processing, while baselines from the remaining observation sessions were temporarily disabled.

## 2.7. BASELINE ANALYSIS AND QUALITY CONTROL OF GNSS OBSERVATIONS

During the GNSS network adjustment process, special attention was given to the analysis and evaluation of the calculated baselines. For a reliable adjustment of the network, only independent baselines should normally be considered, while redundant or dependent baselines must be analyzed and controlled before being included in the final solution.
For each observation session, the number of independent baselines (b) is determined according to the number of GNSS receivers (n) operating simultaneously:

$$b = n - 1 \tag{1}$$

where:

b – number of independent baselines;
n – number of GNSS receivers used during the observation session.

The number of dependent baselines (Nv) generated from a GNSS session is calculated using the following expression:

$$Nv = (n-1) * (n-2)/2 \tag{2}$$

while the total number of possible baselines (Nt) between receivers is determined by:

$$Nt = n * (n-1)/2 \tag{3}$$

In this project, each observation session was performed using three Trimble R8 GNSS receivers, operating simultaneously at different points of the local geodetic support network. In addition, observations from five permanent ALBCORS reference stations were included in the processing procedure [9].
Based on the above equations, the number of available baselines was calculated for each observation session. Although independent baselines are sufficient for network adjustment, redundant baselines provide valuable information for quality assessment, closure analysis, and detection of possible observation errors.

For this reason, in the present study, not all dependent baselines were automatically removed. Only those baselines affected by poor-quality observations, incorrect satellite data, cycle slips, or abnormal behavior were excluded after detailed analysis.
The objective of this procedure was to preserve sufficient redundancy within the network while maintaining the highest possible reliability of the final coordinate solution.

## 2.8. DEFINITION OF CONTROL POINTS AND NETWORK ADJUSTMENT PARAMETERS

A fundamental requirement of the local network was its consistent connection to the national geodetic reference framework. For this purpose, five permanent ALBCORS stations were used as reference control points: Berat, Çorovodë, Fier, Lushnje, and Gramsh.
The ALBCORS stations were treated as fixed control stations in the network adjustment. Their known coordinates constrained the local network and established its spatial relationship with the national reference framework.
The use of five reference stations also provided a redundant geometric connection between the local network and the national framework. Rather than determining the local coordinates independently from a single reference station, the observations were processed relative to several permanent stations distributed around and within the GRoader study region.
The reference stations therefore served two functions. First, they provided the datum constraint required to determine the absolute position of the local network. Second, their multiple connections provided an opportunity to evaluate the consistency of the GNSS observations and the resulting network geometry.
The 9 newly established Gramsh points were treated as unknown stations during the adjustment. Their final coordinates were obtained after the baseline observations were processed and the network adjustment was completed.
The additional observations at MMP-ITU-1987, GR-1, GR-7, and D29HaHpVG were considered separately during quality assessment. Repeated observations of GR-1 and GR-7 were used to assess repeatability, while the observations involving existing reference points were used as independent checks where they were not included as fixed constraints in the final adjustment.
This distinction between control observations used to define the datum and independent observations used for verification is important because an observation cannot provide an independent accuracy assessment if the same information has already been imposed as a fixed constraint in the adjustment.

## 3. RESULTS AND DISCUSSION

The GNSS observations collected during the field campaign were processed and adjusted in Trimble Business Center (TBC). The processing was performed using the five ALBCORS permanent stations—Berat, Çorovodë, Fier, Lushnje, and Gramsh—as fixed control stations. The final processing included baseline quality control, elimination of unsuitable observations, constrained network adjustment, estimation of point precision, and independent verification using repeated observations of existing geodetic points.
The observation campaign was conducted using three Trimble R8 receivers. Six observation sessions were performed, with observation durations of approximately one hour for the individual sessions. The field observations included the newly established points together with repeated observations of MMP-ITU-1987, GR-7, GR-1, and the passive KRGJSH point D29HaHpVG. The original field records indicate successful observations for all six sessions, with GDOP values generally between approximately 2.3 and 3.8 and 4–12 tracked satellites depending on the session and point.

### 3.1. GNSS BASELINE PROCESSING RESULTS

For each observation session, the GNSS data were processed in TBC using GPS and GLONASS observations with a 5-s recording interval and a 20° elevation mask. The five ALBCORS stations were introduced as fixed control stations. The processing strategy considered independent and redundant baselines, allowing the internal consistency of the network geometry to be evaluated.
With three field receivers and five ALBCORS reference stations, the project initially generated 28 possible baselines per observation session, of which 7 were independent and 21 were redundant/dependent. Across the six sessions, this resulted in 42 independent and 126 redundant baselines, for a total of 168 baseline combinations.

During the preliminary processing, some observations were identified as being outside the adopted tolerances. The data were subsequently inspected using the TBC Session Editor, Point Derivation, and GNSS Loop Closure functions. The problematic satellite observations were filtered and unsuitable dependent baselines were excluded. In particular, the processing documented the exclusion of the MMP-ITU-1987–Gramsh baseline and the GR-3–Lushnje baseline after examination of the coordinate differences and loop-closure results. The final network was then processed using the remaining suitable observations.

This procedure is important because the final solution was not obtained simply by accepting every generated baseline. Instead, the observations were subjected to preliminary quality control before the final constrained adjustment.

## 3.2. NETWORK DATUM AND ADJUSTMENT STRATEGY

The five ALBCORS stations—Berat, Çorovodë, Fier, Lushnje, and Gramsh—were introduced as fixed control points in the final network adjustment. Their coordinates therefore defined the connection of the local network to the national geodetic reference framework.

The adjustment was performed as a constrained least-squares network adjustment. The project documentation reports the use of the TBC Network Adjustment function, with the five ALBCORS stations fixed and the coordinates of the observed local points estimated from the processed GNSS vectors. The adjustment produced both coordinate estimates and associated precision information, including horizontal error ellipses and vertical coordinate errors.

The main adjustment statistics for the six observation sessions are summarized in Table 1.

*Tab. 1 Statistical results of the GNSS network adjustments*

| Session | Iterations | Reference factor | Chi-square test (95%) | Confidence level | Degrees of freedom |
|---|---|---|---|---|---|
| S1 | 2 | 1.00 | Passed | 95% | 41 |
| S2 | 2 | 1.01 | Passed | 95% | 62 |
| S3 | 2 | 1.01 | Passed | 95% | 62 |
| S4 | 2 | 0.99 | Passed | 95% | 47 |
| S5 | 2 | 1.00 | Passed | 95% | 71 |
| S6 | 2 | 1.00 | Passed | 95% | 71 |

The adjustment statistics summarized in Table 1 indicate that the six reported session solutions converged within two iterations and had reference factors close to unity. The global Chi-square tests were reported as passing at the 95% confidence level. These results support the internal consistency of the corresponding session adjustments under the adopted stochastic model. Nevertheless, the session statistics should be distinguished from the statistics of a single combined-network adjustment. The global test should also be interpreted together with the individual observation residuals, since an acceptable overall adjustment does not necessarily exclude the presence of individual observations requiring further investigation.

## 3.3. PRECISION OF THE ADJUSTED POINTS

The adjustment results provide individual estimates of horizontal and vertical precision for each observed point. The horizontal uncertainty is represented through the semi-major and semi-minor axes of the error ellipse, while the vertical component is represented by the estimated elevation/height error.

The final selected results for the repeated points are summarized in Table 2.

*Tab. 2 Precision parameters of selected adjusted points*

| Session | Point | Easting error (m) | Northing error (m) | Height error (m) | Semi-major axis (m) | Semi-minor axis (m) |
|---|---|---|---|---|---|---|
| S1 | MMP-ITU-1987 | 0.0038 | 0.0044 | 0.0143 | 0.0056 | 0.0046 |
| S1 | GR-2 | 0.0037 | 0.0044 | 0.0143 | 0.0057 | 0.0043 |
| S1 | GR-3 | 0.0048 | 0.0055 | 0.0159 | 0.0070 | 0.0057 |
| S2 | MMP-ITU-1987 | 0.0039 | 0.0043 | 0.0152 | 0.0055 | 0.0048 |
| S2 | GR-4 | 0.0041 | 0.0044 | 0.0132 | 0.0056 | 0.0050 |
| S2 | GR-5 | 0.0038 | 0.0042 | 0.0130 | 0.0054 | 0.0047 |
| S3 | MMP-ITU-1987 | 0.0034 | 0.0036 | 0.0099 | 0.0045 | 0.0042 |
| S3 | GR-6 | 0.0034 | 0.0036 | 0.0085 | 0.0045 | 0.0043 |
| S3 | GR-7 | 0.0035 | 0.0036 | 0.0085 | 0.0046 | 0.0043 |
| S4 | MMP-ITU-1987 | 0.0032 | 0.0033 | 0.0125 | 0.0042 | 0.0040 |
| S4 | GR-7 | 0.0041 | 0.0041 | 0.0115 | 0.0052 | 0.0050 |
| S4 | GR-8 | 0.0032 | 0.0033 | 0.0103 | 0.0042 | 0.0040 |
| S5 | MMP-ITU-1987 | 0.0031 | 0.0033 | 0.0093 | 0.0041 | 0.0039 |
| S5 | GR-9 | 0.0032 | 0.0034 | 0.0094 | 0.0043 | 0.0040 |
| S5 | GR-1 | 0.0032 | 0.0034 | 0.0096 | 0.0043 | 0.0040 |
| S6 | MMP-ITU-1987 | 0.0029 | 0.0029 | 0.0079 | 0.0036 | 0.0036 |
| S6 | GR-1 | 0.0030 | 0.0030 | 0.0083 | 0.0038 | 0.0037 |
| S6 | D29HaHpVG | 0.0030 | 0.0030 | 0.0045 | 0.0038 | 0.0037 |

The coordinate precision estimates presented in Table 2 indicate that the reported horizontal uncertainties are generally at the millimetre level, whereas the estimated height uncertainties are larger. This difference highlights the importance of evaluating the horizontal and vertical components separately. The values represent adjustment-derived precision estimates and should not be interpreted directly as independently verified absolute positional accuracy. The latter requires comparison with reliable

reference coordinates that are independent of the observations used to determine the adjusted positions.

The results show that the estimated horizontal uncertainties were generally at the millimetre level, with the semi-major axes of the horizontal error ellipses ranging from 0.0036 m to 0.0070 m for the reported observations. The vertical errors were generally below 0.016 m, with the smallest reported value of 0.0045 m obtained for D29HaHpVG in Session 6.

The improvement in precision between the individual sessions is also evident. For example, the MMP-ITU-1987 point had a height error of 0.0143 m in S1, decreasing to 0.0079 m in S6. Similarly, the GR-1 observation in S6 yielded horizontal coordinate errors of 0.0030 m in both east and north and a height error of 0.0083 m.

Repeated occupations of selected points were considered in the assessment of observational consistency. In particular, the observations involving MMP-ITU-1987, GR-1, and GR-7 provided opportunities to compare results obtained during different measurement sessions. Such comparisons can help identify inconsistencies associated with observation conditions or measurement setup. However, repeated observations used in the same network adjustment provide evidence of internal consistency rather than fully independent validation. Their contribution to the final solution must therefore be distinguished from the role of observations reserved exclusively for external quality control.

## 3.4. FINAL COORDINATES OF THE LOCAL NETWORK

The final coordinates were selected after evaluating the repeated observations and the precision obtained in each session. The ellipsoidal coordinates are referred to the GRS80 ellipsoid within the ETRS89/ETRF2000 reference framework. The corresponding geocentric Cartesian coordinates (X, Y, Z) are also provided in Table 3.

*Tab. 3 Final coordinates of the local geodetic network*

| Point | Latitude (GRS80) | Longitude (GRS80) | h (m) | X (m) | Y (m) | Z (m) |
|---|---|---|---|---|---|---|
| GR-1 | N40°42'15.27672" | E19°57'00.86811" | 92.930 | 4551564.506 | 1652158.931 | 4137640.571 |
| GR-2 | N40°42'18.83923" | E19°57'02.06481" | 100.977 | 4551493.288 | 1652162.966 | 4137729.127 |
| GR-3 | N40°42'19.20917" | E19°57'05.81951" | 98.082 | 4551454.154 | 1652242.529 | 4137735.890 |
| GR-4 | N40°42'14.17755" | E19°57'20.83533" | 94.265 | 4551426.285 | 1652607.424 | 4137615.737 |
| GR-5 | N40°42'11.29043" | E19°57'19.63426" | 93.359 | 4551489.855 | 1652600.509 | 4137547.631 |
| GR-6 | N40°42'08.80393" | E19°57'25.12178" | 92.961 | 4551492.620 | 1652738.567 | 4137489.224 |
| GR-7 | N40°42'05.24705" | E19°57'31.56787" | 93.475 | 4551508.583 | 1652905.358 | 4137406.382 |
| GR-8 | N40°42'01.87722" | E19°57'24.41678" | 93.291 | 4551629.474 | 1652770.653 | 4137327.453 |
| GR-9 | N40°42'09.55921" | E19°57'14.98620" | 92.838 | 4551559.459 | 1652509.694 | 4137506.807 |

The final coordinates reported above correspond to the coordinate catalogue obtained from the GNSS network processing. The source document also provides the Cartesian coordinates and projected TMzn coordinates for these points.

The coordinate uncertainties obtained from the adjustment demonstrate that the horizontal position of the established points was determined at the few-millimetre level in the adjustment model, while the estimated ellipsoidal-height uncertainty was generally at the centimetre or sub-centimetre level.

## 3.5. BASELINE AND ADJUSTMENT RESIDUALS

The adjusted observation residuals provide an additional internal quality-control measure. For example, in Session 3 the standardized residuals for the main observations included values of -2.773 for the azimuth of the Fier–Gramsh vector, 1.121 for its ellipsoidal distance, -0.027 for the azimuth of Berat–Gramsh, and 1.932 for its ellipsoidal distance.

In Session 4, the standardized residuals for the Berat–Gramsh ellipsoidal distance, Gramsh–Çorovodë ellipsoidal distance, and GR-8–GR-7 height difference were 2.309, 2.033, and -2.012, respectively. These values were retained within an adjustment that nevertheless passed the global Chi-square test.

The presence of individual standardized residuals approaching or exceeding an absolute value of 2 demonstrates why the adjustment statistics and observation-level quality checks need to be considered together. The final solution was accepted after the iterative processing and removal of observations identified as unsuitable during the preliminary baseline and loop-closure analysis.

The residual analysis complements the global adjustment statistics by providing information about the consistency of individual observations with the estimated network geometry. Standardized residuals should be interpreted according to the definitions and statistical criteria applied by the processing software. Residuals with relatively large absolute values warrant further examination, even when the global Chi-square test is passed. Any decision to retain, down-weight, or reject an observation should be supported by the corresponding processing results and documented quality-control procedure.

## 3.6. DISCUSSION

The numerical results demonstrate that the GNSS network was processed through several complementary quality-control stages. The initial baseline processing identified unsuitable observations, which were subsequently filtered or excluded. The remaining observations were introduced into constrained network adjustments based on five fixed ALBCORS stations.

All six adjustment sessions passed the global Chi-square test at the 95% confidence level, while the network reference factor ranged from 0.99 to 1.01. These results indicate a close agreement between the adopted stochastic model and the post-adjustment observational variance.

The estimated horizontal coordinate errors were generally between approximately 3 and 5 mm for the final observations, while the estimated height errors were predominantly below 1.5 cm. The smallest reported errors were obtained for the S6 observations, where GR-1 had east and north errors of 3 mm and a height error of 8.3 mm, while D29HaHpVG had east and north errors of 3 mm and a height error of 4.5 mm.

Repeated observations and comparisons involving existing geodetic points provided additional information on the consistency of the available coordinate solutions. The GR-7 reoccupation was reported to show millimetre-level coordinate differences, while the comparison involving D29HaHpVG yielded differences of 9 mm in northing, 24 mm in easting, and 15 mm in height. The original processing information should be consulted to confirm whether these observations were excluded from the final adjustment and whether the reported differences represent an independent accuracy assessment.

A distinction must be made between the precision estimated by the least-squares adjustment and the external accuracy of the final coordinates. Adjustment-derived precision describes the uncertainty estimated under the adopted observation and stochastic models, whereas external accuracy requires comparison with sufficiently reliable independent reference information. Consequently, the precision values presented in this study characterize the reported adjustment solutions and should not be considered, on their own, proof of equivalent absolute positional accuracy. This distinction is particularly important when the network is intended to support cadastral and engineering applications with defined accuracy requirements.

Consequently, the results provide quantitative evidence that the established local network can serve as a geodetic control framework for subsequent surveying activities. At the same time, the results indicate that the horizontal and vertical components should be considered separately when defining the accuracy of subsequent cadastral, engineering, topographic, and GIS applications.

The principal contribution of the network is therefore not only the determination of the coordinates of the local points but also the establishment of a controlled and statistically evaluated connection to the national geodetic reference framework through the ALBCORS stations.

The reported adjustment statistics and coordinate precision estimates provide an initial basis for assessing the internal consistency of the Gramsh GNSS network. Nevertheless, the distinction between adjustment-derived precision and independently verified accuracy remains essential. Further confirmation of the final adjustment outputs and documentation of the observations used for independent quality control would strengthen the quantitative validation of the network and its suitability for applications with specific accuracy requirements.

## 4. CONCLUSION

The establishment of the local geodetic support network in the city of Gramsh represents a contribution toward strengthening the geodetic infrastructure of the area and providing a spatial reference framework for future surveying activities.

The developed network consists of 9 newly materialized control points connected to the national geodetic reference framework through five permanent ALBCORS stations. The use of multiple fixed reference stations provided the datum constraint required for the determination of the local coordinates while also introducing redundancy into the connection between the local and national networks.

The GNSS observations were processed using Trimble Business Center and evaluated through baseline quality control, constrained least-squares network adjustment, adjustment statistics, repeated observations, and independent verification measurements. The six adjustment sessions passed the global Chi-square test at the 95% confidence level, with reference factors ranging from 0.99 to 1.01.

The adjusted coordinates of the newly established points and their associated precision estimates provide the principal practical output of the study. The results indicate that the horizontal coordinate precision was generally at the few-millimetre level, while the estimated height precision was generally within the millimetre-to-centimetre range. Repeated and independent observations provided additional evidence of the consistency of the network solution.

The resulting network can therefore provide a locally accessible spatial reference framework for subsequent surveying activities, including cadastral surveys, engineering surveys, GIS applications, infrastructure development, and territorial planning.

The established control points and their associated coordinate information can also support the integration of future geospatial datasets within a common reference framework and provide a basis for the densification or development of similar local GNSS networks in other urban areas of Albania.

## REFERENCES

[1] Land Research Institute's Archive, Tirana, 1996: Bulletin No. 6.

[2] Geofoto SRL, 2007: Final technical report of aerial photography.

[3] Trimble Navigation Limited, September 2003; Real Time Kinematic Surveying, Training Guide, Part Number 33142 40.

[4] Nurçe B., Thesis, 2013: Study of the development of coordinative references of Albania.

[5] Standard on Digital Cadastral Maps and Parcel Identifiers, 2015; International Association of Assessing Officers (IAAO), https://www.iaao.org/media/standards/Standard_Digital_Cadastral_Maps_2015.pdf

[6] Tamrakar, Rabindra Man, (2013), Potential Use of GPS Technology For Cadastral Surveys in Nepal, Nepalese Journal on Geoinformatics, -12, 2070 (2013AD).

[7] Veersema, Adam, (2004), RTK-GPS for Cadastral Boundary Surveying in NSW, School of Surveying and Spatial Information Systems, The university of New South Wales.

[8] Lee, I. and Ge, L., (2006), The performance of RTK-GPS for surveying under challenging environmental conditions, Earth Planets Space.

[9] Öcalan, T. and Tunalioglu, N., (2010), Data communication for real-time positioning and navigation in global navigation satellite systems (GNSS)/continuously operating reference stations (CORS) networks, Scientific Research and Essays Vol. 5(18).

https://doi.org/10.24867/INDIS-2026-EN-844



# GENERATION OF SYNTHETIC B-SCANS USING GPRMAX AND THEIR APPLICATION IN DIFFERENT SCENARIOS

*Željko Bugarinović[1], Aleksandar Ristić[2], Milan Vrtunski[3],Milan Gavrilović[4], Miro Govedarica[5]*

***Summary:***

The detection of underground infrastructure facilities and other inhomogeneities in the soil composition using non-invasive detection technologies has been intensively researched for the last 20 years. GPR scanning technology is the most common for this application. One of the major problems of georadar application is reflected in the interpretation of the obtained scanning results. Namely, the radargram (B-scan) is created by a complex process of convoluted signals of electromagnetic waves, and its correct interpretation usually relies on previous experience. In order to get a better feeling and better understanding of the scanning results, the open source software gprMax was developed through which synthetic radargrams can be generated for different scenes that the user can arbitrarily define. In this paper, several synthetic radargrams were generated and interpreted, taking into account the different number of layers of soil, humidity and similar parameters, which can be encountered in the field of construction.

*Keywords: GPR, gprMax, detection, simulation, construction*

# GENERISANJE SINTETIČKIH RADARGRAMA KROZ GPRMAX I NJIHOVA PRIMENA U RAZLIČITIM SCENARIJIMA

***Rezime:***

Detekcija objekata podzemne infrastrukture i drugih nehomogenosti u sastavu zemljišta primenom neinvazivnih tehnologija detekcije poslednjih 20 godina se intezivno istražuje. Za ovu primenu najzastupljenija je tehnologija skeniranja georadarom. Jedan od većih problema primene georadara ogleda se u načinu tumačenja dobijenih rezultata skeniranja. Naime, radargram (B-sken) nastaje složenim postupkom konvoluiranih signala elektromagnetnih talasa i njegovo ispravno tumačenje obično se oslanja na prethodno iskustvo. Kako bi se stekao bolji osećaj i bolje razumevanje rezultata skeniranja razvijen je softver otvorenog koda gprMax kroz koji se mogu generisati sintetički radargrami za različite scene koje korisnik može proizvoljno da definiše. U ovom radu generisano je i tumačeno više sintetičkih radargrama uzimajući u obzir različit broj slojeva zemljišta, vlage i sličnih parametara, koje se mogu sresti i u oblasti građevinarstva.

*Ključne reči: Georadar, gprMax, detekcija, simulacija, građevinarstvo*

[1] Assistant professor, Faculty of Technical Sciences, Novi Sad, Serbia, zeljkob@uns.ac.rs, https://orcid.org/0000-0002-7237-5130
[2] Full Profesor, Faculty of Technical Sciences, Novi Sad, Serbia, aristic@uns.ac.rs, https://orcid.org/0000-0003-0979-3345
[3] Assistant professor, Faculty of Technical Sciences, Novi Sad, Serbia, milanv@uns.ac.rs, https://orcid.org/0000-0002-1124-871X
[4] Assistant, , Faculty of Technical Sciences, Novi Sad, Serbia, milangavrilovic@uns.ac.rs, https://orcid.org/0000-0003-4671-7544
[5] Full Profesor, Faculty of Technical Sciences, Novi Sad, Serbia, miro@uns.ac.rs, https://orcid.org/0000-0003-1698-0800

## 1. INTRODUCTION

Underground utilities detection as well as determination of soil characteristics is important activity in many areas. Often non-destructive detection technologies are applied among which ground penetrating radar (GPR) is one of the most prominent [1]. GPR is based on emitting of high-frequency electromagnetic waves and detection of reflected signals, from which a result in the form of raster image called radargram is formed [2, 3]. GPR scanning usually is not too complicated and demanding, but processing and results interpretation has a key role in subsequent decision making. Therefore, many authors have had successful attempts at radargram modeling [4, 5]. In order to understand better the forming of radargrams in this paper a gprMax software is used to generate synthetic radargrams. This software tool finds its place in different areas, especially when a number of data is needed for training of neural networks [6, 7] for automated recognition of characteristic shapes in radargrams [8-13] or specific analyses such as moisture content estimation [14]. Also, high costs of real data acquisition lead many researchers to use synthetic data [15, 16]. GprMax is open-source software developed in Python programming language, with some parts implemented in Cython [15]. Simulation is started by creating a *.in file in which, using various commands model geometry and scanning parameters are defined. The process of simulation is based on numerical solution of Maxwell equations, using Finite-Difference Time-Domain (FDTD) method (Figure 1). This is numerical method to calculate the propagation of electromagnetic waves through space and materials. In essence, instead of continuous space, simulation domain is divided into small cells (three-dimensional grid), and time is divided into small time intervals. Then, for each cell and interval values of amplitude for electric and magnetic fields are calculated.

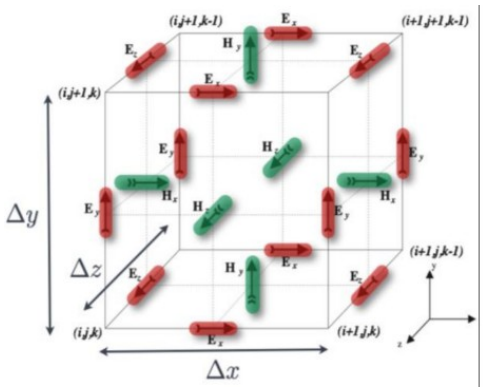


$$\frac{\partial E_x}{\partial t} = \frac{1}{\epsilon}\left(\frac{\partial H_z}{\partial y} - \frac{\partial H_y}{\partial z} - J_{Sx} - \sigma E_x\right)$$
$$\frac{\partial E_y}{\partial t} = \frac{1}{\epsilon}\left(\frac{\partial H_x}{\partial z} - \frac{\partial H_z}{\partial x} - J_{Sy} - \sigma E_y\right)$$
$$\frac{\partial E_z}{\partial t} = \frac{1}{\epsilon}\left(\frac{\partial H_y}{\partial x} - \frac{\partial H_x}{\partial y} - J_{Sz} - \sigma E_z\right)$$
$$\frac{\partial H_x}{\partial t} = \frac{1}{\mu}\left(\frac{\partial E_y}{\partial z} - \frac{\partial E_z}{\partial y} - M_{Sx} - \sigma^* H_x\right)$$
$$\frac{\partial H_y}{\partial t} = \frac{1}{\mu}\left(\frac{\partial E_z}{\partial x} - \frac{\partial E_x}{\partial z} - M_{Sy} - \sigma^* H_y\right)$$
$$\frac{\partial H_z}{\partial t} = \frac{1}{\mu}\left(\frac{\partial E_x}{\partial y} - \frac{\partial E_y}{\partial x} - M_{Sz} - \sigma^* H_z\right)$$

*Figure 1 Time and space discretization for simulation using gprMax*

Input file for simulation (*.in file) contains basic parameters: domain size, time and space discretization, emitted signal, transmitting and receiving antenna, as well as the geometry of the scene. Domain represents the finite space for which Maxwell equations are solved and contains the medium and all objects. Discretization of space and time is defined based on maximum frequency of input signal and relative dielectric constant of a medium. Materials are also defined, although some materials are already pre-defined, such as metal (perfect metallic conductor – pec). Definition of input and receiver involve definition of the type of a signal, antenna central frequency, polarization, as well as coordinates of emitting and receiving antenna. One has to take into account the Perfectly Matched Layer (PML) in order to avoid boundary reflections.

Scene geometry is defined by dimensions and positions of layers of medium and objects. Horizontal layers are most often modelled using parallelepipeds, while objects with circular cross section are modelled using cylinders.

## 2. CREATION OF .IN FILE

Group of command and keywords most often used in *.in files is explained further.

### 2.1. SIMULATION DOMAIN

The first thing that has to be defined is the size of simulation space, that is the dimensions of the finite space for which Maxwell equations will be solved. The command is domain and its syntax is:

#domain: f1 f2 f3.

Parameters f1, f2 i f3 are dimensions in meters along x, y and y axis.

### 2.2. SPACE DISCRETIZATION

Space discretization is defined using command dx_dy_dz:

#dx_dy_dz: f1 f2 f3

Parameters f1, f2 and f3 are discretization steps along x, z and z axis (Δx, Δy i Δz). Spatial discretization is related to discretization of time, with the condition:

$$\Delta t \leq \frac{1}{c\sqrt{\frac{1}{(\Delta x)^2}+\frac{1}{(\Delta y)^2}+\frac{1}{(\Delta z)^2}}} \tag{1}$$

Where c is the speed of light. Smaller values od spatial discretization mean more precise model but increase the number of iterations in simulation.

### 2.3. TIME DOMAIN

The duration of simulation is defined with the command time_window:

#time_window: f1 or #time_window: i1

In the first case duration of simulation is given in seconds (for instance #time_window: 25e-9 for 25 ns), while in the other case a number of iterations is given. Relation between time window, time discretization and number of iterations is given with the expression:

$$t_w = \Delta t\, N_{\text{it}} \tag{2}$$

Where $t_w$ is time window, $\Delta t$ dtime discretization and $N_{it}$ number of iterations. GprMax calculates a required number of iterations using this expression.

### 2.4. MATERIAL

New material is defined using command:

#material: f1 f2 f3 f4 str1

Parameters of this command represent electrical and magnetic properties of the material:
f1 – relative permitivity ($\varepsilon_r$) that describes electrical permitivity of the material relative to vacuum;
f2 – electrical conductivity (σ, S/m), the ability of the material to conduct electrical current;
f3 – relative magnetic permeability ($\mu_r$), permeability of the material to a magnetic field;
f4 – nagnetic losses ($\sigma*$, Ω/m) which represent the part of the energy converted into heat;
str1 – material identificator, that is its name.

gprMax contains pre-defined materials with reserved names: pec, which models perfect electric conductor, and free_space, which represents vacuum with values $\varepsilon_r = 1$ and $\sigma = 0$.

## 2.5. OBJECT

Command #box enables defining an orthogonal parallelopiped with given electromagnetic properties. Most often it is used to model layers of soil, as well as for objects such as concrete slabs and similar structures. Its syntax is:

#box: f1 f2 f3 f4 f5 f6 str1

Parameters f1, f2 amd f3 represent the coordinates of the lower left corner, f4, f5 and f6 represent the coordinates of the upper right corner, while str1 is the identificator of the objects material.
To model cylindrical objects, such as cables and pipes, a command cylinder is used. It enables modelling of a cylinder of arbitrary orientation. Its syntax is:

#cylinder: f1 f2 f3 f4 f5 f6 f7 str1

Parameters f1m f2 and f3 represent the coordinates of the center of one base of the cylinder, f4,f5 and f6, are coordinates of the center of the other base, f7 is cylinder radius and str1 is identificator oif cylinders material.

## 2.6. EXCITATION

Excitation signal of predefined type is defined using comand waveform, with syntax:

#waveform: str1 f1 f2 str2

The parameter str1 is the type of the signal (gaussian or ricker), f1 is the signal amplitude, f2 central frequency and str2 is the name of the signal.
Transmitting antenna parameters are defined using command

#hertzian_dipole: c1 f1 f2 f3 str1

Parameter c1 denotes the polarization plane of the source, parameters f1, f2 and f3 are coordinates of the transmitting antenna and str1 is the identificator of the excitation signal. In 2D models hertzian dipole represents line source fo the current in invariant direction of the simulation.
Recevier antenna is defined using command rx, which determines the points where electromagnetic field is recorded:

#rx: f1 f2 f3

Parameters f1, f2 and f3 represent the coordinates of the receiver, which at the same time defines the distance betweetn transmitting and receiving antenna.
Movement of the antennas through the domain during simulation is defined using src_steps (for transmitting) and rx_steps commands (for receving antenna):

#src_steps: f1 f2 f3

#rx_steps: f1 f2 f3

## 3. CREATED SCENES

In this paper eight scenes are modeled with various levels of complexity, geometry and disposition of objects, as well as different number of soil layers. Scenes are given in ascending order of complexity. Details of each scene are given in Table 1.

*Table 1 Scenes descriptions*

| Scene | Description |
|---|---|
| 1 | One metallic pipa, 10cm diameter, 50cm deep, homogenious soils, dielectric constant 8 |
| 2 | One metallic pipe, 10cm diameter, 50cm deep, three layers of soil, dielectric constants, 8, 15 and 4 |
| 3 | Three pipes (two metallic, 5 and 15cm diameter, one non-metallic, 10cm diameter), three layers of soil, dielectric constants 8, 15 and 4 |
| 4 | Two heating line pipes, 11cm diameter, 80cm deep, in earthen trench |
| 5 | Two heating line pipes, 11cm diameter, 80cm deep, in 90x60cm concrete channel |
| 6 | Two heating line pipes, 11cm diameter, 80cm deep, in 90x60cm reinforced concrete channel |
| 7 | One row of rebar, ⊘20mm, 10cm deep in concrete. |
| 8 | Two rows of rebar ⊘20mm, at 10 and 20cm depth. |

## 4. SIMULATION

Simulation is started in Command Prompt, where gprMax has to be activated in in its working folder. GprMax will generate a given number of synthetic A-scans which are then merged into one synthetic radargram. In the proces, gprMax loads *.in file, generates FDTD grid, and calculates the values of electric and magnetic components allong all axes. During simulation, user can track the number of iterations, its execution poercentage, simulation duration as well as warning and error messages, if there a re any (Figure 2).

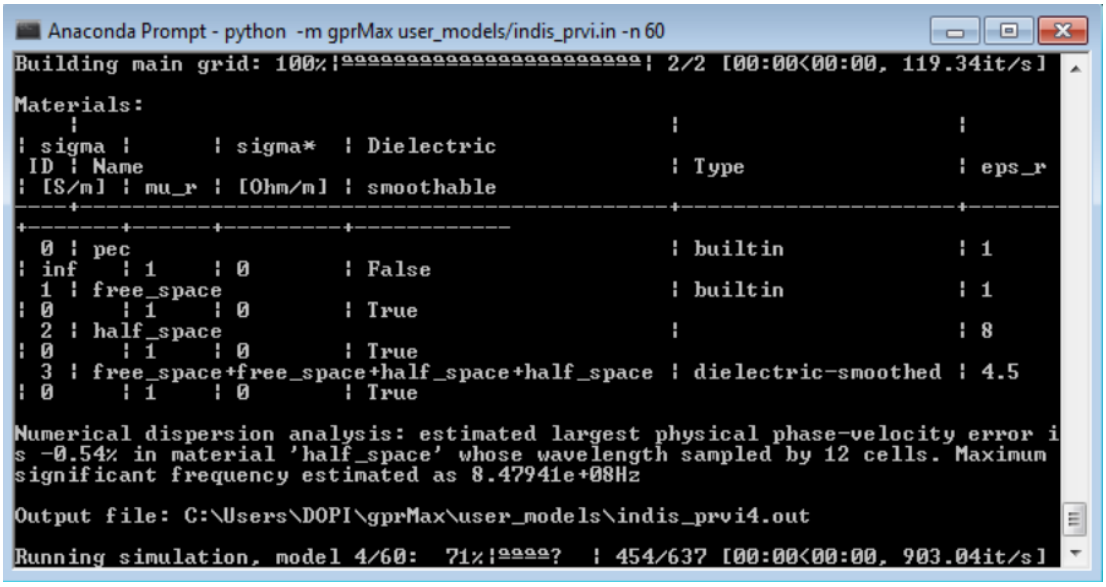


*Figure 2 Command promnt window during gprMax simulation*

## 5. RESULTS AND DISCUSSION

Acquired simulation results for all eight scenes described in Table 1 are represented in Figure 3.

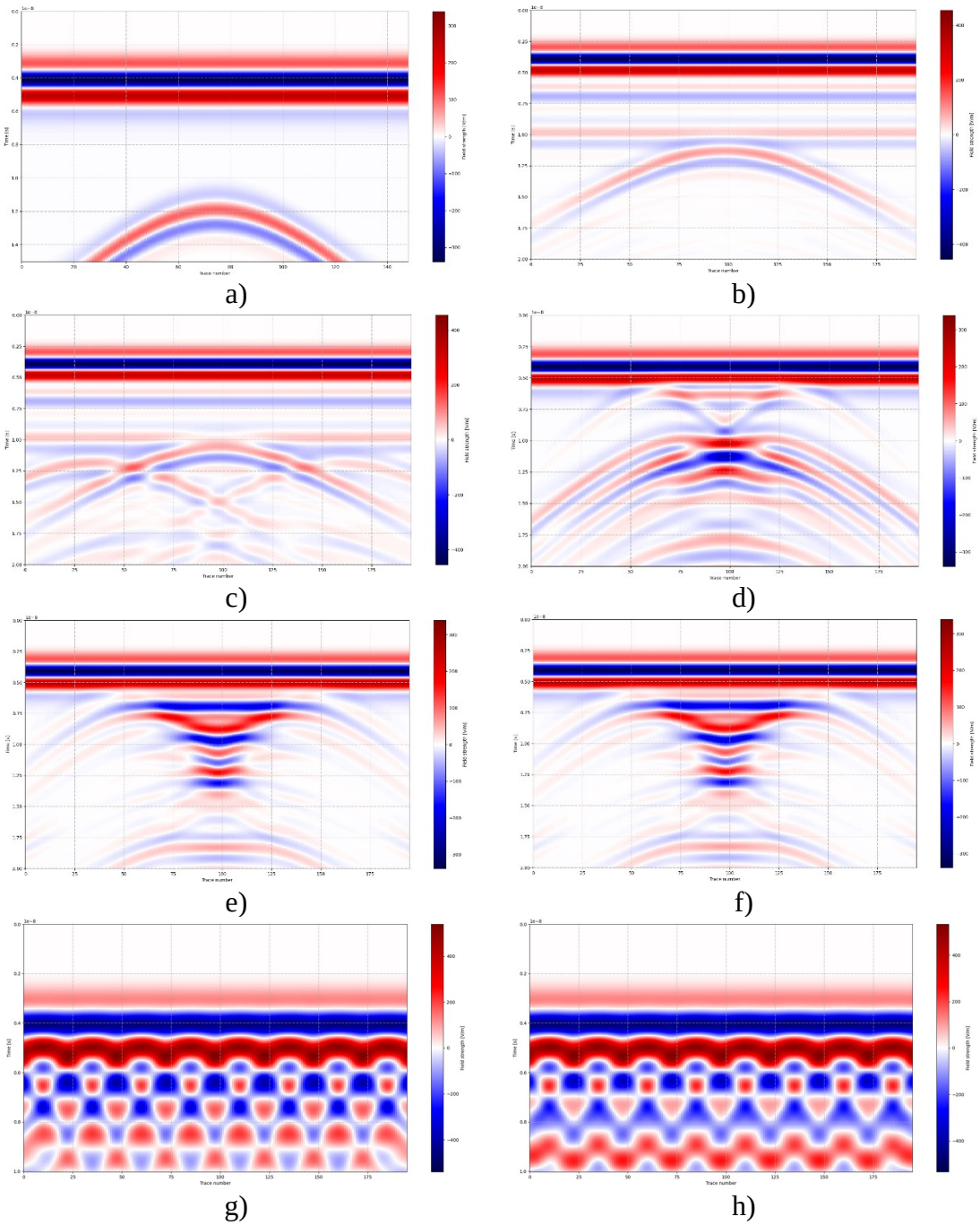


*Figurea 3 Synthetic radargrams generated by gprMax for eight described scenes*

In the first case, one metallic pipe in homogenous soil, hyperbolic reflection can be slearly seen (Figure 3a), with positive value of amplitude. Metallic pipe in soil with three layers, is shown in Figure 3b. Here it can be noticed that the amplitude of hyperbolic reflection is of lower value, compared to the first case. In the case of three pipes in three-layer soil the amplitude is similar to second case, the only difference being overlapping of hyperbolas prongs (Figure 3c). In this case a faint shapes of interferred hyperbolas at bigger depths can appear, which makes the interpretation of such radargrams more complicated. Characteristics of heat line pipes in dirted trench is that, besides the two hyperbolic

reflections from the pipes, a weak reflections can appear as a result of different relative dielectric constants of the trench and surrounding soil (Figure 3d). These hyperbolas are close to the surface and similar to hyperbola. Heat line pipes in the concrete channel yield the reflection of onlu the concrete channel (Figure 3e) and almost identical result is in the case of heat line pipes in reinforced concrete channel (Figure 3f). The main reasons for this is higher level of reflected signal and central frequency of used antenna. The last two examples of synthetic radargrams are for the rebar in concrete. These cases are typical for civil engineering, and results show that there are small differences in reflected signals for the case of one row of compared to two rows of rebar. In case of one row (Figure 3g) the amplitude of reflected signal is degreasing with depth and a number of interferred hyperbolas appear in the zones beneath the original reflections. In case of two rows of rebar (Figure 3h) reflected signal is amplified by the second, deeper row and the number of interferred hyperbolas is lower between two rows of rebar.

## 6. CONCLUSION

In this paper the application of gprMax software for synthetic radargram generation is shown through eight examples. Obtained results show that not only complex scenarios can be simulated, but these simulations can be very helpful in radargram interpretation. Operators not very experienced in data aquisition and interpretation can use synthetic radargrams generated for specific scenario to create an example of expected result. However, obtained results should not be considered a copy of a real radargram for the same scenario. Synthetic radargrams are simulation result in ideal condition, noise-free, in homogeneous layers of soil, without damage on objects of interest and other effects that can have impact to reflected signal. For future consideration, some of these conditions should be taken into account, their imfluence should be assessed, and synthetic radargrams for some more complex scenes should be generated and analyzed.

### ACKNOWLEDGEMENT

This research has been supported by the Ministry of Science, Technological Development and Innovation (Contract No. 451-03-34/2026-03/200156) and the Faculty of Technical Sciences, University of Novi Sad through project “Scientific and Artistic Research Work of Researchers in Teaching and Associate Positions at the Faculty of Technical Sciences, University of Novi Sad 2026” (No. 01-3609/1).

## REFERENCES

[1] Benedetto A., Pajewski L. (2015). *Civil Engineering Applications of Ground Penetrating Radar*. Springer.

[2] Daniels D. J. (1996). Surface Penetrating Radar. *Electronics & Communication Engineering Journal*, Volume 8, No. 4, pp. 165–182.

[3] Jol H. M. (2009). *Ground Penetrating Radar: Theory and Applications* (1st edition). Elsevier, Oxford, United Kingdom.

[4] Bergmann T., Robertsson J. O., Holliger K. (1998). Finite-difference modeling of electromagnetic wave propagation in dispersive and attenuating media. *Geophysics*, Volume 63, No. 3, pp. 856–867. https://doi.org/10.1190/1.1444396

[5] Bourgeois J. M., Smith G. S. (1996). A fully three-dimensional simulation of a ground-penetrating radar: FDTD theory compared with experiment. *IEEE Transactions on Geoscience and Remote Sensing*, Volume 34, No. 1, pp. 36–44. https://doi.org/10.1109/36.481890

[6] Bugarinović Ž., Gavrilović M., Ristić A., Bugarinović M. Š., Radulović A., Govedarica M. (2024). Detection of hyperbolic reflections on real GPR data using YOLO model trained with synthetic data. *2024 47th International Conference on Telecommunications and Signal Processing (TSP)*, pp. 40–44. IEEE. https://doi.org/10.1109/TSP63128.2024.10605917

[7] El-Mahallawy M. S., Hashim M. (2013). Material classification of underground utilities from GPR images using DCT-based SVM approach. *IEEE Geoscience and Remote Sensing Letters*, Volume 10, No. 6, pp. 1542–1546. https://doi.org/10.1109/LGRS.2013.2261796

[8] Ristić A., Bugarinović Ž., Vrtunski M., Govedarica M. (2017). Point coordinates extraction from localized hyperbolic reflections in GPR data. *Journal of Applied Geophysics*, Volume 144, pp. 1–17. https://doi.org/10.1016/j.jappgeo.2017.06.003

[9] Salucci M., Tenuti L., Poli L., Massa A. (2017). Buried object detection and imaging through innovative processing of GPR data. *2017 11th European Conference on Antennas and Propagation (EuCAP)*, pp. 1703–1706. IEEE. https://doi.org/10.23919/EuCAP.2017.7928232

[10] Bugarinović Ž., Vrtunski M., Ristić A., Batilović M., Govedarica M. (2018). Automated data extraction from synthetic and real radargrams of complex structures. *Journal of Environmental and Engineering Geophysics*, Volume 23, pp. 407–421. https://doi.org/10.2113/JEEG23.4.407

[11] Yao H., Pan S., Fan Y., Liu Y., Airey G., Sreeram A., Hou Y. (2025). Intelligent detection of subsurface road targets using a combined numerical simulation and deep learning method. *Computer-Aided Civil and Infrastructure Engineering*, Volume 40, Issue 29, pp. 5808–5820. https://doi.org/10.1111/mice.70121

[12] Meşecan İ., Cico B., Bucak İ. Ö. (2020). Feature vector for underground object detection using B-scan images from GprMax. *Microprocessors and Microsystems*, Volume 76, Article 103116. https://doi.org/10.1016/j.micpro.2020.103116

[13] Meşecan İ., Bucak İ. Ö., Çiço B. (2018). Comparison of histograms of oriented gradients (HOG) and n-row average subtraction (nRAS) using GprMax. *Microprocessors and Microsystems*, Volume 63, pp. 140–146. https://doi.org/10.1016/j.micpro.2018.08.011

[14] Bugarinović Ž., Vrtunski M., Ristić A., Batilović M., Govedarica M. (2026). Application of ground-penetrating radar (GPR) scanning technology in the inspection of concrete structures. *International conference on contemporary theory and practice in construction XVII STEPGRAD XVII*, Volume 1 pp. 1039–1046.

[15] Warren C., Giannopoulos A., Giannakis I. (2016). gprMax: Open source software to simulate electromagnetic wave propagation for ground penetrating radar. *Computer Physics Communications*, Volume 209, pp. 163–170. https://doi.org/10.1016/j.cpc.2016.08.020

[16] Giannopoulos A. (2005). Modelling ground penetrating radar by GprMax. *Construction and Building Materials*, Volume 19, No. 10, pp. 755–762. https://doi.org/10.1016/j.conbuildmat.2005.06.007

https://doi.org/10.24867/INDIS-2026-EN-852



# MONITORING THE SPATIO-TEMPORAL DYNAMICS OF FOREST AREAS USING LANDTRENDR SEGMENTATION OF SATELLITE IMAGE TIME SERIES

*Milan Gavrilović[1], Igor Ruskovski[2], Milka Šarkanović Bugarinović[3], Dušan Jovanović[4], Miro Govedarica[5]*

***Summary:***

The aim of this study is to detect the spatiotemporal dynamics of forest cover in the "Gornje Podunavlje" Special Nature Reserve by applying the LandTrendr algorithm to a time series of Landsat images. Compared to traditional approaches, the algorithm used here treats the entire time series as a continuous process; this reduces sensitivity to atmospheric noise and enables the differentiation of short-term changes from long-term degradation processes. The results, validated at the individual pixel level through comparison with satellite imagery, demonstrate successful detection of vegetation changes, while an RGB visualization of the fitted values provides a quick spatial overview of change distribution across the entire area. The findings confirm that the applied approach is a reliable tool for the long-term monitoring of forest ecosystem dynamics.

*Keywords: LandTrendr, Landsat, remote sensing, segmentation*

# PRAĆENJE PROSTORNO-VREMENSKE DINAMIKE ŠUMSKIH POVRŠINA POMOĆU LANDTRENDR SEGMENTACIJE VREMENSKE SERIJE SATELITSKIH SNIMAKA

***Rezime:***

Cilj ovog rada je detekcija prostorno-vremenske dinamike šumskog pokrivača na području Specijalnog rezervata prirode „Gornje Podunavlje" primenom LandTrendr algoritma nad vremenskom serijom Landsat snimaka. Za razliku od tradicionalnih pristupa, korišćeni algoritam posmatra celu vremensku seriju kao kontinuiran proces, čime se smanjuje osetljivost na atmosferski šum i omogućava razlikovanje kratkotrajnih promena od dugoročnih procesa degradacije. Rezultati, potvrđeni na nivou pojedinačnih piksela poređenjem sa satelitskim snimcima, pokazuju uspešnu detekciju promena vegetacije, dok RGB prikaz fitovanih vrednosti omogućava brz prostorni uvid u distribuciju promena na nivou celog područja. Dobijeni rezultati potvrđuju da je primenjeni pristup pouzdan alat za dugoročno praćenje dinamike šumskih ekosistema.

*Ključne reči: LandTrendr, Landsat, daljinska detekcija, segmentacija*

[1] Teaching assistant, Faculty of Technical Sciences, University of Novi Sad, Novi Sad, Serbia, milangavrilovic@uns.ac.rs, 0000-0003-4671-7544
[2] Teaching assistant, Faculty of Technical Sciences, University of Novi Sad, Novi Sad, Serbia, rus_igor@uns.ac.rs, 0000-0003-2097-4884
[3] Research Associate, Faculty of Technical Sciences, University of Novi Sad, Novi Sad, Serbia, milkasb@uns.ac.rs, 0000-0001-6648-4579
[4] Full professor, Faculty of Technical Sciences, University of Novi Sad, Novi Sad, Serbia, dusanbuk@uns.ac.rs, 0000-0001-6834-0376
[5] Full professor, Faculty of Technical Sciences, University of Novi Sad, Novi Sad, Serbia, miro@uns.ac.rs, 0000-0003-1698-0800

## 1. INTRODUCTION

Forests represent one of the most significant terrestrial ecosystems on the planet, playing a key role in regulating the global climate system and preserving biodiversity [1]. Forest ecosystems also play a central role in mitigating the effects of climate change by absorbing significant amounts of carbon dioxide from the atmosphere [2]. Beyond their climate-related function, forests provide a wide range of ecosystem services essential to both humanity and nature such as protecting soil from erosion and maintaining microclimatic conditions, while also serving as habitats for a vast number of plant and animal species.

Due to various factors, forest ecosystems worldwide are facing increasingly intense pressure that leads to the loss of forest cover and habitat degradation [3], creating a need for reliable methods to continuously monitor their condition and the dynamics of change [4]. Monitoring these changes over time requires approaches capable of detecting both abrupt and gradual changes, as well as distinguishing between temporary vegetation loss and permanent land-use change. Traditional forest monitoring methods, such as field measurements and on-site visual inspections, offer high accuracy and detailed insight into local conditions, yet they are time-consuming, costly, and difficult to implement over large areas. Consequently, satellite imagery, which provides access to long-term data time series, has become an indispensable tool in modern research on forest cover change [5].

Traditional approaches to deforestation detection have primarily relied on methods such as bi-temporal change classification by comparing classified images from two points in time to identify pixels that have undergone a change in land-cover class [6]. Although simple to implement, this method is highly sensitive to phenological differences between images, atmospheric conditions, and the choice of reference years, and it offers no insight into the dynamics of change occurring between the observed time points.

Another previously used method is classification using supervised machine learning (e.g., Random Forest, SVM, Maximum Likelihood) applied to individual images or composites [7], [8]. The main drawbacks of this approach are the need for high-quality, representative training datasets for each class and sensitivity to noise in individual images (clouds, shadows, etc.). Additionally, approaches based on spectral index thresholding [9], [10] detect change when an index value crosses a predefined threshold. Although computationally simple and easy to implement, these approaches have significant limitations. The choice of threshold is often arbitrary and depends heavily on the specific study area. Furthermore, like the previously mentioned methods, this approach does not account for the temporal dynamics of the observed phenomenon but instead treats each change in isolation.

In response to the aforementioned limitations, Kennedy et al. [11] developed the LandTrendr algorithm (Landsat-based Detection of Trends in Disturbance and Recovery), which views change as a continuous process over time. Instead of classifying individual images, LandTrendr fits a series of linear segments to the annual time series of spectral band or index values for each pixel, thereby effectively filtering out random noise (atmospheric interference, shadows, phenological variations) from the actual signal trend [11]. Biophysically relevant parameters, such as the year the change began, its duration, and its magnitude, can be directly derived from the resulting segmented trajectory.

The significance of the LandTrendr algorithm lies in several of its characteristics, such as the ability to distinguish between types of change, meaning the algorithm not only detects that a change has occurred but also determines whether it involves a sudden loss

(e.g., logging, fire) or gradual degradation, while also tracking the recovery process. Furthermore, the segmentation of the entire time series makes the algorithm less sensitive to individual "bad" images compared to bi-temporal approaches.
The aim of this study is to apply the LandTrendr algorithm to a time series of satellite images to detect spatial and temporal patterns of forest loss and recovery in the Gornje Podunavlje region. By analyzing segmented trajectories of spectral bands or indices, the study seeks to identify the locations, timing, and intensity of forest cover changes, thereby contributing to a better understanding of long-term trends.

## 2. STUDY AREA AND DATASETS

### 2.1. STUDY AREA

The Gornje Podunavlje Special Nature Reserve is located in the northwestern part of Bačka, along the left bank of the Danube, within the municipalities of Apatin and Sombor, right next to the borders with Hungary and Croatia (Fig. 1). The reserve covers an area of 19 648 hectares, stretching along a 66-kilometer section of the Danube [12]. The diversity of aquatic, wetland, and terrestrial ecosystems provides a habitat for numerous rare and endangered species; consequently, the area is recognized as a center of ecosystem and species diversity of both national and international importance. For the Republic of Serbia, monitoring changes in forest cover within Gornje Podunavlje is of particular significance given the area's status as a special nature reserve and its role within a transboundary ecological zone; its preservation extends beyond national boundaries and constitutes an obligation within the context of international nature conservation.

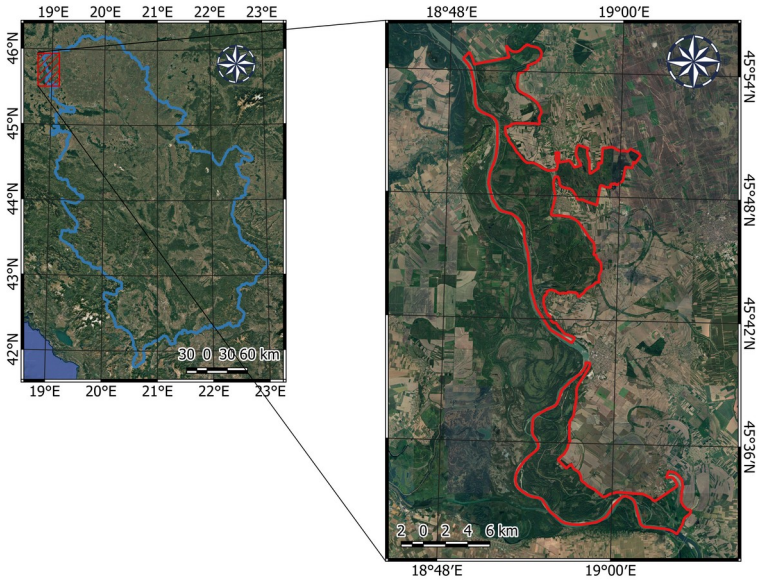


*Fig. 1 Area of interest*

### 2.2. LANDSAT

The Landsat program represents the longest-running continuous satellite imaging mission of the Earth's surface, dating back to the 1972 launch of the Landsat 1 satellite [13]. Over decades of development, the program has encompassed a series of satellite missions, ranging from Landsat 1–3 (featuring the MSS sensor) and Landsat 4–5 (equipped with the Thematic Mapper/TM sensor) to Landsat 7 (featuring the ETM+ sensor, which has operated with partial limitations since 2003 due to a Scan Line Corrector/SLC mechanism failure). A newer generation is represented by Landsat 8 and

Landsat 9, equipped with OLI/OLI-2 and TIRS/TIRS-2 sensors, which offer improved radiometric quality and additional spectral bands compared to earlier missions [13]. Thanks to the overlap and continuity of these missions, a consistent time series of satellite imagery with 30-meter spatial resolution is now available, covering a period of nearly five decades with a 16-day temporal resolution. This unique combination of a long time series, global coverage, and free access to the archive has made the Landsat archive a fundamental data source for research into long-term land-cover changes.

## 3. METHODOLOGY

LandTrendr (Landsat-based detection of Trends in Disturbance and Recovery) is based on a conceptual understanding of change that differs from classical approaches. Instead of treating change as a contrast between states at two isolated points in time, the algorithm views the spectral history of each pixel as a continuous process unfolding over time [14]. The goal is to track state changes that persist over years rather than recording short-term intra-annual trends; consequently, the LandTrendr approach is typically applied to time-series data where a single observation or representative value is selected to represent each year [15]. The algorithm's workflow proceeds through several successive phases [11]:

- time-series preparation,
- anomaly removal,
- identification of initial vertex candidates,
- iterative reduction of the number of vertices,
- selection of the optimal number of segments,
- definition of model constraints and behavioral rules,
- segmented trajectory and derived attributes,
- fitting the trajectory to vertices (Fit-To-Vertex, FTV).

### 3.1. TIME SERIES PREPARATION

For each pixel, a time series of annual values for the selected spectral channel or index is generated (Fig. 2), derived from a single representative (typically the median) image per year [16]. This type of annual aggregation aims to minimize the impact of seasonal (phenological) variations and ensures that all observations in the series correspond to approximately the same period of the growing season; consequently, changes in the time series can be attributed to actual changes on the ground rather than differences in acquisition dates.

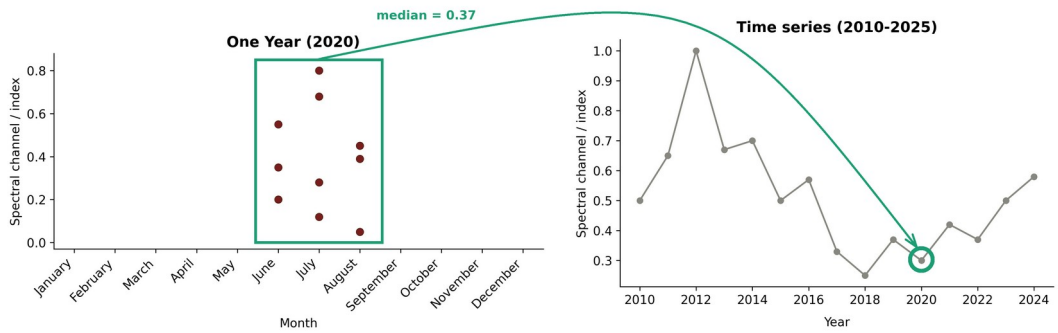


*Fig. 2 Principle of time series formation*

### 3.2. ANOMALY REMOVAL

Prior to segmentation, the algorithm scans the sequence to identify individual, isolated values that deviate significantly from the trend of their neighbors, so-called

"spikes" ,which most likely represent noise (e.g., an unremoved cloud or shadow) rather than an actual change (Fig. 3). These values are smoothed (interpolated based on neighboring points) according to a predefined sensitivity parameter, thereby preventing a single anomaly from being misinterpreted as a change.

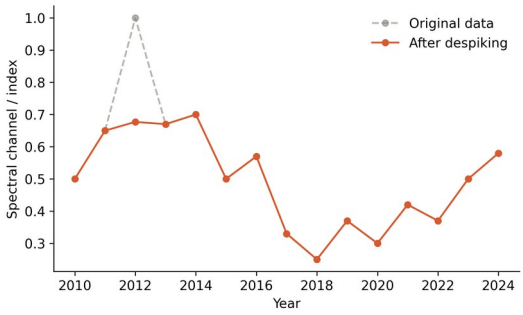


*Fig. 3 Removing anomalies*

## 3.3. IDENTIFICATION OF INITIAL VERTEX CANDIDATES

After removing anomalies, the algorithm identifies all local extrema in the sequence (points where a change in direction occurs). Each such point represents a potential vertex, a candidate for the boundary between two segments. Typically, this stage yields a significantly larger number of candidates than is necessary to describe the trajectory (Fig. 4), as the process captures even minor local fluctuations.

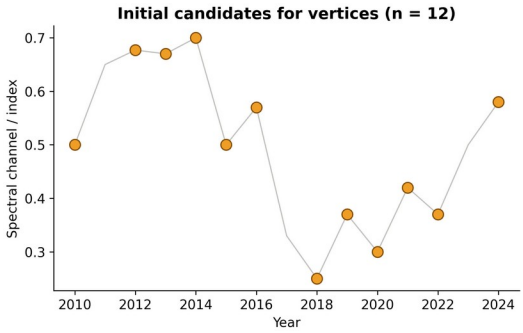


*Fig. 4 Starting vertices*

## 3.4. ITERATIVE REDUCTION OF THE NUMBER OF VERTICES

Starting from an initial (excessively large) set of vertices, the algorithm iteratively reduces the number of vertices until a predefined maximum number of segments is reached (Fig. 5). In each iteration, a series of straight lines (segments) is fitted to the observations based on the current set of vertices, the fitting error is calculated, and the vertex whose removal causes the least degradation in quality is eliminated from the set [11]. This process repeats until the number of remaining vertices reaches a predetermined minimum.

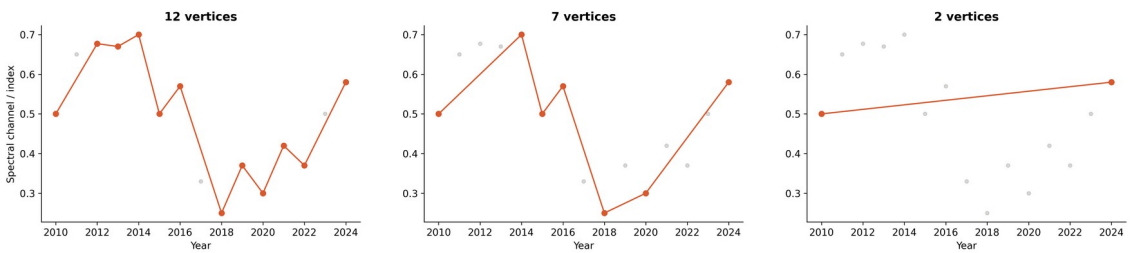


*Fig. 5 Vertex reduction*

## 3.5. SELECTION OF THE OPTIMAL NUMBER OF SEGMENTS

Since a larger number of segments almost always reduces the fitting error, the algorithm does not automatically select the model with the lowest error; instead, it employs a statistical criterion based on the F-test to determine whether adding a new segment yields a statistically significant improvement over a simpler model (Fig. 6) [11]. By comparing models with varying numbers of segments against a specified statistical significance threshold, the algorithm selects the model that strikes the best balance between simplicity and the accurate representation of the actual data trajectory [11].

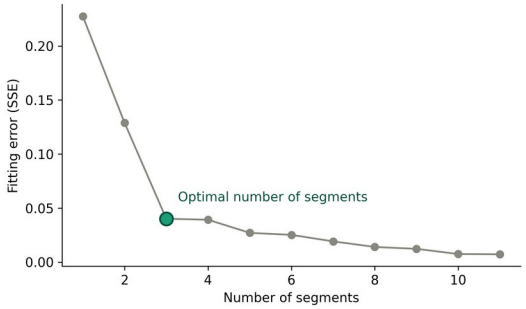


*Fig. 6 Optimization of number of segments*

## 3.6. DEFINITION OF MODEL CONSTRAINTS AND BEHAVIORAL RULES

The segmentation process is further controlled by a set of parameters that constrain the model's behavior in accordance with the known physical characteristics of the process being monitored. For example, a constraint can be defined to prevent the post-change recovery period from being modeled as lasting less than one year (Fig. 7), or to specify the maximum permissible deviation of a segment's slope relative to adjacent segments. Such rules ensure that the final model is not only statistically sound but also consistent with the realistic nature, whether gradual or abrupt, of the change process being analyzed [11].

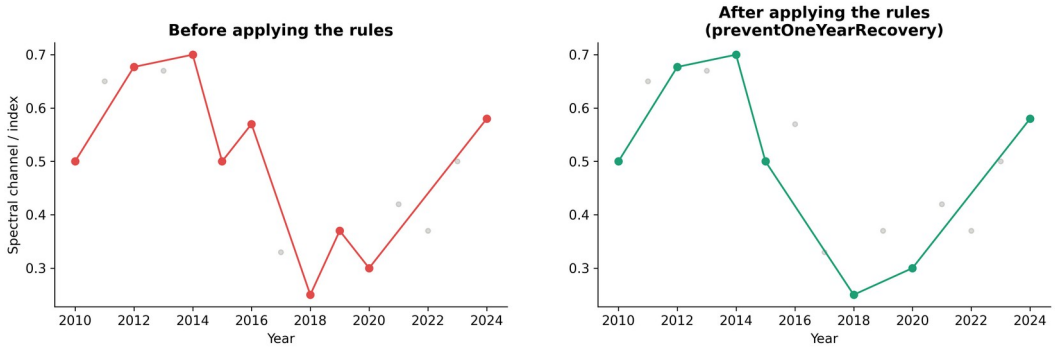


*Fig. 7 Constraining detection of changes shorter than one year*

## 3.7. SEGMENTED TRAJECTORY AND DERIVED ATTRIBUTES

The final result of the segmentation is a series of vertices (defined by a year–value pair) and the segments connecting them. From the simple geometry of each segment (slope, length, and initial and final values), quantitative indicators of the change itself, such as start year, duration, and magnitude, can be directly calculated; these represent the algorithm's primary outputs and the basis for further analysis (Fig. 8).

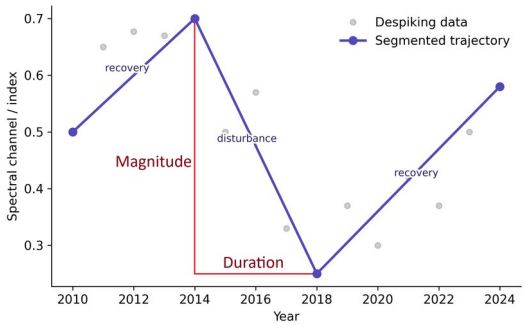


*Fig. 8 Segmented trajectory with attributes*

The following table (Tab. 1) shows the derived attributes obtained by applying the LandTrendr algorithm.

*Tab. 1 Attributes of segmented trajectories*

| Segment | Year of start | Duration [years] | Magnitude | Type |
|---|---|---|---|---|
| **2010-2014** | 2010 | 4 | 0.20 | recovery |
| **2014-2018** | 2014 | 4 | -0.45 | disturbance |
| **2018-2024** | 2018 | 6 | 0.33 | recovery |

## 3.8. FITTING THE TRAJECTORY TO VERTICES (FIT-TO-VERTEX, FTV)

As an additional step, the algorithm allows an interpolated value to be calculated for each year within a segment based on the linear equation of that segment (Fig. 9) [17]. This procedure results in a "cleaned" time series, consistent with the identified trend.

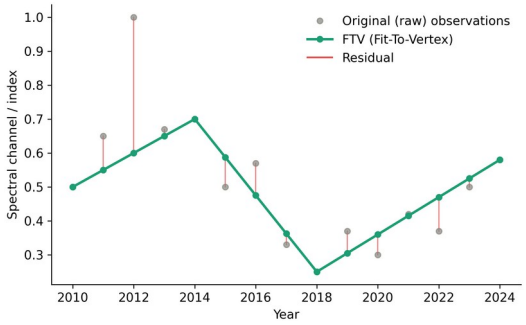


*Fig. 9 Interpolation of new spectral values for each year*

## 4. RESULTS AND DISCUSSION

In the practical part of the work, the described methodology was applied in the area of the Special Nature Reserve “Gornje Podunavlje”, in order to detect the spatio-temporal pattern of forest cover loss and recovery in the period from 1990 to 2025. A study [18] has already addressed the application of the LandTrendr algorithm in this area; however, its analysis was limited to only a portion of the Reserve rather than its entire extent. In contrast, the aim of this study is to examine the algorithm's performance and results when applied to the Reserve's entire area over an extended period, thereby providing a more comprehensive insight into the spatiotemporal dynamics of the forest cover in the region.

## 4.1. MODEL PARAMETERS

Unlike approaches that use recordings throughout the calendar year, in this paper the analysis is limited to the summer period, i.e. the months of June, July and August. The reason for this limitation lies in the need to ensure phenological consistency between annual observations. Vegetation is in full development during the summer months, so its spectral response varies the least. The inclusion of recordings from transition periods (spring, autumn) or winter period, in which the vegetation is in the phase of leafing, leaf fall or dormancy, would introduce additional, phenologically determined variability into the time series, i.e. variability that does not reflect the actual change in forest cover, but rather the seasonal cycle of vegetation. Limiting the analysis to the June–August period ensures that the observed changes in the spectral index time series to the greatest extent reflect real, permanent changes, rather than differences in date or phenophase.

When creating a time series of images, images from the Landsat 5, Landsat 8 and Landsat 9 missions were used, while Landsat 7 was excluded from the analysis. The reason for the exclusion of the Landsat 7 images lies in the failure of the Scan Line Corrector (SLC) mechanism, due to which the images of this mission contain systematic bands of missing data. Before forming annual composites, pixels covered by clouds, cloud shadows and water surfaces were removed from each individual image.

For time series segmentation, NDVI (Normalized Difference Vegetation Index) was used, defined as:

$$NDVI = \frac{\mathrm{NIR} - \mathrm{RED}}{\mathrm{NIR} + \mathrm{RED}} \tag{1}$$

NDVI was selected as an indicator of the state of vegetation due to its wide application and proven sensitivity to changes in the density and vitality of the vegetation cover [19]. In this paper, when creating segments, it is allowed to create a maximum of six segments per pixel, which is enough to describe up to six consecutive periods of change or stability during the observed period, without the model becoming too complex and not following the noise instead of the real trend. Anomaly sensitivity is controlled with a spike threshold of 0.9, which tells the algorithm how much to trust a single value that deviates conspicuously from its neighbors in the sequence. A value of 0.9 means that such a point only slightly approaches the expected (neighboring) value.

In order to avoid that the algorithm accepts as a valid recovery segment the complete regeneration of vegetation lasting only one year, which rarely corresponds to a real biological process, an additional parameter was defined that excludes such segments. To the same end, the maximum allowable speed of recovery is also limited, so that any recovery faster than 4 years is dismissed as biophysically implausible. The threshold for accepting an additional segment is set to 0.05, in order to create a more reliable model, and in the case when two models are similar, the simpler one is chosen, with a smaller number of segments (bestModelProportion = 0.75).

Finally, in order for segmentation to be performed at all for a pixel, the time series was required to contain at least 7 valid (unmasked) annual observations. Pixels with a smaller number of observations were omitted from the analysis. Other parameter values used in this paper correspond to the configuration proposed by Kennedy et al. [11], which is an informal standard in the literature based on the LandTrendr algorithm.

## 4.2. RESULTS FOR SINGLE PIXELS

Before moving on to the analysis of spatial patterns of forest cover loss and recovery at the level of the entire study area, the results of applying the LandTrendr algorithm were first checked at the level of individual pixels. The goal of this step is to confirm that the

segmented trajectories, obtained from the time series of the spectral index, really correspond to real, visible changes in the state of the vegetation in the field, thus validating the reliability of the algorithm before its application to the entire analysis area.

The first example (Fig. 10) shows a long period of stability with high, uniform values of the spectral index until 2019, followed by a sudden and marked drop in values. This pattern is a typical signature of sudden forest loss, such as logging or forest fire, rather than a gradual process of degradation. Satellite imagery unequivocally confirms that the detected change is the result of real forest cover loss, not noise in the data.

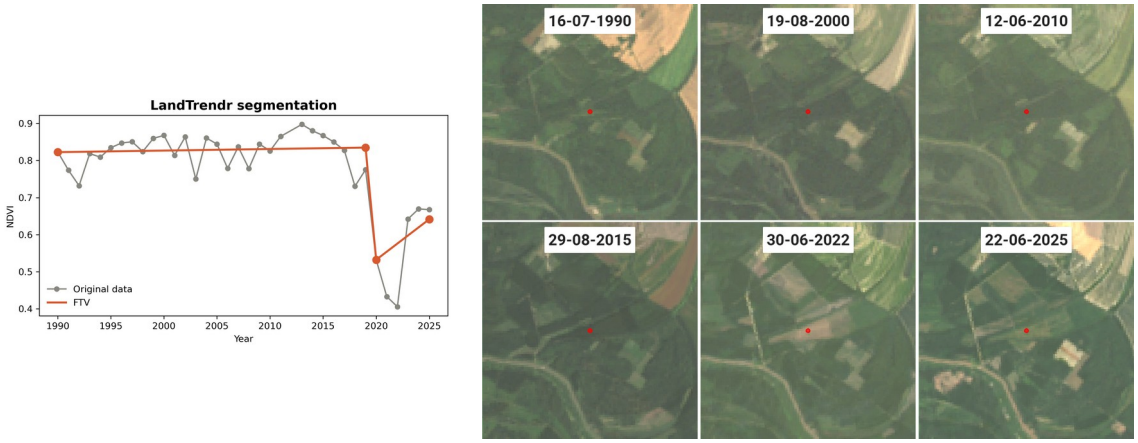


*(a)* *(b)*

*Fig. 10 Deforestation*

The next example (Fig. 11) shows the detected forest cutting and its recovery in the analyzed time interval of 35 years. Unlike the first example, the next image shows a segmented trajectory that has the so-called V-form, ie. a period of stability followed by a sharp decline in 2006, followed by an upward segment that returns the value of the index to a level close to the original until 2010, after which a period of stability follows again.

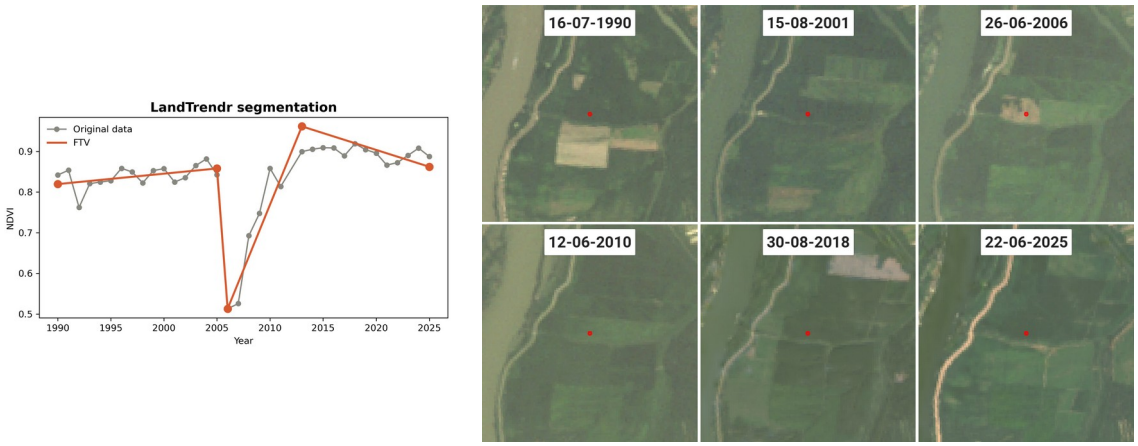


*(a)* *(b)*

*Fig. 11 Recovery after logging*

Unlike the previous two examples, the segmented trajectory here does not show a sudden drop, but rather a continuous decline in index values throughout the observed period, with no signs of recovery (Fig. 12). Such a prolonged, monotonically decreasing trend indicates a permanent change in land use. This is clearly confirmed by satellite imagery, where earlier images show closed forest cover, while images from the later

period reveal regular, geometrically defined plots characteristic of arable agricultural land.

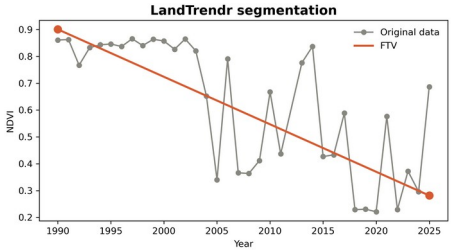


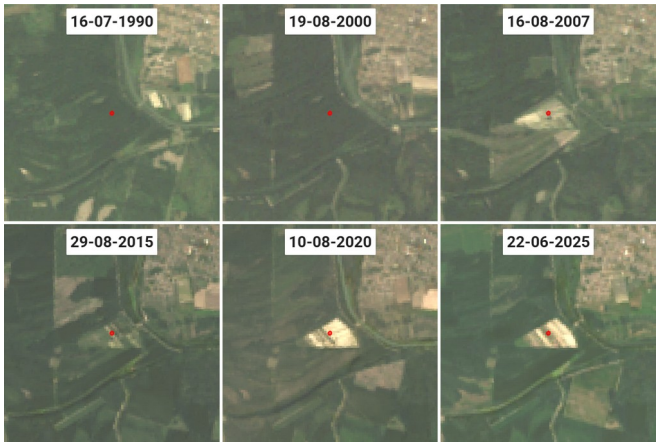


*(a)* *(b)*

*Fig. 12 Transition to arable land*

The segmented trajectory of the next pixel reveals a more complex, multi-segment pattern (Fig. 13). Forest is absent in the initial year (1990), followed by a period of recovery up to 2001; it then disappears again (a drop in 2019), followed by a period without vegetation, before an upward segment appears in 2025, indicating a recovery of the vegetation cover. This recurring cycle: absent-present-absent-present, illustrates the LandTrendr algorithm's ability to detect multiple successive changes within a single time series, rather than just a single isolated event.

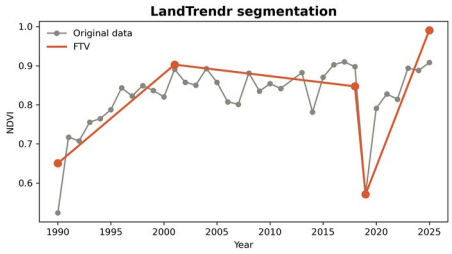





*(a)* *(b)*

*Fig. 13 Detection of multiple consecutive changes within the same time series*

In addition to the pixels where the LandTrendr algorithm reliably detects forest cover changes, a group of pixels yielding significantly less reliable results was also observed —specifically, those located on arable agricultural land. Unlike forest cover, where changes typically reflect long-term, permanent processes, agricultural land is characterized by regular, annual state transitions: from bare, tilled soil through crop development to harvest and the subsequent clearing of the plot. During this cycle, depending on the crop type, NDVI values fluctuate unpredictably over short time intervals (Fig. 14). Since LandTrendr relies on the assumption that the time series reflects a gradual, biophysically meaningful process with clearly defined periods of stability, such high-frequency, irregular fluctuations violate the algorithm's fundamental premises; this manifests as issues such as over-segmentation or an inability to distinguish actual change.

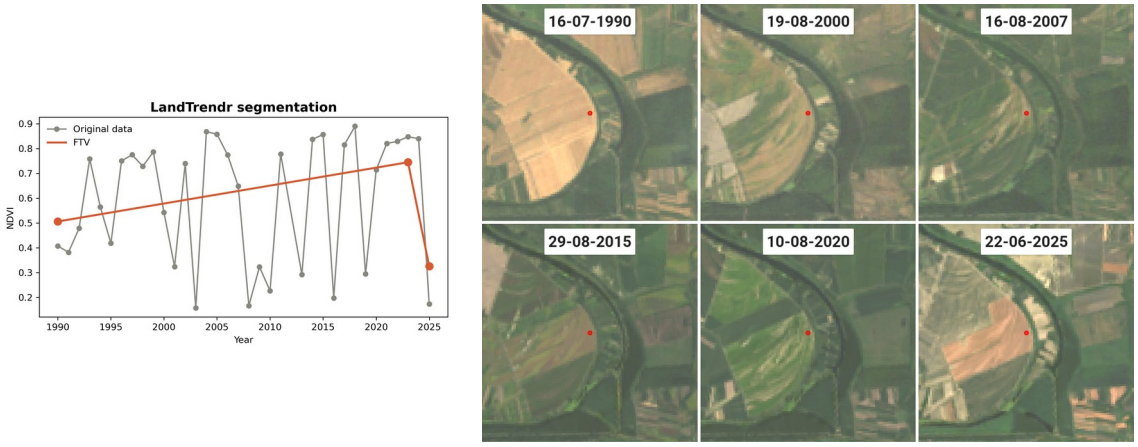


*(a)* *(b)*

*Fig. 14 Time-series segmentation of arable land*

## 4.3. FITTED IMAGES IN RGB MODE

The analysis of individual pixels, presented in the previous chapter, is useful for understanding and validating the fundamental operating principle of the LandTrendr algorithm. However, it is insufficient on its own to capture spatial patterns across the entire study area. To address this, LandTrendr segmentation is applied not merely to select, manually chosen pixels but to every pixel within the study area, thereby generating a segmented trajectory for each one. Based on these trajectories, a separate raster of fitted (FTV) spectral channel or index values is generated for each year of the study period. This process yields an equivalent time series of "cleaned" annual rasters that are free from noise and other transient disturbances while preserving the actual, long-term dynamics of change. The resulting annual fitted rasters are then combined into an RGB display, where fitted channel or index values from three selected, characteristic years of the study period are assigned to the red, green, and blue channels, respectively.

Specifically, this study created an RGB composite in which fitted NDVI values for three characteristic years: 1990 (R), 2007 (G), and 2025 (B) were assigned to the red (R), green (G), and blue (B) channels; this allows a single image to provide insight into vegetation conditions at three distinct points in time within the study period (Fig. 15). Such a visualization enables the easy identification of change types based on pixel color. Areas that maintained a stable NDVI throughout all three years appear white or gray (reflecting an equal contribution from all three channels), whereas areas that lost vegetation during an earlier period and subsequently recovered, or vice versa, take on distinctive, easily discernible colors, depending on which of the three observed years showed low or high NDVI values.

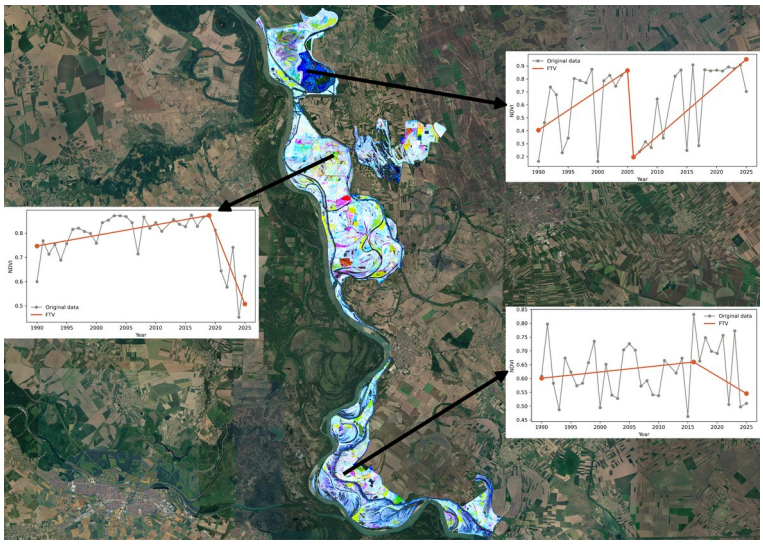

*Fig. 15 Fitted images in RGB mode*

To isolate segments representing truly significant and abrupt changes from the total set of detected segments, an additional filtering step based on two criteria: magnitude and duration of change, was applied to the LandTrendr segmentation results.

Magnitude filtering was set to values exceeding 0.2 in spectral index units. This ensured that only pixels recording a loss greater than this threshold were retained, while segments showing smaller, more gradual spectral index changes were excluded from further analysis. This process eliminates minor, potentially unreliable fluctuations which might stem from residual noise or subtle vegetation changes and retains only those changes pronounced enough to confidently represent an actual loss of vegetation cover.

In addition to magnitude, a duration criterion was applied, targeting segments lasting less than three years. This isolates abrupt, short-term changes such as logging, fire, or extreme weather events causing rapid vegetation loss while excluding segments that reflect gradual, long-term processes (Fig. 16).

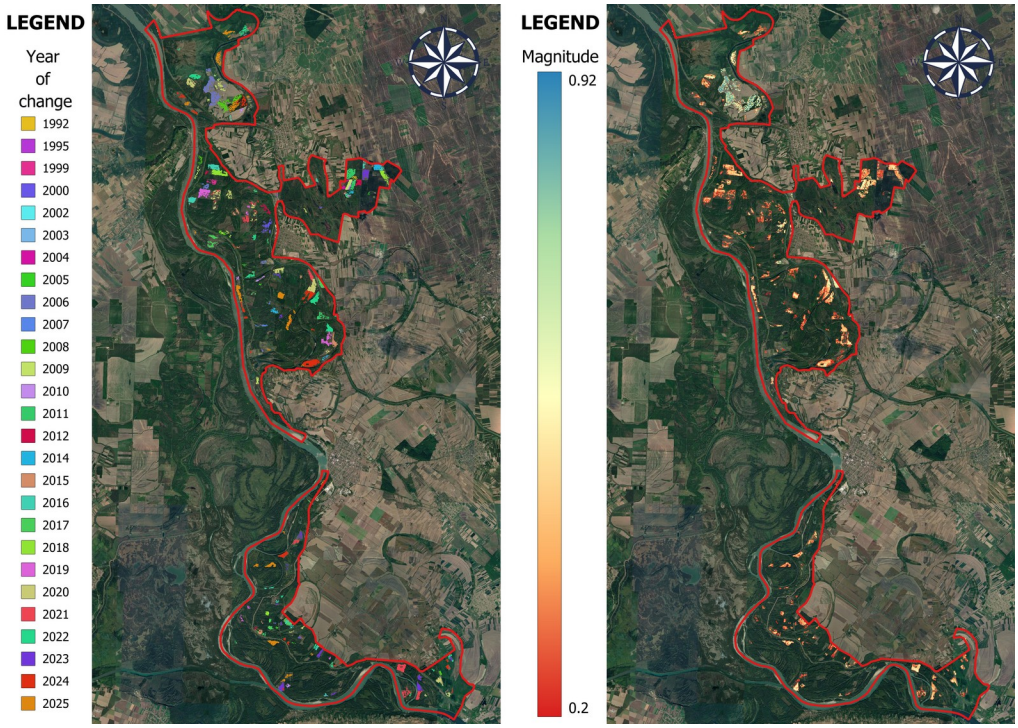


*Fig. 16 Filtered changes shown by year of detection and magnitude*

The attached image (Fig. 17) shows the spatial distribution of detected changes across a portion of the study area. The color of each pixel indicates the year the change was recorded, while the three displayed graphs illustrate segmented NDVI time series for selected locations, confirming the correct detection of vegetation cover changes.

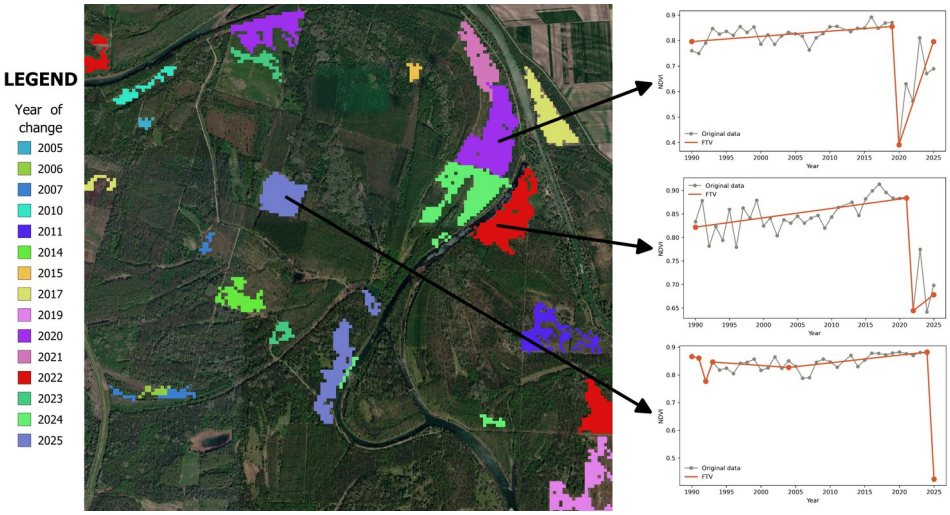


*Fig. 17 Analysis of results using segmented trajectory*

## 5. CONCLUSION

The aim of this study was to apply the LandTrendr algorithm to a time series of satellite images to detect the spatiotemporal dynamics of forest loss and recovery within the “Gornje Podunavlje” Special Nature Reserve. To this end, an annual NDVI time series was constructed from Landsat imagery covering the summer period (June–August) to ensure phenological consistency across observations; subsequently, LandTrendr segmentation was performed to identify change trajectories for each individual pixel.

The results demonstrated that the algorithm successfully detects a wide range of change patterns, spanning from abrupt, short-term losses (such as logging) and gradual vegetation recovery to permanent land-use conversion. Furthermore, generating fitted (FTV) rasters and visualizing them in RGB format provided a quick visual overview of the spatial distribution of these changes across the entire study area, while filtering based on change magnitude and duration allowed for the isolation of pixels undergoing significant changes from the broader set of detected segments.

Compared to traditional forest cover change detection approaches such as bi-temporal classification, supervised machine learning classification, or spectral index thresholding, the method employed in this study offers a distinct advantage by treating the entire time series as a continuous process, rather than reducing change to a contrast between two isolated points in time. On one hand, this significantly reduces sensitivity to atmospheric noise and individual "bad" images which are issues characteristic of methods relying on the comparison of only two points in time, while on the other, it enables the differentiation of short-term changes from long-term ones and allows for the explicit monitoring of recovery dynamics (information that older approaches typically do not provide). An additional advantage is that LandTrendr does not require predefined training samples for each change class, thereby avoiding reliance on the quality and representativeness of reference data which is a major limitation of classification-based approaches.

Despite these advantages, certain limitations of the applied approach were observed during the work. It became evident that LandTrendr segmentation results for pixels classified as arable agricultural land are unreliable; they should neither be interpreted in

the same context as results obtained for forest pixels nor used as indicators of change, given that the regular, cyclical alternation between bare soil and crops systematically violates the algorithm's fundamental assumption regarding the gradual, biophysically meaningful nature of change. Furthermore, while the RGB visualization of fitted values serves as a practical and intuitive tool for rapidly identifying areas affected by change, it is limited by the ability to display only three time points (years) simultaneously; consequently, its informativeness depends heavily on the careful selection of these years, and changes occurring outside or between them may go unnoticed in such a visualization.

Based on the observed limitations, future research could proceed in several directions. First, it is recommended that, in future applications, arable land be excluded from the analysis beforehand using an auxiliary land-use layer (e.g., CORINE Land Cover); this would restrict LandTrendr segmentation exclusively to pixels where the assumption of a long-term trend is justified, namely, forest and natural vegetation cover. Additionally, utilizing higher-resolution input imagery (e.g., Sentinel-2) could facilitate the more precise detection of changes occurring at a smaller spatial scale, while combining the results with field data would enable a more reliable quantitative validation of the derived trajectories.

## ACKNOWLEDGEMENT

This research has been supported by the Ministry of Science, Technological Development and Innovation (Contract No. 451-03-34/2026-03/200156) and the Faculty of Technical Sciences, University of Novi Sad through project “Scientific and Artistic Research Work of Researchers in Teaching and Associate Positions at the Faculty of Technical Sciences, University of Novi Sad 2026” (No. 01-3609/1).

## REFERENCES

[1] Bonan G. B. (2008). Forests and Climate Change: Forcings, Feedbacks, and the Climate Benefits of Forests. *Science*, Volume 320, Issue 5882, pp. 1444–1449. https://doi.org/10.1126/science.1155121

[2] Pan Y., Birdsey R.A., Fang J., Houghton R., Kauppi P.E., Kurz W.A., Phillips O.L., Shvidenko A., Lewis S.L., Canadell J.G., Ciais P., Jackson R.B., Pacala S.W., McGuire A.D., Piao S., Rautiainen A., Sitch S., Hayes D. (2011). A Large and Persistent Carbon Sink in the World’s Forests. *Science*, Volume 333, Issue 6045, pp. 988–993. https://doi.org/10.1126/science.1201609

[3] Potapov P., Tyukavina A., Turubanova S., Hansen M.C., Giglio L., Hernandez-Serna A., Lima A., Harris N., Stolle F. (2025). Unprecedentedly high global forest disturbance due to fire in 2023 and 2024. *Proceedings of the National Academy of Sciences*, Volume 122, Issue 30, p. e2505418122. https://doi.org/10.1073/pnas.2505418122

[4] Rodríguez Paulino E., Schlerf M., Röder A., Stoffels J., Udelhoven T. (2024). Forest disturbance characterization in the era of earth observation big data: A mapping review. *International Journal of Applied Earth Observation and Geoinformation*, Volume 128, p. 103755. https://doi.org/10.1016/j.jag.2024.103755

[5] Hansen M.C., Potapov P.V., Moore R., Hancher M., Turubanova S.A., Tyukavina A., Thau D., Stehman S.V., Goetz S.J., Loveland T.R., Kommareddy A., Egorov A., Chini L., Justice C.O., Townshend J.R.G. (2013). High-Resolution Global Maps of 21st-Century Forest Cover Change. *Science*, Volume 342, Issue 6160, pp. 850–853. https://doi.org/10.1126/science.1244693

[6] Lu D., Mausel P., Brondízio E., Moran E. (2004). Change detection techniques. *International Journal of Remote Sensing*, Volume 25, Issue 12, pp. 2365–2401. https://doi.org/10.1080/0143116031000139863

[7] Jovanović D., Gavrilović M., Borisov M., Govedarica M. (2021). Uporaba Sentinel 1 i Sentinel 2 snimaka u identifikaciji nestalih šumskih površina – studija slučaja Fruška gora (Srbija). *Šumarski List*, Volume 145, Issue 3–4, pp. 127–134. https://doi.org/10.31298/sl.145.3-4.2

[8] Gavrilović M., Ruskovski I., Sladić D., Radulović A., Govedarica M., Jovanović D. (2022). Analysis and Prediction of Spatiotemporal Changes of Urban Areas Using Neural Networks. *International conference on Contemporary Theory and Practice in Construction*, Issue 15, Banja Luka, pp.191-204. https://doi.org/10.7251/STP2215191G

[9] Escuin S., Navarro R., Fernández P. (2008). Fire severity assessment by using NBR (Normalized Burn Ratio) and NDVI (Normalized Difference Vegetation Index) derived from LANDSAT TM/ETM images. *International Journal of Remote Sensing*, Volume 29, Issue 4, pp. 1053–1073. https://doi.org/10.1080/01431160701281072

[10] Liu C.-L., Wang Y.-R., Liu W.-Y. (2025). Multi-index remote sensing for post-fire damage assessment: accuracy, carbon loss, and conservation implications. *Frontiers in Forests and Global Change*, Volume 8. https://doi.org/10.3389/ffgc.2025.1577612

[11] Kennedy R.E., Yang Z., Cohen W.B. (2010). Detecting trends in forest disturbance and recovery using yearly Landsat time series: 1. LandTrendr — Temporal segmentation algorithms. *Remote Sensing of Environment*, Volume 114, Issue 12, pp. 2897–2910. https://doi.org/10.1016/j.rse.2010.07.008

[12] Ristić Z., Matarugić D., Drobnjak D., Božić D., Urošević M. (2012). Fasciolosis of deer in the hunting area of "Gornje Podunavlje" special nature reserve. *Agroznanje*, Volume 13, Issue 3, pp. 501–509. https://doi.org/10.7251/AGRSR1203501R

[13] Wulder M.A., Loveland T.R., Roy D.P., Crawford C.J., Masek J.G., Woodcock C.E., Allen R.G., Anderson M.C., Belward A.S., Cohen W.B., Dwyer J., Erb A., Gao F., Griffiths P., Helder D., Hermosilla T., Hipple J.D., Hostert P., Hughes M.J., Huntington J., Johnson D.M., Kennedy R., Kilic A., Li Z., Lymburner L., McCorkel J., Pahlevan N., Scambos T.A., Schaaf C., Schott J.R., Sheng Y., Storey J., Vermote E., Vogelmann J., White J.C., Wynne R.H., Zhu Z. (2019). Current status of Landsat program, science, and applications. *Remote Sensing of Environment*, Volume 225, pp. 127–147. https://doi.org/10.1016/j.rse.2019.02.015

[14] Pasquarella V.J., Arévalo P., Bratley K.H., Bullock E.L., Gorelick N., Yang Z., Kennedy R.E. (2022). Demystifying LandTrendr and CCDC temporal segmentation. *International Journal of Applied Earth Observation and Geoinformation*, Volume 110, p. 102806. https://doi.org/10.1016/j.jag.2022.102806

[15] Wang W., Zhu L., Li L., Xue X., Feng Y., Xing H. (2023). A LandTrendr Algorithm-Based Study of Forest Disturbance from 2000 to 2020 in Jilin Province, China. *Polish Journal of Environmental Studies*, Volume 32, Issue 1, pp. 309–319. https://doi.org/10.15244/pjoes/153969

[16] Yang B., Wu L., Ju Z., Liu X., Liu M., Zhang T., Xu Y. (2023). Sub-Annual Scale LandTrendr: Sub-Annual Scale Deforestation Detection Algorithm Using Multi-Source Time Series Data. *IEEE Journal of Selected Topics in Applied Earth Observations and Remote Sensing*, Volume 16, pp. 8563–8576. https://doi.org/10.1109/JSTARS.2023.3312812

[17] Kennedy R.E., Yang Z., Gorelick N., Braaten J., Cavalcante L., Cohen W.B., Healey S. (2018). Implementation of the LandTrendr Algorithm on Google Earth Engine. *Remote Sensing*, Volume 10, Issue 5, p. 691. https://doi.org/10.3390/rs10050691

[18] Dedić D. (2024). Application of the LandTrendr Algorithm in the Area of the Special Nature Reserve „Gornje Podunavlje". Bechelor thesis (in Serbian), Faculty of Technical Sciences, University of Novi Sad, Serbia.

[19] Huang S., Tang L., Hupy J.P., Wang Y., Shao G. (2021). A commentary review on the use of normalized difference vegetation index (NDVI) in the era of popular remote sensing. *Journal of Forestry Research*, Volume 32, Issue 1, pp. 1–6. https://doi.org/10.1007/s11676-020-01155-1

https://doi.org/10.24867/INDIS-2026-EN-881



# INVESTIGATION OF TRANSMISSION LINE POLE VERTICALITY USING UAV LIDAR POINT CLOUDS

*Vesko Đorđević[1], Dejan Pavlović[2]*

***Summary:***

Verticality is a key indicator of the structural condition of transmission line poles, as excessive inclination increases eccentric loading of foundations and conductors. This paper presents a method in which conventional total-station surveying of the pole body is replaced by UAV LiDAR scanning, applied to a section of the transmission network in Serbia. Dense point clouds from an RTK-enabled UAV were used to determine the position of characteristic points along the pole, while the foundation corners were independently surveyed by RTK GNSS on the ground, and deviations from the vertical reference axis were computed in two perpendicular planes on five poles selected from a data set of 35 surveyed poles. Measured deviations range from 2 cm to 201 cm, with 83% of the poles exceeding the design tolerance of H/200, showing that UAV LiDAR scanning combined with RTK GNSS surveying offers a considerably faster alternative to conventional surveying while retaining reliable determination of the reference point.

***Keywords**: transmission poles, verticality, UAV LiDAR, point cloud, structural monitoring, deviation analysis*

# ISPITIVANJE VERTIKALNOSTI STUBOVA DALEKOVODA NA OSNOVU UAV LIDAR OBLAKA TAČAKA

***Rezime:***

Vertikalnost predstavlja ključni pokazatelj stanja stubova dalekovoda, jer prekomerno odstupanje od vertikale dovodi do ekscentričnog opterećenja temelja i provodnika. U radu je prikazana metoda kojom se konvencionalna izmera totalnom stanicom, u delu koji se odnosi na telo stuba, zamenjuje UAV laserskim skeniranjem, primenjena na delu prenosne mreže 110/220 kV u Srbiji. Gusti oblaci tačaka sa RTK bespilotne letelice korišćeni su za određivanje položaja karakterističnih tačaka duž stuba, dok su uglovi temelja nezavisno određeni RTK GNSS snimanjem na terenu, a odstupanja od vertikalne referentne ose izračunata su u dve upravne ravni na pet stubova izdvojenih iz skupa od 35 snimljenih stubova. Izmerena odstupanja kreću se od 2 cm do 201 cm, a čak 83% stubova prekoračuje projektovanu toleranciju Δ=H/200, čime se pokazuje da kombinacija UAV laserskog skeniranja i RTK GNSS izmere predstavlja znatno bržu alternativu klasičnoj izmeri, uz zadržanu pouzdanost određivanja referentne tačke.

***Ključne reči:** stubovi dalekovoda, vertikalnost, UAV lasersko skeniranje, oblak tačaka, monitoring konstrukcija, analiza odstupanja*

[1] Chief Executive Officer, MSc Geodetic Engineer, DT Mapping, Kraljevo, Serbia, vdjordjevic@dtmapping.com, ORCID 0009-0007-7524-683X
[2] Geodetic Engineer, DT Mapping, Kraljevo, Serbia, dpavlovic@dtmapping.com
[2]

## 1. INTRODUCTION

Transmission lines represent the primary means of transporting electrical energy over long distances, connecting production facilities (power plants) with transformer stations and consumers. Transmission line conductors are supported by a series of poles – lattice steel or reinforced-concrete structures – whose spacing (span length) depends on the terrain configuration, voltage level and pole type, and typically amounts to several hundred meters. Poles are erected at predetermined locations along the route, on individual reinforced-concrete foundations, so that the conductors and shield wires achieve the prescribed height and safe clearance from the ground and surrounding objects. Owing to the length of the routes, which often extend tens or hundreds of kilometers and pass through varied and difficult-to-access terrain, periodic inspection of transmission line infrastructure represents a demanding yet essential task.

One of the key geometric indicators of a pole's condition is its verticality. Deviation of a pole from the vertical position alters the load distribution within the structure, introduces additional eccentricities under the action of wind, ice and the self-weight of the conductors, and may indicate foundation settlement or instability. For these reasons, periodic verticality inspection of poles is an integral part of the regular maintenance of transmission line corridors, particularly for older lines or lines built on terrain prone to settlement.

The conventional approach to verticality inspection is based on geodetic measurements using a total station, whereby each characteristic point on the pole is surveyed individually. This approach is reliable, but extremely slow when a large number of poles must be inspected along longer transmission line sections, since the measurement time increases proportionally with the number of points and poles, together with a constant need for physical access to the base of each pole and good visibility to every point.

A similar problem has already been addressed in previously published studies – terrestrial laser scanning was used to investigate the verticality of an industrial chimney and the geometry of a bridge [1], while the same research group subsequently applied the same technology to the verticality analysis of sports hall columns, combined with the creation of a 3D model of the structure [2]. Terrestrial laser scanning is more broadly used in geodetic practice for the long-term monitoring of deformations in various structures [3], and specialized algorithms have also been developed for the semi-automatic verticality assessment of complex slender objects from point clouds [4], as well as methods for comparing different approaches to the verticality assessment of circular-base objects [5]. With regard to transmission line poles specifically, UAV laser scanning has been used to assess pole inclination and automatically extract the pole axis from a dense point cloud [6], while a combination of UAV photogrammetry (so-called tilt photography) and terrestrial laser scanning has been used to calibrate and improve the accuracy of deformation measurements on transmission line poles [7], and comparisons of UAV surveys with terrestrial methods show that UAV techniques can achieve accuracy comparable to conventional terrestrial methods for elongated engineering structures as well [8]. Point clouds have also been applied to detect geometric irregularities and damage on other types of tall structures, such as cooling towers [9]. More recently, a similar point-cloud-based approach has been applied to the verticality and deformation analysis of historical structures [10], confirming the wider applicability of the method beyond the power sector.

Similar to several of the aforementioned studies, this paper uses UAV-based laser scanning (LiDAR) for surveying the pole body, combined with an RTK GNSS receiver for determining the foundation reference points. The data used in this paper were collected for a section of the 110/220 kV transmission line owned by AD „Elektromreža

Srbije“, on which a total of 35 poles of different structural types were surveyed (portal type, fir-tree type, reinforced-concrete fir-tree type, and reinforced-concrete barrel type). Owing to the RTK receiver on board the aircraft, each scan was directly georeferenced during the flight, without the need to place markers (ground control points) in the field, further reducing the amount of fieldwork required. Since the base of the poles is typically overgrown with grass and low vegetation, which, unlike gaps in tree canopies, does not allow sufficient laser penetration to the ground, the position of the foundation corners was not reliably obtainable from the aerial point cloud; instead, it was independently surveyed by an RTK GNSS receiver directly in the field for all 35 poles, ensuring a reliable determination of the reference point regardless of the vegetation conditions around the pole.

The objective of this paper is to present, through a specific example, the procedure for determining pole verticality based on a UAV LiDAR point cloud, to compare the results with the design tolerance, and to highlight both the advantages and the limitations of this approach relative to conventional geodetic methods.

## 2. METHODOLOGY

The surveyed transmission line section comprises poles of four structural types, which differ from one another in the number and arrangement of characteristic points at the top of the pole: portal type (10 points), fir-tree type, reinforced-concrete fir-tree type (5 points), and reinforced-concrete barrel type (8 points). The distribution schemes of the characteristic points for the four basic types are shown in Figure 1. The points are numbered so as to correspond to the tops of the load-bearing elements at the top of the pole (cross-arms, pole apex, conductor and shield-wire attachment points), while additional points are also tracked along the pole body, at characteristic elevations where transverse bracing (struts) connects the lateral elements of the structure.

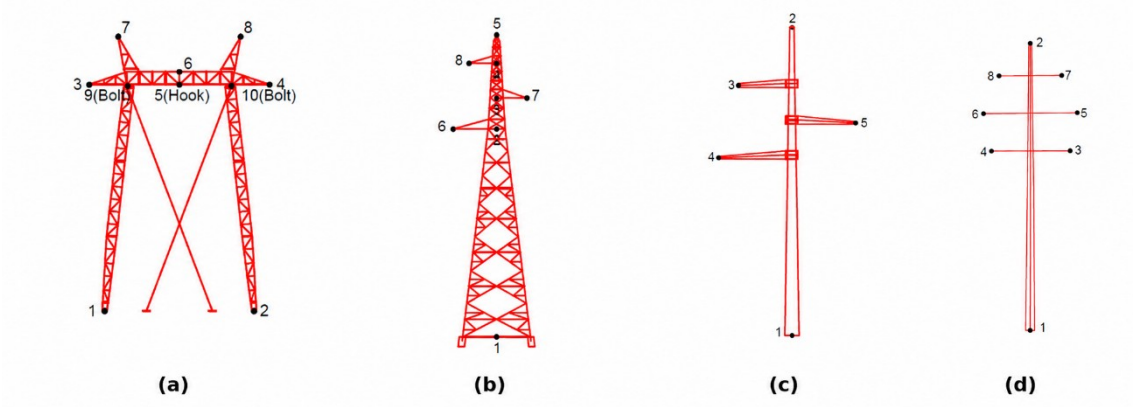


*Fig. 1 Schemes of the characteristic-point arrangement at the top of the pole for four structural types: (a) portal type; (b) fir-tree type; (c) reinforced-concrete fir-tree type; (d) reinforced-concrete barrel type*

The spatial appearance of all four structural types, together with the immediate surroundings of each selected pole, is shown in Figure 2, in the form of a spatial (aerial) view obtained from the UAV point cloud.

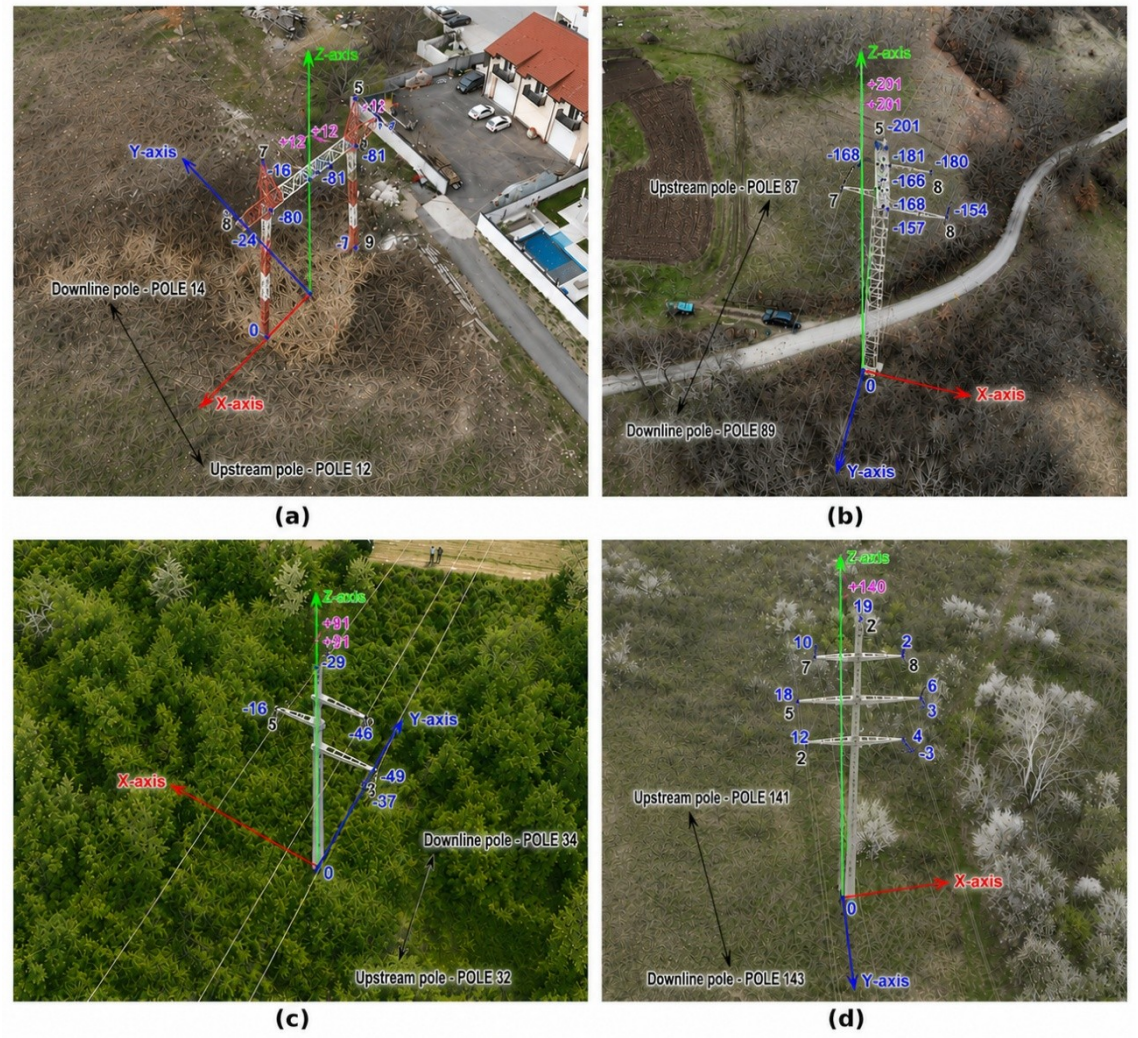


*Fig. 2 Spatial (aerial) view of a representative of each of the four pole structural types from the UAV point cloud: portal type (a), fir-tree type (b), reinforced-concrete fir-tree type (c), and reinforced-concrete barrel type (d)*

The survey was carried out using an unmanned aerial vehicle equipped with a LiDAR sensor and an RTK GNSS receiver, which directly georeferences each scan during the flight, without the need to place markers (ground control points) in the field. Laser pulses emitted from the aircraft are reflected off the surface of the pole and the surrounding terrain; the sensor records the position of each reflection, and where a pulse only partially strikes an obstacle, such as the edge of a branch, multiple returns from a single pulse can be recorded. Combined with the aircraft's own georeferenced trajectory, this yields a dense, georeferenced point cloud that faithfully describes the external geometry of the structure, as schematically shown in Figure 3.

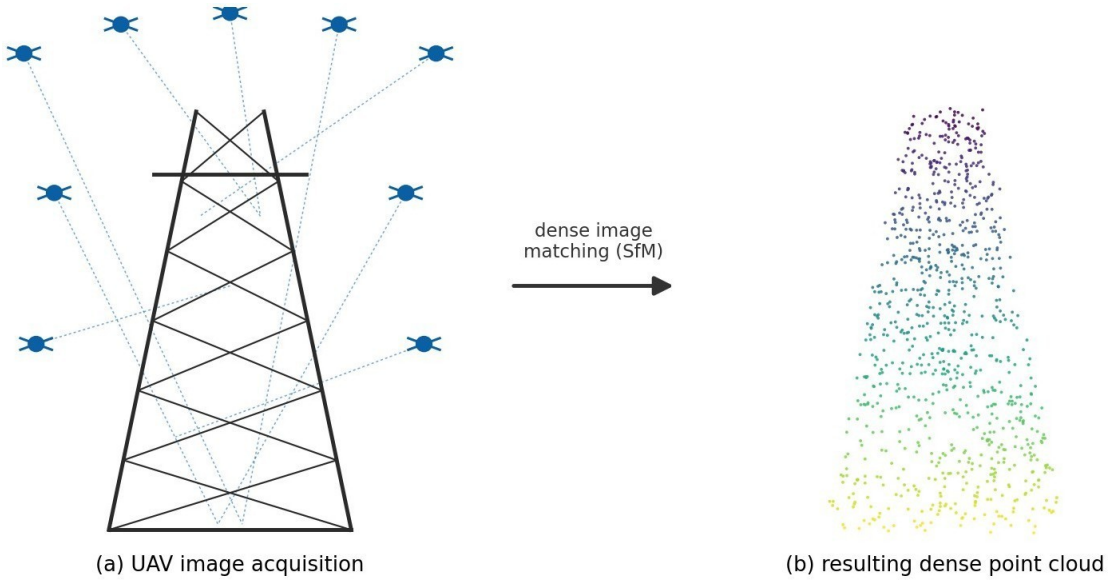


*Fig. 3 Schematic representation of dense point cloud generation through UAV laser scanning: (a) scanning the structure from multiple flight positions; (b) the resulting dense point cloud of the structure*

The point cloud thus obtained, georeferenced within the appropriate coordinate system, forms the basis for all further geometric measurements described in the remainder of this chapter. The appearance of an actual dense point cloud of a fir-tree-type pole, obtained through UAV laser scanning, is shown in Figure 4.

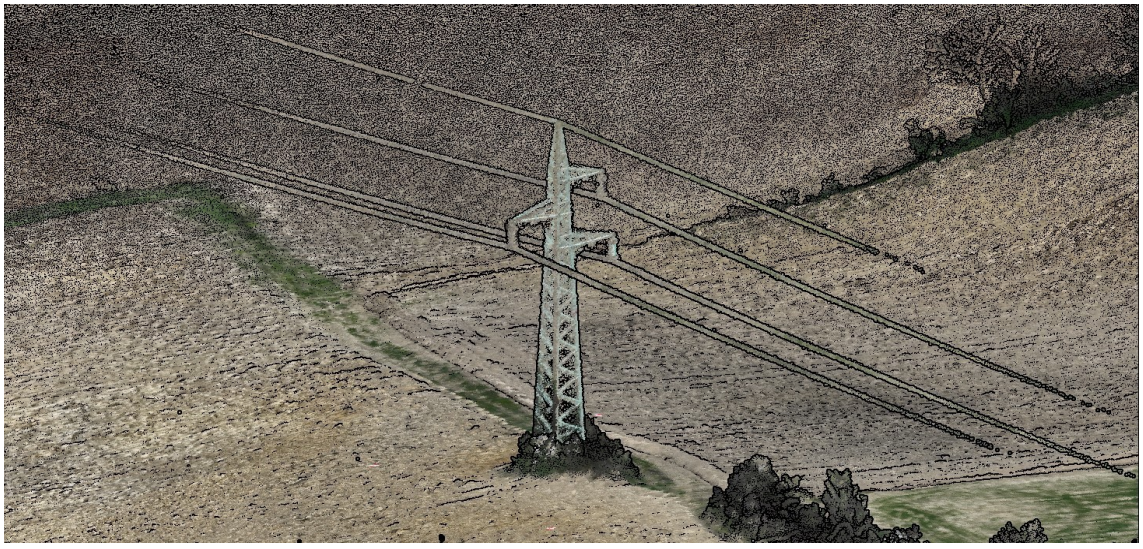

*Fig. 4 Appearance of an actual dense point cloud obtained through UAV laser scanning (fir-tree type)*

Since the base of the poles is typically overgrown with grass and low vegetation, which does not allow sufficient laser penetration to the ground, the position of the foundation corners was not reliably obtainable from the aerial point cloud; instead, it was independently surveyed by an RTK GNSS receiver directly in the field for all 35 poles, ensuring a reliable determination of the reference point regardless of the vegetation conditions around the pole.

A local coordinate system was defined for each pole, with axes X (perpendicular to the transmission line route) and Y (along the route direction). The starting (lowest) point of the Z axis, i.e., of the pole's vertical reference axis, is determined independently of the LiDAR point cloud: the coordinates of all four foundation corners of the pole are

measured in the field using the RTK GNSS receiver, after which the intersection of the diagonals of the measured quadrilateral is adopted as the mean point of the base. From that point, the vertical reference axis extends upward, and the position of the characteristic points along the pole body, from base to top, is read relative to it in both perpendicular planes (X-Z and Y-Z), this time from the UAV LiDAR point cloud. The deviation of each point from the vertical axis is expressed in centimeters, with a sign indicating the direction of inclination – toward the next (+) or toward the previous pole (–) relative to the transmission line route. Since the unmanned aerial vehicle and the field GNSS receiver operate within the same RTK reference system, the field-measured foundation points and the LiDAR point cloud of the pole body lie within a common coordinate system, without the need for subsequent alignment of the two data sets.

The total deviation of the pole top from vertical (Δuk) is calculated as the resultant of the deviation along the Y axis (ΔY) and along the X axis (ΔX), measured between the highest and lowest characteristic points of the pole:

$$\Delta_{uk} = \sqrt{\Delta X^2 + \Delta Y^2} \tag{1}$$

The obtained value is compared with the allowable vertical deviation, which for the observed transmission line section is defined as Δallow = H/200, where H is the pole height. A pole is considered to be within tolerance if Δuk ≤ Δallow.

The reading procedure is illustrated using the example of a fir-tree-type pole with a height of H = 20.55 m (Figure 5), for which the allowable deviation is Δallow = 10 cm. The diagram shows two projections of the pole's vertical – in the Y-axis plane (parallel to the transmission line route) and in the X-axis plane (perpendicular to the route) – with a series of horizontal lines representing the characteristic elevations (elevations of the bracing and of the pole top). The lowest elevation (elevation 0) corresponds to the mean base point obtained from the RTK GNSS survey of the foundation corners, while all higher elevations were read from the UAV LiDAR point cloud. For each elevation, the horizontal deviation of the point relative to the adopted vertical reference line is read, in centimeters.

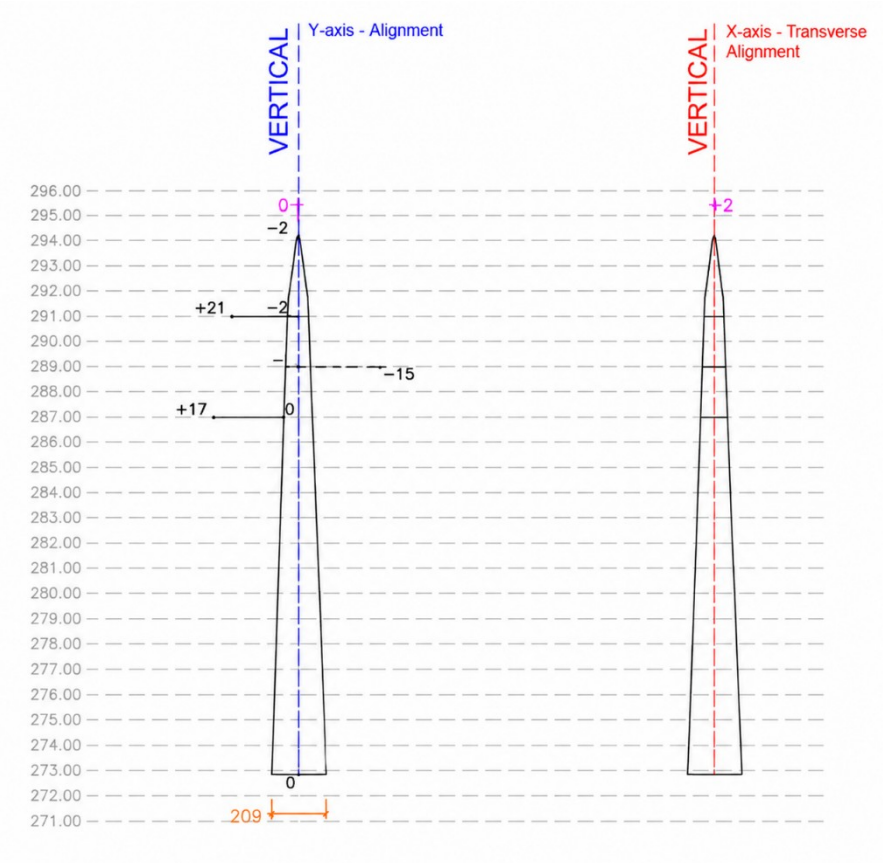


*Fig. 5 Example of a pole vertical-profile diagram (POLE 42, fir-tree type, H = 20.55 m): projections in the Y-axis and X-axis planes with the deviations read at the characteristic elevations*

Figure 6 shows the same pole in a spatial (aerial) view obtained from the UAV point cloud, on which the local axes X, Y, Z and the numbered characteristic points are marked, together with the adjacent poles along the route. This view enables direct verification of whether the characteristic points have been correctly identified on the actual structure and facilitates the interpretation of the deviation sign (+ toward the next pole, – toward the previous pole).

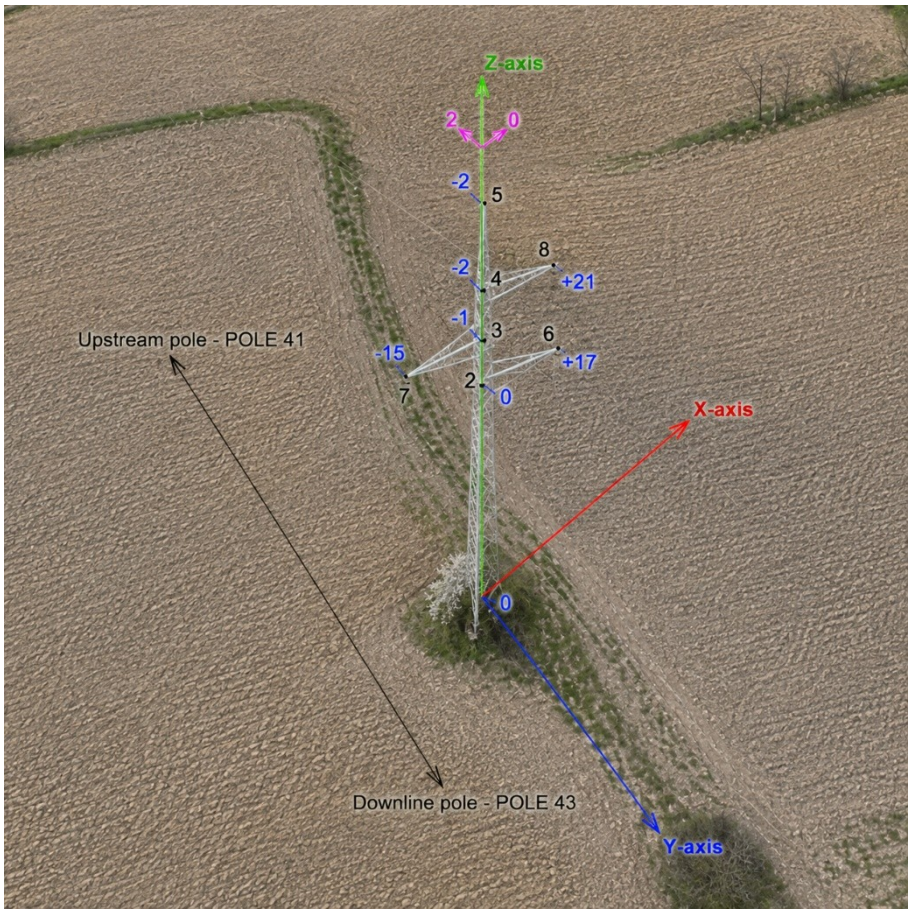


*Fig. 6 Spatial (aerial) view of the pole from the UAV point cloud, with the local axes X, Y, Z and the characteristic points marked (POLE 42)*

Of the 35 poles processed in total, five poles of different structural types and different degrees of deviation from vertical were selected for the purposes of this paper – ranging from a pole that is fully within tolerance (POLE 42, presented in this chapter) to the pole with the most pronounced deviation in the entire data set (POLE 88). Basic data on the selected poles are given in Table 1, while detailed results are presented in the following chapter.

*Tab. 1 Basic data and measured deviations for the five selected poles*

| Pole ID | Pole type | H [m] | Δallow=H /200 [cm] | ΔY [cm] | ΔX [cm] | Δuk [cm] | Assessment |
|---|---|---|---|---|---|---|---|
| Pole 13 | portal | 19,75 | 10 | 16 | 12 | 20 | outside tolerance |
| Pole 42 | fir-tree | 20,55 | 10 | 0 | 2 | 2 | within tolerance |
| Pole 33 | RC fir-tree | 20,91 | 10 | 91 | 29 | 96 | outside tolerance |
| Pole 88 | fir-tree | 31,04 | 16 | 2 | 201 | 201 | outside tolerance |
| Pole 142 | RC - barrel | 26,94 | 13 | 116 | 9 | 116 | outside tolerance |

## 3. RESULTS AND DISCUSSION

The results for the remaining four selected poles (POLE 13, POLE 33, POLE 88 and POLE 142) are presented below, through the vertical-profile diagram and the corresponding spatial (aerial) view from the UAV point cloud.
Pole 13 is of the portal type, with a height of 19.75 m and an allowable deviation of 10 cm. The measured total deviation amounts to 20 cm (ΔY = 16 cm, ΔX = 12 cm), which is twice the allowable value (Figure 7). The diagram shows that the inclination is not linear with height – the largest relative deviation occurs in the upper third of the pole, while the lower elevations are closer to the adopted vertical.

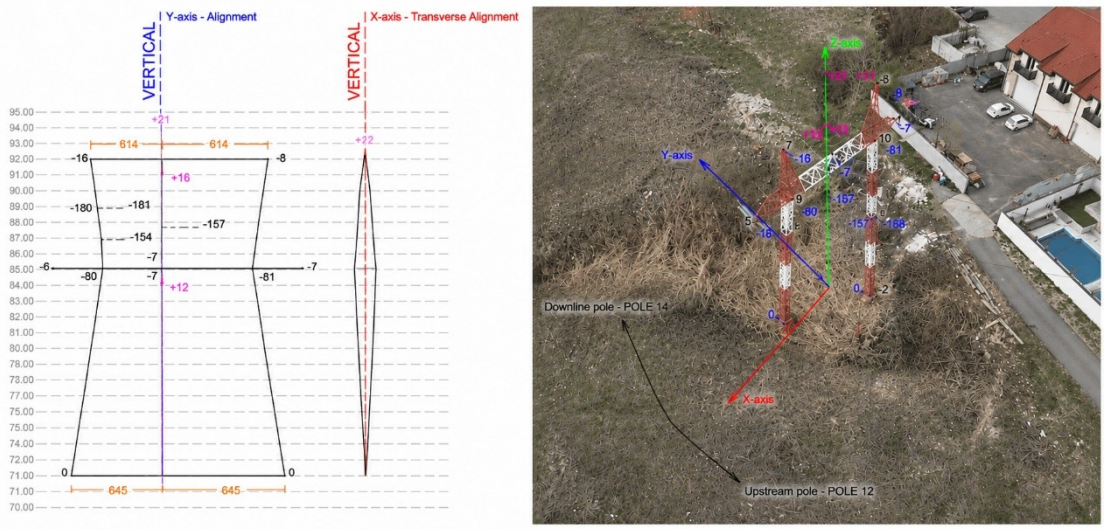


*Fig. 7 POLE 13 (portal type, H = 19.75 m, Δuk = 20 cm): (a) vertical profile; (b) spatial (aerial) view*

Pole 33 (RC fir-tree type, H = 20.91 m) shows a considerably more pronounced deviation – Δuk = 96 cm, i.e., almost ten times the allowable 10 cm (Figure 8). The pole is located in a corridor with dense forest vegetation, clearly visible in the spatial view, which would have completely prevented a reliable reading of the foundation corners from the air. Owing to the field RTK GNSS survey of the base point, independent of the LiDAR point cloud, such conditions nevertheless do not affect the reliability of the adopted reference point or the accuracy of the calculated deviation.

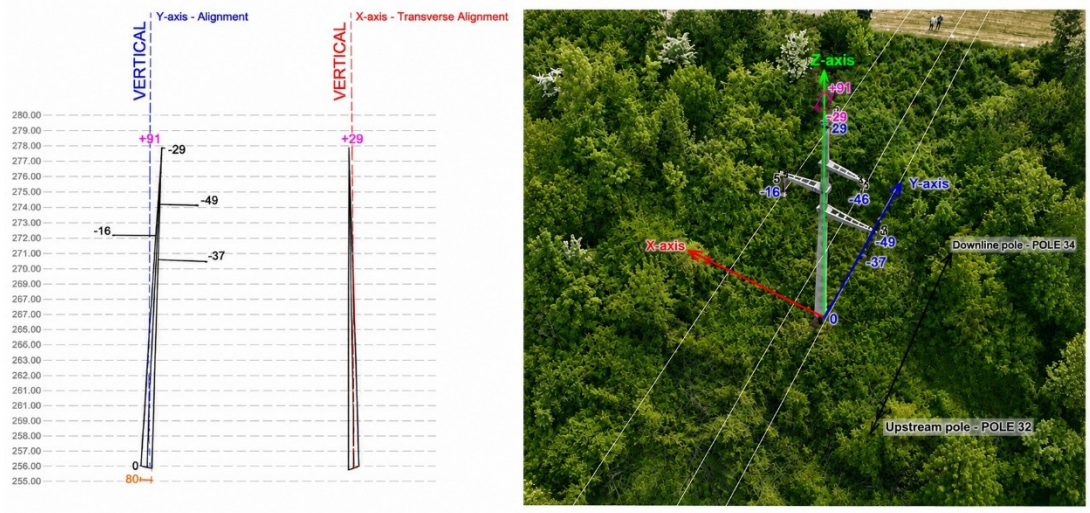


*Fig. 8 POLE 33 (RC fir-tree type, H = 20.91 m, Δuk = 96 cm): (a) vertical profile; (b) spatial (aerial) view in a corridor with dense vegetation*

Pole 88 (fir-tree type, H = 31.04 m) represents an extreme case within the observed data set – the measured total deviation amounts to as much as 201 cm, while the allowable value is 16 cm, meaning that the measured deviation is approximately 12.5 times greater than allowed (Figure 9). The inclination is clearly noticeable already from visual inspection of the spatial view, where the pole's silhouette is visibly offset from the vertical drawn as a dashed line. Such a deviation typically requires an urgent field inspection of foundation stability and, if necessary, corrective intervention.

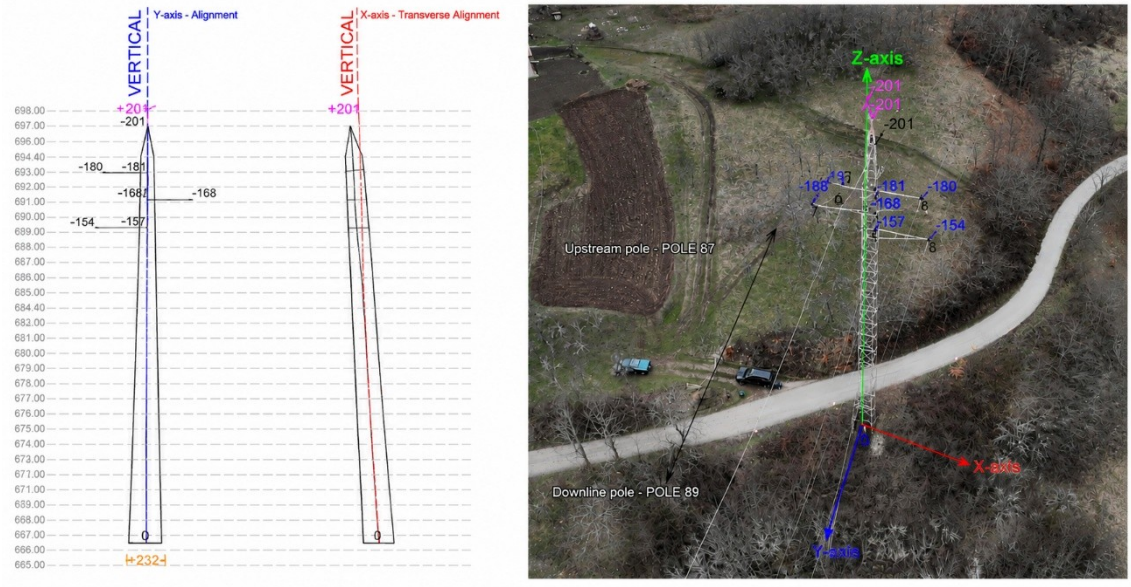


*Fig. 9 POLE 88 (fir-tree type, H = 31.04 m, Δuk = 201 cm) – the most pronounced deviation within the observed data set: (a) vertical profile; (b) spatial (aerial) view*

Pole 142 (RC barrel type, H = 26.94 m) has a measured total deviation of 116 cm against an allowable 13 cm, i.e., approximately nine times the allowable value (Figure 10). It is characteristic that the deviation is almost entirely oriented along the direction of the transmission line route (ΔY = 116 cm), while the deviation perpendicular to the route is negligible (ΔX = 9 cm), which points to a possible cause related to foundation settlement in the direction of the route, rather than lateral displacement.

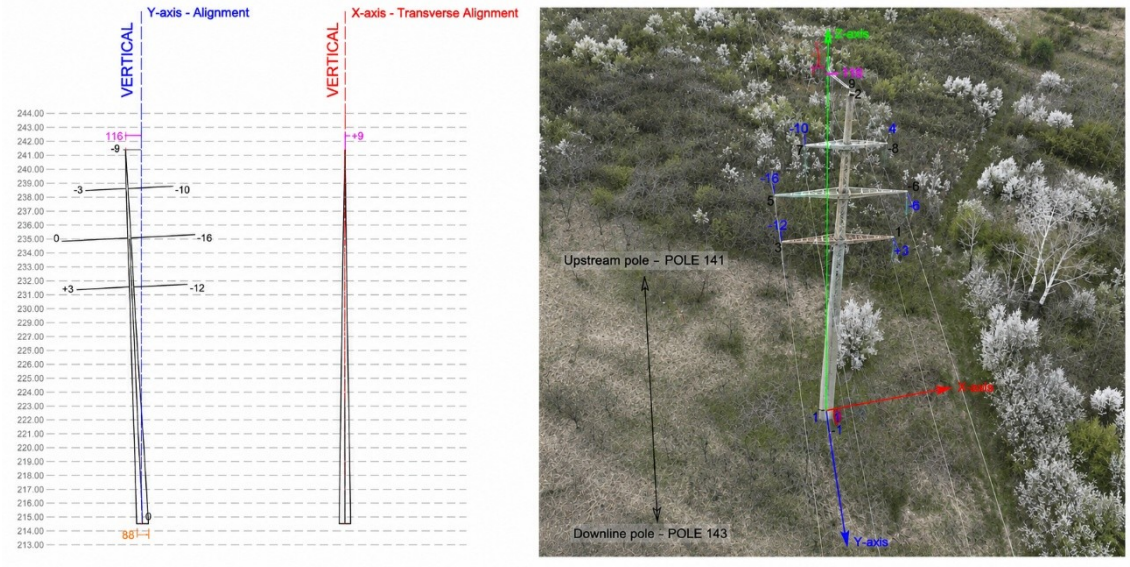


*Fig. 10 POLE 142 (RC barrel type, H = 26.94 m, Δuk = 116 cm): (a) vertical profile; (b) spatial (aerial) view*

Considered at the level of the entire set of 35 surveyed poles, the measured total deviations range from 2 cm to 201 cm, with an average value of about 57 cm. As many as 29 of the 35 poles (83%) exceed the allowable tolerance Δ=H/200, with an average ratio of measured to allowable deviation of approximately 4.6, and up to 15 in the most unfavorable case (Table 2). As an indicative example, the average point cloud density in the vicinity of four of the surveyed poles was found to be approximately 480 points/m²; a systematic density assessment across the entire data set was not performed. Such a high percentage of exceedance, which is not limited to individual, isolated poles, suggests that the cause could be systemic. Several possible explanations may be considered: genuine long-term inclination caused by soil properties along the route, particularly in agricultural areas where several of the surveyed poles are located and where seasonal changes in soil moisture and the use of heavy machinery near the pole bases could contribute to foundation movement; deviations that already occurred during the construction phase and were never corrected; or gradual, long-term soil creep affecting older sections of the line. Determining the exact cause is beyond the scope of this paper and would require additional geotechnical analysis and, ideally, independent validation against a conventional geodetic method on at least a subset of poles; however, the obtained results clearly demonstrate the scale of the problem, which would be considerably more difficult and time-consuming to establish using conventional geodetic inspection on such a large number of poles.

*Tab. 2 Basic statistics of the measured deviations for the set of 35 surveyed poles*

| Parameter | Value |
|---|---|
| Number of surveyed poles | 35 |
| Number (and share) of poles exceeding Δ=H/200 | 29 (83%) |
| Mean total deviation Δuk | 57 cm |
| Minimum / maximum measured deviation | 2 cm / 201 cm |
| Average ratio Δuk / Δallow | ≈ 4,6 |
| Largest ratio Δuk / Δallow (POLE 88) | ≈ 15,1 |

In terms of efficiency, it should be noted that the entire set of 35 poles was processed using data collected in a considerably shorter time than would have been possible with conventional total-station surveying, since the body of all poles along the section is captured in a single (or a few) UAV flight(s), while fieldwork is reduced to a brief RTK GNSS reading of the four foundation corners per pole, instead of lengthy sighting of every point along the entire height of each pole. An additional advantage lies in the fact that, unlike the conventional method, which typically records only a small number of points per pole, an arbitrarily large number of characteristic points can subsequently be read from the UAV point cloud along the entire pole height, providing a considerably more complete insight into the shape of the inclination (e.g., whether the inclination is linear or more pronounced in certain zones, as with Pole 13 in Figure 7).

## 4. CONCLUSION

This paper presents a method for assessing the verticality of transmission line poles based on dense point clouds obtained through UAV laser scanning. The method is illustrated on five poles of different structural types, selected from a set of 35 surveyed poles on a single section of a 110/220 kV transmission line. The measured deviations from vertical range from 2 cm (a pole fully within tolerance) to 201 cm (the most pronounced case within the

observed set), and as many as 83% of all surveyed poles exceed the design tolerance of Δ=H/200.

The results confirm that the conventional approach to verticality inspection, based on geodetic surveying of each characteristic point individually using a total station, represents a slow and labor-intensive procedure, particularly on longer transmission line sections with a large number of poles. The described combination of UAV LiDAR scanning and RTK GNSS surveying retains a brief field visit to the base of each pole (for the GNSS reading of the foundation corners), but entirely eliminates the lengthy total-station reading of every point along the pole body – this is instead carried out subsequently, in the office, from a single UAV point cloud obtained in one flight. This results in a considerably shorter overall field and office working time, as well as a more complete, spatially continuous description of the pole geometry compared with the conventional method, in which the number of measured points per pole is typically limited.

The method, however, is not without limitations. In this paper, vegetation around the pole base was successfully circumvented by combining UAV LiDAR scanning with field RTK GNSS surveying of the foundation corners – since dense grass, unlike gaps in tree canopies, does not allow sufficient laser penetration to the ground for reliable point extraction, the foundation corners were instead surveyed independently using RTK GNSS. The method nevertheless remains partially field-dependent as a result – unlike fully contactless surveying, a brief visit to the base of each pole for GNSS reading is still required, although it is considerably faster than conventional surveying of all points with a total station. In addition, no formal assessment of the overall positional accuracy of the derived deviations (Δuk) was carried out in this study, beyond the reported point cloud density; this is particularly relevant for smaller deviations, such as the 2 cm obtained for Pole 42, which approach the practical measurement uncertainty of the method, and no independent validation against a conventional geodetic method was performed for any of the surveyed poles.

As a direction for further work, the accuracy of the presented method could be validated through independent control measurements using conventional total-station surveying on a subset of poles, together with a formal assessment of point cloud density and positional accuracy across the full data set. Periodic re-surveying of the same section at regular intervals would also allow the observed deviations to be tracked over time, helping to distinguish between deviations that originated during construction and those resulting from ongoing settlement or ground movement along the route. Automating the extraction of characteristic points from the point cloud, currently performed manually, would further reduce the processing time and subjectivity of the procedure.

## ACKNOWLEDGEMENT

The authors would like to thank the surveying company GICOMP d.o.o. and the investor AD „Elektromreža Srbije" – Belgrade, for providing the geodetic data used in this paper.

## REFERENCES

[1] Krnić Đ., Vujinović M., Batilović M., Marković M., Budimirov T. (2023). Investigation of Objects Verticality Using Terrestrial Laser Scanner. 16th International Scientific Conference iNDiS 2023, Vrdnik, Serbia, November 2023.

[2] Marković M.Z., Batilović M., Krnić Đ., Vujinović M., Sušić Z. (2024). Application of Terrestrial Laser Scanning Technology in the Analysis of the Columns Verticality and the Creation of a 3D Model of the Sports Hall. Zbornik radova Građevinskog fakulteta (Journal of Faculty of Civil Engineering), No. 45, 48–59. https://doi.org/10.14415/JFCE-908

[3] Vacca G., Mistretta F., Stochino F., Dessi A. (2016). Terrestrial Laser Scanner for Monitoring the Deformations and the Damages of Buildings. International Archives of the Photogrammetry, Remote Sensing and Spatial Information Sciences, XLI-B5, 453–460. https://doi.org/10.5194/isprsarchives-XLI-B5-453-2016

[4] Matwij W., Lipecki T., Jaśkowski W.F. (2024). Selection of an Algorithm for Assessing the Verticality of Complex Slender Objects Using Semi-Automatic Point Cloud Analysis.

[5] Remote Sensing, 16(3), 435. https://doi.org/10.3390/rs16030435

[6] Hamzić A., Kamber Hamzić D. (2021). Verticality Assessment of the Objects with a Circular Base: Method Comparison. Geodetski Glasnik, No. 52, 42–60. https://doi.org/10.58817/2233-1786.2021.55.52.42

[7] Lu Z., Gong H., Jin Q., Hu Q., Wang S. (2022). A Transmission Tower Tilt State Assessment Approach Based on Dense Point Cloud from UAV-Based LiDAR. Remote Sensing, 14(2), 408. https://doi.org/10.3390/rs14020408

[8] Xia B., Li Z., Huang J., Zeng K., Pang S. (2021). Efficient measurement of power tower based on tilt photography with unmanned aerial vehicle and laser scanning. The Journal of Engineering, 2021(11), 724–730. https://doi.org/10.1049/tje2.12072

[9] Lenda G., Borowiec N., Marmol U. (2023). Study of the Precise Determination of Pipeline Geometries Using UAV Scanning Compared to Terrestrial Scanning, Aerial Scanning and UAV Photogrammetry. Sensors, 23(19), 8257. https://doi.org/10.3390/s23198257

[10] Makuch M., Gawronek P. (2020). 3D Point Cloud Analysis for Damage Detection on Hyperboloid Cooling Tower Shells. Remote Sensing, 12(10), 1542. https://doi.org/10.3390/rs12101542

[11] Zhang J., Zou S., Zhang W., Tian H. et al. (2026). Deformation and disease detection of Tulou based on multi-source 3D point cloud fusion. npj Heritage Science, 14, 66. https://doi.org/10.1038/s40494-026-02333-w

https://doi.org/10.24867/INDIS-2026-EN-894



# DEFORMATION ANALYSIS OF THE ŠELEVRENAC DAM USING THE IWST METHOD

*Anastasija Božić[1], Mehmed Batilović[2], Marko Marković[3], Zoran Sušić[4], Vladimir Bulatović[5]*

***Summary:***

This paper presents the deformation analysis of the Šelevrenac Dam in Serbia, based on measurements from the zero and seventh control epochs. Horizontal displacements were determined based on a two dimensional (2D) geodetic network, while vertical displacements were obtained from a one dimensional (1D) levelling network. The deformation analysis was performed using the Iterative Weighted Similarity Transformation (IWST) method. The estimated displacement values indicate non-uniform distribution of deformations within the dam body. The largest displacements were detected on the upstream slope, where radial and vertical components were dominant. The results confirm the importance of combined 1D and 2D geodetic monitoring for the reliable identification and assessment of dam displacements.

*Keywords: deformation analysis, robust IWST method, dam monitoring, horizontal and vertical displacements*

# DEFORMACIONA ANALIZA BRANE ŠELEVRENAC PRIMENOM IWST METODE

***Rezime:***

U ovom radu prikazan je postupak deformacione analize brane Šelevrenac u Srbiji, na osnovu merenja iz nulte i sedme kontrolne epohe. Horizontalna pomeranja određena su na osnovu dvodimenzionalne (2D) geodetske mreže, dok su vertikalna pomeranja dobijena na osnovu jednodimenzionalne (1D) nivelmanske mreže. Deformaciona analiza sprovedena je primenom iterativne težinske transformacije sličnosti (Iterative Weighted Similarity Transformation). Ocenjene vrednosti pomeranja ukazuju na neravnomernu raspodelu deformacija u telu brane. Najveća pomeranja detektovana su na uzvodnoj kosini, gde su dominantna bile radijalna i vertikalna komponenta pomeranja. Rezultati potvrđuju značaj kombinovanog 1D i 2D geodetskog osmatranja za pouzdanu identifikaciju i ocenu vrednosti pomeranja brane.

*Ključne reči: deformaciona analiza, robusna IWST metoda, osmatranje brane, horizontalna i vertikalna pomeranja*

[1] Teaching Associate, BSc, Faculty of Technical Sciences, University of Novi Sad, Novi Sad, Serbia, anastasija.bozic@uns.ac.rs, ORCID 0009-0004-3350-9097
[2] Assistant Professor, PhD, Faculty of Technical Sciences, University of Novi Sad, Novi Sad, Serbia, mehmed@uns.ac.rs, ORCID 0000-0001-5605-1112
[3] Associate Professor, PhD, Faculty of Technical Sciences, University of Novi Sad, Novi Sad, Serbia, marko_m@uns.ac.rs, ORCID 0000-0003-3666-6325
[4] Full Professor, PhD, Faculty of Technical Sciences, University of Novi Sad, Novi Sad, Serbia, zsusic@uns.ac.rs , ORCID 0000-0002-8885-2659
[5] Full Professor, PhD, Faculty of Technical Sciences, University of Novi Sad, Novi Sad, Serbia, vbulat2003@uns.ac.rs, ORCID 0000-0002-0772-5333

## 1. INTRODUCTION

In modern engineering geodesy, geodetic monitoring plays an important role in observing the behaviour of structures and determining changes in their position over time [1]. This is particularly important for critical infrastructure facilities whose stability directly affects structural functionality and environmental safety. Such facilities include dams, tunnels, bridges and other engineering structures, where the timely detection of displacements is essential for assessing their structural condition [1, 2].

Earth-fill dams are complex engineering structures in which deformation processes may occur already during the construction phase, due to settlement of the foundation soil and compaction of the embankment material. During its lifetime, dam behaviour may be affected by the self-weight of the dam body, consolidation processes, hydrostatic and hydrodynamic loading, changes in reservoir water level, atmospheric effects, seismic actions and other local factors. Therefore, the deformation process of the dam body has a pronounced time-dependent component, which makes it necessary to perform periodic measurements within a predefined geodetic network [1, 2].

Geodetic monitoring of dams aims to provide information on the behaviour of the dam body, structures on and near the dam, as well as the surrounding terrain. Deformation analysis of geodetic networks is performed by analysing changes in the positions of network points through two or more measurement epochs [3-5]. Depending on the network structure, geodetic networks used for deformation analysis can be classified as absolute or relative networks. Absolute networks, which are most commonly applied in the monitoring of dams, consist of reference points stabilized outside the zone of expected deformations and control points located on the monitored object [3, 4]. By comparing adjusted coordinates of points from different epochs, displacement vectors can be determined and a statistical assessment of point stability can be performed [3-5].

In modern deformation analysis, robust methods are increasingly applied, especially in cases where the stability of reference points is not known in advance [6-8]. One of the most widely used robust methods is the Iterative Weighted Similarity Transformation (IWST) method. The advantage of the IWST method lies in its ability to provide a robust estimation of the displacement vector, whereby the influence of points with larger estimated displacements is reduced during the transformation procedure [7-10].

This paper presents the application of the Iterative Weighted Similarity Transformation (IWST) method in the deformation analysis of the Šelevrenac Dam. The analysis utilized results from complementary 1D and 2D geodetic networks, providing horizontal and vertical displacement components, respectively. The deformation analysis was performed with the aim of identifying stable and unstable points and interpreting the spatial distribution of displacements across different parts of the dam structure.

## 2. DEFORMATION ANALYSIS OF GEODETIC NETWORKS

Over the past several decades, numerous methods of deformation analysis have been developed, each based on different mathematical approaches to the assessment of point stability and displacement estimation [10, 11]. Classical methods of deformation analysis, collectively referred to as Conventional Deformation Analysis (CDA), include, among others, the Hannover, Karlsruhe, Delft, Fredericton, München and Caspary methods, each based on different mathematical approaches [10-17]. These methods generally rely on the assumption that the reference points used to define the network datum remain stable between measurement epochs. If unstable points are included in the reference set, they may affect the datum definition and consequently bias the estimated displacement vectors of other network points [4, 10, 11].

To address this limitation, robust approaches to deformation analysis have been developed [7-9, 11]. These approaches enable the estimation of displacement vectors without prior identification of individual stable reference points, while reducing the influence of points with larger estimated displacements during the estimation process [7, 8, 11]. The final classification of points as stable or unstable is then performed by statistical testing of the estimated displacements [9, 18, 19].

Among the robust methods proposed in the literature, the Iterative Weighted Similarity Transformation (IWST) method was introduced by Chen at the University of New Brunswick, Canada, in 1983 [18]. This method has subsequently been applied in several geodetic monitoring studies [3, 19]. For this reason, it is adopted in this paper for the deformation analysis of the Šelevrenac Dam. The mathematical model of the IWST method is described in the following section.

## 2.1. ITERATIVE WEIGHTED SIMILARITY TRANSFORMATION

The IWST method of deformation analysis is based on the mathematical model of robust deformation estimation using differences between adjusted point coordinates. Prior to the deformation analysis, the homogeneity of measurement accuracy between the zero and seventh control epochs is examined on the basis of the a posteriori standard deviations. The IWST procedure includes independent adjustment of both epochs with outlier detection, robust S-transformation of the displacement vector, and statistical testing of point stability using Fisher's test [18, 19].

The deformation model of the IWST method consists of a functional and a stochastic model:

$$d=\begin{bmatrix} d_S \\ d_O \end{bmatrix}=\left(\hat{x}_2-\hat{x}_1\right)-Ht\,, \tag{1}$$

$$\hat{d}_S \sim (1-\tau)\cdot N\left(0\,, diag\left(\sigma_{d_i}^2\right)\right)+\tau\cdot N\left(0\,, diag\left(q\,\sigma_{d_i}^2\right)\right), \tag{2}$$

where $d_S$ and $d_O$ denote the displacement vectors of the reference and object points, respectively; $\hat{x}_1$ and $\hat{x}_2$ are the adjusted coordinate vectors in the zero and control epochs; $H$ is the design matrix of the S-transformation; $t$ is the vector of datum parameters; $\tau$ is a small number taking values from the interval $0 < \tau < 0.5$; $\sigma_{d_i}$ is the accepted standard deviation of the corresponding component of the vector $\hat{d}_S$ of the i-th point; $q\,\sigma_{d_i}$ is the rejected standard deviation of the corresponding component of the vector $\hat{d}_S$ of the i-th point and $q > 1$ [18, 19].

The procedure of the robust S-transformation of the displacement vector is reduced to solving an optimization problem formed by the previously presented functional model and the objective function:

$$\rho(d)=\|d\|_1=\sum|d_i|=min\,. \tag{3}$$

This optimization problem is solved using the Iterative Reweighted Least Squares (IRLS) method:

$$\left.\begin{aligned} \hat{d}^{(k)} &= S^{(k)}\left(\hat{x}_2-\hat{x}_1\right) \\ Q_{\hat{d}}^{(k)} &= S^{(k)}\left(Q_{\hat{x}_1}+Q_{\hat{x}_2}\right)\left(S^{(k)}\right)^T \\ W^{(k+1)} &= diag\left(\ldots, w_{S,i}^{(k+1)}, \ldots\ \ldots, 0, \ldots\right) \end{aligned}\right\}_{k=1,2,\ \ldots} \tag{4}$$

where $S^{(k)}=E-H\left(H^T W^{(k)} H\right)^{-1} H^T W^{(k)}$ is the S-transformation matrix, $W^{(k+1)}$ is the weight matrix; $w_{S,i}^{(k+1)}$ are the weights of the network reference points and *k* is the iteration number. In the first iteration ($k = 1$), the weight matrix is the identity matrix $W = E$. In the subsequent iterations, the weights of the reference points are determined as follows :

$$w_{S,i}^{(k+1)}=\frac{1}{\left|\hat{d}_i^{(k)}\right|+c}, \tag{5}$$

where *c* is a small constant that prevents zero from appearing in the denominator. The iterative procedure is carried out until the differences between two successively transformed displacement vectors $\left|\hat{d}^{(k+1)}-\hat{d}^{(k)}\right|$ become smaller than the adopted tolerance value $\gamma$ [18, 19].

In the final step, point stability is tested to determine whether the estimated displacements are statistically significant or caused by random measurement errors. For this purpose, the null and alternative hypotheses are formulated:

$$H_0: M\left(\hat{d}_i\right)=0 \quad \text{against} \quad H_a: M\left(\hat{d}_i\right)\neq 0. \tag{6}$$

For the purpose of testing these hypotheses, the test statistic is formed:

$$T_i=\left.\frac{\hat{d}_i^T Q_{\hat{d}_i}^{-1} \hat{d}_i}{h_i \hat{\sigma}_0^2}\right|_{H_0} \sim F_{h_i,f}, \tag{7}$$

where $\hat{d}_i$ is the displacement vector of the i-th network point; $Q_{\hat{d}_i}$ is the cofactor matrix of the displacement of the i-th network point; $\hat{\sigma}_0^2=\left(f_1 \hat{\sigma}_{0_1}^2+f_2 \hat{\sigma}_{0_2}^2\right)/f$ is the pooled *a posteriori* variance factor; $f=f_1+f_2$ is the pooled number of degrees of freedom and $h_i=r\left(Q_{\hat{d}_i}\right)$. When testing the hypotheses, the local significance level $\alpha_0$ is used, which is determined on the basis of the adopted value of the global significance level $\alpha$ using the Bonferroni equation:

$$\alpha_0=1-(1-\alpha)^{1/m} \cong \frac{\alpha}{m}, \tag{8}$$

where *m* is the number of network points. If $T_i \leq F_{1-\alpha_0,h_i,f}$, the null hypothesis is not rejected, and the point is classified as stable, meaning that no statistically significant displacement has been detected. When $T_i > F_{1-\alpha_0,h_i,f}$, the null hypothesis is rejected, and the point is classified as unstable, meaning that a statistically significant displacement has been detected [9, 18, 19].

## 3. CASE STUDY: ŠELEVRENAC DAM

The Šelevrenac Dam, located in the vicinity of Krušedolski Prnjavor, Krušedol, and Maradik, has been in operation since 1986. The dam was constructed across the Šelevrenac stream, forming the reservoir commonly referred to as Maradik Lake or Šelevrenac Lake. According to the reservoir volume criterion of the International Commission on Large Dams (ICOLD), the Šelevrenac Dam is classified as a large dam. The spillway is a reinforced-concrete rectangular structure. It is classified as a frontal spillway according to its hydraulic type and as a side spillway according to its position on the left side of the dam. The main characteristics of the dam are presented in Table 1.

*Tab. 1 Main characteristics of the Šelevrenac Dam*

| Characteristic | Value |
|---|---|
| Dam length at the elevation of 131.30 m | 260.50 m |
| Structural height of the dam | 13.9 m |
| Upstream slope inclination | 1:2.5 |
| Downstream slope inclination | 1:2 |
| Dam crest elevation | 131.30 m above sea level (a.s.l.) |
| Maximum water level elevation | 129.70 m a.s.l. |
| Normal water level elevation | 128.00 m a.s.l. |
| Dam crest width | 6.0 m |

Figure 1 shows the Šelevrenac Dam, which represents the monitored structure in this case study.



*Fig. 1 The Šelevrenac Dam*

For the systematic geodetic monitoring of the Šelevrenac Dam, a 1D levelling network and a 2D geodetic network were established. These networks enable the determination of vertical and horizontal displacements, respectively, and are described in the following subsections.

### 3.1. TWO DIMENSIONAL GEODETIC NETWORK

For the purpose of determining the horizontal displacements of the Šelevrenac Dam, a 2D geodetic network was established. This 2D network consists of 7 reference network points (ST1–ST7) and 38 control points stabilized on the dam structure (KT1–KT38). The reference points are distributed outside the zone of expected deformations, while the

control points are distributed over the characteristic parts of the dam structure and associated facilities.

The reference points were materialized by concrete pillars with a forced centering device, except for points ST3 and ST7, which were materialized by bolts embedded in the foundations of existing structures. The control points were materialized by vertically installed brass benchmarks with rounded heads, adapted for prism placement during measurements.

For the determination of horizontal displacements of the dam, a local coordinate system was established. The local coordinate system is defined such that the Y-axis, corresponding to the tangential axis T, is oriented parallel to the dam axis, from point ST2 to point ST1. The X-axis, corresponding to the radial axis R, is perpendicular to the dam axis and oriented upstream. The configuration of the 2D geodetic network, including the reference and control points, observation configuration and adopted local coordinate system, is shown in Figure 2.

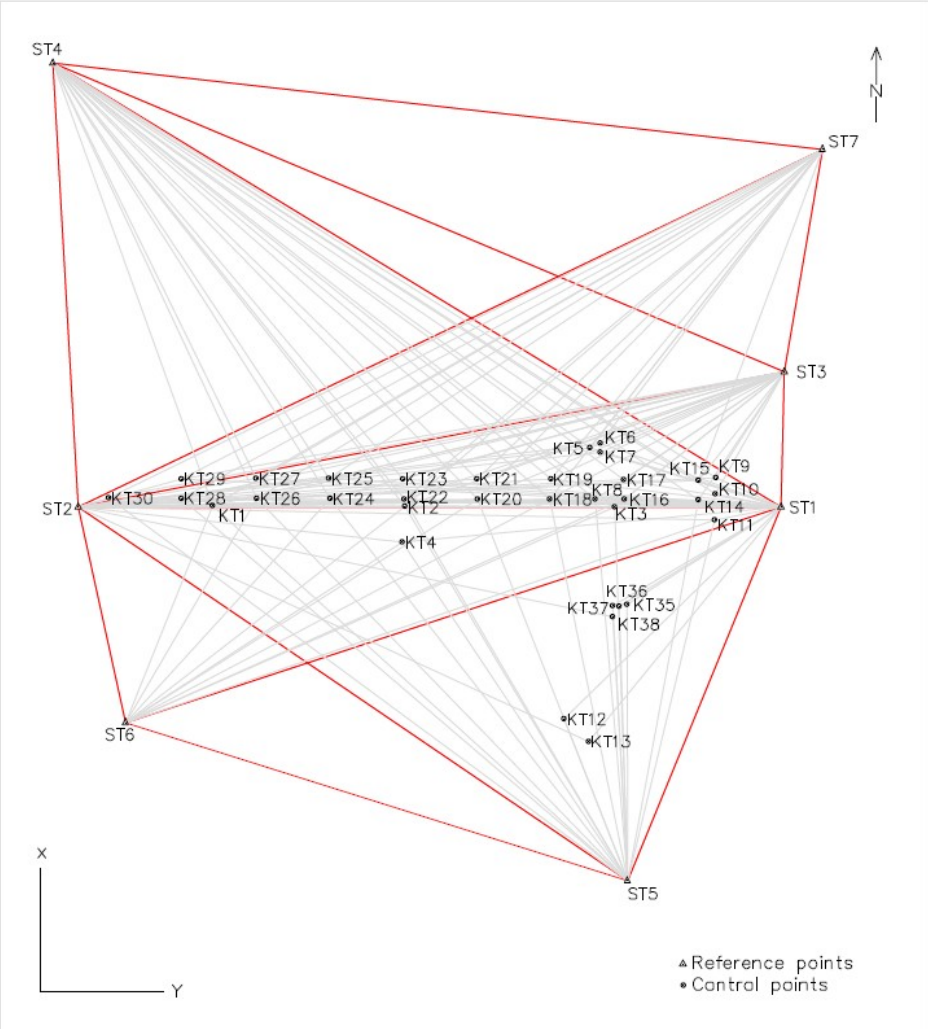


*Fig. 2 2D geodetic monitoring network of the Šelevrenac Dam*

## 3.2. LEVELLING NETWORK

For the purpose of determining the vertical displacements of the dam, a 1D geodetic network was established. The 1D network consists of reference benchmarks R1, R2, R3, R5, R6, R7 and R8, together with points ST1, ST2, ST4, ST5 and ST6, along with 38 control points on the dam (KT1–KT38). Reference benchmarks R1, R2, R3, R5, R6, R7

and R8 are stabilized outside the zone of expected deformations, while ST1, ST2, ST4, ST5 and ST6 are embedded in the pillars of the 2D reference network. The control points are materialized by brass benchmarks designed to enable the determination of both horizontal and vertical displacements. The levelling network layout is designed for the measurement of height differences by the method of geometrical levelling.
In the local coordinate system, vertical displacements are determined along the H-axis, which is perpendicular to the horizontal plane $(Y - X)$ and oriented positively towards the zenith. The height of benchmark R2 is adopted as 100 m, while the heights of the remaining benchmarks are calculated on the basis of the measured height differences in the zero measurement epoch. The configuration of the 1D levelling network, including the position of the reference and control benchmarks and the levelling scheme, is shown in Figure 3.

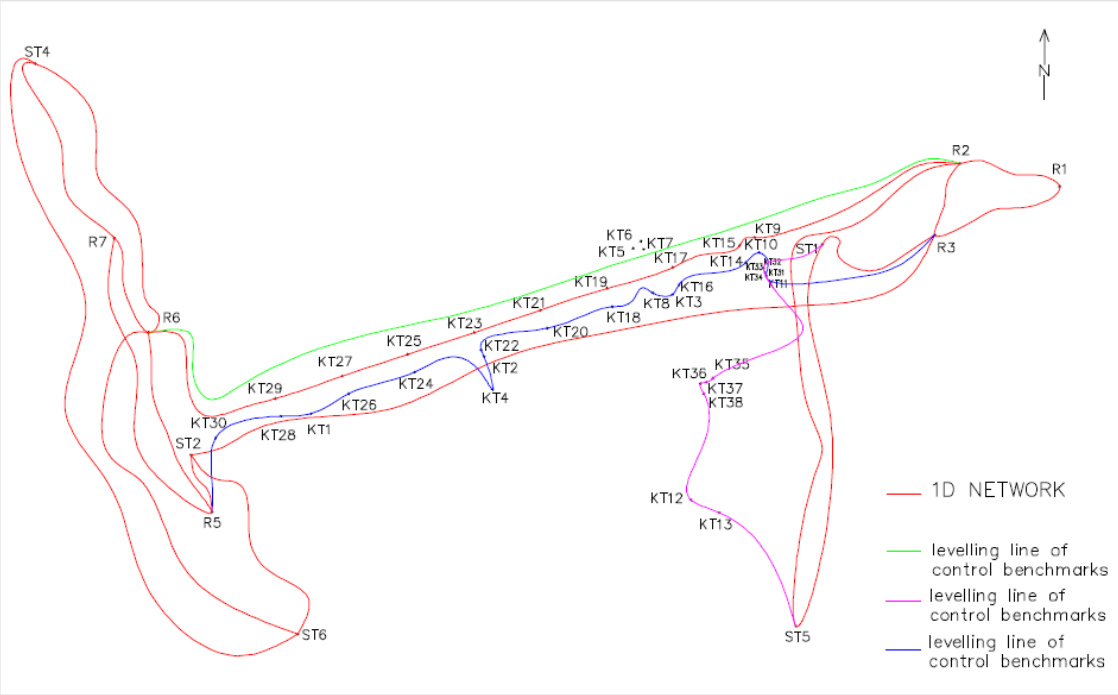


*Fig. 3 1D geodetic monitoring network of the Šelevrenac Dam*

## 3.3. MEASUREMENT EPOCHS AND OBSERVATION PROCEDURE

Geodetic monitoring of the Šelevrenac earth-fill dam has so far included eight measurement epochs: the zero epoch and seven control epochs. These measurements were carried out in the 1D and 2D geodetic networks between 2014 and 2022. This study focuses on the analysis of the zero epoch and the seventh control epoch, observed in April 2022 at a reservoir water level of 124.87 m a.s.l. The observation plan in the seventh control epoch was modified due to field conditions, including limited visibility from the reference points, inaccessible control points and the destruction of reference benchmark R8. As a result, control points KT5–KT7, which were observed in both networks in the zero epoch, were excluded from the measurement procedure altogether, so their displacements could not be determined. Control points KT31–KT34 were observed only in the 1D levelling network in both the zero and the seventh epoch, since their horizontal coordinates could not be determined in the 2D network. Consequently, only vertical displacements were determined for these points.
Measurements in the 2D geodetic network were carried out using a Trimble S6 total station, with a declared angular accuracy of 1" and distance measurement accuracy of 2

mm + 2 ppm. Horizontal directions, zenith angles and slope distances were observed, while horizontal distances were derived from the measured slope distances and zenith angles. Horizontal directions and zenith angles were measured using the gyrus method, with three gyruses in the reference network and two gyruses for observations to the control points. Slope distances were measured in both face positions, with three repetitions in the reference network and two repetitions to the control points. During the measurements, forced centering of the instrument and targets was applied.
Measurements in the 1D geodetic network were carried out by precise geometric levelling using a Leica DNA03 digital level, with a declared accuracy of $U_{1\,km} = 0.3\,mm/\sqrt{km}$. The height differences were measured using Leica invar barcode levelling staffs. The levelling procedure was performed in both directions, with observations taken from the middle.

## 4. RESULTS AND DISCUSSION

After the geodetic measurements and quality control were completed, the final height differences, horizontal directions and distances were used as input data for network adjustment. The 1D and 2D geodetic networks were adjusted using the least-squares method based on the Gauss–Markov model. Both networks were treated as free networks, with the datum defined by minimum trace to reference points ST1–ST7 in the 2D network, and to reference points ST1, ST2, ST4, ST5 and ST6 and R1, R2, R3, R5, R6 and R7 in the 1D network.
Outlier detection in the seventh control epoch was performed using the Data Snooping test. In the 2D network, ten horizontal directions were identified as outliers and excluded from further processing (ST1–ST4, ST2–KT12, ST6–ST1, ST1–KT11, ST2–KT13, ST5–ST6, ST3–KT14, ST6–KT1, ST5–KT35 and ST5–KT36), while no outliers were detected in the 1D network. In addition, the quality of the adjusted networks was evaluated using precision and sensitivity indicators. In the least favourable case, the 2D network enabled the detection of tangential and radial displacements of approximately 5 mm, while the 1D network enabled the detection of vertical displacements of 1.6 mm. The standard deviations of the horizontal coordinates were approximately 1 mm, whereas the standard deviations of point heights ranged from 0.19 mm to 0.41 mm.
The deformation analysis was performed only for the points common to both epochs. Accordingly, control points KT5–KT7 were not included in the analysis of either network, control points KT31–KT34 were not included in the analysis of the 2D network, and reference benchmark R8 was not included in the analysis of the 1D network. The robust S-transformation of the displacement vector was carried out using the IRLS method, which was previously described. The adopted values of the constant $c$ and the tolerance $\gamma$ were 0.01 mm and 0.001 mm, respectively. The estimated displacement vector and the corresponding cofactor matrix were obtained after 15 iterations for the 2D network and 9 iterations for the 1D network. Point stability was analysed using a global significance level of $\alpha = 0.05$, while the local significance level $\alpha_0$ was determined using the Bonferroni equation.
The results of the stability analysis of the reference points of the 2D and 1D networks, including the values of the test statistic, the corresponding quantiles of the $F$-distribution and the estimated horizontal and vertical displacements, are presented in Tables 2 and 3. Reference point ST3 was identified as unstable in the 2D network, with an estimated displacement vector intensity of 5.3 mm, while reference benchmarks R2, R7 and ST1 were identified as unstable in the 1D network, with estimated vertical displacements ranging from −1.7 mm to −4.1 mm.

*Tab. 2 Stability status and estimated displacements of the reference points in the 2D network*

| Point | T | $F_{(0.9987,2,518)}$ | 2D Status | $\hat{d}_Y[mm]$ | $\hat{d}_X[mm]$ | $\hat{d}[mm]$ |
|---|---|---|---|---|---|---|
| ST1 | 1.625 | 6.693 | Stable | 0.060 | 1.751 | 1.752 |
| ST2 | 0.905 | 6.693 | Stable | -0.557 | -0.333 | 0.649 |
| ST3 | 26.459 | 6.693 | Unstable | -3.054 | 4.382 | 5.341 |
| ST4 | 0.982 | 6.693 | Stable | 1.094 | 0.402 | 1.166 |
| ST5 | 3.845 | 6.693 | Stable | -0.010 | -2.400 | 2.400 |
| ST6 | 2.048 | 6.693 | Stable | 1.113 | 0.000 | 1.113 |
| ST7 | 3.454 | 6.693 | Stable | -0.002 | -2.723 | 2.723 |

*Tab. 3 Stability status and estimated displacements of the reference points in the 1D network*

| Point | T | $F_{(0.9989,1,24)}$ | 1D Status | $\hat{d}_H[mm]$ |
|---|---|---|---|---|
| ST1 | 175.623 | 13.706 | Unstable | -4.091 |
| ST2 | 1.591 | 13.706 | Stable | 0.681 |
| ST4 | 9.048 | 13.706 | Stable | -1.793 |
| ST5 | 0.021 | 13.706 | Stable | -0.024 |
| ST6 | 0.968 | 13.706 | Stable | 0.576 |
| R1 | 0.019 | 13.706 | Stable | 0.044 |
| R2 | 33.079 | 13.706 | Unstable | -1.708 |
| R3 | 0.060 | 13.706 | Stable | 0.071 |
| R5 | 2.822 | 13.706 | Stable | 0.848 |
| R6 | 2.612 | 13.706 | Stable | 0.817 |
| R7 | 18.044 | 13.706 | Unstable | -2.301 |

Among the control points, 19 points were identified as horizontally unstable, while 31 points were identified as vertically unstable. Table 4 presents the stability status of the control points in the 2D and 1D networks, the estimated displacements between the zero and seventh control epochs, and the corresponding control point locations. The displacements are presented along the tangential (Y), radial (X) and vertical (H) axes.

*Tab. 4 Stability status and estimated displacements of control points*

| Point | 2D status | $\hat{d}_Y[mm]$ | $\hat{d}_X[mm]$ | 1D status | $\hat{d}_H[mm]$ | Control point location |
|---|---|---|---|---|---|---|
| KT1 | Stable | -0.4 | 1.0 | Unstable | -3.0 | Dam crest |
| KT2 | Stable | 1.5 | -1.8 | Unstable | -5.5 | Dam crest |
| KT3 | Unstable | 0.0 | -4.0 | Unstable | -3.3 | Dam crest |
| KT4 | Unstable | 3.6 | -1.1 | Unstable | -7.3 | Downstream dam slope |
| KT5 | / | / | / | / | / | Bottom outlet gate chamber |
| KT6 | / | / | / | / | / | Bottom outlet gate chamber |
| KT7 | / | / | / | / | / | Bottom outlet gate chamber |
| KT8 | Stable | 0.5 | -2.1 | Unstable | -6.2 | Bottom outlet bridge |

| | | | | | | |
|---|---|---|---|---|---|---|
| | | | | | | foundation |
| KT9 | Stable | 0.4 | 3.0 | Unstable | -3.1 | Spillway floor |
| KT10 | Stable | 0.1 | 1.7 | Unstable | -4.5 | Upper spillway wall |
| KT11 | Unstable | -2.4 | 4.0 | Unstable | -2.8 | Upper spillway wall |
| KT12 | Stable | 0.1 | -3.8 | Unstable | -1.8 | Spillway stilling basin |
| KT13 | Unstable | 2.3 | -6.6 | Unstable | -2.9 | Spillway stilling basin |
| KT14 | Unstable | -3.0 | 6.1 | Unstable | -8.9 | Dam crest edge beam (upstream side) |
| KT15 | Unstable | -1.0 | 8.7 | Unstable | -8.0 | Upstream slope slab |
| KT16 | Unstable | -0.8 | 3.7 | Unstable | -6.4 | Dam crest edge beam (upstream side) |
| KT17 | Unstable | 3.4 | 6.8 | Unstable | -8.6 | Upstream slope slab |
| KT18 | Stable | 0.8 | 2.8 | Unstable | -6.9 | Dam crest edge beam (upstream side) |
| KT19 | Unstable | -1.8 | 54.3 | Unstable | -22.8 | Upstream slope slab |
| KT20 | Unstable | 0.1 | 7.3 | Unstable | -6.4 | Dam crest edge beam (upstream side) |
| KT21 | Unstable | 0.0 | 58.9 | Unstable | -24.0 | Upstream slope slab |
| KT22 | Unstable | 1.1 | 12.8 | Unstable | -6.7 | Dam crest edge beam (upstream side) |
| KT23 | Unstable | 0.8 | 52.7 | Unstable | -21.5 | Upstream slope slab |
| KT24 | Unstable | 1.9 | 8.3 | Unstable | -4.6 | Dam crest edge beam (upstream side) |
| KT25 | Unstable | 1.7 | 48.0 | Unstable | -18.7 | Upstream slope slab |
| KT26 | Unstable | 1.9 | 4.8 | Unstable | -5.7 | Dam crest edge beam (upstream side) |
| KT27 | Unstable | 3.3 | 43.3 | Unstable | -18.4 | Upstream slope slab |
| KT28 | Unstable | 1.8 | 6.5 | Unstable | -5.8 | Dam crest edge beam (upstream side) |
| KT29 | Unstable | 5.4 | 18.3 | Unstable | -8.8 | Upstream slope slab |
| KT30 | Stable | -0.8 | 1.4 | Unstable | -3.8 | Dam crest edge beam (upstream side) |
| KT31 | / | / | / | Unstable | -3.8 | Spillway floor |
| KT32 | / | / | / | Unstable | -7.5 | Spillway floor |
| KT33 | / | / | / | Unstable | -6.6 | Spillway ceiling |
| KT34 | / | / | / | Unstable | -2.3 | Spillway ceiling |
| KT35 | Stable | 0.2 | -2.0 | Stable | -0.5 | Pumping station measuring shaft |
| KT36 | Stable | -1.5 | -1.0 | Stable | -0.3 | Pumping station measuring shaft |

| | | | | | | |
|---|---|---|---|---|---|---|
| KT37 | Stable | 0.5 | -1.5 | Stable | -0.3 | Pumping station manhole |
| KT38 | Stable | -0.1 | 0.4 | Stable | -0.5 | Pumping station manhole |

The individual displacement components between the zero and seventh control epochs are presented graphically in Figures 4–6. The estimated tangential, radial and vertical displacements are shown for all control points included in the measurement procedure, with the points grouped according to their position on the dam structure.

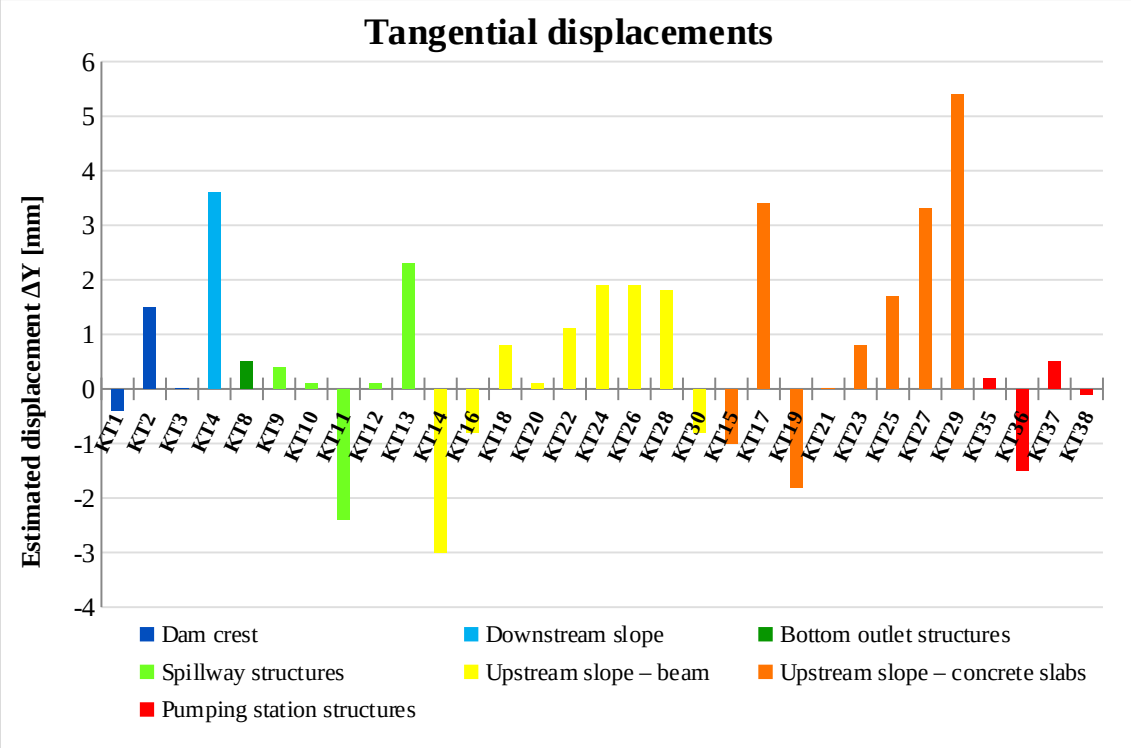


*Fig. 4 Tangential displacements of control points between the zero and seventh control epochs*

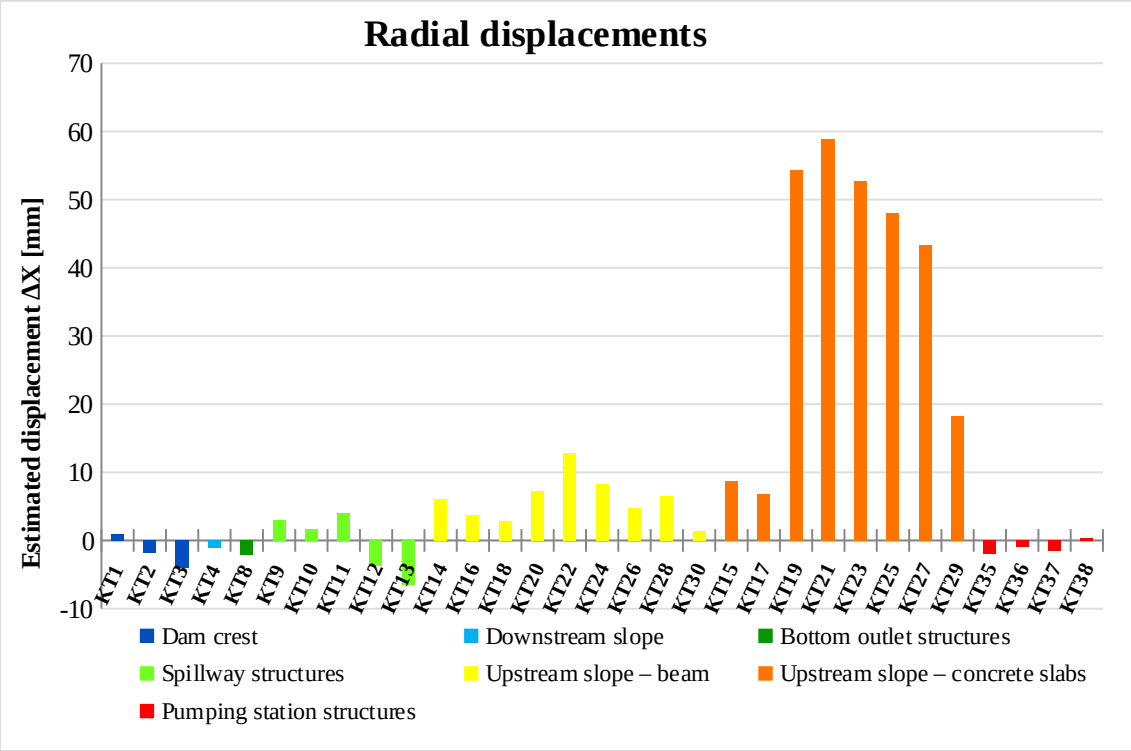


*Fig. 5 Radial displacements of control points between the zero and seventh control epochs*

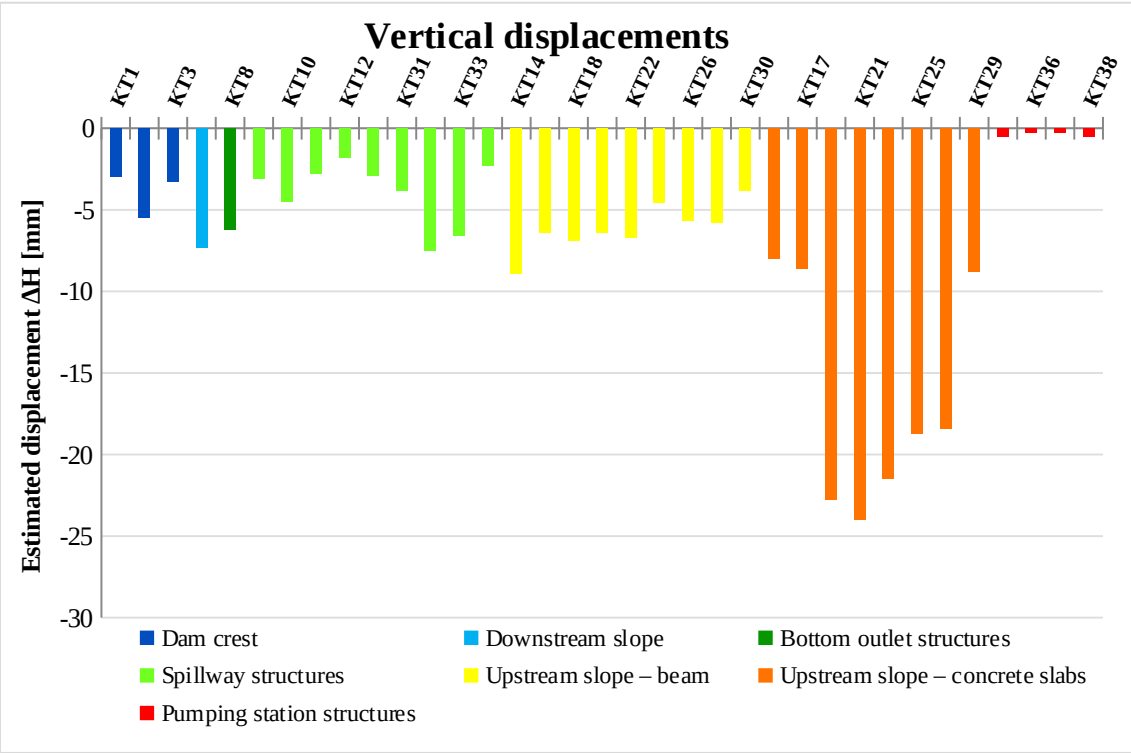


*Fig. 6 Vertical displacements of control points between the zero and seventh control epochs*

The presented graphs and the table of estimated displacements show that the displacements are not uniformly distributed across the dam structure. The most significant displacements were detected at control points KT19, KT21, KT23, KT25, KT27 and KT29 located on the upstream slope. This distribution of displacement components is consistent with the expected effects acting on the dam. The radial component reflects changes in the direction perpendicular to the dam axis, while the vertical component is related to settlement processes. The radial displacements of the control points in the

seventh control epoch range from 18.3 mm to 58.9 mm. The positive displacement values indicate movement towards the upstream side, according to the adopted orientation of the local X-axis. The vertical displacements range from -24.0 mm to -8.8 mm, indicating settlement, since the positive direction of the H-axis is oriented towards the zenith. Such a displacement pattern suggests localized behaviour of the upstream slope, particularly of the concrete slabs.

## 5. CONCLUSIONS

This paper presents the geodetic monitoring and deformation analysis of the Šelevrenac Dam between the zero and seventh control epochs. The analysis was based on the results obtained from the 2D geodetic network, used for the determination of horizontal displacements, and the 1D levelling network, used for the determination of vertical displacements. The network adjustment was performed using the least-squares method based on the Gauss–Markov model, while the deformation analysis was carried out using the IWST method.

The results, presented in both tabular and graphical form, revealed non-uniform deformation behaviour across the dam structure. The most significant displacements were concentrated in the upstream slope zone, where radial displacements reached up to 58.9 mm and vertical displacements reached up to -24.0 mm. The dominance of the radial and vertical components over the tangential component, combined with the spatial distribution of unstable points, suggests localized behaviour of the concrete slabs in this zone rather than a global response of the dam body. The radial displacement component is of particular relevance, as it corresponds to the direction of hydrostatic pressure acting approximately perpendicular to the dam axis. The negative vertical displacement values indicate settlement potentially associated with the self-weight of the dam and localized settlement within the upstream slope zone. The combined interpretation of the 1D and 2D network results provided a clearer distinction between zones with more pronounced deformation behaviour and parts of the dam with more stable behaviour. The applied IWST procedure proved suitable for identifying stable and unstable points, as well as for analysing the spatial distribution of displacements.

Future measurement epochs should continue the systematic geodetic monitoring of the dam, with particular attention to the upstream slope zone where the largest displacements were detected. Given the magnitude of the radial displacements recorded at points KT19, KT21, KT23, KT25, KT27 and KT29, it is recommended to shorten the interval between successive measurement epochs in order to enable timely detection of any acceleration in deformation behaviour. This would allow a more reliable assessment of whether the detected displacements are stabilizing or progressing over time.

### ACKNOWLEDGEMENT

The research has been conducted within the project "Enhancement of teaching and scientific research capacities through the application of modern technologies in the fields of civil engineering, geodesy, and disaster risk management and fire safety", developed at the Department of Civil Engineering and Geodesy, Faculty of Technical Sciences, University of Novi Sad, Serbia.

## REFERENCES

[1] Chrzanowski A., Szostak-Chrzanowski A. (2009). Deformation Monitoring Surveys – Old Problems and New Solutions. *Reports on Geodesy, Volume 87*, Issue 2, pp. 85–103.

[2] Scaioni M., Marsella M., Crosetto M., Tornatore V., Wang J. (2018). Geodetic and Remote-Sensing Sensors for Dam Deformation Monitoring. *Sensors, Volume 18*, Issue 11, Article 3682. https://doi.org/10.3390/s18113682

[3] Taşçi L. (2010). Analysis of Dam Deformation Measurements with the Robust and Non-Robust Methods. *Scientific Research and Essays, Volume 5*, Issue 14, pp. 1770–1779.

[4] Caspary W.F. (2000). *Concepts of Network and Deformation Analysis*. Monograph 11, School of Geomatic Engineering, The University of New South Wales, Sydney, Australia.

[5] Sušić Z., Batilović M., Ninkov T., Bulatović V., Aleksić I., Nikolić G. (2017). Geometric Deformation Analysis in Free Geodetic Networks: Case Study for Fruška Gora in Serbia. *Acta Geodynamica et Geomaterialia, Volume 14*, Issue 3, pp. 341–355. https://doi.org/10.13168/AGG.2017.0017

[6] Setan H., Singh R. (2001). Deformation Analysis of a Geodetic Monitoring Network. *Geomatica, Volume 55*, Issue 3, pp. 333–346. https://doi.org/10.5623/geomat-2001-0039

[7] Caspary W.F., Borutta H. (1987). Robust Estimation in Deformation Models. *Survey Review, Volume 29*, Issue 223, pp. 29–45. https://doi.org/10.1179/sre.1987.29.223.29

[8] Nowel K., Kamiński W. (2014). Robust Estimation of Deformation from Observation Differences for Free Control Networks. *Journal of Geodesy, Volume 88*, Issue 8, pp. 749–764. https://doi.org/10.1007/s00190-014-0719-7

[9] Chen Y.Q., Chrzanowski A., Secord J.M. (1990). A Strategy for the Analysis of the Stability of Reference Points in Deformation Surveys. *CISM Journal ACSGC, Volume 44*, Issue 2, pp. 141–149. https://doi.org/10.1139/geomat-1990-0016

[10] Sušić Z., Batilović M., Ninkov T., Aleksić I., Bulatović V. (2015). Identification of Movements Using Different Geodetic Methods of Deformation Analysis. *Geodetski vestnik, Volume 59*, Issue 3, pp. 537–553. https://doi.org/10.15292/geodetski-vestnik.2015.03.537-553

[11] Batilović M., Kanović Ž., Sušić Z., Marković M.Z., Bulatović V. (2022). Deformation Analysis: The Modified GREDOD Method. *Geodetski vestnik, Volume 66*, Issue 1, pp. 60–75. https://doi.org/10.15292/geodetski-vestnik.2022.01.60-75

[12] Pelzer H. (1971). *Zur Analyse geodätischer Deformationsmessungen*. Deutsche Geodätische Kommission, Reihe C, Heft 164, Verlag der Bayerischen Akademie der Wissenschaften, Munich, Germany.

[13] Heck B. (1983). Das Analyseverfahren des Geodätischen Instituts der Universität Karlsruhe – Stand 1983. In: *Deformationsanalysen '83: Geometrische Analyse und Interpretation von Deformationen Geodätischer Netze*. Schriftenreihe Wissenschaftlicher Studiengang Vermessungswesen der Hochschule der Bundeswehr München, Heft 9, Munich, Germany, pp. 153–182.

[14] Heck B., Kok J.J., Welsch W.M., Baumer R., Chrzanowski A., Chen Y.Q., Secord J.M. (1982). Report of the FIG Working Group on the Analysis of Deformation Measurements. In: Joó I., Detreköi A. (Eds.), *Proceedings of the 3rd International Symposium on Deformation Measurements by Geodetic Methods*, Budapest, Hungary, pp. 337–415.

[15] Chrzanowski A., Chen Y.Q., Secord J.M. (1982). A Generalized Approach to the Geometrical Analysis of Deformation Surveys. In: Joó I., Detreköi A. (Eds.), *Proceedings of the 3rd International Symposium on Deformation Measurements by Geodetic Methods*, Budapest, Hungary.

[16] Welsch W.M. (1982). Description of Homogeneous Horizontal Strains and Some Remarks on Their Analysis. In: *Proceedings of the International Symposium on Geodetic Networks and Computations of the IAG*, Deutsche Geodätische Kommission, Reihe B, Heft 258, Volume 5, Munich, Germany, pp. 188–205.

[17] Caspary W.F. (1984). Deformation Analysis Using a Special Similarity Transformation. In: *Technical Papers, International FIG Engineering Survey Conference*, Washington, D.C., USA, pp. 145–151.

[18] Chen Y.Q. (1983). *Analysis of Deformation Surveys – A Generalized Method*. Technical Report No. 94, Department of Surveying Engineering, University of New Brunswick, Fredericton, Canada.

[19] Sušić Z., Batilović M., Đurović R., Marković M.Z., Vujinović M. (2023). Deformation Analysis of Ratkov Laz Bridge Using Pelzer and IWST Method. *Geodetski vestnik, Volume 67*, Issue 4, pp. 487–504. https://doi.org/10.15292/geodetski-vestnik.2023.04.487-504

https://doi.org/10.24867/INDIS-2026-EN-909



# INFLUENCE OF TEMPERATURE AND LEVELLING STAFF MATERIAL ON THE COLLIMATION ERROR OF THE LEICA DNA03 DIGITAL LEVEL

*Nikolina Gajić[1], Đuro Krnić[2], Marina Davidović Manojlović[3], Vladimir Bulatović[4], Zoran Sušić[5]*

***Summary:***

Precise geometric levelling is one of the most accurate methods for determining height differences, but its accuracy may be affected by environmental conditions and levelling staff characteristics. This paper investigates the collimation error of the Leica DNA03 digital level under two temperature regimes using invar and fiberglass staffs. Measurements were performed according to ISO 17123-2. Considerable differences in the magnitude and stability of the collimation error were observed between the two environmental regimes, while the influence of staff material was less pronounced. Since temperature and measurement environment varied simultaneously, their individual effects could not be separated.

*Keywords: digital level, collimation angle, Leica DNA03, invar staffs, fiberglass staffs, temperature effects*

# UTICAJ TEMPERATURE I MATERIJALA NIVELMANSKIH LETVI NA KOLIMACIONU GREŠKU DIGITALNOG NIVELIRA LEICA DNA03

***Rezime:***

Precizni geometrijski nivelman predstavlja jednu od najtačnijih metoda za određivanje visinskih razlika, ali na njegovu tačnost mogu uticati uslovi sredine i karakteristike nivelmanskih letvi. U radu je analizirana kolimaciona greška digitalnog nivelira Leica DNA03 u dva temperaturna režima, korišćenjem invarskih letvi i letvi od fiberglasa. Mjerenja su sprovedena u skladu sa standardom ISO 17123-2. Utvrđene su značajne razlike u veličini i stabilnosti kolimacione greške između dva režima, dok je uticaj materijala letve bio manje izražen. Pošto su se temperatura i okruženje mjerenja istovremeno mijenjali, njihove pojedinačne uticaje nije bilo moguće razdvojiti.

Ključne reči: digitalni nivelir, kolimacioni ugao, Leica DNA03, invarske letve, letve od fiberglasa, temperaturni uticaji

[1] Teaching Associate, Faculty of Technical Sciences, University of Novi Sad, Novi Sad, Serbia, nikolina.gajic@uns.ac.rs, ORCID 0009-0008-1989-3888
[2] Teaching Assistant, Faculty of Technical Sciences, University of Novi Sad, Novi Sad, Serbia, djuro.geo@uns.ac.rs, ORCID 0000-0003-4481-3209
[3] Research Associate, Faculty of Technical Sciences, University of Novi Sad, Novi Sad, Serbia, marina.davidovic@uns.ac.rs, ORCID 0000-0001-6736-0615
[4] Full Professor, Faculty of Technical Sciences, University of Novi Sad, Novi Sad, Serbia, vbulat2003@uns.ac.rs, ORCID 0000-0002-0772-5333
[5] Full Professor, Faculty of Technical Sciences, University of Novi Sad, Novi Sad, Serbia, zsusic@uns.ac.rs, ORCID 0000-0002-8885-2659

## 1. INTRODUCTION

Precise geometric levelling is considered one of the most important methods for the accurate determination of height differences between points and represents an essential component of engineering surveying, deformation monitoring, and the establishment of vertical control networks [1-2]. According to Schofield [1], levelling remains the principal method for obtaining accurate elevations and forms the basis of many engineering and construction surveying applications where reliable vertical control is required. The development of digital levelling technology has significantly improved the efficiency and reliability of levelling measurements by enabling automatic reading of coded staffs, digital data processing, and reduction of subjective observer errors [3-4]. Among modern digital levels, the Leica DNA03 is widely recognized as a high-precision instrument intended for precise and engineering levelling applications [6,7].

Despite the high level of automation and precision provided by digital levelling systems, measurement results are still influenced by various systematic and random errors [2,5-6]. One of the most important systematic effects is the collimation error, which represents the deviation of the line of sight from the true horizontal direction [5]. The influence of this error becomes particularly significant when unequal sight lengths are used during measurements [5,6]. In addition, the accuracy and stability of levelling measurements are affected by environmental conditions such as refraction, illumination, atmospheric conditions, and temperature variations [2,6].

Temperature changes represent one of the most significant external influences on digital levelling systems because they may affect the instrument, tripod, and levelling staffs [7-8]. Experimental investigations conducted on the Leica DNA03 digital level showed that the values of the collimation angle vary under different temperature conditions, indicating that temperature may influence the stability of the line of sight [9]. Besides the instrument itself, the material characteristics of levelling staffs are also important, especially in high-precision measurements. Invar staffs are characterized by a very low coefficient of thermal expansion and therefore provide greater dimensional stability, while other staff materials are more sensitive to temperature changes [9-10].

Considering the importance of temperature effects and the material properties of levelling staffs, this paper analyses the values of the collimation angle of the Leica DNA03 digital level under two different temperature regimes using invar and fiberglass levelling staffs. The measurements were performed under two different environmental conditions according to the recommendations of the ISO 17123-2 standard [8]. The main objective of the research is to investigate the influence of temperature and staff material on the stability of the collimation angle and the reliability of precise levelling measurements.

## 2. THEORETICAL BACKGROUND

This section reviews the theoretical concepts relevant to the study, including geometric levelling, digital level instrumentation, the collimation error, and the factors - temperature and staff material - known to affect measurement accuracy. The applicable standard for assessing measurement uncertainty is also briefly introduced.

### 2.1. GEOMETRIC LEVELLING

Geometric levelling is one of the most accurate geodetic methods for determining height differences between points and is widely used in engineering surveying, deformation monitoring, construction, and the establishment of vertical control networks [1]. The

method is based on determining height differences using a horizontal line of sight and vertically positioned levelling staffs, typically in midpoint or end levelling configurations [5].

The accuracy of geometric levelling depends on instrument quality, staff stability, environmental conditions, and the applied measurement procedure [1,5]. Instrumental imperfections, atmospheric influences, and observation geometry may affect the results and therefore require careful consideration during field measurements [1,3]. Due to its high-precision and standardized procedures, geometric levelling remains one of the most reliable methods for determining orthometric height differences in geodetic and engineering practice [1,5].

## 2.2. DIGITAL LEVELS AND LEICA DNA03

The development of digital levelling technology has significantly improved the efficiency and automation of levelling measurements. Modern digital levels use optical systems, Charge-Coupled Device (CCD) sensors, and image-processing algorithms to automatically read coded staffs, reducing subjective reading errors and increasing measurement speed and repeatability compared to conventional optical levels [3-4].

Among contemporary instruments, the Leica DNA03 is a high-precision digital level designed for precise and engineering levelling applications (Fig. 1) [6]. It operates with barcode staffs and automatically determines height differences and sight distances through electronic image processing. According to the manufacturer, the instrument achieves a standard deviation of 0.3 mm per 1 km of double-run levelling when used with invar staffs [6]. Its high-precision and automated observation procedure make it suitable for deformation monitoring, precise engineering surveys, and the establishment of high-order vertical control networks [1,10,12].




*Fig. 1 Digital level Leica DNA03*

The Leica DNA03 is equipped with a pendulum compensator with magnetic damping that maintains the horizontality of the line of sight and reduces the influence of minor instrument tilts [6]. However, despite the high level of automation, measurement accuracy may still be affected by factors such as temperature variations, atmospheric refraction, instrument adjustment, staff stability, and observation conditions [3,11,14]. Therefore, regular instrument testing, calibration, and adherence to standardized measurement procedures remain essential for reliable precise levelling results [5].

## 2.3. COLLIMATION ERROR

One of the most important systematic influences affecting the accuracy of geometric levelling is the collimation error. This error occurs when the instrument line of sight deviates from the true horizontal plane, causing a systematic effect in the measured height differences [3,5]. The magnitude of this deviation is commonly expressed by the collimation angle Δi (Fig. 2), which represents the angular difference between the actual line of sight and the ideal horizontal direction [5]. In precise levelling, the determination of height differences with millimetre-level accuracy requires a properly adjusted instrument and a horizontal line of sight; therefore, even small deviations may introduce measurable systematic errors into the observations [1,5].

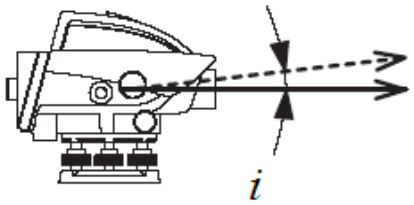


*Fig. 2 Collimation angle*

The influence of the collimation error is directly related to the sight lengths between the instrument and the levelling staffs. When the backsight and foresight distances are equal, the systematic effect of the collimation error is practically eliminated, resulting in a more reliable determination of the height difference. Conversely, when the sight lengths differ, the influence of the collimation error becomes proportional to the difference in sight lengths, introducing a systematic deviation into the measured height difference [5,9].

For this reason, the determination of the collimation angle is commonly based on observations obtained from two different measurement configurations. In the first configuration, the instrument is positioned approximately midway between the staffs, where the influence of the collimation error is minimized due to nearly equal sight lengths [5,9]. In the second configuration, the instrument is placed close to one of the staffs, creating significantly unequal backsight and foresight distances and thereby increasing the effect of the collimation error on the observations [5,9]. By comparing the height differences obtained from these two configurations, the value of the collimation angle Δi can be determined and used to assess the adjustment quality and stability of the instrument line of sight [5,9].

## 2.4. INFLUENCE OF TEMPERATURE ON MEASUREMENT ACCURACY

Temperature is one of the most important environmental factors affecting the performance and stability of digital levelling systems. While surveying instruments are typically calibrated under controlled laboratory conditions, field measurements are often carried out under different environmental conditions [5]. Temperature variations can cause thermal expansion or contraction of instrument components, tripods, and levelling staffs, potentially affecting the line of sight and measurement accuracy [3,10]. Previous studies have shown that temperature changes may influence both the instrument and its accessories, reducing measurement repeatability and accuracy, particularly in high-precision levelling applications [9,11]. The magnitude of these effects depends on the material properties of the equipment used, which is why ISO 17123-2 recommends

allowing instruments to acclimatize to ambient conditions before testing or measurement [8].

### 2.5. LEVELLING STAFFS AND MATERIAL PROPERTIES

Levelling staffs are an essential component of the levelling system, as their dimensional stability directly affects the accuracy of height difference measurements [10-11]. For high-precision levelling, invar staffs are commonly preferred because of their very low coefficient of thermal expansion, which ensures excellent dimensional stability under changing environmental conditions [10]. In contrast, fiberglass staffs exhibit higher thermal expansion and are therefore more susceptible to temperature-induced dimensional changes that may influence measurement accuracy [10,13]. Since modern digital levels use barcode staffs for automatic reading, the thermal behaviour of staff materials remains an important factor in precise levelling, particularly under varying temperature conditions [3-4,6,15].

### 2.6. ISO 17123-2 STANDARD AND MEASUREMENT UNCERTAINTY

The ISO 17123-2 standard provides standardized field procedures for testing levelling instruments under real operating conditions and includes both simplified and full testing methods for evaluating instrument precision and reliability [8]. The simplified procedure is primarily used for assessing the influence of the collimation error through midpoint and end levelling configurations, while the full procedure determines the best achievable precision under field conditions [8]. The reliability of the obtained results can be evaluated through measurement uncertainty, which is commonly estimated from repeated observations and statistical analysis (Type A evaluation), supplemented by information from calibration data and instrument specifications (Type B evaluation) [3,16-17].

## 3. MEASUREMENT SETUP AND METHODOLOGY

To ensure the reliability and reproducibility of the results, a well-defined experimental methodology was applied. This section outlines the instrument and equipment, measurement conditions, measurement geometry, and the observation procedure used during data collection.

### 3.1. INSTRUMENTS AND EQUIPMENT

The experimental part of this research was conducted using a Leica DNA03 digital level in combination with two types of barcode levelling staffs manufactured by the same producer. The first staff set consisted of Leica GPCL2 invar barcode staffs (Fig. 3, left), while the second set consisted of Leica GKNL4M sectional fiberglass barcode staffs (Fig. 3, right) [7]. The use of staffs from the same manufacturer ensured compatibility with the instrument and minimized potential differences arising from design and production characteristics, allowing the investigation to focus primarily on the influence of staff material and temperature conditions on the determined values of the collimation angle.

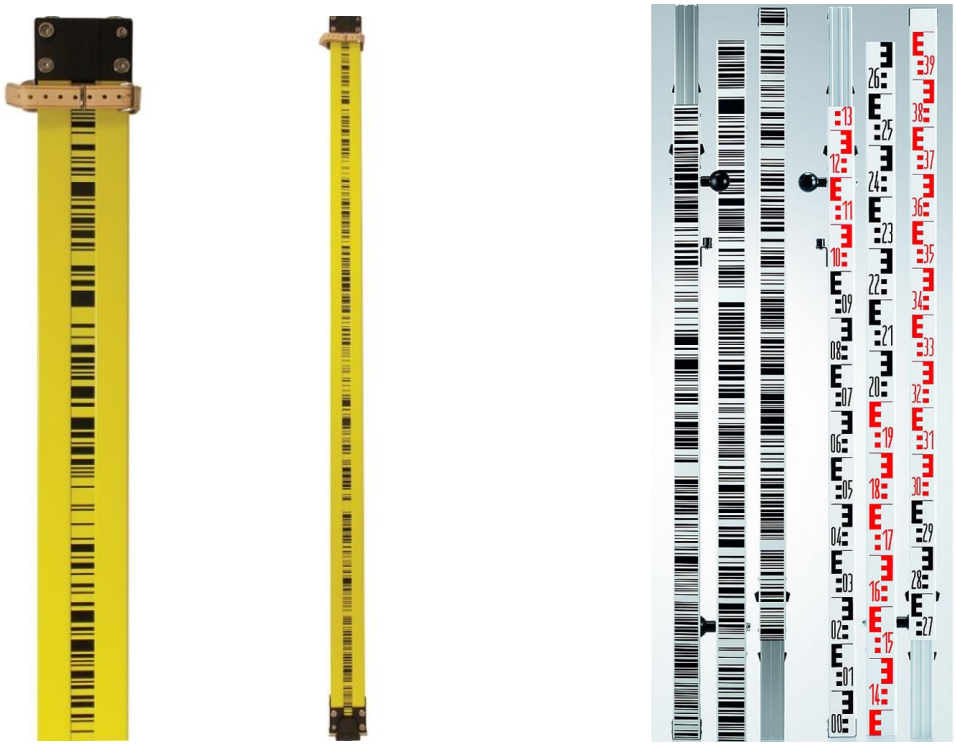

*Fig. 3 Leica invar and fiberglass barcode staffs [7]*

The main technical characteristics of the Leica DNA03 digital level are presented in Table 1 [6].

*Tab. 1 Characteristics of the Leica DNA03 digital level [6]*

| Parameter | Value |
|---|---|
| Accuracy with invar staffs | 0.3 mm |
| Accuracy with standard staffs | 1.0 mm |
| Optical measurements | 2.0 mm |
| Distance measurement accuracy | 1 cm/20 m (500 ppm) |
| Measurement range | 1.8-110 m |
| Resolution of height measurement | 0.01 mm |
| Time for single measurement | approx. 3 s |
| Telescope magnification | 24x |
| Compensator | pendulum compensator with magnetic damping |
| Working temperature | -20°C to +50°C |
| Storage temperature | -40°C to +70°C |

In addition to their thermal properties, the selected levelling staffs differ in several structural characteristics that may affect field observations. The GPCL2 invar staffs are designed for high-precision levelling and provide excellent dimensional stability under varying environmental conditions [7]. In contrast, the sectional fiberglass staffs are lighter and easier to handle but may be more susceptible to environmental influences and mechanical deformation [7]. The main characteristics of the two levelling staff types are summarized in Table 2.

*Tab. 2 Characteristics of the barcode levelling staffs [7]*

| Characteristic | Leica GPCL2 invar staff | Leica GKNL4M fiberglass staff |
|---|---|---|
| Staff type | Invar barcode staff | Sectional fiberglass barcode staff |
| Length | 2.0 m | 1.58-4.0 m |
| Weight | 4.2 kg | 4.4 kg |
| Number of sections | One-piece | 3 connectable sections |
| Circular bubbles | 2 | 1 |
| Handles | 2 attached handles | 2 handles |
| Thermal expansion coefficient | Very low | 10 ppm/°C |
| Intended application | High-precision levelling | General and engineering levelling |

During the measurements, the levelling staffs were manually held by operators (staff holders) and were not mechanically fixed or mounted on supporting devices. This approach was selected in order to simulate standard field measurement conditions commonly encountered in practical levelling operations [1]. Particular attention was paid to maintaining the staffs in a vertical position during observations by using the integrated circular bubbles. Although manually held staffs may introduce minor additional instability compared to fixed setups, the same measurement procedure and observation conditions were consistently maintained throughout all experiments in order to ensure comparability of the obtained results [5].

## 3.2. MEASUREMENT CONDITIONS

The experimental investigation was conducted under two different environmental regimes: low-temperature outdoor conditions (1±1 °C) and moderate-temperature indoor conditions (21±1 °C). These regimes were selected to represent conditions substantially different from those typically encountered during laboratory calibration and testing at approximately 20-22 °C [5]. The indoor measurements were performed during the evening hours, when the measurement area was largely unoccupied and there was minimal movement of people, thereby reducing potential disturbances during the observations. Since temperature and measurement environment varied simultaneously, their individual effects could not be separated; therefore, the observed differences should be interpreted as the combined effect of temperature and associated environmental conditions.

In accordance with ISO 17123-2, the instrument was allowed to acclimatize to ambient conditions for approximately 30 minutes before each measurement session in both regimes [8]. Measurements were conducted on stable ground, with careful vertical positioning of the staffs and controlled instrument setup to minimize refraction and mechanical disturbances. The same pair of staffs of each type and the same tripod were used in both regimes to ensure consistency between the experimental series.

Overall measurement uncertainty may also arise from environmental, instrumental, and operator-related effects [3,11].

## 3.3. MEASUREMENT GEOMETRY

The collimation angle was determined using the from-the-centre method based on two measurement configurations (Fig. 4) [5]. In the first configuration, the instrument was positioned approximately midway between the two levelling staffs (Fig. 4a), resulting in

nearly equal backsight and foresight distances and minimizing the influence of collimation error [5,9].
In the second configuration, the instrument was placed close to one of the staffs (Fig. 4b), producing significantly unequal backsight and foresight distances and increasing the influence of collimation error [5,9]. The collimation angle Δi was calculated by comparing the height differences obtained from the midpoint and end configurations.

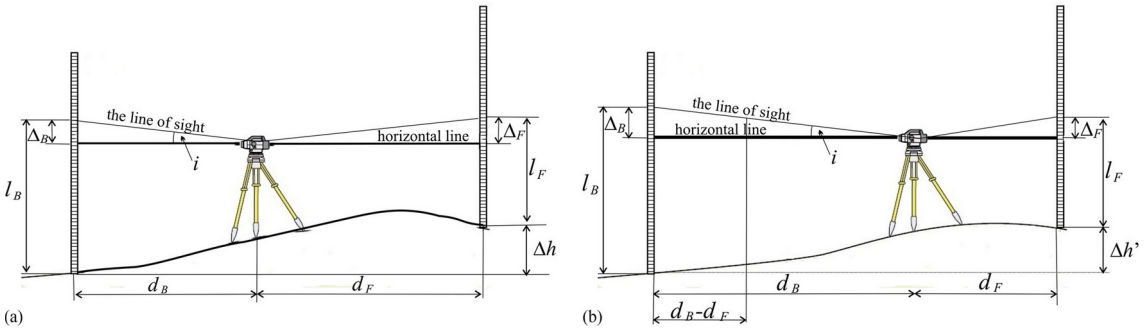


*Fig. 4 Procedure for height difference determination: midpoint (a) and end (b) configurations*

The approximate backsight and foresight distances used in the midpoint configuration are presented in Table 3. As shown, nearly equal sight lengths were maintained for both staff types under the two investigated temperature regimes.

*Tab. 3 Approximate sight lengths in the midpoint configuration*

| Temp. | Staff material | Approximate sight length | |
|---|---|---|---|
| | | Foresight, $d_F$ [m] | Backsight, $d_B$ [m] |
| 1±1°C | Invar | 29.63 | 30.23 |
| | Fiberglass | 29.54 | 30.07 |
| 21±1°C | Invar | 29.68 | 30.33 |
| | Fiberglass | 29.29 | 30.80 |

## 3.4. OBSERVATION PROCEDURE

For each temperature regime and measurement configuration, 10 independent measurement repetitions were performed. During every repetition, 10 individual readings were taken on each levelling staff, after which the arithmetic mean value was adopted as the representative backsight or foresight reading. In order to reduce the possible influence of systematic errors related to instrument positioning, the instrument height was slightly changed between successive repetitions.
The application of multiple readings within a single repetition is consistent with procedures commonly used in investigations of digital levelling precision, as it reduces the influence of random observational errors [11]. For each repetition k, the height difference was determined using the expression:

$$\Delta h_k = \bar{r}_{B,k} - \bar{r}_{F,k}, \tag{1}$$

where $\bar{r}_{B,k}$ is the mean backsight reading and $\bar{r}_{F,k}$ is the mean foresight reading.
For each temperature condition and measurement geometry, the arithmetic mean of all 10 repetitions was subsequently calculated as:

$$\overline{\Delta h}=\frac{1}{n}\sum_{k=1}^{n}\Delta h_k, \tag{2}$$

together with the corresponding experimental standard deviation, following the statistical evaluation principles prescribed in ISO 17123-2 [8]. Based on the obtained mean height differences, the collimation angle was calculated using the following expression:

$$\Delta i=\frac{\Delta h'-\Delta h}{d_B-d_F}\rho'', \tag{3}$$

where $\Delta h$ is the height difference determined in the midpoint configuration (instrument positioned between the staffs), $\Delta h'$ is the height difference determined in the end configuration (instrument positioned near one of the staffs), $d_B$ and $d_F$ are the backsight and foresight distances and $\rho''=(\frac{180}{\pi})\cdot 3600$ - the value of 1 radian expressed in arcseconds.

To evaluate the repeatability and dispersion of the obtained results, the experimental standard deviation was calculated according to the following expression:

$$\sigma=\sqrt{\frac{\sum_{i=1}^{n}(\Delta h_i-\overline{\Delta h})^2}{n-1}}, n=10. \tag{4}$$

## 4. RESULTS AND DISCUSSION

The collimation angle Δi was determined for two temperature regimes and two levelling staff types using the procedure described in Section 3. The results are presented in arcseconds as arithmetic mean values of all measurement repetitions, together with the corresponding standard deviations.

### 4.1. FIRST TEMPERATURE REGIME

The results obtained under low-temperature conditions (1±1°C) indicate relatively stable and consistent values of the collimation error for both staff types and measurement configurations. All calculated Δi values were negative and ranged from -2.48″ to -3.95″, while the corresponding standard deviations varied between 0.41″ and 0.51″, demonstrating good repeatability of the observations.

A comparison of the two staff materials shows that the fiberglass staffs consistently produced larger absolute values of Δi than the invar staffs. The differences ranged from approximately 0.7″ to 1.5″ and may be associated with the lower dimensional stability of fiberglass materials. However, considering the magnitude of the standard deviations, these differences remain relatively small and do not indicate a strong material-dependent effect under low-temperature conditions.

Small differences were also observed between the two levelling configurations. Although these differences were not substantial, they confirm that the estimated value of the collimation error remains sensitive to measurement geometry, even under relatively stable environmental conditions. This behaviour is consistent with the theoretical principles of geometric levelling, according to which the influence of collimation error increases with unequal sight lengths.

The results obtained under the first temperature regime are summarized in Table 4.

*Tab. 4 Results for the first temperature regime*

| Temp. | Staff material | Levelling configuration | Approximate sight length | | Collimation angle $\overline{\Delta i}[”]$ | Standard deviation $\sigma_i[”]$ |
|---|---|---|---|---|---|---|
| | | | Foresight, $d_F$ [m] | Backsight, $d_B$ [m] | | |
| 1±1°C | Invar | End near the foresight staff | 2.35 | 57.48 | -2.92 | 0.41 |
| | | End near the backsight staff | 57.08 | 2.72 | -2.48 | 0.44 |
| | Fiberglass | End near the foresight staff | 2.54 | 57.07 | -3.59 | 0.44 |
| | | End near the backsight staff | 56.97 | 2.65 | -3.95 | 0.51 |

## 4.2. SECOND TEMPERATURE REGIME

The results obtained under moderate-temperature conditions (21±1°C) show considerably larger values of the collimation error compared to those obtained at low temperatures. For both staff materials and measurement configurations, the calculated Δi values ranged from 8.78″ to 11.10″. Compared with the first temperature regime, the average magnitude of the collimation error increased by approximately 12-14 arcseconds, changing from negative to positive values. However, since the two temperature regimes were also associated with different measurement environments (outdoor and indoor conditions), the observed differences cannot be attributed exclusively to temperature.

The corresponding standard deviations were also significantly higher, ranging from 0.90″ to 1.65″. This increase in dispersion suggests reduced measurement stability and greater variability of the observations under moderate-temperature conditions. Such behaviour may be associated with environmental effects acting simultaneously on the instrument, levelling staffs, tripod, and surrounding atmosphere.

Similar to the low-temperature measurements, the fiberglass staffs generally produced slightly larger values of Δi than the invar staffs. Nevertheless, the differences between the two staff materials remained considerably smaller than the differences observed between the two measurement regimes. This indicates that the change in environmental conditions between the two experimental regimes had a substantially greater effect on the determined collimation error than the change in staff material. Because temperature and measurement environment varied simultaneously, their individual contributions cannot be separated based on the present experimental design.

The observed increase in both the magnitude and variability of Δi is consistent with previous investigations that reported temperature-dependent changes in the line-of-sight stability of the Leica DNA03 digital level [9,10].

The results obtained under the second temperature regime are summarized in Table 5.

*Tab. 5 Results for the second temperature regime*

| Temp. | Staff material | Levelling configuration | Approximate sight length | | Collimation angle $\overline{\Delta i}[”]$ | Standard deviation $\sigma_i[”]$ |
|---|---|---|---|---|---|---|
| | | | Foresight, $d_F$ [m] | Backsight, $d_B$ [m] | | |
| 21±1° C | Invar | End near the foresight staff | 2.07 | 57.96 | 10.94 | 1.65 |
| | | End near the backsight staff | 57.95 | 2.03 | 8.78 | 1.30 |
| | Fiberglass | End near the foresight staff | 2.33 | 57.72 | 11.10 | 1.18 |
| | | End near the backsight staff | 57.65 | 2.45 | 9.98 | 0.90 |

Table 6 provides a direct comparison of the average collimation angle values obtained under the two investigated measurement regimes. For both staff types, a clear shift from negative values at 1°C to positive values at 21°C can be observed, resulting in differences of 12.56″ for the invar staff and 14.31″ for the fiberglass staff. In contrast, the differences associated with staff material within the same regime were relatively small. However, since temperature and measurement environment varied simultaneously, the observed changes cannot be attributed exclusively to temperature.

*Tab. 6 Average collimation angle for the two measurement regimes and both staff types*

| Staff type | Δi at 1°C | Δi at 21°C | Difference |
|---|---|---|---|
| Invar | -2.70" | 9.86" | 12.56" |
| Fiberglass | -3.77" | 10.54" | 14.31" |

These findings indicate that environmental conditions should be carefully considered when evaluating the stability of the collimation angle in precise levelling applications.

## 5. CONCLUSION

The experimental investigation revealed considerable differences in the magnitude and stability of the collimation error of the Leica DNA03 digital level between the two measurement regimes. Low-temperature outdoor conditions (1±1°C) yielded small, stable Δi values with low standard deviations, while moderate-temperature indoor conditions (21±1°C) produced substantially larger collimation errors and greater variability. These differences between regimes (exceeding 12″ on average) were considerably greater than those attributable to staff material (generally within 1.5″), with fiberglass staffs consistently producing slightly larger Δi values, consistent with their lower dimensional stability. Since temperature and measurement environment changed simultaneously, their individual effects cannot be separated, and the observed differences should be interpreted as a combined response to the differing environmental

conditions rather than to temperature alone. The experiment also confirmed the influence of measurement geometry, with collimation error increasing under unequal sight lengths, consistent with the theoretical principles of geometric levelling.
These results highlight the need to consider environmental conditions, staff material, and observation geometry in precise levelling, and to perform regular instrument testing and acclimatization. As only two temperature levels and one instrument were tested, no functional temperature-error relationship could be established; future work should cover a broader temperature range under comparable environments and additional instrument types.
In practice, the collimation angle should be checked before each levelling campaign, after transport, and after substantial changes in ambient conditions, particularly when moving between indoor and outdoor environments. Ambient temperature, acclimatization time (approximately 30 min in this study), and staff material should be systematically recorded in the field protocol, together with maintaining approximately equal backsight and foresight distances to minimize residual collimation error.

## ACKNOWLEDGEMENT

The research has been conducted within the project "Enhancement of teaching and scientific research capacities through the application of modern technologies in the fields of civil engineering, geodesy, and disaster risk management and fire safety", developed at the Department of Civil Engineering and Geodesy, Faculty of Technical Sciences, University of Novi Sad, Serbia.

## REFERENCES

[1] Schofield W. (2001). *Engineering Surveying* (5th edition), Butterworth-Heinemann.

[2] Mrkić R. (1991). *Geodetska metrologija*, Naučna knjiga, Beograd.

[3] Rekus D., Kriaučiūnaitė-Neklejonovienė V. (2017). *Peculiarities of Digital Levelling Using Automatic Digital Levels in Civil Engineering Technologies*, Journal of Sustainable Architecture and Civil Engineering, p. 81-86, http://dx.doi.org/10.5755/j01.sace.18.1.17099

[4] Ingensand H. (1999). *The Evolution of Digital Levelling Techniques - Limitations and New Solutions*, FIG, Gävle, Sweden.

[5] Tuno N., Kogoj D. (2012). *Prošlost, sadašnjost i budućnost preciznih optičkih nivelira*. Geodetski glasnik, (43), 21-38.

[6] Leica Geosystems. (2006). *Leica DNA03/DNA10 User Manual*, Leica Geosystems AG, Heerbrugg, Switzerland.

[7] Leica Geosystems. (2023). *Original Accessories Material matters*, Catalog, Leica Geosystems AG, Heerbrugg, Switzerland.

[8] SRPS ISO 17123-2, Optics and optical instruments-Field procedures for testing geodetic and surveying instruments -Part 2: Levels. Serbian Institute for Standardization, Belgrade.

[9] Gučević J., Miljković S., Delčev S., Ogrizović V. (2017). *Effects of Low Temperatures in the Line of Sight of Digital Levels*. J. Surv. Eng. 143(2).

[10] Gučević J., Delčev S., Ogrizović V. (2011). *Determining Temperature Dependence of Collimation Error of Digital Level Leica DNA 03*. Eng. Surv.

[11] Delčev S. (2025). *Errors in Measuring Height Differences in Engineering*, Tehnički vjesnik 32, 2(2025), 775-784, https://doi.org/10.17559/TV-20240707001833

[12] Mazić E., Tuno N., Savšek S., Kogoj D. (2013). *Optimal Sighting Distance of a Leica Geo-Systems DNA03 Digital Level*, Geodetski Vestnik. 57/2. 233-244. UDK: 528.54.001.5

[13] Frukacz M. (2012). The Optimum Procedures of Determining the Coefficient of Linear Thermal Expansion and Calibration of Precise Leveling Rods, FIG, Rome, Italy.

[14] Vestøl O., Eriksson P-O., Jepsen C., Keller K., Mäkinen J., Saaranen V., Valsson G., Hoftuft O. (2014). *Review of current and near-future levelling technology*, Lantmäterirapport, Gävle, Sweden.

[15] Ivanov I. D. (2025). *Errors When Using Telescopic Survey Staff in Geometric Levelling*, Journal scientific and applied research, vol. 29.

[16] JCGM 100:2008 (2008). *Evaluation of measurement data — Guide to the expression of uncertainty in measurement (GUM)*, Joint Committee for Guides in Metrology.

[17] JCGM GUM-1:2023 (2023). *Guide to the expression of uncertainty in measurement - Part 1: Introduction*, Joint Committee for Guides in Metrology.

https://doi.org/10.24867/INDIS-2026-EN-922



# COMPARATIVE ACCURACY ANALYSIS OF A MOBILE SLAM SYSTEM AND TERRESTRIAL LASER SCANNING TECHNOLOGY: A MUSEUM CASE STUDY

*Đuro Krnić[1], Miro Govedarica[2], Mehmed Batilović[3], Andrija Kljajić[4], Marko Marković[5]*

***Summary:***

The paper performs a comparative accuracy analysis of terrestrial laser scanning (TLS) technology and a mobile SLAM system on the example of a museum building. The TLS point cloud was used as the reference dataset, while the SLAM point cloud was analysed as the test dataset. Both datasets were georeferenced into the same coordinate system. The accuracy assessment was conducted on four test areas. The analysis was based on Cloud-to-Cloud (C2C) comparison and supplemented by profiles obtained from point cloud. The results of the C2C indicate that the smallest deviations were obtained in the room, with an RMSE of 0.7 cm, while the largest deviations were recorded in the basement, with an RMSE of 3.3 cm. The profile-based analysis indicated deviations approximately less than 1.0 cm. The results indicate that, in selected profiles, the test SLAM system achieved millimetre-order agreement with the TLS reference system.

*Keywords: SLAM, TLS, accuracy analysis, point cloud, C2C analysis*

# UPOREDNA ANALIZA TAČNOSTI MOBILNOG SLAM SISTEMA I TEHNOLOGIJE TERESTIČKOG LASERSKOG SKENIRANJA NA PRIMERU MUZEJA

***Rezime:***

U radu je izvršena uporedna analiza tačnosti tehnologije terestričkog laserskog skeniranja (TLS) i mobilnog SLAM sistema na primeru objekta muzeja. TLS oblak tačaka korišćen je kao referentan, dok je SLAM oblak tačaka analiziran kao testiran skup podataka. Oba skupa podataka su georeferencirana u isti koordinatni sistem. Ocena tačnosti sprovedena je na četiri test celine. Analiza tačnosti zasnovana je na Cloud-to-Cloud (C2C) poređenju i dopunjena je korišćenjem profila koji su dobijeni iz preseka oblaka tačaka. Rezultati C2C analize ukazuju da su najmanja odstupanja dobijena u sobi sa RMSE od 0.7 cm, dok su najveća odstupanja u podrumu sa RMSE od 3.3 cm. Rezultati analize zasnovane na profilima ukazali su na odstupanja približno ispod 1.0 cm. Rezultati ukazuju da ispitivani SLAM sistem na određenim profilima ostvaruje milimetarsku tačnost u odnosu na TLS referentni sistem.

*Ključne reči: SLAM, TLS, analiza tačnosti, oblak tačaka, C2C analiza*

[1] Teaching assistant, MSc, Faculty of Technical Sciences, University of Novi Sad, Novi Sad, Serbia, e-mail: djuro.geo@uns.ac.rs, ORCID 0000-0003-4481-3209
[2] Full professor, PhD, Faculty of Technical Sciences, University of Novi Sad, Novi Sad, Serbia, e-mail: miro@uns.ac.rs, ORCID 0000-0003-1698-0800
[3] Associate Professor, PhD, Faculty of Technical Sciences, University of Novi Sad, Novi Sad, Serbia, e-mail: mehmed@uns.ac.rs, ORCID 0000-0001-5605-1112
[4] Engineer, MSc, Geodetski biro Kljajic - GBK, Užice, Serbia, gbk@gbk.rs
[5] Associate Professor, PhD, Faculty of Technical Sciences, University of Novi Sad, Novi Sad, Serbia, e-mail: marko_m@uns.ac.rs, ORCID 0000-0003-3666-6325

## 1. INTRODUCTION

Contemporary geodetic and engineering practice increasingly relies on laser scanning technologies (LST). LST enables rapid, contactless and detailed data acquisition of objects and their surrounding environment [1-2]. This type of technology provides the determination of 3D coordinates of a large number of acquired points, which represent a geometric approximation of real-world entities. The LST result is a point cloud used for further analysis. A point cloud can be used for metric analysis, preparation of technical documentation of the existing condition, change monitoring, creation of 3D models and various forms of spatial analysis [3-7]. Due to the aforementioned aspects, such data are today of great importance in geodesy, geoinformatics, civil engineering, architecture, cultural heritage preservation, and many other fields where spatial data are used.

Among laser scanning methods, TLS represents the standard for high accuracy, high point density, and high detail. TLS enables the acquisition of spatial information independently of lighting conditions, which makes it particularly suitable for the production of floor-plan sections, quality control, deformation monitoring and the creation of 3D models [1, 8]. Owing to these characteristics, TLS is used in a large number of studies as the ground truth against which the accuracy of other mapping systems is assessed [9-10]. The main limitations of TLS are reflected in its static operating principle, the need for more scan stations, longer data acquisition and processing times, and higher costs, especially in complex and extensive environments.

The need for faster and more operationally efficient methods of spatial data acquisition has contributed to the development of mobile systems based on the Simultaneous Localization and Mapping (SLAM) algorithm. SLAM devices were initially developed for robotics applications, and numerous studies have used different approaches to solving this problem [11-14]. The SLAM algorithm simultaneously estimates sensor position and reconstructs the surrounding environment. The concept of the SLAM approach is that the sensor location is estimated simultaneously with the environment map, enabling mobile mapping even when GNSS signals are unavailable or unreliable [10]. In geodesy, SLAM systems are particularly relevant because they enable users to collect spatial data in the form of a point cloud in real time as they move through space. Due to their compactness, ease of use, and productivity, these systems have proven particularly suitable for indoor spaces, industrial facilities, narrow and inaccessible areas, and other complex scenarios where TLS would be slower or more operationally demanding.

However, the higher efficiency and mobility of SLAM systems often come with limitations in the accuracy and quality of point clouds. The literature indicates that SLAM devices can provide centimetre-level accuracy and a significantly shorter acquisition time, but they also often produce lower point density, higher noise levels, and lower detail compared with TLS. The quality of the results is additionally influenced by the geometry of the space, the presence or absence of characteristic features, trajectory planning, the possibility of loop closure, and the occurrence of drift error along the trajectory [2, 10]. Closed-loop trajectories are considered one of the basic recommendations for achieving more accurate results when using SLAM algorithms [10,15]. Errors are particularly pronounced in long corridors, spiral staircases and other complex scenes with lower lighting and irregular surfaces. These phenomena can lead to local deformations, loss of detail or reduced reliability of geometric interpretation. Therefore, contemporary research emphasizes the need for a multi-criteria assessment of the quality of SLAM data, which includes not only global accuracy but also local geometric fidelity, noise, and point cloud density.

The comparison of TLS and SLAM systems has both theoretical and practical significance. On the one hand, it enables the limits of applicability of mobile systems to be considered alongside those of static systems. On the other hand, such an analysis provides a basis for selecting the appropriate technology depending on the required level of accuracy, time constraints, the complexity of the object and the intended use of the final product. It is important to examine in which parts of the object SLAM systems provide satisfactory results, and in which segments more pronounced deviations, reduced density or degradation of geometric content occur. In previous studies, TLS has most often been used as the reference point cloud for the assessment of SLAM data through C2C comparison analyses, density analyses, characteristic profiles, and other quality metrics [1, 16, 17].
The aim of this paper is to perform a comparative analysis of TLS and SLAM systems on the example of a museum building, where the TLS point cloud is treated as the reference dataset and the SLAM point cloud as the test dataset. The analysis focuses on assessing the accuracy of the object's geometric characteristics and the ability of both technologies to faithfully represent its spatial and structural elements.

## 2. RELATED WORK

Contemporary studies comparing TLS and SLAM systems are largely focused on examining the relationship between metric reliability, acquisition speed, and suitability for different types of spaces and geometries. Within this framework, the study by Yiğit et al., with a focus on practical application in indoor mapping, compares the TLS method and the wearable mobile laser scanning (WMLS) approach based on the SLAM algorithm. The authors propose a new indoor mapping strategy using a WMLS system as an alternative to TLS. They use four test sections representing a corridor, rooms connected by a corridor, a staircase and a combined indoor/outdoor environment. The authors conclude that the proposed WMLS approach can represent an alternative to TLS in terms of accuracy, with a pronounced time advantage in acquisition. The structure of narrower, more confined spaces shows that results are influenced by scene geometry, reflective surfaces, path complexity, and the presence of vertical changes [1].
Similarly, the study by Szrek et al. compares the TLS method with a SLAM system in the context of 3D reconstruction of objects with different geometric characteristics, including a facade, pillars, a lamp, and a tree. The authors analyse the technical characteristics of the sensors, processing methods, measurement time and cost, and the final accuracy. The approach to solving the problem is considered not only from the aspect of geometric fidelity, but also from the standpoint of practical applicability. The largest deviations were recorded for the facade and pillars, on the order of approximately 7-9 cm, while for the lamp, the deviations were less than 4 cm, and the overall RMSE of the comparison of corresponding dimensions was 5 cm. Based on the results, the authors conclude that SLAM can be successfully used in tasks where centimetre-level accuracy is sufficient, while TLS remains more suitable for objects requiring high accuracy and a high level of detail [2].
The study by Chrbolková et al. compares static and SLAM systems of different generations in a controlled indoor environment. The environment consists of long, straight corridors and recesses, where global, local, and noise-influenced accuracy are assessed. The authors use a reference point cloud obtained by the TLS method and examine five devices: two static scanners, Leica RTC 360 and Trimble X7, and three SLAM systems, GeoSLAM ZEB Horizon RT, Emesent Hovermap ST-X and FARO Orbis. The results show that static scanners retain the highest accuracy, with the Leica RTC360 achieving an overall RMSE of 1.2 mm and the Trimble X7 5.4 mm. The newer

SLAM systems, Emesent Hovermap ST-X and FARO Orbis, achieve RMSE values of 7.3 mm and 8.8 mm, respectively, which represent a significant improvement over the older GeoSLAM ZEB Horizon RT, which has an RMSE of 36.2 mm. Based on the results, the authors conclude that contemporary SLAM systems are approaching the accuracy of static systems, suggesting they can be used for indoor mapping when slightly lower accuracy is acceptable [16].

In the study by Lehtola et al., the focus is not only on comparing several contemporary indoor scanning systems but also on the problem of rigorous point cloud assessment. The authors assume that previous evaluations often rely on manually extracted point subsets and predefined scales, and propose metrics to assess point cloud quality. The metrics evaluate the entire point cloud across all linear scales and can indicate problems such as outliers, over-completeness, and misregistration. The authors compare five commercial indoor mapping systems: Matterport, NavVis, Zebedee, Stencil and Leica Pegasus Backpack, as well as three research systems: Aalto VILMA, FGI Slammer and the Würzburg backpack. The research is conducted at three test sites, and a point cloud obtained by TLS is used as the reference cloud. The results show that the proposed full-point-cloud approach provides a more robust basis for quality assessment than classical methods based on control points or extracted surfaces. According to the short-scale ranking, the best result is achieved by FGI Slammer, followed by Zebedee and NavVis. In individual systems, problems such as outliers in the Würzburg backpack and a double-floor artifact in Stencil were observed. In this way, the authors show that point cloud quality assessment is not expressed solely by accuracy, but also by behaviour across different scales and sensitivity to specific types of errors [17].

## 3. METHODOLOGY

The aim of the methodology is to assess the accuracy and geometric reliability of the SLAM point cloud in relation to the TLS point cloud, using the museum in Sirogojno as a case study. The TLS point cloud is treated as the reference dataset, while the SLAM point cloud is treated as the test dataset. The methodological workflow of the research is shown in Figure 1 and includes all steps up to the interpretation of the results.

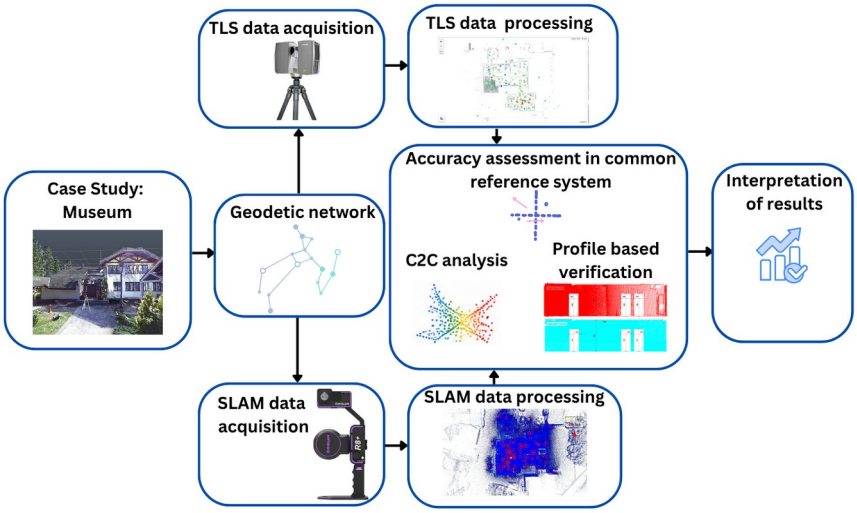


*Figure 1. Methodological workflow for the comparative accuracy assessment*

### 3.1. CASE STUDY

The research was conducted on the museum building in Sirogojno, which was selected as a representative example (Figure 2). The museum is a geometrically complex object

and is therefore suitable for comparative analysis. The building comprises different spatial areas that differ from one another in shape, dimensions and size, with the presence of narrow passages, multiple levels and inaccessible parts.



*Figure 2. Case study object: museum building in Sirogojno*

For the purposes of this research, the areas were analysed according to the type of space and the expected complexity of geometric interpretation. The main test areas were identified as a regular room, a corridor, a staircase and a basement with the TLS station positions also shown for each test area (Figure 3). The TLS station positions shown in Figure 3 indicate that, in certain parts of the test areas, TLS coverage was locally limited by scanner visibility and station distribution. Therefore, some zones captured by the SLAM system were not equally represented in the TLS point cloud or were partially missing.

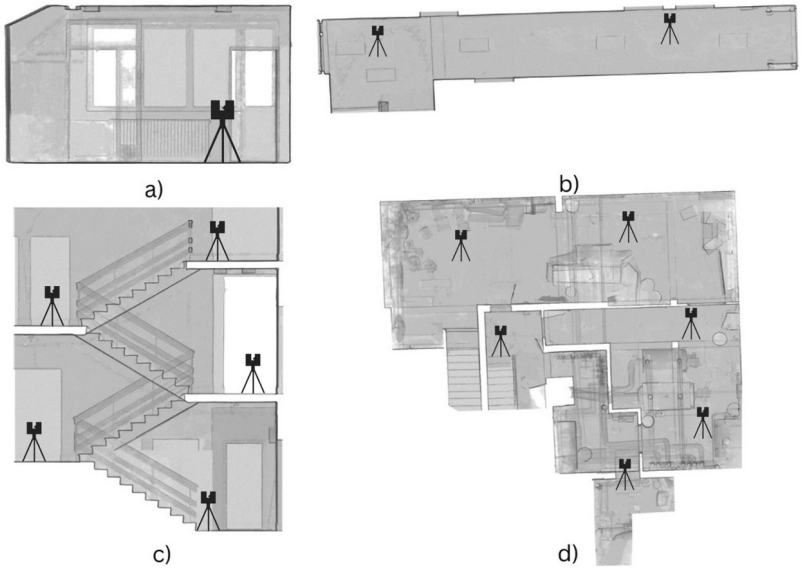


*Figure 3. Test areas used for comparisons with TLS station positions: a) room, b) corridor, c) staircase and d) basement*

The cross-sections of characteristic elements of the building were presented as a supplementary analysis. This division is based on the assumption that different types of space produce different levels of challenge for the SLAM algorithm and for the representation of geometry in the point cloud itself. Regular rooms are suitable for assessing the behaviour of the system under stable and clear conditions. Corridors

enable the analysis of behaviour in long and repetitive parts of the space. Staircases represent a complex case due to the presence of abrupt height changes, pronounced edges and a combination of horizontal and vertical elements. In this paper, the basement is the most spatially complex part of the building in terms of limited visibility, irregular geometry, and the presence of numerous installations and obstacles

## 3.2. INSTRUMENTS AND DATA ACQUISITION

For the purposes of the research, the Trimble TX5 terrestrial scanner and the OmniSLAM R8+ mobile SLAM system were used (Figure 4).




*Figure 4. OmniSLAM R8+ (left) and Trimble TX5 (right)*

The instrument specifications are given in Table 1.

*Table 1. Technical specification of the used laser scanners*

| Parameter | SLAM [18] | TLS [19] |
|---|---|---|
| Laser scanner | OmniSLAM R8+ | Trimble TX5 |
| Operating principle | LiDAR+SLAM+GNSS/IMU | Phase shift |
| Scanning mode | Handheld/backpack/vehicle-mounted | Static terrestrial laser scanning |
| Max. detection range | 0.05-120 m | 0.6-120 m |
| Point rate | 640,000 points/s (up to 3 returns) | 976,000 points/s |
| Range precision | Relative accuracy: 2 mm | ±2 mm at 10 m |
| Field of view (horizontal × vertical) | 360° × 280° | 360° × 300° |
| Weight (without equipment) | 2.1 kg | 5.0 kg |
| Battery life | Approx. 3 h (2 batteries) | Up to 5 h |

## 3.3. GEODETIC NETWORK

For the purposes of the comparative analysis, a geodetic network was established, as the reference framework for georeferencing both datasets. The geodetic network was developed both around the building itself and inside it for all test areas, within a single

coordinate system. The geodetic network is used to determine the positions of spherical targets used for TLS scan registration and the ground control point (GCP) markers used for SLAM point cloud georeferencing.

The network was established using integrated approach method, combining a Trimble S9 HP robotic total station and a Trimble R8s GNSS receiver. The Trimble S9 HP total station used is intended for engineering surveying and provides an angular accuracy of 1″ and distance measurement accuracy of 0.8 mm + 1 ppm when measuring to a prism, and 3.0 mm + 2 ppm in reflectorless mode.

The initial station was determined by resection from four reference points, while the remaining points were established using the forced centering method. The forced centering procedure was applied using fixed tripods and tribrachs, where only the total station and prisms were exchanged between predefined positions. This approach minimizes centering errors of both the instrument and targets and improves the internal consistency of the control network. In addition, the use of the Trimble traverse setup enabled a zero-height workflow, since the optical center of the total station and the prism center are positioned at the same height relative to the tribrach base. This removed the need for manual instrument and target height measurements and reduced potential vertical errors.

For TLS registration, spherical targets were observed with the total station using a sphere target, whose center coincides with the center of the sphere. This enabled the registered TLS scans to be referenced to the established coordinate system. For SLAM processing, GCP markers were observed from the same geodetic network using a mini-prism, with special attention paid to the correct prism orientation during measurement (Figure 5). In this way, both datasets were linked to the same reference framework, ensuring that subsequent differences between the TLS and SLAM point clouds could be interpreted within the same coordinate system.




*Figure 5. Sphere target (left) and GCP marker (right)*

## 3.4. DATA PROCESSING

The processing of TLS and SLAM data was carried out separately, using software tools adapted to the instruments used and to the method of data acquisition. The registration of the point clouds obtained by the TLS method was performed in the FaroSCENE software. Within the TLS data acquisition, a total of 47 scan stations were used, and approximately 503.9 million points were collected. The scan registration was performed using 94 spherical targets with a mean registration error of 2.5 mm. The total time of

TLS data acquisition was 6.5 h. After the registration was completed, the reference TLS point cloud was obtained.
The SLAM data were processed in the OmniSLAM Mapper software. The final SLAM point cloud contained approximately 449.9 million points. A total of 88 control points were used during processing, while the total SLAM data acquisition time was 46 min 50 s. According to the GCP accuracy report, the 3D residual for the control points is 2.7 mm. Data acquisition using SLAM is approximately 8.3 times faster than acquisition using TLS, which reduced field data acquisition time by approximately 88%.
Before the comparative analysis itself, both point clouds were verified (Figure 6). Moving objects were removed, and only the actual overlap area between the TLS and SLAM point clouds was extracted. After basic processing, the TLS and SLAM data were georeferenced into the same reference coordinate system. The TLS acquisition was conducted in January 2025, while the SLAM acquisition was conducted in November 2025. Therefore, the two datasets were acquired approximately 10 months apart, which was considered when interpreting the comparative results.




*Figure 6. Point clouds: Trimble TX5 (above) and OmniSLAM R8+ (below)*

## 3.5. ACCURACY ANALYSIS

The accuracy analysis in this paper is based on the comparison of TLS and SLAM point clouds, where the TLS point cloud represents the reference dataset. The primary objective of this approach is to assess the fidelity of the mobile SLAM system in defining object geometry relative to the high-precision TLS method.
The basic accuracy analysis was carried out using C2C analysis to assess the agreement between the two datasets. The analysis was conducted in CloudCompare software. For each test area, the mean distance, standard deviation, RMSE, and a deviation color map are presented. The computed distances represent absolute nearest-neighbour distances between the two datasets. Therefore, the obtained values describe the geometric agreement between the point clouds and not exclusively the instrumental accuracy of the SLAM system.
It should be particularly emphasized that the TLS and SLAM data acquisitions were not performed in the same time period, which represents an important indicator in the interpretation of the results. The result of the C2C analysis can also be affected by the local absence of a point cloud in one of the applied methods. In other words, if a certain

detail or part of the scene was not equally well captured by the TLS or SLAM method, the obtained C2C deviations may show results affected by errors related to coverage, density and completeness of the point clouds.
After the C2C comparison, the accuracy analysis is extended to the comparison of profiles from the point clouds from both technologies. It is particularly important that cross-sections can reveal phenomena such as wall thickening, edge rounding or the loss of small details.

## 4. RESULTS AND DISCUSSION

This chapter presents the results of the comparative analysis of the TLS and SLAM point clouds for the selected test areas. First, the results of the C2C analysis are presented, through which the basic accuracy analysis of both datasets was performed using basic statistical indicators and deviation color maps. After that, the supplementary profile analysis is presented, enabling a more detailed interpretation of geometric differences on the characteristic elements of the object.

### 4.1. C2C ANALYSIS

The basic assessment of the agreement between the TLS and SLAM point clouds was carried out using C2C analysis. The analysis was performed for four test areas: room, the corridor, the staircase and the basement. For each area, statistical indicators of deviations were calculated, such as the mean deviation, standard deviation and RMSE. In addition to this analysis, color maps of absolute C2C deviations were also generated for each test area, showing the assessment of deviations between the two datasets. The statistical data are presented in Table 2.

*Table 2. C2C analysis report for the test area*

| ID | Scene | Mean distance [cm] | Std deviation [cm] | RMSE [cm] |
|---|---|---|---|---|
| 1 | Room | 0.6 | 0.4 | 0.7 |
| 2 | Corridor | 0.4 | 0.9 | 1.0 |
| 3 | Staircase | 0.4 | 1.8 | 1.9 |
| 4 | Basement | 0.8 | 3.2 | 3.3 |

Although the main focus of this study was the geometric accuracy of the SLAM point cloud relative to the TLS reference point cloud, the density and completeness of the point cloud should also be considered when interpreting the C2C results. These aspects are not analyzed as separate quantitative parameters in this work, but they directly affect the reliability of the comparison. The final density of the point cloud depends on the data acquisition, distance from the object, angle of incidence, scan path, overlap, occlusion, and data processing. Since registration residuals were below 3 mm for both datasets, their influence on centimetre-level C2C discrepancies is considered negligible.
In TLS acquisition, the point density is mainly affected by the scan resolution, distance from the scanner, number and arrangement of scan stations, scan overlap, and local visibility conditions. In this study, the average point density of the TLS point cloud was 62,691 pts/m². In SLAM acquisition, the effective density is influenced by acquisition speed, path length, number of passes over the same area, sensor orientation, and the distance between the sensor and the scanned surfaces, resulting in an average point density of 97,608 pts/m². The higher overall density of the SLAM point cloud relative to the TLS reference is a consequence of the continuous mobile acquisition trajectory and

the closer average sensor-to-surface distances during data collectionFiltering, cleaning, cropping, and possible downsampling during data processing can also alter the final density and completeness of both datasets.

Therefore, in this study, increased C2C deviations in geometrically complex areas cannot be attributed to a deficiency in SLAM point density but rather reflect the geometric accuracy characteristics of the SLAM algorithm itself, particularly in areas with sharp edges, installations, narrow passages, or partially hidden surfaces. In this study, this effect is particularly relevant in basements and stairwells, where obstacles, irregular geometry, and limited visibility reduce the homogeneity and completeness of point clouds.

For the room test area, the obtained results show a mean deviation of 0.6 cm, a standard deviation of 0.4 cm and an RMSE of 0.7 cm. The results indicate moderate agreement between the TLS and SLAM point clouds. The color representation is dominated by the lowest deviations, shown in dark blue (Figure 7). Increased deviations occur in areas where the point cloud is missing, along edges and in zones with weaker coverage.

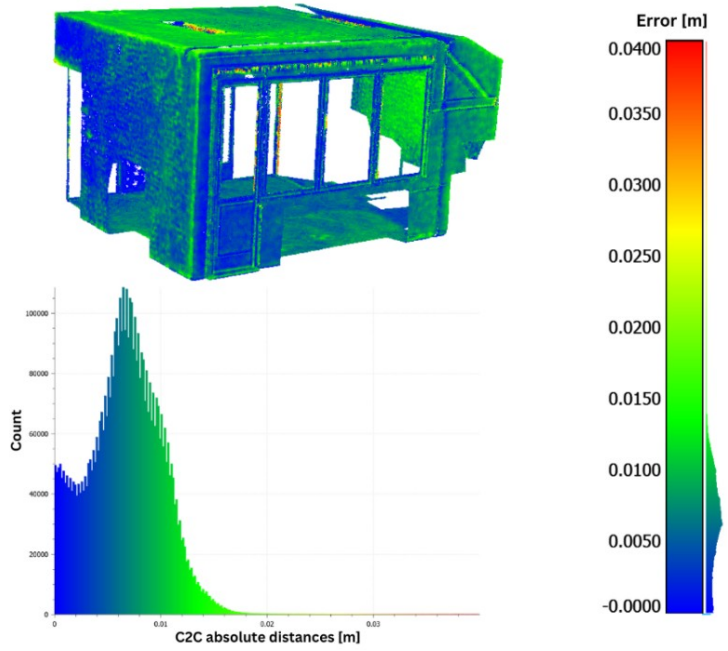


*Figure 7. C2C absolute distance map for the test area "room"*

The corridor showed high geometric agreement between the two datasets, remaining within a range comparable to the room result. The deviation values remained at a few millimeters to approximately one centimeter. On the deviation color map, the majority of the area is shown in dark blue tones, which confirms very good alignment between the two point clouds (Figure 8). Local increases in deviations are observed mainly along the edge areas, at surface junctions, and in the zones of individual openings and geometry interruptions. The RMSE value for this test area is 1.0 cm.

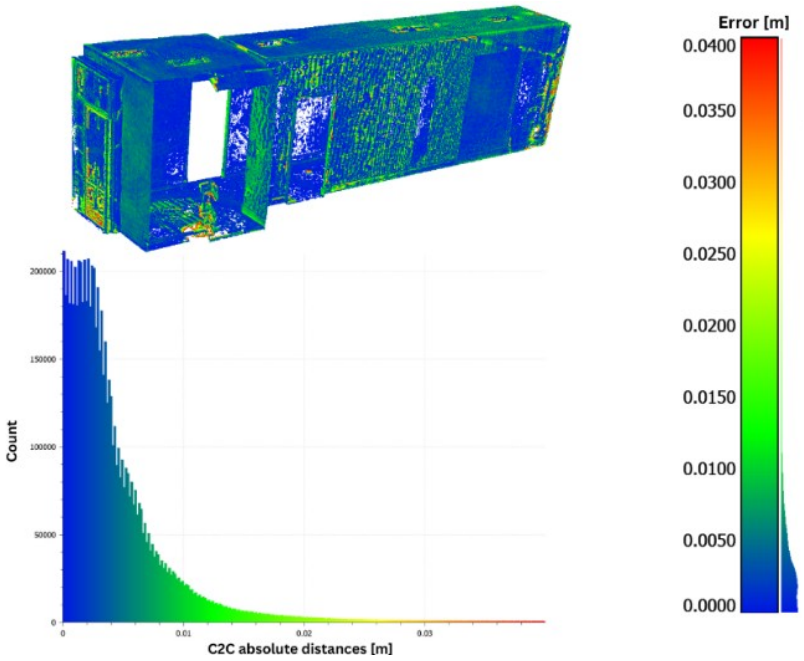


*Figure 8. C2C absolute distance map for the test area "corridor"*

The staircase showed very good agreement between the TLS and SLAM point clouds. The mean deviation is 0.4 cm, while the RMSE value is 1.9 cm. The color representation shows that the largest part of the area has minimal deviations, while larger deviations are more pronounced along the stair edges and in the locations where the scanner was positioned, i.e. where part of the point cloud acquired using TLS technology is missing (Figure 9). The deviations shown for the staircase are very important because this test area represents a spatially demanding geometric unit. The staircase contains abrupt height changes and a large number of sharp transitions. For this reason, larger local deviations are visible on individual parts of the steps and in the edge zones, shown in dark green. The RMSE values remained relatively low, indicating that the SLAM system managed to maintain satisfactory geometric stability in this area.

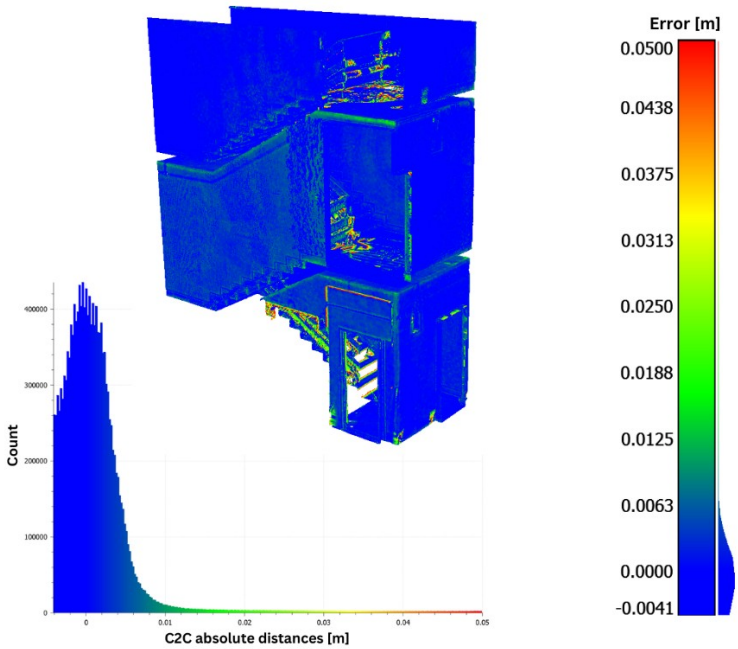


*Figure 9. C2C absolute distance map for the test area "staircase"*

The basement showed the weakest agreement within the C2C analysis. The mean deviation is 0.8 cm, the standard deviation is 3.2 cm, and the RMSE is as high as 3.3 cm. On the deviation color map, the distribution of increased values is clearly visible in the zone of installations, equipment and obstacles (Figure 10). In this paper, the basement represents the most spatially complex scene, with limited visibility, irregular geometry, a large number of occluded parts and locally reduced point cloud homogeneity. The interpretation of the results is also affected by the different time periods of data acquisition, as well as by the possibility that individual details were not equally well captured by both methods.

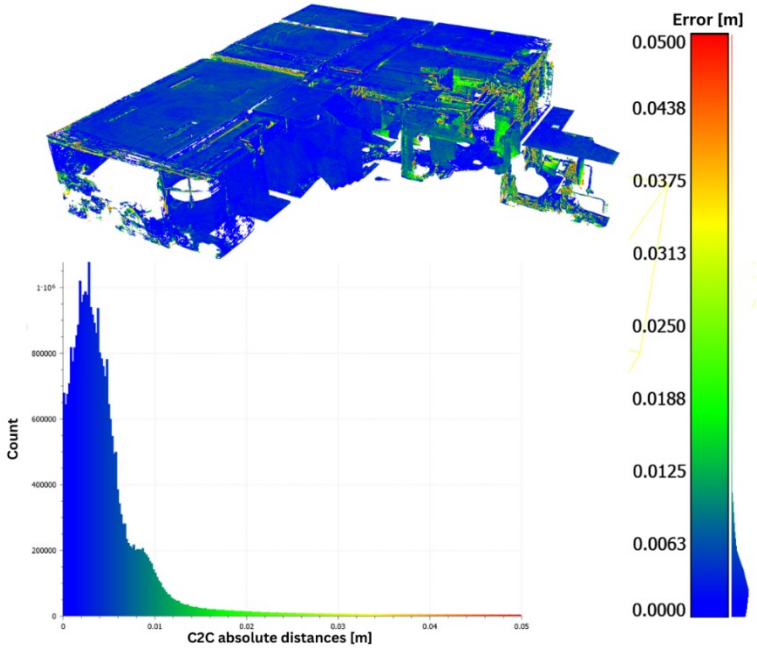


*Figure 10. C2C absolute distance map for the test area "basement"*

The best results were achieved in the room and corridor, as well as for the staircase, while the basement showed larger deviations. For the aforementioned reasons, the C2C deviation analysis is considered the basic analysis and is supplemented by the analysis of profiles obtained from point cloud sections.

## 4.2. PROFILE-BASED LOCAL ACCURACY ANALYSIS

In addition to the global C2C analysis, a supplementary local accuracy assessment was conducted using profiles extracted from both datasets. This step was introduced because cross-sections provide a more granular insight into actual geometric deviations than C2C maps alone. While C2C analysis is effective for identifying the overall spatial distribution of discrepancies, profile-based assessment makes it possible to directly observe geometric effects such as line thickening, edge displacement, local deformation and loss of sharpness.

Two characteristic sections were analyzed: a vertical profile of a first-floor window opening and a horizontal profile of the basement zone, encompassing both external and internal walls. In both cases, the TLS point cloud serves as the reference (shown in red), while the SLAM point cloud is the comparative dataset (shown in blue).

In the vertical window profile, very good agreement between the TLS and SLAM point clouds can be observed, with measured deviations on the order of a few millimetres. In Figure 11, differences of approximately 4.3 mm and 6.3 mm were measured in the upper parts of the section, and about 2.1 mm and 2.2 mm in the lower zone. In some parts, the point cloud obtained by the SLAM system indicates slight thickening and line

irregularity in relation to the TLS reference. The presented result is also consistent with other studies, where TLS profiles usually define edges more clearly, while SLAM profiles may show slight line thickening or reduced edge sharpness.

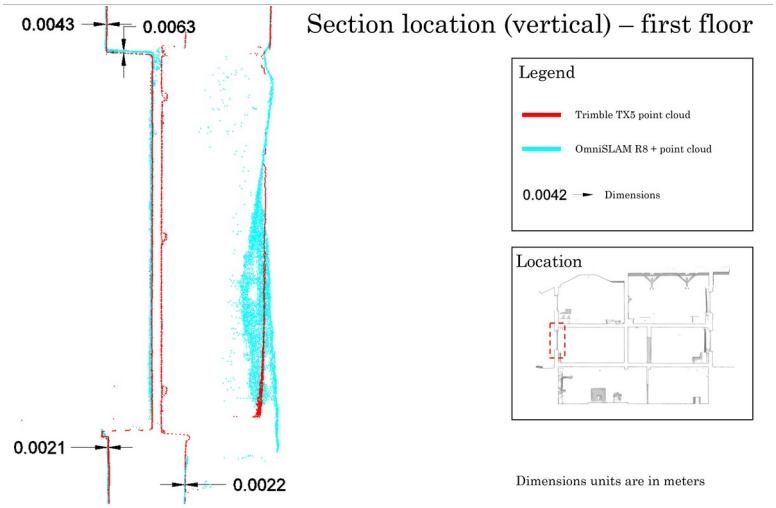


*Figure 11. Vertical profile comparison of the TLS and SLAM point clouds*

The second profile shows a horizontal section extracted in the basement zone. In the section of the external and internal wall, deviations of 3.2–7.2 mm were recorded. The result shown in Figure 12 indicates that, in the case of the SLAM system, the error is more pronounced in scenes with sharp corners and occluded parts of the scene, while better agreement with the TLS reference is achieved on regular and clearly defined elements.

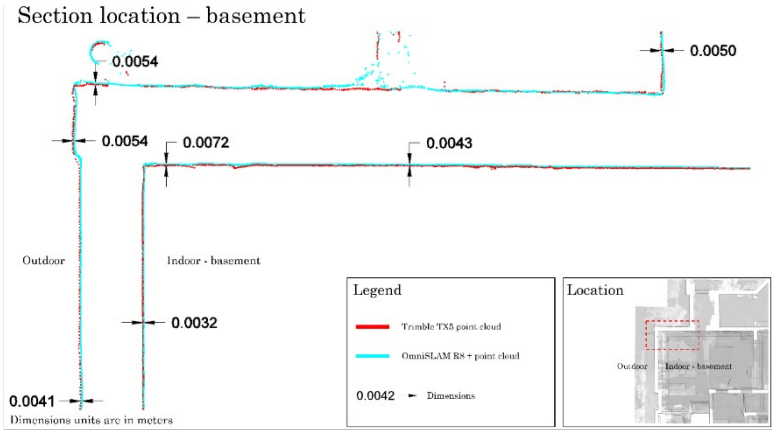


*Figure 12. Horizontal profile comparison of the TLS and SLAM point clouds*

Profile analysis enables a more detailed insight into the geometry of the object at individual structural elements. In this research, the local profiles show that the deviations on the analysed details generally remained within a range below one centimetre. In this way, it was confirmed that local profile analysis represents an important supplementary step in the interpretation of the accuracy analysis of TLS and SLAM point clouds.

## 5. CONCLUSION

In this paper, a comparative analysis of TLS and SLAM systems was carried out on the example of a museum building. The results of the C2C analysis showed that the level of agreement between TLS and SLAM data depends on the type of space and its geometric complexity. The best results were achieved in the room, where the obtained values were

a mean distance of 0.6 cm, a standard deviation of 0.4 cm and an RMSE of 0.7 cm. The basement showed the weakest agreement, with an RMSE value of 3.3 cm.
The supplementary analysis of local profiles confirmed the results of the C2C analysis. In the vertical cross-section through the window opening on the first floor, local deviations on the order of several millimetres were registered. On the other hand, the horizontal cross-section extracted in the basement showed more pronounced deviations, but the accuracy still remained on the order of up to 7.2 mm.
Based on the conducted research, the OmniSLAM R8+ system represents an acceptable alternative to the Trimble TX5 TLS system for as-built documentation of indoor museums, especially when acquisition speed, mobility, and operational efficiency are important requirements. The results indicate that the system can provide high geometric detail and satisfactory agreement with the TLS reference in the analyzed test areas and applications where centimeter-level accuracy is acceptable, while TLS remains preferable for applications requiring millimetre-level geometric fidelity.
For practical applications, using the OmniSLAM R8+ system in complex scenes should involve careful planning of closed-loop paths, a slower, more consistent walking speed, and careful scanning of critical areas. Special attention should be paid to important architectural details, corners, edges, and openings where slower movement can improve data acquisition and image capture for point cloud coloring. The results showed a slight rounding of sharp edges and corners in some parts of the SLAM point cloud, which should be taken into account when using the data for detailed geometric interpretation.
Overall, the results confirm that the choice between TLS and SLAM should not be based only on the nominal accuracy of the instruments, but also on the required level of detail, acquisition conditions, time constraints, and the intended use of the final product. In this context, OmniSLAM R8+ represents a practical and efficient solution for rapid indoor mapping, while additional caution is required in areas with limited visibility, irregular geometry, obstacles, and high geometric complexity.

## ACKNOWLEDGEMENT

The research has been conducted within the project "Enhancement of teaching and scientific research capacities through the application of modern technologies in the fields of civil engineering, geodesy, and disaster risk management and fire safety", developed at the Department of Civil Engineering and Geodesy, Faculty of Technical Sciences, University of Novi Sad, Serbia.

## REFERENCES

[1] Yiğit A. Y., Hamal S. N. G., Ulvi A., Yakar M. (2024). Comparative analysis of mobile laser scanning and terrestrial laser scanning for the indoor mapping. Building Research & Information, Volume 52, Issue 4, pp. 402–417. https://doi.org/10.1080/09613218.2023.2227900.
[2] Szrek A., Romańczukiewicz K., Kujawa P., Trybała P. (2024). Comparison of TLS and SLAM technologies for 3D reconstruction of objects with different geometries. IOP Conference Series: Earth and Environmental Science, Volume 1295, Issue 1, Article 012012. https://doi.org/10.1088/1755-1315/1295/1/012012.
[3] Vujinović M., Krnić Đ., Batilović M., Bulatović V., Sušić Z. (2023). Application of terrestrial laser scanning technology in the procedure of creating as-built projects of objects. Proceedings of the 16th International Scientific Conference iNDiS 2023, Novi Sad, Serbia, p. 111.
[4] Krnić Đ., Vujinović M., Batilović M., Marković M., Budimirov T. (2023). Investigation of objects verticality using terrestrial laser scanner. Proceedings of the 16th International Scientific Conference iNDiS 2023, Novi Sad, Serbia, p. 141.

[5] Skrzypczak I., Oleniacz G., Leśniak A., Zima K., Mrówczyńska M., Kazak J. K. (2022). Scan-to-BIM method in construction: assessment of the 3D buildings model accuracy in terms inventory measurements. Building Research & Information, Volume 50, Issue 8, pp. 859–880. https://doi.org/10.1080/09613218.2021.2011703.
[6] Erdélyi J., Kopáčik A., Kyrinovič P. (2018). Construction control and documentation of facade elements using terrestrial laser scanning. Applied Geomatics, Volume 10, Issue 2, pp. 113–121. https://doi.org/10.1007/s12518-018-0208-4.
[7] Kuzmić T., Marković M., Batilović M., Bulatović V. (2021). Application of terrestrial laser scanning technology for the purpose of creating 3D models of objects. FIG e-Working Week 2021: Smart Surveyors for Land and Water Management - Challenges in a New Reality, Virtually in the Netherlands, 21–25 June.
[8] Jia D., Zhang W., Liu Y. (2021). Systematic approach for tunnel deformation monitoring with terrestrial laser scanning. Remote Sensing, Volume 13, Issue 17, Article 3519. https://doi.org/10.3390/rs13173519.
[9] Tucci G., Visintini D., Bonora V., Parisi E. (2018). Examination of indoor mobile mapping systems in a diversified internal/external test field. Applied Sciences, Volume 8, Issue 3, Article 401. https://doi.org/10.3390/app8030401.
[10] Matellon A., Maset E., Beinat A., Visintini D. (2024). Surface reconstruction from SLAM-based point clouds: results from the datasets of the 2023 SIFET Benchmark. Remote Sensing, Volume 16, Issue 18, Article 3439. https://doi.org/10.3390/rs16183439.
[11] Iocchi L., Pellegrini S. (2007). Building 3D maps with semantic elements integrating 2D laser, stereo vision and IMU on a mobile robot. Proceedings of the 2nd ISPRS International Workshop 3D-ARCH: Virtual Reconstruction and Visualization of Complex Architectures, Zurich, Switzerland.
[12] Jakopec A., Redovniković L., Barković Đ., Zrinjski M. (2023). SLAM i geodezija. Geodetski list, Volume 77(100), Issue 3, pp. 235–271.
[13] Domazetović F., Lončar N., Šaban M. (2024). 3D mapping of karst caves using GeoSLAM technology: potentials and challenges. X AIGeo Italian Young Geomorphologists' Day, p. 24.
[14] Yang B., Chen Y. (2021). Urban Underground Space 3D Semantic Mapping. Technical Report of 2021 ISPRS Scientific Initiatives, ISPRS.
[15] Cadena C., Carlone L., Carrillo H., Latif Y., Scaramuzza D., Neira J., Reid I., Leonard J. J. (2016). Past, present, and future of simultaneous localization and mapping: toward the robust-perception age. IEEE Transactions on Robotics, Volume 32, Issue 6, pp. 1309–1332. https://doi.org/10.1109/TRO.2016.2624754.
[16] Chrbolková A., Štroner M., Urban R., Michal O., Křemen T., Braun J. (2025). A comparative study of indoor accuracies between SLAM and static scanners. Applied Sciences, Volume 15, Issue 14, Article 8053. https://doi.org/10.3390/app15148053.
[17] Lehtola V. V., Kaartinen H., Nüchter A., Kaijaluoto R., Kukko A., Litkey P., Honkavaara E., Rosnell T., Vaaja M. T., Virtanen J.-P., Kurkela M., El Issaoui A., Zhu L., Jaakkola A., Hyyppä J. (2017). Comparison of the selected state-of-the-art 3D indoor scanning and point cloud generation methods. Remote Sensing, Volume 9, Issue 8, Article 796. https://doi.org/10.3390/rs9080796.
[18] OmniSLAM. (n.d.). Mobile SLAM Color 3D Laser Scanner R8+: Product Datasheet. OmniSLAM.
[19] Trimble Navigation Limited. (n.d.). Trimble TX5 3D Laser Scanner: Datasheet. Trimble Navigation Limited.

# DISASTER RISK MANAGEMENT AND FIRE SAFETY

iNDiS 2026

https://doi.org/10.24867/INDIS-2026-EN-938



# PYTHON-BASED AGENT MODELLING IN DISASTER RISK MANAGEMENT EDUCATION: A COURSE-BASED CASE STUDY

*Cveta Lazić*[1], *Tanja Vranić*[2]

***Summary:***

Modelling and simulation are important components of disaster risk management education because they help students understand real risk situations. This paper presents a course-based case study developed within the undergraduate subject Modelling and Simulation in Risk Management. The focus is placed on the use of simple Python-based agent modelling as an introductory educational approach for understanding evacuation scenarios. In the proposed exercise, each agent represents one person in an evacuation process and is described by a small number of attributes. Based on these attributes, students calculate evacuation time and analyse how different assumptions influence the results. Python is used as a simple and accessible tool for connecting input data, assumptions, calculations and interpretation. The case study demonstrates how agent-based thinking can be introduced at an undergraduate level and later transferred to more complex disaster risk scenarios.

*Keywords: disaster risk management; modelling and simulation; Python; agent modelling; evacuation; risk scenarios*

# AGENTSKI PRISTUP ZASNOVAN NA PYTHON PROGRAMSKOM JEZIKU U OBRAZOVANJU ZA UPRAVLJANJE RIZIKOM OD KATASTROFA: STUDIJA SLUČAJA IZ NASTAVNE PRAKSE

***Rezime:***

Modelovanje i simulacija predstavljaju važne komponente obrazovanja u oblasti upravljanja rizikom od katastrofa jer studentima pomažu da razumeju stvarne rizične situacije. Ovaj rad prikazuje studiju slučaja razvijenu u okviru predmeta Modelovanje i simulacija u upravljanju rizikom na osnovnim akademskim studijama. Fokus je stavljen na primenu jednostavnog agentskog modelovanja u programskom jeziku Python kao uvodnog obrazovnog pristupa za razumevanje scenarija evakuacije. U predloženoj vežbi svaki agent predstavlja jednu osobu u procesu evakuacije i opisan je manjim brojem atributa. Na osnovu ovih atributa studenti izračunavaju vreme evakuacije i analiziraju uticaj različitih pretpostavki na rezultate. Python se koristi kao jednostavan i pristupačan alat za povezivanje ulaznih podataka, pretpostavki, proračuna i interpretacije. Studija slučaja pokazuje kako se agentski pristup može uvesti na osnovnim akademskim studijama i kasnije primeniti u složenijim scenarijima rizika od katastrofa.

*Ključne reči: upravljanje rizikom od katastrofa; modelovanje i simulacija; Python; agentsko modelovanje; evakuacija; scenariji rizika*

[1] Teaching Assistant, Faculty of Technical Sciences, University of Novi Sad, Novi Sad, Serbia, cvetalazic@uns.ac.rs, ORCID 0000-0003-2105-6647
[2] Assistant Professor, Faculty of Technical Sciences, University of Novi Sad, Novi Sad, Serbia, tanjanovakovic@uns.ac.rs, ORCID 0000-0001-9971-0384

## 1. INTRODUCTION

In contemporary disaster risk management education, increasing importance is given to approaches that enable students to understand the relationship between data, modelling assumptions and analysis results. In this context, modelling and simulation represent an important part of the teaching process, as they allow complex risk situations to be presented through simplified but analytically clear models. Such an approach is particularly important in the initial stages of education, when students first need to understand the basic logic of models before using more complex software tools.

In previous teaching and research activities in the field of disaster risk management, particular attention was given to the use of disaster databases, GIS tools and spatial layers for identifying hazards, exposure and vulnerable population groups, as well as to evacuation modelling exercises in which persons in a building are represented as agents with defined characteristics [1–3].

This teaching approach should be considered within the broader context of modelling applications in disaster risk management. One example of such applications is the use of modelling to analyse accident scenarios, including accidents at petrol stations [4]. In this way, the introductory Python exercise is not treated as an isolated evacuation example, but as an initial form of model-based thinking that helps students understand more complex disaster risk scenarios at a later stage.

Starting from this context, this paper presents a teaching exercise developed within the course Modelling and Simulation in Risk Management, in which a simple Python model is used to present the basic logic of agent-based evacuation modelling. The aim of the paper is not to replace professional evacuation simulation tools, but to make clear to students the basic procedure of model-based representation of persons, attributes and assumptions that influence evacuation time. In this way, Python is used as an accessible teaching tool for connecting input data, modelling assumptions, calculations and interpretation of results before moving on to more complex software and analytical approaches.

## 2. COURSE CONTEXT: MODELLING AND SIMULATION IN RISK MANAGEMENT

The subject Modelling and Simulation in Risk Management is taught within the undergraduate study programme Disaster Risk Management and Fire Safety. The course connects disaster risk management and fire safety with applied computer science and informatics.

The main objective of the course is to enable students to use modelling methods and information technologies for the analysis and simulation of risk scenarios with potentially catastrophic consequences. The expected outcome is that students become capable of using computers and contemporary software tools to model accidental situations and interpret simulation results in the context of risk management.

The course content includes mathematical foundations of modelling, numerical simulation, applied programming, methodological aspects of modelling and analysis of modelling errors. Special attention is given to spatial simulation, three-dimensional representation, visualization and the use of software tools such as MATLAB, Pathfinder and Google Earth.

The course builds on earlier teaching and research activities in disaster risk management education. Previous work introduced students to the use of disaster databases, GIS tools and spatial layers for identifying hazards, exposure and vulnerable populations [1,2].

Other exercises focused on evacuation modelling, where persons in a building are represented as actors or agents with defined attributes such as speed, initial delay, size and direction of movement [3].

In this paper, Python [5] is introduced as a simple educational tool that supports the same modelling logic. It is not intended to replace professional software such as Pathfinder or GIS tools. Instead, it helps students understand how agents can be represented through structured data, how assumptions are translated into calculations, and how changes in input parameters influence simulation results. This provides a bridge between theoretical concepts, programming exercises and more advanced disaster risk modelling tools.

This introductory Python exercise therefore serves as a foundation for understanding broader entity-oriented modelling concepts that appear in evacuation modelling, BIM environments, and other contemporary digital engineering applications.

## 3. AGENT-BASED THINKING

Agent-based thinking represents a modelling approach in which a system is described through individual entities characterized by their own attributes and properties [6]. Rather than analysing a system only at an aggregate level, this approach focuses on the representation of individual elements and their contribution to the behaviour of the overall system.

In disaster risk management, agents are commonly represented as people, vehicles, buildings, infrastructure components or other exposed assets. Each agent is associated with a set of attributes that influence its role within a model. This way of thinking is particularly valuable in education because it helps students understand how complex system-level outcomes emerge from the characteristics of individual entities.

The concept is not limited to evacuation modelling. Similar principles can also be observed in Building Information Modelling (BIM), where buildings are represented through intelligent digital objects such as walls, doors, rooms and other building elements [7]. Although BIM is not an agent-based simulation system in the strict sense, both approaches rely on the representation of systems through entities characterized by attributes. As illustrated in Figure 1, this shared entity-oriented logic provides a common conceptual foundation for modelling and analysis in different digital environments.

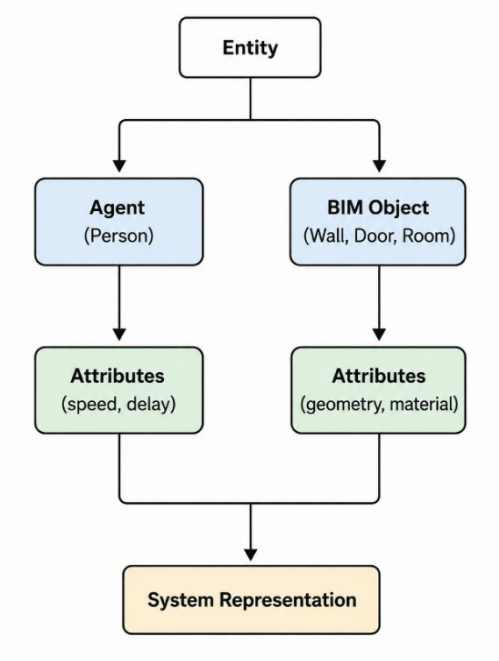


*Figure 1. Entity-oriented modelling logic in agent-based modelling and BIM environments.*

Understanding this relationship helps students transfer the modelling logic learned through simple Python exercises to more advanced modelling environments, including evacuation simulators, BIM-based applications and other digital tools used in engineering and disaster risk management.

## 4. CASE STUDY: SIMPLE PYTHON EXERCISE FOR EVACUATION AGENTS

A simple Python-based exercise is proposed as a practical case study within the course Modelling and Simulation in Risk Management. The purpose of the exercise is not to reproduce the full functionality of professional evacuation simulation software, but to introduce students to the basic logic of agent-oriented modelling. Through this exercise, students learn how a person in an evacuation scenario can be represented as an agent with a small number of attributes, and how these attributes influence the calculated evacuation time.

In this simplified scenario, each agent represents one person who needs to leave a building. The agent is described by four basic attributes: type of person, distance to the exit, walking speed, and initial delay before movement starts. These attributes are intentionally kept simple so that students can focus on the modelling idea rather than on programming complexity.

The evacuation time is calculated using the following expression:

```
Evacuation time = distance to exit / walking speed + initial delay
```

In this expression, distance to exit represents the length of the evacuation path, walking speed represents the assumed movement speed of the agent, and initial delay represents the time needed for the agent to react and start moving. Although simplified, this model introduces an important principle of evacuation modelling: different people may require different evacuation times because they do not have the same movement speed, reaction time or position in the building.

The following Python example can be used in class:

```
agenti = [
```

```
    {"tip": "student", "udaljenost": 40, "brzina": 1.2, "kasnjenje": 5},
    {"tip": "zaposleni", "udaljenost": 55, "brzina": 1.1, "kasnjenje": 8},
    {"tip": "posetilac", "udaljenost": 50, "brzina": 1.0, "kasnjenje": 12},
    {"tip": "smanjena_pokretljivost", "udaljenost": 35, "brzina": 0.6,
"kasnjenje": 15}
]
for osoba in agenti:
    vreme_evakuacije = osoba["udaljenost"] / osoba["brzina"] +
osoba["kasnjenje"]
    print(osoba["tip"], round(vreme_evakuacije, 2))
```

The output of this code gives the evacuation time for each agent. Students can compare the results and identify which agent needs the longest time to leave the building. In the given example, the agent with reduced mobility has a shorter distance to the exit than some other agents, but still requires a longer evacuation time because of lower walking speed and higher initial delay. This helps students understand that evacuation modelling cannot be based only on distance, but must also include the characteristics of the people who are evacuating.

In the next step, students can modify the scenario. For example, they can reduce walking speed to represent smoke, congestion, stairs or panic conditions. They can also increase initial delay to represent delayed alarm perception or uncertainty about the evacuation route. A simple scenario modification can be introduced as follows:

```
faktor_usporenja = 0.8
for osoba in agenti:
    smanjena_brzina = osoba["brzina"] * faktor_usporenja
    vreme_evakuacije = osoba["udaljenost"] / smanjena_brzina +
osoba["kasnjenje"]
    print(osoba["tip"], round(vreme_evakuacije, 2))
```

This second calculation shows how a change in environmental conditions affects all agents in the model. Students can compare the baseline scenario with the modified scenario and discuss how reduced movement speed increases evacuation time. In this way, the exercise introduces the basic idea of scenario analysis.

The exercise can be further extended by asking students to answer several simple questions:

- Which agent has the longest evacuation time in the baseline scenario?
- How does reduced walking speed affect total evacuation time?
- Which attribute has the strongest influence on the result: distance, speed or initial delay?
- How could the model be improved if more data were available?
- What are the limitations of such a simplified model?

The educational value of this exercise is that students can clearly see the connection between data, assumptions and model results. The agent is not presented as an abstract theoretical concept, but as a simple data structure that contains relevant information about one element of the evacuation system. Python is used as a transparent tool for connecting input data, calculation and interpretation.

This exercise also prepares students for more advanced evacuation modelling tools such as Pathfinder [8]. In professional software, agents are described by a larger number of physical and behavioral parameters, while the movement environment is represented in more detail. However, the basic modelling logic remains the same: each agent has

attributes, the environment imposes constraints, and the simulation produces results that must be interpreted from the perspective of risk management.
The same agent-oriented logic can later be transferred to other disaster risk scenarios. In evacuation modelling, the agent is a person. In flood damage assessment, the agent can be a building or an exposed asset. Instead of distance, speed and delay, the relevant attributes may include location, terrain elevation, exposure, vulnerability and expected damage. Therefore, this simple Python exercise serves as an introductory bridge between programming, simulation and disaster risk management decision-making.

## 5. DISCUSSION AND CONCLUSION

The presented case study demonstrates how agent-based concepts can be introduced in disaster risk management education through a simple and transparent Python exercise. Although the proposed model is intentionally simplified, it enables students to understand the fundamental relationship between entities, attributes, modelling assumptions and simulation results. This understanding is often difficult to achieve when students are introduced directly to professional simulation software.
From an educational perspective, the main advantage of the exercise lies in its transparency. Students can clearly observe how evacuation time is calculated, how individual parameters influence the results, and how scenario modifications affect model outputs. Such an approach supports the development of analytical thinking and provides a foundation for understanding more advanced modelling techniques and software environments.
While the exercise does not include the full complexity of professional evacuation simulation software, its purpose is to support the understanding of fundamental agent-based modelling concepts in an educational context.
Overall, the proposed teaching approach provides a practical bridge between theoretical concepts, introductory programming skills and advanced modelling tools. By introducing students to agent-based reasoning through accessible Python examples, the exercise supports the gradual development of competencies required for the analysis of complex disaster risk scenarios and contemporary digital modelling environments. The approach may also serve as a foundation for future educational activities involving BIM-based applications, GIS-supported analyses and professional evacuation simulation platforms.

**ACKNOWLEDGEMENT**

The authors gratefully acknowledge Prof. Dr. Srđan Popov for his strategic guidance, methodological discussions, and internal review during the development of this manuscript.

## REFERENCES (STYLE: LITERATURA)

[1] Novaković T., Simić J., Popović Lj., Popov S., Velemir M., Ćosić Đ., Sakulski D. (2013). Subject ‘Disaster Risk Management’ – Spatial Context. *Proceedings of the International Conference on Information Technology and Development of Education – ITRO 2013*, Technical Faculty “Mihajlo Pupin”, Zrenjanin, Serbia, 28 June, pp. 80-84.

[2] Simić J., Tucakov J., Knežević S., Sremački M., Novaković T., Popović Lj. (2013). Geoinformation Technologies in Education – Persons with Disabilities in Emergencies. *Proceedings of the International Conference on Information Technology and Development of Education – ITRO 2013*, Technical Faculty “Mihajlo Pupin”, Zrenjanin, Serbia, 28 June, pp. 407-411.

[3] Simić J., Novaković T., Duraković N., Mijatov G., Popović Lj., Sremački M., Popov S. (2013). Persons with Disabilities Evacuation – Pathfinder Application. *Proceedings of the International Conference on Applied Internet and Information Technologies – AIIT 2013*, Technical Faculty "Mihajlo Pupin", Zrenjanin, Serbia, 25 October, pp. 446-449.

[4] Simić J., Medić N., Novaković T., Popović Lj., Ćosić Đ. (2015). Aspects of Petrol Station Accident Modeling. *Proceedings of the Scientific Conference Planning, Design, Construction and Building Renewal – iNDiS 2015*, Faculty of Technical Sciences, Novi Sad, Serbia, 25-27 November, pp. 639-646.

[5] Python Software Foundation, Python Documentation. [Online]. Available: https://docs.python.org. [Accessed: 30-May-2026].

[6] Bonabeau E. (2002). Agent-Based Modeling: Methods and Techniques for Simulating Human Systems. *Proceedings of the National Academy of Sciences*, 99(Suppl. 3), 7280–7287.

[7] Succar B. (2009). Building Information Modelling Framework: A Research and Delivery Foundation for Industry Stakeholders. *Automation in Construction*, 18(3), 357–375.

[8] Thunderhead Engineering, Pathfinder User Manual. [Online]. Available: https://www.thunderheadeng.com/docs/2024-2/pathfinder/user-manual/. [Accessed: 30-May-2026].

https://doi.org/10.24867/INDIS-2026-EN-945



# EVACUATION AS A SYSTEM OF MOVEMENT AND BEHAVIOUR: A CASE STUDY OF THE SERBIAN NATIONAL THEATRE IN NOVI SAD

*Teodora Vojnović[1], Mirjana Laban[2], Suzana Draganić[3], Olivera Bedov[4]*

***Abstract:*** *Evacuation performance can be evaluated through analytical calculation or by using modern simulation tools, such as the Pathfinder software package employed in this study. In the case of the Serbian National Theatre in Novi Sad, Serbia, both approaches were applied, and two evacuation scenarios were analysed: the existing arrangement and an improved design incorporating an additional evacuation exit. The analytical assessment produced an evacuation time of 590 s, whereas the simulation results indicated considerably shorter evacuation times of 227.8 s for the existing scenario and 226.5 s for the improved scenario. Although the additional exit contributed to a more balanced distribution of occupant movement, it did not significantly reduce the overall evacuation time. The findings suggest that evacuation efficiency depends not only on the number of available exits, but primarily on the distribution of occupant flows and the organisation of movement throughout the evacuation process.*

***Keywords****: public assembly buildings, evacuation, simulation, fire safety, Pathfinder*

# EVAKUACIJA KAO SISTEM KRETANJA I PONAŠANJA: STUDIJA SLUČAJA SRPSKOG NARODNOG POZORIŠTA U NOVOM SADU

***Rezime:*** Proces evakuacije se može vrednovati analitičkim proračunom ili primenom savremenih simulacionih alata, kao što je programski paket Pathfinder korišćen u ovom radu. Na primeru Srpskog narodnog pozorišta u Novom Sadu primenjena su oba pristupa i analizirana su dva scenarija evakuacije: postojeće stanje i unapređeno rešenje sa dodatnim evakuacionim izlazom. Analitičkim proračunom dobijeno je vreme evakuacije od 590 s, dok su rezultati simulacije pokazali znatno kraća vremena evakuacije - 227,8 s za postojeći i 226,5 s za unapređeni scenario. Iako je dodatni izlaz doprineo ravnomernijoj raspodeli kretanja lica, nije doveo do značajnog skraćenja ukupnog vremena evakuacije. Rezultati ukazuju na to da efikasnost evakuacije ne zavisi samo od broja raspoloživih izlaza, već prevashodno od raspodele tokova kretanja lica i organizacije kretanja tokom čitavog procesa evakuacije.

***Ključne reči:*** *objekti javne namene, evakuacija, simulacija, zaštita od požara, Pathfinder*

[1]MSc in Disaster and Fire Risk Management, BlackRock, Belgrade, Serbia, teodora.vojnovic12345@gmail.com
[2]Full Prof., Faculty of Technical Sciences, University of Novi Sad, Serbia, mirjana.laban.ftn@gmail.com ORCID: 0000-0001-6557-3094
[3]Asst. Prof., Faculty of Technical Sciences, University of Novi Sad, Serbia, suzanav@uns.ac.rs, ORCID: 0000-0003-3803-3484
[4]Teaching Assistant, PhD, Faculty of Technical Sciences, University of Novi Sad, Serbia, olivera.bukvic@uns.ac.rs, ORCID: 0000-0001-8910-1630

## 1. INTRODUCTION

Evacuation is one of the fundamental measures for protecting human life in the event of fire and other emergencies [1]. Its effectiveness depends not only on the building's layout and the capacity of evacuation routes, but also on how occupants perceive risk and respond to emergency conditions.

Public assembly buildings such as theatres are particularly demanding because they combine high occupant densities with complex spatial layouts. During an evacuation, large numbers of people move simultaneously, often causing congestion and reduced walking speeds at critical points within the building.

In practice, evacuation design is most commonly based on analytical calculations that cannot fully represent realistic occupant behaviour or interactions between occupants during evacuation. Consequently, the predicted evacuation process may differ substantially from the movement patterns that develop in an actual emergency.

This paper draws on research conducted for the author's master's thesis [2].

The aim of the study was to evaluate evacuation performance at the Serbian National Theatre in Novi Sad by combining analytical calculations with simulation modelling, to identify the key deficiencies and consider opportunities for improving the system.

The results demonstrate significant differences between the analytical and simulation-based approaches to evacuation assessment. While simulation modelling provided a more realistic representation of occupant movement and evacuation dynamics, both approaches highlighted the importance of identifying critical locations within the evacuation system. The findings indicate that evacuation efficiency is influenced not only by the availability of exits, but also by the distribution of occupant flows and the organisation of movement throughout the building.

## 2. DESCRIPTION OF THE BUILDING AND FIRE SAFETY SYSTEMS

The Serbian National Theatre in Novi Sad is a complex public building with a total floor area of 22,340.58 m². It comprises two basement levels, a ground floor and three upper floors (Figure 1).




*Figure 1. External view of the Serbian National Theatre*

The building contains a main auditorium and a studio theatre, stage areas, circulation zones, corridors, foyers, and associated technical and administrative rooms. This spatial arrangement causes occupant flows to intersect, creating one of the main challenges for evacuation (Figure 2).

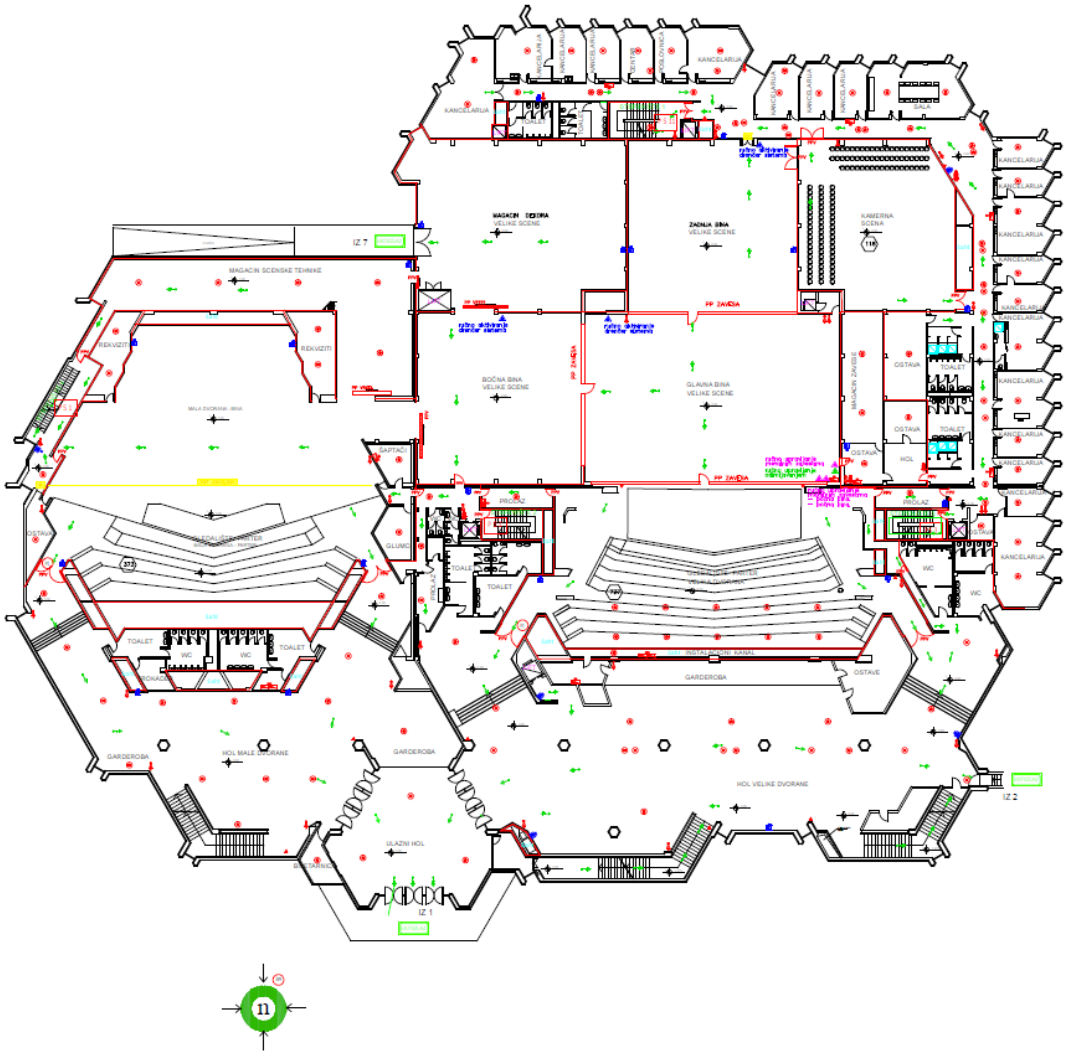

*Figure 2. Ground-floor evacuation plan*

Critical evacuation zones were identified within the circulation areas, primarily in corridors, stairways, and at exits, where bottlenecks form and restrict occupant movement.

The building has a total capacity of 2,997 occupants. For the purposes of this analysis, the ground floor and first floor were examined, representing a total of 1,483 people.

The building is equipped with fire safety systems, including fire detection and alarm, smoke control, fixed fire-extinguishing installations, and emergency lighting. Evacuation routes are defined and marked in accordance with the applicable regulations [3].

## 3. RESEARCH METHODOLOGY

The methodology combines and compares analytical calculation with simulation modelling.
The analytical calculation covers occupant movement through every stage of evacuation, from the initial position to final exit from the building. The parameters considered include travel distance, walking speed, and exit capacity [3].
The calculation was performed in accordance with the applicable regulations and structured by evacuation phases, while accounting for adverse conditions such as passage constrictions, reduced walking speeds when turning, and movement down stairs.
The simulation model was developed in Pathfinder [4] based on the building layout. The spatial model defines rooms, corridors, stairs, and exits, together with the connections between evacuation routes.
Occupant movement was modelled by assigning routes towards the available exits, using the same walking speed of 1.5 m/s as in the analytical calculation. The model assumed that a large number of occupants began moving towards the exits simultaneously, allowing interactions between movement flows and the formation of congestion to be examined.
The simulation makes it possible to analyse the distribution of occupants across evacuation routes, identify critical locations within the building, and examine evacuation dynamics under conditions that more closely reflect actual movement.
Two evacuation scenarios were analysed to compare the existing configuration with the effect of introducing an additional evacuation route.

## 4. RESULTS AND SCENARIO ANALYSIS

This section presents the results of the analytical calculation and simulation modelling for the two evacuation scenarios. Particular attention is given to evacuation time, occupant distribution, and movement dynamics.

The analysis examines how changes in the organisation of evacuation routes affect performance and identifies the critical points within the system.

### 4.1. SCENARIO 1: EXISTING CONFIGURATION

This scenario considers evacuation under the existing conditions, with no changes to the spatial arrangement or evacuation routes. A large number of occupants are assumed to begin evacuating simultaneously. Figure 3 illustrates their initial distribution and assigned evacuation routes. Occupants shown in blue are directed towards Exit 2, located on the eastern side of the building, whereas occupants shown in orange, yellow, and red are directed towards Exit 1, located on the southern side of the building. Several occupant groups converge towards common stairways and exits from the beginning of the simulation, indicating the potential formation of bottlenecks during the subsequent stages of evacuation.

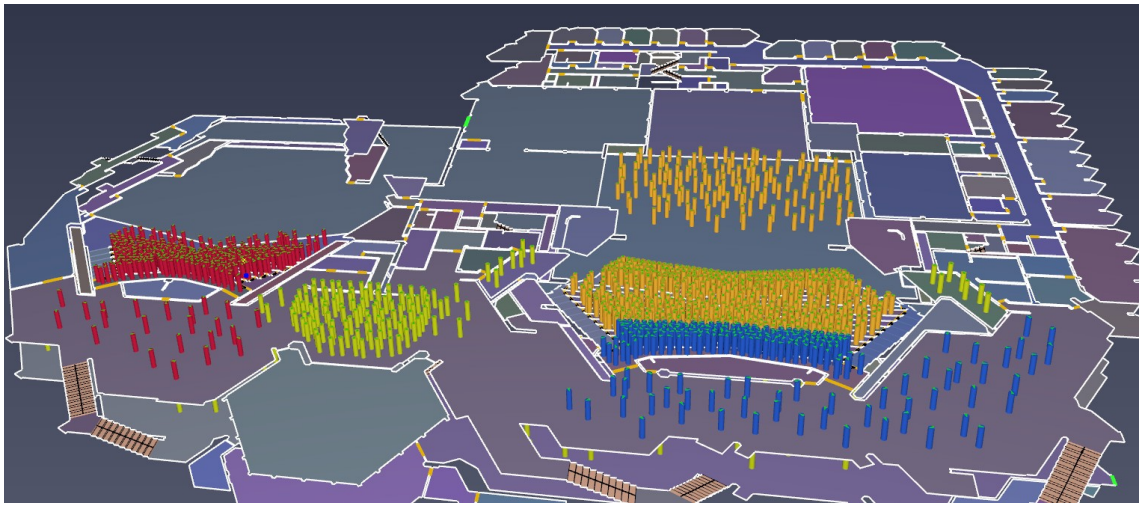

*Figure 3. Scenario 1: Start of the evacuation*

The total evacuation time for this scenario was 227.8 s.

Figure 4 shows the evacuation flow and occupant density after 80 s. The density scale ranges from 0.55 occupants/m² in the blue zones to 3.00 occupants/m² in the red zones. Blue areas represent lower occupant densities, green and yellow areas indicate intermediate densities, while orange and red areas represent the highest occupant concentrations. Increased densities are visible along the main circulation routes, on the stairways, and near the final exits. The orange and red zones identify locations where crowding is most pronounced, indicating the principal bottlenecks within the evacuation system and areas where queues may form.

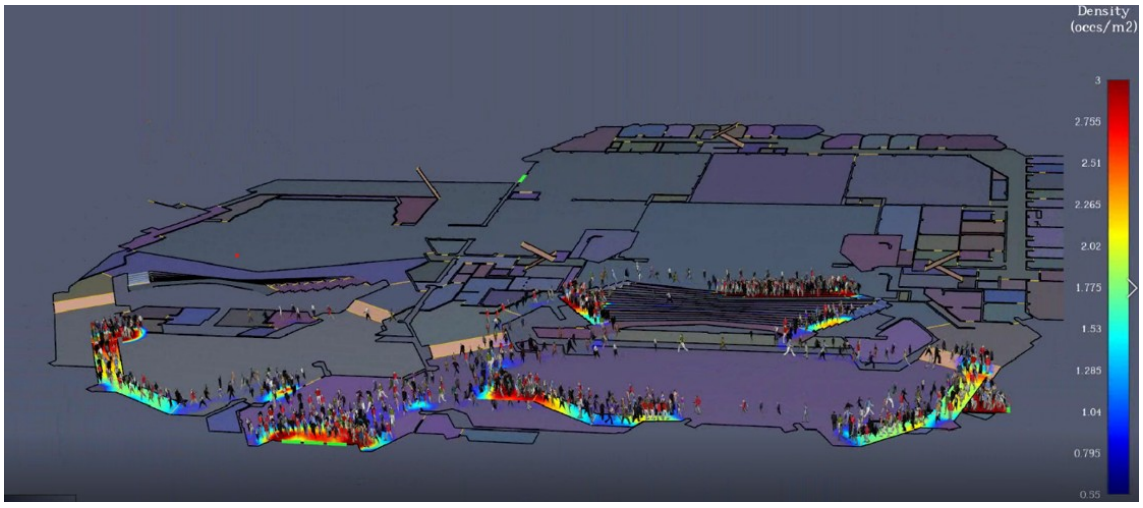


*Figure 4. Scenario 1: Occupant density and evacuation flow after 80 s*

Figure 5 shows the evacuation flow and occupant density after 130 s. The remaining occupants are unevenly distributed across the available evacuation routes, with a pronounced concentration along the route leading towards Exit 2 on the eastern side of the building. The yellow, orange and red zones visible near Exit 2 indicate continued crowding, while Exit 1 on the southern side accommodates considerably fewer occupants. This imbalance in exit utilisation contributes to local congestion despite the availability of an alternative evacuation route.

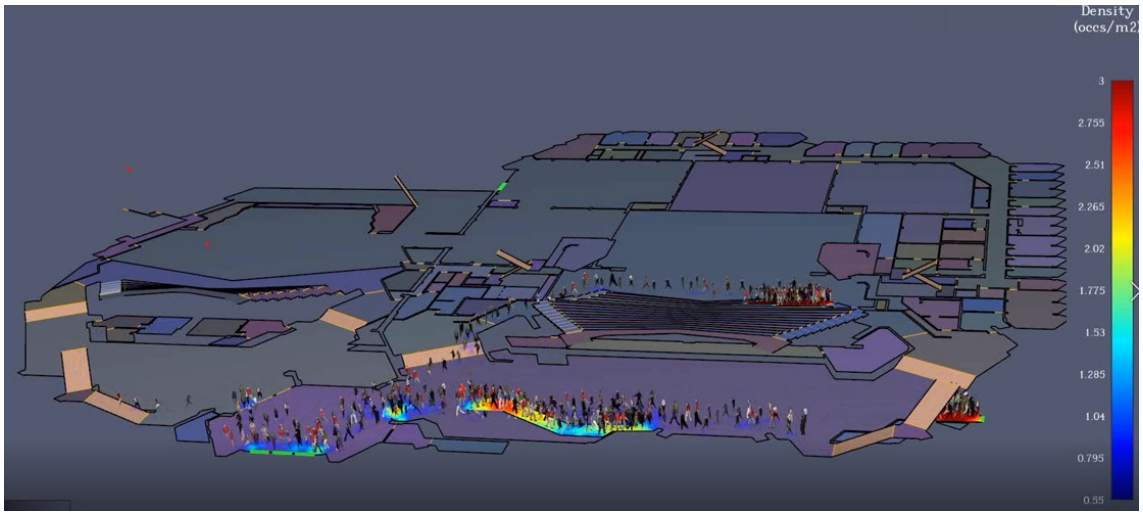


*Figure 5. Scenario 1: Occupant density and evacuation flow after 130 s*

## 4.2. SCENARIO 2: PROPOSED CONFIGURATION

This scenario examines evacuation following the introduction of an external fire escape stair on the eastern side of the building. Figure 6 illustrates the resulting redistribution of occupants according to their assigned evacuation routes. Occupants shown in blue evacuate via the newly introduced external stairway towards Exit 3 on the eastern side of the building. Occupants shown in purple are directed towards Exit 2, also located on the eastern side, while occupants shown in orange, yellow and red evacuate towards Exit 1 on the southern side of the building. Compared with Scenario 1, directing a portion of the occupants towards Exit 3 reduces demand on the existing evacuation routes and provides a more balanced initial distribution of evacuation flows.

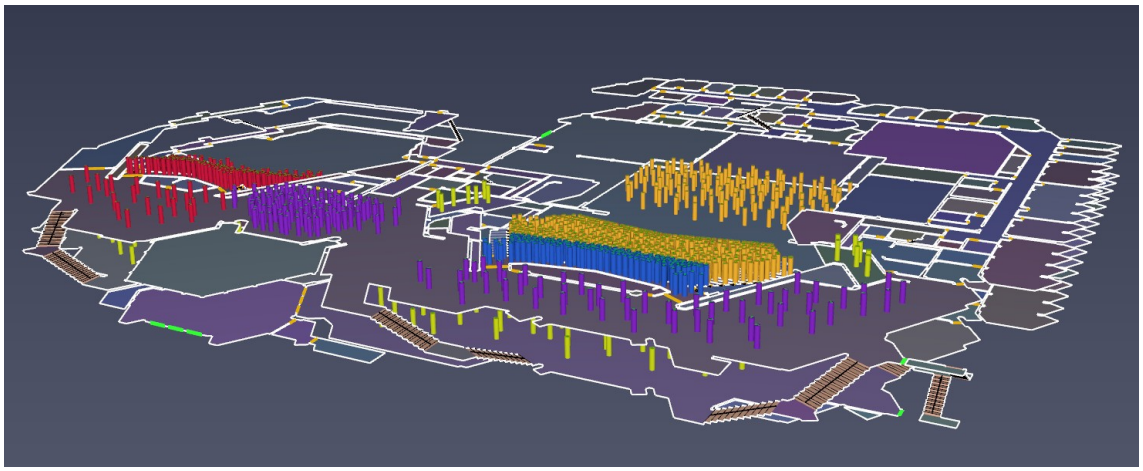

*Figure 6. Scenario 2: Start of the evacuation*

The total evacuation time for this scenario was 226.5 s.

Figure 7 shows the evacuation flow and occupant density after 80 s. Although yellow, orange, and red zones remain visible near stairways, exits, and other constricted circulation areas, the occupant concentrations are distributed more evenly across the available evacuation routes than in Scenario 1. This redistribution reduces demand on

individual routes and indicates improved utilisation of the evacuation network, although localised bottlenecks remain present at several critical locations.

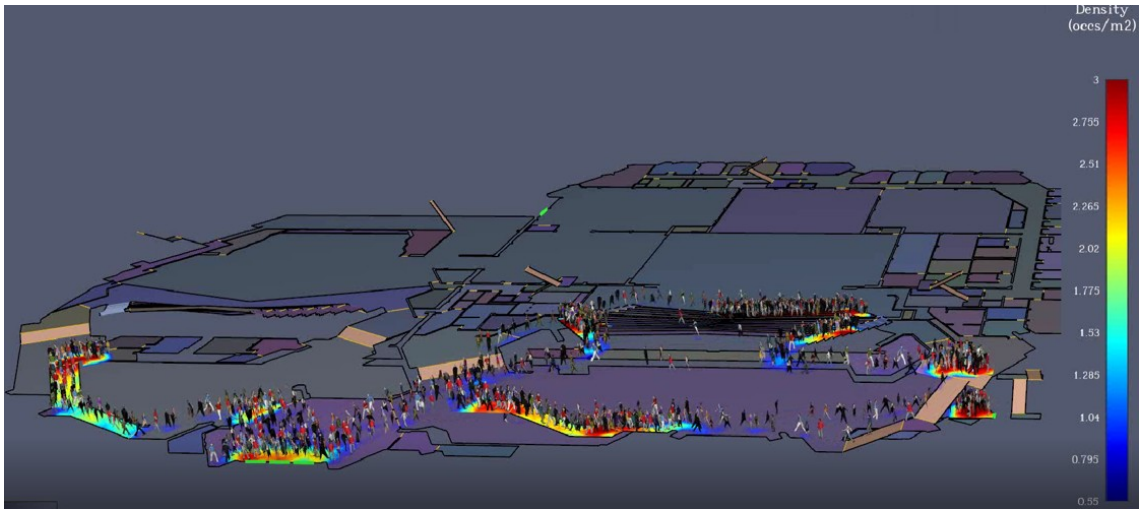


*Figure 7. Scenario 2: Occupant density and evacuation flow after 80 s*

Figure 8 shows the evacuation flow and occupant density after 130 s. Compared with Scenario 1 at the same stage of evacuation, the remaining occupants are distributed more evenly across the available evacuation routes, and the areas of high occupant density are more localised. Nevertheless, yellow, orange and red zones remain visible at several constricted sections of the evacuation network, indicating the continued presence of local bottlenecks. The additional evacuation route therefore reduces demand on individual routes but does not eliminate congestion entirely, which helps explain the limited reduction in the total evacuation time.

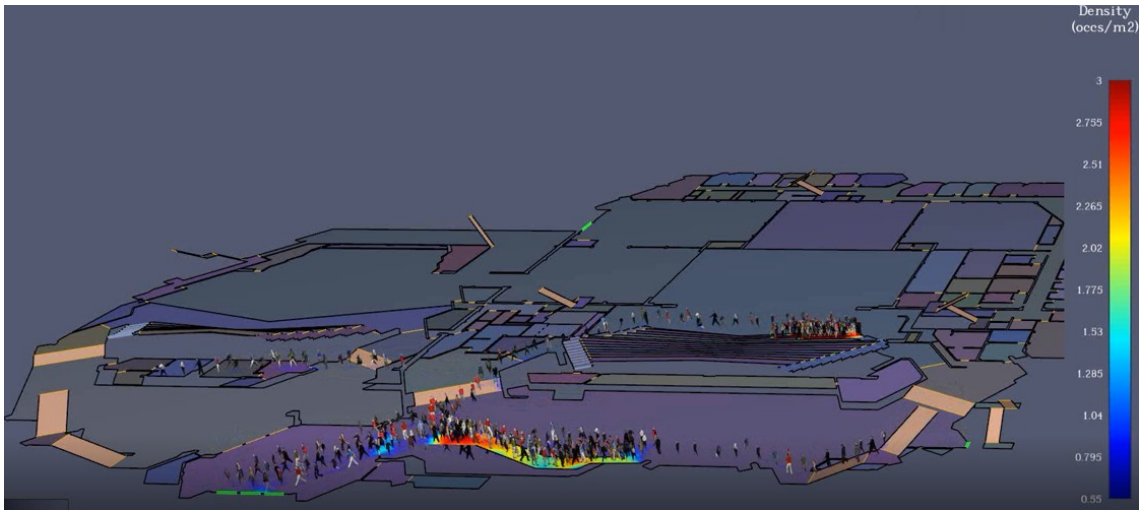


*Figure 8. Scenario 2: Evacuation flow after 130 s*

## 4.3. COMPARATIVE ANALYSIS

The analytical calculation and the two simulation scenarios were compared to examine differences in total evacuation time and occupant movement dynamics. Table 1 presents the results obtained for the three cases.

The total evacuation time calculated analytically was 590 s. The initial phase of the evacuation, from the occupant's initial position to the first exit, was found not to be critical, whereas delays occur in the final phase, i.e., during movement towards the final exits, where congestion develops, and the flow rate is reduced.
The substantial difference between the analytically calculated evacuation time of 590 s and the simulation results of approximately 227 s arises from the conservative, worst-case assumptions underlying the analytical method. In the analytical calculation, occupants are assumed to converge at critical points, whereas the simulation represents a more realistic pattern in which occupants throughout the building begin evacuating simultaneously.

*Table 1. Comparison of the analytical calculation and simulation scenarios*

| Parameter | Analytical model | Simulation scenario 1 existing configuration | Simulation scenario 2 proposed configuration |
|---|---|---|---|
| Total number of occupants | 1,483 | | |
| Total evacuation time (s) | 590 | 227.8 | 226.5 |
| Time to first exit (s) | - | 10.6 | 10.5 |
| Evacuated after 50 s | - | 219 | 267 |
| Evacuated after 80 s | - | 546 | 626 |
| Evacuated after 130 s | - | 1.081 | 1.142 |
| Evacuated after 180 s | - | 1.392 | 1.394 |

The difference between the two simulation scenarios was relatively small, with the proposed configuration reducing the total evacuation time by only 1.3 s. However, the proposed configuration resulted in a faster evacuation rate during the early stages and a more balanced distribution of occupant flows.
Figure 9 compares evacuation progress in the two simulation scenarios.

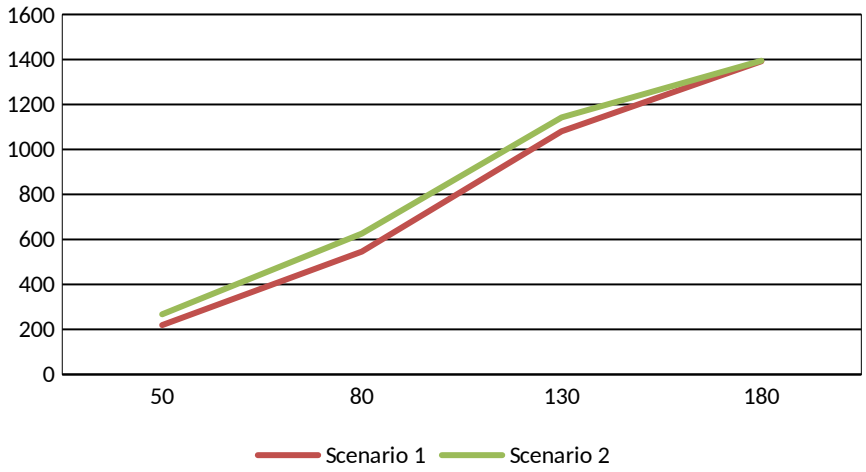


*Figure 9. Comparison of evacuation progress by simulation scenario*

## 5. DISCUSSION

The findings demonstrate that simulation models can support a more detailed understanding and prediction of evacuation performance in complex buildings such as theatres, where high occupant numbers and spatial constraints have a direct bearing on safety.

A key finding is that evacuation time depends not only on the spatial organisation of the building, but also on the interaction between the physical environment and occupant behaviour. The principal value of simulation lies in its ability to reveal critical locations and movement patterns that conventional analytical approaches may not adequately capture.

The results show that bottlenecks, particularly at exits and within circulation areas, can substantially delay evacuation. They also indicate that relatively modest changes in the distribution of evacuation flows can improve evacuation performance, even without a significant reduction in total evacuation time. This suggests that effective improvements do not necessarily require extensive structural alterations.

The comparison with the relevant standards revealed certain deviations, confirming that prescriptive approaches may not fully account for actual human behavior under stressful conditions [5]. Human factors, including collective movement and decision-making under uncertainty, play a decisive role and cannot be disregarded [6].

The approach applied here allows different scenarios to be compared and the effects of changes to evacuation organisation to be assessed more clearly. Without simulation, an evacuation plan remains largely a static representation; the simulation model, by contrast, shows how occupant movement develops over time and where congestion may occur.

These findings can inform improvements to evacuation plans, staff organisation, and occupant training, with the potential to enhance safety substantially without major structural interventions.

The limitations of the models should nevertheless be recognised. They rely on a defined set of assumptions and cannot reproduce every form of occupant behaviour that may arise in an actual emergency. Even so, the approach provides a useful basis for improved evacuation planning and occupant safety.

Simulation methods can therefore make an important contribution to contemporary evacuation planning. Evacuation should be treated as a dynamic process that requires regular review, analysis and improvement.

## 6. CONCLUSION

The results show that compliance with technical requirements, including the provision of an adequate number of evacuation exits, does not necessarily guarantee effective evacuation under real conditions. Even in technically compliant buildings, bottlenecks and congestion can develop, significantly affecting evacuation flow and occupant safety.

Comparison of the scenarios shows that the additional evacuation route improves the distribution of evacuation flows and reduces local congestion, but does not significantly reduce the total evacuation time. This indicates that the effectiveness of an additional exit depends not only on its availability, but also on how evacuation flows are routed and distributed throughout the building.

Evacuation is therefore not solely a technical problem. Human factors, including movement patterns, exit choice and occupant response in an emergency, are equally critical.

Effective evacuation consequently requires a combination of technical and organisational measures, with particular emphasis on appropriate evacuation planning, occupant training and preparedness.

In practice, evacuation is not merely a matter of building design; it also depends on people's ability to respond in an organised and timely manner under actual emergency conditions.

## REFERENCES

[1] Law on Fire Protection, Official Gazette of the Republic of Serbia, Nos. 111/2009, 20/2015 and 87/2018. https://www.paragraf.rs/propisi/zakon_o_zastiti_od_pozara.html

[2] Vojnović, T. (2025). Evacuation Modelling for the Serbian National Theatre in Novi Sad. Master's thesis, Faculty of Technical Sciences, University of Novi Sad.

[3] Rulebook on Technical Requirements for Fire Protection in Residential Buildings, Commercial Buildings and Public-Use Buildings, Official Gazette of the Republic of Serbia, No. 22/2019. https://www.paragraf.rs/propisi/pravilnik-tehnickim-normativima-zastitu-pozara-stambenih-poslovnih-objekata-objekata.html

[4] Thunderhead Engineering. (2021). Pathfinder User Manual.
https://www.thunderheadeng.com/docs/2021-3/pathfinder/user-manual/

[5] Gwynne, S., Galea, E. R., Owen, M., & Lawrence, P. (1999). A review of the methodologies used in the computer simulation of evacuation from the built environment. Building and Environment. https://fseg.gre.ac.uk/fire/Building&Environment_Paper.pdf

[6] Kuligowski, E. (2009). The process of human behaviour in building fires. NIST Technical Note. https://tsapps.nist.gov/publication/get_pdf.cfm?pub_id=902507

https://doi.org/10.24867/INDIS-2026-EN-955



# VOLUNTEERS IN DISASTER RISK MANAGEMENT IN SERBIA: COOPERATION, PUBLIC PERCEPTION AND YOUTH ENGAGEMENT

*Jelena Mirjanić[1], Igor Džolev[2], Jovana Topalić[3], Tiana Milović[4], Mirjana Laban[5],*

***Summary:***

Volunteers play an important role in disaster risk management (DRM), but their effective engagement depends on adequate coordination, training, legal recognition and sustainable funding. This paper examines volunteer involvement in DRM in Serbia, based on surveys conducted within the Interreg Danube Region project InDiMaND in February and March 2026. The findings reveal a gap between the recognised importance of volunteers and the conditions supporting their engagement, while volunteer activities remain primarily focused on emergency response. Although citizens demonstrate a considerable willingness to volunteer, awareness of volunteering opportunities and youth engagement remain challenges. The paper provides insight into the current state of volunteering within Serbia's DRM system and highlights key challenges to its further development.

*Keywords: volunteers; disaster risk management; civil protection; youth engagement;*

# VOLONTERI U UPRAVLJANJU RIZICIMA OD KATASTROFA U SRBIJI: SARADNJA, JAVNA PERCEPCIJA I ANGAŽOVANJE MLADIH

***Rezime:***

Volonteri imaju važnu ulogu u upravljanju rizicima od katastrofa, ali njihovo efikasno angažovanje zavisi od odgovarajuće koordinacije, obuke, pravnog priznanja i održivog finansiranja. Ovaj rad analizira uključenost volontera u upravljanje rizicima od katastrofa u Srbiji, na osnovu anketa sprovedenih u okviru projekta Interreg Dunavskog regiona InDiMaND tokom februara i marta 2026. godine. Rezultati ukazuju na nesklad između prepoznatog značaja volontera i uslova za njihovo angažovanje. Iako je spremnost građana da volontiraju izražena, informisanost o mogućnostima angažovanja i uključivanje mladih ostaju izazovi. Rad pruža uvid u trenutno stanje volontera u sistemu upravljanja rizicima od katastrofa u Srbiji i ukazuje na ključne izazove u njegovom daljem razvoju.

*Ključne reči: volonteri; upravljanje rizicima od katastrofa; civilna zaštita; angažovanje mladih;*

[1] Teach. Asst., Faculty of Technical Sciences, University of Novi Sad, Novi Sad, Serbia, jelena.mirjanic@uns.ac.rs, ORCID 0009-0006-6608-056X
[2] Assoc. Prof., Faculty of Technical Sciences, University of Novi Sad, Novi Sad, Serbia, idzolev@uns.ac.rs, ORCID 0000-0002-7622-7936
[3] Res. Assoc., Faculty of Technical Sciences, University of Novi Sad, Novi Sad, Serbia, jovanatopalic90@uns.ac.rs, ORCID 0000-0001-7854-3257
[4] Res. Assoc., Faculty of Technical Sciences, University of Novi Sad, Novi Sad, Serbia, tiana.milovic@uns.ac.rs, ORCID 0000-0002-3905-7018
[5] Full Prof., Faculty of Technical Sciences, University of Novi Sad, Novi Sad, Serbia, mlaban@uns.ac.rs, ORCID 0000-0001-6557-3094

# 1. INTRODUCTION

Volunteers complement professional services in disaster risk management (DRM): they extend response capacity, connect authorities with local communities and contribute to preparedness and recovery. Their contribution, however, depends on legal status, training, funding and coordination arrangements that differ considerably between countries. The InDiMand project (Interreg Danube Region) explores how volunteer engagement in DRM can be strengthened across the Danube Region, with particular attention to recruitment, coordination, training and long-term retention of young volunteers.
This paper presents the Serbian findings of the InDiMand surveys, conducted in February and March 2026 among institutional stakeholders, volunteer organisations and the general public. Its objective is to describe the current state of volunteer involvement in DRM in Serbia.

## 1.1. NATIONAL CONTEXT

Serbia's DRM system is regulated by the Law on Disaster Risk Reduction and Emergency Management [1], which covers risk assessment and planning, emergency situations, firefighting and rescue units, civil protection, early warning, training and international cooperation. The Sector for Emergency Management within the Ministry of Interior is the lead national body, while local self-government units prepare risk assessments and protection-and-rescue plans together with emergency headquarters at republic, provincial and local level. The 2014 floods were the main trigger for reform. The 2019 EU Civil Protection Mechanism peer review [2] judged the framework comprehensive but recommended more administrative capacity and funding for the Sector for Emergency Management and stronger preparedness, training and public awareness.
The organised volunteer base consists mainly of volunteer fire departments, which are members of firefighter associations and represent a considerable potential for the security of local self-government; the Red Cross of Serbia and its local branches; mountain and search-and-rescue teams, including the Serbian Search and Rescue Organization (OTIS); and civil protection units. Spontaneous volunteers emerge during major events such as floods and the COVID-19 pandemic. General volunteering is governed by the Law on Volunteering [3], which introduces a volunteering contract for long-term engagements and obliges the organiser to insure volunteers against injury and occupational illness. Youth volunteering is promoted through the Law on Youth [4], which defines youth as persons aged 15–30, and the Youth Strategy in the Republic of Serbia [5].

# 2. METHODOLOGY AND SAMPLE

## 2.1. DATA SOURCES

The study uses the Serbian dataset, which contains responses to three of the four InDiMand questionnaires, completed online in Serbian, Hungarian or English:

- Questionnaire for Professional Services,
- Questionnaire for Voluntary Units,
- Questionnaire on Public Knowledge and Attitudes in DRM.

The fourth instrument, aimed at youth volunteers (agreement scale 1–10), received no responses in Serbia (Tab. 1).

*Tab. 1 Respondents by stakeholder group*

| Stakeholder group | Instrument | n | Collection period |
|---|---|---|---|
| Institutional stakeholders | Questionnaire for Professional Services | 35 | 4–26 Feb 2026 |
| Volunteer organisations | Questionnaire for Voluntary Units | 10 | 9–22 Feb 2026 |
| General public | Questionnaire on Public Knowledge and Attitudes in DRM | 103 | 11 Feb–2 Mar 2026 |
| Youth volunteers | Questionnaire for Youth Volunteers | 0 | – |
| **Total** | | **148** | |

All questionnaires were administered as online forms and distributed by e-mail by the Serbian project partner Faculty of Technical Sciences, University of Novi Sad, using a contact database of relevant stakeholders compiled through internet research and from the project partners' contact databases. Participation was voluntary and anonymous.
Single-choice answers are reported as counts and percentages of all respondents in a group. For multiple-choice questions, percentages show the share of respondents who selected an option and therefore add up to more than 100%. Free-text answers were read and grouped manually. All results are descriptive.

## 2.2. LIMITATIONS

The 10 volunteer-organisation responses are too few for percentage-based conclusions and are treated as indicative; four records carry the name of the same unit, so they represent at most seven distinct organisations. The samples are non-probability and self-selected: 30 of 35 institutional respondents are municipal or city administrations, and the public sample is urban (73% live in cities above 100,000 inhabitants), concentrated in the 35–54 age group (50%). No youth volunteer responses exist for Serbia; youth findings are therefore indirect and must be validated through further national fieldwork.

# 3. RESULTS

## 3.1. ROLE OF VOLUNTEERS AND PERCEIVED IMPORTANCE

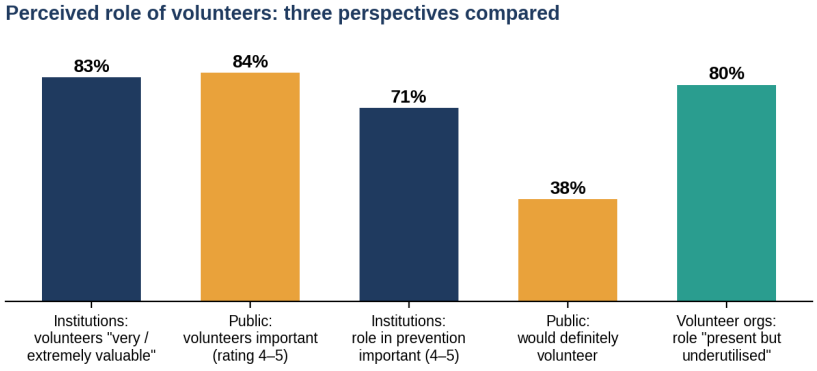


*Fig. 1 Perceived role of volunteers: institutional, public and volunteer-organisation perspectives*

Of 35 institutions, 12 (34%) cooperate with volunteers regularly, 12 occasionally and 4 rarely, while 7 (20%) do not cooperate at all. The institutions that cooperate (28) involve volunteers most often in response-related tasks such as evacuation (16), logistics and supply (16) and search and rescue (12), followed by prevention and awareness activities: public awareness campaigns (14), early warning (12) and risk assessment (9). Recovery is the weakest phase: only 2 of 10 volunteer organisations are active in it, and a single institution mentions recovery work.

Perceived importance is high in all groups (Fig. 1). Institutions rate the importance of volunteers in disaster prevention at 4.1 out of 5 on average, and 29 of 35 (83%) call them very or extremely valuable. The public rates the importance of volunteers at 4.2 out of 5, with 84% giving a score of 4 or 5. At the same time, 8 of 10 volunteer organisations describe their role as “present, but underutilised”. Lower scores are concentrated among municipalities without experience of volunteers: the three institutions that were “not sure” report no or very limited cooperation, so perception is driven by direct experience. The three perspectives are compared in Tab. 2.

*Tab. 2 Role of volunteers from three perspectives*

| Aspect | Institutions (n = 35) | Volunteer organisations (n = 10) | General public (n = 103) |
|---|---|---|---|
| Value of volunteers | 83% very/extremely valuable | 8 of 10: present but underutilised | 84% rate importance 4–5 |
| Typical role | Evacuation, logistics, search and rescue | Fire and flood response, preparedness | Supply delivery (83%), evacuation (82%), first aid (69%) |
| Inclusion in planning | 17 use predefined roles in plans; 5 have no structure | 9 of 10 only partially included in emergency plans | Not asked |
| Training | 1 well-structured programme; 12 do not know | 2 of 10 without structured training; 7 train themselves | 99% say training is needed |
| Main gap | Equipment (66%), volunteers (49%), training (46%) | Legal obstacles (8), no material support (8) | Time (62%), information (50%) |

All three perspectives agree on the importance of volunteers, but the actual role is narrower than the perceived one: volunteers are used mainly as response labour, while their potential in prevention, recovery and planning is not fully exploited.

## 3.2. COOPERATION BETWEEN AUTHORITIES AND VOLUNTEERS

Cooperation is predominantly top-down (Fig. 2A). Of 35 institutions, 20 (57%) state that their own institution initiates cooperation, 7 (20%) that volunteer organisations do, 3 that national coordination does and 1 describes it as mutual; 4 state that nobody does or that they have no volunteers. Volunteer organisations confirm that cooperation depends on personal and local relationships: 9 of 10 report a dedicated contact point and 5 mention ad hoc on-site contact.

Coordination models are a mix of formal and informal arrangements. Institutions use predefined roles in emergency plans (17; Fig. 2B), volunteer liaison officers (5) and central coordination (5), while 6 rely on ad hoc coordination and 5 have no structured coordination. The telephone is the dominant communication channel (Fig. 2C): 31 of 35 institutions (89%), followed by e-mail (12), messaging applications (11) and radio

systems (3); neither institutions nor volunteer organisations mention a shared digital platform. The low use of radio is notable for disaster settings where mobile networks may fail.

Among the 28 institutions that cooperate with volunteers (Fig. 2D), coordination is rated 4.1 out of 5 on average, with 23 (82%) giving a score of 4 or 5; including those without cooperation the mean is 3.7. Volunteer organisations are more reserved: 7 of 10 describe the relationship as positive or functional, but they cite legal and administrative obstacles (8), lack of material support (8), poor communication (6) and lack of formal recognition (6) as the main difficulties (Fig. 2E). Cooperation therefore works well where it already exists, while the legal and financial framework is a hidden source of friction that institutions tend to underestimate.

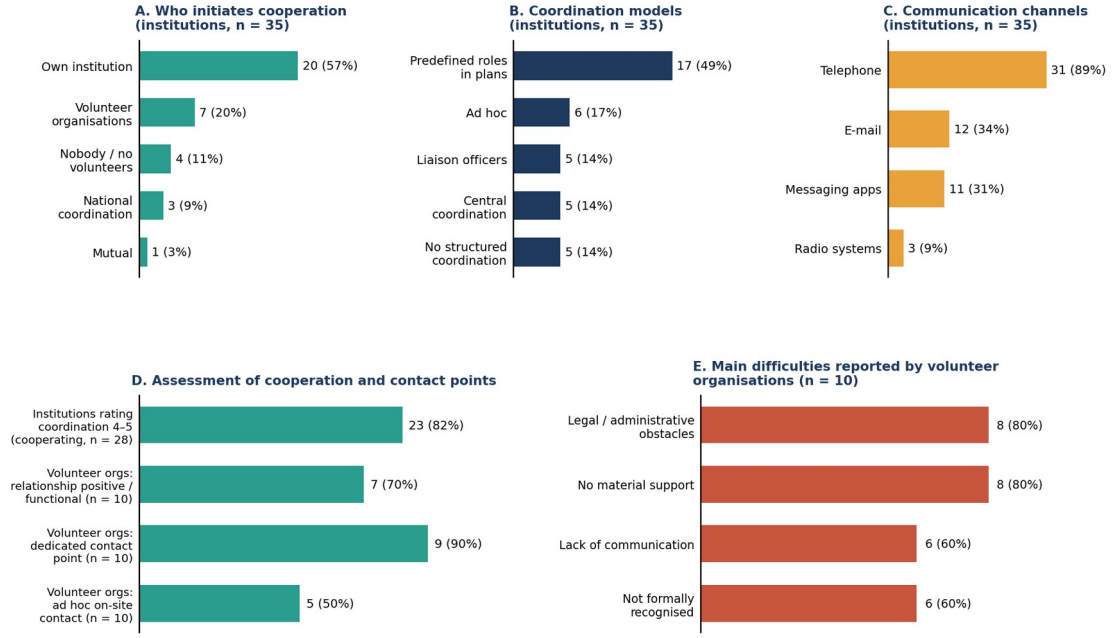


*Fig. 2 Cooperation between authorities and volunteers: (A) initiation, (B) coordination models, (C) communication channels, (D) assessment and contact points, (E) difficulties reported by volunteer organisations*

## 3.3. TRAINING AND FUNDING

Structured training is the weakest element of the system (Fig. 3). Among 35 institutions, only one reports a well-structured volunteer training programme, 9 describe irregular or partial training, 4 minimum training, 9 report none and 12 do not know. Training content is narrow and basic: first aid (24 of 35, 69%), fire safety (16), flood response (13), search and rescue (11) and psychological first aid (7). Logistics, crowd management, risk communication and incident command are not mentioned in any response, although logistics and supply are among the most frequent tasks assigned to volunteers.

The provider landscape is fragmented: training is provided by local authorities, NGOs or volunteer organisations, the Civil Protection Agency or Ministry of Interior structures, national government and the Red Cross, whereas 7 of 10 volunteer organisations train through their own resources. Funding is equally limited: only one institution (3%) reports sufficient funding, 14 (40%) report funding that is not enough, 9 (26%) have no dedicated funding and 11 (31%) do not know. Nine of 10 volunteer organisations consider their financial resources insufficient, and they rely mainly on municipal budgets and private donations.

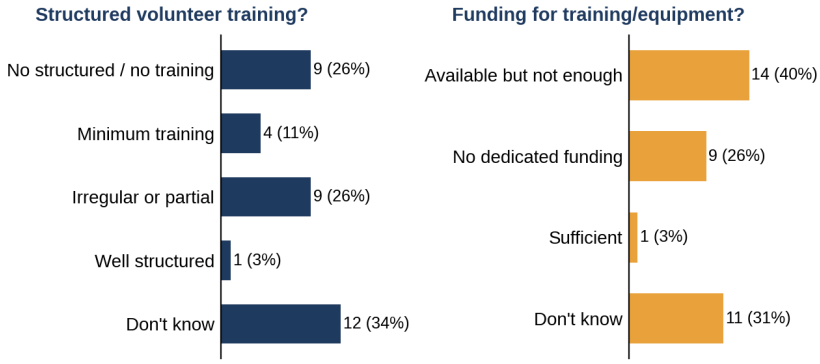


*Fig. 3 Availability of structured volunteer training and of funding (institutions, n = 35)*

## 3.4. CHALLENGES AND BARRIERS

Resource limitations dominate the institutional perspective: lack of equipment (23, 66%), lack of volunteers (17, 49%) and lack of training (16, 46%). Legal barriers follow, with a weak legal framework (12, 34%) and no insurance (8, 23%), while coordination and communication problems are rarely mentioned by institutions (3 respondents) but are reported by 6 of 10 volunteer organisations as lack of communication with authorities. 6 of 10 volunteer organisations report difficulties in recruiting, and 6 of 10 have only 10–25 active volunteers, so even a few departures affect their operational capacity.

## 3.5. PUBLIC PERCEPTION AND MOTIVATION

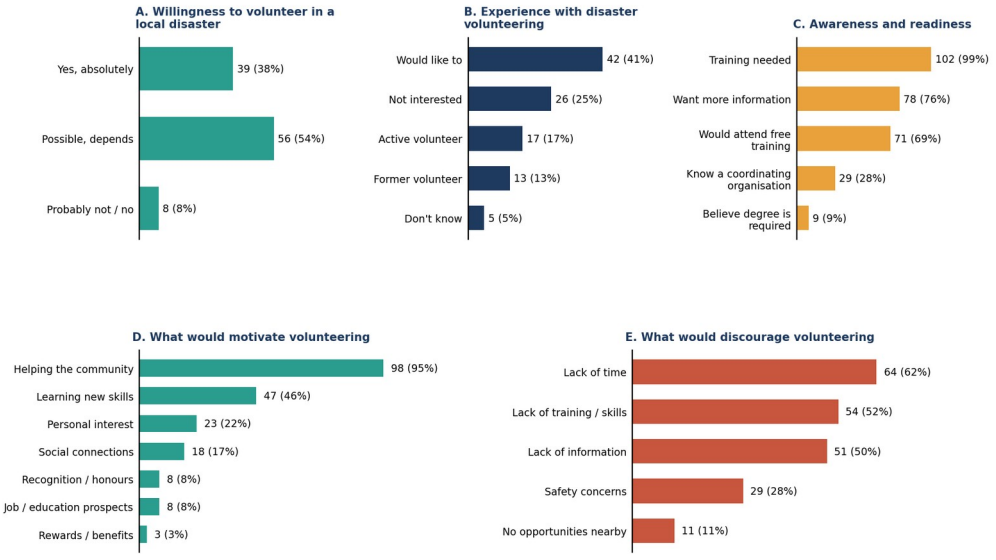


*Fig. 4 Public perception of volunteering: (A) willingness, (B) experience, (C) awareness and readiness, (D) motivating and (E) discouraging factors (general public, n = 103, multiple answers in C–E)*

Public awareness is broad but shallow. Self-rated understanding of what disaster volunteers do averages 3.2 out of 5, only 29 of 103 respondents (28%) know an organisation that coordinates disaster volunteers, and 9 (9%) wrongly believe that a bachelor's degree is required. Nearly all respondents (102) think volunteers need training. Willingness to volunteer in a local disaster is high but conditional (Fig. 4A): 39 (38%) would "absolutely" volunteer, 56 (54%) "depending on the situation" and 8 (8%) probably not. Among the respondents, 30 (29%) have volunteered in civil protection or disasters (17 are currently active and 13 are former volunteers), 42 (41%) have not but

would like to, and 26 (25%) are not interested, while 5 (5%) answered “don’t know” (Fig. 4B). Readiness to learn is strong (Fig. 4C): 71 (69%) would attend a free training and 78 (76%) want more information.

Helping the community is by far the strongest motivation (98 respondents, 95%), followed by learning new skills (47, 46%), while material incentives play a minor role (Fig. 4D). The main barriers (Fig. 4E) are lack of time (64, 62%), lack of training or skills (54, 52%) and lack of information on how to get involved (51, 50%); safety concerns are mentioned by 29 (28%). The gap between willingness (92%), prior participation (29%) and awareness of organisations (28%) is the main recruitment opportunity, and the three leading barriers can be addressed by the system itself through information, accessible training and flexible short-term roles.

## 3.6. YOUTH ENGAGEMENT

Because no youth volunteer questionnaire was returned from Serbia, youth engagement is analysed through proxy indicators from the public survey, in which 20 respondents are aged 18–24 and 21 are aged 25–34; the findings are indicative only (Fig. 5). Only 2 of 20 respondents aged 18–24 (10%) are active volunteers, compared with 21% among those aged 35 and above, and 8 of 20 (40%) are not interested in volunteering, compared with 23% of the older group. Only 15% of the youngest group would “definitely” volunteer in a local disaster (48% among those aged 35+). Among respondents under 35, 3 are active volunteers while 20 would like to volunteer, i.e. roughly seven potential volunteers for every active one.

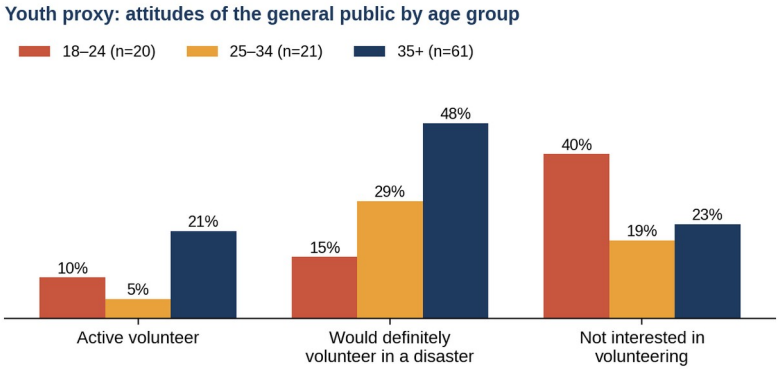


*Fig. 5 Proxy indicators by age group (general public, n = 103)*

Young people are motivated mainly by purpose and skills: 100% of those aged 18–24 are motivated by helping the community and 70% by learning new skills (46% overall), and 60% would probably attend a free training. Their barriers are lack of time (50%), lack of training or skills (55%) and lack of information (55%), with safety concerns more frequent (40%) than overall (28%). Only 3 of 20 (15%) know a disaster-volunteer organisation in their area, against 33% of those aged 35+. Organisations that train weekly or monthly report fewer recruitment difficulties (2 of 5) than those that train rarely or not at all (4 of 5); the numbers are small, but consistent with the view that training capacity supports retention.

## 4. DISCUSSION

The results show that interest is not the main problem; access is. Institutions and citizens value volunteers, and willingness to help is high, but the pathway from willingness to organised, trained and legally protected participation is weak: neither the public nor the

youngest respondents know where to join, and institutions do not report recruitment channels through schools or universities.

Legal status is a binding constraint. All 10 volunteer organisations state that they are legally registered and recognised as legal entities, yet 6 of 10 cite lack of formal recognition as a main challenge. Legal registration only establishes an organisation as a legal entity, whereas formal recognition means a defined role within the DRM system, i.e. inclusion in protection-and-rescue plans, official activation and access to training, insurance and funding. Registered organisations may therefore still be engaged only ad hoc, through personal contacts.

Three good practices were named by the 11 institutions that described a successful model. The Hungarian Firefighters' Association has trained Hungarian-speaking volunteer firefighters in Vojvodina in their mother tongue for 12 years, removing a language barrier and providing a ready-made model for cross-border exchange. The municipalities of the West Morava basin have an agreement on cooperation in risk management, and Kraljevo has involved citizens' associations in local risk assessment. The Municipality of Raška funded the training of its volunteer fire department, while the Red Cross provides an established structure for training, insurance and coordination. Cross-border interest is considerable: 18 of 35 institutions (51%) would support cross-border volunteer cooperation, 15 (43%) answer "maybe" and 7 of 10 volunteer organisations are very interested, but legal and administrative obstacles, insurance, language and lack of information remain barriers.

## 5. CONCLUSION

Volunteers in Serbia are a trusted, locally rooted resource in disaster management, provided mainly by volunteer fire departments, Red Cross and OTIS, and the public is willing to help. Institutions and citizens agree on their importance (83% and 84%), but volunteers are used mainly for emergency response, and they depend on municipal budgets, donations and personal contacts.

The findings are based on small, self-selected samples dominated by municipal administrations and urban citizens, and no youth volunteers responded. Future work should therefore collect youth responses through volunteer fire departments, the Red Cross, mountain rescue and student organisations, and compare the Serbian results with those of the other Danube Region countries participating in InDiMand.

### ACKNOWLEDGEMENT

The research has been conducted within the project "Enhancement of teaching and scientific research capacities through the application of modern technologies in the fields of civil engineering, geodesy, and disaster risk management and fire safety", developed at the Department of Civil Engineering and Geodesy, Faculty of Technical Sciences, University of Novi Sad, Serbia.

## REFERENCES

[1] Law on Disaster Risk Reduction and Emergency Management (2018). *Official Gazette of the Republic of Serbia*, No. 87/2018.

[2] European Commission (2019). *EU Civil Protection Mechanism Peer Review Programme: Serbia*, Review report.

[3] Law on Volunteering (2010). *Official Gazette of the Republic of Serbia*, No. 36/2010.

[4] Law on Youth (2011). *Official Gazette of the Republic of Serbia*, No. 50/2011.

[5] Government of the Republic of Serbia (2023). Youth Strategy in the Republic of Serbia for the Period from 2023 to 2030.

https://doi.org/10.24867/INDIS-2026-EN-963



# INTEGRATION OF KNOWLEDGE MANAGEMENT AND LEAN SIX SIGMA METHODOLOGY IN THE FUNCTION OF CONTINUOUS IMPROVEMENT OF FIRE SAFETY

*Dragan Hristovski*[1], *Vesna Nikolić*[2]

***Summary***

This paper examines the integration of Knowledge Management and Lean Six Sigma methodologies to improve fire safety performance in organizational settings. Fire safety remains a key component of occupational health and risk management, requiring systematic approaches to minimize hazards, improve response efficiency, and ensure regulatory compliance. The study explores how Knowledge Management facilitates the identification, creation, sharing, and application of critical safety knowledge, while Six Sigma provides a data-driven framework for optimizing processes and reducing deficiencies in fire prevention and response systems. A conceptual model is developed to demonstrate the synergistic relationship between Knowledge Management practices and the DMAIC (Define-Measure-Analyze-Improve-Control) cycle of Six Sigma in the context of fire safety. Furthermore, the combined approach supports a proactive safety culture by promoting knowledge sharing and evidence-based decision-making.

*Keywords: Fire Safety, Knowledge Management, Lean Six Sigma, Safety Culture*

# INTEGRACIJA UPRAVLJANJA ZNANJEM I METODOLOGIJE LEAN SIX SIGMA U FUNKCIJI KONTINUIRANOG UNAPREĐENJA ZAŠTITE OD POŽARA

***Rezime***

Ovaj rad ispituje integraciju metodologija upravljanja znanjem i Lean Six Sigma radi poboljšanja učinka zaštite od požara u organizacionim okruženjima. Zaštita od požara ostaje ključna komponenta zdravlja i upravljanja rizicima na radu, zahtevajući sistematske pristupe za minimiziranje opasnosti, poboljšanje efikasnosti reagovanja i osiguravanje usklađenosti sa propisima. Studija istražuje kako upravljanje znanjem olakšava identifikaciju, kreiranje, deljenje i primenu kritičnog znanja o bezbednosti, dok Lean Six Sigma pruža okvir zasnovan na podacima za optimizaciju procesa i smanjenje nedostataka u sistemima za sprečavanje i reagovanje na požare. Razvijen je konceptualni model kako bi se demonstrirao sinergijski odnos između praksi upravljanje znanjem i DMAIC (Definiši-Meri-Analiziraj-Poboljšaj-Kontroliši) ciklusa Six Sigma u kontekstu zaštite od požara. Štaviše, kombinovani pristup podržava proaktivnu kulturu bezbednosti promovišući razmenu znanja i donošenje odluka zasnovanih na dokazima.

*Ključne reči: Zaštita od požara, Upravljanje znanjem, Lean Six Sigma , Kultura bezbednosti*

[1] MSc, PhD student, University of Nis, Faculty of Occupational Safety, R.N.Macedonia, vestak.hristovski@gmail.com, ORCID 0009-0002-2680-4405
[2] Full Prof., Faculty of Occupational Safety, University of Niš, Niš, Serbia, vesna.nikolic@znrfak.ni.ac.rs, ORCID 0000-0002-9163-7116

## 1. INTRODUCTION

Lean principles, originally developed within the Toyota Production System to enhance operational efficiency through cost reduction and productivity improvement, have evolved beyond their traditional characterization as purely manufacturing-oriented strategies. Increasingly, these principles are recognized for their significant contributions to occupational safety and health. In this context, lean safety is a structured, systematic approach to eliminating process inefficiencies and non-value-adding activities that risk worker safety and well-being.

A range of lean tools, including 6S, 5 Whys, Total Productive Maintenance (TPM), Kaizen, Poka-Yoke, Kanban, Value Stream Mapping (VSM) or Process Mapping (PM), Computerized Maintenance Management Systems (CMMS), and Failure Mode and Effects Analysis, are extensively employed within maintenance management frameworks to enhance both operational reliability and safety performance. Among these tools, the 6S methodology is particularly instrumental in promoting workplace safety. By incorporating the practices of Sort, Straighten, Shine, Standardize, and Sustain, augmented by an explicit focus on safety, the 6S system facilitates the creation of an orderly, clean, and well-regulated work environment. Such a structured organization, combined with the elimination of waste and the integration of safety-conscious design, significantly reduces the probability of workplace incidents, including fire-related hazards [1].

Given the inherent complexity of this philosophy, it is essential to rationalize and selectively identify the tools and techniques to be incorporated into the Knowledge Base system at subsequent stages. Particular emphasis is placed on critical enablers such as leadership styles, organizational culture, management commitment, and the strategic alignment of Lean Six Sigma with overarching business objectives. Conversely, the primary barriers to effective implementation are associated with deficiencies in top management engagement, inadequate training, suboptimal project selection, and insufficient allocation of resources.

A novel, generalized conceptual model is proposed for Knowledge-Based Lean Six Sigma, addressing a notable gap in the literature, as no existing framework adequately examines the application of Lean Six Sigma within sustainable building maintenance supported by knowledge management capabilities. The model is structured into three principal phases: Planning, Designing, and Implementation. The Planning and Designing phases collectively establish the strategic dimension of the framework, whereas the Implementation phase operationalizes these strategies at the execution level. Accordingly, the Planning phase serves as the foundational stage, encompassing the definition of the organizational profile, current operational status, and overarching financial and market positioning [2].

Seven principal categories of waste are commonly identified within production and construction environments: Delays, Defects, Unnecessary human motion, Excessive transportation, Surplus inventory, Overproduction, and Inefficiencies associated with the delivery of equipment and materials. To address these inefficiencies, a structured framework has been developed based on Lean Six Sigma principles, aimed at systematically minimizing waste across construction projects. This framework further integrates Lean Six Sigma methodologies with the requirements of ISO 9001 within the DMAIC phases, thereby ensuring a comprehensive, quality-driven approach to process optimization and continuous improvement.

## 2. METHODS

Inadequate safety management systems and deficient housekeeping practices are significant contributing factors to fire incidents [3]. Standardization efforts have significantly contributed to the improvement of the safety system, primarily from the perspective of manageability, clearly defined requirements and integration capabilities [4], but this also leads to various challenges that organizations face when introducing and improving them [5].

The integration of Lean principles with Occupational Safety and Health (OSH) presents a significant challenge, as these paradigms are founded on distinct, and at times competing, objectives. Lean emphasizes eliminating waste within systems, whereas safety management prioritizes reducing risk. A range of Six Sigma tools—such as DMAIC, represented in Table 1, cause-and-effect (fishbone) diagrams, and Failure Mode and Effects Analysis—in conjunction with Lean techniques such as Value Stream Mapping, can be effectively applied to identify, assess, and mitigate risks associated with workplace hazards, including fire incidents, falls, and electrical exposures [6].

*Tab. 1 Six Sigma DMAIC approach*

| | | | |
|---|---|---|---|
| D | Define | Clarify the problem, project goals and customer requirements | Project Charter<br>Problem and goal statements<br>Voice of the Customer (VOC)<br>Suppliers, Inputs, Process, Outputs, Customers (SIPOC) diagram |
| M | Measure | Quantify the current performance | Process Mapping<br>Measurement Systems Analysis (MSA)<br>Mapping the current process in detail<br>Histograms and Frequency Plots |
| A | Analyze | Identify root causes of defects and variation | Fishbone diagrams<br>Pareto Chart<br>5 Whys investigations<br>Hypothesis Testing |
| I | Improvement | Implement and test solutions | Brainstorming and evaluating improvement ideas<br>Failure Mode and Effects Analysis (FMEA)<br>Control Charts<br>Performing Risk Assessments |
| C | Control | Sustain the results and prevent regression | Standard Operating Procedures (SOPs)<br>5S Methodology<br>Developing monitoring dashboards or scorecards<br>Using control charts to track performance |

The fundamental premise of cause-and-effect analysis lies in the systematic identification of sources of variation within a process. To support this analysis, potential causes are typically organized into principal categories—human factors, measurement systems, environmental conditions, methods, materials, and machinery—enabling a structured examination of the underlying drivers of variability, as shown in Figure 1.

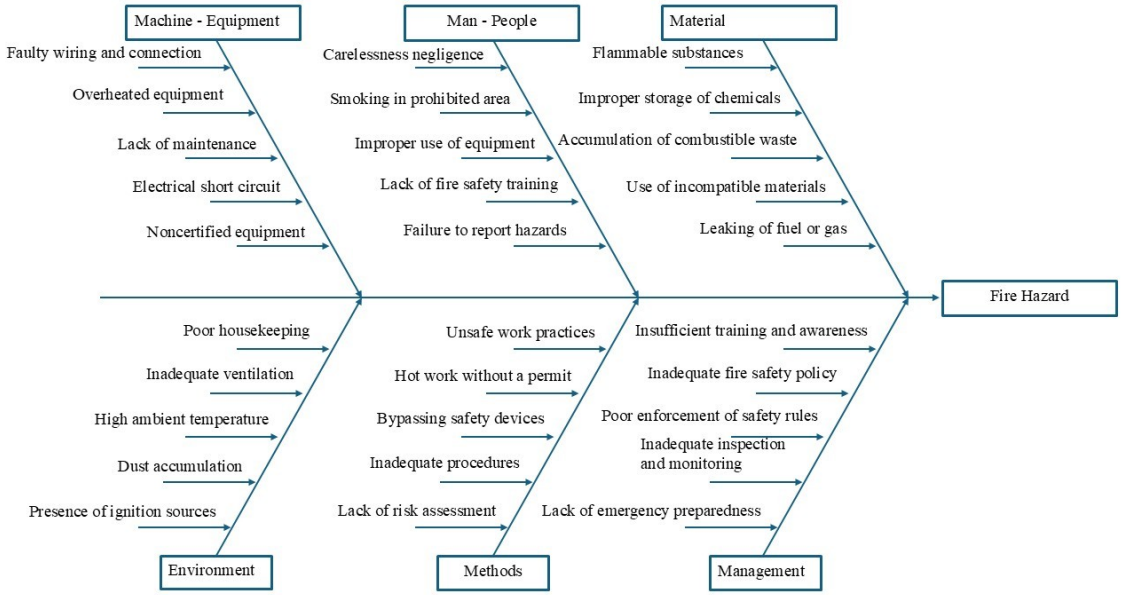


*Fig.1 Causes and effects diagram of fire hazard*

The implementation of the 5S across various operational areas yielded multiple significant benefits, including a reduction in workplace accidents and errors, improved process flow, and more efficient utilization of space. Most notably, it contributed to a substantial enhancement of overall employee safety [6].
Risk management is a systematic process for identifying, evaluating, and prioritizing risks across various domains to support informed decision-making and effective control measures. In this context, Six Sigma aligns closely with risk management principles, incorporating structured methodologies to minimize variability, reduce defects, and mitigate potential process-related risks [7].

## 3. RESULTS AND DISCUSSION

### 3.1. FIRE SAFETY MANAGEMENT IN HIGH-RISE BUILDINGS

Fire may be defined as an uncontrolled combustion process occurring in time and space, characterized by the release of heat and energy, which can potentially lead to significant damage or disaster if not properly contained [8], while Fire safety is defined as a coordinated set of practices aimed at preventing the occurrence of fire, controlling its development and consequences in the event of accidental or intentional ignition, and limiting associated losses to an acceptable level [9], [10].
The field of fire protection engineering is typically founded on five core elements that together form the basis of an effective fire safety framework**:** Building Materials**,** Design**,** Water Supply**,** Fire Extinguishing Systems, Automatic Sprinkler Systems**,** Special Occupancies and Hazards [11].
Integrated approaches to fire preparedness and response, alongside the systematic identification of fire causation factors and the development of long-term sustainable mitigation strategies, have been formulated through consideration of the five core components of fire management [12].
Construction firms should prioritize fire safety as a fundamental organizational objective and cultivate a safety-oriented culture in which all employees consistently recognize fire prevention and control as a critical priority. Fire prevention planning,

encompassing the formulation of a formal Fire Safety Plan, should be fully developed and finalized before the initiation of project activities [13].
Safety planning encompasses the explicit anticipation and preparation of response measures in the event of an accident. In this context, it is essential that such planning incorporates provisions for fire emergencies as well as structured evacuation procedures, ensuring an organized and effective response to potential incidents [14] and the plan should ensure strict compliance with applicable regulatory codes and standards while minimizing the potential risk of fire ignition across all areas of the building [3].

## 3.2. FIRE SAFETY CONCEPTS

A fire safety management program should be grounded in well-established fire safety principles as presented in Figure 2. The systematic and coherent application of these concepts represents the most effective approach to developing a fire safety management system that is both efficient and economically viable.

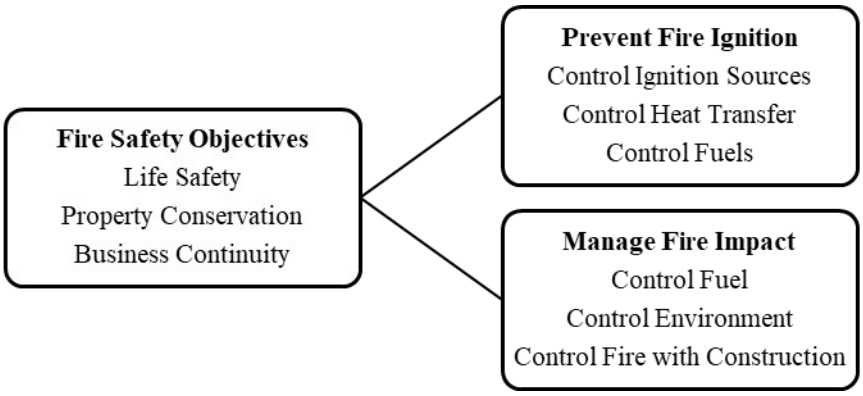


*Fig. 2 An overview of the Fire Safety Concepts Tree*

### 3.2.1. Understanding the Risk and Hazards

The existence of flammable and combustible materials within work environments necessitates the strict prioritization and implementation of effective fire protection strategies. Considering the substantial number of individuals potentially exposed to fire-related hazards, it is essential to establish comprehensive fire safety procedures alongside appropriate protective systems. The principal aim is not only to minimize the likelihood of fire occurrence but also to ensure the safe and efficient evacuation of occupants in the event of an emergency. Furthermore, all employees should actively participate in the ongoing identification, assessment, and management of fire-related hazards, with particular emphasis placed on maintaining adequate separation between potential ignition sources and combustible materials in order to reduce the risk of fire incidents [15].
Residential, occupational, and environmental fires, including bushfires, are frequently associated with severe and often fatal burn injuries. In addition to physical harm, such incidents commonly result in substantial property damage, significant psychological trauma, and, in many cases, loss of life. Although fire safety training initiatives are widely available, existing reports continue to highlight persistent deficiencies in fire safety knowledge, delayed recognition of fire-related threats, and slower evacuation responses within the general population, particularly among younger and older demographic groups [16].

The fire management plan defines the systematic approach through which fire safety is addressed and provides the operational framework by which the building owner manages fire safety throughout the premises. This framework incorporates planning activities, emergency response protocols, and maintenance procedures aimed at ensuring continuous fire protection. In addition, the plan outlines the organizational structure of the personnel responsible for its implementation, clearly specifying their respective roles, functions, and responsibilities. Moreover, the adoption of effective housekeeping practices plays a critical role in minimizing the risk of fire incidents. Consequently, management must ensure that the accumulation of waste materials, as well as the unauthorized storage or stacking of combustible substances, is strictly controlled and prevented, since such conditions may compromise both the safety standards and the operational functionality of the building [17].

### 3.2.2. Importance of Fire Safety Training

Fire prevention and control frameworks emphasize the critical importance of fire safety knowledge in enabling community participation in both fire prevention and emergency preparedness. Accordingly, it is essential that communities are provided with appropriate training to ensure the maintenance of an adequate and sustained level of fire safety awareness. Furthermore, it is equally important that individuals retain sufficient understanding of the necessity to properly maintain functional fire safety equipment, as this directly contributes to effective risk reduction and emergency response capability. In addition to knowledge acquisition, behavioural modification is equally essential in enhancing fire prevention and preparedness. Fire emergencies are inherently highly stressful events, as they typically occur without warning, escalate rapidly, and demand immediate and effective response actions [16].

Fire safety training shall constitute an ongoing and systematic process, initiated from the first day of employment for new staff members and contractors, and sustained through the provision of regular refresher programmes [17]. As with all forms of training, the scope and depth of fire safety instruction are contingent upon the individual’s role and responsibilities, the specific nature of the fire hazards and associated risks, the type of work undertaken, and the characteristics of the working environment. Accordingly, a comprehensive training needs analysis is essential to accurately determine the specific competencies, knowledge areas, and skill sets that must be developed to meet organisational and operational requirements [18].

### 3.2.3. Safety Culture

The concept of “safety culture” within an organisation refers to the collective attitudes, values, and beliefs that shape its approach to safety performance. It is important to acknowledge that the safety culture of a company is largely influenced by the overarching organisational culture in which it operates. This prevailing cultural framework significantly affects the effectiveness of all safety-related functions, including the management and control of fire safety matters [18].

The “fire triangle” provides a simplified conceptual model illustrating the three essential elements required for the initiation and sustained combustion of a fire, as is shown in Figure 3.

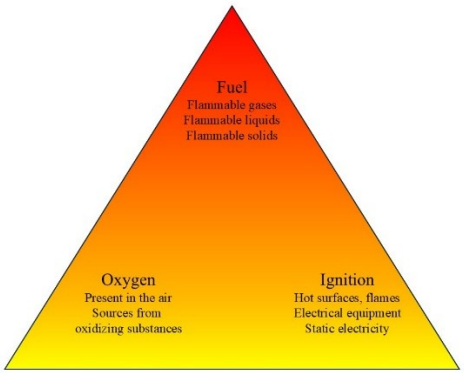


*Fig. 3 Triangle of fire*

## 3.3. KNOWLEDGE MANAGEMENT

Knowledge Management may be defined as a deliberate strategic approach to activating both tacit and explicit knowledge through the creation of enabling contexts, organizational infrastructures, and iterative learning cycles that facilitate access to and utilization of an organization's collective intellectual resources. In practice, many organizations incorporate several stages from the "Road Map to Knowledge Management Results: Stages of Implementation" into their Six Sigma frameworks as well, including the formulation of key strategic directions, the design and implementation of initiatives, and the validation of pilot projects to ensure scalability and the effective institutionalization of processes, presented in Figure 4.

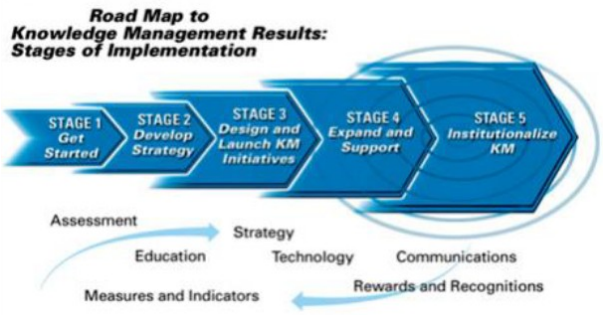


*Fig. 4 Roadmap to Knowledge Management*

Knowledge Management plays a pivotal role in modern knowledge-driven information societies. The integration of Six Sigma methodologies with Knowledge Management principles has the capacity to establish a highly effective and comprehensive managerial framework. In this context, Knowledge-Based Six Sigma (KBSS), representing the convergence of Six Sigma practices and Knowledge Management strategies, is proposed as a strategic approach capable of improving organizational performance through the systematic generation, utilization, and management of organizational knowledge. Knowledge-Based Six Sigma (KBSS) can be conceptualized as an organization-wide management strategy directed toward achieving process quality innovation in accordance with Six Sigma performance standards, while concurrently increasing customer satisfaction. This objective is realized through the structured creation, storage, sharing, and application of knowledge, supported by advanced information technologies, including internet and intranet systems, databases, and other digital communication platforms [19].

Knowledge management represents a systematic organizational approach to the identification, structuring, storage, and dissemination of knowledge across all levels of an enterprise. Through the effective reuse of knowledge assets and the application of established best practices, organizations can enhance operational efficiency, accelerate workflows, and reduce costs associated with repetitive data reprocessing across projects. The transition from the Information Revolution to the Knowledge Revolution is marked by increasing emphasis on structured methodologies alongside information analysis as a foundational basis for decision-making. In this context, Six Sigma aligns with the conceptual framework of Knowledge Management, broadly understood as a process that enhances organizational activities by improving information use and strengthening accountability in decision-making [20].

Continuous training and regular drills are essential to ensure that fire safety knowledge remains salient among personnel on-site, while also providing opportunities to gather feedback for ongoing improvement [13].

Knowledge of the firefighting resources available within one's operational control constitutes a critical factor in determining whether a fire of a given magnitude can be effectively contained with minimal damage or whether it may escalate into a large-scale catastrophic event [21].

## 3.4. KNOWLEDGE MANAGEMENT AND SIX SIGMA

Six Sigma promotes a rigorous and systematic problem-solving methodology designed to support effective project implementation and continuous process improvement. This methodology is structured around the five sequential phases represented by the DMAIC framework, as shown below [22].

D - Define – Knowledge Audit-Identify the fire safety problem and project goals
M - Measure – Actual Process-Collect data on current fire safety performance
A - Analyze – Collaboration-Determine the root causes of risks
I - Improve – Best Practice-Develop and implement solutions to mitigate risks
C - Control – Sustainable Knowledge-Ensure the improvements are sustained

The integration of Knowledge Management (KM) and Six Sigma establishes a proactive, data-driven framework for fire safety management, facilitating a transition from reactive incident response to the systematic prevention of fire-related events. Within this integrated approach, Six Sigma provides a structured, methodical framework to minimize process variability, particularly in areas such as inspections, compliance monitoring, and emergency response. Concurrently, Knowledge Management ensures that tacit and explicit experiential knowledge, including lessons learned from past incidents and operations, is effectively captured, documented, and disseminated across the organization. This synergy enhances organizational learning and supports the sustained improvement of fire safety performance over time [23].

## 3.5. CONNECTING HIGH-RISE FIRE SAFETY TO KNOWLEDGE MANAGEMENT AND LEAN SIX SIGMA

Anomalies that occur during operations, such as false alarms or routine fire drills, are used as critical mechanisms for organizational learning. Rather than being treated as isolated incidents, these events are used as learning points for continuous improvement and optimization of the organization's fire safety knowledge base.

Value Stream Mapping (VSM) is used to systematically visualize and analyze process flows. This process facilitates the identification and elimination of operational waste, such as delays in alarm verification protocols.

The structural reliability of critical life safety systems is optimized through the application of the DMAIC (Define, Measure, Analyze, Improve, Control) framework. This approach aims to minimize variation and mitigate system failures within fire and smoke control mechanisms.

## 4. CONCLUSION

The integration of Knowledge Management (KM) and Lean Six Sigma methodology constitutes a robust and synergistic framework for advancing the continuous improvement of fire safety systems. By systematically capturing, structuring, and disseminating organizational knowledge, Knowledge Management enhances the data-driven rigor of Six Sigma, enabling more precise identification of fire-related risks, root causes, and process inefficiencies. In turn, Six Sigma provides Knowledge Management with a disciplined, analytical structure—through DMAIC (Define, Measure, Analyze, Improve, Control)—that transforms tacit and explicit knowledge into actionable safety interventions.

This integrated approach not only strengthens organizational learning but also fosters a proactive safety culture grounded in evidence-based decision-making. It ensures that lessons learned from past incidents, near-misses, and operational audits are continuously embedded into safety protocols, training programs, and preventive strategies. Consequently, fire safety management evolves from a reactive compliance function to a dynamic, innovation-driven system characterized by reduced variability, enhanced reliability, and sustained risk mitigation.

Furthermore, the convergence of Knowledge Management and Six Sigma supports scalability and adaptability across diverse organizational contexts, allowing continuous refinement of fire safety practices in response to emerging hazards, technological advancements, and regulatory changes. However, the successful implementation of this integration depends on strong leadership commitment, cross-functional collaboration, and the development of a knowledge-sharing culture supported by appropriate digital infrastructures.

The fusion of Knowledge Management and Six Sigma represents a strategic pathway toward achieving operational excellence in fire safety. It enables organizations to institutionalize continuous improvement, minimize fire-related risks, and enhance overall resilience, thereby contributing to safer workplaces and sustainable organizational performance.

Preserving lessons learned from critical events, so that the safety of the entire sector is not left in limbo in the event that an employee retires or transfers to another organizational department.

**ACKNOWLEDGEMENT**

This paper is the result of research funded by the Ministry of Science, Technological Development and Innovation of the Republic of Serbia, Contract No. 451-03-34/2026-03/200148.

## 5. REFERENCES

[1] Salman S. R., Suhaimi N.S., Phuspa S. M, Rahmawati S, Ramli A. (2025). Integrating Lean Principles in Fire Safety Engineering for Private Al-Quran Memorization (Tahfiz) School Buildings: A Conceptual Framework. Universiti Malaysia Pahang Al-Sultan Abdullah Publishing, Vol 5, pp. 106–112. https://doi.org/10.15282/construction.v5i1.11929.

[2] Aldairi JS., Khan MK., Munive JE. (2015). A Conceptual Model for a Hybrid Knowledge-based Lean Six Sigma Maintenance System for Sustainable Buildings. Proceedings of The World Congress on Engineering 2015, pp. 939-944. https://www.iaeng.org/publication/WCE2015/WCE2015_pp939-944.pdf.

[3] Hassanain M. A., Aljuhani M., Hamida, M. B., Salaheldin, M. H. (2022). A Framework for Fire Safety Management in School Facilities. https://doi.org/10.11113/ijbes.v9.n2.901.

[4] Mušicki S., Janaćković G., Vasović D. (2021). Occupational safety and health management system standardization challenges. Proceedings of the 12th International DQM conference on life cycle engineering and management (ICDQM-2021), June 24-25, Prijevor, Serbia, pp. 214-219.

[5] Mušicki S., Janaćković G., Vasović D. (2021). OHS management: development perspectives defined by ISO 45000 series of standards. Proceedings of the XI International Symposium Engineering management and Competitiveness 2021 (EMC 2021), 18-19th June, Zrenjanin, Serbia, pp. 102-107.

[6] Alharthi A. (2015). An Integration of Lean Six Sigma and Health and Safety Management System in Saudi Broadcasting Corporation. A thesis Submitted for the degree of Doctor of Philosophy, Brunel University, London. https://www.academia.edu/66920457/An_integration_of_Lean_Six_Sigma_and_Health_and_Safety_Management_System_in_Saudi_Broadcasting_Corporation, (06.04.2026).

[7] Alharthi A., Sharaf M., Aziz T. (2014). An integrated approach Lean Six Sigma & Risk Management in entertainment and media industry. Proceedings of the 2014 International Conference on Industrial Engineering and Operations Management, Bali, Indonesia, pp. 2917-2927.

[8] Lee P. H, Fu B, Cai W, Chen J, Yuan Z, Zhang L, Ying X. (2018). The effectiveness of an on-line training program for improving knowledge of fire prevention and evacuation of healthcare workers: A randomized controlled trial. https://doi.org/10.1371/journal.pone.0199747,

[9] Nimlyat P., Audu A., Ola-Adisa E., Gwatau D (2017). An evaluation of fire safety measures in high-rise buildings in Nigeria. Sustainable Cities and Society, pp. 774-785, https://doi.org/10.1016/j.scs.2017.08.035

[10] Kodur V., Kumar P., Rafi M. M. (2020). Fire hazard in buildings: review, assessment and strategies for improving fire safety. An International Journal (2020) 4 (1): 1–23, https://doi.org/10.1108/PRR-12-2018-0033

[11] Guyer J. P., (2022). An Introduction to Fire Protection Engineering for Buildings. https://www.cedengineering.ca/userfiles/M03-010%20-%20An%20Introduction%20to%20Fire%20Protection%20Engineering%20for%20Buildings.pdf

[12] Beard N.A. (1986). Towards a systemic approach to fire risk management. Fire Safety Science, pp. 943-952. https://doi.org/10.3801/IAFSS.FSS.1-943

[13] Garis L., Maxim P., Mark K. (2015). Construction Site Fire Safety: A Guide for Construction of Large Buildings. University of the Fraser Valley in British Columbia, https://www.ufv.ca/media/assets/cjsr/Guide-English.pdf

[14] Sears S. K, Sears A. G., Clough H. R. (2008). Construction Project Management. John Wiley & Sons, Inc., Hoboken, New Jersey,

[15] England P. (2020). Fire Precautions During Construction of Large Building. 2020 Forest and Wood Products Australia Limited, https://www.woodsolutions.com.au/sites/default/files/2025-10/WS%20TDG%2020%20-%20Fire%20Precautions%20During%20Construction%20of%20Large%20Buildings.pdf.

[16] Huseyin I., Satyen L., (2006). Fire safety training: Its importance in enhancing fire safety knowledge and response to fire. The Australian Journal of Emergency Management, Vol. 21 No. 4, November 2006, https://search.informit.org/doi/pdf/10.3316/informit.413111012978717,

[17] Yao H. (2014). Fire Safety Management Strategy of Complex Developments. 2014 Elsevier Ltd, Procedia Engineering, pp. 410-420.

[18] Furness A., Muckett M. (2007). Introduction to Fire Safety Management (1st edition). Elsevier, Burlington, MA.

[19] Pinjari H., Teli S. N. (2018). Integrated approach of Six Sigma and Knowledge Management. International Journal of Scientific and Engineering Research (Vol 9, 2018). https://www.researchgate.net/publication/322499522_Integrated_approach_of_Six_Sigma_and_Knowledge_Management.

[20] Jamil Y. M. (2017). Deploying Knowledge Management in DMAIC methodology of Six Sigma projects. 2nd World Conference on Technology, Innovation and Entrepreneurship, 2017, pp. 20-28. https://doi.org/10.17261/Pressacademia.2017.511,

[21] Della-Giustina E. D. (2014). Fire Safety Management Handbook. CRC Press Taylor & Francis Group, Boca Raton, Florida, 2014.

[22] Knop, K.: Using Six Sigma DMAIC Cycle to Improve Workplace Safety in the Company from Automotive Branch: A Case Study, Manufacturing Technology 2022, Vol. 22, No. 3, pp. 297–306. https://doi.org/10.21062/mft.2022.040

[23] Sholanke A. B., Ekhaese E. N., Ekundayo P. A. (2024). Users' Knowledge of Fire Safety Measures in Educational Environment: A Case Study of a College Building in Nigeria. International Journal of Safety and Security Engineering, Vol. 14, No. 1, 2024, pp. 135-143.

# REGISTER OF AUTHORS

Authors are listed alphabetically by surname, with the affiliation given in their paper, the full ORCID iD and the first page of each of their papers in these proceedings.


| Author | Affiliation | ORCID iD | Page |
|---|---|---|---|
| **Marin Allaraj** | Faculty of Civil Engineering, Polytechnic University of Tirana, Albania | – | 725 |
| **Mladen Amović** | Faculty of Architecture-Civil Engineering-Geodesy, University of Banja Luka, Banja Luka, Bosnia and Herzegovina | 0000-0002-5464-0148 | 772 |
| **Aleksandar Andonov Sarev** | GCM, Skopje, North Macedonia | 0009-0004-1533-684X | 504 |
| **Jelena M. Andrić** | European University Cyprus, Nanjing University of Posts and Telecommunications, Nanjing, China | 0000-0002-5343-799X | 471, 482 |
| **Boris Azinović** | Slovenian National Building and Civil Engineering Institute, Ljubljana, Slovenia | 0000-0002-1810-5957 | 264 |
| **Mirjana Bajić** | Real Estate Cadastre Office Zrenjanin, Republic Geodetic Authority, Serbia | – | 684 |
| **Mehmed Batilović** | Faculty of Technical Sciences, University of Novi Sad, Serbia | 0000-0001-5605-1112 | 737, 895, 923 |
| **Miralem Bećić** | Faculty of Technical Sciences, University of Novi Sad, Serbia | 0009-0000-2301-0621 | 603 |
| **Olivera Bedov** | Faculty of Technical Sciences, University of Novi Sad, Serbia | 0000-0001-8910-1630 | 332, 946 |
| **Teo Beker** | Chair of Data Science in Earth Observation, Technical University of Munich, Germany | 0000-0003-1907-4045 | 49 |
| **Pavel Benka** | University of Novi Sad, Faculty of Agriculture, Novi Sad, Serbia | 0000-0001-6229-5180 | 737 |
| **Eduart Bllloshmi** | Faculty of Civil Engineering, Polytechnic University of Tirana, Tirana, Albania | – | 753, 830, 842 |
| **Bogdan Bojović** | Faculty of Civil Engineering Subotica, University of Novi Sad, Subotica, Serbia | 0000-0002-1183-2596 | 695 |
| **Dragan Bojović** | Institute IMS, Belgrade, Serbia | 0000-0002-4900-6177 | 59, 70 |
| **Goran Bošković** | Faculty of Mechanical and Civil Engineering in Kraljevo, University of Kragujevac, Serbia | 0000-0002-4597-922X | 141 |
| **Anastasija Božić** | Faculty of Technical Sciences, University of Novi Sad, Serbia | 0009-0004-3350-9097 | 895 |
| **Ljubomir Budinski** | Faculty of Technical Sciences, University of Novi Sad, Serbia | 0000-0001-7816-0889 | 291, 356, 383 |
| **Željko Bugarinović** | Faculty of Technical Sciences, University of Novi Sad, Serbia | 0000-0002-7237-5130 | 737, 859 |
| **Vladimir Bulatović** | Faculty of Technical Sciences, University of Novi Sad, Serbia | 0000-0002-0772-5333 | 895, 910 |
| **Andrea Buntić** | Department of Geodesy and Geoinformatics, Faculty of Technical Sciences, University of Novi Sad, Serbia | – | 708 |
| **Martin Capuder** | Slovenian National Building and Civil Engineering Institute, Ljubljana, Slovenia | 0009-0002-6984-1804 | 264 |
| **Marina Carević Tomić** | Faculty of Technical Sciences, University of Novi Sad, Serbia | 0000-0003-0209-5747 | 640 |
| **Tomo Cerovšek** | University of Ljubljana, Slovenia | 0000-0003-0523-0473 | 36 |

| Author | Affiliation | ORCID iD | Page |
|---|---|---|---|
| **Meri Cvetkovska** | Ss. Cyril and Methodius University in Skopje, Faculty of Civil Engineering, Skopje, North Macedonia | 0000-0002-9155-6420 | 21, 190 |
| **Nikolina Ćirić Avramović** | Department of Civil Engineering and Geodesy, Faculty of Technical Sciences, University of Novi Sad, Serbia | 0000-0001-5740-0986 | 495, 519 |
| **Danijela Ćirić Lalić** | Faculty of Technical Sciences, University of Novi Sad, Serbia | 0000-0002-4834-6487 | 151 |
| **Marina Davidović Manojlović** | Faculty of Technical Sciences, University of Novi Sad, Serbia | 0000-0001-6736-0615 | 684, 910 |
| **Marija Delić** | Agencija za projektovanje i planiranje LLC, Nikšić, Montenegro | – | 708 |
| **Marijana Divljak** | Radio Television of Vojvodina, Novi Sad, Serbia | – | 538 |
| **Vesko Đorđević** | DT Mapping, Kraljevo, Serbia | 0009-0007-7524-683X | 674, 882 |
| **Radovan Đurović** | University of Montenegro, Faculty of Civil Engineering, Podgorica | – | 708, 753 |
| **Jovana Đurovski** | Faculty of Technical Sciences, University of Novi Sad, Serbia | 0009-0005-7635-0802 | 576 |
| **Ivan Dolibašić** | Tehničko veleučilište u Zagrebu, Zagreb, Hrvatska | – | 415 |
| **Suzana Draganić** | Faculty of Technical Sciences, University of Novi Sad, Serbia | 0000-0003-3803-3484 | 332, 946 |
| **Milan Draganović** | Faculty of Civil Engineering and Architecture, University of Niš, Niš, Serbia | 0009-0001-5907-9388 | 512 |
| **Miroslav Dramićanin** | Faculty of Technical Sciences, University of Novi Sad, Serbia | 0000-0002-9079-0864 | 324 |
| **Gojko Drljača** | Faculty of Civil Engineering, University of Montenegro, Podgorica, Montenegro | 0009-0006-5555-3456 | 91 |
| **Marijana Dukić Mijatović** | Faculty of Technical Sciences, University of Novi Sad, Serbia | 0000-0003-1327-0889 | 151 |
| **Igor Džolev** | Faculty of Technical Sciences, University of Novi Sad, Serbia | 0000-0002-7622-7936 | 229, 238, 276, 428, 956 |
| **Kemal Edip** | Ss. Cyril and Methodius University in Skopje, IZIIS, Skopje, North Macedonia | 0000-0003-3394-510X | 504 |
| **Hejing Feng** | Department of Civil Engineering, Xi'an Jiaotong-Liverpool University, Suzhou, China | – | 482 |
| **Boris Folic** | Innovation Center of the Faculty of Mechanical Engineering, Belgrade, Serbia | 0000-0003-2127-0264 | 70 |
| **Nikolina Gajić** | Faculty of Technical Sciences, University of Novi Sad, Serbia | 0009-0008-1989-3888 | 910 |
| **Jure Galić** | Tehničko veleučilište u Zagrebu, Zagreb, Hrvatska | 0009-0005-2737-2386 | 415 |
| **Jaka Gašper Pečnik** | Slovenian National Building and Civil Engineering Institute, Ljubljana, Slovenia | 0000-0002-8775-8230 | 264 |
| **Milan Gavrilović** | Faculty of Technical Sciences, University of Novi Sad, Serbia | 0000-0003-4671-7544 | 859, 867 |
| **Dalibor Gelo** | Zagreb University of Applied Sciences, Zagreb, Croatia | 0009-0008-5261-107X | 217 |
| **Goran Gorašević** | Faculty of Civil Engineering, University of Montenegro, Montenegro | 0009-0009-4675-8662 | 198 |
| **Miro Govedarica** | Faculty of Technical Sciences, University of Novi Sad, Serbia | 0000-0003-1698-0800 | 772, 859, 867, 923 |

| Author | Affiliation | ORCID iD | Page |
|---|---|---|---|
| **Danijela Gračanin** | Faculty of Technical Sciences, University of Novi Sad, Serbia | 0000-0002-2150-4852 | 151 |
| **Tatjana Grbić** | University of Novi Sad, Faculty of Technical Sciences, Department of Fundamentals Sciences, Novi Sad, Serbia | 0000-0002-4236-7164 | 161 |
| **Sanja Grekulović** | University of Belgrade, Faculty of Civil Engineering, Department of Geodesy and Geoinformatics, Belgrade, Serbia | 0000-0002-2533-1100 | 819 |
| **Nikola Grubić** | Faculty of Civil Engineering and Architecture, University of Niš, Niš, Serbia | – | 512 |
| **Dragan Hristovski** | University of Nis, Faculty of Occupational Safety, R.N.North Macedonia | 0009-0002-2680-4405 | 964 |
| **Biljana Ilić** | Institute IMS, Belgrade, Serbia | 0000-0003-0798-1748 | 276 |
| **Snežana Ilić** | Institute IMS, Belgrade, Serbia | 0000-0003-1641-2301 | 276 |
| **Strahinja Ilić** | Skill Inženjering, Podgorica, Montenegro | – | 198 |
| **Vasilije Ilić** | Dept. of Geodesy & Geoinformatics, Faculty of Civil Engineering Belgrade | 0009-0002-6717-952X | 783 |
| **Andrea Ivanišević** | Faculty of Technical Sciences, University of Novi Sad, Serbia | 0000-0003-3342-7257 | 151 |
| **Gordana Jakovljević** | Faculty of Architecture-Civil Engineering-Geodesy, University of Banja Luka, Banja Luka, Bosnia and Herzegovina | 0000-0003-2784-8370 | 772 |
| **Željko Jakšić** | Faculty of Technical Sciences, University of Novi Sad, Serbia | 0000-0003-3512-1227 | 527 |
| **Ksenija Janković** | IMS Institute, Belgrade, Serbia | 0000-0003-3744-3799 | 207 |
| **Goran Jeftenić** | Faculty of Technical Sciences, University of Novi Sad, Serbia | 0000-0001-5639-4406 | 291, 356, 372, 383 |
| **Milica Jovanoska-Mitrevska** | Ss. Cyril and Methodius University in Skopje, Faculty of Civil Engineering, Skopje, North Macedonia | 0009-0001-2273-5062 | 190 |
| **Đorđe Jovanović** | Faculty of Technical Sciences, University of Novi Sad, Serbia | 0000-0002-6741-0042 | 78 |
| **Dušan Jovanović** | Faculty of Technical Sciences, University of Novi Sad, Serbia | 0000-0001-6834-0376 | 867 |
| **Slobodan Jović** | Faculty of Technical Sciences, University of Novi Sad, Serbia | 0000-0003-2584-5010 | 548 |
| **Milan Jovin** | Department of Civil Engineering and Geodesy, Faculty of Technical Sciences, University of Novi Sad, Serbia | 0009-0004-4422-4230 | 161 |
| **Sofija Kekez-Baran** | Department of Building, Energy and Material Technology, UiT The Arctic University of Norway, Lodve Langes gate 2, Narvik, Norway | 0000-0003-3879-2560 | 310 |
| **Andrija Kljajić** | Geodetski biro Kljajic - GBK, Užice, Serbia | – | 923 |
| **Slobodan Kolaković** | Faculty of Technical Sciences, University of Novi Sad, Serbia | 0000-0002-9859-9669 | 291, 372, 383 |
| **Vladan Komatović** | DT Mapping, Kraljevo, Serbia | – | 674 |
| **Dragana Konstantinović** | Faculty of Technical Sciences, University of Novi Sad, Serbia | 0000-0003-3971-0678 | 548 |
| **Nataša Kopitović Vuković** | Faculty of Civil Engineering, University of Montenegro, Montenegro | 0000-0002-6152-4073 | 198 |

| Author | Affiliation | ORCID iD | Page |
|---|---|---|---|
| **Milena Krklješ** | Faculty of Technical Sciences, University of Novi Sad, Serbia | 0000-0003-4252-258X | 538 |
| **Đuro Krnić** | Faculty of Technical Sciences, University of Novi Sad, Serbia | 0000-0003-4481-3209 | 659, 910, 923 |
| **Sara Krsmanović** | Department of Civil Engineering and Geodesy, Faculty of Technical Sciences, University of Novi Sad, Serbia | 0009-0006-5650-877X | 441, 495, 519 |
| **Panta Krstić** | Department of Civil Engineering and Geodesy, Faculty of Technical Sciences, University of Novi Sad, Serbia | 0000-0001-5519-391X | 183, 441, 495, 519 |
| **Stefan Krstić** | University of Belgrade, Faculty of Civil Engineering, Department of Geodesy and Geoinformatics, Belgrade, Serbia | 0009-0000-2513-7386 | 819 |
| **Danijel Kukaras** | Faculty of Technical Sciences, University of Novi Sad, Serbia | 0000-0003-4726-2799 | 246 |
| **Fation Kurti** | SRP Albanian Engineering, Tirana, Albania | – | 725 |
| **Erta Kushta** | Faculty of Civil Engineering, Polytechnic University of Tirana, Albania | 0009-0002-3957-002X | 725 |
| **Željana Kužet** | Faculty of Technical Sciences, University of Novi Sad, Serbia | 0009-0004-0958-517X | 141 |
| **Mirjana Laban** | Faculty of Technical Sciences, University of Novi Sad, Serbia | 0000-0001-6557-3094 | 276, 946, 956 |
| **Ilija Lalošević** | Faculty of Architecture, University of Montenegro, Podgorica, Montenegro | – | 649 |
| **Ljupcho Lazarov** | Faculty of Civil Engineering, Ss. Cyril and Methodius University in Skopje, Skopje, North Macedonia | 0009-0003-7621-8161 | 102, 128 |
| **Cveta Lazić** | Faculty of Technical Sciences, University of Novi Sad, Serbia | 0000-0003-2105-6647 | 939 |
| **Petar Lazičić** | Faculty of Technical Sciences, University of Novi Sad, Serbia | 0009-0008-2589-7746 | 428 |
| **Željko Lebo** | Tehničko veleučilište u Zagrebu, Zagreb, Hrvatska | – | 415 |
| **Arli Llabani** | Faculty of Civil Engineering, Polytechnic University of Tirana, Albania | 0009-0003-6726-0106 | 725, 753, 830, 842 |
| **Milica Malešić Petković** | Republic Geodetic Authority, Belgrade, Serbia | – | 695 |
| **Vladimir Mandić** | Faculty of Mechanical and Civil Engineering in Kraljevo, University of Kragujevac, Serbia | 0000-0003-3529-171X | 372, 383 |
| **Dragan Manojlović** | Faculty of Technical Sciences, University of Novi Sad, Serbia | 0000-0003-1269-7477 | 78, 114 |
| **Milan Marinković** | Department of Civil Engineering and Geodesy, Faculty of Technical Sciences, University of Novi Sad, Serbia | 0000-0002-1992-302X | 257 |
| **Nikola Marjanović** | Faculty of Technical Sciences, University of Novi Sad, Serbia | – | 453 |
| **Marko Marković** | Faculty of Technical Sciences, University of Novi Sad, Serbia | 0000-0003-3666-6325 | 737, 753, 895, 923 |
| **Marjan Matić** | MHM Projekt, Novi Sad, Serbia | – | 504 |
| **Ranka Medenica Todorović** | Faculty of Technical Sciences, University of Novi Sad, Serbia | 0000-0003-1734-6772 | 640 |

| Author | Affiliation | ORCID iD | Page |
|---|---|---|---|
| **Ivan Mesarović** | Faculty of Technical Sciences, University of Novi Sad, Serbia | 0009-0007-3319-8331 | 372 |
| **Anica Milanović** | Faculty of Architecture-Civil Engineering and Geodesy, University of Banja Luka, Banja Luka, Bosnia and Herzegovina | 0009-0005-5602-150X | 401 |
| **Marija Milanović** | Serbian Railway Infrastructure, Belgrade, Serbia | – | 257 |
| **Marijana Milić** | Faculty of Technical Sciences, University of Novi Sad, Serbia | 0000-0003-1974-2461 | 291, 356, 383 |
| **Miloš Milić** | University of Niš, Faculty of Civil Engineering and Architecture, Niš, Serbia | 0000-0003-3028-0915 | 114 |
| **Tiana Milović** | Faculty of Technical Sciences, University of Novi Sad, Serbia | 0000-0002-3905-7018 | 317, 324, 343, 956 |
| **Jelena Mirjanić** | Faculty of Technical Sciences, University of Novi Sad, Serbia | 0009-0006-6608-056X | 428, 453, 956 |
| **Milica Mirković Marjanović** | Institute IMS, Belgrade, Serbia | 0000-0001-6023-8414 | 276 |
| **Petar Mitrović** | Faculty of Technical Sciences, University of Novi Sad, Serbia | 0009-0002-1291-6924 | 557 |
| **Vladimir Mučenski** | Faculty of Technical Sciences, University of Novi Sad, Serbia | 0000-0001-9830-4747 | 141, 462 |
| **Gordana Nataroš** | Real estate consultant, Novi Sad, Serbia | – | 684 |
| **Dejana Nedučin** | Faculty of Technical Sciences, University of Novi Sad, Serbia | 0000-0002-9828-072X | 538 |
| **Gojko Nikolić** | University of Montenegro, Department of Geography, Nikšić, Montenegro | 0000-0001-8703-2184 | 708 |
| **Vesna Nikolić** | Faculty of Occupational Safety, University of Niš, Niš, Serbia | 0000-0002-9163-7116 | 964 |
| **Oleg Odalović** | Faculty of Civil Engineering, University of Belgrade, Belgrade, Serbia | 0000-0001-6004-824X | 800, 819 |
| **Nermin Palić** | University College „CEPS-Center for Business Studies“, Kiseljak, Bosnia and Herzegovina | 0000-0001-8839-4910 | 190 |
| **Tamara Pantić** | Faculty of Technical Sciences, University of Novi Sad, Serbia | 0009-0003-6341-5692 | 291, 356, 383 |
| **Vladan Pantić** | Faculty of Technical Sciences, University of Novi Sad, Serbia | 0000-0002-3482-9437 | 246 |
| **Jovan Br. Papić** | Ss. Cyril and Methodius University in Skopje, Faculty of Civil Engineering, Skopje, North Macedonia | 0000-0002-2952-302X | 504 |
| **Dejan Pavlović** | DT Mapping, Kraljevo, Serbia | – | 674, 882 |
| **Tomaž Pazlar** | Slovenian National Building and Civil Engineering Institute, Ljubljana, Slovenia | 0009-0003-3857-3293 | 264 |
| **Milutin Pejović** | Dept. of Geodesy & Geoinformatics, Faculty of Civil Engineering Belgrade | 0000-0003-1116-9971 | 783 |
| **Tanja Perčić** | Faculty of Technical Sciences, University of Novi Sad, Serbia | 0000-0001-5517-9659 | 78, 114 |
| **Radovan Perić** | University of Niš, Faculty of Civil Engineering and Architecture, Niš, Serbia | 0009-0003-3022-7898 | 114 |
| **Igor Peško** | Department of Civil Engineering and Geodesy, Faculty of Technical Sciences, University of Novi Sad, Serbia | 0000-0001-9098-3642 | 161 |

| Author | Affiliation | ORCID iD | Page |
|---|---|---|---|
| **Dušan Petković** | Faculty of Civil Engineering, University of Belgrade, Belgrade, Serbia | 0000-0002-8285-9710 | 800 |
| **Dušanka Plazina-Pevač** | IEE Consult s.e. d.o.o., Novi Sad, Serbia | – | 527 |
| **Nikola Postolov** | Faculty of Civil Engineering, Ss. Cyril and Methodius University in Skopje, Skopje, North Macedonia | 0000-0002-4681-5980 | 102 |
| **Petar Praštalo** | Faculty of Architecture-Civil Engineering and Geodesy, University of Banja Luka, Banja Luka, Bosnia and Herzegovina | 0009-0002-1238-1632 | 401 |
| **Aleksandar Pujović** | Western Serbia Academy of Applied Studies, Serbia | 0009-0008-5149-5150 | 343 |
| **Marko Radenković** | BioSense Institute, University of Novi Sad, Novi Sad, Serbia | 0000-0002-0708-2454 | 324 |
| **Una Radivojević** | Faculty of Technical Sciences, University of Novi Sad, Serbia | 0009-0007-1819-0251 | 587 |
| **Dunja Rađenović Veselić** | Faculty of Sciences, University of Novi Sad, Serbia | 0000-0002-6862-4691 | 183 |
| **Dorin Radu** | Faculty of Civil Engineering, Transilvania University of Brașov, Romania | 0000-0001-5043-2723 | 70 |
| **Aleksandra Radujković** | Faculty of Technical Sciences, University of Novi Sad, Serbia | 0000-0003-4863-4486 | 453 |
| **Branko Ranković** | Faculty of Civil Engineering and Architecture, University of Niš, Niš, Serbia | 0009-0001-7358-3038 | 512 |
| **Andrija Rašeta** | Faculty of Technical Sciences, University of Novi Sad, Serbia | 0000-0002-4535-1379 | 59, 161, 229, 238, 428 |
| **Aleksandar Ristić** | Faculty of Technical Sciences, University of Novi Sad, Serbia | 0000-0003-0979-3345 | 859 |
| **Boško Ristić** | Faculty of Technical Sciences, University of Novi Sad, Serbia | – | 548 |
| **Milivoje Rogač** | Faculty of Civil Engineering, University of Montenegro, Podgorica, Montenegro | 0000-0002-6853-6712 | 91 |
| **Igor Ruskovski** | Faculty of Technical Sciences, University of Novi Sad, Serbia | 0000-0003-2097-4884 | 867 |
| **Nikola Santrač** | University of Novi Sad, Faculty of Agriculture, Novi Sad, Serbia | 0000-0001-7183-8511 | 737 |
| **Aleksandar Savić** | University of Belgrade, Faculty of Civil Engineering, Belgrade, Serbia | 0000-0002-1777-6775 | 207 |
| **Vladimir Savić** | Faculty of Technical Sciences, University of Novi Sad, Serbia | 0000-0003-2195-0438 | 614 |
| **Aleksandar Sedmak** | Faculty of Mechanical Engineering, University of Belgrade, Serbia | 0000-0002-5438-1895 | 70 |
| **Simon Sedmak** | Innovation Center of the Faculty of Mechanical Engineering, Belgrade, Serbia | 0000-0002-2674-541X | 70 |
| **Darko Sekulić** | Sub-department for Art and Design, Department for Architecture and Urban Planning, Faculty of Technical Sciences, University of Novi Sad | 0009-0002-1750-2085 | 627 |
| **Mirzo Selimić** | University College „CEPS-Center for Business Studies“, Kiseljak, Bosnia and Herzegovina | 0000-0003-0267-9670 | 190 |

| Author | Affiliation | ORCID iD | Page |
|---|---|---|---|
| **Milena Senjak Pejić** | Faculty of Technical Sciences, University of Novi Sad, Serbia | 0000-0002-1036-1243 | 462 |
| **Marijana Serdar** | Faculty of Civil Engineering, University of Zagreb, Zagreb, Croatia | 0000-0001-8386-7272 | 332 |
| **Šime Serdarević** | Zagreb University of Applied Sciences, Zagreb, Croatia | 0009-0004-9873-4658 | 217 |
| **Bledar Sina** | Faculty of Civil Engineering, Polytechnic University of Tirana, Tirana, Albania | – | 753, 830, 842 |
| **Mirjana Sladić Todorov** | Faculty of Technical Sciences, University of Novi Sad, Serbia | 0000-0003-3666-8865 | 587 |
| **Nataša Slijepčević** | Faculty of Sciences, University of Novi Sad, Serbia | 0000-0002-3866-1205 | 183 |
| **Marko Stanković** | University of Belgrade, Faculty of Civil Engineering, Department of Geodesy and Geoinformatics, Belgrade, Serbia | 0000-0003-2471-0026 | 819 |
| **Dragana Stanojević** | Faculty of Technical Sciences, University of Novi Sad, Serbia | 0000-0003-3471-5656 | 246, 462 |
| **Mia Stantić** | Faculty of Technical Sciences, University of Novi Sad, Serbia | 0009-0008-8309-2612 | 567 |
| **Anka Starčev-Ćurčin** | Faculty of Technical Sciences, University of Novi Sad, Serbia | 0000-0002-1533-3874 | 343 |
| **Danilo Stipić** | Faculty of Technical Sciences, University of Novi Sad, Serbia | 0000-0001-6557-5997 | 291, 356, 383 |
| **Zoran Sušić** | Faculty of Technical Sciences, University of Novi Sad, Serbia | 0000-0002-8885-2659 | 708, 895, 910 |
| **Ivana Šalić** | Vodoopskrba i odvodnja d.o.o., Zagreb, Croatia | – | 217 |
| **Nina Šantek** | Zagreb University of Applied Sciences, Zagreb, Croatia | 0009-0007-6661-6616 | 217 |
| **Milka Šarkanović Bugarinović** | Faculty of Technical Sciences, University of Novi Sad, Serbia | 0000-0001-6648-4579 | 867 |
| **Miloš Šešlija** | Faculty of Technical Sciences, University of Novi Sad, Serbia | 0000-0002-8857-8952 | 183, 441, 495, 504, 512 |
| **Sandra Šlegl** | Faculty of Technical Sciences, University of Novi Sad, Serbia | 0009-0009-3037-1084 | 659 |
| **Olja Šovljanski** | Faculty of Technology Novi Sad, University of Novi Sad, Novi Sad, Serbia | 0000-0002-9118-4209 | 324 |
| **Slobodan Šupić** | Faculty of Technical Sciences, University of Novi Sad, Serbia | 0000-0003-3029-9309 | 246 |
| **Jelena Tatalović** | Faculty of Civil Engineering Subotica, University of Novi Sad, Subotica, Serbia | 0000-0001-7280-919X | 695 |
| **Anja Terzić** | IMS Institute, Belgrade, Serbia | 0000-0002-4762-7404 | 207 |
| **Mirjana Terzić** | Faculty of Technical Sciences, University of Novi Sad, Serbia | 0000-0002-8596-6562 | 462 |
| **Koce Todorov** | Faculty of Civil Engineering, Ss. Cyril and Methodius University in Skopje, Skopje, North Macedonia | 0000-0003-1736-4989 | 102, 128 |
| **Miljana Todorović-Drakul** | Faculty of Civil Engineering, University of Belgrade, Belgrade, Serbia | 0000-0002-8782-0890 | 800 |
| **Dragana Tomašević Pilipović** | Faculty of Sciences, University of Novi Sad, Serbia | 0000-0002-8275-3297 | 183, 495 |

| Author | Affiliation | ORCID iD | Page |
|---|---|---|---|
| **Ana Tomić** | Faculty of Technology Novi Sad, University of Novi Sad, Novi Sad, Serbia | 0000-0002-6338-342X | 324 |
| **Jovana Topalić** | Faculty of Technical Sciences, University of Novi Sad, Serbia | 0000-0001-7854-3257 | 141, 151, 462, 956 |
| **Milan Trivunić** | Fakultet tehničkih nauka, Univerzitet u Novom Sadu, Srbija | 0000-0002-6611-4524 | 527 |
| **Miloš Tutnjević** | Faculty of Architecture-Civil Engineering-Geodesy, University of Banja Luka, Banja Luka, Bosnia and Herzegovina | 0009-0000-7698-143X | 772 |
| **Milan Uljarević** | Power China – Stecol, Novi Sad, Serbia | 0009-0002-7627-1790 | 59 |
| **Dejan Vasić** | Faculty of Architecture, Civil Engineering and Geodesy, University of Banja Luka, Banja Luka, Republic of Srpska, Bosnia and Herzegovina | 0009-0006-9586-729X | 800, 819 |
| **Slavko Vasiljević** | Faculty of Architecture, Civil Engineering and Geodesy, University of Banja Luka, Banja Luka, Republic of Srpska, Bosnia and Herzegovina | 0009-0003-2636-841X | 800 |
| **Viktorija Velinska** | Ss. Cyril and Methodius University in Skopje, Faculty of Civil Engineering, Skopje, North Macedonia | – | 504 |
| **Luka Vidaković** | Labsoft, Novi Sad, Serbia | 0009-0003-6591-2254 | 151 |
| **Teodora Vojnović** | BlackRock, Belgrade, Serbia | – | 946 |
| **Ivan Volarić** | Tehničko veleučilište u Zagrebu, Zagreb, Hrvatska | – | 415 |
| **Riste Volchev** | Ss. Cyril and Methodius University in Skopje, Faculty of Civil Engineering, Skopje, North Macedonia | 0000-0001-9815-9914 | 128 |
| **Milica Vračarić** | Faculty of Technical Sciences, University of Novi Sad, Serbia | 0000-0002-2120-8738 | 640 |
| **Tanja Vranić** | Faculty of Technical Sciences, University of Novi Sad, Serbia | 0000-0001-9971-0384 | 939 |
| **Milan Vrtunski** | Faculty of Technical Sciences, University of Novi Sad, Serbia | 0000-0002-1124-871X | 859 |
| **Radomir Zejak** | Faculty of Civil Engineering, University of Montenegro, Montenegro | 0009-0001-3884-2575 | 198 |
| **Miljana Zeković** | Faculty of Technical Sciences, University of Novi Sad, Serbia | 0000-0002-1327-7063 | 576 |
| **Drago Žarković** | Faculty of Technical Sciences, University of Novi Sad, Serbia | 0000-0002-0560-5231 | 78 |
| **Vladimir Živaljević** | Faculty of Technical Sciences, University of Novi Sad, Serbia | 0000-0002-2808-2664 | 229, 238, 428 |
| **Dragan Živanić** | Faculty of Technical Sciences, University of Novi Sad, Serbia | 0000-0003-2570-0727 | 141 |
| **Višnja Žugić** | Faculty of Technical Sciences, University of Novi Sad, Serbia | 0000-0002-4677-7355 | 557 |

# iNDiS 2026

## ABOUT THE CONFERENCE

iNDiS 2026 is the 17th international scientific conference in the 50-year tradition of iNDiS, held at Fruške Terme, Vrdnik, Serbia, on 4–6 November 2026. It brings together professionals, academics and researchers in Structural and Civil Engineering, Geodesy and Geoinformatics, Architecture and Urban Planning, and Disaster Risk Management and Fire Safety, with an emphasis on applying novel knowledge in civil engineering practice.

## ORGANIZER

University of Novi Sad
Faculty of Technical Sciences
Department of Civil Engineering and Geodesy
Trg Dositeja Obradovića 6, 21000 Novi Sad, Serbia

**indis.gradjevinans.net**

ISBN 978-86-6022-828-6